Transactions of the ASME

HEAT TRANSFER DIVISION
Chairman, J. R. LLOYD
Secretary, A. S. ADORJAN
Senior Technical Editor, G. M. FAETH
Technical Editor, J. V. BECK
Technical Editor, I. CATTON
Technical Editor, R. GREIF
Technical Editor, H. R. JACOBS
Technical Editor, P. J. MARTO
Technical Editor, D. M. McELIGOT
Technical Editor, R. H. PLETCHER
Technical Editor, W. A. SIRIGNANO
Technical Editor, R. VISKANTA

BOARD ON COMMUNICATIONS
Chairman and Vice President
K. N. REID, JR.

Members-at-Large
W. BEGELL
J. T. COKONIS
M. FRANKE
W. G. GOTTENBERG
M. KUTZ
F. LANDIS
J. R. LLOYD
T. C. MIN
R. E. NICKELL
R. E. REDER
F. W. SCHMIDT

President, N. D. FITZROY
Executive Director,
PAUL ALLMENDINGER
Treasurer,
ROBERT A. BENNETT

PUBLISHING STAFF
Mng. Dir., Publ., J. J. FREY
Dep. Mng. Dir., Pub.,
JOS. SANSONE
Managing Editor,
CORNELIA MONAHAN
Sr. Production Editor,
VALERIE WINTERS
Editorial Prod. Asst.,
MARISOL ANDINO

Transactions of the ASME, Journal of Heat Transfer (ISSN 0022-1481) is published quarterly (Feb., May, Aug., Nov.) for $150 per year by The American Society of Mechanical Engineers, 345 East 47th Street, New York, NY 10017. Second class postage paid at New York, NY and additional mailing offices. POSTMASTER: Send address changes to The Journal of Heat Transfer, c/o THE AMERICAN SOCIETY OF MECHANICAL ENGINEERS, 22 Law Drive, Box 2300, Fairfield, NJ 07007-2300.

CHANGES OF ADDRESS must be received at Society headquarters seven weeks before they are to be effective. Please send old label and new address.

PRICES: To members, $24.00, annually; to nonmembers, $150.00. Add $6.00 for postage to countries outside the United States and Canada.

INDEXED by Engineering Information

Journal of Heat Transfer

Published Quarterly by The American Society of Mechanical Engineers

VOLUME 109 • NUMBER 1 • FEBRUARY 1987

ANNOUNCEMENTS

TECHNICAL PAPERS

(Contents continued)

TECHNICAL NOTES

On the Problem of Heat Transfer in a Phase-Change Slab Initially Not at the Critical Temperature

L. N. Gutman
Ben-Gurion University of the Negev,
The Jacob Blaustein Institute
for Desert Research,
Sede Boqer Campus, 84990 Israel

A one-dimensional heat transfer problem in the phase-change slab, one side of which is isothermal while the other is insulated, is considered. Both cases—fusion and solidification—are treated. Slab temperature at the intitial moment is assumed constant and not critical. The main goal of this paper is to find the additional time required for a total phase change, compared with the case of the critical initial temperature. By analogy with perturbation problems in hydrodynamics, an appropriate solution is constructed consisting of an inner and an outer solution. The evaluation of the maximum error of the integral heat balance equation of the slab is treated as an indirect evaluation of the accuracy of the solution obtained. This evaluation shows that the solution can provide sufficient accuracy only in cases in which at least one of the three nondimensional parameters of the problem is small.

1 Introduction

A one-dimensional heat transfer problem for a finite domain (infinite slab), isothermal on one side and insulated on the other, with a moving phase boundary, assuming that an initial temperature is noncritical and that Stefan numbers are small, has recently been considered by Weinbaum and Jiji [1].[1] In that paper a tempting idea is suggested: construction of inner and outer expansions of the solution and then matching these expansions as is done in many mechanical and hydrodynamical perturbation problems (see, for example, Van Dyke [2]). Unfortunately, it seems that in [1] the effect of the noncritical initial temperature (superheating or supercooling) on the process was not explicitly brought out.

The present paper has been prompted by Weinbaum and Jiji [1]. However, in attempting to construct an approximate analytical solution of the same problem, unlike Weinbaum and Jiji [1], we match some inner and outer solutions (not expansions) and consider not only the case of small Stefan numbers, but also the cases when the Stefan number is on the order of one or larger and one of the two other dimensional parameters of the problem is small. The main goal of our paper is to estimate the effect of superheating or supercooling on the process.

2 Formulation of the Problem, Inner and Outer Solutions

The mathematical formulation of the problem is

$$\left.\begin{aligned}
&\frac{\partial T(x,t)}{\partial t}=\alpha\frac{\partial^2 T(x,t)}{\partial x^2} \qquad 0<x<\delta(t),\\
&\frac{\partial T'(x,t)}{\partial t}=\alpha'\frac{\partial^2 T'(x,t)}{\partial x^2} \qquad \delta(t)<x<d,\\
&T'\Big|_{t=0}=T_i;\ \delta(0)=0; \qquad T\Big|_{x=0}=T_a,\\
&T\Big|_{x=\delta}=T'\Big|_{x=\delta}=T_{cr}; \qquad \frac{\partial T'}{\partial x}\Big|_{x=d}=0,\\
&\pm L\frac{d\delta}{dt}=-\alpha c\frac{\partial T}{\partial x}\Big|_{x=\delta}+\alpha' c'\frac{\partial T'}{\partial x}\Big|_{x=\delta},
\end{aligned}\right\} \tag{1}$$

where[2]

$$T_a=\text{consA}\gtrless T\gtrless T_{cr}=\text{consA}\gtrless T'\gtrless T_i=\text{consA} \tag{2}$$

The upper sign in the last equation of (1) and the upper inequality signs in (2) correspond to the case of fusion. Then one should put $T=T_L$, $\alpha=\alpha_L$, $c=C_L$, $T'=T_S$, $\alpha'=\alpha_S$, $c'=C_S$. The lower sign and the inequality signs correspond to the case of solidification and then $T=T_S$, $\alpha=\alpha_S$, $c=C_S$, $T'=T_L$, $\alpha'=\alpha_L$, $c'=C_L$.

We supplement equation (1) by

$$\delta(\theta)=d \tag{3}$$

which specifies the total phase-change time θ.

For the convenience of further transformations, we proceed to nondimensional values (letters with overbars) by the relationships

$$\left.\begin{aligned}
&\bar{x}=x/d,\ \bar{\delta}=\delta/d,\ \bar{t}=\alpha St/d^2,\\
&\bar{T}=(T-T_a)/(T_{cp}-T_a),\ \bar{T}'=(T'-T_i)/(T_{cr}-T_i)
\end{aligned}\right\} \tag{4}$$

and introduce the following notations for nondimensional parameters

$$\left.\begin{aligned}
&\mu=c'|T_{cr}-T_i|/c|T_{cr}-T_a|,\ \nu=\alpha'/\alpha,\\
&S=c|T_{cr}-T_a|/L,\ \tau=\alpha S\theta/d^2
\end{aligned}\right\} \tag{5}$$

where μ and ν as well as S, the Stefan number of the phase change layer, are assumed to be known, and τ is unknown.

Substituting equation (4) into equations (1) and (3), we arrive at the nondimensional problem (the bars over the letters are omitted)

$$\left.\begin{aligned}
&S\frac{\partial T(x,t)}{\partial t}=\frac{\partial^2 T(x,t)}{\partial x^2} \qquad (0<x<\delta(t)),\\
&S\frac{\partial T'(x,t)}{\partial t}=\nu\frac{\partial^2 T'(x,t)}{\partial x^2} \qquad (\delta(t)<x<1),\\
&T'\Big|_{t=0}=\delta(0)=0;\ \delta(\tau)=1 (0\le t\le\tau),\\
&T\Big|_{x=0}=\frac{\partial T'}{\partial x}\Big|_{x=1}=0;\ T\Big|_{x=\delta}=T'\Big|_{x=\delta}=1,\\
&\frac{d\delta}{dt}=\frac{\partial T}{\partial x}\Big|_{x=\delta}+\mu\nu\frac{\partial T}{\partial x}\Big|_{x=\delta}
\end{aligned}\right\} \tag{6}$$

[1] In Weinbaum and Jiji [1] the case of a slab with two isothermal sides has also been considered.

Contributed by the Heat Transfer Division for publication in the JOURNAL OF HEAT TRANSFER. Manuscript received by the Heat Transfer Division May 25, 1985.

[2] Unlike Weinbaum and Jiji [1] we use notations which enable us to consider both cases—fusion and solidification—simultaneously.

Note that equation (6) is valid for both cases, fusion and solidification. Nondimensional T and T' for both of these cases are positive and confined to the interval between 0 and 1.

Proceeding to a solution of the problem (6), we notice that equation (6) has approximate solutions which we interpret as inner and outer solutions of the problem.

The well-known Neumann solution

$$\left.\begin{aligned} T_{in} &= \operatorname{erf}\left[\frac{x}{2}\left(\frac{S}{t}\right)^{1/2}\right]\Big/\operatorname{erf}\lambda \quad (0 \le x \le \delta_{in}), \\ T'_{in} &= \operatorname{erfc}\left[\frac{x}{2}\left(\frac{S}{\nu t}\right)^{1/2}\right]\Big/\operatorname{erfc}(\lambda/\nu^{1/2}) \quad (\delta_{in} \le x \le 1), \\ \delta_{in} &= 2\lambda(t/S)^{1/2} < 1 \end{aligned}\right\} \tag{7}$$

where λ has to be found from the known transcendental equation[3]

$$(e^{\lambda^2}\operatorname{erf}\lambda)^{-1} - \mu\nu^{1/2}\left(e^{\frac{\lambda^2}{\nu}}\operatorname{erfc}\frac{\lambda}{\nu^{1/2}}\right)^{-1} = \pi^{1/2}\lambda/S \tag{8}$$

Note that expressions (7) satisfy exactly all of the equations and conditions (6) with the exception of the insulating condition $\partial T'/\partial x|_{x=1} = 0$ for $t>0$. It is apparent that this condition is satisfied exactly at $t = 0$ and approximately for $t>0$ with an error which increases with time. Inasmuch as expressions (7) satisfy the initial conditions it seems natural to consider expressions (7) as an inner solution of the problem (6).

We now turn to a simpler form of the Neumann solution

$$\left.\begin{aligned} T_{out} &= \operatorname{erf}\left[\frac{x}{2}\left(\frac{S}{t-C}\right)^{1/2}\right]\Big/\operatorname{erf}\kappa \quad (0 \le x \le \delta_{out}), \\ T'_{out} &= 1 \quad (\delta_{out} \le x \le 1), \\ \delta_{out} &= 2\kappa(t-C)^{1/2}S^{1/2} \quad (C < t \le \tau), \\ \tau &= S/4\kappa^2 + C \end{aligned}\right\} \tag{9}$$

where C is a constant, κ is specified by the transcendental equation[4]

$$(e^{\kappa^2}\operatorname{erf}\kappa)^{-1} = \pi^{1/2}\kappa/S \tag{10}$$

One can see that expressions (9) satisfy all equations and boundary conditions from (6) excluding initial conditions for δ and for T'. (If $C = 0$, then $\delta(0) = 0$.) Therefore we interpret (9) as an outer solution. Then C is approximately the additional time needed for total phase change of the slab in comparison with the case of critical initial temperature ($T_i = T_{cr}$) for which expressions (9) are an exact solution, then $\tau = S/4\kappa^2$ and $C = 0$. It seems that for all practical purposes it is more interesting to know a relative additional time which can be specified by the ratio

$$C_r = 4\kappa^2 C/S. \tag{11}$$

3 Matching and Evaluation of the Accuracy of the Solution

To find C, one should match the inner (7) and outer (9) solutions. One can suggest the following matching conditions, understandable from a physical point of view. The sensible heat and latent heat of the slab must not undergo discontinuities at the matching instant t_m. In nondimensional form this means that

$$\left.\begin{aligned} &\int_0^{\delta_{in}} T_{in}\,dx - \mu\int_{\delta_{in}}^{1} T'_{in}\,dx = \int_{T_{out}}^{\delta_{out}} T_{out}\,dx - \mu\int_{\delta_{out}}^{1} T'_{out}\,dx, \\ &\delta_{in} = \delta_{out} \end{aligned}\right\} \quad \text{at } t = t_m \tag{12}$$

Evidently the latter condition also provides the continuity of the function $\delta(t)$ at $t = t_m$. It should be noted that in constructing the approximate solution the temperature fields, as well as the sensible and latent heat fluxes at the instant $t = t_m$, can undergo discontinuities in time. However, owing to conditions (12), this does not violate the energetic balance of the slab.

Thus, the unknown parameters C and t_m are specified by the two conditions (12).

Substituting equations (7) and (9) into conditions (12) yields

$$C = [1 - (\lambda/\kappa)^2]\cdot t_m, \quad t_m = S/4\nu\zeta^2 \tag{13}$$

where ζ has to be found from the transcendental equation

$$a = \zeta + b(e^{-\zeta^2} - \pi^{1/2}\zeta\operatorname{erfc}\zeta) \qquad (\zeta > \lambda/\nu^{1/2}) \tag{14}$$

where

$$\left.\begin{aligned} a &= [(\lambda\operatorname{erf}\lambda)^{-1} - (\kappa\operatorname{erf}\kappa)^{-1}]\lambda/\mu(\pi\nu)^{1/2}, \\ b &= [\pi^{1/2}\operatorname{erfc}(\lambda/\nu^{1/2})]^{-1}. \end{aligned}\right\} \tag{15}$$

The inequality (14) is a consequence of the obvious requirement $\delta_{in} < 1$.

In Appendix A we show that a solution ζ of equation (14) exists and is unique for all a and b, given by equation (15), and also that $\kappa > \lambda$. Therefore, on account of (9), (13), $C>0$ and t_m is confined to the interval between 0 and τ.

Hence, the inner solution (7) should be referred to the interval $0<t<t_m$, and the outer solution (9) to the interval $t_m<t<\tau$.

Proceeding to an evaluation of the accuracy of the approximate solution (7), (9), we turn to an integral relationship, which is convenient to present here in the form

[3] It is known that solution λ of the equation (8) exists and is unique for any positive values S, μ, ν (see Appendix A).

[4] The solution κ of equation (10) exists and is unique for all $S>0$ (see Appendix A).

Nomenclature

- c = specific heat of the phase-changed layer
- c' = specific heat of the layer in which there is no phase change
- C_L = specific heat of the liquid phase
- C_S = specific heat of the solid phase
- d = slab thickness
- L = latent heat of the slab
- T = temperature of the phase-changed layer
- T' = temperature of the layer in which there is no phase change
- T_L = temperature of the liquid phase
- T_S = temperature of the solid phase
- T_{cr} = critical temperature
- T_a = temperature of the isothermal side of the slab
- T_i = initial temperature of the slab
- t = time
- x = coordinate, normal to the boundary of the slab
- α = thermal diffusivity of the phase-changed layer
- α' = thermal diffusivity of the layer in which there is no phase change
- α_L = thermal diffusivity of the liquid phase
- α_S = thermal diffusivity of the solid phase
- δ = thickness of the phase-changed layer
- θ = total fusion or solidification time

$$-\int_0^t \frac{\partial T}{\partial x}\Big|_{x=0} dt + \delta + S\int_0^\delta (1-T)dx + \mu S\left(\delta + \int_\delta^1 T'dx\right) = 0 \tag{16}$$

heat influx taken with opposite sign | latent heat + sensible heat, $0 \le x \le \delta$ | sensible heat, $\delta \le x \le 1$

This relationship is a consequence of (6) and, from a physical point of view, is a dimensional heat balance equation of the slab. The physical meaning of each term in equation (16) is indicated beneath the terms.

It should be stressed that the last three terms in the left-hand side of equation ((16) cannot be negative since $T<1$ and $T'>0$. Therefore for any t the heat influx is larger than any other terms in equation (16).

We attempt to employ equation (16) to estimate indirectly the accuracy of the solution (7), (9). For this we substitute (7) and (9) into (16), which previously was divided term by term by the heat influx term. As a result, we do not obtain zero on the right hand side, but a relative error $\epsilon(t)$ of a violation of the heat conservation law in the slab caused by the approximate nature of the solution (7), (9). Evidently, $\epsilon(t)$ should be presented by a different analytical expression for the intervals of time $(0, t_m)$ and (t_m, τ). However, one can show that both expressions have the same maximum at $t=t_m$. The latter is a consequence of (12) and therefore the conditions of the continuities of the functions $\delta(t)$ and $\epsilon(t)$ at $t=t_m$ are actually equivalent to the energetic conditions (12).

For the interval $(0, t_m)$ $\epsilon(t)$ can be obtained more simply by the relationship

$$\epsilon(t) = -\mu\nu\int_0^t \frac{\partial T_{in}'}{\partial x}\Big|_{x=1} dt \Big/ \int_0^t \frac{\partial T_{in}}{\partial x}\Big|_{x=0} dt \qquad (0 \le t \le t_m) \tag{17}$$

because the spurious heat flux from the surface $x=1$ (which has to be zero in the exact solution) described by expressions (7) causes the error.

Substituting expressions (7) into equation (17) and then putting $t=t_m$ yields the expression for the maximum relative error

$$\epsilon_m = \epsilon(t_m) = (a-\zeta)(\pi\nu)^{1/2} \cdot \mu \mathrm{erf}\lambda \tag{18}$$

This relationship takes into account equations (13)–(15).

One may expect that the application of the approximate solution (7), (9) is expedient, if $\epsilon_m \ll 1$.

According to equation (18) ϵ_m can be small if at least one of the four values λ, μ, ν, or $a-\zeta$ is small. Of course, this implies that the other three factors in equation (18) are no more than on the order of one. However, λ can be small only if $S \ll 1$ or $\mu \gg 1$ (see Appendix A). The latter is evidently not pertinent. Therefore the case $\mu \ll 1$ is actually the case $S \ll 1$. The difference $a-\zeta$ can be small only if μ or ν is small (see Appendix A). Therefore it is enough to consider only three cases: $S \ll 1$ $(\mu \sim \nu \sim 1)$, $\nu \ll 1$ $(\mu \sim 1, S \gtrsim 1)$, $\mu \ll 1$ $(\nu \sim 1, S \gtrsim 1)$. In the last two cases S can be large because $\mathrm{erf}\lambda \lesssim 1$ always. Apparently, if any two of the values S, μ, and ν, or even all of them are small, the relative error becomes smaller. Such cases are not considered in this paper.

4 Consideration of the Three Cases Mentioned

Case 1. $S \ll 1$ $(\mu \sim \nu \le 1)$. In this case (8) and (10) allow an expansion of λ and κ in the power series in $S^{1/2}$.

Retaining the terms with powers of S no greater than 3/2, we have

$$\left.\begin{aligned} \lambda &= \left(\frac{S}{2}\right)^{1/2} \cdot \left[1 - \mu\left(\frac{\nu S}{2\pi}\right)^{1/2} + \left(\frac{\nu\mu^2}{4\pi} - \frac{\mu}{3} - \frac{1}{6}\right)S\right], \\ \kappa &= \left(\frac{S}{2}\right)^{1/2} \cdot \left(1 - \frac{1}{6}S\right) \end{aligned}\right\} \tag{19}$$

Substituting expressions (19) into equations (9), (11), (13), (15), and (18) and then solving equation (14) (see Appendix B) after some transformations, one obtains

$$\tau = t_m = 0.5, \; C_r = \epsilon_m = 0.8\mu(\nu S)^{1/2} \tag{20}$$

Only the first terms are retained in these expansions for the following reason: The method is applicable if the relative error ϵ_m is no more than a few percent, e.g., if $S \lesssim 10^{-3}$ (on the assumption that $\nu \sim \mu \sim 1$). However, then the second terms in the expansions make corrections which are proportional to $S^{1/2}$, e.g., are on the order of a few percent and therefore can be dropped along with all subsequent terms. Expressions (20) lead to the conclusion that if $S \lesssim 10^{-3}$ and $\mu \sim \nu \sim 1$ then the inner solution (7) provides sufficient accuracy for the whole interval $0 \le t \le \tau$ with a negligible value of C_r. If $S \gtrsim 10^{-3}$ and $\mu \sim \nu \sim 1$, the method described does not provide the necessary accuracy.

Case 2. $\nu \ll 1$ $(\mu \sim 1, S \gtrsim 1)$. At first one should solve the transcendental equation (10) numerically (see Appendix B). Then one may treat κ as a given function of S. Since $\nu \ll 1$, then $\lambda/\nu^{1/2} \gg 1$. Therefore, using the known asymptotic expansion of the function erfc for large values of its argument, one can present (8) in the form

$$(e^{\lambda^2}\mathrm{erf}\mu)^{-1} = \pi^{1/2}(1+\mu S)\lambda/S \tag{21}$$

From equations (10) and (21) it follows that λ and κ can be simply related by

$$\lambda = \kappa[S/(1+\mu S)] \tag{22}$$

It follows from Appendix B that if $\nu \ll 1$, one can use (A9) (from Appendix B) which is the asymptotic expression for ζ, stemming from equations (14) and (15) for large values of ζ.

Substituting ζ from equation (A9) into equations (11), (13), and (18), we obtain

$$\left.\begin{aligned} &t_m = S/4A^2, \; C_r = (\kappa^2 - \lambda^2)/A^2 \; (A = a\nu^{1/2}), \\ &\epsilon_m = \pi^{1/2}\mu\nu\lambda\mathrm{erf}\lambda/2A^2\exp[(A^2-\lambda^2)/\nu] \end{aligned}\right\} \tag{23}$$

The graphs of C_r, ϵ_m, as functions of the argument S for three values of μ, 0.5, 1.0, and 1.5, are presented in Fig. 1. Calculating ϵ_m, we set $\nu = 0.05$. As one can see from equation (23) the error ϵ_m decreases with ν. (From point 7 of Appendix A it follows that $A > \lambda$.)

To obtain κ and λ, one can use the graph of $\kappa(S)$ from Fig. 2: If one takes $S/(1+\mu S)$ instead of S in accordance with (22), the graph will give us λ instead of κ. The curve $\kappa/(1+C_r)$ serves for calculating τ, if C_r is found.

The value t_m is not shown on Fig. 1. As our calculations revealed, in the case $\nu \ll 1$, the values t_m are very close to τ (the difference is about a few percent). It means that in the case under consideration, the inner solution works over almost the whole interval $(0, \tau)$. Hence, in that case supercooling or superheating play an important role in the process and must be taken into account.

Case 3. $\mu \ll 1$ $(\nu \sim 1, S \gtrsim 1)$. We shall seek λ in the form of a power series in μ

$$\lambda = \kappa - \lambda_1\mu + \ldots \tag{24}$$

The first term in this expansion is equal to κ because equations (8) and (10) are equivalent, if $\mu = 0$. Substituting equation (24) into equation (8), we obtain by the usual way

$$\lambda_1 = \nu^{1/2}S^2/[S + 2\kappa^2(S+1)]\pi^{1/2}e^{\kappa^2/\nu}\mathrm{erfc}(\kappa/\nu^{1/2}) \tag{25}$$

Also using the expressions (A5) (from Appendix B) for a and b, valid for $\mu \ll 1$, one can solve equation (14) numerically and find ζ for given κ and ν (see Appendix B).

Substituting equation (25) into equations (11), (13), and (18) we find the first terms of the expansion for C_r and for ϵ_m

$$\left.\begin{aligned} &C_r = 2\lambda_1\kappa\mu/\nu\zeta^2 \\ &\epsilon_m = (a-\zeta)(\pi\nu)^{1/2}\mu\mathrm{erf}\kappa \end{aligned}\right\} \tag{26}$$

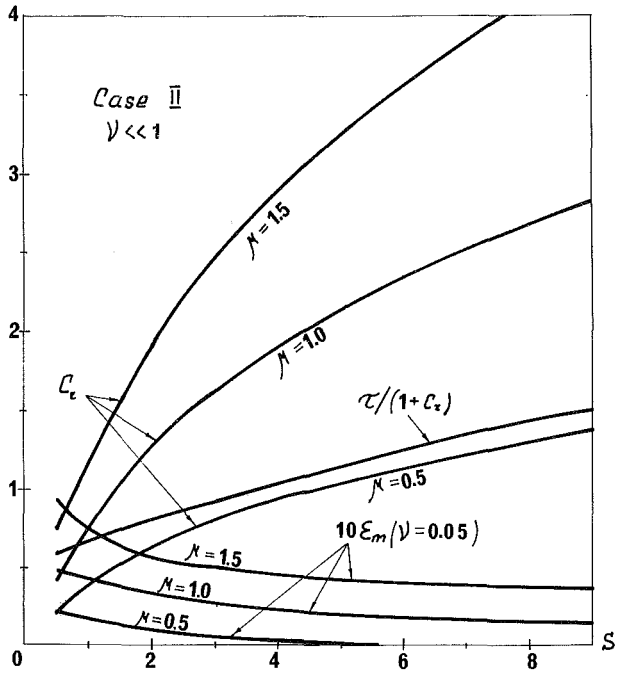

Fig. 1 Graphs of C_r and 10 ϵ_m as functions of S for three values of μ(0.5; 1.0; 1.5) for the case $\nu \ll 1$. The value 10 ϵ_m is calculated for ν = 0.05. The ratio $\tau/(1 + C_r)$, which does not depend on ν and μ, is presented as a function of S. This graph can serve for calculation of τ.

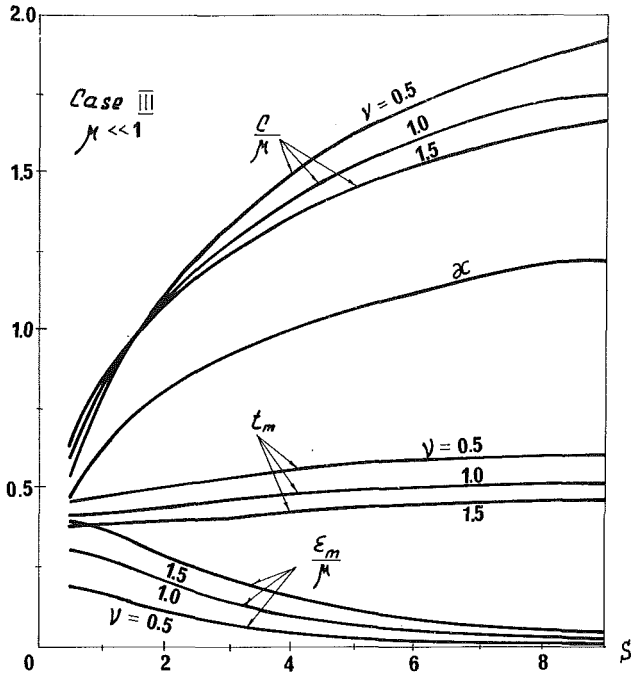

Fig. 2 Graphs of C_r/μ, ϵ_m/μ, and t_m as functions of S for three values of ν (0.5; 1.0; 1.5) for the case $\mu \ll 1$. The value κ, which does not depend on ν and μ, is presented as a function of s.

Now one can calculate t_m, λ_1, and C_r, and ϵ_m with the aid of equations (13), (25), and (26). The values C_r/μ, t_m, and ϵ_m/μ are represented in Fig. 2 as functions of S for three values of ν: 0.5, 1, and 1.5. Also in Fig. 2, the curve $\kappa(S)$ is represented. One can see from Fig. 2 that ϵ_m is small and is a decreasing function of S.

A comparison of the values t_m and τ shows that for the case $\mu \ll 1$, the inner and outer solutions have about equal importance.

This result, along with the curves C_r/μ in Fig. 2, shows that for the case $\mu \ll 1$, the superheating or supercooling can essentially influence τ.

Here we shall present an example of a concrete calculation. Let the nondimensional parameters be $S = 0.5$, $\mu = 0.1$, $\nu = 1.0$. As $\mu \ll 1$, one can use the curves from Fig. 2 to find parameters of interest. We have $C_r = 0.152$, $\kappa = 1.060$, $t_m = 0.528$, $\tau = 1.282$, $\epsilon_m = 0.63$ percent. From equations (25), (26), and (13) we obtain $\lambda_1 = 1.854$, $\lambda = 0.874$, $C = 0.169$. The dependence of the nondimensional δ on nondimensional t is shown by the solid line in Fig. 3. The dependence of ϵ on nondimensional t is shown schematically (only ϵ_m was calculated) by the dotted line.

One can see that the maximum of the relative error ϵ_m is reached at the instant $t = t_m$ at which the curve $\delta(t)$ has a cusp. Evidently there cannot be a cusp in the curve $\delta(t)$, in the exact solution in which the derivative $d\delta/dt$ has to increase gradually with time in the vicinity of $t = t_m$. The fact that such an increase takes place is understandable physically: For $t < t_m$, a significant part of the incoming heat energy is spent not only for the phase change, but also for obtaining the critical temperature.

One can see from Fig. 3 that the instant $t = C$ is the top of the parabola, of which the part corresponding to the interval $t_m < t < \tau$ is the outer solution for $\delta(t)$.

If the curve $\delta_{in}(t)$ is prolonged mentally for $t > t_m$, one can conclude that an estimation of τ only by the inner solution, e.g., by the ratio $S/4\lambda^2$, could be significantly exceeded. In the example under consideration such an excess is about 28 percent.

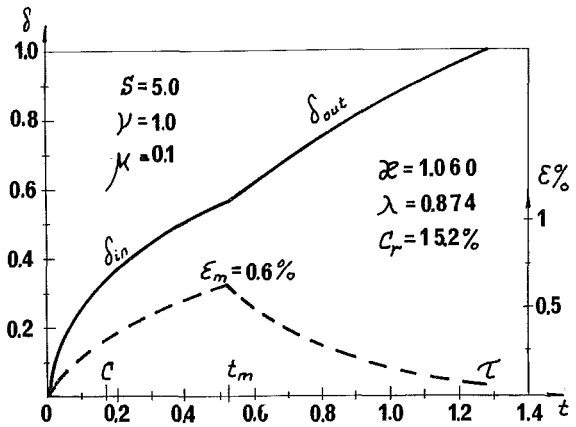

Fig. 3 The nondimensional phase change boundary δ as a function of nondimensional time calculated for S = 5.0, μ = 0.1, and ν = 1.0 from the approximate solution. The energetic error $\epsilon(t)$ in percent is shown schematically by the dotted line. (Only the point ϵ_m was calculated.)

5 Conclusion

Summing up, one can infer that the problem (1)–(3) is approximately solved. Formulae were constructed which allow the approximate calculation of the slab temperaure field and the motion of the phase boundary as well as the total phase-change time and absolute and relative increase of that time in comparison with the case of the initial critical temperature. Special formulas for an estimation of the error of the solution are obtained.

When we constructed the solution, we did not impose any constraints on the nondimensional parameters of the problem. However, it turned out that the method is effective only if at least one of the nondimensional parameters is small or, in other words, if we deal with the problem of perturbations. It should be noticed that only the cases $\nu \ll 1$ or $\mu \ll 1$ can have a practical application. In the case of $10^{-3} < S \ll 1$ one should look for another solution of the problem.

Acknowledgments

I am indebted to Dr. Ch. Charach for many helpful discussions which have attracted my attention to the problem considered. Thanks also go to Prof. L. Berkofsky and A. Molod for editorial assistance, and to R. Roth for typing the manuscript.

References

1 Weinbaum, S., and Jiji, L. M., "Singular Perturbation Theory for Melting or Freezing in Finite Domains Initially Not at the Fusion Temperature," ASME *Journal of Applied Mechanics*, Vol. 44, 1977, pp. 25–30.

2 Van Dyke, M., *Perturbation Methods in Fluid Mechanics*, Academic Press, New York–London, 1964.

3 Grove, W. E., *Brief Numerical Methods*, Prentice-Hall, New York, 1966.

APPENDIX A

Geometric Interpretation of the Transcendental Equations (8), (10), and (14)

A solution λ of equation (8) is the point of intersection of the curves $Z = \varphi(Y) = (\pi^{1/2}e^{Y^2}\mathrm{erf}Y)^{-1}$ and $Z = Y/S + \mu\nu^{1/2}\varphi_C(Y)$, where

$$\varphi_C(Y) = \left[\pi^{1/2}e^{Y^2/\nu}\mathrm{erfc}(Y/\nu^{1/2})\right]^{-1} \tag{A1}$$

κ is a point of intersection of the curve $Z=\varphi(Y)$ and the straight line $Z=Y/S$ (see equation (10)). An elementary investigation reveals that: The curve $Z=\varphi(Y)$ decreases from $Z=\infty$ at $Y=0$ to $Z=0$ at $Y=\infty$ and is concave upward for all Y; the curve $Z=Y/S + \mu\nu^{1/2}\varphi_c(Y)$ increases from $Z=\mu(\nu/\pi)^{1/2}$ at $Y=0$ to $Z=\infty$ at $Y=\infty$ and is also concave upward for all Y. This curve approaches from above to its asymptote $Z=(S^{-1}+\mu)Y$.

From such a geometric interpretation of equations (8) and (10) one can conclude that:

1 Solutions λ of equation (8) and κ of equation (10) exist and are unique for all positive values of the parameters S, μ, and ν.

2 λ is an increasing function of S and a decreasing function of μ.

3 κ is an increasing function of S.

4 If $\mu\neq 0$, then $\lambda<\kappa$ for any values of S and ν ($\lambda=\kappa$ if $\mu=0$).

Proceeding to equation (14), we note that its solution ζ can be represented as the point of intersection of the curve $Z = F(Y) = Y + b(e^{-y^2} - \pi^{1/2}Y\mathrm{erfc}Y)$; $y>\lambda/\nu^{1/2}$; and of the straight line $Z=a$, where a and b are given by equation (15).

An elementary investigation shows that the function $Z=F(Y)$ increases from $Z=\varphi_C(\lambda)$ (φ_C is given by (A1)) at $Y=\lambda/\nu^{1/2}$ ($F'(Y)=0$ at $Y=\lambda/\nu^{1/2}$) to $Z=\infty$ at $Y=\infty$ and is concave upward for all $Y=\lambda/\nu^{1/2}$. When Y increases, the curve $Z=F(Y)$ approaches from above to its asymptote $Z=Y$.

From such a geometric interpretation of equation (14) one can conclude that a solution ζ of equation (14) exists and is unique provided that $N=a-\varphi_C(\lambda)>0$.

On the other hand, with the aid of equations (8) and (10) the value N can be presented in the form

$$N=\left(\frac{1-e^{-\lambda^2}}{\lambda\mathrm{erf}\lambda}-\frac{1-e^{-\kappa}}{\kappa\mathrm{erf}\kappa}\right)\lambda/\mu(\pi\nu)^{1/2} \tag{A2}$$

One can show that the expression $(1-e^{-Y^2})/Y\mathrm{erf}Y$ is a decreasing function of Y and consequently $N>0$ always (see conclusion 4). Therefore:

5 A solution ζ of equation (14) exists and is unique for all positive values of the parameters S, μ, and ν.

6 The difference $a-\zeta$ decreases if N increases, or if a increases. Then ζ also increases. This means that the difference $a-\zeta$ can be small and a and ζ can be large, if either μ or ν is small.

7 $a>\lambda/\nu^{1/2}$ always.

APPENDIX B

Solution of Equations (10) and (14)

We start from the numerical solution of equation (10), which can be presented in the form $Z=f(\kappa)=\varphi(\kappa)-\kappa/S$. Apparently, the curve $f(\kappa)$ decreases from $Z=\infty$ at $\kappa=0$ to $Z=-\infty$ at $\kappa=\infty$ and is concave upward for all κ. This shape of the curve allows us to employ the Newton–Raphson method [3] which can be reduced to the following iterative process

$$\left.\begin{aligned}\kappa_{n+1}&=\kappa_n+(S\varphi_n-\kappa_n)/[1+2S\varphi_n\cdot(\varphi_n+\kappa_n)]\\ \varphi_n&=\varphi(\kappa_n)\qquad n=0,\ 1,\ 2,\ \ldots\end{aligned}\right\} \tag{A3}$$

Iterations converge for any $\kappa_0>0$. We took $\kappa_0=0.5$ and stopped the iterations when $|\kappa_{n+1}-\kappa_n|<10^{-3}$.

Proceeding to equation (14) which we write in the form $Z=F(\zeta)-a=0$; $\zeta>\lambda/\nu^{1/2}$, we note that the shape of the curve $Z=F(\zeta)-a$ also allows use of the Newton–Raphson method.

The iterative formula is

$$\zeta_{n+1}=(a-be^{-\zeta_n^2})/(1-\pi^{1/2}b\mathrm{erfc}\zeta_n)\quad(n=0,\ 1,\ 2,\ \ldots) \tag{A4}$$

We set $\zeta_0=a$, ensuring the convergence of the iterations. As a criterion to stop iterations, we use again $|\zeta_{n+1}-\zeta_n|<10^{-3}$.

As we use (A4) for calculations of the case $\mu\ll 1$, we shall present here the expressions for a and b, valid for small μ

$$\begin{aligned}a&=(S+2\kappa^2)e^{\kappa^2}\varphi_C(\kappa)/[S+2\kappa^2(S+1)]\\ b&=[\pi^{1/2}\mathrm{erfc}(\kappa/\nu^{1/2})]^{-1}\end{aligned} \tag{A5}$$

These expressions are the limit of the expressions (15) when $\mu\to 0$. Obtaining (A5), we took into account equations (8) and (10).

We shall consider now two cases $\zeta-\lambda/\nu^{1/2}\ll 1$ and $\zeta\gg 1$ for which equation (14) has approximate analytic solutions.

In the first case, setting

$$\zeta=\lambda/\nu^{1/2}+\zeta'\qquad(\zeta'\ll 1) \tag{A6}$$

we expand equation (14) in a Taylor series in the vicinity of $\zeta=\lambda/\nu^{1/2}$ and retain the first two terms. Solving the resulting quadratic equation, we have

$$\zeta'=[N/\varphi_C(\lambda)]^{1/2} \tag{A7}$$

If $S\ll 1$, one can construct a power series in $S^{1/2}$ for ζ'. We shall present here the first term of that series. Substituting equation (19) into equations (A1) and (A2) and then into equation (A7) and retaining the first term of the expansion, we get

$$\zeta'=(24)^{-1/2}S=0.204S \tag{A8}$$

One can show that the second term of this series is proportional to $S^{3/2}$. The second possibility for an analytical solution of equation (14) is a construction of the asymptotic expansion of ζ for $\zeta\gg 1$. Using the known asymptotic expansion for erfc and assuming that the second term of this expansion is small in comparison with the first one, we obtain

$$\zeta=a-b/2a^2e^{a^2}\qquad(\zeta\gg 1) \tag{A9}$$

We showed in Appendix A that $a-\zeta\ll 1$ if $N\gg 1$. In other words, (A9) is valid if $N\gg 1$.

A Study of the Relationship Between Free-Stream Turbulence and Stagnation Region Heat Transfer

G. J. VanFossen, Jr.

R. J. Simoneau
Mem. ASME

NASA Lewis Research Center,
Cleveland, OH 44135

A study has been conducted at the NASA Lewis Research Center to investigate the mechanism that causes free-stream turbulence to increase heat transfer in the stagnation region of turbine vanes and blades. The work was conducted in a wind tunnel at atmospheric conditions to facilitate measurements of turbulence and heat transfer. The model size was scaled up to simulate Reynolds numbers (based on leading edge diameter) that are to be expected on a turbine blade leading edge. Reynolds numbers from 13,000 to 177,000 were run in the present tests. Spanwise averaged heat transfer measurements with high and low turbulence have been made with "rough" and smooth surface stagnation regions. Results of these measurements show that, at the Reynolds numbers tested, the boundary layer remained laminar in character even in the presence of free-stream turbulence. If roughness was added the boundary layer became transitional as evidenced by the heat transfer increase with increasing distance from the stagnation line. Hot-wire measurements near the stagnation region downstream of an array of parallel wires has shown that vorticity in the form of mean velocity gradients is amplified as flow approaches the stagnation region. Finally smoke wire flow visualization and liquid crystal surface heat transfer visualization were combined to show that, in the wake of an array of parallel wires, heat transfer was a minimum in the wire wakes where the fluctuating component of velocity (local turbulence) was the highest. Heat transfer was found to be the highest between pairs of vortices where the induced velocity was toward the cylinder surface.

Introduction

In gas turbine blade design, prediction of stagnation region heat transfer is critical because heat flux is usually highest in this region. The heat transfer in the stagnation region can be predicted if the free stream flow is laminar [1]. In the gas turbine, flows are highly turbulent with intensities of 8–15 percent. If the turbulence intensity in the free stream is higher than about 1 percent, heat transfer in the stagnation region is augmented.

Flow in the stagnation region of a turbine blade can be simulated by a cylinder in crossflow. There have been many experimental investigations of the effect of turbulence intensity on heat transfer to a cylinder in crossflow, some of which are given in [2–6]. The bulk of these investigations have measured an increase in heat transfer in the stagnation region for some increased level of free-stream turbulence and then tried to correlate the heat transfer increase to some parameter involving the turbulence intensity. This approach has had limited success. Trends are clearly present but there is great scatter in the data, particularly between the data of different researchers.

The mathematical modeling of stagnation region flow has been divided into several areas. One set of modelers has attempted to develop a turbulence model that can be used to solve the two-dimensional boundary layer equations to predict the level of heat transfer [2, 7, 8]. The results are a correlation of the mixing length or turbulent viscosity and Prandtl number with other flow parameters.

A more plausible model of heat transfer augmentation by free-stream turbulence is the vortex stretching model. It is hypothesized that, as vortical filaments with components of their axes normal to the stagnation line and normal to the free-stream flow are convected into the stagnation region, they are stretched and tilted by the divergence of streamlines and acceleration around the body. Through conservation of angular momentum, this stretching causes the vorticity to be intensified. This increased vorticity is hypothesized to be the cause of the augmented heat transfer in the stagnation region. Some examples of the work on this theory are given in [9–14] and a review of the work is given in [15]. In [9, 10] it was deduced that the mathematical model allowed only turbulent eddies above a certain neutral wavelength to enter the Hiemenz flow [16] boundary layer. Inside the boundary layer, however, shorter wavelengths could be generated by the action of viscosity. The three-dimensional vorticity transport equations were solved for a free-stream velocity that was periodic in the spanwise coordinate. This boundary condition supplied the vorticity to the stagnation region in an orientation that allowed it to be stretched by the mean flow. A few special cases where the period in velocity was near the neutral wavelength have been solved. It was found that the thermal boundary layer was much more sensitive to external vorticity than the hydrodynamic boundary layer.

In [11] measurements of grid turbulence that contained eddies of all orientations near the stagnation point of a circular cylinder showed that eddies with scales much larger than the cylinder diameter were not amplified as they approached the stagnation point. Small-scale eddies, however, were found to be amplified as they approached the cylinder. The measurements of [11] were external to the boundary layer. In [12, 13] a hot wire was used to measure the amplification of turbulence near the stagnation point of both a cylinder and an airfoil. The turbulence was produced by an upstream array of parallel rods. Spectral measurements were then used to deduce a so-called most-amplified scale. Flow visualization with smoke also showed a regular array of vortex pairs near the

Contributed by the Heat Transfer Division for publication in the JOURNAL OF HEAT TRANSFER. Manuscript received by the Heat Transfer Division April 25, 1985.

stagnation point; the array of vortex pairs was clearly outside the theoretical laminar boundary layer.

In [14] vortex formation near the stagnation region of a bluff body from the wakes of an array of parallel wires placed upstream was studied. It was determined that there was a threshold for vortex formation. If the wires were too far upstream or the Reynolds number was too small, no vortices were formed on the bluff body. Heat transfer augmentation in the stagnation region was found to increase sharply when vortices were formed. The size of the vortices was found to scale with the width of the upstream disturbance wake and not with boundary layer thickness.

Calculations and measurements made in [5] concluded that the boundary layer velocity profiles are essentially laminar even in the presence of free-stream turbulence. The temperature field, however, was found more sensitive to free-stream turbulence. This implies that heat transfer will be increased more than skin friction by free-stream turbulence.

A collection of experimental observations has been assembled here in order to construct a picture of this complex phenomenon. Spanwise average heat transfer data are presented to show the effect of free-stream turbulence and surface roughness on the condition (laminar or turbulent) of the thermal boundary layer. Hot-wire measurements are used to show how vorticity from mean velocity gradients is amplified as it approaches the stagnation region. Finally a combination of flow visualization using the smoke wire technique and thermal visualization using liquid crystals is used to show the relationship between vortex pairs produced by mean velocity gradients and the spanwise heat transfer distribution.

Apparatus

Wind Tunnel. All tests were conducted in the wind tunnel shown schematically in Fig. 1. Room air first flowed through a turbulence damping screen with an 18 × 18 mesh of 0.24 mm (0.0095 in.) diameter wire. Large-scale turbulence from the room was then broken up by being passed through a honeycomb of approximately 12,000 plastic soda straws which were 0.64 cm (0.25 in.) in diameter by 19.69 cm (7.75 in.) long. The air then passed through a final damping screen identical to the first. A 4.85:1 contraction (contraction in spanwise direction only) then accelerated the air entering the test section. The maximum velocity attainable in the test section was about 46 m/s (150 ft/s) and the clear tunnel turbulence level was less than 0.5 percent at all flow rates.

The test section was 15.2 cm (6.0 in.) wide by 68.6 cm (27.0 in.) high. The models were mounted horizontally in the tunnel. Hot-wire surveys and smoke wire flow visualization indicated that the center 7.6 cm (3.0 in.) of the tunnel was free from turbulence generated by the sidewall boundary layer. All measurements were confined to this center region of the tunnel test section.

After leaving the test section, the flow passed through a transition section into a 10-in. pipe, through two long radius elbows and a flow straightener and into an orifice run. The orifice plate had a diameter of 19.1 cm (7.5 in.). The flow rates used in these tests were measured with this orifice. Air then passed through a 10-in. butterfly valve which was used to control the flow rate and then to the laboratory altitude exhaust system.

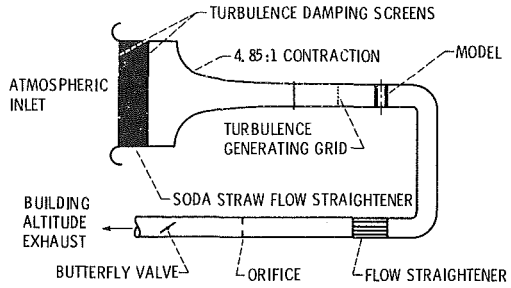

Fig. 1 Schematic of wind tunnel

The temperature of the air entering the wind tunnel was measured by four exposed ball chromel-alumel thermocouples around the perimeter of the inlet. These four temperatures were averaged to give the total (or stagnation) temperature.

Turbulence Generators. For some of the high-turbulence cases, a turbulence generating biplane grid of 0.318 cm (0.125 in.) diameter rods spaced 10 rod diameters apart was installed 79.6 rod diameters upstream of the model leading edge. For the flow visualization tests and some of the heat transfer tests an array of parallel 0.051 cm (0.020 in.) diameter wires spaced 12.5 wire diameters apart was installed 547.5 wire diameters (4.21 cylinder diameters) upstream of the model leading edge. For the spanwise hot-wire traverses the same parallel wire array was used, but the wires were spaced 37.5 wire diameters apart.

Hot Wire. Turbulence measurements were made with a constant-temperature hot-wire anemometer. Signals were linearized and the mean component of velocity was read on an integrating digital voltmeter with an adjustable time constant. The fluctuating component was read on a true rms voltmeter which also had an adjustable time constant. When the hot wire was traversed the analog outputs of both the mean and rms meters were recorded as a function of position on an x–yy' plotter. The hot wire probe was a 4×10^{-6} m diameter, tungsten, single wire probe. The hot wire was calibrated before each use in a free jet of air at nearly the same temperature (±1°C) as the wind tunnel flow. The hot-wire system frequency response was determined to be around 30 kHz by the standard square wave test.

Turbulence scale was estimated by using an autocorrelation of the hot wire signal. The autocorrelation was obtained on a dual channel fast Fourier transform (FFT) spectrum analyzer. The area under the autocorrelation function gave an integral time scale. This time scale was then multiplied by the mean velocity to obtain the integral length scale.

Smoke Wire. Flow visualization was accomplished by using the smoke wire technique described in [17]. A 0.008 cm (0.003 in.) diameter wire was stretched across the tunnel parallel to the cylinder axis slightly below the stagnation plane. The wire was coated with oil, as recommended in [17], by using a cotton swab. A timing circuit was then used to start current flow to heat the wire and vaporize the oil and, after an adjustable delay, fire a strobe light to expose the film. A 35-mm camera with telephoto lens and closeup attachments was used to make high-quality images of the flow and heat transfer patterns in

Nomenclature

D = cylinder diameter, cm
d = rod diameter, cm
e = height of roughness element, cm
h = heat transfer coefficient, W/m^2 • °C
q'' = heat flux, W/m^2
Re = Reynolds number
T = temperature, K
X = distance measured upstream from forward stagnation line, cm
z = spanwise coordinate, cm
θ = circumferential coordinate

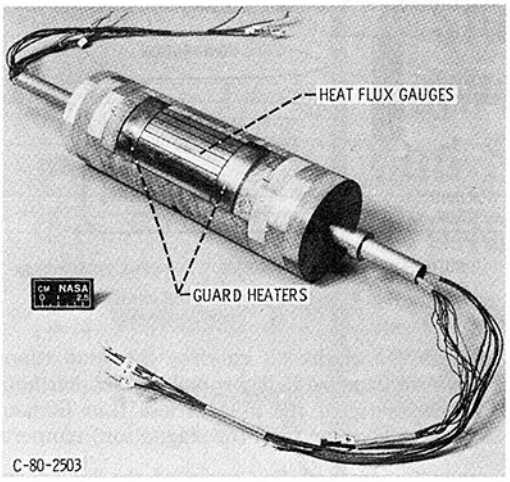

Fig. 2 Spanwise average heat transfer model

the stagnation region. Two strobe lights were used, one from each side of the tunnel. It was found that the best lighting angle for smoke visualization was 90 deg from the viewing angle. This angle was not an optimum angle for the viewing of the liquid crystal models. As explained in [18], if the lighting angle and the viewing angle are not the same, there is a color shift in the liquid crystal. Thus simultaneous smoke and liquid crystal thermal visualization photographs can only be used to obtain qualitative heat transfer results.

Test Specimens

Spanwise Averaged Heat Transfer. Spanwise-averaged heat transfer coefficients were measured on a 6.6 cm (2.6 in.) diameter cylinder (Fig. 2). The cylinder was 15.2 cm (6 in.) long and was made of wood. Heat transfer coefficients around the circumference of the cylinder were measured with electrically heated copper strips. Each strip was 6.6 cm (2.6 in.) long by 0.51 cm (0.21 in.) wide and 0.318 cm (0.125 in.) deep. A Kapton encapsulated electric heater was fastened to the back of each copper strip with pressure-sensitive adhesive. A stainless steel sheathed, closed, grounded ball, chromel-alumel thermocouple was soft soldered into a groove in each copper strip. The copper heat flux gages were embedded in the surface of the cylinder at 10 deg intervals around the circumference. The average gap between copper strips was 0.10 cm (0.04 in.) and was filled with epoxy. There were eight copper strips but only the inner six strips were used as measuring gages; the outer two served as guard heaters to minimize heat loss by conduction. Guard heaters were also used on the ends of the copper strip gages as shown on Fig. 2. A guard heater was also used behind the measuring gages to stop radial heat conduction to the rear of the cylinder. A thin coat of lacquer was sprayed on the surface of the cylinder and the copper gages to keep the copper from oxidizing and changing emissivity. In operation the copper strips were maintained at a constant temperature by a controller described in [19]. The data reduction technique used for the spanwise average model is also described in [19].

For some of the tests, the spanwise average heat transfer model was used to investigate the effect of surface roughness. This was accomplished by spraying a coat of clear lacquer onto the model; sand was then sprinkled on the wet surface from an ordinary salt shaker. Another thin coat of lacquer then held the sand in place. An optical comparator was used to obtain an estimate of the roughness. The maximum height of any one roughness element was found to be 0.0572 cm (0.0225 in.). The average height of the roughness elements above the surface was 0.033 cm (0.013 in.), which gave a relative roughness e/D of 0.005.

An afterbody was used with the cylinder for some tests to eliminate the alternate vortex shedding from the rear of the cylinder. The afterbody consisted of a 5.08 cm (2.0 in.) long straight segment which was tangent to the cylinder surface 90 deg from the stagnation line. A 10 deg wedge then extended downstream and ended in a cylindrical trailing edge 0.3175 cm (0.125 in.) in diameter.

Liquid Crystal Models. Spanwise variations in heat transfer coefficient were mapped using three different models. One of the models was a cylinder with the same dimensions as the spanwise average heat transfer model. The second model had the same dimensions as the spanwise average model plus the afterbody and the third model was scaled to one half the size of the spanwise average plus afterbody.

All the liquid crystal models were constructed using the techniques in [18]. Briefly, a heater element consisting of polyester sheet with a vapor-deposited gold layer was fastened to the model surface with double-sided tape. At the rear of the cylinder, bus bars of copper foil were fastened to the heater edges parallel to the cylinder axis. Silver conductive paint was used to improve electrical conductance between the copper foil and the gold. A commercially available plastic sheet which contained cholesteric liquid crystals was fastened over the heater with double-sided tape.

The gold heater was checked for uniformity in still air using the liquid crystal sheets to monitor temperature gradients. The liquid crystal sheets were calibrated in a water bath. The yellow color was found to indicate a temperature of $54.8 \pm 0.2°C$ ($130.6 \pm 0.4°F$).

In operation, the cylinder was heated by passing an electric current through the gold film. This supplied a uniform heat flux at the surface of the cylinder. Electric power to the model was adjusted so that the area of interest on the surface turned yellow. Neglecting radiation and conduction losses which are small, the heat transfer coefficient can be computed as

$$h = \frac{q''}{(T_{\text{yellow}} - T_{\text{air}})}$$

Thus the yellow color traces an iso-heat transfer coefficient contour on the model.

Traversing Cylinder. Turbulence measurements near the surface of the cylinder were made using a cylinder made of wood that had a hole drilled along a diameter. A hot-wire probe could be inserted through this hole and positioned very close to the surface. The area around the hot wire prongs was filled in with modeling clay to match the contour of the cylinder. The cylinder extended through holes in the tunnel walls; felt was used as a seal between the cylinder and the walls. The cylinder could thus be traversed axially across the tunnel span, carrying the hot wire with it.

Error Analysis

An error analysis was performed for each of the spanwise averaged heat transfer data points by the method of Kline and McClintock [20]. The average error for all the data points was found to be 5.7 percent and the maximum error for any one data point was 7.8 percent. Error estimates of the hot-wire and liquid crystal data were not made.

Results and Discussion

In this section, spanwise-averaged heat transfer distributions around a circular cylinder in cross flow will be presented for high and low free-stream turbulence. The effect of surface roughness will also be presented for both high and low free-stream turbulence. Hot-wire measurements are presented to demonstrate amplification of vorticity in the free stream as the flow approaches the stagnation region. Finally, flow visualization and thermal visualization are combined to show the rela-

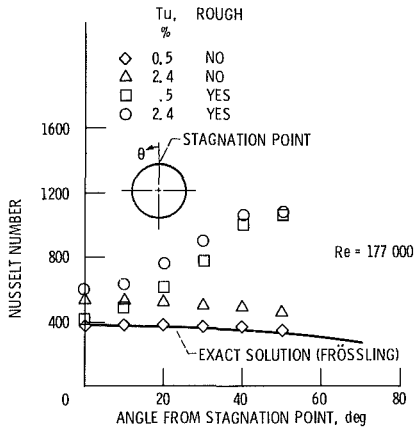

Fig. 3 The effect of free-stream turbulence and surface roughness on spanwise averaged heat transfer for a cylinder in crossflow

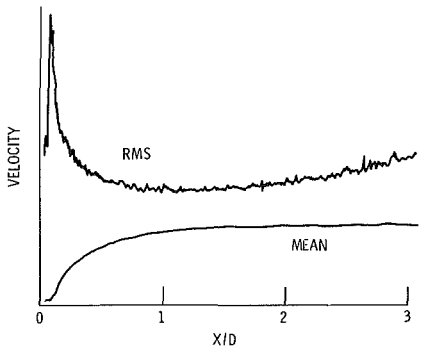

Fig. 4 Streamwise traverse of a hot wire close to the stagnation streamline

tionship between vortex pairs formed in the stagnation region and spanwise variations in surface heat transfer.

Spanwise-Averaged Heat Transfer. Figure 3 shows Nusselt number as a function of angle from the stagnation point for the four cases mentioned above. All of the data on Fig. 3 were taken at a Reynolds number (based on free-stream conditions and cylinder diameter) of 177,000. Low-turbulence data were taken with a clear tunnel and high-turbulence data were taken with a biplane grid. The grid produced turbulence of about 2.4 percent with a scale of 0.50 cm (0.20 in.). Also plotted on the figure is an exact solution of the laminar boundary layer equations from [1]. The data shown on Fig. 3 were for the cylinder without the afterbody; data taken with the afterbody in place were identical within experimental error.

Smooth Surface–Low Turbulence. The agreement between the exact solution and the smooth cylinder, low-turbulence data is well within the experimental error and thus confirms the accuracy of the experimental method (Fig. 3).

Smooth Surface–High Turbulence. For the cylinder placed downstream of the biplane grid (Fig. 3), turbulence increased the heat transfer virtually uniformly around the circumference (measurements were only made up to 50 deg from stagnation) by about 30 percent. This agrees well with the data of other observers; for example, the theory of [2] predicts an increase in Nusselt number at the stagnation point of 27.8 percent for these conditions.

Rough Surface–Low Turbulence. Adding sand roughness to the cylinder surface did not change the heat transfer rate at the stagnation point from the smooth surface case (Fig. 3). As the angle from stagnation increased, however, the heat transfer rate also increased, most likely because boundary layer transition was triggered by the roughness elements.

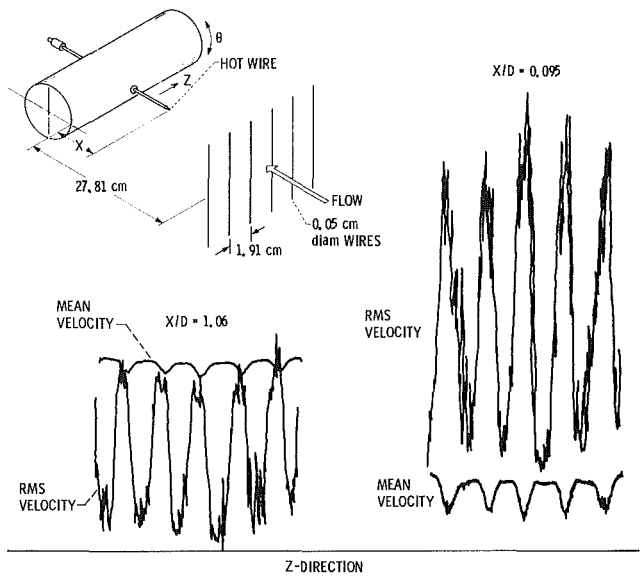

Fig. 5 Spanwise traverses of a hot wire near the cylinder stagnation point (Note: Abscissa of rms and mean velocity plots offset slightly due to pen offset on x-yy′ recorder)

Rough Surface–High Turbulence. The final set of symbols on Fig. 3 is for the sand-roughened surface with 2.4 percent free-stream turbulence. The effect of free-stream turbulence is seen to be greater nearest the stagnation point where the heat transfer rate is again increased by about 30 percent over the low-turbulence case. As the angle from stagnation becomes larger, the high and low-turbulence data (rough surface) merge as the boundary layer becomes more turbulent.

Surface roughness had no effect on heat transfer at the stagnation line but changed the character of the boundary layer in the downstream direction. It seems that the boundary layer on the smooth surface remains laminar in character at the Reynolds numbers tested (i.e., no turbulence is produced within the boundary layer). Free-stream turbulence somehow acts on a laminar boundary layer to agument heat transfer.

Hot Wire Measurements

Streamwise Traverse. A streamwise traverse of a single hot wire was performed with the wire oriented parallel to the 6.6 cm (2.6 in.) diameter cylinder axis and as close as possible to the plane of the stagnation streamline. An array of 0.05 cm (0.02 in.) parallel wires spaced 12.5 wire diameters apart was located 4.21 cylinder diameters (547.5 wire diameters) upstream of the stagnation point. This wire array produced vorticity (gradients in the mean velocity) in an orientation that could be stretched and amplified. The traverse was made from 0.044 to 3.06 cylinder diameters upstream of the stagnation point at a Reynolds number based on cylinder diameter of 177,000. It is typical of all traverses made over the Reynolds number range 31,000 to 177,000. The mean velocity (Fig. 4) fell monotonically as the stagnation region was approached. The fluctuating velocity (rms, Fig. 4), however, first decayed with distance downstream of the grid (decreasing x/D) and then sharply increased and peaked at about 0.085 cylinder diameter upstream from the stagnation point. This peak was far outside the predicted laminar boundary layer thickness of 0.003 cylinder diameter [16]. These results are very similar to those of [12].

Spanwise Traverse. Two spanwise traverses of a hot wire oriented perpendicular to the cylinder axis and centered in the plane of the stagnation streamline were made. The cylinder leading edge was located 4.21 cylinder diameters downstream of an array of 0.05 cm (0.02 in.) diameter parallel wires which were spaced 37.5 wire diameters apart. Both traverses were

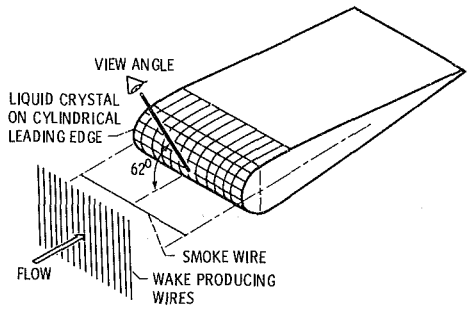

Fig. 6 Physical arrangement of liquid crystal model, wake producing wires, smoke wire, and view angle

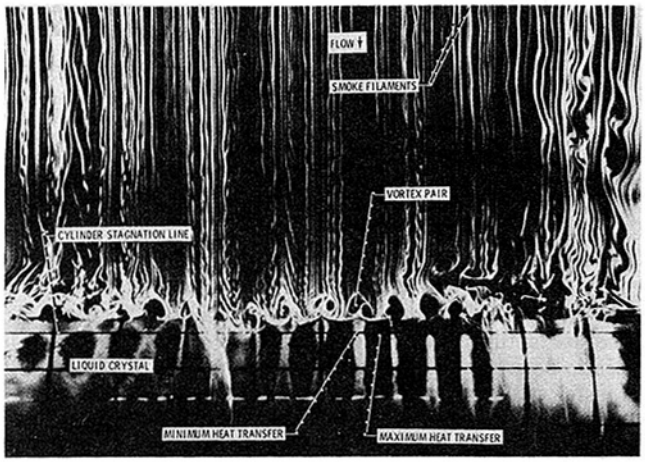

Fig. 7 Combined thermal and flow visualization of cylinder in cross flow

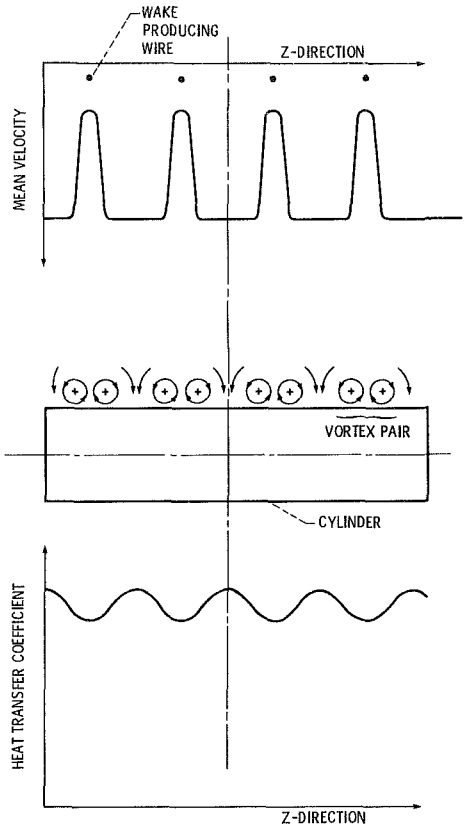

Fig. 8 Schematic showing relationship of wire-produced wakes, vortex pairs, and peaks in heat transfer

made at a Reynolds number based on cylinder diameter of 31,000 and are typical of those for the complete Reynolds number range. Both traverses are presented at the same scale in Fig. 5. For the traverse taken at 1.06 cylinder diameters upstream from the stagnation line, the wire wakes are clearly visible in the mean velocity trace. The turbulent fluctuations are high in the wire wakes and low in the relatively undisturbed flow between wires. At 0.095 cylinder diameters upstream, the level of the mean velocity greatly decreased, but the depth of the wake increased, an indication of increasing vorticity as the stagnation region is approached. The fluctuating component of velocity also increased in the wire wakes as the stagnation region was approached.

Simultaneous Flow—Thermal Visualization. The smoke wire flow visualization technique was combined with the liquid crystal thermal visualization technique to show the relationship between spanwise variations in heat transfer and vortices in the stagnation region. These vortices were formed from the wakes of wires placed upstream of the cylindrical leading edge and arranged as shown in Fig. 6. Figure 7 is a photograph of the leading edge region for the 6.6 cm (2.6 in.) diameter cylindrical leading edge model with afterbody taken at a Reynolds number of 13,000. Note that the Reynolds number for the wires is about 100; for wire Reynolds numbers less than 120, the wakes were laminar (i.e., no Karman trails were formed). The dark lines on the surface of the model were drawn in a 1.27 cm (0.5 in.) square grid pattern for visual scaling.

The smoke shows that a vortex pair was formed from the wake of each wire. The vortices were well outside the theoretical laminar boundary layer. The dark, vertical stripes in the liquid crystal indicate regions of low temperature and thus high heat transfer. Thus, contrary to expectations, the regions of high heat transfer were not under the vortices but between vortex pairs where the free-stream turbulence was lowest. In this region the induced velocity from neighboring vortex pairs was directed toward the cylinder surface. Conversely, the region of minimum heat transfer was directly under the vortex pair. This was the region of highest free-stream turbulence as measured by a hot wire outside the boundary layer. Figure 8 shows schematically the spatial relationship of the wires, wakes, vortex pairs, and the peak in heat transfer.

The heat transfer–vortex pattern was the same for all three of the liquid crystal models. For the cylinder without the afterbody the heat transfer–vortex pattern remained unchanged relative to the model with the afterbody. The half-scale model with afterbody had the same heat transfer pattern but the vortices appeared smaller in diameter at the same free-stream velocity. The spanwise spacing of vortex pairs remained equal to the wire spacing. The Reynolds number for the half-scale model was one half that for the large cylinder with afterbody.

For the half-scale model, the spanwise heat transfer coefficient variation along the stagnation line (i.e., (maximum h − minimum h)/0.5 (maximum h + minimum h)) was 7 percent at a Reynolds number of 16,000 and 16 percent at a Reynolds number of 89,000. This is the same magnitude found for spanwise variations in mass transfer caused by periodic irregularities in a screen [21]. Measurements of heat transfer variation were not made for the other models.

High-speed motion pictures of smoke near the stagnation point of the cylinder without afterbody were taken at a Reynolds number of 13,000. They showed that vortices were formed in the stagnation region but the stagnation point oscillated back and forth due to alternate vortex shedding from the rear of the cylinder.

Vortices such as those in Fig. 7 were only visible for Reynolds numbers based on wire diameter of less than about

120. At higher Reynolds numbers the wire wakes became unstable and finally fully turbulent making it impossible to see the vortices. The heat transfer pattern, however, remained unchanged at all Reynolds numbers indicating that the vortices must still be there but could not be seen. A time exposure photograph was taken in the hope that the random fluctuations from the wire wakes would be averaged out and the relatively steady vortex pattern would thus be made visible. The random fluctuations were indeed averaged out but no steady vortices could be seen.

Summary of Results

This report has presented results of a study to investigate the relationship between free-stream turbulence and heat transfer augmentation in the stagnation region. The effects of free-stream turbulence and surface roughness on spanwise averaged heat transfer were investigated. Turbulence measurements were made upstream of a cylinder placed in the wake of an array of parallel wires that were perpendicular to the cylinder axis. Finally, flow visualization and thermal visualization techniques were combined to show the relationship between vortices in the stagnation region and spanwise variations in heat transfer.

The major conclusions were:

1 Heat transfer in the stagnation region is the highest where turbulent fluctuations were found to be the lowest. This occurred between the wakes formed by parallel wires upstream and perpendicular to the axis of the cylinder. This corresponds to the region between vortex pairs where the velocity induced by the vortices was toward the cylinder surface. Conversely, the lowest heat transfer occurred where the induced velocity was away from the cylinder surface.

2 Vortices formed in the stagnation region from mean velocity gradients are well outside the theoretical laminar boundary layer.

3 The boundary layer downstream of the stagnation point remains laminar in the presence of free-stream turbulence and is forced into transition by surface roughness for the range of Reynolds numbers and turbulence levels tested.

4 Vorticity in the form of mean velocity gradients is amplified as it approaches the stagnation region.

5 Turbulent fluctuating velocity is amplified as it approaches the stagnation region, reaches a peak, and then is damped as it approaches the boundary layer.

6 Surface roughness has no effect on heat transfer at the stagnation point.

7 Free-stream turbulence has the same effect on heat transfer at the stagnation point for smooth and rough cylinders.

References

1 Frossling, N., "Evaporation, Heat Transfer, and Velocity Distribution in Two-Dimensional and Rotationally Symmetrical Laminar Boundary-Layer Flow," NACA TM-1432, 1958.

2 Smith, M. C., and Kuethe, A. M., "Effects of Turbulence on Laminar Skin Friction and Heat Transfer," *Physics of Fluids*, Vol. 9, No. 12, Dec. 1966, pp. 2337–2344.

3 Kestin, J., and Wood, R. T., "The Influence of Turbulence on Mass Transfer From Cylinders," ASME JOURNAL OF HEAT TRANSFER, Vol. 93, No. 11, Nov. 1971, pp. 321–327.

4 Giedt, W. H., "Effect of Turbulence Level of Incident Air Stream on Local Heat Transfer and Skin Friction on a Cylinder," *Journal of the Aeronautical Sciences*, Vol. 18, No. 11, Nov. 1951, pp. 725–730, 766.

5 Hanarp, L. R., and Sunden, B. A., "Structure of the Boundary Layers on a Circular Cylinder in the Presence of Free-Stream Turbulence," *Letters in Heat and Mass Transfer*, Vol. 9, May–June 1982, pp. 169–177.

6 Lowery, G. W., and Vachon, R. I., "Effect of Turbulence on Heat Transfer From Heated Cylinders," *International Journal of Heat and Mass Transfer*, Vol. 18, No. 11, Nov., pp. 1229–1242.

7 Wang, C. R., "Turbulence and Surface Heat Transfer Near the Stagnation Point of a Circular Cylinder in Turbulent Flow," NASA TM-83732, 1984.

8 Gorla, R. S. R., and Nemeth, N., "Effects of Free-Stream Turbulence Intensity and Integral Length Scale on Heat Transfer From a Circular Cylinder in Crossflow," in: *Heat Transfer 1982*, U. Grigull et al., eds., Vol. 3, Hemisphere, Washington, D.C., 1982, pp. 153–158.

9 Sutera, S. P., Maeder, P. F., and Kestin, J., "On the Sensitivity of Heat Transfer in the Stagnation-Point Boundary Layer to Free-Stream Vorticity," *Journal of Fluid Mechanics*, Vol. 16, Part 4, Aug. 1963, pp. 497–520.

10 Sutera, S. P., "Vorticity Amplification in Stagnation-Point Flow and Its Effect on Heat Transfer," *Journal of Fluid Mechanics*, Vol. 21, Part 3, Mar. 1965, pp. 513–534.

11 Britter, R. E., Hunt, J. C. R., and Mumford, J. C., "The Distortion of Turbulence by a Circular Cylinder," *Journal of Fluid Mechanics*, Vol. 92, Part 2, May 28, 1979, pp. 269–301.

12 Sadeh, W. Z., and Brauer, H. J., "Coherent Sub-structure of Turbulence Near the Stagnation Zone of a Bluff Body," *Journal of Wind Engineering and Industrial Aerodynamics*, Vol. 8, No. 1–2, July 1981, pp. 59–72.

13 Sadeh, W. Z., and Sullivan, P. P., "Turbulence Amplification in Flow About an Airfoil," ASME Paper No. 80-GT-111.

14 Hodson, P. R., and Nagib, H. M., "Vortices Induced in a Stagnation Region by Wakes—Their Incipient Formation and Effects on Heat Transfer From Cylinders," AIAA Paper No. 77-790, June 1977.

15 Morkovin, M. V., "On the Question of Instabilities Upstream of Cylindrical Bodies," NASA CR-3231, 1979.

16 Schlichting, H., *Boundary Layer Theory*, 4th ed., McGraw-Hill, New York, p. 78.

17 Jansen, B. J., Jr., "Flow Visualization Through the Use of the Smoke Wire Technique," AIAA Paper No. 81-0412, Jan. 1981.

18 Hippensteele, S. A., Russell, L. M., and Stepka, F. S., "Evaluation of a Method for Heat Transfer Measurements and Thermal Visualization Using a Composite of a Heater Element and Liquid Crystals," ASME JOURNAL OF HEAT TRANSFER, Vol. 105, No. 1, Feb. 1983, pp. 184–189.

19 VanFossen, G. J., et al., "Heat Transfer Distributions Around Nominal Ice Accretion Shapes Formed on a Cylinder in the NASA Lewis Icing Research Tunnel," AIAA Paper No. 84-0017, Jan. 1984.

20 Kline, S. J., and McClintock, F. A., "Describing Uncertainties in Single-Sample Experiments," *Mechanical Engineering*, Vol. 75, No. 1, Jan. 1953, pp. 3–8.

21 Marziale, M. L., and Mayle, R. E., "Mass Transfer From a Circular Cylinder—Effects of Flow Unsteadiness and 'Slight Nonuniformities'," Rensselaer Polytechnic Institute, Troy, New York, Sept. 1984 (NASA CR-174759).

Heat Transfer Effects of a Longitudinal Vortex Embedded in a Turbulent Boundary Layer

P. A. Eibeck
Assistant Professor,
Department of Mechanical Engineering,
University of California—Berkeley,
Berkeley, CA

J. K. Eaton
Associate Professor,
Department of Mechanical Engineering,
Stanford University,
Stanford, CA 94305
Assoc. Mem. ASME

The heat transfer effects of an isolated longitudinal vortex embedded in a turbulent boundary layer were examined experimentally for vortex circulations ranging from $\Gamma/U_\infty\delta_{99} = 0.12$ to 0.86. The test facility consisted of a two-dimensional boundary-layer wind tunnel, with a vortex introduced into the flow by a half-delta wing protruding from the surface. In all cases, the vortex size was of the same order as the boundary-layer thickness. Heat transfer measurements were made using a constant-heat-flux surface with 160 embedded thermocouples to provide high resolution of the surface-temperature distribution. Three-component mean-velocity measurements were made using a four-hole pressure probe. Spanwise profiles of the Stanton number showed local increases as large as 24 percent and decreases of approximately 14 percent. The perturbation to the Stanton number was persistent to the end of the test section, a length of over 100 initial boundary-layer thicknesses. The weakest vortices examined showed smaller heat transfer effects, but the Stanton number profiles were nearly identical for the three cases with circulation greater than $\Gamma/U_\infty\delta_{99} = 0.53$ cm. The local increase in the Stanton number is attributed to a thinning of the boundary layer on the downwash side of the vortex.

Introduction

Longitudinal vortices embedded in boundary layers occur in a large variety of flow situations. Some examples are Taylor–Görtler vortices in boundary layers on concavely curved surfaces, horseshoe vortices formed by an obstruction protruding from a surface, and wingtip vortices impinging on a downstream surface. These flow situations occur in numerous practical devices for which heat transfer rates are important. One well-known example is the gas turbine in which vortices such as skew-induced and Taylor-Görtler vortices interact along the endwalls and blade surfaces. The life of a turbine stage could be significantly reduced by strong, localized heat transfer induced by stationary vortices.

In most practical cases, an embedded vortex has a cross-stream length scale approximately equal to the boundary-layer thickness. Therefore, the vortex is capable of strongly perturbing the boundary-layer structure and modifying the heat transfer characteristics. In addition, longitudinal vortices usually maintain their coherence over a long, streamwise distance, meaning that the heat transfer effects behind an effective vortex generator are likely to be very persistent.

Many researchers have observed longitudinal vortices in various complex flow configurations. However, relatively few have made heat transfer measurements. Numerous workers, including So and Mellor (1972), Ellis and Joubert (1974), Meroney and Bradshaw (1975), and Mayle et al. (1979) found evidence of large longitudinal vortices embedded in turbulent boundary layers developed on concave surfaces. These vortices are sufficiently stable that their presence is apparent in long-time-averaged data. Heat transfer rates in such curved, turbulent flows were measured by Kreith (1955), Thomann (1968), Brinich and Graham (1977), and Mayle et al. (1979). Increases in the average heat transfer rate of 20 to 40 percent over comparable flat-plate values were found. In all cases, the heat transfer measurements were averaged over the span of the facility. Therefore, local heat transfer augmentation due to the longitudinal vortices may have been much larger than 40 percent. It should be noted that destabilization of the boundary layer by concave curvature may cause heat transfer augmentation by some mechanism other than longitudinal vortices. However, flow-visualization work by Jeans and Johnston (1982) indicates that longitudinal vortical structures dominate all other features of the boundary layer on concave surfaces.

Kelleher and co-workers (McCormack et al. (1970), McKee (1973), Flentie (1975), Durão (1977), and Kelleher et al. (1979)) at the Naval Postgraduate School have examined the effects of Taylor–Görtler vortices on heat transfer in laminar boundary layers and duct flows. Local heat transfer rates were increased by as much as 190 percent over flat-plate values. This effect indicates the possible large effects of longitudinal vortices.

Several investigators have carefully examined the passage vortex in turbine cascades. Langston (1980) presented a model of the endwall secondary flow which is based on an experimental study in a turbine cascade (Langston et al., 1977), and Sieverding (1985) gives a summary of the current understanding of these flows. Heat transfer to the endwall of either turbine or vane cascades was measured by Blair (1974), Graziani et al. (1980), Georgiou et al. (1979), Dunn and Stoddard (1978), Hylton et al. (1981), Booth (1975), Dring (1971), Louis (1973), Goldstein and Chen (1985), and Goldstein and Karni (1984). In general, a substantial heat transfer augmentation due to the passage vortex has been observed.

Gaugler and Russell (1984) used flow visualization to study a cascade scaled directly to that used by Hylton et al. (1981). Direct comparisons were then made between the endwall contour plots of Stanton number published by Hylton et al. and the visualization results. The only obvious correlation found was between the horseshoe vortex and the endwall heat transfer maximum near the vane leading edge.

There have been two detailed studies in which isolated vortices or vortex pairs have been purposely introduced into boundary layers. Spangler and Wells (1964) introduced a series of counterrotating vortex pairs into a turbulent boundary layer using rectangular plates mounted normal to the wall but at an angle of attack relative to the oncoming flow. Most of the experiments were done with the common flow (at the center of the vortex pair) moving away from the wall. The

Contributed by the Heat Transfer Division for publication in the JOURNAL OF HEAT TRANSFER. Manuscript received by the Heat Transfer Division April 1, 1985.

Table 1 Boundary-layer characteristics

Streamwise Distance x (cm)	Boundary Layer Thickness δ_{99} (cm)	Displacement Thickness δ^* (cm)	Momentum Thickness θ (cm)	Shape Fractor H	Skin Friction $C_f \times 10^3$	Reynolds Number Re_θ
-28	.837	.120	.089	1.35	4.60	1026
13	1.51	.228	.169	1.35	3.85	1910
44	1.94	.292	.213	1.37	3.57	2385
59	2.05	.319	.234	1.36	3.50	2628
74	2.22	.335	.246	1.36	3.45	2839
104	2.51	.387	.286	1.35	3.33	3267
120	2.66	.418	.308	1.36	3.34	3427
135	2.81	.427	.317	1.35	3.29	3654

data included mean velocity profiles and measurements of the mean skin friction using a floating element force balance. They found that the average skin friction was increased somewhat, suggesting that the heat transfer would also be increased. They used the law of the wall to infer the spanwise variation of the skin friction from the mean velocity profiles and found spanwise variations as large as 20 percent. It should be noted that the law of the wall is not accurate in three-dimensional flows such as the embedded vortex flow. However, their results are probably at least qualitatively correct. Spangler and Wells did not measure heat transfer or turbulence data.

Mehta et al. (1981) studied an isolated vortex embedded in a turbulent boundary layer and an isolated vortex pair in which the common flow was away from the wall. The vortices were generated using half-delta wings mounted in the settling chamber of the wind tunnel. They found that the half-delta wings produced stable and long-lived vortices which had relatively little axial velocity deficit. They measured mean velocity profiles and turbulence quantities primarily using hot-wire anemometry. Like Spangler and Wells, Mehta et al. inferred the skin friction from mean velocity profiles, finding spanwise variations as large as 60 percent. Their turbulence data indicated that conventional eddy viscosity models and even transport equation methods will probably not be able to predict embedded vortex flows. They did not measure either heat transfer or near-wall data.

In summary, several studies have shown that longitudinal vortices may have a substantial effect on heat transfer rates. However, the effect of the longitudinal vortex on heat transfer has never been isolated, and the mechanisms by which it may affect heat transfer rates are as yet not understood. A longitudinal vortex can possibly affect heat transfer rates in three ways. First, the large-scale vortical motion locally changes the mean velocity field and mean temperature field. Secondly, the vortex modifies the turbulence properties in a complex three-dimensional way. This changes the effective diffusivity to heat and therefore affects heat transfer rates. Finally, the vortex may modify the near-wall layers of the boundary layer, the sublayer, and the buffer layer which contribute a large fraction of the total resistance to heat transfer.

The overall objective of the present research program is to increase the physical understanding of the heat transfer effects of a longitudinal vortex in a turbulent boundary layer. The strategy is to introduce vortices of various sizes and strengths into an otherwise unperturbed two-dimensional boundary layer. The effects of the vortex will then be isolated from other effects, such as longitudinal pressure gradient or strong overall three-dimensionality. The experiments provide spatially resolved heat transfer data coupled with three-component velocity measurements. The measurements thus allow association of the local heat transfer behavior with specific features of the vortex. The data also provide a well-documented test case for computational procedures.

Experimental Apparatus

The primary experimental facility was a low-speed, open-circuit, boundary-layer wind tunnel. Air was supplied to the test section by a computer-controlled blower and passed through a turbulence-management section which included a honeycomb, three screens, and a 4.8:1 contraction discharging into the 12.7 cm × 60 cm rectangular test section. The freestream velocity at the inlet plane was 16 m/s, and the freestream turbulence intensity was approximately 0.3 percent. The uniformity of the flow was checked by making span-

Nomenclature

C = specific heat
C_f = skin-friction coefficient $= \tau_0/\rho(U_\infty^2/2)$
h = heat transfer coefficient $= \dot{q}_0''/(T_0 - T_\infty)$
H = vortex generator height
H = shape factor
k = thermal conductivity
Pr = molecular Prandtl number $= \nu/\alpha$
$\dot{q}''$ = heat flux
r_0 = vortex core radius
Re_θ = momentum thickness Reynolds number $= U_\infty\theta/\nu$
Re_x = length Reynolds number $= U_\infty x/\nu$
Re_Γ = vortex Reynolds number $= |\Gamma|/\nu$
St = Stanton number $= h/\rho C U_\infty$
U = mean streamwise velocity
U_∞ = local freestream velocity
V = mean normal velocity
W = mean spanwise velocity
x = spatial coordinate, streamwise direction
y = spatial coordinate, normal direction
Y_c = normal location of vortex center
z = spatial coordinate, spanwise direction
Z_c = spanwise location of vortex center
α = molecular thermal diffusivity
Γ = vortex circulation
δ_{99} = boundary layer thickness
δ^* = displacement thickness
θ = momentum thickness of boundary layer
ν = kinematic viscosity
ρ = fluid density
Ω = vorticity

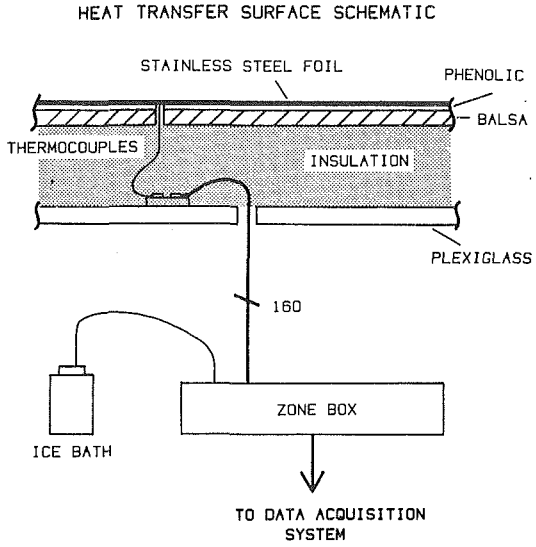

Fig. 1 Sketch of the heat transfer test plate

wise surveys of the mean velocity at several heights above the wall. The peak deviations within the boundary layer were less than 2 percent from the mean, while the freestream was uniform to within 0.1 percent.

The boundary layer of interest developed on one of the 60-cm-wide test-section walls. It experienced a slightly favorable pressure gradient of about -10 Pa/m because the test section was a constant-area channel. The boundary layer was tripped at the entrance to the test section and developed as a two-dimensional turbulent boundary layer. The flow two dimensionality was checked by computing both mass and momentum balances. The centerline mass flux at the test-section exit was within 0.5 percent of the inlet centerline mass flux. All of the terms for an integral momentum balance, including mean velocity and static pressure profiles at the inlet and exit planes and the skin friction along the entire length of the test section, were measured. The momentum equation was found to balance within 0.6 percent of the inlet momentum flux. Table 1 is a summary of the measured boundary layer parameters along the length of the test section.

The heat transfer coefficient was measured on a 60 cm × 117 cm constant-heat-flux surface comprising a segment of the test-section wall. The test plate was positioned to give an unheated starting length of 76 cm from the boundary-layer trip. The plate (see Fig. 1) consists of a thin (0.076 mm), stainless steel foil glued to a 1.6-mm-thick layer of canvas-filled phenolic. The phenolic was backed by a 1.2-cm-thick layer of balsa wood and 5 cm of fiber insulation. Alternating current was supplied to the busbars at either end of the test plate via a variable transformer and a large stepdown transformer. Typical power dissipation was 480 W and this resulted in surface temperatures of approximately 45°C. Heat conduction through the back surface accounted for less than 1 percent of the total heat generation, while conduction along the surface accounted for a smaller fraction, even in regions of high temperature gradient. Therefore, the heat flux from the surface was very uniform, and the heat transfer coefficient could be determined by measuring the difference between the surface and freestream temperatures, typically about 20°C. Radiation loss was estimated to be approximately 2.5 percent of the total heat flux and was accounted for in the final data reduction.

The surface temperature was measured using four spanwise rows of 37 type-K thermocouples (0.076 mm diameter), which were spot-welded to the back surface of the foil. An additional 12 thermocouples were distributed axially along the centerline of the surface. The thermocouple wires were attached to larger-gauge thermocouple extension wire which led to an isothermal zone box. Copper wires were attached between the zone box and the backplane of an HP Model 3495A relay scanner which multiplexed the thermocouple voltages into a Data Precision (Model 3600) digital voltmeter. The freestream temperature was measured with an additional type-K thermocouple connected directly to the zone box. The entire temperature-measurement system was controlled via an IEEE 488 bus from a Digital Equipment MINC Computer.

The power input to the surface was determined by measuring the current supplied and the voltage drop across the surface. The foil was assumed to behave as a purely resistive load, a fact that was confirmed by measuring the phase lag between the current and voltage signal. A Weston Model 904 in-line ammeter was used. The meter was calibrated at a commercial standards lab immediately prior to the experiments. A fine wire was spot-welded to the foil at each end for direct and accurate measurement of the voltage drop using a Fluke Model 88104 digital voltmeter.

The uncertainty in the measurement of the local heat transfer coefficient was estimated by combining uncertainties in the measurement of the power supplied, in the local temperature measurement, and in the correction applied for radiation and conduction losses. The uncertainty in the power measurement was 4 percent, based on instrumentation accuracy and fluctuations in the power during the course of data taking. The temperature measurements were obtained by applying a linear relationship provided by the manufacturer to the thermocouples signals. An uncertainty in the temperature measurements was estimated to be 0.2°C by comparing these measurements with those obtained from 20 individually calibrated surface thermocouples. The total correction for conduction and radiation losses was approximately 3.5 percent of the power supplied. This correction was subject to an uncertainty of about 1 percent, primarily due to uncertainty in the estimate of the surface emissivity. The component uncertainties were combined using the method of Kline and McClintock (1953), resulting in a total uncertainty of 5 percent in the measurement of the heat transfer coefficient.

The heat transfer test plate was qualified by performing a two-dimensional energy balance and by comparing flat-plate values to well-known correlations. Temperature and velocity profiles were measured at two streamwise locations and the convective energy flux was determined by numerical integration of the profiles. The measured increase in the convective energy flux was within 1.7 percent of the power supplied by the test plate.

The measured Stanton numbers for a two-dimensional turbulent boundary layer case were compared with two predictions: an unheated starting length solution assuming constant free-stream velocity and constant heat-flux boundary conditions presented in Kays and Crawford (1980), and the prediction of STAN 5 which includes the slight pressure gradient effects. The measured Stanton number distribution was approximately 6 percent higher than the predictions. The deviation, which is slightly higher than the uncertainty estimate, is most likely due to local drops in surface temperature at the thermocouple locations. This was probably caused by nonuniformities in the metal due to the welding process.

All three components of the mean-velocity field were measured using a four-hole pressure probe described in detail by Youssefmir (1982). This probe is a slight modification of the probe originally designed by Shepherd (1981). It is capable of resolving the velocity vector within a 25 deg cone, which is more than adequate for the present experiments. Three Validyne Model DP45 pressure transducers were used to measure the pressure differences needed by the data-reduction scheme. The probe tip was approximately 3 mm in diameter, making the results somewhat sensitive to velocity gradient. In particular, a negative pitch angle was measured in a region of

Table 2 Vortex characteristics

Case	Vortex Generator		Vortex Properties				
	Height (cm)	Angle of Attack (degrees)	x (cm)	Γ/U_∞ (cm)	$-\Gamma/U_\infty\delta_{99}$	Center Height (cm)	Core Radius (cm)
Base	2	12	30	-0.78	0.60	1.5	0.67
Base	2	12	60	-0.69	0.53	1.57	0.87
Base	2	12	90	-0.57	0.44	1.78	0.97
Base	2	12	120	-0.50	0.38	1.96	1.24
Vortex II	1	12	60	-0.27	0.21	---*	---*
Vortex II	1	12	120	-0.16	0.12	1.25	1.17
Vortex III	2	5	60	-0.27	0.21	1.47	0.86
Vortex IV	2	20	60	-1.06	0.82	1.82	0.71
Vortex V	3	12	60	-1.12	0.86	2.26	0.81

*Method would not converge correctly for these two parameters.

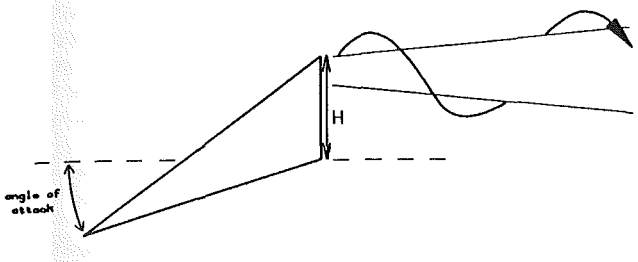

CASE	H (cm)	ANGLE OF ATTACK	VORTEX REYNOLDS #
Base	2	12	7100
Vortex II	1	12	2800
Vortex III	2	5	2800
Vortex IV	2	20	10900
Vortex V	3	12	11500

Fig. 2 Vortex generator characteristics

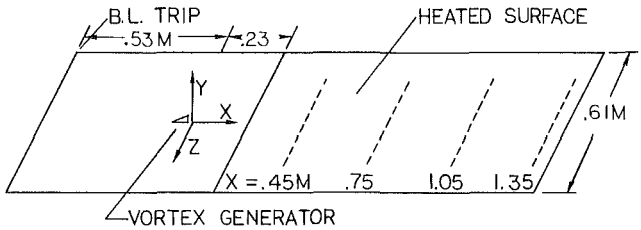

Fig. 3 Coordinate system for data presentation; dashed lines indicate primary temperature-measurement spans

positive velocity gradient. A first-order correction scheme originally proposed by Westphal et al. (1985) was used. The normal and spanwise gradients of the axial velocity were computed by fitting splines to the measured data. Corrections to the pitch and yaw angles were then found by multiplying the gradient by an empirically determined coefficient. The coefficient was found by testing the probe in turbulent boundary layers of varying thicknesses. Westphal et al. estimated the uncertainty in the four-hole probe measurements by testing the probe in well-understood boundary layers and by comparing the measurements to a rotatable cross-wire probe. They concluded that the uncertainty in the pitch and yaw angles was 0.5 deg and the uncertainty in the velocity magnitude was less than 5 percent.

An ordinary total pressure probe 0.7 mm in diameter was used for two-dimensional boundary-layer measurements during the qualification stage of the experiment. The Young and Maas (1936) velocity-gradient correction scheme was used for this proble. The pressure probes were inserted through spanwise slots in the wall opposite the test plate and positioned by a two-axis, computer-controlled traverse mechanism located outside the tunnel. The spanwise slots were sealed by a flexible gasket when in use and a flush-mounting plug when not in use.

The longitudinal vortex was generated by a half-delta wing placed normal to the test wall at an angle of attack relative to the oncoming flow (see Fig. 2). The leading edge of the vortex generator was placed 48 cm downstream of the boundary-layer trip. At this location, the boundary-layer thickness was approximately 1.3 cm and the momentum-thickness Reynolds number was 1700. Five vortex generators were used in order to investigate the effect of changing the vortex strength and height above the surface. Table 2 summarizes the vortex-generator geometries as well as the characteristics of the resulting vortex. As expected, an increase in the vortex-generator size resulted in a larger circulation but also raised the height of the vortex center. An increase in the angle of attack increased the circulation while raising the vortex center only slightly.

The nondimensional vortex circulation ranged from $T/U_\infty\delta_{99}=0.12$ to 0.86. Good data are not available for estimating the vortex circulation for most practical situations, but the present range is probably typical of vortices on curved walls. The data of Mehta et al. (1981) indicate that a typical horseshoe vortex also has a circulation in the present range. However, the three-component velocity measurements of Langston et al. (1977) in a turbine cascade indicate the presence of a much stronger vortex than we were able to generate.

Results and Discussion

Figure 3 defines the coordinate system used for data presentation. The origin of the axial (x) coordinate is located 53 cm downstream of the boundary-layer trip, the approximate location of the vortex-generator trailing edge. The y coordinate is normal to the surface, and the positive z direction is selected to give a right-handed coordinate system, with $z=0$ corresponding to the centerline. The leading edge of the heat transfer surface is at $x=23$ cm, resulting in an unheated starting length of 76 cm measured from the boundary-layer trip.

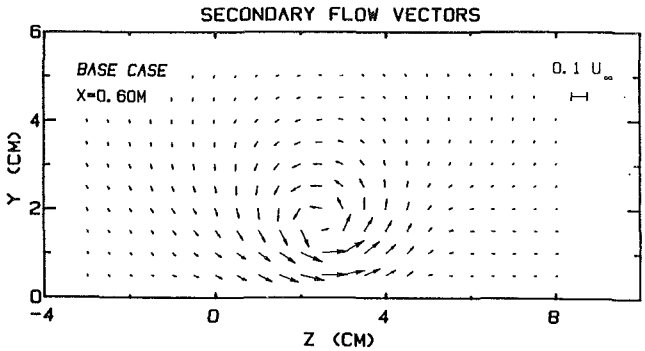

Fig. 4(*a*) Mean-velocity data for the base-case vortex at $x = 60$ cm; secondary flow velocity vectors

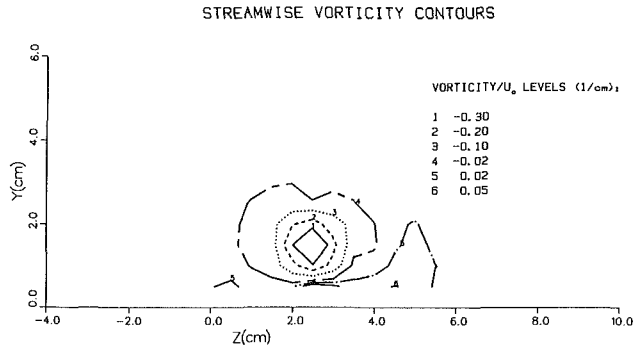

Fig. 4(*b*) Mean-velocity data for the base-case vortex at $x = 60$ cm; axial vorticity = Ω/U_∞

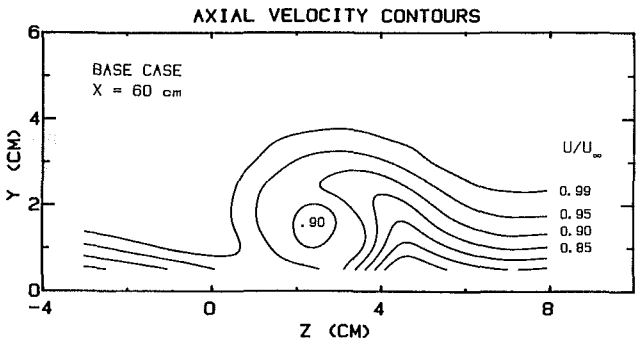

Fig. 4(*c*) Mean-velocity data for the base-case vortex at $x = 60$ cm; axial velocity = U/U_∞

Fluid-Mechanics Results. Detailed mean-velocity data for each of the five vortex cases were measured at $x = 60$ cm and used for the calculation of the vortex properties. The axial development of the vortex for the base case (2-cm-high vortex generator at 12 deg angle of attack) was examined using velocity measurements at four stations ranging from $x = 30$ cm to $x = 120$ cm. As will be shown below, measurements at one axial station are sufficient to define the vortex properties.

The velocity measurements for the base case vortex at $x = 60$ cm illustrate the typical features of the velocity field associated with an embedded longitudinal vortex. Figures 4(*a–d*) present the data in a y–z plane looking in the downstream flow direction. The secondary velocity vectors (V and W components of the velocity vector) shown in Fig. 4(*a*) are very similar to those of a two-dimensional vortex adjacent to a solid wall. The presence of an image vortex below the wall is evidenced by the high crossflow velocities measured near the wall. The presence of the image causes the vortex axis to be skewed at an angle of 3 deg relative to the wind-tunnel centerline. However, there

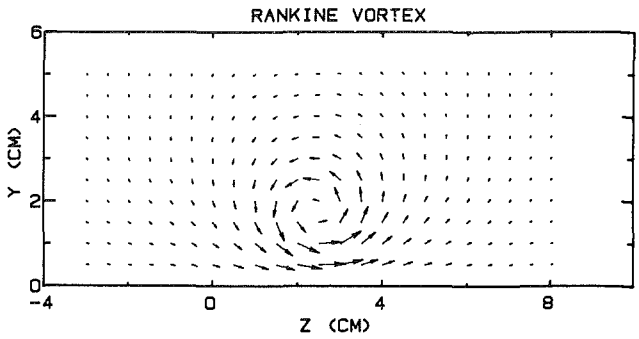

Fig. 5 Rankine vortex modeling for the base-case at $x = 60$ cm

was no evidence of temporal meandering of the vortex in agreement with the recent work of Westphal et al. (1985).

The axial component of the vorticity was estimated by fitting splines to the data in both the normal and spanwise direction and analytically differentiating the splines. A contour plot of the vorticity (Fig. 4*b*) shows the presence of a vortical core surrounded by nonvortical fluid. The vortical core is roughly circular, suggesting that the vortex can be approximately modeled as a Rankine vortex with an image. Figure 5 presents the velocity field for a Rankine vortex with the same circulation and core radius as the measured vortex. The agreement is reasonable except near the upflow region of the vortex. Separation can occur here, leading to the generation of a secondary longitudinal vortex which is not represented in the Rankine vortex model.

The contour plot of the axial velocity (Fig. 4*c*) shows the profound effect the vortex has on the boundary layer. On the upwash side of the vortex, low-speed fluid is lifted away from the wall and the boundary-layer thickness is about twice the undisturbed value. The boundary layer is thinned to less than half its undisturbed thickness on the downwash side of the vortex. High-speed fluid is swept into the near-wall region below the vortex. The relatively weak vortex imposed negligible variations of the static pressure, so an isobar plot of the total pressure would appear identical to Fig. 4(*c*).

Two methods may be used to estimate the integral parameters which describe the vortex, namely, the circulation and the core radius. In the first method,[1] the circulation is estimated by integrating the axial vorticity inside a closed contour. We chose the contour which represents 20 percent of peak vorticity level, to avoid integrating noise. The core radius is then defined as the average radius of the 20 percent contour. The second method uses the Rankine vortex model described above. The data were fitted to the Rankine vortex model using four adjustable parameters: the circulation (Γ), the core radius (r_0), and the coordinates (Y_c and Z_c) of the vortex center. The four parameters were chosen to minimize the error parameter:

$$E(\Gamma, r_0, Y_c, Z_c) = \sum_i |v_i - v_{c_i}| + |w_i - w_{c_i}|$$

where v_i and w_i are the normal and spanwise mean-velocity components at the ith measurement point and the subscript c indicates velocities calculated from the model. The two methods have been found to give comparable results (see Eaton and Pauley (1985)). The Rankine vortex method was used for the data presented in Table 2.

As the vortex developed, the secondary velocities decreased and the core radius increased. Figures 6(*a–c*) show the base-case vortex of Figs. 4(*a–d*) at a downstream location. The peak vorticity level has fallen markedly, but the core has expanded. The axial-velocity contour plots for the two locations look

[1] This method was developed by Dr. R. Westphal of the NASA-Ames Research Center who helped us evaluate our vortex data.

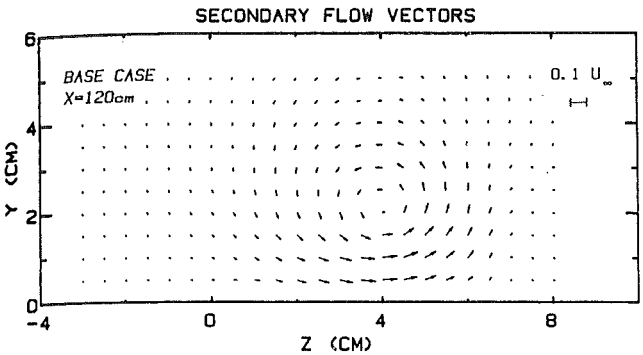

Fig. 6(*a*) Mean-velocity data for the base-case vortex at $x = 120$ cm; secondary flow-velocity vectors

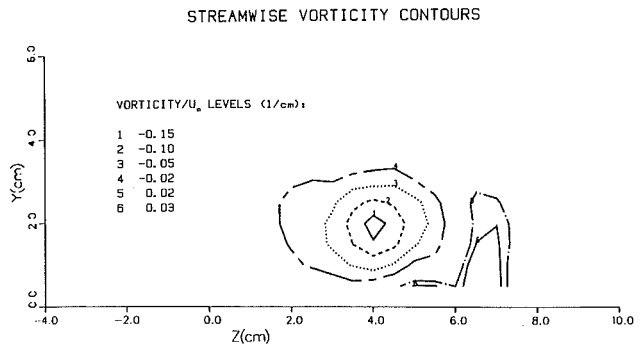

Fig. 6(*b*) Mean-velocity data for the base-case vortex at $x = 120$ cm; axial vorticity = Ω/U_∞

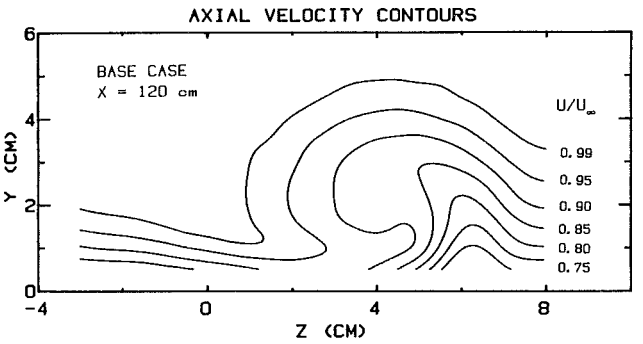

Fig. 6(*c*) Mean-velocity data for the base-case vortex at $x = 120$ cm; axial velocity = U/U_∞

very similar, even though the secondary velocities are considerably lower at the downstream location.

Table 2 gives circulation estimates for the base-case vortex at four axial locations. The circulation decayed quite slowly, despite the fact that the vortex was embedded in a turbulent boundary layer. The circulation at $x = 120$ cm was still over 60 percent of the value at $x = 30$ cm. This finding is consistent with the results of Westphal et al. (1985), who examined vortices developing under both zero and adverse pressure-gradient conditions. The data in Table 2 also show that the vortex lifted slowly away from the surface as it developed. The height of the vortex center for the base case was 1.5 cm at $x = 30$ cm and 1.95 cm at $x = 120$ cm. Because of the slow development of the vortex documented above, it is adequate to define the vortex properties by measurements at one axial location.

Figures 7(*a–d*) show the secondary velocity vectors for the four vortex cases not already shown. Increasing the generator size increases the vortex circulation, the secondary velocities, and the height of the vortex center. Increasing the vortex-generator angle of attack increases the circulation and the

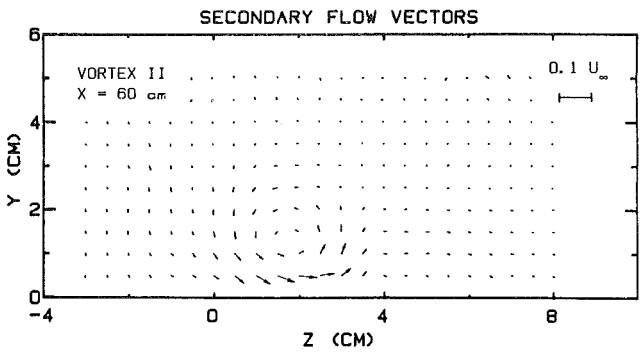

Fig. 7(*a*) Secondary velocity vectors at $x = 60$ cm; 1 cm, 12 deg

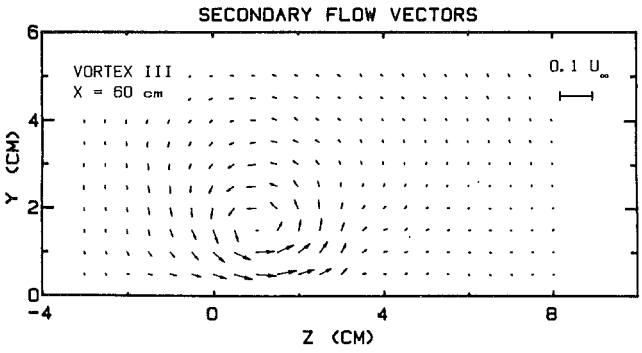

Fig. 7(*b*) Secondary velocity vectors at $x = 60$ cm; 2 cm, 5 deg

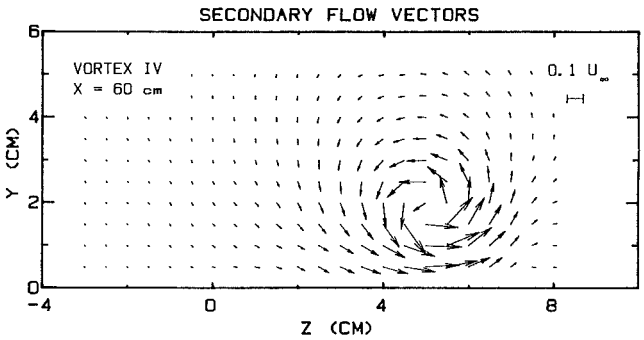

Fig. 7(*c*) Secondary velocity vectors at $x = 60$ cm, 2 cm, 20 deg

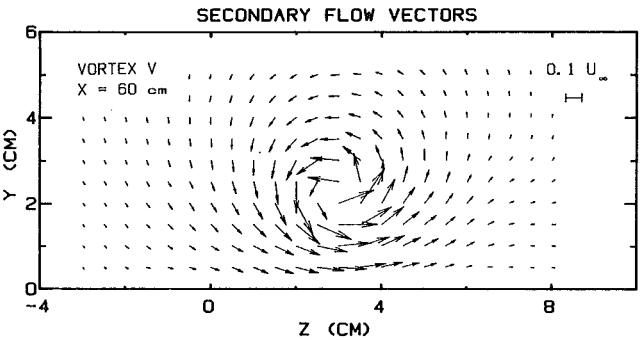

Fig. 7(*d*) Secondary velocity vectors at $x = 60$ cm; 3 cm, 12 deg

secondary velocity magnitudes without significantly changing the core radius. The height of the vortex center increases slightly with increasing angle of attack.

Heat Transfer Results. The heat transfer coefficient data are presented in normalized form as the Stanton number ($St = h/\rho c U_\infty$). The density and specific heat were evaluated at the film temperature, and the local value of U_∞ was used.

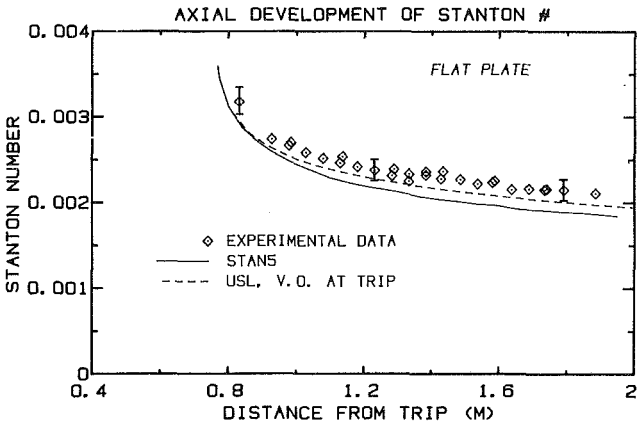

Fig. 8 Stanton number data for the flat plate (note: USL = unheated starting length solution)

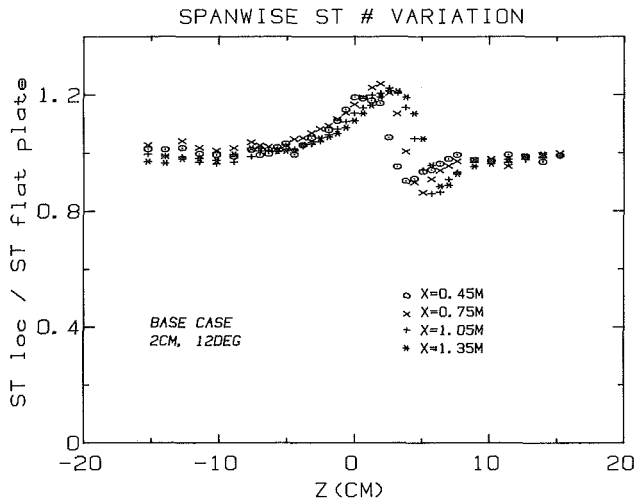

Fig. 9 Stanton number data for the base case

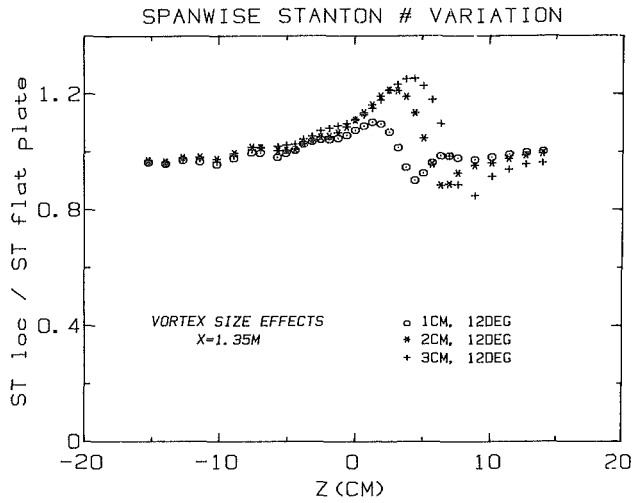

Fig. 10 Stanton number effects of varying the vortex-generator size

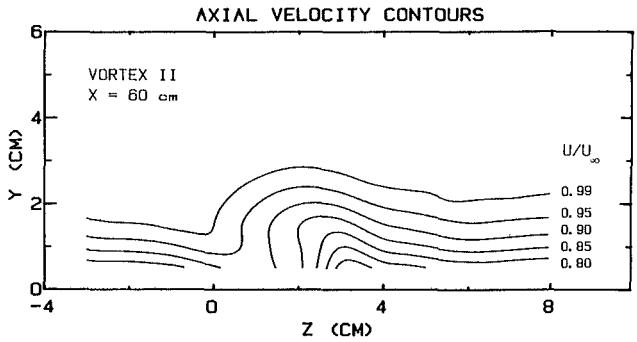

Fig. 11 Axial-velocity contour plot for the 1 cm vortex-generator case at $x = 60$ cm

Figure 8 presents the Stanton number data for the flat plate (no vortex) case along the centerline, and averaged across the tunnel span at the locations of the spanwise thermocouple distribution. These data were used to normalize all the measurements for the vortex cases.

Heat transfer data were measured at the four primary axial locations shown on Fig. 3. The results for the base case are shown in Fig. 9. Several features are immediately apparent. First, the vortex causes a peak augmentation of the local heat transfer coefficient of approximately 25 percent and a local decrease as large as 15 percent. The spanwise variations in the heat transfer coefficient can be directly related to the mean-velocity field. The peak occurs in the downwash region near the point of minimum boundary-layer thickness. The minimum in the Stanton number curve is associated with the upwash region, where warm, low-momentum fluid from the near-wall zone is swept upward to thicken the boundary layer. The heat transfer effects are localized to the immediate vicinity of the vortex, the Stanton number being equal to the flat-plate value away from the vortex.

There is very little axial variation in the heat transfer effects caused by the vortex. The skewing of the vortex axis is obvious, but the peak heat transfer augmentation and the spanwise width of the affected region are unchanged downstream of $x = 90$ cm. The perturbation in the heat transfer coefficient is smaller at locations upstream of $x = 60$ cm (not shown in Fig. 9) probably because the flat-plate Stanton number is higher at this location. Near the leading edge of the heat transfer surface, the thermal boundary layer is so thin that it cannot be significantly perturbed by the vortex. Some data are available at $x = 28$ cm, 5 cm downstream of the leading edge of the heat transfer surface. The effects of the vortex are virtually undiscernible in these data.

The axial development is similar to the base case for all five vortex cases examined. The data at $x = 135$ cm were selected as representative of the heat transfer behavior in the various cases. Figure 10 shows the effect of varying the vortex-generator size, which causes significant changes in the heat transfer behavior. The peak heat transfer augementation is less than 10 percent for the smallest vortex generator, while it is 21 percent and 24 percent for the 2 cm and 3 cm vortex generators, respectively. The minimum heat transfer coefficient is the same for the 1 cm and 2 cm cases, and only slightly lower for the 3 cm case.

The effects on the heat transfer behavior of changing the vortex-generator size can be partially explained by examining an axial velocity-contour plot. The peak heat transfer for the 1-cm-high generator is about 10 percent lower than the base case. A plot of the axial velocity (Fig. 11) shows that the weaker vortex is not capable of thinning the boundary layer to the same degree. However, a vortex even stronger than the base case increases the Stanton number only slightly. The boundary layer may become so thin that it is no longer turbulent, thereby limiting the increase in the Stanton number.

The data and the argument above suggest an asymptotic behavior for the peak Stanton number as a function of vortex circulation. However, further increases in the vortex strength beyond that tested here may result in larger Stanton numbers. The downward velocity could become so large that the downwash region would behave more like an impinging jet than a thinned boundary layer. Asymptotic behavior is

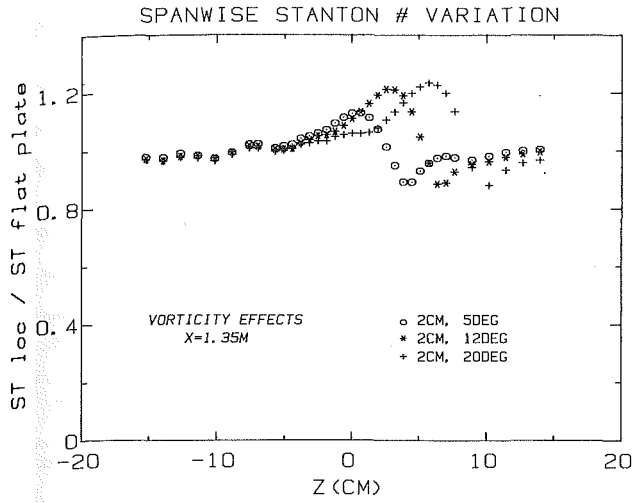

Fig. 12 Stanton number effects of varying the vortex-generator angle

reached very early on the upwash side, where the Stanton number reduction is nearly the same for all of the cases examined.

Figure 12 shows the effect of varying the vortex generator's angle of attack while keeping its size constant. Increasing the angle of attack has the effect of increasing the vortex circulation while changing the vortex height only slightly. The Stanton number curves are nearly identical for the 12 and 20 deg cases, the peak augmentation levels being 21 and 23 percent, respectively. The minimum level is the same for both cases. The only significant difference between the 12 and 20 deg cases is the spanwise location of the vortex. The spanwise velocity of the vortex increases with increasing strength of the image vortex, accounting for the change in spanwise position. The heat transfer effect of the 5 deg vortex generator is much smaller than for the other two cases. The peak Stanton number augmentation is only 14 percent, but the minimum level is the same as for the other two cases. This vortex would cause only a small increase in the spanwise-averaged heat transfer.

The most important feature of the present results is the strong persistence of the heat transfer effects of an embedded vortex. The circulation of the vortex decays slowly, and the secondary velocity magnitude decreases as the core grows. However, the heat transfer effects are virtually unchanged, even for the smallest vortices. The axial length of the test section is of the order of 100 boundary-layer thicknesses, so some decay of the vortex effects should have been expected.

The present results imply that the longitudinal vortex imposes local modifications in the heat transfer coefficient through distortion of the mean flow rather than by modifying the turbulence field or by the larger skin friction magnitude caused by the spanwise flow. Although near-wall turbulence measurements are not available, the data of Westphal et al. (1985) have shown that the turbulence levels are lower than normal in the downwash region of a longitudinal vortex and higher than normal in the upwash region. If these turbulence effects were dominant, they would have resulted in heat transfer behavior opposite to that observed. The crossflow component of the skin friction would also have a small effect on local heat transfer because the vortices are weak. The peak yaw angle for the present cases was approximately 10 deg so the crossflow component of the skin friction had a small effect on the vector magnitude.

It is the influence of the vortex on the mean flow through thinning and thickening of the boundary layer that resulted in the variations in heat transfer. This conclusion can be supported by a very simple calculation. An effective origin is determined for the boundary layer at a given spanwise position by treating that layer as two dimensional. A flat-plate correlation $StPr^{0.4} = 0.0295Re_x^{-0.2}$ from Kays and Crawford (1980) is then used to estimate the heat transfer coefficient. Comparing the results of this procedure for the base case at the thinnest point in the boundary layer and in the undisturbed region away from the vortex, we estimate a local increase in the Stanton number of 27 percent, in good agreement with the data.

The above suggests that the Reynolds analogy between the skin-friction coefficient and the Stanton number may remain valid. Other two-dimensional heat transfer correlations might also apply, possibly leading to simple prediction methods for this flow. Before this can be verified, more details need to be known about the behavior of the boundary layer in the presence of the longitudinal vortex. Such data are available in a full report by Eibeck and Eaton (1985) and will be discussed in a forthcoming paper.

Conclusions

Longitudinal vortices of moderate size and strength have been found to cause a significant perturbation in the heat transfer behavior of an otherwise two-dimensional boundary layer. Local Stanton number increases as great as 24 percent and decreases of 14 percent have been observed, resulting in a net increase in the spanwise-averaged heat transfer coefficient. All of the vortices studied were remarkably persistent, despite the fact that they were embedded in a turbulent boundary layer. The heat transfer effects of the vortex did not decay significantly in any of the cases examined, even though the test section length was over 100 initial boundary-layer thicknesses.

The effects of the longitudinal vortex on the Stanton number can be attributed largely to the distortion of the mean velocity field. Distortion of the turbulence field apparently has little effect on the heat transfer.

The present data provide a useful test case for prediction schemes. A complete specification of the velocity field is available at an early station. Although the work of Mehta et al. (1981) suggests that embedded vortex flows would be very difficult to predict, the present results give reason for optimism. A calculation of the mean-field distortion should be sufficient to provide a good estimate of the Stanton number.

We are unaware of any data which couple velocity measurements with heat transfer measurements for naturally occurring vortices in practical flow fields. Such data would be very useful to determine whether embedded vortices are an important feature in the practical devices. The weakest vortices examined here had a relatively small effect on the local Stanton number and very little effect on the spanwise-averaged heat transfer. Such vortices may appear in flow visualization but actually be of relatively minor importance. On the other hand, stronger vortices can cause a substantial local augmentation of the heat transfer rate, even in a turbulent boundary layer. It is important that the effects of such vortices be recognized by heat transfer prediction schemes.

Acknowledgments

We gratefully acknowledge the financial support of the Department of Energy, Office of Basic Energy Sciences (Project Agreement DE-AT03-83ER13081). We also appreciate the help of Mr. Wayne Pauley, who developed many of the data-reduction codes, and Drs. R. Westphal, R. Mehta, and J. Johnston, with whom we had many useful discussions.

References

Blair, M. F., 1974, "An Experimental Study of Heat Transfer and Film Cooling on Large-Scale Turbine Endwalls," ASME JOURNAL OF HEAT TRANSFER, Vol. 96, pp. 524–529.

Booth, T. C., 1975, "An Analysis of the Turbine Endwall Boundary Layer and Aerodynamic Losses," ASME Paper No. 75-GT-23.

Brinich, P. F., and Graham, R. W., 1977, "Flow and Heat Transfer in a Curved Channel," NASA TND-8464.

Dring, R. P., 1971, "A Momentum Integral Analysis of the Three-Dimensional Turbine End-Wall Boundary Layer," ASME Paper No. 71-GT-6.

Dunn, M. G., and Stoddard, F. J., 1978, "Measurement of Heat Transfer Rate to a Gas Turbine Stator," ASME *Journal of Engineering for Power*, Vol. 101.

Durão, M. C., 1977, "Investigation of Heat Transfer in Straight and Curved Rectangular Ducts Using Liquid Crystal Thermography," M.S. Thesis, Naval Postgraduate School, Monterey, CA.

Eaton, J. K., and Pauley, W. R., 1985, "Techniques for Estimating Scalar Parameters Describing Embedded Longitudinal Vortices," Rept. No. IL-77, Department of Mechanical Engineering, Stanford University, Stanford, CA.

Eibeck, P. A., and Eaton, J. K., 1985, "An Experimental Investigation of the Heat Transfer Effects of a Longitudinal Vortex Embedded in a Turbulent Boundary Layer," Report MD-48, Thermo. Division, Department of Mechanical Engineering, Stanford University, Stanford, CA.

Ellis, L. B., and Joubert, P. N., 1974, "Turbulent Shear Flow in a Curved Duct," *J. Fluid Mech.*, Vol. 64, Part 1, pp. 54–84.

Flentie, D. L., 1975, "An Experimental Study of Taylor–Görtler Vortices in a Curved, Rectangular Channel," M.S. Thesis, Naval Postgraduate School, Monterey, CA.

Gaugler, R. E., and Russell, L. M., 1984, "Comparison of Visualized Turbine Endwall Secondary Flows and Measured Heat Transfer Patterns," ASME *Journal of Engineering for Gas Turbines and Power*, Vol. 106, pp. 168–172.

Georgiou, D. P., Godard, M., and Richards, B. E., 1979, "Experimental Study of the Iso-Heat-Transfer-Rate Lines on the Endwall of a Turbine Cascade," ASME Paper No. 79-GT-20.

Goldstein, R. J., and Chen, H. P., 1985, "Film Cooling on a Gas Turbine Blade Near the End Wall," ASME *Journal of Engineering for Gas Turbines and Power*, Vol. 107, pp. 117–122.

Goldstein, R. J., and Karni, J., 1984, "The Effect of a Wall Boundary Layer on Local Mass Transfer From a Cylinder in Crossflow," ASME *Journal of Engineering for Gas Turbines and Power*, Vol. 106, pp. 260–267.

Graziani, R. A., Blair, M. F., Taylor, J. R., and Mayle, R. E., 1980, "An Experimental Study of Endwall and Airfoil Surface Heat Transfer in a Large-Scale Turbine Blade Cascade," ASME *Journal of Engineering for Power*, Vol. 102, p. 257.

Hylton, L. D., Mihelc, M. S., Turner, E. R., and York, R. E., 1981, *Experimental Investigation of Turbine Endwall Heat Transfer*, AFWAL-TR-81-2077, three volumes.

Jeans, A. J., and Johnston, J. P., 1982, "The Effects of Streamwise Concave Curvature on Turbulent Boundary Layer Structure," Rept. MD-40, Thermosciences Division, Department of Mechanical Engineering, Stanford University, Stanford, CA.

Kays, W. M., and Crawford, M. E., 1980, *Convective Heat and Mass Transfer*, 2nd ed., McGraw-Hill, New York.

Kelleher, M. D., Flentie, D. L., and McKee, R. J., 1979, "An Experimental Study of the Secondary Flow in a Curved, Rectangular Channel," ASME Paper No. 79-FE-6.

Kline, S. J., and McClintock, F. A., 1953, "Describing Uncertainties in Single-Sample Experiments," *Mechanical Engineering*, pp. 3–8.

Kreith, F., 1955, "The Influence of Curvature on Heat Transfer to Incompressible Fluids," *Trans. ASME*, Vol. 77, No. 11, pp. 1247–1256.

Langston, L. S., 1980, "Crossflows in a Turbine Cascade Passage," ASME *Journal of Engineering for Power*, Vol. 102, No. 4, pp. 866–874.

Langston, L. S., Nice, M. L., and Hooper, R. M., 1977, "Three-Dimensional Flow Within a Turbine Cascade Passage," ASME *Journal of Engineering for Power*, Vol. 99, pp. 21–28.

Louis, J. F., 1973, "Investigation of Factors Affecting Heat Transfer to Turbine End Walls," TR-73-93, Air Force Aero-Propulsion Laboratory.

Mayle, R. E., Blair, M. F., and Kopper, F. C., 1979, "Turbulent Boundary Layer Heat Transfer on Curved Surfaces," ASME JOURNAL OF HEAT TRANSFER, Vol. 101, No. 3, pp. 521–525.

McCormack, P. D., Welker, H., and Kelleher, M., 1970, "Taylor-Görtler Vortices and Their Effect on Heat Transfer," ASME JOURNAL OF HEAT TRANSFER, Vol. 92, pp. 101–112.

McKee, R. J., 1973, "An Experimental Study of Taylor–Görtler Vortices in a Curved, Rectangular Channel," Engineer's Thesis, Naval Postgraduate School, Monterey, CA.

Mehta, R. D., Shabaka, I. M. M. A., and Bradshaw, P., 1981, "Imbedded Longitudinal Vortices in Turbulent Boundary Layers," Aspects of Aerodynamic Flows, California State University, Long Beach, CA.

Meroney, R. N., and Bradshaw, P., 1975, "Turbulent Boundary Layer Growth Over a Longitudinally Curved Surface," *AIAA Journal*, Vol. 13, No. 11, pp. 1448–1453.

Shepherd, I. L., 1981, "A Four-Hole Pressure Probe for Fluid Flow Measurements," ASME *Journal of Fluids Engineering*, Vol. 103, pp. 590–594.

Sieverding, C. H., 1985, "Recent Progress in the Understanding of Basic Aspects of Secondary Flows in Turbine Blade Passages," ASME *Journal of Engineering for Gas Turbines and Power*, Vol. 107, pp. 248–257.

So, R. M. C., and Mellor, G. L., 1972, "An Experimental Investigation of Turbulent Boundary Layers Along Curved Surfaces," NASA CR-1940.

Spangler, J. G., and Wells, C. S., Jr., 1964, "Effects of Spiral Longitudinal Vortices on Turbulent Boundary-Layer Skin Friction," NASA-CR-145.

Thomann, H., 1968, "Effect of Streamwise Wall Curvature on Heat Transfer in a Turbulent Boundary Layer," *Journal of Fluid Mechanics*, Vol. 33, Part 2, pp. 283–292.

Westphal, R. V., Eaton, J. K., and Pauley, W. R., 1985, "Interaction Between a Vortex and a Turbulent Boundary Layer in a Streamwise Pressure Gradient," 5th International Symposium on Turbulent Shear Flows, Cornell University, Ithaca, NY.

Young, A. D., and Maas, J. N., 1936, "The Behavior of a Pitot Tube in a Transverse Total-Pressure Gradient," Report No. 1770, Aero. Res. Council.

Youssefmir, P., 1982, "Flow Studies of Full-Coverage Film Cooling on a Convexly Curved Surface," Engineer's Thesis, Department of Mechanical Engineering, Stanford University, Stanford, CA.

Numerical Prediction of Flow and Heat Transfer in a Parallel Plate Channel With Staggered Fins

K. M. Kelkar

S. V. Patankar
Mem. ASME

Department of Mechanical Engineering,
University of Minnesota,
Minneapolis, MN 55455

Fluid flow and heat transfer in two-dimensional finned passages were analyzed for constant property laminar flow. The passage is formed by two parallel plates to which fins are attached in a staggered fashion. Both the plates are maintained at a constant temperature. Streamwise periodic variation of the cross-sectional area causes the flow and temperature fields to repeat periodically after a certain developing length. Computations were performed for different values of the Reynolds number, the Prandtl number, geometric parameters, and the fin-conductance parameter. The fins were found to cause the flow to deflect significantly and impinge upon the opposite wall so as to increase the heat transfer significantly. However, the associated increase in pressure drop was an order of magnitude higher than the increase in heat transfer. Streamline patterns and local heat transfer results are presented in addition to the overall results.

Introduction

Compact heat exchangers are being used increasingly in industrial applications. The flow in these devices is often laminar because of the small dimensions of the passage and low velocities employed. Augmentation of heat transfer in laminar flow is especially important because of the low heat transfer coefficients obtained from smooth channels. Augmentation techniques usually employ fins attached to the heat transfer surfaces so as to provide additional surface area for heat transfer and to cause improved mixing. However, correct arrangement of fins is crucial to have any improvement in heat transfer at all. A study of heat transfer in circumferentially finned tubes [1] shows that, for fluids like air, such fins actually lower the heat transfer because the fins cause the throughflow to detach from the tube wall and reduce the washing of the tube surface. A similar behavior is expected if, in a parallel plate channel, fins are placed on the opposite walls, at the same streamwise location. If, however, the fins are staggered they will cause the flow to deflect and impinge upon the opposite walls thereby increasing the washing action there. The purpose of this paper is to analyze the flow and heat transfer in a parallel plate channel with staggered fins on the two walls as shown in Fig. 1(*a*).

It can be seen that the geometry considered consists of equally spaced transverse fins that are located in a staggered arrangement on the two walls. Figure 1(*b*) shows the details of the geometry of the channel. The fins have the same height F, which provides a partial blockage of the channel of width H. The blockage tends to increase the flow velocity and causes deflection of the main flow so that impingement on one of the walls is created. Fins also lead to recirculation zones, which are expected to augment heat transfer. In this paper, a computational analysis for the steady, two-dimensional, laminar flow is presented. It gives overall results about heat transfer and pressure drop; also the details of velocity and temperature fields provide insight into the physical processes involved.

After the present study was completed, an experimental investigation [2] for the same configuration appeared in the literature. It, however, concentrates on results at rather high Reynolds numbers, mostly in the turbulent flow regime. Only some flow visualization photographs are given for the Reynolds number of 600. Thus, although no direct quantitative comparisons are possible between the present computations and the results of [2], some useful inferences can be drawn from [2] to support the simplifying assumptions employed here. Incidentally, the flow patterns computed in the present work do agree with the flow visualization given in [2].

In the present work, the flow is regarded as steady and laminar, and Reynolds numbers up to 500 are used. For the configuration considered, whether the flow truly remains steady and laminar at these Reynolds numbers is a valid question, because vortex shedding may occur at the fin tips. The evidence provided by [2], however, indicates that the flow is laminar and free of vortex shedding for the Reynolds number of 600. The assumption of steady laminar flow in the present work, therefore, seems to be justified.

Mathematical Formulation

Since the geometry shown in Fig. 1(*a*) contains identical geometric modules, the flow is expected to attain, after a short entrance regime, a periodic fully developed regime, in which the velocity field repeats itself from module to module. This expectation is validated by the results of [2], where the flow became periodic after only 3–5 modules in the entrance region. The concept of a periodic fully developed flow and a solution

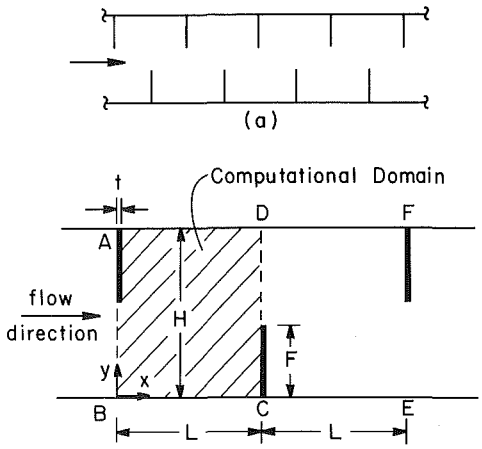

Fig. 1 The geometry considered

Contributed by the Heat Transfer Division for publication in the JOURNAL OF HEAT TRANSFER. Manuscript received by the Heat Transfer Division October 22, 1984. Paper No. 84-HT-70.

procedure for it were described in [3]. It is thus possible to calculate the flow and heat transfer in a typical module such as ABEF shown in Fig. 1(*b*), without the need for the entrance-region calculations. This obviously provides considerable economy of computational effort. A further saving can be obtained in the present case by observing that the flows in the half-modules ABCD and DCEF would exhibit inverted symmetry. It is thus possible to confine the computation to the half-module ABCD. It may be noted that this reduction in effort is available in the present problem because the fins on the two walls are considered to have the same height and the spacing BC equals spacing CE.

Since the basic calculation scheme has been described in detail in [3], the description here will be limited to only the main features of the procedure and to the details associated with the handling of inverted symmetry for the half-module. Also, for the calculation of the periodic temperature field, a modified technique will be described, which is easier to implement than the one given in [3].

Flow Field. The flow is assumed to be laminar and fluid properties to be constant. As explained in [3], the pressure p in a periodically fully developed flow can be expressed by

$$p(x, y) = -\beta x + P(x, y) \tag{1}$$

where β is a constant representing the overall pressure gradient imposed on the flow; βL gives the pressure drop over the region ABCD considered. The quantity $P(x, y)$ behaves in a periodic manner so that

$$P(x, y) = P(x+L, H-y) \tag{2}$$

which expresses the inverted symmetry between the modules ABCD and DCEF. The flow is governed by continuity and momentum equations, which can be written as

$$\frac{\partial u}{\partial x} + \frac{\partial v}{\partial y} = 0 \tag{3}$$

$$\rho\left(u\frac{\partial u}{\partial x} + v\frac{\partial u}{\partial y}\right) = \beta - \frac{\partial P}{\partial x} + \mu\left(\frac{\partial^2 u}{\partial x^2} + \frac{\partial^2 u}{\partial y^2}\right) \tag{4}$$

$$\rho\left(u\frac{\partial v}{\partial x} + v\frac{\partial v}{\partial y}\right) = -\frac{\partial P}{\partial y} + \mu\left(\frac{\partial^2 v}{\partial x^2} + \frac{\partial^2 v}{\partial y^2}\right) \tag{5}$$

The periodic nature of the flow and the inverted symmetry lead to the boundary conditions given by:

Top and bottom wall and fin surfaces:

$$u = 0 \tag{6}$$

$$v = 0 \tag{7}$$

Left and right boundaries:

$$u(0, y) = u(L, H-y) \tag{8}$$

$$v(0, y) = -v(L, H-y) \tag{9}$$

On left and right boundaries, the same conditions hold for all x-direction derivatives of u and v velocities. The negative sign appearing in the periodic boundary condition for v is one of the rather subtle consequences of the concept of inverted symmetry.

Since the boundary conditions do not involve the specification of any inflow velocities, the flow rate through the channel cannot be directly prescribed. On the other hand, the pressure gradient β must be specified for the solution of equations (3)–(5). For a given value of β, there will be a corresponding value of the flow rate in the channel. In a computational solution, it is possible to iteratively adjust various quantities so that the converged solution is obtained for a desired flow or Reynolds number. In this manner, the velocity field can be seen to be completely governed by the Reynolds number Re and the geometric parameters L/H and F/H. The fin thickness t is assumed to be negligible in comparison with the spacing L; thus the ratio t/L is not considered as an additional parameter for the flow field. The Reynolds number and friction factor are defined as

$$\mathrm{Re} = \rho \bar{u} D_H / \mu \tag{10}$$

$$f = \beta D_H / \left(\frac{1}{2}\rho \bar{u}^2\right) \tag{11}$$

where

Nomenclature

C_p = specific heat of fluid at constant pressure
D_H = hydraulic diameter for the channel, equation (13)
F = height of fins, Fig. 1
f = friction factor, equation (11)
H = height of the channel, Fig. 1
h = local heat transfer coefficient on top or bottom wall, equation (25)
$\bar{h}$ = overall heat transfer coefficient, for the half-module based on combined top and bottom surface area only, equation (23)
k = thermal conductivity of the fluid
k_{fin} = thermal conductivity of the fin material
L = separation between fins, Fig. 1
LMTD = log-mean temperature difference for the half-module, equation (24)
Nu = local Nusselt number, equation (26)
$\overline{\mathrm{Nu}}$ = overall Nusselt number, for the half-module, equation (22)
Nu_0 = Nusselt number for channel without fins
P = periodic part of pressure, equation (1)
p = static pressure
Pr = Prandtl number of the fluid $= \mu C_p/k$
Q = total heat transfer rate in the half module
q = local heat flux over the channel surface
q_{av} = average heat flux over the fin surface
Re = Reynolds number, equation (10)
T = temperature
T_b = bulk temperature of the fluid, equation (16)
T_w = constant temperature of the top and bottom walls of the channel
t = thickness of the fins, Fig. 1
u = velocity of the fluid in x direction
$\bar{u}$ = average velocity of the fluid in x direction, equation (12)
v = velocity of the fluid in y direction
x = x coordinate, Fig. 1
y = y coordinate, Fig. 1
β = overall rate of pressure drop, equation (1)
θ = dimensionless temperature, equation (15)
λ = fin-conductance parameter, equation (19)
μ = dynamic viscosity of the fluid
ρ = density of the fluid
ψ_0 = maximum value of normalized stream function in the main recirculating eddy

Subscripts

L, R = left and right faces of the fin
0 = finless channel

$$\bar{u} = \frac{1}{H}\int_0^H u dy \tag{12}$$

$$D_H = 2H \tag{13}$$

It should be noted that the presence of the fins has not been taken into account in defining D_H and $\bar{u}$. The resulting values of f and Re are, therefore, directly comparable to those for a channel without fins.

Temperature Field. The thermal boundary condition employed here is that of constant and equal temperature T_w on the top and bottom surfaces. This condition leads to a thermally developed regime which is periodic in character.

The governing equation for the temperature field is

$$\rho C_p\left(u\frac{\partial T}{\partial x} + v\frac{\partial T}{\partial y}\right) = \frac{\partial}{\partial x}\left(k\frac{\partial T}{\partial x}\right) + \frac{\partial}{\partial y}\left(k\frac{\partial T}{\partial y}\right) \tag{14}$$

In the periodic region, the field of the temperature θ defined by

$$\theta = \frac{T - T_w}{T_b - T_w} \tag{15}$$

repeats identically from module to module. The bulk temperature T_b introduced in equation (15) is given by

$$T_b = \int_0^H |u|Tdy \Big/ \int_0^H |u|dy \tag{16}$$

The absolute value of the velocity u is used here so that the regions with reverse flow are properly represented.

The boundary conditions for temperature are:

Top and bottom walls:

$$T(x, 0) = T(x, H) = T_w \tag{17}$$

Left and right boundaries:

$$\frac{T(0, y) - T_w}{T_b(0) - T_w} = \frac{T(L, H-y) - T_w}{T_b(L) - T_w} \tag{18}$$

where the periodicity in θ and the inverted symmetry has been used. All derivatives of θ in the x direction also obey inverted symmetry on the left and right boundaries.

The boundary conditions on the fin surfaces are dependent on the conduction in the fin material. If the fins are sufficiently thin, the temperature variation within the fin thickness can be ignored. Then, the temperature variation along the fin will be governed by a fin-conductance parameter λ, given by

$$\lambda = k_{\text{fin}} t/(kL) \tag{19}$$

where the conductivity k in the denominator is the fluid conductivity. Such a parameter has been used in [4]. For a very large value of λ, the fins assume uniform temperature equal to T_w. When λ approaches zero, fins become adiabatic.

The solution of equation (14) along with the boundary conditions (17) and (18) presents an eigenvalue problem, since it is the variable θ, and not T, that behaves in a periodic fashion and since the $T_b(x)$ is not known a priori. A procedure to solve this eigenvalue problem has been described in detail in [3]; however, it is somewhat complicated and an easier and more direct procedure is developed here.

To explain the details of the procedure let $0+$ denote the x position of the grid line located to the right of the line AB in Fig. 1(*b*) just inside the calculation domain. The symbol $0-$ indicates the grid line just outside the domain. Similarly, $L+$ and $L-$ will denote the grid line locations to the right and left of DC. If equation (14) for the dimensional temperature T were to be solved numerically, the values of $T(0-, y)$ and $T(L+, y)$ would be required as the neighbor-point temperatures from outside of the calculation domain. Expressions for these can be obtained by employing equation (18) in the following manner

$$\frac{T(0-, y) - T_w}{T_b(0-) - T_w} = \frac{T(L-, H-y) - T_w}{T_b(L-) - T_w} \tag{20}$$

Here T_w is the prescribed wall temperature. In addition, $T_b(0-)$ can be given any arbitrary value (different from T_w). The difference $T_b(0-) - T_w$ represents the scaling factor for the temperature field. In principle, one can establish any arbitrary value of $T_b(0-)$ by adjusting the inlet temperature to the whole channel. It is important to understand that the dimensionless results of the solution are independent of the particular value of $T_b(0-)$ used in the computation. Equation (20) now indicates that $T(0-, y)$ is obtainable in terms of the temperatures within the calculation domain. Since $T(L-, H-y)$ and $T_b(L-)$ would be changing during an iterative solution of the temperature field, the value of $T(0-, y)$ as given by equation (20) should be iteratively updated.

At the right boundary, the outside temperature $T(L+, y)$ is similarly given by

$$\frac{T(L+, y) - T_w}{T_b(L-) - T_w} = \frac{T(0+, H-y) - T_w}{T_b(0-) - T_w} \tag{21}$$

where the periodic nature of the dimensionless temperature of θ has been used. Again, $T(L+, y)$ is to be iteratively calculated in terms of the temperatures within the domain.

The additional parameters required to determine the heat transfer behavior are the Prandtl number Pr and the fin-conductance parameter λ. The overall Nusselt number is defined as

$$\overline{\text{Nu}} = \bar{h}D_H/k \tag{22}$$

where

$$\bar{h} = Q/(2L)(\text{LMTD}) \tag{23}$$

and Q is the rate of total heat transfer over the module ABCD. The quantity $(2L)$ represents the surface area of the top and bottom walls. It should be noted that the extra area provided by the fins is not included in the definition of $\bar{h}$. The resulting values of $\overline{\text{Nu}}$, therefore, are directly proportional to the amount of heat transfer for a given temperature difference. The log-mean temperature difference LMTD is defined as

$$\text{LMTD} = \frac{[T_w - T_b(L)] - [T_w - T_b(0)]}{\ln\{[T_w - T_b(L)]/[T_w - T_b(0)]\}} \tag{24}$$

A local heat transfer coefficient over top and bottom walls was defined as

$$h = q/(T_w - T_b) \tag{25}$$

where q is the local heat flux. The resulting local Nusselt number is given by

$$\text{Nu} = hD_H/k \tag{26}$$

Computational Details. The governing equations were solved numerically. Most of the details of the method can be found in [5]. The SIMPLER procedure as given in [5] was used for handling the flow field.

In the solution of the velocity field, the solid fin region was treated by using a very large value of viscosity in that region. The solution of the flow field for a desired value of Re was obtained as follows. Starting with a tentative value of μ, the velocity field and hence $\bar{u}$ were calculated. With this $\bar{u}$, the viscosity was adjusted to maintain a constant Re. This iterative updating of μ finally led to the converged solution.

All computations were performed on a 50×50 grid. In the x direction, the grid spacing was fine near the fins. In the y direction, the spacing was fine near the top and bottom as well as near the fin tips. Computations for $\text{Re} = 500$, $F/H = 0.5$, and $L/H = 1$ indicated a change of 2 percent in the Nusselt numbers between the solutions of 50×50 and 65×65 grids. As this change is small, the accuracy of the solutions on a 50×50

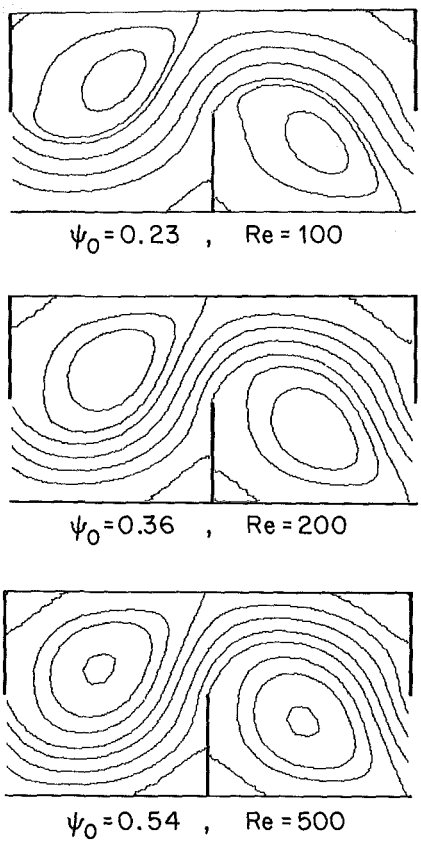

Fig. 2 Velocity fields for different Reynolds numbers

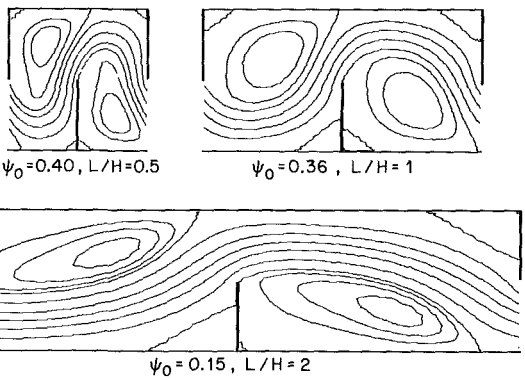

Fig. 3 Velocity fields for different fin spacings

grid was deemed satisfactory. The number of overall iterations of the SIMPLER algorithm ranged from 100 to 400, with the case of Re = 500, $F/H = 0.5$, and $L/H = 1$ requiring the largest computational effort.

The effect of Re on the flow field was studied by varying Re from 100 to 500, while L/H and F/H were maintained at 1 and 0.5 respectively. Calculations were not performed for higher Reynolds numbers because for the complex flow patterns predicted, it is unlikely that the flow will remain laminar for Reynolds numbers that are appreciably greater than 500. The fin spacing L/H was varied from 0.5 to 2 for Re = 200 and $F/H = 0.5$ to study its effect on flow field. To obtain the influence of fin height, F/H was varied from 0.25 to 0.75 for Re = 200 and $L/H = 1$.

For each of the velocity field computed, temperature problem was solved for Pr = 0.7 and Pr = 4 for two values of the fin-conductance parameter $\lambda = 0$ and $\lambda = \infty$. The effect of λ on heat transfer was considered in detail for the case of Re = 500, $L/H = 1$, and $F/H = 0.5$ by varying λ from 0 to ∞.

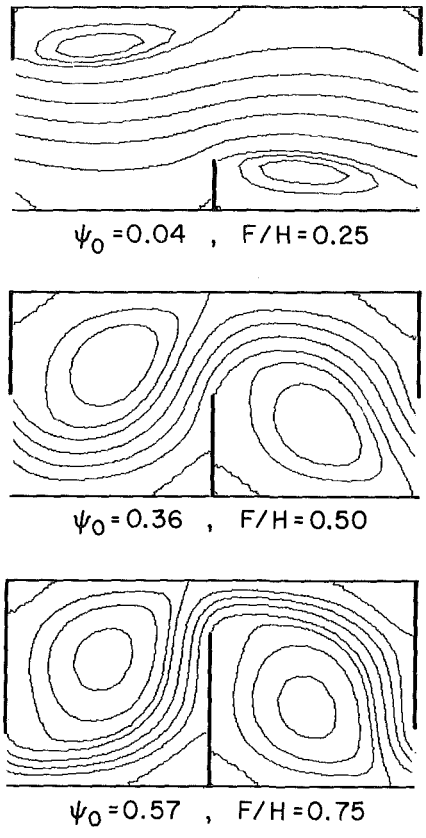

Fig. 4 Velocity fields for different fin heights

Results and Discussion

Flow Field. Streamline plots in Figs. 2–4 show the effect of various parameters on the flow field. Although the computations were confined to the half-module ABCD in Fig. 1(*b*), the streamline patterns have been shown for the complete module in order to facilitate the flow visualization. In all cases, a major portion of the module is occupied by recirculating flow with small secondary recirculations at the base of the fins. It can be seen that the presence of fins causes the flow to bend and impinge significantly on the top and bottom walls and on the upstream surface of fins. The strength of recirculating flow in each case is judged from the value of ψ_0 listed in the figures; ψ_0 is the ratio of the flow rate in the major recirculating eddy to the flow rate of the throughflow.

The effect of Reynolds number on the flow field is shown in Fig. 2. As Re increases, the relative strength and size of the recirculation zone grows causing the throughflow to bend more significantly. The effect of decreasing the fin spacing is qualitatively very similar to increasing Re as is evident in Fig. 3. The effect of increasing fin height is also very similar to that of increasing Re. As shown in Fig. 4, the throughflow is only slightly distorted for short fins, and the distortion becomes more severe as the fin height is increased.

Overall Heat Transfer and Friction Factor. The overall results of the computations are presented in Figs. 5–7 in terms of the ratios $\overline{Nu}/Nu_0$ and $f\mathrm{Re}/(f\mathrm{Re})_0$ where the subscript 0 refers to the unfinned parallel plate channel. The values of Nu_0 and $(f\mathrm{Re})_0$ are 7.54 and 96, respectively. The ratios shown in Figs. 5–7 are above one in almost all cases, indicating the heat transfer augmentation caused by the fins and the associated pressure-drop penalty. For heat transfer, two sets of curves are shown for the limiting cases of highly conducting fins ($\lambda = \infty$) and nonconducting fins ($\lambda = 0$). The improvement in heat transfer for the $\lambda = \infty$ case is due to both the change in

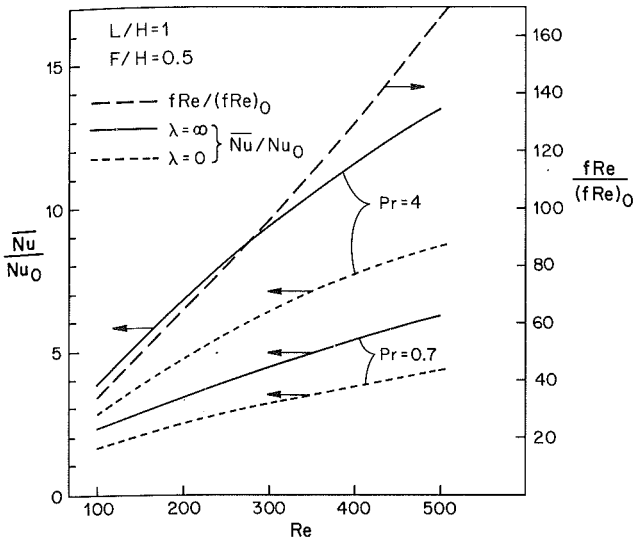

Fig. 5 Variation of friction factor and overall Nusselt number with Reynolds number

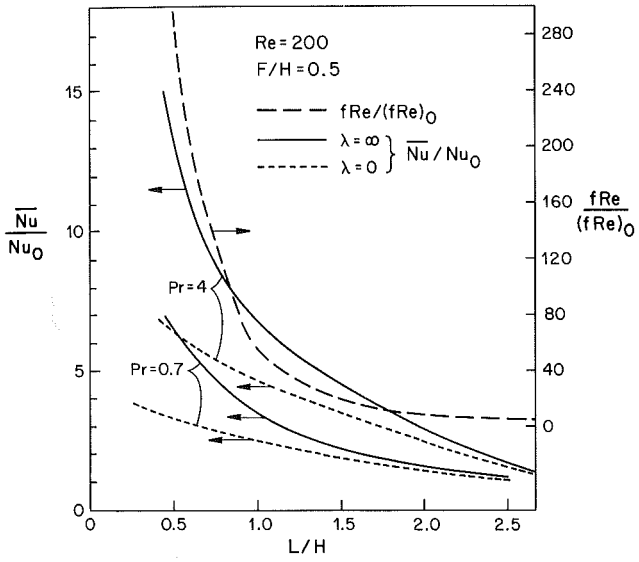

Fig. 6 Variation of friction factor and overall Nusselt number with fin spacing

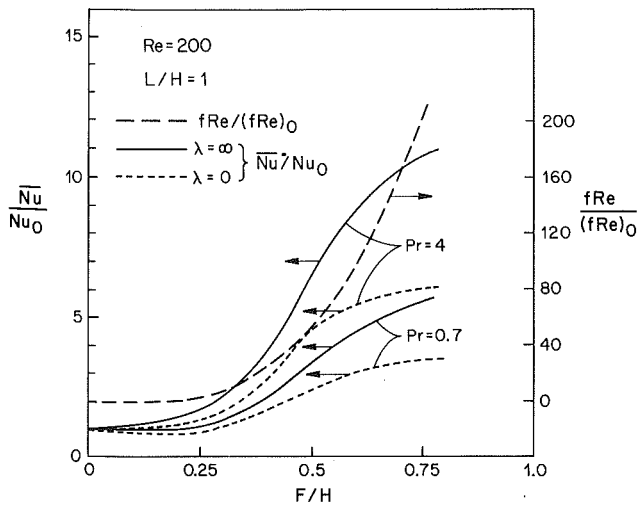

Fig. 7 Variation of friction factor and Nusselt number with fin height

Table 1 Variation of overall Nusselt number with fin-conductance parameter for Re = 500, $L/H = 1$, $F/H = 0.5$

	$\overline{Nu}/Nu_0$	
λ	Pr = 0.7	Pr = 4
0	4.347	8.716
10^{-1}	4.432	8.782
10^{0}	4.584	9.208
10^{1}	5.486	10.913
10^{2}	6.118	12.940
∞	6.233	13.441

the flow pattern and the increased heat transfer area provided by the fins. The augmentation for $\lambda = 0$ case is wholly due to the increase in heat transfer from the channel walls, which is caused by the flow distortion.

The effect of Reynolds number is shown in Fig. 5. In general, both Nu and fRe increase with Reynolds number. The heat transfer rate is higher for the higher Prandtl number and for the conducting fins. Although the heat transfer is augmented by a factor of about 10, the pressure-drop penalty is very large, the $f\text{Re}/(f\text{Re})_0$ values being in excess of 100. The reason for the large pressure drop is the significant blockage and distortion of the flow caused by the fins. It is the same distortion that produces flow impingement on the front face of the fins and on the channel walls, leading to the increased heat transfer.

As already seen in Fig. 3, the flow gets less distorted as the fin spacing is increased. The corresponding effect on friction and heat transfer is shown in Fig. 6. As the fin spacing becomes larger, the behavior approaches that in a finless channel.

The effect of fin height is shown in Fig. 7. As the fin height is increased, the friction-factor ratio can be seen to increase very rapidly. It can be deduced from the flow fields in Fig. 4 that the velocity of the throughflow increases linearly with the fin height. Since the pressure drop is roughly proportional to the square of this velocity, a quadratic rise in fRe is produced. The Nusselt number, on the other hand, tends to rise rather slowly as the fin height is increased beyond 0.5. This is because the thermal boundary layer thickness on the channel wall and the front faces of the fin is approximately proportional to the square root of the throughflow velocity (as in a flat plate boundary layer). Hence the rather slow rise in $\overline{Nu}$ is found for large values of F/H.

Another point to note is that, for Pr = 0.7 and $\lambda = 0$, the ratio of $\overline{Nu}/Nu_0$ is actually below 1 for small values of F/H. This result is qualitatively similar to the decrease in heat transfer reported in [1] for tubes with internal circumferential fins. As shown in Fig. 4 for $F/H = 0.25$, the throughflow does not have any significant tendency to impinge on the channel walls. The recirculation regions formed by the fins, on the other hand, prevent over 50 percent of the channel wall from coming into direct contact with the throughflow. The net result is a decrease in heat transfer in comparison with a finless channel. At higher Prandtl numbers such as Pr = 4, the augmentation caused by the recirculating flow is sufficient to make $\overline{Nu}/Nu_0$ greater than unity.

As shown in Figs. 5–7, the results for highly conducting fins ($\lambda = \infty$) give an overall Nusselt number that is about 30–50 percent higher than that for nonconducting fins ($\lambda = 0$). The typical effect of the fin-conductance parameter on $\overline{Nu}$ is presented for one case in Table 1. For the higher Prandtl number, there is a greater increase in $\overline{Nu}$ associated with the increase in λ. This is because the recirculating flow on the rear faces of the fins becomes more effective for Pr = 4.

Local Heat Transfer. Further insight into the interaction of the fluid flow and heat transfer processes can be obtained by observing the variation of the local heat transfer rates on the channel walls and fin surfaces.

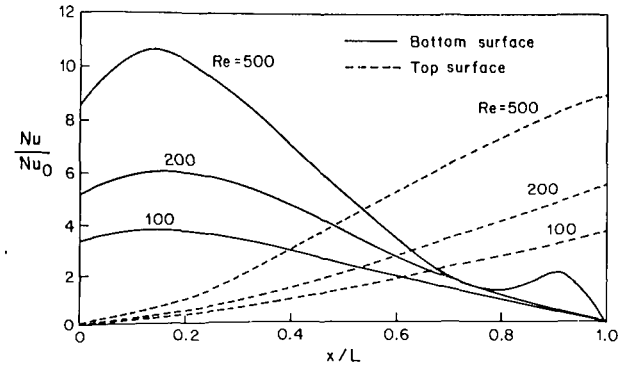

Fig. 8 Effect of Reynolds number on local heat transfer over top and bottom walls for $L/H = 1$, $F/H = 0.5$, $Pr = 0.7$, and $\lambda = \infty$

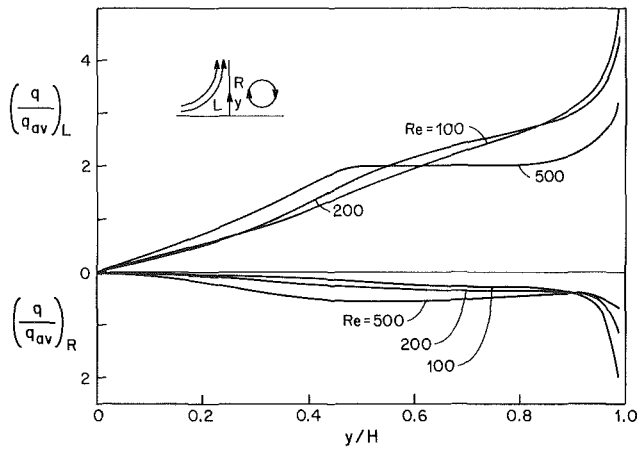

Fig. 9 Effect of Reynolds number on local heat transfer over the fin surface for $L/H = 1$, $F/H = 0.5$, $Pr = 0.7$, and $\lambda = \infty$

Figure 8 shows the behavior of the local Nusselt number on the top and bottom walls of the half-module ABCD shown in Fig. 1(*b*). The corresponding flow fields have been shown in Fig. 2. For the bottom wall, the throughflow first impinges on it and then gradually moves away. This leads to the high local Nusselt numbers in the left half and much lower values on the remainder of the bottom wall. The local maximum in Nu on the left occurs at a point where the impingement of the flow is strongest. It is interesting to note that, for $Re = 500$, the strength of the small recirculation zone on the front face of the fin is high enough to cause a local maximum in Nu near $x/L = 1$.

For the top wall, most of its length in the half-module ABCD is covered by the main recirculating eddy. Only at the right end ($x/L = 1$), the throughflow begins to impinge on the top wall. This explains the variation of Nu shown for the top wall in Fig. 8.

The local variation of the heat transfer on the left and right faces of the fin is presented in Fig. 9. The left face of the fin experiences impingement of the throughflow, while the right face is in contact with the recirculating flow. As a result, the local heat fluxes are, in general, higher on the left face than on the right. On both faces, the local heat transfer is significantly large near the fin tip, since the tip is washed by high velocity throughflow and also experiences large temperature gradients.

For a given Reynolds number and geometry, the flow field is the same whether the fins are conducting or not. Their conductivity, however, influences the temperature field and hence the behavior of local heat transfer. The effect of λ on the variation of Nu for the top and bottom walls is shown in Fig. 10 for one of the Reynolds numbers included in Fig. 8. The two limiting values of fin-conductance parameter, $\lambda = 0$ and ∞, are used. As can be expected, the value of λ has significant influence only near the base of the fin, i.e., near $x/L = 0$ for the top wall and near $x/L = 1$ for the bottom wall. In these regions, the local heat transfer to the channel walls actually increases when $\lambda = 0$ rather than ∞. This is because, if the heat is prevented from going through the fin, some of it will be forced to go through the channel wall.

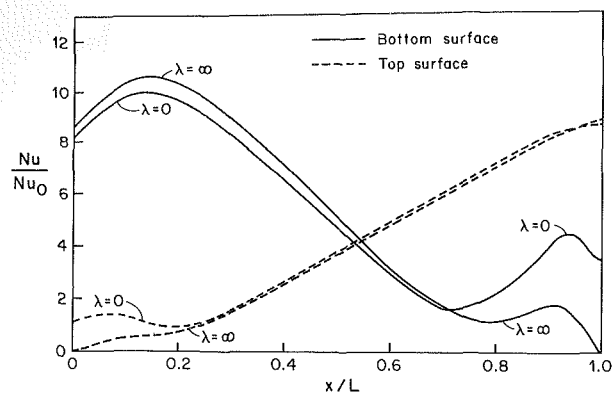

Fig. 10 Effect of fin-conductance parameter on local heat transfer over top and bottom wall for $Re = 500$, $L/H = 1$, $F/H = 0.5$, and $Pr = 0.7$

Concluding Remarks

An analysis has been presented for the flow and heat transfer in a parallel plate channel with staggered fins. The flow is characterized by large recirculation zones and significant flow distortion. A substantial increase in heat transfer is observed especially for high Prandtl-number fluids. However, the increase in the friction factor is an order of magnitude higher than the increase in heat transfer. When the Prandtl number is low, it is found that the use of short fins may indeed decrease the heat transfer. Details of the flow patterns and local heat transfer rates are presented, which give additional insight into the physical phenomena.

Acknowledgments

This research was performed under the auspices of a grant from the National Science Foundation. The computer costs were covered in part by a grant from the University of Minnesota Computer Center.

References

1 Rowley, C. J., "Heat Transfer and Fluid Analysis of Internal Circumferentially Finned Tubes in Laminar Flow," M.S. Thesis, University of Minnesota, Minneapolis, MN, 1981.

2 Berner, C., Durst, F., and McEligot, D. M., "Flow Around Baffles," ASME Journal of Heat Transfer, Vol. 106, 1984, pp. 743–749.

3 Patankar, S. V., Liu, L. H., and Sparrow, E. M., "Fully Developed Flow and Heat Transfer Ducts Having Periodic Variations of the Cross-Sectional Area," ASME Journal of Heat Transfer, Vol. 99, 1977, pp. 180–186.

4 Sparrow, E. M., Baliga, B. R., and Patankar, S. V., "Forced Convection Heat Transfer From a Shrouded Fin Array With and Without Tip Clearance," ASME Journal of Heat Transfer, Vol. 100, 1978, pp. 572–579.

5 Patankar, S. V., *Numerical Heat Transfer and Fluid Flow*, McGraw-Hill, New York, 1980.

Effect of Yaw on Heat Transfer in a Cuplike Cavity Facing a Freestream Flow

E. M. Sparrow

X. Zhang

Department of Mechanical Engineering,
University of Minnesota,
Minneapolis, MN 55455

Wind tunnel experiments were performed to determine the response of the heat transfer coefficient at the base of an open-ended cylindrical cavity to yawed (i.e., nonperpendicular) impingement of the freestream flow on the cavity opening. The experiments encompassed yaw angles from 0 (perpendicular impingement) to 45 deg, cavity depth–diameter ratios from 0 to 0.65, and Reynolds numbers from 4500 to 45,000. In the absence of yaw, very large reductions of the base surface transfer coefficient were brought about by increases of cavity depth. When the freestream flow is yawed relative to the cavity opening the coefficient rebounds from its low no-yaw values, with the rebound being accentuated for large yaw, deep cavities, and high Reynolds numbers. Notwithstanding the rebound, the resulting base surface heat transfer coefficients are lower than those for the no-yaw, zero-depth cavity. Operating conditions are identified for which reductions of the transfer coefficient of 50 percent or more are encountered. On this basis, cavities and recesses appear to be an effective means for reducing heat loss.

Introduction

The heat transfer coefficient at the base of a recession in a surface will be different from that at the surface proper. For example, for a cuplike cylindrical cavity whose opening is perpendicular to an oncoming flow, the heat transfer at the base was much lower than that for the zero-depth cavity [1]. For a shallow cavity whose depth was one-tenth of the cavity diameter, the reduction in heat transfer was about 50 percent, while a reduction by a factor of ten occurred when the depth was about half the diameter. These reductions reflect the inability of the oncoming flow to penetrate the cavity.

The findings of [1] are highly encouraging with regard to the role of recesses in decreasing heat losses and, by inference, suggest that the installation of recesses may serve as an energy conservation measure. However, the results presented in [1] are limited to perpendicular impingement of the freestream on the cavity opening, an orientation which maximizes the resistance to penetration of the cavity by the flow. This is so because fluid which successfully penetrates the cavity must execute a 180 deg turn in order to exit. On the other hand, for nonperpendicular impingement, any fluid which enters the cavity executes a less than 180 deg turn when exiting. From this, it may be expected that nonperpendicular impingement will enable better penetration of the flow into the cavity than does perpendicular impingement. As a consequence, the heat transfer reductions associated with nonperpendicular impingement should not be as great as those associated with perpendicular impingement.

The foregoing discussion provides the groundwork for the research to be reported here, the focus of which is to determine the heat transfer response of recessed surfaces to nonperpendicular impingement. Owing to the availability of perpendicular-impingement results [1] which can serve as a standard of comparison, consideration is given to heat transfer at the base of a cuplike cylindrical cavity. Experiments were performed with the freestream flow oriented at angles 15, 30, and 45 deg relative to perpendicular impingement. At each orientation of the freestream, the cavity depth-to-diameter ratio was varied between 0 and 0.65 in five steps. In addition to the parametric variations of the orientation and the cavity depth, the Reynolds number was systematically varied over a tenfold range from 4500 to 45,000 in seven steps.

The average heat transfer coefficients for the cavity base will be presented from several perspectives. One of these is intended to highlight the effects of nonperpendicular orientation for a cavity of a given depth. Another illustrates the effect of cavity depth for a given orientation. The interaction of the Reynolds number with both the orientation and cavity depth effects is also documented. In addition, the base surface heat transfer for finite-depth cavities with nonperpendicular impingement is compared with that for the no-cavity, perpendicular-impingement case.

Experiments

Experimental Apparatus. In order to obtain results of consistently high accuracy in the presence of well-defined thermal boundary conditions, it was deemed advantageous to use the naphthalene sublimation technique. The mass transfer coefficients measured by employing this technique are readily transformed to heat transfer coefficients by applying the well-established analogy between heat and mass transfer. The resulting heat transfer coefficients correspond to uniform wall temperature at the base surface of the cavity and to a locally and globally adiabatic cavity side wall.

The description of the experimental apparatus is facilitated by reference to Fig. 1, which shows a longitudinal cross section through the cavity assembly. As seen there, the main parts of the assembly are a cylindrical centerbody of diameter D and a sleevelike shroud. The cavity is formed by the front face of the centerbody and the portion of the shroud which extends forward of the centerbody. The cavity depth, denoted by S, can be set at any desired value by displacing the shroud axially with respect to the centerbody and locking it in place.

The centerbody was made from aluminum rod stock with a finished diameter of 3.493 cm. A 0.7-cm-deep recess was machined into the front face of the centerbody to accommodate a layer of solid naphthalene which was implanted by a casting process. The outer wall of the recess was tapered to virtually zero thickness (0.005 cm) at its forward edge. Both the base and the wall of the recess were roughened to aid in the adhesion of the naphthalene.

The centerbody was drilled along its axis to provide an ac-

Contributed by the Heat Transfer Division for publication in the JOURNAL OF HEAT TRANSFER. Manuscript received by the Heat Transfer Division November 5, 1985.

cess hole through which molten naphthalene was poured during the casting procedure. The hole also served to accommodate a shaft which coupled the centerbody to a downstream-positioned support system. To provide both a positive stop for the shaft and a seat for a funnel used during the pouring of the napthalene, the hole was stepped as illustrated in the figure.

In addition to the main axial hole, two smaller axial holes (not shown) were drilled through the centerbody to serve as passage ways for the escape of air displaced from the recess during the casting process. One of the holes also served as a conduit through which lead wires were drawn in order to enable a thermocouple junction to be embedded in the exposed surface of the cast naphthalene.

The shroud was made of brass and was precision bored so that its inside diameter differed by about 0.005 cm from the diameter of the centerbody. The wall thickness of the shroud was 0.35 cm. To help avoid flow blockage effects associated with the finite wall thickness and thereby minimize apparatus-specific effects, the forward extremity of the shroud was beveled at 45 deg to a sharp edge.

The shaft which mated with the aft end of the centerbody was attached at its downstream end to a universal joint. In turn, the joint was affixed to a support stand mounted on the floor of the wind tunnel in which the experiments were performed. The crossflow members of the stand were positioned sufficiently far downstream so that their pressence did not affect the flow about the cavity. The universal joint, in conjunction with angle measurement instruments, enabled the cavity opening to be oriented relative to the freestream at any desired angle. The angle between the perpendicular to the cavity opening and the freestream is designated as θ (see Fig. 1) and will hereafter be referred to as the angle of yaw.

The wind tunnel used for the experiments was operated in the open circuit mode and in suction. Air was drawn from within the building into the tunnel inlet and was delivered to the test section after passing through a set of fine-mesh screens and a 16:1 contraction ratio. The test section had a 30.48 × 60.96 cm (height × width) rectangular test section and a length of 244 cm. The airflow exiting the test section passed through the fan section and a diffuser and then was discharged outside the building. During the course of the experiments, the freestream velocity was varied between about 2.1 and 21 m/s, yielding Reynolds numbers which ranged from about 4500 to 45,000. The freestream turbulence level in this range was 0.4–0.5 percent.

Experimental Procedure and Instrumentation. The setting of the yaw angle θ (Fig. 1) was a two-step process. The first step was to establish the $\theta = 0$ deg orientation of the cavity opening. This was accomplished by employing the oil-lampblack technique. For this purpose, the cavity depth was set at zero, and a suitably fluid mixture of oil and lampblack powder was applied to a sheet of white, plasticized contact paper that had been affixed to the cavity base (which now coincided with the cavity opening). When the airflow was activated, the oil-lampblack mixture revealed the position of the stagnation point on the surface.

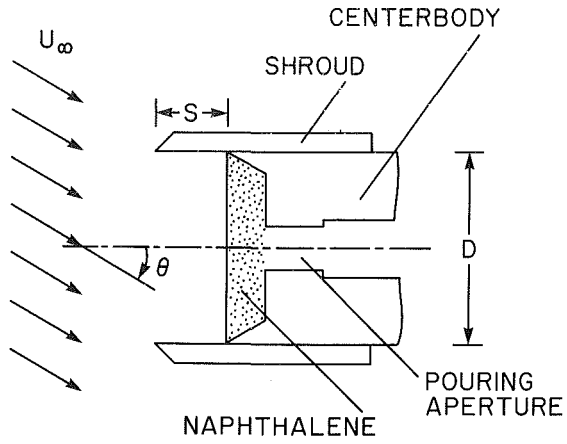

Fig. 1 Cavity assembly

By proper adjustment of the universal joint, the stagnation point was caused to coincide with the center of the circular surface, thereby signaling perpendicular impingement. The setting of the universal joint was defined by two angles, whose values corresponding to the just-obtained perpendicular impingement were recorded as a datum. The angles were read with protractors with 0.5 deg subdivisions.

To achieve non-zero yaw (i.e., nonperpendicular impingement), one of the two angles at the universal joint was held fixed at its datum, while the other was displaced from its datum value by an amount equal to the desired angle of yaw θ.

Prior to the beginning of each data run, a fresh naphthalene layer was cast into the front face of the centerbody. This was accomplished by first removing the naphthalene remaining from the preceding run and then placing the centerbody on a highly polished stainless steel plate with the recess facing downward. This created a mold cavity, into which molten naphthalene was poured with the aid of a funnel. When the centerbody was separated from the casting plate, a naphthalene surface was exposed whose finish was comparable to that of the plate. To prevent extraneous sublimation, the naphthalene surface was covered with a tight-fitting cap.

The capped centerbody was then installed in the wind tunnel for about an hour to attain thermal equilibrium with the airflow, after which it was weighed (with the cap removed). The centerbody was then mated with the shroud, and the capped assembly was installed in the wind tunnel for further equilibration. When steady state had been achieved, the cap was removed and the data run proper initiated.

During the run, periodic readings were made of the thermocouple embedded in the naphthalene surface and of the velocity pressure from an impact tube–static tap combination used to measure the freestream velocity. The tunnel static and barometric pressures were also read. The duration of the run

Nomenclature

A = mass transfer surface area
C = coefficient in Sh–Re correlation
D = diameter of cavity and of cavity base
$\mathfrak{D}$ = mass diffusion coefficient
K = base surface mass transfer coefficient
ΔM = mass loss during data run
n = exponent in Sh–Re correlation
Re = Reynolds number
S = cavity depth
Sc = Schmidt number
Sh = base surface Sherwood number
Sh_0 = Sherwood number for zero-yaw case
$\mathrm{Sh}_{0,0}$ = Sherwood number for zero-yaw, zero-depth case
U_∞ = freestream velocity
θ = angle of yaw (Fig. 1)
ν = kinematic viscosity
ρ_{nw} = naphthalene vapor density at subliming surface
$\rho_{n\infty}$ = naphthalene vapor density in freestream
τ = duration of data run

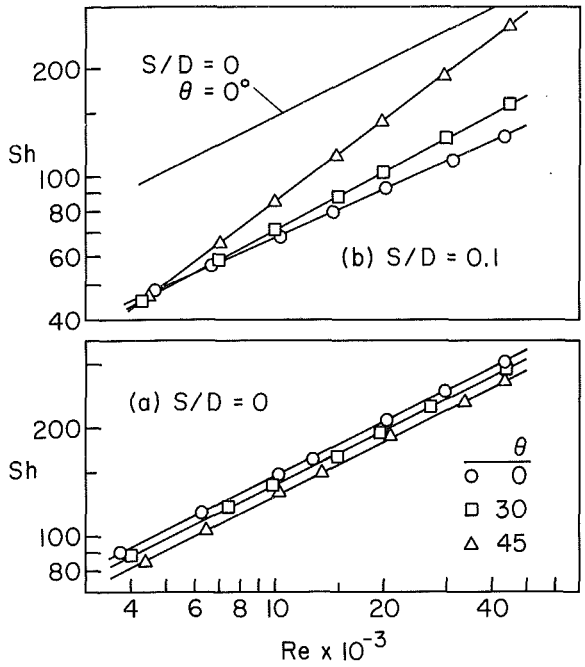

Fig. 2 Base surface Sherwood numbers: (a) $S/D = 0$, (b) $S/D = 0.1$

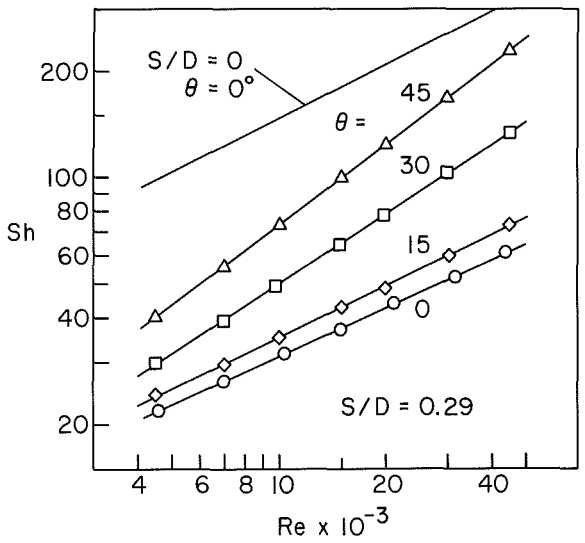

Fig. 3 Base surface Sherwood numbers: $S/D = 0.29$

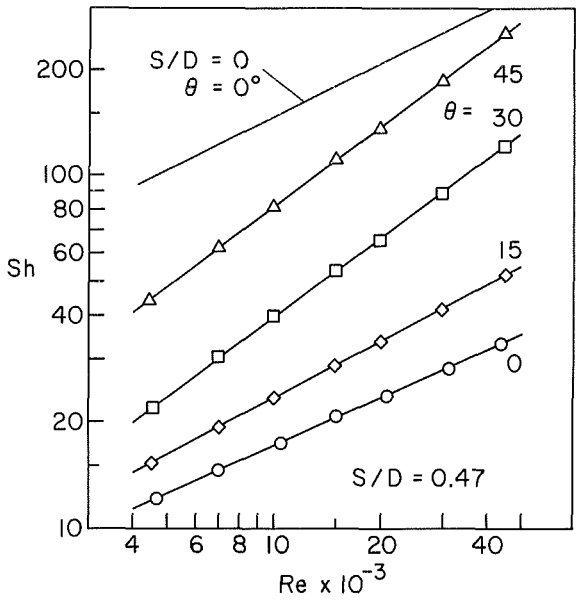

Fig. 4 Base surface Sherwood numbers: $S/D = 0.47$

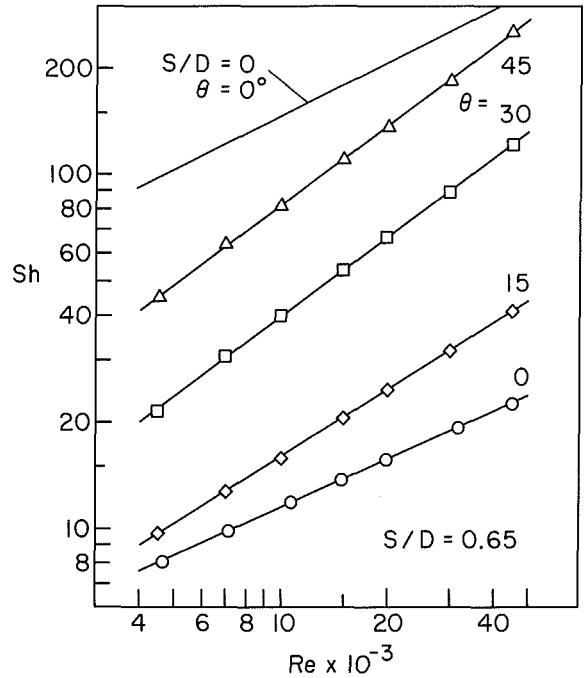

Fig. 5 Base surface Sherwood numbers: $S/D = 0.65$

was chosen to limit the sublimation-related recession of the naphthalene surface to 0.0025 cm. At the termination of the run, the assembly was capped and the centerbody weighed (without the cap). Supplementary runs, made to determine the extent of any extraneous mass losses which might have occurred between the two weighings, yielded a correction of about two percent.

The mass measurements were performed using an electronic analytical balance with a resolution of 0.00001 g, while the velocity and static pressures were read to 0.001 Torr with a solid-state, capacitance-type pressure meter. The thermocouple emfs were read to 1 μV.

Data Reduction

The mass transfer coefficient K at the cavity base surface will be reported in terms of the Sherwood number Sh (which is the mass transfer counterpart of the Nusselt number). These quantities are defined as

$$K = (\Delta M/\tau A)/(\rho_{nw} - \rho_{n\infty}), \qquad \mathrm{Sh} = KD/\mathfrak{D} \tag{1}$$

In this equation, ΔM is the change of mass during time τ due to sublimation at the naphthalene surface A. In the denominator, ρ_{nw} and $\rho_{n\infty}$ respectively denote the densities of naphthalene vapor at the subliming surface and in the freestream. The latter is zero for the present experiments. For the former, it was assumed that solid-vapor equilibrium prevailed at the subliming surface, so that the corresponding vapor pressure-temperature relation for naphthalene [2] could be applied. After the vapor pressure was evaluated using the measured naphthalene surface temperature as input, the density was obtained from the perfect gas law.

The mass diffusion coefficient $\mathfrak{D}$ appearing in the definition of the Sherwood number was evaluated from a formula given by Skelland ([3], p. 51). Also, the $\mathfrak{D}$ values were used to compute the Schmidt number $\mathrm{Sc} = \nu/\mathfrak{D}$ (the mass transfer counterpart of the Prandtl number), where ν is the kinematic

viscosity of air. For all of the data runs, Sc = 2.55, which is within two percent of the empirically based value of 2.5 from [2].

The mass transfer results will be parameterized by the Reynolds number defined as

$$\mathrm{Re} = U_\infty D/\nu \tag{2}$$

The Sherwood numbers are believed to be accurate to two percent.

Results and Discussion

Base Surface Sherwood Numbers. The Sherwood numbers (dimensionless mass transfer coefficients) at the base of the cavity are presented in Figs. 2–5. The results of Figs. 2(*a*) and 2(*b*) respectively correspond to the zero-depth cavity and the $S/D = 0.1$ cavity. The other figures pertain to successively deeper cavities, namely, $S/D = 0.29$, 0.47, and 0.65 in Figs. 3, 4, and 5.

In each figure, the base surface Sherwood number is plotted as a function of the Reynolds number for each of several fixed values of the yaw angle θ. For the $S/D = 0$ and 0.1 cavity depths, for which the results were not very sensitive to yaw, the experiments were performed for $\theta = 0$, 30, and 45 deg, while for the deeper cavities, $\theta = 15$ deg was added to the set. The straight lines passing through the data for a given θ are least-squares fits of the form

$$\mathrm{Sh} = C\mathrm{Re}^n \tag{3}$$

Note that although the results for the $\theta = 0$ deg (perpendicular impingement) case were already available from [1], they were rerun here for verification purposes, and excellent agreement was found to prevail.

For the zero-depth cavity (Fig. 2(*a*)), the Sherwood number decreases slightly due to yaw. Since all three sets of data are well represented by equation (3) with $n = \frac{1}{2}$, the extent of the yaw-related decrease of Sh follows directly from the respective C values, which are 1.47, 1.39, and 1.29 ($\theta = 0$, 30, and 45 deg), corresponding to 5 and 12 percent reductions. The reductions are the result of a longer path length for boundary layer development on the surface (and, hence, a thicker boundary layer) which accompanies an increase in yaw.

The existence of a $\mathrm{Re}^{1/2}$ dependence for all three θ values suggests the presence of laminar boundary layer flow without separation, and this was confirmed by the oil-lampblack visualization technique. Note that the correlation $\mathrm{Sh} = 1.47\mathrm{Re}^{1/2}$ for $\theta = 0$ deg agrees with that of Sogin [2] for a disk situated in crossflow.

For all of the investigated finite-depth cavities, Figs. 2(*b*)-5, the effect of non-zero yaw on the base surface Sherwood number is just opposite to that encountered for the zero-depth cavity. In all of the figures, the lowermost set of data are for the unyawed ($\theta = 0$ deg) cavity and, with progressive increases in yaw, the Sherwood numbers increase monotonically. The yaw-related increases are moderate for shallow cavities such as $S/D = 0.1$ (Fig. 2(*b*)) but become progressively larger with increasing cavity depth. For an intermediate cavity depth such as $S/D = 0.65$ (Fig. 5), yaw gives rise to a tremendous increase in the Sherwood number. For example, an increase in the yaw angle from $\theta = 0$ to 45 deg causes 5.5- and 11-fold increases in the Sherwood number, respectively for Re = 4500 and 45,000.

In each of Figs. 2(*b*)-5, the Sh versus Re distribution for the zero-yaw, zero-depth case is included as a reference line. Note that despite the very large yaw-related increases, the Sh values for the finite-depth cavities did not exceed the reference case in the Reynolds number range investigated here. At larger Reynolds numbers, it appears that the $\theta = 45$ deg Sh distributions for the finite-depth cavities will cross the reference line, but such Reynolds numbers were not attainable in the wind tunnel used here.

Further inspection of Figs. 2(*b*)-5 shows that the enhancement of the Sherwood number due to yaw is greater at the higher Reynolds numbers than at the lower Reynolds numbers. Both larger yaw and higher Reynolds numbers contribute to the ability of the flow to penetrate the cavity. As noted in the Introduction, fluid penetrating the cavity executes a smaller turn when exiting the cavity as the yaw angle increases, thereby making penetration easier. Furthermore, at higher Reynolds numbers, the larger momentum of the oncoming flow facilitates penetration. These factors are the main causes of the yaw-related enhancement of the mass (heat) transfer.

Before leaving Figs. 2(*b*)-5, it is relevant to call attention to the very great reductions in base surface mass (heat) transfer which occur in an unyawed, moderately deep cavity. Referring again to Fig. 5 for $S/D = 0.65$, comparison of the upper and lower curves shows that the Sh values for the latter are only 7–8 percent of those for the former. It was findings such as this which called attention to the possibilities of using recesses and cavities as a means for reducing heat losses. As shown in Fig. 5, large reductions are still possible provided that the yaw angle is not too large. For example, the mass (heat) transfer at the base of a 15 deg yawed cavity of depth $S/D = 0.65$ is 10–12 percent of that for the $S/D = 0$, $\theta = 0$ deg reference case.

Sherwood Number Ratios. To facilitate a direct numerical appraisal of the effect of yaw, the base surface Sherwood number results have been recast in the form of a ratio $\mathrm{Sh}/\mathrm{Sh}_0$. In this ratio, both Sh and Sh_0 correspond to the same values of the cavity depth S/D and Reynolds number Re, but Sh is for finite yaw ($\theta > 0$ deg) while Sh_0 is for no yaw ($\theta = 0$ deg). Thus, the departures of $\mathrm{Sh}/\mathrm{Sh}_0$ from unity are a direct numerical measure of the effect of yaw at fixed S/D and Re.

The $\mathrm{Sh}/\mathrm{Sh}_0$ results ae presented in Figs. 6(*a*), 6(*b*), and 7. Each figure pertains to a fixed yaw angle, respectively $\theta = 15$, 30, and 45 deg. In each figure, $\mathrm{Sh}/\mathrm{Sh}_0$ is plotted as a function of Re for parametric values of S/D. Since the actual experimental data have already been presented in the earlier figures, they have been omitted from Figs. 6 and 7 for simplicity.

From an overview of Figs. 6 and 7, the dramatic growth of $\mathrm{Sh}/\mathrm{Sh}_0$ with the angle of yaw is strongly in evidence. Whereas the largest $\mathrm{Sh}/\mathrm{Sh}_0$ value for $\theta = 15$ deg is about 1.8 (Fig. 6(*a*)), that for $\theta = 45$ deg is about 11 (Fig. 7). In general, at any fixed angle of yaw, the deeper the cavity, the larger is $\mathrm{Sh}/\mathrm{Sh}_0$, i.e., the effect of yaw is accentuated for deeper cavities.

Aside from the zero-depth cavity, for which $\mathrm{Sh}/\mathrm{Sh}_0$ is a constant (< 1), $\mathrm{Sh}/\mathrm{Sh}_0$ increases with Re, which offers testimony to the enhancement of the yaw effect by the Reynolds number. At both $\theta = 15$ and 30 deg, the increase of $\mathrm{Sh}/\mathrm{Sh}_0$ with Re is greater for deeper cavities. For $\theta = 45$ deg, $\mathrm{Sh}/\mathrm{Sh}_0 \sim \mathrm{Re}^{1/4}$ for all $S/D > 0$. This same power law also applies for $S/D = 0.47$ and 0.65 when $\theta = 30$ deg. Thus, for these cases, $\mathrm{Sh}/\mathrm{Sh}_0$ displays a significant Reynolds number dependence.

Another (and final) perspective on the results will now be set forth. Consider as a reference case the zero-yaw, zero-depth cavity and denote the corresponding Sherwood number by $\mathrm{Sh}_{0,0}$. It has already been demonstrated that for any Reynolds number in the investigated range, $\mathrm{Sh}_{0,0}$ is larger than any Sh value corresponding to $\theta > 0$ deg and $S/D > 0$. Thus, although yaw moderates the reductions of mass (heat) transfer due to cavity depth, it may still be advantageous to use cavities or recesses as a heat loss reduction technique.

To explore this issue in a quantitative manner, the ratio $\mathrm{Sh}/\mathrm{Sh}_{0,0}$ has been evaluated. Here, Sh and $\mathrm{Sh}_{0,0}$ correspond to the same Reynolds number, but Sh is for $\theta > 0$ deg and $S/D > 0$ while $\mathrm{Sh}_{0,0}$ is for $\theta = 0$ deg and $S/D = 0$. The $\mathrm{Sh}/\mathrm{Sh}_{0,0}$ results are presented in Figs. 8 and 9, respectively for the ex-

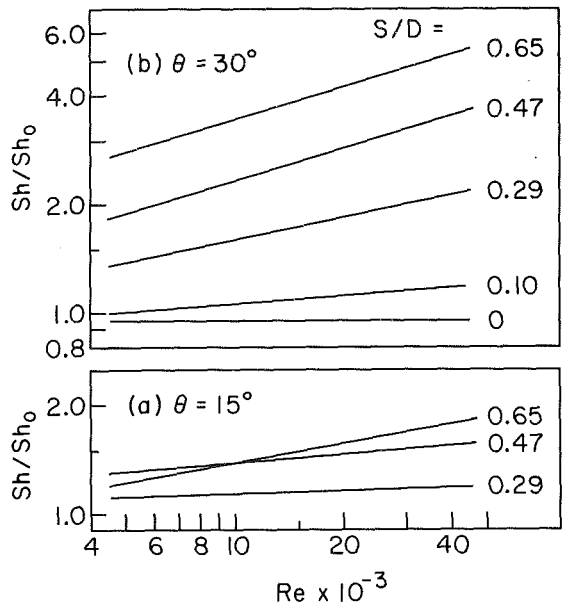

Fig. 6 Comparison of the Sherwood number for a finite-depth, yawed cavity to that for the corresponding unyawed cavity: (a) $\theta = 15$ deg, (b) $\theta = 30$ deg

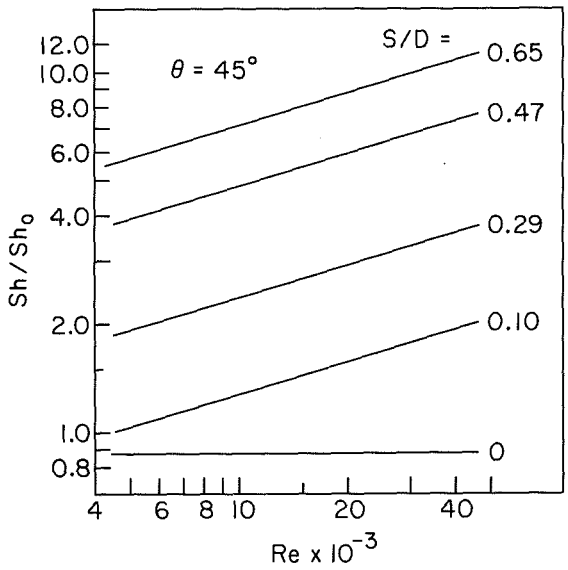

Fig. 7 Comparison of the Sherwood number for a finite-depth, yawed cavity to that for the corresponding unyawed cavity: $\theta = 45$ deg

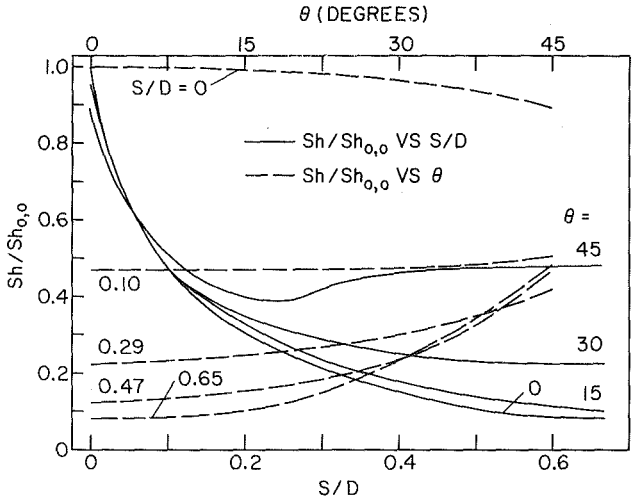

Fig. 8 Comparison of the Sherwood number for a finite-depth, yawed cavity to that for a zero-depth, unyawed cavity: Re = 5000

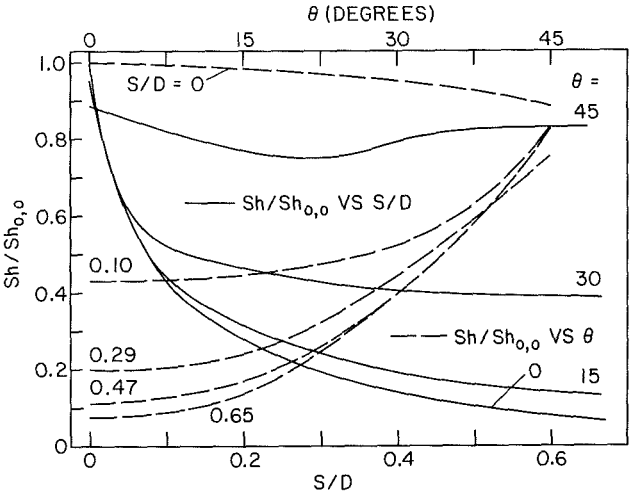

Fig. 9 Comparison of the Sherwood number for a finite-depth, yawed cavity to that for a zero-depth, unyawed cavity: Re = 45,000

tremes of the investigated Reynolds number range, 5000 and 45,000. There are two sets of curves in each figure. The solid lines depict $Sh/Sh_{0,0}$ versus S/D and are referred to the lower abscissa, while the dashed lines represent $Sh/Sh_{0,0}$ versus θ and are referred to the upper abscissa.

Figures 8 and 9 confirm that $Sh/Sh_{0,0} < 1$ for all the investigated operating conditions. From both figures, it is seen that the most rapid dropoff of $Sh/Sh_{0,0}$ with S/D occurs in the range of small S/D. Thereafter, a more gradual variation sets in and, in fact, for the 45 deg yaw, there is a slight increase of $Sh/Sh_{0,0}$ at larger S/D. Small yaw angles (up to 15 deg) do not significantly affect $Sh/Sh_{0,0}$. At larger yaws, $Sh/Sh_{0,0}$ increases rapidly with increasing yaw.

The $Sh/Sh_{0,0}$ values are markedly affected by the Reynolds number. For Re = 5000, if cavities with $S/D < 0.1$ are excluded, it is seen from Fig. 8 that all the measured $Sh/Sh_{0,0}$ values are below 0.5. Therefore, for lower Reynolds numbers, cavities and recesses provide an attractive means for heat loss reduction.

From a comparison of Figs. 8 and 9, it is clear that the $Sh/Sh_{0,0}$ values are higher at the higher Reynolds number. Nevertheless, let $Sh/Sh_{0,0} \leq 0.5$ be taken as the criterion at which cavity-related reductions in mass (heat) transfer are regarded as significant. Then, when $S/D < 0.1$ and $\theta > 30$ deg are excluded, this criterion is fulfilled for the Re = 45,000 case, so that, here again, a cavity can be used effectively for reducing the heat loss.

Concluding Remarks

The mass (heat) transfer coefficients at the base surface of a cuplike cylindrical cavity which faces an oncoming flow have been investigated experimentally. The three parameters which were varied during the course of the work included the angle of yaw θ of the freestream relative to the perpendicular to the cavity opening, the cavity depth – diameter ratio S/D, and the Reynolds number Re.

In the absence of yaw ($\theta = 0$ deg), the Sherwood numbers decreased significantly with cavity depth, rapidly at first and then more gradually. These reductions are on the order of a factor of ten for cavities of intermediate depth ($S/D \sim 0.5$). When the oncoming flow is yawed relative to the cavity open-

ing, the Sherwood number rebounds from its low no-yaw values. The extent of the rebound is greatest at large angles of yaw, deep cavities, and large Reynolds numbers.

Notwithstanding the aforementioned rebound, cavities and recesses provide an effective means for reducing base surface mass (or heat) transfer. At Re = 5000, heat transfer reductions of 50 percent and greater, relative to the no-yaw, zero-depth cavity, were encountered for all S/D, except for $S/D < 0.1$, and for all θ between 0 and 45 deg. A similar finding occurred for Re = 45,000 except that θ values greater than 30 deg must be excluded.

When the cavity is of zero depth, the Sherwood number is quite insensitive to yaw, decreasing slightly as the angle of yaw increases.

References

1 Sparrow, E. M., and Geiger, G. T., "Heat Transfer at the Base of a Cylindrical Cavity Oriented Perpendicular to a Freestream Flow," *International Journal of Heat and Mass Transfer*, Vol. 28, 1985, pp. 2353–2361.

2 Sogin, H. H., "Sublimation From Disks to Air Streams Flowing Normal to Their Surfaces," *Trans. ASME*, Vol. 80, 1958, pp. 61–71.

3 Skelland, A. H. P., *Diffusional Mass Transfer*, Wiley, New York, 1974.

J. W. Baughn
Professor.
Mem. ASME

M. A. Hoffman
Professor.

R. K. Takahashi[1]
Research Assistant.

Daehee Lee
Research Assistant.

Department of Mechanical Engineering,
University of California,
Davis, CA 95616

Heat Transfer Downstream of an Abrupt Expansion in the Transition Reynolds Number Regime

The heat transfer downstream of an axisymmetric abrupt expansion in a pipe in the transition Reynolds number regime has been investigated experimentally. In these experiments the wall of the downstream pipe was heated to give a constant heat flux into the air flow. The ratio of the upstream to downstream pipe diameters was 0.8 and the downstream Reynolds number ranged from 1420 to 8060. Within a narrow range of Reynolds numbers, around 5000, the position of the maximum Nusselt number was found to shift considerably. This interesting behavior may be associated with the flow instabilities in sudden expansions which have been observed by others.

Introduction

The purpose of the present investigation was to provide wall heat transfer data downstream of an axisymmetric abrupt expansion in a pipe in the laminar-to-turbulent transition flow regime. The heat transfer downstream of abrupt pipe expansions for turbulent flow has been investigated experimentally in a number of studies including that by Zemanick and Dougall [1], and more recently by Baughn et al. [2]. These studies all gave results that generally agreed in the location and magnitude of the maximum heat transfer coefficient. It is commonly accepted that this location is at or near the region of reattachment of the separated shear layer. Lengths to the maximum heat transfer coefficient for these turbulent flows ranged typically from 5 to 15 step heights downstream of the expansion. Maximum Nusselt numbers reported in [2] ranged from $2Nu_{DB}$ to $11Nu_{DB}$, where Nu_{DB} is the equivalent fully developed Dittus-Boelter value (i.e., $Nu_{DB}=0.023\ Re^{0.8}Pr^{0.4}$), at the same Reynolds and Prandtl numbers. There have also been a number of computational studies of heat transfer for this type of recirculating flow, for example, that of Chieng and Launder [3].

At the present time, separated flows in the transition flow regime, though studied extensively, are not well understood. Measurements of reattachment lengths downstream of abrupt expansions in the laminar-to-turbulent flow regime were made by Back and Roschke [4] using dye-in-water visualization techniques. They presented data for $d/D=0.385$ showing the reattachment lengths increasing from about zero to 25 step heights from the abrupt expansion as the Reynolds number increased in the laminar flow regime up to an upstream Reynolds number of about 300. While still in the laminar region, their reattachment length then decreased, with increasing Reynolds number, to about 7 step heights, at an upstream Reynolds number of about 800. It then again increased gradually in the transition region to a value of 9 step heights at their maximum Reynolds number, based on the upstream diameter, of 4200 (downstream Reynolds number of 1615). The velocity profile across the entry tube at the abrupt expansion was assumed to be flat. No evidence of flow instabilities was reported.

Recently Sreenivasan and Strykowski [5] reported hot-wire measurements downstream of an abrupt expansion in which the expansion region exhibited an instability. Their measurements showed the flow to be oscillating between a laminar jetlike behavior and a turbulent pipe flow. This indicated that the radial spread of the jet was oscillating. Flow visualization using dye-in-water showed that the jet appeared to be laminar for a distance downstream of the expansion and then suddenly broke down, the dye filling the entire pipe cross-sectional area. The location of the breakdown oscillated back and forth along a pipe length; the degree of oscillation was sensitive to upstream disturbances, and the oscillations occurred only within a narrow range of downstream Reynolds numbers from 750 to 850 (for $d/D=0.50$).

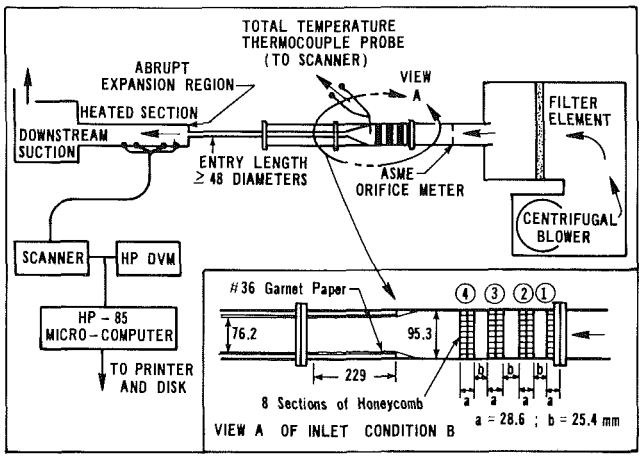

Fig. 1(*a*) Diagram of experimental apparatus showing an enlarged view of the inlet condition B

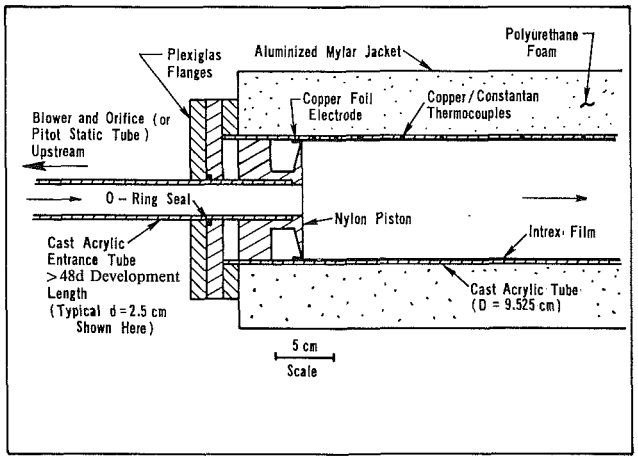

Fig. 1(*b*) Cross section of the apparatus in the region of the abrupt expansion

[1]Present address: Ames Research Center, Moffett Field, CA.

Contributed by the Heat Transfer Division and presented at the 23rd National Heat Transfer Conference, Denver, Colorado, April 1985. Manuscript received by the Heat Transfer Division January 17, 1985.

The only previous heat transfer measurements of axisymmetric abrupt expansions at transitional Reynolds numbers that we are aware of are those of Ede et al. [6]. Although turbulent Reynolds numbers were the major thrust of their study, they do give results at several Reynolds numbers in the laminar and transition regime. Those few results show the same general behavior as our own results but the fact that they heated the upstream tube precludes any direct comparison. Based on their flow visualization results, they make the following comment about their flow instability: " . . . the flow was liable to switch unpredictably from laminar to turbulent, or back again, almost anywhere in the pipe." The flow instabilities observed in both [5] and [6] provide a possible explanation for the heat transfer behavior observed in the present study as described below.

Experimental Apparatus

The experimental apparatus (see Figs. 1*a* and 1*b*) was basically the same as that used by Baughn et al. [2] in acquiring the earlier turbulent flow heat transfer data. The experimental technique uses a gold-coated polyester sheet to obtain a uniform wall heat flux. This technique has many advantages for studying heat transfer in complex flows and is described by Baughn et al. [7]. The main differences in the present apparatus from that of [2] were the use of a smaller orifice plate to measure lower flow rates, and the addition of honeycomb and surface roughening in the upstream, smaller diameter tube to enhance the development of the pipe flow.

A brief description of the apparatus follows. A 1 h.p. squirrel cage blower at the upstream end of the apparatus delivered ambient air into a 9.53 cm diameter tube. The tube contained a 2.32 cm diameter orifice, built to ASME specifications, which was used to measure the flow rate. Downstream of the orifice plate was a section intended to enhance the flow development (an inlet condition). Two different inlet conditions were used and are referred to as A and B in the results. Inlet condition A was a smooth wall with honeycomb at the entrance. Inlet condition B is shown in Fig. 1(*a*) since most of the data were taken with this condition. For this case, honeycomb sections were spaced as shown in Fig. 1(*a*). The first and last pairs of honeycomb had a wire mesh (mesh size of 1.6 mm) sandwiched between them. The flow then converged into a 7.62-cm-dia pipe, 48 diameters (366 cm) long. On the inner surface of this small diameter entry tube was a 23 cm length of sandpaper with grain size of about 1 mm. On the downstream end of this tube was fitted a stationary nylon "piston" which defined the abrupt expansion into the 9.53-cm-dia heated tube (see Fig. 1*b* where the flow is now from left to right). The small-to-large expansion ratio d/D, was 0.80 in these experiments.

Referring to Fig. 1(*b*), the heated large-diameter tube, 18 diameters (172 cm) long, had a transparent, gold-coated polyester sheet glued to its inner surface. This gold-coated sheet, Intrex (a product of Sierracin/Sylmar), was the medium through which an alternating current was passed resulting in electrical resistive heating at the tube inner wall. To minimize circumferential and axial conduction in the tube wall, a cast acrylic tube with a wall thickness of 3.2 mm was used. To minimize radial outward heat losses the tube was covered with 5 cm of polyurethane foam, and to minimize radiation losses the foam was wrapped with an aluminized mylar jacket. Also, in the effort to minimize conduction effects, the nylon piston which formed the abrupt expansion face was designed to have minimal contact with the tube wall, as shown in Fig. 1(*b*).

Wall temperature measurements were made using 36 type T (No. 40 AWG or 0.076 mm diameter) thermocouples which were normally positioned along the top of the tube. The thermocouples were epoxied in holes drilled in the tube wall such that the thermocouple beads were touching the back side of the polyester sheet. The thermocouple axial spacing varied from 0.5 cm near the abrupt expansion to 15 cm near the heated tube exit. The upstream air inlet temperature was measured with a type T thermocouple, mounted on a ceramic support rod, placed in the flow just downstream of the orifice-plate measuring assembly. Thermocouple measurements were made with an HP 3455A digital voltmeter using an HP 85 microcomputer to control an HP 3495A multiplex scanner.

Inlet Flow Conditions

The mean velocity distributions $\bar{U}(r)$, and the streamwise component of the rms turbulence intensity u', were measured at the exit of the small diameter tube (i.e., at the abrupt expansion step) for inlet condition B (used for most of the heat transfer data presented later). The profiles were measured almost across the full diameter and no asymmetry was observed.

The measured velocity distributions are presented and compared to Nikuradse's fully developed profile for his Reynolds number Re_d of 4000 [8] in Figs. 2(*a*) and 2(*b*). From Fig. 2(*a*) we observe that our velocity profiles at an Re_d of 4450 and 5290 are somewhat flatter than Nikuradse's profile. This seems to indicate that at these low Reynolds numbers the flow is nearly, but not completely, fully developed. From Fig. 2(*b*), we see that for the higher upstream Reynolds numbers of about 5980, 6490, and 9600, the profiles fall above Nikuradse's profile for a Re_d of 4000 and very nearly on his profile for 23,000 (not shown for clarity). Considering the uncertainties in Nikuradse's low Reynolds number profiles, this is taken as confirmation that our velocity profiles are essentially fully developed at these Reynolds numbers.

The streamwise turbulent intensity measurements normalized by the mean flow velocity are shown in Fig. 2(*c*). These have been compared to earlier fully developed measurements on a completely different apparatus at a Reynolds number of 13,000 [9]. The agreement with our measured values at Re_d of 6980 and 9600 can be seen to be very good (except very close to the tube wall), again indicating that fully developed flow has essentially been achieved. For the lower Reynolds number of 4836, we have not found other data for comparison.

Heat Transfer Measurements

All measurements were made after the flow had attained

Nomenclature

d = upstream tube diameter
D = heated tube (downstream) diameter
H = step height $= (D-d)/2$
k = air thermal conductivity
Nu = Nusselt number
$\mathrm{Nu}_{\mathrm{DB}}$ = Nusselt number determined by the Dittus-Boelter Equation
$\mathrm{Nu}_{\max}$ = maximum Nusselt number
q_e'' = local electrical heating per unit area
q_l'' = local heat-flux conduction loss into wall
Re = downstream Reynolds number based on D
Re_d = upstream Reynolds number based on d
T_b = local air bulk temperature
T_f = local film temperature
T_w = local wall temperature
x = axial position downstream of abrupt expansion step
θ = angular position around tube (0 deg is at the top)

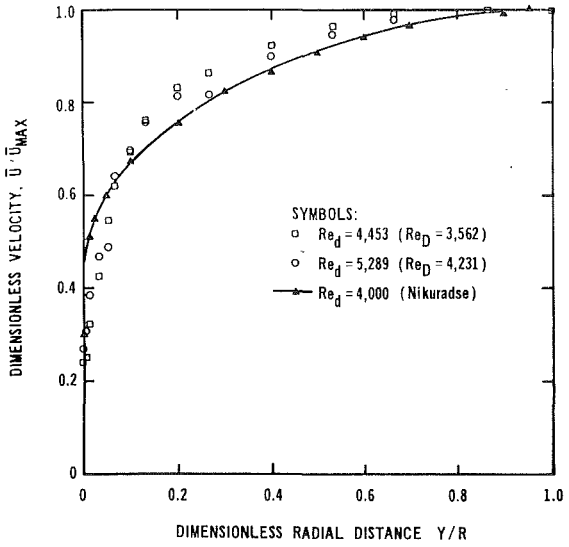

Fig. 2(a) Measured mean velocity profiles at the exit of the small-diameter tube (i.e., at the abrupt expansion step) for the lower Reynolds numbers for inlet condition B (rough)

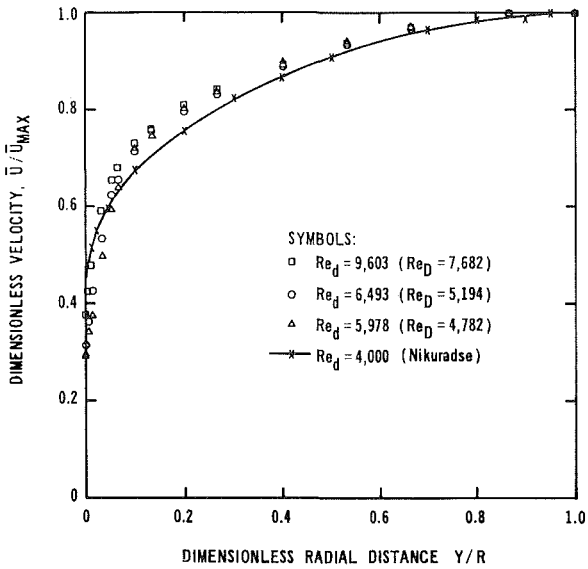

Fig. 2(b) Measured mean velocity profiles at the exit of the small-diameter tube at the higher Reynolds numbers for inlet condition *B* (rough)

steady state, determined when the difference between the temperature of any of the wall thermocouples and the inlet temperature became constant (typically taking 30 to 90 min from the start of heating at each Reynolds number). Reference electrical heat fluxes used in most runs were chosen so that the wall temperature minus bulk temperature difference typically ranged from about 5 to 20°C. This mild heating rate was chosen to reduce the complexities of buoyancy and temperature-dependent viscosity, while still maintaining a high enough temperature difference to keep measurement uncertainties small.

Downstream Reynolds numbers ranged from 1420 to 8060. Redundant runs, made weeks apart, were used to check the repeatability of the measurements. Runs with both the reference heat flux and 50 percent of the reference heat flux were made to try to evaluate the effects of buoyancy. To check for axial symmetry, runs were also made with the heated tube rotated 180 deg, such that the wall-mounted thermocouples were at the bottom of the tube.

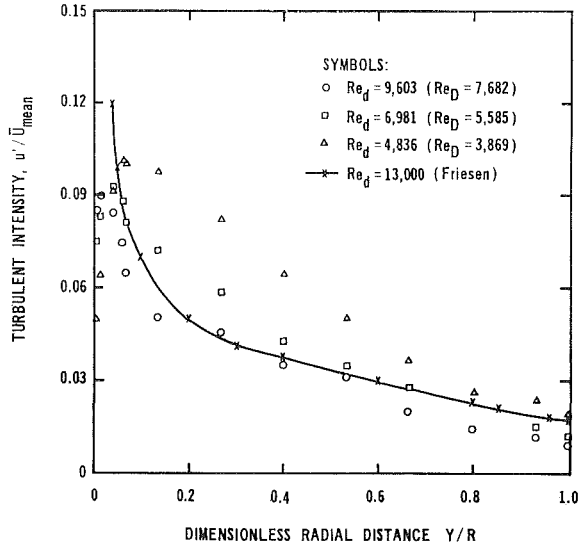

Fig. 2(c) Turbulence intensity measurements at the exit of the small-diameter tube for inlet condition *B* (rough)

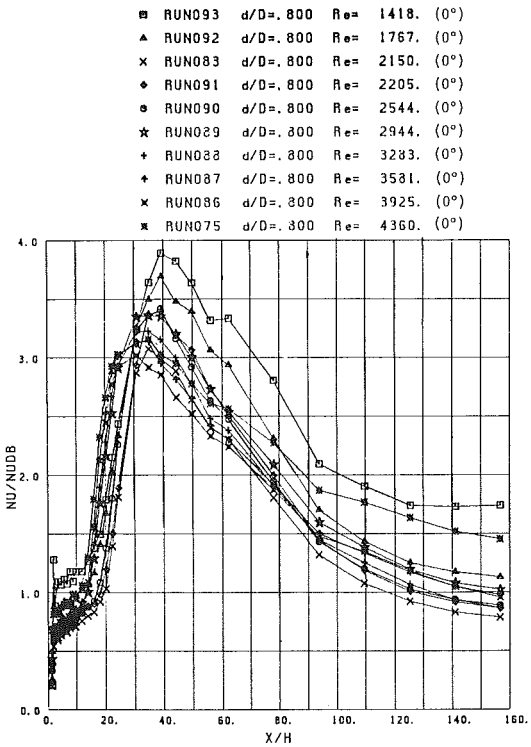

Fig. 3 Nusselt number data for a series of runs at low downstream Reynolds numbers with the thermocouples at the top of the heated tube ($\theta = 0$ deg) for inlet condition *B* (rough)

Data Reduction

The data reduction scheme follows the same procedure used in [2]. The main features are described briefly.

The local Nusselt number was calculated as

$$\mathrm{Nu}(x) = (D/k)[q_e''(x) - q_l''(x)]/[T_w(x) - T_b(x)]$$

where $q_e''(x)$ is the local electrical heat flux produced in the gold coating and $q_l''(x)$ is the local wall conduction loss determined by a conduction analysis (two-dimensional). $T_w(x)$ is the local wall temperature measured by the thermocouples and $T_b(x)$ is the calculated local bulk temperature. The values for k above (and also for the kinematic viscosity in the Reynolds

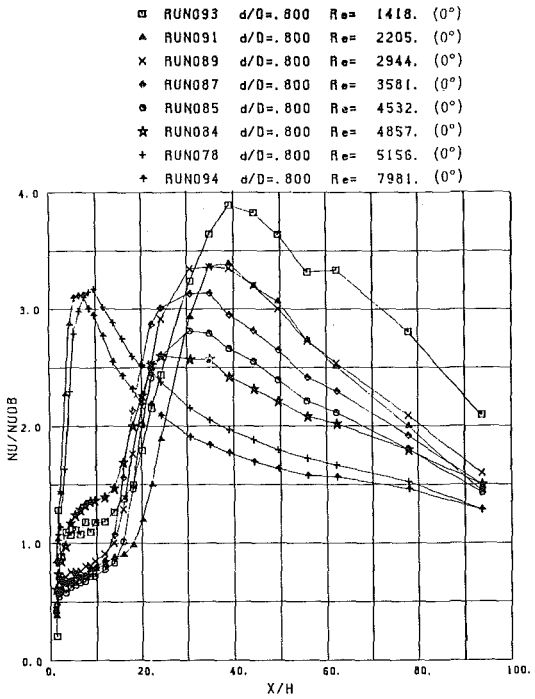

Fig. 4 Enlarged horizontal scale for the results of Fig. 3 (note: the computer connects the data points with straight lines)

number) were evaluated at the local film temperature, $T_f = 0.5(T_w(x) + T_b(x))$.

The measurement uncertainties in the reported results, estimated with odds of 20:1, using a standard uncertainty analysis, are as follows: The uncertainties in the Reynolds numbers are about ±2.3 percent at all Reynolds numbers; the uncertainties in the Nusselt numbers range from about ±6.6 percent at the peak Nusselt numbers to about ±2 percent at the lowest Nusselt numbers.

Results and Discussion

Figure 3 shows the Nusselt number results for a range of low downstream Reynolds numbers. On the abscissa H is the step height ($H = 0.5(D-d)$) and $x = 0$ is at the step. The Nusselt number is ratioed to the equivalent fully developed pipe flow value of Dittus-Boelter at the same Reynolds and Prandtl numbers for ease of comparison with other published results.

Note that the Nusselt number has its minimum at or near the corner of the expansion as can be seen more clearly on the expanded scale of Fig. 4. As the flow proceeds downstream a maximum Nusselt number is obtained, presumably near the region of reattachment of the shear layer. The Nusselt number then falls gradually and asymptotically toward its fully developed value. At the lowest Reynolds numbers the maximum Nusselt number occurs 30 to 40 step heights downstream of the expansion. As the Reynolds number is increased to near 4857 the distance to the maximum Nusselt number (and presumably reattachment) decreases, as shown in Fig. 3 (and in more detail in Fig. 4). A second peak in the Nusselt number is seen to begin forming at a position of about 9 step heights for runs at Re = 4532 and 4857. At these Reynolds numbers the oscillations or instabilities described in [5, 6] may be occurring. The measurements presented here represent a time-averaged heat transfer coefficient since the transient time scale of the wall temperature change is much longer than the time scale of the oscillations or instabilities, based on the oscillation time scales observed in [5].

In these data, as the Reynolds number is further increased, the location of maximum Nusselt number jumps abruptly to

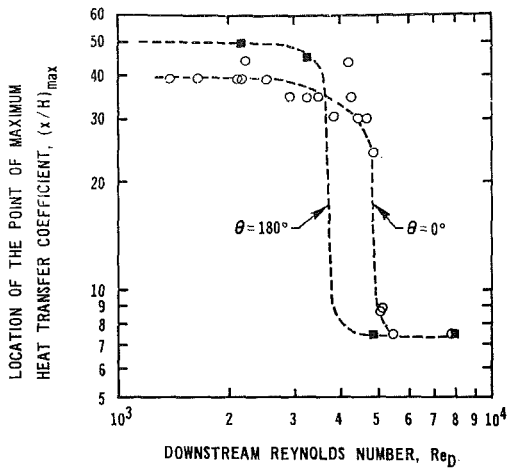

Fig. 5 Estimated location of the point of maximum Nusselt number for inlet condition B (rough) for θ = 0 deg (top) and θ = 180 deg (bottom of the tube) (dashed curves shown only to aid in interpretation)

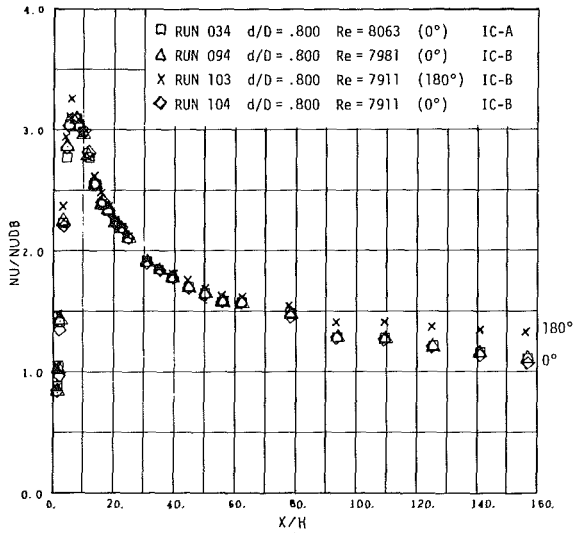

Fig. 6 Several runs at a downstream Reynolds number near 8000 to compare results for inlet condition B (rough) to an earlier run with inlet condition A (smooth)

about 10 step heights. As the flow rate is increased even further (up to about a Reynolds number of 8000) the location of the maximum Nusselt number approaches about 7 step heights, in agreement with the results in [2]. The abruptness of the jump in the location of the maximum Nusselt number is emphasized in Fig. 5. (The slight scatter in the results may be caused by uncertainties in determining the location of the maximum due to the flatness of the peaks as can be seen from Figs. 3 and 4.) This abrupt decrease in the location of the maximum Nusselt number on the top of the tube at 0 deg is at a downstream Reynolds number of about 5000 (upstream Reynolds number of about 6250). For the bottom of the tube this transition occurs at a downstream Reynolds number of about 4000 (upstream Re about 5000). These results are qualitatively similar to those reported by Back and Roschke [4]. However, their decrease occurred over a range of upstream Reynolds numbers starting at about 300 and finishing at about 800 for their d/D of 0.385. We have no explanation for these differences in the results at the present time, except to note that the transition Reynolds number appears to increase with d/D. This is supported by the data of Ede et al. [6].

This jump in the position of reattachment was also observed in the flow visualization studies of a single backward-facing step by Sinha et al. [10]. Sinha reported a gradual rise, with Reynolds number, in the length to reattachment at laminar

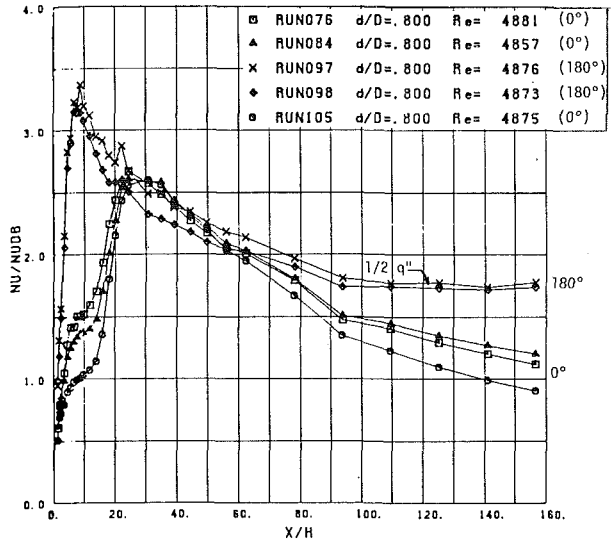

Fig. 7 Several runs at a downstream Reynolds number of about 4870 for inlet condition *B* (rough); run 097 heat flux was half the reference rate

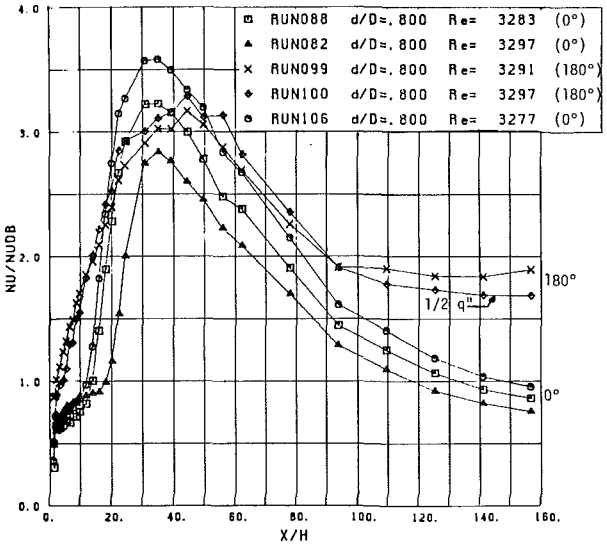

Fig. 8 Several runs at a downstream number of about 3300 for inlet condition *B* (rough); run 100 heat flux was half the reference rate

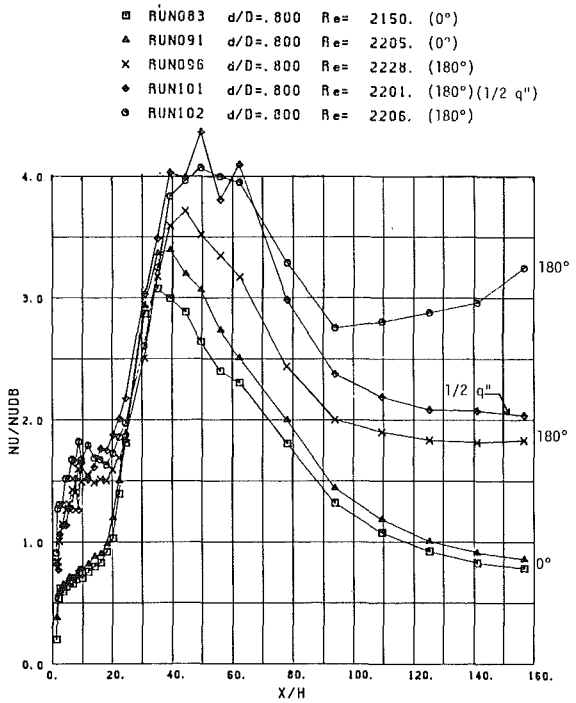

Fig. 9 Several runs at a downstream Reynolds number of about 2200 to show the variability from run to run and the effect of thermocouple location for inlet condition *B* (rough); run 101 heat flux was half the reference rate

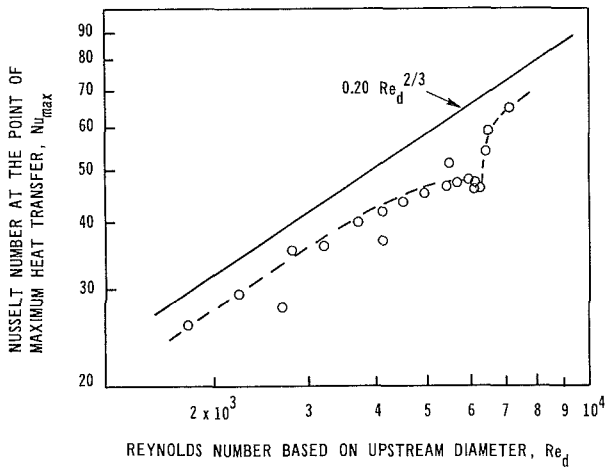

Fig. 10 Comparison of the suggested variation of the maximum Nusselt number point [1] with our data for $\theta = 0$ deg (dashed curve shown only to aid in interpretation)

flow up to a maximum of 21 step heights, following by a sudden decrease at transition to a constant value of about 6 step heights for a Reynolds number based on step height of about 900. Two major differences stand out when comparing our results to Sinha's. First, our maximum values of the length to the position of maximum Nusselt number of about 30 to 40 step heights are much longer than for his backward-facing step. This may be due to the axial symmetry of our flow. Second, we did not observe the gradual rise in the reattachment length Reynolds number, in the laminar flow regime reported in [4, 10]. This gradual rise could occur at Reynolds numbers lower than we tested for our $d/D = 0.8$.

Additional runs, not presented in this report, were made using various other upstream inlet conditions of surface roughness, ranging from no roughening to extreme roughening with 3.5-mm-dia spheres glued to the wall in place of the sandpaper. The results show the same general behavior but with the abrupt change in the position of the maximum Nusselt number occurring at slightly different Reynolds numbers, the more severe initial roughness cases giving the lower "transition" Reynolds numbers, as one might expect.

In order to determine whether the flow was axisymmetric, the heated tube was rotated 180 deg such that the wall thermocouples, normally located along the top of the tube ($\theta = 0$ deg), were positioned at the bottom ($\theta = 180$ deg). In addition, duplicate runs were made at 0 deg (and also at 180 deg in some cases) to check on reproducibility of the data.

Figure 6 shows $\theta = 0$ deg and $\theta = 180$ deg results for a downstream Reynolds number of approximately 8000 (upstream of 10,000). Note the excellent agreement between all runs, with only a slight but growing difference for x/H greater than 60, possibly due to buoyancy effects at very large x/H or downstream exit effects. This region was of little interest in this study. These results indicate that the flow at this higher Reynolds number (above the transitional Reynolds number of approximately 5000 shown in Fig. 5) is axisymmetric and highly reproducible. Furthermore, at this Reynolds number the flow can be seen to be insensitive to the inlet conditions (compare Run 034 which uses inlet condition A,

smooth, to the other runs with inlet condition B, rough, in Fig. 6). This supports the earlier conclusions regarding a fully developed inlet condition.

Figure 7 is for a downstream Reynolds number of about 4870 (upstream of 6100), which is very close to the transition Reynolds number of Fig. 5 for the top of the tube. We now find a strong Nusselt number asymmetry starting at the abrupt expansion step. Also, the position of maximum heat transfer is now far downstream at x/H values of about 30 for the top of the tube (0 deg) while it has remained at x/H of about 7 to 8 at 180 deg (i.e., close to where it was at the higher Reynolds number of Fig. 6). Thus, it appears that the flow instability is triggered at a lower Reynolds number near the bottom of the tube as previously shown in Fig. 5. The data for the two 180 deg (bottom) runs of Fig. 7 show good repeatability even though Run 097 has half the surface heat flux of Run 098. This implies that at this Reynolds number (and corresponding Rayleigh number) there are very small buoyancy effects near the bottom of the tube. However, the differences between the Nusselt numbers at 0 and 180 deg at large x/H are now larger than in Fig. 6, indicating that some buoyancy or exit effects may exist downstream of $x/H=60$.

At the top, the three 0 deg runs of Fig. 7 show good reproducibility in the position of maximum heat transfer and in the value of the maximum Nu. However, in the very sensitive region near the abrupt expansion step, we see slightly different time-averaged Nusselt number behavior. Also, for x/H values beyond about 60 some differences begin to appear in the three 0 deg runs; these are probably due to small differences in heating conditions from run to run and hence in the temperature-difference-driven buoyancy effects which can cause small but noticeable differences in the Nusselt number at large x/H.

It should be noted that the asymptotic Nusselt number ratio at large x/H is less than unity for one 0 deg run on Fig. 7 (and for all 0 deg runs on Figs. 8 and 9). This undershoot in the Nusselt number is not surprising since Nu_{DB} is not the correct asymptotic correlation for the Nusselt number at these Reynolds numbers, but is only used as a reference value. The correct average Nusselt number for fully developed flow in this transition region lies between the laminar value of 4.36 and Nu_{DB}. It should also be noted that our downstream flow does not reach fully developed conditions.

As the downstream Reynolds number is reduced to about 3300 (i.e., below the transition Reynolds number of Fig. 5) the results shown in Fig. 8 exhibit additional interesting effects. Now the position of maximum heat transfer on the bottom (180 deg) is also far downstream at about x/H of 45, while at the top it has stayed around 30 to 35. This indicates that the bottom transition Reynolds number is somewhat lower (around 4000) than the top transition Reynolds number as shown in Fig. 5.

The reproducibility shown in Fig. 8 is very good at low values of x/H and in the region of the maximum heat transfer. However, it is clearly not as good overall as in Fig. 7. At the top ($\theta=0$ deg), the systematic differences between the three runs may be due to a combination of small differences in flow conditions and in free convection effects due to small differences in heating conditions (which would be more important at the lower Reynolds numbers). At 180 deg, Run 100 was at half the heat flux of Run 099, and this difference is probably the cause of the noticeably lower Nusselt numbers at large x/H for Run 100.

Figure 9 shows results for the lowest downstream Reynolds number of about 2200 (upstream Re_d of about 2750). The behavior near the top (at 0 deg) is very similar to that of Figs. 7 and 8, both of which are for Reynolds numbers below the top transition Reynolds number of about 5000. The reproducibility of the two 0 deg runs can be seen to be very good. At 180 deg, the reproducibility at low x/H values is also very good. We now clearly see a second local maximum in the Nusselt number developing near an x/H of about 10.

The results at higher x/H values for three runs at 180 deg (bottom) shown in Fig. 9 are clearly not consistent. We suspect that Run 096 is in error but cannot prove this. The other two runs exhibit a behavior at large x/H consistent with the higher Reynolds number Runs 100 and 099 of Fig. 8, but more pronounced. That is, Run 101 (at half the heat flux of Run 102) has much lower Nusselt numbers at large x/H than Run 102. This again is attributed to lower buoyancy effects at the lower heat flux.

The $Re^{2/3}$ dependence of the maximum Nusselt number proposed by Zemanick and Dougall [1] for the higher Reynolds number turbulent flows appears to hold for lower Reynolds numbers as well, as seen in Fig. 10. The results deviate from the $Re^{2/3}$ dependency only in the transition region, but then return toward this $Re^{2/3}$ slope as the Reynolds number is increased. Our data generally lie about 15 percent below the 0.20 $Re^{2/3}$ line of [1], as did our results for fully turbulent flow reported in [2].

Conclusions

Heat transfer measurements downstream of an axisymmetric abrupt expansion at transitional Reynolds numbers have been presented. The results are particularly interesting, since they show that a sudden change in the location of the maximum Nusselt number occurs at a "transition" Reynolds number. For our upstream conditions, this transition Reynolds number was about 5000 at $\theta=0$ deg (based on the downstream diameter, with $d/D=0.8$). This heat transfer behavior may be due to a flow instability which others have previously observed in flow visualization studies. At Reynolds numbers below this transition Reynolds number, the heat transfer is not axisymmetric.

Acknowledgments

The authors gratefully acknowledge the support of the National Science Foundation for this research under Grant No. MEA-8103657. Dr. Win Aung was the program manager. We also wish to acknowledge the many valuable discussions with Professor Brian Launder of the University of Manchester Institute of Science and Technology.

References

1 Zemanick, P. P., and Dougall, R. S., "Local Heat Transfer Downstream of Abrupt Circular Channel Expansion," ASME *Journal of Heat Transfer*, Vol. 92, 1970, pp. 53–60.

2 Baughn, J. W., Hoffman, M. A., Launder, B. E., and Takahashi, R. K., "Local Heat Transfer Downstream of an Abrupt Expansion in a Circular Channel With Constant Wall Heat Flux," ASME JOURNAL OF HEAT TRANSFER, Vol 106, 1984, pp. 789–796.

3 Chieng, C. C., and Launder, B. E., "On the Calculation of Turbulent Heat Transport Downstream From an Abrupt Pipe Expansion," *Numerical Heat Transfer*, Vol. 3, 1980, pp. 189–207.

4 Back, L. H., and Roschke, E. J., "Shear-Layer Flow Regimes and Wave Instabilities and Reattachment Lengths Downstream of an Abrupt Circular Channel Expansion," ASME *Journal of Applied Mechanics*, Vol. 39, 1972, pp. 677–681.

5 Sreenivasan, K. R., and Strykowski, P. J., "An Instability Associated With a Sudden Expansion in a Pipe Flow," *Phys. Fluids*, Vol. 26, No. 10, 1983.

6 Ede, A. J., Morris, R., and Birch, E. S., "The Effect of Abrupt Changes of Diameter on Heat Transfer in Pipes," NEL Report No. 73, National Engineering Laboratory, East Kilbridge, Glasgow, Scotland, Dec. 1962.

7 Baughn, J. W., Takahashi, R. K., Hoffman, M. A., and McKillop, A. A., "Local Heat Transfer Measurements Using an Electrically Heated Thin Gold-Coated Plastic Sheet," ASME JOURNAL OF HEAT TRANSFER, Vol. 107, 1985, pp. 953–959.

8 Schlichting, J., *Boundary Layer Theory*, 4th ed., McGraw-Hill, New York, 1960, p. 505.

9 Friesen, T. V., "Design and Testing of an Apparatus Which Provides Hydrodynamically Fully-Developed Flow in a Circular Duct," Master of Eng. Project Report, Mechanical Engineeirng Dept., University of California, Davis, Mar. 1981.

10 Sinha, S. N., Gupta, A. K., and Oberai, M. M., "Laminar Separating Flow Over Backsteps and Cavities, Part I: Backsteps," *AIAA Journal*, Vol. 19, No. 12, 1981, pp. 1527–1530.

Local Heat Transfer Measurements in Turbulent Flow Around a 180-deg Pipe Bend

J. W. Baughn
Mechanical Engineering Department,
University of California,
Davis, CA 95616

H. Iacovides

D. C. Jackson

B. E. Launder

Department of Mechanical Engineering,
University of Manchester,
Institute of Science and Technology,
Manchester, England

The paper reports extensive convective heat transfer data for turbulent flow of air around a U*-bend with a ratio of bend radius:pipe diameter of 3.375:1. Experiments cover Reynolds numbers from* 2×10^4 *to* 1.1×10^5. *Measurements of local heat transfer coefficient are made at six stations and at five circumferential positions at each station. At* $Re = 6 \times 10^4$ *a detailed mapping of the temperature field within the air is made at the same stations. The experiment duplicates the flow configuration for which Azzola and Humphrey [3] have recently reported laser-Doppler measurements of the mean and turbulent velocity field. The measurements show a strong augmentation of heat transfer coefficient on the outside of the bend and relatively low levels on the inside associated with the combined effects of secondary flow and the amplification/suppression of turbulent mixing by streamline curvature. The peak level of Nu occurs halfway around the bend at which position the heat transfer coefficient on the outside is about three times that on the inside. Another feature of interest is that a strongly nonuniform Nu persists six diameters downstream of the bend even though secondary flow and streamline curvature are negligible there. At the entry to the bend there are signs of partial laminarization on the inside of the bend, an effect that is more pronounced at lower Reynolds numbers.*

Introduction

Turbulent flow in a pipe bend is fundamental to many engineering components in the thermal power area, especially those associated with convective heat transport. As two examples we mention the liquid side of a shell-and-tube heat exchanger and the interior cooling passages of turbine blades. The flow geometry is moreover sufficiently basic that, even for laminar flow, it has been the subject of numerous experimental, analytical, and numerical studies.

In the turbulent flow regime the extensive pitot tube explorations by Rowe [1] of the approach to its fully developed state of flow in a gently curved U-bend threw considerable light on the markedly different flow structure at different positions in the bend. More recently two LDA explorations have helped provide more extensive mappings of the flow structure. Enayet et al. [2] measured the distribution of streamwise mean and rms fluctuating velocity along several lines traversing the duct cross section at five stations within and downstream of a 90-deg bend with mean bend radius 2.8 times the pipe diameter. The mean velocity profiles showed clearly the piling up of low-momentum fluid on the inside of the bend by the secondary flow. This slow-moving fluid was further retarded by the adverse pressure gradient encountered by the flow on the inside as it passed from the curved bend to the straight exit tangent. The study by Azzola and Humphrey [3] obtained measurements of the mean and rms values of both the streamwise and the circumferential (secondary) components along the diametral line at right angles to the duct's plane of symmetry. The data were obtained for two turbulent Reynolds numbers ($Re \simeq 5.74 \times 10^4$ and 1.1×10^5) and at a total of 12 stations including five, at one-diameter intervals, immediately downstream of the bend. Their measurements of the secondary flow, summarized in Fig. 4 and discussed more fully in Section 3, show in quantitative detail a number of the qualitative inferences drawn by Rowe [1], including the reversal of the secondary flow in the center of the pipe by 135 deg into the bend.

No correspondingly detailed sets of data for heat transfer in circular-sectioned pipe bends are available. Local heat transfer coefficients for turbulent, nominally fully developed flow in a coil have been reported by Seban and McLaughlin [4]. Their experiments, carried out over a range of Reynolds number, showed mean levels of heat transfer coefficient some 50 percent above those for a straight tube and a circumferential variation of Nu of about 2:1, the levels diminishing monotonically from the outside to the inside of the bend. Qualitatively this behavior is to be expected: The secondary flow continually removes hot fluid[1] from the outside of the

Contributed by the Gas Turbine Division of THE AMERICAN SOCIETY OF MECHANICAL ENGINEERS and presented at the 31st International Gas Turbine Conference and Exhibit, Düsseldorf, Federal Republic of Germany, June 8–12, 1986. Manuscript received at ASME Headquarters January 10, 1986. Paper No. 86-GT-53.

[1] Assuming a heated tube wall

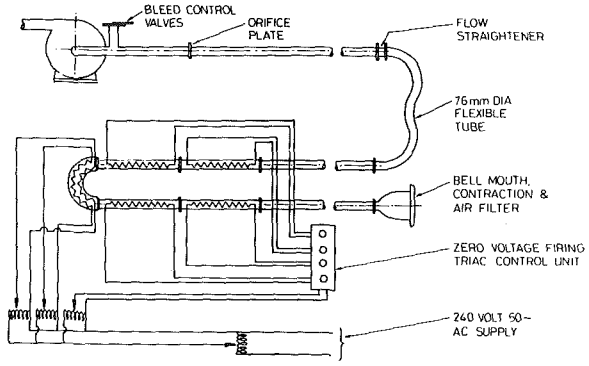

Fig. 1 Schematic view of test section

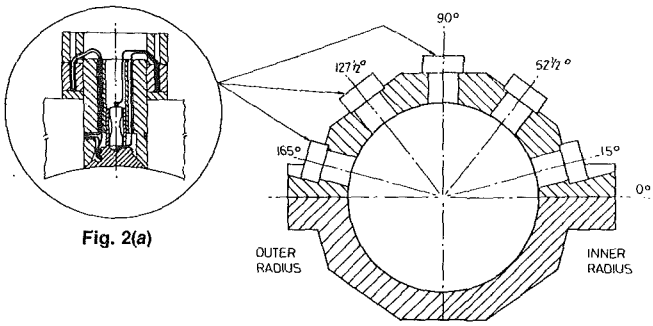

Fig. 2(a)

Fig. 2(b)

Fig. 2 (a) Cross section of U-bend; (b) enlarged view of heat flux meter

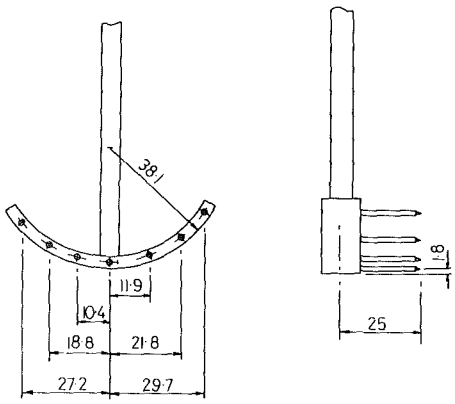

Fig. 2(c) Thermocouple rake

bend and transports it to the inside. There is a further contributor to the circumferential nonuniformity. Streamline curvature will tend either to dampen or augment turbulent mixing depending on whether the mean angular momentum increases or decreases with radius (here referenced to the center of curvature of the streamline, not the pipe center) [5]. This effect reduces thermal mixing on the inside of the bend and increases it on the outside, i.e., its effect on the heat transfer coefficient is in the same sense as that of the secondary flow.

The aim of the experimental work presented in this paper has been to provide detailed information about the convective heat transfer coefficient and thermal field in a *developing* flow around a bend, a more complicated and more important situation from a practical standpoint than fully developed flow. Because of the desirability of having flow-field data as well (since convection by the secondary flow and modifications to the fluctuating velocity are the agencies determining the level of heat transfer coefficient), the experiment has been designed to replicate the geometry and boundary conditions of the 180-deg-bend experiments of Azzola and Humphrey [3]. Together, those experiments and the present ones provide the corresponding mapping for the circular tube that the recent experiments by Chang, Humphrey, and Modavi [6] and Johnson and Launder [7] have reported for the square-sectioned U-bend.

Apparatus, Instrumentation, and Experimental Procedure

The test section, shown in Fig. 1, consisted of a 76-mm-dia circular-sectioned U-bend with inlet and exit tangents each 50 diameters long, 25 of which were instrumented for heating (see Fig. 1). A short perspex spacer was interposed between the flanges separating the heated and unheated parts of the inlet/exit tangents to keep heat conduction to the unheated sections to unimportant levels. The apparatus was designed to provide a nearly uniform wall-temperature boundary condition, the tangent tubing being made from sections of thick-walled drawn aluminum tubing while the 180-deg bend itself was machined in two symmetric halves from solid aluminum blocks. The mean radius of the bend was 6.75 times the pipe radius. The sections of the inlet and outlet tangents, each 0.95 m in length, were flanged and spigoted at their ends to facilitate their connection together without mismatch at the pipe wall; for the same reason the upper and lower halves of the 180-deg bend were also spigoted.

The flow entered the test seciton via a 16:1 area contraction. The flow in the inlet tangent was rather sensitive to the flaring of the bellmouth and some of the earlier tests (shown in Figs. 5, 6(*a*), and 6(*b*)) were taken without the contraction as this led to a more symmetric velocity distribution. A hot-wire traverse along the vertical diameter revealed that the maximum difference between the two halves of the velocity profile was 4.2 percent. Later tests, with a redesigned bellmouth in place, achieved a further improvement in symmetry. Air was drawn through the rig by a 10-hp blower which provided a maximum test section Reynolds number of 1.1×10^5. Flow rates were monitored by an orifice plate located in a separate section leading to the blower; the plate itself and associated pipework conformed with BS1042.

Thermal measurements were made at five stations in the bend (15, 55, 90, 125, and 165 deg) and at six diameters downstream. The data comprised local heat transfer rates measured at five circumferential positions in the top half of the bend (Fig. 2). These were measured by heat-flux gauges developed at UMIST from an earlier design of Kraabel, Baughn, and McKillop [8] and described in detail in Baughn et al. [9]. Briefly, a conical copper block providing the heating surface, with a small resistor embedded at its center, was enveloped by a cylindrical body of low thermal conductivity epoxy (Fig. 2(*b*)). The unit was flush mounted with the surface

Nomenclature

D = pipe diameter
Nu = Nusselt number based on temperature difference between wall and pipe center
r = radial coordinate
Re = Reynolds number $\equiv DW_b/\nu$
T = temperature
T_A = ambient temperature
T_b = bulk temperature
T_W = wall temperature
V = circumferential component of mean velocity
w' = rms streamwise fluctuating velocity
W = longitudinal component of mean velocity
W_b = bulk average velocity through the pipe
ν = fluid kinematic viscosity

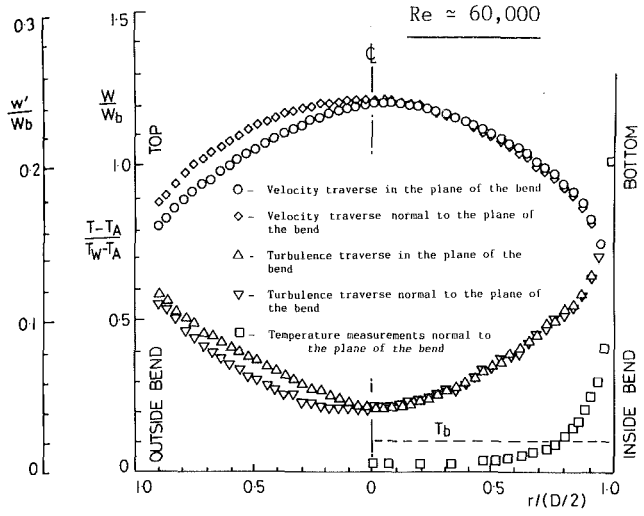

Fig. 3 Bend inlet mean and turbulence velocity profiles and temperature profile measured two diameters upstream of the bend

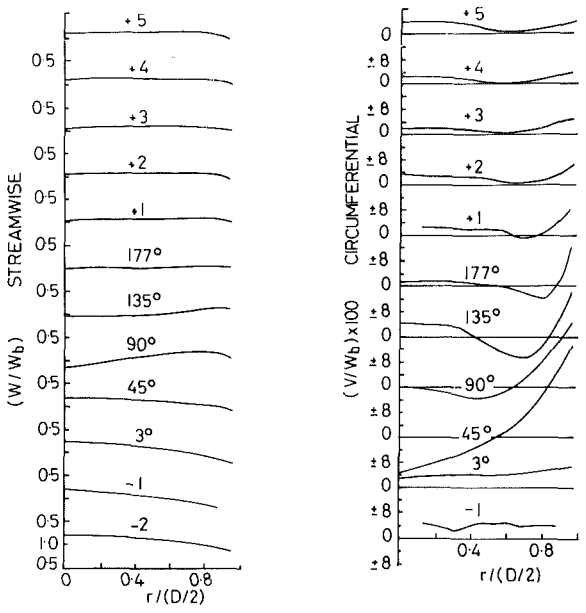

Fig. 4(a) **Fig. 4(b)**

Fig. 4 Normalized streamwise and circumferential velocity profiles along a radius perpendicular to a symmetry plane at a Reynolds number of 57,400; data of Azzola and Humphrey [3]

of the pipe bend. Heat input to the resistor was adjusted until the cone temperature was brought to that of the surrounding pipe (to within 0.015°C) details of instrumentation and procedure being given in [9]. Accurate measurement of the current supply to the resistor and the voltage applied across it enabled the heat flux through the exposed area of the sensor to be calculated. Prior to their use in the present study, the gauges were extensively tested in a straight pipe [9].

At one Reynolds number, temperature distributions within the air stream were made by means of a thermocouple rake consisting of seven PTFE insulated chromel-alumel thermocouples of 0.2-mm diameter (Fig. 2(*c*)). These were held by a tufnol (low thermal conductivity) support bar curved to match the radius of the pipe, thus allowing all seven thermocouples to record temperatures close to the wall. The rake was traversed vertically covering the lower half of the bend. Because of the time-consuming nature of this mapping, other tests merely recorded – with a single thermocouple – the temperature at the bend center. Unlike the rake, the single probe could be inserted and removed through the stem access hole without disassembling the bend.

The heat supply to the bend itself and to the inlet and exit tangents was provided by self-adhesive heat tape (Clayborn Labs. Inc.) affixed to the outside of the bend with approximately 12-mm spacing between adjacent tracks. The tape on the straight sections was wound helically while for the bend section 20 single tracks running axially were applied to the upper and lower halves of the bend. The electrical connections allowed the heating current to 20 tracks on the outer half of the bend (10 each from the upper and lower halves) to be controlled separately from the 20 on the inside. A two-dimensional finite-difference heat-conduction analysis indicated that at the inside surface of the tube temperature variations arising from the discrete heating on the outside amounted to no more than 2 percent of the temperature difference between the wall and ambient values. There was found to be a larger variation in wall temperature in the streamwise direction (~7 percent) arising from changes in both the bulk temperature and the velocity field as the air passes around the bend. This variation was of course taken into account in evaluating the Nusselt number data presented in Section 3.

Before the test program began, the apparatus was checked for leaks by sealing off the pipework and pressurizing the rig. Thereafter velocity profiles were taken at two diameters upstream of the bend to establish that the flow was acceptably symmetric and to provide well-defined entry conditions. Figure 3 shows the mean and rms axial velocity profiles for both vertical and horizontal traverses; the horizontal traverse already shows a shift of the airflow toward the inside of the bend induced by the upstream effects of the bend on the pressure field. To verify that the cold-rig flow-field data (obtained by the Berkeley group) would be representative of flow conditions in the heated duct, the mean profile was measured again with a pitot tube with the duct both heated and unheated. No significant differences in the profile were noted with the pipe wall temperature 20°C above that of the entering fluid, both showing complete agreement with the cold-flow profile obtained by the hot wire.

The heat transfer measurements were taken at three nominal Reynolds numbers: 2×10^4, 6×10^4, and 11×10^4. The two higher Reynolds numbers correspond closely with those for which the velocity field has been mapped by Azzola and Humphrey [3]. In our work the greatest attention has been given to the middle Reynolds number. Data have been obtained with the nominal wall temperature 10°C and 20°C above that of the air at inlet. Iacovides [10] has provided a detailed analysis of experimental uncertainties. Based on this we estimate that the Nusselt number data are accurate to within ±4 percent at the highest Reynolds number with 20°C overheat (where uncertainties are least) and to within ±10 percent for a 10°C overheat at $Re = 2 \times 10^4$ (where uncertainties are greatest).

Presentation and Discussion of Results

First we re-examine the mean velocity field data of Azzola and Humphrey [3] summarized in Fig. 4 to provide a background for presenting the thermal measurements. The velocities were taken along the vertical diametral line perpendicular to the plane of geometric symmetry. Fully developed pipe flow at entry leads to a rapid development of secondary velocities which, by 45 deg into the bend, reach a peak value of about 30 percent of the bulk streamwise velocity, the maximum occurring very close to the wall. The secondary motion carries slow-moving fluid near the pipe wall to the inside of the bend; correspondingly, faster-moving fluid close to the symmetry plane migrates toward the outside of the bend giving the classical single-cell vortex. By 90 deg into the bend, the convection of fluid by the secondary motion shifts the peak in streamwise velocity near the pipe wall with a minimum at the

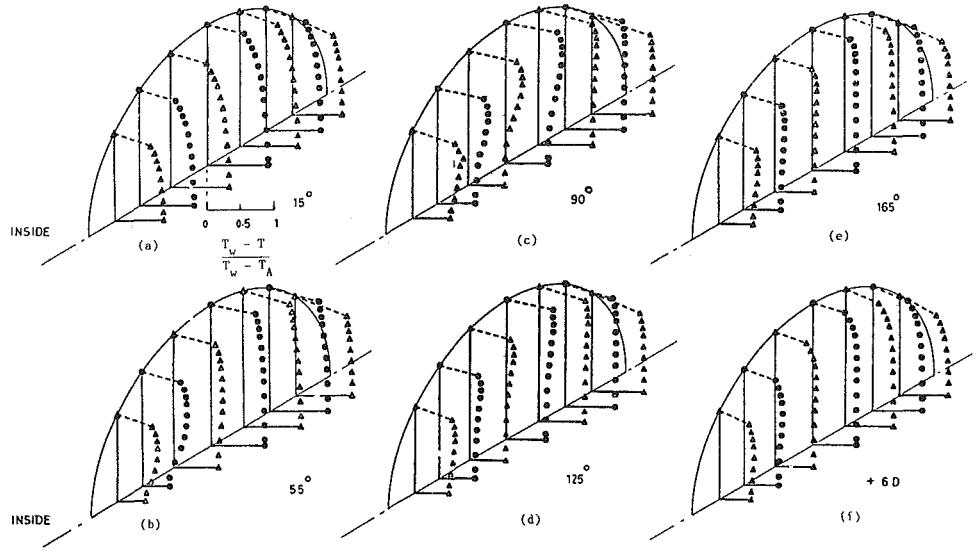

Fig. 5 Normalized temperature profiles in U-bend; Re ≃ 60,000; $\Delta T \simeq 20°C$

pipe center. Because of this inversion the radial pressure gradient now acts to drive fluid near the pipe center to the *inside* of the bend (135 deg) and this reverse stirring makes the streamwise velocity virtually uniform along the measurement line (177 deg to four diameters downstream).

Figure 5 provides the corresponding temperature mapping obtained in the present explorations at a nominal bulk Reynolds number of 6×10^4 and for the tube wall heated to about 20°C above ambient. The variation of $(T_w - T)/(T_w - T_i)$ along seven vertical lines is shown; the center line is the same as that on which the velocity profiles of Fig. 4 were obtained. Here T_w is the wall temperature, T the local air temperature, and T_i the air temperature at inlet to the pipe. At 15 deg into the bend the temperature field differs little from that found in a straight pipe: Along each traverse line the normalized temperature rises monotonically from the wall to the symmetry plane while along the symmetry plane itself the temperature is nearly symmetric with respect to the pipe center.

A sharply different picture has developed by 55 deg. Along the two traverse lines closest to the inside of the bend, a deep trough in normalized temperature appears in the vicinity of the symmetry plane associated with hot air from the immediate proximity of the bend wall being lifted away from the surface and carried toward the pipe center by the secondary flow. Along the third line there is only a weak dip in normalized temperature at this station and none at all along the fourth (the diametral line); this is because at these locations the secondary motion has brought fluid at only a slightly different temperature than that originally occupying that position. Over the outer half of pipe a reverse picture emerges: Here the secondary flow "imports" faster moving, cooler fluid (i.e., with larger normalized temperatures).

The temperature field at 90 deg is very much a continuation of the developments seen at 55 deg. There is now a marked dip in temperature along the center traverse line, a feature which matches the dip in streamwise velocity noted above in Fig. 4. The profiles at 125 deg and 165 deg, like the corresponding velocity profiles, now show little variation along the traverse lines though there remains a significant rise in (normalized) temperature from the inside to the outside of the bend. By six diameters downstream of the bend the re-establishment of new thermal boundary layers on the pipe wall is evident.

The overall picture that emerges from the temperature-field data is one that is fully compatible with the Azzola–Humphrey velocity measurements. Indeed, because the present measurements provide a view of the temperature field over the whole cross section, they allow a fuller, more quantifiable impression than could be gained from the flow-field data alone.

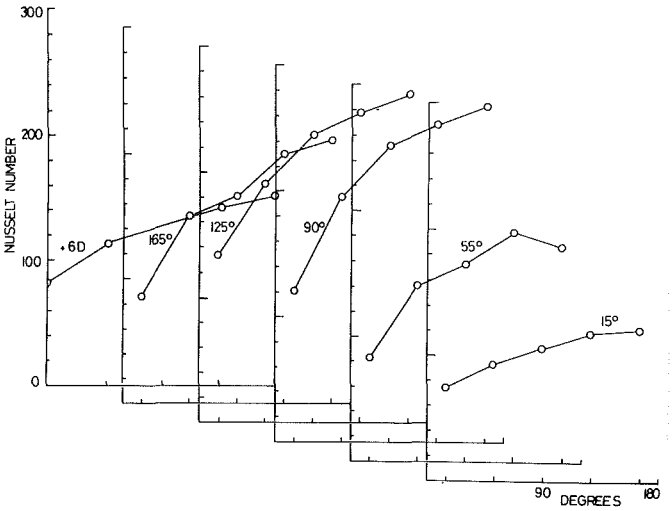

Fig. 6(a) Circumferential distribution of Nusselt number at six stations in and downstream of U-bend; $\Delta T \simeq 20°C$; Re ≃ 6×10^4; thermocouple rake in duct

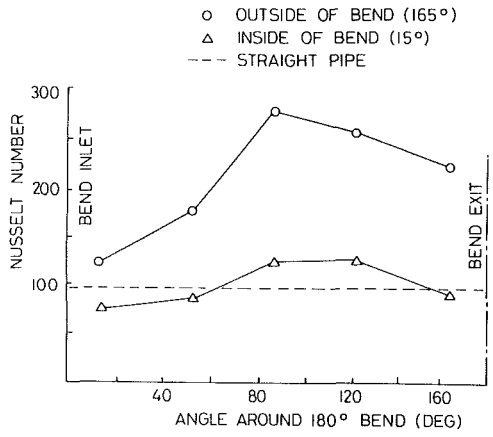

Fig. 6(b) Variation of Nusselt number around the 180-deg bend at a Reynolds number of 60,000; $\Delta T \simeq 20°C$; thermocouple rake in duct

The measured heat transfer coefficients, expressed in terms

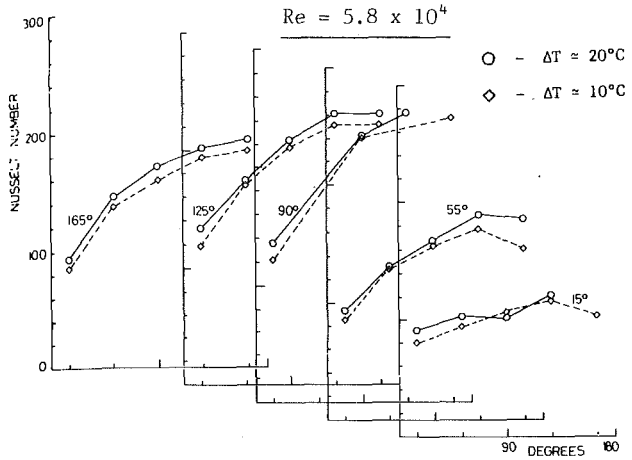

Fig. 7 Circumferential distribution of Nusselt number at five stations in U-bend

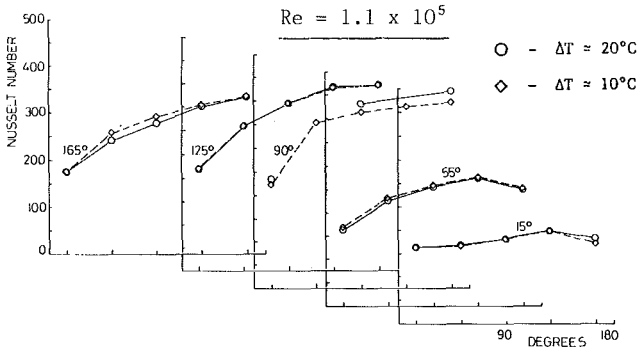

Fig. 8 Circumferential distribution of Nusselt number at five stations in U-bend

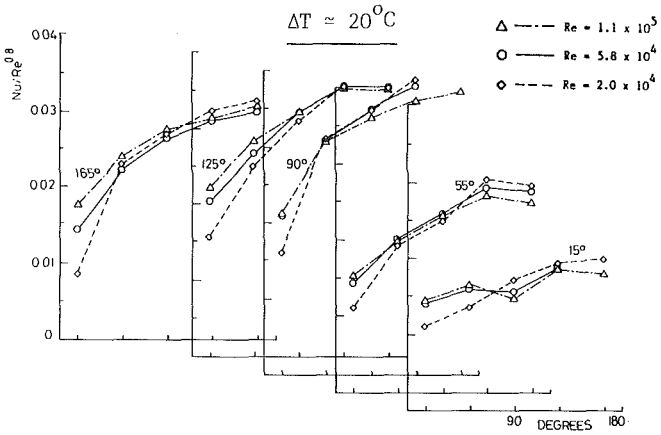

Fig. 9 Variation of $Nu/Re^{0.8}$ around U-bend for tests at three Reynolds numbers

of Nusselt number, are presented in Figs. 6(*a*) and 6(*b*). The "point" values reported are in fact an average over the face of the heat flux meter whose extremities extend ±8 deg about the center (the angular location of which is indicated in the figures). From *predictions* of this test case [11] we infer that this average value will differ negligibly from the local value at the center of the heat flux meter except at the position nearest the inside of the bend where at some positions the reported value may be up to 2 percent too high. It is emphasized that in the definition of Nu the temperature difference is that between the local wall value and the air temperature *at the center* of the tube. This basis was adopted because the bulk mean temperature at any station could not be determined with great precision since the experiments were with a (nearly) uniform wall temperature. Figures 6(*a*) and 6(*b*) relate to precisely the test conditions for which the interior temperature profiles were obtained – indeed, the rake was still in place, pushed down as far as possible while the measured heat fluxes were obtained around the top half of the duct. Perhaps the first thing to notice is that even by 15 deg an appreciable circumferential variation of heat flux has developed. Much stronger circumferential variations are found as one proceeds around the bend, a development due partly to the secondary flow (the "impingement" of cool fluid on the outer wall will obviously raise heat transfer rates) and partly to the modifications to the turbulent mixing, augmentation occurring on the concave surface and damping on the inside of the bend. The maximum mean level of Nu occurs at 90 deg. The variation from the inside to the outside of the bend is also largest there: Extrapolation to 0 deg suggests an outer-to-inner variation of 3:1. (Figure 6(*b*) helps to underline that the main changes in the level of Nu occur over the outer half of the bend.) The mean level and the circumferential variation of Nusselt number fall gradually over the second half of the bend due to decay of secondary flow (see Fig. 4(*b*)). Even six diameters downstream, however, there is still a 2:1 variation in Nu between (what had been) the inside and outside of the bend. The reason for this seems to be that due to the virtual disappearance of the secondary flow the hottest fluid, which during passage around the bend accumulated on the inside, simply stays there (Fig. 5(*f*)) until eventually the (relatively) slow process of turbulent diffusion restores axial symmetry to the temperature field. Evidently, however, this occurs only far downstream of the region examined in the present experiments.

More extensive heat-flux measurements in the bend itself were made in which just the centerline temperature was measured; in this way the risk of affecting the surface heat flux pattern with the thermocouple rake was avoided. Figure 7 shows the distributions of Nusselt number for nearly the same Reynolds number as Fig. 6 for two temperature differences: 20°C (as in Fig. 6) and 10°C. In a few positions the heat-flux gauge went "open circuit" during the test, which is why data points are occasionally missing. The variation is very similar to that shown in Fig. 6, though on average the levels are lower by 5 percent. For the test in which the temperature difference was reduced to 10°C the average levels of Nu lie 8 percent below those for a 20°C temperature difference. Two earlier tests, in which just the heat transfer rates were measured, also showed the same effect, i.e., the heat fluxes divided by the temperature difference at inlet was 8–10 percent less at the lower heating rate. The decrease in density associated with heating could be expected to raise the Nusselt number in a curved pipe by two mechanisms. Firstly, the secondary flow driving force is raised since the lowest density fluid is also the slowest moving. Secondly, there will be some tendency for cooler (denser) turbulent eddies to centrifuge to large radii thus promoting mixing on the outside of the bend (though dampening it on the inside). Neither mechanism looks powerful enough to have a significant effect, however, when such small density differences are involved. We note, moreover, that at a Reynolds number of 1.1×10^5, for which results are shown in Fig. 8, there are no significant differences between the 20°C and 10°C experiments. Now, at this higher Reynolds number precision is greater because heat input rates are greater and heat losses of smaller significance. Our view is thus that the apparent sensitivity to ΔT, shown in the data at $Re = 5.8 \times 10^4$, is probably not a real effect. The values obtained with the larger temperature difference are thus preferred.

Finally, Fig. 9 shows the results of consolidating data for three Reynolds numbers: the two for which data are shown above and for 20,000. In all cases the measured Nusselt number is divided by $Re^{0.8}$ for the test in question. While the data for the three tests broadly collapse together, there is evidently a diminution in the ratio of outer:inner heat transfer

coefficient as the Reynolds number is raised, due mainly to a marked increase in Nusselt number on the inside of the bend, or, conversely, a sharp fall as Re is lowered. The indication seems to be that the diminished turbulent mixing near the inner wall is causing the viscous sublayer to become thicker at the lowest Reynolds number causing a substantial increase in thermal resistance. This is qualitatively similar to the effects found in other boundary layer flows subject to damping of turbulence. Indeed, for flows in coils it is known (see, for example, Sreenivasan and Strykowski [12]) that at Reynolds numbers below 10^4 the flow on the inside of the bend may become laminar even though turbulent flow is maintained on the outside.

Concluding Remarks

A detailed mapping has been provided of the thermal field in turbulent flow around a circular-sectioned **U**-bend for conditions corresponding to those for which Azzola and Humphrey have reported velocity field data. Together, the two experiments give a comprehensive documentation of the processes of convective heat transport in a complex but well-defined three-dimensional turbulent flow. It is hoped that they will provide a searching test case for the three-dimensional flow computation procedures that are now becoming widely available for industrial design purposes.

Among the most striking results to emerge were:

- the large circumferential variation of heat transfer coefficient that developed by only 15 deg into the bend: nearly a 2:1 ratio for $Re = 2 \times 10^4$;
- the attainment of maximum mean heat transfer coefficient at 90 deg into the bend at which station the maximum circumferential variation was also recorded;
- the persistence of strong circumferential nonuniformities in Nusselt number six diameters downstream of the bend.

Acknowledgments

The research has been sponsored by the U.S. Office of Naval Research (Power Program) through Grant N00014-83-G-0021 for which we express our gratitude and thanks. Special recognition must go to two UMIST technician staff: Mr. D. Cooper provided outstanding assistance in the design of the heat-flux meters, in constructing the apparatus, and in providing support during test runs. Mr. R. Lever brought his remarkable machining skills to bear in fabricating the 180-deg-bend test section and many other precision-machined items in the test rig. Our thanks go also to Mrs. L. J. Ball who prepared the camera-ready manuscript with her usual and appreciated care.

Authors are listed alphabetically.

References

1 Rowe, M., *J. Fluid Mech.*, Vol. 43, 1970, p. 771.

2 Enayet, M. M., Gibson, M. M., Taylor, A. M. K. P., and Yianneskis, M., *Int. J. Heat and Fluid Flow*, Vol. 3, 1982, p. 211.

3 Azzola, J., and Humphrey, J. A. C., "Developing Turbulent Flow in a 180° Curved Pipe and Its Downstream Tangent," Report LBL-17681, Lawrence Berkeley Laboratory, Univ. California, 1984 [see also *Proc. 2nd Int. Conf. on Laser Anemometry*, Lisbon, 1984].

4 Seban, R. A., and McLaughlin, E. F., *International Journal of Heat and Mass Transfer*, Vol. 6, 1963, p. 387.

5 Bradshaw, P., AGARDograph 169, 1973.

6 Chang, S. M., Humphrey, J. A. C., and Modavi, A., *Physico-Chemical Hydrodynamics*, Vol. 4, 1983, p. 243.

7 Johnson, R. W., and Launder, B. E., *Int. J. Heat and Fluid Flow*, Vol. 6, 1985, p. 171.

8 Kraabel, J. S., Baughn, J. W., and McKillop, A. A., ASME *Journal of Heat Transfer*, Vol. 102, 1980, p. 576.

9 Baughn, J. W., Cooper, D., Iacovides, H., and Jackson, D. C., "An Instrument for the Measurement of Heat Flux From a Surface With Uniform Temperature," *Rev. Scientific Inst.*, May 1986.

10 Iacovides, H., Ph.D. thesis, University of Manchester, Faculty of Technology, 1986.

11 Iacovides, H., and Launder, B. E., "ASM Predictions of Turbulent Momentum and Heat Transfer in Coils and **U**-Bends," *Proc. 4th Int. Conf. on Num. Meth. in Laminar and Turbulent Flow*, 1985, pp. 1023–1045.

12 Sreenivasan, K. R., and Strykowski, P. J., "Stabilization Effects in Flow Through Helically Coiled Pipes," *Experiments in Fluids*, Vol. 1, 1983, p. 48.

Flow Visualization Studies on Secondary Flow Patterns in Straight Tubes Downstream of a 180 deg Bend and in Isothermally Heated Horizontal Tubes

K. C. Cheng
Mem. ASME

F. P. Yuen

Department of Mechanical Engineering,
University of Alberta,
Edmonton, Alberta, Canada

Photographs are presented for secondary flow patterns in a straight tube (x/d = 0 ~ 70) *downstream of a 180 deg bend* (*tube inside diameter* d = 2.54 *cm, radius of curvature* R_c = 12.7 *cm*) *and in an isothermally heated horizontal tube* (*tube inside diameter* d = 2.54 *cm, heated length* l = 46.2 *cm*) *with free convection effects. Each test section is preceded by a long entrance length with air as the flowing fluid. For curved pipes, the Dean number range is* K = 99 *to* 384. *At the exit of the 180 deg bend, the onset of centrifugal instability in the form of an additional pair of Dean vortices near the central outer wall occurs at a Dean number of about* K = 100. *The developing secondary flow patterns in the thermal entrance region of an isothermally heated horizontal tube are shown for the dimensionless axial distance* $z = 0.8 \times 10^{-2}$ *to* 1.83 (*Re* = 3134 ~ 14) *for a range of constant wall temperatures* $\bar{T}_w$ = 55 ~ 65°C *with entrance air temperature at about* 25°C. *The secondary flow patterns shown are useful for future comparisons with predictions from numerical solutions.*

1 Introduction

The secondary flows caused by centrifugal force effects in curved pipes and by buoyancy force effects in the thermal entrance region of isothermally heated or cooled tubes are known to be important in laminar forced convection heat transfer and the related literature is quite extensive because of their practical importance in heat transfer equipment applications.

After the classical works of Graetz (1883) and Nusselt (1910) on pure forced convection in the thermal entrance region of isothermally heated tubes with fully developed laminar flow, the buoyancy effect on the thermal entrance region problem (Graetz problem) were studied by such well-known investigators as Drew [1], Colburn [2], and many others in recent years. The earlier results are well summarized by McAdams [3]. For the Graetz problem with significant buoyancy effects in horizontal isothermal tubes, the classical method of solution is not applicable and one must employ a numerical solution [4]. For the uniform wall temperature boundary condition, the buoyancy effect first appears in the Leveque solution region near the thermal entrance depending on Rayleigh number [4] and the bulk temperature approaches the wall temperature in the fully developed forced convection region with the asymptotic Nusselt number Nu_∞ = 3.66. Because of the heat transfer mechanism, the correlation of heat transfer data on laminar mixed convection in an isothermal horizontal tube [5] is very difficult. It is believed that flow visualization studies on developing secondary flow patterns in the thermal entrance region of an isothermally heated horizontal tube with free convection effects will provide some insight into the heat transfer mechanism and complement the existing theoretical and experimental investigations reported in the literature.

After the classical work of Dean [6, 7] on fully developed laminar flow in curved pipes, many theoretical and experimental investigations on flow and forced convective heat transfer in curved pipes have been carried out. The literature was surveyed recently by Berger et al. [8] and Masliyah and Nandakumar [9]. One notes that heating and cooling coils are used extensively in heat transfer equipment and the physiological applications of curved tubes dealing with flow patterns and wall shear stress in arteries are given by Pedley [10].

Numerical solutions of fully developed laminar flow in curved pipes or ducts usually yield secondary flow patterns. For laminar flow in a curved pipe, it is generally understood that the secondary flow consists of a pair of symmetric counterrotating vortices in a cross section normal to the main flow. However, it is not clear whether the secondary flow eventually decays or changes into other flow patterns as the Reynolds number increases to the turbulent flow regime. It is observed that for flow in curved pipes the pressure increases monotonically from the inner convex curved wall toward the concave curved outer wall across the cross section due to the centrifugal forces caused by the curvature effect. However, the centrifugal force increases and then decreases toward the outer concave wall after reaching a maximum value along a line parallel to the horizontal axis. Thus, the region near the concave outer wall is potentially unstable and centrifugal instability (Dean's instability) phenomena [11] may occur. Dean's instability phenomenon in the form of an additional pair of counterrotating vortices occurring near the center of the concave outer wall has been observed by flow visualization for fully developed laminar flow in curved square channels at a certain Dean number [12]. It is thus speculated that a centrifugal instability phenomenon may occur for other geometric shapes such as curved circular or semicircular pipes. Indeed, recent numerical solutions for fully developed laminar flow in curved pipes reveal the occurrence of the abovenoted centrifugal instability for curved semicircular tubes [13] and curved circular tubes [14, 15]. Recently, flow visualization studies of secondary flow patterns and centrifugal instabilities in curved circular and semicircular pipes were reported [16]. It is noted that flow visualization studies on secondary flow patterns in or downstream from the 90 or 180 deg bend reported in the literature are rather limited. The local heat transfer measurements in and downstream from a U-bend were reported by Moshfeghian and Bell [17] and the pertinent

Contributed by the Heat Transfer Division for publication in the JOURNAL OF HEAT TRANSFER. Manuscript received by the Heat Transfer Division April 24, 1984. Paper No. 84-HT-62.

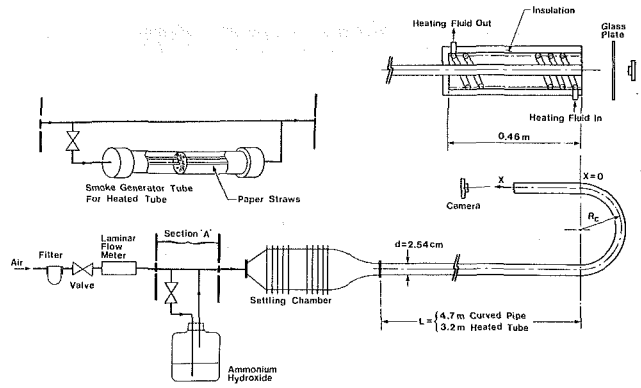

Fig. 1 Schematic diagram of experimental apparatus

literature can be found there. The effect of a 90 deg bend on flow in the bend or flow in the straight tube downstream was also studied experimentally by several investigators. It is evident that theoretical and experimental studies on flow in or downstream of 90 or 180 deg bends should be complemented by flow visualization studies on developing or decaying secondary flow patterns across the cross section normal to the main flow.

The main purpose of this paper is to present a series of photographs on secondary flow patterns at the exit of a 180 deg bend and in the downstream region of straight tube for a range of Reynolds numbers (Re = 283 ~ 1807) and on developing secondary flow patterns in the thermal entrance region of isothermally heated horizontal tubes with significant free convection effects. The flow visualization was facilitated by injecting smoke into air.

2 Experimental Parameters

The experimental parameters for steady viscous flow in curved circular pipes are curvature ratio (ratio of tube inside diameter to coil diameter) $d/2R_c$, Reynolds number $\mathrm{Re} = \bar{W}d/\nu$, and Dean number $K = \mathrm{Re}(d/2R_c)^{1/2}$. For this investigation, $d = 2.54$ cm and $R_c = 12.7$ cm, Re = 283 ~ 1807, and $K = 99 \sim 384$.

For an isothermally heated horizontal tube, the experimental parameters are Reynolds number, Rayleigh numbers $\mathrm{Ra}_1 = g\beta(\bar{T}_w - T_0)d^3/\nu\kappa$, $\mathrm{Ra}_2 = g\beta(\bar{T}_w - \bar{T}_c)d^3/\nu\kappa$, and dimensionless axial distance $z = (1/d)/\mathrm{RePr}$. For this study, $d = 2.54$ cm, $l = 46.2$ cm, $\bar{T}_w = 55 \sim 65°\mathrm{C}$, Re = 15 ~ 3271, $\mathrm{Ra}_1 = 3.65 \times 10^4 \sim 6.3 \times 10^4$, and $\mathrm{Ra}_2 = 8.94 \times 10^3 \sim 4.67 \times 10^4$.

3 Experimental Apparatus and Procedure

The experimental appartus for a 180 deg bend with a downstream straight tube is shown schematically in Fig. 1. The 180 deg bend was machined from two pieces of plexiglass block symmetric in the plane of the curved pipe axis. The downstream straight section utilizes plexiglass tubes with different lengths. The smoke was generated by passing air over ammonium hydroxide and injecting hydrochloric acid through a hypodermic needle ahead of the 180 deg bend. The secondary flow patterns were observed at the exit of the 180 deg bend ($x = 0$) and at various downstream sections at a distance x from the outlet of the 180 deg bend. A slit light source was provided by a slide projector. Room compressed air was used and the air flow rate was measured by Meriam laminar flow element. The entrance length after settling chamber was 4.7 m to ensure fully developed laminar flow at the inlet of the bend.

For combined free and forced convection tests in a horizontal tube, the 180 deg bend was replaced by a copper tube (inside diameter $d = 2.54$ cm, heating length $l = 46.2$ cm) with heating jacket (double-pipe heat exchanger) and hot water was circulated at high speed between the constant-temperature bath and the test section in the counterflow direction. To promote turbulence, a coil was inserted in the annular space and the test section was insulated to prevent heat loss. The inlet and outlet bulk temperatures of the heated fluid (hot water) to the heating section were measured using 0.7 mm o.d. sheathed iron-constantan thermocouples. The inlet and outlet centerline air temperatures in the test section were measured by type T thermocouples (diameter = 0.254 mm). All thermocouples were initially calibrated using a quartz thermometer. A maximum error is ± 0.3°C. It was confirmed that the inlet and outlet hot water temperatures are nearly equal and the average temperature was taken as the average tube wall temperature $\bar{T}_w$. The smoke was generated by burning Chinese straw paper sticks inside a copper tube (see Fig. 1). The smoke generator tube was installed before the settling chamber. The secondary flow patterns were observed at the exit of the isothermally heated section where the heated air leaves as a jet. A glass plate was installed between the camera and the exit of the test section to protect the camera.

4 Results and Discussion

4.1 Secondary Flow Patterns at the Exit of the 180 deg Bend (curvature ratio $d/2R_c = 0.10$). In view of the centrifugal instability phenomenon causing the onset of an additional pair of counterrotating vortices near the center of the outer concave wall at a certain Dean number for fully developed laminar flow in a curved pipe revealed by recent numerical solutions [14, 15], the experimental confirmation of this phenomenon is of particular interest. It should also be noted that three types of secondary flow patterns for fully developed laminar flow in curved pipes are reported in the existing literature for small Dean numbers ($K \lesssim 20$), large Dean numbers $K \gtrsim 200$, and intermediate Dean numbers. The secondary streamline patterns for small Dean numbers were identified by Dean's analysis [6, 7] based on a perturbation solution. The secondary streamline patterns for the intermediate range of Dean numbers were identified by various numerical solutions in recent years up to about $K = 400$ [15]. The secondary streamline patterns for the large Dean number range are a physical model based on potential core and bound-

Nomenclature

d = inside diameter of curved tube or heated tube
g = gravitational acceleration
K = Dean number = $\mathrm{Re}(d/2R_c)^{1/2}$
l = heated tube length
Pr = Prandtl number = ν/κ
Ra_1 = Rayleigh number = $g\beta(\bar{T}_w - T_0)d^3/\nu\kappa$
Ra_2 = Rayleigh number = $g\beta(\bar{T}_w - T_c)d^3/\nu\kappa$
R_c = radius of curvature for curved pipe
Re = Reynolds number = $\bar{W}d/\nu$
T_c, T_0, $\bar{T}_w$ = centerline air temperature at thermal entrance, unheated air temperature, and average tube wall temperature, respectively
$\bar{W}$ = average axial air velocity
x = distance from the exit of 180 deg bend
z = dimensionless axial distance from thermal entrance = $(1/d)/\mathrm{RePr}$
β = coefficient of thermal expansion
κ = thermal diffusivity
ν = kinematic viscosity

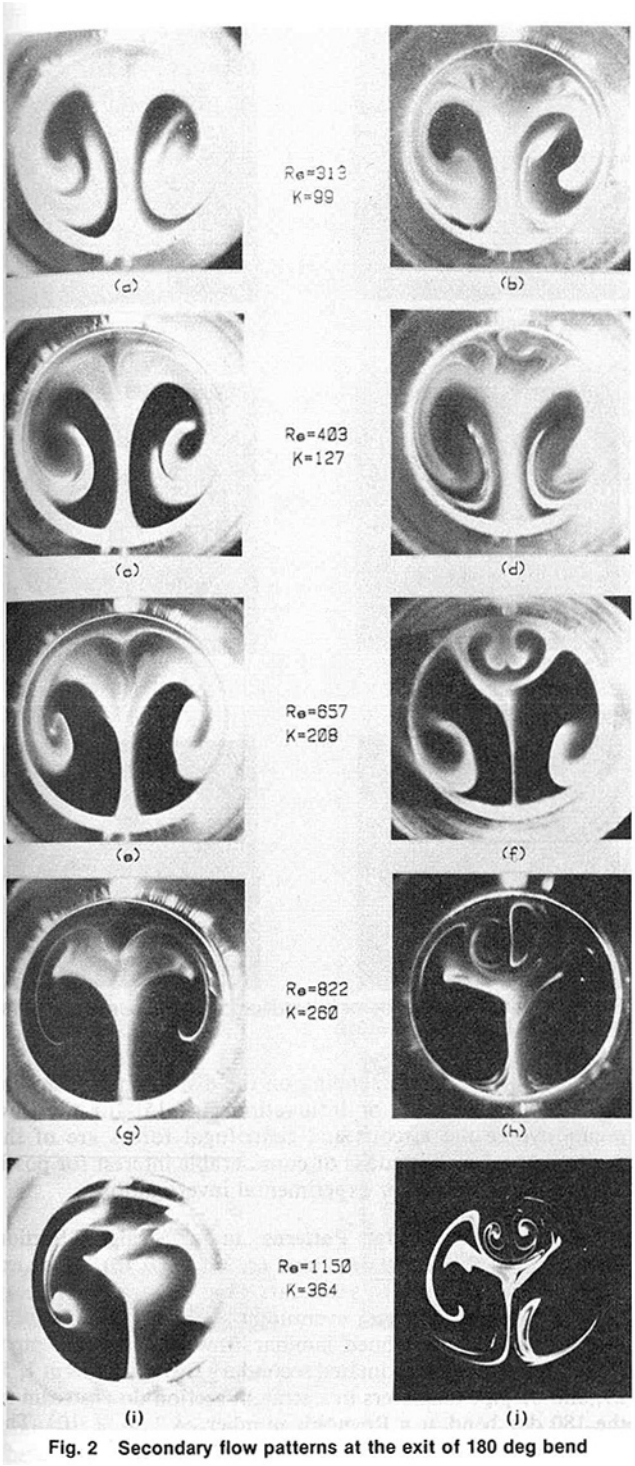

Fig. 2 Secondary flow patterns at the exit of 180 deg bend

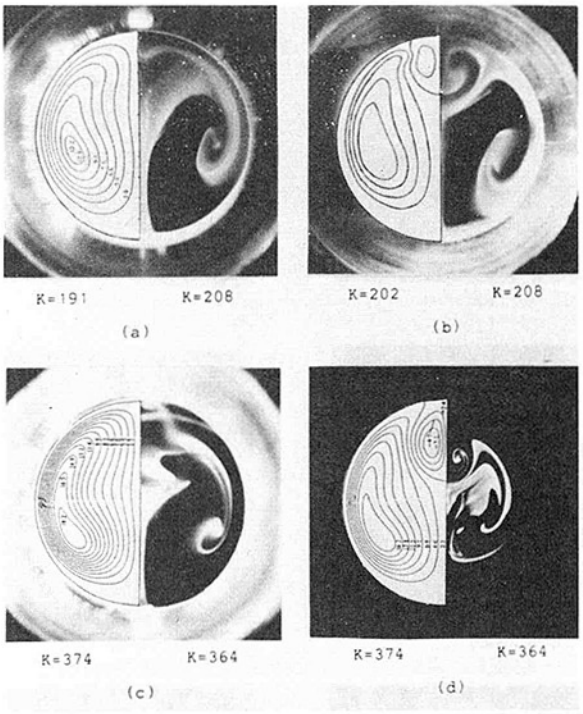

Fig. 3 Comparison between numerical solution and present flow visualization study: (*a*) Collins and Dennis [21]; (*b*) Nandakumar and Masliyah [14]; (*c*) and (*d*) Dennis and Ng [15]

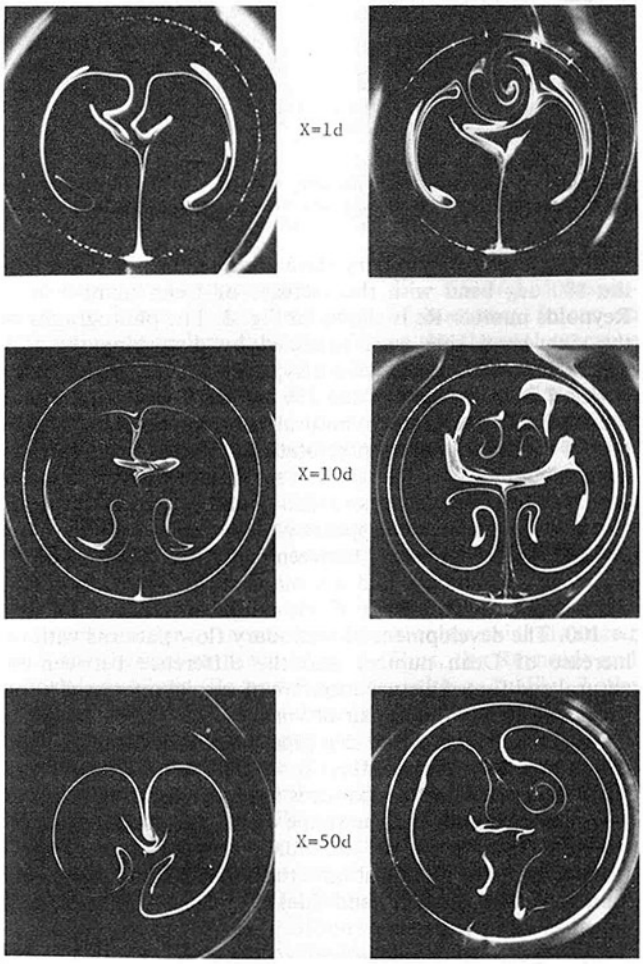

Fig. 4 Secondary flow patterns in a straight section downstream of 180 deg bend at Re = 403, K = 127

ary layer approximation near the pipe wall. The core-boundary layer model enabled several investigators to obtain theoretical solutions for large Dean number flow regime [18]. Apparently the onset of centrifugal instability poses some questions regarding the validity of the physical models used for large Dean number flow. Thus, the precise details of the secondary flow patterns for the large Dean number flow regime up to transition to turbulent flow should be studied by both numerical methods and flow visualization. In this connection, it is proposed that one or more pairs of the additional counterrotating vortices obsered at a certain Dean number in curved rectangular channels with various aspect ratios [12, 19], curved semicircular tubes [13, 16], curved circular tubes [14, 15], and various other geometric shapes to be identified in future investigations be called "Dean vortices." It is in-

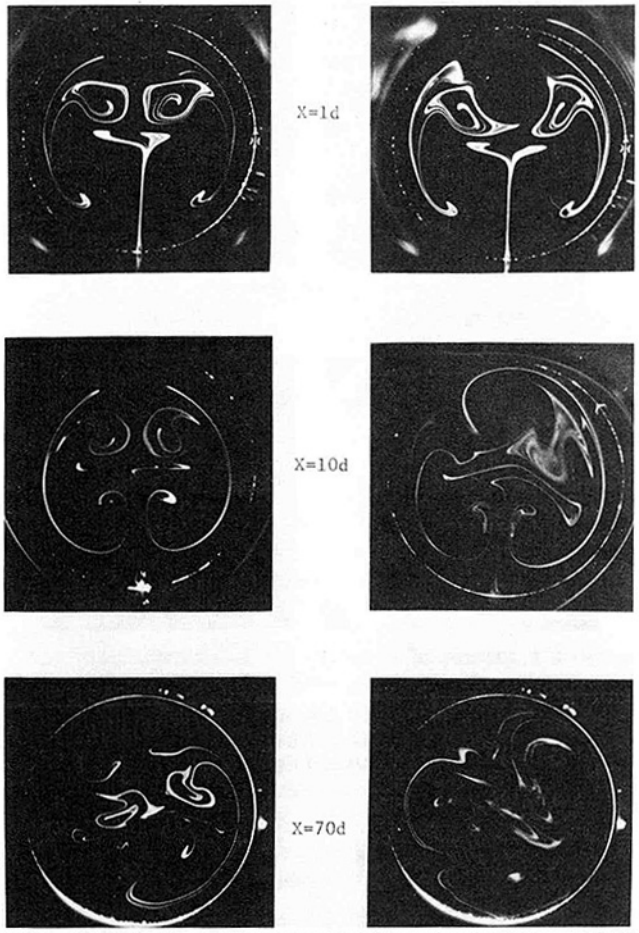

Fig. 5 Secondary flow patterns in a straight section downstream of 180 deg bend at Re = 657, K = 208

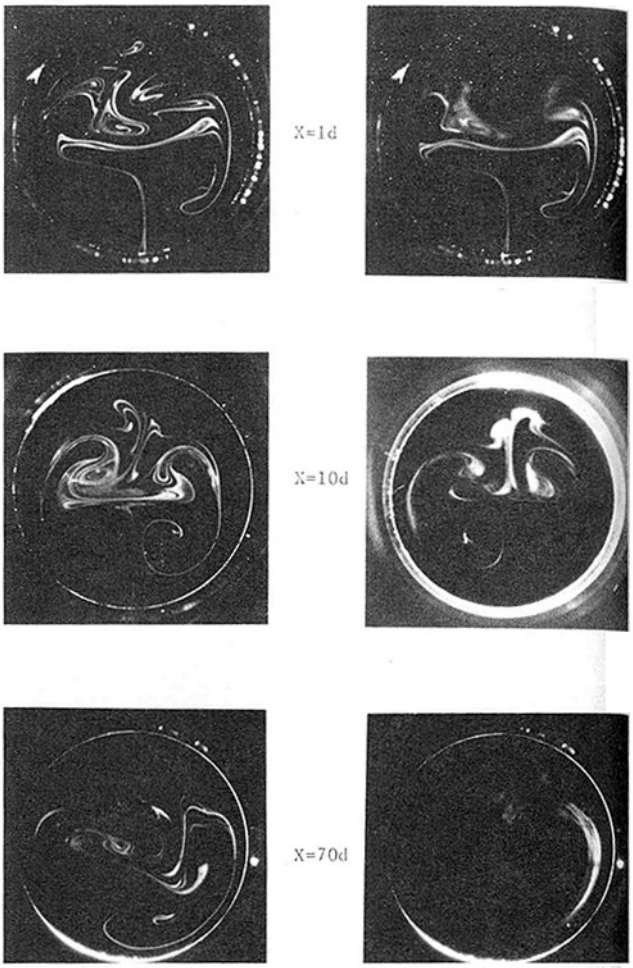

Fig. 6 Secondary flow patterns in a straight section downstream of 180 deg bend at Re = 986, K = 312

teresting to observe that Taylor, Gortler, and Dean vortices are all longitudinal vortices but they are different in nature and origin.

The change of secondary streamline pattern at the exit of the 180 deg bend with the increase of Dean number K or Reynolds number Re is shown in Fig. 2. The photographs on the right-hand side were obtained by disturbing the flow across the cross section using a hypodermic needle at a 90 deg position from the start of the 180 deg bend whereas those on the left-hand side represent natural disturbances. At $K = 99$, a pair of the additional counterrotating vortices (Dean vortices) appears and at $K = 127$ one can see clearly the formation of the Dean vortices. The numerical solutions reveal that four-vortex solution already appears at $K = 113.3$ [14] and $K = 114.2$ [15]. The agreement between numerical solution and experiment is reasonable and one may conclude that the critical Dean number for the onset of centrifugal instability is about $K = 100$. The development of secondary flow patterns with the increase of Dean number and the difference between the natural and forced disturbances are of special interest. The existence of an additional pair of vortices near the outer wall of the cross section in a 180 deg pipe bend was noted by Rowe [20] at high Reynolds number Re $= 2.36 \times 10^5$ ($K = 4.72 \times 10^4$). His secondary flow patterns were inferred from both the yaw measurements and the shape of the pressure contours.

Figure 3 compares the secondary flow patterns obtained from the flow visualization study (right-hand side) and numerical solution (left-hand side) [14, 15, 21]. Figures 3(a, c) reveal a pair of symmetric vortices at $K \sim 200$ and 370, respectively. Figures 3(b, d) show four-vortex patterns with a pair of Dean vortices near the outer concave wall. Apparently, at Dean numbers $K \sim 200$ and 370, two solutions may exist for a given Dean number, depending on the disturbance. The subject of dual solutions or bifurcation [14, 15] for the flow regime where the viscous and centrifugal forces are of the same order of magnitude is of considerable interest for possible future theoretical or experimental investigations.

4.2 Secondary Flow Patterns in a Straight Section Downstream of the 180 deg Bend ($d/2R_c = 0.10$). One expects that the intensity of secondary flow will gradually decay after a 180 deg bend and eventually revert to the Poiseuille profile for fully developed laminar flow in a straight pipe. Rowe [20] shows the estimated secondary flow patterns at 1, 5, 29, and 61 pipe diameters in a straight section downstream of the 180 deg bend at a Reynolds number of 2.36×10^5. The gradual decay of secondary flow patterns is shown in Figs. 4, 5, and 6 for Dean numbers $K = 127$, 208, and 312, respectively, at three selected downstream distances. It is noted that the photographs on the right-hand side were again obtained by disturbing the flow using a hypodermic needle at the 90 deg position across the cross section from the start of the 180 deg bend and those on the left-hand side represent natural disturbances. It is observed that the secondary flow still persists at a downstream position $x = 70d$.

At $K = 127$, the changes of the shapes for Dean vortices are clearly seen and the interaction between the Dean vortices and the original primary vortices as a function of downstream distance x is of interest. At $x \gtrsim 50d$, the secondary flow patterns appear to be unstable. The secondary flow patterns in the downstream section become more complicated at $K = 208$ since yet another additional pair of vortices appears to form below the Dean vortices at $x = 1d$. The new vortices are still

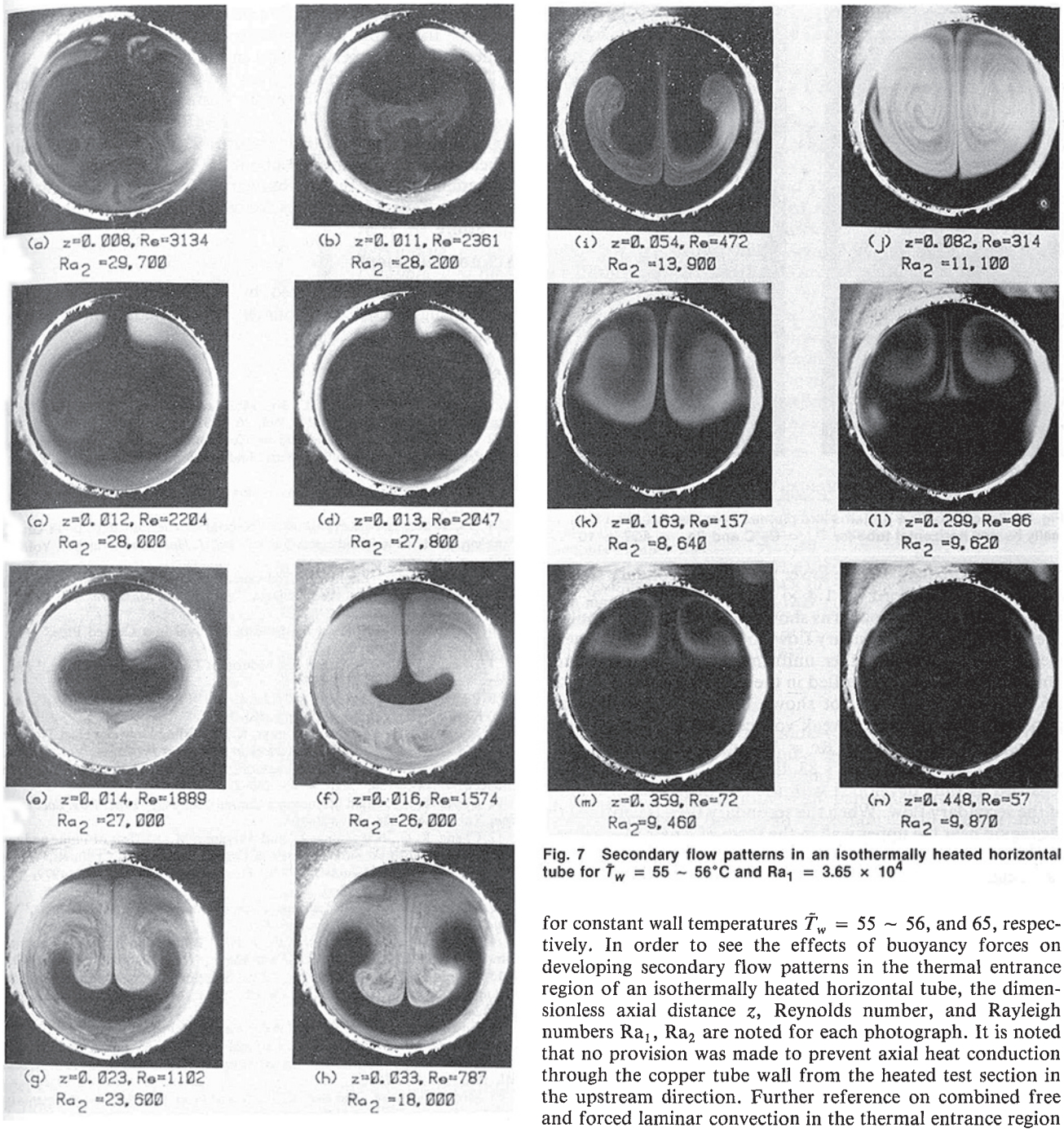

Fig. 7 Secondary flow patterns in an isothermally heated horizontal tube for $\bar{T}_w = 55 \sim 56°C$ and $Ra_1 = 3.65 \times 10^4$

observed at $x = 40d$. At $K = 208$, the detailed appearance of the Dean vortices is not clear but the boundary of the territory can be recognized. At $K = 312$, a small disturbance by the hypodermic needle at 90 deg position from the start of the 180 deg bend was found to have a considerable effect on secondary flow patterns in the downstream straight section. For this case, the boundary of the Dean vortices becomes vague at $x \geq 15d$.

4.3 Secondary Flow Patterns at the Exit of an Isothermally Heated Horizontal Tube. For this series of experiments, the heated tube length was fixed at $l = 46$ cm ($l/d = 18.1$) and the smoke was generated by burning Chinese paper sticks inside the copper tube installed before the settling chamber. A large number of photographs were obtained covering the constant wall temperature range $\bar{T}_w = 55 \sim 93°C$ and Reynolds number range Re = 14 ~ 3134. However, only typical examples of secondary flow patterns are shown in Figs. 7 and 8 for constant wall temperatures $\bar{T}_w = 55 \sim 56$, and 65, respectively. In order to see the effects of buoyancy forces on developing secondary flow patterns in the thermal entrance region of an isothermally heated horizontal tube, the dimensionless axial distance z, Reynolds number, and Rayleigh numbers Ra_1, Ra_2 are noted for each photograph. It is noted that no provision was made to prevent axial heat conduction through the copper tube wall from the heated test section in the upstream direction. Further reference on combined free and forced laminar convection in the thermal entrance region of an isothermally heated horizontal tube can be found in some recent works [22–24].

The photographs for $\bar{T}_w = 55 \sim 65°C$ (Figs. 7 and 8) are arranged in order of increasing dimensionless axial distance z from the thermal entrance ($z = 0$). Thus, the Reynolds and Rayleigh numbers (Re and Ra_2) vary with z. In Fig. 7, the changing secondary flow patterns with z are of particular interest. The secondary flow patterns in photographs (*a*)–(*d*) are qualitatively similar and are characterized by a thin ascending boundary layer along the tube wall and a fairly complicated flow in the core region. Because of rather large values of $ReRa_2 = (5.69 \sim 9.31) \times 10^7$, the flow is believed to be laminar but flow in the core region is rather complicated for $z \lesssim 0.013$ due to Re > 2000. Photographs (*e*)–(*h*) reveal different features for secondary flow patterns. For the range $z = 1.4 \times 10^{-2}$ to 3.3×10^{-2}, the secondary flow in the upper part is clearly divided into left and right-hand regions whereas the demarcation line for the lower part is not so clear due

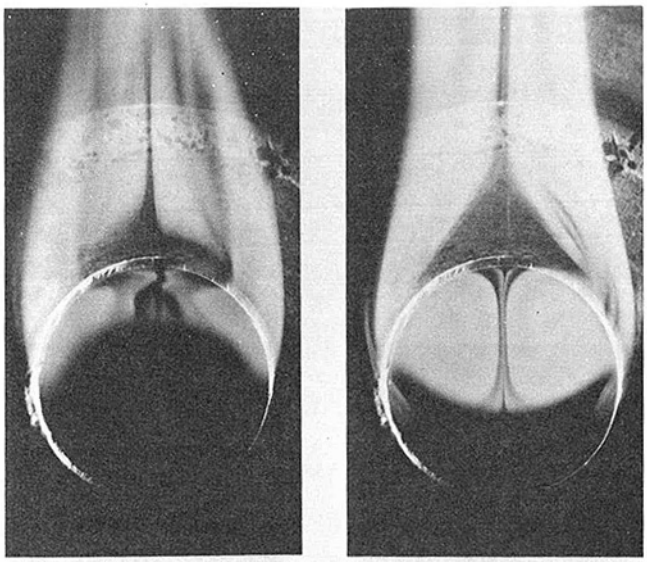

Fig. 8 Secondary flow patterns and plumes from the exit of an isothermally heated horizontal tube for $\bar{T}_w = 65°C$ and $Ra_1 = 4.37 \times 10^4$

probably to mixing near the lower wall. The secondary flow is found to be stable for $z \gtrsim 1.4 \times 10^{-2}$.

The secondary flow patterns shown in (*i*) and (*j*) are familiar ones except that the secondary flow does not seem to exist near the lower wall due to rather uniform air temperature there. This trend is further magnified in the downstream region $z \gtrsim 1.63 \times 10^{-1}$. Although not shown because of rather weak secondary flow, a pair of weak vortices is still observed near the upper wall at $z = 1.83$, Re = 14, and $Ra_2 = 8.94 \times 10^3$. Further downstream at $z > 1.83$, the temperature field may be regarded as fully developed with the complete disappearance of the secondary flow. When the secondary flow is confined to the region near the upper wall in the form of a pair of vortices, the heated secondary flow leaves as a plume upward and this particular feature is illustrated in Fig. 8 for $z = 1.63 \times 10^{-1}$ and 4.48×10^{-1}. In interpreting the secondary flow patterns, one must recognize the roles of Reynolds and Rayleigh numbers since the heated tube length was fixed.

One may gain more insight regarding the free convection effect by comparing the secondary flow patterns for the identical dimensionless axial distance z (or Reynolds number) for different wall temperatures. Further photographic results at higher wall temperatures are shown in [25]. At higher Rayleigh number, the fully developed temperature field is approached earlier at small values of z. This observation agrees with the theoretical results for large Prandtl number fluid [5]. Since the heated test tube length is fixed, the secondary flow patterns near the thermal entrance ($z = 0$) after the onset of free convection effect cannot be obtained in this flow visualization study.

5 Concluding Remarks

The main purpose of this paper is to present the secondary flow patterns in the downstream straight section of a 180 deg bend and in isothermally heated horizontal tubes with free convection effects. Further details for secondary flow patterns in a downstream straight section after the 180 deg bend with $x/d = 1$ to 70 and Dean numbers $K = 127$, 208, and 312 are presented in [25]. The secondary flow patterns at the exit of the 180 deg bend are shown for Dean number range $K = 99$ to 384. The onset of centrifugal instability at Dean number of about $K = 100$ in the form of an additional pair of vortices (Dean vortices) near the central outer wall region is believed to be of considerable theoretical and practical interest. The secondary flow patterns in the postcritical regime up to transition to turbulent flow remain to be investigated both numerically and experimentally in the future.

The developing secondary flow patterns in the thermal entrance region of an isothermally heated horizontal tube are presented for $z = 0.8 \times 10^{-2}$ to 1.83 (Re = 3134 ~ 14) for a range of constant wall temperatures $\bar{T}_w = 55 \sim 65°C$ with unheated air temperature at about 25°C. The stablizing effect of secondary flow due to buoyancy forces for flow regime with inlet Reynolds numbers Re ≥ 2300 should be studied in the future.

Acknowledgments

This work was supported by the Natural Sciences and Engineering Research Council of Canada through an operating grant.

References

1 Drew, T. B., Hogan, J. J., and McAdams, W. H., "Heat Transfer in Streamline Flow," *Trans. AIChE*, Vol. 26, 1931, pp 81–117.

2 Colburn, A. P., "A Method of Correlating Forced Convection Heat Transfer Data and a Comparison With Fluid Friction," *Trans. AIChE*, Vol. 29, 1933, pp. 174–210.

3 McAdams, W. H., *Heat Transmission*, 3rd ed., McGraw-Hill, New York, 1954, p. 235.

4 Ou, J. W., and Cheng, K. C., "Natural Convection Effects on Graetz Problem in Horizontal Isothermal Tubes," *Int. J. Heat Mass Transfer*, Vol. 20, 1977, pp. 953–960.

5 Hieber, C. A., "Laminar Mixed Convection in an Isothermal Horizontal Tube: Correlation of Heat Transfer Data," *Int. J. Heat Mass Transfer*, Vol. 25, 1982, pp. 1737–1746.

6 Dean, W. R., "Note on the Motion of Fluid in a Curved Pipe," *Phil. Mag.*, Vol. 4, 1927, pp. 208–223.

7 Dean, W. R., "The Streamline Motion of Fluid in a Curved Pipe," *Phil. Mag.*, Vol. 5, 1928, pp. 673–695.

8 Berger, S. A., Talbot, L., and Yao, L. S., "Flow in Curved Pipes," *Ann. Rev. Fluid Mech.*, Vol. 15, 1983, pp. 461–512.

9 Masliyah, J. H., and Nandakumar, K., "Swirling Flow and Heat Transfer in Coiled and Twisted Pipes," *Advances in Transport Processes*, Vol. 4, 1984.

10 Pedley, T. J., *The Fluid Mechanics of Large Blood Vessels*, Cambridge University Press, 1980, Chap. 4, pp. 160–234.

11 Dean, W. R., "Fluid Motion in a Curved Channel," *Proc. Roy. Soc. London*, Vol. 121A, 1928, pp. 402–420.

12 Cheng, K. C., Nakayama, J., and Akiyama, M., "Effect of Finite and Infinite Aspect Ratios on Flow Patterns in Curved Rectangular Channels," *Flow Visualization (Tokyo, Japan, 1977)*, Hemisphere, Washington, 1979, pp. 181–186.

13 Masliyah, J. H., "On Laminar Flow in Curved Semicircular Ducts," *J. Fluid Mech.*, Vol. 99, 1980, pp. 469–479.

14 Nandakumar, K., and Masliyah, J. H., "Bifurcation in Steady Laminar Flow Through Curved Tubes," *J. Fluid Mech.*, Vol. 119, 1982, pp. 475–490.

15 Dennis, S. C. R., and Ng, M., "Dual Solutions for Steady Laminar Flow Through a Curved Tube," *Q. J. Mech. Appl. Math.*, Vol. 35, 1982, pp. 305–324.

16 Cheng, K. C., Inaba, T., and Akiyama, M., "Flow Visualization Studies of Secondary Flow Patterns and Centrifugal Instability in Curved Circular and Semicircular Pipes," *Third Int. Symposium on Flow Visualization*, Ann Arbor, MI, 1983, pp. 761–766.

17 Moshfeghian, M., and Bell, K. J., "Local Heat Transfer Measurements in and Downstream From a U-Bend," ASME Paper No. 70-HT-82.

18 Mori, Y., and Nakayama, W., "Study on Forced Convective Heat Transfer in Curved Pipes (1st Report, Laminar Region)," *Int. J. Heat Mass Transfer*, Vol. 8, 1965, pp. 67–82.

19 Sugiyama, S., Hayashi, T., and Yamazaki, K., "Flow Characteristics in the Curved Rectangular Channels (Visualization of Secondary Flow)," *Bulletin of the JSME*, Vol. 26, 1983, pp. 964–969.

20 Rowe, M., "Measurements and Computations of Flow in Pipe Bends," *J. Fluid Mech.*, Vol. 43, 1970, pp. 771–783.

21 Collins, W. M., and Dennis, S. C. R., "The Steady Motion of a Viscous Fluid in a Curved Tube," *Q. J. Mech. Appl. Math.*, Vol. 28, 1975, pp. 133–156.

22 Yousef, W. W., and Tarasuk, J. D., "Free Convection Effects on Laminar Forced Convective Heat Transfer in a Horizontal Isothermal Tube," ASME JOURNAL OF HEAT TRANSFER, Vol. 104, 1982, pp. 145–152.

23 Hishida, M., Nagano, Y., and Montesclaros, M. S., "Combined Forced and Free Convection in the Entrance Region of an Isothermally Heated Horizontal Pipe," ASME JOURNAL OF HEAT TRANSFER, Vol. 104, 1982, pp. 153–159.

24 Kato, K., Watanabe, E., Ogura, T., and Hanzawa, T., "Effect of Natural Convection on Laminar Flow Heat Transfer in Horizontal Circular Tubes," *J. Chem. Engg. Japan*, Vol. 15, 1982, pp. 355–361.

25 Cheng, K. C., and Yuen, F. P., "Flow Visualization Studies on Secondary Flow Patterns in Curved Tubes and Isothermally Heated Horizontal Tubes," 22nd National Heat Transfer Conference, 1984, Paper No. 84-HT-62.

Flow Visualization Experiments on Secondary Flow Patterns in an Isothermally Heated Curved Pipe

K. C. Cheng

F. P. Yuen

Department of Mechanical Engineering,
University of Alberta,
Edmonton, Alberta, Canada

Secondary flow patterns at the exit of a 180 deg bend (tube inside diameter d = 1.99 cm, radius of curvature R_c = 10.85 cm) are presented to illustrate the combined effects of centrifugal and buoyancy forces in hydrodynamically and thermally developing entrance region of an isothermally heated curved pipe with both parabolic and turbulent entrance velocity profiles. Three cases of upward, horizontal, and downward-curved pipe flows are studied for constant wall temperatures T_w = 55–91°C, Dean number range K = 22–1209 and ReRa = 1.00×10^6–8.86×10^7. The flow visualization was realized by the smoke injection method. The secondary flow patterns shown are useful for future comparison with numerical predictions and confirming theoretical models. The results can be used to assess qualitatively the limit of the applicability of the existing correlation equations for laminar forced convection in isothermally heated curved pipes without buoyancy effects.

Introduction

The thermal entrance region problem (Graetz problem) for fully developed laminar flow in a straight tube with constant wall temperature was solved first by Graetz [1] in 1885 and independently by Nusselt [2] in 1910. Historically, it is of particular interest to note that Graetz obtained the first analytical solution for developing thermal boundary layer inside a tube (parabolic problem) preceding the proposal of general laminar boundary layer concept for flow on a flat plate by Prandtl in 1904. The analytical solution for fully developed laminar flow in curved pipes was first obtained by Dean [3, 4] in 1927 for very low Dean number flow regime. Fully developed free and forced laminar convection in uniformly heated horizontal pipes was solved by Morton [5] in 1959 for low Rayleigh number flow regime. In recent years, the buoyancy force effects on laminar forced convection in vertical and horizontal tubes and centrifugal force effects on laminar forced convection in curved pipes have been studied by many investigators both theoretically and experimentally. It is only recently that the combined buoyancy and centrifugal force effects on laminar forced convection heat transfer have been reported in the literature [6–13]. The relevant references can be found in [6–13] and the literature review will not be repeated here.

The secondary flows caused by buoyancy forces in straight tubes and by centrifugal forces in curved pipes have significant effects on laminar forced convective heat transfer. When the buoyancy effects are significant in curved pipes, one must consider the inclination of the plane of curvature and the direction of flow (upward or downward). Recent numerical and flow visualization studies [14–17] reveal the appearance of a four-vortex secondary laminar flow in curved pipes at a certain Dean number. The additional pair of counterrotating vortices is caused by centrifugal instability near the concave outer wall and is known as Dean vortices. It is thus expected that the secondary flow patterns for laminar flow in heated or cooled curved pipes will be very complicated depending on the inclination of the plane of curvature and the direction of flow (upward or downward). It is expected that the secondary flow caused by both centrifugal and buoyancy forces will depend on Dean number K and the product of Reynolds and Rayleigh numbers ReRa.

The purpose of this paper is to present a series of photographic results on secondary flow patterns observed at the exit of a 180-deg bend (tube inside diameter d = 1.99 cm, radius of curvature R_c = 10.85 cm) for horizontal and vertical curved pipe configurations with parabolic laminar or turbulent entrance flow and constant wall temperature T_w = 55–95°C. Air at room temperature was the flowing fluid. The flow visualization was made possible using smoke generated by burning a bundle of straw paper sticks in a smoke generator tube. Since flow visualization experiments were made by varying Reynolds number with fixed curved pipe length (πR_c), the photographic results obtained represent the secondary flow patterns in the thermal entrance region of an isothermally heated curved pipe by using an inverse Graetz number. The photographic results provide physical insight into the heat transfer mechanism for laminar forced convection in curved pipes with buoyancy effects. Flow visualization studies are also useful in confirming the theoretical models for numerical and analytical solutions of mixed convection problems in curved pipes. The secondary flow patterns are presented to illustrate the simultaneous effects of centrifugal and buoyancy forces in the thermal entrance region of isothermally heated horizontal and vertical (upward or downward flow) curved pipes. It should be pointed out that theoretical (numerical or analytical) solution of the problem under consideration is extremely difficult.

Table 1 Ranges of experimental parameters

Air flow rate	18.9–1033.6 cm^3/s
Mean velocity	6.05–331.0 cm/s
Reynolds number Re	73–3989
ReRa	$9.49\times10^5 - 8.86\times10^7$
Rayleigh number Ra_1	$1.74\times10^4 - 3.09\times10^4$
Dean number K	22–1209
Prandtl number (air)	0.71
Pipe wall temperature T_w	55–95°C
$(d/2R_c)^{1/2}$	0.3032

Experimental Parameters

The experimental parameters for the present investigation are: curvature ratio $d/2R_c$, Reynolds number, Dean number, constant wall temperature, Rayleigh (or Grashof) number, inclination angle of the plane of curvature from the horizontal direction, and direction of flow. For this investigation, only horizontal and vertical curved pipe configurations were considered. The entrance flow at the start of 180-deg bend was parabolic for laminar flow case and in effect thermally and hydrodynamically developing flow in an isothermally heated

Contributed by the Heat Transfer Division and presented at the ASME Winter Annual Meeting, Miami Beach, FL, November 1985. Manuscript received by the Heat Transfer Division November 1, 1985.

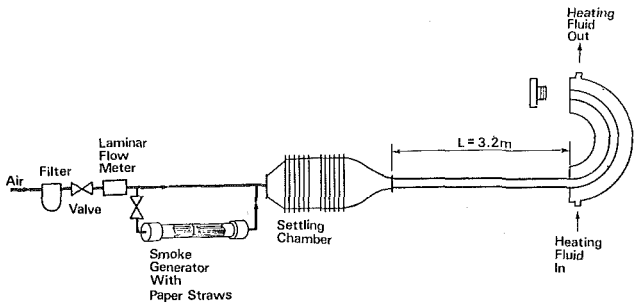

Fig. 1 Schematic diagram of experimental apparatus

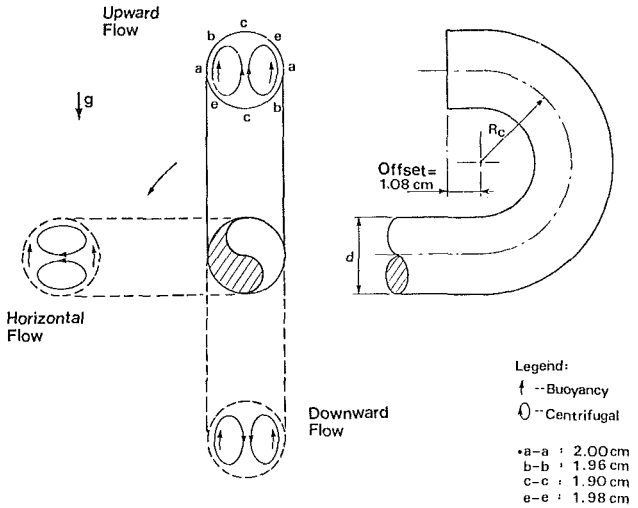

Fig. 2 Vertical and horizontal curved pipes

curved pipe was studied. The ranges of experimental parameters for this investigation are listed in Table 1.

Experimental Apparatus and Procedure

A schematic diagram of the experimental apparatus is shown in Fig. 1. Since the curved tube was rolled from a straight copper tube, the tube diameter at the exit of 180-deg bend was not uniform and the results of measurements are shown in Fig. 2 for reference. The water jacket for heating was made from a flexible heat-resistant hose (o.d. = 4.2 cm). The hose was clamped on two 2.5-cm-long copper end pieces soldered on the tube bend forming the curved annular space for double-pipe heat exchanger. A helical coil was inserted in the annular space for heat transfer augmentation and the test section was insulated with 3.8 cm Armaflex pipe insulation to prevent heat loss. Figure 2 also shows an offset of 1.08 cm between the end of water jacket and the center of the radius of curvature. Hot water from a large constant-temperature tank was circulated through the annular space in the direction parallel to the air flow.

The inlet and outlet bulk temperatures of heating hot water were measured by 0.7 mm o.d. sheathed iron-constantan thermocouples and the outlet centerline air temperature was measured by a type T thermocouple (o.d. = 0.254 mm). All thermocouples were initially calibrated using a quartz thermometer (HP-2807A) with a maximum error of $\pm 0.1°C$. Since the temperature difference between the inlet and outlet bulk temperatures of the hot water were found to be rather small considering the measurement error, the average value was taken as the average tube wall temperature T_w.

As shown in Fig. 1, a straight entrance length of 3.2 m was provided between the settling chamber and the start of the 180-deg bend to ensure a fully developed parabolic velocity profile at the entrance of the test section for $Re \leq 2300$. Room air from a compressor was used and the air flow rate was measured by a Meriam laminar flow element and a Dwyer inclined manometer. The experimental error was estimated to be ± 1.75 percent. Flow visualization was made possible by burning a bundle of paper straws inside a smoke generator tube located in front of the settling chamber.

The experimental technique was similar to that used in earlier investigations [16–18]. By passing a sheet of light provided by a 500 W slide projector, the secondary flow pattern can be observed at the exit of the isothermally heated curved tube section. The heated air was discharged directly into the atmosphere as a jet. Three different cases of horizontal curved pipe, vertical curved pipe with upward flow, and vertical curved pipe with downward flow, as shown in Fig. 2, were studied. A Nikon FM2 single lens reflex camera with a 50 mm micro lens was used together with Kodak Tri-X black and white film and camera settings of f3.5 and 1/2-1/8 s.

Results and Discussion

The main interest here is to study the secondary flow patterns resulting from the interaction between centrifugal and buoyancy forces for three different geometric configurations (see Fig. 2). Physically, the Dean number K can be considered as the ratio of the centrifugal force to the viscous force and the parameter ReRa represents the ratio of the buoyancy force to the viscous force.

In contract to the theoretical results [7, 8] for similar problems reported in the literature, the flow visualization technique using smoke injection method enables one to study a wider range of parametric values and the ranges $22 \leq K \leq 1209$ and $9.49 \times 10^5 \leq ReRa \leq 8.86 \times 10^7$ were reached in this investigation.

Since the heated curved pipe length is fixed, an increase in the parameter ReRa for a constant wall temperature may be regarded as an increase in Reynolds number or a decrease in the dimensionless axial distance from the thermal entrance, $(1/d)/RePr$, which is an inverse Graetz number representing the thermal entrance distance. It is noted that no provision was made to prevent axial heat conduction through the copper tube from the heated section in the upstream direction since a

Nomenclature

g = gravitational acceleration
K = Dean number = $Re(d/2R_c)^{1/2}$
l = heated tube length
Pr = Prandtl number = ν/κ
Ra = Rayleigh number = $g\beta(T_w - (T_c + T_0)/2) \cdot d^3/\nu\kappa$
Ra_1 = Rayleigh number = $g\beta(T_w - T_0)d^3/\nu\kappa$
R_c = radius of curvature for curved pipe
Re = Reynolds number = wd/ν
T_c, T_0, T_w = centerline air temperature at pipe exit, unheated air temperature, and average (constant) pipe wall temperature, respectively
w = average axial air velocity
β = coefficient of thermal expansion
κ = thermal diffusivity
ν = kinematic viscosity
ϕ = angular position from start of bend

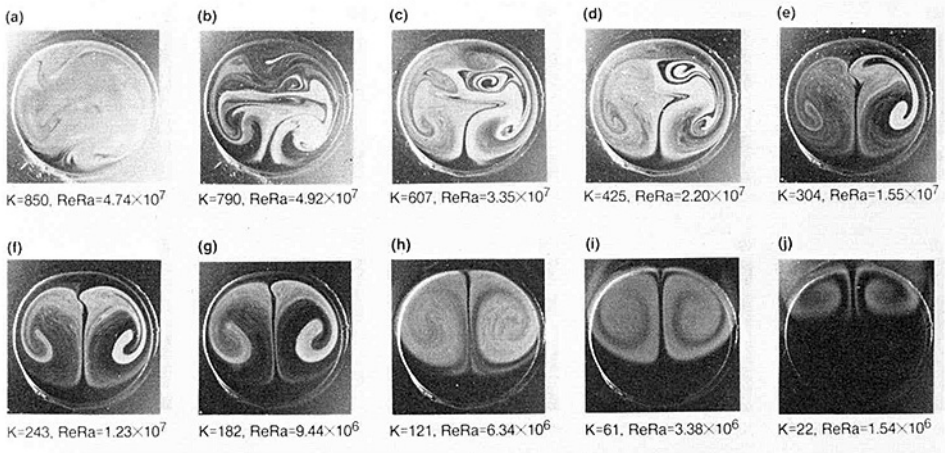

Fig. 3 Secondary flow patterns in a vertical curved pipe with upward flow for $T_w = 76°C$ and $Ra_1 = 2.57 \times 10^4$

180-deg bend was made from a piece of straight tube. The photographic results for secondary flow patterns for laminar flows in the unheated curved pipe and isothermally heated horizontal pipe are presented in [17].

Photographs for Vertical Curved Pipe With Upward Flow (Fig. 3). The photographs for secondary flow pattern are arranged in the order of decreasing Dean numbers in Fig. 3 for an average wall temperature of 76°C. The directions of the centrifugal forces and buoyancy forces are coplanar but they may not be in phase depending on the angular position ϕ from the start of bend. Without buoyancy force effect, the secondary flow develops gradually from the start of bending to the end of the 180-deg bend. It is generally understood that the centrifugal forces induce a pair of symmetric counterrotating vortices in a cross section normal to the main flow and the fluid in the central core moves toward the concave outer wall. The buoyancy force effect may be negligible at the start of bending (see Fig. 2). Its effect increases with the angle of bend but the buoyancy force along the cross section decreases to zero momentarily at the 90-deg bend position. The effect then increases again from the 90-deg bend position to the 180-deg bend position. The buoyancy forces also induce a pair of symmetric vortices.

The secondary flows caused by centrifugal and buoyancy forces are in phase in the region $\phi = 0$ and 90 deg but are 180 deg out of phase in the region $\phi = 90$ and 180 deg. The intensity of secondary flow due to the centrifugal forces increases monotonically in the 180-deg bend until a fully developed flow is reached. The discussion here is only qualitative since the interaction between the two regions of vortices may occur due to the internal or external disturbances. The secondary flow pattern observed at the exit of the 180-deg bend represents the effects of the complicated interaction process of centrifugal and buoyancy forces in the 180-deg bend section.

In Fig. 3, the top of each photograph represents the outside of the bend and the bottom represents the inside of the bend. At K = 850 in Fig. 3, the buoyancy forces are seen to be dominating over the centrifugal forces and the secondary flow patterns are not very clear probably due to smoke diffusion at high secondary flow velocity. In photograph (*b*) of Fig. 3, one sees the dividing streamline in the lower part caused by centrifugal forces. In the upper part the centrifugal forces and buoyancy forces are apparently of the same order of magnitude resulting in a rather complicated secondary flow with several vortices seen clearly and no symmetry can be observed. At K = 850 in (*a*), the Reynolds number is 2805 exceeding the critical Reynolds number of 2300 for straight tube flow. It is seen that a laminar flow still persists at K = 850. The secondary flow patterns shown in (*c–f*) can be identified as somewhat similar to those of isothermal flow in curved pipes [16, 17] and one may infer that the centrifugal forces are dominating over the buoyancy forces for the parametric values shown.

At $K \leq 182$, apparently the buoyancy forces dominate over the centrifugal forces in (*g–j*) and the symmetric secondary flow patterns are similar to those observed in the thermal entrance region of an isothermally heated horizontal tube [17]. The black crescent region is caused by thermal plume effect at the exit since the flow speed is small. At K = 22, the centrifugal force effect is very weak and the curvature effect may be negligible practically. When the secondary flow disappears completely, a fully developed flow for the limiting Nusselt number $Nu_\infty = 3.66$ is approached for the constant wall temperature case.

It is of interest to note that the secondary flow pattern at K = 850 represents that near the thermal entrance with small inverse Graetz number and K = 22 represents secondary flow pattern at larger inverse Graetz number. At K = 425 and 607 in Fig. 3, one sees clearly the eyes of an additional pair of vortices located near the outer wall of the bend and the interaction between the left-hand and right-hand regions is appreciable in the upper part of the curved pipe.

Photographs for Horizontal Curved Pipe Flow (Figs. 4–6). This case is of considerable practical interest since many cooling or heating coils are used in this geometric configuration. Intuitively, this case can be considered as a combination of centrifugal force effect in an isothermal flow in a curved tube and buoyancy effect in an isothermally heated horizontal straight tube. The secondary flow patterns for the average wall temperatures $T_w = 56$, 76, and 91°C are shown in Figs. 4, 5, and 6, respectively. In each photograph, the left-hand side represents the concave outer wall of the bend and the right-hand side represents the convex inner wall of the bend. For the horizontal curved pipe shown (see Fig. 2), the buoyancy forces act in the upward direction and the centrifugal forces act toward the left and the two forces are always perpendicular to each other in the 180-deg bend section. The secondary flow patterns at the exit of the 180-deg bend represent the outcome of a hydrodynamically and thermally developing entrance region.

The secondary flow patterns in Fig. 4 for $T_w = 56°C$ will be examined first. At K = 850 and 729, the centrifugal force effect can be seen from the dividing streamline near the right-hand wall (inner bend). The flow pattern near the outer wall is not very clear at K = 850 due to smoke diffusion but several vortices are clearly seen at K = 729. At K = 607, one observes six

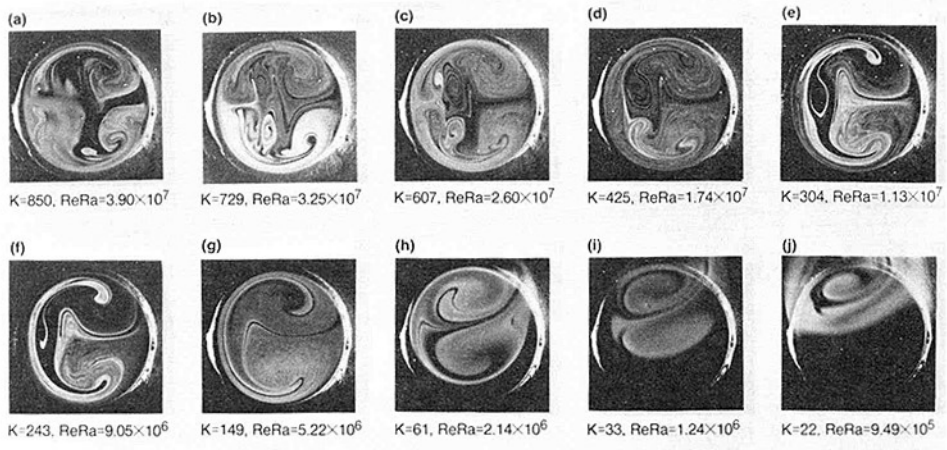

Fig. 4 Secondary flow patterns in a horizontal curved pipe for $T_w = 56°C$ and $Ra_1 = 1.80 \times 10^4$

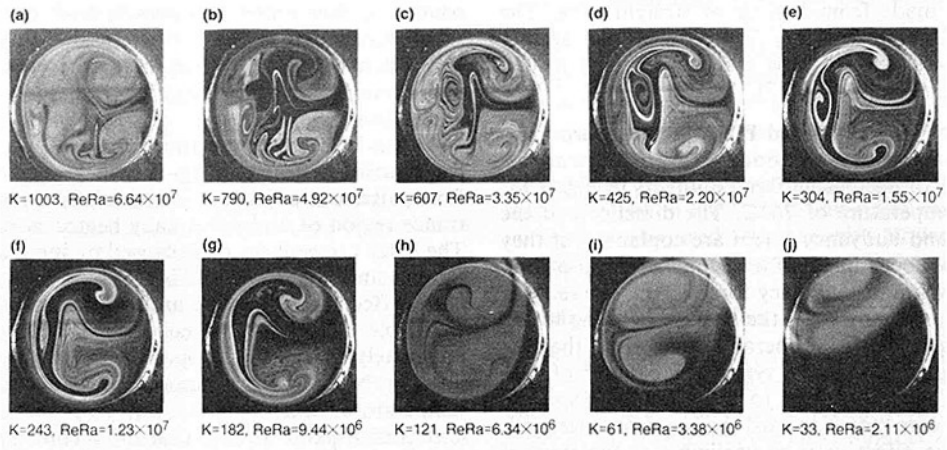

Fig. 5 Secondary flow patterns in a horizontal curved pipe for $T_w = 76°C$ and $Ra_1 = 2.57 \times 10^4$

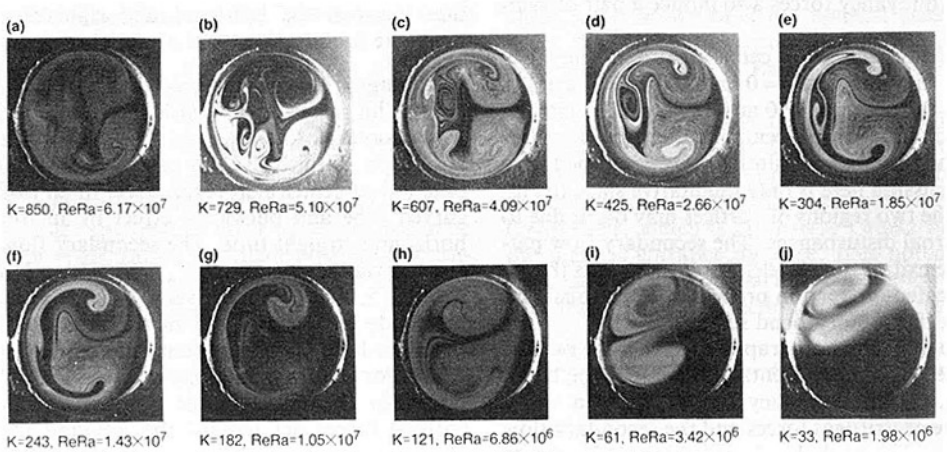

Fig. 6 Secondary flow patterns in a horizontal curved pipe for $T_w = 91°C$ and $Ra_1 = 3.02 \times 10^4$

vortices and four vortices remain at K = 425. One also sees a heated air layer near the outer wall and the trend becomes more apparent at K = 304 and 243 where only one cell remains near the outer wall. The flow pattern is more complicated in the region near the outer wall where the centrifugal instability occurs. The additional vortices or cell near the outer wall in (*b–f*) are caused by centrifugal instability but are subject to buoyancy effect.

The centrifugal and buoyancy forces are of the same order of magnitude at K = 850 but centrifugal forces are dominant over the buoyancy forces for K = 729, 607, and 425. As Dean number K decreases from K = 304 to 22, the buoyancy effect

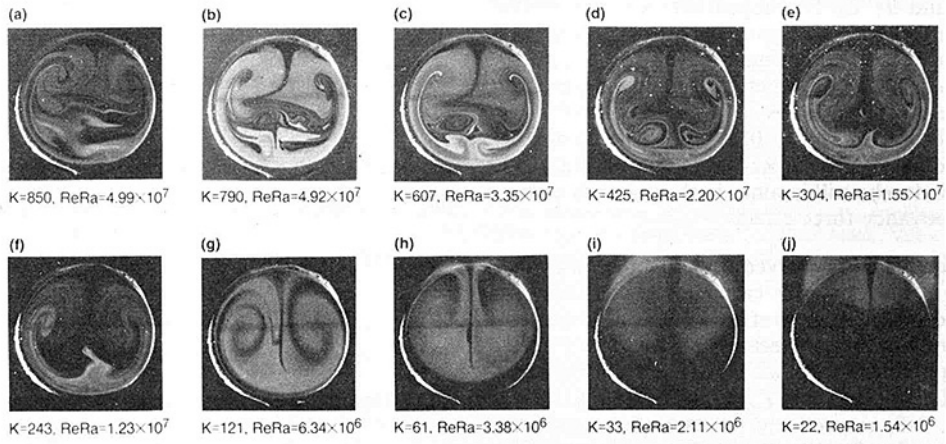

Fig. 7 Secondary flow patterns in a vertical curved pipe with downward flow for $T_w = 76°C$ and $Ra_1 = 2.57 \times 10^4$

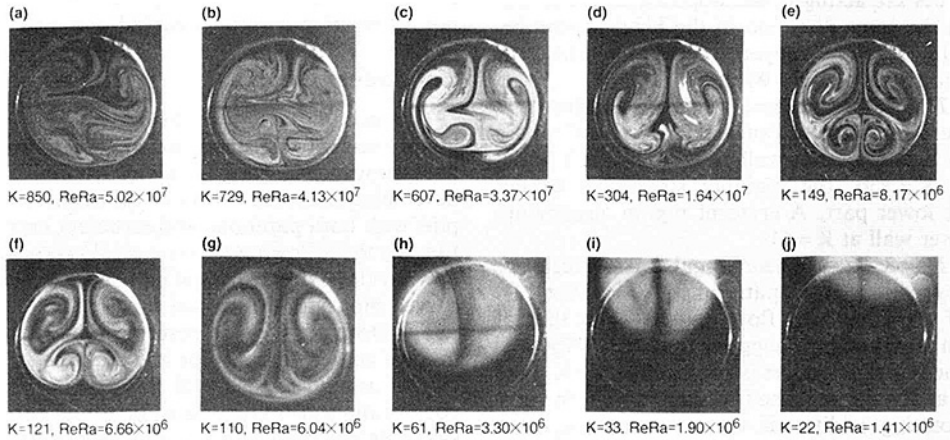

Fig. 8 Secondary flow patterns in a vertical curved pipe with downward flow for $T_w = 85°C$ and $Ra_1 = 2.84 \times 10^4$

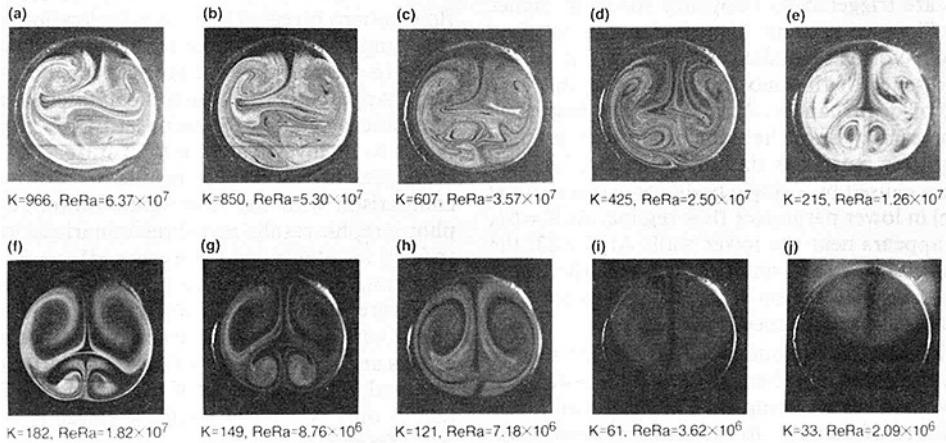

Fig. 9 Secondary flow patterns in a vertical curved pipe with downward flow for $T_w = 91°C$ and $Ra_1 = 3.02 \times 10^4$

increases gradually over the centrifugal force effect and the distortion of the dividing streamline due to the centrifugal forces is of particular interest. At K = 61, a crescent region (black part) appears near the lower wall and the area of the region with secondary flow decreases with further decrease of Dean number. The lifting of the secondary flow pattern is due to the buoyant jet leaving from the exit of the 180-deg bend.

The centrifugal and buoyancy force effects on secondary flow patterns at wall temperature $T_w = 76$ and 91°C are qualitatively similar to the case with $T_w = 56°C$ and the effect of wall temperature increase can be seen in Figs. 5 and 6. In studying the secondary flow pattern, it is of interest to note the distortion of the dividing streamline caused by buoyancy effect. For K = 607 to 243 in Fig. 5, the dividing streamline is diverted upward near the outer wall and is lifted near the inner wall. At K = 243, the secondary flow patterns are quite similar

for $T_w = 56$, 76, and 91°C. The appearance of the crescent region and the lifting of the secondary flow region with decreasing area are due to the thermal plume effect at the exit. The secondary flows in these isothermally heated pipes show no symmetry since two body forces act in perpendicular directions. Although not shown at K = 1033, the Reynolds number is Re = 3406 exceeding the critical Reynolds number Re = 2300 but the flow is found to be still laminar in the presence of both centrifugal and buoyancy force effects.

Photographs for Vertical Curved Pipe With Downward Flow (Figs. 7–9). Intuitively, this case can be considered as a combination of centrifugal force effect in an isothermal flow in a curved tube and buoyancy effect in an isothermally heated vertical tube with downward flow. The secondary flow patterns for the wall temperatures $T_w = 76$, 85, and 91°C are presented in Figs. 7–9, respectively. In each photograph the top represents the convex inner wall and the bottom represents the concave outer wall of the bend. At any angular position in the initial 90-deg bend ($\phi = 0 - 90$ deg), the centrifugal forces and buoyancy forces are acting in the opposite direction but they are acting in the same direction in the bend section between $\phi = 90$ and 180 deg. The buoyancy force along the cross section is momentarily zero at $\phi = 90$ deg.

In Fig. 7 with $T_w = 76$°C, the centrifugal force effects are clearly seen in the Dean number range K = 607 to 243 and a layer of heated air near the lower wall due to buoyancy forces is also seen. At K = 850, the dividing streamline cannot penetrate into the lower part. A crescent region already appears near the lower wall at K = 61.

In Fig. 8 with $T_w = 85$°C, the centrifugal force effects are clearly seen in the secondary flow patterns for K = 607 to 121. The distortion of the secondary flow pattern from that of isothermal flow in a curved pipe suggests that at K = 966 and 850 (see Fig. 9), the buoyancy effect is appreciable. At K = 149 and 121 in Figs. 8 and 9, one sees the four-vortex pattern and a pair of counterrotating additional vortices near the lower (outer) wall can be identified as Dean vortices caused by centrifugal instability in the region near the concave wall. Since Dean vortices are not observed for the case $T_w = 76$°C (see Fig. 7) in the same Dean number range, one may conclude that the Dean vortices are triggered by buoyancy forces at higher wall temperature. Since no external disturbances are required for the onset of four-vortex secondary flow pattern, it is concluded that the presence of the buoyancy forces in this case could be a source of disturbances. At K = 110, the buoyancy and centrifugal forces may be of the same order of magnitude and the secondary flow pattern is similar to the familiar secondary flow pattern caused by a single body force (centrifugal or buoyancy force) in lower parameter flow regime. At K = 61, a crescent region appears near the lower wall. At K = 22, the secondary flow is confined to a small region near the upper wall and the fully developed region with $Nu_\infty = 3.66$ for constant wall temperature is approached.

In Fig. 9 with $T_w = 91$°C, the buoyancy effects are seen to be appreciable in the Dean number range K = 966 – 425 and the secondary flow patterns are complex. The heated air layers near the side walls are of interest. In the Dean number range K = 215 to 149, the four-vortex secondary flow patterns are seen with a good symmetry. At K = 121, two heated air layers can be seen extending from the bottom to the top. At K = 61, a crescent region appears near the bottom and the lifting effect is due to thermal plume effect at the exit.

Although not depicted in Fig. 7, the unsteady, oscillating Dean vortices were observed in the range $110 \leq K \leq 180$ for $T_w = 76$°C. At higher wall temperature, the Dean vortices become more stable over a wider Dean number range. The onset of the four-vortex secondary flow patterns is of considerable theoretical interest. The experimental data based on flow visualization are shown in Fig. 10 for reference. The experimental data are too few to define clearly an instability region for the onset of four-vortex flow pattern. It is of interest to note that the four-vortex secondary flow pattern was not observed in a vertical curved pipe with upward flow.

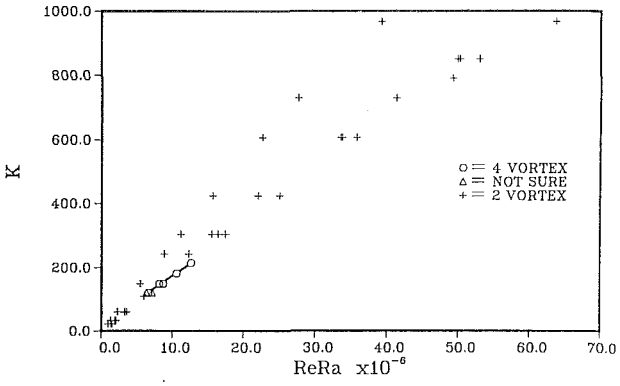

Fig. 10 The onset of four-vortex secondary flow pattern

Concluding Remarks

The secondary flow patterns at the exit of a 180-deg bend are presented to illustrate the combined effects of centrifugal and buoyancy forces in hydrodynamically and thermally developing entrance region of an isothermally heated curved pipe with both parabolic and turbulent entrance velocity profiles for the following three cases: (1) vertical curved pipe with upward flow, (2) horizontal curved pipe flow, and (3) vertical curved pipe with downward flow.

The Dean vortices are observed only in the downward flow inside a curved vertical pipe and the onset of Dean vortices occurs at around K = 121 and $ReRa \geq 6.66 \times 10^6$. The case of convection heat transfer in a horizontal curved pipe is of considerable practical interest. The secondary flow patterns for the case of horizontal curved pipe are quite skewed since the buoyancy and centrifugal forces are perpendicular to each other.

It is of interest to observe that the four-vortex secondary flow pattern revealed by flow visualization can be obtained by superimposing the two counterrotating vortices for the first mode ($n = 1$) and the four vortices for the second mode ($n = 2$) [19]. Apparently the theoretical interpretation of physical phenomena relating to the onset of centrifugal instability remains to be investigated in the future.

At present, theoretical results are not available for direct comparison with the flow visualization results. The present photographic results reveal relaminarization phenomena, centrifugal instability, and buoyancy effects on secondary flow in isothermally heated curved pipe with different orientations of curvature plane. The distortion of secondary flow from that of isothermal flow in a curved pipe represents the buoyancy effects and the symmetry of the secondary flow field cannot be assumed. The symmetry of the secondary flow can be maintained only when the viscosity effect is dominant over the body force effect.

The present flow visualization results provide physical insight into the convective heat transfer mechanism inside an isothermally heated curved pipe with buoyancy and centrifugal force effects. The present photographic results are believed to be useful for future theoretical and experimental studies on heated and cooled curved pipes.

Acknowledgments

This work was supported by the Natural Sciences and Engineering Research Council of Canada through an operating grant.

References

1 Graetz, L., "Uber die Warmeleitungsfahigkeit von Flussigkeiten," *Ann. d. Physik*, Vol. 18, 1883, pp. 79–94; Vol. 25, 1885, pp. 337–357.

2 Nusselt, W., "Die Abhangigkeit der Warmeubergangszahl von der Rohrlange," *Z. der Deut. Ing.*, Vol. 54, 1910, pp. 1154–1158.

3 Dean, W. R., "Notes on the Motion of Fluid in a Curved Pipe," *Phil. Mag.*, Vol. 4, 1927, pp. 208–223.

4 Dean, W. R., "The Streamline Motion of Fluid in a Curved Pipe," *Phil. Mag.*, Vol. 5, 1928, pp. 673–695.

5 Morton, B. R., "Laminar Convection in Uniformly Heated Horizontal Pipes at Low Rayleigh Numbers," *Q. J. Mech. Appl. Math.*, Vol. 12, 1959, pp. 410–420.

6 Yao, L. S., "Entry Flow in a Heated Straight Tube," *J. Fluid Mech.*, Vol. 88, 1978, pp. 465–483.

7 Yao, L. S., and Berger, S. A., "Flow in Heated Curved Pipes," *J. Fluid Mech.*, Vol. 88, 1978, pp. 339–354.

8 Futagami, K., Aoyama, Y., and Abe, F., "Forced and Free Combined Convective Laminar Heat Transfer in a Helically-Coiled Tube," *Trans. Japan Soc. Mech. Engrs.*, Vol. 47B, 1981, pp. 1995–2003.

9 Prusa, J., and Yao, L. S., "Numerical Solution of Fully-Developed Flow in Heated Curved Tubes," *J. Fluid Mech.*, Vol. 123, 1982, pp. 503–522.

10 Akiyama, M., Kikuchi, K., Cheng, K. C., Suzuki, M., and Nishiwaki, I., "Mixed Laminar Convection of the Thermal Entry Region in Curved Rectangular Channels," *ASME–JSME Thermal Engineering Joint Conf.*, 1983, Vol. 3, pp. 27–33.

11 Lee, J. B., Simon, H. A., and Chow, J. C. F., "Buoyancy in Laminar Curved Tube Flows," *ASME–JSME Thermal Engineering Joint Conf.*, 1983, Vol. 3, pp. 133–139.

12 Akiyama, M., Suzuki, Ma., Cheng, K. C., Suzuki, Mi, and Nishiwaki, I., "Mixed Convection Problems in the Entrance Region of Curved Circular Tubes," *Trans. Japan Soc. Mech. Engrs.*, Vol. 50B, 1984, pp. 1197–1204.

13 Yao, L. S., "Heat Convection in a Horizontal Curved Pipe," ASME JOURNAL OF HEAT TRANSFER, Vol. 106, 1984, pp. 71–77.

14 Nandakumar, K., and Masliyah, J. H., "Bifurcation in Steady Laminar Flow Through Curved Tubes," *J. Fluid Mech.*, Vol. 119, 1982, pp. 475–490.

15 Dennis, S. C. R., and Ng, M., "Dual Solutions for Steady Laminar Flow Through a Curved Tube," *Q. J. Mech. Appl. Math.*, Vol. 35, 1982, pp. 305–324.

16 Cheng, K. C., Inaba, T., and Akiyama, M., "Flow Visualization Studies of Secondary Flow Patterns and Centrifugal Instability in Curved Circular and Semicircular Pipes," *Flow Visualization III*, pp. 531–536.

17 Cheng, K. C., and Yuen, F. P., "Flow Visualization Studies on Secondary Flow Patterns in Curved Tubes and Isothermally Heated Horizontal Tubes," ASME Paper No. 84-HT-62.

18 Cheng, K. C., and Yuen, F. P., "Flow Visualization Studies on Secondary Flow Patterns for Mixed Convection in the Thermal Entrance Region of Isothermally Heated Inclined Pipes," *Fundamentals of Forced and Mixed Convection*, ASME HTD-Vol. 42, 1985, pp. 121–130.

19 Yao, L. S. private communication, 1985.

R. S. Amano
Associate Professor.
Mem. ASME

A. Bagherlee
Research Assistant.

R. J. Smith
Student.

T. G. Niess
Student.

Department of Mechanical Engineering,
University of Wisconsin—Milwaukee,
Milwaukee, WI 53201

Turbulent Heat Transfer in Corrugated-Wall Channels With and Without Fins

A numerical study is performed examining flow and heat transfer characteristics in a channel with periodically corrugated walls. The complexity of the flow in this type of channel is demonstrated by such phenomena as flow impingement on the walls, separation at the bend corners, flow reattachment, and flow recirculation. Because of the strong nonisotropic nature of the turbulent flow in the channel, the full Reynolds-stress model was employed for the evaluation of turbulence quantities. Computations are made for several different corrugation periods and for different Reynolds numbers. The results computed by using the present model show excellent agreement with experimental data for mean velocities, the Reynolds stresses, and average Nusselt numbers. The study was further extended to a channel flow where fins are inserted at bends in the channel. It was observed that the insertion of fins in the flow passage has a visible effect on flow patterns and skin friction along the channel wall.

Introduction

A corrugated-wall channel is often used as a passage in a heat exchanger device for the purpose of heat transfer enhancement. The study of corrugated-wall channel heat exchangers has been conducted experimentally during the past decade [1–3]. Goldstein and Sparrow [1] investigated local mass transfer rates in a corrugated wall channel by using the naphthalene sublimation technique. Izumi et al. [2] and O'Brien and Sparrow [3] measured heat transfer rates by using thermocouples. The geometry considered by Izumi et al. was a channel with a 90 deg bend angle, while that of O'Brien and Sparrow has a 120 deg bend angle. Izumi et al. used a corrugation period as a parameter by holding the fluid properties fixed, while O'Brien and Sparrow obtained heat transfer rates for several different Prandtl numbers with a fixed corrugation geometry. Except for the case of Goldstein and Sparrow [1] the other studies mentioned above were performed in turbulent regions (Re = 2000–20,000).

A numerical study was performed by Faas and McEligot [4] for laminar flows for the channels with 90 deg bends and with the corrugation periods ranging from 1 to 2. Both laminar and turbulent flows were considered by Amano [5] for the 90 deg bend channels with the corrugation period between 2 and 4. In the latter study, the standard k–ϵ model was employed along with a special three-layer near-wall model to account for the wall viscous effect in the evaluation of the local Nusselt number for turbulent flow computations. Although the slope of the Nusselt number on the Reynolds number agrees with the experimental data of Izumi et al. [2], the computed Nusselt numbers in the turbulent flow regime were 10–20 percent lower than measured values. In order to improve the prediction of Nusselt number, the full Reynolds-stress model (RSM) was employed for a flow in an infinitely long channel with two right-angle bends [6]. It was shown that the average Nusselt numbers computed by using the RSM were about 20 percent higher than those obtained by using the k–ϵ model, and consequently agreed well with experimental data. This is because the turbulence level predicted in the recirculating region by the k–ϵ model is much lower than shown by the Reynolds-stress model, thus resulting in lower heat transfer rates in the channel. In addition, the RSM can take nonisotropic effects into account, which are strong in the recirculating region. Moreover, the large deflection of the flow due to separation and reattachment adjusts the level of each Reynolds stress through the pressure-strain correlation.

This paper is a continuation of Amano [5], but here the RSM is incorporated in order to take all the stress behaviors into account in a complex flow region. Since channels with corrugation periods of 2–4 were used in [5], periods of less than 2 are mainly considered in the present paper. The results are compared with the data in literature. In addition, fin plates are inserted in the flow passage in order to investigate the local flow characteristic variations. The discussion of the computed results follows the sections dealing with mathematical models and numerical method.

Mathematical Models

The governing differential equations for the present flow geometry shown in Fig. 1 are the continuity, momentum, and energy equations. For the evaluation of the Reynolds kinematic stresses $\overline{u_iu_j}$, the full Reynolds-stress transport equations are employed rather than approximating the stresses with the Boussinesq viscosity model. The transport equation is given as

$$U_k \frac{\partial}{\partial x_k}(\overline{u_iu_j}) = G_{ij} - \frac{2}{3}\delta_{ij}\epsilon + C_D \frac{\partial}{\partial x_k}\left(\frac{k}{\epsilon}\overline{u_ku_m}\frac{\partial \overline{u_iu_j}}{\partial x_m}\right) + \overline{\frac{p}{\rho}\left(\frac{\partial u_i}{\partial x_j} + \frac{\partial u_j}{\partial x_i}\right)} \quad (1)$$

where

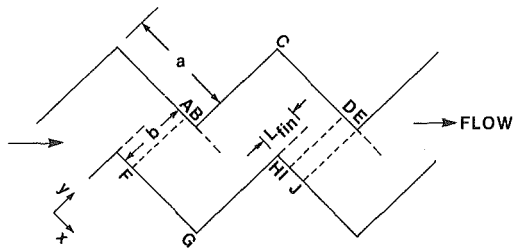

Fig. 1 Corrugated wall channels

Contributed by the Heat Transfer Division for publication in the JOURNAL OF HEAT TRANSFER. Manuscript received by the Heat Transfer Division October 10, 1985.

Table 1 Constants used in turbulence model

C_1	C_2	C_3	C_4	C_D	C_k	C_ϵ	$C_{\epsilon 1}$	$C_{\epsilon 2}$	C_μ
1.5	0.4	0.125	0.015	0.25	0.1	0.3	1.45	1.92	0.09

$$G_{ij} = -\left(\overline{u_j u_k}\,\frac{\partial U_i}{\partial x_k} + \overline{u_i u_k}\,\frac{\partial U_j}{\partial x_k}\right) \tag{2}$$

and where the pressure-strain correlation (the last term on the RHS of equation (1)) is approximated by the return-to-isotropy hypothesis of Rotta [7], the interaction with mean strains by Daly and Harlow [8], and the wall correction by Launder et al. [9]

$$\overline{\frac{p}{\rho}\left(\frac{\partial u_i}{\partial x_j} + \frac{\partial u_j}{\partial x_i}\right)} = -C_1\epsilon\left(\frac{\overline{u_i u_j}}{k} - \frac{2}{3}\delta_{ij}\right) - C_2\left(G_{ij} - \frac{2}{3}\delta_{ij}G\right) \tag{3}$$

$$-\left[C_3\epsilon\left(\frac{\overline{u_i u_j}}{k} - \frac{2}{3}\delta_{ij}\right) + C_4(G_{ij} - H_{ij})\right]f_w$$

$$G = -\overline{u_i u_j}\,\frac{\partial U_i}{\partial x_j} \tag{4}$$

$$H_{ij} = -\left(\overline{u_i u_k}\,\frac{\partial U_k}{\partial x_j} + \overline{u_j u_k}\,\frac{\partial U_k}{\partial x_i}\right) \tag{5}$$

$$f_w = \frac{k^{3/2}}{\epsilon z} \tag{6}$$

and

$$1/z = 1/x + 1/y \tag{7}$$

where x and y denote the distance to the nearest wall. The turbulence time scale k/ϵ is determined by solving the transport equations of k and ϵ

$$U_l\frac{\partial k}{\partial x_l} = -\overline{u_i u_l}\,\frac{\partial U_i}{\partial x_l} + \frac{\partial}{\partial x_l}\left[\left(\nu + C_k\,\frac{k}{\epsilon}\,\overline{u_i u_l}\right)\frac{\partial k}{\partial x_i}\right] - \epsilon \tag{8}$$

$$U_l\frac{\partial \epsilon}{\partial x_l} = +\frac{\partial}{\partial x_l}\left[\left(\nu + C_\epsilon\,\frac{k}{\epsilon}\,\overline{u_i u_l}\right)\frac{\partial \epsilon}{\partial x_i}\right]$$

$$-\frac{\epsilon}{k}\left(C_{\epsilon 1}\,\overline{u_i u_l}\,\frac{\partial U_i}{\partial x_l} + C_{\epsilon 2}\epsilon\right) \tag{9}$$

The energy equation is given as

$$U_l\frac{\partial T}{\partial x_l} = \frac{\partial}{\partial x_l}\left[\left(\frac{\nu}{\mathrm{Pr}} + \frac{\nu_t}{\mathrm{Pr}_t}\right)\frac{\partial T}{\partial x_l}\right] \tag{10}$$

where the velocity-scalar fluctuation correlation that determines the turbulence diffusion flux $-\overline{u_l T'}$ is replaced by the Boussinesq viscosity approximation and the turbulent kinematic viscosity is evaluated by $C_\mu k^2/\epsilon$. The second-order closure has not been adopted for the energy equation because the transport model for $u_l T'$ is not well defined for the complex recirculating flows. The coefficients used in the above equations are summarized in Table 1.

Numerical Method

The solution method of the transport equations stated in the preceding section is based on the control volume approach of Patankar [10] with the convection-diffusion treatment of Amano [11].

The computational domain of the flow field is the region ABCDEJIHGF (in Fig. 1). This region consists of two cycles (ABCDIHGF) and the additonal region (DEJI). For computations of laminar flows, only one cycle of the corrugated wall channel may be used with a periodic inlet/outlet condition; however, a two-cycle system is needed for complex turbulent flow computations because of numerical instability. In turbulent flow equations more nonlinear transport coefficients appear which results in a very poor history of convergence performance in the course of the iteration process. In addition, a two-pass procedure is employed. That is, the computation was started out with a constant prescribed inlet condition at AF and an outflow condition at EJ. With a line relaxation method, computations were iterated until relative residual sources of all the transport equations decreased below 2 percent. Then the periodic condition was activated by transferring the updated values at the section DI to the inlet section AF. Finally, the computation was terminated when all the relative residual sources became less than 0.1 percent.

At the wall boundaries, the momentum, energy, and the turbulence kinetic energy are evaluated from the "law of the wall" while the energy dissipation rate is determined from the

Nomenclature

a = step height
b = channel width
$C_1, C_2, C_3, C_4, C_D, C_k, C_\epsilon, C_{\epsilon 1}, C_{\epsilon 2}, C_\mu$ = constants used in turbulence model
f = average skin friction factor
f_w = function for wall correction
G = generation rate of turbulence kinetic energy
G_{ij} = generation rate of the Reynolds stresses
H_{ij} = secondary generation rate of the Reynolds stresses
k = turbulence kinetic energy
L_f = length of fin
$\underline{\mathrm{Nu}}$ = local Nusselt number
$\overline{\mathrm{Nu}}$ = average Nusselt number
p = pressure fluctuation
P = mean pressure
Pr = Prandtl number
Pr_t = turbulent Prandtl number
$\dot{q}_w$ = wall heat flux
Re = Reynolds number based on $2b$
T = temperature
T_b = bulk temperature
T_w = wall temperature
T' = fluctuating temperature
u = fluctuating velocity (x direction)
U = mean velocity
U_{in} = inlet velocity
U_m = average mean velocity
v = fluctuating velocity (y direction)
x, y = Cartesian coordinates
Γ = thermal conductivity
δ_{ij} = Kronecker delta
ϵ = energy dissipation rate
μ = dynamic molecular viscosity
ρ = density

Subscripts

i, j, k, l, m = tensor notations

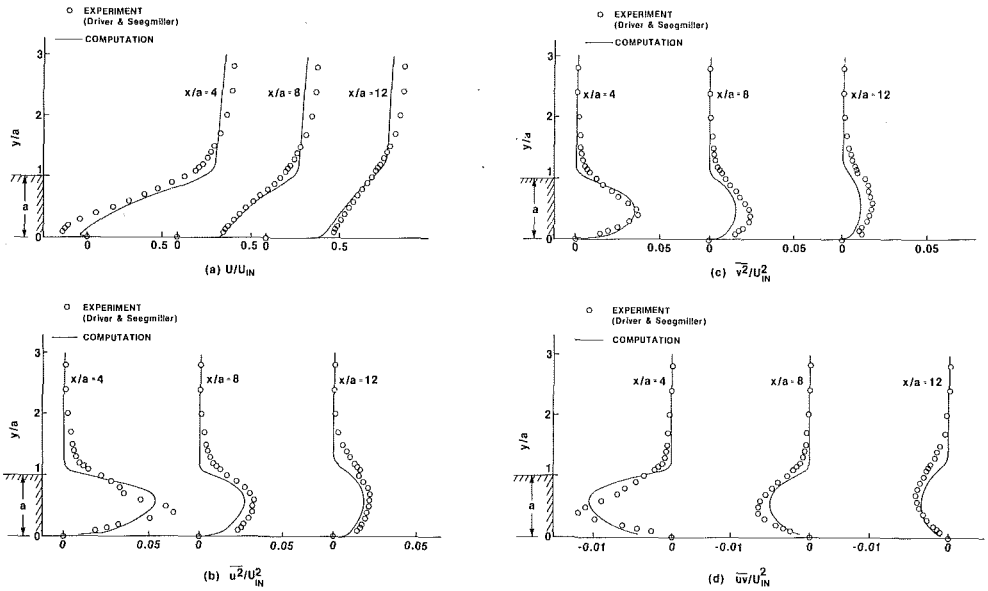

Fig. 2 Velocity and the Reynolds-stress profiles in a backward-facing step flow

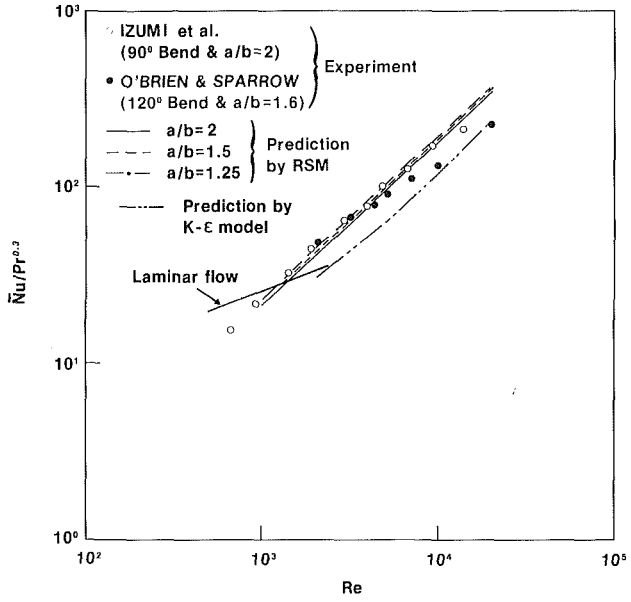

Fig. 3 Average Nusselt number as a function of Reynolds number

"local equilibrium condition," which gives linear variation of the turbulence length scale from the solid wall.

The average friction factor is computed as

$$f = -\frac{b}{\rho U_m^2}\frac{\Delta P}{L} \tag{11}$$

where L is the distance between corresponding planes and ΔP is the average pressure drop between these planes.

The local Nusselt number is obtained by the following equation

$$\mathrm{Nu} = \frac{(\dot{q}_w/\Gamma)2b}{|T_w - T_b|} \tag{12}$$

where the constant heat flux condition is employed. The bulk temperature T_b is determined as

$$T_b = \frac{\int T|U|dy}{\int |U|dy} \tag{13}$$

where the integrals are to be carried over the cross-sectional area of the channel. The absolute value of the velocity is taken so that the regions with reverse flows are also properly represented. Accordingly, the averaged Nusselt number is defined as

$$\overline{\mathrm{Nu}} = \frac{2b}{x\Gamma}\int h dx \tag{14}$$

where

$$h = \mathrm{Nu}\Gamma/2b \tag{15}$$

Results and Discussion

Validation Test of the Reynolds Stresses. Due to lack of experimental data for corrugated wall channel flows, the present numerical model cannot be justified for all the variables obtained. In particular, turbulence quantities such as the Reynolds stresses need to be compared with some experimental data. For this reason, data for a backward-facing step flow were chosen to perform a validation test of the Reynolds stresses since the wall region behind a step is similar to the flow field along the wall ABCDE in Fig. 1.

Figure 2 shows the computed results of the mean velocity and the Reynolds-stress distributions in the region behind the step. These results are compared with the experimental data of Driver and Seegmiller [12]. Here 52 × 52 grid points are used for the computational region of $50a \times 5a$ which was determined after a number of grid tests for a grid-independent state. In both recirculating and recovering regions, agreement between the present computations and the experimental data is reasonably good (within 30 percent).

Average Nusselt Number and Skin Friction Coefficients. Figure 3 shows $\overline{\mathrm{Nu}}/\mathrm{Pr}^{0.3}$ as a function of Reynolds number. The experimental data of both Izumi et al. [2] and O'Brien and Sparrow [3] are used for comparison with the present computations. The geometry considered by O'Brien and Sparrow has a bend of 120 deg and $a/b = 1.6$ whereas that by Izumi et al. has a bend of 90 deg and $a/b = 2$. The experimental data of Izumi et al. ($a/b = 2$) and those of O'Brien and

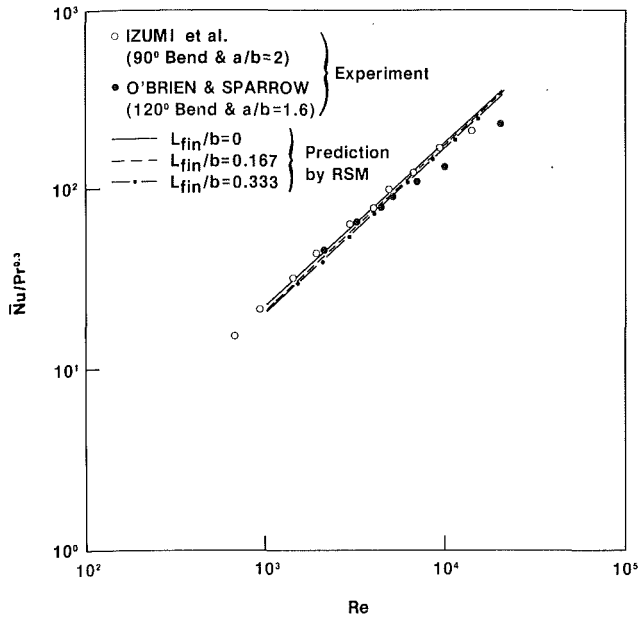

Fig. 4 Average Nusselt number as a function of Reynolds number

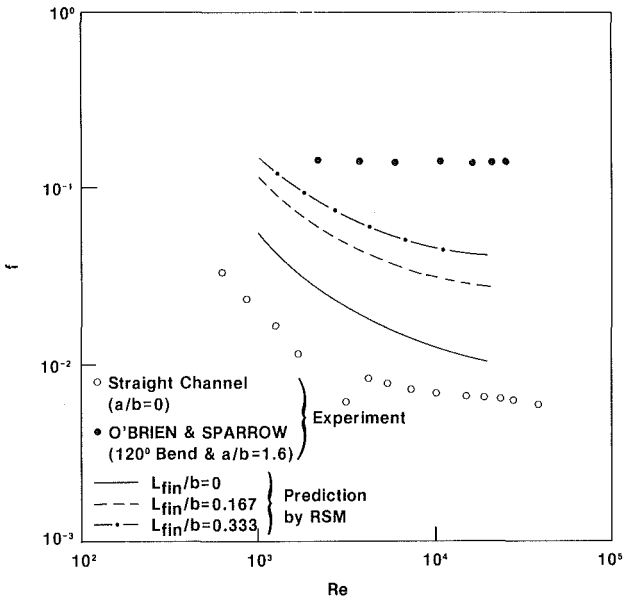

Fig. 6 Average skin friction coefficient as a function of Reynolds number

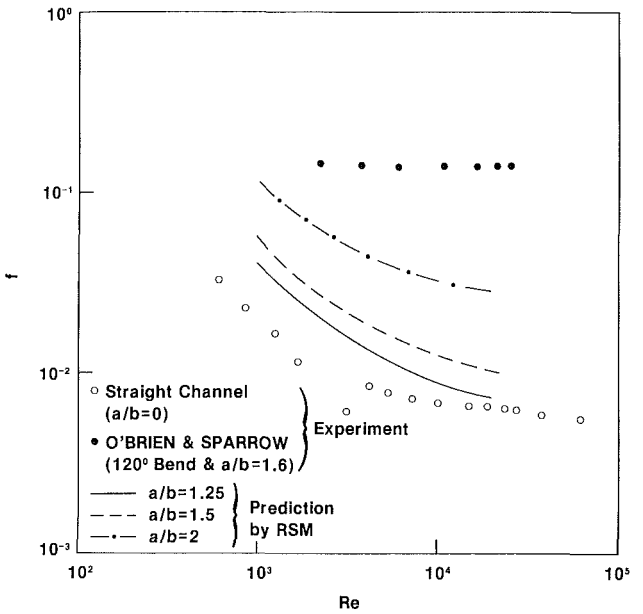

Fig. 5 Average skin friction coefficient as a function of Reynolds number

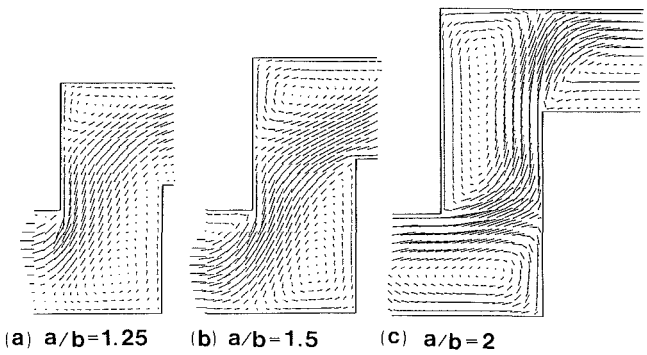

Fig. 7 Velocity vectors in channels

Sparrow (a/b = 1.6) also show similar levels at lower Reynolds number flows. However, the Nusselt numbers of O'Brien and Sparrow show a smaller slope which results in lower levels at higher Reynolds number flows. The discrepancy may be mainly due to the difference in the channel's bend angle.

For a/b = 2, the computations by the k-ϵ model [5] and the present model (RSM) are also compared. It is noteworthy that the RSM improves the prediction by 30 percent compared with the k-ϵ model when compared with the experimental data for the channel with a 90 deg bend. This observation is consistent with the case of an infinitely long channel with two bends [6] in which it was also discerned that the prediction of the Nusselt number was improved by 20–30 percent by employing the RSM. This is because the turbulence levels in recirculating regions are correctly evaluated since the RSM accounts for nonisotropic behavior of the Reynolds stresses.

In Fig. 3 the computations for a/b = 1.5 and 1.25 are also shown. It is observed that the difference in the Nusselt number created by the change in corrugation period is minor showing only a 2–3 percent decrease from a/b = 1.5 to 2.0.

Figure 4 shows the Nusselt number variation when a fin is inserted at each corner of the bend (see Fig. 1). As we see later in Fig. 8, the flow pattern changes if fins are inserted in the flow field. However, the insertion of a fin does not seem to alter the average Nusselt number more than 10 percent between L_f/b = 0 and 0.333.

Figure 5 shows the skin friction coefficient as a function of Reynolds number. Unlike the case of the Nusselt number, the computed skin friction depends strongly on the corrugation period a/b. As is expected, the level of the skin friction becomes lower as a/b decreases. The ultimate case is the straight channel with a/b = 0 whose experimental data are also shown in this figure.

In Fig. 5, the experimental data of O'Brien and Sparrow are also compared. As is shown, their experimental data are two to four times higher than the computations for a/b = 2.0. Since there are not enough experimental data with different geometries for further comparison, it is difficult to discuss the reliability of both experimental and computed results. However, because the trend in Fig. 5 is similar to the Moody

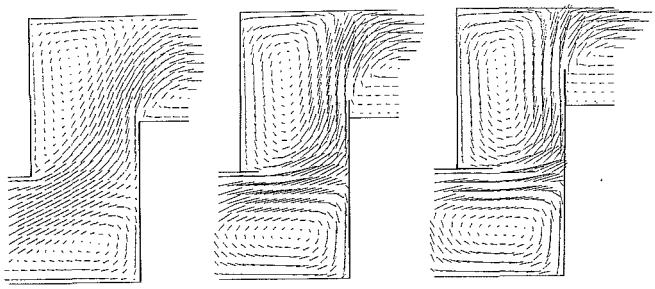

(a) $L_{fin}/b=0$ (b) $L_{fin}/b=0.167$ (c) $L_{fin}/b=0.333$

Fig. 8 Velocity vectors in channels

chart, it is plausible that the results are considerably sensitive to the roughness of the channel. Thus, we need to investigate further for the wall surface effect on the levels of friction factor.

In Fig. 6 the friction factors for the case when the fin is inserted in the flow passage are shown. Here, the effect of the fin is significant giving higher friction factors for longer fins than the case where there is no fin. In the following discussion, the local flow pattern will be considered.

Velocity and the Reynolds-Stress Profiles. Figures 7 and 8 represent, respectively, the velocity vectors in the channels with and without fins inserted. Figure 7 shows the difference of the flow pattern as the corrugation period a/b changes. For smaller a/b the separated flow creates higher convection toward the opposite side of the corner. As a/b increases, however, the flow with higher convection impinges almost normally on the opposite side of the wall (see the case of $a/b = 2.0$). Also the recirculating region expands as a/b becomes larger.

The effect of the fins is shown in Fig. 8. As is presented, the convectively accelerated flow along the fin deflects at the fin passage resulting in stronger impingement on the opposite side of the wall. As a result this highly accelerated flow causes more friction effect along the wall.

Computed mean velocities and the Reynolds stresses in the channel where $a/b = 1.5$ and $Re = 3000$ are shown in Fig. 9. As was observed in the preceding figures of velocity vectors, the mean velocity profile varies as the length of the fin increases. For example, at section B, the location of the peak of the mean velocity shifts toward the inner convex corner as the length of the fin becomes longer, and the peak value increases accordingly. This high velocity gradient causes correspondingly higher levels of the Reynolds stresses in the midsection of the flow passage. The levels of $\overline{u^2}$ and $\overline{v^2}$ interchange in the next bend section (cross section CH) showing a relatively high level of $\overline{v^2}$ and a low level of $\overline{u^2}$ because the y component of velocity is predominant over the x component mean velocity. The peak of $\overline{u^2}$ appears at the midsection of passage DI due to a high mean strain rate. On the contrary the peak of $\overline{v^2}$ at the same passage occurs near point D since the flow deflection caused by the separation at H generates the energy of $\overline{v^2}$.

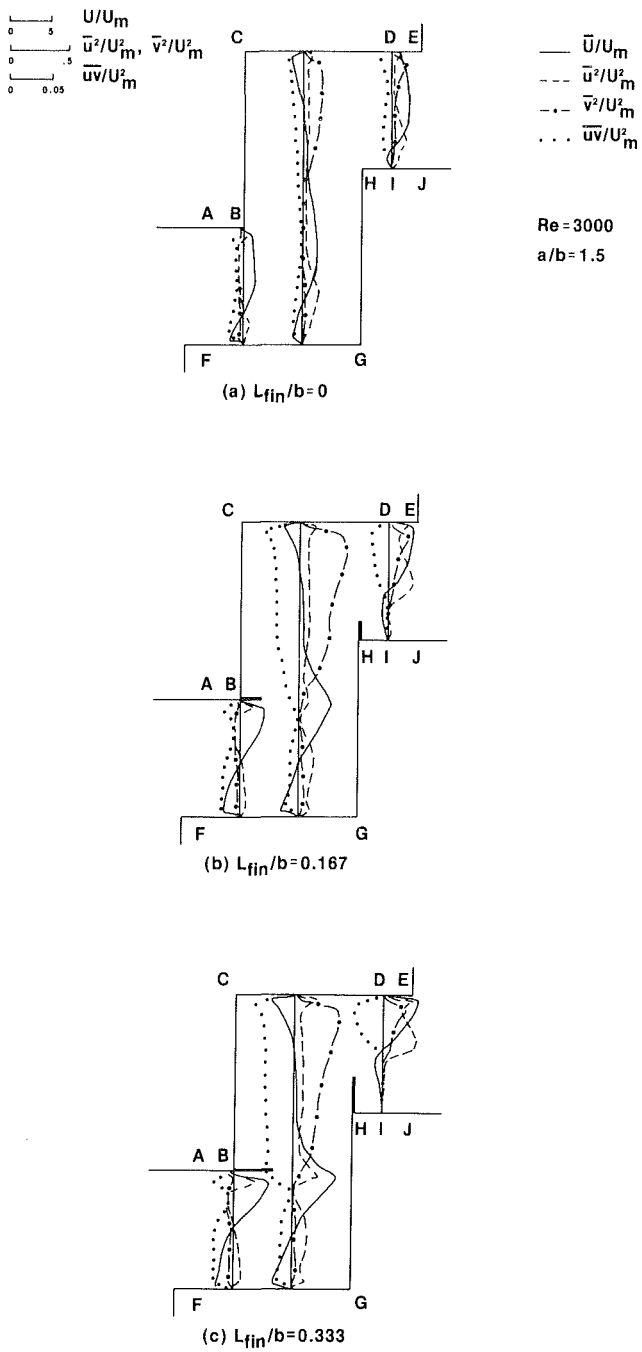

Fig. 9 Velocity and the Reynolds-stress profiles in a corrugated wall channel ($a/b = 1.5$, $Re = 3000$)

Conclusions

Mathematical and numerical models are developed for the study of flow and heat transfer rates in corrugated wall channels where complex turbulent flows are created. The following conclusions emerge from this study:

1 Because the flow field created in such a channel is highly nonisotropic, the second-moment closure approach is required to analyze these turbulent flows. The Reynolds stress model has been successfully applied. As a result the stress levels obtained by using the present model showed reasonable results within 30 percent error.

2 The average Nusselt numbers computed with the RSM are improved about 30 percent compared with predictions obtained by the standard k-ϵ model. This is because the RSM can evaluate the recirculating region correctly.

3 By inserting fins in the flow passage, the flow pattern and the skin friction rates change considerably. However, the effect of the insertion of fins on the heat transfer rate is small.

Acknowledgments

This work was supported by NASA Lewis Research Center under grant No. NAG 3-546 monitored by Mr. Thomas VanOverbeke.

References

1 Goldstein, L., and Sparrow, E. M., "Heat/Mass Transfer Characteristics for Flow in a Corrugated Wall Channel," ASME JOURNAL OF HEAT TRANSFER, Vol. 99, 1977, pp. 187–195.

2 Izumi, R., Yamashita, H., Kaga, S., and Miyajima, N., "Fluid Flow and Heat Transfer in Corrugated Wall Channels—Experimental Study for Many Bends," *Proceedings of the 19th JSME Symposium on Heat Transfer*, 1982, Paper No. A101.

3 O'Brien, J. E., and Sparrow, E. M., "Corrugated-Duct Heat Transfer, Pressure Drop, and Flow Visualization," ASME JOURNAL OF HEAT TRANSFER, Vol. 104, 1982, pp. 410–416.

4 Faas, S. E., and McEligot, D. M., "Convective Heat Transfer for Ship Propulsion," Report No. 1248-7, ONR, Aerospace and Mechanical Engineering Department, University of Arizona, 1980.

5 Amano, R. S., "A Numerical Study of Laminar and Turbulent Heat Transfer in a Periodically Corrugated Wall Channel," ASME JOURNAL OF HEAT TRANSFER, Vol. 107, 1985, pp. 564–569.

6 Amano, R. S., "A Numerical Study of Turbulent Heat Transfer in a Channel With Bends," presented at the 23rd National Heat Transfer Conference, Denver, Aug. 1985, ASME Paper No. 85-HT-20.

7 Rotta, J. C., "Statistische Theories Nichthomogener Turbulenz," *Zeitschrift fur Physik*, Vol. 129, 1951, pp. 547–572.

8 Daly, B. J., and Harlow, F. H., "Transport Equations of Turbulence," *The Physics of Fluids*, Vol. 13, No. 11, 1970, pp. 2634–2649.

9 Launder, B. E., Reece, G. J., and Rodi, W., "Progress in the Development of a Reynolds-Stress Turbulence Closure," *Journal of Fluid Mechanics*, Vol. 68, 1975, pp. 537–566.

10 Patankar, S. V., *Numerical Heat Transfer and Fluid Flow*, McGraw-Hill, New York, 1980.

11 Amano, R. S., "Development of Turbulent Near-Wall Model and Its Application to Separated and Reattached Flows," *Numerical Heat Transfer*, Vol. 7, 1984, pp. 59–75.

12 Driver, D. M., and Seegmiller, H. L., private communications, 1985.

Effects of Several Roughness Elements on an Insulated Wall for Heat Transfer From the Opposite Smooth Heated Surface in a Parallel Plate Duct

K. Ichimiya
Associate Professor,
Department of Mechanical Engineering,
Yamanashi University,
Kofu, Yamanashi 400, Japan

Experiments were carried out to examine the effects of several roughness elements on the insulated wall opposite the smooth heated plate for the heat transfer with air flowing through a parallel plate duct. The local heat transfer coefficient, the velocity distribution, the turbulence intensity, and the pressure drop were measured. An optimum pitch of roughness elements for the augmentation of heat transfer exists for each space between two parallel plates. Additionally, the correspondence between the heat transfer and the flow situation is also examined. Acceleration and turbulence produced by roughness elements contribute to the increase of the local heat transfer coefficients on the smooth heated plate. Thermal performance is evaluated at constant pumping power.

Introduction

Turbulence promoters or roughness elements have been used to improve the heat transfer in various heat exchangers. A number of reports [1-7] have been published on the heat transfer characteristics with roughness elements for forced convection.

These roughness elements have been set on a heat transfer surface. The mechanism of augmented heat transfer is complicated since the effects of the extended surface and turbulence generation are combined. Therefore, it is important in a fundamental sense to examine the effectiveness of roughness elements alone for the heat transfer.

These previous investigations consider the fully developed heat transfer situation. However, most practical applications include not only the fully developed region, but also the developing region. Thus the local heat transfer and flow situations should be clarified from the first element to the developed region.

In recent years, for a single turbulence promoter, experiments have been performed not only with a turbulence promoter on a heated surface, but also with a circular tube placed over the heated surface with a small clearance [8], or a contraction by using a segment [9] or a slat blockage [10]. The author has already examined the effect of a single roughness element set on the upper insulated plate of a parallel plate duct for the local heat transfer coefficient on the opposite smooth heated wall [11]. However, considering practical applications, the characteristics of heat transfer and flow situation should be examined experimentally for several roughness elements, rather than for a single element.

The present paper basically describes the characteristics of the local heat transfer and the flow in the developing region by using air as a fluid when roughness elements are placed on the insulated wall opposite the smooth heated plate. The behavior of the local heat transfer coefficients, the relationship between heat transfer and flow, and the thermal performance are examined with variations in the pitches of the roughness elements, the size of a duct, and the Reynolds number.

Contributed by the Heat Transfer Division and presented at the ASME-JSME Joint Thermal Engineering Conference, Honolulu, Hawaii, March 1983. Manuscript received by the Heat Transfer Division September 14, 1984.

Experimental Facility and Procedure

Experimental Facility. The schematic diagram of the experimental facility is shown in Fig. 1. The test section set on the suction side of a blower (f), is composed of a parallel plate duct whose width and length are 300 mm and 2420 mm, respectively, and whose upper plate is insulated. Air (indicated by the arrows in Fig. 1) flowed through a bell-like mouth entrance, which possibly reduced the effect of the entrance edge. The flow rate was measured by traversing the pitot tube (c) across the sectional area. Square roughness elements (d) (refer to Fig. 2) made of acrylic material and 10 mm in height, were set on the bottom of the upper plate with pitch *Pi* at the 1640 mm from the entrance, thus perturbing the flow.

The heating section ($a_1 - a_1$) of the bottom plate consisted of a smooth copper plate and rubber heaters (Ni-Cr heaters were arranged closely and insulated by thin rubber), which supplied uniform heat flux by alternating current. The thickness of the copper plate was 1.2 mm. The generated heat was transferred to the air after the wall conduction in the copper plate, as shown in Fig. 2. Heated surface temperatures were measured by the calibrated copper-constantan thermocouples whose diameter was 0.1 mm and which were set on

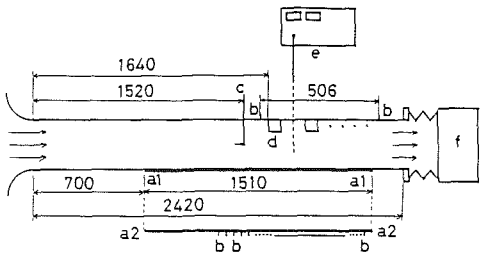

a1-a1 : Heated surface
a2-a2 : Acrylic plate
b : Pressure taps
c : Pitot tube
d : Roughness elements
e : Hot wire anemometer
f : Blower

Fig. 1 Experimental facility

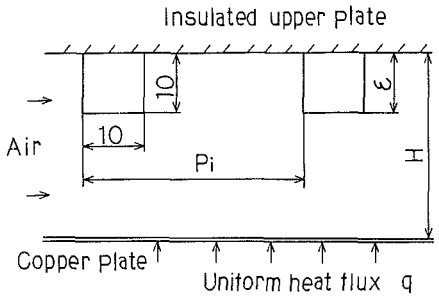

Fig. 2 Test section with roughness elements

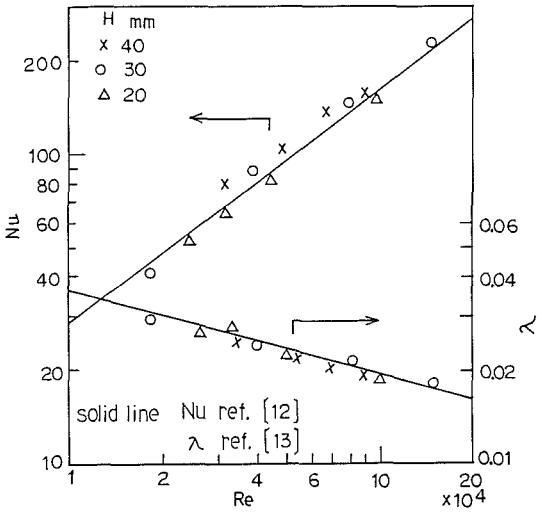

Fig. 3 Heat transfer and friction factor from smooth parallel plates (uniform heat flux on one side, the other insulated)

the back of the heated plate along the center line of the flow passage. The upper part of the heated plate was supported and insulated by an acrylic plate and the insulated materials. Additionally, a subheater was affixed between the insulation materials to compensate for heat loss from the under part.

For the flow experiment the heated plate was replaced by a smooth acrylic plate (a_2–a_2) with pressure taps (b). The local velocity and turbulence intensity were simultaneously measured by a thermoanemometer (e) (Kanomax, System 7114) under an unheated condition. A probe (I-type) was inserted from the upper plate to traverse across the section and along the flow direction at 10-mm intervals. The static pressure distribution was also measured by 53 pressure taps.

Table 1 Experimental conditions

Reynolds number	$10^4 \sim 1.9 \times 10^5$
Heat flux q W/m^2	477 ~ 745
Space between upper plate and bottom plate H mm	20, 25, 30, 35, 40
Pitch of roughness elements Pi mm	20, 30, 40, 50, 70, 100, 150, 200

Experimental Procedure. In order to obtain the local heat transfer coefficient, the entrance temperature of the air was measured directly and the mixed mean temperature of the air T_m at any arbitrary point was calculated by the flow rate and the net heat flow. The local heat transfer coefficient was evaluated by the following equation

$$\alpha = \frac{q}{T_w - T_m}$$

This local heat transfer coefficient is the heat transfer after the wall conduction in the copper plate. The percentage of the axial conduction in the copper plate was from 2 to 4 percent in the present study. Measurements were started after steady state was attained.

In the first stage, heat transfer experiments were performed in a smooth parallel plate duct without roughness elements. These results agreed fairly well with values of Nu on one side of a heated plate duct obtained by Hatton [12], as shown in Fig. 3. In the next step, experiments for the roughness elements proceeded after these elements were aligned lengthwise beneath the width of the upper insulated plate (the length of the roughness element being the same as the width of the parallel plate) at a constant pitch.

In the flow experiments, friction factors for the smooth duct were compared with the experimental equation for the rectangular duct obtained by Jones [13]. Although the values are a little lower, they coincide generally well for the whole region, as shown in Fig. 3. It was recognized that the velocity distribution showed the fully developed turbulent values within the center two thirds of the cross-sectional area. The

Nomenclature

D_H = hydraulic diameter = $2H$, m, mm
f_R = friction factor for the duct with roughness elements
H = space between the upper plate and the bottom plate, mm
k = thermal conductivity, W/m•K
Nu = Nusselt number = $\alpha \cdot D_H/k$
Nu_{max} = maximum Nusselt number
Nu_0 = Nusselt number for smooth duct
Pi = pitch of roughness elements, mm
q = heat flux, W/m^2
Re = Reynolds number = $U_m \cdot D_H/\nu$
T_m = mixed mean temperature, K
T_w = heated surface temperature, K
X = distance from the starting point of heating, mm
X' = distance from the starting point of the roughness element, mm
$\tilde{U}$ = local time-averaged velocity, m/s
U_m = mean velocity across the sectional area, m/s
U_0 = maximum velocity across the sectional area of a smooth duct, m/s
$\sqrt{U'^2}/\tilde{U}$ = intensity of turbulence
$\tilde{U}/U_0$ = velocity ratio
α = local heat transfer coefficient, W/m^{2}K
α_0 = minimum heat transfer coefficient before the first roughness element, W/m^{2}K
ϵ = height of a roughness element, mm
λ = friction factor for smooth duct
ν = kinetic viscosity, m^2/s

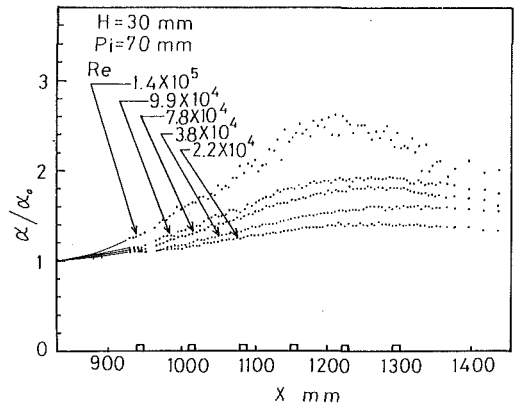

Fig. 4(*a*) Local heat transfer coefficient with Re as a parameter

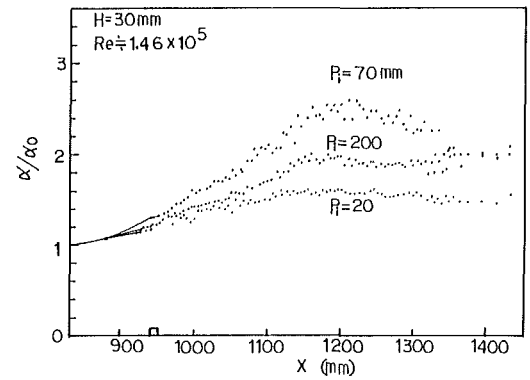

Fig. 4(*b*) Local heat transfer coefficient with *Pi* as a parameter

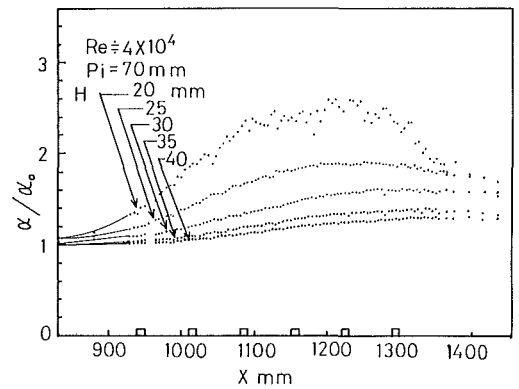

Fig. 4(c) Local heat transfer coefficient with *H* as a parameter

flow was found to be two dimensional near the center of the section and was determined by using the ratio of local time-averaged velocity and the maximum time-averaged velocity without roughness elements $\bar{U}/U_0$, local turbulence intensity $\sqrt{\overline{U'^2}}/\bar{U}$, and the ratio of the static pressure difference (Δp being the pressure difference between the entrance and the local point) and the dynamic pressure by mean velocity $\Delta p/(1/2\rho U_m{}^2)$. The mutual relation between flow and heat transfer was then investigated.

The experimental conditions are listed in Table 1.

Experimental Results and Discussion

Local Heat Transfer Coefficient. The ratio of local heat transfer coefficient and minimum heat transfer coefficient before the first roughness element α/α_0 is shown in Fig. 4(*a*, *b*, *c*). Figure 4(*a*) displays α/α_0, for pitch $Pi=70$ mm and

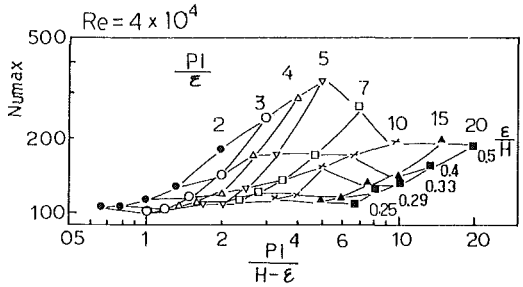

Fig. 5 Relationship between Nu_{max} and $Pi/(H-\epsilon)$

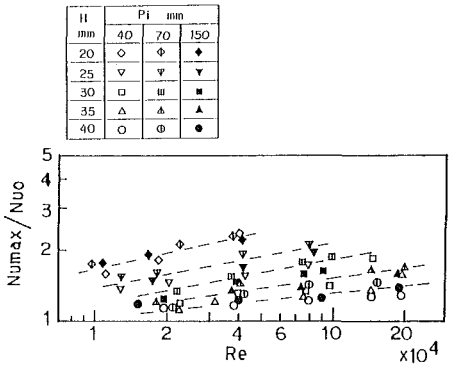

Fig. 6 Relationship between Nu_{max}/Nu_0 and Re

$H=30$ mm, as a parameter of Reynolds number Re. The value of α_0 is approximately the developed heat transfer coefficient of a smooth parallel plate duct with $H=30$ mm. While local heat transfer coefficients approach the fully developed value along the direction from the starting point of heating, they generally begin to increase before the first roughness element and show a small peak under the first roughness element. They continue to increase to a large maximum α_{max} after the developing region, and then decrease gradually behind the last roughness element. The decrease in α prior to the last element for large Re is disturbing due to the flow situation (recirculating effect). The magnitude of α/α_0 increases with Reynolds number for the constant spacing and the constant pitch of roughness elements. Figure 4(*b*) shows that the local heat transfer coefficient is higher in comparatively medium pitch ($Pi=70$ mm) rather than the small pitch $Pi=20$ mm or the larger pitch $Pi=200$ mm. This tendency means an optimum pitch, which gives the best effect for the heat transfer, exists for each space H. Figure 4(*c*) shows the effect of the space H on the local heat transfer. It is clear that the effect is much higher for a smaller distance between the roughness element and the heated surface. The magnitude of α_{max}/α_0 is 1.25 for $H=40$ mm and on the other hand, it is 2.6 for $H=20$ mm. Within our experimental conditions, α_{max}/α_0 approaches to about 3.5 and the position of the maximum moves downstream with H.

The relationship between Nu_{max} and the pitch of roughness elements for each spacing is shown in Fig. 5 for $Re=4\times10^4$. The abscissa represents the dimensionless pitch, while the ordinate is the maximum Nusselt number. Each signal displays a condition for space and pitch. Figure 5 describes the existence of an optimum pitch for the spacing, as described above. Namely, Nu_{max} takes a peak at dimensionless pitch $Pi/\epsilon=5\sim10$ for each dimensionless height $\epsilon/H=0.25\sim0.5$. Figure 6 shows the relationship between Nu_{max}/Nu_0 and Re. While Nusselt number Nu_0 in a smooth parallel plate duct is approximated by the relation $Nu_0=0.028Re^{0.75}$ for air [12], Nu_{max}/Nu_0 is represented by Re^n, whose index n changes with H. Index n varies from 0.10 for $H=40$ mm to about 0.38 for

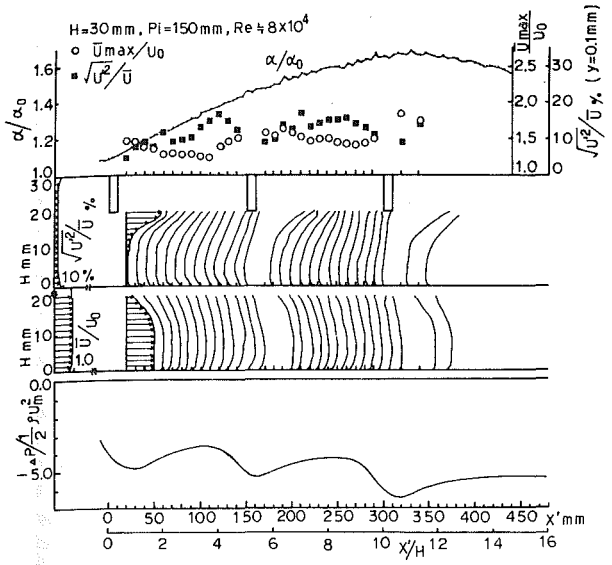

Fig. 7(a) Correspondence between heat transfer and flow situation, $Pi = 150$ mm

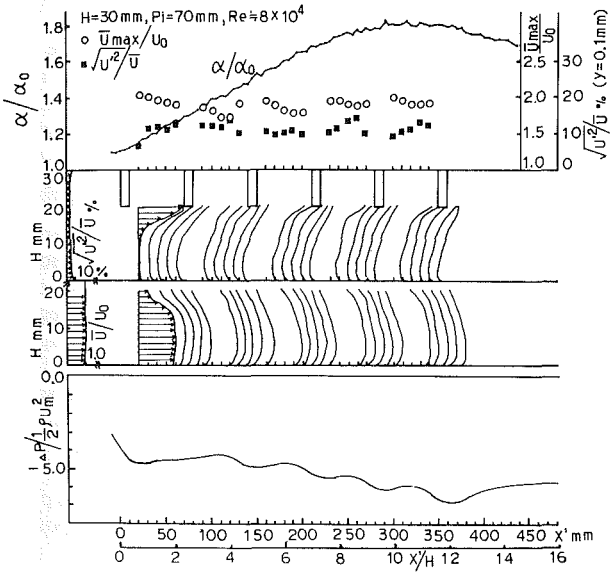

Fig. 7(b) Correspondence between heat transfer and flow situation, $Pi = 70$ mm

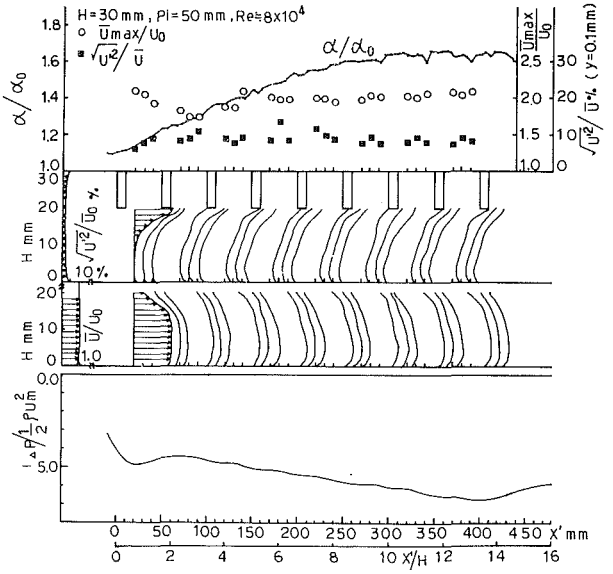

Fig. 7(c) Correspondence between heat transfer and flow situation, $Pi = 50$ mm

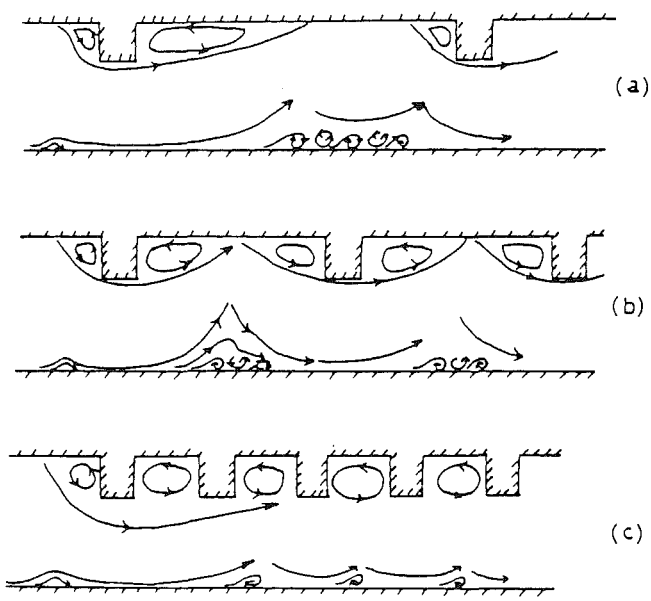

Fig. 8 Flow patterns

$H = 20$ mm. Consequently, Nu_{max} depends on $Re^{(0.85 \sim 1.13)}$ more heavily than Nu_0 in a smooth parallel plate duct.

Relationship Between Heat Transfer and Flow. This section examines how heat transfer relates to the flow behavior. Figures 7(*a*, *b*, *c*) show the correspondence between heat transfer and flow for $Re = 8 \times 10^4$ and $H = 30$ mm in the cases $Pi = 150$, 70, and 50 mm. The upper diagram for the above figures shows the local heat transfer ratio α/α_0, the maximum velocity ratio U_{max}/U_0 and the turbulence intensity $\sqrt{U'^2/\bar{U}}$ at a vertical distance from the smooth surface $y = 0.1$ mm. The middle two diagrams show the velocity and the turbulence intensity distribution along the flow direction. These distributions are compared with the values of a smooth parallel plate duct on the left side. The bottom diagram displays the dimensionless static pressure difference $\Delta p/(1/2\rho U_m{}^2)$.

In Fig. 7(*a*) ($Pi = 150$ mm), the maximum velocity is largest under the roughness element, decreases along the flow direction, and then increases before the next roughness element. On the other hand, the turbulence intensity near the smooth plate (corresponding to heated surface) is low under the roughness element, increases gradually along the flow direction and reaches a maximum of 20 percent. Then it decreases before the next roughness element. Consequently, it is recognized that the increase of the flow acceleration and turbulence intensity near the heated plate causes the increase of the local heat transfer coefficient. In Fig. 7(*b*) ($Pi = 70$ mm), according to the velocity distribution, the flow suddenly accelerates near the first roughness element and the maximum value occupies the lower part of the cross sectional area. Consequently, the velocity distribution is flattened. However, the area of the maximum value decreases longitudinally and the distribution is warped along the flow direction. The static pressure recovers between the second and the third roughness element and then varies periodically in the downstream region for $Pi = 70$ mm (Fig. 7*b*). The magnitude of the maximum velocity behind the first roughness element also continues to decrease until the third roughness element (upper diagram). This demonstrates that the effect of the first roughness element is stronger within the next two pitches. Turbulence intensity near

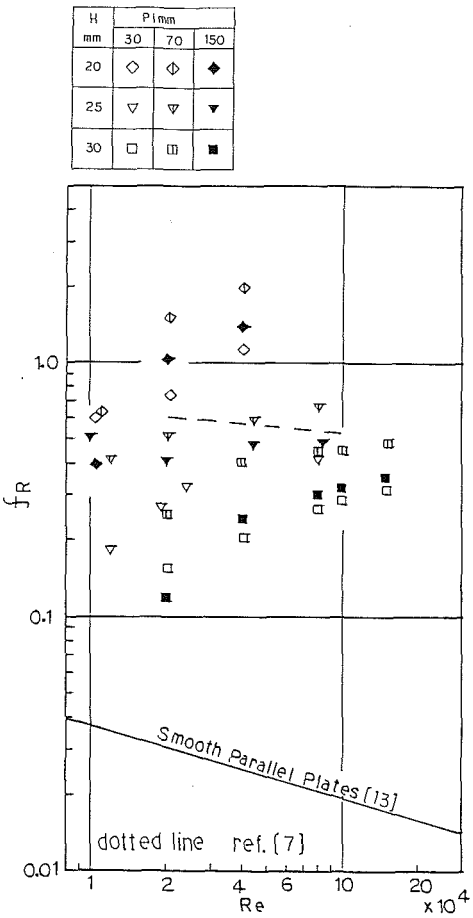

Fig. 9 Friction factor

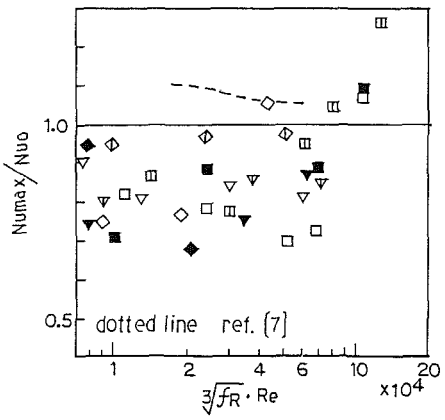

Fig. 10 Thermal performance

the smooth surface and the maximum velocity change periodically after the fourth roughness element. On the other hand, the local heat transfer coefficient attains and maintains the maximum value (upper diagram). The abovenoted data are emphasized after the sixth roughness element in $Pi = 50$ mm (Fig. 7*c*). The maximum value of the turbulence intensity near the heated surface in $Pi = 50$ mm is smaller than that in $Pi = 150$ mm. By the above results, while the reduction of pitch causes the decrease of the local turbulence intensity and the increase of the local acceleration, the enlargement of pitch produces the inverse phenomena. Consequently, the existence of an optimum pitch represents the situation in which the effects of the acceleration and the turbulence intensity are mixed mutually and properly.

Flow Visualization. Furthermore, the flow behavior is examined by flow visualization (fluid: water, medium: dye). The experimental conditions are: The height of roughness element $\epsilon = 30$ mm, the space of a duct $H = 100$ mm, and the Reynolds number $\mathrm{Re} = 7000$. While this does not correspond exactly to the heat transfer experiment, this may be contributed to the qualitative explanations. Figures 8(*a*, *b*, *c*) indicate the flow patterns for three kinds of pitches. For the large pitch (Fig. 8*a*), two separated regions are produced between two roughness elements. Behind the accelerated area, small clockwise and anticlockwise rotating eddies are generated on the smooth surface corresponding to the reattached region on the upper plate. With decreasing pitch, two separated flow regions on the upper plate are in contact with each other (Fig. 8*b*). Under the corresponding region on the heated surface, the flow rolls up, and near the bottom plate small eddies are generated. At comparatively small pitches, a separated flow region occurs between two roughness elements and becomes a recirculating closed vortex (Fig. 8*c*). Acceleration by the first roughness element starts and contributes to the acceleration within the next two or three roughness elements. After that, small eddies are generated on the heated surface, and contribute to the increase of local turbulence intensity in Fig. 7. These flow patterns depend on the ratio Pi/ϵ and the space of the duct H or $H - \epsilon$.

Friction Factor. Friction factor for a pressure drop through the section with roughness elements is shown in Fig. 9. The solid line represents that of a smooth parallel plate duct. The dotted line displays the friction factor of a parallel plate duct with roughness elements of both plates ($\epsilon = 8$ mm, $H = 44.5$ mm, area ratio which roughness elements occupies cross section $2\epsilon/H = 0.36$) [7]. This is in the middle of the present friction factor for $H = 25$ mm and 30 mm. In previous papers, fluid resistance through a fully developed region had been described as a friction factor for fluid passage with roughness elements. Evaluation for the developing region is needed since both regions are involved in practical applications, for instance, in heat exchangers. Present friction factors are $9 \sim 60$ times greater in magnitude than that of a smooth duct since a roughness element occupies $33 \sim 50$ percent of the cross section, and are largest for medium pitch, which are optimum on heat transfer for each space H. While friction factor generally does not depend on Re in the rough tube, the present data tend to increase with Re. This tendency corresponds to the increase of α_{max}/α_0 with Re.

Thermal Performance. In the constant channel length and uniform heat flux, the thermal performance is evaluated by comparing heat transfer coefficients for channels with and without roughness elements per unit pumping power. Pumping power is proportional to $f_R \cdot \mathrm{Re}^3$. Hence in Fig. 10, the performance is shown by the ratio of the maximum Nusselt number Nu_{max}, and the value for smooth channel Nu_0 at the same $\sqrt[3]{f_R} \cdot \mathrm{Re}$. Present data are compared with experimental values [7] for a parallel plate duct with roughness elements on heated surfaces ($2\epsilon/H = 0.36$), and shows that the passage with medium pitch and narrow space gives higher performance at high Reynolds number ($\mathrm{Nu}_{max}/\mathrm{Nu}_0 > 1.0$), namely, $\mathrm{Nu}_{max}/\mathrm{Nu}_0$ tends to increase with $\sqrt[3]{f_R} \cdot \mathrm{Re}$. Consequently, in the present case, heat transfer from a smooth surface opposite the rough surface is more effective for a comparatively narrow passage and high Reynolds number than that from the rough surface on a heater plate.

Concluding Remarks

Experiments have been performed to examine the effect of several roughness elements located on the insulated upper wall on the heat transfer of the opposite wall in a parallel plate duct.

The effect of roughness elements on heat transfer increases with the Reynolds number. A large pitch causes the increase of local turbulence intensity, while a small pitch causes the increase of an accelerated region rather than that of local turbulence intensity. Acceleration and turbulence near the heated surface produced by roughness elements contribute to the increase of the local heat transfer coefficient. If acceleration and turbulence are combined properly with each other by changing the pitch, an optimum pitch of roughness elements for the augmentation of heat transfer exists for each space between two parallel plates. The ratio of the maximum Nusselt number under the condition of the constant pumping power shows the excellent performance at high Reynolds numbers and medium pitch of roughness elements in a narrow passage.

Based on the results described above, it would seem important to take into account the effects of roughness elements for the heat transfer on the opposite wall in design (for instance, heat exchangers and heat removal from high-temperature gas-cooled reactors or gas-cooled nuclear fusion).

Acknowledgments

I would like to express appreciation to Professor S. Hasegawa, Kyushu University, and Professor R. Shimomura, Fukui Institute of Technology, who presented valuable comments and advices to this study, and to Mr. M. Yokoyama, who helped me in the process of the experiment.

References

1 Nunner, W., "Wärmeubergang und Druckabfall in Rauhen Rohren," VDI-Forschungsheft 455, Series B, Vol. 22, 1956.

2 Dipprey, D. F., and Sabersky, R. H., "Heat and Momentum Transfer in Smooth and Rough Tubes at Various Prandtl Numbers," *International Journal of Heat and Mass Transfer*, Vol. 6, 1963, pp. 329–353.

3 Gomelauri, V., "Influence of Two-Dimensional Artificial Roughness on Convective Heat Transfer," *International Journal of Heat and Mass Transfer*, Vol. 7, 1964, pp. 653–663.

4 Williams, F., and Watts, J., "The Development of Rough Surfaces With Improved Heat Transfer Performance and a Study of the Mechanism Involved," *Proceedings of 4th International Heat Transfer Conference*, FC-5.5, 1970, pp. 1–11.

5 Webb, R. L., Eckert, E. R. G., and Goldstein, R. J., "Heat Transfer and Friction in Tubes With Repeated-Rib Roughness," *International Journal of Heat and Mass Transfer*, Vol. 14, 1971, pp. 601–617.

6 Lewis, M. J., "An Elementary Analysis for Predicting the Momentum and Heat Transfer Characteristics of a Hydraulically Rough Surface," ASME JOURNAL OF HEAT TRANSFER, Vol. 97, 1975, pp. 249–254.

7 Tanasawa, I., Nishio, S., Takano, K., and Tado, M., "Enhancement of Forced Convection Heat Transfer in Rectangular Channel Using Turbulence Promoters," *ASME/JSME Thermal Engineering Joint Conference*, Vol. 1, 1983, pp. 395–402.

8 Fujita, H., Takahama, H., and Yamashita, R., "The Forced Convective Heat Transfer on a Plate With a Cylinder Inserted in the Boundary Layers," *Transactions of the Japan Society of Mechanical Engineers*, Vol. 42, 1976, pp. 2828–2836.

9 Koram, K. K., and Sparrow, E. M., "Turbulent Heat Transfer Downstream of an Unsymmetric Blockage in a Tube," ASME JOURNAL OF HEAT TRANSFER, Vol. 100, 1978, pp. 588–594.

10 Sparrow, E. M., Koram, K. K., and Charmahi, M., "Heat Transfer and Pressure Drop Characteristics Induced by a Slat Blockage in a Circular Tube," ASME JOURNAL OF HEAT TRANSFER, Vol. 102, 1980, pp. 64–70.

11 Ichimiya, K., Hasegawa, S., and Yamasaki, K., "Effects of a Single Artificial Roughness Element on the Heat Transfer From a Smooth Heated Wall in a Parallel Plates Duct," *Transactions of the Japan Society of Mechanical Engineers*, Vol. 46, 1980, pp. 482–491.

12 Hatton, A. P., and Quarmby, A., "The Effect of Axially Varying and Unsymmetrical Boundary Conditions on Heat Transfer With Turbulent Flow Between Parallel Plates," *International Journal of Heat and Mass Transfer*, Vol. 6, 1963, pp. 903–913.

13 Jones, O. C., "An Improvement in the Calculation of Turbulent Friction in Rectangular Ducts," *Transactions ASME*, Vol. 98, 1976, pp. 173–181.

Effects of Crossflow Temperature on Heat Transfer Within an Array of Impinging Jets

L. W. Florschuetz
Mem. ASME

C. C. Su[1]
Assoc. Mem. ASME

Department of Mechanical and Aerospace Engineering, Arizona State University, Tempe, AZ 85287

Two-dimensional arrays of circular air jets impinging on a heat transfer surface parallel to the jet orifice plate are considered. In the experimental model the jet flow, after impingement, was constrained to exit in a single direction along the channel formed by the jet orifice plate and heat transfer surface. In addition to the crossflow that originated from the jets following impingement, an initial crossflow was present that approached the array through an upstream extension of the channel. By varying the initial crossflow temperature, the mixed-mean crossflow temperature approaching each spanwise jet row n ($T_{m,n}$) *was varied independently of the jet temperature* (T_j). *For each row, the effect of* $T_{m,n}$ *relative to* T_j *on the heat flux opposite the row was determined. Results are formulated in terms of parameters defined for each individual spanwise row domain: a crossflow-to-jet temperature difference influence factor* (η_r) *and a Nusselt number* (Nu_r) *as functions of jet Reynolds number, crossflow-to-jet mass flux ratio, and geometric parameters. Effects of row position within the array are also considered. It was found that* η_r *and* Nu_r *are nominally independent of row position after the first two rows.*

Introduction and Background

When impinging jets are utilized for internal cooling of gas turbine components the overall cooling scheme configuration may be such that the jets are subject to a crossflow. Even if the cooling air is supplied to the component at a single temperature, the crossflow air approaching a jet may be at a higher temperature than the jet air because of upstream heat addition to the air comprising the crossflow. In addition to the effect of the crossflow on the flow field of the impinging jet, which may in turn affect the heat rate at the impingement surface, there will also be the effect of the crossflow temperature relative to the jet temperature on the impingement surface heat rate.

Most prior studies of heat transfer to single impinging jets or single spanwise rows of impinging jets subject to a crossflow were performed with the crossflow temperature essentially identical to the jet temperature; see, e.g., Metzger and Korstad [1], Sparrow et al. [2], and Goldstein and Behbahani [3]. Bouchez and Goldstein [4], however, did study the effect of crossflow temperature relative to jet temperature on impingement heat transfer for a single circular jet.

Holdeman and Walker [5], Srinivasan et al. [6], and Wittig et al. [7] studied the temperature profile development downstream of a row of jets mixing with a confined crossflow which approached the jets at a temperature different from the jet temperature. Since these studies were motivated by interest in dilution zone mixing in gas turbine combustion chambers, surface heat transfer characteristics in those cases where impingement did occur were not of interest and were approximately adiabatic during these tests. Therefore, heat fluxes were not determined.

Two-dimensional arrays of circular jets impinging on a heat transfer surface opposite the jet orifice plate produce conditions in which individual jets or rows of jets in the array are subject to a crossflow the source of which is other jets within the array itself. In gas turbine applications the flow from the jets is often constrained to exit essentially in a single direction along the channel formed by the jet orifice plate and the impingement surface. Such configurations are also encountered in a wide variety of process and thermal control applications. Examples include cooling of electronic equipment, drying of paper and textiles or other thin layers or films, annealing of metals, and glass tempering operations.

Experimental studies of impingement surface heat transfer for such configurations motivated by gas turbine applications were reported, e.g., by Kercher and Tabakoff [8], Florschuetz et al. [9, 10], Saad et al. [11], and Behbahani and Goldstein [12]. In these studies the effect of the temperature of the crossflow approaching a spanwise jet row within the array relative to the jet temperature was not explicitly determined. In fact, such a determination cannot be made from these types of tests, i.e., when (1) the jet air source is from a single plenum, (2) the only crossflow arises from upstream jets within the array, and (3) the type of thermal boundary condition at the impingement surface (e.g., uniform temperature or uniform flux) is fixed. Under such conditions the crossflow temperature approaching a given spanwise row within the array cannot be independently varied.

Saad et al. also reported spanwise-average, streamwise-

[1] Current address: Chun-Shan Institute of Science and Technology, Lungtan, Taiwan, Republic of China.

Contributed by the Gas Turbine Division of THE AMERICAN SOCIETY OF MECHANICAL ENGINEERS and presented at the 31st International Gas Turbine Conference and Exhibit, Düsseldorf, Federal Republic of Germany, June 8–12, 1986. Manuscript received at ASME Headquarters January 10, 1986. Paper No. 86-GT-55.

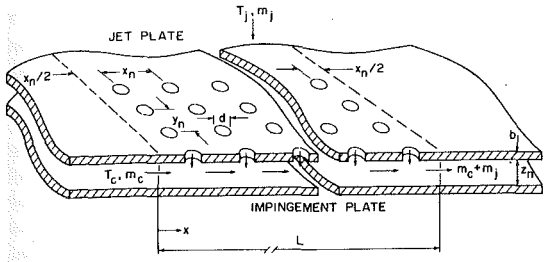

Fig. 1 Array of circular jets with an initial crossflow

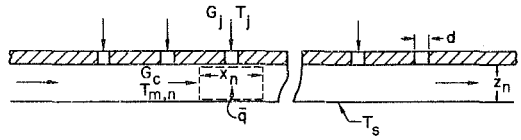

Fig. 2 Definition of individual spanwise row domain and associated parameters

resolved Nusselt numbers for one array geometry at a single jet flow rate for three different initial crossflow rates approaching the array from an upstream extension of the channel formed by the jet orifice plate and the impingement surface. The magnitude of the initial crossflow temperature relative to the jet temperature was not indicated. Presumably the temperature of the air in the initial crossflow plenum was the same as that for the air in the main jet array plenum.

Florschuetz et al. [13] reported experimental results for two-dimensional arrays of circular jets with an initial crossflow approaching the array (Fig. 1). The initial crossflow originated from a separate plenum so that its flow rate and temperature could be independently controlled relative to the jet flow rate and temperature. Spanwise-average, streamwise-resolved (regional-average) Nusselt numbers and values of a parameter η, representing the influence of initial crossflow temperature relative to jet temperature, were determined as a function of overall array flow parameters for a range of geometric parameter values.

Subsequently some of the raw data from that study, combined with some newly obtained data utilizing the same test facility, were further analyzed in an attempt to determine regional-average Nusselt numbers and η values defined solely in terms of parameters associated with the individual spanwise row opposite the given impingement region. The objectives were to: (1) explicitly account for the effect on the impingement heat flux opposite an individual spanwise jet row within an array of the crossflow temperature approaching the row relative to the temperature at which the jet flow is introduced; and (2) determine if the application of the results in such a form could be generalized to apply to individual rows of a larger class of arrays or subarrays having similar geometries but an arbitrary number of spanwise rows in the overall array or in each subarray. A subarray would be one or more contiguous spanwise rows of jet holes having a uniform hole diameter, hole spacing, and hole pattern which are part of a larger overall array; see, e.g., Florschuetz and Tseng [14].

Overview of Problem Formulation

The basic test model geometry and nomenclature are shown schematically in Fig. 1. Most of the jet arrays tested in the presence of an initial crossflow had uniform inline hole patterns as illustated in Fig. 1. However, two jet arrays were also tested for corresponding staggered patterns in which alternate spanwise rows were offset by one-half a spanwise hole spacing.

For steady-state conditions, heat rates could be measured for regional areas centered opposite spanwise hole rows, covering the span of the impingement heat transfer surface, with a streamwise length of one streamwise hole spacing. Thus, the regional average heat flux $\bar{q}$ associated with any given spanwise row of the array (Fig. 2) could be determined. It was desired to obtain the basic set of heat transfer characteristics for the case of constant fluid properties. Hence, the tests were conducted at relatively small temperature differences; e.g., the maximum surface-to-jet temperature difference utilized was about 35 K.

Now consider $\bar{q}$ as a function of parameters associated with the domain of an individual spanwise row n as specified in Fig. 2. The mass flux at the jet exit plane G_j and the mean mass flux for the crossflow approaching row n, G_c, are specified.

Nomenclature

c_p = specific heat at constant pressure
d = jet hole diameter
G_c = crossflow mass flux averaged over channel cross-sectional area at entrance to individual spanwise row domain
G_j = jet mass flux at individual spanwise row based on jet hole area
$\bar{G}_j$ = mean jet mass flux over entire array
h_r = regional average heat transfer coefficient defined in terms of individual spanwise row parameters, equation (1)
k = thermal conductivity of fluid
L = streamwise length of jet plate and impingement surface (Fig. 1)
m_c = initial crossflow rate
m_j = total jet flow rate
Nu_r = regional average Nusselt number defined by equation (1) = $h_r d/k$
Pr = Prandtl number
$\bar{q}$ = regional average impingement surface heat flux (Fig. 2)
r_r = regional average recovery factor defined in terms of individual spanwise row parameters, equation (2)
Re_j = individual spanwise row jet Reynolds number = $G_j d/\mu$
$\overline{\mathrm{Re}}_j$ = mean jet Reynolds number over entire array = $\bar{G}_j d/\mu$
t_j = static temperature at jet exit plane
T_j = jet plenum temperature (assumed same as mixed-mean total temperature at jet exit plane)
$T_{m,n}$ = mixed-mean total temperature over channel cross section at one-half streamwise hole spacing upstream of row n
T_s = impingement surface temperature
$T_{\mathrm{rec},r}$ = recovery temperature defined as impingement surface temperature for $\bar{q} = 0$ and $T_{m,n} = T_j$
$T_{\mathrm{ref},r}$ = fluid reference temperature defined as temperature at impingement surface for $\bar{q} = 0$ and specified $T_{m,n}$ and T_j
x = streamwise coordinate (Fig. 1)
x_n = streamwise jet hole spacing
y_n = spanwise jet hole spacing
z_n = channel height (jet exit plane-to-impingement surface spacing)
ϵ_r = regional average heat flux $\bar{q}$ for $T_s = T_j = T_{m,n}$, see equation (1)
η_r = regional average fluid temperature difference influence factor defined in terms of individual spanwise row parameters, equation (1)
μ = dynamic viscosity of fluid
ρ = density of fluid

The mixed-mean total temperature at the jet exit plane T_j is specified as the characteristic jet temperature. The characteristic crossflow temperature is specified as the mixed-mean total temperature $T_{m,n}$ at the channel cross section located at the upstream edge of the impingement surface region immediately opposite row n; i.e., one-half streamwise hole spacing upstream of row n. Mixed-mean total temperatures are selected as characteristic fluid temperatures since they will normally be available based on energy balances carried out upstream of their respective control surfaces. Since in the present case the objective is to cool the surface by designing impinging jets into the system, the jet flow is considered to be the primary flow, while the crossflow is considered the secondary flow. Thus, it is convenient to consider $(T_s - T_j)$ as the primary temperature potential and consider the conditon $T_{m,n}$ different from T_j as a secondary effect. Working from the differential energy equation and boundary conditions written in terms of total temperature for the individual spanwise row domain indicated in Fig. 2, retaining the dissipation term, but assuming constant fluid properties and a uniform specified impingement surface temperature T_s, it may be shown using linear superposition arguments that the regional average heat flux can be expressed in the form [15]

$$\bar{q} = (k/d)\mathrm{Nu}_r[(T_s - T_j) - \eta_r(T_{m,n} - T_j)] + \epsilon_r \quad (1)$$

In this equation ϵ_r represents the heat flux which would occur if all three temperatures were equal. $\mathrm{Nu}_r = h_r d/k$ may be regarded as the Nusselt number and h_r as the heat transfer coefficient for the special case when $T_{m,n} = T_j$ and recovery effects are absent; and η_r may be regarded as a fluid temperature difference influence factor reflecting the strength of the influence on the heat flux when $T_{m,n}$ differs from T_j. The subscript r is used to emphasize that the parameters are defined for an individual spanwise *row* domain.

It is customary in the heat transfer literature when considering recovery effects to define a recovery temperature and a corresponding normalized form, the recovery factor. The recovery temperature is normally defined as the steady-state surface temperature corresponding to a zero surface heat flux. However, in the present problem, the zero heat flux surface temperature for a given jet temperature will be influenced not only by recovery effects but also by the level of the crossflow temperature relative to the jet temperature. It is also noted that we are considering a uniform impingement surface temperature boundary condition and are concerned with regional average heat fluxes. Therefore, a recovery temperature $T_{\mathrm{rec},r}$ is defined as the surface temperature for a zero mean heat flux, $\bar{q} = 0$, under the condition that $T_{m,n}$ is the same as T_j. In the present problem the recovery factor could be defined in terms of either characteristic crossflow or characteristic jet flow conditions. It is here defined in terms of jet flow conditions because the jet flow is considered the primary flow

$$r_r = (T_{\mathrm{rec},r} - t_j)/[(G_j/\rho)^2/2c_p] \quad (2)$$

With these definitions of recovery temperature and recovery factor equation (1) may be recast in the form

$$\bar{q} = (k/d)\mathrm{Nu}_r[(T_s - T_j) - \eta_r(T_{m,n} - T_j) + (1 - r_r)(G_j/\rho)^2/2c_p] \quad (3)$$

By dimensional analysis based on the governing differential equations and boundary conditions for the velocity and temperature fields it may be shown [15] that the parameters Nu_r, η_r, and r_r may be considered as functions of the following individual row parameters:

Geometric parameters $(x_n/d, y_n/d, z_n/d)$

Flow and fluid parameters $(\mathrm{Re}_j, G_c/G_j, \mathrm{Pr})$

where $\mathrm{Re}_j = G_j d/\mu$. In general, there will also be a dependence on the normalized velocity and temperature profiles of the crossflow and the jet flow at their respective boundaries of the individual row domain. The profiles are considered normalized by the mean velocities and mixed-mean total temperatures at the respective boundaries.

An alternative formulation of the regional average heat flux equation (3) and an alternative interpretation of the fluid temperature difference influence factor η_r can be obtained by defining a fluid reference temperature $T_{\mathrm{ref},r}$ as equivalent to the surface temperature for a zero regional average heat flux $\bar{q}$. ($T_{\mathrm{ref},r}$ should not be confused with the recovery temperature, $T_{\mathrm{rec},r}$.) Setting $T_s = T_{\mathrm{ref},r}$ and $\bar{q} = 0$ in equation (3) one obtains, with the aid of equation (2)

$$\eta_r = (T_{\mathrm{ref},r} - T_{\mathrm{rec},r})/(T_{m,n} - T_j) \quad (4)$$

Substituting this back into (3) one obtains, again with the aid of (2)

$$\bar{q} = (k/d)\mathrm{Nu}_r(T_s - T_{\mathrm{ref},r}) = h_r(T_s - T_{\mathrm{ref},r}) \quad (5)$$

Equations (2), (4), and (5) together are equivalent to equation (3).

In general, for problems like the one under consideration here with two characteristic fluid temperatures, a reference temperature defined as equivalent to the surface temperature at zero surface heat flux will depend on both recovery effects and the magnitude of one fluid temperature relative to the other (here $T_{m,n}$ relative to T_j). However, for $r_r = 1$, the recovery temperature is equal to the jet total temperature, $T_{\mathrm{rec},r} = T_j$, so that for this important special case

$$\eta_r = (T_{\mathrm{ref},r} - T_j)/(T_{m,n} - T_j) \quad (6)$$

and $T_{\mathrm{ref},r}$ is influenced only by $T_{m,n}$ and T_j.

The η_r parameter defined and utilized in the present work is similar to "effectiveness" parameters often utilized in connection with film cooling problems. However, in film cooling problems the injected (or jet) flow is normally considered as the secondary flow, whereas in the present jet impingement problem we consider the jet flow as the primary flow. It may also be noted here that we choose not to use the term adiabatic wall temperature in referring to the fluid reference temperature $T_{\mathrm{ref},r}$ defined above. This term is misleading unless one is dealing with a uniform heat flux heat transfer surface. In the present study the impingement heat transfer surface was isothermal. Furthermore, the reference temperature is defined as the surface temperature for a zero regional average heat flux. For an isothermal surface (or isothermal region on a surface) to have a zero heat rate (or zero average heat flux), the local heat flux need not be zero everywhere over the surface (or region) and therefore the surface (or region) need not be adiabatic.

The η_r parameter defined in the present work is similar, but not identical, to the η parameter defined by Bouchez and Goldstein [4] in their study of a single impinging jet in a crossflow. Differences are, first, as in film cooling studies, they considered the crossflow as the primary flow; and second, their η parameter was appropriately defined in terms of a local adiabatic wall temperature as a reference temperature, since their results were obtained for an adiabatic wall rather than an isothermal surface.

Experimental Approach and Data Reduction

The basic experimental facility was that originally used for a comprehensive series of noninitial crossflow tests [9, 10, 16] but for the present study, set up in a modified form suitable for conducting tests with initial crossflow. A complete description of the original facility may be found in [17] and a description of the initial crossflow configuration in [18].

The length L (Fig. 1) of the jet plate and impingement plate sections was 12.7 cm. The interchangeable jet plates each had ten spanwise rows of holes. The initial crossflow was introduced through two closely spaced spanwise rows of holes

located 24.1 cm upstream of the jet array entrance ($x=0$ in Fig. 1). The heat transfer test plate (i.e., the impingement plate and its upstream extension) was constructed of individual copper-segment/heater asemblies arranged such that regional average heat fluxes $\bar{q}$ as defined in Fig. 2 could be determined opposite each row of holes, while the entire heat transfer test surface was maintained at a nominally isothermal condition. The jet holes were square edged with diameters of either 0.127 or 0.254 cm, and lengths equal to their diameters.

For a given test run, a basic jet orifice plate geometry and channel height were selected. These are specified in the following form: $B(x_n/d, y_n/d, z_n/d)I$ where B designates the particular jet plate length (L = 12.7 cm) and I designates the inline hole pattern for which most of the initial crossflow tests were conducted (S is used to designate a staggered hole pattern). Once the geometry was fixed, setting the total jet flow rate and the initial crossflow rate resulted in a set of fixed values for the independent dimensionless parameter sets summarized in the preceding section following equation (3). Measured distributions of the jet and crossflow mass fluxes G_j and G_c over the spanwise rows were reported by Florschuetz and Isoda [19]. The exhaust pressure at the exit of the jet array channel was one atmosphere.

Referring to equation (1) it is clear that for the fixed conditions described in the preceding paragraph, measurement of three independent data sets ($\bar{q}$, $T_s - T_j$, $T_{m,n} - T_j$) would permit determination of Nu_r, η_r, and ϵ_r. These data sets were obtained as follows. The value of T_j was fixed nominally at ambient temperature level. Then a uniform maximum T_s was set such that $T_s - T_j \simeq 35$ K by individually adjusting $\bar{q}$ at each copper segment of the heat transfer test plate, including those in the initial crossflow channel. The initial crossflow plenum temperature was fixed roughly midway between T_j and the maximum T_s. This condition gave one data set. Keeping T_j and the initial crossflow plenum temperature fixed, a second set was obtained by adjusting each $\bar{q}$ to roughly half the prior values. The third set was obtained with the initial crossflow plenum temperature set approximately equal to T_j and the segment heater power inputs set to zero.

In reducing the data $T_{m,n}$ was evaluated via an energy balance over a control volume encompassing the height of the channel and extending from the initial crossflow plenum to a cross section of the channel located one-half a streamwise hole spacing upstream of row n. This energy balance required as input information: (*i*) the measured heat rates from each segment of the test plate up to but not including the segment opposite row n, (*ii*) the initial crossflow plenum temperature and the initial crossflow rate, and (*iii*) the jet plenum temperature and the jet mass flux at each spanwise row of the array preceding row n.

Results and Discussion

In many applications involving impinging jets in the presence of a crossflow, surface-to-fluid temperature differences are typically large enough and coolant flow velocities low enough such that recovery effects are negligible. Thus, in applying an equation in the form of equation (3), or similar forms, precise information on recovery factors is not required. Since equation (3) is formulated in terms of total fluid temperatures for the jet flow and the crossflow, neglecting the term containing the recovery factor is equivalent to assuming a recovery factor of unity. Therefore, though often negligible, recovery effects are still accounted for to a good approximation since the recovery factors r_r ordinarily are close to unity [20]. Nusselt numbers Nu_r and fluid temperature difference influence factors η_r, or equivalent results, are the primary parameters required. However, based on experimental data from the present study it was shown in [20] that for model tests conducted at nominally ambient pressure and temperature levels with small hole diameters recovery effects,

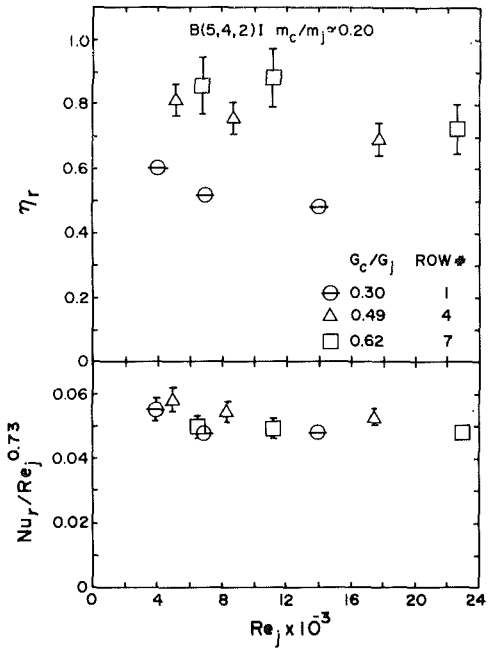

Fig. 3 Effect of jet Reynolds number on η_r and Nu_r for $(x_n/d, y_n/d, z_n/d)$ = (5, 4, 2) inline array geometry

as represented by the last term ϵ_r of equation (1) or the final term in the square brackets of equation (3), may in certain cases be quite significant in affecting the determination of η_r while at the same time having only minor or negligible effect on the determination of Nu_r.

In the present section we first consider the influence of Re_j and G_c/G_j on the dependent parameters Nu_r and η_r. Then the effects of the normalized velocity and temperature profiles at the upstream control surfaces of the individual row domains are examined. These normalized profiles depend, of course, on the history of the flow upstream of the row being considered which, in turn, depends on the position of the row within the array. Understanding the significance of these effects is of primary importance in assessing the validity of applying individual row heat transfer characeristics measured for a given array to individual rows of other arbitrary arrays (i.e., longer or shorter or nonuniform arrays) for a given individual row parameter set (Re_j, G_c/G_j, x_n/d, y_n/d, z_n/d). Examination of these effects also answers the following question: What is the minimum number of spanwise rows needed for testing in order to apply the results with confidence to downstream rows within larger arrays?

In figures throughout this section composite experimental uncertainties associated with individual data points, determined by the method of Kline and McClintock [21], are indicated by vertical bars attached to the data point symbols (if they exceed the height of the symbol). See [15] for details. It may be noted that larger uncertainties in η_r values for downstream rows resulted primarily from the decrease in $T_{m,n} - T_j$ which occurred in the downstream direction, plus the increasing number of values for measured heat rates and jet mass fluxes which entered the energy balance for the determination of $T_{m,n}$.

Effect of Jet Reynolds Number. The bulk of the tests were conducted at a mean jet Reynolds number of 10^4. However, four of the twelve geometries were tested at three nominal mean jet Reynolds numbers of 6×10^3, 10^4, and 2×10^4 for fixed m_c/m_j, so that G_c/G_j for any given spanwise row also remained fixed. Results for the (5, 4, 2) I geometry are shown in Fig. 3. For clarity, only the results based on data for rows 1, 4, and 7 are presented in the figures. The Nu_r values were normalized by $\mathrm{Re}_j^{0.73}$ for direct comparison. The exponent on Re_j

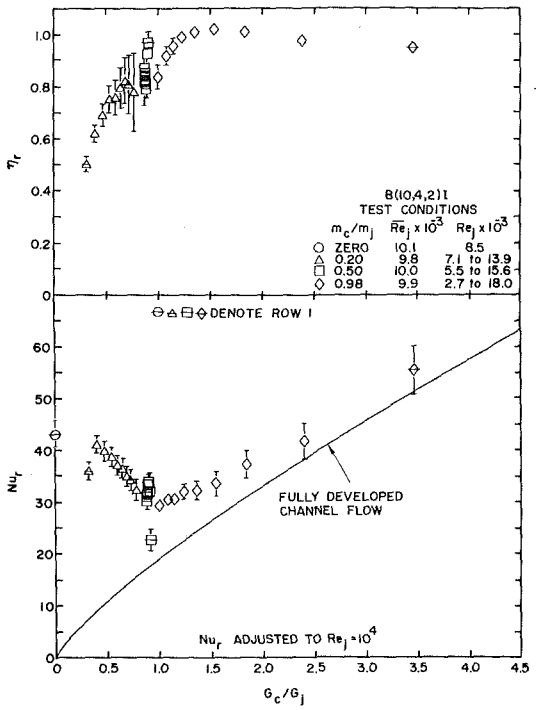

Fig. 4 Effect of crossflow-to-jet mass flux ratio on η_r and Nu_r for (x_n/d, y_n/d, z_n/d) = (10, 4, 2) inline array geometry

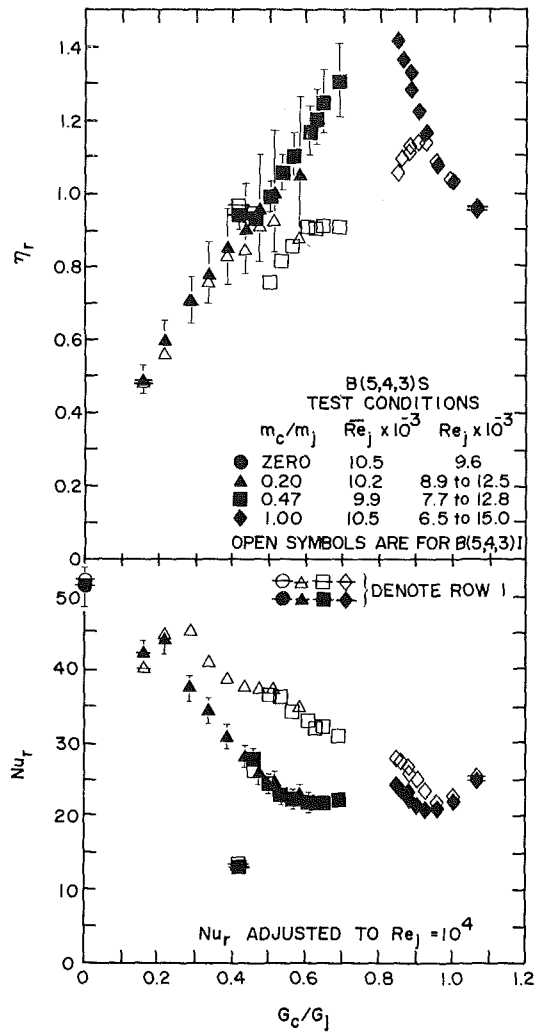

Fig. 5 Effect of crossflow-to-jet mass flux ratio on η_r and Nu_r for (x_n/d, y_n/d, z_n/d) = (5, 4, 3) geometry: comparison of inline (open points) and staggered (solid points) arrays; uncertainty intervals for inline case similar to those shown for staggered case

is from the previous noninitial crossflow jet array impingement correlation reported by Florschuetz et al. [10].

Considering experimental uncertainty, the η_r values appear to be relatively insensitive to Re_j, while the Reynolds number dependence of $Re_j^{0.73}$ accounts quite well for the Nusselt number variation. Results based on data from the remaining rows for the (5, 4, 2) *I* case and the additional cases not shown here also support these general conclusions. Variations, though still small, are sometimes more noticeable at upstream rows and smaller values of Re_j.

Effects of Crossflow-to-Jet Mass Flux Ratio. The dependence of η_r and Nu_r on G_c/G_j is shown in Figs. 4–6 for three of the inline array geometries tested and in Figs. 5 and 6 for two staggered geometries. The values of Nu_r were adjusted to $Re_j = 10^4$ according to $Nu_r \propto Re_j^{0.73}$. The values of η_r were plotted for the Re_j at which they were measured, since as discussed in the preceding paragraph η_r is relatively insensitive to Re_j. The values of the independent overall array parameters, m_c/m_j and $\overline{Re}_j$, and the range of Re_j for the test conditions are shown in the legend. Values of Nu_r at $G_c/G_j = 0$ are for the first row of zero initial crossflow tests. η_r at the first row of an array with no initial crossflow is by definition zero. Values of η_r and Nu_r at downstream rows cannot be obtained from data for zero initial crossflow tests since the crossflow mixed-mean temperatures approaching individual rows cannot be varied independently when the jet flow is from a single plenum and the type of thermal boundary condition at the impingement surface is fixed. Horizontal lines are added to the symbols for all data from row 1 of the array. This permits one to more easily identify from which row each data point was obtained since the points lie in sequence to the right or left of the first row point depending on whether G_c/G_j increased or decreased from upstream to downstream.

First consider η_r. On theoretical grounds we should expect that as G_c/G_j goes to zero η_r also goes to zero and that as G_c/G_j increases η_r asymptotically approaches one. Furthermore, if all the parameters (x_n/d, y_n/d, z_n/d, Re_j) plus the normalized velocity and temperature profiles at the entrance to each individual row domain (or the flow history) were in fact held constant we would expect a single smooth curve for η_r versus G_c/G_j joining the two limits. Allowing for experimental uncertainty, the bulk of the data points for η_r in Fig. 4 are quite consistent with the above described pattern.

For Nu_r versus G_c/G_j we would expect a finite value of Nu_r for $G_c/G_j = 0$ which then decreases with increasing G_c/G_j, since we normally expect the presence of a crossflow to diminish the heat transfer capability of an impinging jet. If G_c/G_j is increased far enough, however, we would expect Nu_r to increase again eventually approaching values for a fully developed channel flow, as the crossflow completely dominates. The fully developed channel flow curve shown in Fig. 4 is for turbulent flow between parallel planes with one side adiabatic and the other side heated, based on results presented by Kays and Crawford [22]. Examining Fig. 4, it appears that the bulk of the data points for Nu_r do indeed follow these overall trends.

However, for each of the 12 geometric configurations tested there were some individual data points which clearly did not follow the overall trends described above (see, e.g., Figs. 4–6) and in some cases groups of points which only marginally fell in the overall trend of the bulk of the data points (see, e.g., Fig. 5).

For both η_r and Nu_r the individual data points which clearly deviated from the overall trends of the other points were always for the upstream rows of the array, primarily row 1 and to a lesser extent row 2. This result may be attributed to the differences in the normalized velocity and temperature

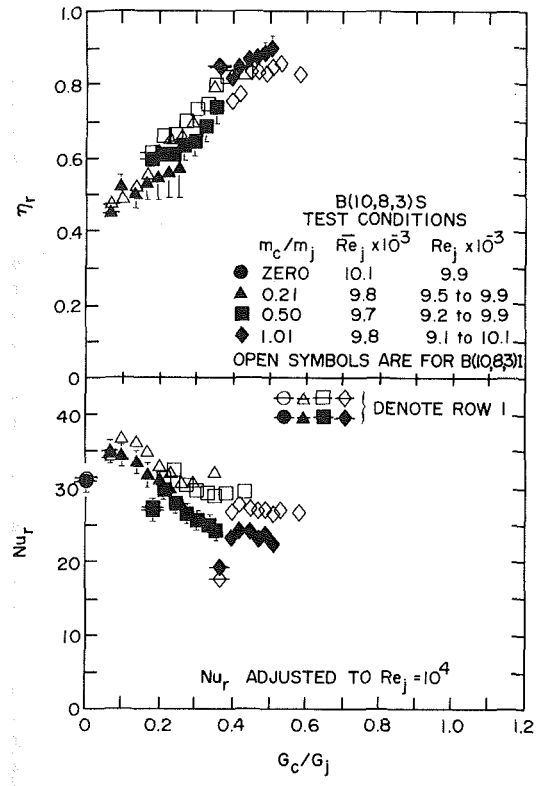

Fig. 6 Effect of crossflow-to-jet mass flux ratio on η_r and Nu_r for (x_n/d, y_n/d, z_n/d) = (10, 8, 3) geometry: comparison of inline (open points) and staggered (solid points) arrays; uncertainty intervals for inline case similar to those shown for staggered case

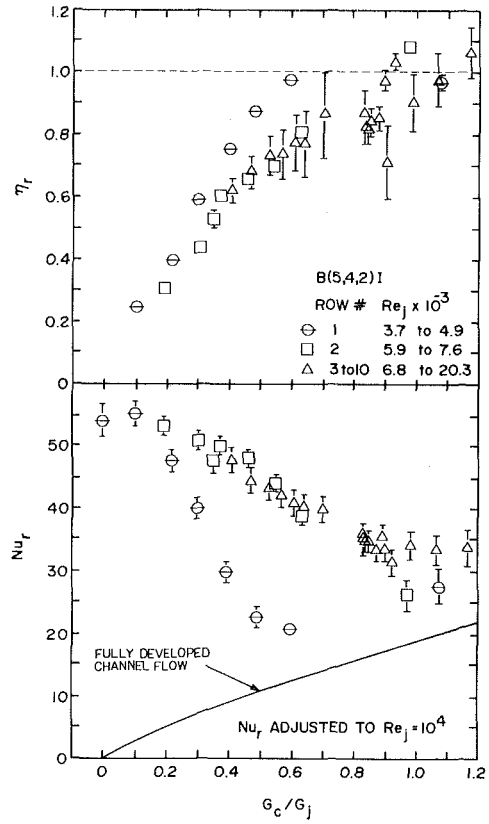

Fig. 7 Effect of crossflow-to-jet mass flux ratio on η_r and Nu_r by row number for (x_n/d, y_n/d, z_n/d) = (5, 4, 2) inline array geometry

profiles at the entrances to the individual row domains (flow history effects), which should be most pronounced for row 1 as compared with downstream rows. This is clearly illustrated in Fig. 7 for the (5, 4, 2) *I* geometry which includes additional data points at smaller increments of G_c/G_j for rows 1 and 2 obtained from extra tests conducted for this particular geometry. These results show that for small values of G_c/G_j the trend of both η_r and Nu_r is independent of the row number (and therefore the flow history). However, as G_c/G_j increases the trends for row 1 clearly begin to separate from those for the downstream rows. The effects of individual spanwise row normalized entrance profiles are discussed in more detail later.

Returning to Fig. 5, several additional observations are in order. Values of η_r greater than unity occurred in the case of four geometric configurations including both the inline and staggered hole patterns of the (5, 4, 3) array (Fig. 5). These occurred only for G_c/G_j of order unity or larger when the crossflow exerts a dominant influence on the impingement surface heat flux. Consider the interpretation of η_r in terms of the reference temperature defined for a zero regional average heat flux, equation (6). η_r greater than unity occurs for $T_{\text{ref},r}$ greater than the mixed-mean total temperature $T_{m,n}$. After the row where $T_{\text{ref},r}$ becomes equal to $T_{m,n}$ ($\eta_r = 1$), the crossflow is controlling the heat flux. Proceeding downstream $T_{\text{ref},r}$ may decrease very slowly because the temperature of the jet flow can now influence $T_{\text{ref},r}$ only after mixing with the crossflow since it no longer impinges directly on the heat transfer surface, while $T_{m,n}$ will have decreased more since its value is independent of the degree of mixing between the two flow streams. Thus η_r may become larger than unity. As a practical matter knowledge of these values of η_r would normally not be required since jet array designs in which the crossflow negates the cooling effect of the jet would not be utilized. It is useful for design purposes, however, to know the point at which the presence of the jet is rendered useless by the crossflow.

The Nu_r data indicate that for some configurations (e.g., Fig. 6) the presence of a small crossflow increases Nu_r slightly relative to the zero crossflow value before it begins to decrease with further increases in G_c/G_j. It appears that in these cases a direct contribution to the heat transfer rate by a small crossflow outweighs any degradation of the heat transfer contribution of the impinging jet caused by the small crossflow. Further increases in G_c/G_j then cause a decline in Nu_r which then tends to level off. If in these cases G_c/G_j were increased even more, Nu_r would presumably begin to increase again ultimately approaching heat transfer rates equivalent to those of a fully developed channel flow, as was in fact observed for some of the other cases (e.g., Fig. 4).

Flow History Effects. The individual spanwise row heat transfer parameters η_r and Nu_r have been presented as functions of the independent parameters for the row domain (x_n/d, y_n/d, z_n/d, Re_j, G_c/G_j). These formulations account for the effects of both the average mass flux G_c and the mixed-mean total temperature of the crossflow at the entrance to an individual spanwise row domain. As noted in the problem formulation section there is also, in general, a dependence of the heat transfer parameters on the normalized velocity and temperature profiles at the domain entrance. The profiles are considered normalized with respect to the average velocity and mixed-mean temperature of the crossflow at the domain entrance. These normalized profiles depend in turn, of course, on the details of the flow history upstream of the domain. Two domains having identical values for the independent parameter set noted above may have different normalized entrance profiles (flow histories). Different flow histories may occur for different hole patterns, e.g., inline versus staggered, or because of the streamwise position of a row within the array. In the interests of generalizing the applicability of the individual row parameters Nu_r and η_r, it is important to consider the sensitivity of these parameters to the flow history.

For the array geometries under consideration here it is reasonable to consider the available flow development length

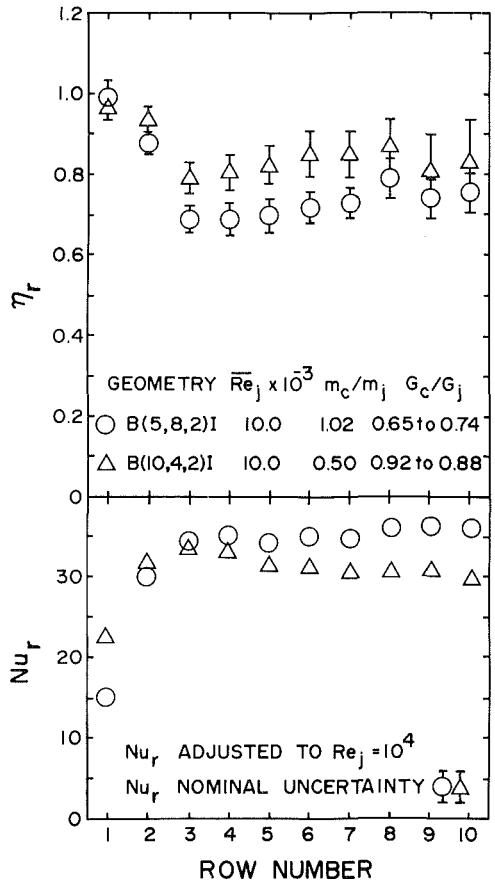

Fig. 8 Effect of flow history on η_r and Nu_r for $(x_n/d, y_n/d, z_n/d)$ = (5, 8, 2) and (10, 4, 2) inline array geometries

upstream of the entrance to a given domain as extending from the control surface marking the entrance of the domain to the nearest upstream spanwise row of jet holes. In the present tests this length for the initial crossflow channel upstream of the array was fixed at 24.1 cm, ranging from 16 to 95 hydraulic diameters depending on the channel height. Channel heat transfer coefficients just upstream of the entrance to the array were in good agreement with prior results for large aspect ratio rectangular ducts with one large side heated [18]. It may therefore be assumed that the velocity and temperature profiles at the entrance to the array were spanwise uniform.

Now consider the individual row domains. The available development length upstream of the domain associated with row 1 was the same as that for the overall array. For rows downstream of row 1, it ranged from 5/12 hydraulic diameters for geometries with $(x_n/d, z_n/d)$ = (5, 3) to 2.5 hydraulic diameters for geometries with $(x_n/d, z_n/d)$ = (10, 1). These available development lengths were 38 times smaller than those upstream of row 1 (and of the array). It is reasonable to suppose that the row domain entrance velocity and temperature profiles downstream of row 1 were not spanwise uniform.

Flow history effects associated with hole pattern are discussed first followed by those associated with row position within the array.

Hole Pattern. Results for corresponding inline and staggered arrays are compared in Figs. 5 and 6. The η_r data points for the array with large hole spacing (10, 8, 3), Fig. 6, are essentially independent of hole pattern flow history to within experimental uncertainty, while the staggered array Nu_r data begins to fall noticeably below the inline array data as G_c/G_j increases. For the array with closer hole spacing (5, 4, 3), Fig. 5, η_r is independent of hole pattern for smaller values of G_c/G_j but for increasing G_c/G_j the η_r data points for the staggered array fall significantly above those for the inline array with values rising above unity, then decreasing to unity again as G_c/G_j approaches one, with the staggered array points again coinciding with those for the inline array. An explanation for η_r greater than one was discussed in the preceding subsection. Apparently η_r for the (5, 4, 3) staggered array falls above that for the inline array because increased mixing between the crossflow and jet streams for the staggered array causes the crossflow to begin to dominate at smaller values of G_c/G_j (about 0.5) than for the inline case. This is also indicated by the comparison of the Nu_r data. The more rapid decrease of Nu_r for the staggered array is arrested near $G_c/G_j = 0.5$ while the slower decrease of Nu_r for the inline array continues. Then as G_c/G_j approaches unity the crossflow becomes dominant for the inline array as well and both η_r and Nu_r for the two arrays again coincide as they do for small values of G_c/G_j. Because of the complexity of the flow fields involved, explanations of observed heat transfer characteristics for staggered arrays relative to inline arrays must remain speculative. Hippensteele et al. [23] presented a comparison of an inline and a staggered array using thermal visualization with liquid crystals which also indicated higher heat rates for the inline array.

Row Position Within Array. For a specific array geometry $(x_n/d, y_n/d, z_n/d, L/x_n$, hole pattern), as m_c/m_j is increased a value is reached for which G_c/G_j becomes essentially uniform over all spanwise rows of the array [19]. This condition occurred, at least approximately, for several of the test runs in the present study, thus providing, in each of these cases, heat transfer results from a single test having a uniform G_c/G_j, but with varying flow history (depending on row number). Since the individual row Reynolds number increases from upstream to downstream, Nu_r values were adjusted to correspond to $Re_j = 10^4$ according to $Nu_r \propto Re_j^{0.73}$. It may also be recalled that η_r was found to be relatively insensitive to Re_j. Thus, we have results from individual test cases for which, to a good approximation, the only remaining independent parameter that may affect η_r or Nu_r is the flow history (i.e., row number).

Sample results of this type for η_r and Nu_r as a function of row number for two different array geometries are shown in Fig. 8. Generally these results indicate that η_r and Nu_r become relatively insensitive to flow history after the first two rows of the array; the normalized velocity and temperature profiles at the row domain entrance are presumably approaching an approximately fully developed condition. Or stated another way, a reasonable entrance length for the array appears to be two rows. These results imply further that the application of test results obtained for a crossflow approaching a single line of jets to individual downstream jet rows within a two-dimensional array could result in serious errors, but that results based on the third row of an array could be applied as a good approximation for rows downstream of the third row. That is, for such application, test results for an array having at least three rows should be obtained.

These plots show clearly (as did Figs. 4–7) that Nu_r at row 1 is often significantly smaller than at downstream rows for the same Re_j and G_c/G_j. This is presumably because the entire crossflow interacts directly with the jets at row 1, whereas for any given downstream row the bifurcation of the crossflow caused by upstream jets tends to decrease the direct interaction of the crossflow with jets in the given downstream row. This effect is more pronounced for inline arrays than for staggered arrays as is indicated by the comparisons in Figs. 5 and 6. There, for intermediate values of G_c/G_j (large enough to have a significant effect but still small enough so the crossflow is not dominating), staggered versus inline Nu_r values for the same G_c/G_j are identical at row 1, whereas for downstream rows Nu_r for the staggered arrays at the same G_c/G_j is larger than the row 1 value by a smaller increment than for the inline

arrays. The crossflow bifurcation is less significant in decreasing direct interaction between jets and crossflow for the staggered case because of the offset of the jets immediately upstream of the row in question. Where differences are significant, η_r at the same G_c/G_j tends to be larger at row 1 than at downstream rows and for staggered arrays than for inline arrays, presumably for the same reasons suggested above in connection with Nu_r.

Finally, note that different combinations of m_c/m_j and row position within an array can result in the same G_c/G_j, but will have differing flow histories. Consider Nu_r in Fig. 5. When the ranges of G_c/G_j from tests at different m_c/m_j overlap, the sets of Nu_r data points from the different tests for a given hole pattern are generally quite consistent; and when the ranges of G_c/G_j do not overlap it appears that the sets of points are also generally quite consistent in that they lie on or close to a single smooth curve which could be drawn through them. Thus, with the important exception of row 1 and sometimes row 2 and then only at intermediate values of G_c/G_j, these flow history effects on Nu_r are not significant.

Turning to η_r (Fig. 5) for the inline case (open data points), the different sets of points which result from tests at different m_c/m_j do not appear overall as consistent as they are for Nu_r, though the larger experimental uncertainties for some of the η_r data points at downstream rows make it more difficult to draw precise conclusions. The η_r points from the $m_c/m_j = 0.47$ test (open squares), beginning at row 1 and proceeding downstream, first drop below the points from the $m_c/m_j = 0.20$ test (open triangles), then at row 3 (the third square point) the trend reverses with the points appearing to asymptotically approach an imaginary line extrapolated from the $m_c/m_j = 0.20$ set (triangles). Similar trends, though sometimes less pronounced, were also present for some of the other geometries tested.

The most probable explanation of these trends is flow history effects. Approaching row 1 the crossflow is entirely initial crossflow. For succeeding rows considered at the same G_c/G_j and mixed-mean total temperature, the further downstream the row, the larger the fraction of the crossflow which originated from upsteam jets, but at the same time a larger fraction of the crossflow originating from upstream jets becomes more thoroughly mixed in the crossflow stream before reaching the row. Thus, for rows immediately following row 1 the zero regional average heat flux surface temperature $T_{\mathrm{ref},r}$ [see equation (6)] is directly influenced by the cooler part of the crossflow originating from upstream jets and is smaller relative to the mixed-mean temperature than at row 1. For rows farther downstream $T_{\mathrm{ref},r}$ increases again relative to the mixed-mean temperature because more of the jet contribution to the crossflow has mixed with the crossflow stream before interacting with the surface.

As additional evidence that the observed pattern of the η_r data points under discussion may be attributed to flow history effects, a comparison of all data sets for $x_n/d = 5$ with those for $x_n/d = 10$, other parameters being held constant, showed the behavior attributed above to flow history effects is less pronounced for $x_n/d = 10$ than for $x_n/d = 5$ presumably because of the smaller available flow development length between rows for the latter case.

Conclusions

The advantage of the individual spanwise row formulation is that, to the extent that the flow history effect is not significant, results for Nu_r and η_r at specified (x_n/d, y_n/d, z_n/d, Re_j, G_c/G_j) can be applied at arbitrary rows of an array whereas Nusselt numbers and η values defined in terms of overall array parameters [13, 15] can be applied only at a specified spanwise row location x/L within an array of a specified number of rows L/x_n for specified (x_n/d, y_n/d, z_n/d, Re_j, m_c/m_j).

A complete set of results for Nu_r, η_r, and r_r for ten different inline array geometries (x_n/d, y_n/d, z_n/d) and two staggered array geometries is presented in both graphic and tabular form in [15]. Selected results have been presented and discussed in the present paper emphasizing the effects on η_r and Nu_r of Re_j, G_c/G_j, and various flow history effects. For a presentation of recovery factors and discussion of recovery effects see [15] or [20]. The specific conclusions for η_r and Nu_r summarized below are based on the complete set of results.

Results in Terms of Row Parameters. (1) η_r is relatively insensitive to Re_j.

(2) As should be expected the η_r data appear to extrapolate to zero (jet flow dominates) as G_c/G_j goes to zero. As G_c/G_j increases, the η_r data, in their overall trend, asymptotically approach unity (crossflow dominates) or in cases where the range of G_c/G_j was not large enough it appears that they would extrapolate asymptotically to unity. Values of η_r greater than unity were observed in some cases for G_c/G_j of order unity or greater. Possible explanations were discussed in the Results section.

(3) As z_n/d is increased, η_r increases somewhat more rapidly with G_c/G_j. For the smallest channel heights, $z_n/d = 1$, η_r reaches unity as G_c/G_j reaches about 2. For $z_n/d = 2$ the η_r data reach unity, or if extrapolated appear to reach unity, as G_c/G_j approaches unity, while for $z_n/d = 3$, they either reach or would extrapolate to unity for G_c/G_j smaller then unity but never less than 0.5.

(4) η_r is relatively insensitive to x_n/d and y_n/d.

(5) Nu_r is proportional to Re_j^n where $n = 0.73$.

(6) The overall trend of Nu_r is decreasing as G_c/G_j increases from zero. However, Nu_r increases slightly in some cases for $G_c/G_j << 1$, before the decreasing trend begins. If G_c/G_j becomes large enough for the crossflow to dominate, Nu_r begins to increase again and approaches values equivalent to those for a parallel plate channel flow with one side heated. This behavior generally occurs as η_r is approaching unity.

(7) In contrast with η_r, Nu_r is relatively insensitive to z_n/d over the range covered, but sensitive to hole spacings. For fixed Re_j and G_c/G_j, Nu_r decreases as both x_n/d and y_n/d increase.

Flow History. (1) Both Nu_r and η_r are insensitive to flow history for $G_c/G_j << 1$. For larger values of G_c/G_j both Nu_r and η_r for spanwise uniform crossflow (e.g., at row 1) may differ significantly from values for nonuniform crossflow (e.g., at downstream rows) for fixed geometric parameters. Therefore, results for a single jet in a crossflow or a single row of jets in a crossflow cannot, in general, be applied to individual rows beyond row 1 for a two-dimensional array.

(2) Values of Nu_r and η_r beyond row 2 are insensitive to flow history for fixed geometric parameters. Therefore, they can be applied to individual rows of an array of arbitrary length for rows beyond row 2.

(3) Based on points (1) and (2) above it is recommended that if measurements are to be made for application to a two-dimensional array, the minimum array length utilized for testing should be three rows.

(4) When the flow history develops from a staggerd hole pattern with the smallest hole spacing, Nu_r is smaller and η_r is larger than when the flow history develops from the corresponding inline pattern. For the largest hole spacings the effect on Nu_r is much smaller and the effect on η_r is insignificant.

(5) When differing flow histories arise from differing combinations of initial crossflow and upstream jet flow, the effects on Nu_r are not very significant for any of the array geometries studied. The effects on η_r vary from insignificant to moderate depending on the magnitude of G_c/G_j and (x_n/d, y_n/d, z_n/d). It does appear, as would be expected, that increasing x_n/d tends to minimize the effect of flow history.

References

1 Metzger, D. E., and Korstad, R. J., "Effects of Cross Flow in Impingement Heat Transfer," ASME JOURNAL OF ENGINEERING FOR POWER, Vol. 94, 1972, pp. 35–41.

2 Sparrow, E. M., Goldstein, R. J., and Rouf, M. A., "Effect of Nozzle-Surface Separation Distance on Impingement Heat Transfer for a Jet in a Crossflow," ASME JOURNAL OF HEAT TRANSFER, Vol. 97, 1975, pp. 528–533.

3 Goldstein, R. J., and Behbahani, A. I., "Impingement of Circular Jet With and Without Crossflow," *International Journal of Heat and Mass Transfer*, Vol. 25, 1982, pp. 1377–1382.

4 Bouchez, J. P., and Goldstein, R. J., "Impingement Cooling From a Circular Jet in a Crossflow," *International Journal of Heat and Mass Transfer*, Vol. 18, 1975, pp. 719–730.

5 Holdeman, J. D., and Walker, R. E., "Mixing of a Row of Jets With a Confined Crossflow," *AIAA Journal*, Vol. 15, 1977, pp. 243–249.

6 Srinivasan, R., Berenfeld, A., and Mongia, H. C., *Dilution Jet Mixing Program—Phase I Report*, NASA Contractor Report 168031, Garrett Turbine Engine Company, Phoenix, AZ, 1982.

7 Wittig, S. L. K., Elbahar, O. M. F., and Noll, B. E., "Temperature Profile Development in Turbulent Mixing of Coolant Jets With a Confined Hot Cross Flow," ASME Paper No. 83-GT-220.

8 Kercher, D. M., and Tabakoff, W., "Heat Transfer by a Square Array of Round Air Jets Impinging Perpendicular to a Flat Surface Including the Effect of Spent Air," ASME *Journal of Engineering for Power*, Vol. 92, 1970, pp. 73–82.

9 Florschuetz, L. W., Berry, R. A., and Metzger,D. E., "Periodic Streamwise Variations of Heat Transfer Coefficients for Inline and Staggered Arrays of Circular Jets With Crossflow of Spent Air," ASME JOURNAL OF HEAT TRANSFER, Vol. 102, 1980, p. 132–137.

10 Florschuetz, L. W., Truman, C. R., and Metzger, D. E., "Streamwise Flow and Heat Transfer Distributions for Jet Array Impingement With Crossflow," ASME JOURNAL OF HEAT TRANSFER, Vol. 103, 1981, p. 337–342.

11 Saad, N. R., Mujumdar, A. S., Abdel Messeh, W., and Douglas, W. J. M., "Local Heat Transfer Characteristics for Staggered Arrays of Circular Impinging Jets With Crossflow of Spent Air," ASME Paper No. 80-HT-23.

12 Behbahani, A. I., and Goldstein, R. J., "Local Heat Transfer to Staggered Arrays of Impinging Circular Air Jets," ASME *Journal of Engineering for Power*, Vol. 105, 1983, pp. 354–360.

13 Florschuetz, L. W., Metzger, D. E., and Su, C. C., "Heat Transfer Characteristics for Jet Array Impingement With Initial Crossflow," ASME JOURNAL OF HEAT TRANSFER, Vol. 106, 1984, pp. 34–41.

14 Florschuetz, L. W., and Tseng, H. H., "Effect of Nonuniform Geometries on Flow Distributions and Heat Transfer Characteristics for Arrays of Impinging Jets," ASME *Journal of Engineering for Gas Turbines and Power*, Vol. 107, 1985, pp. 68–75.

15 Florschuetz, L. W., and Su, C. C., *Heat Transfer Characteristics Within an Array of Impinging Jets—Effects of Crossflow Temperature Relative to Jet Temperature*, NASA Contractor Report 3936, Department of Mechanical and Aerospace Engineering, Arizona State University, Tempe, AZ, 1985.

16 Metzger, D. E., Florschuetz, L. W., Takeuchi, D. I., Behee, R. D., and Berry, R. A., "Heat Transfer Characteristics for Inline and Staggered Arrays of Circular Jets With Crossflow of Spent Air," ASME JOURNAL OF HEAT TRANSFER, Vol. 101, 1979, pp. 526–531.

17 Florschuetz, L. W., Metzger, D. E., Takeuchi, D. I., and Berry, R. A., *Multiple Jet Impingement Heat Transfer Characteristics—Experimental Investigation of Inline and Staggered Arrays With Crossflow*, NASA Contractor Report 3217, Department of Mechanical Engineering, Arizona State Unversity, Tempe, AZ, 1980.

18 Florschuetz, L. W., Metzger, D. E., Su, C. C., Isoda, Y., and Tseng, H. H., *Jet Array Impingement Flow Distributions and Heat Transfer Characteristics—Effects of Initial Crossflow and Nonuniform Array Geometry*, NASA Contractor Report 3630, Department of Mechanical and Aerospace Engineering, Arizona State University, Tempe, AZ, 1982.

19 Florschuetz, L. W., and Isoda, Y., "Flow Distributions and Discharge Coefficient Effects for Jet Array Impingement With Initial Crossflow," ASME *Journal of Engineering for Power*, Vol. 105, 1983, pp 296–304.

20 Florschuetz, L. W., and Su, C. C., "Recovery Effects on Heat Transfer Characteristics Within an Array of Impinging Jets," *Heat Transfer and Fluid Flow in Rotating Machinery*, W. J. Yang, ed., Hemisphere Publishing Corp., Washington, DC, 1987, pp. 375–387.

21 Kline, S. J., and McClintock, F., "Describing Uncertainties in Single Sample Experiments," *Mechanical Engineering*, Vol. 75, Jan. 1953, pp. 3-8.

22 Kays, W. M., and Crawford, M. E., *Convective Heat and Mass Transfer*, 2nd ed., McGraw-Hill, New York, 1980.

23 Hippensteele, S. A., Russel, L. M., and Stepka, F. S., "Evaluation of a Method for Heat Transfer Measurements and Thermal Visualization Using a Composite of a Heater Element and Liquid Crystals," ASME JOURNAL OF HEAT TRANSFER, Vol. 105, 1983, pp. 184–189.

A Convection Calibration Method for Local Heat Flux Gages

G. J. Borell
Harris Corporation, GASD,
Melbourne, FL 32902
Assoc. Mem. ASME

T. E. Diller
Mechanical Engineering Department,
Virginia Polytechnic Institute
and State University,
Blacksburg, VA 24061
Mem. ASME

An apparatus for calibrating local heat flux gages in convective air flows is described. Heat transfer from a "hot" gage to a "cold" fluid was measured using a guarded hot-plate technique. The system was used to calibrate Gardon-type circular foil heat flux gages of 1/8 in. and 1/16 in. outer diameters. The results indicate that the calibration curves are nonlinear, which is different from the linear calibration obtained using the standard radiation technique. The degree of nonlinearity matches the analysis which accounts for the effect of the temperature distribution in the gage foil. The effect of this temperature distribution can be neglected in the standard radiation calibration but is often significant in convection applications. These results emphasize the importance of calibrating heat flux gages in thermal environments similar to those in which they will be used.

Introduction

Circular foil heat flux gages were introduced by Gardon [1] for measurement of thermal radiation. Later, Gardon introduced the miniaturization of these meters [2] and described their use in studies of convection heat transfer. These circular foil gages, illustrated in Fig. 1, consist of a thin constantan foil which is welded to the end of a hollow copper cylinder. A copper wire is secured to the center of the foil. Two copper-constantan thermocouples are thus created, one at the center and one at the edge of the foil. Heat enters the foil and flows radially, creating a temperature gradient along the foil. The difference in emf between the two thermocouples is read as a voltage output from the gage and is proportional to the heat flux entering or leaving the foil. Fortunately, the thermal conductivity of constantan and the emf of the copper-constantan thermocouple vary almost identically with temperature. Therefore, the gage output versus heat flux is not a function of gage temperature over a wide temperature range.

A number of researchers have used circular foil gages in convection studies (e.g., [2–7]). The American Society of Testing and Materials has compiled a list of guidelines for the use of these gages to measure heat transfer [8]. The standard calibration procedure for circular foil gages uses radiative heat fluxes [8, 13, 14]. Because a hot source is used to radiate to a cooled gage, very little radiation is emitted from the gage and any temperature gradient in the foil is not important to the heat exchange. Consequently, these radiation calibrations produce a linear relationship between heat flux and voltage output.

The temperature gradient developed across the foil during convection measurements, however, can cause significant errors in the results [2, 9–11]. Striegl and Diller [3] use an approximate correction for this error in the gage output as a function of the convective heat flux. A nonlinear calibration arises due to the inherent temperature variation across the foil. The temperature distribution in the foil also has an effect on the measurement of net radiation *from* the gage.

Previous researchers using these gages in convection environments have often simply used the linear response based on the manufacturer's calibration to determine heat transfer rates. Large errors can arise using this simplification. One of the purposes of the present research is to check the measurement accuracy and proper application of circular foil gages by calibrating them directly in convection heat transfer.

Gage Analysis

The following explains, expands, and improves a circular-foil gage analysis originally given by Striegl and Diller [3]. The analysis shows the difference in gage response between a radiation application, where the effect of temperature gradient in the foil can be neglected, and a convection application, where the effect of the foil temperature gradient can be significant. For convective applications, the boundary condition on the foil surface is best represented by a constant heat transfer coefficient h. Conversely, the commonly used radiation boundary condition is constant heat flux. The corresponding solutions for the temperature distribution [3, 9] (assuming adiabatic conditions on the backside of the foil) are for radiation ($q_r = \text{const}$)

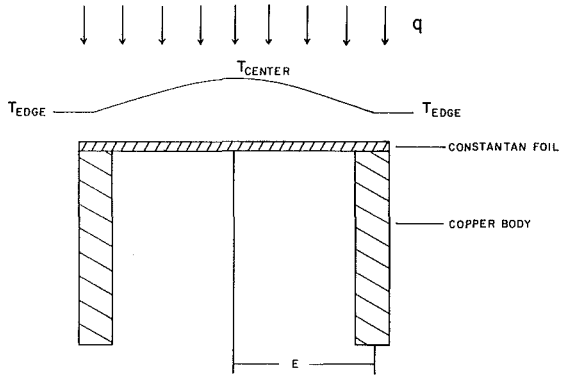

Fig. 1 A Gardon-type thin foil heat flux gage

$$T - T_p = \frac{q_r}{4kt}(R^2 - r^2) \tag{1}$$

and for convection ($h = \text{const}$)

$$T - T_a = (T_p - T_a)\frac{I_0\left(\lambda \frac{r}{R}\right)}{I_0(\lambda)} \tag{2}$$

where $\lambda^2 = R^2 h/kt$.

The output emf from the gage is proportional to the temperature difference across the foil, $T_0 - T_p$. This is related to the heat flux by integrating equations (1) and (2). For radiation, this is

$$T_0 - T_p = \frac{Q_r}{4\pi kt} \tag{3}$$

where Q_r is the total gage heat transfer. For the convection case the center-to-edge temperature difference is

$$T_0 - T_p = \frac{I_0(\lambda) - 1}{I_0(\lambda)}(T_a - T_p) \tag{4}$$

and the total heat transfer to the gage is

Contributed by the Heat Transfer Division for publication in the JOURNAL OF HEAT TRANSFER. Manuscript received by the Heat Transfer Division April 17, 1985. Paper No. 84-HT-45.

$$Q_c = \pi R^2 h \frac{(2/\lambda)I_1(\lambda)}{I_0(\lambda)} (T_a - T_p) \tag{5}$$

Combining equations (4) and (5) relates the measured temperature difference across the gage to the total heat transfer to the gage. The expansion of the Bessel functions for small λ is also shown

$$T_0 - T_p = \frac{Q_c}{\lambda^2 \pi k t} \frac{I_0(\lambda) - 1}{I_1(\lambda)} \cong \frac{Q_c}{4\pi k t} \left(\frac{1 + \lambda^2/16}{1 + \lambda^2/8} \right) \tag{6}$$

By comparing equations (3) and (6) it is apparent that for the same total heat transfer to the gage, the gage output, which is $E = K_2(T_0 - T_p)$, is smaller for convection than for radiation. To obtain the same gage output, these equations show that Q_c must be larger than Q_r

$$\frac{Q_c}{Q_r} = \frac{(\lambda/2)I_1(\lambda)}{I_0(\lambda) - 1} \cong \frac{1 + \lambda^2/8}{1 + \lambda^2/16} \tag{7}$$

Moreover, because of the drop in temperature difference relative to the air, compared to the undisturbed plate, the average gage heat flux in convection is lower than that to the undisturbed plate. Since the undisturbed plate heat flux is

$$q_p = h(T_a - T_p) \tag{8}$$

the ratio of the gage average heat flux (equation (5)) to the plate heat flux for convection applications is

$$\frac{q_c}{q_p} = \frac{(2/\lambda)I_1(\lambda)}{I_0(\lambda)} \cong \frac{1 + \lambda^2/8}{1 + \lambda^2/4} \tag{9}$$

Therefore, to determine h accurately, the output of the gage must be corrected for both of these effects. One method to express the total correction is to define a heat transfer coefficient inferred from the radiation calibration

$$h_i = \frac{q_r}{(T_a - T_p)} \tag{10}$$

This is the value determined from the gage if no correction is made. The true heat transfer coefficient for convection from the plate is defined as h by equation (8) and is given the symbol h_c to clearly indicate that it is the value determined after correction of the gage measurements. The ratio of these two heat transfer coefficients is then

$$\frac{h_c}{h_i} = \frac{q_p}{q_r} = \left(\frac{q_p}{q_c} \right) \left(\frac{q_c}{q_r} \right) \tag{11}$$

The terms in equation (11) can be evaluated from equations (7) and (9) to obtain the result

$$\frac{h_c}{h_i} = \lambda^2/4 \frac{I_0(\lambda)}{I_0(\lambda) - 1} \tag{12}$$

where $\lambda^2 = R^2 h_c / kt$ as given in equation (2). For small values of λ, the Bessel functions can be approximated as

$$\frac{h_c}{h_i} \cong \frac{1 + \lambda^2/4}{1 + \lambda^2/16} \cong 1 + \frac{3}{4} (\lambda^2/4) \tag{13}$$

In terms of the sensitivity factor of the gage, equation (13) can be expressed as

$$\frac{h_c}{h_i} \cong \frac{1}{1 - \frac{3}{4} \frac{f h_i}{K_2}} \tag{14}$$

where f is the linear factor determined by the usual radiation calibration

$$f = E/q_r = \frac{K_2 \pi R^2}{Q_r} (T_0 - T_p) = \frac{K_2 R^2}{4kt} = \frac{\lambda^2 K_2}{4h_c} \tag{15}$$

Equation (14) is the same as presented by Striegl and Diller [3] except for an additional factor of 3/4, which gives an improved approximation of equation (12). The error introduced by the approximation used in equations (13) and (14) is small for the reported experimental measurements ($\lambda < 0.65$). Even for $\lambda = 0.8$, which corresponds to a 12 percent gage correction, the value of h_c/h_i is within 0.1 percent of the exact solution (equation 12).

Alternatively, the correction of the gage output can be expressed in terms of the corrected temperature. Rearrangement of equation (12) into this format gives the corrected heat flux as

$$q_p \cong h_i[(T_a - T_p) + C(T_0 - T_p)] \tag{16}$$

where the quantity multiplying h_i can be regarded as a corrected temperature difference. Unfortunately, C is not a constant, but is a function of λ

$$C = \frac{I_0(\lambda) - (1 - \lambda^2/4)I_0^2(\lambda)}{[I_0(\lambda) - 1]^2} \tag{17}$$

In the limit as $\lambda \to 0$, the value of C is 0.75. The value of C increases as λ increases (e.g., when $\lambda = 0.8$, $C = 0.85$). Malone [9] used an effective gage temperature of this form, with a constant factor of 0.75 for the value of C. As seen from these results, this is correct only in the limit as λ approaches zero.

The analysis presented does not include the effect of heat transfer down the gage center wire. Others [9, 15, 16] have in-

Nomenclature

A = area
C = correction factor, equation (17)
e_e = absolute external error
E = gage output, mV
f = gage sensitivity, mV/(W/m^2)
f_a = apparent gage sensitivity, equation (21)
h = heat transfer coefficient, W/(m^2-K)
h_{av} = average heat transfer coefficient over the center plate, W/(m^2-K)
h_c = corrected heat transfer coefficient in convection, W/(m^2-K)
h_i = heat transfer coefficient based on isothermal gage surface assumption, W/(m^2-K)
I_0, I_1 = Bessel functions
k = thermal conductivity, W/(m-K)
K_2 = thermoelectric constant for copper constantan = 0.042 mV/°C
P = power, W
q = heat flux, W/m^2
Q = heat, W
Q_b = heat loss from backside, W
Q_s = heat loss from surface of insulation strips, W
r = radial coordinate from gage center
R = gage radius
R_h = electric resistance of center plate heater, Ω
t = foil thickness
T = temperature
T_0 = gage center temperature
V = rms voltage
X = amplification factor of amplifier, mV/mV
ϵ = surface emissivity
λ = dimensionless parameter, equations (2) and (12)
σ = Stefan–Boltzmann constant = 5.67 × 10^{-8} W/(m^2-K^4)

Subscripts

a = air
c = convection
g = gage
p = plate
r = radiation
T = total
∞ = surroundings

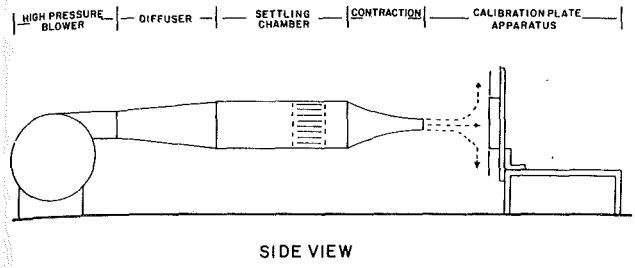

Fig. 2 The flow system

cluded this effect in their analyses for radiation, particularly for the influence on transient response characteristics. Because the results have indicated that the effect was a function of only the material properties and gage geometry for steady-state transfer, and not dependent on the heat flux, it changes only the gage sensitivity f. Since f was determined from experimental calibration, the center wire heat transfer was not included in the analysis. It may be a source of discrepancy, however, between the gage sensitivities determined from radiation and convection calibrations because of the different fluxes and temperatures typically used.

Experimental Apparatus

The calibration apparatus consists of a large free jet at room temperature impinging on a heated flat plate containing the heat flux gage. At the center of this jet is a region of nearly constant heat transfer coefficient. With an isothermal plate and known heat input to the plate, the heat flux from the gage can be determined.

Flow System. The large free jet is created by a small wind tunnel (Fig. 2). A high-pressure blower provides the air supply. The wind tunnel consists of a circular-to-rectangular diffuser, a settling chamber, and a contraction. The settling chamber includes two screens separated by a section of flow straighteners. The contraction ratio is 4.74:1. A square free jet, with velocities of up to 60 m/s, 0.102 m (4 in.) on a side, exits the contraction. The jet impinges on a square stationary flow shield 0.667 m on each side with a square hole, 0.286 m per side, in the center. The calibration plate is positioned immediately behind this hole. The plate and shield apparatus is positioned perpendicular to the jet about 0.6 m from the wind tunnel outlet. This gave the best heat transfer uniformity over the plate. The calibration plate can be traversed through the flow field while behind the large flow shield. Since the large flow shield is stationary and the calibration plate always fills the hole in the shield, the flow remains unchanged during traverses of the flow field.

Calibration Plate. The calibration plate (Fig. 3) consists of a square center plate, 15.2 cm (6 in.) on a side, made of 1.27 cm (1/2 in.) thick aluminum. At the center of this plate is a mounting for the heat flux gage to be calibrated, Thirteen type-T thermocouples are embedded in the plate flush with the top surface. They are located three per side, evenly spaced 1.27 cm from the edge, and one near the center. The side perimeter of this plate has balsa wood, 0.48 cm (3/16 in.) thick, glued to the edge to reduce side losses. Four guard plates, 5.1 cm (2 in.) × 15.2 cm (6 in.) × 1.27 cm (1/2 in.) aluminum surround the center plate as shown in Fig. 3. Each guard plate has a thermocouple embedded directly across from the corresponding one in the center plate. Wire resistance heaters covered with silicone rubber are mounted under each plate. Five variable power supplies, one connected to each heater, allow individual control of the temperature of each plate. The outside perimeter of each guard plate is lined with 1.9 cm (3/4 in.) of Armaflex insulation.

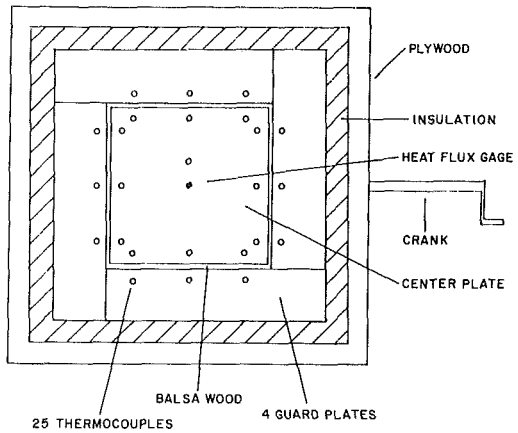

Fig. 3 The calibration plate

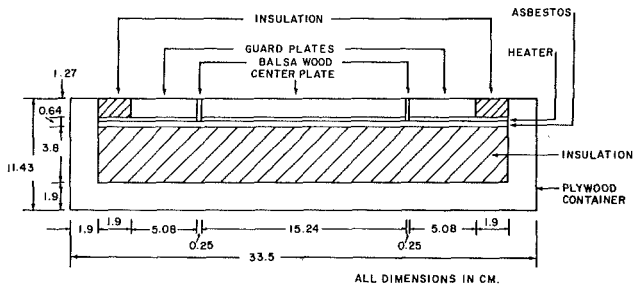

Fig. 4 Cross-sectional view of the calibration plate

Behind the plate system is 0.6 cm of asbestos mill board for stability and 3.8 cm (1-1/2 in.) of Armaflex insulation to reduce back losses. The entire system sits in a plywood box, shown in Fig. 4. The thermocouple, heater, and gage wires thread through the heaters, asbestos, Armaflex, and plywood. The bottom side of the plywood box has the sliding component of a Uni-Slide traversing mechanism mounted in the center. The stationary part of the Uni-Slide is mounted on a stand situated perpendicular to the floor as shown in Fig. 2. The Uni-Slide system produces a voltage that denotes the position of the gage relative to the center of the jet. A small square flow shield, 0.47 m per side with a 0.26 m hole in the center, mounts around the guard plates to form a 0.47 m per side square flat plate.

This system was designed such that the losses through the sides and back would be small. In a typical test the center plate was isothermal to approximately 1°C, which was generally 5 percent of the total ΔT, and the guard plates were kept at temperatures within 0.2°C of the center plate temperature. Heat fluxes from the front surface of the plate ranged from 650 to 4000 W/m^2 depending on the jet velocity and ΔT. Losses from the sides of the plate occur from the center plate to the guard plates and from the center plate to the top surface of the balsa wood. The error introduced by the small differences in temperature between the center plate and guard plates was negligible. The balsa wood, while restricting heat flow to the guard heaters, contributed added surface area on the top face. The heat loss from the center plate which went through the balsa wood and left by surface convection was modeled and included (< 3 percent).

Test Procedure. After the air jet was activated, the power to each of the heaters was adjusted until the center plate and guard plates were at equal steady-state temperatures. The plate and air stream temperatures were recorded from a Doric 410A digital thermocouple readout calibrated to an accuracy of 0.1°C. The input voltage to the center heater was recorded from a Hewlett-Packard 3466A Digital Voltmeter and the input power calculated from $P = V^2/R_h$, where $R_h = 78.0\ \Omega$ is the

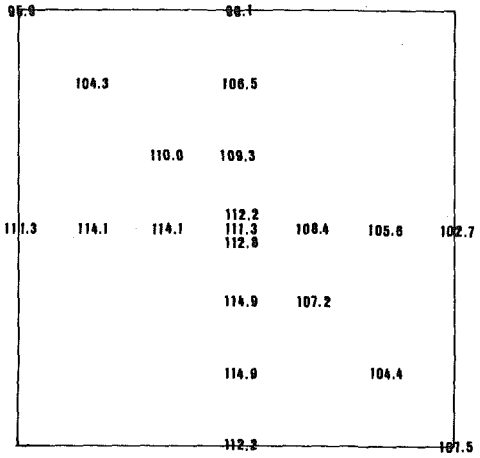

Fig. 5 A typical distribution of heat transfer coefficient (W/m^2K) over the center plate looking in the direction of the free jet

electrical resistance of the heater. The resistance was found to be constant to within 0.6 percent in the operating temperature range. The output from the heat flux gage was fed to a Thermogage High Gain DC amplifier which amplified the signal by a factor of 484.5. It should be noted here that the signal from the gage was so small (50 μV) for these heat fluxes that it was very susceptible to electrical noise. The gage leads were shielded and the shield and the plate were securely grounded.

From the amplifier the gage signal was fed to an X–Y plotter. The traversing mechanism was used to obtain the entire variation of heat flux across the center plate by traversing the calibration plate relative to the fixed jet. The trasverse was performed slowly in both directions to insure that there was no effect of plate motion on the measured heat flux. The result was a plot of the gage output versus position on the X–Y plotter. The entire system could also be rotated such that vertical or diagonal traverses through the flow field were possible. During these traverses the temperature near the gage was monitored and found to be stable throughout the traverse. A test case was run in which the gage was traversed horizontally, vertically, and diagonally through the flow field. Part of the distribution of h is shown in Fig. 5. From this distribution the average h over the entire plate was estimated to be within 1 percent of the average h determined from the horizontal traverse only. Therefore, a horizontal traverse was found to be a good representation of the conditions over the entire plate.

Data Reduction. The total heat transfer from the top surface of the center plate can be expressed as

$$Q_T = h_{av}A_T(T_p - T_a) + \sigma(\epsilon_p A_p + \epsilon_g A_g)(T_p^4 - T_\infty^4) \quad (18)$$

The average plate temperature T_p was calculated as the average of the 13 temperatures from the center plate. Q_T represents the input power less back and side losses

$$Q_T = V^2/R_h - Q_{\text{losses}} \quad (19)$$

The losses, however, are a function of h_{av}. Therefore, an iterative scheme was used with equations (18) and (19) to determine h_{av} and the losses. Iteration continued until the value of h_{av} converged to within ± 0.1 percent.

The losses from the back side of the plate were calculated using a steady-state one-dimensional conduction analysis. The heat transfer resistance of the asbestos insulation, plywood, and backside natural convection was used to estimate the heat loss relative to the front side. In all cases this was less than 1.5 percent.

A finite difference scheme was used to determine the side losses to the balsa wood surface between the measurement plate and guard plates Q_s. The assumptions made were: (1) constant plate temperature, (2) constant h over the balsa wood surface, and (3) center plate temperature equal to guard plate temperature. The calculated heat loss from the balsa wood surface was less than 3 percent for all cases.

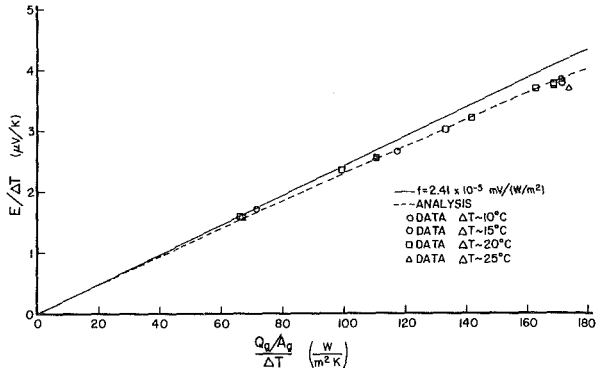

Fig. 6 Calibration curves for the Medtherm heat flux gage

The total heat transfer from the gage, assuming a uniform temperature T_p, was

$$Q_g = h_{av}A_g(T_p - T_a) + \epsilon_g A_g \sigma(T_p^4 - T_\infty^4) \quad (20)$$

using the measured plate heat transfer along with equations (18) and (19) to evaluate h_{av}. This represents the heat transfer that a "perfect" gage should measure without any temperature disruption. The effect of the *actual* gage temperature distribution was included in evaluating the gage sensitivity as follows. An apparent gage sensitivity was determined for each individual test by dividing the gage output by the gage heat flux from equation (20)

$$f_a = E/(Q_g/A_g) \quad (21)$$

This value of f_a is smaller than the true sensitivity f because of the smaller voltage output (E) for convection, and it is a function of the heat flux level because of the nonlinear gage output for convection (e.g., Fig. 6). Consequently, the true gage sensitivity f had to be obtained by correcting for the effect of the nonuniform gage temperature in convection. Because the experimental gage sensitivity and the size of the correction were not initially known, an iteration procedure was necessary to obtain the average gage sensitivity from the measurements for each gage.

The procedure began with evaluation of the apparent heat transfer coefficient h_i for each measurement from

$$h_i = \frac{E/f - \epsilon_g \sigma(T_p^4 - T_\infty^4)}{T_p - T_a}, \quad (22)$$

where the gage temperature was again assumed equal to the plate temperature. A value for f was initially assumed equal to the value supplied by the manufacturer. The resulting values of h_i were used with equation (14) to obtain the corrected values of heat transfer coefficient for convection

$$h_c = h_i \frac{1}{1 - \frac{3}{4}\frac{fh_i}{K_2}} \quad (23)$$

In terms of the parameters in the analysis, the ratio of the true gage sensitivity to the apparent value can be expressed as

$$\frac{f}{f_a} = \frac{q_p}{q_r} = \frac{h_c}{h_i} \quad (24)$$

This was then used to calculate a new value of the corrected gage sensitivity for each test. The *average* value of f for all of the tests for a particular gage was then used to recalculate new values beginning with equation (22). Iteration was continued until the average value of f converged to within 0.1 percent. This value of f should be the same as the manufacturers' f obtained from radiation calibration.

Table 1 Experimental test values for gage 1

TEST	(T_p-T_a) (°C)	OUTPUT (mV)	h_i (W/m^2-K)	h_c/h_i	f (mV/W/m^2)
10	9.6	0.0367	149.7	1.069	0.238 E-04
11	19.0	0.0563	148.1	1.068	0.234 E-04
12	19.9	0.0741	147.3	1.068	0.236 E-04
13	25.4	0.0935	145.2	1.067	0.225 E-04
14	10.3	0.0275	101.5	1.046	0.237 E-04
15	21.4	0.0551	98.7	1.044	0.242 E-04
16	26.4	0.0673	97.9	1.044	0.240 E-04
17	20.4	0.0648	124.1	1.056	0.236 E-04
18	20.7	0.0338	59.3	1.026	0.254 E-04
19	20.8	0.0793	147.4	1.068	0.236 E-04
20	20.2	0.0605	116.2	1.053	0.236 E-04
21	20.4	0.0753	144.5	1.066	0.241 E-04
22	18.6	0.0442	90.2	1.040	0.249 E-04
23	20.6	0.0338	59.6	1.026	0.252 E-04
24	10.2	0.0182	63.2	1.028	0.255 E-04
				Average	0.241 E-04

Table 2 Experimental test values for gage 2

TEST	(T_a-T_p) (°C)	OUTPUT (mV)	h_i (W/m^2-K)	h_c/h_i	f (mV/W/m^2)
42	9.8	0.0070	69.9	1.011	0.953 E-05
43	20.0	0.0126	62.2	1.010	0.965 E-05
44	31.0	0.0190	60.6	1.010	0.959 E-05
45	10.7	0.0136	133.3	1.022	0.889 E-05
46	19.2	0.0241	132.8	1.022	0.886 E-05
47	20.4	0.0239	123.0	1.020	0.894 E-05
48	20.4	0.0161	80.1	1.013	0.961 E-05
49	20.1	0.0178	90.8	1.015	0.899 E-05
50	10.5	0.0109	107.6	1.018	0.872 E-05
51	20.5	0.0204	103.6	1.017	0.886 E-05
52	20.4	0.0208	106.3	1.017	0.847 E-05
53	20.2	0.0199	101.6	1.017	0.854 E-05
				Average	0.905 E-05

Although the gage sensitivity f can be expressed analytically in terms of the gage geometric parameters and material properties, equation (15), it does not provide an accurate determination of f because of the limitation on manufacturing tolerances. This is one reason why individual calibrations are always necessary for each gage.

Results

Calibration tests were run on two gages at different values of h (adjusted by changing the velocity of the jet) and different values of ΔT from the plate to air stream. The heat transfer coefficients ranged from approximately 60 to 170 W/(m^2-K) (jet velocities from 9 m/s to 54 m/s) and the plate-to-airstream ΔT ranged from 10°C to 30°C.

Fifteen tests were conducted on gage 1 (Medtherm, 0.32 cm (1/8 in.) o.d.). Figure 6 plots gage output/ΔT versus the measured heat flux/ΔT from the plate as determined from equation (20). These data are uncorrected for the effects of the nonisothermal gage surface. The straight line on the figure indicates the gage sensitivity ($f = 2.41 \times 10^{-5}$ mV/(W/m^2), see Table 1) as determined experimentally using equations (22)–(24). This sensitivity matches the standard calibration of the gage done by the manufacturer to within 1 percent. The dashed line represents the analytical correction of the calibration line for convection as represented by equation (23). Applying this correction assumes that most of the heat flux is convective rather than radiative. It is apparent from the figure that the experimental results agree well with the analysis

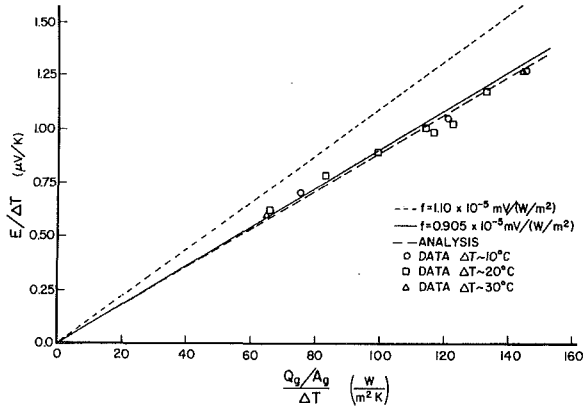

Fig. 7 Calibration curves for the Thermogage heat flux gage

throughout the range of heat flux and also are independent of ΔT. For this gage, correction factors reach 7.7 percent at $h_c = 180$ W/(m^{2}K) ($\lambda^2 = 0.41$).

Data in Table 1 illustrate the repeatability of the calibration system. The 95 percent confidence interval of the experimentally determined f values was 1.9 percent. An external error analysis, described in the Appendix, yields an error estimate of 1.5 to 3.5 percent for the measurements, including both uncertainty and bias errors. Because the largest uncertainty was in the voltage output of the gage, the range of uncertainties reflects the range of gage outputs covered. The average estimated uncertainty of the 15 tests was 1.9 percent.

Twelve tests were conducted on gage 2 (Thermogage, 0.16 cm (1/16 in.) o.d.). The results are shown in Fig. 7 and Table 2. Because this was a smaller gage, some modification of the calibration plate was necessary. In addition, this gage had no threads on the outside to anchor it in place and therefore had a tendency to slip in and out slightly. Consequently, it was more difficult to position the gage exactly flush with the surface and to insure good thermal contact between the gage and plate. The gage was subjected to the available range of heat flux and ΔT.

The data clearly show a discrepancy between the manufacturer's value of sensitivity and the experimental value. The manufacturer's value is $f = 1.10 \times 10^{-5}$ mV/(W/m^2) while the present experimental value is $f = 0.905 \times 10^{-5}$ mV/(W/m^2) (average value from Table 2), a difference of 17.7 percent. A possible explanation is that the gage changed calibration sometime after shipping and before the set of calibration tests. Other researchers have cautioned about this problem [8]. Possibly, the foil could not withstand the pressure of the air jet and deformed. The appearance of the foil was noticeably changed during the 75 hr of testing, which probably also affected the surface emissivity.

Data gathered for gage 2 also show some nonlinearity of the calibration curve. Using $f = 0.905 \times 10^{-5}$ mV/(W/m^2) as experimentally determined, the convection correction for this gage is smaller because the gage is less sensitive. The correction reaches only 2.9 percent at $h_c = 180$ W/(m^2-K) ($\lambda^2 = 0.16$). The assumption of a linear response introduces less error with this gage because of the lower gage sensitivity. This lower sensitivity, however, increases the measurement error. Although the accuracy of the output voltage reading is the same as for the larger gage, the output itself is smaller by a factor of three. Hence, the error associated with the voltage measurement is greater. An external error analysis (Appendix A) indicates measurement errors from 2.3 to 6.4 percent with an average for all 12 tests of 3.2 percent. From the data in Table 2, the 95 percent confidence interval for the values of f determined from the calibration system was 3.0 percent. This interval is almost twice that for the more sensitive gage 1.

Discussion

The results from the two heat flux gages calibrated in the convection environment clearly show the nonlinearity of the calibration curve. The degree of nonlinearity depends on the gage sensitivity and the convection heat transfer coefficient as the analysis indicates. Although the needed corrections of the measured heat flux were small for the ranges and gages tested, the analysis and experimental trends indicate that for the larger gage outputs often reported in the literature the needed corrections would be much larger. As shown by equation (15) the correction is approximately proportional to the gage center-to-edge temperature difference, which determines the gage output voltage.

The experimental tests also indicated that for the range tested the accuracy of the circular foil gages is mainly limited by the ability to read accurately the small output signal. The 95 percent confidence intervals for the measurements with both gages were close to the average of the estimated uncertainties. For most of the tests the uncertainty in the gage output voltage was the largest portion of the estimated error.

The gage sensitivity was purposely kept small to minimize the perturbation of the thermal boundary layer due to the presence of the gage. Although no analysis was found for this effect for a stagnation flow, the analysis by Woodruff et al. [11] for the perturbation of a flat plate was applied. For the test conditions and gage sensitivities used the effect of the nonisothermal condition due to the gage was estimated as less than a few percent. Gages of higher sensitivity, although more desirable because of larger output signals, have a larger ΔT across the foil which increases the effect of this disruption of the thermal boundary layer.

The experimental data verify the analytical results and hence the significance of the temperature distribution in the foil. It should be emphasized that the resulting correction for h_c given in equations (12) and (13) arises from two sources. The first is a smaller voltage output from the gage because the average air-to-surface temperature difference is smaller than that for the undisturbed surface. Therefore, the gage actually receives less heat flux than the adjacent plate surface. The second source of error is that because of the nonuniform distribution of the heat flux, a convection boundary condition produces a smaller center-to-edge temperature difference than an equal size radiation flux to the gage surface. Therefore, the gage output is less for the convection condition than for constant heat flux. The first effect has generally been recognized while the second has not.

The temperature distribution in the gage foil could also cause a significant effect for a net heat flux *leaving* the gage by radiation. The gage output is lower than the isothermal case for the same two reasons as for the convection boundary condition. For gage 1 with $f = 2.41 \times 10^{-5}$ mV/(W/m^2) and an edge temperature of 1000 K radiating to the ambient at 300 K (radiative flux of $\sim 50{,}000$ W/m^2 which produces a gage ΔT of ~ 30°C) the error would be ~ 10 percent. The error increases as the net heat flux or the gage sensitivity increases, although gage temperatures this high are not normally achievable because of the material limitations.

The calibration system designed and used in this research is not limited to the calibration of circular foil heat flux gages. Any instrument that measures a steady-state heat flow could be used with only minor adjustments to the system. Instruments such as those introduced by Kraabel et al. [17], Achenbach [18], and more abundant "sandwich" gages [19] could all be calibrated in the present system. For most of the range currently tested the estimated uncertainty in the calibration plate measurements was 1.5 percent. This was generally smaller than the uncertainty in the voltage readings from the gages tested.

Conclusions

The conclusions and recommendations deduced from this research are listed:

1 A circular foil heat flux gage has a nonlinear calibration curve in convection which differs from the linear calibration resulting from the standard radiation technique.

2 The theoretical correction derived for convection measurements appears to match the experimental results.

3 With proper care and calibration, circular-foil heat flux gages can measure local heat flux accurately and repeatably.

4 The results obtained in convection show the effect of the nonuniform temperature in the circular foil on heat flux measurements. The same effect would occur in measurements of a net radiation heat flux *from* the gage. This effect should be carefully considered.

5 An accurate calibration system is described and demonstrated for testing local heat flux gages in a convective air flow.

Acknowledgments

The support of the Department of Energy, Grant No. DE-A505-82ER12022, is gratefully acknowledged. This is a project in the program of Dr. Oscar P. Manley, Division of Engineering and Geosciences of the Office of Basic Energy Sciences.

References

1 Gardon, R., "An Instrument for the Direct Measurement of Intense Thermal Radiation," *Review of Scientific Instruments*, Vol. 24, No. 5, 1953, pp. 366–370.

2 Gardon, R., "A Transducer for the Measurement of Heat Flow Rate," ASME JOURNAL OF HEAT TRANSFER, Vol. 82, 1960, pp. 396–398.

3 Striegl, S. A., and Diller, T. E., "The Effect of Entrainment Temperature on Jet Impingement Heat Transfer," ASME JOURNAL OF HEAT TRANSFER, Vol. 106, 1984, pp. 27–33.

4 Trimmer, L. L., Matthews, R. K., and Buchanan, T. D., "Measurement of Aerodynamic Heat Rates at the Von Karman Facility," *International Congress of Instrumentation in Aerospace Simulation Facilities Record*, IEEE/AES, 1973, pp. 35–44.

5 Hollworth, B. R., and Berry, R. D., "Heat Transfer From Arrays of Impinging Jets With Large Jet-to-Jet Spacing," ASME JOURNAL OF HEAT TRANSFER, Vol. 100, 1978, pp. 352–357.

6 Luckey, D. W., and L'Ecuyer, M. R., "Stagnation Region Gas Film Cooling – Spanwise Angled Injection from Multiple Rows of Holes," NASA Contractor Report 165333, Apr. 1981.

7 Pirovano, A., Viannay, S., and Jannot, M., "Convection Naturelle en Regime Turbulent le Long d' une Plaque Plane Verticale," *Heat Transfer 1970*, Vol. IV, 1970, Paper No. NC1.8.

8 American Society for Testing and Materials, "Measurement of Heat Flux Using a Copper-Constantan Circular Foil Heat-Flux Gage," *ASTM Book of Standards*, Standard 511-73, Part 41, 1980, pp. 733–737.

9 Malone, E. W., "Design and Calibration of Thin-Foil Heat Flux Sensors," *ISA Transactions*, Vol. 7, 1968, pp. 175–179.

10 Bachmann, R. C., Chambers, J. T., and Giedt, W. H., "Investigation of Surface Heat Flux Measurements With Calorimeters," *ISA Transactions*, Vol. 4, 1965, pp. 143–151.

11 Woodruff, L. W., Hearne, L. F., and Keliher, T. J., "Interpretation of Asymptotic Calorimeter Measurements," *AIAA Journal*, Vol. 5, No. 4, 1967, pp. 795–797.

12 Thibault, J., and Hoffman, T. W., "A Heat Flux Meter to Determine the Local Heat Flux Density During a Quenching Experiment," *Int. J. Heat Mass Transfer*, Vol. 22, 1979, pp. 177–184.

13 Brookley, C. E., "A Method for the Rapid Calibration of Circular Foil Calorimeters to 500 Btu/ft^2 second," Thermogage, Inc., Mar. 1969.

14 "General Description of Calibration Procedures for Heat Flux Transducers and Infrared Radiometers," Medtherm Corporation.

15 Keltner, N. R., and Wildin, M. W., "Transient Response of Circular Foil Heat Flux Gages to Radiative Fluxes," *Rev. Sci. Instrum.*, Vol. 46, 1975, pp. 1161–1166.

16 Ash, R. L., and Wright, R. E., "Design Considerations for Gardon Heat Flux Sensors," 6th AIAA Thermodynamics Conference, Tullahoma, TN, Apr. 1971, Paper No. 71-470.

17 Kraabel, J. S., Baughn, J. W., and McKillop, A. A., "An Instrument for the Measurement of Heat Flux from a Surface With Uniform Temperature," ASME JOURNAL OF HEAT TRANSFER, Vol. 102, 1980, pp. 576–578.

18 Achenbach, E., "Total and Local Heat Transfer From a Smooth Circular Cylinder in Crossflow at High Reynolds Number," *International Journal of Heat and Mass Transfer*, Vol. 18, 1975, pp. 1387–1396.

19 Thompson, W. P., "Heat Transfer Gages," in: *Fluid Dynamics, Methods of Experimental Physics*, Vol. 18B, R. J. Emrich, ed., Academic Press, New York, 1981, Chap. 7, pp. 663–685.
20 Rabinowicz, E., *An Introduction to Experimentation*, Addison-Wesley, New York, 1970.

APPENDIX

An external error estimate was performed on the calibration system. The final result of a calibration test is a value of the gage sensitivity f given by the equation

$$f = \frac{E}{h_{av}(T_p - T_a) + \epsilon_g \sigma (T_p^4 - T_\infty^4)} \tag{A1}$$

where

$$h_{av} = \frac{V^2/R_h - Q_s - Q_b - \sigma(\epsilon_p A_p + \epsilon_g A_g)(T_p^4 - T_\infty^4)}{A_T(T_p - T_a)} \tag{A2}$$

Errors associated with E, X, V, R_h, T_p, T_∞, ϵ_p, Q_s, and Q_b are included. No attempt is made to account for error in area measurements or manufacturer-supplied values of gage emissivity. If the value of gage emissivity changes (due to loss of the surface coating) or the value is unknown, an additional error of 1 or 2 percent would need to be included.

The errors associated with each term are as follows:

$e_{h_{av}} = 0.01\ h_{av}$	due to uncertainties in the heat transfer profile
$e_E = 0.8\ \mu$V	zeroing inaccuracies of the amplifier and high frequency fluctuation of the signal
$e_{T_p} = 0.1$°C	measurement accuracy of the digital thermocouple readout
$e_X = 3.0$	the amplifier calibration curve is not perfectly linear
$e_V = 0.5$ V	fluctuation in readout of the digital voltmeter
$e_{R_h} = 0.5\ \Omega$	variation of resistance of center heater with temperature
$e_{\epsilon_p} = 0.05$	accounts for 25 percent error in the value of ϵ_p
$e_{T_\infty} = 2$°C	the possible difference between the surrounding air temperature measured and the surroundings temperature desired
$e_{Q_s} = 0.2$ W	accounts for 40 percent error in the finite difference approximation
$e_{Q_b} = 0.1$ W	accounts for 50 percent error in the simplified one-dimensional analysis

These errors were summed by the method in [20].

Natural Convection Heat Transfer Characteristics of Simulated Microelectronic Chips

K.-A. Park

A. E. Bergles

Heat Transfer Laboratory,
Department of Mechanical Engineering,
Iowa State University,
Ames, IA 50011

Microelectronic circuits were simulated with thin foil heaters supplied with d-c power. The heaters were arranged in two configurations: flush mounted on a circuit board substrate or protruding from the substrate about 1 mm. Heat transfer coefficients (midpoint) were obtained with two heater heights (5 mm, 10 mm) and varying width (2 mm ~ 70 mm), in water and R-113. The height effect for single flush heaters agrees qualitatively with conventional theory; however, even the widest heaters have coefficients higher than predicted due to leading edge effects. The heat transfer coefficient increases with decreasing width, with the coefficient for 2 mm being about 150 percent above that for 20 mm ~ 70 mm. This is attributed to three-dimensional boundary layer effects. The protruding heaters have a coefficient about 15 percent higher. Data were obtained for in-line and staggered arrays of flush heaters with varying distance between heaters. Coefficients for the upper heaters are below those for lower heaters, with the differences diminishing as the vertical or horizontal spacing increases. For the protruding heaters, the upper heaters have higher coefficients than the lower heaters.

Introduction

Extreme miniaturization of electronic devices has reintroduced the thermal problem. The failure of microelectronic chips increases exponentially as the junction temperature increases. It is important in the packaging of these microelectronic chips to predict the heat transfer characteristics for all anticipated modes of heat transfer. Natural convection is an important mode of heat transfer for both air and liquid cooling.

Microelectronic chips should be modeled as uniform heat flux devices; due to their small size, the flow is laminar. The existing natural convection correlations, experimental and analytical, for uniform heat flux from vertical plates were obtained from heating surfaces that were large in at least one dimension (the width) (Goldstein and Eckert, 1960; Vliet, 1969; Fujii and Fujii, 1979). The heat dissipation area of typical chips is very small in two dimensions (about 5 mm × 5 mm). The interactions among chips are of considerable importance in predicting the thermal behavior of the chips. In general, a limited amount of data exists for such small distributed heat sources, either single or in arrays.

Baker (1972, 1973) found midpoint heat transfer coefficients for resistor chips, flush-mounted on a substrate, which were twice as wide as they were high: 4.6 mm × 2.3 mm, 9.8 mm × 4.9 mm, and 20 mm × 10 mm. The surfaces were placed vertically in air and liquid Freon-113 (R-113). His data with R-113 illustrate the observed large increases in heat transfer coefficients above those expected for natural convection. Baker suggested qualitatively that the increases were due to leading edge and side flow effects. He also showed that conduction to the substrate was relatively unimportant.

Carey and Mollendorf (1977) mentioned the increased complexity of the three-dimensional flows associated with small heating elements. They investigated the temperature fields in an adiabatic wall above flush-mounted circular and square heaters in water. Sufficient data were presented for one small square heater (4.7 mm × 4.7 mm) so that a single value of the heat transfer coefficient could be calculated. This coefficient was 110 percent higher than the predicted value.

In reviewing the existing literature, no previous experimental studies of arrays of small heaters on a vertical surface have been found. Sparrow and Faghri (1980) numerically solved boundary layer equations for the problem of two in-line wide vertical flush mounted heaters (assumed isothermal) for natural convection in air. Jaluria also numerically solved this problem for multiple wide heaters (1981, 1982a) and experimentally and numerically studied two line sources (1982b). He also solved the more general equations for two in-line wide vertical heaters using finite difference methods (1984). The differences between the solutions of boundary layer theory and the more general equations increase as Grashof number decreases.

Experimental studies on heater interactions were done with arrays of wires (Lieberman and Gebhart, 1969; Pera and Gebhart, 1975) and small tubes (Tokura et al., 1983; Masters, 1972). The general observation is that heat transfer at the upper heaters is enhanced by the buoyancy-driven flow of the lower heaters; however, the enhancement is partially offset by the higher fluid temperature. Also of related interest, there are many analytical and experimental works on the plumes induced from single wide heat sources (Cary and Mollendorf, 1977; Hardwick and Levy, 1973; Jaluria and Gebhart, 1977; Sparrow et al., 1978; Kishinami and Seki, 1983).

The purpose of the present study was to clarify the dependence of heat transfer performance on heater size through a systematic experimental investigation. In the simulated multichip module, the development and interaction of the plumes of small heat sources is very complicated; thus, it is not easy to solve the problem numerically. A practical first step is to obtain physical understanding by experimentation.

Experimental Apparatus and Procedure

Single Flush Heaters. Two working fluids, Freon-TF (R-113) and water, were used to determine the influence of test section size on natural convection heat transfer. R-113 was selected as its properties are similar to those of dielectric liquids commonly used for direct immersion cooling of microelectronic components. The R-113 experiments were done in an insulated tank 273 mm × 127 mm of 152 mm height with a plexiglass cover as shown in Fig. 1. A pyrex beaker of 4 liter capacity (16 cm diameter) was used for experiments with distilled water. The distilled water was

Contributed by the Heat Transfer Division and presented at the 23rd National Heat Transfer Conference, Denver, CO, August 4–7, 1985. Manuscript received by the Heat Transfer Division November 25, 1985.

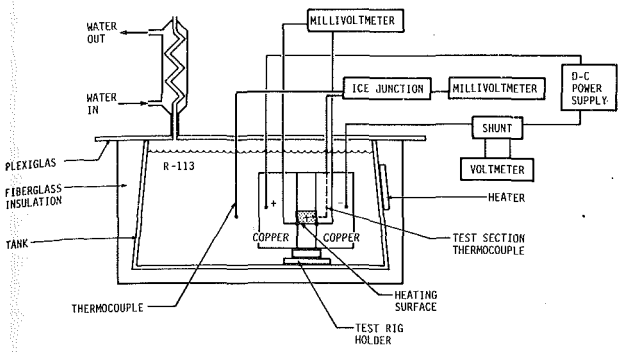

Fig. 1 Experimental apparatus

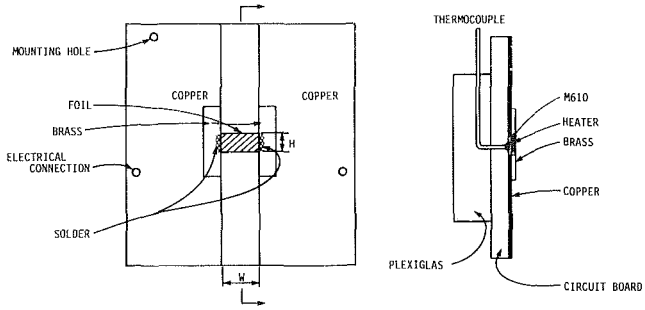

Fig. 2 Test section details

deaerated by preboiling. Room temperature conditions were reestablished throughout the pool before the experiments. The pool temperature was maintained close to room temperature (25 ~ 30°C) during the experiments.

A circuit board (glass epoxy G-10) clad with copper on one side was the basis of the test section, as shown in Fig. 2. The copper cladding in the center was removed by a razor blade to make room for the foil heater.

Three kinds of foil were used in this experiment: 25.4-μm-thick steel, for R-113, and 10-μm-thick constantan and 12.7-μm-thick nichrome for both water and R-113. M610 epoxy resin (Measurements Group, Inc.) was used to bond the foil to the circuit board. The foil and copper cladding were then very carefully soldered to the 25.4-μm brass foil for the electrical connections. The resulting small protrusion of the power connections should not have affected the heat transfer. Direct-current power to the test section was supplied by a 50 A power supply. The final assembly simulated a chip flush with the substrate. The area of the exposed surface was measured by an optical microscope. The surface was left in the original polished condition and cleaned with Freon TF degreaser. Plexiglass was added for insulation and to guide the thermocouple wires to the back side of the circuit board.

A single thermocouple was placed at the back center of each foil: The junction was electrically insulated from the heater. The midpoint of the heaters was chosen as being representative of the thermal performance of a chip. Two types of thermocouples (iron-constantan 40 gauge and copper-constantan 36 gauge) were used for this experiment. The copper-constantan thermocouples were used in all but five test sections. It was confirmed by calculation and experiment for both types of thermocouples that the conduction loss through the leads was negligible.

The main variable in this experiment was the width of the heated surface. Two different heights (5 mm and 10 mm) were employed with variations in width from about 2 mm to 70 mm. In all cases a smooth leading edge was provided by a 50-mm section of the circuit board. A similar strip was at the trailing edge. All test sections were vertically oriented about 60 mm below the free surface of the pool.

Arrays and Protruding Heaters. The main difference in the array experiments was that multiple foil heaters (5 mm × 5 mm) were installed on strips of circuit board. These strips were then stacked with various combinations of plain circuit boards and sandwiched with copper bus bars and plexiglass retainers as shown in Fig. 3. To avoid contact resistance problems, the heaters were joined at both ends with soldered shorting strips. The staggered surfaces were arranged simply by sliding the heater strips. Arrays of in-line and staggered flush surfaces are shown in Fig. 4(*a–c*).

Microelectronic chips normally protrude from the substrate. To better conform to this real situation, an experimental program was also developed to study single, protruding simulated chips and an array of such chips. Small pieces of the bare circuit board were added to simulate the shape of the microchips as shown in Fig. 4(*d*, *e*). The chip model (4.9 mm × 5.3 mm wide) was built out so that the face of the heating foil was 1.1 mm from the substrate. This is comparable to actual thermal chips studied previously (Hwang and Moran, 1981; Oktay, 1982).

Multiple heaters were tested individually to assess any bias resulting from thermocouple installation and other construction variables. The heat transfer coefficients fell within a band of ± 3.5 percent from average values for the flush heaters and ± 3 percent for the protruding heaters. This is due to the usual experimental uncertainty; no significant bias was observed. Also, the resistance of each heater was measured, since variations in resistance would affect the individual heater power during multiple heater operation. The variation in resistance about the mean was ± 3.5 percent for both types of heaters.

Data Reduction. The nominal heat flux, calculated from the voltage drop across the heater and current across a calibrated shunt, was corrected for the back side heat loss and heat loss to the electrical connections. These heat loss corrections, evaluated at the midpoint of the test section, were about 10 ~ 15 percent for a 5 mm × 5 mm surface. The main correc-

Nomenclature

C_p = specific heat at constant pressure
G = vertical pitch between the heaters
g = gravitational acceleration
Gr_c^* = modified Grashof number at center of heater = $(g\beta q'' H^4/16k\nu^2)$
H = height of the test section
h = heat transfer coefficient
k = thermal conductivity
$\overline{\mathrm{Nu}}$ = average Nusselt number = hH/k
Nu_c = Nusselt number at center of heater = $hH/2k$
P = horizontal pitch between the heaters
Pr = Prandtl number $C_p\mu/k$
q_c'' = heat flux at center of heater
$\overline{\mathrm{Ra}}$ = average Rayleigh number = $(g\beta\Delta TH^3/\nu^2)\mathrm{Pr}$
Ra_c^* = Rayleigh number at center of heater = $\mathrm{Gr}_c^*\mathrm{Pr}$
Ra_w^* = Rayleigh number based on width of heater
T_b = bulk temperature
T_w = wall temperature
ΔT = temperature difference between wall and bulk fluid
W = width of the test section
β = coefficient of expansion
μ = dynamic viscosity
ν = kinematic viscosity

Subscripts

b = bottom test section
m = middle test section
s = boundary layer solution
t = top test section

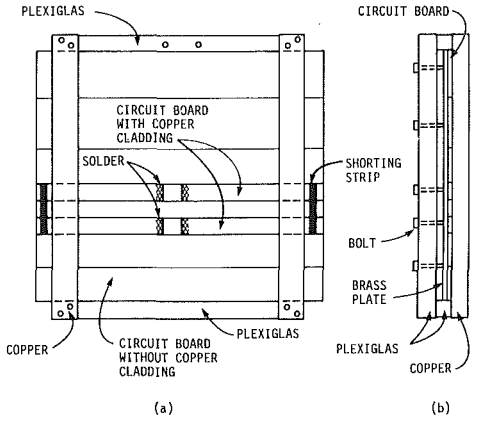

Fig. 3 Test-section assembly for multiple heaters: (*a*) front view, (*b*) view from left

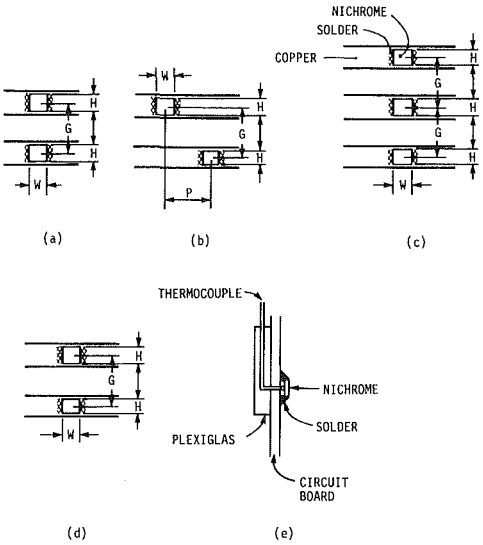

Fig. 4 Schematic layouts of flush heaters (*a*, *b*, *c*) and protruding heaters (*d*), and protruding heater detail (*e*)

tion was heat loss to the back side. The very small temperature drop between the thermocouple junction and the outer foil surface was neglected (Park, 1985).

Heat flux profiles were not uniform because of the heat loss to electrical connections at the edges of the heater. With this type of heating, it is not possible to get uniform heat flux conditions for small heat sources (Park, 1985).

The heat losses to the back side for heaters in an array should be different from those for single heaters. It is expected that the heat loss corrections to the back side for the single heaters are similar to those for arrays of heaters because the heaters in arrays were rather widely spaced. The heat loss corrections to the back side for arrays of heaters were applied in the same way as for single heaters. Errors in this correction would be larger when many heaters are involved and the heaters are placed close to each other.

The Nusselt number was based on the heat flux and wall temperature at the midpoint of the test section. In accordance with this local assessment of heat transfer performance, the modified Rayleigh number was also evaluated at the midpoint. The estimated uncertainty in Nu_c is 3.4 percent and the uncertainty in Ra_c is 6.7 percent.

Properties of working fluids were evaluated at the film temperature, the average of the local surface and pool temperatures (i.e., $(T_w + T_b)/2$). The properties as functions of temperature were obtained from Jensen (1980) for R-113 and Morcos and Bergles (1974) for distilled water.

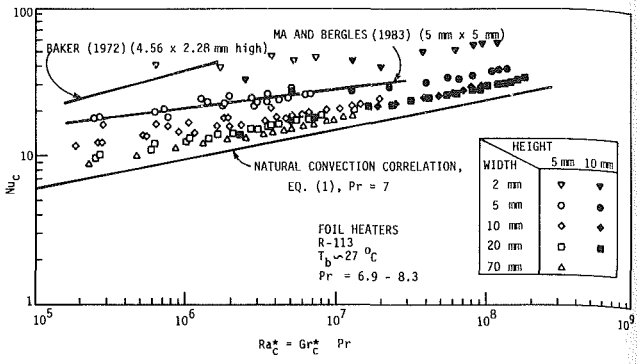

Fig. 5 Natural convection data for test sections of various width (R-113)

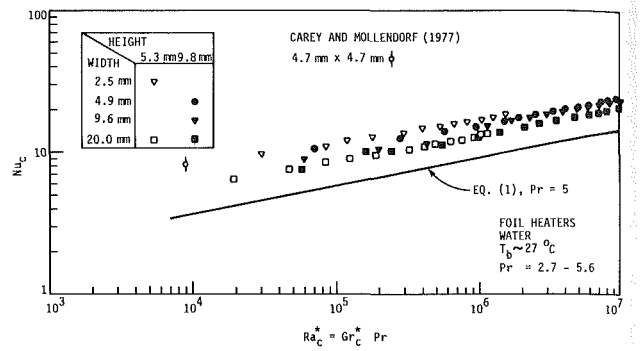

Fig. 6 Natural convection data for test sections of various width (water)

Experimental Results and Discussion

Single Flush Heaters. The experimental data for the 5-mm and 10-mm-high heaters in R-113 are shown in Fig. 5. The base line in this figure is the Fujii and Fujii correlation of laminar boundary layer solutions for a vertical surface with constant heat flux (Fujii and Fujii, 1976)

$$Nu_{c,s} = \left(\frac{Pr}{4 + 9\sqrt{Pr} + 10Pr}\right)^{1/5} (Gr_c^* Pr)^{1/5} \quad (1)$$

For $Pr = 7$, the Pr function is 0.59, essentially the same as the constant value of 0.6 found empirically by Vliet (1969).

The data of Ma and Bergles (1983) for a 5 mm × 5 mm test section, using a similar type of construction, are in very good agreement with the present data. The heat transfer coefficient clearly increases as the width is reduced. The chip size (5 mm × 5 mm) test section has a heat transfer coefficient 80 to 100 percent greater than that for the widest test section. A similar width effect was obtained for the 9.86-mm-high test section. This suggests that the height effect is taken care of by the usual Nu_c-Ra_c^* presentation. It is noted, however, that the heat transfer coefficients for the widest test section are 20 percent higher than predicted by equation (1).

With water, the experimental results for varying width with two different heights are shown in Fig. 6. The single data point of Carey and Mollendorf (4.7 mm × 4.7 mm heater) is somewhat higher than interpolated and extrapolated data of the present study. The width effect with water is much less pronounced than that for R-113. There was no effect of heating surface material on either set of natural convection data, as expected.

Qualitative Explanation for Wide Plate Deviation From the Classical Solution. It is apparent from Figs. 4 and 5 that the present data are not in good agreement with the "textbook" boundary layer similarity solution. Consider first the 20 percent deviation of the widest test section. While not really addressed in the very limited experimental literature for uniform-

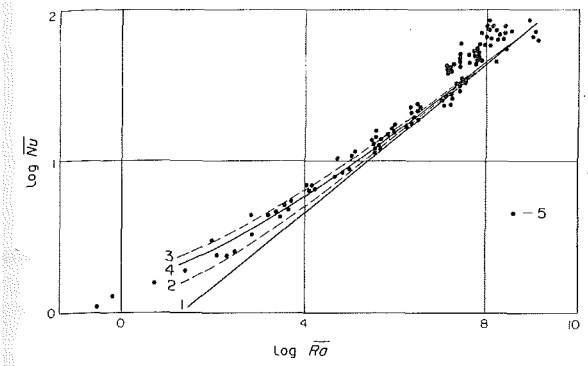

Fig. 7 Comparison between calculation and experiments on the basis of the mean heat transfer coefficient: (1) boundary-layer theory, (2) with external flow taken into account, (3) with the leading edge effect taken into account, (4) with the trailing edge and wake effects taken into account, (5) experiment (Ede, 1967) (from Martynenko et al. (1984))

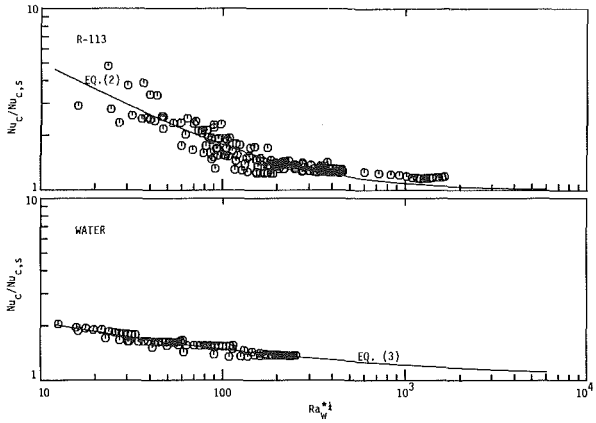

Fig. 8 Comparison between experimental data and correlations using Ra_W^* based on width of heater

ly heated test sections, the extensive literature for uniform temperature heaters does consider this deviation in great detail.

Baker (1972, 1973) assumed a uniform temperature chip and suggested that the leading edge effect is similar to that occurring in forced convection. This explanation does not seem to be correct.

Scherberg (1962) has called attention to the inadequacy of the boundary layer similarity solution in the vicinity of the leading edge of real heaters. According to this simplified theory, the isotherms converge at the leading edge and an infinite heat transfer coefficient is predicted at this point. In reality, there is upstream conduction to nose pieces or, in the present case, the substrate. Furthermore, in this region of very low velocity, upstream conduction in the fluid is significant. The main effect is starting of the free convection flow below the heater; the velocities at the heater are higher, but the effect decreases with increasing distance from the leading edge. Scherberg (1962, 1964, 1965) obtained integral solutions that incorporated these effects; however, the emphasis was on the formidable mathematical details rather than predicting heat transfer coefficients.

Most investigators have considered only the fluid flow and not the conjugate problem involving the heater. Mathematically, the boundary layer solutions represent asymptotic solutions to governing equations that are valid at very large Grashof numbers. Accordingly, numerous perturbation solutions that are valid at small and moderate Grashof numbers have been attempted, e.g., Suriano et al. (1965). Increased heat transfer coefficients are predicted. Complications due to the discontinuous boundary condition at the plate edge are also recognized, e.g., Messiter and Linan (1976).

The most recent summary of the analytical situation is presented by Martynenko et al. (1984). As shown in Fig. 7, the average predicted coefficients (perturbation solution) for a uniform wall temperature plate increase when the interaction with the external flow is taken into account and increase further when the upstream induced flow, due to conduction in the fluid, is taken into account. Trailing edge and wake effects reduce the heat transfer coefficient, an effect that is opposite to that predicted by Messiter and Linan (1976). In any event, there is ample theoretical evidence for increased heat transfer coefficients and, as shown in Fig. 7, the data seem to support predictions. The origin of these data is not noted by Ede (1967); however, the other experimental evidence is considerable.

Goldstein and Eckert (1960) observed that the temperature of a uniformly heated plate, as obtained by an interferometer, did not agree with boundary layer predictions near the leading edge. This was attributed to conduction to the electrical connections, and the leading edge data were ignored when the comparison with boundary layer theory was made. Eichhorn (1962) found that the free convection boundary layer originated below a uniform temperature plate, due to heating of the upstream insulating strip. Brodowicz (1968) studied uniform temperature plates with various leading edge geometries. He confirmed establishment of free convection upstream of the normal heated surface, but did not report heat transfer coefficients. Gryzagoridis (1971) obtained local heat transfer coefficients interferometrically that conclusively demonstrated the increase in heat transfer coefficient at low Grashof number.

Qualitative experiments were conducted as a part of the present program. Dye was injected into the water with near-zero velocity at the nose of the heater. The dye streamers confirmed that there was an upstream velocity at the leading edge due to conduction to the substrate and fluid.

Correlation of the Width Effect. Although three-dimensional effects have been observed with large plates, no analyses or correlations have been proposed. In their tests of large, uniformly heated, vertical plates, Fujii and Imura (1972) observed that wall temperatures at the center were higher than toward the sides. Wall temperatures at the sides were measured at 15 mm (100 mm × 50 mm high) and 20 mm (150 mm × 300 mm high) from the side edges. They speculated that this was due to transverse conduction in the fluid.

Oosthuizen (1965) observed that the average heat transfer coefficients for a vertical, isothermal heater (203 mm × 813 mm high) in air were higher than the predicted values. This was attributed to width effects even though the heater was quite wide. The width enhancement of the heat transfer coefficients was smaller as Ra increased. He correlated the width effects with nondimensional Ra based on the width. He further confirmed these effects with two isothermal heaters (254 mm high, 203 mm and 762 mm wide) (1967). Data for the 203-mm-wide heater were higher than those for the 762-mm-wide heater. Recently, Oosthuizen and Paul (1985) numerically solved the boundary layer equations with additional terms for the transverse direction in the momentum and energy equations. In general, the width effects observed by Oosthuizen are qualitatively similar to the results of the present study. However, it is difficult to make use of his results due to the very large wide heaters used as compared with the present heaters.

Induced flow at the sides of the present small heaters was also observed with side injection of dye. A Bernoulli effect due to lowering of pressure in the plume induces a flow from the sides of the heater.

The width effect depends on the relation of the transverse conduction heat transfer to the energy convected in the ver-

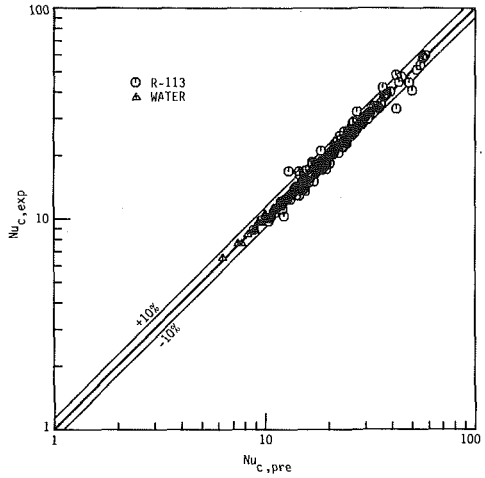

Fig. 9 Comparison between predicted and experimental Nusselt number

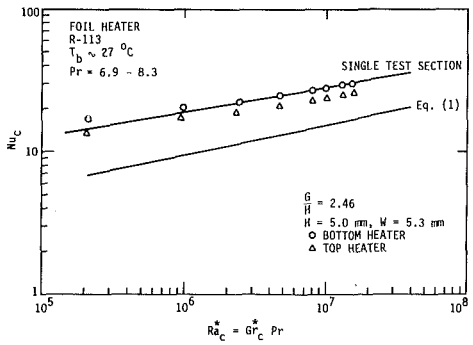

Fig. 10 Typical data for two flush in-line heaters

tical direction. The trends shown in Figs. 5 and 6 are expected; that is, the Nusselt number increases as the width decreases, but the percentage increase is less as the Rayleigh number increases.

A correlation of the width effect was attempted using Ra_w^* based on the width as supported by Oosthuizen and Paul (1965, 1967, 1985). The Churchill-Usagi (1972) technique and Marquart nonlinear regression (Statistical Analysis System package) were used to generate the correlations. For R-113

$$\frac{Nu_c}{Nu_{c,s}} = \left[1 + \frac{362.5}{Ra_w^{*0.2732}}\right]^{0.4752} \tag{2}$$

For water

$$\frac{Nu_c}{Nu_{c,s}} = \left[1 + \frac{2.234}{Ra_w^{*0.08862}}\right]^{1.077} \tag{3}$$

The data are compared with this correlation in Fig. 8. The main problem with this type of correlation is lack of agreement with the boundary layer solution $Nu_{c,s}$ for wide heaters, due to leading edge effects mentioned above.

The experimental results show that the width effect is negligible at about 70 mm. The width was nondimensionalized by dividing it by this asymptotic width. This nondimensionalized width is adopted as the parameter characterizing the conduction effect. Another form of the correlation is chosen as

$$Nu_c = \alpha\ Ra_c^{*\delta} \tag{4}$$

The values of α and δ were evaluated by the Churchill-Usagi (1972) technique so that the Nusselt number approaches the limiting value for $W = 70$ mm as the width is increased. The optimized constants and exponents were obtained for R-113 as

$$\alpha = 0.906\left[1 + \frac{0.0111}{(W/W_\infty)^{3.965}}\right]^{0.2745} \tag{5}$$

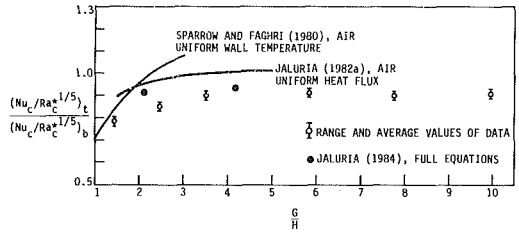

Fig. 11 Heat transfer coefficient ratios for two flush in-line heaters (numerical studies represent average values)

$$\delta = 0.184\left[1 + \frac{2.64 \times 10^{-5}}{(W/W_\infty)^{9.248}}\right]^{-0.0362} \tag{6}$$

where

$$W_\infty = 70\ \text{mm}$$

and for water as

$$\alpha = 0.906\left[1 + \frac{0.09886}{(W/W_\infty)^{4.08}}\right]^{0.04654} \tag{7}$$

$$\delta = 0.184\left[1 + \frac{2.219 \times 10^{-9}}{(W/W_\infty)^{9.834}}\right]^{-0.003966} \tag{8}$$

In formulating the correlation for water, 70 mm was again taken as the limiting value. Since actual data were not available for $W = 70$ mm, it was assumed that the offset from the similarity solution was the same as for R-113, i.e., 20 percent.

The comparison between predicted and experimental Nu_c is shown in Fig. 9. More than 95 percent of the data are within ± 10 percent of the correlation. It was not possible to obtain a single correlation for both R-113 and water. The reasons for this are not clear at the present time. More work with additional fluids is required as it would be desirable to have a general correlation. In any event, The R-113 correlation should be valid for the dielectric fluids of interest in immersion cooling of microelectronic components.

Arrays of the Flush Heaters. An in-line array of two test sections was tested with the variation of distance between the heating surfaces ranging from $G/H = 1.42$ to 9.94. Typical results for $G/H = 2.46$ are presented in Fig. 10. The top test section has a substantially lower heat transfer coefficient.

The ratios of $Nu_c/Ra_c^{*1/5}$ for the top and bottom test sections are plotted for all values of G/H in Fig. 11. This ratio compensates for the slight differences in heat flux and film fluid properties between top and bottom heaters, due to the different substrate heat loss correction. The average values and the ranges for all ratios tested are given; however, the variations of these ratios are very small. As the distance between the test sections increases, the heat transfer coefficient for the top surface increases until G/H is about 3.5. The heat transfer coefficient ratios then remain constant at about 0.9 for higher values of G/H.

The present results are compared with the analytical results for wide strips in air. Both Sparrow and Faghri (1980) and Jaluria (1982b) found that the average heat transfer coefficient on the upper surface exceeded that for the lower surface at large G/H. The results of Sparrow and Faghri (1980) and Jaluria (1981, 1982b) are quite different. The boundary conditions, uniform wall temperature and uniform heat flux, respectively, should not make a difference due to use of ratios. Furthermore, the use of the average values should not pose a problem as the average coefficient for small plates is close to the midpoint value. It is important to note that Jaluria's numerical results (1984), obtained by solving the more general equations, are lower than results obtained by solving the boundary layer equations (1981, 1982b). The implication is that as the assumptions for numerical methods become closer

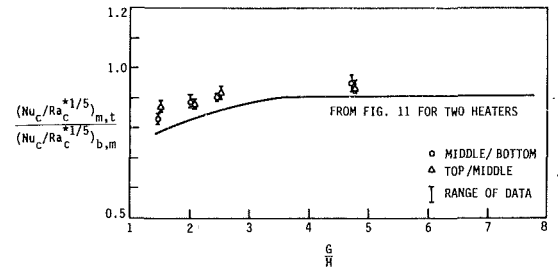

Fig. 12 Heat transfer coefficient ratios for three flush in-line heaters: middle/bottom and top/middle

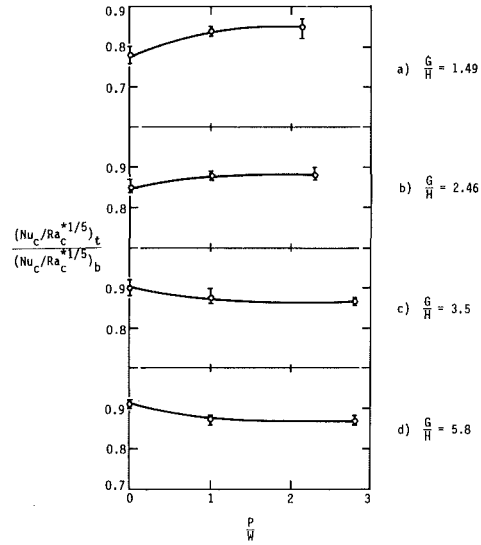

Fig. 13 Heat transfer coefficient ratios for staggered arrays of two flush surfaces

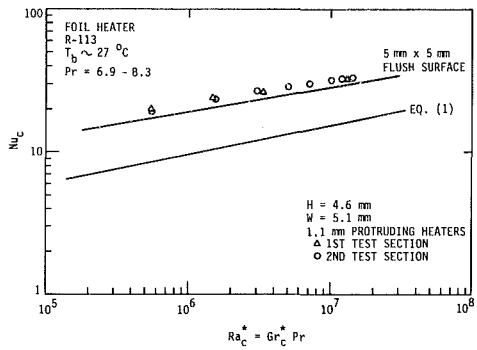

Fig. 14 Natural convection data for a single protruding heater

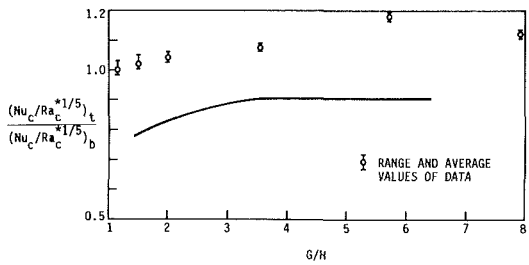

Fig. 15 Heat transfer coefficient ratios for two protruding in-line heaters

to real conditions, the numerical results become closer to the experimental results.

Physically, the heat transfer at the top surface is influenced by the velocity and temperature profiles of the plume from the bottom heater. Apparently, this influence extends beyond the maximum G/H considered in the present test. It is expected that the coefficient ratio will increase beyond $G/H \sim 10$ and eventually approach 1.0. We have no explanation for the intermediate asymptote of 0.9. Carey and Mollendorf (1977) reported a monotonic decrease in surface temperature above a flush heat source; hence, no intermediate asymptote is to be expected.

An in-line array with three test sections was studied with variation of the distance between heaters. The data for the bottom surface are similar to those for a single test section. The heat transfer coefficient clearly decreases with an increasing number of vertical heaters, but the decrease is less as the distance between heaters increases, as shown in Fig. 12. The ratios of coefficients for the middle to the bottom heater are in approximate agreement with the above results for two heaters. The differences could be due to the small construction differences noted earlier. The ratios of coefficients for top and middle or middle and bottom surfaces are included in Fig. 12. It is clear that for all cases considered, as the distance between heaters increases, the heat transfer coefficients for the upper surfaces increase.

The results for arrays of staggered surfaces are shown in Fig. 13 ($P/W=0$ represents the in-line case). In all tests, the bottom heater had about the same heat transfer coefficient while the top heater responded differently. When G/H is small and P/W is very large, the thermal plume from the bottom heater does not extend to the top offset heater, and the ordinate should approach unity. This suggests that if the data were extended to large P/W, the curves would rise and asymptotically approach 1.0.

At small G/H, the increase in the coefficient for the top heater could be due to removal of that heater from the high temperature of the plume. At large G/H, the plume temperature has decayed to the point where it has little effect; however, the beneficial transverse conduction heat transfer for the top heater is reduced by the lower plume. The heat transfer coefficient thus decreases.

Protruding Surfaces. As shown in Fig. 14, the natural convection data for the protruding surfaces are about 14 percent higher than those of the flush surfaces and about 120 percent higher than the predicted values. The increase in heat transfer coefficient above that for the flush surface is likely due in part to increased flow disturbance at the leading edge and trailing edge. The side flow hitting the heated surface could have a higher velocity for the protruding surface than for the flush surface. That would also increase the heat transfer coefficient.

Experimental results were obtained with two in-line protruding heaters with variation of spacing from $G/H=1.15$ to 7.93. The data for the bottom heater agreed well with results for the single test section. Heat transfer coefficients for the top surface are slightly higher than those for the bottom surface. The coefficient ratios for the top and bottom test sections are plotted for various values of G/H in Fig. 15. The average values and the ranges are given; once again the variation of these ratios is very small. As the space between test sections increases, the heater transfer coefficient of the top surface increases. It is quite significant that the top coefficient is always greater than the bottom coefficient; however, at large G/H it is expected that the ratio will return to unity. The enhancement is most likely due to the leading edge disturbance at the top heater.

Conclusions

The effect of test section width in natural convection has been documented with small heaters in R-113 and water. The heat transfer coefficient increases with decreasing width, with the effect greater in R-113 than in water. The data for the

widest test section are about 20 percent above the classical prediction. This is attributed to leading edge effects which have been documented analytically and experimentally. The present correlations of the data appear to be the first that have been attempted for small heaters.

An experimental study of arrays of small (5 mm × 5 mm) heaters was carried out in natural convection. The natural convection tests utilized two or three heaters in-line or staggered. With in-line flush heaters, the heat transfer coefficients for the upper heaters are lower than those for the bottom heater. As the distance between the heaters increases, the heat transfer coefficients for the upper surfaces increase. In a staggered array, the heat transfer coefficient for the top heater increases as transverse distance between heaters increases at small G/H; however, the opposite effect is observed at large G/H.

The heat transfer coefficient for a single protruding heater is about 14 percent higher than that for a flush surface. Heat transfer coefficients for the top heater in an array are higher than those for the bottom heater, in contrast to the results for the flush heaters, and increase as the distance between heaters increases.

Acknowledgments

This study was supported by IBM Corporation, Data Systems Division, Poughkeepsie, NY. The assistance of Mr. R. C. Chu and Dr. P. W. Ing of IBM is appreciated.

References

Baker, E., 1972, "Liquid Cooling of Microelectronic Devices by Free and Forced Convection," *Microelectronics and Reliability*, Vol. 11, pp. 213–222.

Baker, E., 1973, "Liquid Immersion Cooling of Small Electronic Devices," *Microelectronics and Reliability*, Vol. 12, pp. 163–193.

Brodowicz, K., 1968, "An Analysis of Laminar Free Convection Around Isothermal Vertical Plate," *International Journal of Heat and Mass Transfer*, Vol. 11, pp. 201–209.

Carey, V. P., and Mollendorf, J. C., 1977, "The Temperature Field Above a Concentrated Heat Source on a Vertical Adiabatic Surface," *International Journal of Heat and Mass Transfer*, Vol. 20, pp. 1059–1067.

Churchill, S. W., and Usagi, R., 1972, "A General Expression for the Correlation of Rates of Transfer and Other Phenomena," *AIChE Journal*, Vol. 18, pp. 1121–1128.

Ede, A. J., 1967, "Advances in Free Convection," *Advances in Heat Transfer*, Vol. 4, Academic Press, New York, pp. 1–64.

Eichhorn, R., 1962, "Measurement of Low Speed Gas Flows by Particle Trajectories: a New Determination of Free Convection Velocity Profiles," *International Journal of Heat and Mass Transfer*, Vol. 5, pp. 915–928.

Fujii, T., and Imura, H., 1972, "Natural-Convection Heat Transfer From a Plate With Arbitrary Inclination," *International Journal of Heat and Mass Transfer*, Vol. 15, pp. 755–767.

Fujii, T., and Fujii, M., 1976, "The Dependence of Local Nusselt Number on Prandtl Number in the Case of Free Convection Along a Vertical Surface With Uniform Heat Flux," *International Journal of Heat and Mass Transfer*, Vol. 19, pp. 121–122.

Goldstein, R. J ., and Eckert, E. R. G., 1960, "The Steady and Transient Free Convection Boundary Layer on a Uniformly Heated Vertical Plate," *International Journal of Heat and Mass Transfer*, Vol. 1, pp. 208–218.

Gryzagoridis, J., 1971, "Leading Edge Effects on the Nusselt Number for a Vertical Plate in Free Convection," *International Journal of Heat and Mass Transfer*, Vol. 16, pp. 517–520.

Hardwick, N. E., and Levy, E. K., 1973, "Study of the Laminar Free-Convection Wake Above an Isothermal Vertical Plate," ASME JOURNAL OF HEAT TRANSFER, Vol. 95, pp. 289–294.

Hwang, U. P., and Moran, K. P., 1981, "Boiling Heat Transfer of Silicon Integrated Circuits Chip Mounted on a Substrate," *Heat Transfer in Electronic Equipment*, HTD-Vol. 20, ASME, pp. 53–59.

Jaluria, Y., 1981, "Buoyancy-Induced Flow Due to Isolated Thermal Sources on a Vertical Surface," *Natural Convection*, HTD-Vol. 16, ASME, pp. 25–33.

Jaluria, Y., 1982a, "Buoyancy-Induced Flow Due to Isolated Thermal Sources on a Vertical Surface," ASME JOURNAL OF HEAT TRANSFER, Vol. 104, pp. 223–227.

Jaluria, Y., 1982b, "Natural Convection Flow Due to Line Thermal Sources on a Vertical Adiabatic Surface," *Proceedings, 7th International Heat Transfer Conference*, U. Grigull et al., eds., Hemisphere Publishing Corp., Washington, D.C., Vol. 2, pp. 147–152.

Jaluria, Y., 1984, "Interaction of Natural Convection Wakes Arising From Thermal Sources on a Vertical Surface," *Fundamentals of Natural Convection/Electronic Equipment*, HTD-Vol. 32, ASME, pp. 67–76.

Jaluria, Y., and Gebhart, B., 1977, "Buoyancy-Induced Flow Arising From a Line Thermal Source on an Adiabatic Vertical Surface," *International Journal of Heat and Mass Transfer*, Vol. 20, pp. 153–157.

Jensen, M. K., 1980, "Boiling Heat Transfer and Critical Heat Flux in Helical Coils." Ph.D. Dissertation, Iowa State University, Ames, IA.

Kishinami, K., and Seki, N., 1983, "Natural Convective Heat Transfer on an Unheated Vertical Plate Attached to an Upstream Isothermal Plate," ASME JOURNAL OF HEAT TRANSFER, Vol. 105, pp. 759–766.

Lieberman, J., and Gebhart, B., 1969, "Interactions in Natural Convection From an Array of Heated Elements, Experimental," *International Journal of Heat and Mass Transfer*, Vol. 12, pp. 1385–1396 .

Ma, C.-F., and Bergles, A. E., 1983, "Boiling Jet Impingement Cooling of Simulated Microelectronic Chips," *Heat Transfer in Electronic Equipment*, HTD-Vol. 28, ASME, pp. 3–10.

Martynenko, O. G., Berezovsky, A. A., and Sokovishin, Y. A., 1984, "Laminar Free Convection From a Vertical Plate," *International Journal of Heat and Mass Transfer*, Vol. 27, pp. 869–881.

Masters, G. F., 1972, "Arrays of Heated Horizontal Cylinders in Natural Convection," *International Journal of Heat and Mass Transfer*, Vol. 15, pp. 921–933.

Messiter, A. F., and Linan, A., 1976, "The Vertical Plate in Laminar Free Convection: Effects of Leading and Trailing Edges and Discontinuous Temperature," *Journal of Applied Mathematics and Physics*, Vol. 27, pp. 633–651.

Morcos, S. M., and Bergles, A. E., 1974, "Combined Forced and Free Laminar Convection in Horizontal Tubes," Technical Report ISU-ERI-Ames-74008, Iowa State University, Ames, IA.

Oktay, S., 1982, "Departure From Natural Convection (DNC) in Low-Temperature Boiling Heat Transfer Encountered in Cooling Micro-Electronic LSI Devices," *Proceedings, 7th International Heat Transfer Conference*, U. Grigull et al., eds., Hemisphere Publishing Corp., Washington, D. C., Vol. 4, pp. 113–118.

Oosthuizen, P. H., 1965, "An Experimental Analysis of the Heat Transfer by Laminar Free Convection From a Narrow Vertical Plate," *The South African Mechanical Engineer*, Vol. 14, pp. 153–158.

Oosthuizen, P. H., 1967, "A Further Experimental Study of the Laminar Free Convective Heat Transfer From Narrow Vertical Flat Plates in Air," *The South African Mechanical Engineer*, Vol. 16, pp. 182–184.

Oosthuizen, P. H., and Paul, J. T., 1985, "Numerical Study of Free Convective Heat Transfer From Narrow Vertical Flat Plates," *Proceedings, 10th Canadian Congress of Applied Mechanics*, pp. C23–C24.

Park, K.-A., 1985, "Heat Transfer Characteristics of Simulated Microelectronic Chips Under Normal and Enhanced Conditions," Ph.D. Dissertation, Iowa State University, Ames, IA.

Pera, L., and Gebhart, B., 1975, "Laminar Plume Interactions," *Journal of Fluid Mechanics*, Vol. 68, Part 2, pp. 259–271.

Scherberg, M. G., 1962, "Natural Convection Near and Above Thermal Leading Edges on Vertical Walls," *International Journal of Heat and Mass Transfer*, Vol. 5, pp. 1001–1010.

Scherberg, M. G., 1964, "Natural Convection from Wall Sections of Arbitrary Temperature Distribution by an Integral Method," *International Journal of Heat and Mass Transfer*, Vol. 7, pp. 501–516.

Scherberg, M. G., 1965, "Natural Convection at a Thermal Leading Edge on a Vertical Wall," *International Journal of Heat and Mass Transfer*, Vol. 8, pp. 1319–1331.

Sparrow, E. M., and Faghri, M., 1980, "Natural Convection Heat Transfer from the Upper Plate of a Colinear, Separated Pair of Vertical Plates," ASME JOURNAL OF HEAT TRANSFER, Vol. 102, pp. 623–629.

Sparrow, E. M., Patankar, S. V., and Abel-Wahed, R. M., 1978, "Development of Wall and Free Plumes Above a Heated Vertical Plate," ASME JOURNAL OF HEAT TRANSFER, Vol. 100, pp. 184–190.

Suriano, F. J., Yang, K.-T., and Donlon, J. A., 1965, "Laminar Free Convection Along a Vertical Plate at Extremely Small Grashof Numbers," *International Journal of Heat and Mass Transfer*, Vol. 8, pp. 815–831.

Tokura, I., Saito, H., Kishinami, K., and Muramoto, K., 1983, "An Experimental Study of Free Convection Heat Transfer From a Horizontal Cylinder in a Vertical Array Set in Free Space Between Parallel Walls," ASME JOURNAL OF HEAT TRANSFER, Vol. 105, pp. 102–107.

Vliet, G. C., 1969, "Natural Convection Local Heat Transfer on Constant-Heat-Flux Inclined Surfaces," ASME JOURNAL OF HEAT TRANSFER, Vol. 91, pp. 511–516.

Secondary Flow Effects in High Tip Speed Free Convection

P. W. Eckels
Mem. ASME

J. H. Parker, Jr.

A. Patterson

Westinghouse Research Laboratories,
1310 Beulah Road,
Pittsburgh, PA 15235

Experimental analyses of the effects of secondary flows on heat transfer in high tip speed rotating apparatus are not readily available. This paper provides data on the heat transfer within two different test modules which were rotated at high speed with the heat transfer surfaces perpendicular and parallel to the Coriolis acceleration. One module contained a heated wall and another a parallel plate free convection experiment. Uniform heat fluxes were maintained. Rayleigh numbers in excess of 10^{15} were achieved with liquid helium as the transfer medium. Some of the findings are that secondary flows can reduce heat transfer by as much as 60 percent in single-phase heat transfer, the transitions to fully turbulent flow are in agreement with existing prediction methods, the critical heat flux in two-phase flow boiling is significantly increased, forced convection correlations underpredict single-phase thermosyphon performance, and the usual nondimensional parameters of free convection establish similitude between various fluids and speeds. These results suggest that techniques used to enhance heat transfer in the rotating frame should be verified by tests in the rotating frame.

Introduction

The need for higher efficiency and power density gas turbines has placed greater demands on the available heat transfer surface in these machines. In his review of heat transfer in gas turbines, Taylor (1980) identifies several methods used to improve internal blade cooling, notes that it is largely an experimental science, and identifies a need for research to identify the effects of rotation on heat transfer. Metzger and Mayle (1983) review several techniques used for cooling blades and again note the experimental nature of the ongoing research studies. Several papers (Florschuetz et al., 1981; Bergles, 1969; Webb, 1978) present heat transfer data relevant to the techniques used to enhance internal blade cooling. However, there are few data in the open literature that experimentally address the effects of secondary flows and boundary layer stabilization on heat transfer and its augmentation in high tip speed apparatus.

In this paper we present data taken with a high tip speed apparatus using liquid helium as the heat transport media. Our objectives were twofold: to obtain data that was specifically related to the field windings of a superconducting generator and, equally important, to explore the effects of boundary layer stabilization and secondary flows in a geometry of more analytical interest, a set of heated parallel plates forming a radial channel. The channel walls were heated electrically and their temperature rise was measured as the walls were individually and simultaneously heated while oriented so that the Coriolis vector was either parallel to the wall or perpendicular to it in different tests.

The experiments were designed to address the following questions:

Is a buoyancy-induced flow analysis coupled through a heat transfer correlation such as Dittus–Boelter, see Eckert (1950) for example, adequate to predict the free convective flow and heat transfer in thermosyphons at high tip speeds?

Do the rotationally induced secondary flows always degrade heat transfer in free convection systems as they dissipate the buoyant energy available to circulate the bulk flow?

Do existing flow regime correlation methods (Lezius and Johnston, 1976) allow prediction of the regimes in which secondary flows and boundary layer stabilization will exist and allow the designer to adequately predict their existence and effects in a given geometry?

Do nondimensional representations of the flow and heat transfer allow accurate extrapolation of the performance of rotating systems from model tests through similitude?

Background

Secondary flows and boundary layer stabilization occur because of the well-known effects of conservation of angular momentum, Coriolis acceleration, and centrifugal acceleration. Although more subtle effects exist in rotating flows (Greenspan, 1968), these are not dominant in radial channels and influence only the overall module design. Conservation of angular momentum can cause the radially inward flowing fluid to rotate in the channel because of excess angular momentum if the aspect ratio of the channel is sufficiently large. If this excess angular velocity exists, it is evidenced in the Coriolis acceleration effects and flow stability. Unstable flow conditions caused by angular momentum exist when the local angular momentum is zero or opposite in sense to the system rotation (Monin and Yaglom, 1971).

Coriolis acceleration produces the most interesting effects on free convection of the three mechanisms. In an isothermal flowing channel, the velocity profile produces a Coriolis acceleration gradient that is very strong at high tip speeds. If the Coriolis vector is perpendicular to the channel wall with radial inflow, the boundary layer on the trailing wall is stabilized (thickened) and on the leading wall it is destabilized (thinned). Thickening of the boundary layer occurs because the fluid has excess tangential velocity as it moves radially inward and so the high radial velocity fluid tends to move away from the trailing wall. Mixing of the high radial velocity fluid into the boundary layer on the trailing wall is thus inhibited causing boundary layer thickening. By the same mechanism, mixing is promoted on the leading wall and produces thinning of the boundary layer. Because all of the high velocity fluid has this net body force in the direction of the leading wall, the physical situation is similar to that of forced convection across a horizontal plate heated from below and the thinning may be manifest in the formation of streamwise Taylor–Gortler (Schlichting, 1960) vortices as a secondary flow. For a more exact discussion of these phenomena the reader is referred to Johnston et al. (1972). In the corner flow region of the isothermal channel the velocity gradients produce a helical flow but it

Contributed by the Heat Transfer Division for publication in the JOURNAL OF HEAT TRANSFER. Manuscript received by the Heat Transfer Division December 3, 1985.

is not significant in these tests because the minimum channel aspect ratio is 20. Heating the walls in this case increases the body force on the fluid and amplifies the effects of the secondary flows when compared to isothermal flows.

With the Coriolis vector parallel to an isothermal wall, a helical vortex or roll cell flow pattern is formed, depending on the channel depth. Here again, if the walls are heated, the result is to increase the vigor of the secondary flow. Although friction and heat transfer are increased with this secondary flow pattern in forced flow (Mori, 1971), if buoyancy is the only energy source inducing flow, the helical vortex pattern dissipates some of the energy available to motivate the flow and the resulting effect on the heat transfer is uncertain.

The centrifugal acceleration produces a body force that is greatest within the heated boundary layer in radially inward free convection flows. This has the effect of accelerating or thinning the boundary layer in comparison to the thickness that would exist for the same bulk flow in forced convection and could be expected to increase the heat transfer over that which forced-flow correlations such as the Dittus-Boelter correlation would predict.

Hydrodynamic Stability

It is well known that turbulent energy production can obliterate organized secondary flows and some stability studies are well known for their ability to predict the breakdown of the flow or stabilized boundary layer. For geometries that have the Coriolis vector normal to the heated surface, Lezius and Johnson (1976) have produced a flow map derived from the observations of the forced flow of water in a rotating channel with the Coriolis vector normal to the wall. They deal specifically with the formation of secondary flows on the trailing wall and stabilization of the leading wall boundary layer with radial outflow. The secondary flows form on the leading wall with radial inflow. Considering the stabilized boundary layer on the trailing wall with radial inflow, it would be expected that boundary layer stability analysis (Chandrasekhar, 1961; Schlichting, 1960) of a wall cooled from below by forced convection would describe that condition. The Richardson number (Ri) is the appropriate parameter and the stratification breaks down when Ri $<$ 0.0417.

When the Coriolis vector is parallel to the wall, the secondary flow pattern and its driving force are very similar to those of forced flow in a curved pipe. This flow pattern persists for all Reynolds numbers although it is of lesser importance at high Reynolds numbers because the fraction of the flow area with a velocity deficit is reduced. Since the designer is generally seeking the most compact heat transfer surface, all three of these effects are likely to be encountered as channel dimensions are minimized.

Apparatus

The high tip speed rotating dewar used in these tests is described by Litz et al. (1982) and Eckels et al. (1985, 1986) and is only briefly reviewed here. The rotating apparatus consists of an outer dewar into which an inner dewar containing the test volume is inserted. Access to the experimental volume shown in Fig. 1 requires 4 hr enabling the test modules to be changed in one day. The rotating dewar cooling system can operate continuously in the self-regulating mode or in the batch fill mode at high internal pressure. An onboard microprocessor (Intel 8748) controls the data acquisition, sensing which experiment is active and processing its data into digital form for FM transmission from the rotating frame to a laboratory microcomputer. The onboard data acquisition program is interrupt driven through optical links to the heaters which are energized by the laboratory computer through slip rings. Four different heat transfer tests contained in modules can be placed in the dewar for test.

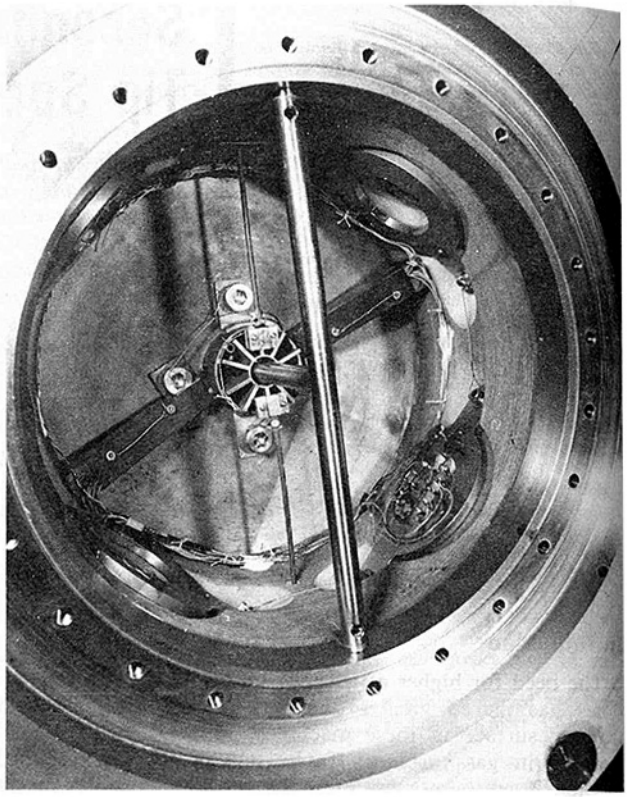

Fig. 1 Rotating dewar test chamber showing the parallel plate module at 4 o'clock

Winding Simulation Module. The winding simulation module is described in detail by Eckels et al. (1982, 1986) and is very briefly described here. In the module, three stacks of simulated copper conductors shown in Fig. 2 are separated by 0.381 mm G-10 CR strips that form cooling channels 7.62 mm wide. The three stacks of bars form three solid walls 91.0 mm long and 68.6 mm high radially. Silicon diode thermometers

Nomenclature

A_s = wetted cooling surface, m^2
c_p = constant pressure specific heat, kJ/kg-K
Gr = Grashof number = $r \cdot \omega^2 \cdot \beta \cdot \Delta T \cdot L^3 \cdot \rho^2 / \mu^2$
h = heat transfer coefficient, W/m^2-K
k = thermal conductivity, W/m-K
L = channel length = 0.0686 m
Nu = Nusselt number = $h \cdot L/k$
Pr = Prandtl number = $c_p \cdot \mu/k$
q'' = surface heat flux, W/m^2
r = radius, m
R = heater resistance, Ω
Ra = Rayleigh number = Gr•Pr
Ri = Richardson number = $-(r \cdot \omega^2/\rho) \cdot (d\rho/dy) / (dU/dy)_w^2$
U = helium velocity, m/s
V = heater voltage, V
y = coordinate normal to the wall, m
β = thermal coefficient of expansion, 1/K
ΔT = temperature difference, K
μ = dynamic viscosity, kg/m-s
ρ = density, kg/m^3
ω = angular speed, 1/s

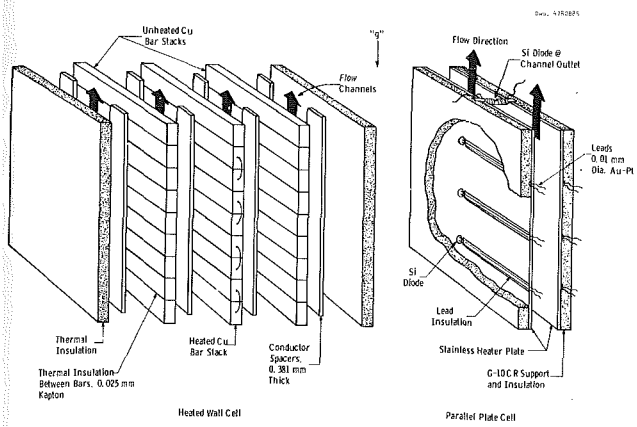

Fig. 2 Views of the heat transfer surfaces tested

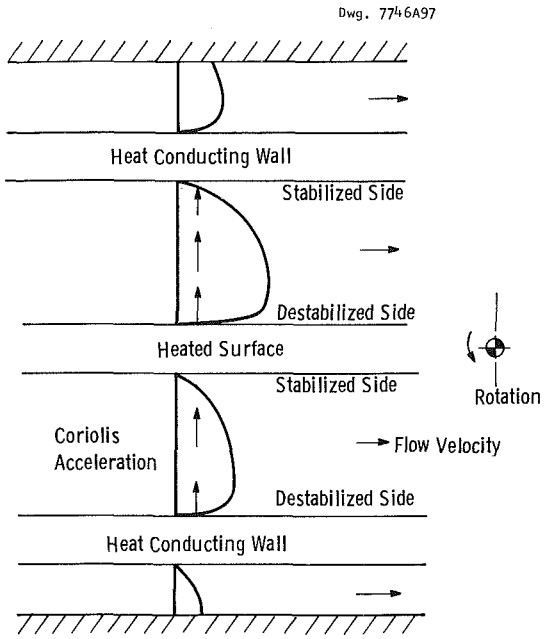

Fig. 3 Diagram of the velocity profiles in the straight section

are positioned in the first, middle, and last bar and in the helium inlet and outlet streams at midchannel. Only the center wall was heated, but the other two walls can conduct heat from the primary cooling channel over to the next set of channels as seen in Fig. 3. Extreme care was exercised to prevent the radial flow of heat in the copper walls and to prevent its flow from the ends of the bars. Summarizing the description, the winding simulation module contained a wall generating a uniform heat flux cooled by free convection radial channels.

Uniform Heat Flux Parallel Plate Module. Figure 1 shows the parallel plate module installed in the heat transfer rig for the test. The module contained two heating plates that were spaced 0.015 in. (0.38 mm) apart and which could be individually or simultaneously heated. These components are also shown in Fig. 2. Stainless steel (301) shim stock 0.025 mm (0.001 in.) thick was bonded to G-10 CR plates to provide the uniform flux plates and their thermal insulation. Differential thermal expansion between the stainless and G-10 was minimized by machining the flat G-10 surface at a suitable angle to the warp and fill laminations and the effects of the uncompensated cooldown contraction incompatibility remaining were minimized by bonding with an adhesive that retains some ductility at low temperature, Bostic 400. Si diode sensors were bonded to the stainless with GE lacquer before bonding the stainless to the G-10. Their leads were also bonded to the stainless over an insulating layer of cigarette paper. Because the thermal conductivity of the stainless is low, correction must be made for the temperature drop through the uniformly generating stainless plate. Offsetting the temperature drop error through the stainless is the sensor temperature drop due to heat conducted down the leads into the G-10 and from the sensor body to the G-10. The correction from surface to back wall (peak) temperature is given as $q'' \cdot t/(2 \cdot k)$ where $K = 0.00048T^{1.2}$, an effective value based upon computation of the various thermal resistances.

Experimental Technique

Following cooldown, the rotating dewar is filled with liquid helium and spun to establish an isothermal condition in the test chamber. The number of heat pulses in a 1-min run, their time interval and voltage are entered. Typically six 0.5-s pulses are initated in 1 min with various voltages (50, 75, 100, 150, 200, and 250 in ascending or descending sequence) applied to the heater. Conductor temperatures, dewar temperatures, fluid temperatures, voltage, and current are logged during the minute-long run. Mean pressure in the test section is calculated by assuming a linear decay of pool depth with time or from level measurements.

Reduction of the data to heat flux, heat transfer coefficient and temperature difference is accomplished by computing heat flux as $q'' = V^2/(R \cdot A_s)$. In computing heat flux, the conductor spacers are presumed adiabatic but the error due to that assumption is less than 1 percent. Heat transfer coefficient is defined as $h = q''/(\Delta T)$. Helium temperature is measured at the inlet and outlet. Temperature difference is taken as that between the mean copper and inlet helium. The data correlation variables used are derived from an early analysis by Eckert (1950) in which turbulent thermosyphon flows were found to be described by the nondimensional groups Nu and $Gr \cdot Pr$ or Ra. Closed-cell thermosyphon data and some free convection experiments have been correlated at high Gr numbers by $Gr \cdot Pr^2$ to eliminate the viscosity dependence. Because some of these data span the transposed critical and because of the associated strong Pr variations, we were able to evaluate the correlation forms $Gr \cdot Pr$ versus $Gr \cdot Pr^2$ for convection loops. Correlation using $Gr \cdot Pr^2$ decreased the data correlation coefficient in this case. The thermodynamic condition at which properties should be evaluated is not clearly defined by existing experiments. Constant wall temperature natural draft cooling channels have been found by Elenbaas (1949) to have the highest correlation coefficient using wall temperature for all properties excepting the coefficient of thermal expansion, which is evaluated at the inlet fluid temperature. That method is used in this presentation of the data. Another consideration in compressible fluid thermosyphon analysis in the rotating frame is that adiabatic expansion and compression of the flowing coolant produce fluid temperature changes. Compression temperature rises are eliminated by the rotating rig's copper heat exchanger but radial inflow adiabatic expansion decreases the temperature between channel inlet and outlet by 0.2 K (McCarty, 1972). Because it is of little consequence no attempt has been made to isolate and eliminate that effect.

Experimental Results

The winding simulation tests were quite hardware specific, but still much information of a general nature can be gleaned from the data. Of more analytical interest are the tests using parallel plates, which are designed to simulate a geometry frequently used in the analysis of convective flows. One of the most important factors in these tests is the very strong influence of the compressibility of liquid helium (McCarty, 1972) on the data which is particularly evident when boiling

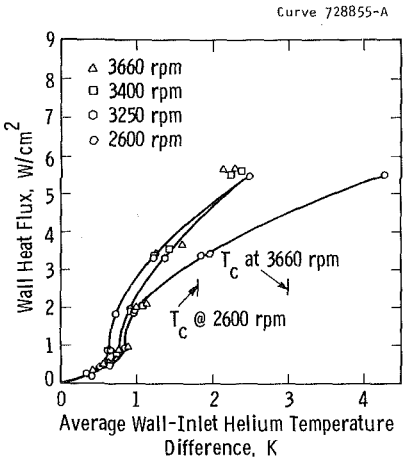

Fig. 4 Heat flux versus temperature difference for the winding straight section for several speeds

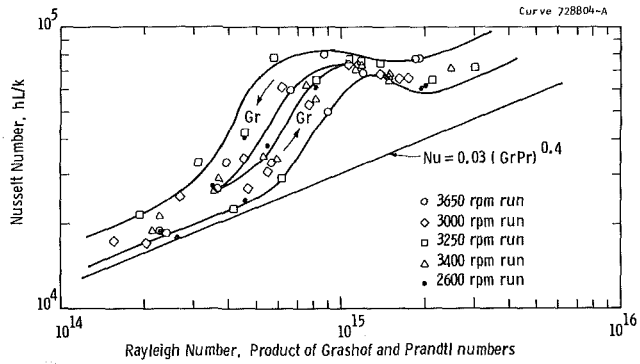

Fig. 5 Correlation of heat transfer in the winding straight section; Coriolis vector is perpendicular to the heated surface

occurs or the transposed critical trajectory of thermodynamic states is closely approached within the test module. The large density changes experienced by the fluid tend to emphasize the secondary effects of rotation on the flow patterns. Fortunately, the variety of thermodynamic conditions in these tests includes boiling, near critical, and also supercritical data so the heat transfer in each mode can be compared.

Coriolis Vector Normal to the Heated Wall. In the winding straight section, the Coriolis acceleration is perpendicular to the heated surface as shown in Fig. 3. Considering for a moment isothermal flow, the trailing side of the channel is stabilized (tending toward laminar flow) and the leading side is destabilized and tends to form streamwise Taylor–Gortler vortices. Heating the wall intensifies both of these phenomena. Although it is not possible to a priori predict the effect of streamwise vortices on heat transfer, stratification will reduce the heat transfer coefficient because heat transmitted from both sides of the heated surface encounters a stabilized boundary layer eventually (see Fig. 3), so a laminar-turbulent transition is expected in the heat transfer data.

Figure 4 shows the heat flux from the wetted surface versus temperature difference for several families of velocity. Features of the plot are indications of repeatability from the low ΔT data, the strong nonlinear variations in q'' versus ΔT, and the span of the transposed critical temperatures. The temperatures with the lowest signal-to-noise ratio are the low values of ΔT and these group exceedingly well. In Fig. 4 we see very strong nonlinear variations in q'' versus ΔT which can be typical of data spanning the transposed critical or data recording a transition in flow regime. Shown on Fig. 4 is a band indicating the range of transposed critical temperatures encountered in these experiments. The occurrence of the steep

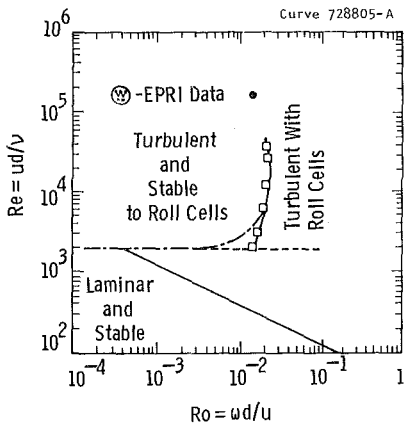

Fig. 6 Neutral stability boundary for laminar Poiseuille and turbulent channel flow (two-layer model): □, calculated neutral states; — - —, estimated neutral states; for Lezius and Johnston (1976)

rise in q'' precedes the approach to the transposed critical band, indicating a probable transition in the flow regime to full turbulence. This conclusion is supported by the high-speed data which are not influenced at all by the transposed critical region but which nevertheless display the characteristic transition.

Figure 5 shows the data of Fig. 4 correlated by the variables Nu and Ra. Shown in the same figure is the linearized equation of performance of the thermosyphon computed by conventional buoyancy induced circulation techniques (Eckert, 1950). The circulation computation is for a rectangular channel with three sides adiabatic and one long side heated, but it differs from the actual test channel which transfers heat through the opposite wall to a channel beyond. If the heat transfer to the second channel is impedance free, an increase of 40 percent over the adiabatic wall computation might be expected, thus explaining some of the theory–measurement difference. The most striking feature of the data is the hysteresis type loop generated by increasing and decreasing heat flux to vary Gr. As heat flux is increased, the lower curve is generated with a steep rise as the flow becomes fully turbulent. Decreasing heat flux generates the upper curves because turbulence persists in the channel for the 10 s between pulses despite all thermometers indicating thermal equilibrium for 8.5 s. If pulses are initiated 20 s apart, the lower curve is retraced as heat flux is decreased. Persistence of the turbulence is attributed to the very low viscosity of liquid helium (McCarty, 1972). The steep rise accompanying the turbulent transition goes well above either correlation line to a possible correlation that may be 25 percent higher than the lower line. This is the result of thinning of the boundary layers by the high ambient g field of rotation.

Another interesting aspect of the data is the comparison of the transition indicated by heat transfer with existing theory and experiment. Figure 6 is reproduced from Lezius and Johnston (1976) and indicates by a solid circle our estimate of the transition point at 3650 rpm ($Ra = 6 \times 10^{14}$). Considering the approximate computation scaling and nonsmooth inlet, the comparison is fortuitous.

Coriolis Vector Parallel to the Heated Wall. In the winding end turn region the Coriolis vector is oriented transverse to the flow and parallel to the heated surface. If the turbulent energy production is not large enough, a longitudinal helical vortex secondary flow is formed. Isothermal channels form a vortex pair but heating one wall and cooling the opposite results in a dominant vortex. Thus, similar but more vigorous vortices occupying nearly the full channel are to be expected with the Coriolis vector parallel.

Figure 7 shows the heat flux versus mean wall-inlet helium

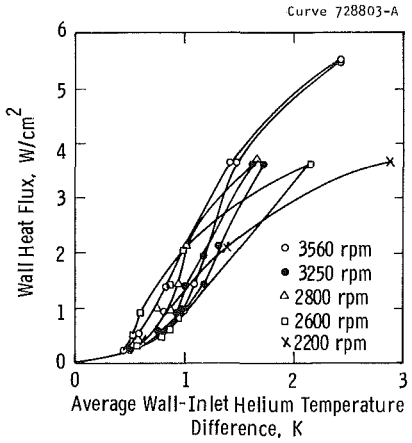

Fig. 7 Heat flux versus temperature difference for the winding end turn section for several speeds

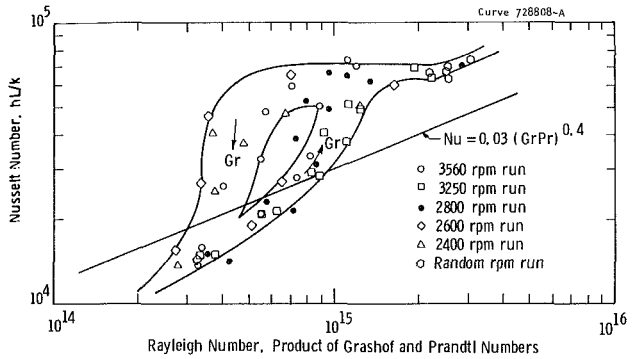

Fig. 8 Heat transfer correlation for the end turns; Coriolis vector is transverse to the flow and parallel to the heat surface

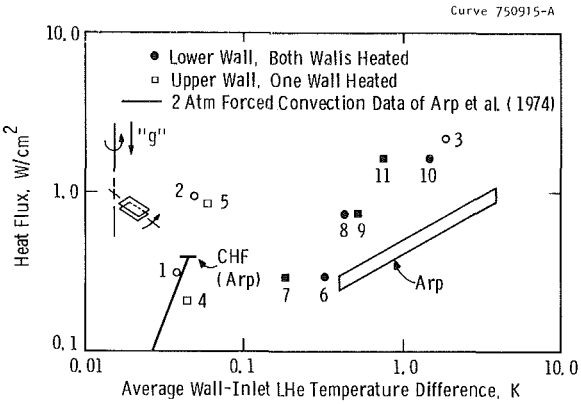

Fig. 9 Rotating, parallel plate free convection heat flux versus temperature difference at 2500 rpm; average pressure = 2 atm; Coriolis vector is parallel to the heated surface

temperature difference for various angular speeds. Results similar to the perpendicular Coriolis vector case (Fig. 4) are seen. Figure 8 is the correlation Nu versus Ra and it is quite different from the straight section. At the lower Ra numbers, secondary flows reduce the heat transfer remarkably. The data seem to approach the turbulent natural convection correlation, $Nu = 0.13\ Ra^{0.3}$. According to McAdams (1954), turbulent natural convection would be the minimum heat transfer coefficient obtained in mixed flow in this case.

At higher Ra numbers the data seem to converge to a fully turbulent correlation similar in slope and magnitude to that with the normal Coriolis vector. This is expected for cases where turbulent energy production fully mixes the flow and the boundary layer is thinned by the high ambient g field. The data at high Ra number are again insufficient to demonstrate a unique correlation of all speeds.

Between the extremes again we see the hysteresis type curve produced with increasing and decreasing Ra numbers (heat rate is the only variable in each run). The transition to turbulence occurs with similar conditions as the straight section and again there seems to be a rise of Nu number above the turbulent correlation value; perhaps because of fluid property changes traversing the transposed critical. A less abrupt change to turbulence is seen with increasing heat flux in this data set and it is because the helical secondary flow is not associated with a stability type transition but is more of a diminishing of importance of the secondary flow as the channel turbulent velocity profile becomes more uniform. In this case the hysteresis loop is more prominent because the secondary flows are more persistent. It should be noted that all of the speed curves except 3560 rpm tend to shift to the right with increasing speed and tend to diminish the abruptness of the transition. The reason for the departure of the 3560 rpm data from the general trend is not known but it could be related to more vigorus turbulent energy production at higher speed.

Coriolis Vector Parallel to the Heated Channel. The uniformly generating, parallel flat plate tests were run only with the plates orthogonal to the rotating axis. With the shaft vertical, one of the plates is cooled from below and the other one is cooled from above, similar to the end turn orientation of the winding cell. Unfortunately, due to funding limitations, the program ended before the parallel plates could be tested with the Coriolis vector perpendicular to the walls. However, as will be seen, the data from the two modules concerning flow regimes are very similar; however, a direct comparison of the stabilized surface heat transfer performance compared to the destabilized surface performance is unavailable.

In this data set, the major secondary flow expected is a helical flow, either single or double with one or two sides heated, respectively. Generally speaking, the secondary flow will persist to higher velocities with the lower side heated because gravitational buoyancy favors that flow. With two sides heated the space for the flow is halved, thus reducing the impact of the secondary flow. It must also be remembered that with the channel major dimension aligned with the plane of rotation, the flow can rotate excessively as it moves radially inward because of conservation of angular momentum. To the degree that excessive rotation occurs, the Coriolis induced secondary flows are enhanced or diminished.

The channel tests were run after the winding tests and methods were changed slightly to adapt to the knowledge gained in the earlier tests. In this case the heaters were programmed in a rising voltage sequence only. Because of the residual turbulence decreasing voltage sequences were avoided. Each heater was pulsed through its sequence and then both were pulsed together. At the time of these tests the bore of the rotor was operating at 0.5 atm and so the mean pressure in the channel at 2500 rpm was 2.0 atm. These results are discussed separately as phase change phenomena. Figure 9 displays the data in a conventional boiling format with some flow boiling results from Arp et al. (1974). Data points 1–5 are with single sides heated, while 6 and 7, 8 and 9, and 10 and 11 are pairs with two sides heated. Note that with single sides being heated, the side cooled from below has a higher temperature rise for a given heat flux despite the average angular acceleration of 1300 g. Even a weak earth gravity seems to influence the data! The critical heat flux exceeds 0.9 W/cm^2 with one side heated. With two sides heated the critical heat flux is apparently reduced by more than half indicating the expected nonlinearities in flow boiling driven by natural circulation. Note that the present nucleate boiling data and Arp's are similar despite the different geometries in the two tests and

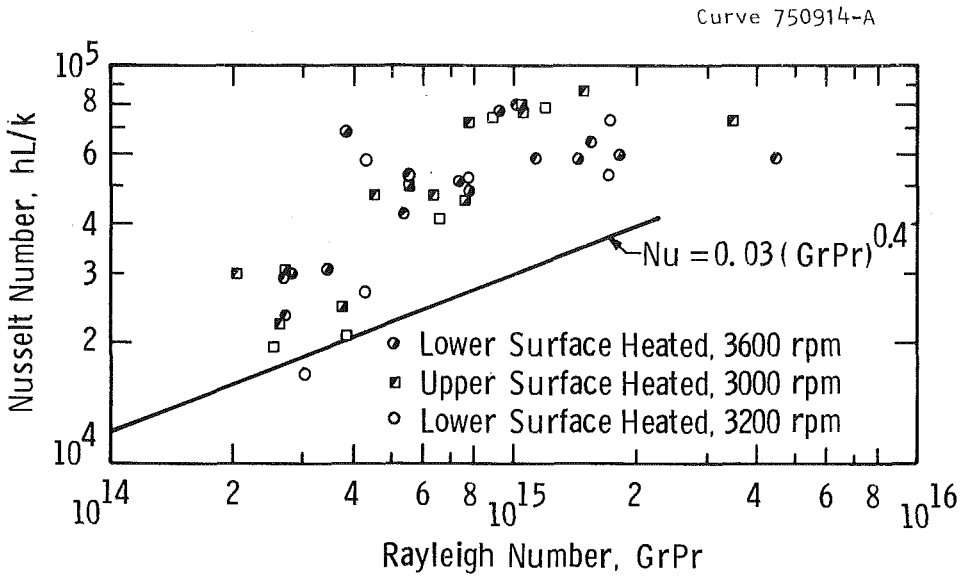

Fig. 10 Correlation of parallel plate free convection heat transfer data at high rotational speed

that the slope of the nucleate boiling curves determined by the two data sets (points 1-2 and 4-5) are equal.

Above the critical heat flux, the low heat flux data lie close to the curve of forced convection boiling from Arp (1974), but as the heat flux increases the high ambient g field enables higher heat fluxes to be transferred for the same temperature difference. This is not unexpected since buoyant forces tend to thin the boundary layer and improve heat transfer. Clearly the high g field has a strong influence on the vapor film next to the wall and precludes the computation of heat transfer performance from two-phase pressure drop and forced convection boiling correlations. The effect of the buoyancy or centrifugal acceleration on the heated fluid is also evident in the nucleate boiling data: The slope of the higher g boiling curve is larger.

The heat transfer runs at 3000, 3200, and 3600 rpm are in the supercritical or near critical domain. Figure 10 shows the remaining parallel plate heat transfer data as Nu number versus Ra number. The similarity of the shape of the parallel plate data to that of the winding data is obvious. Above, it was indicated that the departure of the data from the usual $Ra^{0.4}$ dependence is the result of the effects of secondary flows. Here again, the same variations exist but the data are much closer to the transposed critical trajectory of states because the dewar is operating in the self-regulating mode with reduced test chamber pressure. However, again it can be said that the 3600 rpm data do not approach the transposed critical, yet they are indistinguishable from the correlated form of the rest of the data. However, the two points furthermost to the right at 3000 and 3200 rpm are displaced because the averaging of temperatures for property evaluation resulted in the fluid properties of these two points being evaluated on the transposed critical and the high Prandtl number so obtained shifted the data to the right. No improved performance, i.e., higher Nu, near the transposed critical is detectable for these points because of the natural averaging of performance over the radial extent of the channel.

Several additional comments are noteworthy, but because of the difficulty of placing instrumentation in the high speed rotating cryogenic environment, insufficient data exists to take these additional comments out of the realm of useful speculation.

The high Ra number data group in Fig. 10 shows that the surface cooled from below yields the highest level of heat transfer and that the difference seems to be statistically significant. This is evidenced in the figure as the square point markers lying above the circles. The difference in performance of the two surfaces is consistent whether one or two surfaces are heated simultaneously and the reason for it is not known. However, if it is correct that earth gravity stabilizes the upper surface boundary layer against secondary flows and secondary flows are responsible for the performance differences, then it follows that the secondary flow must impede heat transfer. Examining the winding module data seems to allow this reasoning since the high Ra number Nu correlation generally lies above the lower Nu correlation as previously discussed.

The middle grouping of data shows no preference for a side with superior performance, but the lower grouping of data does show interesting, consistent characteristics when examined in terms of walls heated individually or simultaneously. When individually heated, the upper surface performance is inferior to that of the lower surface at low Ra. However, when simultaneously heated, there is a reversal in performance with the upper surface being consistently better in performance. With both sides heated the secondary flow associated with a given side can only operate over one-half of the channel width making the channel more stable against the formation of secondary flows. Under these circumstances, earth gravity may be more effective at limiting secondary flows in the upper half-channel and therefore improving the upper surface performance. Some support exists for this rationale in that the simultaneously heated surfaces consistently perform better than the individually heated surfaces where the Ra number allows the formation of strong secondary flows. Again, this analysis is speculative in nature.

Another interesting bit of data is the thermal response of the unheated wall under various conditions. At low Ra numbers, the opposite wall always shows a temperature rise associated with heat transferred from the bulk fluid at all three thermometer stations along the channel. From Fig. 10 it is evident that angular speed has less influence on Ra number than heat flux because each grouping of points corresponds to a heat rate and each speed is represented throughout that grouping. At low Ra, i.e., low heat flux, the rise of the opposite wall is uniform and about 50 percent of the average rise of the heated wall. At intermediate Ra numbers, the rise of the opposite wall is reduced to 10 to 20 percent of that of the heated wall and a linear increase along the channel is observed. This may indicate that turbulent energy production is reducing the significance of the secondary flows. At the higher Ra numbers, the first two thermometer stations located at 25 and

50 percent of the channel length on the opposite unheated wall drop in temperature as would be expected of helium being adiabatically expanded as it flows radially inward. At high Ra numbers the third thermometer records an increase of about 10 percent of the heated wall rise. The intermediate and higher Ra number wall temperature variations are consistent with reduced boundary layer thickness which is typically proportional to $Gr^{-0.33}$. The uniformity of temperature of the unheated wall at low Ra numbers could be produced by the combination of secondary flows and counterrotation of the fluid in the channel caused by conservation of angular momentum.

Conclusions

Thermosyphons can be designed to transfer heat at rates well in excess of natural convection limits, but data reported here show that under certain conditions the effects of Coriolis acceleration can reduce heat transfer in rotating channels by as much as 60 percent. Conventional buoyancy-induced flow analysis and conventional heat transfer correlations for supercritical flow provide a good indicator of heat transfer coefficients in rotating thermosyphons if regimes of strong secondary flow are avoided, but conventional heat transfer correlations do not adequately describe the thinning of the boundary layer produced by high rotational g fields and the resulting improved heat transfer of high tip speed surfaces.

These data indicate that the regimes of secondary flow can be predicted in high tip speed apparatus and that the secondary flows degrade heat transfer. The worst degradation of heat transfer occurs with the Coriolis vector parallel to the heated surface indicating that designers should avoid that geometry if possible.

Turbulence is shown to exist in liquid helium filled channels for more than 10 s after the turbulence generating mechanism has ceased.

Nucleate boiling in high tip speed environments is minimally influenced by the g field when compared to forced flow boiling except that the critical heat flux is increased. Note that these tests were run with LHe, a relatively low liquid–vapor differential density fluid. Film boiling is considerably improved by the high tip speed environment at higher superheats.

Correlation of these data is not improved by using $Gr \cdot Pr^2$ instead of $Gr \cdot Pr$. Occasionally $Gr \cdot Pr^2$ is used as a correlating parameter for turbulent flow because it eliminates the viscosity parameter from the Rayleigh number.

Acknowledgments

The authors express their appreciation for cofunding of this program by the Electric Power Research Institute and the Westinghouse Electric Corporation Steam Turbine Generator Division under contract number RP 1473-1.

References

Arp, V., Girratano, P. J., Hess, R. C., and Jones, M. C., 1974, "Heat Transfer in Pulsed Superconducting Magnets," National Bureau of Standards Interim Report, NBSIR 74-363, Jan.

Bergles, A. E., 1968, "Survey and Evaluation of Techniques to Augment Convective Heat and Mass Transfer," *Progress in Heat and Mass Transfer*, Permagon Press, Vol. 1, p. 323.

Eckels, P. W., Buttyan, J., Parker, J. H., Jr., and Patterson, A., 1985, "Superconducting Generator Cooling System Simulation," *Cryogenics*, Vol. 25, No. 6, p. 471.

Eckels, P. W., Parker, J. H., Jr., Patterson, A., and Murphy, J. H., 1982, "Heat Transfer Correlations for a Cryostable Alternator Field Winding," *Advances in Cryogenic Engineering*, Vol. 27, R. W. Fast, ed., p. 357.

Eckels, P. W., Parker, J. H., Jr., and Litz, D. C., 1986, "Heat Transfer to Helium Fluid Under High Speed Rotation," EPRI Report No. EL-, Palo Alto, CA 94304, to be published.

Eckert, E. R. G., and Jackson, T. W., 1950, "Analytic Investigation of Flow and Heat Transfer in Coolant Passages of Free Convection Lqiuid-Cooled Turbines," NACA RM E50D25.

Elenbaas, W., 1949, "Dissipation of Heat by Free Convection, Parts I and II," Philips Research Report 3, N. B. Philip's Gloeilampenfabrfrieken, Eindhoven, The Netherlands.

Florschuetz, L. W., Truman, C. R., and Metzger, D. E., 1981, "Streamwise Flow and Heat Transfer Distributions for Jet Array Impingement With Crossflow," ASME JOURNAL OF HEAT TRANSFER, Vol. 103, p. 337.

Greenspan, H. P., 1968, *The Theory of Rotating Fluids*, Cambridge University Press, London.

Johnston, J. P., Halleen, R. M., and Lezius, D. K., 1972, "Effects of Spanwise Rotation on the Structure of Two-Dimensional Fully Developed Turbulent Channel Flow," *Journal of Fluid Mechanics*, Vol. 56, p. 533.

Lezius, D. K., and Johnston, J. P., 1976, "Roll-Cell Instabilities in Rotating Laminar and Turbulent Channel Flows," *Journal of Fluid Mechanics*, Vol. 77, p. 153.

Litz, D. C., Moore, W. G., Eckels, P. W., and Mallick, G. T., 1982, "High Tip Speed Test Rig to Study Natural Convection in Liquid Helium," *Advances in Cryogenic Engineering*, Vol. 27, R. W. Fast, ed., p. 799.

McCarty, R. D., 1972, "Thermophysical Properties of Helium-4 from 2 to 1500 K with Pressures to 1000 Atmospheres," National Bureau of Standards Technical Note 631.

Monin, A. S., and Yaglom, A. M., 1971, *Statistical Fluid Mechanics*, Translation edited by J. L. Lumley, MIT Press, Cambridge, MA, p. 97.

Mori, Y., Fukada, T., and Nakayama, W., 1971, "Convective Heat Transfer in a Rotating Radial Circular Pipe, 2nd report," *International Journal of Heat and Mass Transfer*, Vol. 14, p. 1807.

Schlichting, H., 1960, *Boundary Layer Theory*, McGraw-Hill, New York.

Taylor, J. R., "Heat Transfer Phenomena in Gas Turbines," ASME Paper No. 80-GT-172.

Webb, R. L., 1978, "Toward a Common Understanding of the Performance and Selection of Roughness for Forced Convection," ASME Paper No. 78-WA-61.

Combined Heat and Mass Transfer by Natural Convection in a Vertical Enclosure

O. V. Trevisan[1]

A. Bejan
Mem. ASME

Department of Mechanical Engineering
and Materials Science,
Duke University,
Durham, NC 27706

The phenomenon of natural convection caused by combined temperature and concentration buoyancy effects is studied analytically and numerically in a rectangular slot with uniform heat and mass fluxes along the vertical sides. The analytical part is devoted to the boundary layer regime where the heat and mass transfer rates are ruled by convection. An Oseen-linearized solution is reported for tall spaces filled with mixtures characterized by Le = 1 and arbitrary buoyancy ratios. The effect of varying the Lewis number is documented by a similarity solution valid for Le > 1 in heat-transfer-driven flows, and for Le < 1 in mass-transfer-driven flows. The analytical results are validated by numerical experiments conducted in the range $1 \le H/L \le 4$, $3.5 \times 10^5 \le Ra \le 7 \times 10^6$, $-11 \le n \le 9$, $1 \le Le \le 40$, *and* $Pr = 0.7, 7$. *"Massline" patterns are used to visualize the convective mass transfer path and the flow reversal observed when the buoyancy ratio* n *passes through the value* -1.

Introduction

The subject of this study is formed by what emerges as a new class of flows driven by buoyancy in closed cavities, namely, the natural circulation driven by density variations due to the combined presence of temperature and concentration gradients in the solution that fills the cavity. A fundamental investigation of the combined heat and mass transfer process effected by this class of flows is demanded by contemporary engineering questions such as the migration of contaminants through buildings, passive solar system components, shallow bodies of water, etc., and the role of convection during the growth of a crystal.

Review papers and monographs published during the last decade [1-4] show that the fundamental research devoted to natural convection in enclosures has focused exclusively on flows driven by the buoyancy effect due to temperature variations alone. The flows addressed in the present study are identified for the first time as an important research area by Ostrach [5] in his 1982 Keynote Paper in Munich. Consequently, the first and only study devoted to this topic was published not long ago by Kamotani et al. [6]. The experiments of Kamotani et al. [6] had as objective the mass transfer and flow pattern in shallow enclosures ($H/L = 0.13$-0.55) filled with one fluid ($Pr = 7$, $Sc = 2100$), in cases where the combined buoyancy effect is dominated by the buoyancy due to concentration gradients ($N = 4$-40, where N is the buoyancy ratio in a box with specified side-to-side ΔT and ΔC, $N = \beta_C \Delta C / \beta \Delta T$).

The combined heat and mass transfer enclosure flow considered in this study and by Kamotani et al. [6] is related to the established and very active area of "double-diffusive" convection research. The most recent review of this activity is the one published by Viskanta et al. [7], who stress that "the two requirements for the occurrence of double-diffusive convection are that the fluid contain two or more components with different molecular diffusivities and that these components make opposing contributions to the vertical density gradients." As a departure from the main focus of double-diffusive convection, our study deals with the phenomenon of natural convection in a vertical slot, where the combined buoyancy effect is due to the horizontal density gradient caused by heat and mass transfer from the side. Furthermore, in our study the buoyancy effects of mass transfer (concentration gradient) and heat transfer (temperature gradient) do not necessarily oppose one another; in other words, the value of the buoyuancy ratio n is not restricted to a narrow range around -1.

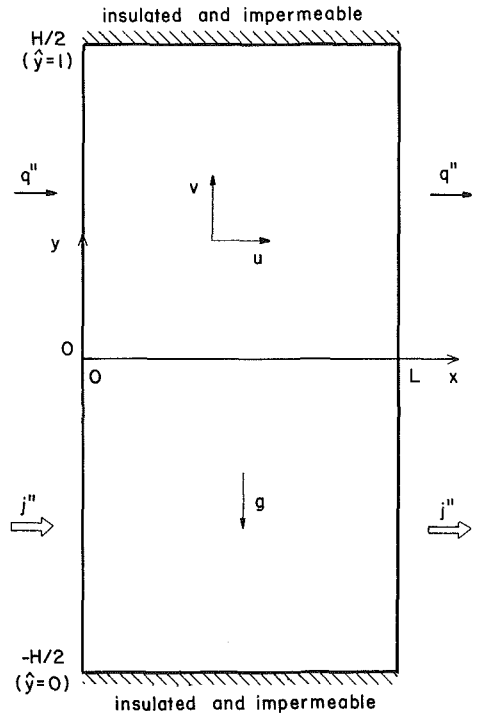

Fig. 1 Schematic of a vertical enclosure filled with fluid and subjected to heat and mass transfer from the side

The present study contributes concrete analytical and numerical solutions for calculating heat and mass transfer rates across tall vertical cavities, in a domain of Prandtl numbers, Schmidt numbers, and buoyancy ratios that is considerably wider than in [6]. In line with the overall engineering objective of this study, the simultaneous heat and mass transfer effect is modeled as one characterized by uniform fluxes (q'', j'', Fig. 1); this model is more appropriate for vertical cavities heated by radiation [8] and subjected to mass transfer where the resistance to mass transfer through the side wall is comparable with or greater than the resistance to mass transfer posed by the natural circulation.

[1] Present address: Department of Mechanical Engineering, University of Campinas ("UNICAMP"), 13100 Campinas, SP Brazil.

Contributed by the Heat Transfer Division for publication in the JOURNAL OF HEAT TRANSFER. Manuscript received by the Heat Transfer Division April 23, 1985.

Analysis of the Boundary Layer Regime

The fluid system selected for analysis is shown in Fig. 1. The top and bottom walls of the two-dimensional cavity are impermeable and adiabatic, while the vertical walls are impermeable and covered by uniform distributions of heat flux q'' and mass flux j''

$$q'' = -k\left(\frac{\partial T}{\partial x}\right)_{x=0,L} \tag{1}$$

$$j'' = -D\left(\frac{\partial C}{\partial x}\right)_{x=0,L} \tag{2}$$

The two analyses reported in this section are of the boundary layer type. The boundary layer-approximated equations that govern the steady-state conservation of mass, momentum, energy, and constituent in each vertical boundary layer region are

$$\frac{\partial u}{\partial x} + \frac{\partial v}{\partial y} = 0 \tag{3}$$

$$0 = \nu \frac{\partial^2 v}{\partial x^3} + g\beta \frac{\partial T}{\partial x} + g\beta_c \frac{\partial C}{\partial x} \tag{4}$$

$$u \frac{\partial T}{\partial x} + v \frac{\partial T}{\partial y} = \alpha \frac{\partial^2 T}{\partial x^2} \tag{5}$$

$$u \frac{\partial C}{\partial x} + v \frac{\partial C}{\partial y} = D \frac{\partial^2 C}{\partial x^2} \tag{6}$$

These equations have been further approximated by invoking the Boussinesq-incompressible fluid model, where β and β_C represent the thermal and concentration expansion coefficients (these and other symbols are defined in the Nomenclature). The inertia terms that usually appear on the left-hand side of equation (4) have been neglected based on the assumption that the fluid has a Prandtl number greater than one [9].

Oseen-Linearized Solution. An analytical solution for the combined heat and mass transfer problem can be constructed along the lines of the Oseen – linearized solution reported in [8] for the classical problem in which the buoyancy effect is due solely to temperature variations in the fluid. Due to space limitations and since the present heat and mass transfer solution is a generalization of the pure heat transfer solution [8], we report only the main steps and conclusions of the analysis.

The main features of the boundary layer regime revealed by the heat-transfer-driven flows of [8] are

1 a constant (altitude-independent) boundary layer thickness

2 a motionless and stratified core region

3 side wall temperatures that increase linearly with altitude at the same rate as the core temperature

Translated to the present problem, these features suggest the following transformation

$$T(x, y) = t(x) + T_0 + ay \tag{7}$$

$$C(x, y) = c(x) + C_0 + by \tag{8}$$

where the constants T_0 and C_0 are the reference temperature and concentration measured in the geometric center of the cavity, and a and b are the constant vertical gradients of temperature and concentration. The functions $t(x)$ and $c(x)$ account for the temperature and concentration profile shapes in the boundary layer region. Outside the boundary layer region that lines the left wall (Fig. 1) the vertical velocity v as well as functions t and c satisfy the condition

$$\lim_{x\to\infty} (t, c, v) = 0 \tag{9}$$

Subjecting the governing equations (4)–(6) to the transformation (7), (8) yields, in order,

$$0 = v''' + \frac{g}{\nu}(\beta t' + \beta_C C') \tag{10}$$

$$av = \alpha t'' \tag{11}$$

$$bv = Dc'' \tag{12}$$

Eliminating t and c between equations (10) – (12) we obtain

$$v^{IV} + \gamma^4 v = 0 \tag{13}$$

with the notation $\gamma = [g\beta a(1+n)/(\alpha\nu)]^{1/4}$, where n is the buoyancy ratio for a system with prescribed heat flux and mass flux, $n = \beta_C b\alpha/(\beta a D)$. The solution that satisfies equation (13), the no-slip boundary condition at $x = 0$, and equation (9) is

Nomenclature

a = core temperature gradient
b = core concentration gradient
B = parameter defined in equation (30)
c = concentration boundary layer profile
c_p = specific heat at constant pressure
C = concentration of constituent (i)
C_1 = constant
D = mass diffusivity of constituent (i) through the fluid mixture
f = similarity concentration profile
g = gravitational acceleration
Gr = Grashof number = Ra/Pr
H = enclosure height
j'' = mass flux from the side
k = thermal conductivity
L = enclosure thickness (horizontal dimension)
Le = Lewis number = α/D
M = massfunction, equations (45), (46)
n = buoyancy ratio = $\beta_c b\alpha/(\beta a D)$
Nu = overall Nusselt number, equation (23)
Pr = Prandtl number = ν/α
q'' = heat flux from the side
Ra = Rayleigh number = $g\beta q'' H^4/(\alpha\nu k)$
Sh = overall Sherwood number, equation (24)
t = temperature boundary layer profile
T = temperature
u, v = horizontal and vertical velocity components
u_C, v_C = velocity components in the concentration boundary layer region
u_0 = interfacial flow velocity (through the side wall)
x, y = horizontal and vertical coordinates
α = thermal diffusivity
β = thermal expansion coefficient
β_c = concentration expansion coefficient
γ = parameter = $[g\beta a(1+n)/(\alpha\nu)]^{1/4}$
δ_C = concentration boundary layer thickness
δ_T = thermal boundary layer thickness
η = similarity variable, equation (30)
ν = kinematic viscosity
ρ = density of fluid mixture
ψ = stream function
ω = vorticity function
$(\,)_0$ = reference values
$(\hat{\ })$ = dimensionless variables

$$v = C_1 \exp(-2^{-1/2}\gamma x) \sin(2^{-1/2}\gamma x) \tag{14}$$

The corresponding expressions for $t(x)$ and $c(x)$ are obtained immediately by integrating equations (11), (12) subject to conditions (9). The resulting expressions for $t(x)$ and $c(x)$ have the unknown constant C_1 as a factor: Two expressions for C_1 are obtained by subjecting $t(x)$ and $c(x)$ to the heat and mass transfer boundary conditions (1), (2)

$$C_1 = 2^{1/2}\frac{\gamma\alpha q''}{ka} = 2^{1/2}\frac{\gamma j''}{b} \tag{15}$$

in other words $a/b = \alpha q''/(kj'')$. In view of the centrosymmetry of the flow, temperature and concentration fields, the results of this entire analysis may be summarized as

$$T = \pm 2^{1/2}\frac{q''}{k\gamma}\exp(-2^{-1/2}\gamma x)\cos(2^{-1/2}\gamma x) + T_0 + ay \tag{16}$$

$$C = \pm 2^{1/2}\frac{j''}{D\gamma}\exp(-2^{-1/2}\gamma x)\cos(2^{-1/2}\gamma x) + C_0 + by \tag{17}$$

$$v = \pm 2^{1/2}\frac{\gamma\alpha q''}{ka}\exp(-2^{-1/2}\gamma x)\sin(2^{-1/2}\gamma x) \tag{18}$$

where the (+) and (−) signs differentiate between the left-side and the right-side boundary layer solutions (in the solution for the right side the horizontal coordinate x is measured from the right wall into the fluid).

Regarding the unknown core gradients a and b, it was shown in [8] that at any y, the vertical enthalpy flow must be balanced by thermal diffusion downward through the core

$$\int_0^L \rho c_p v T\, dx = \int_0^L k\frac{\partial T}{\partial y}\, dx \tag{19}$$

Condition (19), which is conceptually the same as the aggregate (heat and fluid flow) end condition proposed as improvement on the original Oseen-linearized solution to this problem [9, 10], yields

$$a = 2^{-1/4}\frac{q''}{k(\gamma L)^{1/2}} \tag{20}$$

The corresponding integral condition of zero net mass transfer in the vertical direction

$$\int_0^L vC\,dx = \int_0^L D\frac{\partial C}{\partial y}\, dx \tag{21}$$

yields

$$b = 2^{-1/4}\frac{j''}{D(\gamma L)^{1/2}} \tag{22}$$

The solution is now complete; however, an important limitation of this solution is brought to light by eliminating a and b between equations (15), (20), and (22). We obtain $\alpha = D$; in other words the Oseen-linearized solution is valid for fluids with a Lewis number Le = 1 and with an arbitrary buoyancy ratio n.

The engineering conclusion of the above analysis is one compact formula for the overall Nusselt number and the overall Sherwood number

$$\mathrm{Nu} = \frac{q''}{k\Delta T/L} = 2^{-3/2}\gamma L \tag{23}$$

$$\mathrm{Sh} = \frac{j''}{D\Delta C/L} = 2^{-3/2}\gamma L \tag{24}$$

where ΔT and ΔC are the side-to-side temperature difference and concentration difference (note that ΔT and ΔC are y independent). Recalling the definition of γ, equations (23) and (24) can be rewritten as

Table 1 Similarity concentration profile for heat-transfer-driven flows where Le >> 1 (the same as the similarity temperature profile for mass-transfer-driven flows where Le << 1)

η	f	f'
0.0	1.536	−1.000
0.5	1.046	−0.936
1.0	0.619	−0.755
1.5	0.304	−0.501
2.0	0.116	−0.257
2.5	0.033	−0.095
3.0	0.006	−0.023
3.5	0.001	−0.004
4.0	0.000	−0.000

$$\mathrm{Nu} = \mathrm{Sh} = 0.34\left(\frac{L}{H}\right)^{8/9}\mathrm{Ra}^{2/9}\,|1+n|^{2/9} \tag{25}$$

where Ra is the Rayleigh number based on imposed heat flux, $\mathrm{Ra} = g\beta q'' H^4/(\alpha\nu k)$.

Similarity Solution. In view of the Le = 1 limitation of the preceding theory, it is useful to provide an alternative analytical description of the effect of Lewis number on quantities such as Nu and Sh. We found that such a description is possible in the two buoyancy ratio extremes, in so-called heat-transfer-driven flows ($|n| << 1$) and in mass-driven-flows ($|n| >> 1$). The mathematical course followed by the analysis of the two extremes is the same in both cases, therefore in the interest of brevity we illustrate only the analysis of heat-transfer-driven flows.

In heat-transfer-driven flows the distribution of constituent does not influence the flow pattern and the heat transfer rate. The flow and temperature fields in this extreme are obtained by setting $n = 0$ in the preceding solution. Relative to the boundary layer structure assumed for the flow and temperature fields, the thickness of the concentration boundary layer will be influenced by the Lewis number α/D. Consider the range of values Le >> 1 describing concentration boundary layers that are much thinner than the driving thermal boundary layer. Inside the concentration boundary layer the vertical velocity distribution approaches

$$v = \left(\frac{\partial v}{\partial x}\right)_{x=0} x \tag{26}$$

where $v(x)$ is given by equation (18). Therefore, in the limit Le → ∞ the problem of determining the concentration field and the mass transfer rate begins with substituting equation (26) and $u = 0$ in the constituent conservation equation (6)

$$(2^{1/4}\gamma^{5/2}\alpha L^{1/2})x\frac{\partial C}{\partial y} = D\frac{\partial^2 C}{\partial x^2} \tag{27}$$

This equation can be solved subject to conditions of uniform mass flux at $x = 0$, and uniform concentration $C = C_0$ outside the concentration boundary layer (this last condition is validated by numerical experiments for Le >> 1; e.g., Fig. 3*d*). The similarity formulation of the problem is

$$f''' + \frac{\eta^2}{3}f' - \frac{\eta}{3}f = 0 \tag{28}$$

$$f'(0) = -1, \qquad f(\infty) = 0 \tag{29}$$

where

$$\eta = \hat{x}(\hat{y}/B)^{-1/3}, \quad f = \frac{C - C_0}{j''H/D}\left(\frac{\hat{y}}{B}\right)^{-1/3}$$

$$\hat{x} = x/H, \quad \hat{y} = (y + H/2)/H, \quad B = 2^{1/4}\gamma^{5/2}\alpha L^{1/2}\mathrm{Le}H^2 \tag{30}$$

This problem was solved numerically using the fourth-order Runge–Kutta scheme and the standard shooting method. Equation (28) was integrated from $\eta = 0$ to $\eta > 10$ using as step size $\Delta\eta = 0.001$ and as shooting success criterion $f < 10^{-4}$. The

Table 2 Summary of analytical results and respective domains of validity (Pr > 1 fluids)

Analytical results		Domain of validity			
Nu	Sh	$\|n\|$	Le	Nu	Sh
equation (25)	equation (25)	$0-\infty$	1	$>>1$	$>>1$
equation (25)	equation (31)	$<<1$	$>>1$	$>>1$	$>>1$
equation (32)	equation (25)	$>>1$	$<<1$	$>>1$	$>>1$

solution is listed in Table 1. Of interest is the overall Sherwood number prediction made possible by this solution

$$\mathrm{Sh}=\frac{j''}{D\Delta C/L}=0.445\ \mathrm{Ra}^{5/27}\mathrm{Le}^{1/3}\left(\frac{L}{H}\right)^{58/54} \tag{31}$$

where, as before, ΔC represents the H-averaged concentration difference between the vertical sides of the enclosure.

The analogous analysis of mass-transfer-driven flows ($|n|>>1$) in the limit of relatively thin thermal boundary layers ($\mathrm{Le}<<1$) yields the overall Nusselt number expression

$$\mathrm{Nu}=\frac{q''}{k\Delta T/L}=0.445(\mathrm{Ra}\,|n|)^{5/27}\mathrm{Le}^{-1/3}\left(\frac{L}{H}\right)^{58/54} \tag{32}$$

The mass transfer rate in such flows is covered by the earlier result, equation (25).

In ending the analytical part of the present study, it is important to stress the "distinct boundary layer" assumption on which both analyses are based. Noting the diffusion-referenced definition of the Nusselt and Sherwood numbers, the distinct boundary layer assumption means $\mathrm{Nu}>>1$ and $\mathrm{Sh}>>1$. Table 2 directs the reader to the three regimes addressed analytically in this study and their respective (Nu, Sh) formulas.

Numerical Experiments

The objective of the numerical experiments conducted in the second part of this study was to demonstrate the validity of the analytical results summarized in Table 2. The dimensionless problem statement considered for numerical analysis is:

Equations

$$\mathrm{Gr}\left(\hat{u}\frac{\partial\hat{\omega}}{\partial\hat{x}}+\hat{v}\frac{\partial\hat{\omega}}{\partial\hat{y}}\right)=\nabla^2\hat{\omega}+\frac{\partial\hat{T}}{\partial\hat{x}}+n\frac{\partial\hat{C}}{\partial\hat{x}} \tag{33}$$

$$\hat{\omega}=-\nabla^2\hat{\psi} \tag{34}$$

$$\mathrm{Ra}\left(\hat{u}\frac{\partial\hat{T}}{\partial\hat{x}}+\hat{v}\frac{\partial\hat{T}}{\partial\hat{y}}\right)=\nabla^2\hat{T} \tag{35}$$

$$\mathrm{Ra\ Le}\left(\hat{u}\frac{\partial\hat{C}}{\partial\hat{x}}+\hat{v}\frac{\partial\hat{C}}{\partial\hat{y}}\right)=\nabla^2\hat{C} \tag{36}$$

Boundary Conditions

$$\hat{\psi}=\frac{\partial\hat{\psi}}{\partial\hat{x}}=0,\quad \frac{\partial\hat{T}}{\partial\hat{x}}=\frac{\partial\hat{C}}{\partial\hat{x}}=-1 \text{ at } \hat{x}=0,\ \frac{L}{H} \tag{37}$$

$$\hat{\psi}=\frac{\partial\hat{\psi}}{\partial\hat{y}}=0,\quad \frac{\partial\hat{T}}{\partial\hat{y}}=\frac{\partial\hat{C}}{\partial\hat{y}}=0 \text{ at } \hat{y}=0,\ 1 \tag{38}$$

Notation

$$\hat{x}=x/H,\quad \hat{y}=(y+H/2)/H,\quad \hat{u},\ \hat{v}=\frac{u,\ v}{\mathrm{Gr}\nu/H} \tag{39}$$

$$\hat{\omega}=\frac{\omega}{\mathrm{Gr}\nu/H^2},\quad \hat{\psi}=\frac{\psi}{\mathrm{Gr}\nu},\quad \hat{u}=\frac{\partial\hat{\psi}}{\partial\hat{y}},\quad \hat{v}=-\frac{\partial\hat{\psi}}{\partial\hat{x}} \tag{40}$$

$$\hat{T}=\frac{T-T_0}{q''H/k},\quad \hat{C}=\frac{C-C_0}{j''H/D} \tag{41}$$

It is worth noting that by writing $\hat{\psi}=0$ in equations (37) and (38) we have assumed that relative to the flow field the solid walls are impermeable (the same assumption is built into the analyses reported in the preceding section). In the concluding section of this paper we rely on scale analysis to show that the impermeable-wall feature of the flow field is not necessarily incompatible with the existence of mass transfer through the wall-fluid interface.

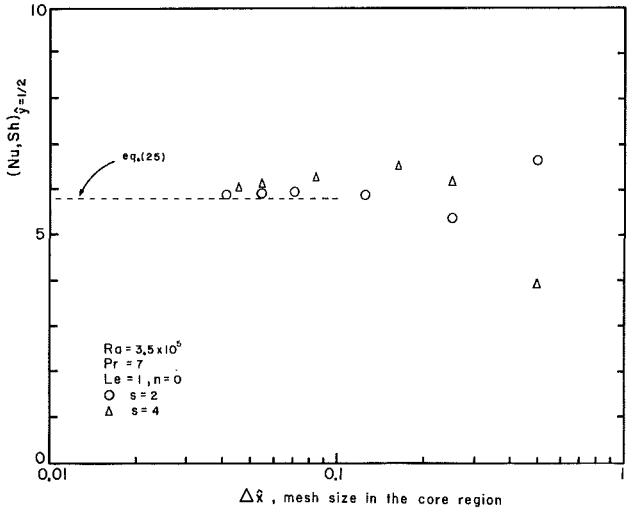

Fig. 2 The effect of mesh size on the accuracy of numerical heat and mass transfer calculations

The numerical method consisted of discretizing equations (33)–(38) using the control-volume formulation developed by Patankar [11]. The power-law scheme was used to calculate both the heat and mass fluxes across each of the control volume boundaries. A Gauss-Seidel iterative routine was employed to solve the discretized equations. The procedure of updating the values of $\hat{\psi}$, $\hat{T}$, and $\hat{C}$ was repeated until the following convergence criterion was satisfied

$$\frac{\sum_{ij}|\tau_{R+1}-\tau|}{\sum_{ij}|\tau_{R+1}|}<10^{-5} \tag{42}$$

with the subscript R representing the iteration order. Use of underrelaxation for the vorticity, the temperature, and the concentration was needed to obtain converged solutions. Suitable values for the relaxation parameters vary between 0.3 and 0.8 for the vorticity and between 0.5 and 0.8 for both concentration and temperature. In all the cases reported in the present study the agreement between the last two estimates of each of the overall Nusselt and Sherwood numbers was better than one percent. In the present formulation, the diffusion-referenced definitions (23), (24) are

$$\mathrm{Nu}=\frac{L}{H}\left(\int_0^1\Delta\hat{T}d\hat{y}\right)^{-1} \tag{43}$$

$$\mathrm{Sh}=\frac{L}{H}\left(\int_0^1\Delta\hat{C}d\hat{y}\right)^{-1} \tag{44}$$

Table 3 Summary of numerical results for natural convection in a cavity with combined heat and mass transfer (Le = 1, Pr = 7; the results in parentheses correspond to Pr = 0.7).

H/L	Ra ($\times 10^6$)	$n+1$	m/s	Nu, Sh	(Nu, Sh)$_{\hat{y}=1/2}$
1	0.35	0	32/4	1.04 (1.04)	1.05 (1.05)
		1		4.83 (4.78)	5.88 (5.82)
		±2		5.73 (5.72)	6.83 (6.87)
		±4		6.88 (6.76)	8.05 (7.92)
		±10		8.67 (8.44)	9.86 (9.55)
2	0.35	4	32/4	7.74	8.74
	0.70			9.19	10.24
	1.4			10.88	11.96
	3.5			13.51	14.58
	7.0			15.85	16.86
4	0.35	4	40/4	8.51	9.17
	0.70			10.12	10.88
	1.4			11.90	12.72
	3.5			14.70	15.58
	7.0			17.27	18.18

Table 4 Numerical results for heat-transfer-driven flows in fluids with large Lewis number ($n = 0$, $H/L = 1$, Pr = 7, Ra = 3.5×10^5; the results in parentheses correspond to Pr = 0.7)

Le	Nu	Sh	$\Delta C_{\hat{y}=1/2}$	$\Delta C_{\hat{y}=0,1}$	s
2	4.81 (4.78)	6.46 (6.47)	0.1340 (0.1325)	0.2173 (0.2173)	4
4	4.81 (4.78)	8.15 (8.17)	0.1104 (0.1088)	0.1733 (0.1737)	4
10	4.81 (4.78)	10.99 (11.01)	0.0837 (0.0824)	0.1322 (0.133)	4
20	4.77 (4.76)	13.93 (13.9)	0.0658 (0.0651)	0.1086 (0.1096)	5
40	4.70 (4.70)	18.00 (17.8)	0.0512 (0.0512)	0.0867 (0.0875)	7

The domain of Fig. 1 was decomposed into an array of $(m-2) \times (p-2)$ control volumes. The four boundaries were treated as strings of control volumes with zero thickness. The mesh size was nonuniform so that thinner control volumes could be placed closer to the walls. The width (or height) of a near-boundary control volume was equal to a fraction $1/s$ of the width (or height) of an interior control volume. The number of thinner control volumes placed near the boundaries was s. Therefore, in order to maintain m and p constant, the core region was covered by a grid that was coarser than the uniform grid with the same overall m and p values. Relative to uniform grids, the use of nonuniform grids with thinner near-wall control volumes improved the convergence of the numerical solutions.

The effect of mesh size on the converged solution is illustrated by the test presented in Fig. 2, where the abscissa parameter is the mesh size in the core region. Although a grid with a core mesh size as small as 0.05 (for example, one with $m = 28$ and $s = 4$, or one with $m = 24$ and $s = 2$) provided accurate results for overall Nu and Sh estimates, in this study we used $m = p = 32$ for square-shaped domains. For solutions in tall domains, $H/L > 1$, the number of control volumes in the vertical direction m was increased up to 44 in such a way that $(m-2s)/(p-2s)$ was always equal to H/L. Regarding parameter s, whose effect on accuracy is also illustrated in Fig. 2, its value was set high enough so that at least two control volumes were always located inside the thinnest boundary layer region.

Each flow is characterized by a set of five numerical values (Ra, Pr, n, H/L, Le): The flows selected for numerical analysis are intended to document systematically the effect of one dimensionless group at a time, and in this way to test the analytical arm of this study.

Table 3 summarizes the overall heat and mass transfer results obtained in a domain filled with a solution with Prandtl number of order one or greater (Pr = 0.7 and 7) and Lewis number equal to one. Shown in Table 3 are the effects of varying the Rayleigh number, the buoyancy ratio, and the slenderness ratio of the enclosure. The main features of the flow pattern in the boundary layer regime are illustrated in Fig. 3(*a*), while the temperature and concentration fields (which are identical when Le = 1) are shown in Fig. 3(*b*). Note that the features of these fields are consistent with the assumptions (1)–(3) adopted as foundation for the Oseen-linearized solution.

The Le = 1 data of Table 3 can be used to test the Oseen-linearized solution. Figure 4 shows that the effect of buoyancy ratio on Nu (or Sh) is as predicted in equation (25) (in Fig. 4, Ra = 3.5×10^5 and $-11 \le n \le 9$). The agreement between equation (25) and numerical data improves as $|n|$ increases, i.e., as the circulation accelerates and the boundary layers become thinner (more distinct).

In Fig. 5 we see that the effect of H/L and Ra on numerical results is the same as the effect predicted analytically via equation (25). The agreement between numerical results and equation (25) improves steadily as the slenderness ratio H/L and Ra increase. The numerical Nu, Sh data exhibited in Figs. 4 and 5 represent overall Nusselt and Sherwood number values (the fifth column in Table 3). Even better agreement between analysis and numerical results would be recorded if Figs. 4 and 5 showed the local Nu and Sh values computed at midheight, i.e., in that part of the enclosure where the assumed purely parallel boundary layer flow structure comes closest to the structure revealed by numerical experiments (the midheight local Nu and Sh data are listed in the sixth column of Table 3).

In the numerical results discussed so far the Lewis number was fixed at Le = 1. The effect of varying the Lewis number is illustrated by the sequence of concentration patterns of Figs. 3(*b–d*) drawn for a heat-transfer-driven flow in the boundary layer regime ($n = 0$, Pr = 7, Ra = 3.5×10^5). As the Lewis number decreases from Le = 1 in Fig. 3(*b*) to Le = 0.1 in Fig. 3(*c*), the concentation boundary layers thicken and merge in the core region of the enclosure. The reverse trend is observed as Le increases from Le = 1 in Fig. 3(*b*) to Le = 10 in Fig. 3(*d*): Relative to the driving velocity and temperature layers of Figs. 3(*a, b*), the concentration boundary layer becomes thinner. At the same time, the core concentration distribution becomes nearly constant [this last feature is consistent with the $f(\infty) = 0$ boundary condition (29) invoked in the development of the similarity solution (31)].

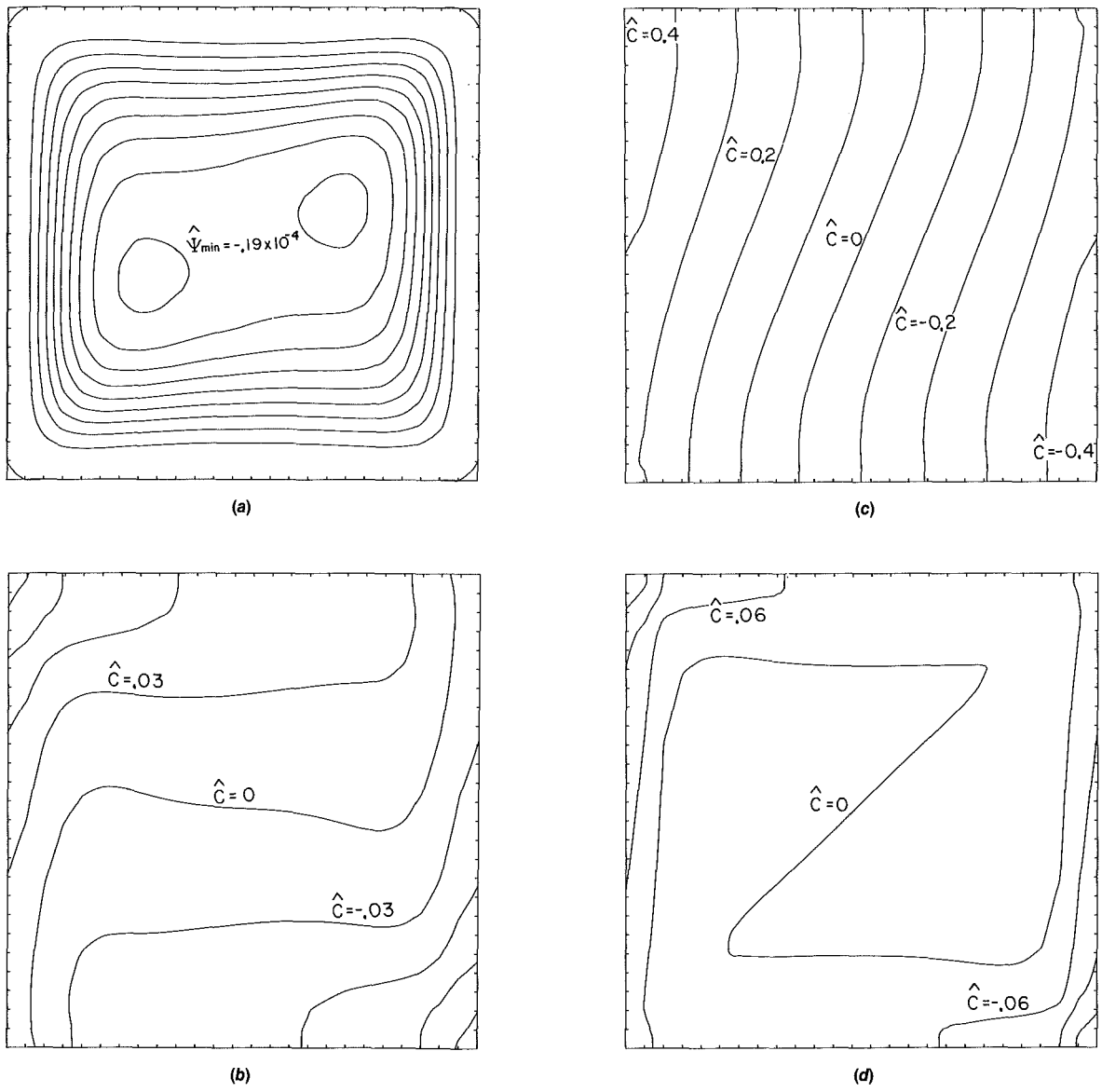

Fig. 3 Examples of flow, temperature, and concentration patterns in the boundary layer regime ($H/L = 1$, $Pr = 7$, $n = 0$, $Ra = 3.5 \times 10^5$); (*a*) streamlines, (*b*) isotherms for all values of Le, and lines of constant concentration when $Le = 1$, (*c*) concentration pattern when $Le = 0.1$, (*d*) concentration pattern when $Le = 10$

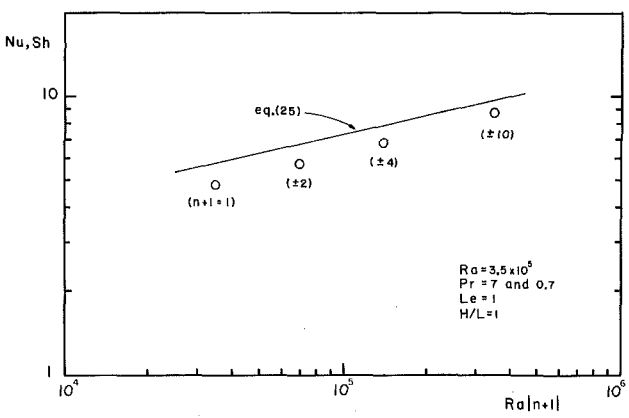

Fig. 4 The effect of buoyancy ratio on the overall heat and mass transfer rates

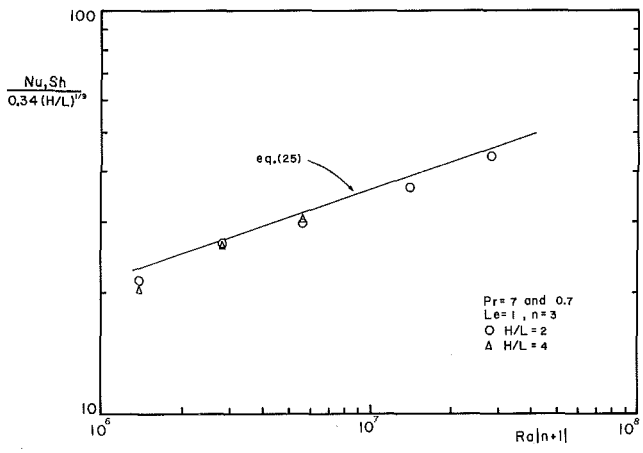

Fig. 5 The effect of cavity aspect ratio *H/L* on the overall heat and mass transfer rates

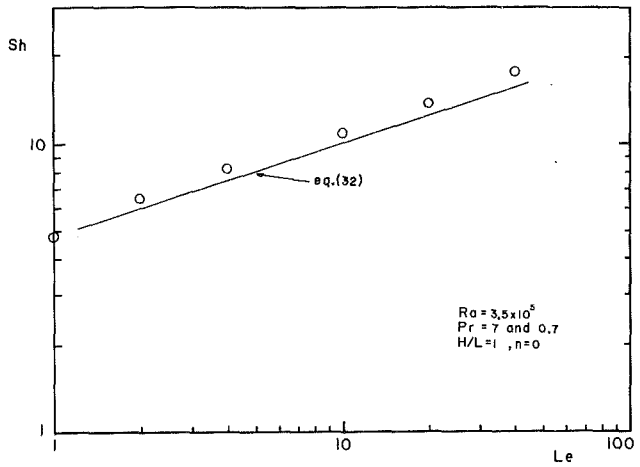

Fig. 6 ***The effect of Lewis number on the overall Sherwood number in heat-transfer-driven flows in the boundary layer regime***

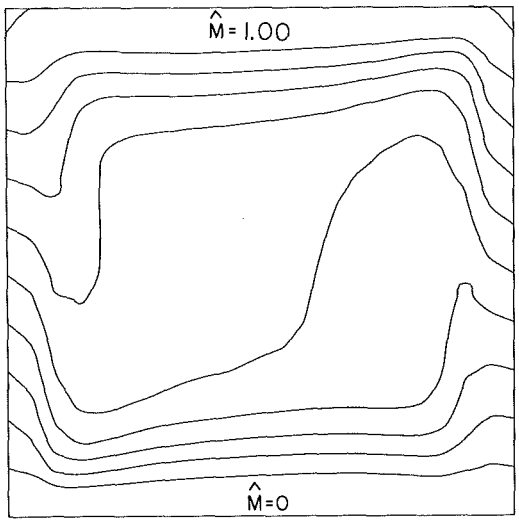

(a)

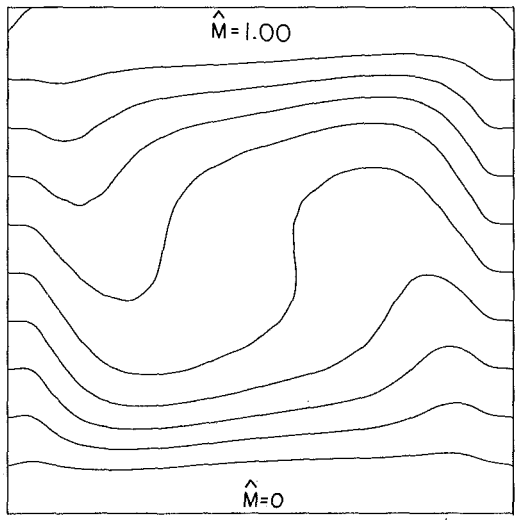

(b)

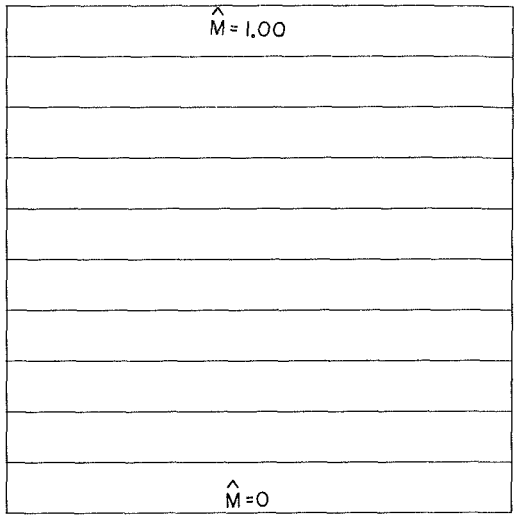

(c)

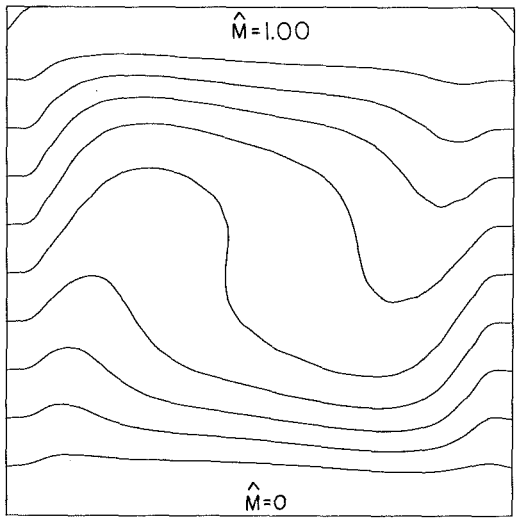

(d)

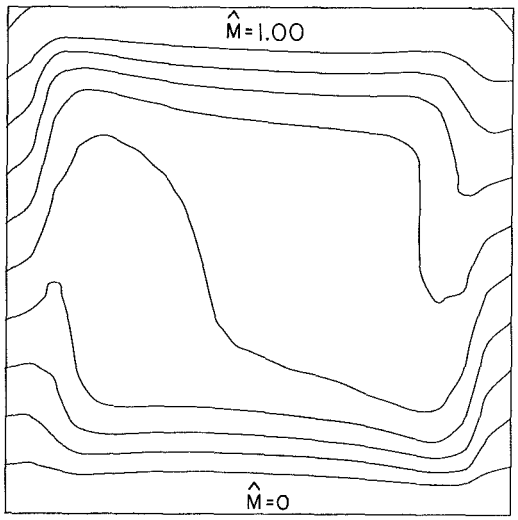

(e)

Fig. 7 Massline patterns showing the effect of varying the buoyancy ratio n through the flow-reversal condition $n = -1$ ($Ra = 3.5 \times 10^5$, $H/L = 1$, $Le = 1$, $Pr = 7$); (a) $n = -4$, (b) $n = -1.1$, (c) $n = -1$, (d) $n = -0.9$, (e) $n = 2$

The numerical runs chosen to test the effect of Le on the overall mass transfer rate are assembled in Table 4. Figure 6 displays these results next to the similarity solution (31), and shows that the $Le^{1/3}$ dependence predicted analytically is supported by the trend revealed by numerical experiments. Given the analogy between the tasks of deriving equation (31) and equation (32), the numerical test presented in Fig. 6 validates also the Nusselt number formula for mass-transfer-driven flows in fluids with $Pr > 1$ and $Le < 1$, equation (32).

Tables 3 and 4 show also that by changing the Prandtl number from 0.7 to 7 we do not register meaningful changes in the overall heat and mass transfer rates. This finding is consistent with the theoretical results (25) and (31), which show that in the parametric domain where these results are valid they should be independent of Pr.

"Masslines" for the Visualization of Convective Mass Transfer

We use the opportunity presented by the combined heat and mass transfer phenomenon discussed in this paper to extend the convective heat transfer concept of "heatlines" [4, 12] to the graphic presentation of convective mass transfer. The motivation for such an extension is conceptually analogous to what led to the idea of heatlines, namely, patterns of constant concentration lines [e.g., Figs. 3(*b–d*)] may be useful in setting up approximate analytical solutions and in understanding the direction of mass transfer near solid walls (where fluid motion is minimal); however, they are inappropriate as indicators of the direction of total (convective plus diffusive) mass transfer. Following the analytical definition of heat function, in conjunction with the two-dimensional field of Fig. 1 we define the "massfunction" $M(x, y)$

$$\frac{\partial M}{\partial y} = u(C - C_0) - D\frac{\partial C}{\partial x} \tag{45}$$

$$-\frac{\partial M}{\partial x} = v(C - C_0) - D\frac{\partial C}{\partial y} \tag{46}$$

so that M satisfies the constituent conservation equation (36) indentically. Employing one more time the nondimensionalization method of equations (39)–(41), the dimensionless massfunction is

$$\hat{M} = \frac{M}{j'' H} \tag{47}$$

and, taken together, equations (45), (46) yield

$$\nabla^2 \hat{M} = \mathrm{RaLe}\left[\frac{\partial}{\partial \hat{y}}(\hat{u}\hat{C}) - \frac{\partial}{\partial \hat{x}}(\hat{v}\hat{C})\right] \tag{48}$$

The mass function boundary conditions corresponding to equations (37), (38) are

$$\hat{M} = \hat{y} \text{ at } \hat{x} = 0, L/H \tag{49}$$

$$\hat{M} = 0, 1 \text{ at } \hat{y} = 0, 1 \tag{50}$$

Figure 7 shows a sequence of massline patterns obtained by solving equations (48)–(50) for a relatively high Rayleigh number in a square domain with $Le = 1$. The five-graph sequence was constructed for the additional objective of illustrating the effective of varying the buoyancy ratio n through the critical value $n = -1$ associated with the perfect cancellation of opposing buoyancy effects. In flows driven primarily by mass transfer [$n = -4$ in Fig. 7(*a*); $n = 2$ in Fig. 7(*e*)], the masslines show clearly the existence of distinct vertical boundary layer region and the "channeling" of convective mass transfer through horizontal corridors lining the top and bottom walls. As the quantity $(n + 1)$ changes sign in going from Fig. 7(*a*) to Fig. 7(*e*) to Fig. 7(*e*), the circulation sense changes from counterclockwise to clockwise; this change is reflected by the shape of the masslines.

As the buoyancy ratio n approaches and passes through -1, Figs. 7(*b–d*), the boundary layer character of the convective mass transfer process is inhibited to the point that pure mass diffusion (horizontal masslines) rules at $n = -1$, Fig. 7(*c*). Again, as the quantity $(n + 1)$ changes sign from Fig. 7(*b*) to Fig. 7(*d*), the circulation changes direction and so does the convection mass transfer through the core region.

One final observation concerns the centrosymmetry exhibited by the massline patterns of Fig. 7. This feature is not present in the patterns of heatlines reported for a related heat transfer problem in [12], where it was shown that in general the heatline patterns do not share the centrosymmetry property of the temperature and streamline patterns. However, there is one special case (i.e., definition of massfunction or heatfunction) that renders the corresponding patterns centrosymmetric: that special definition was used here in equations (45), (46), and consists of using the concentration *difference* $C - C_0$ as concentration field in the definition of the M field. Note that C_0 is the enclosure-averaged concentration. Should M have been defined as in [12], the difference $C - C_0$ would have been replaced by C in equations (45), (46) and the resulting massline pattern would have lacked the centrosymmetry property. In addition, the massline pattern would not have been unique, because a new pattern can be plotted for each new reference concentration that is used to specify C numerically.

The lack of uniqueness of the heatline patterns defined and plotted in [12] was not realized at the time. We use the opportunity afforded by the present mass transfer study to propose that in order to generate heatline and massline patterns that are *centrosymmetric* and *unique*, the heatfunction and massfunction should be defined based on $(T - T_0)$ and $(C - C_0)$, where the reference values T_0 and C_0 are enclosure-averaged quantities (i.e., properties measured in the center of the enclosure).

Concluding Remarks

In this article we developed analytical means for calculating the combined heat and mass transfer rates for natural convective driven by temperature and concentration gradients in a vertical slot. The analysis focused on the boundary layer regime, where the heat and mass transfer rates exceed the pure diffusion estimates, and succeeded to reveal in closed form the role played by dimensionless groups such as the Lewis number, Rayleigh number, and buoyancy ratio. The analytical results were later tested and extended by means of direct numerical solutions to the complete governing equations. In the graphic-presentation phase of this study, we introduced the concept of "masslines" as a tool for visualizing convection mass transfer.

One advantage of combining theory with direct numerical simulations is that the theory "organizes" the numerical effort, that is, it defines its purpose, it shows how to correlate the emerging information (thus minimizing the numerical effort and maximizing the return on investment) and, finally, it shows the domain in which the overall study is valid. Regarding the validity domain of the present study, we use this opportunity to comment critically on the correctness of the assumption that the flow field is characterized by zero velocity normal to a solid wall: We made this assumption to obtain equations (14), (27), (37), and (38). As was argued by one anonymous reviewer of this manuscript, the impermeable wall assumption seems to contradict the assumption of the existence of mass transfer through the wall.

In a few steps of scale analysis we can show that the existence of mass transfer at the wall does not necessarily invalidate the impermeable-wall feature of the flow field. For simplicity, consider a single vertical wall with a heat-transfer-driven boundary layer ($n = 0$), for which the relevant scales of the thermal boundary layer of thickness δ_T are

$$\delta_T \sim H\,\mathrm{Ra}^{-1/5}, \quad v \sim \frac{\alpha}{H}\,\mathrm{Ra}^{2/5}, \quad u \sim \frac{\alpha}{H}\,\mathrm{Ra}^{1/5} \tag{51}$$

These scales follow from the assumption that the flow is driven by uniform heat flux and that $\mathrm{Pr} > 1$ ([4], pp. 120, 130–133). If, as in our analyses, the Lewis number is of order one or greater, the thickness of the concentration boundary layer δ_C does not exceed δ_T ([4], p. 323; also [13, 14])

$$\frac{\delta_C}{\delta_T} \sim \mathrm{Le}^{-1/3} \leq 1 \tag{52}$$

Therefore, the scales of the δ_C-thin layer are

$$\delta_C \sim \mathrm{Le}^{-1/3} H\,\mathrm{Ra}^{-1/5} \tag{53}$$

$$v_C \sim \frac{\delta_C}{\delta_T} v \sim \mathrm{Le}^{-1/3} \frac{\alpha}{H}\,\mathrm{Ra}^{2/5} \tag{54}$$

$$u_C \sim \frac{\delta_C}{\delta_T} u \sim \mathrm{Le}^{-1/3} \frac{\alpha}{H}\,\mathrm{Ra}^{1/5} \tag{55}$$

In the high Rayleigh number regime, the smaller of the two velocity scales (u_C, v_C) is u_C. Therefore, if the actual velocity through the wall-fluid interface (u_0) is to be negligible, then in an order of magnitude sense we must have

$$u_0 < u_C \tag{56}$$

The u_0 scale is proportional to the mass flux through the wall

$$u_0 = \frac{j''[\text{kg of constituent/m}^2\text{/s}]}{\rho[\text{kg of mixture/m}^3]} \tag{57}$$

wherre ([4], p. 323, and [13, 14])

$$j'' \sim \frac{(C_0 - C_\infty)D}{H}\,\mathrm{Le}^{1/3}\mathrm{Ra}^{1/5} \tag{58}$$

Criterion (56) becomes

$$\frac{C_0 - C_\infty}{\rho}\,\mathrm{Le}^{-1/3} < 0(1) \tag{59}$$

In conclusion, according to equation (59) it is permissible to treat the flow as one confined by impermeable walls if

- Le is sufficiently large
- $(C_0 - C_\infty)/\rho$ is sufficiently small, i.e., the solution is dilute
- Le is large and the solution is dilute

According to criterion (59), the $\mathrm{Le} > 0(1)$ similarity solution that ended with equations (31), (32) is always compatible with the negligible u_0 assumption. The $\mathrm{Le} = 1$ Oseen-linearized solution that led to equation (25) is valid if $\Delta C << \rho$, which is a reasonable assumption in most mass transfer calculations.

One purely numerical study that included the effect of mass transfer on the fluid velocity normal to the side walls is that of Jhaveri and Rosenberger [15]. In the present notation, Jhaveri and Rosenberger's results were obtained for heat-transfer-driven flows ($n = 0$), in a shallow enclosure ($H/L = 0.1$), containing a fluid with $\mathrm{Pr} = 0.7$ and $\mathrm{Le} = 0.71$, in the relatively low Rayleigh number range 2.3×10^3 to 2.3×10^4 (note: their Rayleigh number is based on the side-to-side temperature difference). In the same study, the value of the $(C_0 - C_\infty)/\rho$ ratio of equation (59) was fixed at 0.1; since Le was of order 0(1), criterion (59) suggests that the walls could safely be modeled as impermeable relative to the flow field, if the Rayleigh number is high enough to approach the boundary layer regime discussed in this paper. However, the low Rayleigh number range $10^3 - 10^4$ places Jhaveri and Rosenberger's study in the "shallow enclosure limit," where the end-to-end thermal resistance is influenced by the effectivness of the horizontal counterflow as a long heat exchanger ([4], p. 167). In other words, a comparison between the present results and Jhaveri and Rosenberger's is not possible. The appropriateness of neglecting the "interfacial flow" as the Rayleigh number increases was also stressed by Jhaveri and Rosenberger ([15], p. 58).

Finally, we draw attention to another study that used the same impermeable-wall model as in the present study: Gray and Kostin [16] simulated numerically the transient convection generated in a two-dimensional rectangular domain by a catalytic reaction that occurs along the two side walls. The reaction contributes a combined heat and mass transfer effect from both sides (hence the natural circulation); however, as the reaction eventually goes to completion, the temperature once again becomes uniform throughout the fluid, and the flow ceases.

References

1 Ostrach, S., "Natural Convection in Enclosures," *Adv. Heat Transfer*, Vol. 8, 1972, pp. 161–227.

2 Catton, I., "Natural Convection in Enclosures," *6th Int. heat Transfer Conf. Toronto, 1978*, Vol. 6, 1979, pp. 13–43.

3 Jaluria, Y., *Natural Convection Heat and Mass Transfer*, Pergamon, Oxford, 1980.

4 Bejan, A., *Convection Heat Transfer*, Wiley, New York, 1984, Chap. 5.

5 Ostrach, S., "Natural Convection Heat Transfer in Cavities and Cells," *7th Int. Heat Transfer Conf., Munich, 1982*, Vol. 1, 1983, pp. 365–379.

6 Kamotani, Y., Wang, L. W., Ostrach, S., and Jiang, H. D., "Experimental Study of Natural Convection in Shallow Enclosures With Horizontal Temperature and Concentration Gradients," *Int. J. Heat Mass Transfer*, Vol. 28, 1985, pp. 165–173.

7 Viskanta, R., Bergman, T. L., and Incropera, F. P., "Double-Diffusive Natural Convection," in: *Natural Convection: Fundamentals and Applications*, S. Kakac, W. Aung, and R. Viskanta, eds., Hemisphere, Washington, DC, 1985, pp. 1075–1099.

8 Kimura, S., and Bejan, A., "The Boundary Layer Natural Convection Regime in a Rectangular Cavity With Uniform Heat Flux From the Side," ASME JOURNAL OF HEAT TRANSFER, Vol. 106, 1984, pp. 98–103.

9 Gill, A. E., "The Boundary Layer Regime for Convection in a Rectangular Cavity," *J. Fluid Mech.*, Vol. 26, 1966, pp. 515–536.

10 Bejan, A., "Note on Gill's Solution for Free Convection in a Vertical Enclosure," *J. Fluid Mech.*, Vol. 90, 1979, pp. 561–568.

11 Patankar, S. V., *Numerical Heat and Fluid Flow*, Hemisphere, Washington, D.C., 1980.

12 Kimura, S., and Bejan, A., "The 'Heatline' Visualization of Convective Heat Transfer," ASME JOURNAL OF HEAT TRANSFER, Vol. 105, 1983, pp. 916–919.

13 Bejan, A., "The Method of Scale Analysis: Natural Convection in Fluids," in: *Natural Convection: Fundamentals and Applications*, S. Kakac, W. Aung, and R. Viskanta, eds., Hemisphere, Washington, DC, 1985, pp. 75–94.

14 Khair, K. R., and Bejan, A., "Mass Transfer to Natural Convection Boundary Layer Flow Driven by Heat Transfer," ASME JOURNAL OF HEAT TRANSFER, Vol. 107, 1985, pp. 979–981.

15 Jhaveri, B. S., and Rosenberger, F., "Expansive Convection in Vapor Transport Across Horizontal Rectangular Enclosures," *J. Crystal Growth*, Vol. 57, 1982, pp. 57–64.

16 Gray, W. G., and Kostin, M. D., "Natural Convection, Diffusion and Chemical Reaction in a Catalytic Reactor: Numerical Results," *The Chemical Engineering Journal*, Vol. 8, 1974, pp. 1–10.

A. O. Demuren[1]
Research Fellow.
Mem. ASME

W. Rodi
Professor.
Mem. ASME

Institute for Hydromechanics,
University of Karlsruhe,
D-7500 Karlsruhe,
Federal Republic of Germany

Three-Dimensional Numerical Calculations of Flow and Plume Spreading Past Cooling Towers

The paper reports on the application of an existing three-dimensional computer code to the calculation of the flow and temperature field past cooling towers. The code uses a rectangular grid so that the round tower geometry has be approximated by steps. Simulations are presented of various idealized laboratory studies carried out with cylindrical cooling tower models with the ratio of plume exit to cross-wind velocity varying in the range 0.2 to 1.7 and the densimetric Froude number in the range ∞ to 2. By comparison with the experimental results it is shown that the computer model is capable of reproducing the main features of the complex flow and temperature field past cooling towers including the downwash effect at strong cross winds. The quantitative agreement is not always entirely satisfactory, and suggestions are made for improving the computer model.

1 Introduction

A variety of mathematical models have been developed for calculating the dilution and spreading of cooling tower plumes. Most practical calculations are carried out with one-dimensional integral models (see, e.g., Schatzmann and Policastro, 1984). With suitable empirical input, these models have produced fairly good predictions of the global features of thermal plumes in many situations. However, integral methods cannot account for certain important effects, like downwash, except in an entirely empirical way, and they cannot simulate details of the flow field and mixing characteristics. For this, a field method is required which solves the original three-dimensional equations. Benqué et al. (1976), Viollet (1977), and Egler and Ernst (1979) have developed field methods based on simplified parabolic equations which allow one to describe only flows with a predominant direction. The former two use rather simple turbulence models (empirical relations for the eddy viscosity and diffusivity), whereas Egler and Ernst solved transport equations for various turbulence quantities. The parabolic models cannot predict the complex flow field in the vicinity of the cooling tower, and in particular not the bending-over of the plume and the separation behind the tower in a cross wind. This can be simulated realistically only by solving the original three-dimensional elliptic equations. Crawford (1977) and Pernecker (1979) reported on some calculations with elliptic methods employing very simple turbulence models, but few comparisons with experiments were presented. Botros and Brzustowki (1978) calculated the flow field and temperature distribution for a situation similar to a cooling tower plume, namely for a diffusion flame issuing from a chimney into a cross wind. They employed a three-dimensional elliptic numerical model incorporating the more refined k–ϵ turbulence model. Some of the most important features could be reproduced by the model, but the accuracy of the computations suffered from the inability to use a sufficiently fine numerical grid.

The present paper reports on the first stage of the development of a field method which allows the realistic simulation of the important details of the near-field as well as of the plume development over larger distances downwind without excessive computing cost. This is achieved by combining an elliptic model for the near-field with a computationally more economic parabolic model for covering longer stretches downstream of the immediate vicinity of the tower. The present paper reports on the testing of the near-field, elliptic model component which is the locally elliptic procedure of Rodi and Srivatsa (1980) developed for computing jets in a crossflow and extended by Demuren and Rodi (1982) for flows around obstacles. The method uses a rectangular numerical grid so that the round tower shape has to be approximated by steps. The turbulent transport of momentum and heat is determined with the aid of the k–ϵ model which has shown a fair degree of universality in many applications (Rodi, 1980, 1984). For situations where buoyancy effects are important, a simple buoyancy-extended form of this model is employed as described in Rodi (1980). Applications of the calculation method to several idealized cylindrical cooling tower situations (see Fig. 1) studied in the laboratory are presented. Further results are provided in Demuren and Rodi (1985). The main aim of the investigation was to show whether the calculation method tested is capable of reproducing the most essential characteristics of the idealized situations studied.

2 Mathematical Model

2.1 Governing Differential Equations. The time-averaged partial differential equations governing the steady, three-dimensional turbulent flow and temperature field above and around cooling towers may be written in tensor notation as:

Continuity equation:

$$\frac{\partial \rho U_i}{\partial x_i} = 0 \tag{1}$$

Momentum equations:

$$\rho U_j \frac{\partial U_i}{\partial x_j} = -\frac{\partial P}{\partial x_i} + \frac{\partial}{\partial x_j}(-\rho \overline{u_i u_j}) + g_i(\rho - \rho_\infty) \tag{2}$$

Temperature equation:

$$\rho U_j \frac{\partial T}{\partial x_j} = \frac{\partial}{\partial x_i}(-\rho \overline{u_i T'}) \tag{3}$$

Equation of state:

$$\rho = \rho(T) \tag{4}$$

The Boussinesq approximation has not been invoked in these equations, i.e., the density variation is accounted for in

[1] Presently: Senior Lecturer, Faculty of Engineering, University of Lagos, Lagos, Nigeria.

Contributed by the Heat Transfer Division for publication in the JOURNAL OF HEAT TRANSFER. Manuscript received by the Heat Transfer Division February 14, 1986.

all terms. The local density is related to the quantity causing the density differences (here the temperature) by an equation of state (4). The correlations $-\rho\overline{u_i u_j}$ and $-\rho\overline{u_i T'}$ appearing respectively in the momentum equation (2) and in the temperature equation (3) represent the diffusive transport of momentum and heat by the turbulent motion. $-\rho\overline{u_i u_j}$ act as turbulent (or Reynolds) stresses and $-\rho\overline{u_i T'}$ as heat fluxes, and these correlations need to be determined by a turbulence model before the above mean-flow equations can be solved.

Here, the k–ϵ model described in detail by Rodi (1980) is employed. This relates the turbulent stresses via the eddy viscosity concept to the mean velocity gradients

$$-\rho\overline{u_i u_j} = \mu_t\left(\frac{\partial U_i}{\partial x_j}+\frac{\partial U_j}{\partial x_i}\right)-\frac{2}{3}\rho k\delta_{ij} \tag{5}$$

and in an analogous way the turbulent heat fluxes to the temperature gradients

$$-\rho\overline{u_i T'} = \Gamma_t\frac{\partial T}{\partial x_i} \tag{6}$$

The model assumes that the local state of turbulence is characterized by the turbulent kinetic energy k and by the rate of its dissipation ϵ. The eddy viscosity is related to these parameters by

$$\mu_t = c_\mu\rho\frac{k^2}{\epsilon} \tag{7}$$

The eddy diffusivity is calculated from the eddy viscosity via a turbulent Prandtl number

$$\Gamma_t = \frac{\mu_t}{\sigma_t} \tag{8}$$

The parameters k and ϵ are obtained from the following semi-empirical transport equations

$$\rho U_i\frac{\partial k}{\partial x_i} = \frac{\partial}{\partial x_i}\left(\frac{\mu_t}{\sigma_k}\frac{\partial k}{\partial x_i}\right)+\rho P+\rho G-\rho\epsilon \tag{9}$$

$$\rho U_i\frac{\partial \epsilon}{\partial x_i} = \frac{\partial}{\partial x_i}\left(\frac{\mu_t}{\sigma_\epsilon}\frac{\partial \epsilon}{\partial x_i}\right)+c_1\frac{\epsilon}{k}\rho P + c_3\frac{\epsilon}{k}\rho G - c_2\rho\frac{\epsilon^2}{k} \tag{10}$$

where

$$P = \frac{\mu_t}{\rho}\left(\frac{\partial U_i}{\partial x_j}+\frac{\partial U_j}{\partial x_i}\right)\frac{\partial U_i}{\partial x_j} \tag{11}$$

is the rate of production of turbulent kinetic energy due to the interaction of turbulent stresses and mean velocity gradients and

$$G = -\beta g\frac{\mu_t}{\rho\sigma_t}\frac{\partial T}{\partial y} \tag{12}$$

is the production or destruction of the turbulent kinetic energy by buoyancy forces. The latter causes the turbulence to be damped under stably stratified situations. The empirical constants in the above turbulence model are taken from Rodi (1980) as: $c_\mu = 0.09$, $c_1 = 1.44$, $c_2 = 1.92$, $c_3 = 1.44$, $\sigma_k = 1.0$, $\sigma_\epsilon = 1.3$, $\sigma_t = 0.5$. As was discussed in Rodi (1980) the constant c_3 multiplying the buoyancy term in the ϵ equation (10) does not have a universal value. Here the value suitable for vertical buoyant jets ($c_3 = c_1$) is taken which may not be entirely satisfactory for those parts of the plume where this is bent over in the wind direction.

2.2 Boundary Conditions. The mathematical model was applied to simulate the flow above and around model cooling towers placed in a wind or water tunnel. The computational domain has the following boundaries: inflow plane, outflow plane, three wind-tunnel walls at the top, the ground, and the far side (in the water tunnel experiments the top boundary is the free surface), a symmetry plane (only one half of the flow field is calculated), the surface wall of the cooling tower, and the circular exit plane of the tower. In general, boundary conditions need to be specified for all dependent variables at all boundaries.

At the symmetry plane and also the free surface treated as such, the normal gradients of all variables are prescribed as zero except that the normal velocity itself is set zero. At the wind or water tunnel walls, the wall function procedure described in detail in Launder and Spalding (1974) is employed. In this procedure, the viscous sublayer is bridged by relating the velocity components parallel to the wall and the value of k and ϵ at the first grid point (located outside the viscous sublayer) to the resultant friction velocity. In particular, use is made of the "universal" logarithmic velocity distribution and the assumption that the turbulence is in local equilibrium (shear production P = dissipation ϵ) at the first grid point.

At the inflow plane, which was located 12 tower diameters upstream of the tower, the longitudinal velocity U_∞ was assumed uniform and the other velocities are set to zero. Uniform inflow profiles were also prescribed for T, k, and ϵ, with the experimental value taken for T_∞ and small values

Nomenclature

C = concentration
c = constants in turbulence model
D = internal diameter of model cooling tower
Fr = densimetric Froude number at tower exit = $V_j/\sqrt{(gD(\rho_\infty-\rho_j)/\rho_\infty}$
G = buoyancy production/destruction of turbulent kinetic energy
g = acceleration due to gravity
g_i = component of g in the coordinate direction x_i
H = height of model cooling tower
H_T = height of the wind or water tunnel
k = kinetic energy of turbulence
P = pressure, shear production of turbulent kinetic energy
R = jet to cross-flow velocity ratio = V_j/U_∞
Re = Reynolds number = $U_\infty D/\nu$
T, T' = mean, fluctuating temperature
T^* = normalized temperature = $(T-T_\infty)/(T_j-T_\infty)$
U, V, W = mean velocity components in x, y, z directions
U_i, u_i = mean, fluctuating velocity component in direction x_i
U_∞ = average crossflow velocity
V_j = average jet exit velocity
x, y, z = longitudinal, vertical, lateral coordinates
x_i = coordinates in tensor notation
β = volumetric expansion coefficient
Γ_t = turbulent diffusion coefficient of T
δ_{ij} = the Kronecker delta = 0, if $i \neq j$; and 1, if $i = j$
ϵ = dissipation rate of k
μ = molecular viscosity
μ_t = turbulent (or eddy) viscosity
ν = kinetic viscosity = μ/ρ
ρ = density
σ_t = turbulent Prandtl/Schmidt number

Subscripts

j = jet exit
∞ = condition in crossflow

given to the latter quantities ($k_\infty = 0.005\ U_\infty^2$, $\epsilon = k_\infty^{3/2}/0.2H_T$, where H_T = tunnel height). The outflow plane was positioned far enough downstream from the cooling tower so that the velocity, temperature, and k as well as ϵ conditions at that plane have no influence on the calculation of the flow and temperature field in the vicinity of the tower. Upstream influences from that boundary are transmitted only through pressure, and the boundary condition imposed is to set the second streamwise derivative of the pressure to zero.

The finite difference method for solving the governing equations employs a rectangular numerical grid so that the round shape of the tower must be approximated by steplike surfaces. The tower walls are considered adiabatic so that the heat flux through the step surfaces was set to zero. The wall function procedure described above is applied also to all the step surfaces, relating the near-wall longitudinal velocity components U to the friction on the longitudinal surfaces and the lateral velocity components W to the friction on the adjacent lateral surfaces so that, effectively, the resultant velocity near the real surface is related to the resultant wall friction. A more ideal way of resolving the flow near the cooling-tower surface is, of course, to employ a boundary-fitted grid, and the development of a method using such a grid is under way. Initial calculations with a body-fitted grid have shown, however, that even with this method the resolution of the boundary layer developing on the surface is difficult and expensive for the large Reynolds numbers occurring in reality, as the boundary layers are very thin compared with the extent of the flow domain that has to be covered.

The tower exit conditions were matched as far as possible to those prevailing in the experiments. Hence the mass flow rates, as well as the heat and momentum fluxes of the plume at the exit, were matched to the experimental conditions. Previous calculations (see Demuren, 1983) have shown that the velocity distribution downstream of the exit plane was relatively insensitive to the exact way in which the exit hole was approximated in the numerical calculation, so long as these conditions were satisfied. The plume exit velocity and temperature were prescribed as uniform. Calculations were also carried out with a constant total pressure imposed as exit boundary condition, but the predicted results were not significantly different for the test cases considered here. The jet exit kinetic and dissipation rates were again given low values ($k_j = 0.001\ V_j^2$, $\epsilon_j = k_j^{3/2}/0.5D$).

2.3 Solution Procedure. The partial differential equations (1)–(3), (9), and (10) were solved with a modified version of the locally elliptic three-dimensional procedure of Rodi and Srivatsa (1980) which is an extension of the well-known parabolic procedure of Patankar and Spalding (1972). The procedure treats only the reverse flow region as fully elliptic, the rest of the flow being treated as partially parabolic (only the pressure is treated as elliptic; see Pratap and Spalding, 1976) which, compared with a fully elliptic procedure, makes it more economical in storage. The method employs a hybrid (central/upwind) differencing scheme for approximating the convection terms. This was found by Demuren (1983) to cause excessive numerical diffusion in certain jet-in-a-crossflow situations. The quadratic upstream weighted scheme (QUICK) proposed by Leonard (1979) was found to perform well in that study but could not be employed successfully in the present one because it produced severe undershoots, especially in the temperature, near the top of the cooling tower. The calculations with the hybrid scheme to be presented below must therefore be expected to be influenced by a certain amount of numerical diffusion. This will be discussed further in connection with grid-refinement tests performed.

3 Results and Discussion

3.1 Test Cases. The numerical model was applied to simulate various laboratory flows involving cylindrical cooling-tower models. The main influence parameters were the ratio of plume exit to cross-wind velocity, R, the densimetric Froude number, Fr, and the tower-height-to-diameter ratio, H/D. The first experiment is the water-model study of Viollet (1977) who carried out detailed measurements of the velocity (by LDA) and tracer concentration field for one virtually nonbuoyant situation (Fr = 70). Less detailed concentration measurements were reported also for a few buoyant situations. The second set of experiments is the wind-tunnel study by Andreopoulos (1986). He could realize densimetric Froude numbers as low as 3.3 by discharging heated air and measured the velocity components (except in reverse flow regions) and the temperature distribution with a four-sensor hot wire. Earlier, Vrettos (1984) had performed temperature measurements with thermocouples in the same wind tunnel with the same cooling tower model. The Reynolds numbers were all in the range 10,000–40,000, which is considerably lower than in real-life situations. Andreopoulos and Vrettos used tripping wires on the upwind surfaces of their tower model to simulate the flow separation at higher Reynolds numbers. Viollet did not use such a device; he studied the sensitivity of the dilution along the plume center line to the variation in Reynolds number for one case ($R = 2.0$, Fr = 5). He observed that the influence on the dilution is small once the Reynolds number is above 20,000.

For simulating the water-tunnel experiments, Batchelor's (1967) relation between the water density and temperature was used. For the wind-tunnel experiments, the local density of air was related to the temperature by the ideal gas law.

3.2 Computational Details. The computations were carried out with a 63 × 31 × 32 grid in the x, y, and z directions in all cases. This grid was chosen after calculations with a much coarser 32 × 12 × 11 grid and grid dependency tests had been performed (see discussion below on Fig. 3). The grid was fairly coarse near the boundaries of the solution domain and concentrated near the tower. With this grid, an average core memory of 500 K words was required. About 600 iterations were necessary to achieve convergence at a cost of 28 s per iteration on a CYBER 205 computer. A total run therefore took typically 4.5 hr. It should be mentioned that the vector capabilities of the CYBER 205 machine could not be utilized as the computer code has not yet been vectorized.

3.3 Model Predictions. For the virtually nonbuoyant situation studied by Viollet (1977), the calculated and measured velocity vectors and isotherms (in this case temperature acts as a tracer and corresponds to the measured dye concentration) are shown for the symmetry plane ($z = 0$) in Fig. 1. Additional results for off-symmetry planes are reported by Demuren and Rodi (1985). The velocity vectors indicate that a very complex flow field develops above and behind the tower. One peculiarity of this case with fairly large R (= 1.7) is the presence of two reverse-flow regions, one behind the plume near the top of the tower and the other behind the tower itself near the floor, but both part of a complex three-dimensional flow. The former region, which involves a stronger vortex, appears to be caused by the bending-over jet entraining fluid from downstream, and the latter by flow separation behind the tower. The length of each of these regions extends to about 1.5–2 diameters downstream of the tower. The upward velocity downstream of the reverse-flow regions is caused by the flow "filling" the wake behind the bending-over jet, as was also observed in the jet-in-a-crossflow measurements of Andreopoulos and Rodi (1984). This upward motion is strengthened by the longitudinal vortex generated by the bending-over jet as shown in Fig. 2 and discussed below. Away from the symmetry plane, this vortex consists of a downward motion which explains the downward component of the velocity vectors observed at the plane $z/D = 1.3$ (see

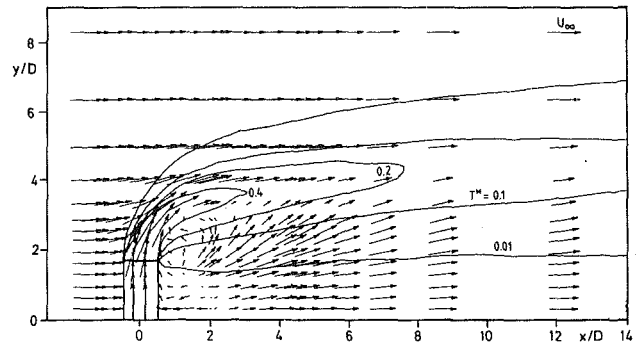

Fig. 1(a) Calculations

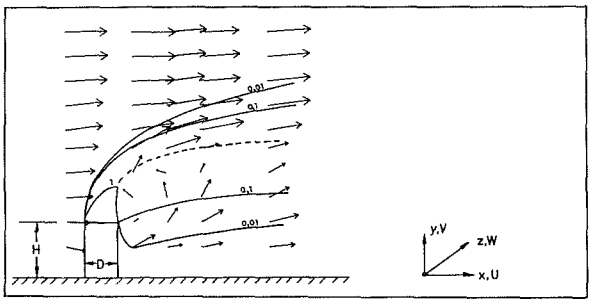

Fig. 1(b) Measurements of Viollet (1977)

Fig. 1 Velocity vectors and isotherms in symmetry plane ($z = 0$) for case studied by Viollet (1977); $R = 1.7$, Fr = 70 (nonbuoyant)

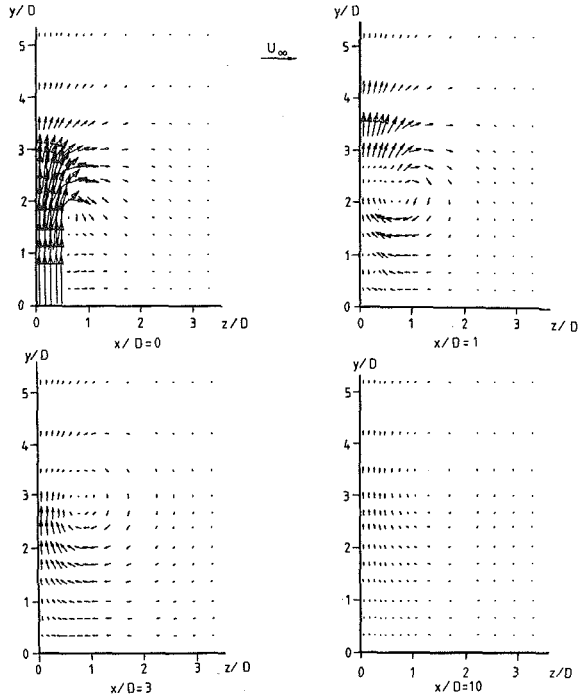

Fig. 2 Calculated velocity vectors in cross-sectional planes for case studied by Viollet (1977); $R = 1.7$, Fr = 70 (nonbuoyant)

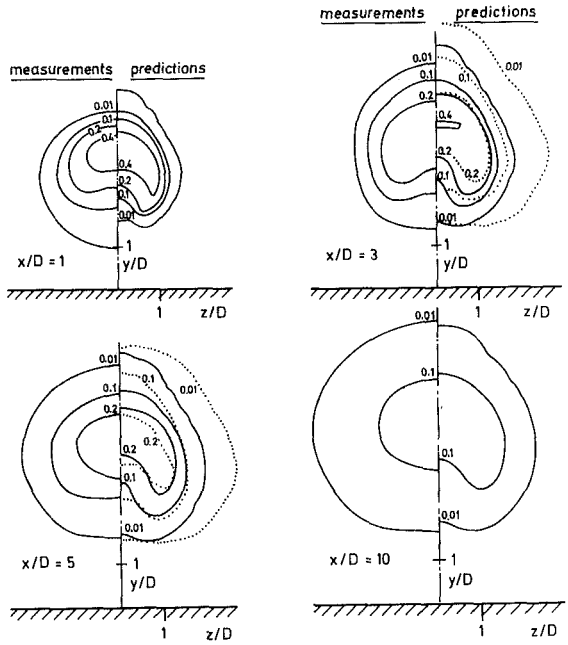

Fig. 3 Cross-sectional isotherms (lines of constant T^*) for case studied by Viollet (1977); $H/D = 1.64$, $R = 1.7$, Fr = 70 (nonbuoyant), ——— calculation with 63 × 31 × 32 grid, . . . calculation with 32 × 12 × 11 grid

Demuren and Rodi, 1985). Behind the tower, the plume does not show any downwash in this case of fairly large R. Even though there may not be agreement in all details, the calculated velocity field can be seen to be very similar to the measured one. The features just discussed can also be observed from the measured velocity vectors. In any case, the complex flow structure in the vicinity of the tower is reproduced much better than by the fully parabolic calculations presented by Viollet (1977). The isotherms are also in fairly good agreement; a more detailed comparison follows.

As is well known, the bending-over of rolled-up vortex sheets in the lee of jets in a crossflow leads to longitudinal vortices which persist quite a way downstream from the jet discharge. Figure 2 shows calculated velocity vectors in cross-sectional planes at various distances from the tower, illustrating clearly the formation and the decay of the longitudinal vortices. Figure 3 compares predicted and measured isotherms (rather lines of constant concentration) at various cross sections. The distortion of the isotherms to kidney shape caused by the longitudinal vortices appears to be somewhat overpredicted by the model. Also, the measured plume has a larger downward spreading just behind the tower, which is somewhat surprising in view of the measured velocity field. Apart from these discrepancies, however, the agreement is quite good and would probably be sufficient for practical purposes. Calculations obtained with the coarser 32 × 12 × 11 grid are also included in Fig. 3 as dotted lines in order to show the sensitivity to grid refinement. The coarse grid calculations show generally more spreading due to numerical diffusion, especially in the outer and upper part of the plume. The fine-grid calculations may still suffer from some numerical diffusion (further grid refinement was not possible), but to a much lesser extent. Calculations of the Froude-number influence on the center-line dilution in Viollet's (1977) cases are presented below in Fig. 8.

Figures 4–7 compare calculated and measured velocity vectors and isotherms in the center plane ($z = 0$) for the cases studied experimentally by Andreopoulos (1986). It is evident that the plume bends over much more quickly in these cases with $R \leq 0.5$ compared with Viollet's (1977) case with $R = 1.7$.

The calculated bending-over and its dependence on R are in general agreement with the experiments. The calculations indicate that at these lower R values there is now only one reverse-flow region with an eddy rotating in clockwise direction. This region extends to $2D$–$2.5D$ downstream of the tower. The faster bending-over reduces the wake behind the plume so that the wake behind the cylinder becomes dominant as R becomes smaller. As a consequence, it is the wake behind the cylinder that requires "filling" so that the inclination of the velocity vectors downstream of the reverse-flow region is reversed and for $R = 0.2$ (Figs. 6 and 7) is actually downward, indicating a "filling" of the cylinder wake with fluid from the bent-over plume. Hence, in this case, there is clearly a

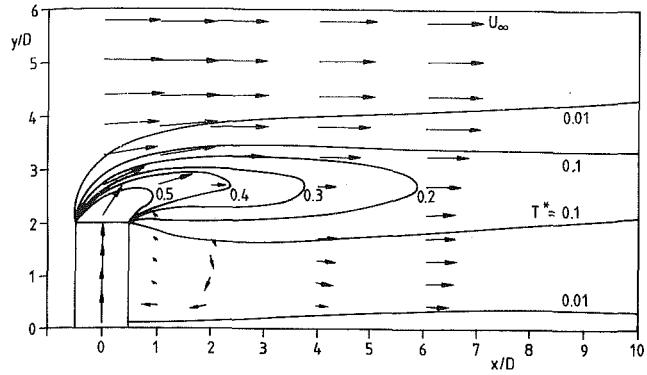

Fig. 4(*a*) Calculation

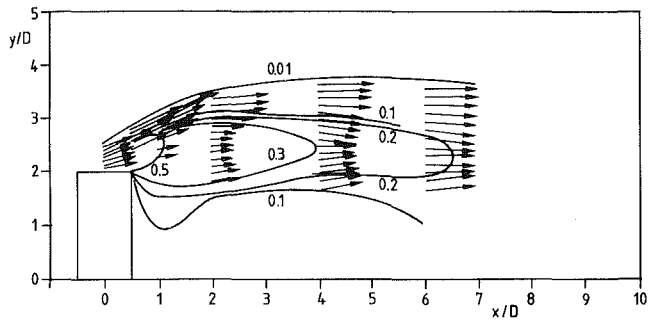

Fig. 4(*b*) Measurements

Fig. 4 Velocity vectors and isotherms in center plane for Andreopoulos' (1986) case; $H/D = 2.0$, $R = 0.5$, Fr = 8.7

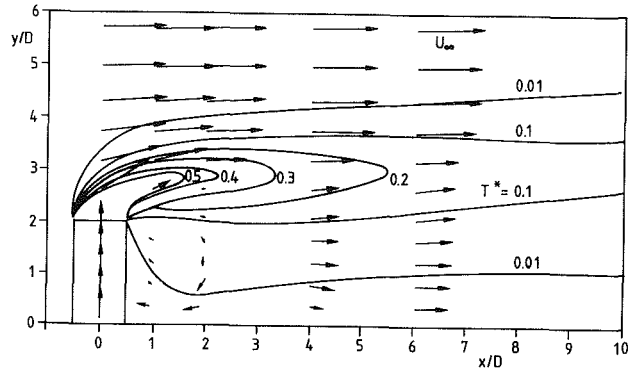

Fig. 5(*a*) Calculation

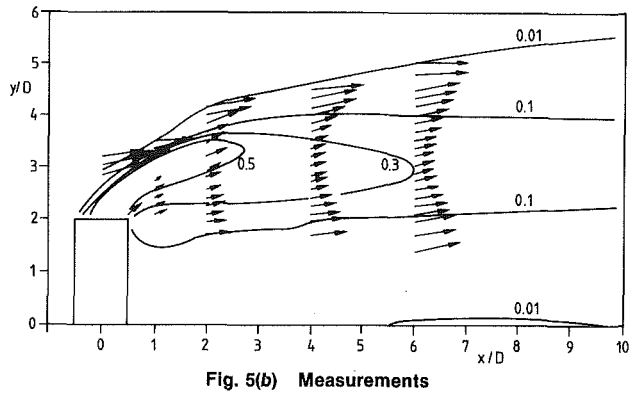

Fig. 5(*b*) Measurements

Fig. 5 Velocity vectors and isotherms in center plane for Andreopoulos' (1986) case; $H/D = 2.0$, $R = 0.5$, Fr = 3.3

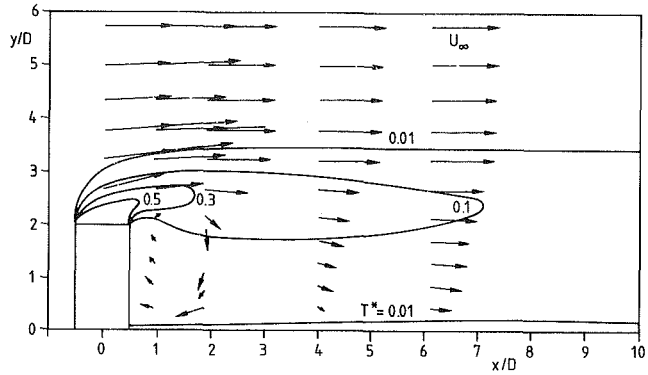

Fig. 6(*a*) Calculation

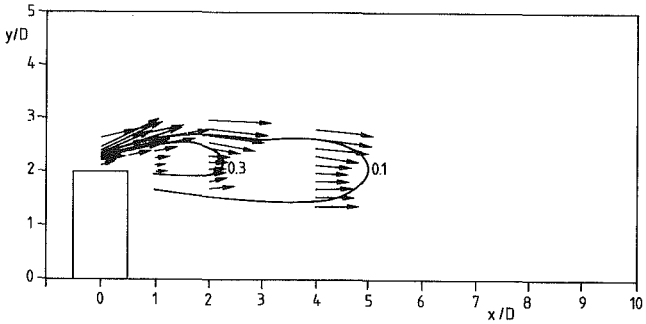

Fig. 6(*b*) Measurements

Fig. 6 Velocity vectors and isotherms in center plane for Andreopoulos' (1986) case; $H/D = 2.0$, $R = 0.2$, Fr = 8.6

downwash effect. In the region immediately behind the cylinder, measurements were not available for comparison but the measurements at stations $x/D = 4$ and 6 further downstream show much less velocity deficit than the calculations, indicating a much smaller separation region. Also, the measured velocity vectors near the top of the tower at $x/D = 1$ are contrary to the recirculating motion obtained in the calculations. However, the sketches of Andreopoulos (1986) based on flow visualization observations and an inspection of the corresponding film taken by Andreopoulos clearly reveal the presence of a recirculating motion of the type obtained in the calculations, extending about 2 diameters downstream of the tower model. These flow pictures are fully consistent with the calculation results. It is not clear at present why the measured velocity vectors hardly show any velocity deficit behind the tower model.

The effect of buoyancy on the velocity field is not very strong in the calculations. The results show a slightly more pronounced dip in the velocity profile at the location of the plume indicating a somewhat stronger wake of the bent-over plume, which may be explained by the slower bending due to the lifting of the jet by buoyancy forces. As a consequence, there is a more pronounced upward motion in the case of $R = 0.5$ and a reduced downward motion in the case of $R = 0.2$. All these effects are much more pronounced in the experiments which show a strong dip in the velocity profiles associated with an upward motion, indicating a fairly strong wake of the bent-over plume. Again, the measured behavior in the wake of the cylinder is not easy to understand.

Figures 4–7 also compare calculated and measured isotherms in the center plane. Although not all the details of the temperature field are well predicted, the bending-over of the plume and the extent of the various isotherms is in general accord with the measurements, at least for the weakly buoyant situations with Fr = 8.6. At the higher wind velocity ($R = 0.2$), a clear downwash effect can be observed in both calculations and measurements. Concerning the influence of buoyancy on

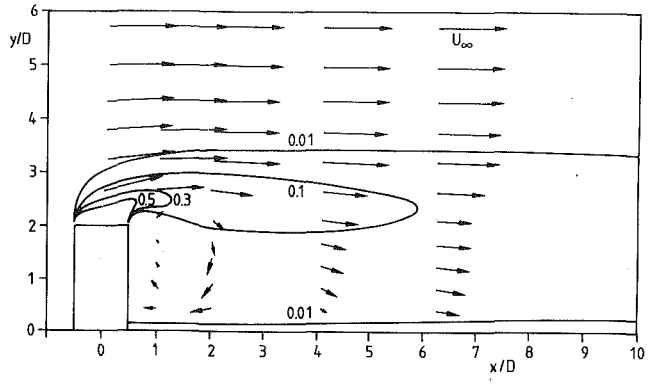

Fig. 7(a) Calculation

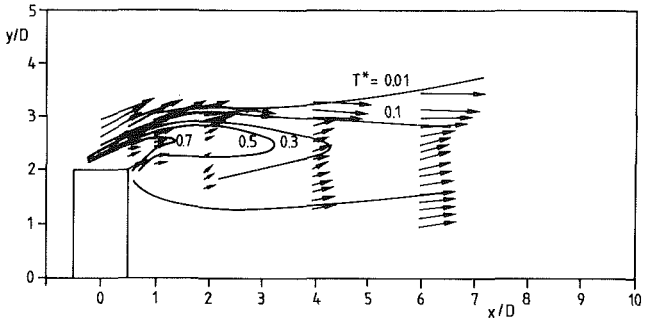

Fig. 7(b) Measurements

Fig. 7 Velocity vectors and isotherms in center plane for Andreopoulos' (1986) case; $H/D = 2.0$, $R = 0.2$, Fr = 3.3

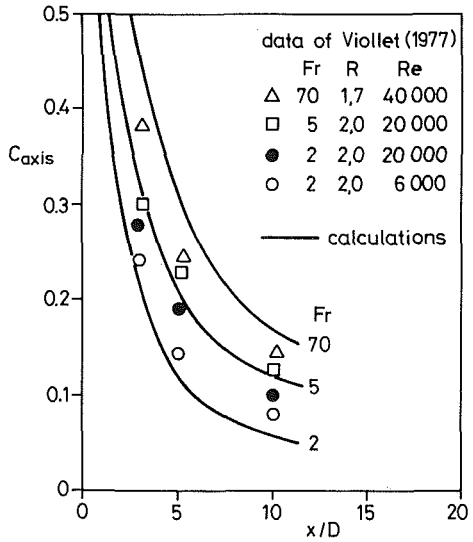

Fig. 8 Decay of concentration on the plume axis for the cases studied by Viollet (1977)

the temperature field, there is agreement between calculations and measurements only close to the tower exit. For $R = 0.5$, the 0.5 isotherm extends farther downstream in the case with stronger buoyancy, indicating less dilution in this region. This is probably due to the acceleration of the jet due to buoyancy forces. In the case with $R = 0.2$ the cross-wind effects dominate in the bending-over region so that buoyancy has little influence. Farther downstream, the calculations indicate increased dilution (isotherm areas are smaller) for the case with stronger buoyancy while the experiments show the opposite trend, i.e., the 0.1 and 0.3 isotherms extend farther downstream. The calculated trend conforms with the observed behavior in vertical buoyant jets (see Chen and Rodi, 1980) and is also in line with Viollet's (1977) measurements, which

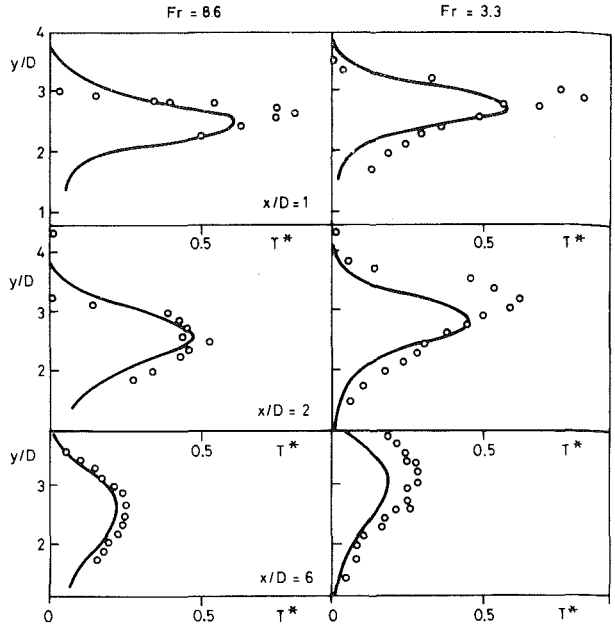

Fig. 9 Comparison of predicted normalized vertical temperature profiles in the center plane with the measurements of Andreopoulos (1986), $R = 0.5$, $H/D = 2.0$

were however for a higher velocity ratio R. Figure 8 displays his measured decay of the center-line concentration (and hence also dilution), and calculations are included for the virtually nonbuoyant case (Fr = 70) and for the buoyant cases with Fr = 5 and Fr = 2. The quantitative agreement between calculated and measured concentration decay is not particularly good, but the dependence on Fr is in agreement with the measurements, which show increased dilution when Fr is reduced. It is not clear at present whether a reversal of this trend must be expected for lower velocity ratios R as indicated by Andreopoulos' (1986) measurements.

Figure 9 illustrates more clearly agreement and discrepancies between the calculated and measured temperature distributions for the cases of Andreopoulos with $R = 0.5$. The figure compares profiles of the normalized temperature T^* along the center plane for the two Froude number situations. In general, the predictions show somewhat lower temperature peaks than the measurements, which is indicative of excessive mixing. This may be due to various reasons. Firstly, the computational grid may still not have been fine enough in the vicinity of the plume exit in order to guarantee proper resolution of the rapidly varying flow properties in this region. Associated with this is probably also some numerical (or false) diffusion causing extra mixing. Further grid refinement to eliminate any numerical inaccuracies was not possible. Another possible contributor to the excessive mixing, not related to the numerical procedure, is the buoyancy treatment in the turbulence model. As was mentioned already this may not be entirely suitable for relatively low velocity ratios R, in which the plume bends over quickly and the flow is predominantly horizontal. In this case the reduction of mixing by the stable stratification setup is not reproduced sufficiently by the model, particularly so for the lower Froude number case. A more general form of the buoyancy terms in the model equations would be desirable. The possible shortcomings discussed appear not to be very serious for the higher Froude number case as the agreement between predictions and measurements is altogether quite good. On the other hand, the calculations for the highly buoyant case at Fr = 3.3 show less rising of the plume due to buoyancy effects than was observed in the experiments. In this case, excessive mixing is more effective as the lower temperatures and higher velocities in the plume caused by it would both reduce the influence of the

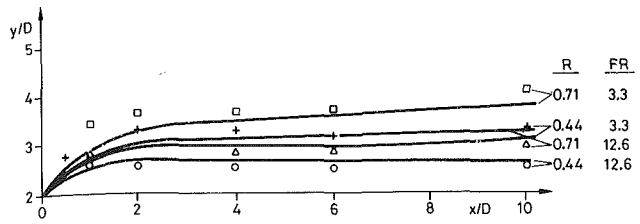

Fig. 10 Comparison of predicted plume trajectories (lines) with measurements (symbols) of Vrettos (1984), $H/D = 2.0$

buoyancy forces and hence lead to an underprediction of the buoyancy effect. The reduction of excessive mixing is therefore more important in highly buoyant cases than in mildly buoyant ones. Temperature profiles for four additional cases studied experimentally by Vrettos (1984), which are reported in Demuren and Rodi (1985), show similar trends.

The behavior of plume lifting can be studied better by looking at the trajectories. For four different situations measured by Vrettos (1984) Fig. 10 shows a comparison of the predicted trajectories based on the maximum temperature along the center plane with his measurements. The calculated trajectories are somewhat lower than the measured ones for the highly buoyant cases ($Fr = 3.3$). This trend is reversed for the cases with mild buoyancy ($Fr = 12.6$). The largest disagreement exists in the near-field ($x/D < 2$) where the buoyancy effects are strongest and the mixing of the plume with the cross flow is highest. These findings are consistent with those discussed in connection with the vertical temperature profiles. In general the trajectories can be considered to show reasonable agreement with the experiments. They indicate only slight downwash effects; beyond four diameters downstream of the tower they are almost parallel to the ground. It appears that stronger downwash effects are present only for velocity ratios even lower than 0.44; they were certainly observable for $R = 0.2$ as discussed above.

4 Concluding Remarks

Calculations of the flow and temperature field past cooling towers with an existing three-dimensional computer code have shown that, for the idealized situations considered, the most important features can be simulated reasonably well. This includes the complex flow pattern in the immediate vicinity of the tower and the downwash at strong cross winds, the formation and decay of longitudinal vortices, and the trajectory and spreading of the plume under various conditions. The effect of the cross wind, which was studied in the range $0.2 < R < 1.7$, was well reproduced in the calculations. The quantitative agreement with the laboratory experiments was not in all cases entirely satisfactory; in some cases the measurements appeared less plausible than the predictions, but it became clear that the lifting effect of buoyancy on the plume in the initial region was underpredicted. This was concluded to be due to excessive mixing caused partly by an inaccurate numerical solution (numerical diffusion) and partly by the turbulence model. Also, the computing times required are rather high for practical applications. The employment of a curvilinear grid fitted to the cooling tower geometry suggests itself as the most promising and natural improvement of the calculation method. However, preliminary calculations with such a grid (being the same at all horizontal planes) have shown that the simultaneous resolution of the boundary layer development around the tower and of the complex flow in the wake is even more costly and that the use of a grid fitted to the cooling tower geometry is not very suitable for the flow above the tower top. Of course, the accuracy can also be improved by employing a higher-order discretization method, but at the same time controlling the over- and undershoots, and by modifying the turbulence model to achieve a more realistic simulation of the influence of buoyancy. The computing time could be reduced drastically by vectorizing the computer code. While such work is in progress, the existing calculation method can be used for predicting trends and is capable of producing answers that are often of sufficient accuracy.

5 Acknowledgments

The work reported here was supported by the Deutsche Forschungsgemeinschaft. The calculations were carried out on the CYBER 205 computer of the University of Karlsruhe, using a highly modified version of program FLAIR of CHAM Ltd., London, which is based on the algorithm of Patankar and Spalding (1972). The help of Mr. Ohlböter with the computations is gratefully acknowledged.

6 References

Andreopoulos, J., 1986, "Wind Tunnel Experiments on Cooling-Tower Plumes, Part 1: In Uniform Cross Flow," Report No. SFB 210/E/18, University of Karlsruhe, Karlsruhe, Federal Republic of Germany.

Andreopoulos, J., and Rodi, W., 1984, " Experimental Investigation of Jets in a Cross Flow," *J. Fluid Mech.*, Vol. 138, pp. 93–127.

Batchelor, G. K., 1967, *An Introduction to Fluid Dynamics*, Cambridge University Press, Cambridge, England.

Benqué, J. P., Caudron, L., and Viollet, P. L., 1976, "Modèle Tridimensionnel de Calcul de Panaches émis dans l'Atmosphère," Société Hydrotechnique de France, XIVes Journées de l'Hydraulique, Question V, Rapport 1, Paris, France.

Botros, P. E., and Brzustowski, 1978, "An Experimental and Theoretical Study of the Turbulent Diffusion Flame in Cross Flow," *Proc. 17th Symposium on Combustion*, The Combustion Institute, Pittsburgh, PA, USA.

Chen, C. J., and Rodi, W., 1980, *Vertical Turbulent Buoyant Jets—A Review of Experimental Data*, HMT Series Vol. 4, Pergamon Press, Oxford, England.

Crawford, T. L., 1977, "Numerical Modelling of Complex Two- and Three-Dimensional Flow and Diffusion Problems in the Natural Air Environment," Ph.D. Thesis, University of Waterloo, Canada.

Demuren, A. O., 1983, "Numerical Calculations of Steady Three-Dimensional Turbulent Jets in Cross Flow," *Computer Methods in Applied Mechanics and Engineering*, Vol. 37, pp. 309–328.

Demuren, A. O., and Rodi, W., 1982, "Calculation of Three-Dimensional Turbulent Flow Around Car Bodies," *Proceedings of Symposium on Vehicle Aerodynamics*, Wolfsburg, Federal Republic of Germany.

Demuren, A. O., and Rodi, W., 1985, "Three-Dimensional Numerical Calculations of Flow and Plume Spreading Past Cooling Towers," Report No. SFB 210/T/17, University of Karlsruhe, Karlsruhe, Federal Republic of Germany.

Egler, W., and Ernst, G., 1979, "Dreidimensionales Ausbreitungsmodell für Kühlturmschwaden," *Fortschrittsberichte der VDI-Zeitschriften*, Reihe 15.

Launder, B. E., and Spalding, D. B., 1974, "Numerical Computation of Turbulent Flows," *Computer Methods in Applied Mechanics and Engineering*, Vol. 3, pp. 269–289.

Leonard, B. P., 1979, "A Stable and Accurate Convective Modelling Procedure Based on Quadratic Upstream Interpolation," *Computer Methods in Applied Mechanics and Engineering*, Vol. 19, pp. 59–98.

Patankar, S. V., and Spalding, D. B., 1972, "A Calculation Procedure for Heat, Mass and Momentum Transfer in Three-Dimensional Parabolic Flows," *International J. Heat Mass Transfer*, Vol. 15, pp. 1787–1805.

Pernecker, L., 1979, "Une Tentative de Calcul Tridimensionnel des Champs de Vitesse, de Pression et de Temperature autour d'un Aérorefrigérant," EDF Report No. HE 041/79.03.

Pratap, V. S., and Spalding, D. B., 1976, "Fluid Flow and Heat Transfer in Three-Dimensional Duct Flows," *Int. J. Heat Mass Transfer*, Vol. 13, pp. 1183–1188.

Rodi, W., 1980, *Turbulence Models and Their Application in Hydraulics*, International Association for Hydraulic Research, Delft, Netherlands.

Rodi, W., 1984, "Examples of Turbulence-Model Applications," in: *Turbulence Models and Their Applications*, Vol. 2, Collection de la Direction des Etudes et Recherches, Electricité de France, édition Eyrolles, Paris, France.

Rodi, W., and Srivatsa, S. K., 1980, "A Locally Elliptic Calculation Procedure for Three-Dimensional Flows and Its Application to a Jet in a Cross Flow," *Computer Methods in Applied Mechanics and Engineering*, Vol. 23, pp. 67–83.

Schatzmann, M., and Policastro, A. J., 1984, "An Advanced Integral Model for Cooling Tower Plume Dispersion," *Atmospheric Environment*, Vol. 18, pp. 663–674.

Viollet, P. L., 1977, "Etude de Jets dans des Courants Transversiers et dans des Milieux Stratifiés," Dissertation, Université Pierre et Marie Curie, Paris, France.

Vrettos, N., 1984, "Experimentelle Untersuchung der Ausbreitung von Kühlturmschwaden im Windkanal," Diploma Thesis, University of Karlsruhe, Karlsruhe, Federal Republic of Germany.

Convective Heat Transfer in the Impingement Region of a Buoyant Plume

R. L. Alpert
Factory Mutual Research Corporation,
Norwood, MA 02062
Mem. ASME

Fires of hazardous scale generate turbulent plumes within which convective heat transfer to surfaces can be important. Relatively little work has been done on developing reliable convective heat transfer correlations applicable to such large-scale flows. The present study, confined to heat transfer rates within the plume impingement region on a ceiling, achieves plume Reynolds numbers an order of magnitude beyond those of previous work by performing laboratory-scale experiments at elevated ambient pressures. Flow disturbances which normally cause scatter in plume heat transfer data are reduced as a consequence of this technique. It is shown that impingement zone Nusselt number depends on the 0.61 power of plume Reynolds numbers in the range of 10^4 to 10^5. This result is between the 1/2 power dependence expected for strain rate control (forced jet impingement) and the 2/3 power expected for buoyancy control of turbulent heat transfer rates.

Introduction

Fires of hazardous scale occur both inside and outside of buildings. Such large-scale fires generate plumes which transfer heat by convection and radiation to surrounding objects, e.g., building ceilings, steel beams, and exterior structures. Within the plume itself, convective heat transfer to surfaces can be very important because of the high gas velocities and large-scale turbulent eddies induced by the gravitational body force.

There has been a long history of laminar and turbulent forced convection heat transfer measurements in a laminar free stream. However, relatively little work has been done on developing heat transfer correlations for turbulent free streams, especially those driven by buoyancy. For turbulent jet impingement on a heated flat plate, Donaldson et al. [1] find that the Stanton number near the stagnation point decreases as the $-1/2$ power of the turbulent jet Reynolds number (Nusselt increasing as the square root of Reynolds), in the same manner as the Stanton number for a laminar jet. Based on a review of the work in [1] and on other data, Cooper [2] recommends that this Reynolds number dependence is also applicable to heat transfer rates in the buoyant plume stagnation zone.

Heat transfer rates due to impingement of a turbulent, buoyant plume on a flat ceiling have been measured by You and Faeth [3]. These measurements are limited to theoretical plume Reynolds numbers ($2b \cdot U_m/\nu$, where $2b$ is the Gaussian velocity width, U_m is centerline velocity, and ν is kinematic viscosity based on centerline gas temperature) an order of magnitude below that for hazardous fires. You and Faeth presume that the $-1/2$ power of Reynolds number is appropriate because of the similarity of the flow to that with a forced jet.

From the preceding discussion there appears to be a practical need to obtain a scientific correlation for convective heat transfer rates in a large-scale buoyant plume. To simplify the problem, the present study is confined to the case of hazardous-scale plume impingement on a ceiling. Only the stagnation zone within the plume turning region is examined. A wide range of plume Reynolds numbers (up to those characteristic of practical situations) is achieved by performing laboratory scale experiments at elevated ambient pressures. This elevated pressure technique has been used previously by Saunders [4] to study buoyant flows and by de Ris et al. [5], Kanury [6], and Alpert [7] to study fuel burning rates in fires at 1/11 of full scale. An additional benefit of the technique is a reduction in the flow disturbances which can cause scatter in plume heat transfer data.

Experiment

In order to study convective heat transfer in the buoyant plume impingement region, a fully developed turbulent plume is produced by a burning fuel such that the weakly buoyant thermal plume relations [8] are applicable at the measurement location. This asymptotic plume region has been found by Cox and Chitty [9] to exist above a point well within the flame zone. Flame heights are typically one source diameter, with measurements being made three to six source diameters above the fuel surface. The experimental apparatus described below and sketched in Fig. 1 is contained within a 2.5 m^3 pressure vessel consisting of a 1.2-m-dia horizontal cylinder.

Because the flames from burning polyoxymethylene (POM) are nonluminous, radiation effects are minimized by using a POM pool fire as a plume source. Somewhat greater luminosity is evident in the POM flame at elevated air pressures, with experiments by Kanury [6] showing that up to 10 percent of the theoretical energy release appears as radiation for 73-mm-dia POM pool fires over a wide range of pressures. In spite of any such luminosity, the radiant heat flux at the measurement station should be less than 1/10 of the convective heat flux. Absorbed radiant flux is further reduced to less than 1 percent of the convective flux by the use of gold-plated sensors.

The buoyant plume for the POM fire impinges on a water-heated, 4.76-mm-thick, square copper ceiling (0.41 m × 0.41 m), suspended on four rods a distance of 0.305 m above the POM fuel surface and 0.6 m below the top of the cylindrical pressure vessel. The fuel bed consists of a 51-mm, 76-mm, or 102-mm-dia aluminum pan filled with 50 to 200 g of POM beads. This pan is mounted on a ceramic board platform connected via an insulating acrylic rod directly to a 900 g full-scale, strain-gage type load transducer for accurate measurement of mass loss rates (see sketch in Fig. 1).

The copper ceiling is instrumented with Gardon-type heat flux gages flush with the ceiling surface at radial distances from the pool fire axis of 6.4 mm, 20 mm, and 38.6 mm. To reduce errors from foil temperature gradients, as discussed by

Contributed by the Heat Transfer Division for publication in the JOURNAL OF HEAT TRANSFER. Manuscript received by the Heat Transfer Division February 4, 1986.

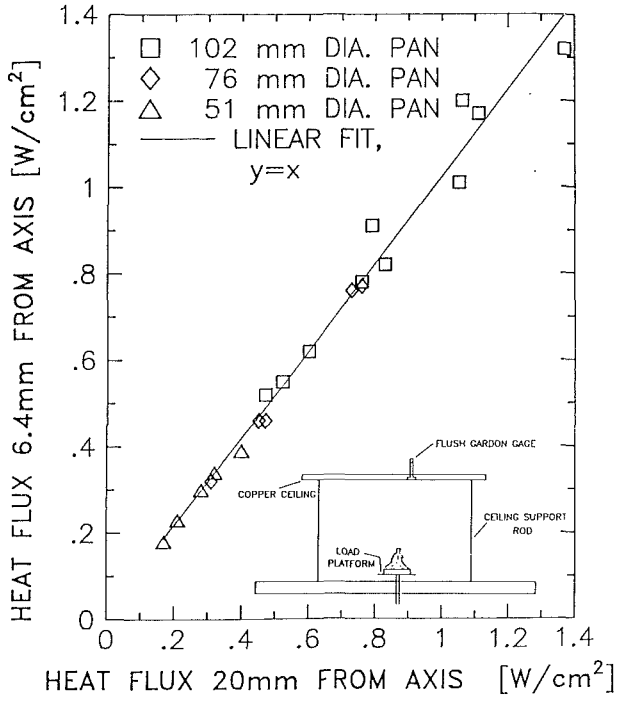

Fig. 1 Comparison of ceiling heat fluxes at 6.4 and 20 mm from plume axis; reproducibility of average heat flux values is ± 3.5 percent

Striegl and Diller [10], the Gardon gages are of low sensitivity, 5–10 W/cm² mV. A nonradiating hot-air jet is used to calibrate the gold-plated gages, which have a radiation absorptivity of 10 percent.

Bare thermocouple beads fabricated from 25.4 μm chromel-alumel wire are at the same three radial distances from the plume axis and about 6 mm below the ceiling surface. The thermocouple beads will be well outside the ceiling thermal boundary layer, which is estimated to be less than 0.3 mm thick in the stagnation zone due to low kinematic viscosity at elevated pressure (see [11], p. 251). An additional set of three thermocouple beads of the same type is located about 0.6 m beyond the edge of the ceiling so that the temperature distribution in the ambient can be measured.

Measurements of the rate of heat transfer to the ceiling in the plume impingement region are made at elevated absolute air pressures of 5.8, 11.2, 21.4, and 31.6 atmospheres. To prevent condensation of plume water vapor, the entire experiment is operated at an ambient temperature of 40 – 50°C by circulating hot water inside the pressure vessel and inside cooling tubes on the copper ceiling. Further details about the experiment are given in [12].

Experimental Results

Examination of transducer outputs from each experiment shows that mass loss rates, heat fluxes, and gas temperatures are nearly steady during the following time intervals after complete flame spread on the pool fire: 2-12 s at 31.6 atm; 3 – 30 s at 21.4 atm; 5 – 40 s at 11.2 atm; and 6 – 50 s at 5.8 atm. Within these intervals, there is no significant increase in ambient gas temperature. Average values for each measurement have been obtained from linear regression fits to data obtained during the above quasi-steady periods.

The plume radius ($1/e$ velocity radius) at the 0.305 m ceiling height should be more than 37 mm. Thus, the heat flux gages and thermocouples at 6.4 and 20 mm from the axis should all be within the plume impingement region rather than in the ceiling jet. Average values of heat flux at these two locations are indeed nearly the same as shown in Fig. 1 (time-average temperatures measured at 6.4 and at 20 mm are also nearly identical). This is especially encouraging because the gage at the 20 mm radius had only about one-half the sensitivity of the gage at 6.4 mm.

From the measurements of excess gas temperature ΔT_p in the plume impingement region (either at the 6.4 mm or the 20 mm radial location) together with the fuel mass loss rate, it is possible to calculate the height z of the thermocouples above the effective origin of the thermal plume generated by the fire. In this way, it can be determined if the plume has approached, at ceiling level, the following asymptotic state described by Morton et al.

$$\frac{\Delta T_p}{T_\infty} = \frac{3.16}{g}\left(\frac{\dot{Q}g}{p}\right)^{2/3} / z^{5/3} \tag{1}$$

where p is the ambient pressure (related to the ambient temperature T_∞ by $p = \rho_\infty R T_\infty$) and $\dot{Q}$ is the heat release rate convected in the plume.

Values of z calculated from equation (1) (assuming a POM heat of complete combustion of 15,481 J/g) are seen in Fig. 2 to be nearly independent of plume Reynolds number and generally quite close to the actual ceiling height above the fuel surface. The plume generated by the POM pool fires thus appears to be a well-defined, fully developed flow.

Global Stanton Number Correlations. As shown in [12], the classic Stanton number St is proportional to the global parameter $\dot{q}'' H^2/\dot{Q}$, where $\dot{q}''$ is the measured heat flux to the ceiling impingement region a distance H above the plume origin. Time-averaged values of this global Stanton number are correlated in Fig. 3 as a function of time-averaged, plume Reynolds number. The regression power law fit shown has a correlation coefficient of 0.88 and implies a Nusselt number (which equals the product of Stanton, Reynolds, and Prandtl numbers) varying as $\mathrm{Re}^{0.57}$. There appears to be a small effect

Nomenclature

b = plume radius at which $U = U_{max}/e$, m
g = acceleration of gravity, m/s²
H = distance of ceiling above the plume origin, m
h = heat transfer coefficient, W/m²K
L = characteristic flow length, m
$\dot{m}$ = fuel mass loss rate, g/s
Nu = Nusselt number = $2b\dot{q}''/\lambda\Delta T$
p = absolute air pressure, Pa
$\dot{Q}$ = convective heat release rate in plume, W
$\dot{q}''$ = net heat flux to ceiling, W/cm²
Re = Reynolds number
Re_p = plume Reynolds number = $2bU_{max}/\nu_{max}$
r = radial distance from plume axis, m
St = Stanton number = 0.045 • $\dot{q}'' H^2/\dot{Q}$
T_∞ = ambient gas temperature at 191 mm below ceiling, K
ΔT = excess of gas temperature above circulating hot water temperature, K
ΔT_p = excess of gas temperature above ambient gas temperature, K
U = upward gas velocity in plume, m/s
z = height above effective plume origin, m
δ = boundary layer thickness, m
λ = gas thermal conductivity, W/mK
ν = gas kinematic viscosity, m²/s

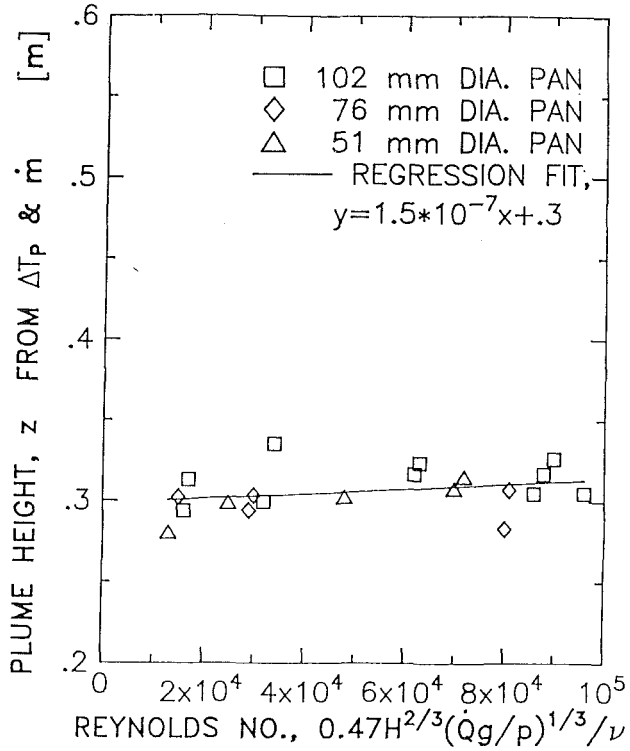

Fig. 2 Calculation of plume height from POM mass loss and gas temperature measurements; reproducibility of average excess gas temperature values is ± 3.5 percent

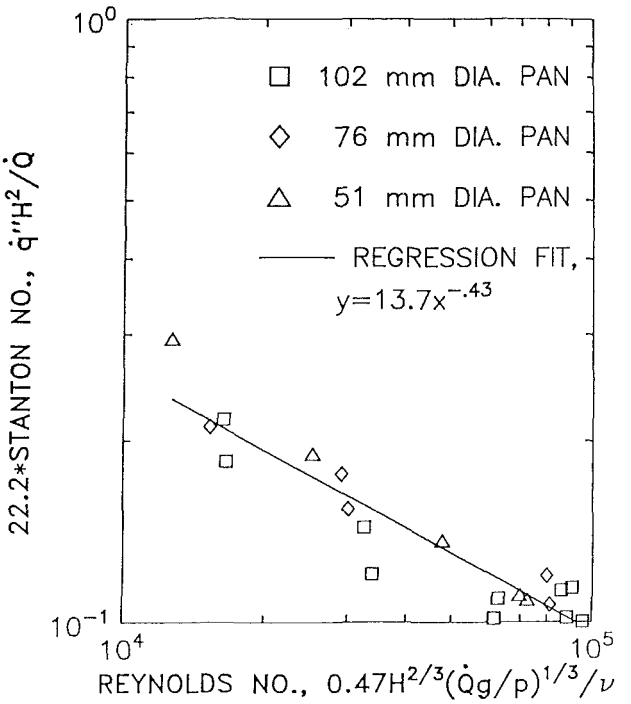

Fig. 3 Global Stanton number correlation for plume stagnation zone

of fuel diameter on the correlation. If only tests with the 76 and 51 mm dia fuels are considered, there is much less data scatter and a dependence on Re closer to the $-1/2$ power is indicated ($St = 23.2\ Re^{-0.48}$), with a regression coefficient of 0.95.

All relevant data (flame height < 55 percent of the 58–940 mm total ceiling height) obtained by You and Faeth [3] are shown in Fig. 4 along with data from the present study. Taking the You and Faeth data alone, a best power law fit yields a

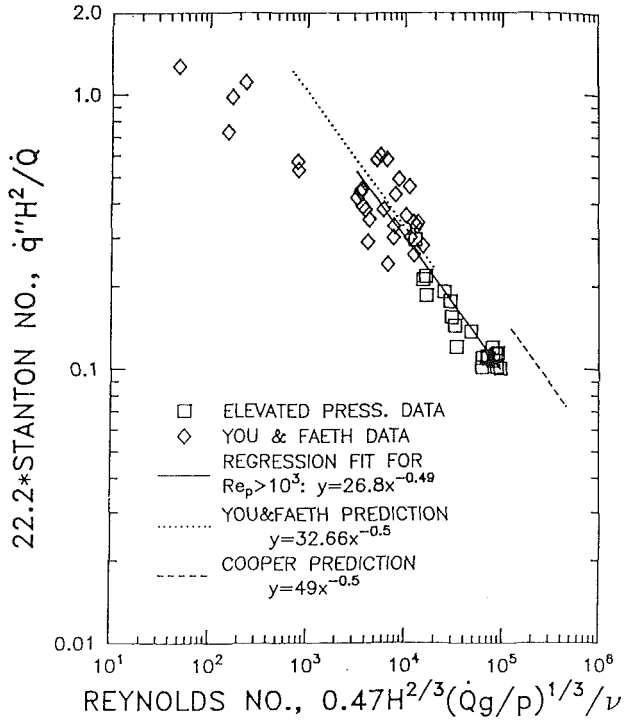

Fig. 4 Comparison with results of [2, 3]

Reynolds number dependence of only the -0.23 power. You and Faeth assumed a -0.5 power dependence for Reynolds number in their data analysis in order to conform with the laminar jet theory and then determined a numerical coefficient that would give the best agreement.

When both the present elevated pressure data and the You and Faeth data for a turbulent plume are examined in Fig. 4, it is seen that there is good agreement between the two classes of measurements in the very limited overlap region. Beyond the overlap region, the elevated pressure measurements clearly have a Reynolds number dependence which is entirely consistent with the You and Faeth data for a fully turbulent ($Re > 1480$, critical Rayleigh number of 9×10^9) plume. The global heat transfer expressions recommended for the plume stagnation zone by Cooper [2] and by You and Faeth [3] are also provided in Fig. 4. There is good agreement between these recommended correlations and the combined set of data in the *turbulent regime*.

Local Nusselt Number Correlation. Because measurements of the local temperature difference ΔT between the plume gas in the impingement region and the heat flux gage are available, a heat transfer coefficient h can be computed directly from the ratio $\dot{q}''/\Delta T$. The resultant local Nusselt number h^*2b/λ (where λ is thermal conductivity based on centerline gas temperature) should be insensitive to temperature stratification in the ambient or to the exact ambient temperature value. In addition, the convective component of the fire heat release rate $\dot{Q}$ need not be computed when the Nusselt number is obtained in this way. Although $\dot{Q}$ is needed to compute the plume Reynolds number, only the cube root of $\dot{Q}$ is required so that any errors in $\dot{Q}$ should be unimportant.

Values of Nusselt number obtained from the measured heat flux nearest the plume axis and the associated excess gas temperature are shown in Fig. 5 as a function of plume Reynolds number. The correlation of data in this figure is seen to be quite successful, with a correlation coefficient of 0.96 for the fit having a 0.61 power of Re. If Stanton–Reynolds coordinates were used, the corresponding fit would have a -0.39

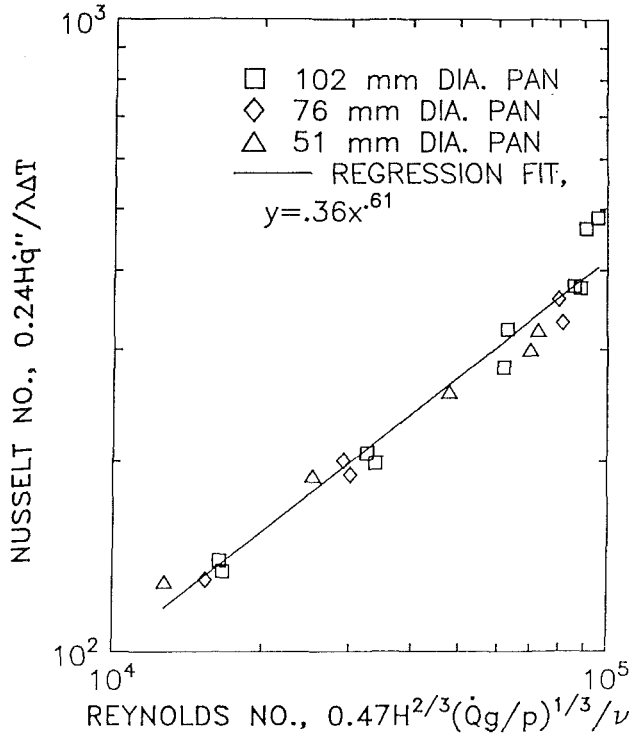

Fig. 5 Local Nusselt number correlation for plume stagnation zone

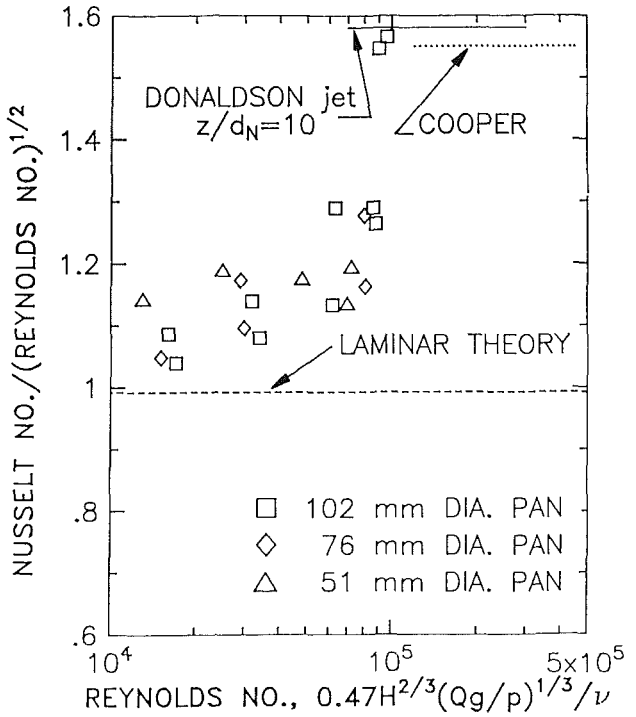

Fig. 6 Comparison with measurements of Donaldson et al. [1] and prediction of Cooper [2]

power of Reynolds number. A similar correlation result, with a 0.64 power of Re, is obtained when all Nusselt numbers are corrected (see [10]) for the actual elevated temperature distribution of the Gardon gage surface.

Discussion

The expected dependence of Stanton or Nusselt numbers on plume flow Reynolds number can be derived by examining the critical length scales associated with the flow kinematic viscosity ν. Typically, the smallest such length scale will control heat transfer rates due to fluid flow. A mean strain rate or boundary-layer length scale δ is given by $(\nu L/U)^{1/2}$, where L/U is the flow time scale. Since the heat transfer coefficient h is proportional to gas thermal conductivity λ divided by the critical heat transfer length scale, then

$$\mathrm{Nu} = \frac{hL}{\lambda} \sim \frac{L}{\delta} \sim \frac{L}{(\nu L/U)^{1/2}}$$

The preceding relation shows that the Nusselt number Nu should be proportional to $(LU/\nu)^{1/2}$, or the square root of the flow Reynolds number. Here, L would be the length determining the strain rate in the flow, such as plume radius b in the impingement region. Heat transfer relations such as this apply to bodies (e.g., spheres) submerged in forced convective flow. When the turbulent kinetic energy in the flow has been generated by surfaces, such as in pipes or on a flat plate, the Nusselt number at the pipe or flat plate surface is proportional to the 0.8 power of Reynolds number.

Another critical length scale [13] which may be important due to the effect of buoyancy is given by $(\nu^2/(g\Delta T/T_\infty))^{1/3}$, or equivalently, by $(\nu^2 L/U^2)^{1/3}$, since the buoyancy-induced velocity U at a height L is proportional to $((g\Delta T/T_\infty)L)^{1/2}$. As a result

$$\mathrm{Nu} \sim \frac{hL}{\lambda} \sim \frac{L}{(\nu^2 L/U^2)^{1/3}} \sim \left(\frac{U^2 L^2}{\nu^2}\right)^{1/3}$$

or, the Nusselt number is proportional to the 2/3 power of the flow Reynolds number. Here, L would be the length determining the buoyant velocity levels, which in an asymptotic plume is proportional to plume radius b.

Depending upon the relative importance of strain rate and buoyancy, a variation in the power of Reynolds number from 1/2 up to 2/3 could thus be expected for the Nusselt number relation in the plume impingement region. Cooper [2] has developed a correlation for plume heat transfer rates to a flat ceiling, both in the impingement region and in the ceiling jet region. For the plume impingement zone, Cooper has adopted an average of the results of You and Faeth [3] and of Donaldson et al. [1], recommending that the Nusselt number should depend on the square root of Reynolds number as in [1, 3]. This Reynolds number dependence would imply that plume impingement heat transfer rates are dominated by strain rate boundary layer processes.

Impingement zone local heat transfer correlations obtained in the present study with a buoyant plume can be compared to those obtained by Cooper [2] and by Donaldson et al. [1] for a forced jet and to laminar, stagnation point heat transfer rates predicted by Donaldson et al. [1]. This comparison is shown in Fig. 6. Donaldson et al. use a characteristic length r_5 in their work, where r_5 is the radius at which the jet velocity is 1/2 the peak value. By assuming a Gaussian velocity profile, it is found that $r_5 = 0.833\ b$, where b is the "1/e" velocity radius. As a result,

$$\frac{\mathrm{Nu}_5}{\sqrt{\mathrm{Re}_5}} = \frac{0.645\ \mathrm{Nu}_{2b}}{\sqrt{\mathrm{Re}_{2b}}}$$

These relations have been used to plot the laminar and turbulent jet lines from Donaldson et al. [1] in terms of the total plume or jet width $2b$. Note that the actual turbulent jet data from [1] only cover the Reynolds number range from 7×10^4 to 3×10^5 and correspond to a distance z of 10 nozzle diameters d_n, while the plume data from the present study correspond to a ceiling height/pool fire diameter ratio of from 3 to 6. The correlation recommended by Cooper is seen in Fig. 6 to be close to the turbulent jet results of Donaldson et al., covering a similar range of plume Reynolds number.

Data from the present study on plume impingement heat transfer imply that, unlike the turbulent jet case, $\mathrm{Nu}/\sqrt{\mathrm{Re}}$ is

indeed dependent on Reynolds number. Note that the expanded ordinate in Fig. 6 amplifies the modest difference in Nusselt number (see Fig. 5) between the two highest Reynolds number data points and the remainder of the data. Experimental values of $Nu/\sqrt{Re}$ are greater than expected for a laminar jet, but somewhat less than expected for a forced turbulent jet in the Reynolds number range of 10^4 to 10^5. The present buoyant plume local Nusselt number measurements show a Reynolds number dependence of 0.61 (see Fig. 5), somewhere between that expected for strain rate control and buoyancy control. Obviously, more heat transfer data are needed for objects immersed within the plume before a firm conclusion can be reached about the proper Nusselt–Reynolds number relation.

Conclusions

It has been shown that for plume impingement on a smooth ceiling, the impingement zone global Stanton number depends on the -0.43 power of plume Reynolds number in the range of 10^4 to 10^5. This conclusion is reinforced by using the data on gas temperatures to obtain local Nusselt numbers without recourse to the heat release rate measurements, yielding a more reliable Stanton number dependent on the -0.39 power of Reynolds number. Based on these results, it appears that plume buoyancy causes heat transfer rates in the impingement region of the ceiling to differ somewhat from forced convection rates in the stagnation zone of a turbulent jet. For plume Reynolds numbers near 10^5 (Rayleigh numbers of $10^{15}-10^{16}$) the following heat transfer correlations are recommended for use in the ceiling impingement zone: $Nu=0.36Re^{0.61}$ or $St=0.51Re^{-0.39}$.

This work has also shown that the elevated pressure technique is an excellent method for obtaining buoyant plume heat transfer measurements since atmospheric disturbances causing data scatter can be avoided.

Acknowledgments

The author is pleased to acknowledge Dr. John de Ris and Dr. Michael Delichatsios of Factory Mutual Research Corporation for providing both the inspiration for this study and continuing assistance throughout the course of the program. This research was cosponsored by Factory Mutual Research Corporation and the National Science Foundation under NSF Grant No. CPE-8213100 for the study of "Convective Heat Transfer to Surfaces in Diffusion Flame Plumes."

References

1 Donaldson, C. duP., Snedeker, R. S., and Margolis, D. P., "A Study of Free Jet Impingement, Part 2, Free Jet Turbulent Structure and Impingement Heat Transfer," *Journal of Fluid Mechanics*, Vol. 45, Part 3, 1971, pp. 477–512.

2 Cooper, L. Y., "Heat Transfer From a Buoyant Plume to an Unconfined Ceiling," ASME JOURNAL OF HEAT TRANSFER, Vol. 104, No. 3, 1982, pp. 446–451.

3 You, H. Z., and Faeth, G. M., "Ceiling Heat Transfer During Fire Plume and Fire Impingement," *Fire and Materials*, Vol. 3, No. 3, 1979, pp. 140–147.

4 Saunders, O. A., "The Effect of Pressure Upon Natural Convection in Air," *Proceedings of the Royal Society A*, Vol. 157, 1936, p. 278.

5 de Ris, J., Kanury, A. M., and Yuen, M. C., "Pressure Modeling of Fires," *Fourteenth International Symposium on Combustion*, The Combustion Institute, 1973, pp. 1033–1044.

6 Kanury, A. M., "Pressure Modeling of Pool Fires With a Variety of Polymers," *Fifteenth International Symposium on Combustion*, The Combustion Institute, 1975, pp. 193–202.

7 Alpert, R. L., "Pressure Modeling of Fires Controlled by Radiation," *Sixteenth International Symposium on Combustion*, The Combustion Institute, 1977, p. 1489.

8 Morton, B. R., Taylor, G. I., and Turner, J. S., "Turbulent Gravitational Convection From Maintained and Instantaneous Sources," *Proceedings of the Royal Society A*, Vol. 236, 1956, p. 1.

9 Cox, G., and Chitty, R., "A Study of the Deterministic Properties of Unbounded Fire Plumes," *Combustion and Flame*, Vol. 39, 1980, pp. 191–209.

10 Striegl, S. A., and Diller, T. E., "The Effect of Entrainment Temperature on Jet Impingement Heat Transfer," ASME JOURNAL OF HEAT TRANSFER, Vol. 106, 1984, pp. 27–33.

11 Schlichting, H., *Boundary Layer Theory*, McGraw-Hill, New York, 1960.

12 Alpert, R. L., "Convective Heat Transfer in the Impingement Region of a Buoyant Plume," Factory Mutual Research Corporation, Technical Report J.I. No. OJON1.BU, RC85-BT-2, 1985.

13 Delichatsios, M. A., Factory Mutual Research Corporation, personal communication, 1985.

Free Convective Heat Transfer Over a Nonisothermal Body of Arbitrary Shape Embedded in a Fluid-Saturated Porous Medium

A. Nakayama
Associate Professor.
H. Koyama
Professor.

Dept. of Energy and
Mechanical Engineering,
Shizuoka University,
3-5-1 Johoku, Hamamatsu, 432 Japan

The problem of free convective heat transfer from a nonisothermal two-dimensional or axisymmetric body of arbitrary geometric configuration in a fliud-saturated porous medium was analyzed on the basis of boundary layer approximations. Upon introducing a similarity variable (which also accounts for a possible wall temperature effect on the boundary layer length scale), the governing equations for a nonisothermal body of arbitrary shape can be reduced to an ordinary differential equation which has been previously solved by Cheng and Minkowycz for a vertical flat plate with its wall temperature varying in an exponential manner. Thus, it is found that any two-dimensional or axisymmetric body possesses a corresponding class of surface wall temperature distributions which permit similarity solutions. Furthermore, a more straightforward and yet sufficiently accurate approximate method based on the Kármán–Pohlhausen integral relation is suggested for a general solution procedure for a Darcian fluid flow over a nonisothermal body of arbitrary shape. For illustrative purposes, computations were carried out on a vertical flat plate, horizontal ellipses, and ellipsoids with different minor-to-major axis ratios.

Introduction

The investigation of free convection from an outer surface of a heated body in a fluid-saturated porous medium is of great interest for geophysical and engineering applications [1]. For example, convection of underground water around hot intrusions as a result of volcanic activities or tectonic movements may well be modeled as free convection from a heated body embedded in a porous medium. Modern technologies such as underground heat exchangers for energy storage and recovery, and temperature-controlled reactors, also require a further exploration of the mechanism of free convection in porous media. Many other examples can be found in practical engineering applications.

Wooding [2] attacked the problem of free convection about a line source and a point source as well as free convection above two heated vertical plates embedded in a porous medium, using the boundary layer approximations analogous to the classical viscous theory. Following a boundary layer approach similar to this, McNabb [3] treated free convection above a horizontal heated plate in a porous medium. Possible similarity solutions were discussed by Avduyevskiy et al. [4] and Cheng and Minkowycz [5] for a vertical flat plate and by Cheng and Chang [6] for a horizontal surface, assuming that the wall temperature distributions follow a power function of distance. Moreover, Minkowycz and Cheng [7] investigated free convection from a vertical cylinder in a porous medium, including the transverse curvature effect on local heat transfer rates. The local similarity and local nonsimilarity models suggested by Sparrow and Yu [8] were employed to treat such nonsimilar boundary layers.

Recently, convective heat transfer over curved surfaces of heated bodies associated with cylindrical and spherical canisters for nuclear waste disposal in subsea beds has begun to attract a great deal of attention. Nilson [9] used a curvilinear coordinate system with boundary layer approximations to investigate the effects of both surface inclination and transverse curvature on the temperature profile. An elegant transformation was proposed by Merkin [10] who showed that similarity solutions exist for all two-dimensional isothermal bodies of arbitrary shape. This transformation was extened by Cheng [11] to the mixed convection problem on a horizontal cylinder and a sphere. All these analyses, however, have been restricted to isothermal bodies, despite the fact that, in practical situations, the surface temperature of a body is often found to vary significantly in the streamwise direction. Minkowycz et al. [12] considered mixed convection from nonisothermal bodies. Numerical calculations based on the local nonsimilarity method were carried out for a horizontal cylinder and a sphere varying the degree of buoyancy effects. In their analysis, the vertical coordinate was transformed into a pseudosimilarity variable following Merkin [10], while the streamwise coordinate was transformed to measure the buoyancy effects such that the origin of the transformed coordinate corresponds to the pure forced convection case. However, asymptotic solutions for the pure free convection case were not possible since the case corresponds to an infinite value of their buoyancy parameter.

In the present paper, the problem of free convection from nonisothermal bodies embedded in a saturated porous medium of infinite extent is considered. A nonisothermal body may be either two dimensional or axisymmetric with an arbitrary shape. A general transformation is suggested below to deal with nonisothermal bodies of arbitrary shape. It will be shown that any two-dimensional or axisymmetric body shape possesses a corresponding class of the wall temperature distributions which permit the similarity solution. It is particularly interesting to note that, through this generalized transfomation, the resulting equations become identical to those for a vertical flat plate with its wall temperature varying as a power function of vertical distance. For illustrative purposes, local heat flux expressions will be presented for a vertical flat plate, a horizontal cylinder, a sphere, horizontal ellipses, and ellipsoids. Furthermore, a simple integral procedure based on the Kármán–Pohlhausen integral relation is proposed for a speedy and yet accurate estimation of local heat transfer rates. Comparison of the resulting approximate

Contributed by the Heat Transfer Division for publication in the JOURNAL OF HEAT TRANSFER. Manuscript received by the Heat Transfer Division January 17, 1986.

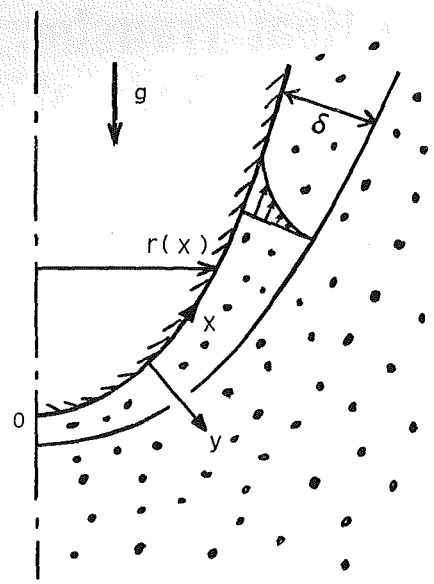

Fig. 1 Physical model and coordinates

results with those from the exact solution reveals excellent performance of the approximate method.

Governing Equations and Transformation

The physical model and its boundary layer coordinate system are shown in Fig. 1, where x is the coordinate to measure distance around a body surface from a lower stagnation point, and the coordinate y is set everywhere perpendicular to the body surface. The body under consideration may be plane or axisymmetric, and its geometric configuration is described by the function $r(x)$. The body may be nonisothermal, and its temperature $T_w(x)$ as a function of x exceeds the ambient temperature T_e everywhere. Thus, there is an upward convective fluid movement as a result of the buoyancy force.

Under the usual boundary layer approximations along with the Boussinesq approximation, the governing equations, namely, the equation of continuity, Darcy's law, and the energy equation are given by

$$\frac{\partial}{\partial x} r^* u + \frac{\partial}{\partial y} r^* v = 0 \tag{1}$$

$$\frac{\partial u}{\partial y} = \frac{K\beta}{\nu} g_x \frac{\partial T}{\partial y} \tag{2}$$

and

$$u \frac{\partial T}{\partial x} + v \frac{\partial T}{\partial y} = \alpha \frac{\partial^2 T}{\partial y^2} \tag{3}$$

where

$$r^* = \begin{cases} 1: \text{ plane flow} \\ r(x); \text{ axisymmetric flow} \end{cases} \tag{4a}$$

and

$$g_x = g\left[1 - \left(\frac{dr}{dx}\right)^2\right]^{1/2} \tag{4b}$$

In the preceding equations, u and v are the Darcian velocity components in the x and y directions, and T is the local temperature. The tangential component of the accelration due to gravity g is indicated by g_x which is related to the local surface inclination through equation (4b). Furthermore, K is the peremability; ν, the kinematic viscosity; α, the equivalent thermal diffusivity of the porous medium; and β, the coefficient of thermal expansion. The appropriate boundary conditions for the problem are

$$y = 0: \qquad v = 0, \qquad T = T_w(x) \tag{5a, b}$$

$$y \to \infty: \qquad u = 0, \qquad T = T_e \tag{5c, d}$$

where the subscripts w and e refer to the wall and boundary layer edge, respectively. The continuity equation (1) can automatically be satisfied by introducing the stream function ψ such that

$$u = \frac{1}{r^*} \frac{\partial \psi}{\partial y} \tag{6a}$$

and

$$v = -\frac{1}{r^*} \frac{\partial \psi}{\partial x} \tag{6b}$$

We now introduce the following general transformations

$$\psi = \alpha r^* (\mathrm{Ra}_x I)^{1/2} f(x, \eta) \tag{7a}$$

$$T - T_e = \Delta T_w \theta(x, \eta) \tag{7b}$$

$$\eta = \frac{y}{x} (\mathrm{Ra}_x / I)^{1/2} \tag{7c}$$

where

$$\Delta T_w(x) = T_w - T_e \tag{8a}$$

$$\mathrm{Ra}_x = \frac{K\beta \Delta T_w g_x x}{\nu\alpha} \tag{8b}$$

and

$$I(x) = \frac{\int_0^x \Delta T_w^3 g_x r^{*2} dx}{\Delta T_w^3 g_x r^{*2} x} \tag{8c}$$

Ra_x is the local Rayleigh number and η is the proposed pseudosimilarity variable. The function I as defined by equation (8c) adjusts the scale in the normal direction according to a given body geometry and its surface temperature distribution. Obviously the function I reduces to unity for the special

Nomenclature

f = dimensionless stream function
g = acceleration due to gravity
h = local heat transfer coefficient
I = function associated with a deviation from unity
k = thermal conductivity
K = permeability
Nu_x = local Nusselt number
q_w = local surface heat flux
r = function representing wall geometry
r^* = 1 for plane flow and r for axisymmetric flow
Ra_x = local Rayleigh number
T = temperature
u, v = Darcian velocity components
x, y = boundary layer coordinates
α = thermal diffusivity
β = coefficient of thermal expansion
γ = ratio of horizontal axis to a vertical axis
δ = boundary layer thickness
ζ = shape parameter
η = similarity variable
θ = dimensionless temperature
λ = exponent associated with wall temperature increase
ν = kinematic viscosity
ψ = stream function

Subscripts

e = boundary layer edge
w = wall

case of an isothermal flat plate. Substitution of equation (7) into equations (2)–(6) yields

$$f''=\theta' \tag{9a}$$

$$\theta''+\left(\frac{1}{2}-nI\right)f\theta'-nIf'\theta=-xI\left(\theta'\frac{\partial f}{\partial x}-f'\frac{\partial\theta}{\partial x}\right) \tag{9b}$$

with boundary conditions given by

$$\eta=0: \qquad f=0, \qquad \theta=1 \tag{10a, b}$$

$$\eta\to\infty: \qquad f'=0, \qquad \theta=0 \tag{10c, d}$$

and the Darcian velocities are

$$u=(\alpha/x)\,\mathrm{Ra}_x f' \tag{11a}$$

and

$$v=(\alpha/x)\,(\mathrm{Ra}_x/I)^{1/2}\left[\left(nI-\frac{1}{2}\right)f-Ix\frac{\partial f}{\partial x}-\left(I\frac{d\ln g_x r^*}{d\ln x}+2nI-\frac{1}{2}\right)\eta f'\right] \tag{11b}$$

where

$$n(x)=\frac{d\ln\Delta T_w}{d\ln x} \tag{12}$$

The primes in the above equations denote differentiation with respect to η. Equation (9*a*) may readily be integrated with equations (10*b*) and (10*d*) as

$$f'=\theta \tag{13}$$

Substituting the preceding equation into equations (9*b*) and (10) yields

$$f'''+\left(\frac{1}{2}-nI\right)ff''-nI(f')^2=-xI\left(f''\frac{\partial f}{\partial x}-f'\frac{\partial f'}{\partial x}\right) \tag{14}$$

with boundary conditions, namely,

$$\eta=0: \qquad f=0, f'=1 \tag{15a, b}$$

$$\eta\to\infty: \qquad f'=0 \tag{15c}$$

Solution Procedure

The resulting partial differential equation can be integrated using available solution methods such as the local nonsimilarity method [8]. For many boundary layer problems, however, the so-called "local similarity solution" is found sufficiently accurate [7]. When the values of x or $\partial f/\partial x$ and $\partial f'/\partial x$ are small, the right-hand-side term of equation (14) may be neglected. Thus, all derivatives with respect to x vanish under this local similarity approximation, and equation (14) reduces to

$$f'''+\left(\frac{1}{2}-nI\right)ff''-nI(f')^2=0 \tag{16}$$

The preceding equation may now be regarded as an ordinary differential equation in the η direction, since nI is a function of x alone, and can be prescribed at any given station. Any standard numerical integration scheme (such as Runge–Kutta) can be used to solve the above equation for a given lumped parameter nI. It is most interesting to note that the numerical solutions, thus furnished for possible nI values, may readily be translated to any particular two-dimensional or axiymmetric body of arbitrary shape with arbitrary wall temperature distribution using the lumped parameter nI as given by

$$nI=\frac{d\ln\Delta T_w}{d\ln x}\frac{\int_0^x\Delta T_w^3 g_x r^{*2}dx}{\Delta T_w^3 g_x r^{*2}x} \tag{17}$$

As will be shown shortly, the above parameter nI is directly related to the power law exponent λ of the similarity (exact) solutions. Thus, the numerical values, for the similarity solutions given below, are readily available for the foregoing local similarity procedure. Since both the local similarity and local nonsimilarity methods are described thoroughly elsewhere [7–9, 12], further discussions on the nonsimilar flow case will not be given here.

The exact solutions to equation (16) are possible when the lumped parameter nI remains constant in the streamwise direction. One such obvious case is an isothermal body of arbitrary shape. Since $n = 0$, equation (16) reduces to

$$f'''+\frac{1}{2}ff''=0 \tag{18}$$

The case has been treated by Merkin [10]. Similarity solutions for the case of free convection around nonisothermal curved surfaces, however, do not seem to have been reported so far. Thus, to seek possible similarity solutions, we rewrite equation (17) using a new transformed variable as

$$nI=\frac{d\ln\Delta T_w}{d\ln\xi}\frac{\int_0^\xi\Delta T_w^3 d\xi}{\Delta T_w^3\xi} \tag{19a}$$

where

$$\xi\equiv\int_0^x g_x r^{*2}dx \tag{19b}$$

Equation (19*b*) along with (4*b*) suggests that the variable ξ for the plane flow case corresponds to the distance (elevation) measured vertically from a lower stagnation point, while that for the axisymmetric flow case corresponds to the volume segment cut by a horizontal plane. Equation (19*a*) also suggests that the similarity solutions exist when the wall temperature varies according to

$$\Delta T_w\propto\xi^\lambda \tag{20}$$

Substitution of equation (20) into (19*a*) leads to a simple relation between the lumped parameter nI and the constant exponent λ

$$nI=\frac{\lambda}{1+3\lambda} \tag{21}$$

Hence, equation (16) reduces to

$$f'''+\frac{1+\lambda}{2(1+3\lambda)}ff''-\frac{\lambda}{1+3\lambda}(f')^2=0 \tag{22}$$

The resulting equation is identical to the one derived by Cheng and Minkowycz [5] for a vertical flat plate with its wall temperatures varying as $\Delta T_w\propto x^\lambda$. (We note that f and η in their work correspond to $f/(1+3\lambda)^{1/2}$ and $\eta/(1+3\lambda)^{1/2}$ in our notation, respectively.) Hence, the numerical values obtained by Cheng and Minkowycz for a flat plate are directly applicable to bodies of arbitrary shape of the present concern. (A straightforward procedure to find $f(\eta)$ satisfying the boundary conditions given by equations (15) may be to iterate on $f''(0)$ by carrying out the integration of equation (22) with equations (15*a*), (15*b*), and a guessed value $f''(0)$, so that equation (15*c*) is satisfied eventually. The upper bound of the integration, namely, $\eta\to\infty$, was replaced by $\eta = 10$ in our calculations with an increment of $\Delta\eta = 0.02$, since it was

found sufficiently far from the wall surface in all cases treated here.)

Upon finding the f distribution for a given value of λ, the local surface heat flux q_w may be computed from

$$q_w = -k \left.\frac{\partial T}{\partial y}\right|_{y=0} \tag{23}$$

which can alternatively be expressed in terms of dimensionless variables as

$$\mathrm{Nu}_x \equiv \frac{q_w x}{\Delta T_w k} = [-f''(0)](\mathrm{Ra}_x/I)^{1/2} \tag{24}$$

where the function I under the relation given by equation (19*a*) reduces to

$$I = \frac{1}{1+3\lambda} \frac{\xi}{g_x r^{*2} x} \tag{25}$$

Integral Method

The Kármán-Pohlhausen integral relation has been widely used for Newtonian fluids [e.g., 13-15] and even for non-Newtonian fluids [16, 17]. Chen [18] and Bejan [19] extended the integral method to the Darcain fluid flows on flat surfaces in fluid-saturated porous media. In the following, a general integral treatment based on the Kármán-Pohlhausen integral relation is suggested for the approximate analysis of free convective Darcian fluid flow over a nonisothermal body of arbitrary shape.

With the boundary conditions given by equations (5*c*, *d*), equation (2) may be integrated as

$$u = \frac{K\beta g_x}{\nu} (T - T_e) \tag{26}$$

Integration of the energy equation (3) along with the continuity equation (1) yields

$$\frac{d}{dx} \int_0^\delta r^* u (T - T_e) dy = -r^* \alpha \left.\frac{\partial T}{\partial y}\right|_{y=0} \tag{27}$$

where δ is the boundary thickness. Further consideration of the energy equation (3) at the wall gives the following auxiliary relation

$$u_w \frac{dT_w}{dx} = \alpha \left.\frac{\partial^2 T}{\partial y^2}\right|_{y=0} \tag{28}$$

The profile for the velocity and temperature distributions may be specified by a one-parameter family as follows

$$u/u_w = \theta = \left(1 - \frac{y}{\delta}\right)^\zeta \tag{29}$$

Upon substituting this profile into equations (27) and (28), integrations and differentiations are carried out to obtain the following two distinct expressions for δ^2

$$(\delta/x)^2 \mathrm{Ra}_x = 2\zeta(1+2\zeta) I^* = \zeta(\zeta - 1)/n \tag{30a}$$

where

$$I^* \equiv \frac{\int_0^x \frac{\zeta}{1+2\zeta} \Delta T_w^3 g_x r^{*2} dx}{\frac{\zeta}{1+2\zeta} \Delta T_w^3 g_x r^{*2} x} \tag{30b}$$

These two expressions in the right-hand side of equation (30*a*) lead to a characteristic equation for the shape parameter ζ which may vary in the streamwise direction for the general case of nonsimilar flows. Since the function I^* also involves the unknown shape parameter ζ, the characteristic equation is implicit in ζ, and the determination of the streamwise variation of ζ requires an interactive procedure at each integration step, such as the one successfully employed for the film condensation problem [15]. However, for the similar boundary layers developed over bodies of arbitrary shape with ΔT_w characterized by equation (20), the shape parameter ζ remains constant, and the preceding characteristic equation reduces to a remarkably simple algebraic equation between the shape parameter ζ and the exponent λ already introduced for the wall temperature distribution as

$$\zeta = \frac{1+2nI}{1-4nI} = \frac{1+5\lambda}{1-\lambda} \tag{31}$$

By virtue of equations (31) and (30*a*), an approximate expression for the local Nusselt number may be obtained as

$$Nu_x = \zeta \frac{x}{\delta} = \left[\frac{1+5\lambda}{6(1+3\lambda)}\right]^{1/2} (\mathrm{Ra}_x/I)^{1/2} \tag{32}$$

Naturally, the resulting expression is identical to equation (24) derived through the similarity transformation, except that the multiplicative constant $[-f''(0)]$ in the exact expression is replaced by $[(1 + 5\lambda)/6(1 + 3\lambda)]^{1/2}$ in the approximate expression.

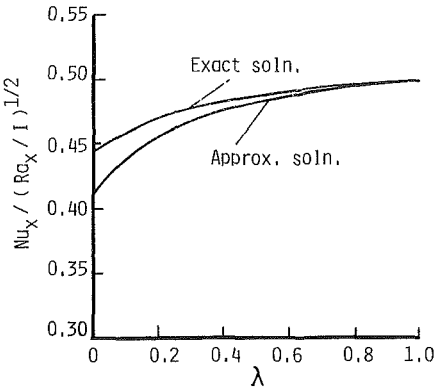

Fig. 2 Comparison of approximate and exact solutions

Results and Discussion

The present analysis has revealed that a certain class of similarity solutions exist even for a nonisothermal body of arbitrary geometric configuration. It is particularly interesting to note that any two-dimensional or axisymmetric body shape has a corresponding class of the wall temperature distributions (described by equation (20)) which permit the similarity solutions. General expressions for the local Nusselt number have been reduced through both the similarity transformation procedure and the Kármán-Pohlhausen integral procedure once for all possible two-dimensional and axisymmetric bodies. These two expressions are presented together in Fig. 2, where the abscissa variable is the exponent λ, while the ordinate variable is taken as $\mathrm{Nu}_x/(\mathrm{Ra}_x/I)^{1/2}$ such that a direct comparison of the multiplicative constants is possible. Although the approximate formula (equation (32)) tends to underestimate the heat transfer level, it appears to give a close approximationto the exact solution over a wide range of the exponent λ.

To appeciate the generality acquired in the present solution procedure, free convective flows over nonisothermal plates, horizontal ellipses and ellipsoids (including a horizontal circular cylinder and a sphere as special cases) embedded in a porous medium will now be treated as illustrative cases. The transformed variable ξ as defined by equation (19*b*) corresponds as follows

$\xi = gL_r(x/L_r)$: vertical plates (33*a*)

$\xi = gL_r(1 - \cos\phi)$: horizontal ellipses (33*b*)

$\xi = gL_r^3\gamma^2\left(\frac{1}{3}\cos^3\phi - \cos\phi + \frac{2}{3}\right)$: ellipsoids (33*c*)

where

$$\phi = \sin^{-1}(r(x)/\gamma L_r) \tag{33d}$$

Thus, the lower (front) and upper (rear) stagnation points are located at $\phi = 0$ and π, respectively. The symbol L_r denotes referenced lengths such as a plate height and a vertical semi-axis of an ellipse or an ellipsoid, while γ stands for the ratio of a horizontal axis to a vertical axis. The function I may be computed according to equation (25) from

$$I = \frac{1}{1+3\lambda} : \qquad \text{vertical flat plates} \quad (34a)$$

$$I = \frac{1}{1+3\lambda} \frac{(\sin^2\phi+\gamma^2\cos^2\phi)^{1/2}}{\int_0^\phi (\sin^2\phi+\gamma^2\cos^2\phi)^{1/2}d\phi} \frac{1-\cos\phi}{\sin\phi} : \qquad \text{horizontal ellipses} \quad (34b)$$

$$I = \frac{1}{1+3\lambda} \frac{(\sin^2\phi+\gamma^2\cos^2\phi)^{1/2}}{\int_0^\phi (\sin^2\phi+\gamma^2\cos^2\phi)^{1/2}d\phi} \frac{\cos^3\phi-3\cos\phi+2}{3\sin^3\phi} : \qquad \text{ellipsoids} \quad (34c)$$

Consequently, the local surface heat flux of the primary interest may be evaluated from

$$q^* = [-f''(0)](1+3\lambda)^{1/2}(x/L_r)^{\frac{3\lambda-1}{2}} : \qquad \text{vertical flat plates} \quad (35a)$$

$$q^* = [-f''(0)](1+3\lambda)^{1/2} \frac{\sin\phi}{[(1-\cos\phi)(\sin^2\phi+\gamma^2\cos^2\phi)]^{1/2}} \left(\frac{1-\cos\phi}{2}\right)^{\frac{3\lambda}{2}} : \qquad \text{horizontal ellipses} \quad (35b)$$

$$q^* = [-f''(0)](1+3\lambda)^{1/2} \frac{\sin^2\phi}{\left[\left(\frac{1}{3}\cos^3\phi-\cos\phi+\frac{2}{3}\right)(\sin^2\phi+\gamma^2\cos^2\phi)\right]^{1/2}} \times \left(\frac{\cos^3\phi-3\cos\phi+2}{4}\right)^{\frac{3\lambda}{2}} : \qquad \text{ellipsoids} \quad (35c)$$

where

$$q^* \equiv \left(\frac{q_w L_r}{\Delta T_{wr} k}\right) \Big/ \left(\frac{K\beta\Delta T_{wr} g L_r}{\alpha\nu}\right)^{1/2} \tag{35d}$$

ΔT_{wr} is the wall-ambient temperature difference at a trailing edge or a rear stagnation point. Fortunately, the local surface heat flux q^* expressions for ellipses and ellipsoids, namely, equations (35*b*) and (35*c*), do not require any numerical integrations with respect to ϕ. (Numerical integrations would be needed if we were to evaluate Nu_x instead; see equations (24) and (34).)

The surface wall temperature distributions which permit similarity solutions are plotted in Figs. 3(*a*) and 3(*b*) for ellipses and ellipsoids, rexpectively. The ordinate variable is chosen to be the wall-ambient temperature difference ΔT_w normalized by its value at the rear stagnation point ΔT_{wr}. The wall temperature rise near the front stagnation point becomes steeper for smaller λ, and an inflection point appears when $\lambda > 1/2$ for ellipses, and $\lambda > 1/4$ for ellipsoids. The surface local heat fluxes on a horizontal circular cylinder and a sphere ($\gamma = 1$) computed from equations (35*b*) and (35*c*) are presented in Figs. 4(*a*) and 4(*b*), respectively. As λ increases, the local surface heat flux distribution diverges from that for the isothermal case ($\lambda = 0$), which has previously been treated by Cheng [20]. The location of the maximum heat flux consistently moves downstream. This trend can be appreciated in consideration of the relationship $q_w \propto \Delta T_w/\delta$ with the fact that ΔT_w increases steeply near the front stagnation point, while δ approaches infinity at the rear stagnation point. Both figures indicate a close similarity between the heat flux distributions of a horizontal circular cylinder and a sphere. The heat flux variation over a sphere (shown in Fig. 4*b*), however, is somewhat more concentrated within the region away from the front and rear stagnation points, as a result of a three-dimensional geometric effect.

Figures 5(*a*) and 5(*b*) show the local surface heat flux distributions over isothermal ellipses and ellipsoids, for three different values of γ, namely, $\gamma = 0.5$, 1, and 2. Naturally, the distribution for a small γ (i.e., a slender body) exhibits a pattern similar to that of a vertical flat plate (namely, $q_w \propto$

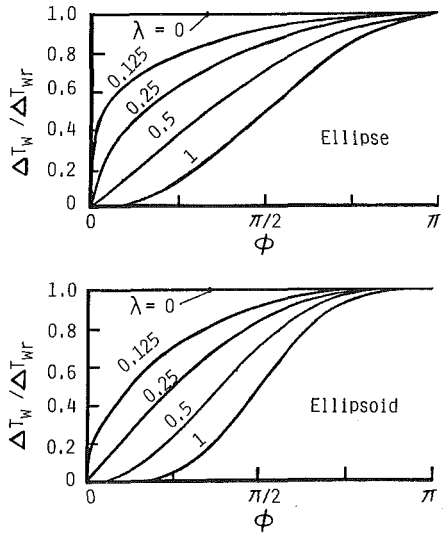

Fig. 3 Wall temperatures distributions: (*a*) ellipses; (*b*) ellipsoids

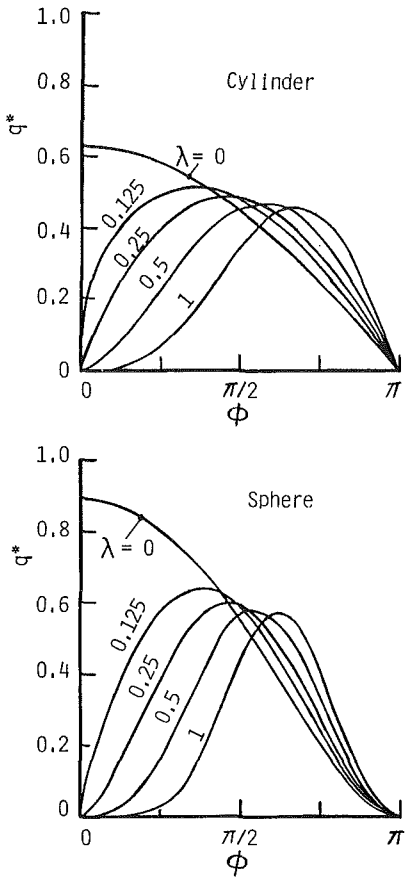

Fig. 4 Effect of wall temperature distributions on local heat fluxes: (a) a horizontal circular cylinder: (b) a sphere

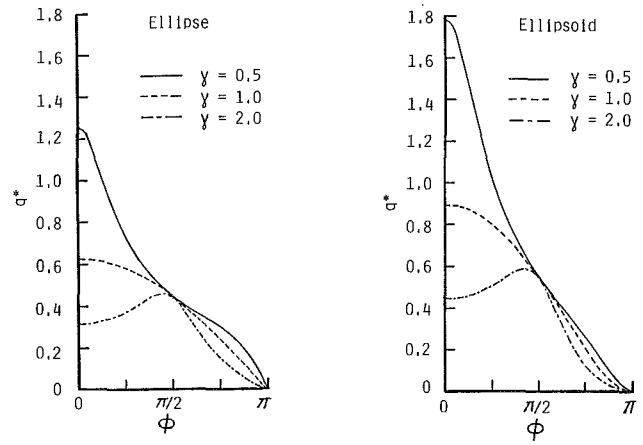

Fig. 5 Geometric effect on local heat fluxes: (a) horizontal ellipses; (b) ellipsoids

$x^{-1/2}$). The heat flux for a larger $\gamma(>1)$, on the other hand, increases away from the front stagnation point, and attains a maximum, as the flow accelerates due to a significant streamwise increase in g_x. But, as the boundary layer thickens quickly, it decreases downstream, resulting in a nonmonotonic variation of the surface heat flux. It is also interesting to note that the q^* values at $\phi = \pi/2$ are at the same level for all values of γ. (See equations (35*b*) and (35*c*).)

Conclusions

In this study, similarity solutions have been obtained for the problem of free convection heat transfer of a Darcian fluid about a nonisothermal body of arbitratry geometric configuration. The resulting ordinary differential equation turns out to be identical to that of a vertical flat plate with its wall temperature varying exponentially. It is found that all two-dimensional and axisymmetric bodies possess corresponding classes of similarity solutions, when the wall temperature varies according to a power function of the transformed variable ξ, which measures the elevation from a front stagnation point for the case of two-dimensional bodies, and the volume segment cut by a horizontal plane for the case of axisymmetic bodies.

An attempt was also made to attack the same problem by means of the Kármán–Pohlhausen integral procedure. A general closed-form formula has been reduced for the local surface heat flux distribution over a nonisothermal body of arbitrary shape. Comparison of the approximate solution against the exact solution reveals a high accuracy acquired in the present integral method.

Illustrative calculations were carried out on a vertical flat plate, various horizontal ellipses, and ellipsoids. The calculated results substantiate the validity of the present analysis.

References

1 Cheng, P., "Heat Transfer in Geothermal Systems," *Advances in Heat Transfer*, Vol. 14, 1978, pp. 1–105.

2 Wooding, R. A., "Convection in a Saturated Porous Medium at Large Rayleigh Number or Peclet Number," *J. Fuid Mech.*, Vol. 15, 1963, pp. 527–544.

3 McNabb, A., "On Convection in a Porous Medium," *Proc. 2nd Australasian Conf. on Hydraulics and Fluid Mech.*, University of Auckland, New Zealand, 1965, pp. c 161–c 171.

4 Avduyevski, V. S., Kalashnik, V. N., Kopyatevich, R. M., "Investigation of Free-Convection Heat Transfer in Gas-Filled Porous Media at High Pressures," *Heat Transfer—Soviet Research*, Vol. 10, 1978, pp. 136–144.

5 Cheng, P., and Minkowycz, W. J., "Free Convection About a Vertical Flat Plate Embedded in a Saturated Porous Medium With Application to Heat Transfer From a Dike," *J. Geophysics Research*, Vol. 82, 1977, pp. 2040–2044.

6 Cheng, P., and Chang, I., "Buoyancy Induced Flows in a Saturated Porous Medium Adjacent to Impermeable Horizontal Surfaces," *Int. J. Heat Mass Transfer*, Vol. 19, 1976, pp. 1267–1272.

7 Minkowycz, W. J., and Cheng, P., "Free Convection About a Vertical Cylinder Embedded in a Porous Medium," *Int. J. Heat Mass Transfer*, Vol. 19, 1976, pp. 805–813.

8 Sparrow, E. M., and Yu, H. S., "Local Non-similarity Thermal Boundary Layer Solutions," ASME JOURNAL OF HEAT TRANSFER, Vol. 93, 1971, pp. 328–334.

9 Nilson, R. H., "Natural Convective Boundary Layer on Two-Dimensional and Axisymmetric Surfaces in High-Pr Fluids or in Fluid Saturated Porous Media," ASME JOURNAL OF HEAT TRANSFER, Vol. 103, 1981, pp. 803–807.

10 Merkin, J. H., "Free Convection Boundary Layers on Axisymmetric and Two-Dimensional Bodies of Arbitrary Shape in a Saturated Porous Medium," *Int. J. Heat Mass Transfer*, Vol. 22, 1979, pp. 1416–1462.

11 Cheng, P., "Mixed Convection About a Horizontal Cylinder and a Sphere in a Fluid Saturated Porous Medium," *Int. J. Heat Mass Transfer*, Vol. 25, 1982, pp. 1245–1247.

12 Minkowycz, W. J., Cheng, P., and Chang, C. H., "Mixed Convection About a Non-isothermal Cylinder and Sphere in a Porous Medium," *Numerical Heat Transfer*, Vol. 8, 1985, pp. 349–359.

13 Schlichting, H., *Boundary Layer Theory*, 6th ed., McGraw-Hill, New York, 1968.

14 Nakayama, A., Koyama, H., and Ohsawa, S., "An Approximate Solution Procedure for Laminar Free and Forced Convection Problems," *Int. J. Heat Mass Transfer*, Vol. 26, 1983, pp. 1721–1726.

15 Nakayama, A., and Koyama, H., "An Integral Treatment of Laminar and Turbulent Film Condensation on Bodies of Arbitrary Geometrical Configuration," ASME JOURNAL OF HEAT TRANSFER, Vol. 107, 1985, pp. 417–423.

16 Acrivos, A. M., Shah, M. J., and Petersen, E. E., "Momentum and Heat Transfer in Laminar Boundary Layer Flows on Non-Newtonian Fluids Past External Surfaces," *AIChE Journal*, Vol. 6, 1960, pp. 312–317.

17 Nakayama, A., Shenoy, A. V., and Koyama, H., "An Analysis for Forced Convection Heat Transfer From External Surfaces to Non-Newtonian Fluids," *Warme- und Stoff.*, Vol. 20, 1986, pp. 219–227.

18 Cheng, P., "Convective Heat Transfer in Porous Layers by Intergral Methods," *Letters in Heat and Mass Transfer*, Vol. 5, 1978, pp. 243–252.

19 Bejan, A., *Convection Heat Transfer*, Wiley, New York, 1984, pp. 367–371.

20 Cheng, P., "Natural Convection in Porous Media: External Flows," in: *Natural Convection Fundamental and Applications*, W. Aung, S., Kakac, and R. Viskanta, R., Martinus Nijhoff Publishers, The Hague, the Netherlands, 1985.

Hin-Sum Law

J. H. Masliyah

K. Nandakumar

Department of Chemical Engineering,
University of Alberta,
Edmonton, Alberta, T6G 2G6 Canada

Effect of Nonuniform Heating on Laminar Mixed Convection in Ducts

Combined convection flow in square, circular, and semicircular ducts was numerically studied for axially uniform heat flux. The peripheral condition is that of the top half of the duct is insulated while the bottom half is heated. For the case of a square duct, dual solutions are obtained where the secondary flow is characterized either with two or four vortices. Regions of dual solutions have been mapped in the parameter space of aspect ratio and Grashof number. For the case of a circular duct, only the solution characterized by two vortices is obtained.

Introduction

Combined free and forced convection flows, i.e., mixed convection flows, have been studied extensively for various enclosure shapes and thermal boundary conditions. Due to the superposition of the buoyancy effects on the main flow there is a secondary flow in the form of a vortex recirculation pattern. For the case of circular and square ducts with the boundary conditions of uniform axial flux and uniform peripheral temperature, Chang and Hwang [1] and Hwang and Cheng [2] found that the secondary flow is characterized by a two-vortex recirculation pattern. Recently Chou and Hwang [3] extended the work for higher values of ReRa. They observed a change in flow behavior from a two-vortex recirculation pattern to a four-vortex pattern, but they did not observe dual solutions or hysteresis behavior.

Recently, Nandakumar et al. [4] extended the aforementioned studies using a numerical solution of the flow and energy equations for a higher Grashof number and found that above a critical Grashof number, the mixed convection problem exhibited a dual solution. In one solution a two-vortex pattern emerges while in the other solution a four-vortex pattern evolves. Such a dual solution or flow bifurcation can be obtained as follows: Starting with a low Grashof number as the initial condition for the iterative solution procedure, a converged solution is obtained. Such a solution exhibits a two-vortex flow pattern. On *slowly* increasing the Grashof number, new solutions are obtained, all of which exhibit a two-vortex flow pattern. Once a critical Grashof number is reached, say, Gr_u, the flow pattern becomes that of a four-vortex type. On further increasing the Grashof number, such a pattern is preserved. Now, decreasing Grashof number *slowly* the four-vortex pattern can be preserved until a new critical Grashof number Gr_l is reached. For a Grashof number smaller than Gr_l the flow pattern becomes that of a two-vortex one. As $Gr_u > Gr_l$, a hysteresis loop is present and a dual solution is thus exhibited for $Gr_l < Gr < Gr_u$.

Recently, Patankar et al. [5] examined the case of mixed convection flow in a circular tube for the thermal boundary condition of axially uniform flux with a peripheral boundary condition of the top half of the cylinder insulated and its bottom half heated at a specified flux. They predicted a flow transition from a two-vortex pattern to a four-vortex one above a Grashof number of about 100,000. They however did not report dual solutions.

The work of Patankar et al. together with our earlier experience with a mixed convection flow having a different thermal boundary condition [4], and isothermal flow in curved tubes [6, 7], have been the motivating factors in our decision to re-examine this problem.

Contributed by the Heat Transfer Division for publication in the JOURNAL OF HEAT TRANSFER. Manuscript received by the Heat Transfer Division June 10, 1985.

In this paper mixed convection flow in circular and square ducts will be examined for a thermal boundary condition of axially uniform flux. Along the periphery, the top half of the duct is insulated while the bottom half is heated at a specified flux. Patankar et al. [5] have examined an identical set of thermal boundary conditions, noting that such nonuniform heating can arise in solar collectors. The present work however is motivated by the multiplicity characteristics of this heat transfer problem.

Governing Equations

Three coordinate systems were employed. A Cartesian system of coordinates is used for the straight rectangular ducts. Circular cylindrical and bipolar coordinates are used for the case of circular and semicircular straight ducts. The bipolar coordinate system has been used successfully elsewhere [7] in studying the bifurcation phenomena in curved tubes. In such studies the ability to change the geometric shape gradually and smoothly from a semicircular duct to a circular duct through several intermediate moon shaped configurations is essential. The resulting solution should of course be independent of the choice of the coordinate system. But the region of attraction of stable solutions is strongly influenced by the shape of the geometry and the coordinate system used.

The equations of motion and energy for the mixed convection problem are formulated in the stream function–vorticity form. The viscous dissipation and compressibility effects in the energy equation are neglected. The Boussinesq approximation is invoked to account for the temperature variation of density in the body force term. Furthermore, the thermal boundary condition of axially uniform heat flux has been imposed on the energy equation.

The equations of motion and energy for the fully developed, mixed free and forced convection are given in dimensionless form as

Stream function equation

$$\nabla^2\psi = -\Omega \tag{1}$$

Axial vorticity equation

$$\nabla^2\Omega - (\mathbf{v}\cdot\nabla)\Omega = B \tag{2}$$

Axial velocity equation

$$\nabla^2 w - (\mathbf{v}\cdot\nabla w) = -1 \tag{3}$$

Energy equation

$$\nabla^2\phi - \mathrm{Pr}(\mathbf{v}\cdot\nabla\ \phi) = +\frac{w}{\langle w\rangle}\frac{1}{A} \tag{4}$$

The condition of axially constant heat flux is reflected in the right-hand side of equation (4). The quantity A is given by

Table 1 Expansion of equations (1)–(4) in various coordinates

Quantity	Cartesian (y, x, z)	Cylindrical (θ, r, z)	Bipolar (ξ, η, z)
$(\mathbf{v}\cdot\nabla)$	$\left(v_x \frac{\partial}{\partial x}+v_y \frac{\partial}{\partial y}\right)$	$\left(v_r \frac{\partial}{\partial r}+\frac{v_\theta}{r}\frac{\partial}{\partial \theta}\right)$	$f_1\left(v_\xi \frac{\partial}{\partial \xi}+v_\eta \frac{\partial}{\partial \eta}\right)$
∇^2	$\frac{\partial^2}{\partial x^2}+\frac{\partial^2}{\partial y^2}$	$\frac{\partial^2}{\partial r^2}+\frac{1}{r}\frac{\partial}{\partial r}+\frac{1}{r^2}\frac{\partial^2}{\partial \theta^2}$	$f_1^2\left(\frac{\partial^2}{\partial \xi^2}+\frac{\partial^2}{\partial \eta^2}\right)$
B (body force)	$\mathrm{Gr}\frac{\partial \phi}{\partial x}$	$\mathrm{Gr}\left\{\cos\theta \frac{\partial \phi}{\partial r}-\frac{\sin\theta}{r}\frac{\partial \phi}{\partial \theta}\right\}$	$-\mathrm{Gr}\left[\sin\xi \sinh\eta \frac{\partial \phi}{\partial \xi}+(-1+\cos\xi\cosh\eta)\frac{\partial \phi}{\partial \eta}\right]$
Stream function	$v_x=-\frac{\partial \psi}{\partial y}$	$v_r=-\frac{1}{r}\frac{\partial \psi}{\partial \theta}$	$v_\xi=-f_1\frac{\partial \psi}{\partial \eta}$
	$v_y=\frac{\partial \psi}{\partial x}$	$v_\theta=\frac{\partial \psi}{\partial r}$	$v_\eta=f_1\frac{\partial \psi}{\partial \xi}$

Note: $f_1 = \cosh\eta - \cos\xi$.

$$A = \text{flow area}/a^2$$

where a is the radius for the circular geometry or half side of the duct for a rectangular geometry. The vector operators in equations (1)–(4) for the various coordinates are defined in Table 1. The flow and energy equations were rendered dimensionless as follows:

$$\psi=\psi'/\nu,\ \Omega=\Omega'/(\nu/a^2),\ w=\frac{w'}{\left(-\frac{dp'}{dz'}\right)(a^2/\mu)},$$

$$x=x'/a,\ y=y'/a,\ r=r'/a,\ z=z'/a,$$

$$\phi=\frac{T-T_b}{(Q'/k)},\ \mathrm{Gr}=Q'g\,\beta\,a^3/k\nu^2$$

The definition of the Grashof number is from Patankar et al. The secondary velocities were rendered dimensionless using (ν/a). The term dp'/dz' is the axial pressure gradient and it is constant for a fully developed flow. For the case of the bipolar coordinates, the transformation $\eta = 0.5(e^{\beta} - 1)$ has been found useful in providing more grid points near the coordinate $\eta = 0$. The bipolar coordinates are such that a semi-infinite domain must be spanned in the η-coordinate direction. But the finite-difference method requires the selection of a finite domain. Choosing $\beta = 3$ ($\eta = 9.5428$) spans most of the physical space with $r = 0.99986$ (as opposed to the exact value of unity). In this manner the singularity at $\eta = \infty$ is avoided.

The boundary conditions for the stream function and vorticity arise out of imposing the no-slip condition on the wall and the symmetry condition along $x = 0$. The thermal boundary conditions are given by:

Cartesian coordinates

$$\frac{\partial \phi}{\partial n}=0 \qquad \text{for the insulated portion of the wall} \qquad (5a)$$

$$\frac{\partial \phi}{\partial n}=\pm\frac{1}{2(1+\gamma)} \qquad \text{for the heated wall} \qquad (5b)$$

Circular coordinates

$$\frac{\partial \phi}{\partial r}=0 \qquad \text{for } 0<\theta<\frac{\pi}{2} \qquad (6a)$$

(top semicircular wall)

$$\left.\frac{\partial \phi}{\partial r}\right|_{r=1}=\frac{1}{\pi} \qquad \text{for } -\frac{\pi}{2}<\theta<0 \qquad (6b)$$

(bottom semicircular wall)

Nomenclature

a = half side of square tube or radius of cylinder
A = flow area/a^2
C_1 = heated perimeter, equation (8)
D_e = equivalent diameter, 4 • flow area/wetted perimeter
f = Fanning friction factor = $\tau_w/(1/2\,\rho\,\langle w\rangle^2)$
g = gravitational acceleration
Gr = Grashof number = $Q'\,g\,\beta\,a^3/k\,\nu^2$
k = thermal conductivity
Nu = average Nusselt number = $D_e\,h/k$
p' = pressure, dimensional
P = wetted perimeter, equation (10)
Q' = heat transfer rate per unit length of duct
r = r'/a = radial coordinates
Re = Reynolds number = $D_e'\langle w\rangle\,\rho/\mu$
T = temperature, dimensional
v = secondary velocity = $v'/(\nu/a)$
w = axial velocity
x = Cartesian coordinates = x'/a
y = Cartesian coordinates = y'/a
β = thermal expansion coefficient
γ = aspect ratio
η = bipolar coordinate
θ = cylindrical coordinate
μ = viscosity
ν = kinematic viscosity
ξ = bipolar coordinate
ρ = density
τ_w = shear stress at wall
ϕ = temperature
ψ = stream function = ψ'/ν
Ω = axial vorticity = $\Omega'/(\nu a^2)$

Subscripts

l = lower value
u = upper value
x = x direction
y = y direction
η = η direction
ξ = ξ direction

Superscripts and Symbols

'(prime) = dimensional quantity
$\langle\ \rangle$ = average quantity

Table 2 Grid sensitivity for circular geometry; Pr = 0.7, full circle

Gr	Grid	$f\mathrm{Re}/f\mathrm{Re}_0$	$\mathrm{Nu}/\mathrm{Nu}_0$
100,000	21×21	1.4773	3.564
	21×31	1.4838	3.282
	31×31	1.4864	3.280
400,000	21×21	1.8398	5.265
	21×31	1.7544	4.375
	31×41	1.7578	4.120

Bipolar coordinates

$$\left.\frac{\partial\phi}{\partial\xi}\right|_{\xi=3\pi/2}=0 \qquad \text{for } 0<\eta<\infty \qquad (7a)$$

(top semicircular wall)

$$f_1\left.\frac{\partial\phi}{\partial\xi}\right|_{\xi_{\min}}=-\frac{1}{C_1} \qquad \text{for } \xi=\xi_{\min} \qquad (7b)$$

(bottom wall of the duct)

where C_1 is the circumference of the lower heated portion of the duct. The shape of the duct can be changed by selecting different values of ξ_{min}. For a circular duct $\xi_{min} = \pi/2$ and $C_1 = \pi$. For a semicircular duct with a flat lower portion, $\xi_{\min} = \pi$ and $C_1 = 2$. For any other value of $\xi_{\min}$ we obtain a moon-shaped duct with a heated length given by

$$C_1=\frac{4}{\sin\xi_{\min}}\left[\frac{\pi}{2}-\tan^{-1}\sqrt{\frac{1-\cos\xi_{\min}}{1+\cos\xi_{\min}}}\right] \qquad (8)$$

In addition one must satisfy the overall energy balance which is given by

$$\int_{-1}^{1}\int_{0}^{\gamma}\phi\, w\, dx\, dy=0 \qquad \text{Cartesian coordinates} \qquad (9a)$$

$$\int_{0}^{1}\int_{-\pi/2}^{\pi/2}\phi\, r\, w\, d\theta\, dr=0 \qquad \text{Circular coordinates} \qquad (9b)$$

$$\int_{0}^{\infty}\int_{\xi_{\min}}^{3\pi/2}\frac{\phi w}{f_1^2}\,d\xi d\eta=0 \qquad \text{Bipolar coordinates} \qquad (9c)$$

The Fanning friction factor is obtained from

$$f\mathrm{Re}=2D_eA/(P<w>) \qquad (10)$$

and the average Nusselt number is given by

$$\mathrm{Nu}=D_e/(C_1<\phi_w>) \qquad (11)$$

where A is the dimensionless flow area, D_e is the equivalent diameter and C_1 is the heated perimeter. The average Nusselt number is based on the duct equivalent diameter.

The governing partial differential equations were discretized using central difference approximations. As both diffusive and convective mechanisms are important in this problem, central difference approximations were preferred over the upwind differencing scheme as the latter might introduce parasitic effects and false scaling as shown by Strikwerda [8]. The resulting algebraic equations were solved in the order of ϕ–Ω–ψ–w until convergence was attained. For the rectangular duct most of the solutions were obtained with a uniform grid of 21 × 21 over the domain $0 < x < \gamma$ and $-1 < y < 1$. The adequacy of this grid size was verified by reproducing previously obtained solutions by Cheng and Hwang [1] for the case of peripherally uniform temperature boundary. For Gr = 500,000 (with a four-vortex pattern) a grid refinement from 21 × 21 to 21 × 41 resulted in the following changes in macroscopic quantities: fRe and Nu changed from 27.046 and 8.898 for the coarse grid to 27.014 and 8.879 for the fine grid. Nevertheless, the coarse grid was used as well over 300 simulations were required to determine the stability boundaries shown in Fig. 5. The uncertainty in the critical points was reduced to about 5 percent and are indicated by the length of the arrow in Fig. 5. The macroscopic results for the circular geometry were found to be much more sensitive to the choice of grid size. A measure of this dependence is shown in Table 2. A grid size of 31 × 41 was used for this geometry.

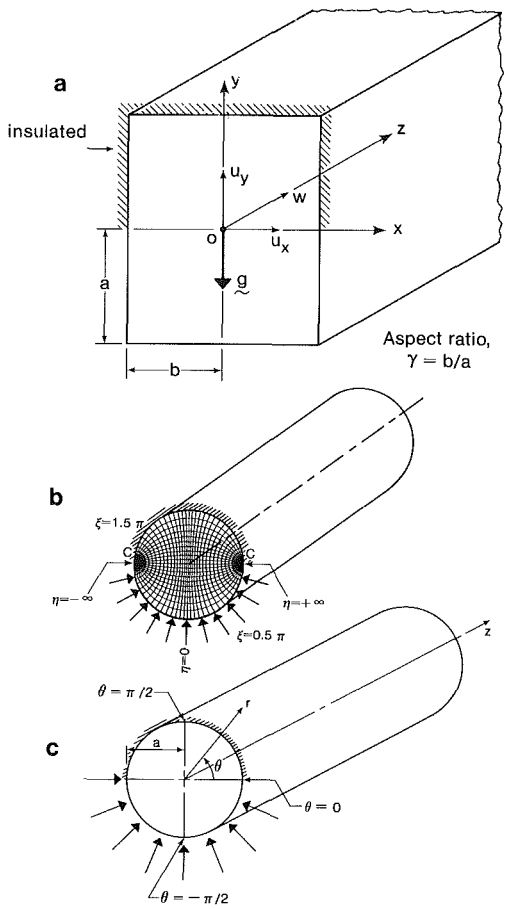

Fig. 1 (*a*) Cartesian coordinate system; (*b*) bipolar coordinate system; (*c*) circular coordinate system

Rectangular Ducts

The variation of the friction factor and Nusselt number with Grashof number for a square duct for Pr = 0.7 is shown in Figs. 2 and 3. Both the friction factor and Nusselt number data show a hysteresis behavior as Grashof number is *gradually* increased and then gradually decreased. For Gr < 89,800 only a two-vortex solution is present while for Gr > 170,000 only a four-vortex solution can be obtained. Between these two limits, both types of solutions are possible. Similar behavior was observed by Nandakumar et al. [4] for the case of mixed flow in a square duct with boundary condition of constant axial flux and uniform peripheral wall temperature.

It might be instructive to give the details on how the results of Figs. 2 and 3 are obtained. Starting with a converged solution for a small Grashof number, say 10,000, as the initial guess of the field, a converged solution was then obtained for a slightly higher Grashof number, say 15,000. Using the solution at Gr = 15,000 a new solution at a still slightly higher Grashof number, say 20,000, was then obtained. These solutions are given by the curve ABC in Figs. 2 and 3. The solution exhibits a two-vortex pattern. On further increasing the Grashof number beyond its value at C, the solution exhibits a four-vortex flow pattern and such a pattern is maintained on further increasing the Grashof number. On *gradually* decreasing the Grashof number from its value at D, curve DC′B′ is followed and such a curve is for a four-vortex flow pattern. However, on further decreasing the Grashof number below its value at B′, the solution becomes that of a two-

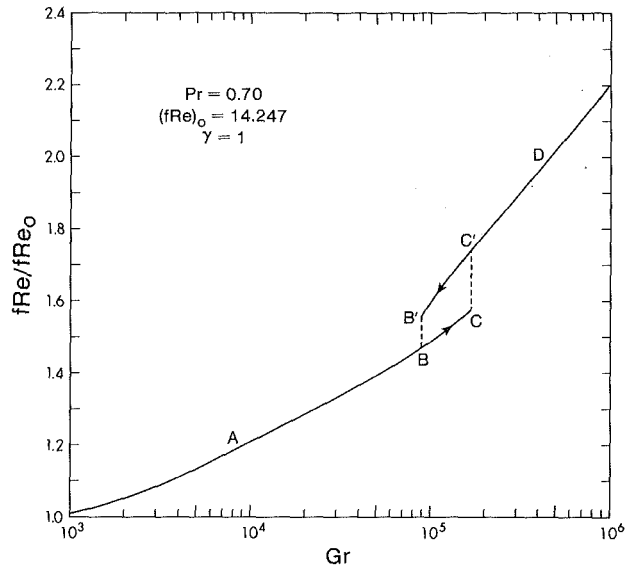

Fig. 2 Friction factor variation with Grashof number for a square duct

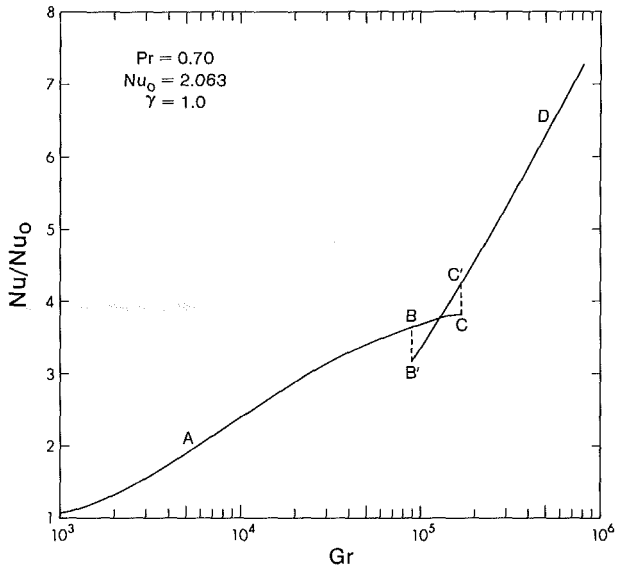

Fig. 3 Nusselt number variation with Grashof number for a square duct

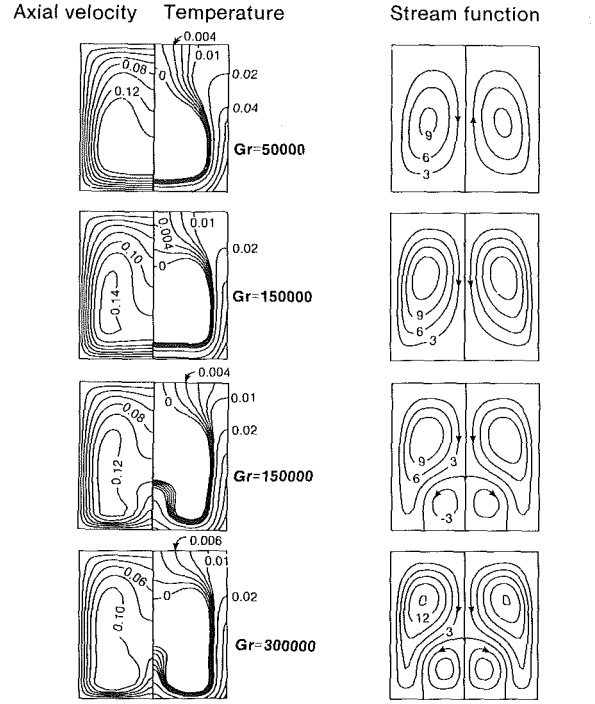

Fig. 4 Contours of axial velocity, temperature, and stream function for a square duct

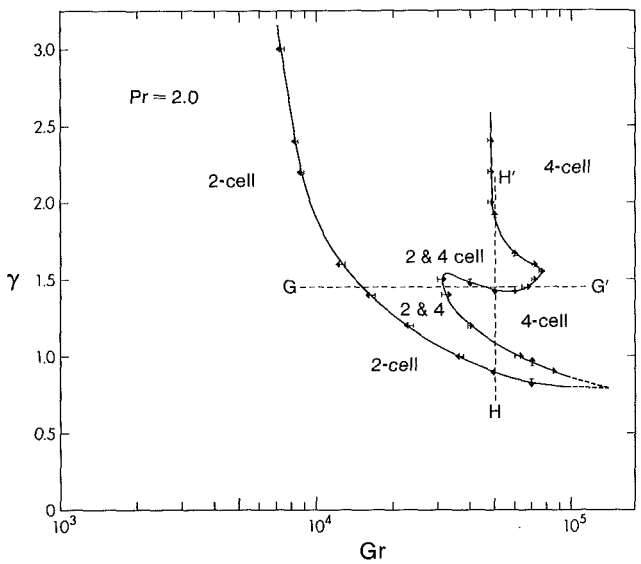

Fig. 5 Map of dual solution region in the Grashof number-aspect ratio space for Pr = 2.0

vortex pattern. A further decrease in Gr retraces the curve BA. A hysteresis behavior is present and the unfolding of such a phenomenon, when the aspect ratio γ is changed, can be interpreted in terms of a cusp catastrophy as done by Benjamin [9, 10] in his experiments on the Taylor problem with a finite geometry.

Figure 4 shows a series of contour plots for axial velocity, temperature, and stream function. At a Grashof number of 50,000 only a two-vortex pattern is observed. The axial velocity and temperature show a boundary layer structure with sharp gradients close to the lower wall, i.e., in the direction of gravitational force. Both two and four-vortex patterns are observed at a Grashof number of 150,000. The additional vortices attach themselves to the lower duct wall and are fairly intense. At a Grashof number of 300,000 only a four-vortex pattern is observed.

The variation of the critical Grashof numbers (i.e., points corresponding to BB′ and CC′ in Figs. 2 and 3) with the aspect ratio is shown in Fig. 5, for a Prandtl number of 2.0. First observe the effect of Prandtl number on the critical points at $\gamma = 1$. The upper critical point has moved from 170,000 for Pr = 0.7 to 62,500 for Pr = 2.0. Similarly the lower critical point has changed from 89,800 at Pr = 0.7 to 37,500 at Pr = 2.0. The hysteresis behavior is still present, but occurs at a much earlier flow condition. As the aspect ratio γ is increased, the range of Grashof number over which hysteresis is exhibited increases. The arrows in Fig. 5 indicate the uncertainty in the critical Grashof number or aspect ratio values, i.e., starting at any point inside the dual solution region and changing the parameter values by a small value, such that the boundary is crossed, would result in a flow pattern change. The bisection method used in this work cannot determine these critical points precisely, but can only bracket them within a range.

As the aspect ratio is decreased, the two-vortex solution remains stable for higher values of Grashof number. The critical curves (the loci of critical points) show some interesting behavior over a narrow range of aspect ratio of 1.4 to 1.55.

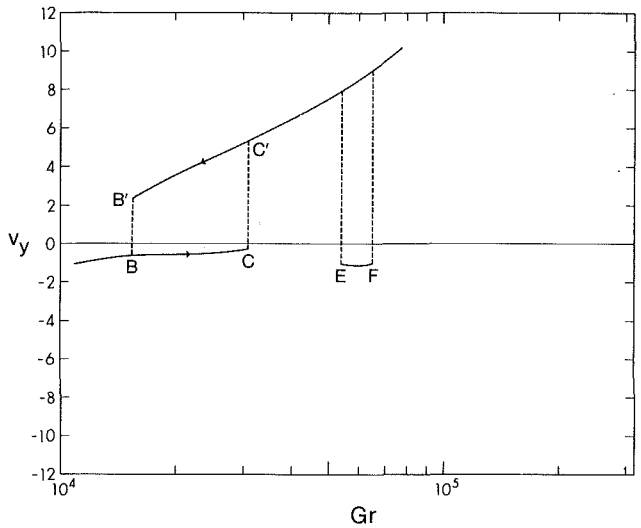

Fig. 6 Bifurcation diagram for a fixed aspect ratio, i.e., 1.45; corresponds to section GG′ in Fig. 5

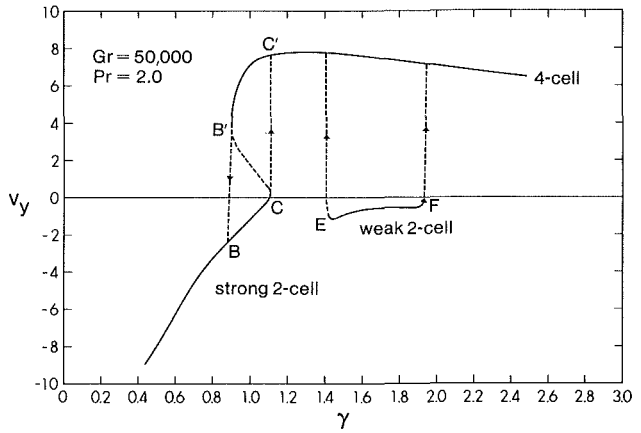

Fig. 7 Bifurcation diagram for a fixed Grashof number of 50,000; corresponds to section HH′ in Fig 5

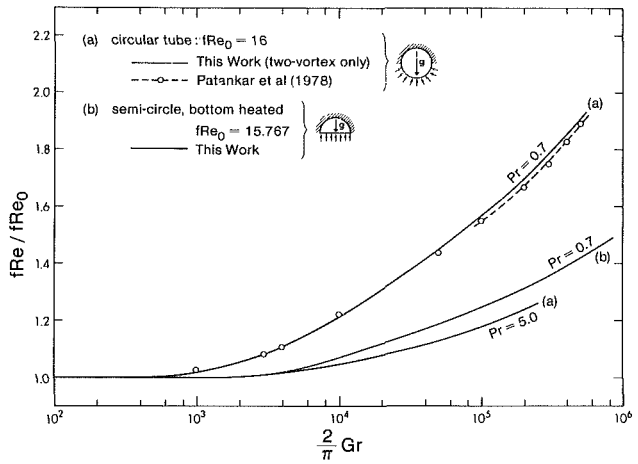

Fig. 8 Friction factor variation with Grashof number for circular and semicircular ducts

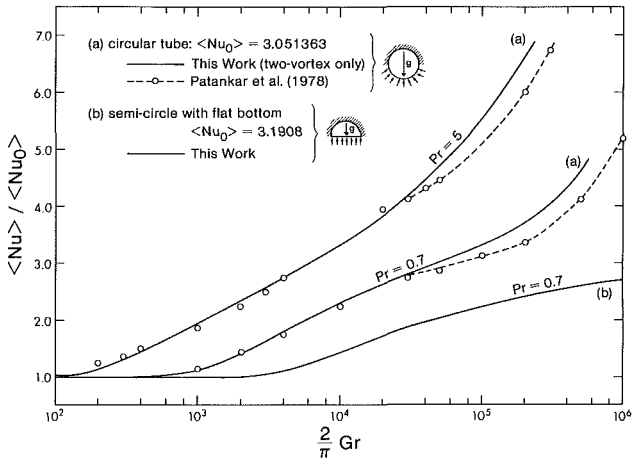

Fig. 9 Nusselt number variation with Grashof number for circular and semicircular ducts

These are illustrated with the help of a bifurcation diagram in Figs. 6 and 7. Figure 6 shows a section through GG′ in Fig. 5, i.e., for a fixed aspect ratio of $\gamma = 1.45$. The changes in the vertical velocity component $v(x=0, y=0.8)$ at a fixed point are followed as the Grashof number is changed. This point is chosen because the velocity changes direction as the flow pattern changes. The hysteresis behavior with respect to Gr is evident between BB′ and CC′. However, there is a second, isolated two-vortex solution region between E and F. A similar phenomenon has been reported by Cheng et al. [11] for flow through a curved pipe. Figure 7 shows a similar plot along a section HH′ in Fig. 5, i.e., for a fixed Grashof number but varying aspect ratio. The second, isolated two-vortex solution region around EF is seen to be weak in circulation. The strength of the primary two-vortex solution is high to begin with, but decreases rapidly as the aspect ratio is increased. Similar phenomena known to exist are the Taylor problem [9] and the Dean problem [7]. The effect of other geometric shapes is investigated next.

Circular Ducts

The variation of the friction factor and Nusselt number for circular ducts at $Pr = 0.7$ and 5 and for a semicircular duct at $Pr = 0.7$ are presented in Figs. 8 and 9. For these three cases, a two-vortex solution was the only flow obtained over the range of Grashof numbers investigated here. Figure 10 shows the

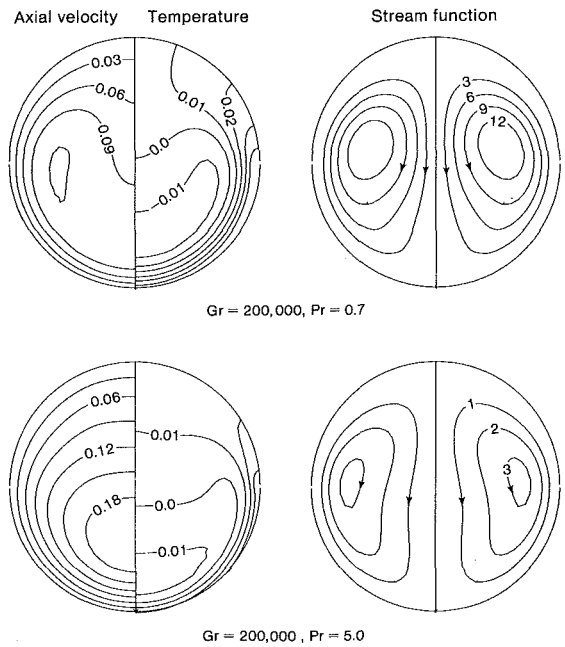

Fig. 10 Contours of axial velocity, temperature, and stream function for a circular duct

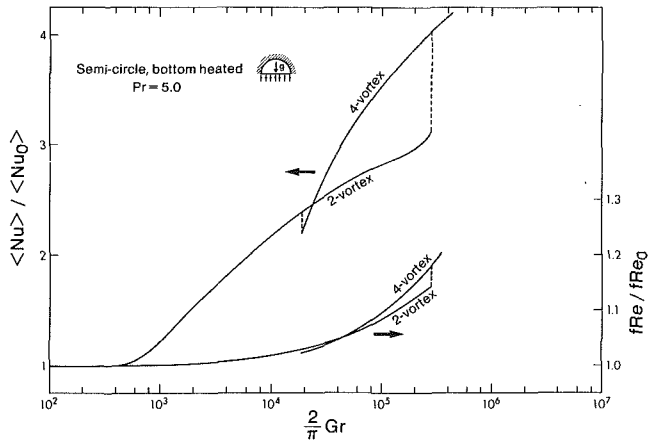

Fig. 11 Friction factor and Nusselt number variation with dual solution for Pr = 5.0 in a semicircular duct

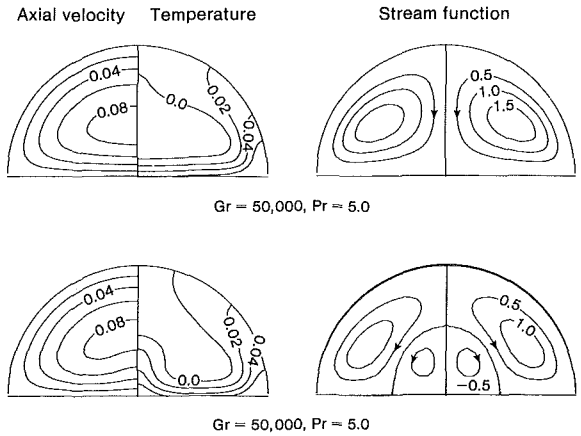

Fig. 12 Contours showing dual solutions for Pr = 5 in a semicircular duct

contours of stream function, axial velocity, and temperature for a circular duct for Pr = 0.7 and 5.0. At higher Prandtl numbers the temperature contour shows a plateau in the core and thus the secondary flow is weak. This is accompanied by a lower friction factor as seen in Fig. 8. There is, however, a sharp temperature gradient close to the lower portion of the wall for Pr = 5, a situation conducive to the formation of the alternate four-vortex pattern. Yet we could not establish a converged four-vortex solution as a stable dual solution at high Gr for any of the three cases. The central difference method used in this study always converged to a stable two-vortex flow. These results for a circular duct are in contradiction to those of Patankar et al. [5]. All of their macroscopic results like fRe and Nu show a sudden change in the slope between Grashof numbers of 100,000 and 200,000. This appears to be accompanied by a change in flow pattern from a two-vortex to a four-vortex pattern. They however do not observe dual solutions at higher Grashof number, i.e., they do not predict a two-vortex flow also at these high Grashof numbers. The fRe and Nu values calculated in this study are in reasonable agreement with those of Patankar et al. [5] for Gr of up to about 100,000. This is not surprising as both studies predict a two-vortex pattern in this region. At higher Grashof numbers, the difference is attributed to the different flow patterns observed in these two studies.

Although our reason to initiate this study was to show that dual solutions are possible for this geometry, a four-vortex solution or a dual solution could not be established at these Prandtl numbers from the same discretized equations of motion. Two factors appear to influence the onset of four-cell solution. Increasing Prandtl number appears to aid the formation of four-cell flow at earlier Gr. We have seen an example of this in the square geometry. Secondly a flat wall geometry facing the body force appears to aid in the formation of four-cell pattern. This has been observed in earlier studies as well [4, 6, 7]. This was the motivating factor in our choice of the bipolar coordinate system. In this coordinate system, the coordinate ξ can be changed in small steps from π to $\pi/2$, effecting a gradual change in geometry from a semicircle to a full circle (see Fig. 1*b*). We were successful in establishing a four-cell solution for a semicircular duct with a flat bottom wall at Pr = 5.0. The results for fRe and Nu are shown in Fig. 11 and the contours of flow and temperature fields are shown in Fig. 12. For this case the range of Gr over which dual solutions are present is fairly large.

Using the converged four-cell solution for the above case as the initial guess, the semicircular geometry was changed gradually to a full circle by changing the lower boundary ξ. This was done in an attempt to see whether the four-cell pattern could be preserved for the circular geometry at Pr = 5. However, in all the cases we studied, the four-cell initial profile lost its stability and converged to a two-cell pattern. Patankar et al. used the Spalding difference scheme (SDS) for the pressure-temperature-velocity variables in cylindrical coordinates. The SDS is essentially a central difference scheme at low flow conditions and an upwind difference scheme at higher flow conditions. Since they predicted a four-cell pattern at Pr = 5 for a circular geometry, we were motivated to examine the effect of numerical scheme on such flow transition. Hence we solved the stream function vorticity form of the equations of motion in cylindrical coordinates using the upwind weighted difference scheme of Raithby and Torrance [12]. Still only a two-vortex pattern was generated and the results were consistent with the earlier ones. Hence, at this stage, we can only conclude that the four-cell solution cannot be observed as a stable one in a circular geometry over the range of Gr investigated here for Pr < 5.0.

Hence it appears that the nonlinear coupling between the flow and energy equations has the potential for exhibiting multiple solutions. However, the realization of such multiplicities appears to depend on the duct geometry and fluid properties. Experimental verification of these phenomena is required to remove the uncertainties caused by numerical difficulties over certain ranges of parameter values.

Concluding Remarks

The presence of the natural convection due to the buoyancy force has marked influence on the flow Nusselt number. The dual solutions obtained for the case of a square duct are in accord with previously published results for a different thermal boundary condition. The results for a circular duct exhibited only a two-vortex flow pattern contradictory to the Patankar et al. studies in which a four-vortex flow pattern was obtained above a certain critical Grashof number. Further work is necessary to resolve this discrepancy.

Acknowledgments

The authors wish to thank the Natural Science and Engineering Research Council of Canada for financial support. Computing facilities on an Array Processor (FPS164) were made possible through an equipment grant from NSERC.

References

1 Cheng, K. C., and Hwang, G. J., "Numerical Solution for Combined Free and Forced Laminar Convection in Horizontal Rectangular Channels," ASME Journal of Heat Transfer, Vol. 91, 1969, pp. 59–66.

2 Hwang, G. J., and Cheng, K. C., "Boundary Vorticity Method for Con-

vective Heat Transfer With Secondary Flow," *Heat Transfer*, Vol. 4, 1970, Paper No. NC3.5.

3 Chou, F. C., and Hwang, G. J., "Combined Free and Forced Laminar Convection in Horizontal Rectangular Channels for High ReRa," *The Canadian Journal of Chemical Engineering*, Vol. 62, 1984, pp. 830-836.

4 Nandakumar, K., Masliyah, J. H., and Law, H. S., "Bifurcation in Steady Lamianr Mixed Convection Flow in Horizontal Ducts," *Journal of Fluid Mechanics*, Vol. 152, 1985, pp. 145-161.

5 Patankar, S. V., Ramadhyani, S., and Sparrow, E. M., "Effect of Circumferentially Non-uniform Heating on Laminar Combined Convection in a Horizontal Tube," ASME JOURNAL OF HEAT TRANSFER, Vol. 100, 1978, pp. 63-70.

6 Masliyah, J. H., "On Laminar Flow in Curved Semi-circular Ducts," *Journal of Fluid Mechanics*, Vol. 99, 1980, pp. 469-479.

7 Nandakumar, K., and Masliyah, J. H., "Bifurcation in Steady Laminar Flow Through Curved Tubes," *Journal of Fluid Mechanics*, Vol. 119, 1982, pp. 475-490.

8 Strikwerda, J. C., "Upwind Differencing, False Scaling and Nonphysical Solutions to the Driven Cavity Problem," *J. Comp. Physics*, Vol. 47, 1982, pp. 303-307.

9 Benjamin, T. B., "Bifurcation Phenomena in Steady Flows of a Viscous Fluid, I. Theory," *Proc. Roy. Soc., London*, Vol. A359, 1978, pp. 1-26.

10 Benjamin, T. B., "Bifurcation Phenomena in Steady Flows of a Viscous Fluid, II. Experiments," *Proc. Roy. Soc., London*, Vol. A359, 1978, pp. 27-43.

11 Cheng, K. C., Lin, R.-C., and Ou, J.-W., "Fully Developed Lamianr Flow in Curved Rectangular Channels," ASME *Journal of Fluids Engineering*, Vol. 98, 1976, pp. 41-48.

12 Raithby, G. D., and Torrance, K. E., "Upstream-Weighted Differencing Schemes and Their Applications to Elliptic Problems Involving Fluid Flow," *Computers and Fluids*, Vol. 2, 1974, pp. 191-206.

P. D. Symolon
General Electric Company,
Schenectady, NY 12301
Assoc. Mem. ASME

N. E. Todreas
Department of Nuclear Engineering,
Massachusetts Institute of Technology,
Cambridge, MA 02139
Fellow ASME

W. M. Rohsenow
Department of Mechanical Engineering,
Massachusetts Institute of Technology,
Cambridge, MA 02139
Fellow ASME

Criteria for the Onset of Flow Recirculation and Onset of Mixed Convection in Vertical Rod Bundles

In a vertical rod bundle with forced upflow and a nonuniform radial power profile, the potential for flow reversal into the low power side of the bundle exists due to buoyancy forces. In this paper a criterion is developed to predict the onset of flow recirculation in rod bundles. The criterion is validated with experimental data for flow recirculation in water-cooled bare rod bundles and with the results of a standard multichannel rod bundle code. A criterion for the onset of mixed convection is also given. Thus, the boundaries between the forced convection, mixed convection, and recirculation regimes are identified. Results are expressed on a flow regime map in terms of the dominant dimensionless parameters (the Reynolds number and a buoyancy parameter B*) *and as a closed-form equation.*

1 Introduction

In recent years there has been an increased interest in predicting the temperature and flow fields in nuclear reactor rod bundles operating under low flow conditions. This regime, where buoyancy effects become important, is called the mixed convection flow regime.

In a rod bundle with a radial power gradient operating at sufficiently low flows, buoyancy forces cause a lateral crossflow from the low power to the high power side of the bundle. For extremely low flows, flow recirculation (downflow) may occur if the crossflow is large enough.

Thus three flow regimes may be identified: forced convection, mixed convection, and recirculation. These regimes are illustrated in Fig. 1. In the forced convection regime the momentum and energy equations may be solved independently, while in mixed convection they are coupled through the buoyancy term. The recirculation regime is actually a subset of the mixed convection regime, but the solution method must allow for the existence of reverse flows in the rod bundle.

The purpose of this paper is to identify the boundaries between these flow regimes and to construct flow regime maps for these flow conditions. In [1] a criterion for the onset of mixed convection was developed based on the same model to be given here, and is included in this paper. The criterion for the onset of recirculation is developed and presented using the same dimensionless parameters as used for the mixed convection criterion.

There are several reasons why such criteria are needed for nuclear reactor design and safety analysis. The first is that the identification of the flow regime allows determination of the complexities which the numerical tools used to analyze the flow conditions must be capable of handling. For example, analysis of the buoyancy-induced transverse flow which occurs in the mixed convection regime requires a numerical tool effectively incorporating the transverse momentum equation. On the other hand analysis of the recirculation regime requires a solution method which allows for the existence of reverse flow as well as strong transverse flow. The optimum transient analysis approach is one which applies increasing complex numerical capability as the transient progresses through these flow regime boundaries. The second need, specific to the recirculation criterion, is to provide a simple measure for assuring that excursion into the recirculation regime does not occur.

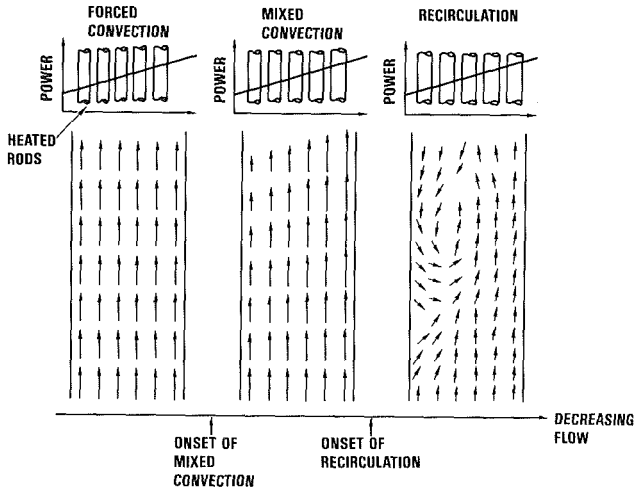

Fig. 1 Road bundle flow regimes

While further work is ongoing internationally to show that any thermal excursion within the recirculating region is self-limiting, current safety analysis practice precludes excursion into this regime.

To develop these criteria, a simple two-channel model of the rod bundle was formulated. Alternately, parametric studies based on the detailed numerical code COBRA-WC [6] could have been performed as a basis for developing these criteria. However, the two-channel model permits an analytic solution which yields both the governing dimensionless parameters and physically versus empirically based equations for the criteria. These results are presented in terms of both a flow regime map and closed form equations.

Flow recirculation in rod bundles has been observed experimentally by several investigators. Recirculation was observed in a water-cooled 2 × 6 rod bundle for controlled flow transients for a step change in power with half the bundle unheated [2]. Flow recirculation existed in one of the three steady-state runs in the 2 × 6 rod bundle [3]. Recirculation was also observed by Wang [4] in a four-rod bundle, but no data were given to indicate under what conditions the recirculation occurred. In this paper new recirculation data in a 4 × 4 rod water-cooled bundle is presented. The recirculation criterion developed here is compared with all these data as well as Westinghouse blanket bundle sodium data which operated near the onset of the recirculation boundary.

The body of this paper is organized as follows. In Section 2

Contributed by the Heat Transfer Division for publication in the JOURNAL OF HEAT TRANSFER. Manuscript received by the Heat Transfer Division December 17, 1984. Paper No. 84-HT-101.

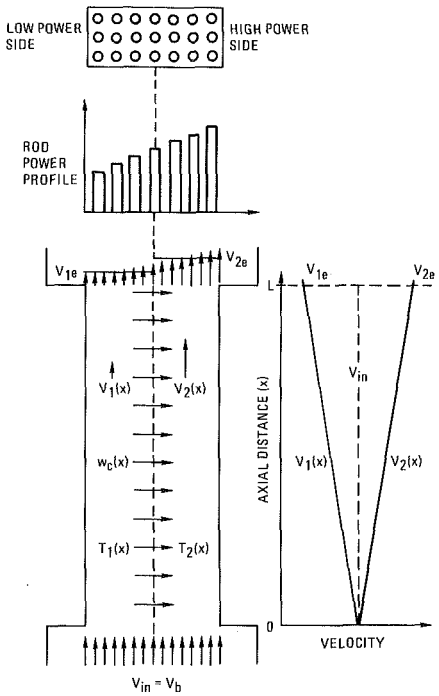

Fig. 2 Two-channel model of a rod bundle

the two-channel model, which is the framework for the criteria, is developed; then additional models necessary for the recirculation criterion are presented in Section 3. In Section 4, the essence of the formulation is distilled into two key parameters which govern mixed convection in rod bundles. The experimental determination of the onset of flow recirculation is descibed, then model results are compared with the experimental data in Sections 5 and 6, respectively. In Section 7, the final results are presented in terms of flow regime maps for the onset of mixed convection and onset of recirculation.

2 Two-Channel Model

2.1 Model Development. In the two-channel approach, the bundle is modeled as two interacting channels as shown in Fig. 2. Each channel is characterized by a bulk velocity and temperature which vary axially. The two channels interact through radial heat conduction, turbulent and wire wrap induced coolant mixing, and buoyancy induced crossflow. The following assumptions are employed in the model: (*a*) neglect axial conduction, (*b*) neglect unsteady terms, and (*c*) Boussinesq approximation. Details of the development of the two-channel model may be found in [5]; the procedure is outlined here.

Conservation equations for mass, momentum, and energy are written for each channel in accordance with the above assumptions and are given in the appendix. By convention, channel 2 always refers to the channel with higher power input. Since our objective is to develop a simple model which yields results in terms of the dominant physical parameters, numerical methods will be avoided and an approximate analytical solution will be found. We use the method of trial solution with undetermined parameters. The functional form of the solution for the velocity field [$V_1^*(x^*)$ and $V_2^*(x^*)$] is to be specified to within two undetermined parameters: the net buoyancy-induced crossflow fraction C and a velocity profile shape function $f(x^*)$. These two parameters will next be incorporated into the velocity field.

The crossflow parameter C is defined as the fraction of the cold channel (channel 1) inlet flow which is redistributed to the hot channel

$$C = \frac{\int_0^L w_c dx}{\rho V_{in} A_1} = (1 + 1/R) \int_0^1 w_c^* dx^* \tag{1}$$

A mass balance for channel 1 gives the crossflow parameter as

$$C = 1 - V_{1e}^* \tag{2}$$

A bundle mass balance gives

$$V_{1e}^* R + V_{2e}^* = 1 + R \tag{3}$$

It follows from equations (2) and (3) that

$$V^*_{1e} = 1 - C \tag{4}$$

and

$$V_{2e}^* = 1 + RC \tag{5}$$

The crossflow parameter C is a key variable in the model, since it is a measure of the importance of the buoyancy-induced crossflow. A small value for C gives the onset of mixed convection condition. The onset of recirculation is expected to occur when C is close to one, so that $V_{1e}^* = 0$.

Nomenclature

A_i = area of channel i, or subchannel i
A_b = bundle area
A^* = defined by equation (30)
A_i^* = dimensionless subchannel area = A_i/A_b
B^* = dimensionless buoyancy term defined by equation (27)
C = buoyancy-induced crossflow parameter defined by equation (1)
C_f = skin friction coefficient in friction factor correlation: $f = C_f/\mathrm{Re}^m$
D = rod diameter
D_{ei} = hydraulic diameter of channel $i = 4A_i/P_{wi}$, where P_{wi} is wetted perimeter of channel i
D_{eb} = bundle hydraulic diameter $= 4A_b/P_{wb}$
D_H = bundle hydraulic diameter $= 4A_b/P_{Hb}$, where P_{Hb} is the bundle heated perimeter
E^* = dimensionless lateral energy transport due to mixing and conduction = $w_t^* + K^*$
f_i = friction factor for channel i
f = bundle friction factor
$f(x^*)$ = velocity profile shape function
F_D = flow development factor in equation (25)
F_i = integrated friction term defined by equation (10)
F_c = integrated friction term defined by equation (18)
Gr_q = $D_{eb}^4 g\beta q''/K\nu^2$ = Grashof number based on average heat flux
K_1, K_2 = energy integral coefficients defined by equations (12) and (13)
K = thermal conductivity
K^* = dimensionless conduction term defined by equation (16)
l = centroidal distance between channels 1 and 2
L = bundle heated length
m = exponent in friction factor correlation: $f = C_f/\mathrm{Re}^m$
P = rod-to-rod pitch
P_H = heated perimeter
P_{wi} = wetted perimeter of channel i
P_i = fraction of bundle power input to channel i
p_i = pressure in channel i
Pr = Prandtl number = $\mu c_p/K$
q'' = rod heat flux
q_i' = power input per unit axial length for channel i
Q_b = bundle power input

To allow direct integration of the conservation equations, we assume some velocity profile shape to give a functional relationship for the velocity variation with x^*. It follows from equations (4) and (5) that the most general form is

$$V_1^*(x^*) = 1 - Cf(x^*) \tag{6}$$

and

$$V_2^*(x^*) = 1 + RCf(x^*) \tag{7}$$

where $f(x^*)$ must satisfy the boundary conditions $f(0) = 0$ and $f(1) = 1$. From continuity, the cross flow is given by

$$w_c^* = \frac{1}{1+R}\frac{dV_2^*}{dx} = \frac{RCf'(x^*)}{1+R} \tag{8}$$

If $f(x^*) = x^*$, the crossflow profile is uniform and the channel velocities vary linearly from the inlet to the outlet, as shown in Fig. 2. The corret $f(x^*)$ must be obtained from the results of a numerical solution of the conservation equations (e.g. COBRA [6]), but for now the general form is used. This leaves C as the only undetermined parameter in equations (6) and (7).

Since the velocity field as given by equations (6) and (7) already satisfies continuity, only the momentum and energy equations need be considered further. Equations (6) and (7) are substituted into the momentum and energy equations. The momentum equations [equations (A3) and (A4)] are then integrated to give the channel pressure drops, which are set equal to each other. The buoyancy term of the resulting equation $[\rho\beta(T_2 - T_1)]$ is evaluated by combining and integrating the energy equations [equations (A5) and (A6)]. Thus the six conservation equations are combined into a single dimensionless equation for C

$$\begin{aligned}
&① \quad 0 = 2RC + (RC)^2 - C\left(1 + \frac{1}{2}C\right)(R-1)\\
&② \quad + \frac{(1+R)^3}{R} w_t^* C\overline{f(x^*)}\\
&③ \quad + \frac{1}{2}\left(\frac{L}{D_{e2}}F_2 - \frac{L}{D_{e1}}F_1\right)\\
&④ \quad - 4\frac{L}{D_{eb}}\frac{L}{D_H}\frac{\mathrm{Gr}_q}{\mathrm{Re}^3\mathrm{Pr}}(K_2P_2 - K_1P_1)
\end{aligned} \tag{9}$$

where

$$F_i = \int_0^1 f_i V_i^{*2} dx^* \quad (i = 1, 2) \tag{10}$$

$$\overline{f(x^*)} = \int_0^1 f(x^*)dx^* \tag{11}$$

$$K_2 = (1+R)\int_0^1 \left[\frac{1}{\mu(x^*)}\int_0^{x^*}\frac{\mu(x^*)}{1+RCf(x^*)}dx^*\right]dx^* \tag{12}$$

$$K = (1+1/R)\int_0^1 \left[\frac{1}{\mu(x^*)}\int_0^{x^*}\frac{\mu(x^*)}{1-Cf(x^*)}dx^*\right]dx^* \tag{13}$$

$$\mu(x^*) = [1+RCf(x^*)]\exp\left\{E^*x^*\left[\frac{1+R}{1+RCf(x^*)} + \frac{1+1/R}{1-Cf(x^*)}\right]\right\} \tag{14}$$

$$E^* = w_t^* + K^* \tag{15}$$

and

$$K^* = \frac{1}{\mathrm{RePr}}\frac{w}{l}\frac{LD_{eb}}{A_b} \tag{16}$$

The term labeled ① represents inertial and axial momentum transported laterally by the crossflow. Term ② represents momentum transport due to mixing. Terms ③ and ④ are friction and buoyancy, respectively. The factor $K_2P_2 - K_1P_1$ in the buoyancy term was obtained by integrating the energy equation and depends on C and E^*. E^* is the dimensionless lateral energy transport due to mixing (w_t^*) and heat conduction (K^*). In [5] program RECIRC was written to evaluate the terms in equations (10) to (13) for any $f(x^*)$ and any friction factor correlation and to solve equation (9) by numerical iteration.

To determine an appropriate expression for $f(x^*)$, results of the COBRA code [6] were used to determine $f(x^*)$ at onset of recirculation conditions. COBRA is a multichannel rod bundle code which handles buoyancy-induced flow redistribution and flow recirculation. The resulting $f(x^*)$ was input to program RECIRC. Then, by exercising the model, it was determined that using $f(x^*) = x^*$ resulted in an error in the recirculation Reynolds number of at most 8 percent when compared to model results using the true (COBRA predicted) $f(x^*)$. Based on this result $f(x^*) = x^*$ was used for all model predictions.

Nomenclature (cont.)

Q_i = power input to subchannel i
Q_i^* = power input parameter defined by $Q_i^* = Q_i/Q_b$
R = ratio of channel areas = A_1/A_2
Ra_D = Rayleigh number based on rod diameter
Re = bundle Reynolds number = $D_{eb}V_b/\nu$
T_i = temperature in channel i
V_b = bundle averaged velocity
V_i^* = dimensionless velocity in channel $i = V_i/V_b$
V_{edg}^* = dimensionless velocity in edge subchannel at the onset of recirculation
V_i = velocity in channel i
w_c = mass crossflow rate per unit length
w_c^* = dimensionless mass crossflow parameter = $w_cL/\rho V_bA_b$
w_t = mixing parameter
w_t^* = dimensionless mixing parameter = $w_tL/\rho V_bA_b$
w = width available for interchannel conduction and mixing
x = axial distance
x^* = dimensionless axial distance = x/L
β = volumetric expansion coefficient
δ = constant of proportionality in equation (19)
ΔT_B = bulk temperature rise
$\mu(x)$ = defined by equation (14)
ν = kinematic viscosity
ρ = density
Γ = defined by equation (24)

Subscripts

1, 2 = pertaining to channel 1 or 2
b = pertaining to bundle
crit = critical value at the onset of recirculation
D = based on rod diameter
e = exit value
edg = pertaining to edge subchannel, where recirculation occurs
i = pertaining to channel i, or subchannel i
in = inlet value
L, T = pertaining to laminar or turbulent flow, respectively
min = minimum value

Superscripts

* = indicates dimensionless parameter
c = critical value at the onset of recirculation

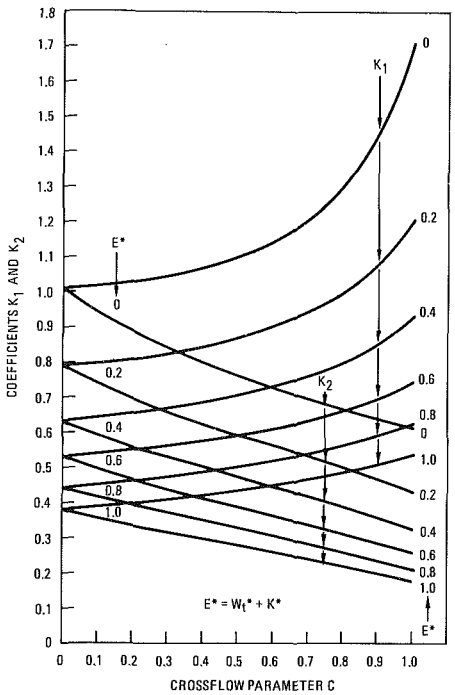

Fig. 3 K_1 and K_2 as a function of C and E^* for $f(x^*) = x^*$ and $R = 1$

Figure 3 gives a plot of K_2 and K_1 [equations (12) and (13)] as a function of C and E^* for the case that $f(x^*) = x^*$ and $R = 1$. This plot is used to evaluate the power skew term $K_2P_2 - K_1P_1$ in the buoyancy term of equation (9). From the results of Fig. 3 it follows that for a fixed power skew, the value of $K_2P_2 - K_1P_1$ decreases with an increase of E^* or C. Physically, this means that radial energy transport due to heat conduct, mixing, and buoyancy-induced crossflow results in a decrease in the buoyancy term.

Considerable simplification of the model occurs if the friction factor is expressed as $f = C_f/\mathrm{Re}^m$ and if uniform crossflow $[f(x^*) = x^*]$ is assumed since equations (10) and (11) can then be integrated analytically. With these simplifications and with $R = 1$, equation (9) becomes

$$0 = C(2+C) + 4Cw_t^* + \frac{1}{2}\frac{C_f}{\mathrm{Re}^m}F_c\frac{L}{D_{eb}} - 4\frac{L}{D_{eb}}\frac{L}{D_H}(K_2P_2 - K_1P_1)\frac{\mathrm{Gr}_q}{\mathrm{Re}^e\mathrm{Pr}} \tag{17}$$

where

$$F_c = \frac{(1+C)^{3-m} + (1-C)^{3-m} - 2}{(3-m)C} \tag{18}$$

For laminar flow ($m = 1$) it follows from equation (18) that $F_c = C$.

2.2 Criteria for Onset of Mixed Convection and Recirculation From the Two-Channel Model. The prediction of the conditions for the onset of flow recirculation and onset of mixed convection is made using equation (9) or its simpler form, equation (17). These equations, which are the result of combining the six conservation equations, physically represent the balance of friction, inertia, and buoyancy forces such that the two channels have a common pressure drop.

The onset criteria is obtained by fixing C (the fraction of the cold channel inlet flow redistributed to the hot channel) in equations (9) and (15) at the appropriate value corresponding to each criterion. The C value for the onset of recirculation is derived in the next section and is given by equation (23). The C value for onset of mixed convection is established in [1] as 0.01.

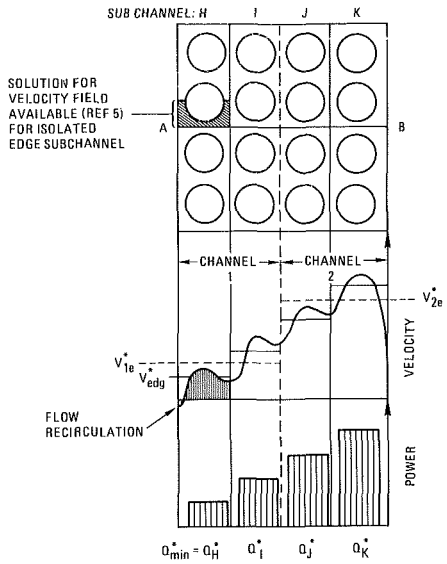

Fig. 4 Velocity field at onset of recirculation

Alternately, equations (9) and (17) can be used to calculate the value of C corresponding to identified bundle operating conditions. With C known, the velocity and temperature field in the two-channel system can easily be found from equations (6), (7), (A5), and (A6).

3 Auxiliary Models and Input Parameters

In this section models are developed for the critical value of C at the onset of recirculation (C_{crit}) and the two-channel mixing parameter (w_t^*). The appropriate friction factor correlation is also discussed. These parameters are required as input to equation (17).

3.1 Model for the Critical Value of C at the Onset of Recirculation. To use the two-channel model to predict the onset of flow recirculation, we require a model for the value of C at which recirculation is expected to occur. This will involve consideration of intersubchannel (between subchannels) and intrasubchannel (within a subchannel) buoyancy effects which were neglected in the two-channel model. In this subsection a model is developed to estimate the critical value of C.

To apply this model, the bundle must be further subdivided into subchannels containing rows of rods at constant power, as shown in Fig. 4 for a 4 × 4 rod bundle. The bundle is divided into four subchannels labeled H, I, J, and K. Also shown in Fig. 4 is a typical power distribution and velocity profile (along line AB) at the onset of recirculation condition. Note that recirculation is initiated in the edge subchannel in the low power side of the bundle. Recirculation may occur while the net flow in the subchannel is upward ($V_{edg}^* > 0$). This occurs when the power gradient is relatively flat and is due to the intrasubchannel buoyancy effects within the recirculation subchannel. If intrasubchannel effects are unimportant, then the onset of recirculation is expected to occur with $V_{edg}^* = 0$. In deriving the model, the following assumptions are made:

(a) The onset of recirculation condition exists when the recirculation subchannel average velocity is V_{edg}^*. This assumption allows for intrasubchannel buoyancy effects when $V_{edg}^* > 0$.

(b) The mean velocity in the other subchannels (V_i^*) is assumed proportional to $Q_i^* - Q_{min}^*$, so the higher the subchannel power, the higher the subchannel average velocity. This assumption allows for intersubchannel buoyancy effects.

From the above assumptions it follows that the subchannel averaged velocities at the onset of recirculation are

$$V_i^* = \delta(Q_i^* - Q_{min}^*) + V_{edg}^* \qquad i = \mathrm{H, I, J, K} \tag{19}$$

where δ is a constant of proportionality. Equation (19) gives the average velocity in each subchannel i. The dimensionless bundle continuity equation is

$$\sum_b V_i^* A_i^* = 1 \tag{20}$$

where Σ_b indicates the sum is taken over all subchannels in the bundle (subchannels H, I, J, and K in Fig. 4). Using equation (20) with the velocity field of equation (19), the constant δ may be evaluated, and substituted back into equation (19), to give

$$V_i^* = \frac{(1 - V_{\text{edg}}^*)(Q_i^* - Q_{\text{min}}^*)}{\sum_b (Q_i^* - Q_{\text{min}}^*) A_i^*} + V_{\text{edg}}^* \tag{21}$$

A mass balance for channel 1 allows V_{1e}^* to be found

$$V_{1e}^* = 2 \sum_{\text{ch 1}} V_i^* A_i^* \tag{22}$$

where $\Sigma_{\text{ch 1}}$ indicates the sum is taken over all subchannels in channel 1 (subchannels H and I in Fig. 4).

Substituting equation (21) into equation (22), and equation (22) into equation (2) gives the critical value of C

$$C_{\text{crit}} = 1 - 2(1 - V_{\text{edg}}^*)\Gamma - 2V_{\text{edg}}^* \tag{23}$$

where

$$\Gamma = \frac{\sum_{\text{ch 1}} A_i (Q_i^* - Q_{\text{min}}^*)}{\sum_b A_i (Q_i^* - Q_{\text{min}}^*)} \tag{24a}$$

For the bundle shown in Fig. 3, $Q_{\text{min}}^* = Q_H^*$ and equation (24a) becomes

$$\Gamma = \frac{A_1^*(Q_1^* - Q_H^*)}{A_1^*(Q_1^* - Q_H^*) + A_J^*(Q_J^* - Q_H^*) + A_K^*(Q_K^* - Q_H^*)} \tag{24b}$$

Equation (23) gives the critical value of C at the onset of recirculation. The parameters Γ and V_{edg}^* account for the inter-subchannel and intrasubchannel buoyancy effects, respectively. Γ is determined from equation (24) and V_{edg}^* can be estimated from a solution for the edge subchannel velocity field at the onset of recirculation. In [7] numerical study was performed to determine the onset of flow recirculation for fully developed laminar flow in isolated (zero crossflow) edge subchannels. The onset was expressed in terms of a critical Rayleigh numbers (Ra_D^c) which depended on the P/D ratio. In [5] it was shown that V_{edg}^* could be expressed in terms of Ra_D^c by

$$V_{\text{edg}}^* = 4\left(\frac{D}{D_{eb}}\right)^4 \frac{D_{eb}}{D_H} \frac{1}{\text{Ra}_H^c} \frac{\text{Gr}_q}{\text{Re}} Q_{\text{min}}^* F_D \tag{25}$$

where F_D is a factor inserted to account for flow development effects. For fully developed flow, $F_D = 1.0$, while for developing flow, $F_D < 1.0$, and depends on L/D_{eb}, Re, Pr, and Gr_q. However, the functional dependence on F_D on these parameters has not been found. Thus, C_{crit} can be determined from equations (23), (24), and (25). Next the mixing parameter w_l^*, which must be input to equation (17), will be determined.

3.2 Mixing Model for Buoyancy-Dominated Flows. During the recirculation test, turbulent flow was observed in heated subchannels of the rod bundle due to instabilities caused by the buoyancy forces. In the unheated subchannels, the flow remained laminar because there were no buoyancy-induced instabilities and the Reynolds number was low. Similar observations were made in [2].

The turbulence in the flow resulted in a lateral energy transport which reduced the buoyancy forces and inhibited the onset of recirculation. It was found that the model predictions could be improved if the lateral mixing is accounted for by a semi-empirical model. The development of this model is given in [5]. The model is based on a modified mixing length hypothesis where the fluctuations in the velocity are assumed to be due to buoyancy forces which are produced when a fluid lump moves into a region of different temperature. It can be shown that under these conditions, the mixing between the two channels may be expressed as

$$w_l^* = 1.75 \frac{D_{eb}}{D_H} \sqrt{\frac{l}{D_H}} \frac{wL}{A_b} \sqrt{\frac{\text{Gr}_q}{\text{Pr Re}^{2.4}}} Q_{\text{min}}^* \tag{26}$$

where 1.75 and 2.4 are constants which were calibrated against the experimental data. In the above equation, if $Q_{\text{min}}^* = 0$ (row H unheated) the mixing is zero. This is consistent with the experimental observation of laminar flow in the unheated subchannels of the bundle.

3.3 Friction Factor Correlation. Both forced convection and mixed convection friction factor correlations were employed in this model in [5]. It was found that using mixed convection correlations did not significantly improve the predictions, though they increased the mathematical complexity of the model. For the predictions which follow, standard forced convection rod bundle friction factor correlations will be employed (for $P/D = 1.25$, laminar: $f = 88/\text{Re}$, turbulent: $f = 0.319/\text{Re}^{0.25}$).

4 Identification of the Dominant Dimensionless Parameters in the Model

Calculating the values of the terms of equation (17) for both laminar and turbulent flow at both onset of recirculation and onset of mixed convection conditions has led to the conclusion that the friction and buoyancy terms dominate the mixing and inertia terms. Equating the friction and buoyancy terms of equation (17) and isolating Re to one side gives (for laminar flow: $C_f = C_{fL}$, $m = 1$)

$$\frac{1}{8}\text{Re}^2 = \frac{L}{D_H} \frac{\text{Gr}_q}{\text{Pr}} \frac{K_2 P_2 - K_1 P_1}{C_{fL} C} \equiv B^* \tag{27}$$

Utilizing the above definition of B^*, for laminar flow ($f = C_{fL}/\text{Re}$), equation (17) can be written as

$$B^* = \frac{\text{Re}^3}{4}\left[A^* + \frac{1}{2\text{Re}}\right] \tag{28}$$

For turbulent flow ($f = C_{fT}/\text{Re}^m$), equation (17) becomes

$$B^* = \frac{\text{Re}^3}{4}\left[A^* + \frac{1}{2\text{Re}^m} \frac{F_c}{C} \frac{C_{fT}}{C_{fL}}\right] \tag{29}$$

In equations (28) and (29), A^* is given by

$$A^* = \frac{2 + C + 4\, w_l^*}{C_{fL} L/D_{eb}} = \frac{\text{Inertia} + \text{Crossflow} + \text{Mixing}}{\text{Friction}} \tag{30}$$

The parameter A^* in equations (28) and (29) gives the relative importance of inertia and lateral momentum transported by crossflow and mixing. In these equations the magnitude of A^* is small relative to the second term. It is stressed that equations (28) and (29) are not approximate formulations but express the same relationship as equation (17). Equations (28) and (29) can be expressed functionally as follows

$$\text{Laminar: } B^* = f_n(\text{Re}, A^*) \tag{31}$$

$$\text{Turbulent: } B^* = f_n(\text{Re}, A^*, F_c/C, C_{fT}/C_{fL}) \tag{32}$$

For rod bundle geometries, the ratio C_{fT}/C_{fL} is nearly constant, and as C varies from 0.01 to 1 the ratio F_c/C varies

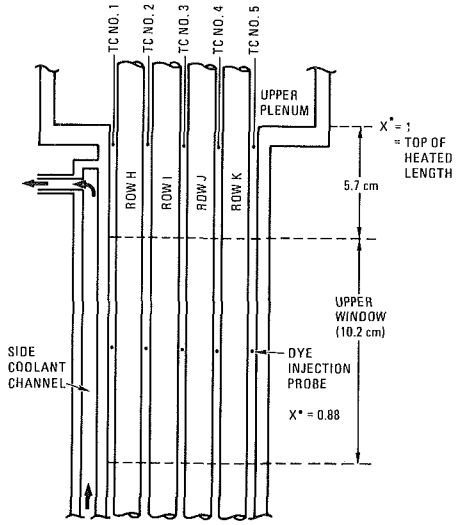

Fig. 5 Upper region of MIT 4 × 4 rod bundle

from 1.75 to 1.72, so it too may be treated as a constant. As discussed above, the parameter A^* is not very important. Since A^*, F_c/C, and C_{fT}/C_{fL} are either negligible or nearly constant, it follows from equations (31) and (32) that Re and B^* are the dominant dimensionless parameters governing the onset of mixed convection and onset of recirculation in rod bundles. The parameter B^* represents the relative importance of buoyancy induced flow redistribution. Note that the ratio Gr_q/Pr in B^* is independent of fluid thermal conductivity. The effect of heat conduction is incorporated into K_1 and K_2 through the parameter K^* [equation (16)]. A high-conductivity coolant will inhibit the onset of recirculation and onset of mixed convection. Note that the mixing parameter (w_t^*) enters both the momentum equation (through A^*) and the energy equation (through B^* via K_1 and K_2). The effect of w_t^* on A^* is small, but its effect on B^* is not. Next, the experimental determination of the onset of recirculation will be discussed, then comparisons will be made of predictions and test data.

5 Experimental Determination of the Onset of Flow Recirculation

The Massachusetts Institute of Technology (MIT) 4 × 4 rod bundle was used to experimentally determine the onset of recirculation over a wide range of bundle power inputs and radial power profiles [5]. The upper portion of the bundle is shown in Fig. 5. A dye injection probe was used to inject a neutral density dye tracer near the outlet of the bundle in any of the five gaps. The dye was observed through the top window and indicated whether upflow or downflow existed in the injection subchannel. The top window was used because recirculation starts at the top of the bundle. For a given power input and radial power profile, the bundle flow rate was varied until the onset of recirculation was observed; that is, the transition from upflow to downflow. In all of the cases investigated, downflow occurred first in the edge subchannel most distant from the high power side of the bundle.

A plexiglass side wall coolant channel is located on one wall of the bundle. Cold water can be passed through this channel to simulate the effect of interassembly heat transfer. The bundle was wrapped with fiberglass insulation to prevent heat loss. The coolant flow to both the bundle and the side channel could be measured, as well as the bulk inlet and outlet temperatures.

The six radial power profiles which were employed are given in Table 1. Power profiles 1, 2, and 3 were with 1, 2, and 3 rows uniformly heated. Profile 4 is a linear power gradient

Table 1 Power profiles used during MIT recirculation tests

	Rod Row Power: $Q_i^* = Q_i/Q_b$			
Profile Number	Q_H^*	Q_I^*	Q_J^*	Q_K^*
1	0	0	0	1
2	0	0	1/2	1/2
3	0	1/3	1/3	1/3
4	0	1/6	2/6	3/6
5[1]	α	α	β	β
6	1/10	2/10	3/10	4/10

[1]Step power change such that $2(\alpha + \beta) = 1$

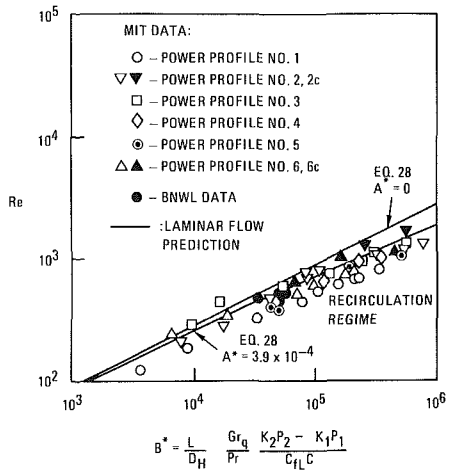

Fig. 6 Onset of recirculation data correlated with B^* parameter

with one row unheated. Profile 5 is a step change in power with all rods heated. Profile 6 is a 4:1 linear power gradient with all rods heated, which is typical of the liquid metal fast breeder reactor (LMFBR) radial blanket assembly.

6 Comparison of the Model Results With Experimental Data

For comparison, the model predictions and experimental data are plotted on Re-B^* coordinates in Fig. 6. The results of these comparisons are discussed in this section. Prediction of the onset of recirculation is given by equations (28) and (29) with C_{crit} found from equation (23) and w_t^* found from equation (26). The laminar flow prediction [equation (28)] is drawn in for $A^* = 0$ (mixing and inertia negligible so that friction and buoyancy are in balance) and for $A^* = 3.90 \times 10^{-4}$ (corresponding to $C = 1.00$, $C_{fL} = 88$, $L/D_{eb} = 87.6$, $w_t^* = 0.0$). It is concluded from Fig. 6 that:

(a) Including friction and buoyancy only ($A^* = 0$) gives a conservative estimate of the onset of recirculation.

(b) Use of Re-B^* coordinates correlates recirculation data reasonably well for a wide range of bundle operating conditions.

Detailed data comparisons will be discussed next.

6.1 Comparison of Model Results With MIT Recirculation Data. Power profiles 1 to 4 all have at least one row of rods unheated ($Q_{min}^* = 0$, so that $V_{edg}^* = 0$ and $w_t^* = 0$); hence, intrasubchannel buoyancy effects and coolant mixing

are unimportant. It follows from equation (23) that $C_{crit} = 1$ for profiles 1 and 2, $C_{crit} = 0.375$ for profile 3, and $C_{crit} = 0.696$ for profile 4. The agreement for profiles 2, 3, and 4 was found to be excellent (within ±25 percent), while the model prediction for profile 1 consistently overestimated Re_{crit} by 40 percent (see Fig. 6).

For power profile 5, the power in the left half of the bundle was fixed at 100 W/rod while the power in the right half was varied from 1500 W/rod (15:1 gradient) to 100 W/rod (uniform power), and the onset of recirculation was measured for each case. The primary purpose of these runs was to determine when the approximation of neglecting intrasubchannel buoyancy effects ($V^*_{edg} = 0$) fails. It was found that for power gradients of 2:1 and smaller, using $V^*_{edg} = 0$ caused the model to have no meaningful solution [i.e., B^* becomes negative because $K_1P_1 > K_2P_2$]. However, if equation (25) is used to evaluate V^*_{edg}, good agreement is obtained if $F_D = 0.3$. Thus, for relatively flat power profiles, the intrasubchannel buoyancy drives the flow recirculation, but fully developed flow cannot be assumed. Since F_D cannot be estimated a priori, predicting recirculation for lower power gradients must be considered an unresolved issue. An analysis which accounts for flow development effects is needed to predict the low power gradient and uniform power recirculation data. The data for profile 5 (excluding the uniform power and 1:1 power gradient data) are given in Fig. 6, and the agreement with the model prediction is quite good.

For profile 6, if $V^*_{edg} = 0$ and the mixing model [equation (26)] were used, the model predicted the onset of recirculation to within ±15 percent, as shown in Fig. 6. Intrasubchannel buoyancy effects did not appear to be significant for this power profile.

Six runs were made using profiles 2 and 6 (labeled 2*c* and 6*c* in Fig. 6) to examine the effect of side channel cooling on the onset of recirculation. Side channel cooling simulates the interassembly heat transfer which occurs in LMFBR rod bundles. The effect of radial heat transfer from the low power side of the bundle was to cause recirculation to occur at a higher Reynolds number than for the corresponding adiabatic bundle case. To model the effect of side channel cooling with the two-channel model, the power lost through the cold wall was subtracted from the power in the four rods closest to the cold wall. The power skew parameters (P_1 and P_2) and Grashof number were calculated accordingly. All model predictions were within ±30 percent of the data (see Fig. 6), indicating that the model effectively handles interassembly heat transfer effects.

6.2 Comparison of Model Results With Battelle Northwest Laboratories (BNWL) Recirculation Data. Flow recirculation was reported to occur in the BNWL 2 × 6 rod bundle under transient (three runs in [2] and steady-state (one run in [3] conditions. All runs were with a 1:0 power gradient (half the rods heated). As seen in Fig. 6, the model prediction and BNWL recirculation data are in good agreement, suggesting that the quasi-steady-state approximation is valid.

6.3 Comparison With Westinghouse Advanced Reactor Division (WARD) LMFBR Blanket Bundle Test Data. A series of steady-state and transient tests was performed at WARD on a sodium-cooled LMFBR wire wrapped rod bundle. Flow recirculation was not observed in any of the tests. In [8] the recirculation criterion was employed to predict the flow regime for selected WARD tests. The calculated results agreed with the WARD data with the exception of one run for which the criterion predicted the existence of recirculation while no recirculation was observed for the test run. Since the data are not at the onset of recirculation, no WARD points are included in Fig. 6.

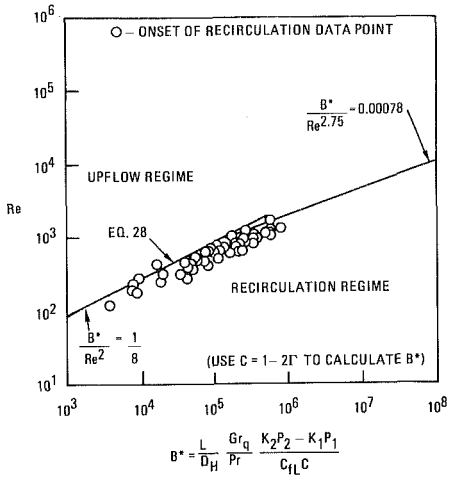

Fig. 7(*a*) Flow regime map for the onset of recirculation ($C = 1\text{-}2\Gamma$)

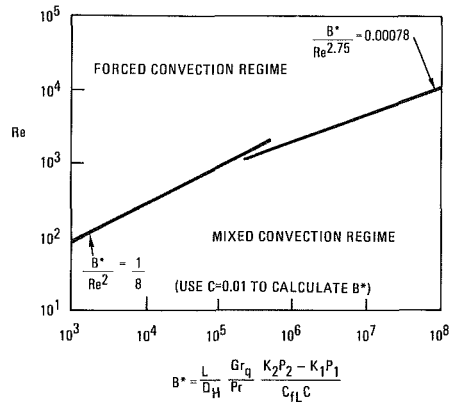

Fig. 7(*b*) Flow regime map for the onset of mixed convection ($C = 0.01$)

7 Flow Regime Map for the Onset of Recirculation and Onset of Mixed Convection in Rod Bundles

Having identified the dominant dimensionless parameters, a flow regime map may be developed by plotting both the model prediction and the data on Re–B^* coordinates as shown in Fig. 6. For conservatism and simplicity, $A^* = 0$ will be used. It follows from equations (28) and (29) that for $A^* = 0$ both criteria are given simply as

$$\text{Laminar: } \left(f = \frac{C_{fL}}{Re}\right); \quad \frac{B^*}{Re^2} = \frac{1}{8} \tag{33}$$

and

$$\text{Turbulent: } \left(f = \frac{C_{fT}}{Re^{0.25}}\right); \quad \frac{B^*}{Re^{2.75}} = \frac{1.735}{8}\frac{C_{fT}}{C_{fL}} = 0.00078 \tag{34}$$

where F_c/C is equated to its mean value of 1.735. The reason the two criteria can be expressed by the same set of equations is that the crossflow effect C, upon which both criteria are based, is incorporated into B^*.

In Fig. 7(*a*), the results of Fig. 6 are reproduced on a larger scale, and the predictions for the turbulent flow regime [equation (29)] are included. Note that no experimental data exist for the turbulent regime due to boiling in the rod bundle at high Gr_q. Figure 7(*a*) is the flow regime map for the onset of flow recirculation in rod bundles. (For the onset of recirculation, the parameter B^* is calculated with $C_{crit} = 1 - 2\Gamma$ [equation (23) with $V^*_{edg} = 0$].) For this case the regime above the

onset line is upflow, and the regime below the line is recirculation. Figure 7(*b*) is the flow regime map for the onset of mixed convection in rod bundles. For the onset of mixed convection the parameter B^* is calculated with $C = 0.01$. It was shown in [1] that $C = 0.01$ gives the point at which the buoyancy-induced crossflow becomes significant. For this case the regime above the onset line is forced convection, and the regime below the line is mixed convection. A sample calculation showing how to use the criteria is provided in [10]. For both criteria, Fig. 3 is used to determine K_1 and K_2.

Figure 7(*a*) bears some similarity to the flow regime map for mixed convection in tubes [9], suggesting that the dominant physical mechanism may be the same for tubes and rod bundles. For both cases, buoyancy results in a lateral crossflow toward the location of greatest heat input, distorting the velocity profile, and for severe conditions causing flow recirculation. Recirculation occurs when momentum deficient fluid is unable to penetrate the adverse pressure gradient established by buoyancy forces.

Summary, Conclusions, and Recommendations

An analytical model has been derived governing mass, momentum, and energy transfer in a rod bundle using a two-channel approach. The model has been validated by comparison with experimental data and COBRA code results. The dominant dimensionless parameters governing mixed convection in rod bundles have been identified with results expressed in analytical form and in terms of a flow regime map.

For profiles 1 to 4 and the BNWL data, the agreement was surprisingly good (maximum error = 40 percent) considering that no empiricism was used for the predictions. This demonstrates that the model itself is on a firm fundamental base. For profiles 5 and 6 (which had heated rods in the recirculation subchannel) the effects of mixing (w_t^* model) had to be accounted for, and empirical constants were introduced into the mixing model. For power gradients of 2:1 and less, intrasubchannel buoyancy effects must be accounted for. Attempts to model this failed (V_{cdg}^* model) because the flow was not fully developed.

Based on the results discussed above, it is recommended that future efforts be directed toward developing adequate models for intrasubchannel buoyancy effects for developing flow. Obtaining recirculation data at higher Reynolds numbers and for low Prandtl number fluids would further validate the model.

Acknowledgment

This work was financially supported by DOE. The laboratory assistance of Tsing Huang is also acknowledged.

References

1 Symolon, P. D., Todreas, N. E., and Rohsenow, W. M., "Criterion for the Onset of Mixed Convection in Vertical Bare and Wire Wrapped Rod Bundles," in: *Thermal Hydraulics of Nuclear Reactors*, ANS 700081, M. Merilo ed., Santa Barbara, 1983, pp. 1391-1402.

2 Bates, J., and Kahn, E., "Investigation of Combined Free and Forced Convection in a 2 × 6 Rod Bundle During Controlled Flow Transients," *AIChE Symposium Series on Heat Transfer*, Orlando, Vol. 76, 1980, pp. 215-230.

3 Quigley, M., McMonagle, C., and Bates, J., "Investigation of Combined Free and Forced Convection in a 2 × 6 Rod Bundle," Battelle Northwest Laboratories Report BNWL-2216, 1977.

4 Wang, S. F., "Natural Convection Effects in Isolated and Interconnecting Subchannels of a Reactor Fuel Assembly," Ph.D. Thesis, Massachusetts Institute of Technology, Department of Nuclear Engineering, Jan. 1981.

5 Symolon, P. D., "Mixed Convection in Vertical Rod Bundles," Ph.D. Thesis, Massachusetts Institute of Technology, Department of Mechanical Engineering, Sept. 1982.

6 George, T. L., "COBRA-WC: A Version of COBRA for Single-Phase Multiassembly Thermal Hydraulic Transient Analysis," Pacific Northwest Laboratory Report PNL-3259, July 1980.

7 Wang, S. F., Rohsenow, W. M., and Todreas, N. E., "Subchannel Friction Factor for Bare Rod Arrays Under Mixed Convection Conditions," in: *Decay Heat Removal and Natural Convection in Fast Breeder Reactors*, Hemisphere, Washington, 1981.

8 Huang, T. T., and Todreas, N. E., "Application of the MIT Two-Channel Model to Predict Flow Recirculation in WARD 61 Pin Blanket Tests," Massachusetts Institute of Technology Report DOE/ET/37240, 104TR, Jan. 1983.

9 Metias, B., and Eckert, E. G., "Forced, Mixed and Free Convection Regimes," ASME JOURNAL OF HEAT TRANSFER, May 1964, pp. 295-296.

10 Symolon, P. D., Todreas, N. E., and Rohsenow, W. M., "Criteria for the Onset of Flow Recirculation and Onset of Mixed Convection in Vertical Rod Bundles," ASME Paper No. 84-HT-101.

APPENDIX

Two-Channel Model Conservation Equations

This appendix presents the two-channel conservation equations, which were derived with the following assumptions: (*a*) neglect axial conduction, (*b*) neglect unsteady terms, and (*c*) Boussinesq approximation. The six conservation equations are

Mass conservation:

$$w_c = \rho A_2 \frac{dV_2}{dx} \tag{A1}$$

$$w_c = -\rho A_1 \frac{dV_1}{dx} \tag{A2}$$

Momentum conservation:

$$-\frac{dp_1}{dx} = \rho V_1 \frac{dV_1}{dx} - \frac{w_t}{A_1}(V_2 - V_1) + \frac{1}{2}\rho V_1^2 \frac{f_1}{D_{e1}} + \rho_1 g \tag{A3}$$

$$-\frac{dp_2}{dx} = \rho V_2 \frac{dV_2}{dx} + \frac{1}{A_2}(w_t + w_c)(V_2 - V_1) \tag{A4}$$

$$+\frac{1}{2}\rho V_2^2 \frac{f_2}{D_{e2}} + \rho_2 g \tag{A4}$$

Energy conservation:

$$\rho V_1 \frac{dT_1}{dx} = \frac{q_1'}{A_1 C_p} + \frac{1}{A_1}\left[w_t + \frac{K \cdot w}{l \cdot C_p}\right](T_2 - T_1) \tag{A5}$$

$$\rho V_2 \frac{dT_2}{dx} = \frac{q_2'}{A_2 C_p} - \frac{1}{A_2}\left[w_t + w_c + \frac{K \cdot w}{l \cdot C_p}\right](T_2 - T_1) \tag{A6}$$

In the equations above, ρ_1 and ρ_2 are local densities (functions of x) while ρ is the bundle average density.

Measurements of Laminar Mixed Convection Flow Adjacent to an Inclined Surface

N. Ramachandran
Assoc. Mem. ASME

B. F. Armaly
Mem. ASME

T. S. Chen
Fellow ASME

Department of Mechanical and Aerospace Engineering, University of Missouri—Rolla, Rolla, MO 65401

Measurements of laminar mixed forced and free convection air flow adjacent to an upward and a downward facing, isothermal, heated inclined surface (at 45 deg) are reported. Local Nusselt number and the velocity and temperature distributions are presented for both the buoyancy assisting and the buoyancy opposing flow cases for a range of buoyancy parameter $0 \leq \xi \leq 5$ ($\xi = \mathrm{Gr}_x/\mathrm{Re}_x^2$). The measurements are in good agreement with predictions which define a laminar mixed convection regime for buoyancy assisting flow as $0.1 \leq \xi \leq 7$, and for buoyancy opposing flows as $0.06 \leq \xi \leq 0.25$ for this inclination angle of 45 deg. Simple mixed convection correlations for the local and average Nusselt numbers for inclined surfaces are also presented and they agree very well with predicted results. As expected, the local Nusselt number increases with increasing buoyancy parameter for assisting flows and decreases for opposing flows. For a given buoyancy parameter and Reynolds number, a downward facing surface provides essentially the same Nusselt number as the upward facing surface for the conditions examined in the experiment.

Introduction

Combined forced and free convection or mixed convection flows arise in many transport processes in engineering devices and in nature. A review of published results on mixed convecton in laminar boundary layer flow has been reported recently by Chen et al. (1985) and clearly identifies the scarcity of experimental results in this convection regime. Mixed convection in laminar boundary layer flow along vertical and horizontal surfaces has been thoroughly examined numerically by Ramachandran et al. (1983, 1985). Experimental measurements were also reported for the vertical flat surface geometry by Ramachandran et al. (1985). In contrast, mixed convection flow along inclined surfaces has been examined only numerically for a limited range of buoyancy parameters for both uniform wall temperature and uniform surface heat flux by Mucoglu and Chen (1979) and by Moutsoglou et al. (1980). The absence of any experimental mixed convection measurements for the inclined surface geometry has motivated the present study.

The investigation was carried out to measure detailed velocity and temperature distributions for both the buoyancy assisting flow and the buoyancy opposing flow along an upward facing and a downward facing surface that is maintained at a uniform temperature and inclined at 45 deg. The results were used to validate numerical predictions for this geometry. A schematic of the flow cases considered in this study is shown in Fig. 1. This study represents an extension of an earlier work by Ramachandran et al. (1985) on mixed convection measurements adjacent to a vertical surface.

Experimental Apparatus and Procedure

The experimental investigation was performed in a low-turbulence (with free-stream turbulence intensity of less than 1 percent), open circuit wind tunnel which could be rotated and fixed at any desired inclination angle. An aluminum plate (30 cm wide by 104 cm long and 1.58 cm thick) which could be maintained at a desired temperature level uniformly by controlling the electrical energy input to six independent heating elements was used for the test surface. Velocity and temperature measurements were made by a single boundary-layer wire probe using the appropriate control bridge (constant resistance and constant current) in the hot-wire anemometer. The normal motion of the probe (relative to the plane of the heated surface) was controlled by a stepper motor and by a sweep drive unit capable of moving the probe to within 0.02 mm of a desired location. The movement of the probe along the other two directions (along the plate length and across its width) was manually controlled by a lead screw to an accuracy level of 1 mm. This traversing capability was utilized to scan through the boundary layer and throughout the flow domain over the heated surface. Data acquisition and reduction were performed on a PDP 11/23 computer. The probe was calibrated for the range of velocities and temperatures encountered in the experiment. These calibrations were checked periodically and were repeated if any deviations were detected. A detailed description of the tunnel, heated test surface, instrumentation, and experimental pro-

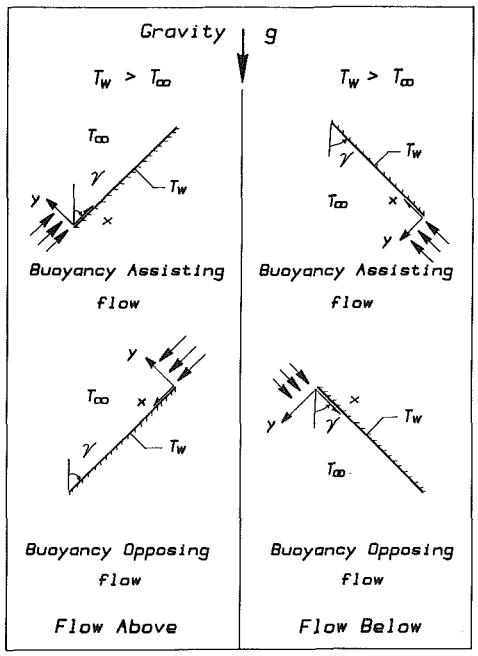

Fig. 1 Schematic of flow geometry

Contributed by the Heat Transfer Division and presented at the ASME Winter Annual Meeting, Miami, Florida, November 17-21, 1985. Manuscript received by the Heat Transfer Division June 28, 1985.

cedure is given by Ramachandran et al. (1985). The uncertainty associated with temperature measurements was determined to be 0.1°C and with velocity measurements was 8 percent for low velocity (0 to 0.5 m/s) and 2 percent for higher velocities.

The tunnel and the test surface were fixed at 45 deg in either the buoyancy assisting or the buoyancy opposing flow condition and with either flow above or flow below the heated test surface. A steady-state, uniform plate temperature level was maintained for a given free-stream velocity and then both the temperature and the velocity distributions were measured at various axial locations at the centerline of the test surface. Free-stream velocity and surface temperature were adjusted to cover a wide range of the buoyancy parameter. Local heat transfer rates and Nusselt numbers were determined from the measured temperature distributions. The procedure is the same as the one outlined by Ramachandran et al. (1985). The tunnel and its instrumentations were tested by examining the two limiting cases of the pure free and the pure forced laminar convective flow and these measurements compared very well with predicted values. The temperature of the test surface T_w was varied from the ambient temperature (T_∞ = 25°C) to 95°C in the experimental study.

Analysis and Correlations

The numerical solution of mixed convection flow adjacent to a flat surface inclined with an acute angle γ from the vertical has been reported by Mucoglu and Chen (1979) and by Moutsoglou et al. (1980). The governing boundary layer equations can be written as

$$\frac{\partial u}{\partial x}+\frac{\partial v}{\partial y}=0 \tag{1}$$

$$u\frac{\partial u}{\partial x}+v\frac{\partial u}{\partial y}=-\frac{1}{\rho}\frac{\partial p}{\partial x}\pm g\beta(T-T_\infty)\cos\gamma+\nu\frac{\partial^2 u}{\partial y^2} \tag{2}$$

$$0=-\frac{1}{\rho}\frac{\partial p}{\partial y}\pm g\beta(T-T_\infty)\sin\gamma \tag{3}$$

$$u\frac{\partial T}{\partial x}+v\frac{\partial T}{\partial y}=\alpha\frac{\partial^2 T}{\partial y^2} \tag{4}$$

The forced flow is above the heated surface when γ is measured in the clockwise direction and below the heated surface when it is measured in the opposite direction as shown in Fig. 1. The streamwise pressure gradient induced by the buoyancy force can be related to the temperature difference through equation (3) as

$$-\frac{1}{\rho}\frac{\partial p}{\partial x}=\pm g\beta\sin\gamma\frac{\partial}{\partial x}\int_y^\infty(T-T_\infty)dy \tag{5}$$

where the plus and minus signs on the right-hand side of the equation pertain, respectively, to flow above and below the surface. The second term on the right-hand side of equation (2) represents the buoyancy force, and its plus and minus signs refer to upward and downward forced flows, respectively. The boundary conditions for equations (1)–(4) are

$$\begin{aligned} &u=v=0,\ T=T_w \text{ at } y=0\\ &u\to u_\infty,\ T\to T_\infty \text{ as } y\to\infty \end{aligned} \tag{6}$$

The finite difference solution of equations (1)–(4), which was presented by Mucoglu and Chen (1979), was implemented to examine this flow regime in more detail, i.e., for buoyancy assisting and opposing flows above the surface and also below the surface, in an effort to develop simple predictive correlations for the local and average Nusselt numbers. For comparison, when needed with experimental results, the numerical solution was carried out for the same value of the buoyancy parameter as that maintained during an experimental run. This procedure eliminated any errors which could have resulted from a graphic interpolation of numerical results. The Prandtl number used in the computations was 0.7.

The predictions reveal that for the major portion of this mixed convection regime with the values of the buoyancy parameter ξ smaller than 8 and for inclination angles smaller than 75 deg, the parameter $\mathrm{Nu}_x\mathrm{Re}_x^{-1/2}$ is almost independent of the Reynolds number. In addition, for that limited range of parameters the induced streamwise pressure gradient ($\partial p/\partial x$) could be almost neglected in the solution. Thus, for that range of parameters, predictions of convective flow above the heated surface will be almost the same as those for convective flow below the heated surface under the same flow conditions. This fact was also verified from the measurements of heat transfer with air flow above and below the heated plate as will be discussed later. In the present study, however, the induced streamwise gradient term appearing in the governing equations was retained during the numerical solution in order to examine the entire range of inclination angles and buoyancy

Nomenclature

$F_1(\mathrm{Pr})$, $F_2(\mathrm{Pr})$ = functions defined in equations (8) and (10), respectively
F' = u/u_∞, dimensionless velocity
g = gravitational acceleration
h, $\bar{h}$ = local and average heat transfer coefficients
Gr_x = $g\beta(T_w - T_\infty)x^3/\nu^2$, local Grashof number
Gr_L = $g\beta(T_w - T_\infty)L^3/\nu^2$, Grashof number based on L
k = thermal conductivity
L = length of plate in flow direction
Nu_x, Nu_F, Nu_N = $q_w x/k(T_w - T_\infty)$, local Nusselt numbers for mixed, pure forced, and pure free convection, respectively
$\overline{\mathrm{Nu}}$, $\overline{\mathrm{Nu}}_F$, $\overline{\mathrm{Nu}}_N$ = $\bar{h}L/k$, average Nusselt numbers for mixed, pure forced, and pure free convection, respectively
p = pressure
Pr = Prandtl number
Re_x = $u_\infty x/\nu$, local Reynolds number
Re_L = $u_\infty L/\nu$, Reynolds number based on L
T = fluid temperature
T_w = wall temperature
T_∞ = free-stream temperature
u = axial velocity component
u_∞ = free-stream velocity
v = transverse velocity component
x = axial coordinate
y = transverse coordinate
α = thermal diffusivity
β = coefficient of thermal expansion
γ = inclination angle from the vertical
η = pseudosimilarity variable = $y(u_\infty/\nu x)^{1/2}$
θ = $(T - T_\infty)(T_w - T_\infty)$, dimensionless temperature
μ = dynamic viscosity
ν = kinematic viscosity
ξ = $\mathrm{Gr}_x/\mathrm{Re}_x^2$, local buoyancy parameter
ξ_L = $\mathrm{Gr}_L/\mathrm{Re}_L^2$, buoyancy parameter based on L
ρ = density

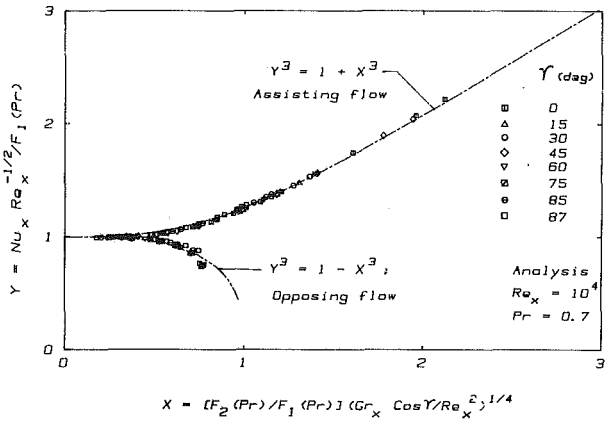

Fig. 2 Comparison of correlation with analysis

parameters and to insure a greater level of accuracy in the presented results.

The concept which was employed by Churchill (1977) to correlate the mixed convection local Nusselt number Nu_x, by using the pure forced convection value Nu_F and the pure free convection value Nu_N, was utilized in this study in order to develop a simple mixed convection correlation for the inclined surface geometry. Such a correlation takes the following general form

$$Nu_x^n = Nu_F^n \pm Nu_N^n \tag{7}$$

where the plus sign is used for buoyancy assisting flow and the minus sign for buoyancy opposing flow. This correlation was tested by comparing its results with the predicted mixed convection values, and it appears to provide a very good agreement when the magnitude for the exponent n is chosen as three ($n = 3$). The specific correlations that were used in these calculations and the comparisons with predicted mixed convection results are discussed in the following section.

The correlation for the local Nusselt number in the limit of pure forced convection is taken from Kays and Crawford (1980) as

$$Nu_F Re_x^{-1/2} = 0.332\,Pr^{1/3} = F_1(Pr) \tag{8}$$

and that in the pure free convection limit was reported by Ede (1967) as

$$Nu_N = (Gr_x \cos\gamma)^{1/4} F_2(Pr) \tag{9}$$

where

$$F_2(Pr) = 0.75[2\,Pr^2/(5 + 10\,Pr + 10\,Pr^{1/2})]^{1/4} \tag{10}$$

For the purpose of representing the comparison between the predicted values and those obtained from the correlations, it is convenient to express the mixed convection local Nusselt number as given by equation (7) in the form

$$Nu_x Re_x^{-1/2}/F_1(Pr) = \{1 \pm [F_2(Pr)(\xi \cos\gamma)^{1/4}/F_1(Pr)]^3\}^{1/3} \tag{11}$$

where

$$\xi = Gr_x/Re_x^2 \tag{12}$$

The plus and minus signs that appear in equation (11) pertain to buoyancy assisting and buoyancy opposing flows, respectively. Equation (11) has the form $Y = (1 \pm X^3)^{1/3}$. Comparisons between the correlation and the predicted results for the buoyancy assisting and buoyancy opposing flows are shown in Fig. 2 in a Y versus X plot. It is clear from the figure that the correlation provides a simple and accurate means for calculating mixed convection Nusselt numbers for inclined surfaces. Further it can be seen that the correlation agrees well (to within 5 percent) over the present range of parameters with the predicted values for the inclination angle 0 deg $\leq \gamma \leq$ 87 deg.

The correlation proposed in equation (7) was also explored for the average Nusselt number, i.e.,

$$\overline{Nu}^3 = \overline{Nu}_F^3 \pm \overline{Nu}_N^3 \tag{13}$$

where $\overline{Nu}$, $\overline{Nu}_F$, and $\overline{Nu}_N$ are the average Nusselt numbers for mixed, pure forced, and pure free convection, respectively. The proposed correlations for the local Nusselt number were used to develop expressions for the average Nusselt number and they were used in equation (13) to evaluate the correlated mixed convection values. The above-mentioned expressions are

$$\overline{Nu}_F = 2F_1(Pr)Re_L^{1/2} \tag{14}$$

$$\overline{Nu}_N = (4/3)F_2(Pr)(Gr_L \cos\gamma)^{1/4} \tag{15}$$

By utilizing equations (13)–(15) the average mixed convection Nusselt number can be expressed as

$$\overline{Nu}Re_L^{-1/2}/2F_1(Pr) = \{1 \pm [2F_2(Pr)(\xi_L \cos\gamma)^{1/4}/3F_1(Pr)]^3\}^{1/3} \tag{16}$$

Numerically predicted values for the average mixed convection Nusselt number compare very well with the correlated results from equation (16), which is similar in form to equation (11). Thus, Fig. 2 can also be utilized to determine the average mixed convection Nusselt number if Y is selected as $[\overline{Nu}Re_L^{-1/2}/2F_1\ (Pr)]$ and X as $[2F_2(Pr)(\xi_L \cos\gamma)^{1/4}/3F_2(Pr)]$ in the figure.

It should be pointed out that the heat transfer results, which have been generated for a wide range of inclination angle $0 \leq \gamma \leq 87$ deg and were used to assess the local and the average Nusselt number correlations, did not account for any turbulence or instabilities that could develop at high buoyancy parameter or high inclination angles. Thus care should be used when applying these results outside the laminar mixed convection domain which must be established experimentally for different inclination angles. For example, for the experimental geometry of 45 deg inclination angle the regime of laminar mixed convection was established experimentally to be $Gr_x \leq 10^5\ Re_x^{0.96}$.

Experimental Results and Discussion

The velocity and temperature distributions for the buoyancy assisting cases of flow above and below the heated surface, maintained at a constant temperature and at an inclination angle of $\gamma = 45$ deg (see Fig. 1 for surface orientation) were measured for the buoyancy parameter ξ in the range of $0 \leq \xi \leq 5$ for Reynolds numbers $5000 \leq Re_x \leq 60{,}000$. The highest experimental buoyancy parameter corresponds to $X = 1.6$ on the abscissa of Fig. 2. The highest value for the buoyancy parameter was limited by the maximum safely attainable plate temperature of 95°C and the lowest velocity of 0.3 m/s. The high free-stream velocity was associated with a low plate-free stream temperature difference to provide experimentally low buoyancy parameters and the low free-stream velocity was associated with the high plate-free stream temperature difference to provide experimentally high buoyancy parameters. Flow visualization was performed for each condition to insure the two dimensional, laminar nature of the flow. The laminar mixed convection domain for this geometry was established from flow visualization to be approximately $Gr_x < 10^5\ Re_x^{0.96}$. This relation provides a higher critical Grashof number than the numerically predicted value by the linear instability theory (Chen et al., 1982) for thermal instability of mixed convection adjacent to an inclined plate.

For the above stated flow regime and for inclination of 45 deg, it was numerically predicted and experimentally verified that the case of flow above the heated surface provides essen-

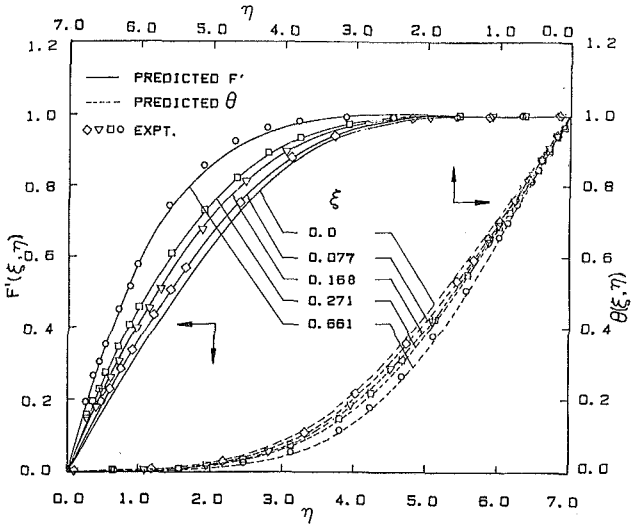

Fig. 3 Velocity and temperature distribution, buoyancy assisting flow

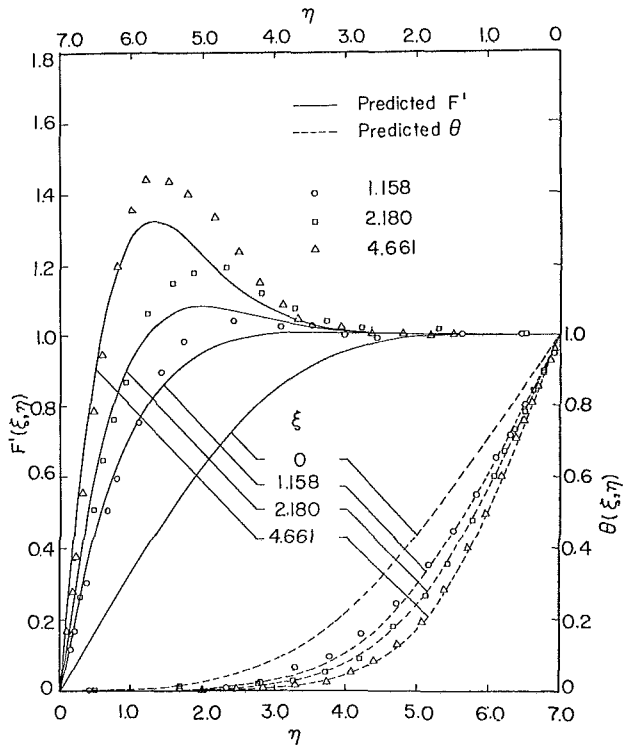

Fig. 4 Velocity and temperature distribution, buoyancy assisting flow

tially the same results as the case of flow below the heated surface. In addition, for all practical purposes, the dimensionless velocity and temperature can be considered as being a function of the buoyancy parameter ξ and the pseudosimilarity variable η for all Reynolds numbers. Similarly, the local expression $Nu_x Re_x^{-1/2}$ may be regarded as being only a function of the buoyancy parameter ξ.

Representative measurements of velocity and temperature distributions through the boundary layer for the assisting flow case are represented in Figs. 3 and 4. In these figures, the solid and the dashed lines represent, respectively, the predicted velocity and temperature distributions from the numerical solution of the governing equations for the indicated value of the buoyancy parameter. As indicated earlier, nonsimilarity variables ξ and η can be used alone to describe accurately this flow regime and for that reason the local Reynolds number is not shown in these figures. Figures 3 and 4 represent the experimental results for buoyancy assisting flow above the inclined heated plate, but measurement for assisting flow below the heated plate for similar range of ξ yielded almost similar velocity and temperature distributions and hence they are not included in these figures. This finding verifies the analytical observation mentioned earlier.

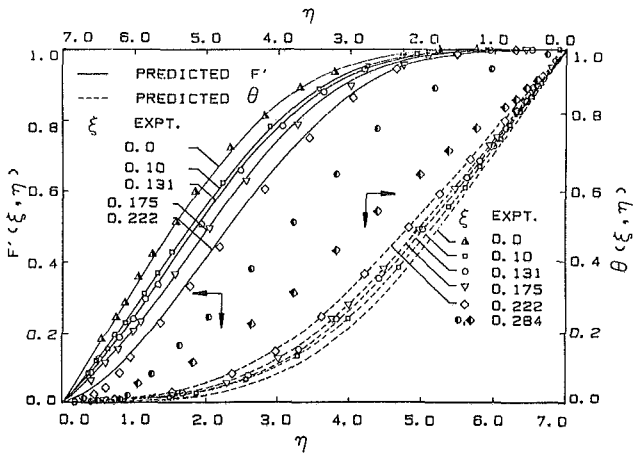

Fig. 5 Velocity and temperature distribution, buoyancy opposing flow

The predicted velocity and temperature distributions for pure forced convection ($\xi = 0$) are presented in each figure for comparison. Measured velocity and temperature data were reduced and transformed into the (ξ, η) coordinate system for comparison with the predicted values. Fluid properties were evaluated at the film temperature, $T_f = (T_w + T_\infty)/2$. These figures demonstrate that measured velocity and temperature distributions are in very good agreement with the predictions. The agreement between the measured and predicted temperature distributions is better than that for the velocity distributions. This is because the velocity field is more sensitive to changes in the value of the buoyancy parameter than the temperature field and this sensitivity increases for higher buoyancy parameter. As the buoyancy parameter increases, both the velocity and temperature boundary layer thicknesses decrease and the velocity and temperature gradients at the wall increase, causing an increase in both the Nusselt number and the friction coefficient. It is also evident that the measured velocity distributions show a slightly higher overshoot than the predictions. For example, at a buoyancy parameter of $\xi = 4.661$ the experimental results deviate by 9.77 percent from the predicted values (the uncertainty in measured velocity in that region is approximately 8 percent).

The air tunnel which was used to study the buoyancy assisting mixed convective flow was rotated appropriately to examine the buoyancy opposing flow case. For this case the suction fan was at the bottom of the tunnel and the leading edge of the plate was pointing upward toward the inlet section of the tunnel. The same statements which were made earlier for buoyancy assisting flow cases regarding the effect of the local Reynolds number and the flow disposition (either above or below the inclined heated surface) are also applicable for the buoyancy opposing flow cases. Measurements for this flow condition were limited to a buoyancy parameter range of $0 \leq \xi \leq 0.222$, because flow reversal occurs when $\xi \geq 0.25$. The hot-wire anemometer cannot detect the flow direction and could not be used to explore the reversed flow region. In fact, the governing equations for this case also failed to yield converged numerical solution for values of buoyancy parameter ξ larger than 0.25, because the model cannot be used in regions where flow reversal occurs. Measured velocity and temperature distributions for the opposing flow case are presented in Fig. 5. In this figure, the solid and the dashed lines represent, respectively, the velocity and temperature

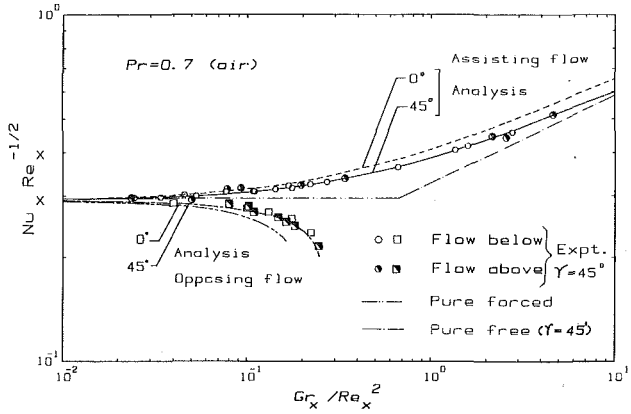

Fig. 6 Measured and predicted results for buoyancy assisting and opposing flow

distributions predicted by the numerical solution of the governing equations. Measured velocities and temperatures are in reasonable agreement with the predicted values (within 10 percent), but this agreement is not as good as the one reported for the buoyancy assisting flow case. As the buoyancy parameter increases, the velocity and temperature gradients at the wall decrease, causing a decrease in both the local Nusselt number and the local friction coefficient. The measured results for a buoyancy parameter larger than 0.222 clearly demonstrate the existence of a flow reversal region near the wall.

The measured temperature distribution was used to determine the temperature gradient at the wall which was in turn utilized to determine the local Nusselt number. The uncertainty associated with determining the temperature gradient at the wall and consequently the Nusselt number was determined to be less than 5 percent. The variation of the deduced Nusselt number as a function of the buoyancy parameter is presented in Fig. 6. The predicted local Nusselt numbers which are shown in this figure are for $Re_x = 60{,}000$ for both the buoyancy assisting and buoyancy opposing flow cases. The Reynolds numbers for the various experimental points are not shown in this figure because, as was established earlier, they can be considered as being independent of this paramater in the present experimental range. It is seen that the agreement between the measured and the predicted results is very good. For buoyancy assisting flow, the mixed convection results asymptotically approach the pure forced ($\xi = 0$) and pure free ($\xi = \infty$) convection limits, and the mixed convection Nusselt numbers are higher than the equivalent pure forced or pure free convective flow. The regime of mixed convection based on a 5 percent departure in the local Nusselt number from pure forced and pure free convection results is represented by the buoyancy parameter range of $0.10 \leq \xi \leq 7.0$. The influence on the velocity distribution, however, becomes significant at a much smaller buoyancy parameter. The local Nusselt numbers can be 25 percent higher than the corresponding pure forced or pure free convection values in this region of buoyancy assisting flow.

The local Nusselt numbers for the buoyancy opposing flow cases are also presented in Fig. 6, along with the numerically predicted values. Good agreement (better than 10 percent) is seen between the experimental and the predicted values. As the buoyancy parameter increases, the temperature and the velocity gradients at the wall decrease, causing the heat transfer to decrease gradually and then rapidly in the vicinity of flow reversal at $\xi \geq 0.25$. For the buoyancy opposing flow case, the mixed convection Nusselt numbers could be significantly lower than the corresponding pure forced convective values. Figure 6 contains measured data from the two cases of flow above and below the heated surface for buoyancy assisting and buoyancy opposing flow conditions. It is quite clear from these results that in the experimental range, the two cases are essentially identical. This was verified also from the numerical solution of the governing equations.

Conclusions

Detailed study of laminar convection boundary layer flow adjacent to inclined isothermal surfaces is reported for buoyancy assisting and buoyancy opposing flow conditions. Simple and accurate correlations for the local and average Nusselt numbers are presented for all inclination angles. Measured velocity and temperature distributions and local Nusselt numbers for a surface inclination angle of 45 deg are reported and they compare well with predicted results, with deviation of less than 10 percent. The local Nusselt number increases with increasing buoyancy parameter for the buoyancy assisting flow and decreases for the buoyancy opposing flow. The velocity distributions for the buoyancy assisting flow exhibit a significant overshoot above the free-stream value and the velocity field is found to be more sensitive to the buoyancy effect than the temperature field. The mixed convection domain, defined as the region where the local Nusselt numbers resulting from mixed convection calculations deviate by more than 5 percent from either the pure forced or the pure free convection value, is given by $0.1 \leq \xi \leq 7.0$ for the buoyancy assisting flow case and $0.06 < \xi < 0.25$ for the buoyancy opposing flow case.

It was verified that flows above and below the heated surface yielded essentially similar heat transfer results in the experimentally measured ranges of Reynolds and Grashof numbers. In addition, the dimensionless velocity and temperature distributions can be considered as being only a function of ξ and η, and the local expression $Nu_x Re_x^{-1/2}$ as being only a function of ξ, for all Reynolds numbers.

Acknowledgments

This study was supported in part by two grants from the National Science Foundation (NSF MEA 81-11673 and NSF MEA 83-00785).

References

Chen, T. S., Moutsoglu, A., and Armaly, B. F., 1982, "Thermal Instability of Mixed Convection Flow Over Inclined Surfaces," *Numerical Heat Transfer*, Vol. 5, pp. 343-352.

Chen, T. S., Armaly, B. F., and Aung, W., 1985, "Mixed Convection in Laminar Boundary-Layer Flow," in; *Natural Convection: Fundamentals and Applications*, S. Kakac, W. Aung, and R. Viskanta, eds., Hemisphere, New York, pp. 699-725.

Churchill, S. W, 1977, "A Comprehensive Correlating Equation for Laminar, Assisting, Forced and Free Convection," *AIChE Journal*, Vol. 23, No. 1, pp. 10-16.

Ede, A. J., 1967, "Advances in Free Convection," in: *Advances in Heat Transfer*, Vol. 4, pp. 1-64.

Kays, W. M., and Crawford, M. E., 1980, *Convective Heat and Mass Transfer*, 2nd ed., McGraw-Hill, New York.

Moutsoglou, A., Tzuoo, S. K. L., and Chen, T. S., 1980, "Mixed Convection in Boundary Layer Flows Over Inclined Surfaces," *AIAA 15th Thermophysics Conference*, Snowmass, CO, July 14-16, 1980, Paper No. AIAA-80-1525.

Mucoglu, A., and Chen, T. S., 1979, "Mixed Convection on Inclined Surfaces," ASME JOURNAL OF HEAT TRANSFER, Vol. 101, pp. 422-426.

Ramachandran, N., Armaly, B. F., and Chen, T. S., 1983, "Mixed Convection Over a Horizontal Plate," ASME JOURNAL OF HEAT TRANSFER, Vol. 105, pp. 420-423.

Ramachandran, N., Armaly, B. F., and Chen, T. S., 1985, "Measurements and Predictions of Laminar Mixed Convection Flow Adjacent to a Vertical Surface," ASME JOURNAL OF HEAT TRANSFER, Vol. 107, pp. 636-641.

R. D. Skocypec[1]
Mem. ASME

D. V. Walters

R. O. Buckius
Mem. ASME

Department of Mechanical and Industrial Engineering, University of Illinois at Urbana-Champaign, Urbana, IL 61801

Spectral Emission Measurements From Planar Mixtures of Gas and Particulates

An experimental system is developed that forms a hot layer of gas and particulates flowing through a test section with cooled walls. The test section forms a one-dimensional planar layer, allows intrusive probes to characterize the medium in terms of particle loading and temperature, and allows radiometric measurements of the normally directed spectral energy emitted from the medium. Gas flow, gas composition, and particle flow are controlled. An experimental investigation is undertaken yielding spectral normally directed emittance data obtained from a well-characterized layer containing gaseous constituents of carbon dioxide and nitrogen, and solid particles of BNi-2, a boron nickel alloy. Emittance data are presented and exhibit the effects of particulate scattering, including the extension of the 4.3 μm carbon dioxide band wings. Emittance data are compared to analytical predictions.

Introduction

Advancement in the field of radiative heat transfer requires a balance between analytical and experimental investigations. Analytical modeling has progressed sufficiently to include more complex and detailed phenomena. Radiative heat transfer from high-temperature media, consisting of spectrally absorbing gas and particulates, is presently being analytically modeled [1, 2]. Experimental works considering heat transfer in such media are very limited in number and specific in scope. Also, virtually no controlled fundamental experiments investigating radiative heat transfer in participating media have been performed at high temperatures.

Emission/absorption experiments are considered to be those which do not scatter radiant energy. This classification includes single-phase experiments, in which the medium is strictly gaseous or solid, and are viewed as single line-of-sight problems. The gas experiments generally measure an absorptance along a specified path through the medium (e.g., [3, 4]). Temperature, partial pressure, and path length for the gases are controlled. Measurements of emission from solids can be obtained by either: (1) measuring reflectance and, if necessary, transmittance, invoking an energy balance and Kirchhoff's law (e.g., [5, 6]), (2) making a calorimetric measurement (e.g., [7]), or (3) performing a radiometric measurement (e.g., [8, 9]). Reference [10] has a very good review of solid emission measurements. A good overview of the pitfalls related to thermal emittance work has been presented by Harrison [11] and Richmond et al. [12]. Single particle emittance experiments have been attempted by simultaneously levitating and heating a particle with lasers [13]. Experimental investigations of flame emission on both total (e.g., [14, 15]) and spectral (e.g., [16]) bases have been presented. In rocket plume applications, attempts at predicting the heat transfer agreed poorly with observations (e.g., [17]). More recent experimental efforts [18] have been undertaken to model rocket plumes in a controlled environment.

All of the above investigations can be performed at high temperatures and are generally concerned only with a single line of sight since inscattering is usually negligible. In contrast, light scattering experiments investigate scattering media with visible wavelength sources at room temperatures (e.g., [19, 20]). Reflectance and transmittance values are generally measured. The analytical extension of these experiments into the infrared region is termed light modeling [21].

Thus, a variety of experiments have been performed investigating radiative transfer in solids, gases, and aerosols. Emission, absorption, reflection and transmission at both high temperatures and room temperatures have been measured. None, however, have examined emission from planar media containing real gases and particulates at high temperatures in which both nongray absorption and multiple scattering effects were present simultaneously. The goal of the investigation is to obtain infrared radiation heat transfer measurements in the form of normally directed emission data from a high-temperature, one-dimensional, well-characterized layer containing a real gas and particulates.

Before outlining the systems and measurement methods of the experiment, the pertinent parameters are discussed. The primary radiative variables are system temperature T, total pressure P_T, the product of absorbing gas partial pressure and path length P_AL, single scattering albedo ω_S, and scattering optical depth κ_{SL}. These variables are specified in terms of more fundamental variables as: $P_AL = x_f \cdot P_T \cdot L$, $\omega_S = \sigma/(\alpha_S + \sigma) = Q_{sc}/Q_{ex}$, and $\kappa_{SL} = (\sigma + \alpha_S)L = A_c \cdot Q_{ex} \cdot N \cdot L$. N is also defined in terms of the particle volume fraction (particle volume per unit volume) f_v, as $N = 6 f_v/\pi d^3$. The scattering and extinction efficiencies can be determined from the well-known Mie theory (e.g., [22]) using the complex refractive index of the particle material $\bar{n}$ and the size parameter $x = \pi d/\lambda$. Thus, the basic variables become: T, P_T, x_f, L, d, f_v, and $\bar{n}$.

Experimental System

Flow Loop Components. A steady state flow system (see Fig. 1) was designed to obtain a reasonably isothermal hot medium with cold walls. The degree of isothermality is, in part, governed by the gas flow rate. The pressure and flow rate of the gas from cylinders containing a mixture of a known concentration of carbon dioxide in nitrogen are regulated and controlled prior to entering the laminar flow element (LFE) (Meriam 50 MW 20-1) for measurement of the gas flow rate. The standard relationship for laminar duct flow, the calibration curve supplied with the LFE, and the density and dynamic viscosity of the mixture are used to determine the gas mass flow rate for the gas compositions investigated. The gas, after passing through the laminar flow element, flows primarily through the electric heating unit. A very small amount of gas

[1] Presently at Sandia National Laboratories, Division 1512, Albuquerque, NM 87185.

Contributed by the Heat Transfer Division and presented at the National Heat Transfer Conference, Denver, CO, August 1985. Manuscript received by the Heat Transfer Division April 29, 1985.

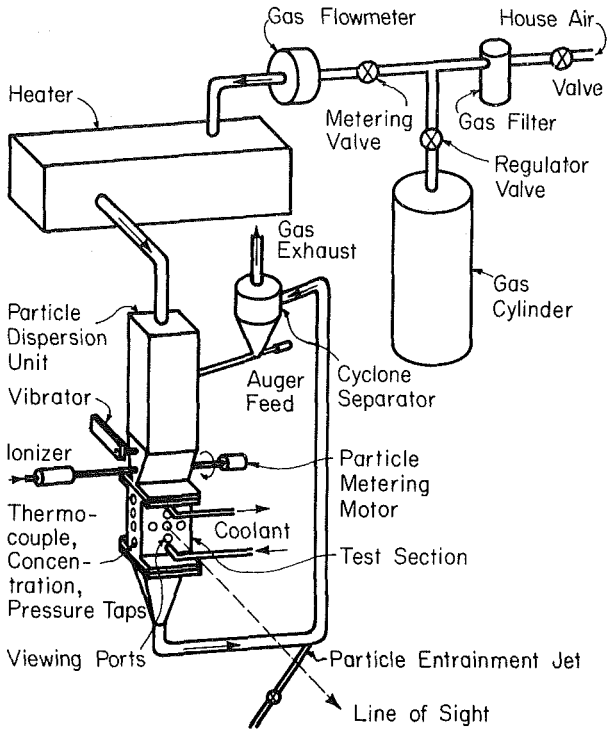

Fig. 1 Schematic diagram of experimental system

is diverted to flow through the gas ionizer discussed below. The gas heater (ThermCraft, Inc.) is a compact 2.4 kW unit which can heat 1.2 g/s of gas to a temperature of 1061 K.

Particle Dispersion Unit. Upon leaving the heater, the hot gas flows to the particle dispersion unit (PDU), which is designed to dispense particulates into the gas phase uniformly. It consists of two chambers: an interior chamber with a porous stainless steel plate over the top and tapered walls at the bottom, and an exterior chamber which forms a slot passage for gas flow around the interior chamber. The particulate is held in the interior chamber, maintaining it at a temperature near that of the gas. There is a slight separation at the bottom between the walls of the interior chamber where a knurled 0.79 cm (5/16 in.) o.d. stainless steel shaft rotates. A 0.079-cm-wide annular slot remains between one side of the shaft and the wall, allowing the particulates contained in the interior chamber to be fed into the hot gas stream flowing around the chamber. The rotational speed of the shaft governs the amount of particulate admitted to the gas.

Directly below the rotating shaft, on either side of the slot, are two 17-gauge stainless steel hypodermic tube manifolds which admit ionized gas to the system. The compact ionizer used in this experiment (3M Model 906) has a Polonium 210

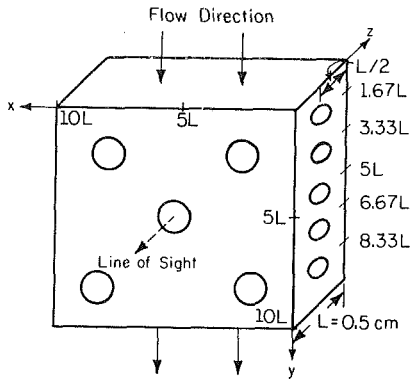

Fig. 2 Location of directional axes and radiometric and probe ports in the test section medium

source with an activity of 20 mCi emitting alpha particles which interact with the gas flowing over the source to create ions. This neutralizes any electrostatic charge of the aerosol to improve homogeneity. To insure uniform flow of particulate out of the interior chamber of the PDU, the chamber is vibrated using a simple cantilever concept with a striker at one end.

Test Section. The hot two-phase mixture flows downward into the test section. The test section slot dimensions (0.5 cm deep, 5.0 cm wide, see Fig. 2) are chosen based on radiative conditions, manageable gas flow rates, and particle feeding abilities. The test section has a 10-to-1 depth-to-width ratio because a number of investigations (e.g., [23]), in attempting to develop more realistic models for cloud analysis, have shown that a slab whose thickness is one-tenth of the side dimensions can be accurately modeled by a one-dimensional slab. To reduce the effect of the walls, the primary walls are cooled with flowing tap water and all interior slot walls are painted with an infrared flat black paint (3M ECP-2200 Solar Absorber Coating), designed for high-temperature service. The paint has a typical nonselective absorptance of 0.96 and typical normal emittance of 0.86.

The test section is made of copper (except for the outer plates of the cooling jackets) to maintain temperature uniformity. Five radiometric viewing ports are located in the front primary wall. There is one port in the center of the wall and one each placed 1.75 cm (11/16 in.) on either side horizontally and vertically. The viewing port consists of a threaded brass rod with a 0.635-cm (1/4 in.) diameter hole through the center (painted black). A 1-mm-thick, 0.864-cm-dia optical window (T-12 of Harshaw Chemical Company) is epoxied onto the end facing the hot medium and is flush with the inner surface of the wall. Brass plugs with no windows or viewing holes are placed in the four threaded ports not being used at any given time. The effect of the window on the one dimensionality of the test section is analytically determined to be under 2 percent

Nomenclature

A_c = geometric cross section
d = particle diameter
D = geometric diameter
d_{32} = volume to surface area average diameter
f_v = particle volume fraction
L = length
$\dot{m}$ = mass flow rate
N = particle number density
$\tilde{n}$ = complex refractive index
P = pressure
P_A = absorbing gas partial pressure
P_AL = product of absorbing gas partial pressure and path length
P_T = total pressure
Q_{ex} = extinction efficiency
Q_{sc} = scattering efficiency
T = temperature
x = Mie size parameter
x_f = mole fraction of absorbing gas species
α_S = absorption coefficient
ΔP = differential pressure
ϵ'_λ = spectral directional emittance
θ = polar angle
κ_S = optical depth = $(\alpha_S+\sigma)y$
λ = wavelength
μ = cos θ
ρ = density
σ = scattering coefficient
ω_S = scattering albedo = $\sigma/(\alpha_S+\sigma)$

Subscripts

g = gas quantity
L = evaluated at the total perpendicular layer depth
p = particle quantity

in the worst case. Also, the wall temperature is monitored and is isothermal within 1 K (±0.5 K).

Five 0.635-cm (1/4 in.) diameter threaded access holes are available every 1.27 cm (1/2 in.) downstream along both side walls. Threaded brass positioners are constructed with an axial hole which allows 18-gauge (0.124 cm (0.049 in.) o.d.) stainless steel hypodermic tubing to slide through. Two intrusive probes, for temperature and particle volume fraction measurements, have 18-gauge tubing for positioning and protection. The axial hole is offset 0.152 cm (0.060 in.) from the center of the positioner so that when the positioner is rotated 180 deg the tube traces a semicircle with endpoints at the test section walls. A probe contained within 18-gauge tubing is slid through the positioner to a desired cross-stream location and locked with the tube fitting. Rotation of the positioner locates the probe at any depth position within the medium. With five downstream ports, many locations in the medium can be accessed.

Upon leaving the test section the hot medium is funneled into 3.175 cm (1.25 in.) stainless steel pipe to the cyclone separator [24] at the top of the loop. The particulate that has been separated from the gas is fed to a small conical feeding hopper directly beneath the cyclone. An auger feed transports the particulate horizontally to the interior chamber of the PDU. It can transport enough particulate to maintain a steady state at the highest PDU feed rate.

To keep the medium hot, all components in the loop except the test section are insulated with as much Carborundum Fiberfrax H Durablanket ceramic fiber insulation as possible. Typically at least a 7.62-cm (3 in.) radial blanket is used.

The calibration of the particle dispersion unit is determined under conditions most representative of operating conditions. Calibration is accomplished by weighing the particulate obtained when the PDU shaft is rotating for a given time period. The calibration tests are performed using air flowing at about 2.4 g/s with the heater at 505 K. Repeatability for all conditions is within 9 percent and typically is within 3 percent. The stability and repeatability of the particulate dispersion unit under steady-state test conditions are better than this due to the inherent transient nature of the calibration test.

Probes. The degree to which the medium in the test section matches the desired conditions is monitored. The three independent variables – temperature, total pressure, and particle volume fraction – all require a type of probe for characterization. Total pressure is measured by connecting one of the ten access ports in the test section to an absolute pressure transducer.

Local test section gas temperature is measured using chromel-alumel (type K) thermocouples at five possible downstream positions and any cross-stream location. Omega-clad thermocouple wire (a solid Inconel-600 sheathed cable containing 36-gauge chromel-alumel wires insulated from each other and from the sheath by highly compacted magnesium oxide), is fixed into an 18-gauge stainless steel tube which has a single 0.79-mm (1/32 in.) diameter hole drilled through the tube 0.119 cm (3/64 in.) from one end. The bead, located in the center of the hole, is shielded by the hypodermic tube on the sides toward the cold walls, it is easily positioned, and the probe has a 1.24-mm (0.049 in.) o.d. The radiative effect of the cold walls on the equilibrium temperature of the thermocouple bead is reduced by the radiation shield between the bead and the walls, while maintaining gas flow over the bead. Additionally, the thermocouple wires are thin and well insulated to reduce the error due to conduction from the bead.

To determine the uniformity of particle loading, a probe is required that yields relative local particle volume fraction data. Only relative information is necessary since the average particle loading is known from the calibration of the PDU. A fiber optic probe is designed to minimize flow disturbance.

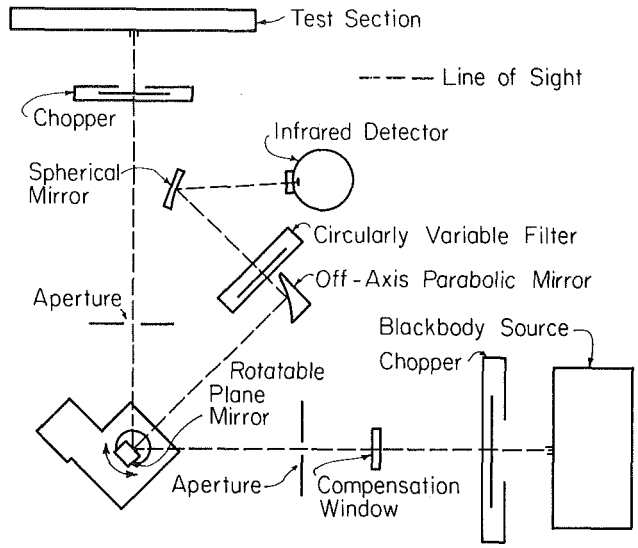

Fig. 3 Schematic diagram of optical system

The ends of two fiber optic cables are positioned a fixed distance apart by the probe. A 0.95 mW helium–neon laser is focused with a lens into the external end of one cable (the emitter cable). The energy is transmitted across the fixed gap inside the medium into the receptor cable. The transmission gap (3.5 mm wide) is positioned from one side with 18-gauge hypodermic tubing. A bundle of six fiber optic receptor cables is epoxied within it (to increase the transmission signal), with the external end of the bundle aligned with a PIN silicon photodiode. The connector between the fiber optic receptor bundle and the emitter cable is a small piece of hypodermic tubing, which slips over both ends of the cables and has the transmission gap machined out. It is painted black to reduce reflection.

The fiber optic cable is a plastic-clad silicon fiber (a low-loss silicon polymer-clad fused quartz core fiber) with a core diameter of 200 μm and an acceptance angle of 30 deg. The cable is extremely fragile, is easily broken and has a temperature limit of 473 K. It is noted that movement of the cable generates changes in curvature of its shape and alters the transmission signal (due to a change in cable loss). To minimize movement of the cable, it is slid inside stainless steel tubing for much of the distance between the focusing lens and the access port of the test section. Because of the cable loss problem for analog signal transmission, comparison between results of different directional scans cannot be made on an absolute scale. However, the desired relative measurements within a directional scan are possible and normalized comparisons between scans are made. The thermocouple and fiber optic probes are removed when the emittance data are being obtained.

Optical System. The emission measurements are made radiometrically and thus require an optical system, depicted in Fig. 3. Beginning at the test section, the first component is an optical chopper to modulate the energy at the desired frequency (910 Hz). The energy next passes through an aperture set at 0.508-cm (0.20 in.) diameter (to define the field of view of the detector) and is reflected off a rotatable plane mirror into the off-axis parabolic reflector. The plane mirror can be rotated about its vertical axis by a stepper motor driven rotator. The off-axis parabolic reflector focuses collimated energy parallel to the optic axis into the focus of the paraboloid, at which point the circularly variable filter (CVF) is placed. The CVF spectrally resolves the energy incident to it with a resolution of 1.5 percent half bandwidth. The CVF consists of three optical wedges (Optical Coating Laboratory, Inc. CV-2.5/14.5-L)

Table 1 Particle size distribution of BNi-2 particulates by Coulter Counter measurement

Diameter range, μm	Proportion within range
under 6.35	0.005
6.35–8.0	0.01
8.0–10.8	0.02
10.08–12.7	0.045
12.7–16.0	0.20
16.0–20.2	0.29
20.2–25.4	0.36
25.4–32.0	0.07

placed in circumferential slots in an aluminum wheel. Calibration of the CVF is accomplished by taking a spectral transmission scan of polystyrene film and comparing the well-defined spectral distribution to known spectral locations.

A concave front surface spherical mirror with a focal length of 75 mm is used to reflect the energy passing through the CVF onto the infrared detector element. A custom semiconductor detector (Santa Barbara Research Center) includes two different elements located side by side. The elements used are a photovoltaic InSb element (0.0314 cm^2) with ultimate sensitivity in the spectral band 0.5 to 5.5 μm, and a HgCdTe photoconductive element (0.04 cm^2) with a spectral response band to 14.5 μm. The detector position is adjusted to obtain an optimum signal strength using a three-dimensional translation stage.

The normally directed energy from the test section is compared to the normally directed energy from a blackbody (Infrared Industries Model 464 with Temperature Controller 101-B) at the test section temperature. Consequently, a blackbody source with an attached aperture is located symmetrically with the test section about the line of sight to the off-axis parabolic reflector. Similarly positioned in front of the blackbody is another optical chopper and aperture. An optical window identical to that of the test section is placed in the line of sight between the blackbody and plane mirror. Rotation of the plane mirror is all that is necessary to direct either the test section energy or blackbody reference energy to the detector. In this manner both the blackbody energy and energy from the layer pass through similar optical paths. The modulated signal is amplified and directed to a lock-in amplifier.

The difficulty in accurately directing infrared energy through the optical system makes identical optical paths for the test section and blackbody energy impossible. The amount of misalignment is determined using a heat source constructed of a 330 Ω carbon resistor imbedded in a small cylinder of copper. The copper cylinder is coated on one end with the same high emittance 3M black paint used inside the test section. The coated end, used as the infrared source, is identical in dimension to the test section viewing port. A low emittance polished aluminum disk surrounds the coated end to provide a radiation shield. The copper cylinder can be mounted in two nylon bases, one fitting the test section viewing port, the other fitting the aperture attached to the blackbody. The source can thus be placed directly into the test section or blackbody line of sight.

The initial alignment of the optical system is performed using a helium-neon laser. All optical components, except the plane mirror, are then fixed, as is the detector. The plane mirror alone is used to direct energy from either the test section or the blackbody into the detector. The optical paths are now checked for alignment with the heat source. The source is first placed in the test section viewing port and the plane mirror is rotated to reflect the maximum source energy into the detector. The detector voltage signal is recorded. The source is next placed in the blackbody aperture, and the plane mirror is again rotated to reflect the maximum source energy into the detector. The detector voltage signal is again recorded. Since the energy source is identical for the two source positions, any

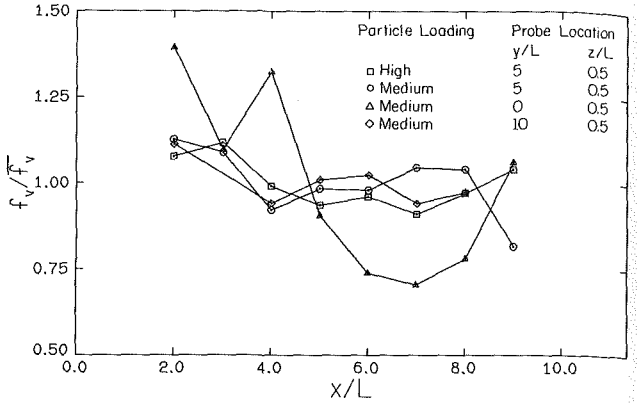

Fig. 4(a) Relative particle volume fraction scans in the x direction within the medium

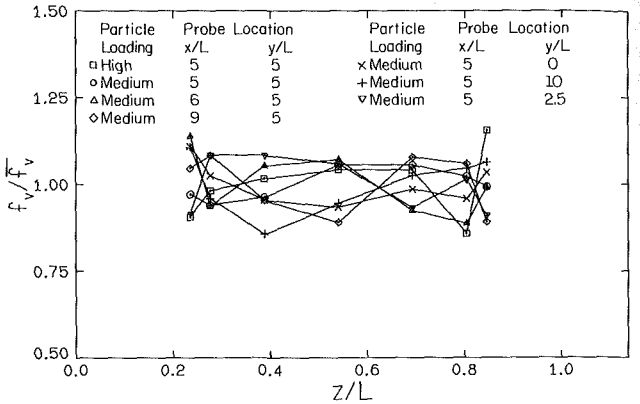

Fig. 4(b) Relative particle volume fraction scans in the z direction within the medium

discrepancy between the two voltage values must be due only to a small optical misalignment. Thus, the ratio of the blackbody voltage to the test section voltage gives the alignment correction factor for this system.

Physical Characterization of the Medium. Physically, the medium is described by the geometric shape of the layer and identification of the gas and particulate phases. The layer depth is 0.5 cm for all cases with a width and downstream distance of 5.0 cm. The three gas mixtures investigated are: 100 percent nitrogen (99.995 percent minimum purity, with a typical analysis of 0.4 ppm CO, 1.3 ppm H_2O, 1.6 ppm O_2, less than 1 ppm H_2, less than 0.1 ppm T.H.C.); 50 percent carbon dioxide, balance nitrogen; and 100 percent carbon dioxide (Coleman grade). The gas cylinders for all gas mixtures are rolled prior to use to insure a well-mixed homogeneous gas.

The solid particulate consists of a boron nickel alloy BNi-2 commonly used as a nickel-based brazing compound. This material is used because it is available as micron-sized spheres with a very peaked size distribution, and can withstand operating temperatures. When it is dispersed in the gas phase, a reasonably uniform two-phase medium can be generated. BNi-2 is a homogeneous alloy satisfying the American Metal Standard specification 4777. It has the following chemical analysis (weight percent): 2.99 boron, 0.020 carbon, less than 0.10 cobalt, 7.06 chromium, 3.02 iron, 4.40 silicon, 82.4 nickel and cobalt. The material is formed into spheroid-ellipsoids by vacuum induction melting and argon atomization (gas atomization). The particle size distribution is presented from a Coulter Counter analysis described in Table 1. The mean diameter of interest is the volume to surface area average d_{32} [25], which is 21.4 μm with a variation of 5.4 μm. The density of the particulate is 7770 kg/m^3 by null pyc-

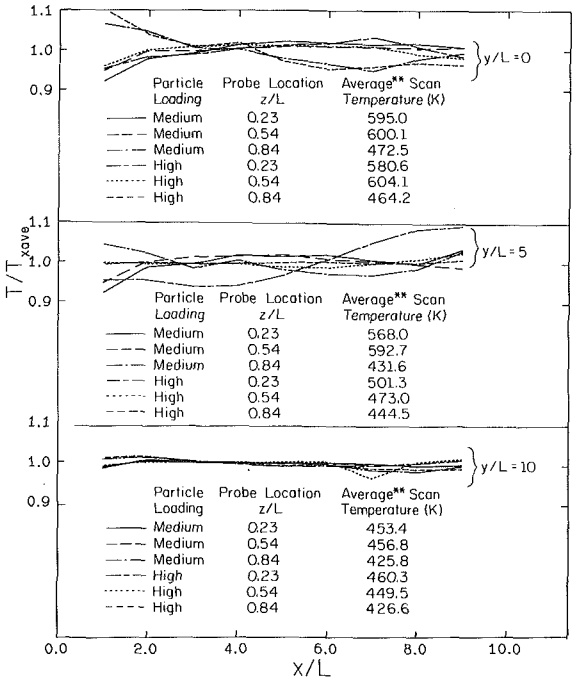

Fig. 5 Normalized temperature scans in the *x* direction within the medium (average of temperature at all points in the scan)**

nometer measurement. The particulate is baked at 480 K and then deagglomerated, giving excellent flowability.

Radiative Characterization of the Medium. The medium is radiatively characterized by determining the degree of one dimensionality (already discussed), homogeneity, and isothermality of the layer, assuming the following are known: gas partial pressure, total pressure, geometric depth, and optical or radiative properties of the particulate. The homogeneity and isothermality of the layer are determined by taking scans with the fiber optic and thermocouple probes in all directions within the medium. Figure 2 indicates the directional axes and port positions within the medium. Data are taken at eight or nine x locations, five y locations, and seven z locations.

The fiber optic scans are obtained at a temperature near the limit of the fiber optic cable (425 K) with low, medium, and high particle loadings in air. Figures 4(*a*) and 4(*b*) plot f_v information at different locations within the layer. Although additional scans were taken, only medium and high particle loadings representative of conditions during emittance measurements are presented. Each set of data is an average of a number of repeated scans (three to six each) and each set is referenced to the average f_v for that scan (i.e., averaged over the direction plotted at the location indicated). The magnitude of the particle loading is observed to not affect the relative distribution. Therefore, the intermediate particle loading is expected to be representative. The data generally remain within 10 percent of the average, except at probe location $y/L = 0$. These data are taken at the top of the test section and the greater observed variation in x/L is believed to be due to entrance flow, and is not observed at any of the downstream locations. Interestingly, in Fig. 4(*b*) the data at the top of the test section do not exhibit this large of a variation in the z direction. Due to the cable loss problem and the sensitivity to vibration, and the particle feeding variation of the PDU (as discussed earlier), the f_v values are comparaable to the variations noted. In view of this, and the fact that no consistent trend is noted, the medium is believed to have a homogeneous particle loading within measurable limits.

Thorough temperature scans of the layer are made at various layer temperature settings to determine the degree of

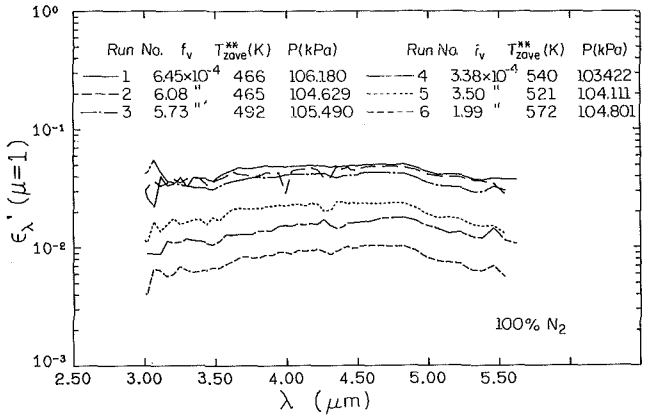

Fig. 6(*a*) Normally directed spectral emittance for layers having a gaseous constituent of 100 percent nitrogen (see Fig. 7 for test section temperature scans in the *z* direction; ** average of temperature at three center points)

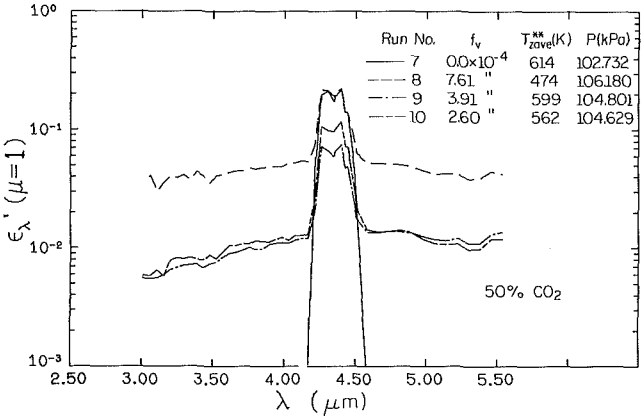

Fig. 6(*b*) Normally directed spectral emittance for layers having a gaseous constituent of 50 percent carbon dioxide in a nitrogen balance (see Fig. 7 for test section temperature scans in the *z* direction; ** average of temperature at three center points)

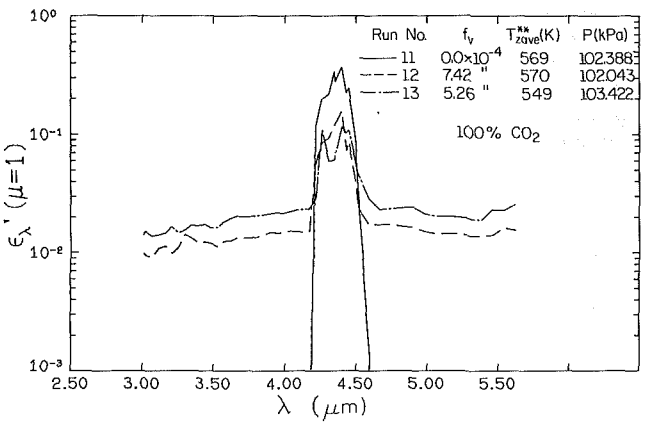

Fig. 6(*c*) Normally directed spectral emittance for layers having a gaseous constituent of 100 percent carbon dioxide (see Fig. 7 for test section temperature scans in the *z* direction; ** average of temperature at three center points)

isothermality. The data presented in Fig. 5 are taken at higher layer temperatures and exhibit larger temperature variations than other scans which are not presented. Figure 5 shows temperature scans in the x direction (see Fig. 2 for direction notation) for medium and high particle loadings (representative of conditions during emittance measurements) and probe locations at the middle and extremes in the y and z directions. Ten temperature readings are taken at each point and averaged. The top set of scans is at the top location of the

test section ($y/L = 0$), the middle set at $y/L = 5$, and the bottom set at $y/L = 10$. The temperature scans are normalized with respect to the average temperature of each scan. Under all conditions investigated, the temperature variation in the x direction is under 10 percent. A temperature drop greater than desired in the y direction is observed, although a consistent drop is not noted when all data (including those not presented) are considered. The largest temperature gradient occurs in the z direction, and specific z direction test section temperature scans are presented with the emittance data in the following section.

Results and Discussion

Before presenting the emittance results, a typical data run is described and a discussion of the expected experimental uncertainty is given. The system is warmed to thermal steady-state conditions with laboratory air flowing for 2–3 hr. During warmup the detector is cooled to an operating temperature of 77 K with liquid nitrogen.

An interactive procedure with the laboratory computer is used to obtain the temperature z scan at $x/L = 5$, $y/L = 5$. Ten temperatures are taken at each of seven z positions and averaged. The three centermost points are then averaged and are taken as the average test section temperature. The temperature of the blackbody is set to this average temperature and the resulting particle volume fraction in the test section (based on the average temperature) is also determined. The CVF is positioned with a locating slit in the optical line of sight. The slit is only used to reposition the CVF wheel prior to a spectral scan and is replaced in the optical path by the CVF wedges during a scan. The plane mirror is then rotated to reflect the maximum test section energy into the detector. After the lock-in amplifier sensitivity has been entered in the laboratory computer that controls the experiment, and the CVF has been moved to the correct position, a spectral scan of the test section energy is obtained. The CVF slit is repositioned in the line of sight, the plane mirror is rotated to reflect the maximum blackbody energy into the detector line of sight, and the entire emittance measurement procedure is repeated for the blackbody energy. An emittance scan takes approximately an hour to complete.

The data of interest, spectral-directional (normally directed) emittance, are obtained by first taking the ratio of the voltage generated by the system (lock-in amplifier output voltage) in response to the energy from the test section, to the voltage generated in response to the energy from the blackbody. These ratios, multiplied by the alignment correction factor, give the emittance data. The uncertainties associated with the electronic processing equipment are small relative to other uncertainties and are not discussed. The errors introduced by the optical system are difficult to quantify, and they are minimized by correcting the emittance values with the experimentally determined alignment correction factor. The error associated with the blackbody energy is governed by the ability to set and maintain the blackbody temperature. With an uncertainty of about 1.4 K (1 K by manufacturer specification and 1 K from a curve fit to the calibration curve) in the blackbody temperature, energy uncertainties of the order of 1.8 percent are expected.

The primary uncertainty is due to the determination of the particle volume fraction for the layer, with f_v evaluated as $(\rho_g \dot{m}_p)/(\dot{m}_g \rho_p)$. Although the particle volume should be included in the denominator, the particle volume is very small relative to the gas volume (typically a factor of 10^{-4}) and it is not included. The gas density is known from the ideal gas law and test section pressure and average temperature. The particle density is known and the gas mass flow rate is determined from the laminar flow element. The particle mass flow rate is obtained from the PDU calibration. The primary uncertainties are the particle mass flow rate, known within 9 percent, and the test section local temperature, indicated to be the average temperature within 10 percent. These uncertainties generate an uncertainty in f_v of 13.5 percent.

The optical thickness is determined from $\kappa_{SL} = 1.5\, Q_{ex}\, f_v\, L/d_{32}$, as previously discussed. The extinction efficiency is taken as 2 for the range of experimental conditions with minimal error. The uncertainty in f_v yields an uncertainty in optical depth of the same amount. For representative conditions, an uncertainty of under 15 percent is expected in the emittance values for a layer of particulates in nonparticipating gas.

The effect of the wall on the emittance measurements is determined to be small for the conditions of interest. An estimate of the wall effect is obtained by comparing the Planck function for the wall temperature to the Planck function for a layer temperature at the same wavelengths. The ratio is on the order of 0.01. However, the medium is not black but has an emittance of 0.1 or greater. Consequently, the wall effect is on the order of 10 percent for a nonparticulate layer. In the gas bands, though, emittances much larger than 0.1 are observed so the 10 percent wall effect is a worst case. This was experimentally verified in the pure gas runs by observing that the energy levels in spectral locations between the bands were very low (on the order of or less than 0.01 of the band signal levels). When particulates are present in the layer the transmitted energy from the wall is reduced. In addition, the energy level at all wavelengths is greater with particulates present. The amount of wall energy reflected and transmitted through the medium is a function of particulate properties, clouding the issue. Laboratory observations and analytical calculations just discussed indicate, however, that no corrections are necessary for conditions of interest.

The spectral emittance values for 13 data runs are presented in Figs. 6(*a–c*), grouped in terms of the gaseous constituents. The optical thickness for any run can be easily determined using $\kappa_{SL} = 700.93\, f_v$. The emittance for the particulate in nonparticipating nitrogen gas in Fig. 6(*a*) shows the expected trend: As the particle volume fraction increases the emittance increases. However, as will be discussed below, temperature has a strong influence on the spectral directional emittance data ϵ'_λ. The banded nature of carbon dioxide emittance is evident when compared to the relatively gray emittance of the particulate, as seen in Fig. 6(*a*) and in the windows of the carbon dioxide bands in Figs. 6(*b*) and 6(*c*). Also, as the concentration of carbon dioxide increases, the emittance within the bands is shown to increase as expected.

An initial inspection of the pure particulate emittance in Fig. 6(*a*) and the particle emittance in the windows of the gas bands in Figs. 6(*b*) and 6(*c*) yields the conclusion that the temperature of the medium is an important factor in the emittance data obtained. Comparisons between runs having similar temperatures exhibit expected trends. For example, Runs 4 and 13 have temperatures within 9 K, and Run 13 has a higher f_v and correspondingly higher spectral emittance values. However, as the temperature of the medium increases a decrease in emittance is observed in all cases. For example, Run 8 and Run 12 have very close f_v values but Run 8 has an average temperature almost 100 K lower than Run 12. The emittance of Run 8 is much larger than that for Run 12 even though the particle loading is comparable. The temperature dependence of the data is discussed further below.

The gas and particulate emittance data in Figs. 6(*b*) and 6(*c*) exhibit gray particle emittance in the windows of the gas bands. The banded emittance of carbon dioxide is also observed. Additionally, the 4.3-μm band is observed to broaden toward the larger wavelength direction as f_v increases. That is, the wings of the absorption band are seen to extend farther out from the band head when scattering particulates are present

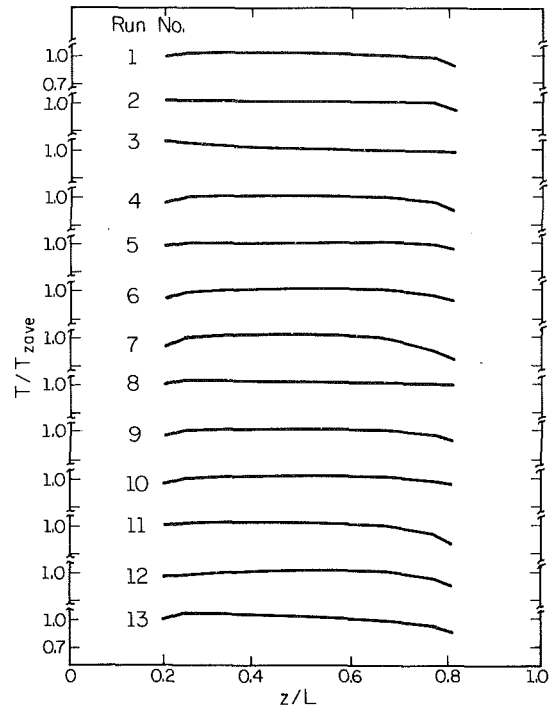

Fig. 7 Normalized temperature scans in the z direction for emittance plots

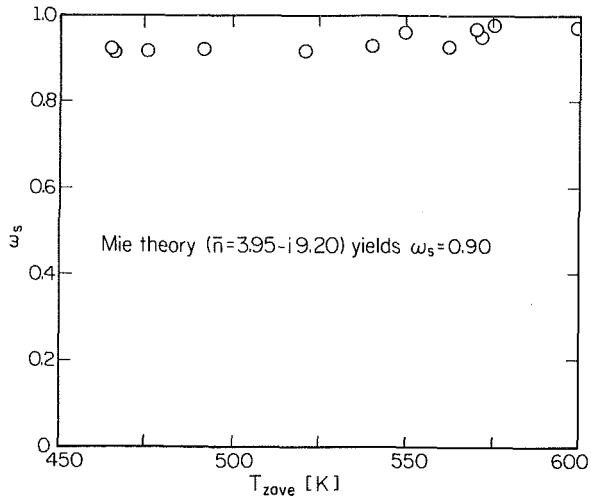

Fig. 8 Effective layer albedo versus layer temperature

than when no particulates are present [1]. Figures 6(*b*) and 6(*c*) both exhibit this effect and for 100 percent CO_2 in Fig. 6(*c*) the wing extension is clearly shown. The extension occurs in only one direction for the 4.3-μm band because this band is not a centered band but instead has a fixed upper band limit (upper in terms of wavenumber, therefore a lower limit in terms of wavelength). Note from Fig. 6(*a*) that the particulate emittance is very flat in this spectral region so the particulate is not expected to generate the effect observed in the band wings.

Figure 7 presents z direction test section temperature scans at $x/L = y/L = 5$ for the emittance data runs of Figs. 6(*a–c*). The temperature scans are normalized with respect to the average temperature of the three centermost data points. The layer temperature is very uniform over the center region in the z direction, between z/L of 0.2 and 0.8, before dropping near the cold wall. For comparison, the wall temperature (290 K), if plotted in Fig. 7, would have a value near 0.5.

Comparisons of the data to analytical calculations are made with varying degrees of assumptions required. An effective albedo of the particulate is obtained by matching the emittance data for the particulate to analytical predictions. A number of steps must be taken before a direct comparison can be made between the emittance data and analytical results. The particulate data presented in Figs. 6(*a–c*) are spectral normally directed emittances from layers having quasi-isothermal temperature distributions as indicated in Fig. 7. The particulate emittance values are noted to be virtually gray so that the data can also be viewed as total directional emittances. An emittance value is read from Figs. 6(*a–c*) at a wavelength of approximately 3.6 μm that is representative of the spectral data. The optical thickness of the layer is determined as indicated above using the known particle volume fraction value for each run. A factor necessary to correct for the cold boundary region in the test section is determined from an analysis of emission from a nonisothermal scattering layer with a nonparticipating gas phase [26].

To estimate the hemispherical flux from the normally directed intensity measured experimentally a factor is obtained from an analysis of an isothermal scattering layer [26]. A factor ranging from 1.4 to 1.7 (flux to intensity ratio) is obtained for the optical thickness of each run. The ratio values agree well with other published values [27]. Applying these two factors to the data, one to account for the cold boundary region and one to account for the directional measurement, yields an equivalent total hemispherical emittance from an isothermal layer at T_{av} with the known optical depth κ_{SL}. The only unknown is the single scattering albedo ω_S. If Mie theory is used with a complex refractive index representative of nickel ($\bar{n} = 3.95 - i9.20$) [28], the average cosine is 0.55, indicating that anisotropy of the particle scattering exists. Thus, anisotropic scaling relations [29] are used to scale the anisotropic values of ω_S and κ_{SL} to isotropic values. By matching the equivalent experimental emittance discussed above and the calculated total hemispherical emittance (for an isothermal layer at T_{av} with the scaled values of ω_S and κ_{SL}), the effective ω_S is determined. When the effective albedo determined in this manner is plotted versus the average layer temperature for each run, a dependence of albedo on layer temperature is observed (see Fig. 8). The scattering albedo predicted by Mie theory using a refractive index representative of nickel (as above) is 0.90. This value is very representative of those presented in Fig. 8. The temperature variation is believed to result from property variations since other investigations [13, 30] have similarly observed property variations with temperature.

Another comparison of the data to analytical calculations is performed using Edwards' wide-band scaling relations [3] for a nonisothermal, pure gas layer. A value of the directional band emittance for a homogeneous, pure gas layer with a known temperature distribution is calculated. This emittance value, calculated for the 4.3-μm CO_2 band, can be compared to the equivalent experimental value found for the pure gas runs by numerical integration of the 4.3-μm band data. Pure gas Runs 7 and 11 are amenable to this process. Run 7 involves 50 percent CO_2 with an average temperature of 614 K. The analytical and experimental values of the directional band emittance differ by 20 percent for this run. Run 11 involves 100 percent CO_2 with an average temperature of 569 K, and the analytical and experimental emittances differ by only 2.2 percent. The agreement between the emittance values for the two cases is quite good considering experimental uncertainties, the expected accuracy of the exponential wide-band model and the nonisothermal scaling technique.

Conclusions

An experimental investigation has been undertaken yielding spectral normally directed emittance data obtained

radiometrically from a well-characterized layer containing gaseous constituents of carbon dioxide and nitrogen, and solid particulate of BNi-2. The medium has been characterized to be one dimensional, reasonably isothermal, and homogeneous within measurable limits. Emittance data have been presented for wavelengths between 3.0 and 5.5 μm for layers having: gas components of 100 percent nitrogen, 50 percent CO_2/50 percent N_2, and 100 percent CO_2; particle volume fractions up to 7.6×10^{-4}; temperatures between 475 K and 650 K; total pressures near 1 atm; and a geometric depth of 0.5 cm. The data exhibit the effects of particulate scattering. The gray nature of particulate emittance is evident for data runs when nonparticipating nitrogen is the gas constituent and in the windows of the carbon dioxide bands. The gas band emittance is observed in both pure gas runs and for gas and particulate runs. An extension of the 4.3-μm carbon dioxide band wings due to scattering is noted and is very apparent in the 100 percent carbon dioxide data. It is found that the effective albedo of the layer is a function of average layer temperature.

Acknowledgments

This work has been supported, in part, by the National Science Foundation under Grant No. MEA 83-05370.

References

1 Skocypec, R. D., and Buckius, R. O., "Total Hemispherical Emittances for CO_2 or H_2O Including Particulate Scattering," *Int. J. Heat Mass Transfer*, Vol. 27, 1984, pp. 1-13.

2 Skocypec, R. D., Walters, D. V., and Buckius, R. O., "Total Hemispherical Emittances for Isothermal Mixtures of Combustion Gases and Scattering Particulate," *Comb. Sci. Tech.*, Vol. 47, 1986, pp. 239-252.

3 Edwards, D. K., "Molecular Gas Band Radiation," in: *Advances in Heat Transfer*, Vol. 12, T. F. Irvine and J. P. Hartnett, eds., Academic Press, New York, 1976, pp. 115-193.

4 Tien, C. L., and Giedt, W. H., "Experimental Determination of Infrared Absorption of High Temperature Gases," in: *Advances in Thermophysical Properties at Extreme Temperatures and Pressures*, S. Gratch, ed., ASME 1965.

5 Birkebak, R. C., Hartnett, J. P., and Eckert, E. R. G., "Measurement of Radiation Properties of Solid Materials," *Prog. in Int. Research on Thermodynamic and Transport Properties*, ASME, New York, 1962, pp. 563-574.

6 Sherell, F. G., and Shahrokhi, F., "Determination of Hemispherical Emittance by Measurements of Infrared Bihemispherical Reflectance," *Prog. in Astronautics and Aeronautics*, Vol. 24, 1970, pp. 169-183.

7 Gaumer, R. E., McKellar, L. A., Streed, E. R., Frame, K. L., and Grammer, J. R., "Calorimetric Determination of Thermal Radiation Characteristics," *Prog. in Int. Research on Thermodynamic and Transport Properties*, ASME, New York, 1962, pp. 575-582.

8 Pisoni, C., and Ruffino, G., "Equiradiance Method for Measurement of Emissivity," *Proc. 7th Symp. on Thermophysical Properties*, ASME, New York, 1977, pp. 265-267.

9 DeWitt, D. P., Taylor, R. E., and Riddle, T. K., "High Temperature Computer Controlled Emissometer for Spectral and Total Measurements on Conducting and Non-conducting Materials," *Proc. 7th Symp. on Thermophysical Properties*, ASME, New York, 1977, pp. 256-264.

10 Richmond, J. C., "Measurement of Thermal Radiation Properties of Materials," *High Temperatures–High Pressures*, Vol. 11, 1979, pp. 355-381.

11 Harrison, W. N., "Pitfalls in Thermal Emission Studies," *Measurement of Thermal Radiative Properties of Solids*, NASA SP-31, 1962, pp. 3-9.

12 Richmond, J. C., Harrison, W. N., and Shorten, F. J., "An Approach to Thermal Emittance Standards," *Measurement of Thermal Radiative Properties of Solids*, NASA SP-31, 1962, pp. 403-421.

13 Dowling, J. M., and Randall, C. M., "Infrared Emissivities of Micron-Sized Particles of C, MgO, Al_2O_3, and ZrO_2 at Elevated Temperatures," AFRPL-TR-77-14, Apr. 1977.

14 Hottel, H. C., and Mangelsdorf, H. G., "Heat Transmission by Radiation From Nonluminous Gases. II. Experiment Study of Carbon Dioxide and Water Vapor, *Trans. Am. Inst. Chem. Engrs.*, Vol. 31, 1935, pp. 517-549.

15 Gabriel, C. T., and Beer, J. M., "Measurements of Radiative Heat Flux From Synthetic Fuel and Coal-Slurry Flames," ASME Paper No. 83-WA/HT-107.

16 Buckius, R. O., and Tien, C. L., "Infrared Flame Radiation," *Int. J. Heat Mass Transfer*, Vol. 20, 1977, pp. 93-106.

17 Bartky, C. D., and Bauer, E., "Predicting the Emittance of a Homogeneous Plume Containing Alumina Particles," *J. Spacecraft*, Vol. 3, 1966, pp. 1523-1527.

18 Konopka, W., Calia, V. S., Reed, R. A., and Oman, R. A., "Controlled Hot Gas/Particle Experiments for Validation of a Standardized Infrared Radiation Model," AFRPL-8-31, 1980.

19 Graber, M., and Cohen, A., "Multiple Scattering: Theoretical Calculations Compared With Experimental Dye-Laser Measurements," *J. Opt. Soc. Am.*, Vol. 65, 1975, pp. 1306-1310.

20 Brewster, M. Q., and Tien, C. L., "Radiative Transfer in Packed/Fluidized Beds: Dependent Versus Independent Scattering," ASME JOURNAL OF HEAT TRANSFER, Vol. 104, 1982, pp. 573-579.

21 Adrianov, V. N., "Modeling Radiant Heat Transfer by Means of Visible Light," *Heat Transfer–Soviet Research*, Vol. 8, 1976, pp. 94-104.

22 van de Hulst, H. C., *Light Scattering by Small Particles*, Dover, New York, 1981.

23 Liou, K. N., and Ou, S. C., "Infrared Radiative Transfer in Finite Cloud Layers," *J. Atm. Sci.*, Vol. 36, 1979, pp. 1985-1996.

24 Hestroni, G., ed., *Handbook of Multiphase Systems*, McGraw-Hill, New York, 1982.

25 Buckius, R. O., and Hwang, D. C., "Radiation Properties for Polydispersions: Application to Coal," ASME JOURNAL OF HEAT TRANSFER, Vol. 102, 1980, pp. 99-103.

26 Skocypec, R. D., and Buckius, R. O., "Photon Path Length Analysis of Radiative Heat Transfer in Planar Layers With Arbitrary Temperature Distributions," *J. Quant. Spectrosc. Radiat. Transfer*, Vol. 35, 1986, pp. 109-120.

27 Crosbie, A. L., "Apparent Radiative Properties of an Isotropically Scattering Medium on a Diffuse Substrate," ASME JOURNAL OF HEAT TRANSFER, Vol. 101, 1979, pp. 68-75.

28 Siegel, R., and Howell, J., *Thermal Radiation Heat Transfer*, 2nd ed., McGraw-Hill, New York, 1981.

29 Lee, H., and Buckius, R. O., "Scaling Anisotropic Scattering in Radiation Heat Transfer for a Planar Medium," ASME JOURNAL OF HEAT TRANSFER, Vol. 104, 1982, pp. 68-75.

30 Whitson, M. E., Jr., "Handbook of the Infrared Optical Properties of Al_2O_3, Carbon, MgO and ZrO_2," The Aerospace Corp. Report TR-0075(5548)-2, (SAMSO report TR-75-131), Vols. I and II, June 1975.

Transient Radiative Cooling of a Droplet-Filled Layer

R. Siegel
NASA Lewis Research Center,
Cleveland, OH 44135
Fellow ASME

A proposed lightweight radiator system for waste heat dissipation in space would eject streams of coolant in the form of small, hot liquid droplets. The droplets would lose radiative energy by direct exposure to the very low-temperature environment of space, and would then be collected for reuse. The cooling behavior of a layer composed of many small droplets was studied by numerical solution of the radiative integral equations. Since there is mutual interference for radiative energy dissipation, an array droplet will cool more slowly than if each drop is exposed individually. Since liquid metal droplets may be used, the study includes results for conditions with high scattering. For optically thin regions, especially with high scattering, the temperature distribution is sufficiently uniform that the cooling can be computed using the approximation of a constant layer emittance. For optically thick layers starting at uniform temperature, the temperature distributions become nonuniform with time. It was found that the cooling process goes through a starting transient; a constant emittance condition is then achieved where the emittance is lower than that for a layer at uniform temperature.

Introduction

The dissipation of waste heat for a power generation device in space requires some type of heat radiator. It has been proposed (Mattick and Hertzberg, 1981) that hot liquid droplets could be sprayed through space freely exposed, and then be collected after losing a portion of their energy by transient radiative cooling. The direct exposure to space could provide good heat dissipation characteristics with possibly a relatively lightweight design. Some analysis of the radiative cooling of a layer filled with droplets has been given by Mattick and Hertzberg (1981), and in some of their other publications. The purpose of the present work is to study in more detail some aspects of the transient radiative cooling process for this type of absorbing and scattering layer.

Transient cooling of radiating layers has been studied during the past 30 years. The early literautre has been reviewed by Viskanta and Bathla (1967), where transient radiation from an absorbing layer was analyzed. A brief review of transient radiative cooling is given in Chap. 18 of Siegel and Howell (1981). Some additional references of interest are Kubo (1984), Bathla and Viskanta (1968), Lii and Ozisik (1972), and Viskanta and Anderson (1975). It is not feasible to include here a detailed survey of the literature.

The intent of the present work is to provide additional information about the cooling of an emitting, absorbing, and scattering layer. The effect of the nonuniform temperature distribution that develops across the layer thickness is compared with simplified cooling results obtained using a constant layer emittance, which assumes a uniform temperature distribution at all times. Comparisons with the simplified theory become poor when the layer is optically thick, and are especially poor when the scattering albedo is small. A high albedo tends to provide a more uniform temperature across the layer. The high scattering also causes the radiative source function within the layer to be practically uniform. For this condition, a simple approximate solution was developed. A high scattering albedo yields slow cooling rates.

When the layers are optically thick and the scattering is not high, both the temperature distribution and the radiative source function are highly nonuniform and change with time. It was found, however, that the emittance of the layer, based on the instantaneous mean temperature, achieves a constant value after an initial starting transient; this value is lower than the emittance for a layer at uniform temperature. This constant emittance leads to a simplified theory for the later part of the cooling transient.

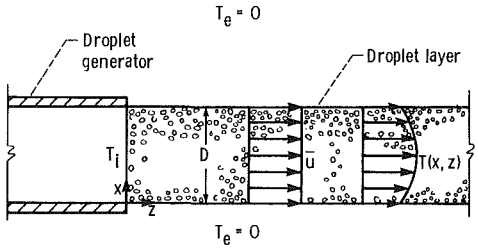

Fig. 1 Geometry of droplet-filled layer

Analysis

The droplet layer as shown in Fig. 1 exits from the droplet generator at $z=0$ and is traveling through space with a uniform velocity $\bar{u}$. The layer has a constant thickness D. Its extent in the direction normal to the x–z plane is large relative to D, so that variations in that normal direction are neglected. The layer temperature at $z=0$ is uniform at T_i, and becomes a function of x and z as the layer cools by radiating energy to the environment at $T_e=0$. The droplets in the layer emit, absorb, and scatter radiation. Since each droplet receives radiation from many directions, the scattering can be specified as isotropic to a good approximation. The velocity $\bar{u}$ is assumed large enough so that temperature variations in the z direction are small compared with those in the x direction.

For the specified conditions, the energy equation for cooling the droplet layer is

$$\rho c_p \bar{u} \frac{\partial T}{\partial z} = -\frac{\partial q_r}{\partial x} \qquad T(x,\, z=0) = T_i \tag{1}$$

where the term $\partial q_r/\partial z$ for radiative transfer in the z direction has been neglected relative to $\partial q_r/\partial x$. Since the velocity is constant, it is convenient to let τ be the cooling time after the droplets leave the droplet generator, and use the transformation $\tau = z/\bar{u}$. The energy equation and initial condition then become

$$\rho c_p \frac{\partial T}{\partial \tau} = -\frac{\partial q_r}{\partial x} \qquad T(x,\, \tau=0) = T_i \tag{2}$$

In terms of the optical coordinate $\kappa = (a+\sigma_s)x$ this becomes

$$\frac{\rho c_p}{a+\sigma_s} \frac{\partial T}{\partial \tau} = -\frac{\partial q_r}{\partial \kappa} \qquad T(\kappa,\, \tau=0) = T_i \tag{3}$$

Contributed by the Heat Transfer Division for publication in the JOURNAL OF HEAT TRANSFER. Manuscript received by the Heat Transfer Division February 4, 1986.

The derivative in radiative flux is given by Siegel and Howell (1981) as

$$-\frac{\partial q_r}{\partial \kappa}=2\pi\int_0^{\kappa_D} I(\kappa^*,\ \tau)E_1(\,|\kappa-\kappa^*|)d\kappa^*-4\pi I(\kappa,\ \tau) \qquad (4)$$

where the source function I for an absorbing and scattering region is given by

$$I(\kappa,\ \tau)=(1-\Omega)\frac{\sigma T^4(\kappa,\ \tau)}{\pi}+\frac{\Omega}{2}\int_0^{\kappa_D} I(\kappa^*,\ \tau)E_1(\,|\kappa-\kappa^*|)d\kappa^* \qquad (5)$$

Equation (4) is substituted into equation (3), and equation (5) is used to eliminate the integral containing I. This yields the energy equation in the form

$$\frac{\rho c_p}{a+\sigma_s}\frac{\partial T}{\partial \tau}=4\frac{(1-\Omega)}{\Omega}[\pi I(\kappa,\ \tau)-\sigma T^4(\kappa,\ \tau)] \qquad (6)$$

Equation (6) is to be solved simultaneously with the source function equation (5). Using the dimensionless variables in the Nomenclature, the equations become

$$\tilde{I}(X,\ \tilde{\tau}) = (1-\Omega)\tilde{T}^4(X,\ \tilde{\tau})+\frac{\kappa_D\Omega}{2}\int_0^1 \tilde{I}(X^*,\ \tilde{\tau})E_1(\kappa_D\,|X-X^*|)dX^* \qquad (7a)$$

$$\frac{\partial \tilde{T}}{\partial \tilde{\tau}} = \kappa_D\frac{(1-\Omega)}{\Omega}[\tilde{I}(X,\ \tilde{\tau})-\tilde{T}^4(X,\ \tilde{\tau})] \qquad \tilde{T}(X,\ 0)=1 \quad (7b)$$

The forms in equations (7) are not convenient when the scattering is zero ($\Omega=0$). For this case substitute $\tilde{T}^4(X,\ \tilde{\tau})$ from equation (7*a*) into (7*b*) to obtain the following form which is independent of Ω

$$\frac{\partial \tilde{T}}{\partial \tilde{\tau}}=-\kappa_D\left[\tilde{I}(X,\ \tilde{\tau})-\frac{\kappa_D}{2}\int_0^1 \tilde{I}(X^*,\ \tilde{\tau})E_1(\kappa_D\,|X-X^*|)dX^*\right] \qquad (8)$$

Equation (7*a*) shows that for $\Omega=0$, $\tilde{I}(X,\ \tilde{\tau})=\tilde{T}^4(X,\ \tilde{\tau})$, so that equation (8) becomes the energy equation for $\tilde{T}$

$$\frac{\partial \tilde{T}}{\partial \tilde{\tau}}=-\kappa_D\left[\tilde{T}^4(X,\ \tilde{\tau})-\frac{\kappa_D}{2}\int_0^1 \tilde{T}^4(X^*,\ \tilde{\tau})E_1(\kappa_D\,|X-X^*|)dX^*\right] \qquad (9)$$

By use of an accurate integration subroutine, equations (7) can be solved numerically to yield $\tilde{T}(X,\ \tilde{\tau})$ and $\tilde{I}(X,\ \tilde{\tau})$. Starting with $\tilde{T}(X,\ 0)=1$, equation (7*a*) was solved by iteration using $\tilde{I}(X,\ 0)=1$ as an initial guess. This initial function was inserted into the integral on the right side. The difference between the right-hand side and the trial $\tilde{I}$ was multiplied by an acceleration factor of 1.2 and the result added to the trial $\tilde{I}$ to obtain a new $\tilde{I}$ with which to continue the iteration. The iteration was continued until the relative change in $\tilde{I}$ converged to within at least four decimal places for all X values. The $\tilde{I}$ and $\tilde{T}$ were then inserted into the right-hand side of (7*b*) and the resulting $\partial\tilde{T}/\partial\tilde{\tau}$ used to extrapolate $\tilde{T}$ forward to the next time. The calculations were checked by reducing the ΔX and $\Delta\tilde{\tau}$ intervals. Usually 40 ΔX intervals were used across the width of the droplet layer. The size of $\Delta\tilde{\tau}$ depended on the cooling rate which was a function of the parameters κ_D and Ω. Equation (9) was solved in a similar manner but did not require an iteration loop.

The solution requires an accurate integration technique. Since $E_1(0)=\infty$, care must be taken as X^* approaches X. Since the integral of E_1 is $-E_2$, and $E_2(0)=1$, the integration was carried out analytically for a very small region near the singularity with $\tilde{I}$ or $\tilde{T}$ assumed constant over this region. The calculations were checked by reducing the size of this region to be sure its size had no effect. The integrations in the regions away from the singularity were performed with a Gaussian integration subroutine available in the computer library. Solutions were quite rapid, in the range of several minutes or less on an IBM 370 computer. In a few cases where both κ_D and Ω were large, more time was required, about 30 min. The solution was carried forward until the temperatures had cooled to 20 percent of their initial values.

After obtaining the $\tilde{T}(X,\ \tilde{\tau})$ and $\tilde{I}(X,\ \tilde{\tau})$ distributions, some auxiliary information was calculated. The energy of the layer at τ relative to that at $\tau=0$ was obtained from the following integration

$$\frac{\text{Energy at } \tau}{\text{Energy at } \tau=0}=\frac{1}{DT_i}\int_0^D T(x,\ \tau)dx = \int_0^1 \tilde{T}(X,\ \tilde{\tau})dX\equiv\tilde{T}_m(\tilde{\tau}) \qquad (10)$$

Nomenclature

a = absorption coefficient of absorbing-scattering layer
A_d = projected area of drop
c_p = specific heat of droplet layer
$c_{p,d}$ = specific heat of droplet material
D = thickness of absorbing-scattering layer
E_a, E_s = efficiency factors for absorption and scattering
E_1, E_2, E_3 = exponential integral functions, $E_n(x)=\int_0^1 \mu^{n-2}\exp(-x/\mu)d\mu$
I = source function in absorbing-scattering layer; $\tilde{I}=\pi I/\sigma T_i^4$
N = number of droplets in a unit volume of layer
q = heat loss per unit area and time from surface of droplet layer
q_r = radiative heat flow per unit area and time
R_d = radius of spherical drop
T = absolute temperature; $\tilde{T}=T/T_i$
T_e = temperature of surrounding environment
T_i = initial temperature of radiating layer
T_m = integrated mean temperature across layer at any time during cooling transient; $\tilde{T}_m=T_m/T_i$
$\tilde{T}_{m,s}$ = value of $\tilde{T}_m$ when $\epsilon_{m,s}$ first applies
$\tilde{u}$ = velocity of the droplet layer
x, z = coordinates across and along the layer
X = dimensionless variable = x/D
X^* = dummy variable of integration
ϵ = emittance of layer
ϵ_c = emittance for layer at constant temperature
ϵ_m = emittance based on instantaneous value of T_m
$\epsilon_{m,s}$ = steady value of ϵ_m achieved after initial transient
κ = optical coordinate = $(a+\sigma_s)x$
κ_D = optical thickness = $(a+\sigma_s)D$
κ^* = dummy variable of integration
ρ = density of droplet layer
ρ_d = density of droplet material
σ = Stefan–Boltzmann constant
σ_s = scattering coefficient of droplet layer
τ = time from start of cooling; $\tilde{\tau}=(4\sigma T_i^3/\rho c_p D)\tau$
τ_s = time at which ϵ_m becomes $\epsilon_{m,s}$
Ω = albedo for scattering = $\sigma_s/(a+\sigma_s)$

If $q(\tau)$ is defined as the heat loss rate per unit area at one side of the layer, then

$$2q(\tau) = -\rho c_p \frac{\partial}{\partial \tau} \int_0^D T(x,\tau) dx$$

In dimensionless form, the energy radiated from one side of the droplet layer is

$$\frac{q(\tilde{\tau})}{\sigma T_i^4} = -2 \int_0^1 \frac{\partial \tilde{T}}{\partial \tilde{\tau}} (X, \tilde{\tau}) dX \tag{11}$$

This integral is readily calculated from equation (7*b*) at each $\tilde{\tau}$ step.

Another quantity of interest is to examine an emittance $\epsilon_m(\tilde{\tau})$, based on the instantaneous energy being radiated away and on the instantaneous mean temperature of the sheet

$$\epsilon_m(\tilde{\tau}) \equiv \frac{q(\tilde{\tau})}{\sigma T_m^4(\tilde{\tau})} = \frac{q(\tilde{\tau})/\sigma T_i^4}{\tilde{T}_m^4(\tilde{\tau})} \tag{12}$$

The $\tilde{T}_m(\tilde{\tau})$ is the integral defined in equation (10).

Cooling of Droplet Layer at Uniform Temperature. If the droplet layer were at a uniform temperature at each time during the cooling process, then the layer emittance would remain constant; this is called ϵ_c. The cooling equation for this simplified case is given by

$$2\epsilon_c \sigma T_m^4(\tau) = -\rho c_p D \frac{dT_m}{d\tau} \tag{13}$$

This is placed in dimensionless form and integrated with the initial condition $\tilde{T}_m(0) = 1$ to yield

$$\tilde{T}_m = \left(1 + \frac{3}{2} \epsilon_c \tilde{\tau}\right)^{-1/3} \tag{14}$$

This is a useful result with which the general solution can be compared.

By substituting equation (14) into equation (12), the instantaneous rate of heat loss for a droplet layer at uniform temperature is

$$q(\tilde{\tau})/\sigma T_i^4 = \epsilon_c \left(1 + \frac{3}{2} \epsilon_c \tilde{\tau}\right)^{-4/3} \tag{15}$$

Evaluation of ϵ_c Values. For various κ_D and Ω, the ϵ_c is found numerically by using the results from equation (11) at the first time iteration when, from the specified initial condition, the temperature is uniform across the layer. These values are plotted and tabulated later. There are also some special cases that can be obtained analytically; these cases are useful, and can also be used to check some of the numerical results.

For absorption only (no scattering), equation (9) applies. The ϵ_c is conveniently obtained by using this equation at $\tilde{\tau} = 0$ where $\tilde{T} = 1$

$$\frac{\partial \tilde{T}}{\partial \tilde{\tau}} = -\kappa_D \left[1 - \frac{\kappa_D}{2} \int_0^1 E_1(\kappa_D |X - X^*|) dX^*\right]$$

$$= -\frac{\kappa_D}{2} \{E_2(\kappa_D X) + E_2[\kappa_D(1-X)]\}$$

Then from equations (11) and (12) the emittance for a constant temperature layer with absorption only is

$$\epsilon_c = \kappa_D \int_0^1 \{E_2(\kappa_D X) + E_2[\kappa_D(1-X)]\} dX = 1 - 2E_3(\kappa_D) \tag{16}$$

This result can also be obtained from equation (17-46) in Siegel and Howell (1981).

For an optically thin layer $E_3(\kappa_D) \approx 1/2 - \kappa_D + \ldots$, so that $\epsilon_c = 2\kappa_D$. Then equation (14) becomes in the optically thin limit

$$\tilde{T}_m = (1 + 3\kappa_D \tilde{\tau})^{-1/3} \tag{17}$$

Now consider some ϵ_c values for conditions when both absorption and scattering are present. Analytical results can be obtained when the layer is optically thin. When κ_D is small, it might be expected that both T and I would tend to become uniform with X; this was verified by examining the numerical solutions. Then, as an approximation in equation (7*a*), the $\tilde{I}$ is taken out of the integral, and the integration performed to yield

$$\tilde{I}(\tilde{\tau}) = (1-\Omega)\tilde{T}^4(\tilde{\tau}) + \Omega \tilde{I}(\tilde{\tau}) \left(1 - \frac{1}{2} \{E_2(\kappa_D X) + E_2[\kappa_D(1-X)]\}\right) \tag{18}$$

This cannot be valid unless the function of X on the right side becomes independent of X. For small arguments, $E_2 \to 1$; hence, the equation becomes valid for layers that are optically very thin. In this instance, $\tilde{I} \to (1-\Omega)\tilde{T}^4$. If the quantity $E_2(\kappa_D X) + E_2[\kappa_D(1-X)]$ is examined for small κ_D values, it is found not to vary much over the thickness of the droplet layer. To a very close approximation for small κ_D, equation (18) can be replaced by its integrated average value over the thickness. Then solving for $\tilde{I}$

$$\tilde{I}(\tilde{\tau}) \approx \left\{1 + \frac{\Omega}{2\kappa_D(1-\Omega)} [1 - 2E_3(\kappa_D)]\right\}^{-1} \tilde{T}^4(\tilde{\tau})$$

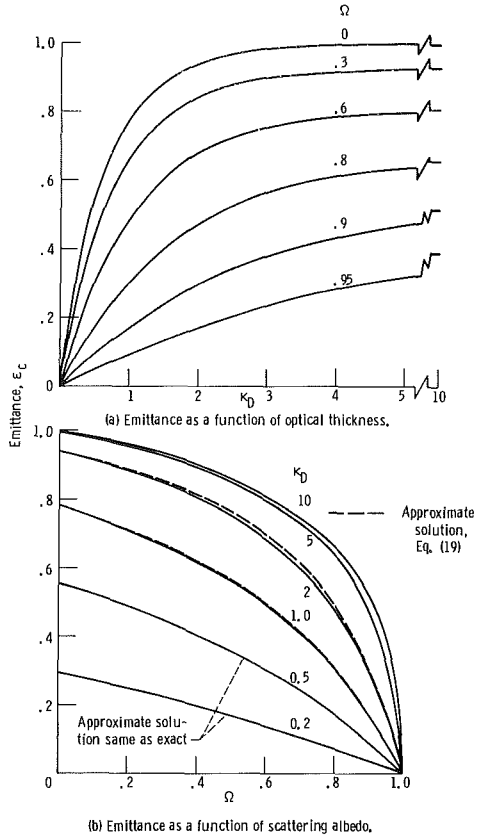

Fig. 2 Emittance for droplet layer at uniform temperature

Table 1 Emittance values for droplet layer at uniform temperature, ϵ_c

Optical thickness, κ_D	Scattering albedo, Ω					
	0	0.3	0.6	0.8	0.9	0.95
0.2	0.296	0.225	0.140	0.0748	0.0386	0.0197
.5	.557	.449	.303	.172	.0926	.0481
1.0	.781	.667	.490	.304	.173	.0926
2	.940	.846	.681	.475	.297	.170
3	.982	.900	.757	.566	.382	.233
4	.994	.918	.786	.612	.436	.281
5	.998	.924	.798	.637	.470	.317
10	1.000	.933	.808	.659	.518	.389

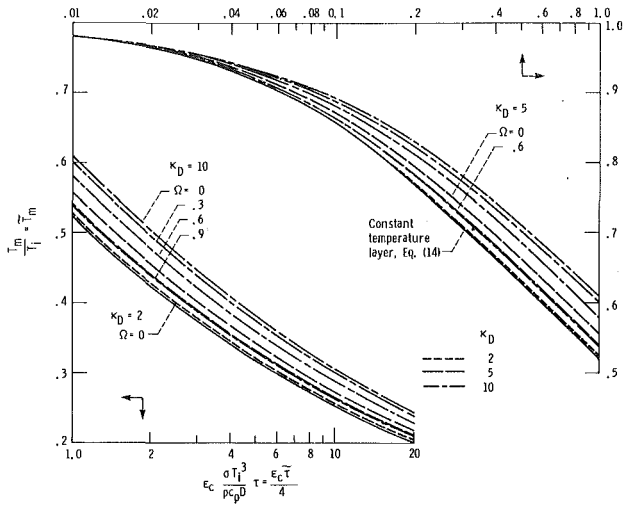

Fig. 3 Cooling curves for droplet layer

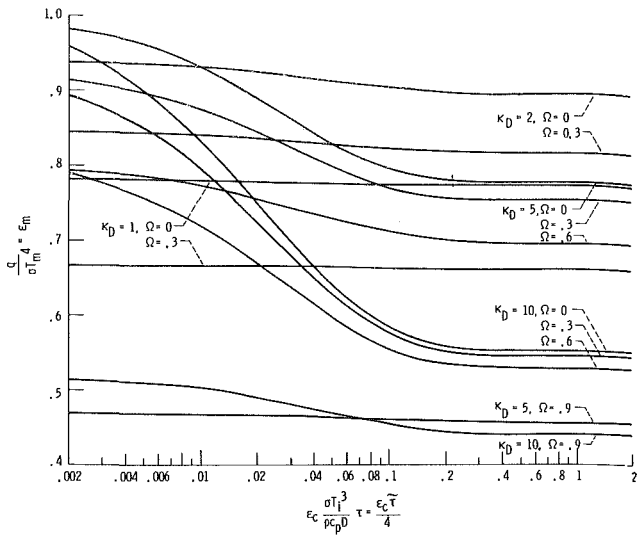

Fig. 4 Transient values of emittance based on instantaneous values of heat loss and mean temperature

It follows from equation (7*b*) that

$$\frac{\partial \tilde{T}}{\partial \tilde{\tau}} = \kappa_D \frac{(1-\Omega)}{\Omega} \left\{ \frac{1}{1 + \frac{\Omega}{2\kappa_D(1-\Omega)}[1-2E_3(\kappa_D)]} - 1 \right\} \tilde{T}^4(\tilde{\tau})$$

and hence

$$\epsilon_c = \frac{1-2E_3(\kappa_D)}{1 + \frac{\Omega}{2\kappa_D(1-\Omega)}[1-2E_3(\kappa_D)]} \tag{19}$$

Although this relation was obtained for optically thin conditions, comparisons with the numerical results will show that it has a more general applicability. This is because the $\tilde{T}$ and $\tilde{I}$ remain fairly uniform in some instances even when κ_D is not small.

Cooling Relations for a Layer Filled With Spherical Droplets of Radius R_d. The absorption and scattering coefficients for a droplet cloud can be written in terms of efficiency factors and the droplet projected area as

$$a = E_a A_d N = E_a \pi R_d^2 N \tag{20}$$

$$\sigma_s = E_s A_d N = E_s \pi R_d^2 N \tag{21}$$

The density and specific heat of the droplet dispersion can be expressed in terms of properties of the droplet material, and the total volume of the droplets within a unit volume of the layer

$$\rho c_p = \rho_d c_{p,d} \frac{4}{3} \pi R_d^3 N \tag{22}$$

The dimensionless time $\tilde{\tau}$ contains ρc_p and hence the droplet number density N. The $\kappa_D = (E_a + E_s)\pi R_d^2 N D$ also contains N. This results in some confusion, since both $\tilde{\tau}$ and κ_D will change if the number density is changed during optimization studies. For this reason some results will be given in terms of the following dimensionless time

$$\frac{\sigma T_i^3 (E_a + E_s)}{\rho_d c_{p,d} R_d} \tau = \frac{\tilde{\tau}\kappa_D}{3} \tag{23}$$

For a given droplet type, size, and temperature, the quantity on the left depends only on the time. The cooling will be examined for various values of κ_D, which contains the number density and layer thickness.

Results and Discussion

The transient solutions described in the Analysis were started from a uniform layer temperature. Hence the emittance values calculated at the start of the first time increment are for a uniform temperature distribution, and a nonuniform source function $I(x, 0)$ as obtained by iteration of equation (7*a*). The ϵ_c values for a uniform temperature layer, obtained as described in the Analysis, are in Fig. 2 and Table 1. The values are functions of the optical thickness κ_D and the scattering albedo Ω. Some of these results are in Mattick and Hertzberg (1981); they are given here in more detail and will be needed in the development that follows.

In Fig. 2(*a*), the ϵ_c are presented as a function of κ_D for various values of Ω. The curve for $\Omega = 0$ is given by the analytical solution in equation (16) and was also obtained numerically from equation (9). The analytical solution was one check on the numerical method, and agreement was within 10^{-3}. For each value of Ω, the ϵ_c increases as the optical thickness increases. The ϵ_c decreases as Ω is increased, as this corresponds to more highly reflecting droplets that do not emit well. The results are given in Fig. 2(*b*) in terms of Ω with each curve being for a constant κ_D. As Ω goes to unity, the droplets do not emit energy, and the sheet emittance decreases to zero. This figure is used to compare with the results from the approximation in equation (19), which was obtained by having both T and I not vary appreciably across the layer at each time. As expected, the agreement is excellent for optically thin layers, and the approximation remains very good for $\kappa_D = 1$. For thicker layers the approximation is good when the scattering is large; this distributes the small amount of emitted radiation throughout the layer, and tends to make T and I uniform across the layer.

The transient cooling of the droplet layer will now be examined. Since $\tau = x/\bar{u}$, these results give the cooling behavior as a function of distance as the droplet layer moves through space. The energy in the layer divided by the initial energy is given in Fig. 3 as a function of dimensionless time multiplied by the emittance ϵ_c for a constant temperature layer. From equation (10), this energy ratio is equal to $T_m(\tau)/T_i \equiv \tilde{T}_m$. The abscissa that was used was taken from the simple cooling expression in equation (14) for a layer that is at uniform temperature throughout the transient. The cooling curve from equation (14) is shown on the figure, and deviations from it provide the effect of the nonuniform temperature distribution that develops during the cooling process. All of the curves are very close together for short times as they all start from a

Table 2 Values of $\epsilon_{m,s}$ and $\tilde{T}_{m,s}$ (at $\epsilon_c\tilde{\tau}_s/4=0.4$) [In each entry $\epsilon_{m,s}$ is upper value; $\tilde{T}_{m,s}$ is lower value.]

Optical thickness, κ_D	Scattering albedo, Ω			
	0	0.3	0.6	0.9
2	0.895	0.816	0.669	0.297
	.669	.667	.665	.665
5	.777	.752	.695	.456
	.697	.691	.681	.666
10	.551	.544	.528	.440
	.743	.736	.719	.678

uniform temperature condition and hence agree with the simplified model. Curves from the numerical solution of equations (7*a*) and (7*b*), and from equation (9) for $\Omega=0$, are given for various κ_D and Ω.

The scattering by the droplets tends to equalize the radiative energy across the layer. Hence the temperature distributions across the layer tend to become somewhat more uniform as Ω is increased; this effect depends on κ_D. This will be illustrated later by giving typical temperature profiles during the cooling process. For each κ_D, the limiting case of $\Omega=0$ provides the largest temperature variations across the layer; hence attention is first directed to the curves for $\Omega=0$ in Fig. 3. For $\kappa_D=0.5$ and 1.0, the solution for $\Omega=0$ agrees very well with the analytical solution for a uniform temperature layer. This is also true for any Ω, since for $\Omega>0$ the temperature profiles become increasingly more uniform as Ω is increased. Hence for $\kappa_D\leq 1$ and any Ω, the cooling process can be accurately calculated using the simple expression in equation (14) with the ϵ_c obtained from Fig. 2 or Table 1 (or equation (19) can be used).

For $\kappa_D=2$ and $\Omega=0$, the cooling curve in Fig. 3 is at $\epsilon_c\tilde{\tau}/4$ values that are only about 3 percent greater than those from equation (14). For $\Omega>0$ the difference in abscissa values is even less. Thus the result in equation (14) can be used with good accuracy for $\kappa_D\leq 2$. For $\kappa_D=5$ and $\Omega=0$, the curve in Fig. 3 is significantly to the right of the uniform temperature cooling curve; using the simple uniform temperature theory would be in error by about 25 percent. This difference becomes less when Ω is increased, as shown by the curves for $\Omega=0.3$, 0.6, and 0.9. The curve for $\kappa_D=5$ and $\Omega=0.9$ is only slightly to the right of the simple cooling curve. For $\kappa_D=10$ the results are of the same general nature as for $\kappa_D=5$, except that the curves are further to the right. A value of $\Omega=0.9$ is not large enough to make the temperature profiles fairly uniform; hence the curve for $\kappa_D=10$ and $\Omega=0.9$ is somewhat to the right of the simple uniform temperature cooling curve.

It is now interesting to observe in Fig. 3 that, after an initial transient period of $\epsilon_i\tilde{\tau}/4\approx 0.4$, all of the curves are parallel to the simple cooling curve from equation (14). This indicates that a new constant emittance has been achieved after the temperature profiles have developed with time, even though the temperature profiles continue to change with time. This is analogous to the Graetz solution for forced convection in a tube at uniform wall temperature; in this instance the Nusselt number approaches a constant value as the distance from the tube entrance becomes large. An emittance based on the instantaneous heat loss and the instantaneous mean temperature is given by equation (12) as $\epsilon_m(\tau)=q(\tau)/\sigma T_m^4(\tau)$, which was calculated in the numerical solution from equations (10) and (11). The $\epsilon_m(\tau)$ are given in Fig. 4 for various κ_D and Ω. In all instances the $\epsilon_m(\tau)$ reaches a steady value, and this is achieved at essentially the same value of $\epsilon_c\tilde{\tau}/4$ for all κ_D and Ω. This steady ϵ_m value is called $\epsilon_{m,s}$, and for each κ_D and Ω it is smaller than the corresponding ϵ_c value as a result of the temperature variations across the droplet layer. The outer regions of the layer are cooler than the mean temperature, and

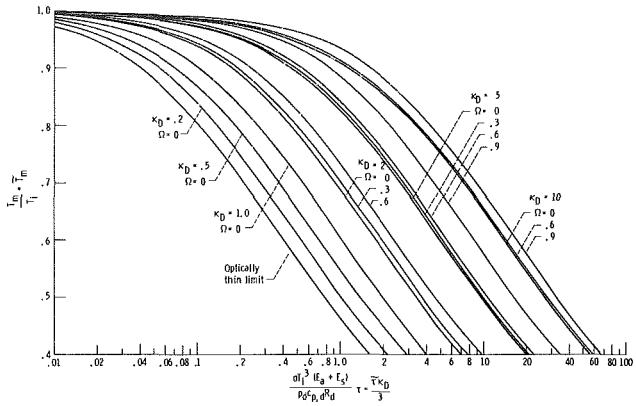

Fig. 5 Cooling curves for droplet layer

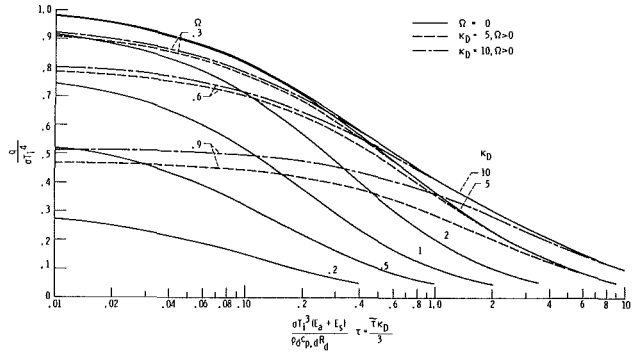

Fig. 6 Heat loss rates from droplet layer

hence less energy is radiated away than for a layer at constant temperature. For $\kappa_D=2$ and $\Omega=0$, the limiting $\epsilon_{m,s}$ is only 5 percent lower than ϵ_c. For optically thick layers, however, there is a substantial difference between the $\epsilon_{m,s}$ and ϵ_c values. For $\kappa_D=2$, the $\epsilon_{m,s}$ values are larger than for $\kappa_D=1$, but when the optical thickness is further increased to 5 the $\epsilon_{m,s}$ decreases; the increase in optical thickness, which tends to increase emission, is insufficient to overcome the effect of the nonuniform temperature distribution. The $\epsilon_{m,s}$ values are summarized in Table 2 for $\kappa_D\geq 2$; for smaller κ_D the $\epsilon_{m,s}\approx\epsilon_c$.

If the value $\epsilon_c\tilde{\tau}/4=0.4$ is selected from Fig. 4 as being at the end of the starting transient, then the cooling curves can be calculated for larger values by integrating equation (13) using $\epsilon_{m,s}$ rather than ϵ_c and starting with an initial $\tilde{T}_{m,s}$ at $\epsilon_c\tilde{\tau}_s/4=0.4$. This integration yields the relation for $\tilde{T}_m(\tilde{\tau})$

$$\frac{\epsilon_c\tilde{\tau}}{4}=\frac{1}{6}\frac{\epsilon_c}{\epsilon_{m,s}}\left(\frac{1}{\tilde{T}_m^3}-\frac{1}{\tilde{T}_{m,s}^3}\right)+\frac{\epsilon_c\tilde{\tau}_s}{4}$$

$\tilde{T}_{m,s}$ values are given in Table 2, as obtained from the numerical solution. By comparison with the curves in Fig. 3, this use of a constant $\epsilon_{m,s}$ gives good results for $\tilde{T}_m$ decreasing to 0.2 and possibly for even longer times; the transient numerical calculations were not continued for $\tilde{T}_m<0.2$ because the energy radiated became very small and was not of practical interest.

As presented in the Analysis in relation to equation (23), it is useful for purposes of interpretation to present results in terms of a dimensionless time that does not contain the number density of droplets or the layer thickness; these quantities will then appear only in the parameter κ_D. The cooling curves are presented in this form in Fig. 5. It is evident that a layer that is optically very thin will cool most rapidly since the radiation from individual droplets is not significantly obstructed by other droplets in the layer. The limiting curve for an optically thin region, which is the same as for cooling a single black droplet, is obtained from equation (17) and is the curve far-

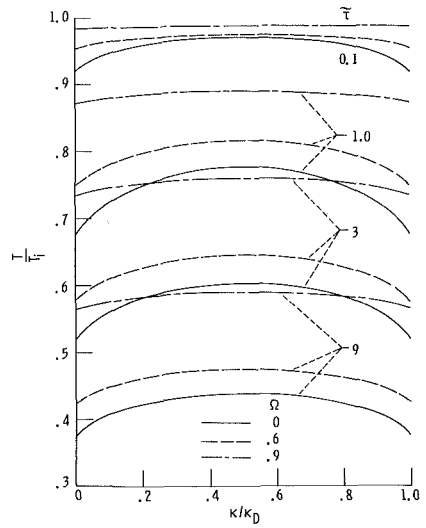

(a) Optical thickness of layer = 2.

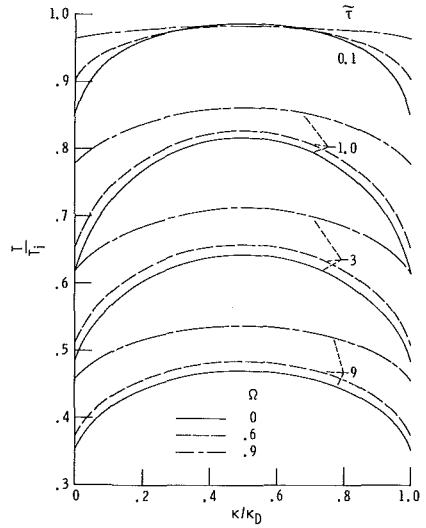

(b) Optical thickness of layer = 5.

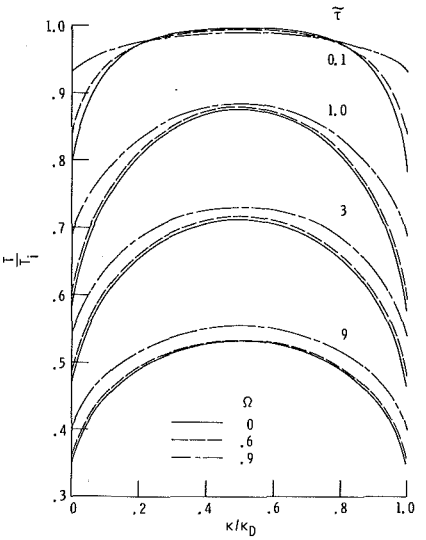

(c) Optical thickness of layer = 10.

Fig. 7 Temperature distributions during transient cooling

thest to the left. As the optical thickness κ_D is increased, the curves are displaced to the right, as longer cooling times are required for the mean temperature to decrease to a specified level. For $\kappa_D = 0.2$, 0.5, and 1, the results from the numerical solution that have a temperature distribution across the layer agree within negligible error with the results from equation (14) for a constant temperature layer. The results shown are all for $\Omega = 0$. For $\Omega > 0$ there is even closer agreement with equation (14) because scattering makes the temperature distributions more uniform. Hence for $\kappa_D \leq 1$, equation (14) can be used, with ϵ_c values from Fig. 2, to calculate accurate cooling results. For $\kappa_D = 2$, the cooling times calculated numerically for $\Omega = 0$ are only about 3 percent longer than predicted by equation (14); hence, for $\kappa_D = 2$ equation (14) provides an adequate engineering approximation for all Ω. For $\kappa_D = 5$ and $\Omega = 0$ the results assuming a constant temperature layer are no longer correct. With the temperature distribution taken into account, the layer cools more slowly because the temperature near the outside of the layer is decreased and the radiating ability is thus lowered. When Ω is increased, more cooling time is required since the droplet emission is decreased. Results are given in Fig. 5 for $\Omega = 0.3$, 0.6, and 0.9 for $\kappa_D = 5$ and for $\Omega = 0.6$ and 0.9 for $\kappa_D = 10$.

The instantaneous heat loss rates from the surface of the droplet layer are given in Fig. 6. The simple expression in equation (15) gives good results for κ_D up to about 1.0. The effect of scattering is quite significant early in the cooling process, but it becomes small as the cooling time increases.

Typical temperature profiles are shown in Fig. 7 for cooling to about 40 percent of the original energy in the droplet layer. At early times, the curves for high scattering tend to be much flatter than the curves for $\Omega = 0$. The curves for $\Omega = 0$ always have the largest temperature variation across the layer. Figure 7(*c*) shows, however, that for $\kappa_D = 10$ the curves for high scattering ($\Omega = 0.9$) tend to become quite similar in shape to those for $\Omega = 0$.

Concluding Remarks

An analysis was made of the transient cooling of a layer filled with many small radiating droplets that absorb, emit, and scatter radiation. The cooling results were compared with a simplified theory that assumes a uniform temperature distribution across the layer at all times. The simplified theory was found adequate for optical thicknesses of the layer less than about two for any value of the scattering albedo. For larger optical thicknesses the nonuniform temperature distribution must be taken into account as the simplified theory will underestimate the required cooling time. For these cases an emittance was defined based on the instantaneous heat loss from the layer and its instantaneous mean temperature which is proportional to the energy remaining in the layer. An interesting feature was found wherein the cooling process passes through a starting transient after which a constant emittance is achieved that is lower than the emittance for a uniform temperature layer. This provides a simplified theory for the later portion of the transient cooling process.

References

Bathla, P. S., and Viskanta, R., 1968, "Effect of Surroundings on the Transient Energy Transfer in a Layer of Radiating Gas," *Applied Scientific Research*, Vol. 19, pp. 182–197.

Kubo, S., 1984, "Unsteady Radiative Heat Transfer in a Scattering-Dominant Medium," *AIAA Journal*, Vol. 22, pp. 1804–1809.

Lii, C. C., and Ozisik, M. N., 1972, "Transient Radiation and Conduction in an Absorbing, Emitting, Scattering Slab With Reflective Boundaries," *Intl. Journal Heat and Mass Transfer*, Vol. 15, pp. 1175–1179.

Mattick, A. T., and Hertzberg, A., 1981, "Liquid Droplet Radiators for Heat Rejection in Space," *Journal of Energy*, Vol. 5, pp. 387–393.

Siegel, R., and Howell, J. R., 1981, *Thermal Radiation Heat Transfer*, 2nd ed., Hemisphere, Washington, D.C.

Viskanta, R., and Anderson, E. E., 1975, "Heat Transfer in Semitransparent Solids," *Advances in Heat Transfer*, Vol. 11, Academic Press, New York.

Viskanta, R., and Bathla, P. S., 1967, "Unsteady Energy Transfer in a Layer of Gray Gas by Thermal Radiation," *ZAMP*, Vol. 18, pp. 353–367.

Spectral and Total Radiation Properties of Turbulent Hydrogen/Air Diffusion Flames

J. P. Gore
S.-M. Jeng[1]
G. M. Faeth
Fellow ASME

Department of Aerospace Engineering,
University of Michigan,
Ann Arbor, MI 48109-2140

A study of the structure and radiation properties of round turbulent hydrogen/air diffusion flames is described. Measurements were made of mean and fluctuating streamwise velocity, mean temperatures, species concentrations, spectral radiation intensities, and radiant heat fluxes. The measurements were used to evaluate predictions based on the laminar flamelet concept and narrow-band radiation models both ignoring (using mean properties) and considering (using a stochastic method) effects of turbulence/radiation interactions. State relationships found by correlating auxiliary measurements in laminar flames proved to be almost equivalent to conditions for local thermodynamic equilibrium. Structure and radiation predictions were reasonably good for present test conditions. Effects of turbulence/radiation interactions were significant for these flames, causing almost a 100 percent increase in spectral radiation intensities, in comparison to mean property predictions, upstream of the flame tip.

Introduction

This study is an extension of earlier work on the structure and radiation properties of turbulent methane/air and propane/air diffusion flames (Jeng and Faeth, 1984a, b, c; Jeng et al., 1982, 1984). The present study considers turbulent hydrogen/air diffusion flames both theoretically and experimentally. This investigation closely parallels a companion study of turbulent carbon monoxide/air diffusion flames (Gore et al., 1986). The present study and Gore et al. (1986) provide information on nonluminous flames having relatively simple chemistry and radiation properties in order to simplify interpretation of results. The objective of the present study was to obtain new measurements of the structure and radiation properties of tubulent hydrogen/air diffusion flames and to use the results to evaluate models of the process. The following description of the study is brief; additional details and a complete tabulation of data are provided by Gore (1986).

Faeth and Samuelson (1985) recently reviewed past studies of turbulent hydrogen/air diffusion flames; therefore, only the important results from past studies will be discussed here. Bilger (1976), Dibble et al. (1984a, b), Driscoll et al. (1982), Drake et al. (1981, 1982, 1984a, b), Johnson et al. (1984), Starner and Bilger (1980, 1981), and Starner (1983) have reported extensive measurements and analyses of turbulent hydrogen/air diffusion flames, using coflowing jet configurations. These results suggest that the hydrogen air system has local properties nearly equal to thermodynamic equilibrium conditions; however, effects of differential diffusion, radical superequilibrium, and departure from equilibrium near points of flame attachment have been reported. Analysis of these flows using the conserved-scalar formalism, in conjunction with state relationships based on thermodynamic equilibrium, and a Favre-averaged k–ϵ–g turbulence model has been reasonably successful (Bilger, 1976; Drake et al., 1982). However, none of these studies has considered the radiation properties of the flames.

Past work on the radiative properties of turbulent diffusion flames was recently reviewed by Faeth et al. (1985). Surprisingly, there has been relatively little work reported for hydrogen/air flames. An exception is the study of Fishburn and Pergament (1979), who undertook a comprehensive analysis of the spectral radiation properties of large-scale hydrogen flames in still air. Flame structure was predicted using a mixing—length model of turbulence with Arrhenius expressions to prescribe turbulent reaction rates. Radiation properties were found from a narrow-band analysis, using the approach described by Ludwig et al. (1973), and based on predicted mean properties. Encouraging agreement was obtained between predictions and measurements, aside from some difficulties in predicting flame widths. However, the use of Arrhenius expressions to estimate the structure of turbulent diffusion flames, is certainly not consistent with present understanding of turbulent diffusion flame structure (Bilger, 1976) and structure measurements were not available for the flames used to evaluate the radiation predictions.

An important issue for turbulent flames is the effect of turbulent fluctuations on flame radiation, i.e., turbulence/radiation interactions. Current practice, e.g., Fishburn and Pergament (1979) and Ludwig et al. (1973), is to ignore turbulence/radiation interactions and base predictions on mean scalar properties. On the other hand, simplified analyses of flame radiation, reported by Cox (1977) and Kabashnikov and Kmit (1979), suggest that turbulent fluctuations can increase radiative heat fluxes in flames by up to 300 percent from predictions based on mean properties.

Prompted by this inconsistency, Jeng et al. (1984), Jeng and Faeth (1984c), and Gore et al. (1986) studied both the structure and radiative properties of turbulent methane and carbon monoxide/air diffusion flames. Flame structure was analyzed along the lines proposed by Bilger (1976, 1977) yielding reasonably good agreement between predictions and measurements. Spectral radiation intensities were predicted using the narrow-band model described by Ludwig et al. (1973). Computations were carried out using both mean properties along a radiation path and a stochastic method to allow for turbulence/radiation interactions. The comparison between predictions and measurements of spectral radiation intensities was encouraging. Furthermore, differences between mean property and stochastic predictions suggested only modest effects of turbulence radiation interactions, e.g., stochastic predictions were 10 percent higher for carbon

[1]Currently at the Center for Laser Applications, University of Tennessee Space Institute, Tullahoma, TN 37383.

Contributed by the Heat Transfer Division and presented at the AIAA/ASME Thermophysics Conference, Boston, MA, June 1986. Manuscript received by the Heat Transfer Division February 14, 1986.

monoxide/air flames and 20 - 30 percent higher for methane/air flames than predictions based on mean properties. Such differences are modest in comparison to uncertainties of typical flame structure models and even the uncertainties of the narrow-band model itself. However, since different fuels yielded somewhat different degrees of turbulence/radiation interactions, the universality of this observation is clearly limited.

The objective of the present investigation was to further test these ideas by considering turbulent hydrogen/air diffusion flames as a natural counterpart of carbon monoxide/air diffusion flames, since both are related to hydrocarbon/air diffusion flames but are less complex. Although study of radiation properties was the main objective, structure measurements were also completed so that predictions of scalar structure of the present test flames could be evaluated. Experimental and theoretical methods were similar to Jeng and Faeth (1984a, b, c) and Jeng et al. (1982, 1984). Mean and fluctuating velocities, mean temperatures, species concentrations, spectral radiation intensities, and radiative heat fluxes were measured for two turbulent hydrogen/air diffusion flames to allow some consideration of flame scale. The measurements were used to evaluate predictions of radiation properties. Structure measurements in laminar diffusion flames were also undertaken, in order to test the applicability of the thermodynamic equilibrium assumption for state relationships needed by the analysis.

The paper begins with a discussion of experimental and theoretical methods. Results concerning the state relationship measurements and the structure of the turbulent diffusion flames are then described. The paper concludes with descriptions of predicted and measured spectral radiation intensities and radiative heat fluxes.

Experimental Methods

Test Arrangement. Experimental methods were similar to past work; therefore, they will only be briefly described. Hydrogen was injected vertically upward, from a water-cooled burner, into still air. The burner had a screened plenum, followed by a 25:1 contraction which terminated in a 5-mm-dia exit passage. The burner was housed in a screened enclosure to reduce room disturbances. The burner could be traversed in three directions, to accommodate rigidly mounted optical instrumentation.

An uncooled concentric-tube burner was used for the laminar flame measurements. The hydrogen flowed from a central tube (14.3 mm in diameter) with a coflow of air from a concentric port having an inside diameter of 102 mm. The burner flows were smoothed using a bed of stainless-steel balls and honeycomb (1 mm hexagonal cells × 25 mm long) which was flush with the burner exit. The flames were shielded from drafts with a concentric cylindrical quartz tube (115 mm inside diameter) which extended 10 mm beyond each measuring plane. Fine-mesh screen was used to shield the upper portions of the flame.

Instrumentation

Velocities. Mean and fluctuating velocities were measured using a single-channel laser-Doppler anemometer (LDA). The LDA was operated in the dual-beam forward-scatter mode using frequency shifting to eliminate directional bias and ambiguity. Seeding levels were high; therefore, the analog output of the burst-counter signal processor was integrated directly to yield time averages without velocity bias. The measuring volume had a diameter of 0.24 mm and a length of 0.72 mm. Analysis indicated that gradient broadening effects were small, except near the downstream end of the potential core. Uncertainties (95 percent confidence) of mean and fluctuating velocities were less than 5 percent (Gore, 1986).

Temperatures. Mean temperatures were measured using a butt-welded thermocouple constructed out of 0.075 mm-dia Pt/Pt–10 percent Rh wires. The region of the junction was somewhat enlarged, having a diameter of roughly 0.2 mm. The junction wires were mounted on heavier lead wires, spaced 12 mm apart, to provide a traversable probe. The theromocouple output was recorded with an integrating digital voltmeter. Temperature measurements were not corrected for radiative heat losses and are estimated to be 100–200 K too low in the hottest parts of the flames (Gore, 1986).

Species Concentrations. Compositions were measured in the turbulent flames by isokinetic sampling at the mean gas velocity (water-cooled probe with an inlet diameter of 2 mm) and analysis with a gas chromatograph. Samples were analyzed on a dry basis using a gas chromatograph having a hot-wire detector. Water vapor concentrations were then estimated from mass balances, accounting for the local ambient humidity. The gas chromatograph was calibrated with known gas mixtures. Aside from uncertainties in the density weighting of isokinetic sampling in turbulent flames, to be quantified later, uncertainties in composition measurements are less than 15 percent (Gore, 1986).

Concentration measurements in the laminar flames employed a quartz sampling probe which operated choked (0.1–0.2 mm inlet with a 0.75 mm probe tip radius). Chromatography methods and uncertainties were similar to the turbuent flame measurements.

Spectral Radiation Intensities. Spectral radiation intensities were measured for radial paths through the flames using a 250-mm grating monochromator with a pyroelectric detector (Oriel Corp., models 7240 and 7084). The field of view was roughly 10 mm in diameter with a 1.2 deg field angle. A water-cooled aperture between the flame and the monochromator prevented overheating of the instrument. Various gratings and order-sorting filters were used to cover the wavelength range 1–4 μm, which includes the 1.38, 1.87, and 2.7 μm bands of water vapor. The system function of the monochromator was calibrated using a blackbody source heated by a furnace. Higher-order harmonics of known wavelengths from a mercury arc and a He-Ne laser were used to calibrate the

Nomenclature

a = acceleration of gravity
d = burner exit diameter
g = square of mixture fraction fluctuations
k = turbulent kinetic energy
$\dot{m}_o$ = burner mass flow rate
$\dot{Q}$ = heat release rate
$\dot{Q}_{rad}$ = radiative heat loss from flame
Re = burner Reynolds number
Ri = burner Richardson number
T = temperature
u = streamwise velocity
v = radial velocity
x = height above burner
ϵ = rate of dissipation of turbulence kinetic energy
ν = kinematic viscosity
ρ = density

Subscripts

c = centerline quantity
o = burner exit condition

Superscripts

$[\tilde{}]$, $[\tilde{}]'$ = time-averaged mean and fluctuating quantity
$[\tilde{}]$, $[\tilde{}]''$ = Favre-averaged mean and fluctuating quantity

Table 1 Summary of turbulent flame test conditions[a]

Reynolds number[b]	5722	3000
Richardson number[c]	0.4×10^{-5}	1.5×10^{-5}
Measured		
u_o, m/s	108.4	66.3
$k_o^{1/2}/u_o$	0.23	0.184
$\dot{Q}$, kW	23.8	12.5
$\dot{Q}_{rad}/\dot{Q}$, percent	8.7	10.2
Hydrogen flow Rate, mg/s[d]	200	105

a Flow directed vertically upward from a 5-mm-dia passage, in still air at NTP.
b $Re = u_o d/\nu$ based on fuel gas properties at exit.
c $Ri = ad/u_o^2$.
d Commercial Grade, Linde Division of Union Carbide.

wavelength readout. Uncertainites in these measurements were less than 20 percent (Gore, 1986).

Radiative Heat Fluxes. Total radiative heat flux distributions were measured along the base and the axis of the turbulent flames using a gas-purged, water-cooled sensor (Medtherm, Type 64P-10-22, with a 150° viewing angle). The sensor was positioned so that the flame boundaries were entirely within viewing angle, except for points far from the burner exit, which contribute very little to the radiative flux in any event. Uncertainties of these measurements were less than 10 percent (Gore, 1986).

Test Conditions. Test conditions, for the two turbulent hydrogen air diffusion flames studied, are summarized in Table 1. Relatively high burner exit velocities were used; however, the low density of hydrogen still resulted in Reynolds numbers barely in the turbulent flow regime at the burner exit. This places stress on the turbulence model, which was generally developed using approximations appropriate for high-Reynolds-number flows. Initial Richardson numbers were relatively low; nevertheless, effects of buoyancy were still appreciable, particularly near the end of the visible flame zone (visible due to low levels of impurities in the hydrogen fuel), for the lowest Reynolds number flame.

Initial conditions for the present flames were defined by measuring $\bar{u}$, $\bar{u}'$, and $\bar{v}'$ at $x/d = 2$, which was the position nearest the exit which was accessible to the LDA. The initial turbulence kinetic energy distribution was estimated from these measurements, assuming that radial and tangential velocity fluctuations were equal. Initial values of ϵ were estimated from the rate of decay of velocity fluctuations in the potential core.

Theoretical Methods

Flame Structure. Theoretical methods were similar to past practice (Jeng and Faeth, 1984a, b, c, Jeng et al., 1982, 1984) and will only be described briefly. A k–ϵ–g model together with the conserved-scalar method was used to estimate flame structure, assuming: (1) boundary layer approximations for an axisymmetric flame with no swirl, (2) negligible mean kinetic energy, (3) equal exchange coefficients for all species and heat, (4) negligible radiative energy exchange within the flames, and (5) buoyancy only affects the mean flow. Assumption (1) and (2) represent conditions of the experiments. Assumption (3) is widely adopted for analysis of turbulent mixing in gases and is reasonably satisfactory at high Reynolds numbers. Assumption (4) is justified by the relatively small radiative heat loss fractions of present flames; see Table 1. Assumption (5) has been shown to provide reasonably good predictions of mean properties in turbulent diffusion flames having similar initial conditions (Jeng and Faeth, 1984a, b; Gore et al., 1986). The Favre-averaged formulation of Bilger (1976) was adopted (although details differ) which involves governing equations for mean conservation of mass, momentum and mixture fraction and modeled governing equations for k, ϵ, and g. All model contants were fixed by measurements in constant- and variable-density noncombusting jets (Jeng and Faeth, 1984a).

The laminar flamelet approximation was used to relate scalar properties to the mixture fraction, along the lines proposed by Bilger (1977) and Liew et al. (1981). Together with the previous assumptions, this implies that scalar properties are only a function of mixture fraction, termed the state relationships. In the past, state relationships for turbulent hydrogen/air diffusion flames have been prescribed by assuming local thermodynamic equilibrium (Bilger, 1976). This approximation was tested here by developing state relationships based on auxiliary measurements in corresponding laminar diffusion flames, similar to Bilger (1977), Liew et al. (1981), Gore et al. (1986), and Jeng and Faeth (1986a, b). The laminar flamelet state relationships were only used for the mass fractions of major gas species. Temperatures and densities were computed as a function of mixture fraction, assuming that each flame lost the measured fraction of chemical energy release by radiation. The calculations for temperature and density used the Gordon and McBride (1971) chemical equilibrium algorithm.

Spectral Radiation Intensities. The equation of radiative transfer was solved for various paths through the flames, ignoring scattering and using the narrow-band analysis of Ludwig et al. (1973). The analysis considered all the gas bands in the region of interest, e.g., the 1.38, 1.87, 2.7, and 6.3 μm bands of water vapor. The Goody statistical narrow-band model was used in conjunction with the Curtis–Godson approximation for a nonhomogeneous gas path. A slightly modified version of the computer algorithm RADCAL, developed by Grosshandler (1980), was used for the computations.

Spectral intensity computations are straightforward when turbulence/radiation interactions are ignored. The structure analysis provides both time- and Favre-averaged mean scalar properties along the radiation path. Properties needed for the calculations are taken to be time averages.

The stochastic analysis was used to gain insight concerning turbulence/radiation interactions. This involves dividing the gas path into discrete eddies, having lengths equal to the local dissipation length scale. Estimates of characteristic eddy sizes and lifetimes were obtained using the approach described by Shuen et al. (1985). Each eddy is assumed to have uniform properties. The properties of each eddy are found by randomly sampling its time-averaged probability density function of mixture fraction and obtaining scalar properties for this mixture fraction from the state relationships. Once properties of all eddies along the gas path are specified, spectral intensities are calculated similar to the mean property method. Random sampling continues in this manner, until sufficient realizations have been computed to obtain statistically significant results.

Radiative Heat Fluxes. Computations of radiative heat fluxes are a straightforward extension of the spectral radiaton intensity computations using the discrete transfer method of Lockwood and Shah (1981). This involves determining the spectral intensity for various wavelengths and paths passing through the point in question (120 paths to the sensor location in this instance, allowing for symmetry) and then summing over both wavelengths and paths to find the total radiative heat flux. Paths are chosen to cover the region viewed by the detector with the contribution of each weighted according to the solid angle it intercepts and the angle of the path normal to

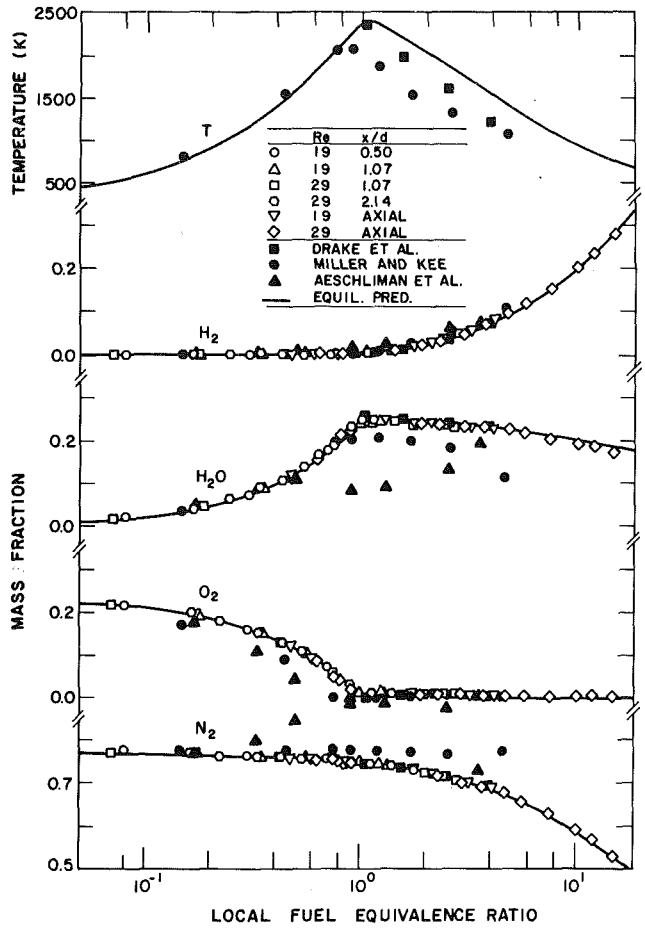

Fig. 1 Hydrogen/air state relationships

the detector surface. The spectal response of the detector was considered during these computations. The present calculations were based on mean property preditions to shorten computation time.

Results and Discussion

State Relationships. Measurements of temperatures and species concentrations for hydrogen/air diffusion flames are illustrated in Fig. 1. Results illustrated include present sampling measurements in laminar flames, and Raman spectroscopy measurements by Aeschliman et al. (1979) in a laminar flame and by Drake et al. (1981, 1984b) giving instantaneous values in turbulent flames. Concentration and temperature predictions by Miller and Kee (1977), for laminar conditions ($Re < 100$), were reduced to state-relationship form and are also shown on the figure. Finally, predictions based on the assumption of adiabatic thermodynamic equilibrium using the Gordon and McBride (1971) algorithm are included. The present measurements and those of Drake et al. (1981, 1984b) exhibit close approach to thermodynamic equilibrium for major gas species, suggesting universality of these properties with respect to fuel equivalence ratio, and thus mixture fraction. It is widely accepted that hydrogen/oxygen kinetics are fast (Bilger, 1976); therefore, this result is perhaps to be expected. The temperature measurements of Drake et al. (1981, 1984b), however, are somewhat below adiabatic conditions even though radiative heat losses in their test flames were relatively small. They attributed this behavior, which was most noticeable near the jet exit, to finite-rate chemistry causing superequilibrium concentrations of OH. Later measurements established that this was indeed the case (Drake et al. 1984a), with the large enthalpy of formation of the excess OH being responsible for lower temperature (~ 200 K lower). The earlier result of Aeshliman et al. (1979) and Miller and Kee (1977) diverge appreciably from equilibrium predictions; however, these findings are not supported by the more recent measurements. A factor in this behavior may be differential diffusion at low Reynolds numbers. which is a particular problem for this flame system due to the large molecular diffusivity of hydrogen. Since the present flames have larger residence times and greater radiation heat losses than those of Drake et al. (1981, 1984b), the procedure adopted for constructing state relationships was to ignore effects of OH superequilbrium but to allow for radiative heat losses during thermodynamic equilibrium computations. The resulting state relationships for the composition of major gas species were virtually identical to those illustrated in Fig. 1, while temperatures were somewhat lower. Fortunately, uncertainties in temperature levels are much less critical for predictions of radiation from nonluminous gas bands than is the case for blackbody radiation.

Flame Structure. Structure measurements and predictions along the axis of the two flames are illustrated in Figs. 2 and 3. Recall that time-averaged velocities were measured while Favre averages were predicted. The differences between these averages are less than 10 percent for mean velocities and generally less than 20 percent for velocity fluctuations (except near the flame tip where differences for velocity fluctuations approach 40 percent) with the Favre-averaged values being lower for present flame conditions (Starner and Bilger, 1981; Faeth and Samuleson, 1985). The analyis only yields k; therefore, $\tilde{u}''$ has been estimated for plotting in the figures, assuming isotropic turbulence ($\tilde{u}''^2 = 2k/3$), which is consistent with other turbulence model assumptions. If the usual levels of anisotropy observed along the axis of jets is assumed ($\tilde{u}''^2 = k$), predictions would be roughly 20 percent higher. Mean velocities along the axis are predicted reasonably well. Predicted values of $\tilde{u}_c''$ are generally lower than the measured $\tilde{u}_c'$, which is consistent with potential differences between the two averages and typical levels of anisotropy for this variable. Near and beyond the flame tip there is also additional production of turbulence due to turbulence/buoyancy interactions which have not been considered in the analysis (Jeng et al., 1982). This effect accounts for the rapid increase of $\tilde{u}_c'$ for $x/d > 60$, which is not suggested by the predictions. The fact that the increase is greater for the lower Reynolds number flame (compare Figs. 2 and 3) supports the idea that the effect is due to buoyancy.

The analysis provides both time- and Favre-averaged scalar properties; therefore, predictions in Figs. 2 and 3 include both averages, since the degree of density weighting of the measurements is unknown. For present conditions, however, differences between these averages are not large. As noted earlier, temperature measurements were not corrected for radiative heat losses and are 100–200 K too low in the hottest portions of the flow. Considering effects of radiation and uncertainties in the type of average measured, however, the comparison between predicted and measured temperatures is reasonably good.[2] Predicted and measured concentrations are in reasonable agreement as well. The main discrepancy appears to be a tendency to slightly overestimate the rate of development of the higher Reynolds number flame (Fig. 2), thus underestimating the flame length.

Spectral Radiation Intensities. The structure evaluation suggests that the present model provides reasonable predictions of mean properties for the flames under consideration; therefore, we turn to a discussion of radiation properties. Measurements

[2]Temperature measurements could not be extended farther upstream than shown in Figs. 2 and 3, due to burnout of the probe.

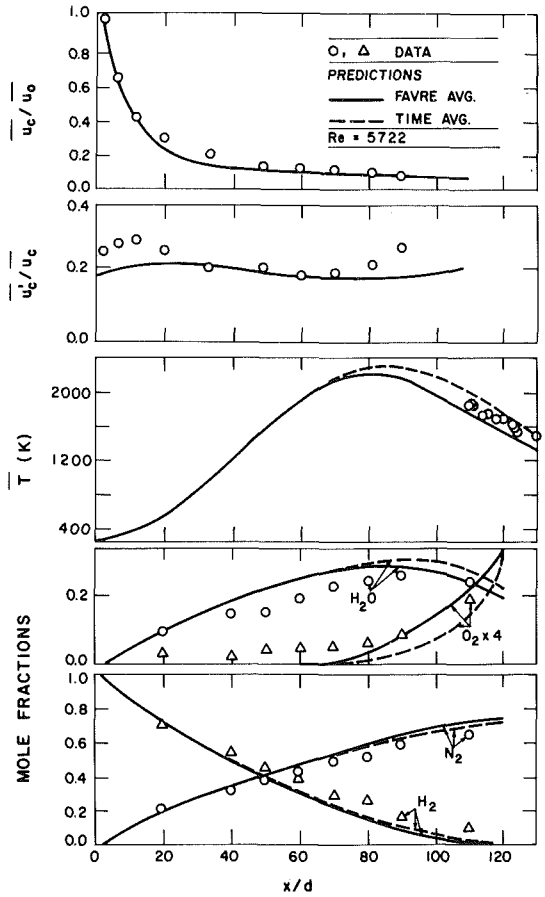

Fig. 2 Structure predictions and measurements along the axis: Re = 5722

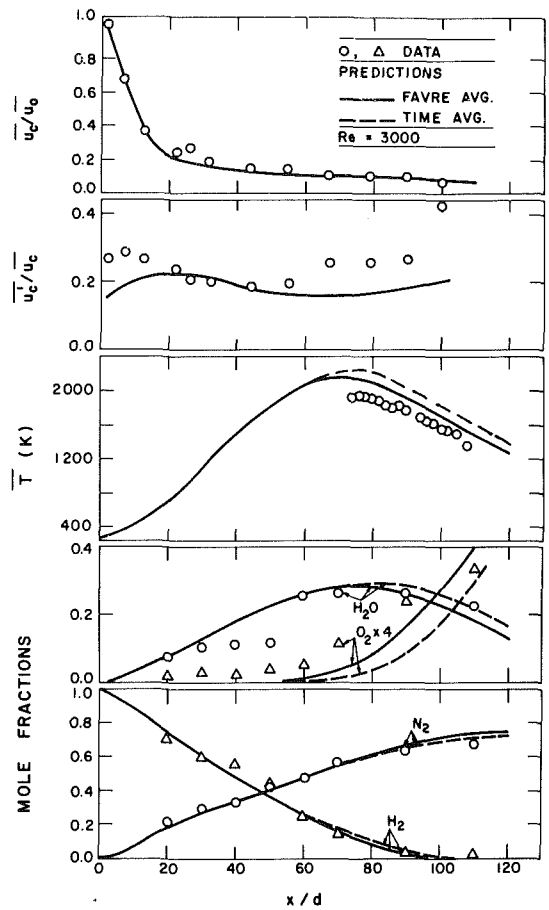

Fig 3 Structure predictions and measurements along the axis: Re = 3000

and predictions of spectral radiation intensities for the two flames are illustrated in Figs. 4 and 5. Measurements were undertaken for horizontal, radial paths at x/d = 50, 90, and 130. Results for x/d = 130 are not shown for the lower Reynolds number flame, since this position is well beyond the flame tip and spectral intensities were too low to be measured with acceptable levels of accuracy. Predictions using both the mean-property and stochastic methods are also shown on the figures.

Spectral radiation intensities in Figs. 4 and 5 are dominated by the 1.38, 1.87, and 2.7 μm bands of water vapor. Intensities also increase gradually beyond 4 μm, as the broad 6.3-μm band of water vapor is approached. The stochastic method generally yields higher values of spectral radiation intensities than the mean property method, ca. 2:1. This suggests greater effects of turbulence/radiation interactions for hydrogen/air diffusion flames than either carbon monoxide/air or methane/air diffusion flames where differences between the two method were generally less than 30 percent (Jeng et al., 1984; Gore et al., 1986). This behavior is caused by the rapid variation of radiation properties (i.e., temperature and water vapor concentration) with mixture fraction near the stoichiometric condition. Thus predictions of the two methods tend to merge in the far field; however, this region also has relatively small radiation intensities for the present test conditions.

Measured spectral radiation intensities are generally between the two predictions with discrepancies on the order of 20 percent for each. This is very encouraging since both structure and radiation properties are predicted; and uncertainties in the narrow-band model, and also the structure model, are within the same range. An exception to this performance is the x/d = 130 position for the higher Reynolds number flame (Fig. 4). The position is just beyond the flame tip, where spectral radiation intensities decrease very rapidly with increasing distance. Present structure predictions tend to underestimate the length of this flame, as noted earlier, and this is largely responsible for the discrepancies seen in Fig. 4.

Radiative Heat Fluxes. Measurements and predictions of total radiative heat fluxes to points surrounding the present turbulent flames are illustrated in Fig. 6 and 7. Two sets of predictions are shown, one considering the spectral response of the heat flux sensor used for the total radiative heat flux measurements (denoted 1–6.3 μm), the other considering heat fluxes resulting from the spectral range 1–10 μm. The latter illustrates the potential affect of the 6.3-μm band of water vapor, which was largely omitted from the response range of the present heat flux sensor.

Figure 6 is an illustration of results for the detector facing the flame axis and traversing in the vertical direction at a distance of 575 mm from the axis. The radiative heat flux is highest near the flame tip, $x/d \leq 100$ and 80 for the high and low Reynolds number flames. Figure 7 is an illustration of the results for a detector facing vertically upward in the plane of the burner exit and traversing radially outward. In this case, the radiative heat flux decreases monotonically with increasing radial distance. Although peak mean temperatures and compositions are the same for both flames, radiative heat fluxes are lower for the lower Reynolds number flame due to its smaller dimensions. Buoyancy caused the flames to be shorter and narrower at lower Reynolds numbers for the present test range. This effect would disappear at higher Reynolds numbers, where flame structure is relatively independent of Reynolds number.

Predictions allowing for the response of the present heat

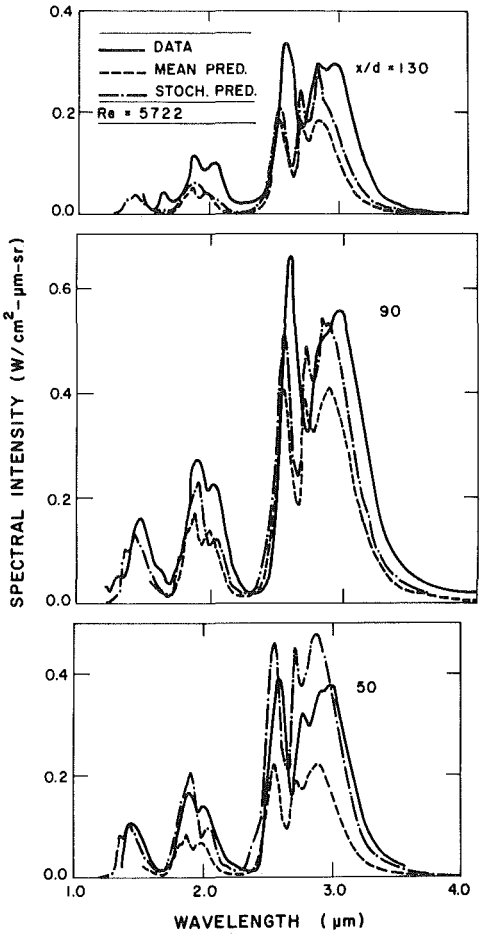

Fig .4 Spectral radiation intensities for radial paths through the axis: Re = 5722

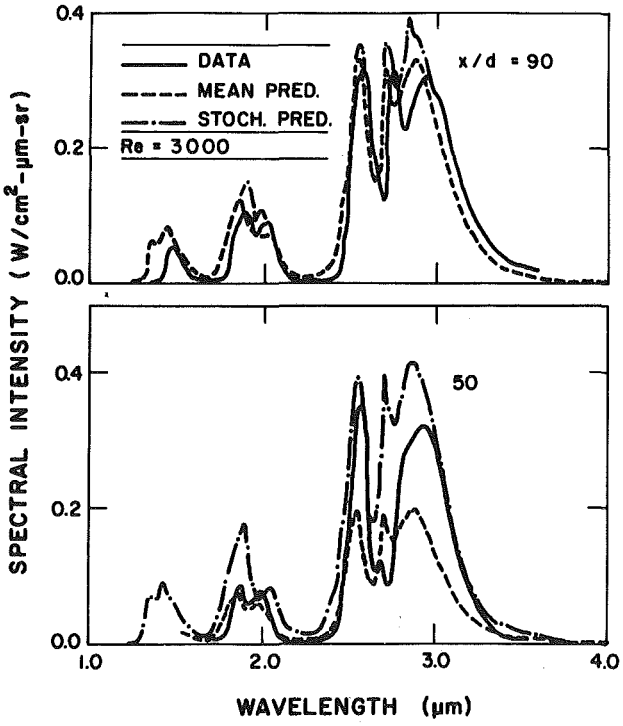

Fig .5 Spectral radiation intensities for radial paths through the axis: Re = 3000

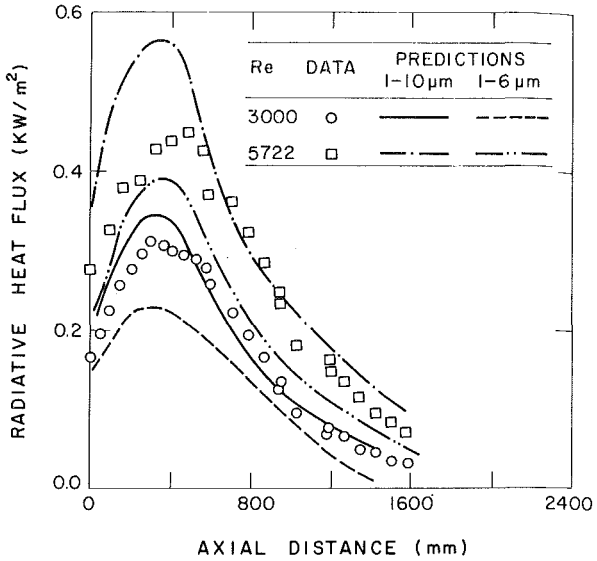

Fig. 6 Total radiative heat fluxes along the axis

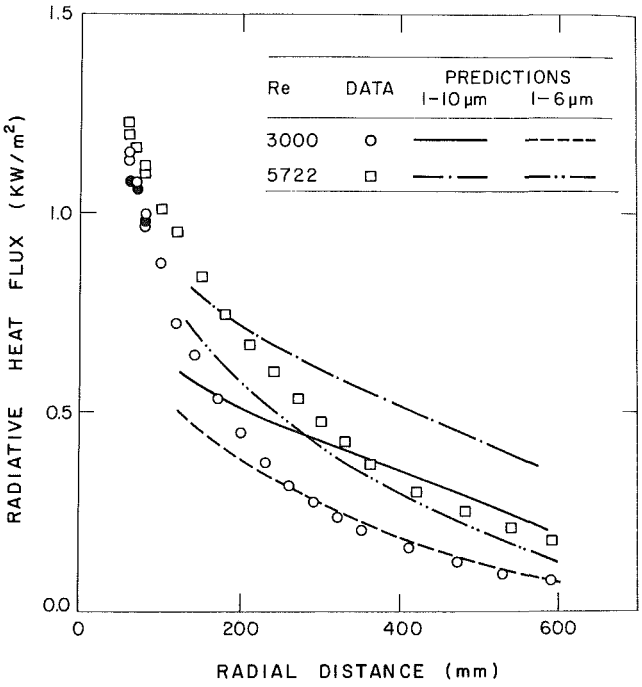

Fig. 7 Total radiative heat fluxes in the plane of burner exit

flux sensor (denoted 1–6.3 μm) tend to underestimate measurements in Figs. 6 and 7 by roughly 20 percent. This parallels the underestimation of spectral radiation intensities using the mean property method (Figs. 4 and 5). Nevertheless, it is encouraging that present methods provide reasonably good predictions of trends toward reduced radiative heat fluxes as the Reynolds number is reduced for present test conditions. Predictions of heat fluxes with and without the 6.3-μm water vapor band included indicate that this band contributes roughly 30 percent to the heat flux and should be considered for radiation analysis of hydrogen/air diffusion flames. Water vapor bands at wavelengths larger than 10 μm, however, were not significant for present conditions.

Conclusions

The major conclusions of the study are as follows:

1 For the range of conditions examined here, state rela-

tionships for hydrogen/air diffusion flames closely approximated conditions for local thermodynamic equilibrium, modified by radiative heat losses. This behavior satisfies the universality requirements of the laminar flamelet state relationships, making such flames good candidates for analysis using this method.

2 The present k–ϵ–g conserved-scalar analysis for structure was in reasonbaly good agreement with measurement, using measured initial conditions with all empirical constants fixed by results for noncombustiing jets. This agreement is surprising, and perhaps fortuitous, since present flames had relatively low Reynolds numbers in comparison to the range used to develop the turbulence model.

3 The present radiation analysis achieved reasonably good predictions of spectral radiation intensities and radiative heat fluxes, similar to past experience with turbulent carbon monoxide/air and methane/air diffusion flames. Discrepancies between measurements and predictions of both the mean property and stochastic methods were on the order of 20 percent, which is comparable to uncertainties in the narrow-band radiation model, and also the structure model.

4 Effects of turbulence/radiation interactions were very significant for the present flames, with stochastic predictions being as much as twice the mean property predictions. In contrast, turbulence/radiation interactions caused less than a 30 percent increase in spectral radiation intensities for carbon monoxide/air and methane/air diffusion flames. This difference is caused by the relatively rapid variation of radiation properties (water vapor concentration and temperature) near stoichiometric conditions for hydrogen/air diffusion flames.

Acknowledgments

This research was carried out while the authors were members of the Department of Mechanical Engineering at The Pennsylvania State University, University Park, Pennsylvania. The research was supported by the United States Department of Commerce, National Bureau of Standards, Grant No. 60NANB4D0032, with B. J. NcCaffrey of the Center for Fire Research serving as Scientific Officer.

References

Aeschliman, D. P., Cummings, J. C., and Hill, R. A., 1979, "Raman Spectroscopic Study of a Laminar Hydrogen Diffusion Flame in Air," *J. Quant. Spectrosc. Radiat. Trans.*, Vol. 21, pp. 293-307.

Bilger, R. W., 1976, "Turbulent Jet Diffusion Flames," *Prog. Energy Combust. Sci.*, Vol. 1, pp. 87-109.

Bilger, R. W., 1977, "Reaction Rates In Diffusion Flames," *Comb. Flame*, Vol. 30, pp. 277-284.

Cox, G., 1977, "On Radiant Heat Transfer From Turbulent Flames," *Comb. Sci. and Tech.*, Vol. 17, pp. 75-78.

Dibble, R. W., Kollmann, W., and Schefer, R. W., 1984a, "Conserved Scalar Fluxes Measured in Turbulent Nonpremixed Flame by Combined Laser Doppler Velocimetry and Laser Raman Scattering," *Comb. Flame*, Vol. 55, pp. 307-321.

Dibble, R. W. Schefer, R. W., and Kollman, W., 1984b, "Measurements and Predictions of Scalar Dissipation in Turbulent Jet Flames," *Twentieth Symposium (International) on Combustion*, The Combustion Institute, Pittsburgh, PA, pp. 345-352.

Driscoll, J. F., Schefer, R. W., and Dibble, R. W., 1982, "Mass Fluxes $\rho' u'$ and $\rho' v'$ Measured in a Turbulent Nonmpremixed Flame," *Nineteenth Symposium (International) on Combustion*, The Combustion Institute, Pittsburgh, PA, pp. 477-485.

Drake, M. C., Lapp, M., Penney, C. M., and Warshaw, S., 1981, "Measurements of Temperature and Concentration Fluctuations in Turbulent Diffusion Flames Using Pulsed Raman Spectroscopy," *Eighteenth Symposium (International) on Combustion*, The Combustion Institute, Pittsburgh, PA, pp. 1521-1531.

Drake, M. C., Bilger, R. W., and Starner, S. H., 1982," Raman Measurements and Conserved Scalar Modeling in Turbulent Diffusion Flames," *Nineteenth Symposium (International) on Combustion*, The Combustion Institute, Pittsburgh, PA, pp. 459-467.

Drake, M. C., Pitz, R. W., Lapp, M., Fenimore, C. P., Lucht, R. P., Sweeney, D. W., and Laurendeau, N. M., 1984a, "Measurements of Superequilibrium Hydroxyl Concentrations in Turbulent Nonpremixed Flames Using Saturated Fluorescence," *Twentieth Symposium (International) on Combustion*. The Combustion Institute, Pitttsburgh, PA, pp. 327-335.

Drake, M. C., Pitz, R. W., and Lapp, M., 1984b, "Laser Measurements on Nonpremixed Hydrogen-Air Flames for Assessment of Turbulent Combustion Models," AIAA Paper No. 84-0544.

Faeth, G. M., Jeng, S-M., and Gore, J. P., 1985, "Radiation from Flames," *Heat Transfer in Fire and Combustion Systems*, C. K. Law, L. Jaluria, W. W. Yuen, and K. Miyasaka, eds., HTD-Vol. 45, ASME, New York, pp. 137-151.

Faeth, G. M., and Samuelson, G. S., 1985, "Fast-Reaction Non-premixed Combustion," *Evaluation of Data on Simple Turbulent Flows*, W. C. Strahle and S. G. Lekoudis, eds., AFOSR TR-85 0880.

Fishburne, E. S., and Pergament, H. S., 1979, "The Dynamics and Radiant Intensity of Large Hydrogen Flames," *Seventeenth Symposium (International) on Combustion*, The Combustion Institute, Pittsburgh, PA, pp. 1063-1073.

Gordon, S., and McBride, B. J., 1971, "Computer Program for Calculation of Complex Chemical Equilibriuum Compositions, Rocket Performance, Incident and Reflected Shocks, and Chapman-Jouget Detonations," NASA SP-273.

Gore, J. P., 1986, "A Theoretical and Experimental Study of Turbulent Flame Radiation," Ph.D. Thesis, The Pennsylvania State University, University Park, PA.

Gore, J. P., Jeng, S. M., and Faeth, G. M., 1986, "Spectral and Total Radiation Properties of Turbulent Carbon Monoxide/Air Diffusion Flames," AIAA Paper No. 86-0294.

Grosshandler, W. L., 1980, "Radiative Heat Transfer in Nonhomogeneous Gases: A Simplified Approach," *Int. J. Heat Mass Trans.*. Vol. 23, pp. 1447-1459.

Jeng, S.-M., Chen, L.-D., and Faeth, G. M., 1982, "The Structure of Buoyant Methane and Propane Diffusion Flames," *Nineteenth Symposium (International) on Combustion*, The Combustion Institute, Pittsburgh, PA, pp. 349-358.

Jeng, S.-M., and Faeth, G. M., 1984a, "Species Concentrations and Turbulence Properties in Buoyant Methane Diffusion Flames," ASME JOURNAL OF HEAT TRANSFER, Vol. 106, pp. 721-727.

Jeng, S.-M., and Faeth, G. M., 1984b, "Predictions of Mean and Scalar Properties in Turbulent Propane Diffusion Flames," ASME JOURNAL OF HEAT TRANSFER, Vol. 106, pp. 891-893.

Jeng, S.-M., and Faeth, G. M., 1984c, "Radiative Heat Fluxes Near Turbulent Buoyant Methane Diffusion Flames," ASME JOURNAL OF HEAT TRANSFER, Vol. 106, pp. 886-888.

Jeng, S.-M., Lai, M.-C., and Faeth, G. M., 1984, "Nonluminous Radiation in Turbulent Buoyant Axisymmetric Flames," *Comb. Sci. and Tech.*, Vol. 40, pp. 41-53.

Johnson, S. C., Dibble, R. W., Schefer, R. W., Ashurst, W., T., and Kollmann, W., 1984, "Laser Measurements and Stochastic Simulations of Turbulent Reacting Flows," AIAA Paper No. 84-0543.

Kabashnikov, V..P., and Kmit, G. I., 1979, "Influence of Turbulent Fluctuations on Thermal Radiation," *J. Applied Spectroscopy*, Vol. 31, pp. 963-967.

Liew, S. K., Bray, K. N. C., and Moss, J. B., 1981, "A Flamelet Model of Turbulent Non-premixed Combustion," *Comb. Sci. and Tech.*, Vol. 27, pp. 69-73.

Lockwood, F. C., and Shah, N. B., 1981, "A New Radiation Solution Method for Incorporation in General Combustion Prediction Procedures," *Eighteenth Symposium [International] on Combustion*, The Combustion Institute, Pittsburgh, PA, pp. 1405-1414.

Ludwig, C. B., Malkmus, W., Reardon, J. E., and Thomson, J. A., 1973, *Handbook of Infrared Radiation From Combustion Cases*, NASA SP-3080.

Miller, J. A., and Kee, R. J., 1977, "Chemical Nonequilibrium Effects in Hydrogen-Air Laminar Jet Diffusion Flames," *J. Phys. Chem.*, Vol. 81, pp. 2534-2542.

Shuen, J.-S., Solomon, A. S. P., Zhang, Q.-F., and Faeth, G. M., 1985, "Structure of Particle-Laden Jets: Measurements and Predictions," *AIAA J.*, Vol. 23, pp. 396-404.

Starner, S. H., and Bilger, R. W., 1980, "LDA Measurements in a Turbulent Diffusion Flame with Axial Pressure Gradient," *Comb. Sci. Tech.*, Vol. 21, pp. 259-276.

Starner, S. H., and Bilger, R. W., 1981, "Measurements of Scalar-Velocity Correlations in a Turbulent Diffusion Flames," *Eighteenth Symposium (International) on Combustion*, The Combustion Institute, Pittsburgh, PA, pp. 921-930.

Starner, S. H., 1983, "Joint Measurements of Radial Velocity and Scalars in a Turbulent Diffusion Flames," *Comb. Sci. Tech.*, Vol. 30, pp. 145-169.

Thermal Response of Unconfined Ceilings Above Growing Fires and the Importance of Convective Heat Transfer

L. Y. Cooper

D. W. Stroup

National Bureau of Standards, Gaithersburg, MD 20899

A procedure is developed to calculate the thermal response of unconfined nonburning ceilings above growing fires. The procedure uses an algorithm for conduction into the ceiling material. It takes account of heat transfer due to radiation from the combustion zone to the ceiling surface, and due to reradiation from the ceiling to the floor and furnishings. Finally, the procedure uses a previously developed algorithm for convective heat transfer to the ceiling from the fire-plume-driven ceiling jet. The procedure is used to predict radial-dependent surface temperature histories of typical ceiling materials under a variety of different realistic levels of hazardous fire energy generation rates and combustion zone-ceiling separation distances. The results give an indication of the influence of convective heat transfer on peak ceiling thermal response, losses from fire plume gases, and radial variations and peak values of ceiling-to-floor irradiation during enclosure fires.

Introduction

In [1, 2] an algorithm was developed to estimate the radial- and time-dependent convective heat transfer to unconfined ceilings above growing fires. Together with an account of radial-dependent radiant heat transfer to and from the ceiling, it would appear that such an algorithm is required to predict the thermal response of the ceiling material from the time of fire initiation (when the ceiling and lower gas temperature is at a uniform ambient temperature, T_{amb}), to critical times during the course of hazardous fires (when the temperature field of the ceiling material can have significant variation in both thickness and radial position, r, from the ceiling–fire plume impingement point). Examples of such critical times might be those times when near-ceiling fire detectors and/or fusible sprinkler links are actuated, when the ceiling surface reaches an ignition or failure temperature, and when radiation from the ceiling to occupants or combustible furnishings below reaches critical levels.

The importance of position-dependent ceiling response to an understanding of hazardous fire phenomena, in general, does not appear to have been previously studied. To do so is a major objective of this work.

As pointed out in [1], at relatively early times subsequent to the ignition of a fire the unconfined ceiling fire scenario depicted in Fig. 1 is relevant to enclosure fire scenarios where ceiling surfaces are inherently confined. Also, as discussed in [3, 4], even at later times during enclosure fires when the inevitable upper layer of elevated temperature gases has partially filled the enclosure, analytic methods for describing the unconfined ceiling fire scenario can still be directly used to predict continuing changes in the fire-generated enclosure response.

This work represents the first stage of an investigation of the response of real ceiling materials above typical hazardous fires. This first-stage effort deals with the response of ceilings in the unconfined ceiling fire scenario. Subsequent stages will use the present procedures together with the ideas of [3, 4] to study confined ceiling, enclosure fire scenarios.

Model for the Ceiling Response

Figure 1 is a sketch of the fire scenario under consideration. A fire, modeled as a point source of total time-dependent energy release rate $Q(t)$, is initiated a distance H below an expansive (unconfined) ceiling. Because of their elevated temperature the products of combustion of the fire are driven upward by buoyancy. These products generate a turbulent plume of upward-moving, elevated temperature gases. The fraction of Q which effectively acts to heat the plume gases and drive the plume's upward momentum is taken to be $1-\lambda_r$, where λ_r is approximately the fraction of Q lost by radiation from the combustion zone.

Heat Transfer at the Lower Ceiling Surface. As indicated in Fig. 1, the radiant energy $\lambda_r Q$ is assumed to be radiated uniformly outward from the fire. The radiant flux $q''_{rad\text{-}fire}$, incident on the lower surface of the ceiling at a distance r from the plume–ceiling impingement point, is, therefore,

$$q''_{rad\text{-}fire} = [\lambda_r Q/(4\pi H^2)][1+(r/H)^2]^{-3/2} \quad (1)$$

The fire plume gases continue to rise and entrain air from the ambient environment. When their upward movement is blocked by the ceiling, they spread radially outward forming a relatively thin, turbulent, ceiling jet.

As was done in equation (1), radiation absorption and emission of the ceiling jet will be neglected throughout this paper.

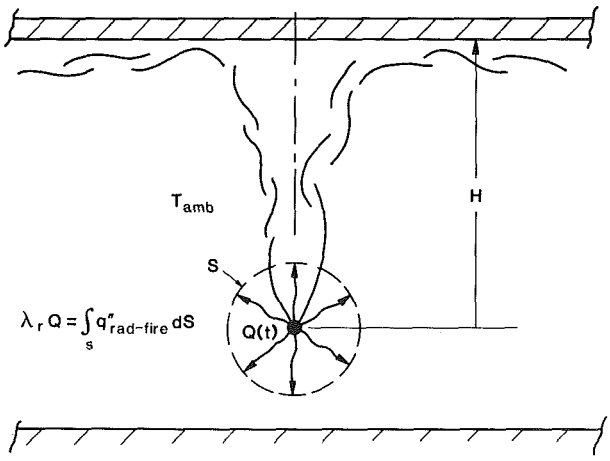

Fig. 1 The unconfined ceiling fire scenario

Contributed by the Heat Transfer Division for publication in the JOURNAL OF HEAT TRANSFER. Manuscript received by the Heat Transfer Division February 3, 1986.

In the case of the early time, unconfined ceiling, fire scenario under consideration, this neglect is justified, for example, if one anticipates effective ceiling jet thicknesses of the order of a few tenths of a meter and absorption coefficients of the order of a few tenths of an inverse meter.

Heat is transferred by convection from the ceiling jet to the lower surface of the ceiling. At an arbitrary time after ignition and up to moderate values of r/H, this radial-dependent heat flux, $q''_{\text{conv},L}$, can be estimated from [1, 2]

$$q''_{\text{conv }L} = h_L(T_{ad} - T_{s,L}) \tag{2}$$

where $T_{s,L}$ is the then-current, absolute temperature of the lower surface of the ceiling, and T_{ad}, a characteristic gas temperature, is the temperature that would be measured adjacent to the lower ceiling surface under the condition of an adiabatic ceiling. h_L and T_{ad} of equation (2) can be estimated [2] from

$$h_L/\tilde{h} = \begin{cases} 8.82\text{Re}_H^{-1/2}\text{Pr}^{-2/3}[1-(5.0-0.284\text{Re}_H^{0.2})(r/H)], \\ 0 \le r/H < 0.2 \\ \\ 0.283\text{Re}_H^{-0.3}\text{Pr}^{-2/3}(r/H)^{-1.2}\dfrac{(r/H-0.0771)}{(r/H+0.279)}, \\ 0.2 \le r/H \end{cases} \tag{3}$$

$$\frac{(T_{ad}-T_{\text{amb}})}{T_{\text{amb}}Q_H^{*2/3}} = \begin{cases} 10.22 - 14.9\, r/H, \; 0 \le r/H \le 0.2 \\ \\ 8.39 f(r/H), \; 0.2 \le r/H \end{cases} \tag{4}$$

$$f(r/H) = \frac{1 - 1.10(r/H)^{0.8} + 0.808(r/H)^{1.6}}{1 - 1.10(r/H)^{0.8} + 2.20(r/H)^{1.6} + 0.690(r/H)^{2.4}}$$

where

$$\tilde{h} = \rho_{\text{amb}} C_p g^{1/2} H^{1/2} Q_H^{*1/3}; \; \text{Re}_H = g^{1/2} H^{3/2} Q_H^{*1/3}/\nu_{\text{amb}}$$
$$Q_H^* = (1-\lambda_r)Q/[\rho_{\text{amb}} C_p T_{\text{amb}} (gH)^{1/2} H^2] \tag{5}$$

and where Pr, ρ_{amb}, C_p, and ν_{amb} are the Prandtl number (taken to be 0.7), density, specific heat, and kinematic viscosity of the ambient air. In the above, Q_H^* is a dimensionless number representing the relative strength of the fire, and Re_H is a characteristic Reynold's number of the fire plume at the elevation of ceiling impingement.

As time goes on, $T_{s,L}$, initially at T_{amb}, begins to increase. At all times this surface is assumed to diffusely radiate to the initially ambient temperature, expansive, lower floor surface and to exposed surfaces or furniture or other items. In response to this radiation the temperatures of these surfaces also increase with time. For times of interest here, it is assumed that these "floor" temperature increases are always relatively small compared to the characteristic increases of $T_{s,L}$. Accordingly, at a given radial position of the lower ceiling surface, the net radiation exchange between the ceiling and the floor, furniture, etc., surfaces below can be approximated by a net reradiation flux

$$q''_{\text{rerad},L} = \sigma(T_{s,L}^4 - T_{\text{amb}}^4)/(1/\epsilon_L + 1/\epsilon_{\text{floor}} - 1) \tag{6}$$

where σ is the Stefan–Boltzmann constant and ϵ_L and ϵ_{floor} are the effective emittance/absorptance of the assumed grey, lower ceiling surface and floor/furniture surfaces, respectively.

Heat Transfer From the Upper Ceiling Surface. Heat is transferred through the ceiling, and eventually the temperature of its upper surface, assumed to be exposed to a constant T_{amb} environment and cavity surface, begins to rise.

The rate of heat transfer from the upper surface has convective and radiative components, $q_{\text{conv},U}$ and $q_{\text{rerad},U}$, respectively, which can be estimated from

$$q_{\text{conv},U} = h_U(T_{s,U} - T_{\text{amb}}); q_{\text{rerad},U} = \sigma(T_{s,U}^4 - T_{\text{amb}}^4)/(1/\epsilon_U + 1/\epsilon_{\text{cav}} - 1) \tag{7}$$

where $T_{s,U}$ is the instantaneous, radius-dependent upper surface temperature, h_U is an effective heat transfer coefficient, and ϵ_U and ϵ_{cav} are the effective emittance/absorptance of the assumed grey, upper ceiling and cavity surfaces, respectively. The value for h_U to be used in the present calculations will be [5]

$$h_U = 1.675\,|T_{s,U} - T_{\text{amb}}|^{1/3} \text{W/m}^2(T \text{ in K}) \tag{8}$$

The Basis of the Lower Surface Convective Heat Transfer Model. The development of the equation (2)–(4) model for $q''_{\text{conv},L}$, with h_L based on $T_{ad} - T_{s,L}$, was motivated by results of a series of small scale, constant Q, fire plume-driven ceiling

Nomenclature

C_p = specific heat at constant pressure
g = acceleration of gravity
H = fire-to-ceiling distance
$\tilde{h}$ = characteristic heat transfer coefficient
h_L, h_U = convective heat transfer coefficient at lower and upper surface
k = thermal conductivity
N = number of ceiling node points
Q = fire's energy release rate
Q_H^* = a dimensionless value of Q
$q''_{\text{conv},L}$, $q''_{\text{conv},U}$ = convection from the lower and upper surface
q''_L, q''_U = net incident flux to lower and upper surface
$q''_{\text{rad-fire}}$ = direct radiation from the fire
$q''_{\text{rerad},L}$, $q''_{\text{rerad},U}$ = net reradiation from the lower and upper surface
Re_H = plume Reynold's number, equation (5)
r = radius from plume-ceiling impingment point
T = absolute temperature field of ceiling
T_{ad} = temperature adjacent to an adiabatic ceiling
T_{amb} = ambient temperature
$T_{s,L}$, $T_{s,U}$ = absolute temperature of lower and upper surface
t = time from ignition
Z = in-depth ceiling coordinate
α = thermal diffusivity
δZ = distance between node points in ceiling
ϵ_L, ϵ_U, ϵ_{floor}, ϵ_{cav} = emittance/absorptance of grey lower, upper, floor and cavity grey surfaces
λ_r = fraction of Q radiated from fire
λ_{conv} = fraction of Q convected to ceiling
ν_{amb} = ambient kinematic viscosity
ρ_{amb} = ambient density
σ = Stefan–Boltzmann constant

jet experiments reported in [6]. In those tests an unconfined steel plate ceiling was heated from ambient to steady-state conditions. Correlation of the data revealed that $h_L/\bar{h}$ could be reasonably modeled as a function only of r/H, and was relatively independent of t, Q, and H. (Re_H for these experiments varied in the narrow range $1.5 \times 10^4 < \mathrm{Re}_H < 2.0 \times 10^4$.) Motivated by the observation in [7] that inertial forces dominate buoyancy forces from plume impingement to moderate r/H in plume-driven ceiling jets, and based on several related considerations, this small-scale experimental result was generalized in [1, 2] to yield the present results of equations (2)–(4).

It is of interest to relate the model of equations (2)–(4) to $q''_{\mathrm{conv},L}$ data acquired in tests of [8, 9], similar in scale to those of [6], but with the unconfined ceiling uniformly at $T_{s,L} = T_{\mathrm{amb}}$. Those heat flux measurements would relate directly to fluxes to ceilings under transient conditions, but only at early times into the heating.

Correlations in [8, 9], successfully supported by an integral analysis of the ceiling jet flow, can be recast into the equation (2)-type form. Thus, those studies conclude that

For $t = 0$, i.e., $T_{s,L} = T_{\mathrm{amb}}$:

$$q''_{\mathrm{conv},L} = (Q/H^2)\mathrm{Re}_H^{-1/2}\mathrm{Pr}^{-3/5}(1-\lambda_r)^{1/6}w(r/H) = h_L(T_{ad} - T_{s,L})$$

$$w(r/H) = \begin{cases} 38.6, & 0 \le r/H < 0.16 \\ 1.88(r/H)^{-1.65}, & 0.16 \le r/H \end{cases}$$

Since local values of T_{ad} could not be expected to provide a good approximation to local maximum gas temperatures at $t = 0$, one may argue that the right-hand formulation in the above, albeit correct (by definition), is artificial. However, as $T_{s,L}$ increases with time, T_{ad} would indeed begin to provide a reasonable approximation to the maximum gas temperature, and the utility of an equation (2) formulation would be justified. If, as suggested by the transient heating experiments of [6], the $h_L/\bar{h}$ distribution does not change significantly with time, then in a remarkably simple and unifying way the heat transfer model being used here provides a means of estimating $q''_{\mathrm{conv},L}$ and the transient thermal response of the ceiling not just at $t = 0$, but for all times during the course of the heating. The idea of a constant $h_L/\bar{h}$ distribution is a major feature of the equation (2) formulation. However, as discussed in [2], the equation (3) estimate for h_L is derived using data sources other than those of [8, 9]. Thus, for example, except at $r/H = 0$, the h_L that would be obtained from the above equation with the use of equation (4) for T_{ad} would have a different Re_H dependence than would the h_L of equation (3).

While it is reasonable to use the $q''_{\mathrm{conv},L}$ estimate of equations (2)–(4) in the present work and as an algorithm in compartment fire model computer codes, it is clear that further development of the integral methods of [7–9] will lead to significant future advances in this regard.

The Boundary Value Problem for the Ceiling, and the Method of Its Solution. The absolute temperature field $T(r,t)$ in the ceiling material is assumed to be governed by the Fourier heat conduction equation. Initially, the ceiling is taken to be of uniform temperature T_{amb}. The rates of heat transfer to the lower and upper surfaces, q''_L and q''_U, respectively, are given by

$$Q''_L = q''_{\text{rad-fire}} + q''_{\mathrm{conv},L} - q_{\mathrm{rerad},L};\ q''_U = -q_{\mathrm{conv},U} - q_{\mathrm{rerad},U} \quad (9)$$

For times of interest here, radial gradients of q''_L and q''_U are assumed to be small enough so that conduction in the ceiling is quasi-one dimensional in space, i.e., $T = T(Z, t; r)$, where Z is the in depth ceiling coordinate.

An algorithm for solving the above problem was developed. Q, λ_r, H, properties of the ambient environment, ceiling thickness, and material properties are specified along with the position of radial locations of interest. The solution to the heat conduction equation for the ceiling at every specified radial position is by finite differences. The algorithm for this was taken from [10, 11]. For a given calculation, $N \le 20$ equally spaced points are positioned at the surfaces and through the thickness of the ceiling. The spacing δZ is selected to be large enough (based on a maximum time step) to insure stability of the calculation. Throughout a calculation, time steps are made small enough so that, at a given lower surface node, the temperature increase for each time step never exceeds one percent of the then-current value of T at that node.

Convective Heat Transfer From the Plume Gases – Enthalpy Flux in the Ceiling Jet. A key parameter in enclosure fire modeling is the net rate of heat transfer from the plume–ceiling jet gases to the enclosure boundaries. The value of this can play a very important role in a determination of the temperature history of the upper "smoke" layer of enclosure fires. For the unconfined ceiling scenario, one anticipates that convection dominates this heat transfer and, as mentioned earlier, that it is reasonable to neglect radiative transfer to and from the relatively thin ceiling jet.

The rate of convective heat transfer to the lower ceiling surface out to radius r will be expressed as a fraction, λ_{conv}, of Q according to

$$\lambda_{\mathrm{conv}}(r, t)Q(t) = 2\pi \int_0^r q''_{\mathrm{conv},L}(r, t)r\,dr \quad (10)$$

Thus, of the total instantaneous energy release rate Q of the fire, $\lambda_r Q$ is lost to bounding surfaces of the enclosure by radiation from the combustion zone and, within a circle of radius r, $\lambda_{\mathrm{conv}}Q$ is lost by convection from the ceiling jet.

At a given radius, the total enthalpy flux of the ceiling jet is $(1 - \lambda_r - \lambda_{\mathrm{conv}})Q$. A reliable estimate for the enthalpy flux of these diluted products of combustion is required in enclosure fire modeling since these are the ceiling jet gases which, when eventually blocked by a vertical wall, will be turned back to develop into the potentially hazardous upper smoke layer.

In the present calculations the value of λ_{conv} at an arbitrary value of r is obtained as follows: At a given instant of time in the calculation, $q''_{\mathrm{conv},L}$ is approximated by a piecewise linear function of r which passes through the $q''_{\mathrm{conv},L}$ values previously computed at the selected radial positions. This function is then integrated according to equation (10) to yield λ_{conv} as a piecewise quadratic function of r.

Radiative Flux From the Ceiling to Lower Targets. One measure of the hazard of an enclosure fire is the radiative flux to nonburning combustible target items. The main concern is the onset of remote ignitions which could rapidly lead to flashover. Radiation from the combustion zone contributes to the remote target flux, but even for items shielded from direct fire radiation, illumination from lower ceiling surface radiation alone can lead to flashover. This latter radiative flux will decrease with distance from the fire and will vary with the orientation of the target surface.

The present algorithm includes a capability for calculating downward radiative flux from the ceiling to horizontal target surfaces. This is obtained with the use of the commonly available view factor between a disk (and, from this, an annulus), and a parallel but otherwise arbitrarily positioned differential target surface element. At a given instant of time in a calculation, this view factor is used to compute the total ceiling-to-target radiant flux as follows: The ceiling is divided into a disk (center at the plume impingement point) of radius $0.1H$, and 99 concentric, contiguous annuli of ring width $0.1H$. The temperature of the disk and of each annulus is assumed uniform at the position of its average radius, at which location the temperature is estimated from linear interpolations between previously computed, current ceiling

Table 1 Description of the four ceiling constructions

Material	Thickness m	k, $Wm^{-1}K^{-1}$	α, $m^2 s^{-1}$	Reference
Fiber insulation board	0.0127	0.04	1.2×10^{-7}	[14]
Gypsum board	0.0127	0.134	1.577×10^{-7}	[11]
Concrete	0.0508	0.92	4.2×10^{-7}	[14]
Steel	0.003175	46.	1.20×10^{-7}	[15]

Table 2 Description of the six fire scenarios

H, m \ Q, kW =	101.2	1000.	9883.	0.1054 $(t/s)^2$ (t in s)
2.0	x $Q_H^* = 0.01048$	x $Q_H^* = 0.1035$		x
5.0		x $Q_H^* = 0.01048$	x $Q_H^* = 0.1035$	x

temperatures. Appropriate view factors are used, and the radiative flux from the disk and from each annulus to the target location of interest is computed and summed sequentially starting from the plume axis. The summation is stopped when the flux contribution of an annulus is less than one percent of the largest of the previous single annuli contributions at the current time step. If the latter condition is still not achieved by the outermost annulus (i.e., at $r/H = 10.$), then the entire calculation for that target location is assumed to be invalid. Note that this computation can exceed the moderate r/H limitation of equation (2).

Calculations for the Response of a Variety of Different Ceiling Constructions to Different Fire Threats

Descriptions of the Ceiling Constructions and Fire Threats. The algorithm described in the last section was exercised for fire scenarios involving four typical ceiling constructions identified by ceiling material and thickness in Table 1, and six fire scenarios identified by the Q–H pairs marked with an x in Table 2. The response of each of the ceiling constructions to each of the fire scenarios was calculated. Each of these 24 calculations was carried out to 300 s. In all calculations T_{amb}, ρ_{amb}, C_p, and ν_{amb} were taken as 300K, 1.177 kg/m^3, 1004. Ws/(kgK) and 0.1568×10^{-4} m^2/s, respectively; $\epsilon_U = \epsilon_L = \epsilon_{floor} = \epsilon_{cav} = 1$ (black body surfaces); and $\lambda_r = 0.35$. For typical hazardous flaming fires, λ_r does not vary significantly from this value [12]. The ceiling response was computed at 28 values of r, where the r/H for these were $r/H = 0.$, 0.1, 0.2, 0.3, 0.4, 0.5, 0.6, 0.7, 0.8, 0.9, 1.0, 1.25, 1.50, 1.75, 2.00, 2.25, 2.50, 2.75, 3.00, 3.5, 4.0, 4.5, 5.0, 6.0, 7.0, 8.0, 9.0, 10.0.

The fire scenarios of Table 2 involve the two fire-to-ceiling distances 2 m and 5 m, and four different Q's. $H = 2$ m would relate, say, to slightly elevated fires in residential-type occupancies, where a typical floor-to-ceiling height is 2.4 m. $H = 5$ m relates to fires in larger spaces such as places of assembly or commercial storerooms.

Besides the Q–H pair which defines a given fire scenario, the corresponding value of Q_H^* is also displayed in Table 2. Note that the "odd" values $Q = 101.2$ kW at $H = 2$ m and 9883 kW at $H = 5$ m were chosen to exactly reproduce the two Q_H^* values of 0.01048 and 0.1035, which correspond to the 1000 kW fires of $H = 5$ m and $H = 2$ m, respectively. Thus, for example, effects of a dimensionless $Q_H^* = 0.01048$ fire strength is predicted here for two dramatically different physical fire scenarios.

Of the different Q's, the 101.2 kW level is characteristic of fires in small chairs or large wastepaper baskets; the 1000 kW level is characteristic of peak levels of fires in bedding or in upholstered couches; and the 9883 kW level is characteristic of a 1 – 1.5 m^2 fuel spill fire, or of peak levels of fires in a variety of typical arrangements of stacked commodities, as identified in Table 4.1 of [13]. Finally, as identified in Table 4.2 of [13], the t^2 fire of Table 2 is characteristic of the growth stages of fires in various diverse arrangements of combustibles, e.g., wood pallets stacked 3 m high.

General Results of the Calculations. Some results of the aforementioned calculations are presented in Fig. 2(*a–f*). Each one of the six figure groups is associated with the ceiling responses to one of the six fire threats. Plots of three of the several variables of the ceiling responses, which were obtained during the course of a calculation, are presented in each figure group, one variable for each figure of the group. The left-hand figures present plots of the peak ceiling temperature increase $T_{s,L}(r=0, t) - T_{amb}$ versus t. The center figures present plots of the radial distribution of the normalized $T_{s,L}$'s, $[T_{s,L}(r, t) - T_{amb}]/[T_{s,L}(r=0, t) - T_{amb}]$, for $t = 10$ s and 300 s (note that the discontinuities in the slopes of these plots at $r/H = 0.2$ reflect the corresponding discontinuities in the h_L and T_{ad} approximations of equations (3) and (4)). The right-hand figures present plots of $\lambda_{conv}(r, t)$ also for 10 s and 300 s. Although not presented here, it is noteworthy that plots of the numerical results in the center figures were also obtained in log-log coordinates, and that no unifying trends were apparent.

Discussion of Overall Results. The results of Figs. 2(*a–f*) provide insight into the early time response of real and significantly different ceiling constructions to typical hazardous fires developing in expansive enclosure geometries. Within the specific limitations discussed above, the computation algorithm can be used to estimate the response of any other nonburning ceiling construction or arbitrarily specified Q–H combinations.

Results for the two pairs of identical Q_H^* fire scenarios can be compared in Figs. 2(*a*) and 2(*c*) ($Q_H^* = 0.01048$) and in Figs. 2(*b*) and 2(*d*) ($Q_H^* = 0.1035$). Considering the significant differences in the values of Q and H, the lower ceiling surface temperature responses (i.e., the left and center figures) for a given Q^* are remarkably similar. This is especially true for the $r = 0$ temperature histories. Thus, it appears that for constant Q fires, and for a fairly wide range of H values, it may be possible to describe the unconfined ceiling impingement point temperature response with reasonable accuracy by specifying Q_H^* alone instead of the Q–H (or Q_H^*–H) pair.

The response of the ceilings is strongly influenced by the characteristic dimension H of the enclosure fire problem. Thus, the center plots of Fig. 2 indicate significant variation of $T_{s,L}$ with r/H variations of the order of 1. When attempting to

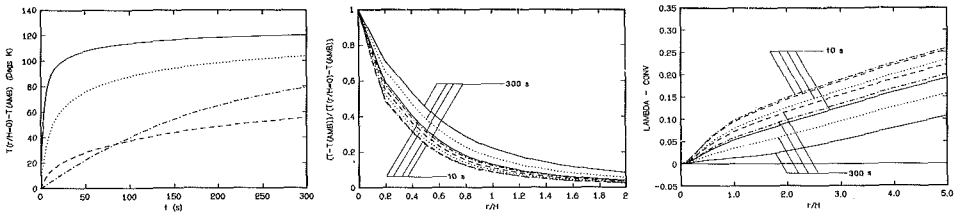

(a) Q,H=101.2kW, 2m

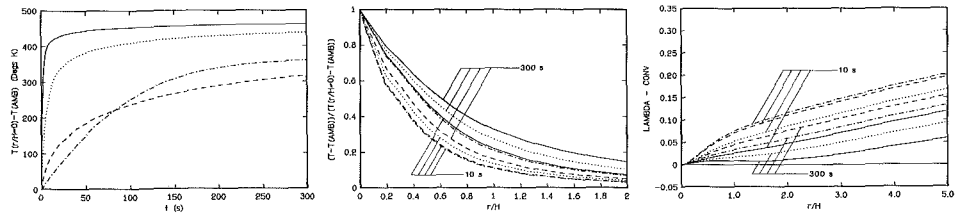

(b) Q,H=1000kW,2m

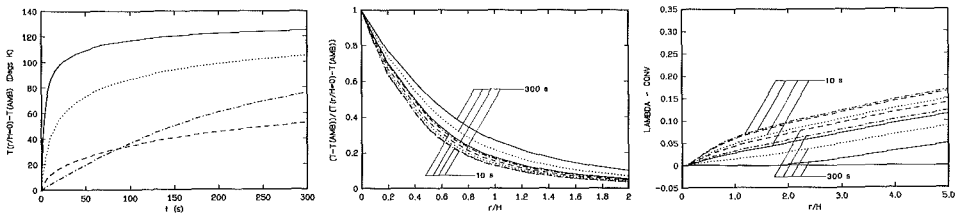

(c) Q,H=1000kW,5m

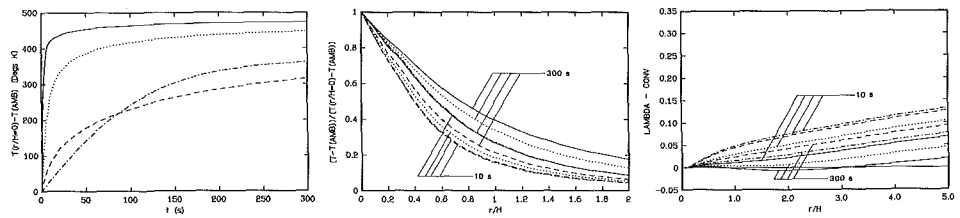

(d) Q,H=9883kW,5m

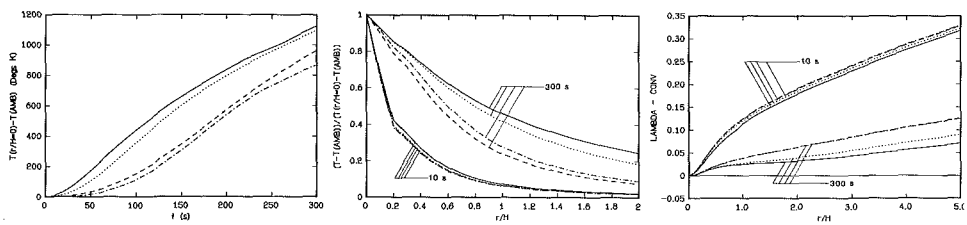

(e) Q,H=0.1054 t^2 kW, 2 m (t in seconds)

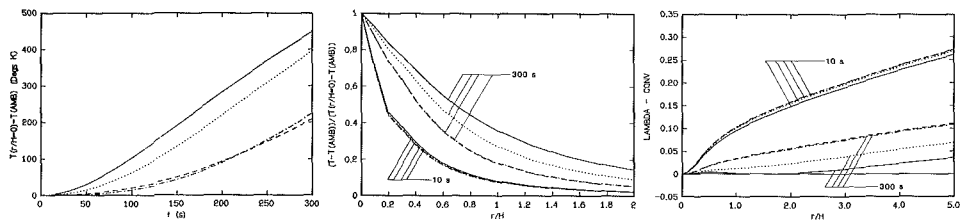

(f) Q,H=0.1054 t^2 kW, 5 m (t in seconds)

Fig. 2 Responses of different ceiling constructions of Table 1 (insulation board ———, gypsum board . . . , concrete ···, steel — · —) to fire scenarios of Table 2: (*a*) *Q*, *H* = 101.2 kW, 2 m; (*b*) *Q*, *H* = 1000 kW, 2 m; (*c*) *Q*, *H* = 1000 kW, 5 m; (*d*) *Q*, *H* = 9883 kW, 5 m; (*e*) *Q*, *H* = 0.1054 t^2 kW, 2 m; (*f*) *Q*, *H* = 0.1054 t^2 kW, 5 m (*t* in s)

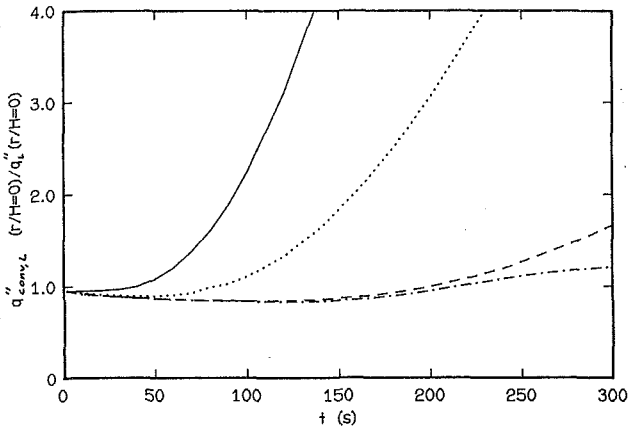

Fig. 3 Plot of $q''_{conv,L}$ $(r=0, t)/q''_L$ $(r=0, t)$ for different ceiling constructions of Table 1 (see legend of Fig. 2) to the fire scenario Q, $H=0.1054t^2$ kW, 2 m (t in s)

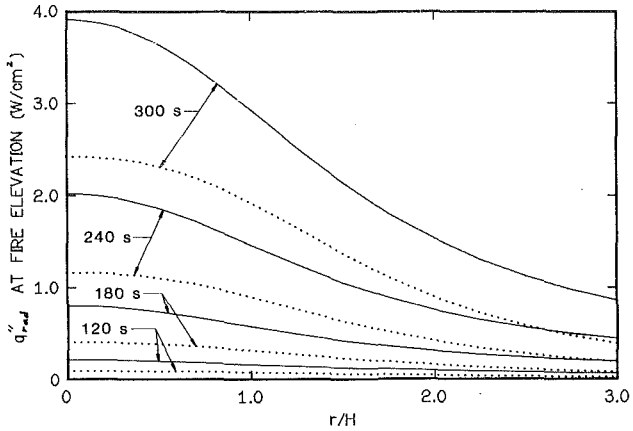

Fig. 5 Plots of radiant flux to remote targets from the gypsum board ceiling responding to the fire scenario Q, $H=0.1054\ t^2$ kW, 2 m; nonzero $q''_{conv,L}$ ——, $q''_{conv,L}=0$ . . . . (t in s)

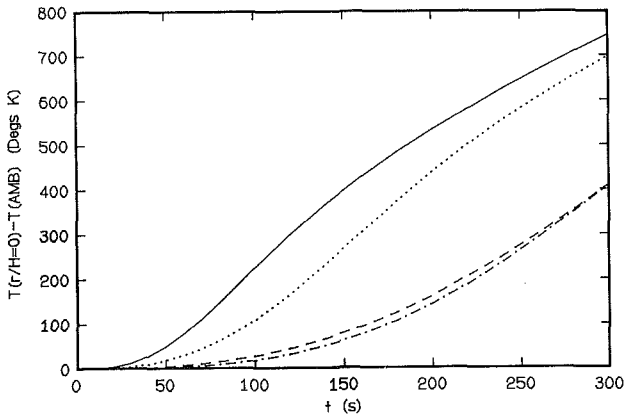

Fig. 4 Plot of $T_{s,L}$ $(r=0, t)-T_{amb}$ for different ceiling constructions of Table 1 (see legend of Fig. 2) to the fire scenario Q, $H=0.1054\ t^2$ kW, 2 m with $q''_{conv,L}=0$ (t in s)

model enclosure fire environments, this suggests that calculations of the ceiling response in terms of a simple spatial average may not be adequate.

On the Importance of Convective Heat Transfer

The significant impact of radiation heat transfer on enclosure fire environments is well known. The corresponding importance of convective heat transfer, however, is not clear and enclosure fire models have taken this effect into account in only the most rudimentary manner.

Predicting Ceiling Temperatures. The importance of ceiling surface temperatures to fire hazard analyses is mentioned in the introduction. The present calculations indicate that, in general, convective heat transfer to the lower ceiling surface is significant in the sense that reliable estimates of its values are required if such temperature predictions are to be made with reasonable accuracy.

To illustrate this, plots of $q''_{conv,L}$ $(r=0, t)/q''_L(r=0, t)$ are presented in Fig. 3 for the previously calculated 2 m, $Q\sim t^2$ fire scenario. The result is typical of that of the other fire scenarios considered here, in that at all times considered, $q''_{conv,L}(r, t)$ at $r=0$ (and indeed, at all r) is generally of the order of $q''_L(r, t)$.

To further illustrate the significance of $q_{conv,L}$ on $T_{s,L}$, the ceiling response to the 2 m, $Q\sim t^2$ fire scenario was calculated a second time under a condition of $q_{conv,L}=0$. The results for $T_{s,L}(r=0, t)-T_{amb}$ are plotted in Fig. 4, which is to be compared to the left-hand plots of Fig. 2(*e*). For example, consider a papered gypsum board ceiling with an ignition temperature of 700 K. Then, for the 2 m, $Q\sim t^2$ fire scenario, the left-hand gypsum board plot of Fig. 2(*e*) indicates that ignition of the ceiling will occur at approximately 110 s while the calculations of Fig. 4, which neglect convection, indicate that ignition will occur at 190 s.

Radiation to Remote Targets. Another key to successful fire hazard analysis is prediction of the ignition of target surfaces removed from the immediate vicinity of a fire's combustion zone. Such ignition would typically occur on account of radiant fluxes from the hot ceiling surface, from the upper hot smoke layer, and from the flame itself.

Depending on target orientation and elevation, direct flame radiation, which diminishes inversely as the square of the distance from the combustion zone, could be significant for targets close to the fire. This component of radiant flux to remote targets will not be considered here.

At early times during enclosure fires when smoke layer accumulations are still not significant and when the present type of unconfined ceiling calculations are directly applicable, radiation from these layers will be negligible. Even when smoke layer thicknesses become a significant fraction of H, they can still be optically thin to the extent that gas radiation to remote target surfaces will not be significant. Under the two latter circumstances (at least), and at targets sufficiently removed from walls, overhead radiation will be determined by the temperature distribution of the lower ceiling surface.

In predicting remote ignition of targets under expansive ceilings, the fact that ceiling temperature distributions are distinctly nonuniform is key. Thus, one expects that the peak value of $T_{s,L}$ at $r=0$, as well as its r distribution, is important in establishing the levels of remote target irradiation. Also, one anticipates that significant reductions of $T_{s,L}$ with r, suggested in the center plots of Fig. 2, lead to a significantly reduced threat of remote ignition far from the fire.

Based on these observations and on earlier remarks, it would appear that the radial dependence of convective heat transfer to the lower ceiling surface can play an important role in predicting remote ignition/flashover threats during enclosure fires.

To illustrate this conclusion quantitatively, the overhead radiant flux to horizontal remote targets a distance H below the gypsum board ceiling is plotted versus r/H and at different times in Fig. 5 for the 2 m, $Q\sim t^2$ fire. These fluxes were obtained using the $T_{s,L}$ presented in the left and center plots of Fig. 2(*e*), and the target radiation calculation scheme de-

scribed earlier. For comparison, the radiation flux for the same ceiling construction and fire, but with $q_{conv,L}=0$ (i.e., corresponding to the gypsum $T_{s,L}$ of Fig. 4), is also plotted in Fig. 5.

As can be seen in Fig. 5, there is a significant reduction of overhead flux to targets which are removed distances of the order of H from the fire. Also, neglect of convection appears to lead to serious underestimates of peak fluxes when they reach typical hazardous levels of 2 W/cm^2 and above. For example, at 300 s, the peak predicted flux level of 3.91 W/cm^2 is reduced to 62 percent of its value (2.42 W/cm^2) if convection is neglected.

Net Heat Transfer From the Enclosure Gases. When λ_{conv} is a significant fraction of $1-\lambda_r$ (which, as assumed here, is typically equal to 0.65) then the net rate of heat transfer from the enclosure gases to ceilings would definitely be required to predict temperature histories of enclosure fire environments. However, if λ_{conv} is relatively small, then such heat transfer estimates may not be important.

The right-hand plots of Fig. 2 indicate that λ_{conv} is of the order of 0.1 or less for small to moderate r/H. Except for very early times, this is also true for larger r/H. For the purposes of estimating net enthalpy flux in the ceiling jet this would seem to suggest that accurate estimates of the convective loss to the ceiling may not be critical in the calculation of average, enclosure smoke layer temperatures. Careful scrutiny of the situation does not, however, provide any real confidence in such a conclusion.

For early times, when it is hoped that the present unconfined-ceiling type of calculation provides reliable estimates of ceiling response, modeling of fire growth is key. In this regard early time ceiling responses to the $Q\sim t^2$ fires of Figs. 2(*e*) and 2(*f*) are particularly relevant. But it is exactly for these fire scenarios, and at early times, that the values of λ_{conv} are relatively large. Furthermore, the most direct practical use for early time calculations would be for prediction of fire detector/sprinkler link response. It is exactly for such a purpose that the details of the convection problem (i.e., the time-dependent temperature and velocity field of the ceiling jet) are likely to play an important role.

For later times, when upper layer growth becomes a prominent feature of the enclosure environment, there is an indication in Figs. 4 and 5 of [3] that there may be a significant enhancement in values of λ_{conv} over unconfined ceiling values. As indicated in the introduction, by using the procedures developed here together with ideas presented in [3, 4], the next stage of this investigation will, hopefully, provide more definitive insight into this question.

Summary of Conclusions and Future Work

The algorithm developed here was used to predict the response of a variety of realistic ceiling constructions to different fire scenarios. The algorithm is designed to be useful up to moderate values of r/H and at times subsequent to ignition which are small enough (dependent on the size of the enclosure, and on the size and location of the fire) that the unconfined ceiling scenario of Fig. 1 is still relevant. Besides the specific results presented in the figures, the following is a summary of some general results which were indicated by the calculations.

Significant variations in ceiling response and lower target irradiation occur over intervals of radial distance from the fire of the order of H.

Some quantitative similarity in ceiling response is obtained for constant Q fire scenarios which have identical Q_H^*. For such scenarios, and for a fairly wide range of H, it appears that unconfined ceiling impingement point temperature response can be predicted with reasonable accuracy by specifying the single, dimensionless, fire strength parameter Q_H^*.

Convective heating along with radiative heating and cooling has a significant effect on the magnitude of the ceiling's lower surface temperature, and, as a result, on the magnitude of heat transfer by radiation from this surface to targets below.

Net convective heat transfer to enclosure ceilings can be a significant fraction of Q at early times during growing fires. At later times, when an elevated temperature, upper smoke layer starts to fill an enclosed space, the situation in this regard is unclear. It is hoped that this situation will be clarified in the next stage of this investigation.

In general, the results of the calculations presented here are plausible, and they provide useful insight into the response of real ceilings to hazardous fires. Nevertheless, no data presently exist to compare theory with experiment. In this regard, a program at the National Bureau of Standards to measure ceiling response in reduced-scale fire experiments is now underway.

Acknowledgments

This work was supported by the U.S. Department of Health and Human Services, The Bureau of Mines and the National Park Service of the U.S. Department of Interior, and the Federal Aviation Administration of the U.S. Department of Transportation.

References

1 Cooper, L. Y., "Heat Transfer From a Buoyant Plume to an Unconfined Ceiling," ASME JOURNAL OF HEAT TRANSFER, Vol. 104, 1982, pp. 446–451.

2 Cooper, L. Y., and Woodhouse, A., "The Buoyant Plume-Driven Adiabatic Ceiling Temperature Revisited," ASME JOURNAL OF HEAT TRANSFER, Vol. 108, 1986, pp. 822–826.

3 Cooper, L. Y., "Convective Heat Transfer to Ceilings Above Enclosure Fires," *19th Symp. (Inter.) on Combustion*, 1982, pp. 933–939.

4 Cooper, L. Y., "A Buoyant Source in the Lower of Two, Homogeneous, Stably Stratified Layers," *20th Symp. (Inter.) on Combustion*, 1984, pp. 1567–1573.

5 Yousef, W. W., Tarasuk, J. D., and McKeen, W. J., "Free Convection Heat Transfer from Upward-Facing Isothermal, Horizontal Surfaces," ASME JOURNAL OF HEAT TRANSFER, Vol. 104, 1982, pp. 493–499.

6 Veldman, C. C., Kubota, T., and Zukoski, E. E., "An Experimental Investigation of the Heat Transfer From a Buoyant Gas Plume to a Horizontal Ceiling – Part 1: Unobstructed Ceiling," Cal. Institute of Technology, report prepared for NBS/CFR, NBS-GCR-77-97, 1975.

7 Alpert, R. L., "Turbulent Ceiling-Jet Induced by Large-Scale Fires," Combustion Science and Technology, Vol. 11, 1975, pp. 197–213.

8 You, H-Z., and Faeth, G. M., "Ceiling Heat Transfer During Fire Plume and Fire Impingement," *Fire and Materials*, Vol. 3, 1979, pp. 140–147.

9 You, H-Z., "An Investigation of Fire-Plume Impingement on a Horizontal Ceiling: 2 – Impingement and Ceiling Jet Regions," *Fire and Materials*, Vol. 9, 1985, pp. 46–55.

10 Emmons, H. W., "The Prediction of Fires in Buildings," *17th Symp. (Inter.) on Combustion*, 1979, pp. 1101–1111.

11 Mitler, H. E., and Emmons, H. W., "Documentation for the Fifth Harvard Computer Fire Code," Home Fire Project Tech. Rpt. 45, Harvard University, 1981.

12 Cooper, L. Y., "A Mathematical Model for Estimating Available Safe Egress Time in Fires," *Fire and Materials*, Vol. 6, 1982, pp. 135–144.

13 NFPA 204M, *Guide for Smoke and Heat Venting*, National Fire Protection Association, 1982.

14 Thomas, P. H., and Bullen, M. L., "On the Role of $k\rho C$ of Room Lining Materials in the Growth of Room Fires," *Fire and Materials*, Vol. 3, 1979, pp. 68–73.

15 Carslaw, H. S., and Jaeger, J. C., *Conduction of Heat in Solids*, 2nd ed., Oxford, 1959.

Selective Radiative Preheating of Aluminum in Composite Solid Propellant Combustion

M. Q. Brewster[1]
Assistant Professor of Mechanical Engineering.
Assoc. Mem. ASME

R. Patel[1]
Graduate Research Assistant.

Department of Mechanical and Industrial Engineering,
University of Utah,
Salt Lake City, UT 84112

A two-phase model has been developed to study aluminum (Al) particle preheating through selective radiation absorption in composite solid propellants. The two phases considered are one strongly absorbing particle (Al) phase and another weakly absorbing matrix (ammonium perchlorate (AP), binder and catalyst particle) phase surrounding the Al phase. Separate energy balance equations for the Al and matrix phases are developed. Both the matrix and the Al phase are assumed to be nonemitting, anisotropically scattering, absorbing media. The parameters identified which strongly influence Al preheating and melting are Al size, mass fraction, burn rate, and level of incident radiant flux. It was found that large Al mass fractions and small Al particle sizes promote lower Al temperatures. The effect of adding submicron iron oxide burn rate catalyst particles on aluminum preheating was also investigated. It was found that the addition of small amounts of catalyst can theoretically reduce Al temperatures significantly by dominating the optical properties. These results should prove useful to propellant formulators in trying to reduce the problem of unwanted Al agglomeration.

Introduction

It has been observed that during the combustion of aluminized (aluminum-containing) composite solid propellants, some of the aluminum particles agglomerate before they leave the surface of the propellant [1-4]. Typically, aluminum particles with mean diameters of 5-30 μm may be mixed in the propellant formulation. Yet combustion bomb studies [1-4] indicate that aluminum agglomerates as large as 300 μm leave the burning propellant surface. This agglomeration results in two kinds of loss. The first loss is the energy that escapes due to the fact that the large agglomerates have insufficient residence time to burn completely. The second loss is the two-phase flow loss occurred in dragging the large agglomerates out through the nozzle. Both types of loss reduce the specific impulse of the rocket motor.

It is conceivable that the problem of unwanted aluminum agglomeration could be substantially reduced by maintaining the temperature of the aluminum particles below the melting temperature (933 K). To study the factors which influence the temperature variation of the aluminum particles, a heat transfer model has been developed. Among the factors investigated which influence the aluminum particle temperature are aluminum particle size and mass fraction, the level of radiant flux incident from the rocket motor, and the nature of the propellant matrix surrounding the aluminum.

The type of propellant studied was an ammonium perchlorate (AP)/hydrocarbon/aluminum (Al) composite propellant with properties similar to the space shuttle propellant. Bimodal AP was considered. Taken together the AP oxidizer and hydrocarbon binder constitute the matrix which surrounds the Al particles (see Fig. 1). Since the matrix is usually relatively transparent to thermal radiation and since significant levels of radiant flux are likely to be present, in aluminized propellant motors due to the abundance of aluminum (Al) and aluminum oxide (Al_2O_3) particles suspended in the gas phase it is quite possible for the Al particles embedded in the propellant to be preferentially heated and become hotter than the surrounding matrix. Furthermore the low thermal conductivity of AP (k_{AP} = 0.04186 W/m K) inhibits heat conduction between the Al particles and matrix and thus preserves separate and distinct matrix and Al particle temperatures. By tailoring the propellant's thermal radiative absorption and scattering properties it should be possible, in theory at least, to minimize or at least reduce the Al particle temperatures. Perhaps it would be possible to maintain the Al particles below the melting temperature. These considerations are the basis for this theoretical study.

Definition of Model

The model developed consists of two phases, a particle phase which represents the oxide-coated Al particles, and a matrix phase which represents the AP, binder, and any submicron particle additives such as Fe_2O_3. Small micron-size particles such as Fe_2O_3 are included in the matrix phase since their small size would guarantee thermal equilibrium with the surrounding matrix (Fig. 1). The incident radiation was assumed to be blackbody radiation at a temperature T_R. The actual level of radiant flux that exists in an aluminized propellant motor is a matter of uncertainty and a topic of current research [5-7]. Therefore a more elaborate description of the incident radiation is not warranted here.

For theoretical purposes all particles (AP, Fe_2O_3, and Al) were treated as spherical and monodisperse. Although the actual particles under consideration are not spherical there is no systematic deviation from sphericity which would warrant a

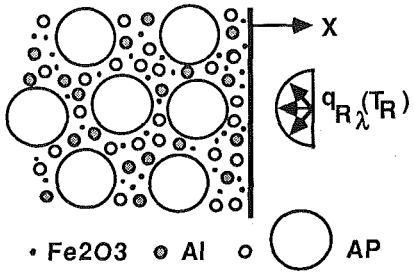

Fig. 1 Aluminized composite propellant with bimodal AP blend

[1]Present address: University of Illinois, Urbana, IL.

Contributed by the Heat Transfer Division and presented at the National Heat Transfer Conference, Denver, CO, August 1985. Manuscript received by the Heat Transfer Division May 1, 1986.

nonspherical analytical treatment. Also, the neglect of particle size distribution about the modal particle sizes is a very reasonable one here for composite propellants.

Finally each phase was assumed to be a nonemitting, anisotropically scattering, absorbing homogeneous medium. The assumption of homogeneity was made only to maintain analytical tractability of the problem. In fact nonhomogeneous features of the propellant, such as pockets of Al particles forming between the large AP particles, certainly have an influence on the Al particle heating behavior. However, treatment of these effects is beyond the scope of this work and discussion of nonhomogeneous effects (without radiative heating considerations) may be found elsewhere [8].

Analysis

As the propellant is assumed to be nonemitting ("cold medium" [9] or "scattering" [10] approximation) the radiative transfer equation is decoupled from the energy equations and solved by the two-flux method [11] which assumes a semi-isotropic intensity distribution.

The two-flux radiative transfer equations are

$$\frac{dI_\lambda^+}{dx} = -(\bar{a}_\lambda + \bar{\sigma}_\lambda) I_\lambda^+ + \bar{\sigma}_\lambda I_\lambda^- \tag{1}$$

$$-\frac{dI_\lambda^-}{dx} = -(\bar{a}_\lambda + \bar{\sigma}_\lambda) I_\lambda^- + \bar{\sigma}_\lambda I_\lambda^+ \tag{2}$$

where equation (1) is a radiative energy balance on rays traveling in the forward or "+" direction and equation (2) the same for rays traveling in the backward or "−" direction (see Fig. 1). The two-flux absorption and scattering coefficients are given in equations (3) and (4) [11]

$$\bar{a}_\lambda = 2(a_{\lambda B} + a_{\lambda \mathrm{AP}_1} + a_{\lambda \mathrm{AP}_2} + a_{\lambda \mathrm{Al}} + a_{\lambda F}) \tag{3}$$

$$\bar{\sigma}_\lambda = 2(\sigma_{\lambda \mathrm{AP}_1} b_{\mathrm{AP}_1} + \sigma_{\lambda \mathrm{AP}_2} b_{\mathrm{AP}_2} + \sigma_{\lambda \mathrm{Al}} b_{\mathrm{Al}} + \sigma_{\lambda F} b_F) \tag{4}$$

The individual component absorption and scattering coefficients are given by equations (5) and (6) where the subscript i represents large AP, small AP, Fe_2O_3, or Al (B stands for binder)

$$a_{\lambda i} = \frac{1.5 f_{vi} Q_{ai}}{D_i} \quad \text{except } a_{\lambda B} = \frac{f_{vB} 4\pi k_B}{\lambda} \tag{5}$$

$$\sigma_{\lambda i} = \frac{1.5 f_{vi} Q_{si}}{D_i} \tag{6}$$

The two-flux back-scatter fraction for each particle component is given by equations (7) and (8)

$$b_i = \frac{1}{2} \int_0^1 \int_{-1}^0 P_i(\mu, \mu') d\mu' \, d\mu \tag{7}$$

$$P_i(\mu, \mu') = \frac{1}{\pi} \int_{\theta_0}^{\theta_\pi} \frac{p(\theta) \sin\theta \, d\theta}{[(1-\mu^2)(1-\mu'^2) - (\cos\theta - \mu\mu')^2]^{1/2}} \tag{8}$$

where $P_i(\mu, \mu')$ is the phase function in the slab geometry for radiation scattered from the μ' direction into the μ direction and $p(\theta)$ is the single particle scattering phase function.

The limiting angles in equations (8) θ_0 and θ_π are defined as [12]:

$$\cos\theta_0 = \mu\mu' + (1-\mu^2)^{1/2}(1-\mu'^2)^{1/2} \tag{9}$$

$$\cos\theta_\pi = \mu\mu' - (1-\mu^2)^{1/2}(1-\mu'^2)^{1/2} \tag{10}$$

Solution of equations (1) and (2) with the boundary conditions

(1) at $x \to -\infty$; $I_\lambda^+ \to$ finite value (11)

(2) at $x = 0$; $I_\lambda^-(0) = (1-R) \frac{q_{R\lambda}}{\pi} + R I_\lambda^+$ (12)

(where R is the hemispherical spectral reflectivity and $q_{R\lambda}/\pi$ = (uniform) incident intensity) gives

Nomenclature

C = specific heat
C_1 = constant defined by equation (16)
C_λ = constant defined by equation (15)
$C_{0\lambda}$ = constant defined by equation (32)
D = diameter
I = intensity
N = number density of particles
N_1, N_2, N_3 = parameters in equation (35)
P = phase function in slab geometry
Q = scattering or absorption efficiency
R = hemispherical spectral reflectivity
T = temperature
a = absorption coefficient
a_0 = constant defined by equation (25)
a_1 = constant defined by equation (26)
a_2 = constant defined by equation (27)
b = backscatter fraction
e = charge of electron
f_v = volume fraction
h = heat transfer coefficient
k = imaginary part of refractive index ($\tilde{n} = n - ik$); also thermal conductivity
m = mass fraction; also mass of electron
n = real part of refractive index ($\tilde{n} = n - ik$)
p = single scatter phase function
q = heat flux
r = rate of burning
x = particle size parameter = $\pi D n_B/\lambda$; also slab coordinate
α_1 = constant defined by equation (33)
γ_λ = constant defined by equation (14)
γ = constant defined by equation (39)
$\gamma_1, \gamma_2, \gamma_3$ = parameter defined in equation (35)
θ = polar angle in single particle geometry
λ = wavelength in vacuum
μ = cosine of polar angle in slab geometry for incoming ray
μ' = cosine of polar angle in slab geometry for outgoing ray
ρ = density
σ = scattering coefficient
ω = angular frequency
$\omega_{01}, \omega_{02}, \omega_{03}$ = parameters defined in equation (35)

Subscripts

Al = aluminum
AP = ammonium perchlorate
B = binder
F = Fe_2O_3 catalyst
R = incident radiation
s = surface (at $x = 0$); also scattering
a = absorption
i = index used for AP_1, AP_2, Al, and F
∞ = matrix (AP, B, and F)
λ = spectral quantity

Superscripts

$\pm$ = forward and backward direction
$\bar{}$ = (overbar) two flux value

$$2\pi[I_\lambda^+(x)+I_\lambda^-(x)]=2C_\lambda\exp[\gamma_\lambda x] \tag{13}$$

where

$$\gamma_\lambda=[\tilde{a}_\lambda(\tilde{a}_\lambda+2\tilde{\sigma}_\lambda)]^{1/2} \tag{14}$$

$$C_\lambda=\pi C_1\left[1+\frac{1}{\tilde{\sigma}_\lambda}[\tilde{a}_\lambda(\tilde{a}_\lambda+2\tilde{\sigma}_\lambda)]^{1/2}+\frac{1}{\tilde{\sigma}_\lambda}(\tilde{a}_\lambda+\tilde{\sigma}_\lambda)\right] \tag{15}$$

$$C_1=\frac{(1-R)q_{R\lambda}/\pi}{\frac{1}{\tilde{\sigma}_\lambda}[\tilde{a}_\lambda(\tilde{a}_\lambda+2\tilde{\sigma}_\lambda)]^{1/2}+\frac{1}{\tilde{\sigma}_\lambda}(\tilde{a}_\lambda+\tilde{\sigma}_\lambda)-R} \tag{16}$$

Multiplying the left-hand side of equation (13) by $a_{\lambda i}$ gives $2\pi a_{\lambda i}[I_\lambda^+(x)+I_\lambda^-(x)]$ which has the interpretation of the radiant power absorbed by specie i in a differential slab element of propellant per unit volume per unit wavelength. These terms will appear as source terms in the particle and matrix energy equations.

Separate steady-state energy equations for the matrix and aluminum particle phase are written

Matrix:

$$(\rho C)_\infty f_{v\infty}\, r\frac{dT_\infty}{dx}=k_\infty f_{v\infty}\frac{d^2T_\infty}{dx^2}+\pi D_{Al}^2\left(\frac{2k_\infty}{D_{Al}}\right)(T_{Al}-T_\infty)N_{Al}+\pi\int_0^\infty \tilde{a}_{\lambda\infty}(I_\lambda^+ +I_\lambda^-)d\lambda \tag{17}$$

Aluminum:

$$f_{vAl}\,\rho_{Al}\,C_{Al}\,r\frac{dT_{Al}}{dx}=\pi D_{Al}^2\left(\frac{2k_\infty}{D_{Al}}\right)(T_\infty-T_{Al})N_{Al}+\pi\int_0^\infty \tilde{a}_{Al\lambda}(I_\lambda^+ +I_\lambda^-)d\lambda \tag{18}$$

where

$$k_\infty=\frac{f_{vB}k_B+f_{vAP}k_{AP}+f_{vF}k_F}{f_{v\infty}} \tag{19}$$

$$(\rho C)_\infty=\frac{f_{vB}\rho_B C_B+f_{vAP}\rho_{AP}C_{AP}+f_{vF}\rho_F C_F}{f_{v\infty}} \tag{20}$$

$$f_{v\infty}=f_{vB}+f_{vAP}+f_{vF} \tag{21}$$

$$\tilde{a}_{\lambda\infty}=\tilde{a}_{\lambda B}+\tilde{a}_{\lambda AP}+\tilde{a}_{\lambda F} \tag{22}$$

$$N_{Al}=\frac{6f_{vAl}}{\pi D_{Al}^3} \tag{23}$$

In equation (23) the Al particle number density is related to the volume fraction through the volume of a single particle, $\pi D_{Al}^3/6$. The above equations are coupled through the conduction term $h(T_{Al}-T_\infty)$; $h=2k_\infty/D_{Al}$. Here, the limiting result for spherical conduction to infinite surroundings, Nu = 2, has been used [13]. Also the temperature of single particles has been lumped (assumed uniform) due to the poor matrix conductivity. This is justified by the fact that the Biot number (which is a measure of the ratio of conductive resistance to heat flow inside the Al particles to conductive resistance outside the particle) is very small [14]

$$\text{Biot No.}=h(D_{Al}/6)/k_{Al}=(1/3)(k_\infty/k_{Al})<<0.1$$

The coupled energy and transfer equations are reduced to

$$\frac{d^3T_\infty}{dx^3}+a_2\frac{d^2T_\infty}{dx^2}+a_1\frac{dT_\infty}{dx}+a_0\int_0^\infty \tilde{a}_\lambda C_\lambda e^{\gamma_\lambda x}d\lambda+\frac{1}{k_\infty f_{v\infty}}\int_0^\infty \tilde{a}_{\lambda\infty}C_\lambda e^{\gamma_\lambda x}d\lambda \tag{24}$$

where

$$a_0=\frac{12}{\rho_{Al}\,D_{Al}^2\,C_{Al}\,r\,f_{v\infty}} \tag{25}$$

$$a_1=\frac{-12(\rho C)_\infty}{\rho_{Al}\,D_{Al}^2\,C_{Al}}-\frac{12\,f_{vAl}}{D^2{}_{Al}\,f_{v\infty}} \tag{26}$$

and

$$a_2=\frac{-(\rho C)_\infty\, r}{k_\infty}+\frac{12\,k_\infty}{D^2{}_{Al}\,\rho_{Al}\,C_{Al}\,r} \tag{27}$$

The solution of this equation is

$$T_\infty(x)=\left[T_s-T_0-\int_0^\infty C_{0\lambda}\,d\lambda\right]e^{\alpha_1 x}+\int_0^\infty C_{0\lambda}\,e^{\gamma_\lambda x}d\lambda+T_0 \tag{28}$$

where the boundary conditions used are

$$(1)\ T_\infty(0)=T_s \tag{29}$$

$$(2)\ T_\infty(x\to-\infty)=T_0 \tag{30}$$

$$(3)\ dT_\infty/dx(x\to-\infty)=0 \tag{31}$$

The constants appearing in the solution for $T_\infty(x)$ are

$$C_{0\lambda}=\frac{-C_\lambda\left[a_0\tilde{a}_\lambda+\left(\frac{\tilde{a}_{\lambda\infty}}{k_\infty f_{v\infty}}\right)\gamma_\lambda\right]}{\gamma_\lambda{}^3+\gamma_\lambda{}^2a_2+\gamma_\lambda a_1} \tag{32}$$

and

$$\alpha_1=\frac{-a_2+(a_2^2-4a_1)^{1/2}}{2} \tag{33}$$

The Al particle temperature can then be determined as

$$T_{Al}(x)=T_\infty(x)+\frac{D^2{}_{Al}(\rho C)_\infty\, r\,f_{v\infty}}{12\,k_\infty\,f_{vAl}}\left\{\alpha_1\cdot(T_\infty(x)-T_0)+\int_0^\infty C_{0\lambda}e^{\gamma_\lambda x}(\gamma_\lambda-\alpha_1)d\lambda\right\}$$

$$\frac{-D_{Al}^2\,f_{v\infty}}{12\,f_{vAl}}\left\{\alpha_1^2(T_\infty(x)-T_0)+\int_0^\infty C_{0\lambda}e^{\gamma_\lambda x}(\gamma_\lambda^2-\alpha_1^2)d\lambda\right\}$$

$$-\frac{D_{Al}^2}{12\,k_\infty\,f_{vAl}}\int_0^\infty \tilde{a}_{\lambda\infty}\,C_\lambda\,e^{\gamma_\lambda x}d\lambda \tag{34}$$

It should be noted that the effect of conductive heat feedback from the hot gaseous flame zone on Al heating has not been neglected. It has been implicitly included in the surface temperature boundary condition T_s. The energy balance equations (17) and (18) apply only to the solid propellant region ($x \geq 0$). The boundary condition at $x = 0$ could be taken as $k_\infty\, dT_\infty/dx\ (x=0)=q_c$, the conductive heat feedback from the gas zone (ignoring latent energy due to phase change at the surface). However the value of q_c (and any possible phase change present) is known with less certainty than the surface temperature. Hence the surface temperature boundary condition is adopted. The particular value used here is 625 K which is based on the best currently available information [15].

Radiative Properties

The absorption and scattering efficiencies $Q_{a\lambda i}$ and $Q_{s\lambda i}$ for the AP and Al particles were determined from the fundamental optical constants $\tilde{n}=n-ik$. The values for the Al particles were taken to be $\tilde{n}=1.7-i\,0.1$ for all wavelengths, which is characteristic of the oxide coating which inevitably forms on the aluminum particles before propellant mixing due to atmospheric oxidation [16]. The optical constants for AP were determined from the dispersion equations [17, 18]

$$n^2-k^2=[1.4833]^2+\sum_{i=1}^{3}\frac{N_i e^2}{m\,\epsilon_0}\frac{\omega_{0i}^2-\omega^2}{(\omega_{0i}{}^2-\omega^2)^2+\gamma_i{}^2\omega^2} \tag{35}$$

$$2nk = \sum_{i=1}^{3} \frac{N_i e^2}{m\ \epsilon_0} \frac{\gamma_i \omega}{(\omega_{0i}{}^2 - \omega^2)^2 + \gamma_i{}^2 \omega^2} \tag{36}$$

where

$N_1 = 0.252 \times 10^{19}$, cm^{-3}
$N_2 = 0.188 \times 10^{19}$
$N_3 = 0.405 \times 10^{19}$
$\omega_{01} = 58.7 \times 10^{13}$, s^{-1}
$\omega_{02} = 25.4 \times 10^{13}$
$\omega_{03} = 19.8 \times 10^{13}$
$\gamma_1 = 1.66 \times 10^{13}$, s^{-1}
$\gamma_2 = 1.76 \times 10^{13}$
$\gamma_3 = 0.746 \times 10^{13}$

which are valid over the range of wavelengths from 0.4 to 14 μm [18]. Over this range of wavelengths it was determined from Fourier-Transform Infrared Spectrometer (FTIR) measurements that the AP transmits between 0.4 and 2.7 μm, 3.8 and 4.3 μm, and 11.8 and 14.0 μm [19]. The AP absorbs between 2.7 and 3.8 μm and 4.3 and 11.8 μm. Since the AP dispersion equations give small nonzero values for k in the known transmissive regions, k is set equal to zero in those regions.

Absorption and scattering efficiencies are determined either by Mie theory or the laws of geometric optics, depending on the value of the particle size parameter $x = \pi D n_B/\lambda$. For opaque regions of wavelength (all wavelengths for Al and selective as noted above for AP) the efficiencies and single-scatter phase function are calculated from Mie theory for $x < 5$. For $x > 5$ the geometric optics results are used assuming a diffusively reflecting particle with the hemispherical reflectively equal to normal reflectivity [9]. The value of $x = 5$ is the approximate recommended lower limit for opaque particles, for which geometric optics gives suitable heat transfer results [9]. For transmissive wavelength regions (AP only) Mie theory is used for values of $x < 50$. For $x > 50$ geometric optics results are used with the Fraunhofer diffraction contribution to forward scatter removed. A larger lower limit ($x = 50$) is necessary for transparent particles due to the strong component of forward scattering.

The binder was assumed to be nonabsorbing with a refractive index of $n_B = 1.6$. This is a reasonable representation of most hydrocarbon binders which have a few very narrow infrared absorption bands and refractive indices ranging between 1.4 and 1.7. This assumption was made because the imaginary component k_B is not readily known and its inclusion was judged to have a very small effect on the temperature predictions.

Limiting Solution

To clarify the roles of some of the major parameters and to help debug the computer program of the full solution a limiting solution was developed using the following assumptions:

1 Transparent matrix phase ($\bar{a}_\infty = 0$)
2 Grey medium
3 $f_{v\mathrm{Al}}$ or m_{Al} very small
4 No scattering ($\bar{\sigma} = 0$)
5 No interface reflectance ($R = 0$)
6 $\alpha_1 >> \gamma$
7 $|a_1/a| >> |a_2|, |\bar{a}|$

Assumptions (6) and (7) may be verified by substituting realistic propellant properties into the definitions of those constants. With the above assumptions the modified constants are obtained as

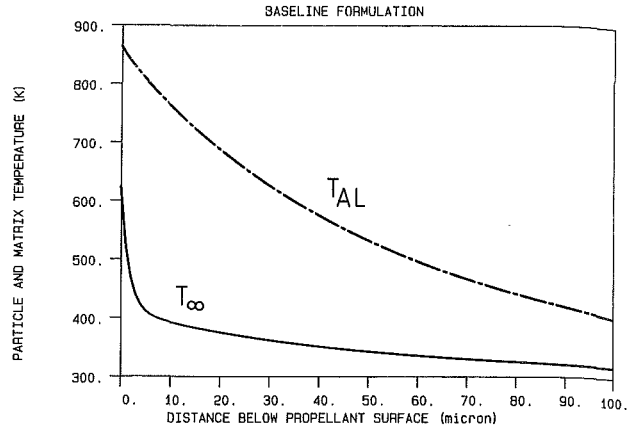

Fig. 2 Al particle and matrix temperatures for baseline formulation

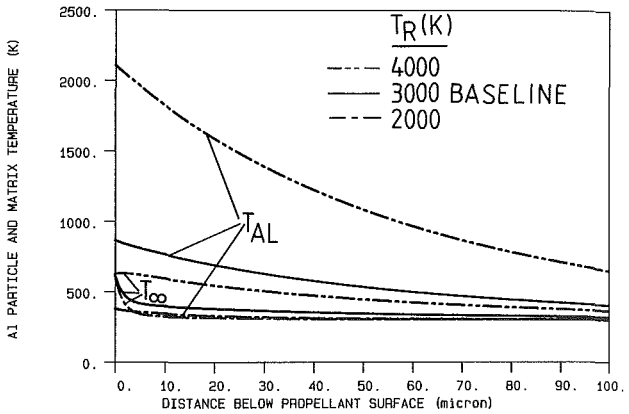

Fig. 3 Effect of blackbody incident radiation temperature

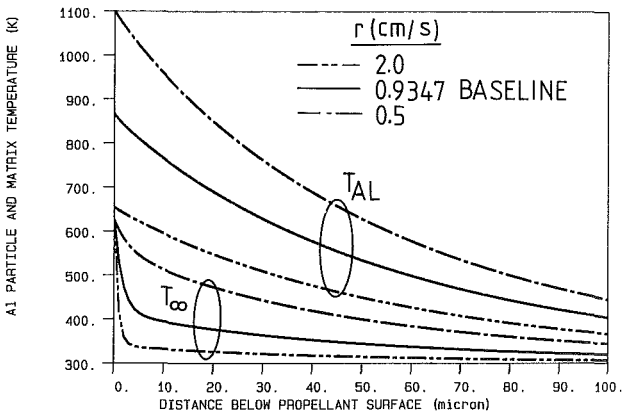

Fig. 4 Effect of propellant burn rate

$$\alpha_1 = \frac{(\rho C)_\infty r}{k_\infty} \tag{37}$$

$$C_0 = \frac{-q_R\ a_0\ \bar{a}}{\gamma^3 + \gamma^2 a_2 + \gamma a_1} \tag{38}$$

$$\gamma = \bar{a} \tag{39}$$

and equation (32) evaluated at the surface $x = 0$ reduces to

$$T_{\mathrm{Al}_0} - T_s = \frac{q_R\ Q_{a\mathrm{Al}}\ D_{\mathrm{Al}}}{4\ k_\infty} \tag{40}$$

Also, for large black ($\sigma = 0$) Al particles ($D_{\mathrm{Al}} \geq 10\ \mu$m) the absorption efficiency approaches unity $Q_{a\mathrm{Al}} \to 1$, giving

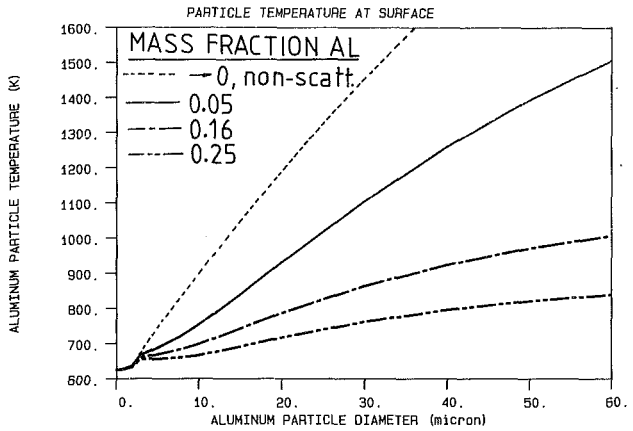

Fig. 5 Effect of Al particle diameter and mass fraction

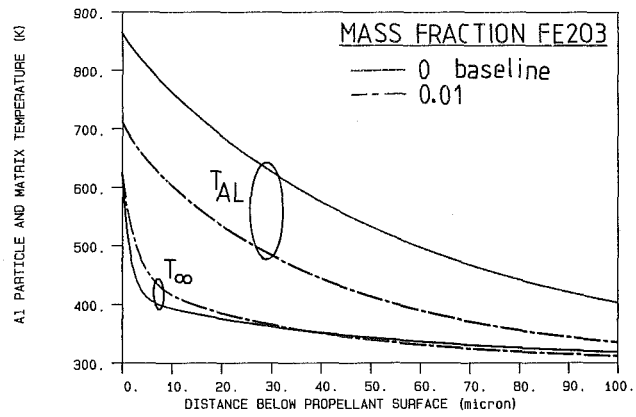

Fig. 6 Effect of Fe_2O_3 on Al particle and matrix temperature profiles

$$T_{Al_0} - T_s = \frac{q_R D_{Al}}{4 k_\infty} \tag{41}$$

Equation (41) can also be obtained directly from (18) by letting the left-hand side go to zero or from a simple energy balance on a single particle, recognizing that the effective surface area for absorbing a diffuse incident flux is $\pi D^2_{Al}/2$ (not the projected area $\pi D^2_{Al}/4$ as would be the case for a collimated flux).

Now the influence of the key parameters can be seen easily. The temperature difference between the selectively absorbing particles and transparent matrix is larger for large incident fluxes, small matrix conductivities, and large particle diameters. Assuming values of T_R = 3000 K, k_∞ = 0.04186 W/m K (10^{-4} cal/cm s K) gives the following results for the limiting case:

D_{Al}, μm	$T_{Al} - T_s$, K
10	275
30	826
100	2750

Results and Discussion

A formulation similar to the space shuttle solid rocket booster (SRB) propellant was chosen as a baseline case against which to test variations in various parameters. The parameters for the baseline formulation were as follows:

$D_{AP_1} = 24$ μm	$D_{AP_2} = 180$ μm	$D_{Al} = 30$ μm
$m_{AP_1} = 0.21$	$m_{AP_2} = 0.49$	$m_{Al} = 0.16$
$r = 0.9347$ cm/s	$n_B = 1.6$	$k_B = 0$
$T_R = 3000$ K	$T_s = 625$ K	$T_0 = 300$ K
$n_{Al} = 1.7$	$k_{Al} = 0.1$	$m_F = 0$

The predicted particle and matrix temperature profiles for this case, T_{Al} and T_∞, are predicted in Fig. 2. The selectively absorbing Al particles maintain a consistently hotter temperature profile. For this case the Al particles would reach approximately 860 K at the surface, which is below the melting temperature (933 K). However the fact that the Al particles are actually concentrated in the spaces between AP and particles would result in higher temperatures than those indicated here [8].

To test which parameters most strongly influence the Al particle temperature, each parameter in the baseline formulation was varied keeping all others the same. The parameters which were found to have little influence on the particle and matrix temperature profiles were the large/small AP slit, the AP size (both small and large), the total AP mass fraction,

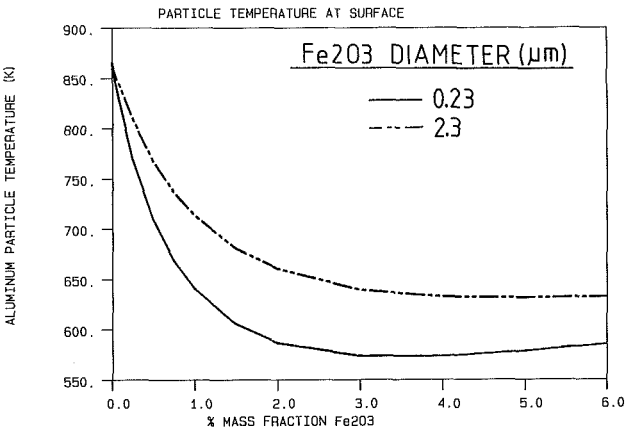

Fig. 7 Effect of Fe_2O_3 on Al particle surface temperature

and the imaginary component of refractive index for the Al particles, k_{Al}.

Two parameters which had a large effect on T_p but which are difficult to control independent of other ballistic considerations are the characteristic blackbody temperature of the incident radiation T_R (Fig. 3) and the burn rate r (Fig. 4). For obvious reasons low incident fluxes and high burn rates favor lower Al temperatures. While little is known about the level of radiant flux present in aluminized propellant motors and controlling that flux would be difficult, it is important to recognize that it is a major parameter in determining the temperature of the Al particles.

Of the parameters over which the propellant formulator has control the two which indicate promise for use in reducing the Al particle temperature are the Al mass fraction and Al diameter (Fig. 5). Large mass fractions favor lower Al temperatures. This is due to the increase in thermal capacity which accompanies an increase in m_{Al}. In general small diameters also favor lower Al temperature. For a given Al mass fraction as the Al diameter decreases the conduction of absorbed energy to the matrix becomes more efficient and the Al temperature decreases, approaching the matrix temperature. For comparison the limiting case ($m_{Al} \to 0$) discussed earlier is also shown in Fig. 5. The straight portion of the curve ($D_{Al} \geq 2$–3 μm) corresponds to the geometric optic scattering regime ($Q_a \to 1$) and the curved portion of the curve ($D_{Al} \leq 2$ μm) corresponds to transition through the Mie region to the Rayleigh limit where Q_a is proportional to D_{Al}.

Finally the effects of adding small quantities of Fe_2O_3 burn rate catalyst are indicated in Figs. 6 and 7. Because these particles are so small (typically less than one micron) even very small quantities (1–2 percent) added to the propellant will

significantly alter the optical properties. The Fe_2O_3 optical properties were modeled here by the assumed values of $n = 1.8$ and $k = 0.6$ [20–24] which result in rather highly absorptive behavior.[2] The main effect of these particles is to absorb radiation which would have otherwise been absorbed by the Al and thereby reduce the Al particle temperature while increasing the matrix temperature near the surface (Fig. 6). Above a certain concentration (approximately 3 percent in Fig. 7), however, it appears that the energy absorbed by the Fe_2O_3 is being conducted to the Al, as the Al temperature increases slightly at higher Fe_2O_3 concentrations. These results suggest that it may be worth investigating the use of highly scattering or reflective powder additives to reduce Al heating.

Conclusions

A model for radiative preheating of aluminum particles in AP composite propellants has been developed. The model identifies which parameters have a strong influence on the aluminum particle temperature. These are aluminum size and mass fraction, burn rate, and level of radiant flux. In general, smaller aluminum particles and larger Al mass fractions promote lower temperatures. Parameters were also identified which have little effect on Al temperature. These were total AP mass fraction, small/large AP split, surface temperature, Al extinction coefficient, and large AP size. In addition the size of small AP had a weak effect. The effect of adding Fe_2O_3 catalyst particles was also modeled. It was shown that small amounts of Fe_2O_3 can significantly alter the optical properties of the propellant and therefore the Al heating process. While the Al temperatures predicted by this model are probably low due to the neglect of nonhomogeneous (pocket) effects, these results should prove useful in formulating propellants which minimize the problem of unwanted Al agglomeration.

Further research should now be directed at developing a model which combines radiative heating with nonhomogeneous effects.

Acknowledgments

Support for this work from the Southeastern Conference on Electrical Engineering Education under subcontract 83 RIP 42 and the National Science Foundation under Grant CBT 8351243 is gratefully acknowledged. Additional support from Morton Thiokol Inc. and the University of Utah Research Committee was also appreciated.

[2]Note added in press: A recently discovered reference [25] indicates that Fe_2O_3 is actually nonabsorbing between 1.2 and 14 μm.

References

1 Sambamurthi, J. K., Price, E. W., and Sigman, R. K., "Aluminum Agglomeration in Solid-Propellant Combustion," *AIAA Journal*, Vol. 22, 1984, pp. 1132–1138.

2 Brundige, W. N., and Caveny, L. H., "Low Burning Rate Aluminized Propellants in Acceleration Fields," *AIAA Journal*, Vol. 22, 1984, pp. 638–646.

3 Beckstead, M. W., Richards, R. S., and Brewster, B. S., "Distributed Combustion Effects on Particle Damping," *AIAA Journal*, Vol. 22, 1984, pp. 383–387.

4 Gany, A., Caveny, L. H., and Summerfield, M., "Aluminized Solid Propellants Burning in a Rocket Motor Flowfield," *AIAA Journal*, Vol. 16, 1978, pp. 736–739.

5 Worster, B. W., "Particulate Infrared Radiation in Aluminized Solid Fuel Rocket Plumes," *Journal of Spacecraft and Rockets*, Vol. 11, 1974, pp. 260–262.

6 Pearce, B. E., "Radiative Heat Transfer Within a Solid-Propellant Rocket Motor," *Journal of Spacecraft and Rockets*, Vol. 15, 1978, pp. 125–128.

7 Edwards, D. K., and Bobco, R. P., "Effect of Particle Size Distribution on the Radiosity of Solid Propellant Rocket Motor Plumes," presented at AIAA 16th Thermophysics Conference, June 23–25, 1981, Palo Alto, CA, Paper No. AIAA-811-052.

8 Cohen, N. S., "A Pocket Model for Aluminum Agglomeration in Composite Propellants," *AIAA Journal*, Vol. 21, 1983, pp. 720–725.

9 Siegel, R., and Howell, J. R., *Thermal Radiation Heat Transfer*, 2nd ed., McGraw-Hill, New York, 1981.

10 Chandrasekhar, S., *Radiative Transfer*, Dover, New York, 1960.

11 Brewster, M. Q., and Tien, C. L., "Examination of the Two-Flux Model for Radiative Transfer in Particulate Systems," *International Journal of Heat and Mass Transfer*, Vol. 25, 1982, pp. 1905–1906.

12 Brewster, M. Q., "Radiative Transfer in Packed and Fluidized Beds," Ph.D. Thesis in Mechanical Engineering, University of California, Berkeley, CA, 1981.

13 Bird, R. B., Stewart, W. E., and Lightfoot, E. N., *Transport Phenomena*, Wiley, New York, 1960, p. 409.

14 Incropera, F. P., and DeWitt, D. P., *Fundamentals of Heat and Mass Transfer*, Wiley, New York, 1985.

15 Salita, M., Morton Thiokol/Wasatch Division, Brigham City, UT, private communication.

16 Rieger, T. J., "On the Emissivity of Alumina/Aluminum Composite Particles," *Journal of Spacecraft and Rockets*, Vol. 16, 1979, pp. 438–439.

17 Moss, T. S., *Optical Properties of Semi-Conductors*, Butterworths Scientific Publications, 1959, p. 16.

18 Patel, R. S., and Brewster, M. Q., "Optical Constants of Propellant-Grade Ammonium Perchlorate," *AIAA Journal*, Vol. 24, No. 11, 1986, pp. 1878–1880.

19 Patel, R. S., "Selective Radiative Pre-heating of Aluminum in Composite Solid Propellant Combustion," M.S. Thesis, University of Utah, 1985.

20 Valkonen, E., and Karlsson, B., "Spectral Selectivity of a Thermally Oxidized Stainless Steel," *Solar Energy Materials*, Vol. 7, 1982, pp. 43–50.

21 Douglass, D. L., and Pettit, R. B., "The Selective Solar Absorptance of In-Situ Grown Oxide Films on Metals," *Solar Energy Materials*, Vol. 4, 1981, pp. 383–402.

22 Popova, S. I., Tolstykh, T. S., and Ivlev, L. S., "Optical Constants of Fe_2O_3 in the Infrared Range of the Spectrum," *Opt. Spectrosc.*, Vol. 35, 1973, pp. 551–552.

23 Szklarska, Z., and Jurek, J., "Ellipsometric Studies on Iron Oxide Film Growth at 100 to 350°C," *Corrosion–NACE*, Vol. 32, 1976, pp. 294–297.

24 Morl, K., Ropke, U., Knappe, B., Lehmann, J., Perthel, R., and Schroder, H., "Optical Properties of Sputtered Fe_2O_3 Films," *Thin Solid Films*, Vol. 60, 1979, pp. 49–53.

25 Shafey, H. M., "Studies on Radiative Heat Transfer in Dispersed Media With Application to Painted Layers," Ph.D. Thesis in Mechanical Engineering, Kyoto University, Kyoto, Japan, 1981, p. 21.

I. Catton
Mem. ASME

J. O. Jakobsson

Mechanical, Aerospace & Nuclear Engineering, School of Engineering, University of California, Los Angeles, CA 90024

The Effect of Pressure on Dryout of a Saturated Bed of Heat-Generating Particles

The results of an experimental investigation of pressure effects on dryout heat flux in a volume-heated porous bed are reported. Several porous beds of near-uniform-sized particles were studied at pressures up to 5 atm. The beds were saturated with water, Freon-113, acetone, and methanol. Simple scaling of the Freon-113 results is used to yield results valid for water pressures from 1 atm to 37.3 atm.

Introduction

Dryout heat flux in a volume-heated porous medium is defined as the total heat generated within the porous medium per unit horizontal cross-sectional area that causes a portion of the porous medium to "dry out". Dryout is recognized by observing that the temperature at some spot within the porous medium begins to increase monotonically above the saturation temperature of the coolant with time. This phenomenon can also occur if a saturated porous medium is depressurized too rapidly.

As a result of the importance of dryout phenomena to reactor safety, both for the liquid metal fast breeder reactor (LMFBR) and for the light water reactor (LWR), more than 50 papers were published during the past decade. Some of the earliest experiments were conducted by Sowa et al. [1]. They bottom heated a sodium-saturated UO_2 bed but failed to achieve dryout. They also proposed the first dryout model, which was forgotten for many years. Since their model was based on a flooding correlation, it is more suitable for beds of large particles. Later, Gabor et al. [2] studied a water-saturated UO_2 bed with heat generation in the water. They noted channels at the top portion of the bed and observed a decrease in dryout heat flux as the bed height increased. They also noted that bottom-heated beds had a lower dryout heat flux than volumetric-heated beds. Gabor et al. [3] continued the research using water and sodium-saturated UO_2 beds. They found that subcooling in the overlying pool had only a minor effect on the dryout heat flux.

Keowen [4] inductively heated beds of steel and lead particles with water as coolant. Keowen's measured dryout heat fluxes were much higher than those of Gabor et al. [2, 3]. The main cause was the use of larger particles. In all of the above studies, the bed particle size was not varied systematically. Keowen's work was extended by Dhir and Catton [5] at UCLA. The found that the dryout heat flux was independent of bed thickness in deep beds. They used their deep-bed data to develop a semi-empirical model, for prediction of dryout heat flux valid for beds with particle sizes less than 1 mm.

Hardee and Nilson [6] studied natural convection and boiling in a porous bed. They developed a model based on conservation of mass, momentum, and energy and obtained the dryout heat flux by maximizing the heat flux. The model is found to be similar to the Dhir and Catton model. They also suggested that subcooling the overlying pool would increase the dryout heat flux by the ratio of the sensible heat of the subcooling to the latent heat of evaporation.

Dhir and Catton [7] also considered the effect of beds of mixed particle sizes. They found that for a 50–50 mixture (by volume) of 0.9 mm and 0.36 mm particles their dryout data lay between the predictions for uniform beds of 0.9 mm or 0.36 mm particles. Dhir [8] extended this work and considered two mixtures: 75 percent 0.36 mm, 25 percent 0.9 mm; and 20 percent 3.25 mm, 60 percent 0.9 mm, 20 percent 356 μm. He found that a mean particle diameter obtained by adding resistances due to each fraction of particles led to predictions that compared reasonably well with the data.

Barleon and Werle [10] studied dryout with particles larger than one millimeter. They found that most models overpredicted dryout heat flux for large particles. Later, Ostensen and Lipinski [11] proposed that dryout heat flux varied as the square root of the particle diameter by assuming flooding controls dryout. Since both Ostensen et al. [11] and Sowa et al. [1] used flooding correlations, their correlations are similar. At almost the same time three other similar flooding models were developed by Dhir et al. [12], Theofanus et al. [13], and Henry et al. [14]. All of these models are restricted to beds of large particles.

Lipinski extended the Hardee and Nilson work [6] and Shires and Steven's model [15] to develop a dryout model which is claimed to have no empirical constraints. The Lipinski model [16] was found to fit experimental data well for beds of small and large particles. Later he extended their previous model to a more general one-dimensional model [17].

Somerton et al. [18] studied dryout of deep beds of large particles. They found that the amount of coolant above the bed can affect the dryout heat flux. Presently, there are no models that properly account for this effect.

To our knowledge no experimental measurements of the effect of pressure on dryout heat flux in porous media have been made although predictions have been presented [19]. Thus, the present study consists of an experimental investigation of dryout heat flux in volumetrically heated porous media at different pressures. The beds were made of steel particles of sizes 0.59–0.79 mm, 1.6 mm, 3.2 mm, and 4.8 mm. Bed heights were varied from 10.0 to 21.0 cm, with the bed diameter equal to 6.1 cm. The overlying liquid ratio, a measure of the amount of coolant above the bed, was varied from 0.0 to 2.0, and the pressure range was from 1 to 5.76 atm absolute. Freon-113 and water were used as coolants with some runs made using acetone and methanol as coolants.

Since Freon-113 and water are thermodynamically similar fluids, the results of dryout heat flux as a function of pressure can be scaled quite nicely. The results can be presented as a reduced dryout heat flux as a function of reduced pressure and geometry only, allowing the Freon-113 results to represent water up to 37.3 atm.

In this study the effect of the overlying liquid and bed height were also tested for beds of uniform-sized particles. Finally, the experimental results were compared to some of the theoretical models.

Contributed by the Heat Transfer Division for publication in the JOURNAL OF HEAT TRANSFER. Manuscript received by the Heat Transfer Division August 27, 1984.

Scaling of Dryout Heat Flux

Experimental measurement of dryout heat flux in a porous media are difficult to perform at high pressure. A strong apparatus is needed and the cost of building it is high. Therefore, it was desirable to use similar fluids so that dryout can easily be achieved and be scaled to represent high-pressure behavior. Pressure scaling was shown to be possible for all thermodynamically similar fluids by Lienhard and Schrock [20] and Lienhard and Watanabe [21]. Lienhard and Schrock observed in 1961 that Zuber's expressions for $q_{\max}$ and $q_{\min}$ [22] depend only upon thermodynamic variables since the transitions are dictated hydrodynamically and are not influenced by transport processes. All these thermodynamic properties can be expressed as a function of the reduced pressure P_r. This then permits the formulation of reduced heat fluxed $(q_{\max})_r$ and $(q_{\min})_r$, which, according to the law of corresponding states, should have the same functional dependence upon P_r for all substances. Formal application of the law of corresponding states leads them to correlations of the form

$$\frac{q_{\min}}{q_s} \text{ and } \frac{q_{\max}}{q_s} = f(P_r, \quad \text{geometry})$$

with the scaling heat flux defined by

$$q_s = \left[\frac{8}{3}\,\frac{g^3\sigma^3 M P_c^7}{RT_c(\rho_l-\rho_v)^4}\right]^{3/4}$$

Using q_s to scale the dryout heat flux data from measurements using Freon-113 allows one to estimate the dryout heat flux for water at pressures up to 37 atm. The acetone and methanol results did not scale well enough to be useful. As shown by many models, the dryout heat flux varies as d_p^2 in the small-particle region, whereas it varies as $d_p^{1/2}$ in the large-particle region. For different liquids the transition diameter d_p^* may not be the same, so the scaling method cannot be used directly in the small particle region even if it works quite well for the large particles. Thus, the scaling method needs to be modified to extend to the small-particle region.

First of all, we need to find the transition particle diameter which divides the small particle regime from the large particle region. The Ostensen and Lipinski model [11] and Dhir and Catton model [5] wre chosen to represent the dryout behavior for the large and small-particle regimes, respectively. The transition particle diameter can be derived by calculating the intersection point of those two models. It is

$$d_p^* = 184\,\frac{(1-\epsilon)}{\epsilon}\left[\frac{\nu_l^2}{g}\right]^{1/3}\left[\frac{1}{1+(\rho_l/\rho_v)^{1/4}}\right]^{4/3} \tag{1}$$

One can relate the intersection of the small particle dryout heat flux for different fluids with the large particle dryout heat flux curve by

$$\frac{q_{d_1}}{q_{s_1}} = \frac{q_{d_2}}{q_{s_2}}\left[\frac{d_{p_2}^*}{d_{p_1}^*}\right]^{3/2} \tag{2}$$

where the subscripts 1 and 2 refer to fluid, 1 and 2. Choosing a liquid, the scaling factor is

$$q_s = \begin{cases} \left[\dfrac{8M\,g^3\sigma^3 P_c^7}{3RT_c(\rho_l-\rho_v)^4}\right]^{3/4} & \text{large particles } (d_p \geq 1.6 \text{ mm}) \\ \left[\dfrac{8M\,g^3\sigma^3 P_c^7}{3RT_c(\rho_l-\rho_v)^4}\right]^{3/4}\left[\dfrac{d_{p_w}^*}{d_p^*}\right]^{3/2} & \text{small particles } (d_p < 1.6 \text{ mm}) \end{cases} \tag{3}$$

where the subscript w refers to water, which is one of the most commonly used liquids in the nuclear industry.

Experimental Apparatus and Procedure

A schematic of the experimental apparatus used to study the effect of pressure on dryout is shown in Fig. 1. It consists of a thick-walled glass tube (6.1 cm i.d., 7.1 cm o.d.) closed at the bottom. The tube holds a debris bed of steel particles and the coolant. The bed was inductively heated with a multiturn copper coil (radius of curvature 5.8 cm). The coil was powered by a 10 kW, 463 kHz Cycle-Dyne radio frequency generator. A reflux condenser was used to condense the large amounts of vapor generated during the runs. The condenser is a section of helically coiled copper tubing and is housed above the bed in the same kind of glass as the thick-walled glass tube. It is fastened to the top of the glass tube with a flange and collar.

A flask of nitrogen under high pressure was used to keep pressure on the system and a pressure regulator was used to set and maintain the desired pressure. Another flask was connected to the system to damp out pressure fluctuations that might occur during boiling. A small amont of nitrogen was constantly bled out of the system. Four thermocouples in the debris bed were connected to an X–Y recorder to calibrate the power and to occasionally check the temperatures during boiling. Mild steel particles of diameter 0.59 to 0.79 mm and stainless steel particles of diameters 1.6 mm, 3.2 mm, and 4.8 mm were used to form the porous bed. A majority of the experiments were conducted using Freon-113 and water; some used acetone and methanol.

Nomenclature

d = particle diameter
h_{fg} = latent heat of vaporization, J/kg
g = acceleration due to gravity, m/s^2
L_B = bed depth, m
L_C = overlying coolant depth, m
M = molecular weight
P = pressure, Pa
P_r = reduced pressure
P_C = critical pressure, Pa
q_d = dryout heat flux, kW/m^2
q_{d_r} = reduced dryout heat flux
$q_{\max}$ = peak heat flux, kW/m^2
$q_{\min}$ = minimum heat flux, kW/m^2
q_s = scaling factor for dryout heat flux, kW/m^2
R = gas constant, Pa m^3/K
T = temperature, K
T_C = critical temperature, K
T_r = reduced temperature
γ = overlying liquid ratio, L_C/L_B
ϵ = porosity
μ_l = dynamic viscosity, liquid, Ns/m^2
μ = dynamic viscosity, vapor, Ns/m^2
ρ_l = liquid density, kg/m^3
ρ_v = vapor density, kg/m^3
σ = surface tension, N/m
φ = liquid fraction in the bed

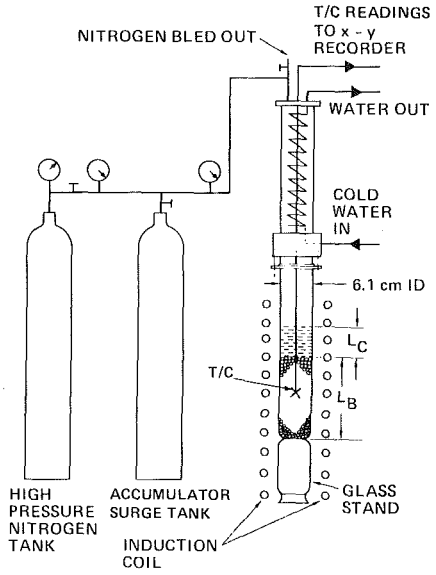

Fig. 1 Experimental apparatus for measurement of pressure effect on dryout

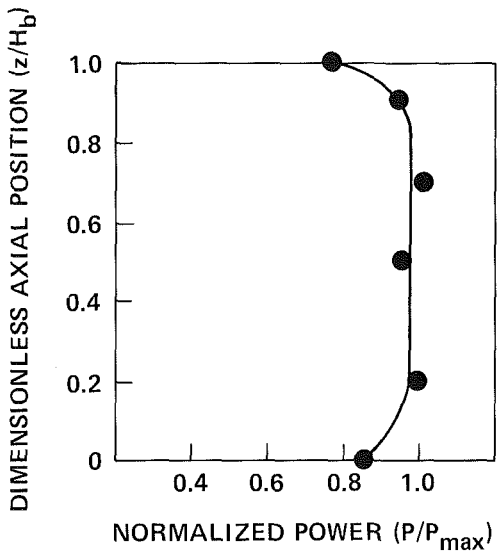

Fig. 2 Uniformity of bed power generation: Axial power profile

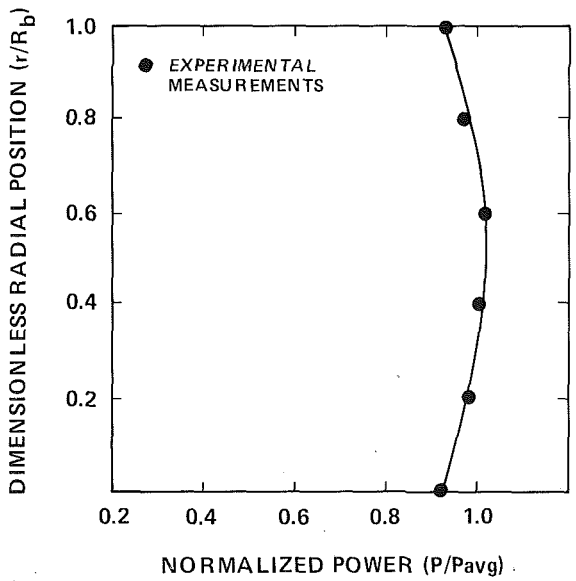

Fig. 3 Uniformity of bed power generation: Radial power profile

Table 1 Thermophysical properties used to calculate the volumetric heating rate

	C_P, J/kg-K	ρ, kg/m^2	
Steel	4.605×10^2	7.82×10^3	(*s*)
Freon-113	9.128×10^2	1565.0	(*l*)
Water	4.174×10^3	989.0	(*l*)
Acetone	2.276×10^3	750.8	(*l*)
Methanol	2.794×10^3	747.8	(*l*)

Power Calibration

The power input into the bed was determined by an adiabatic startup process. At 1 atm absolute pressure, with both the debris bed and the coolant in the tube, the power was turned on, and the temperature increase was recorded. After cooling the bed down to almost ambient temperature, this was repeated for another power setting and a calibration curve established. A temperature record was made using a copper-constantan thermocouple encased in a 1-mm glass rod embedded in the bed and connected to an X-Y recorder. The input heat flux corresponding to the temperature increase

$$q=[\epsilon\,\rho_l C_P+(1-\epsilon)\rho_s C_{Ps}]H_b\,\frac{dT}{dt} \tag{4}$$

The heat flux is based on the cross-sectional area of the glass tube (total bed power divided by bed volume times bed height). The porosity was measured and taken to be 0.4 in all cases. Table 1 gives the thermophysical properties which were used to calculate the volumetric heating rate.

The spatial power distibution within the bed was checked and found to be almost uniform in the axial and radial direction. This was done by placing the thermocouples radially at several elevations as well as axially at several radii. Typical profiles are shown in Figs. 2 and 3. Therefore, typically one thermocouple near the middle of the bed was used for the bed power calibration. Further discussion of the uniformity of the heating can be found in [4, 5, 18].

Identifying Dryout

Three methods were used to identify the power at which the bed dries out: visual observation, temperature measurement, and reflood time measurement. Visual observation is not a good method because dryout can, and in most cases does, occur within the bed and out of sight. The temperature increase measurement was, at first glance, thought to be a good method, but turned out not to be consistent. The reason for this is that a thermocouple may not be properly located at the place where dryout first occurs, so no temperature increase would be measured unless the heating period was very long.

Somerton et al. [18] suggested the reflood time be used to determine the dryout point. Reflood time is defined as the time it takes the coolant, displaced from the bed by the boiling process, to re-enter when the power is turned off. This time can be measured very accurately by watching how the liquid front moves up to a predetermined point at the surface of the bed, when the power is turned off. Once a dryout spot forms, the reflood time will increase because the local superheat must first be removed by evaporation. For heating rates below dryout, the reflood time is constant, but once the dryout limit has been reached, the reflood time increases with increasing power and the amount of time at a power setting. A typical graph of the reflood time is shown in Fig. 4 where the load meter reading is directly proportional to the power. A careful study of this method was carried out. To verify that the reflood time was an appropriate indicator of dryout, the physical location of the dryout was found (with some difficulty) and its temperature was measured. Figure 4 shows that the time to reflood increases monotonically with time at power beyond the dryout point. This implies a linear heatup in the

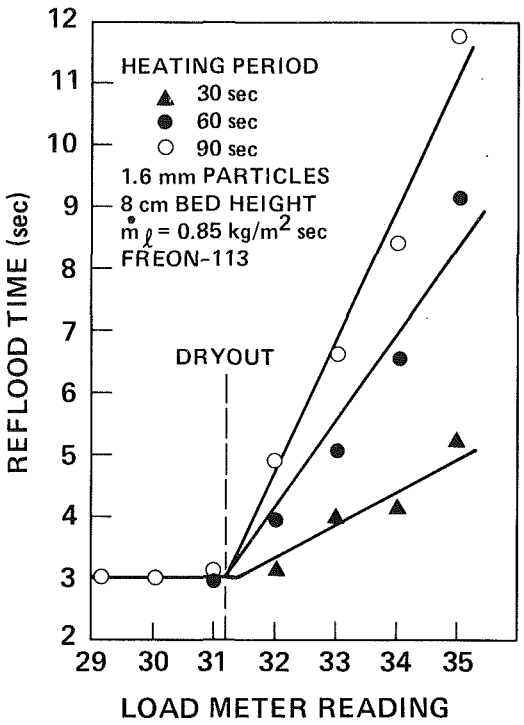

Fig. 4 Effect of different heating periods on the reflood time

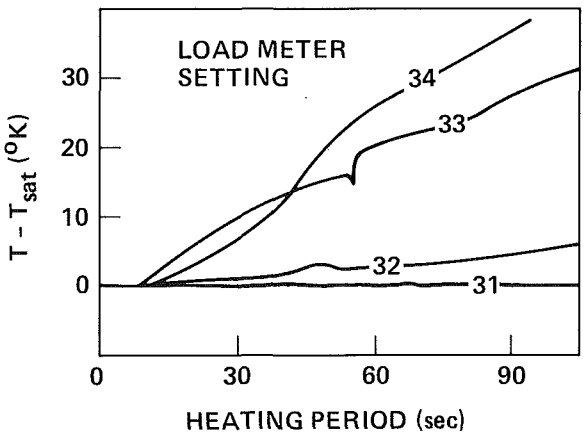

Fig. 5 Temperature-time behavior for various load meter settings

dry part of the bed, which is better seen in Fig. 5. It is clear that dryout has occurred. The dry region becomes superheated and the excess energy (above the saturation temperature) must be removed before boiling will cease. The reflood time method was therefore chosen as the preferred method for determining the dryout heat flux.

Test Procedure

The test procedure was the same for each particle size and each coolant. A predetermined bed was installed in the glass tube and coolant added to obtain a certain overlying liquid height. The load meter was calibrated following the procedure described above. An arbitrary power setting was chosen and the machine and power maintained constant for 1.5 min. When the power was turned off the reflood time was measured. The reflood time was then plotted as a function of the load meter setting (see Fig. 4, and the dryout point found. The load meter calibration procedure was repeated at load meter readings around the dryout point to obtain a power calibration curve that could be used for different pressure and flow rates. The dryout point was then found for different system pressures as before. After each run the amount of overlying liquid was checked to make sure it had stayed constant.

Experimental Error

The principal error in this experiment is in measuring the power input to the bed. The error is from the following:

1 The power can only be set to within 0.5 (full scale = 100) of the load meter reading.

2 When calibrating the power, the temperature time history plot was assumed to be linear, but it was not. Error was therefore introduced in estimating the slope.

3 Both the radial and axial power profiles have been considered uniform, even though they have a slight tapering off of the power at both ends of the bed (see Figs. 2 and 3). Consequently the measured bed power is slightly overestimated.

4 The porosity of the bed may vary from 0.38 to 0.42; 0.40 is used in all calculations.

5 The height of the bed can only be measured to within ± 0.2 cm.

6 Values of the thermophysical properties used to calculate the input power were assumed to be constants.

Assuming that the errors are random, the uncertainty in dryout heat flux, found from equation (4), is

$$\frac{dq_d}{q_d}=\left[\left[\frac{dH_b}{H_b}\right]^2+\left[\frac{d\left(\frac{dT}{dt}\right)}{\frac{dT}{dt}}\right]^2+\left[1-\frac{\rho_s C_{ps} H_b\left(\frac{dT}{dt}\right)}{q_d}\right]^2\left[\frac{d\epsilon}{\epsilon}\right]^2\right]^2 \tag{5}$$

For a typical case we would have

$$\frac{dH_b}{H_b}=0.02$$

where the largest particles are 0.2 cm and the smallest bed height is 10.0 cm. By looking at some temperature history plots of the power calibration, it was observed that the error in this plot could be ±15 percent. Therefore we have

$$\frac{d\left(\frac{dT}{dt}\right)}{\frac{dT}{dt}}=0.15$$

and

$$\left[1-\frac{\rho_s C_{ps} H_b\left(\frac{dT}{dt}\right)}{q_d}\right]\frac{d\epsilon}{\epsilon}=0.05$$

The resulting error in q_d is

$$\frac{dq_d}{q_d}=\pm[(0.02)^2+(0.15)^2+(0.05)^2]=\pm 0.16$$

Thus, an uncertainty of ±16 percent should be expected in the experimental measurements of the dryout heat flux. The greatest part of this uncertainty is in determining the slope of the temperature record or in equation (4). This was therefore done many times and the average slope taken in those cases where accurate results were necessary. Also, as was mentioned earlier, a power calibration curve was established instead of

Table 2 Dryout heat flux (kW/m^2) as a function of bed depth L_B and overlying liquid ratio γ; Freon-113 at 1 atm absolute

L_B (cm)	d_p [mm]	γ 0.0	0.5	1.0	1.5	2.0	2.5
5.0	.59 - .79	43.9	(44.0)*	44.0	43.9	43.9	44.0
	1.6	92.3, 96.2	108.6,114.2	108.6	(109)	108.6	(109)
	3.2	215	216	216	(215)	(215)	(215)
	4.8						
10.0	.59 - .79	47.3, 46.0	47.5	49.0	(47.0)	49.7	(47)
	1.6	184.8	201.1	191.2	200.0, 193	192.0	(195)
	3.2	224	282	266	272	265	(270)
	4.8	308.3	(308)	308.3	(308)	306.6	(308)
15.0	.59 -.79	46.4	42.3	48.5	(48)	(48)	
	1.6	163.9	180.7	201.5	196.0	(200)	
	3.2	232	251, 263	265			
	4.8	308	(308)	308	(308)	(308)	
20.0	.59 -.79	52.5	53.0	(53.0)	(53.0)		
	1.6	149.0	163.9	183.9			
	3.2	203.0	220.0	268.0			
	4.8	310	310	(310)	(310)		

*( ) denotes estimates obtained by interpolation

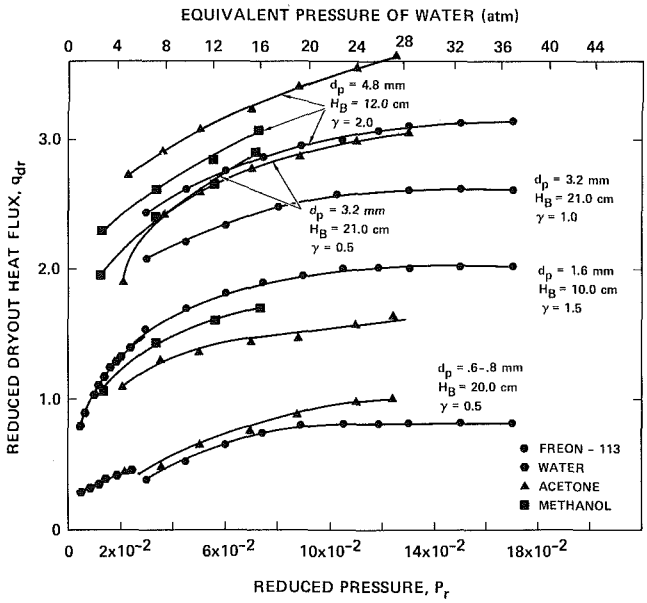

Fig. 6 Reduced dryout heat flux as a function of reduced pressure

just calibrating each dryout point. The best curve was then visibly fitted to the calibration points and read off this curve when the dryout heat flux was determined.

Experimental Results

The study was carried out for four particle sizes: 0.59–0.79 mm, 1.6 mm, 3.2 mm, and 4.8 mm. Freon-113 and acetone were used as coolants for all the particle sizes, water was used with the 1.6 mm and 0.59–0.79 mm particles and methanol with the 1.6 mm, 3.2 mm, and 4.8 mm particles. Experimental measurements are tabulated in the appendix.

Using Freon-113 as a coolant, the effects of the overlying liquid ratio γ and the bed height H_B were investigated for all the particle sizes. The results are presented in Table A.1 in the appendix. The results have been summarized in Table 2. During these runs H_B was varied from 5.0 to 21.0 cm and γ from 0.0 to 2.0. The bed diameter was constant at 6.1 cm.

The effects of pressure on the dryout flux were investigated for all the particle sizes using Freon-113 as a coolant. The results are presented in Table A.1 of the appendix. The pressure range was from 0.23 to 5.76 atm absolute. Using water as a coolant, the effects of pressure on the dryout flux were investigated for the 1.6 mm and 0.59–0.79 mm particles. The pressure range was from 1 to 5.08 atm absolute. The results are presented in Table A.2 in the appendix. Acetone was used as a coolant for all particle sizes for the pressure range from 1 to 5.76 atm absolute. The results are presented in Table A.3 in the appendix. Some limited results for methanol are presented in Table A.4.

All the experimental results are summarized in Fig. 6 in nondimensional form.

Effects of Bed Depth and Overlying Liquid

Previous investigators have shown that the dryout heat flux is dependent on bed height for shallow beds and independent of the depth for deep beds. To make sure that the bed would be deep enough some runs were made where bed height was varied systematically. While looking at the effects of bed depth on dryout it was found that the results depended very much on how much coolant was above the bed. Results of this investigation are tabulated in Table 2. The tabulated values of dryout clearly show that when a bed is "deep enough" is a function of the overlying liquid ratio characterized by γ. For $\gamma = 0.5$, a bed of 3.2 mm particles is deep enough at a depth of about 20.0 cm, but for an overlying liquid ratio $\gamma = 1.0$ it is deep enough when $L_B = 11.0$ cm. The data show that the dryout heat flux is lower at $\gamma = 0.5$ than at $\gamma = 1.0$ for a 21.0 cm deep bed, but the overlying liquid ratio γ no longer affects dryout heat flux for an 11.0 cm bed when $\gamma \geq 0.5$. This is an interesting result; the finding that the overlying liquid ratio has more of an effect on the dryout of deep beds than on the dryout of shallow beds might explain why there is so much scatter in the experimental results of other investigations, since the ratio is usually not mentioned.

Similar results were obtained for particle diameters of 1.6 mm and bed depths $H_b \geq 10.0$ cm, i.e., more effect of γ on dryout of deep beds than shallow ones and that a deeper bed is required for it to be a "deep bed" when the ratio is low. However, for $H_b \leq 10.0$ cm the results are somewhat surprising. The dryout heat flux falls rapidly with smaller bed depth and the overlying liquid ratio does not seem to have more effect when the bed depth is as small as 5.0 cm.

The results for the smallest particle size show that neither γ nor the bed depth seems to have much effect on the dryout heat flux. The scatter in the results shows that the zero overlying liquid height experiment must be conducted very carefully, especially for the smallest particles, since the dryout heat flux is so low.

When the particles are large ($d_p = 4.8$ mm), the dryout heat flux is insensitive to both H_B and γ, just like the smallest particles. However, since the results in the table were not repeated, and this experiment must be conducted very carefully, the results should be viewed with caution. A dryout heat flux of around 307 kW/m^2 for large particles in Freon-113 is in reasonable agreement with results of Barleon and Werle [10].

Several different mechanisms could lead to dryout of the debris bed. For small particles, friction in the bed dominates [5], whereas for large particles, $d_p > 1.5$ mm, Counter Current Flow Limiting (CCFL) will take place above the bed or within the interstitial spaces near the top. Zuber [22] addressed CCFL above a heated surface. Here the surface will influence

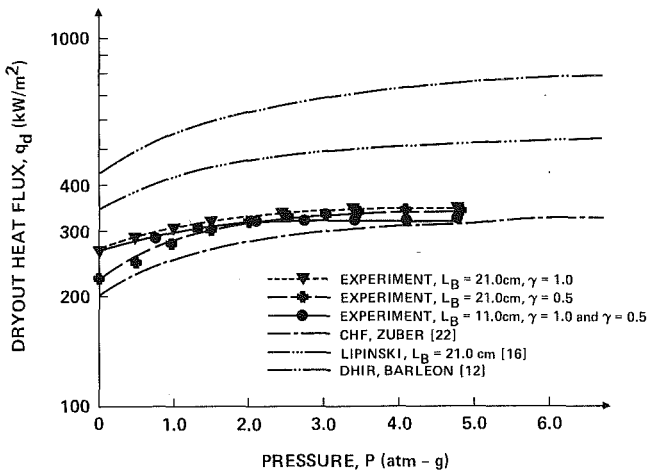

Fig. 7 Comparison of experimental results with models for a bed of 3.2 mm particles (Freon-113)

Table 3 Some thermophysical properties used to calculate dryout heat flux

P(atm)	T_{sat}(°C)	$\rho_\ell\left(\frac{kg}{m^3}\right)$	$\rho_v\left(\frac{kg}{m^3}\right)$	$\mu_\ell x10^3\left(\frac{N\,sec}{m^2}\right)$	$\mu_v x10^5\left(\frac{N\,sec}{m^2}\right)$	$\sigma\left(\frac{N}{M}\right)$	$\hat{h}_{fg}\left(\frac{J}{kg}\right)$
FREON							
1.0	47.8	1510.0	7.45	0.504	1.078	14.8×10^{-3}	146,742
2.0	70.0	1453.0	14.21	0.400	1.123	12.5×10^{-3}	138,932
3.2	87.8	1405.0	22.46	0.339	1.170	10.7×10^{-3}	131,791
4.3	98.9	1374.0	29.25	0.308	1.190	9.6×10^{-3}	123,860
5.4	110.0	1340.0	37.71	0.282	1.257	8.5×10^{-3}	120,254
6.1	115.6	1323.0	42.54	0.269	1.269	7.9×10^{-3}	117,789
ACETONE							
1.14	60	745.8	2.44	0.224	0.891	18.63×10^{-3}	500.8×10^3
2.13	80	722.3	4.31	0.194	0.951	16.19×10^{-3}	478.8×10^3
2.82	90	710.0	5.59	0.181	0.982	14.98×10^{-3}	467.2×10^3
3.68	100	697.3	7.14	0.170	1.014	13.79×10^{-3}	455.1×10^3
WATER							
1.0	100.0	958	0.611	0.288	1.203	58.9×10^{-3}	2.247×10^6
2.0	120.6	942	1.124	0.238	1.281	54.9×10^{-3}	2.198×10^6
3.0	133.9	931	1.644	0.214	1.331	52.1×10^{-3}	2.163×10^6
4.0	144.1	922	2.162	0.197	1.369	50.0×10^{-3}	2.198×10^6
5.0	152.2	914	2.660	0.187	1.398	48.2×10^{-3}	2.108×10^6
6.0	159.3	907	3.177	1.180	1.423	46.8×10^{-3}	2.084×10^6
7.0	165.5	901	3.687	0.173	1.443	45.4×10^{-3}	2.061×10^6
8.0	170.5	896	4.092	0.168	1.463	44.3×10^{-3}	2.047×10^6
9.0	175.2	891	4.493	0.162	1.480	43.3×10^{-3}	2.031×10^6
10.0	179.8	886	4.980	0.158	1.495	42.2×10^{-3}	2.015×10^6
METHANOL							
.23	70	742.7	1.464	0.305	1.127	18.48×10^{-3}	1.096×10^6
1.78	80	732.4	2.084	0.271	1.162	17.56×10^{-3}	1.075×10^6
2.52	90	721.8	2.907	0.242	1.197	16.61×10^{-3}	1.051×10^6
3.48	100	710.8	3.984	0.217	1.233	15.63×10^{-3}	1.026×10^6
4.73	110	699.3	5.373	0.194	1.269	14.62×10^{-3}	0.999×10^6

Surface Tension for Freon-113 was calculated with $\sigma = 20.0 \times 10^{-3}$

$$\left(1-\frac{T(°C)}{214.7}\right)^{1.2}\left(\frac{N}{m}\right)$$

the vapor streams in a way that will modify the critical heat flux. Dhir and Barleon [12] based their analysis on CCFL occurring in the interstitial spaces at the top of the bed. The most restrictive mechanism should control and lead to dryout of the bed. At this time it is difficult to predict which will govern for a specific bed configuration.

For an experimental study of the effects of pressure on dryout heat flux, a particular bed depth and overlying liquid ratio must be chosen for each particle size. In the work reported here, the two components were selected so that the dryout heat flux would be independent of an increase in γ or bed depth for Freon-113. For water, the same geometry was then selected for the corresponding particle size, so that the scaled results could be compared.

Effect of Pressure

The objective of this work was to study the effect of pressure on dryout heat flux. The results can be seen in Fig. 6. In Fig. 6 the reduced dryout heat flux is plotted as a function of the reduced pressure. As would have been expected from Fig. 2, the dryout at 1 atm absolute pressure is lower for $\gamma = 0.5$, than $\gamma = 1.0$ for a 21.0 cm deep bed at low pressures, but does not depend on γ when $\gamma > 0.5$ for an 11.0 cm deep bed of 3.2 mm particles. Figure 7 also shows that the dryout heat flux increases with increasing pressure and since the effects of the ratio disappear at high pressure, the rate of increase is greater at $\gamma = 0.5$ for deep beds than for larger values of γ.

The results for particles of diameter 0.59–0.79 mm and 4.8 mm in Freon-113 are also shown in Fig. 6. For the small particles, a bed of 20.0 cm was used with the ratio $\gamma = 0.5$, since it does not affect the dryout heat flux. For large particles, a bed of $H_B = 12.0$ cm with $\gamma = 2.0$ was used. This was chosen so that even if Tsai et al. [23] were right about the effect of γ on dryout heat flux for beds of large particles, γ would be large enough to make the results independent of bed height and γ. It can also be seen that the increase in dryout heat flux is less for smaller particles. This is because the resistance to flow within the bed, rather than the "flooding" limit near the top of the bed, determines the dryout heat flux in beds of small particles.

The effect of pressure on the dryout heat flux when acetone is used as a coolant was measured for all particle sizes and the bed configuration for each particle size was the same as for Freon-113. Here, as for Freon-113, the dryout heat flux increases with increasing pressure.

Reaching the dryout heat flux in water requires a higher power than when Freon-113 is used. Due to limited power supply it was therefore only possible to reach dryout with particle size $d_p \leq 1.6$ mm. The experiment was run for the 1.6 mm and 0.59–0.79 mm particles. The 1.6 mm bed was 10 cm deep and the overlying liquid ratio γ was 1.5; the other bed was 20.0 cm deep, with $\gamma = 0.5$. These configurations were used so the results could be compared to the Freon-113 results with the same geometry. The pressure dependence here is the same as for Freon-113 and acetone.

The fourth coolant used was methanol. Runs were made with particle sizes of 1.6 mm, 3.2 mm, and 4.8 mm. The 1.6 mm particle bed was 10.0 cm deep and had an overlying liquid ratio γ of 1.5. The 3.2 mm bed was 20.0 cm deep with $\gamma = 0.5$ and the 4.8 mm bed was 12.0 cm deep with $\gamma = 1.5$. These are the same configurations that were used with the other coolants and the results can therefore be compared after scaling (see Fig. 6).

Comparison of Data With Model Predictions

To establish how well existing models predict dryout heat flux, experimental results were compared with the dryout models derived by Lipinski [16], Dhir and Barleon [12], and with the pool boiling critical heat flux q_{CHF} given by Zuber [22]. Here, Zuber's prediction of CHF is thought to represent CCFL taking place above the bed. Comparison was also made with the model derived by Dhir and Catton [5] for the smallest particles and with the model of Sowa et al. [1] for the largest particles. The model of Theofanus and Saito [24] was not used since it is essentially the same as Sowa's model. The theoretical properties needed to calculate the dryout heat flux for the various models are given in Table 3.

In Fig. 7 a comparison is made of model predictions with data for the 3.2 mm particle bed saturated with Freon-113. It indicates that although the experimental data are somewhat higher than Zuber's [22] CHF model, in particular at 1 atm absolute, it best predicts the magnitude and the trend of the data. The trend of Lipinski's [16] model is similar to Zuber's although somewhat higher than the data and the Dhir Barleon [12] prediction is much too high. All the models predict maximum dryout heat flux for Freon-113 at 8.6 atm gage.

The comparison made in Fig. 8 for 4.8 mm particles lead to conclusions similar to those above, i.e., that the Zuber model best predicts the trend of the data and that the Lipinski [10]

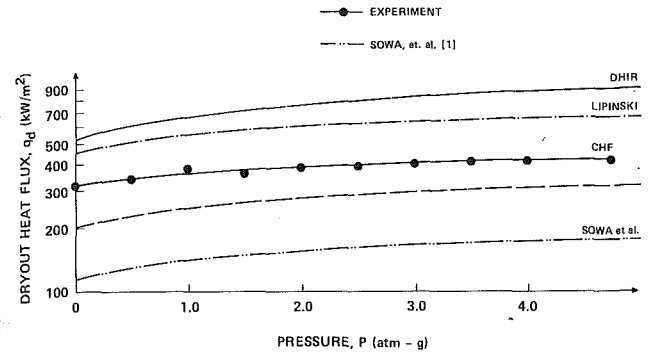

Fig. 8 Comparison of experimental results with models for a 12 cm deep bed of 4.8 mm particles (Freon-113, γ = 2.0)

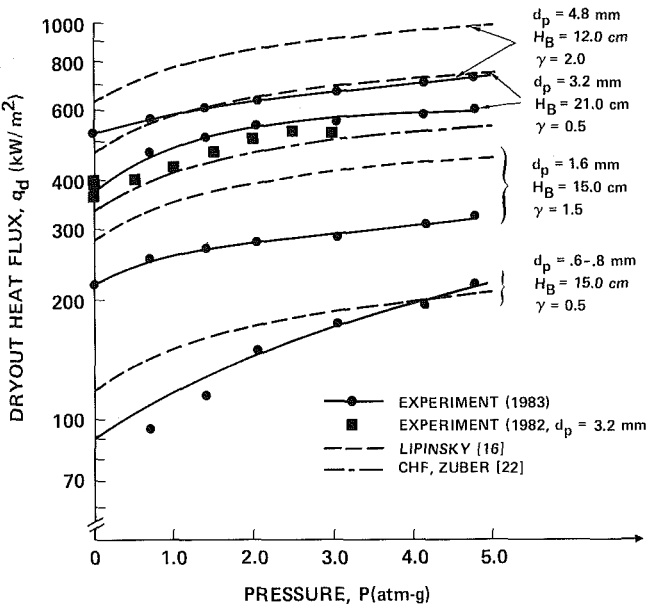

Fig. 9 Comparison of experimental results with Lipinski's model and CHF (acetone)

and Dhir Barleon [12] models overpredict the data. The model developed by Sowa et al. [1] severly underpredicts dryout. However, the distinctions between the results of the figures should be understood. Zuber's prediction of dryout is for a horizontal flat plate and is therefore not physically correct for a porous medium. The other models attempted to represent the physical processes expected in a porous medium and, as a result, are particle size dependent. It is, therefore, just a coincidence if Zuber's model and any other model coincide at any time.

Figure 9 shows the comparison of experimental results for acetone with predictions from Lipinski's model [16] and Zuber's CHF [22], for the 3.2 mm particles. Here, as for Freon-113, the models show the same trend as is displayed by the data while overpredicting the data. The Dhir-Barleon model (see Fig. 10), although theoretically based, has an empirically obtained constant. The constant was adjusted to match data obtained by Barleon and Werle [25] with water as a coolant. The reason this model overpredicts the results of the current experiment might therefore be that temperature measurements were used to identify dryout heat flux and if a thermocouple is not placed where dryout first occurs the dryout data are going to be too high. Zuber's critical heat flux prediction is in close agreement with the data. This agreement is coincidental and holds true only for this particular particle size, liquid, and the ratio γ.

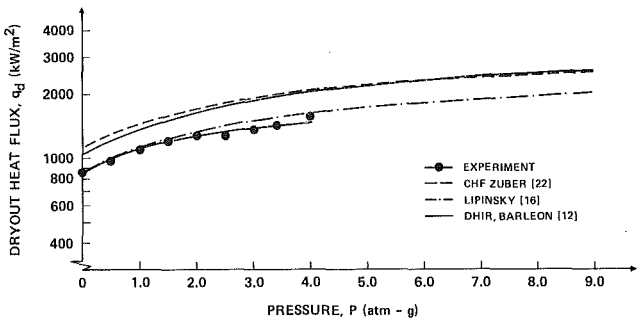

Fig. 10 Comparison of experimental results with models for a 10 cm deep bed of 1.6 mm particles (water, γ = 0.5)

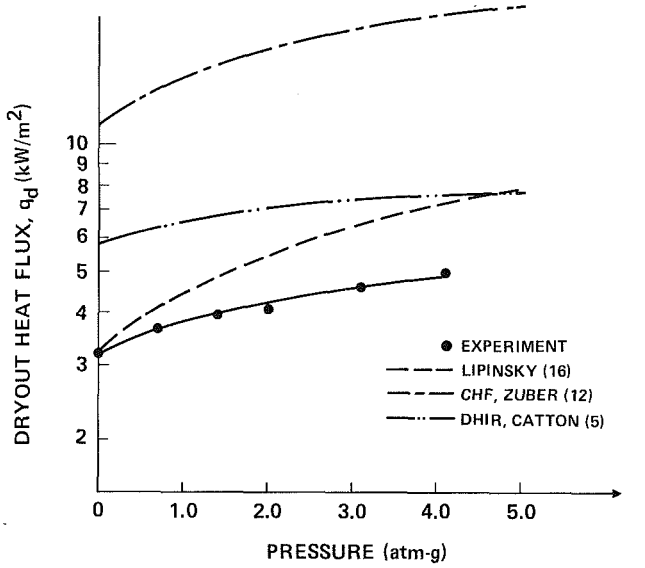

Fig. 11 Comparison of experimental results with models for a 15 cm bed of 0.59-0.79 mm particles (water, γ = 0.5)

A comparison of the data for a 1.6 mm particle bed saturated with water and the models can be seen in Fig. 10. As before, the data trend is the same as for the models and it is interesting to see how well the Lipinski model predicts the results for dryout heat flux in water. This similarity in the trend of dryout heat flux with pressure lends some strength to the assumptions made by Squarer et al. [19] that the pressure effect can be predicted based on CHF behavior with pressure. In Fig. 11, which shows data for small particles, all the models overpredict the results, but the trend of the Dhir-Catton model is correct.

Scaling of Results

The concept for scaling the dryout heat flux explained earlier was applied to the experimental results of this study; these results are shown in Fig. 6. The reduced dryout heat flux $q_d/q_s = q_{dr}$ is plotted in these figures as a function of reduced pressure with geometry as a parameter. It can be seen that the Freon-113 results fall on the same curve as the water results for the 1.6 mm particles and very close to the Freon-113 results for the smallest particles. The Freon-113 results, therefore, represent water up to 37.3 atm absolute. The reason the water results are a bit too high for the 0.59-0.79 mm particles might be that these results had to be obtained by using direct temperature measurement instead of the reflood method. As explained in the previous chapter, this could lead to higher measured dryout heat fluxes. It should be noted that the scaling factor for dryout heat flux q_s is almost a constant for each coolant: 1.305×10^5, 1.057×10^6, 1.970×10^5, and $3.240 \times$

Table 4 Critical temperature and pressure of the coolant used in this study

Liquid	T_c, °C	P_c, atm
Freon-113	214.0	33.7
Acetone	235.0	46.9
Methanol	239.5	78.7
Water	374.1	217.9

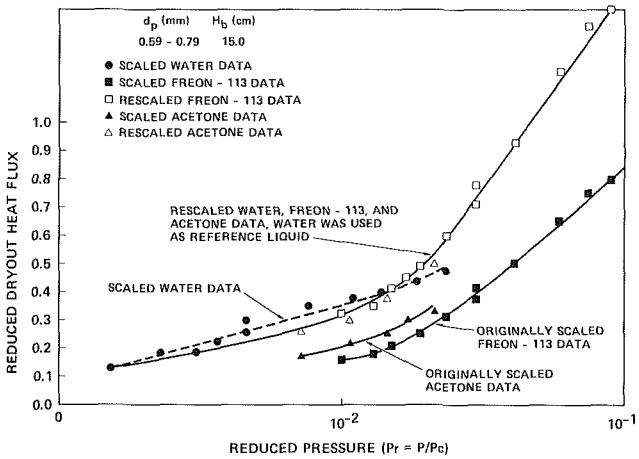

Fig. 12 Reduced dryout data versus reduced pressure

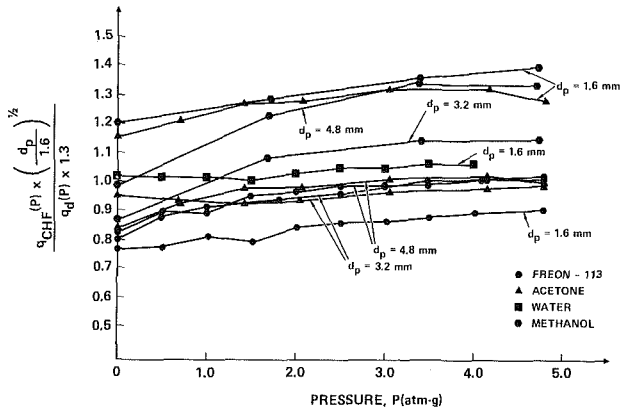

Fig. 13 An approach to scaling debris bed dryout data

10^5 W/m^2 for Freon-113, water, acetone, and methanol, respectively, based on the critical pressures and temperatures given in Table 4.

The acetone and methanol results do not coincide with the Freon-113 results in Fig. 6. The reason for this difference is probably just that the scaling factor needs some further work for it to be good for all fluids. The fact that the overlying liquid ratio is not the same for the 3.2 mm particles in different fluids does not make much difference at high pressure.

As mentioned earlier, the proposed scaling approach does not scale data for small particles very well unless the transition particle size is used to rescale q_s as shown in equation (3). On Fig. 12, the data of water, Freon-113, and acetone for small particles (d_p = 0.59–0.79 mm) are shown for both scalings. As one can see the original scaling method failed to scale those data into a single curve. Thus, the scaling method can be extended to the small particle region, by rescaling q_s with d_{pr}^*.

Another method to scale all the data for particles of $d_p \geq$ 1.6 mm was tried and the results are shown in Fig. 13. It was noticed that the dryout heat flux results for 1.6 mm particles did not deviate much from Zuber's predicted CHF [22] especially in the case of Freon-113. The parameter

$$\frac{1}{1.3}\,\frac{q_{\mathrm{CHF}}(P)}{q_d(P)}\left[\frac{d_p}{1.6}\right]^{1/2}$$

was calculated for all fluids. This parameter is close to being a constant and in most cases is within 30 percent of the mean value.

Conclusions

The following conclusions may be drawn from this experimental study:

1 The results of the experiments in this study indicate that of the models tested, Zuber's prediction of CHF [22] and Lipinski's model [16] best predict the effect of pressure on the dryout heat flux in a debris bed (i.e., the trend). Lipinski's model generally best predicts the value of the dryout flux, for all the coolants tested, since it is particle size dependent, while Zuber's prediction of CHF is not. In general, however, all the models are poor.

2 For a debris bed of 1.6 mm and 3.2 mm steel particles and with Freon-113 as coolant, the bed depth beyond which the dryout flux does not vary with bed depth (i.e., "deep bed") depends on γ. Larger bed depth is required to achieve a deep bed when γ is reduced (see Table 2).

3 The effect of γ on the dryout heat flux disappears at high pressure.

4 The effect of pressure on dryout heat flux in porous media can be scaled so that the dimensionless dryout heat flux is only a function of reduced pressure and geometry. Freon-113 can be used in the experiments to represent water. However, this scaling is not very good for acetone and methanol.

5 The scaling method can be modified to scale the small-particle data.

Acknowledgments

The Electrical Power Research Institute is gratefully acknowledged for its support of this project.

References

1 Sowa, E. S., Hesson, J. C., Gebner, R. H., and Goldfuss, G. T., "Heat Transfer Experiments Through Beds of UO_2 in Boiling Sodium," *Trans. ANS*, Vol. 14, 1971, p. 725.

2 Gabor, J. D., Hesson, J. C., Baker, L. Jr., and Cassulo, J. C., "Simulation Experiments on Heat Transfer From Fast Reactor Fuel Debris," *Trans. ANS*, Vol. 15, 1972, p. 836.

3 Gabor, J. D., Sowa, E. S., Baker, L., Jr., and Cassulo, J. C., "Studies and Experiments on Heat Removal for Fuel Debris in Sodium," *Proceedings of ANS Fast Reactor Safety Meeting*, Beverly Hills, CA, Apr. 1974, Paper No. CONF-740401, p. 823.

4 Keowen, R. S, "Dryout of a Fluidized Particle Bed With Internal Heat Generation," M.S. Thesis, University of California, Los Angeles, CA, 1974.

5 Dhir, V. K., and Catton, I., "Study of Dryout Fluxes in Beds on Inductively Heated Particles," USNRC NUREG-0252, 1974.

6 Hardee, H. C., and Nilson, R. H., "Natural Convection in Porous Media With Heat Generation," *Nuclear Science and Engineering*, Vol. 63, 1977, pp. 119–132.

7 Dhir, V. K., and Catton, I., "Effect of Particle Size Distribution and Non-heated Constituents on Debris Bed Dryout," *Proceedings of the Post-Accident Heat Removal (PAHR) Information Exchange Meeting*, ANL-788-10, 1977, p. 67.

8 Dhir, V. K., "Dryout Heat Fluxes in Debris Beds Containing Particles of Different Size Distributions," *Proceedings of the International Meeting on Fast Reactor Safety Tech.*, Seattle, WA, Aug. 19–23, 1972.

9 Squarer, D., and Peoples, J. A., "Dryout in Inductively Heated Beds With and Without Forced Flow," *Trans. ANS*, Vol. 34, 1980, pp. 537–538.

10 Barleon, I., and Werle, H., "Debris Bed Investigations With Adiabatic and Cooled Bottom," *Proceedings of the 9th Meeting of the Liquid Metal Boiling Working Group*, Rome, Italy, June 1980.

11 Ostensen, R. W., and Lipinski, R. J., "A Particle Bed Dryout Model Based on Flooding," *Nuclear Science and Engineering*, Vol. 79, 1981.

12 Dhir, V. K., and Barleon, L., "Dryout Heat Flux in a Bottom Heated Porous Layer," *Trans. ANS*, Vol. 38, 1981, pp. 385–386.

13 Theofanus, T. G., and Saito, M., "An Assessment of Class 9 (Core-Melt) Accidents for PWR Dry-Containment Systems," PNE-81-148, Purdue University, West Lafayette, IN, June 1981.

14 Henry, R. E., and Fauske, H. K., "Core Melt Progression and the Attainment of a Permanently Coolable State," presented at the Meeting on Light Water Reactor Safety, Sun Valley, ID, Aug. 1981.
15 Shires, G. L., and Stevens, G. F., "Dryout During Boiling in Heated Particulate Beds," AEEW-M1779, UKAEA, Winfrith, England, 1980.
16 Lipinski, R. J., "A Particulate Bed Dryout Model With Upward and Downward Boiling," *Trans. ANS*, Vol. 35, 1980, pp. 358–360.
17 Lipinski, R. J., "A One-Dimensional Particle Bed Dryout Model," *Trans. ANS*, Vol. 38, 1981, pp. 386–387.
18 Somerton, C., Catton, I., and Thompson, L., "An Experimental Investigation Into Dryout in Deep Debris Beds," ASME Winter Annual Meeting, Washington, D.C., 1981, Paper No. 81-WA/HT-17.
19 Squarer, D., Pieczynski, A. T., and Hochreiter, L. E., "Effect of Debris Bed Pressure, Particle Size, and Distribution on Degraded Core Coolability," *Nucl. Sci. and Eng.*, Vol. 80, 1982.
20 Lienhard, J. H., and Schrock, V. E., "The Effect of Pressure Geometry and the Equation of State Upon the Peak and Minimum Boiling Heat Flux," ASME JOURNAL OF HEAT TRANSFER, Vol. 85, 1963, p. 261.
21 Lienhard, J. H., and Watanabe, K., "On Correlating Peak and Minimum Boiling Heat Fluxes With Pressure and Heater Configuration," ASME JOURNAL OF HEAT TRANSFER, Vol. 87, 1965, p. 94.
22 Zuber, N., "Hydrodynamic Aspects of Boiling Heat Transfer," AECU-4439, Physics and Mathematics, 1959.
23 Tsai, F. P., Jakobsson, J. O., Catton, I., and Dhir, V. K., "Dryout of an Inductively Heated Bed of Steel Particles With Subcooled Flow From Below," *Proceedings of 2nd Int'l Meeting of Nuclear Reactor Thermal Hydraulics*, ANS/ASME, Santa Barbara, CA, Jan. 1983.
24 Theofanus, T. G., and Saito, M., "An Assessment of Class 9 (Core Melt) Accidents for PWR Dry-Containment Systems," PNE-81-148, Purdue University, West Lafayette, IN, June 1981.
25 Barleon, L., and Werle, H., "Dependence of Dryout Heat Flux on Particle Diameter for Volume and Bottom-Heated Debris Beds," KFK 3138, Nov. 1981.

APPENDIX

Experimental Measurements of the Effect of Pressure on Dryout Heat Flux

Experimental measurements of the effect of pressure on dryout heat flux are presented in the following tables:

Table	Fluid	Particle Sizes (mm)
A.1	Freon-113	0.59–0.79, 1.6, 3.2, and 4.8
A.2	Water	0.59–0.79 and 1.6
A.3	Acetone	3.2
A.4	Methanol	1.6, 3.2, and 4.8

Table A.1 Measurements of dryout heat flux for Freon-113 coolant

d_p(mm)	H_b(cm)	γ	P(atm)	q_d(kW/m^2)
.59 – .79	5.0	0.0	1.0	41.6, 43.9
"	"	1.0	"	44.0
"	"	1.5	"	43.9
"	"	2.0	"	34.9
"	"	2.5	"	44.0
"	10.0	0.0	"	47.3, 46.0
"	"	0.5	"	47.5
"	"	1.0	"	49.0
"	"	2.0	"	49.7
"	15.0	0.0	"	46.4
"	"	0.5	"	42.3
"	"	1.0	"	48.5
"	20.0	0.0	"	42.5, 37.5, 33.0
"	"	0.5	"	53.0
"	20.0	0.5	1.0	53.0
"	"	"	1.0	53.0
"	"	"	1.5	66.5
"	"	"	2.0	84.8
"	"	"	2.5	98.2
"	"	"	3.0	103.8
"	"	"	3.5	107.0
"	"	"	4.0	"
"	"	"	4.5	"
"	"	"	5.0	"
"	"	"	5.8	"
1.6	5.0	0.0	1.0	92.3, 96.2
"	"	0.5	"	108.6, 114.2
"	"	1.0	"	108.6
"	"	2.0	"	108.6
"	10.0	0.0	"	184.8
"	"	0.5	"	201.1
"	"	1.0	"	191.2
"	"	1.5	"	192.3, 200.0
"	"	2.0	"	192.0
"	15.0	0.0	"	163.9
1.6	15.0	0.5	"	181
"	"	1.0	"	202
"	"	"	2.5	308
"	"	"	3.5	328
"	"	"	4.0	335
"	"	"	5.1	336
"	"	"	5.8	336
"	"	1.0	1.0	269, 271
"	"	"	1.5	290
"	"	"	2.0	305
"	"	"	2.7	318
3.2	21.0	1.0	3.4	336
"	"	"	4.4	339
"	"	"	5.8	339
4.8	10.0	0.0	1.0	308
"	"	1.0	"	308
"	"	2.0	"	307
"	15.0	0.0	"	308
"	"	1.0	"	308
"	12.0	2.0	1.0	318
4.8	12.0	"	1.5	342
"	"	"	2.0	380, 372
"	"	"	2.5	366
"	"	"	3.0	384
"	"	"	3.5	393
"	"	"	4.0	400
"	"	"	4.4	406
"	"	"	5.1	409
"	"	"	5.8	411
"	20.0	0.0	1.0	310
"	"	0.5	1.0	310
.59 – .79	15.0	1.5	0.33	20
.59 – .79	15.0	1.5	0.5	23
.59 – .79	15.0	1.5	0.67	33
.59 – .79	15.0	1.5	0.8	43
.59 – .79	15.0	1.5	1.0	49

Table A.1 cont

1.6	15.0	1.5	0.33	133
1.6	15.0	1.5	0.5	157
1.6	15.0	1.5	0.67	172
1.6	15.0	1.5	0.8	186
1.6	15.0	1.5	1.0	196
3.2	15.0	1.5	0.33	181
3.2	15.0	1.5	0.5	215
3.2	15.0	1.5	0.67	235
3.2	15.0	1.5	0.8	252
3.2	15.0	1.5	1.0	265
4.8	15.0	1.5	0.33	228
4.8	15.0	1.5	0.5	257
4.8	15.0	1.5	0.67	280
4.8	15.0	1.5	0.8	296
4.8	15.0	1.5	1.0	313
"	"	1.5	"	196
"	20.0	0.0	"	149
"	"	0.5	"	164
"	"	1.0	"	184
"	7.5	0.0	"	132
"	"	1.0	"	192
"	11.0	1.5	1.0	200, 193
"	"	"	2.0	239
"	"	"	2.5	239
"	"	"	3.0	246
"	"	"	3.5	264
1.6	11.0	1.5	4.0	264
"	10.0	"	4.4	260
"	10.0	"	5.1	260
"	"	"	5.8	264
"	11.0	0.0	1.0	224
"	"	0.5	"	281, 282, 279
"	"	0.5	"	272.0
"	"	1.0	"	266
"	"	1.5	"	272
"	10.0	2.0	"	265
"	15.0	0.0	"	232
"	"	0.5	"	251, 263
"	"	1.0	"	265.0
"	21.0	0.0	"	203.0
"	"	0.5	"	220, 232, 215
"	"	1.0	"	268.0
"	25.0	0.5	"	239, 224, 226
"	11.0	0.5	1.0	270
"	"	"	2.0	296
"	"	"	3.1	326
"	"	"	4.4	320
"	"	"	5.9	326
1.6	11.0	1.0	1.0	260, 272
"	"	"	1.7	285
"	"	"	2.4	307
"	"	"	3.1	318
3.2	11.0	1.0	3.7	320
"	"	"	5.1	320
"	"	"	5.8	324
"	"	2.0	1.0	265
"	"	"	1.5	277
"	"	"	2.0	302
"	"	"	2.5	302
"	"	"	3.0	317
"	"	"	3.5	334
"	"	"	4.0	335
"	21.0	0.5	1.0	225, 200
"	"	"	1.5	245
"	"	"	2.0	275

Table A.2 Dryout measurements of heat flux for water coolant

d_p(mm)	H_b(cm)	γ	P(atm)	q_d(kW/m^2)
*.59–.79	15.0	0.5	1.0	320
"	"	"	1.7	365
"	"	"	2.4	395
"	"	"	3.0	410
"	"	"	4.1	460
"	"	"	5.1	495
1.6	10.0	1.5	1.0	855
"	"	"	1.5	960
"	"	"	2.0	1150, 1100
"	"	"	3.5	1215
"	"	"	4.0	1350
"	"	"	4.4	1430
"	"	"	5.1	1521
.59 – .79	15.0	1.5	0.33	138
.59 – .79	15.0	1.5	0.5	191
.59 – .79	15.0	1.5	0.67	212
.59 – .79	15.0	1.5	0.8	244
.59 – .79	15.0	1.5	1.0	276
1.6	15.0	1.5	0.33	350
1.6	15.0	1.5	0.5	498
1.6	15.0	1.5	0.67	572
1.6	15.0	1.5	0.8	678
1.6	15.0	1.5	1.0	795
3.2	15.0	1.5	0.33	570
3.2	15.0	1.5	0.5	720
3.2	15.0	1.5	0.67	820
3.2	15.0	1.5	0.8	975
3.2	15.0	1.5	1.0	1030
4.8	15.0	1.5	0.33	996
4.8	15.0	1.5	0.5	1124
4.8	15.0	1.5	0.67	1250
4.8	15.0	1.5	0.8	1314
4.8	15.0	1.5	1.0	1431

*) For this particle size the dryout was found with direct temperature measurement

Table A.3 Measurements of dryout heat flux for acetone coolant

d_p(mm)	H_b(cm)	γ	P (atm)	q_d(kW/m^2)
3.2	21.0	0.5	1.0	392, 363, 412
"	"	"	1.5	500
"	"	"	2.0	432
"	"	"	2.5	472
"	"	"	3.0	472, 514
"	"	"	3.5	530
"	"	"	4.0	520
.59 - .79	15.0	1.5	0.33	36
.59 - .79	15.0	1.5	0.5	47
.59 - .79	15.0	1.5	0.67	50
.59 - .79	15.0	1.5	0.8	59
.59 - .79	15.0	1.5	1.0	67
1.6	15.0	1.5	0.33	183
1.6	15.0	1.5	0.5	211
1.6	15.0	1.5	0.67	248
1.6	15.0	1.5	0.8	266
1.6	15.0	1.5	1.0	282
3.2	15.0	1.5	0.33	273
3.2	15.0	1.5	0.5	325
3.2	15.0	1.5	0.67	335
3.2	15.0	1.5	0.8	361
3.2	15.0	1.5	1.0	390

Table A.4 Measurement of dryout heat flux for methanol coolant

d_p (mm)	H_b (cm)	γ	P (atm)	q_d(kW/m^2)
1.6	10.0	1.5	1.0	349
"	"	"	2.7	468
"	"	"	4.4	521
"	"	"	5.8	560
3.2	20.0	0.5	1.0	629
"	"	"	2.7	783
"	"	"	4.4	865
"	"	"	5.8	944
4.8	12.0	1.5	1.0	736
"	"	"	2.7	848
"	"	"	4.4	922
"	"	"	5.8	1001

Boiling Heat Transfer in a Shallow Fluidized Particulate Bed

Y. K. Chuah
Postdoctoral Fellow,
Solar Energy Research Institute,
Golden, CO 80401

V. P. Carey
Associate Professor,
Department of Mechanical Engineering,
University of California,
Berkeley, CA 94720
Mem. ASME

Experimental data are presented which indicate the effects of a thin layer of unconfined particles on saturated pool boiling heat transfer from a horizontal surface. Results are presented for two different types of particles: (1) 0.275 and 0.475-mm-dia glass spheres which have low density and thermal conductivity, and (2) 0.100 and 0.200-mm-dia copper spheres which have high density and thermal conductivity. These two particle types are the extremes of particles found as corrosion products or contaminants in boiling systems. To ensure that the surface nucleation characteristics were well defined, polished chrome surfaces with a finite number of artificial nucleation sites were used. Experimental results are reported for heat fluxes between 20 kW/m² and 100 kW/m² using water at 1 atm as a coolant. For both particle types, vapor was observed to move upward through chimneys in the particle layer, tending to fluidize the layer. Compared with ordinary pool boiling at the same surface heat flux level, the experiments indicate that addition of light, low-conductivity particles significantly increases the wall superheat, whereas addition of heavier, high-conductivity particles decreases wall superheat. Heat transfer coefficients measured in the experiments with a layer of copper particles were found to be as much as a factor of two larger than those measured for ordinary pool boiling at the same heat flux level. The results further indicate that at least for thin layers, the boiling curve is insensitive to layer thickness. These results are shown to be consistent with the expected effects of the particles on nucleation, fluid motion, and effective conductivity in the pool at or near the surface. The effect of surface nucleation site density on heat transfer with a particle layer present is also discussed.

Introduction

In a number of situations of technological interest, particulate contaminants may be introduced into a system in which boiling occurs. Residue from manufacturing processes, precipitation of dissolved contaminants, and corrosion products are possible sources of particulates in evaporators in power or refrigeration systems. In time, a layer of accumulated particles may cover portions of the heated surface, locally altering the vaporization process.

During chemical or food processing, it is often necessary to boil solid–liquid slurries in which particles tend to settle into a layer on horizontal surfaces. Boiling in an unconfined layer of particulate debris can also occur in accident scenarios for liquid-cooled nuclear reactors.

The dryout characteristics of the boiling process in an unconfined particulate bed have been the subject of several recent studies. These studies have uncovered several important features of this boiling process. In their experiments with water and UO_2 particles, Gabor et al. (1974) observed the formation of channels which facilitated the escape of vapor. In shallow beds, these channels extend through the full depth of the bed, while for deep beds, they exist only in the top portion of the bed. The reported "spontaneous leveling" of the bed suggests that it was at least partially fluidized.

Later studies by Dhir and Catton (1977), Jones (1982), and Carey et al. (1986) confirmed the channel mechanism of vapor release and the fluidizing effect of vapor motion through the layer. The experimental results of Carey et al. (1986) also indicated that if the setting velocity of the particles is low, a significant quantity of particles may be suspended in the liquid pool above the layer by vapor-generated turbulence. This was shown to produce very unusual dryout behavior.

The effect of added particulates on pool boiling has also been studied for particles that remain completely suspended in the liquid pool. Eisenberg (1964) studied the dryout characteristics of the pool-boiling process in non-Newtonian suspensions. Yang and Wanat (1968) experimentally determined the pool boiling heat transfer for a horizontal flat plate and cylinder in solid–liquid slurries. In general, they found that as the solid concentration increased, the surface superheat for a given heat flux also increased. Hence, the effectiveness of the heat transfer process is reduced as the solid concentration increases.

In contrast, a recent study by Yang and Maa (1984) indicates an opposite trend. As the concentration of Al_2O_3 powder in water increased, they found that the boiling heat transfer from a horizontal cylinder was enhanced. Their measured data indicate that for a given heat flux level, the required wall superheat decreases as the concentration of Al_2O_3 increases.

The studies described above provide considerable insight into the effects of particulates on boiling transport. However, none of these studies has examined the effect of an unconfined particulate layer on the boiling heat transfer from a horizontal surface. The studies of boiling in particulate layers mentioned above have considered only the dryout behavior. The studies of boiling in slurries have considered only low-concentration slurries of very small particles (less than 3 μm) which have very low settling velocities. For these slurries, the time required for a significant quantity of particles to settle onto the heated surface is much larger than the duration of the experiments. Hence, these experiments consider boiling in a suspension of particles with no layer present on the surface.

The objective of the present study was to experimentally determine the effects of a layer of unconfined particles on boiling heat transfer from a horizontal surface. This type of circumstance will arise when the particulates in the boiling system are large and/or heavy with significant setting velocities. We report experimental results for two different types of particles: 0.275 and 0.475-mm-dia glass spheres, which have low density and low conductivity, and 0.100 and

Contributed by the Heat Transfer Division and presented at the National Heat Transfer Conference, Denver, CO, August 1985. Manuscript received by the Heat Transfer Division May 20, 1985.

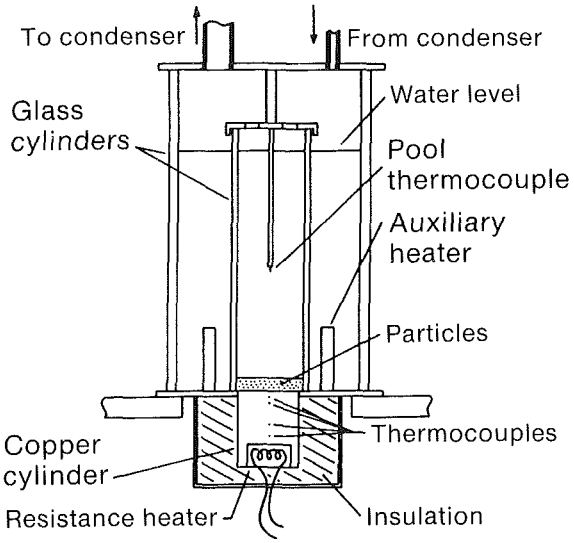

Fig. 1 Experimental apparatus

0.200-mm-dia copper spheres which have high density and conductivity. These two particle types are representative of the extreme combinations of settling velocity and conductivity for particles found as corrosion products or contaminants in boiling systems. The data indicate that the presence of the particle layer may enhance or inhibit heat transfer depending on the conditions. In addition to experimental measurements, an approximate model analysis is also presented which attempts to account for the principal effects of the particle layer on boiling heat transfer. The shifts in the boiling curve predicted by this model are consistent with those observed experimentally for both glass and copper particles.

Experimental Procedure and Results

The experimental apparatus used in our tests is shown schematically in Fig. 1. A thick copper cylinder was heated from below by an electric resistance heater. The copper cylinder was insulated to ensure only vertical upward transfer of heat in the copper. The heat flux to the top surface of the cylinder, i.e., the heated surface, was determined from thermocouple measurements of the temperature gradient in the cylinder. The uncertainty in the measured heat flux is estimated to vary from ± 10 percent at the lowest flux to ± 1 percent at the highest heat flux. The mean heated surface temperature was determined by extrapolating the measured subsurface temperature profile. A least-squares method was used in the extrapolation. The boiling process in and above the particle layer was visually observed through the glass walls of the test section.

Table 1 Description of the particles used

Material	Nominal Diameter (μm)	Density (g/cm^3)	Thermal Conductivity (W/m°C)
Copper	100	8.9	398.
Copper	200	8.9	398.
Glass	275	2.8	1.30
Glass	475	2.8	1.30

In the experiments, distilled water was added to both the test section and the annulus to a height of about 15 cm. The water in the annulus was kept at the saturation temperature by the two auxiliary heaters to prevent heat from leaking from the test section. Before adding particles to the test section, a boiling curve was first obtained for pure water alone. To obtain the boiling curve, the heat flux was gradually increased by increasing the level of power supply to the heater. After each increase, thermocouple readings of the temperature profile in the copper cylinder were allowed to stabilize before they were recorded. The boiling curve was then obtained by calculating the heat flux and heated surface temperature using the temperature readings taken after each increase in heat flux.

There were four types of particles used in the experiments. There were two sizes of glass spheres used, with nominal diameters of 275 μm and 475 μm, as well as two sizes of copper spheres with a nominal diameters of 100 and 200 μm. The relevant physical properties of the particles are listed in Table 1.

After obtaining the pool-boiling curve for the liquid alone, a measured quantity of particles was added to the test section. Then the boiling curve for this system was determined using the same procedure described above. When this was complete, more particles were added to the test section and the boiling curve for this system was again determined using the same procedure. This process was repeated to determine the boiling curve for several different layer thicknesses.

All the particles used in these tests have terminal velocities that are high enough so that even at the highest heat flux levels, there was no significant suspension of particles in the pool above the layer. Virtually all the particles remained in the fluidized layer on the surface. The quantity of particles was weighed before it was added to the test section so the total mass of particles in the layer was known for each test. Assuming a bed porosity of approximately 0.4, the height of the bed can then be computed using the mass of particles, the particle density and the diameter of the test section which is 5.1 cm.

Nomenclature

A = surface area
A_{tot} = total area of heated surface
h = heat transfer coefficient = $q''/\Delta T_S$
H = mean thickness of particle layer
k = thermal conductivity
n = nucleation site density (number of sites/unit area)
Pr = Prandtl number
q'' = heat flux
Q_{tot} = total heat transfer rate form surface
ΔT = wall to ambient temperature difference
ΔT_S = surface superheat
β = constant in equation (7)
γ = constant in equation (7)
λ = constant in equation (1)
ξ = constant in equation (9)
Ω = particle volume fraction in layer

Subscripts

CF = conditions at which layer is completely fluidized
f = liquid properties
F = pertaining to portion of layer which is fluidized
m = liquid–particle mixture properties
NF = pertaining to portion of layer which is not fluidized
P = conditions with particle layer present
PB = conditions for ordinary pool boiling
s = solid properties

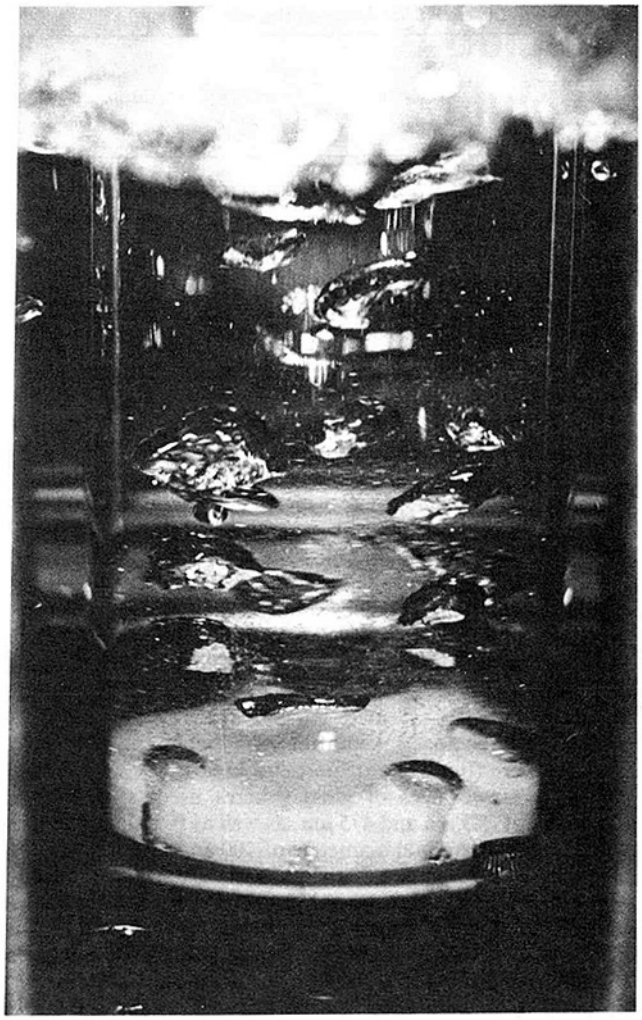

Fig. 2 Fluidized-bed boiling with 275-μm glass particles; heat flux: $q'' = 21.2$ kW/m^2, bed height: $H = 1.0$ cm

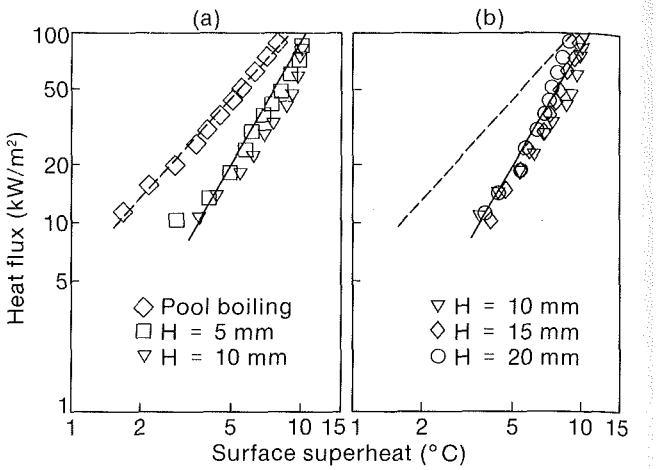

Fig. 3 Saturated boiling data for layers of 275-μm-dia glass beads at various layer heights on the chrome surface with seven artificial cavities. The broken line is the pool boiling curve and the solid line is the prediction of equation (15).

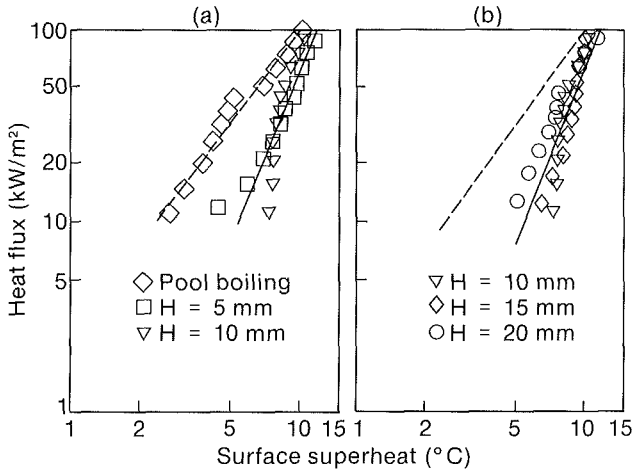

Fig. 4 Saturated boiling data for layers of 475-μm-dia glass beads at various layer heights on the chrome surface with seven artificial cavities. The broken line is the pool boiling curve and the solid line is the prediction of equation (15).

The porosity of the layer is taken to be 0.4 since that is the value usually associated with incipient fluidization of a fluidized bed of spherical particles (see Wallis, 1969).

To evaluate the interaction between the surface nucleation conditions and the boiling process in the layer, a plain surface and two surfaces with different arrays of artificial cavities were used. One of the surfaces with artificial cavities has 7 cavities while the other has 19 cavities. For both surfaces the cavities were distributed uniformly over the surface. Each of the cavities was a cylindrical hole 0.8 mm in diameter and approximately 0.5 mm deep. Since the copper is soft, all three surfaces were chrome plated to ensure that particle collisions would not erode the surface and/or change its nucleation characteristics.

For each particle and surface combination tested, a pool-boiling curve for liquid alone was determined prior to taking data at different particle layer heights. This ensured that a meaningful comparison could be made between the ordinary pool-boiling curve and the curves obtained with the particle layer present.

Figure 2 is a photograph of the boiling process in the particle layer as seen through the test section walls. In this particular experiment, the heat flux was 21.2 kW/m^2 and the surface was covered with a 10-mm-thick layer of 0.275-mm-dia glass beads. This figure vividly shows the escape of vapor through the chimneys at discrete locations in the layer. The

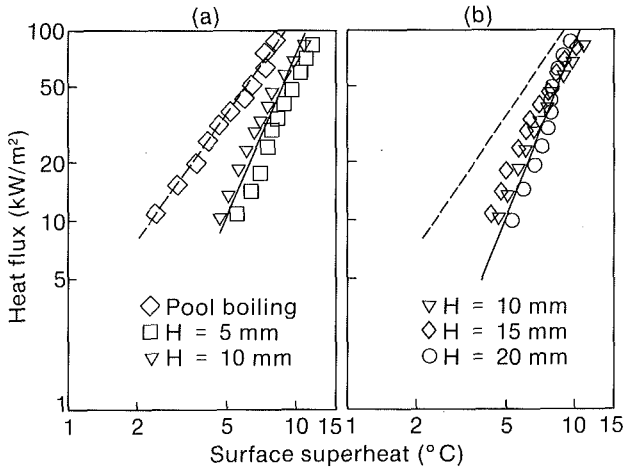

Fig. 5 Saturated boiling data for layers of 275-μm-dia glass beads at various layer heights on the chrome surface with 19 artificial cavities. The broken line is the pool boiling curve and the solid line is the prediction of equation (15).

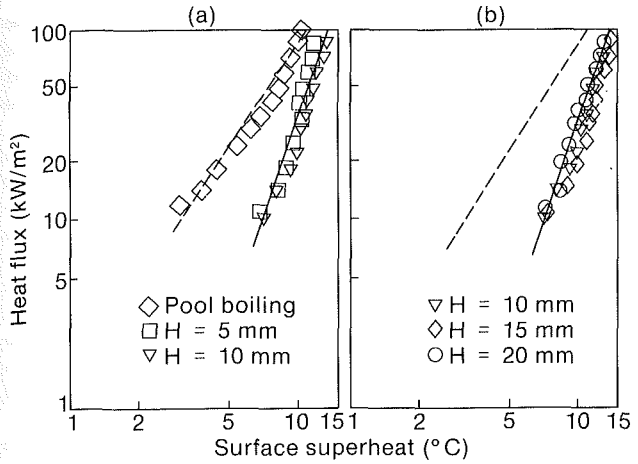

Fig. 6 Saturated boiling data for layers of 475-μm-dia glass beads at various layer heights on the chrome surface with 19 artificial cavities. The broken line is the pool boiling curve and the solid line is the prediction of equation (15).

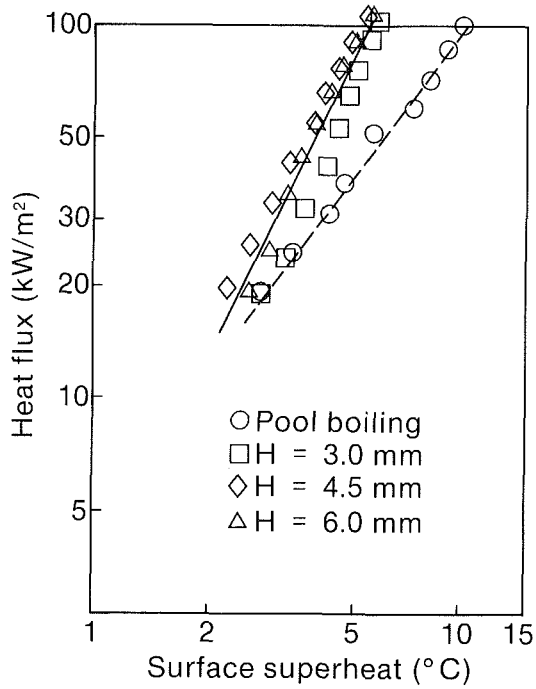

Fig. 7 Saturated boiling data for layers of 200-μm-dia copper beads at *various layer heights on the chrome surface with 19 artificial cavities.* The broken line is the pool boiling curve and the solid line is the prediction of equation (15).

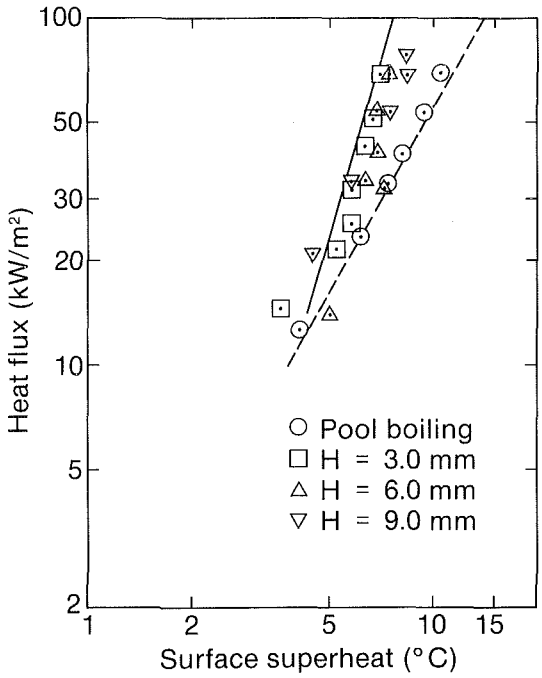

Fig. 8 Saturated boiling data for layers of 100-μm-dia copper beads at various layer heights on the chrome surface with 19 artificial cavities. The broken line is the pool boiling curve and the solid line is the prediction of equation (15).

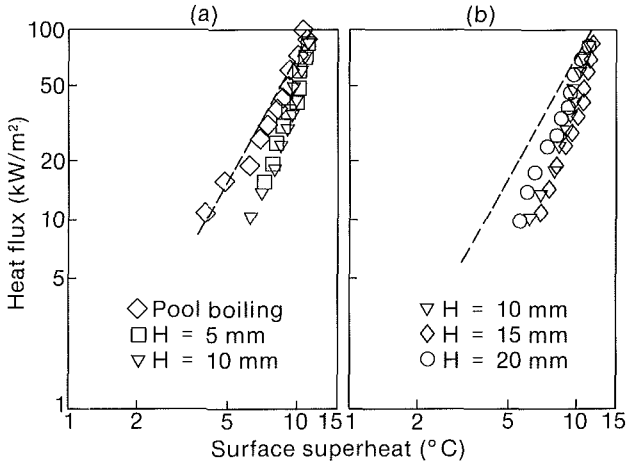

Fig. 9 Saturated boiling data for layers of 475-μm-dia glass beads at various layer heights on the plain chrome-plated surface. the broken line *is the pool boiling curve.*

frequency of bubble release from the layer at these locations was found to increase as the heat flux increased.

At low heat flux levels, vapor bubbles grow at one or more nucleation sites in the vicinity of a chimney, sometimes coalescing as they grow. When the buoyancy of the accumulated vapor becomes large enough to overcome the weight of the overlying particles, the vapor moves upward and escapes the layer. Growth of vapor bubbles at the nucleation sites then begins anew, and the process repeats.

At high heat fluxes, so much vapor is moving upward through the layer that an almost permanent column of vapor is present in the chimney. At both high and low heat flux levels, the upward motion of vapor appeared to fluidize the layer, at least in the chimney regions. At low heat flux, portions of the particle bed between the chimneys did not appear to be fluidized, while at high heat flux levels, almost all of the layer appeared fluidized.

Figures 3–9 show the results of the heat transfer experiments. In each of the figures, the boiling data for experiments with layers of different heights are compared with the boiling curve obtained for ordinary pool boiling with the same surface. A curve is also shown which is a least-squares fit to the pool boiling data. Because many of the data points for the particle layers lie close together, two plots are used in some of the figures to show the data for different heights of the particle bed.

There are several interesting trends that can be seen in Figs. 3–9. In general, for a given heat flux level, addition of the layer of glass particles increased the surface superheat ΔT_S relative to the ordinary pool boiling result. In contrast, the presence of a layer of copper particles was found to decrease ΔT_S relative to the pool boiling curve. The shifts in the boiling

curves are relatively small, only about 2-4°C. However, since the driving temperature difference for heat transfer is also only a few degrees, this amounts to a sizable change in the heat transfer coefficient.

For a layer of glass beads, the shift of the boiling curve relative to that for ordinary pool boiling is large at low heat flux, and diminishes as the heat flux increases. The boiling curves with the particles present seem to merge with the pool boiling curves at a heat flux of about 100 kW/m^2. For layer depths greater than 5 mm, the size of the glass beads and the depth of the particle layer have almost no effect on the shift of the boiling curve. However, this also suggests that for layer depths smaller than those tested here, the position of the curve may depend more strongly on layer thickness.

The shift in the boiling curve for a layer of copper particles is seen to be quite different than that observed for the glass beads. The shift relative to the pool curve is small at low heat flux and increases slowly with heat flux. As was found for the glass beads, the depth of the layer is seen to have almost no effect on the shift in the boiling curve for the range of layer heights tested here.

To ensure that the shifts in the boiling curves were not due to hysteresis effects or changes in the surface condition, tests were run to repeat measurements and to take data with both increasing and decreasing heat flux. In all such tests, the repeatability of the data was very good and no hysteresis effects were found. The trends in the data and the mechanisms which appear to cause them are discussed in the next section.

Discussion

The presence of the particle layer on the heated surface apparently affects the boiling process in three ways. First, particles resting on the surface may provide additional potential nucleation sites for vapor generation. If there are few active sites on the surface itself, this may enhance the transport by agitating the fluid near the surface in areas that otherwise would transfer heat only by natural convection.

The enhancement due to added nucleation sites will be greatest for very smooth surfaces at low superheat. For rough surfaces with many available sites, or at higher wall superheats where even smooth surfaces have many active sites, the particles may have little effect on nucleation behavior.

The particle layer also is expected to have an effect on the motion of the fluid near the surface. For ordinary pool boiling at low superheat levels, the active nucleation sites are few and widely spaced. Consequently, the effectiveness of the heat transfer in regions between the sites is dependent on the vigor of the liquid flow induced by bubble motion at the nucleation sites. With the particle layer present, the region in the immediate vicinity of the vapor chimneys is fluidized by the upward vapor motion which promotes strong agitation of the adjacent mixture of liquid and particles.

At low heat flux, the region between the chimneys appears to be virtually unaffected by bubble motion in the fluidized chimney regions. The presence of the settled particle layer in these regions inhibits convective motion of liquid near the surface. Heat transfer in these regions is then mostly by conduction, with some convective effects within the porous structure of the layer. Hence, at low heat flux levels, the presence of the layer retards heat transfer by convection over portions of the surface between chimney sites, and thereby tends to reduce the overall effectiveness of heat transfer from the surface.

However, at high heat flux levels, it is expected that the density of nucleation sites will increase and their mean spacing will decrease. A single chimney may then be fed by several active nucleation sites. Consequently, as the heat flux increases, there may be more chimneys spaced closer together, and the agitation in the chimney regions may become more vigorous. As a result of these trends, the layer will become more thoroughly fluidized as the heat flux increases. The decrease in heat transfer effectiveness due to reduced convective transport in unfluidized regions of the bed is therefore expected to diminish as the heat flux increases.

The third major effect of the particle layer on the heat transfer mechanism results from the difference between the thermal conductivity values for the solid particles and the liquid. If the conductivity of the particles is much higher or lower than the conductivity of the liquid, the effective conductivity of the mixture of liquid and particles in the layer may be significantly different from the conductivity of pure liquid. This may increase or decrease the ability of the medium to conduct heat and thereby alter the overall effectiveness of heat transfer from the surface. For a given heat flux, this could change the required surface superheat.

To further investigate these mechanisms, an approximate analysis of their effects on the boiling process will be developed here. Note that the analysis which follows is not intended to be a general model of the boiling process. The data currently available are too limited to validate such a model. This approximate analysis is presently primarily as an attempt to determine whether the trends in the data are explainable in terms of these mechanisms.

For a given heat flux at the surface, the addition of more active nucleation sites will tend to enhance heat transfer and thereby reduce the required wall superheat. As discussed by Lienhard (1981), for ordinary pool boiling at low heat flux, the required superheat ΔT_S decreases as the nucleation site density n_{PB} increases, in the manner

$$\Delta T_{SPB} \propto n_{PB}^{-\lambda} \tag{1}$$

If we assume that the required superheat varies with nucleation site density in about the same way with particles present, it may be expected that

$$\frac{\Delta T_{SP}}{\Delta T_{SPB}} \propto \left(\frac{n_P}{n_{PB}}\right)^{-\lambda} \tag{2}$$

where the subscript P denotes values with particles present and PB denotes values for pool boiling of pure liquid at the heat flux.

As mentioned above, at low heat fluxes, only the portion of the layer in the immediate vicinity of the vapor chimneys appears to be fluidized. In these fluidized regions, liquid motion is relatively unrestricted. Consequently, the heat transfer mechanism usually present near the surface in ordinary pool boiling is not expected to be strongly affected by the presence of the particles. In regions that are not fluidized, heat transfer is much lower than it would be for ordinary pool boiling because the particle layer inhibits convective liquid motion.

Since the heated surface is made of copper, it is expected that lateral conduction will keep the surface temperature nearly uniform despite the variation in heat transfer effectiveness caused by partial fluidization. Consequently, the heat flux in the fluidized and nonfluidized regions are expected to differ. Note that the experimentally measured heat flux q'' is a mean value averaged over the entire surface.

If the bed is partially fluidized and the surface superheat is assumed to be uniform, the total heat transfer from the surface is therefore expected to equal the sum of the contributions from the fluidized (F) and nonfluidized (NF) regions

$$\dot{Q}_{\text{tot}} = h_P A_{\text{tot}} \Delta T_S = h_F A_F \Delta T_S + h_{NF} A_{NF} \Delta T_S \tag{3}$$

which can be rearranged to obtain

$$\frac{h_P}{h_F} = \frac{A_F}{A_{\text{tot}}} + \frac{h_{NF}}{h_F}\left(\frac{A_{NF}}{A_{\text{tot}}}\right) \tag{4}$$

The heat transfer coefficient in the fluidized region is expected to be virtually the same as that for ordinary pool boiling at the

same conditions. Since the h value in the nonfluidized region is expected to be much smaller than h in the fluidized region, as a first approximation we can neglect the second term on the right side of (4). This, of course, is only valid when A_F is significantly larger than zero. Based on these surmises, we can rewrite (4) approximately as

$$\frac{h_P}{h_{PB}} = \frac{A_F}{A_{\text{tot}}} \tag{5}$$

It was further observed during the experiments that as the measured mean heat flux increased, the fraction of the layer which was fluidized also increased, until at some threshold value q''_{CF} the bed was virtually completely fluidized. This suggests that

$$\frac{A_F}{A_{\text{tot}}} = F_1(q''/q''_{CF}) \tag{6}$$

where $F_1 \to 0$ as $q''/q''_{CF} \to 0$, $F_1 \to 1$ asymptotically as q'' increases, and F_1 is virtually equal to 1 for q'' greater than q''_{CF}. An approximate functional form for F_1 might be

$$F_1 = \frac{1}{1+\beta(q''/q''_{CF})^{-\gamma}} \tag{7}$$

The form of equation (7) was chosen somewhat arbitrarily. Since our objective here is only to relate the trends in our data to the physical mechanisms described above, we will adopt equation (7) as a suitable approximation of the functional form of F_1 between its expected limiting behaviors at large and small q''.

Combining equations (5) and (6) at a given mean heat flux level, and noting that $h = q''/\Delta T_S$, yields

$$\frac{\Delta T_{SP}}{\Delta T_{SPB}} \propto \frac{1}{F_1(q''/q''_{CF})} \tag{8}$$

It should be noted that equation (8) accounts only for the effect of partial fluidization of the layer on heat transfer.

As described above, if the conductivity of the particles differs significantly from that of the liquid, then the effective conductivity of the liquid-saturated layer will also differ from the value for liquid alone. For ordinary pool boiling, the well-known Rohsenow (1952) correlation suggests that for a given heat flux

$$\Delta T_S \propto k_f^{-\xi} \tag{9}$$

where ξ is approximately 1.7. Forster and Zuber's (1955) correlation suggests a similar relation with ξ approximately equal to 1.4. If the mixture of particles and liquid in the layer is considered to be a composite material with an appropriately defined mean conductivity k_m, it is therefore expected that

$$\frac{\Delta T_{SP}}{\Delta T_{SPB}} \propto \left(\frac{k_f}{k_m}\right)^{\xi} \tag{10}$$

The mean conductivity of the particle layer may be estimated using the relation developed by Brailsford and Major (1964) for a matrix of spheres filled with a fluid

$$k_m = \frac{k_f\left[1-2\Omega\left(\frac{1-k_s/k_f}{2+k_s/k_f}\right)\right]}{1+\Omega\left(\frac{1-k_s/k_f}{2+k_s/k_f}\right)} \tag{11}$$

Although the three mechanisms considered above would appear to act independently, further investigation is needed to fully determine whether they are completely independent. However, if as a first approximation, we assume that they do act independently, the physical arguments described above suggest that the effects of the particle layer on wall superheat at a fixed heat flux is given by a relation of the form

$$\frac{\Delta T_{SP}}{\Delta T_{SPB}} \propto \left(\frac{n_P}{n_{PB}}\right)^{-\lambda} \frac{1}{F_1(q''/q''_{CF})}\left(\frac{k_f}{k_m}\right)^{\xi} \tag{12}$$

As mentioned earlier, two of the heated surfaces used in these studies had an array of either 7 or 19 artificial cavities. The edge of each heater surface also usually provided several additional potential nucleation sites. During the pool boiling experiments without particles, it was observed that all the artificial sites and a few locations around the edge of the heater surface were active. With the exception of these locations, the polished surfaces used in our study had only very small natural cavities which were not observed to be active at the low to moderate superheat levels in our experiments. Even though they appear to be one nucleation site, the artificial cavities may actually contain one or more crevices within them which are potentially active nucleation sites. As the wall heat flux and superheat increase, more of these tiny crevices within the cavity may become active, producing vapor more rapidly at these locations. The rate of bubble generation and release at the artificial sites was observed to increase with heat flux, but no additional natural sites on the surface became active.

The artificially produced cavities and those at the edge of the heater surface provided an abundance of nucleation sites at all heat flux levels studied here. Furthermore, as described above, the number of active sites did not change significantly with heat flux in the pool boiling tests without particles. Consequently, the addition of particles is expected to produce virtually no change in the active nucleation site density on the surface from that for ordinary pool boiling. This was visually confirmed by noting that addition of a small quantity of particles to the test section during ordinary pool boiling produced no detectable change in the observed number of nucleation sites (i.e., $n_P = n_{PB}$). Hence, in experiments with these surfaces, this mechanism should not contribute significantly to the shift in the boiling curve. If this hypothesis is correct, we can then write equation (12) as

$$\frac{\Delta T_{SP}}{\Delta T_{SPB}} \propto \frac{1}{F_1(q''/q''_{CF})}\left(\frac{k_f}{k_m}\right)^{\xi} \tag{13}$$

If we adopt (7) as a suitable functional form for F_1, equation (13) becomes

$$\frac{\Delta T_{SP}}{\Delta T_{SPB}} = \left[1+\beta\left(\frac{q''}{q''_{CF}}\right)^{-\gamma}\right]\left(\frac{k_f}{k_m}\right)^{\xi} \tag{14}$$

where β, γ, and ξ are unknown constants. Assuming that partial fluidization of the bed and the change in effective conductivity are the dominant effects, we have replaced the proportional sign with an equal sign in (14). The ratio k_f/k_m can be evaluated using equation (11). Assuming a layer porosity of 0.4, this yields values of 0.67 and 0.18 for glass and copper particles, respectively.

At the present time, we do not have sufficient data to develop a general technique to predict the heat flux at which the bed becomes fully fluidized. Physically, it is expected that q''_{CF} may vary with the size and density of the particles, the properties of the liquid and vapor, and, to some extent, on the distribution of nucleation sites on the heated surface. In another recent study, Gabor et al. (1984) experimentally examined the fluidization of a layer of particles in a liquid pool by an upward air flow through the layer. Tests were conducted in water using glass beads with different diameters. Their results suggest that for thin layers, the superficial gas velocity required for full fluidization of the bed is only weakly dependent on the size of the particles. At layer depths less than 30 mm, full fluidization of the layer was obtained at an air velocity between 30 to 80 mm/s for all glass beads with diameters between 127 μm and 562 μm. During visual observation of the boiling process, the layer appeared to be fully fluidized in all our tests at a heat flux of approximately 100 kW/m^2, which

corresponds to a superficial vapor velocity of about 74 mm/s. Hence, our observation and the results of Gabor et al. (1984) suggest that the size and the terminal velocity of the particles do not strongly affect the vapor flux required for full fluidization. For the purposes of this analysis, we will therefore take $q''_{CF} = 100$ kW/m^2 as a known constant.

The above discussion suggests that, for the surfaces with artificial cavities, the dominant effects of the particle layer are represented by equation (14). To test this hypothesis, our results were analyzed to find values of β, γ, and ξ which would fit all available data for these surfaces. When the resulting values of these constants are substituted into (14) we obtain

$$\frac{\Delta T_{SP}}{\Delta T_{SPB}} = \left[1 + 0.50\left(\frac{q''}{q''_{CF}}\right)^{-0.6}\right]\left(\frac{k_f}{k_m}\right)^{0.6} \tag{15a}$$

where

$$q''_{CF} = 100 \text{ kW/m}^2 \tag{15b}$$

and k_m is determined from equation (11). The value of ξ that best fits our data is much different from the value of 1.4 to 1.7 suggested by the pool boiling correlations mentioned previously. It is interesting to note that for many forced and free convection circumstances, well-known correlations predict that the Nusselt number is proportional to Pr^a where a is between 0.25 and 0.4. This implies that in flows of this type, for a given heat flux, ΔT is proportional to k^{-b}, where b is between 0.6 and 0.75. It may be that the stronger dependence of ΔT_S on k_f in pool boiling is a result of the fact that the magnitude of the liquid conductivity affects both the bubble growth process and the convection resulting from agitation caused by bubble growth and release.

The presence of particles in our system certainly affects the convection caused by bubble agitation. However, they may have little effect on bubble growth, particularly since the particles are typically large compared with the superheated liquid layer under and around the bubble as it grows. The value of ξ which best fits our data, $\xi = 0.6$, is, in fact, quite close to the range associated with single-phase forced or free convection, as described above. Hence, the shift in the boiling curve may be proportional to $(k_f/k_m)^{0.6}$ because only the convective agitation mechanism of the boiling process is affected.

Equation (15*a*) using (15*b*) is shown with the corresponding experimental data in Figs. 3–8 for surfaces with either 7 or 19 artificial cavities. It can be seen in the figures that the relation given by (15*a*) matches the data very well in all cases.

Considering the spectrum of surface conditions, particle sizes and conductivities represented in Figs. 3–8, the good agreement appears to confirm the assumptions of the approximate analysis discussed above. The boiling curves apparently shift position relative to the ordinary pool boiling curve partly because of the higher effective conductivity of the layer near the surface. The results also suggest that partial fluidization of the bed causes the curve to shift to the right by an amount that decreases as the heat flux increases.

An additional series of experiments were run with 475-μm glass beads with a chrome-plated heated surface with no artificial cavities. The data from these tests are shown in Fig. 9. It can be seen from this figure and Figs. 4 and 6 that the shift in the boiling curves with particles present is less for the plain chrome surface than for the surfaces with artificial cavities.

This may be a consequence of the fact that, for the surface with no artificial cavities, the presence of the particles is likely to provide additional sites for nucleation on the surface. This would more thoroughly agitate the layer, resulting in better heat transfer. This, in turn, would reduce the required surface superheat at a given heat flux, tending to shift the boiling curve somewhat to the left. Overall, the combined effects of nucleation augmentation, partial bed fluidization, and effective layer conductivity may still shift the curve to the right relative to the pool boiling curve for this surface. However, the amount of the resulting shift is expected to be less than if no nucleation augmentation occurred. The arguments noted above suggest that the reduced shift in the boiling curve observed for the chrome surface without artificial cavities is a consequence of enhanced nucleation on the surface. Unfortunately, the ratio n_P/n_{PB} could not be quantified in these tests because the nucleation sites were hidden beneath the layer.

Conclusions

The results of this study reveal several interesting characteristics of the boiling process in a thin particle layer covering a heated horizontal surface. Vapor bubbles generated by the vaporization process have been observed to escape through vapor chimneys which extend through the layer to the heated surface. Motion of vapor to, and upward through the chimneys was found to at least partially fluidize the layer. The fraction of the layer fluidized in this manner was observed to increase with increasing heat flux.

Experimental measurements indicate that a particle layer on the heated surface may increase or decrease the surface superheat at a given heat flux, depending on the characteristics of the system. The size of the particles and the depth of the particle layer were found to have little effect on heat transfer from the surface for the systems studied here.

An approximate analysis of the boiling process has been presented which postulates that the shift in the boiling curve due to the addition of a particle layer can be explained in terms of three distinct effects: (1) enhanced nucleation, (2) partial fluidization of the layer, and (3) the change of the effective conductivity of the medium near the surface. For our experiments using surfaces with artificial cavities, the presence of the particles appeared to have little effect on the density of active nucleation sites. For these surfaces, the effect of the particles on the boiling process appears to be primarily a consequence of the other two mechanisms noted above.

Based on the approximate analysis, an equation was developed which predicts the shift in the boiling curve caused by the presence of the particle layer. This relation was found to fit all our data for glass and copper particles on the surfaces with artificial cavities. The excellent agreement between the data and this relation strongly supports the assumptions used in the approximate analysis. Specifically, it suggests that particles with a thermal conductivity higher than that of the liquid tend to enhance conduction of heat near the surface in both the fluidized and nonfluidized regions. This enhancement is expected to reduce the mean thermal boundary layer thickness near the wall.

In addition, the results also suggest that with the layer of particles present, the thermal boundary layer may be nonuniform over the surface. The thermal boundary layer is expected to be very thin in fluidized regions which are agitated by the vapor motion, and relatively thicker in nonfluidized regions where heat is transferred by conduction or natural convection.

Two effects of the particle layer, enhanced nucleation and the increase in the effective conductivity, act to enhance heat transfer. This suggests, and our data appear to confirm, that a thin layer of high conductivity particles can actually be an effective means of enhancing pool boiling heat transfer in some circumstances.

Acknowledgments

Support for this research was provided by the National Science Foundation under research grant No. MEA-8307212.

References

Brailsford, A. D., and Major, K. G., 1964, *British J. of Applied Physics*, Vol. 15, pp. 313–319.

Carey, V. P., Markovitz, E., and Chuah, Y. K., 1986, "The Effect of Turbulence Suspended Light Particles on Dryout for Pool Boiling From a Horizontal Surface," ASME JOURNAL OF HEAT TRANSFER, Vol. 108, pp. 109–116.

Dhir, V., and Catton, I., 1977, "Dryout Heat Fluxes for Inductively Heated Particulate Beds," ASME JOURNAL OF HEAT TRANSFER, Vol. 99, pp. 250–256.

Eisenburg, D. M., 1964, "Boiling Burnout Heat Flux Measurements in a Non-Newtonian Suspension," *AIChE J.*, Vol. 10, pp. 684–687.

Forster, H. K., and Zuber, N., 1955, "Dynamics of Vapor Bubbles and Boiling Heat Transfer," *AIChE Journal*, Vol. 1, pp. 531–535.

Gabor, J. D., Cassulo, J. C., Fountain, D., and Bingle, J. D., 1984, "Gas Fluidization of Solids in a Stationary Liquid," presented at the 1984 AIChE Annual Meeting, San Francisco, CA, Nov. 25–29, 1984.

Gabor, J. D., Sowa, E. S., Baker, L., Jr., and Cassulo, J. C., 1974, "Studies and Experiments on Heat Removal From Fuel Debris in Sodium," ANS. Fast Reactor Safety Meeting, Los Angeles, CA.

Jones, S. W., 1982, "A Study of Dryout Heat Fluxes," Ph.D. Dissertation, Northwestern University, Evanston, IL.

Lienhard, J. H., 1981, *A Heat Transfer Textbook*, Prentice-Hall, Inc., Englewood Cliffs, NJ, Chap. 10.

Rohsenow, W. M., 1952, "A Method of Correlating Heat Transfer Data for Surface Boiling of Liquids," *Trans. ASME*, Vol. 74, pp. 969–975.

Wallis, G. B., 1969, *One-Dimensional Two-Phase Flow*, McGraw-Hill, NY, Chaps. 4 and 8.

Yang, W. J., and Wanat, R. L., 1968, "Nucleate Pool Boiling of Slurries on a Horizontal Plate and Cylinder," *Chem. Engrg. Prog. Symp. Ser.*, Vol. 64, pp. 126–130.

Yang, Y. M., and Maa, J. R., 1984, "Boiling of Suspension of Solid Particles in Water," *Int. J. Heat Mass Transfer*, Vol. 27, pp. 145–147.

Application of a Multifield Model to Reflooding of a Hot Vertical Tube: Part 1—Model Structure and Interfacial Phenomena

M. Kawaji
Department of Reactor Safety Research,
Japan Atomic Energy Research Institute,
Tokai Mura, Japan

S. Banerjee
Department of Chemical
and Nuclear Engineering,
University of California,
Santa Barbara, CA 93106
Mem. ASME

This is the first of a series of two papers reporting on a study of reflooding of a hot vertical tube. A mechanistic model of reflood is developed using a multifield modeling approach to analyze experimental data reported previously [1]. In Part 1 of this paper, the mathematical model for the thermohydraulic processes during reflood is derived from the general two-field conservation equations, and its structure is examined. Linear stability of the equation system is analyzed incorporating consideration of phase pressure differences. For inverted annular flow, the system is stable to short-wavelength perturbations and captures long-wavelength interfacial instabilities. The length of the most unstable waves is also derived in the analysis and agrees well with the available data. For dispersed flow, the system is predicted to become unstable if the Weber number exceeds a critical value of 8. In Part 2 [2], constitutive relations for reflood are fomulated and model is numerically solved for comparison with experimental data.

Introduction

When an initially hot vertical tube is reflooded with subcooled water from the bottom, various two-phase flow patterns appear above the quench front. Phenomenological modeling of hydrodynamic and thermal aspects of the reflooding process is important in analysis of the reflood phase of postulated Loss-of-Coolant Accidents in nuclear power plants.

If the injected water is still subcooled at the quench front, an inverted annular flow pattern appears immediately above the quench front, with a liquid core which is separated from the wall by a thin annular vapor film. Flow visualization experiments involving a heated quartz tube revealed little vapor entrainment in the liquid and the presence of interfacial waves as shown in Fig 1. The heat transfer in this region is quite good because the vapor film is thin and the presence of interfacial wave enhances heat transfer. Further downstream the inverted annular flow regime breaks up and a dispersed flow regime is established where the vapor phase may be significantly superheated. Drops of various sizes are entrained in the vapor stream and evaporate as they move downstream.

In both of these flow regimes, mechanical and thermal nonequilibrium exists between the liquid and vapor phases. The model that best describes nonequilibrium two-phase flow is the multifield model. A two-field version of such a model has been used successfully for prediction of refilling and rewetting of a horizontal tube by Chan and Banerjee [3, 4]. However, Chan and Banerjee showed that careful consideration of forces on each phase is necessary if a model of this type is applied. In particular, the small, but significant, differences of pressure between phases (and pressure variations over interfaces) have important effects on the stability of the governing equations and on wave phenomena in the vicinity of the quench front. The wave phenomena were shown in turn to affect rewetting when the liquid is subcooled at the quench front [3, 4].

Although reflood of a vertical tube may involve different mechanisms, the same case in considering the momentum interactions between the phases is required for two reasons.

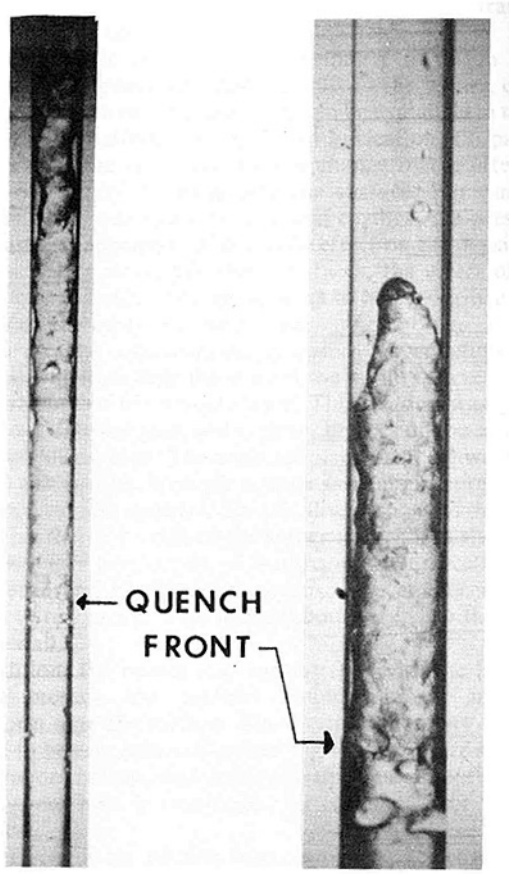

Fig. 1 Inverted annular flow regime

First, the interfacial waves in inverted annular flow may influence heat transfer and their characteristics should be captured in the model if possible. Second, the two-field model is unstable if some of the real physical effects involved in momentum interactions are ignored. Numerical techniques of good accuracy, with low numerical diffusion and dispersion, cannot be used unless the model is stable.

Thus, a two-field model of reflood has been developed con-

Contributed by the Heat Transfer Division for publication in the JOURNAL OF HEAT TRANSFER. Manuscript received by the Heat Transfer Division November 19, 1984.

sidering the phasic pressure difference in order to interpret the experimental data reported previously [1, 5], and to understand the mechanisms that govern hydrodynamics and heat transfer in the inverted annular and dispersed flow regimes.

In this paper, the structure of the two-field model equations, linear stability analysis of the hydraulic equation system, and the interfacial wave phenomena for the inverted annular flow will be discussed. In a separate paper [2], constitutive relations, the numerical solution scheme, and the comparisons of predictions with the experimental results will be presented.

Mathematical Formulation

The volume and time-averaged conservation equations for one-dimensional two-phase flow are given below. For simplicity, the average of products of the dependent variables has been replaced by the product of the averages—a good assumption for the inverted annular flow and dispersed flow situations that are modeled here.

$$\frac{\partial}{\partial t}(\rho_l \alpha_l) + \frac{\partial}{\partial z}(\rho_l \alpha_l U_l) = -m_l''' \tag{1}$$

$$\frac{\partial}{\partial t}(\rho_v \alpha_v) + \frac{\partial}{\partial z}(\rho_v \alpha_v U_v) = m_l''' \tag{2}$$

$$\frac{\partial}{\partial t}(\rho_l \alpha_l U_l) + \frac{\partial}{\partial z}(\rho_l \alpha_l U_l U_l) + \alpha_l \frac{\partial P_l}{\partial z} - \Delta P_{li} \frac{\partial \alpha_l}{\partial z} = \tau_i''' - \tau_{wl}''' - \rho_l \alpha_l g - m_l''' U_i \tag{3}$$

$$\frac{\partial}{\partial t}(\rho_v \alpha_v U_v) + \frac{\partial}{\partial z}(\rho_v \alpha_v U_v U_v) + \alpha_v \frac{\partial P_v}{\partial z} - \Delta P_{vi} \frac{\partial \alpha_v}{\partial z} = -\tau_i''' - \tau_{wv}''' - \rho_v \alpha_v g + m_l''' U_i \tag{4}$$

$$\frac{\partial}{\partial t}(\rho_l \alpha_l h_l) + \frac{\partial}{\partial z}(\rho_l \alpha_l U_l h_l) = q_{lH}''' - m_l''' h_{l,\text{sat}} \tag{5}$$

$$\frac{\partial}{\partial t}(\rho_v \alpha_v h_v) + \frac{\partial}{\partial z}(\rho_v \alpha_v U_v h_v) = q_v''' + m_l''' h_{v,\text{sat}} \tag{6}$$

The derivation of these equations with particular emphasis on the treatment of the pressure terms has been presented by Banerjee and Chan [6]. The equations are applicable to various two-phase flow situations, provided the interfacial mass, momentum, and energy transfer terms and pressure differences are expressed by apppropriate constitutive relations for a particular flow regime. The energy equations have been simplified by assuming that the kinetic energy and axial conduction terms are negligible.

To capture transient effects such as interfacial waves, transient terms are retained in the conservation equations. However, in transient two-field models, complex characteristics may arise from constitutive models, and assumptions concerning the treatment of the pressure, stress, and transient flow forces at the interface between the two phases. The nature of the mathematical characteristics of the two-phase flow equations with regard to stability has been discussed by Travis et al. [7], Stuhmiller [8], Ramshaw and Trapp [9], Lyczkowski et al. [10], and Arai [11] among others. Real characteristics can be obtained, however, by a careful treatment of the pressure difference across the interface and pressure variations over the interface which lead to a numerically stable system that can predict the behavior of one-dimensional interfacial waves [12]. In this study, the conservation equations given above are adapted to describe the inverted annular and dispersed flow hydrodynamics and heat transfer which are important in analyzing the process of reflooding of a hot vertical tube. Equations (1)–(4) are also analyzed for stability in this paper and are solved together with the energy equations and various constitutive relations in [2].

Inverted Annular Flow. When the inverted annular flow patterns photographed during the quartz-tube quench experiments [1] were examined, bubbles were seldom observed in the liquid column above the quench front. This indicated nearly all the vapor generated at the liquid–vapor interface flowed upward in the vapor film. Waves were also observed at the liquid–vapor interface, growing in amplitude with height above the quench front. The stability of the liquid–vapor interface in inverted annular flow was first analyzed by Jensen [13], in connection with prediction of the liquid core breakup, but in simplified form under Cartesian coordinates. The interfacial waves seem to be important in enhancing heat transfer in inverted annular film boiling as suggested by Edelman et al. [14]. There was, however, no evidence in our study [1] of the liquid column rewetting the wall surface in the inverted annular region above the quench front. If such wall–liquid contact did occur, it was for such brief periods that it could not be detected.

Based on these observations, a one-dimensional two-field model of the inverted annular flow in a tubular flow channel was developed using the conservation equations given previously. Both the liquid and vapor phases are assumed to be incompressible and the liquid is assumed to flow in the center of the flow channel, being always separated from the channel wall by a thin vapor film as shown in Fig. 2. Therefore, the wall–liquid shear term, τ_{wl}''', is dropped from the liquid momentum equation.

Nomenclature

a = length of semiminor axis of an oblate spheroid
b = length of semimajor axis of an oblate spheroid
D_l = liquid core diameter
g = gravity
h = enthalpy
h_{fg} = latent heat of vaporization
Im = imaginary part
k = wave number
m_l''' = interfacial mass transfer per unit volume out of the liquid
n = number density of drops
P = pressure
ΔP_{ki} = $\langle P_{ki} \rangle - \langle P_k \rangle$
q'' = heat flux
q_{lH}''' = heat transfer to subcooled liquid per unit volume
R = inner radius of the flow channel
R_d = mean radius of drops
t = time
U = velocity
U_r = $U_v - U_l$
We = Weber number
X = droplet shape factor
Y = solution vector
z = axial coordinate
α_l = volume fraction of liquid
α_v = void fraction
β = ρ_l/ρ_v
δ = vapor film thickness
θ = angular position
λ = wavelength
ρ = density
σ = surface tension coefficient
τ''' = shear force per unit volume
ω = wave frequency
$\langle\ \rangle$ = volume average

Superscripts

d = drops
evap = vaporization
i = vapor–liquid interface
k = phase
ki = at vapor–liquid interface just inside phase k
l = liquid
sat = saturation
v = vapor
w = wall

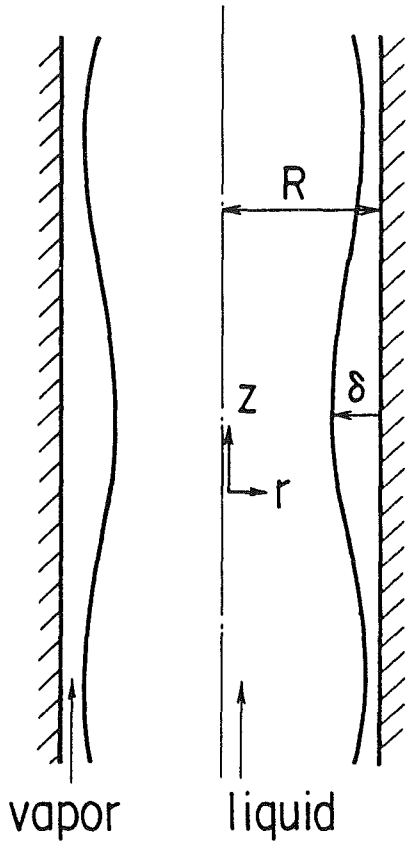

Fig. 2 Inverted annular flow geometry

For an inverted annular flow, the pressure difference between the two phases arises due to surface tension and vapor generation at the interface. The difference in pressure is, in general, an important factor in stabilizing the interface between the two phases. For example, in a horizontal stratified flow of liquid at bottom and vapor at top, gravity and surface tension forces influence and limit the interfacial wave growth. In an inverted annular flow, where liquid and vapor phases flow vertically upward, gravity should have little effect on interfacial stability. However, surface tension effects are important in determining wave phenomena in such cases.

In film boiling situations, an additional interfacial force arises due to vapor generation at the liquid–vapor interface. When the interface approaches the hot channel wall, a large amount of heat is transferred to the liquid and used for vaporization. As a result of the thrust force of vapor leaving the interface, liquid is pushed away from the hot wall. Vapor thrust is, however, expected to be significant only in regions very close to the wall.

The pressure difference between the liquid and vapor phases is thus considered to be made up of two terms

$$P_v - P_l = \Delta P_{vt} + \Delta P_{st} \tag{7}$$

where ΔP_{vt} = pressure difference due to vapor thrust; and ΔP_{st} = pressure difference due to surface tension. Considering the geometry of the interface shown in Fig. 2, the pressure difference due to surface tension is given by

$$\Delta P_{st} = -\sigma\left(\frac{1}{R\sqrt{\alpha_l}} + \frac{\partial^2 \delta}{\partial z^2}\right) \tag{8}$$

where

$$\delta = R(1-\sqrt{\alpha_l}) \tag{9}$$

In order to calculate ΔP_{vt}, the amount of heat used for vaporization at the interface q''_{evap} is used. Assuming all of the vapor generated at the interface enters the vapor film in the direction normal to the interface, the vapor thrust term is given by [5]

$$\Delta P_{vt} = -\frac{1}{\rho_v}\left(\frac{q''_{\text{evap}}}{h_{fg}}\right)^2 \Big/ \left(1+\left(\frac{\partial \delta}{\partial z}\right)^2\right) \tag{10}$$

The evaporative heat flux is given by a constitutive relation for energy partition that will be described in [2].

The pressure difference term ΔP_{ki} appearing in equations (3) and (4) is the difference between the volume-averaged phase pressure at the interface, but just within the phase, and the volume-averaged phase pressure, i.e.,

$$\Delta P_{ki} = <P_{ki}> - <P_k> \tag{11}$$

where P_{ki} is defined at the interface but just within phase k. This term arises, for example, when gravity acts normal to the interface as in a horizontal stratified flow, or when flow separation occurs at the interface, e.g., over a wave crest. For inverted annular flow, this term is considered to be negligibly small for both phases.

The stability of the hydraulic equation system, i.e., equations (1)–(4), with the phase pressure difference terms described above, will be examined later in this paper.

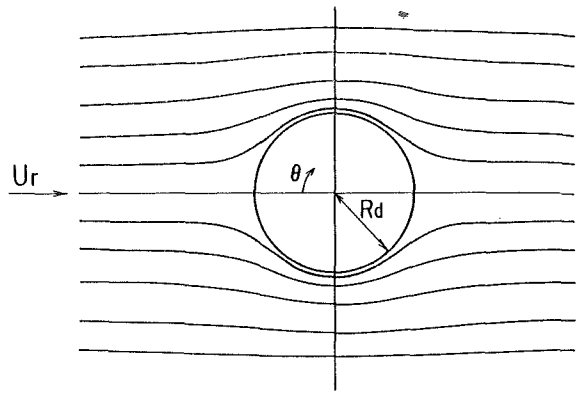

Fig. 3 Potential flow about a spherical droplet

Dispersed Droplet Flow. For dispersed droplet flow, we assume drops of mean radius R_d with a mean velocity U_l flowing in a vapor stream along a flow channel. Considering a single droplet, the average pressures of vapor and liquid phases are different due mainly to the surface tension effect. In the present analysis, we neglect the effects of interfacial mass transfer and virtual mass. We can then simply express the phasic pressure difference as follows

$$P_l - P_v = \frac{2\sigma}{R_d} \tag{12}$$

The pressure difference terms ΔP_{li} and ΔP_{vi} are now examined in detail. If the secondary flow in the droplet is assumed to be nonexistent, then the ΔP_{li} term can be assumed to be zero. On the other hand, the ΔP_{vi} term can be significantly larger depending on the vapor flow field around the droplet. This term can be analytically evaluated if the pressure distribution on the surface of the drop is known. The simplest case amenable for analytical study is that of potential flow about a sphere, shown in Fig. 3, in which the pressure distribution is given by the following expression [15]

$$P_{vi} = P_v + (1/8)\rho_v U_r^2(9\cos^2\theta - 5) \tag{13}$$

where

$$U_r = U_v - U_l \tag{14}$$

Integrating equation (13) around the droplet, we obtain the following expression for ΔP_{vi}

$$\Delta P_{vi} = -(1/4)\rho_v U_r^2 \tag{15}$$

The stability of the hydraulic equation system with the phasic pressure difference terms incorporated in momentum equations will be examined next for inverted annular and dispersed droplet flows.

Linear Stability Analysis

The stability of the two-field equation system is of great importance if numerical solutions are to be obtained. The numerical instabilities are related to the modeling of the phasic interaction terms which may, in some cases, lead to the mathematical characteristics of the equations becoming complex.

The linear stability analysis of the hydraulic equation system (equations (1)–(4)) can show whether the solution to the present two-field equation system, which incorporates interfacial forces due to surface tension and vapor thrust, is stable to perturbations of varying wavelength. For the present analysis, both phases are assumed to be incompressible. By substituting the liquid and vapor continuity equations into the momentum equations and using the relation

$$\alpha_l + \alpha_v = 1 \tag{16}$$

the following hydraulic equation system is obtained for the linear stability analysis

$$\rho_l \frac{\partial \alpha_l}{\partial t} + \rho_l \alpha_l \frac{\partial U_l}{\partial z} + \rho_l U_l \frac{\partial \alpha_l}{\partial z} = -m_l''' \tag{17}$$

$$-\rho_v \frac{\partial \alpha_l}{\partial t} + \rho_v \alpha_v \frac{\partial U_v}{\partial z} - \rho_v U_v \frac{\partial \alpha_l}{\partial z} = m_l''' \tag{18}$$

$$\rho_l \alpha_l \frac{\partial U_l}{\partial t} + \rho_l \alpha_l U_l \frac{\partial U_l}{\partial z} + \alpha_l \frac{\partial P_l}{\partial z} - \Delta P_{li} \frac{\partial \alpha_l}{\partial z} = \tau_i''' - \tau_{wl}''' - \rho_l \alpha_l g - m_l''' (U_i - U_l) \tag{19}$$

$$\rho_v \alpha_v \frac{\partial U_v}{\partial t} + \rho_v \alpha_v U_v \frac{\partial U_v}{\partial z} + \alpha_v \frac{\partial P_v}{\partial z} + \Delta P_{vi} \frac{\partial \alpha_l}{\partial z} = -\tau_i''' - \tau_{wv}''' - \rho_v \alpha_v g - m_l''' (U_v - U_i) \tag{20}$$

To analyze the stability of the liquid–vapor interface for a particular flow pattern, the pressure difference terms in the momentum equations must be replaced by appropriate expressions that describe the forces involved in interfacial momentum transfer.

Inverted Annular Flow. For the inverted annular flow regime, the difference in phasic pressures arises due to surface tension and vapor thrust forces as has been discussed. The pressure difference terms ΔP_{li} and ΔP_{vi} are zero for the present case and are dropped from equations (19). The pressure term in the liquid momentum equation is then expressed in terms of the vapor pressure P_v,

$$\alpha_l \frac{\partial P_l}{\partial z} = \alpha_l \frac{\partial P_v}{\partial z} - \alpha_l \left(\frac{\partial \Delta P_{vt}}{\partial z} + \frac{\partial \Delta P_{st}}{\partial z} \right) \tag{21}$$

in order to maintain a set of dependent variables consisting of α_l, U_l, U_v, and P_v. When equations (7) through (10) are used to evaluate the derivative terms in equation (21), the following liquid momentum equation is obtained

$$\rho_l \alpha_l \frac{\partial U_l}{\partial t} + \rho_l \alpha_l U_l \frac{\partial U_l}{\partial z} + \alpha_l \frac{\partial P_v}{\partial z} - \frac{\sigma}{2R\sqrt{\alpha_l}} \frac{\partial \alpha_l}{\partial z} - \frac{\sigma R \sqrt{\alpha_l}}{2} \frac{\partial^3 \alpha_l}{\partial z^3} = \tau_i''' - \rho_l \alpha_l g - m_l''' (U_l - U_i) \tag{22}$$

We note that in obtaining the above equation, only the terms linear in the first and second derivatives of α_l with respect to z have been retained and terms containing their product have been dropped. In addition, the effect of interfacial vaporization will be neglected in the following analysis, so that the results may be compared with those obtained in an adiabatic simulation to be discussed in the next section.

To perform the stability analysis, a perturbation of the form $\exp[i(kz - \omega t)]$ is introduced into the solution vector, $Y = (\alpha_l, U_l, U_v, P_v)$, and the equations are linearized in the perturbation variables. The resulting equations can be written in matrix form as follows

$$\begin{bmatrix} U_l - \frac{\omega}{k} & \alpha_l & 0 & 0 \\ -\left(U_v - \frac{\omega}{k}\right) & 0 & \alpha_v & 0 \\ A & \rho_l \alpha_l \left(U_l - \frac{\omega}{k}\right) & 0 & \alpha_l \\ 0 & 0 & \rho_v \alpha_v \left(U_v - \frac{\omega}{k}\right) & \alpha_v \end{bmatrix} \cdot \begin{bmatrix} \tilde{\alpha}_l \\ \tilde{U}_l \\ \tilde{U}_v \\ \tilde{P}_v \end{bmatrix} = 0 \tag{23}$$

where $A = (k^2/2)\,\sigma R\sqrt{\alpha_l} - \sigma/2R\sqrt{\alpha_l}$. In obtaining equation (23), we have assumed that there are no differential terms in the constitutive relations. Thus, added mass effect is neglected. For a nontrivial solution to exist, the determinant of the coefficient matrix must be zero. This condition gives the following dispersion relation

$$\frac{\omega}{k} = \left(\frac{B}{\rho^*}\right) \pm \left[\left(\frac{B}{\rho^*}\right)^2 - \frac{C - \alpha_v A}{\rho^*}\right]^{1/2} \tag{24}$$

where $B = \alpha_v \rho_l U_l + \alpha_l \rho_v U_v$; $C = \alpha_v \rho_l U_l^2 + \alpha_l \rho_v U_v^2$; and $\rho^* = \alpha_v \rho_l + \alpha_l \rho_v$. For stability in a linear sense, $\mathrm{Im}(\omega) \le 0$. This is satisfied when the condition given below is true

$$|U_v - U_l| < \left[\left(\frac{k^2 \sigma R}{2\sqrt{\alpha_l}} - \frac{\sigma}{2R\alpha_l^{3/2}}\right)\left(\frac{\alpha_v}{\rho_v} + \frac{\alpha_l}{\rho_l}\right)\right]^{1/2} \tag{25}$$

For waves of short wavelength (large k), the limit on relative velocity is seen to increase according to equation (25). Thus, the present two-field equation system is expected to be stable to perturbations of short wavelength or high frequency even for a large velocity difference between the liquid and vapor phases.

For waves of suficiently long wavelength (small k), the stability limit on relative velocity is reduced and approaches zero. When the relative velocity exceeds this limit, waves of long wavelength due to Kelvin–Helmholtz instability are expected to grow in amplitude. Interfacial waves of long wavelengths have been observed in flow visualization experiments and measured in adiabatic inverted annular flow experiments as will be discussed shortly.

It is noted that in equation (25) the terms describing surface tension arising out of curvature in the radial and axial directions have opposite signs. The surface tension term for the radial direction has a negative sign and reduces the stability limit, indicating that it is not a stabilizing force. Physically, this force should have a destabilizing effect rather than a stabilizing effect for the following reason. When the interface is perturbed from an equilibrium position, the surface tension force becomes larger at places where radius is smaller and the interface is further pulled in toward the center, instead of being restored to the equilibrium position.

If the same analysis is performed for the hydraulic equations with the pressure difference term set equal to zero (i.e., $P_l = P_v$), the resulting phase velocity ω/k has a complex value for any relative velocity greater than zero, and the solution is

expected to be unstable to both short and long-wavelength perturbations. In particular, the short-wavelength instabilities have no physical basis.

Dispersed Droplet Flow. A similar analysis for the dispersed droplet flow can be performed but a fifth equation is needed to complete the system of equations, since an additional dependent variable R_d has been introduced to the system through the pressure difference term. In terms of this added variable, the liquid volume fraction can be expressed as follows

$$\alpha_l = \frac{4}{3}\pi R_d^3 n \tag{26}$$

where n = number density of drops. As the drops travel along the flow channel, both n and R_d change, resulting in net variation of α_l.

In the present analysis, the variables n and R_d are used instead of α_l as the fourth and fifth dependent variables, in addition to U_l, U_v, and P_v. To complete the hydraulic equation system, however, a fifth equation is necessary. For this, we consider a simple problem of the behavior of a droplet of radius R_d subjected to a gas stream with a relative velocity U_r, as shown in Fig. 3. For such a droplet, the external pressures at the forward and rear stagnation points ($\theta = 0$ and π, respectively) and at the equator ($\theta = \pi/2$) are given, respectively, by the following equations

$$P_{vi}(\theta = 0 \text{ or } \pi) = P_v + \frac{1}{2}\rho_v U_r^2 \tag{27}$$

$$P_{vi}(\theta = \pi/2) = P_v - \frac{5}{8}\rho_v U_r^2 \tag{28}$$

Due to this external pressure difference, the droplet is expected to be pressed at stagnation points deforming into an oblate spheroidal shape, which is an ellipsoid formed by rotating an ellipse about its minor axis. Unless the droplet breaks up, these forces tending to deform the droplet are balanced by surface tension, which tends to restore a spherical shape. Photographic observations of liquid drops either suddenly introduced into an air stream [16] or moving at a steady speed [17] show clearly that the drops become flattened and spheroidal in shape. Ryan's experiments involving drops of water with surfactant added to reduce surface tension further show that the degree of flattening increases with decreasing surface tension as expected.

For the present analysis, we assume that the semiminor and semimajor axes of the spheroid at equilibrium state are equal to a and b, respectively. Furthermore, we assume the potential flow about a sphere is still applicable and approximate the pressure distribution on the surface of a spheroid by equation (13). Then, at equilibrium, the following relationship must hold between the dynamic pressure and surface tension at the stagnation points and at the equator, respectively

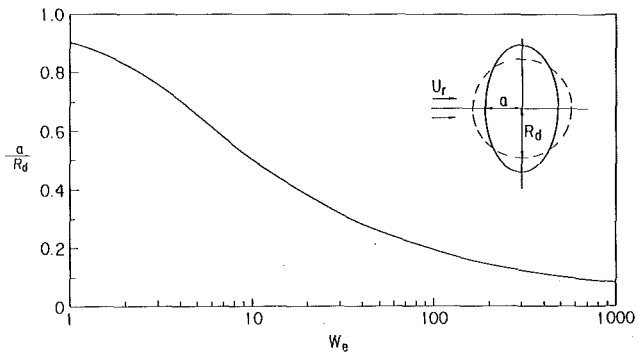

Fig. 4 Variation of shape factor with Weber number

$$P_l - P_v - \frac{1}{2}\rho_v U_r^2 = \frac{2\sigma}{R_d} X^2 \tag{29}$$

$$P_l - P_v + \frac{5}{8}\rho_v U_r^2 = \frac{\sigma}{R_d}(X^{1/2} + X^{-5/2}) \tag{30}$$

where $X = a/R_d$ (shape factor). Substracting equation (29) from (30) and rearranging, we obtain the following equation describing the degree of flattening the droplet is subjected to in order to balance the forces originating from the dynamic pressure of the vapor phase

$$\text{We} = \frac{\rho_v U_r^2 2R_d}{\sigma} = \frac{16}{9}(X^{1/2} + X^{-5/2} - 2X^2) \tag{31}$$

A nondimensional parameter appearing on the left-hand side of equation (31) is identified to be the Weber number defined in terms of the droplet's mean diameter and relative velocity. The shape factor satisfying equation (31) for various values of Weber number is plotted in Fig. 4. As the relative velocity or Weber number is increased, the droplet is predicted to become more flattened in shape, as expected from physical intuition. The use of pressure distribution for the potential flow about a sphere rather than a spheroid tends to overestimate the degree of flattening for a given Weber number; however, we adopt the present approach to simplify the analysis. If a more accurate description is desired, an analytical solution for potential flow about an oblate spheroid should be used instead.

To obtain the fifth equation necessary for the stability analysis, we assume that the shape factor remains constant and differentiate equation (31) with respect to z (or t). The following equation is obtained to complete the equation system for stability analysis

$$\frac{2}{U_r}\frac{dU_r}{dz} + \frac{1}{R_d}\frac{dR_d}{dz} = 0 \tag{32}$$

Substituting equations (12) and (15) into the pressure difference terms of the momentum equations, and performing a similar analysis as described for the inverted annular flow, the following dispersion relation for the droplet flow is obtained

$$\left(\frac{\omega}{k}\right) = \frac{\rho_l U_l + \rho_v U_v - 4\sigma/R_d U_r}{\rho_l + \rho_v} \pm \left[\frac{64\sigma^2}{R_d^2 U_r^2} + \frac{16\sigma}{R_d}(\rho_l - \rho_v) + \rho_v U_r^2\left(\frac{\alpha_l}{\alpha_v}(\rho_l + \rho_v) - 4\rho_l\right)\right]^{1/2} / 2(\rho_l + \rho_v) \tag{33}$$

For stability, the condition given below has to be satisfied.

$$\text{We} < \frac{16(\beta - 1) \pm 16[(\beta + 1 - \alpha_l/\alpha_v)(\beta + 1)]^{1/2}}{\beta(5 - 1/\alpha_v) - 1/\alpha_v + 1} \tag{34}$$

where

$$\beta = \rho_l/\rho_v \tag{35}$$

We first note that in the limit $\alpha_v = 1.0$, equation (34) simplifies to

$$\text{We} < 8 \tag{36}$$

The stability criterion obtained above implies breakup of drops for a given dispersed flow system when the Weber number, defined by equation (31), exceeds a critical value.

Table 1 Critical Weber number for various density ratios and void fractions

ρ_l/ρ_v	α_v					
	0.3	0.5	0.7	0.9	0.95	1.0
10	20.95	10.75	8.96	8.23	8.11	8.0
100	19.36	10.68	8.96	8.23	8.11	8.0
1000	19.22	10.67	8.96	8.23	8.11	8.0

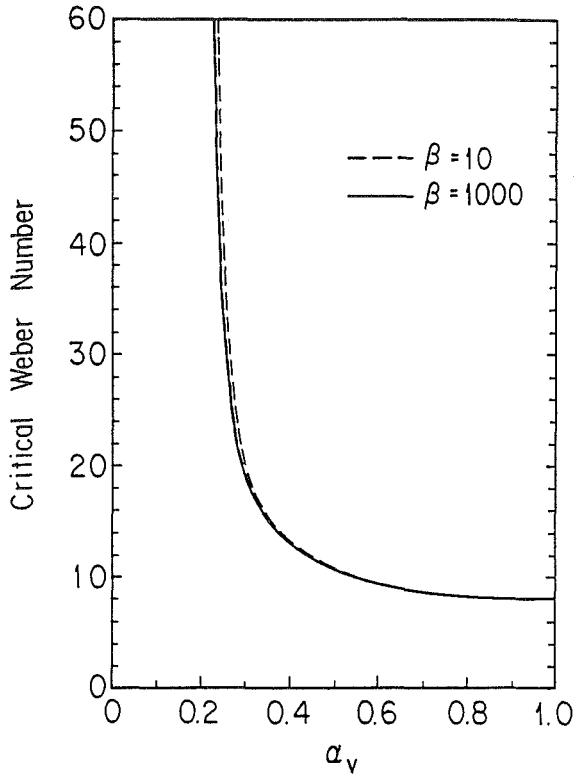

Fig. 5 Variation of critical Weber number with void fraction

For various density ratios and void fractions, the values of the critical Weber number predicted by equation (34) are tabulated in Table 1 and also plotted in Fig. 5. The effect of density ratio is small. As void fraction is decreased from unity, the critical Weber number is predicted to increase gradually. The validity of this predicted behavior is not clear at present due to the lack of experimental data concerning the breakup of drops in a confined flow channel. However, as Sleicher [18] pointed out, an increase in droplet concentration or liquid volume fraction for a given drop diameter in our case is likely to reduce the level of turbulence in the gas stream and should lead to a larger critical Weber number.

An infintely large critical Weber number is obtained as void fraction decreases to a value of 0.2. In reality, however, the dispersed flow usually exists for void fractions greater than about 0.8. At lower values, droplet coalescence, collision, and breakup processes will be important and the present analysis is no longer applicable. It is also noted here that the present analysis is limited to the well-established dispersed flow, for example, in regions well downstream of the inverted annular flow in reflooding of a hot vertical tube. The assumption of potential flow about a sphere has limited validity in the transition region where the liquid core in inverted annular flow destabilizes and breaks up into slugs, ligaments, and various large and small droplets. In this region, the mechanisms responsible for droplet breakup may be quite different from those relevant to well-developed dispersed flow with high void fraction and the situations of droplet breakup in a free gas stream which are discussed below.

The breakup of drops in a free gas stream has been investigated in the past both experimentally and theoretically. For cases where the inertial force and surface tension dominate the viscous effects, the droplet breakup can be specified by a critical Weber number [19]. Hinze [20] suggested further that the value of the critical Weber number should depend on the rate of droplet acceleration with respect to the gas stream. Various cases have been investigated in the past ranging from a drop suddenly exposed to a high-velocity gas stream to that of a drop moving in a gas stream at a terminal speed. For these two extreme cases, Hinze [19] recommends critical Weber numbers of 13 and 22, respectively.

The experimental data of Haas [16] for the breakup of mercury drops in air indicate a critical value of 10, while Hanson et al. [21] obtained values ranging from 7 to 17 for the breakup of water and methyl alcohol drops by air blast. On the other hand, the experimental data of Lane [22] and Ryan [17] involving a water drop placed in a vertical wind tunnel and held stationary by an upward flow of air indicate critical values of 10 and 12, respectively. Wallis [23] suggests that a drop moving in an infinite medium at its terminal speed will break up at a critical Weber number equal to 8, in agreement with equation (36). Kataoka et al. [24] also suggests a critical Weber number of 8 ~ 17 for a large drop falling at its terminal speed.

The stability criterion derived from the present analysis is consistent with the available data on droplet breakup in a gas stream. Furthermore, Ryan's data [17] indicate that the degree of maximum flattening before breakup, defined by the ratio a/b, is nearly constant at a value of 0.4 for drops of varying surface tension and maximum equivalent spherical diameter between 4.4 mm and 9.1 mm. The limiting value of a/b equal to 0.4 corresponds to the shape factor a/R_d of 0.54 and from equation (31) the Weber number of 8.4, which is also close to the critical value found in the present stability analysis.

If the ΔP_{vi} term is neglected in the above analysis, then the stability condition expressed by equation (36) is obtained for all void fractions and density ratios. This shows that the ΔP_{vi} term accounting for the nonuniformity of the interfacial pressure distribution tends to enhance the stability of the dispersed flow system, a result consistent with that reported by Pauchon and Banerjee [25].

Interfacial Waves in Inverted Annular Flow

From the dispersion relation obtained for the inverted annular flow, equation (24), the wavelength of maximum growth rate can be obtained by differentiating the imaginary part of the angular frequency, Im(ω), with respect to the wave number k, and by setting the derivative equal to zero.

$$\frac{\partial \mathrm{Im}(\omega)}{\partial k} = \frac{\partial}{\partial k}\left[-\left(\frac{B}{\rho^*}\right)^2 k^2 + \left(\frac{C + \frac{\sigma\alpha_v}{2R\sqrt{\alpha_l}}}{\rho^*}\right)k^2 - \frac{1}{2}\frac{k^4\alpha_v\sigma R\sqrt{\alpha_l}}{\rho^*}\right]^{1/2} = 0 \tag{37}$$

We can then solve for k_m, the wave number of the most unstable waves as

$$k_m = \alpha_l^{-1/4}(\sigma R)^{-1/2}\left[\frac{\alpha_l\rho_l\rho_v(U_v - U_l)^2}{\alpha_v\rho_l + \alpha_l\rho_v} + \frac{\sigma}{2R\sqrt{\alpha_l}}\right]^{1/2} \tag{38}$$

The wavelength for the maximum growth rate is then given by

$$\lambda_m = \frac{2\pi\alpha_l^{1/4}(\sigma R)^{1/2}}{\left[\frac{\alpha_l\rho_l\rho_v(U_v - U_l)^2}{\alpha_v\rho_l + \alpha_l\rho_v} + \frac{\sigma}{2R\sqrt{\alpha_l}}\right]^{1/2}} \tag{39}$$

The validity of equation (39) can only be determined by comparison with the measured wavelengths. Although the behavior of the interfacial waves were photographed in our flow visualization experiments as shown in Fig. 1, it was not possible to determine the relative velocity due to continuous vapor generation at the liquid–vapor interface. The only com-

Table 2 Experimental conditions for De Jarlais' experiments [26]

Test series	Inner diameter of tube, cm	D_l, cm	Void fraction	$\frac{\sqrt{2}\pi}{\sqrt{\alpha_v \alpha_l}}$	Gas species
A7	1.66	0.425	0.934	17.8	N_2
B2	1.36	0.763	0.685	9.6	N_2, He, Freon-12
B3	1.36	0.902	0.560	9.0	N_2, He, Freon-12
C1	0.90	0.604	0.549	8.9	N_2
C2	0.90	0.763	0.281	9.9	N_2

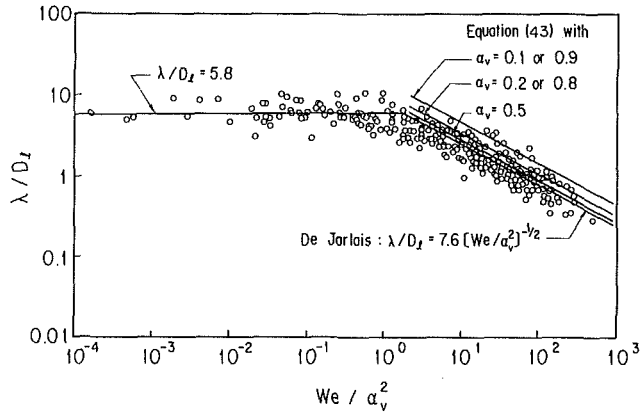

Fig. 6 Interfacial wave data and correlation developed by De Jarlais [26]

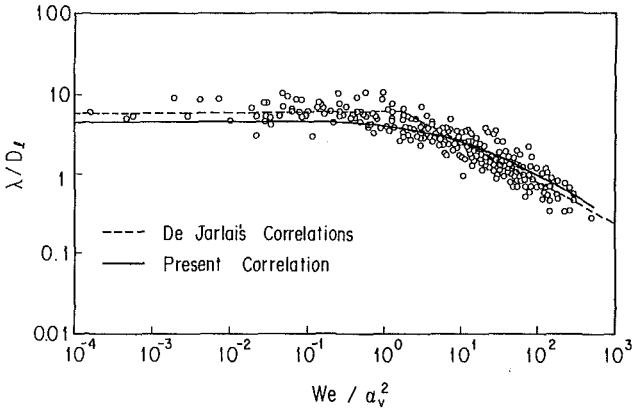

Fig. 7 Comparison of predictions with De Jarlais' data and correlations [26]

parison that could be made for these cases was a qualitative one based on numerical calculations and comparisons with the flow visualization experiments. However, adiabatic experiments in a round tube have been performed by De Jarlais [26], and the interfacial wavelength data were systematically obtained for downward inverted annular flow using a photographic technique. De Jarlais used water, and nitrogen, Freon-12 or helium for the gas, and performed experiments under the conditions summarized in Table 2.

De Jarlais correlated his interfacial wavelength data as shown in Fig. 6. At low relative velocities, the ratio of wavelength to liquid core diameter λ/D_l was determined to be roughly constant at about a value of 5.8. At large relative velocities, the wavelength decreased and the ratio λ/D_l was correlated by De Jarlais using a Weber number as follows

$$\frac{\lambda}{D_l} = 7.6[\mathrm{We}/\alpha_v^2]^{-1/2} \tag{40}$$

or

$$\frac{\lambda}{D_l} = 6.5[\mathrm{We}/\alpha_v^2]^{-0.46} \tag{41}$$

where

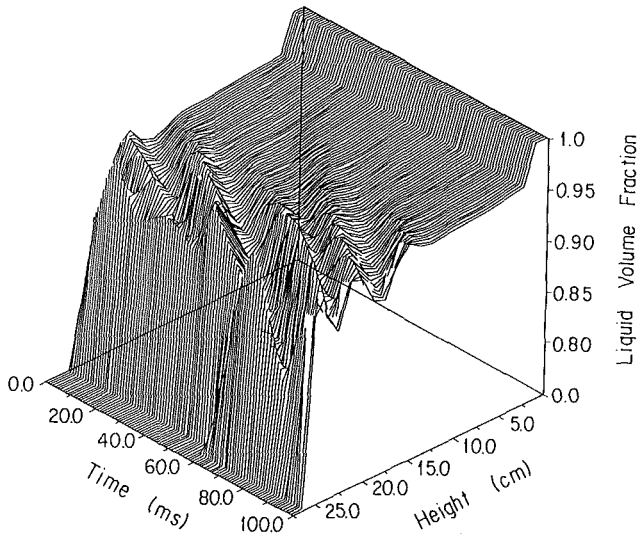

Fig. 8 Interfacial waves predicted by a two-fluid model of inverted annular flow

$$\mathrm{We} = \frac{\rho_v (U_v - U_l)^2 D_l}{\sigma} \tag{42}$$

We will now compare the expression for λ/D_l obtained from the linear stability analysis of the two-field formulations, i.e., equation (39) with D_l replacing $2R\sqrt{\alpha_l}$, with the De Jarlais correlations. Equation (39) indicates that the wavelength decreases with increasing relative velocity between the vapor and liquid phases. For sufficiently large relative velocities, the surface tension term in the denominator becomes insignificant and equation (39) can be simplified and written in terms of the Weber number as

$$\frac{\lambda_m}{D_l} = \frac{\sqrt{2}\pi}{\sqrt{\alpha_v \alpha_l}} [\mathrm{We}/\alpha_v^2]^{-1/2} \tag{43}$$

In deriving this expression, the liquid density was assumed to be much greater than that of vapor, and the volume fractions of vapor and liquid are of the same order of magnitude, i.e., $\alpha_v \rho_l >> \alpha_l \rho_v$. These assumptions are justified for the range of experimental conditions covered by De Jarlais.

The difference between equations (40) and (43) is found only in the leading coefficient. The leading coefficient in equation (43) is computed for void fractions used in experiments as listed in Table 2. The values are only slightly larger than De Jarlais' value of 7.6 for all cases except the void fraction of 0.934. The reasons for the theory for the 0.934 void fraction deviating from the correlation (and data) are not clear. It appears that the theory somewhat overpredicts the effect of void fraction. Equation (43) is also plotted in Fig. 6 for several values of void fraction. Agreement is excellent as the curves from equation (43) lie only slightly above that of De Jarlais' correlation. It is also noted that when the contribution of the surface tension terms in the denominator of equation (39) is considered, the wavelength predicted would be slightly smaller and the curves are expected to be in even better agreement.

As the relative velocity is reduced and the surface tension term dominates in the denominator, equation (39) simplifies to the following expression.

$$\lambda/D_l = 4.44 \quad (44)$$

The wavelength to liquid diameter ratio is predicted to be constant at a value of 4.44, which is closer to the value of 4.508 obtained by Rayleigh for a liquid jet [27] than De Jarlais' value of 5.8.

To compare equation (39) with De Jarlais' data and correlations over the entire range of relative velocities, the wavelength to liquid diameter ratio was evaluated using equation (39) for the experimental conditions covered by De Jarlais (excluding cases with void fraction of 0.934) and plotted in Fig. 7 against the parameter (We/α_v^2), also evaluated for the same conditions. The theoretical lines for the different void fractions, excluding $\alpha_v = 0.934$, lie very close together and are shown as one line. A smooth transition is seen for the predicted wavelength between large and small relative velocities. Good agreement is obtained among equation (39), experimental data, and De Jarlais' correlations for all conditions.

It is apparent that De Jarlais' choice of the parameter (We/α_v^2) in correlating the interfacial wavelength data for sufficiently large relative velocities is supported on theoretical grounds by the results of the present analysis. In comparison with De Jarlais' correlations, however, our expression given by equation (39) has the advantage of describing the interfacial waves with a single expression over the entire range of relative velocities. It is also remarkable how well the theoretical calculations compare with the experimental data.

Finally, when the inverted annular flow equations with interfacial vaporization were solved using the constitutive relations and numerical methods described in [2], interfacial waves were indeed calculated as shown in Fig. 8. The waves calculated have a significant effect on heat transfer in the region above the quench front. In addition, the interfacial waves eventually grow sufficiently in amplitude and lead to transition between the inverted annular and dispersed flow regimes. Calculations related to this transition are discussed in [2].

Conclusions

A two-field model of the inverted annular and dispersed droplet flows encountered in reflooding of a tubular flow channel is presented. The model consists of mass, momentum and energy conservation equations derived from a generalized, one-dimensional, two-field model. The phasic pressure difference terms have been included in the momentum equations of both phases and linear stability analyses of the hydraulic equations are performed. For inverted annular flow, these terms are shown to be important in achieving stability to short wavelength numerical instabilities, but allow prediction of long-wavelength Kelvin–Helmholtz instabilites, which appear physically as interfacial waves. For dispersed flow, the system is predicted to be unstable if the Weber number defined in terms of the mean droplet diameter and relative velocity exceeds a critical value of 8.

An expression for the wavelength of the most unstable interfacial waves in inverted annular flow is also obtained from the dispersion relation. The expression is successful in predicting the interfacial wave data obtained by De Jarlais for adiabatic, inverted annular flow in a glass tube.

Acknowledgments

The authors would like to acknowledge support for this work from the National Science Foundation under Grant No. CPE-81-12667.

References

1 Kawaji, M., Ng, Y. S., Banerjee, S., and Yadigaroglu, G., "Reflooding With Steady and Oscillatory Injection, Part I: Flow Regimes, Void Fraction, and Heat Transfer," ASME JOURNAL OF HEAT TRANSFER, Vol. 107, Aug. 1985, pp. 670–678.

2 Kawaji, M., and Banerjee, S., "Application of a Multifield Model to Reflooding of a Hot Vertical Tube: Part 2—Analysis of Experimental Results," in preparation for ASME JOURNAL OF HEAT TRANSFER.

3 Chan, A. M. C., and Banerjee, S., "Refilling and Rewetting of a Hot Horizontal Tube, Part II: Structure of a Two-Fluid Model," ASME JOURNAL OF HEAT TRANSFER, Vol. 103, May 1981, pp. 287–292.

4 Chan, A. M. C., and Banerjee, S., "Refilling and Rewetting of a Hot Horizontal Tube, Part III: Application of a Two-Fluid Model to Analyze Rewetting," ASME JOURNAL OF HEAT TRANSFER, Vol. 103, Nov. 1981, pp 653–659.

5 Kawaji, M., "Non-Equilibrium Two-Phase Flow: Reflooding of a Hot Vertical Tube," Ph.D. Thesis, Department of Nuclear Engineering, University of California, Berkeley, CA, 1984.

6 Banerjee, S., and Chan, A. M. C., "Separated Flow Models, Part I: Analysis of the Averaged and Local Instantaneous Formulations," *Int. J. Multiphase Flow*, Vol. 6, 1980, pp. 1–24.

7 Travis, J. R., Harlow, F. H., and Amsden, A. A., "Numerical Calculations of Two-Phase Flows," *Nuclear Science and Engineering*, Vol. 61, 1976, pp. 1–10.

8 Stuhmiller, J. H., "The Influence of Interfacial Pressure Forces on the Character of Two-Phase Flow Model Equations," *Int. J. Multiphase Flow*, Vol. 3, 1977, pp. 551–560.

9 Ramshaw, J. D., and Trapp, J. A., "Characteristics, Stability, and Short Wavelength Phenomena in Two-Phase Flow Equation Systems," *Nuclear Science and Engineering*, Vol. 66, 1978, p. 93–102.

10 Lyczkowski, R., Gidaspow, D., Solbrig, C. W., and Hughes, E. D., "Characteristics and Stability Analyses of Transient One-Dimensional Two-Phase Flow Equations and Their Finite Difference Approximations," *Nuclear Science and Engineering*, Vol. 66, 1978, pp. 378–396.

11 Arai, M., "Characteristics and Stability Analysis for Two-Phase Flow Equation Systems With Viscous Terms," *Nuclear Science and Engineering*, Vol. 74, 1980, pp. 77–83.

12 Agee, L. J., Banerjee, S., Duffey, R. B., and Hughes, E. D., "Some Aspects of Two-Fluid Models and Their Numerical Solutions," presented at the *Second OECD/NEA Specialists' Meeting on Transient Two-Phase Flow, Paris*, June 1978.

13 Jensen, R. T., "Inception of Liquid Entrainment During Emergency Cooling of Pressurized Water Reactors," Ph.D. Thesis, Department of Mechanical Engineering, Utah State University, 1972.

14 Edelman, Z., Elias, E., and Naot, D., "Optical Illustration of Liquid Penetration to the Vapour Film in Inverted Annular Boiling," *Int. Journal of Heat and Mass Transfer*, Vol. 26, No. 11, Nov. 1983, pp. 1715–1717.

15 Milne-Thompson, L. M., *Theoretical Hydrodynamics*, 5th ed., MacMillan, New York, 1968.

16 Haas, F. C., "Stability of Droplets Suddenly Exposed to a High Velocity Gas Stream," *AIChE Journal*, Vol. 10, No. 6, Nov. 1976, pp. 920–924.

17 Ryan, R. T., "The Behavior of Large, Low-Surface-Tension Water Drops Falling at Terminal Velocity in Air," *Journal of Applied Meteorology*, Vol. 15, Feb. 1976, pp. 157–165.

18 Sleicher, C. A., "Maximum Stable Drop Size in Turbulent Flows," *AIChE Journal*, Vol. 8, No. 4, Sept. 1962, pp. 471–477.

19 Hinze, J. O., "Fundamentals of the Hydrodynamic Mechanism of Splitting in Dispersion Process," *AIChE Journal*, Vol. 1, 1955, pp. 289–295.

20 Hinze, J. O., "Critical Speeds and Sizes of Liquid Globules," *Appl. Sci. Res.*, Vol. A1, 1948, pp. 273–288.

21 Hanson, A. R., Domich, E. G., and Adams, H. S., "Shock Tube Investigation of the Breakup of Drops by Air Blasts," *Physics of Fluids*, Vol. 6, No. 8, Aug. 1963, pp. 1070–1080.

22 Lane, W. R., "Shatter of Drops in Streams of Air," *Ind. Eng. Chem.*, Vol. 43, No. 6, June 1951, pp. 1312–1317.

23 Wallis, G. B., "The Terminal Speed of Single Drops or Bubbles in an Infinite Medium," *Int. J. Multiphase Flow*, Vol. 1, 1974, pp. 491–511.

24 Kataoka, I., Ishii, M., and Mishima, K., "Generation and Size Distribution of Droplet in Annular Two-Phase Flow," ASME *Journal of Fluids Engineering*, Vol. 105, June 1983, pp. 230–238.

25 Pauchon, C., and Banerjee, S., "Interface Momentum Interaction Effects in the Averaged Multifield Model: I. Void Propagation in Bubbly Flows," accepted for publication in *Int. J. Multiphase Flow*, 1985.

26 De Jarlais, G., "An Experimental Study of Inverted Annular Flow Hydrodynamics Utilizing an Adiabatic Simulation," NUREG/CR-3339, ANL-83-44, Mar. 1983.

27 Lamb, H., *Hydrodynamics*, 6th ed., Cambridge University Press, Cambridge, United Kingdom, 1932.

N. Moussiopoulos
Lecturer.

G. Ernst
Professor.

Institut für Technische Thermodynamik,
Universität Karlsruhe,
Karlsruhe, Federal Republic of Germany

Thermal Performance of Spray Cooling Ponds at Zero Wind Velocity

The present model allows predictions of the thermal performance of spray cooling ponds in the case of zero wind velocity. Droplet cooling is described by modeling of the heat and water vapor transfer to the air. Temperature and humidity of air are obtained by the numerical solution of transport differential equations. Detailed results are presented and discussed. Predictions are in good agreement with the observed thermal performance of spray cooling ponds. Results are utilized for a check of assumptions made by NTU models.

1 Introduction

Spray cooling ponds are an alternative to evaporating cooling towers for heat rejection into the atmosphere. In the USA, spray cooling systems are used at several power plants for supplemental cooling. In Western Europe, the use of spray cooling ponds is restricted because of their high land requirements. Nevertheless, spray cooling can be of interest even in European countries, if the needed area is available [1]. Recently systems with fixed pipes have been proposed as emergency cooling systems in the Federal Republic of Germany. For this application the mechanical simplicity of spray cooling ponds is appreciated.

This paper deals with predictions of the thermal performance of spray cooling ponds achieved with the mathematical model ASCONA (Algorithm for Spray Cooling Numerical Analysis). After a description of the model, detailed results for the thermal performance of spray cooling ponds are presented. Subsequently, these results are compared with predictions achieved with NTU models.

2 Model Description

Spray cooling is based on heat transfer to air and to the evaporating water. Correspondingly, the air density decreases and a large-scale convective air flow is established above the spray cooling pond. Additional vertical momentum is transferred to the air by the upward and downward-moving droplets. As the velocity of upward-moving droplets is at all levels higher than that of downward-moving droplets [2], the transfer of upward vertical momentum predominates; hence, this mechanism enhances the convective air flow driven by buoyancy forces.

Most of the existing models describing the performance of spray systems combine basic parameters into a dimensionless group (e.g. NTU, Number of Transfer Units, and SER, Spray Energy Release) to be determined directly from observed performance [3, 4]. The principal difficulty in applying these models for predictions of the thermal performance is that the local wet-bulb temperature in the spray region has to be known. Several approximations have been introduced for obtaining the local wet-bulb temperature. Porter and Chen [3], for instance, utilize an appropriate constant average wet-bulb temperature derived from an empirically evaluated interference factor (cf. equation (29)). Chen and Trezek [4] suggest an averaging of the initial and final wet-bulb temperatures depending on the wind velocity. On the basis of an analysis of the air-vapor dynamics, Chaturvedi and Porter [5] propose an expression for the interference factor depending on the distance windward into the spray region.

In contrast to previous models, the mathematical model ASCONA allows a description of the convective air flow and of heat and mass transfer in the spray region; it requires neither empirical information from field measurements nor an adaptation of model constants. In the present paper the set of differential equations is formulated with respect to cylindrical coordinates and is numerically solved for spray cooling ponds of equivalent circular surface area for the critical case of zero wind velocity. The droplet size is modeled by means of the Sauter mean diameter, which is the characteristic diameter giving the proper ratio between total volume and total surface area [6].

The mean droplet density in the spray region is given by

$$\bar{n} = \frac{6\dot{M}_W \tau_o}{\rho_W \pi d^3} \cdot \frac{1}{h_{sp} A_{sp}} \tag{1}$$

The arrangement of the spray nozzles is assumed to provide a horizontally homogeneous droplet distribution in the spray region. Consideration of mass conservation for the droplets allows the calculation of the vertical variation of the droplet density for upward or downward-moving droplets

$$n(y) = \bar{n} \cdot \frac{h_{sp}}{\tau_o |w(y)|} \tag{2}$$

where the vertical droplet velocity w follows from the equation of motion for droplets [2, 7]. The horizontal droplet velocity component is neglected, as it is in general small compared to the vertical component; furthermore, it does not affect the momentum exchange between droplets and air (contributions of individual droplets cancel out) and it has only a minor influence on the kinetics of heat and mass transfer.

The air flow field is described by solving the vorticity transport equation and the Poisson equation for the stream function. Turbulent diffusion is taken into account by means of a modified version of the k–ϵ model. A detailed description of the hydrodynamic part of the model is given in [2, 7].

Temperature and absolute humidity of air are obtained by solving the transport differential equations

$$\nabla(\mathbf{u}t) = \nabla(a_T \nabla t) + C_t \tag{3}$$

$$\nabla(\mathbf{u}x) = \nabla(\delta_T \nabla x) + C_x \tag{4}$$

In the case of saturated air, x represents the sum of water vapor and content of (recondensed) droplets ($x = x_G + x_K$). The air velocity $\mathbf{u}$ results from the calculated stream function. The eddy conductivity a_T and the eddy diffusivity δ_T are calculated from the eddy viscosity assuming $\mathrm{Pr}_T = \mathrm{Sc}_T = 1$.

For nonsaturated air, the source terms C_t and C_x correspond to the rates of heat and mass transfer

Contributed by the Heat Transfer Division for publication in the JOURNAL OF HEAT TRANSFER. Manuscript received by the Heat Transfer Division December 10, 1985.

$$C_x = C_{x_G} = \dot{m} \tag{5}$$

$$C_t = \frac{1}{c_{pM}} \dot{q} \tag{6}$$

If the air is saturated, a part of the evaporating water has to recondense. The resulting latent heat leads to an additional heating of the air

$$C_x = C_{x_G} + C_{x_K} = \dot{m} \tag{7}$$

$$C_{x_K} = \chi \dot{m} \tag{8}$$

$$C_t = \frac{1}{c_{pM}} (\dot{q} + \chi \dot{m} r_o) \tag{9}$$

where χ indicates which part of the transferred water vapor recondenses. χ depends on the local heating of air and the temperature dependence of the saturation humidity

$$C_{x_G} = (1-\chi)\dot{m} = C_t \left(\frac{\partial x_s}{\partial t}\right)_p \tag{10}$$

Using equations (9) and (10) one gets

$$\chi = \frac{1 - \frac{\dot{q}}{\dot{m} c_{pM}} \left(\frac{\partial x_s}{\partial t}\right)_p}{1 + \frac{r_o}{c_{pM}} \left(\frac{\partial x_s}{\partial t}\right)_p} \tag{11}$$

This expression is discussed below.

The rates of heat and mass transfer are calculated for upward and downward-moving droplets from the heat and mass rejected per unit surface area by a single droplet

$$\dot{q} = \left(q' \pi d^2 \frac{n}{\rho_A}\right)_{\text{up}} + \left(q' \pi d^2 \frac{n}{\rho_A}\right)_{\text{down}} \tag{12}$$

$$\dot{m} = \left(m' \pi d^2 \frac{n}{\rho_A}\right)_{\text{up}} + \left(m' \pi d^2 \frac{n}{\rho_A}\right)_{\text{down}} \tag{13}$$

Linear kinetic expressions are used for the calculation of q' and m'

$$q' = \alpha (t_W - t) \tag{14}$$

$$m' = \begin{cases} \sigma (x_s(t_W) - x), & x < x_s(t) \\ \sigma (x_s(t_w) - x_s(t)), & x \geq x_s(t) \end{cases} \tag{15}$$

The approximation usually introduced of completely mixed droplets [4] is justified for the case to be discussed below, i.e., $d = 2$ mm and a mean value of 350 W/(m^{2}K) for the predicted heat transfer coefficient in the air phase, see Fig. 2: While the Biot number ($\text{Bi} = \alpha d/\lambda_W$) is nearly equal to unity, the effects of oscillation and internal circulation considerably enhance heat transfer in the interior of the droplets. Therefore, in the present work the heat transfer resistance inside the droplets is neglected.

The heat transfer coefficient α is obtained from the Nusselt number ($\text{Nu} = \alpha d/\lambda_A$) proposed by Schlünder [8], which is very similar to the widely used Ranz–Marshall expression [9] but is valid for Reynolds numbers up to 10^7

$$\text{Nu} = 2 + \sqrt{\text{Nu}_L^2 + \text{Nu}_T^2} \tag{16}$$

$$\text{Nu}_L = 0.664 \sqrt{\text{Re}} \sqrt[3]{\text{Pr}} \tag{17}$$

$$\text{Nu}_T = \frac{0.037 \text{Re}^{0.8} \text{Pr}}{1 + 2.44(\text{Pr}^{2/3} - 1)\text{Re}^{-0.1}} \tag{18}$$

where L and T as subscripts denote "laminar" and "turbulent," respectively. The Reynolds number is calculated with the relative velocity between droplets and air and the Sauter mean diameter.

The mass transfer coefficient follows from the similarity of heat and mass transfer implying a psychrometric ratio equal unity, i.e.

$$\frac{\alpha}{\sigma c_{pM}} = 1 \tag{19}$$

Equations (12)–(15) and (19) allow a discussion of the quantity χ which has been introduced as the recondensing part of the transferred water vapor. Assuming that heat and water vapor are transferred from droplets of uniform temperature ($t_W > t$) to saturated air, equation (11) can be rewritten as

Nomenclature

A = interfacial area of droplets and air
A_{sp} = surface area of spray region
a_T = eddy conductivity
c_{pM} = specific heat of humid air
C_t, C_x = source terms
c_W = specific heat of liquid water
d = Sauter mean diameter
f = interference factor
h_s = specific enthalpy of saturated air per unit mass of dry air
h_{sp} = spraying height
$\dot{M}$ = mass flow rate
$\dot{m}$ = rate of mass transfer per kg dry air
m' = rate of mass transfer per unit area
n = droplet density
NTU = number of transfer units
Nu = Nusselt number
p = pressure
Pr = Prandtl number
Pr_T = turbulent Prandtl number
$\dot{Q}$ = total heat rejection
$\dot{q}$ = rate of heat transfer per kg dry air
q' = rate of heat transfer per unit area
R = gas constant
r = radius
R_i = inner radius of the spray region
R_o = outer radius of the spray region
r_o = heat of vaporization of water
Re = Reynolds number
Sc_T = turbulent Schmidt number
T = thermodynamic temperature
t = air temperature
t_{CW} = cold water temperature
t_W = droplet temperature
t_{wb} = wet-bulb temperature
t_{WW} = water temperature before spraying
Δt_{wb} = wet-bulb degradation
$\mathbf{u}$ = air velocity
w = droplet velocity
x = absolute humidity
x_s = saturation humidity
y = height
α = heat transfer coefficient
δ_T = eddy diffusivity
η = spray cooling effectiveness
λ = thermal conductivity
ρ = density
σ = mass transfer coefficient
τ = time
τ_o = spray residence time
ϕ = relative humidity

Subscripts

A = air
a = ambient
G = water vapor
K = recondensed water
W = water

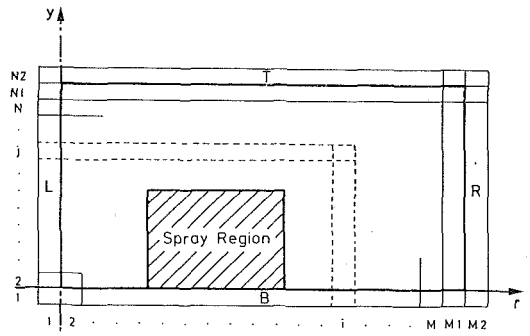

Fig. 1 Numerical grid

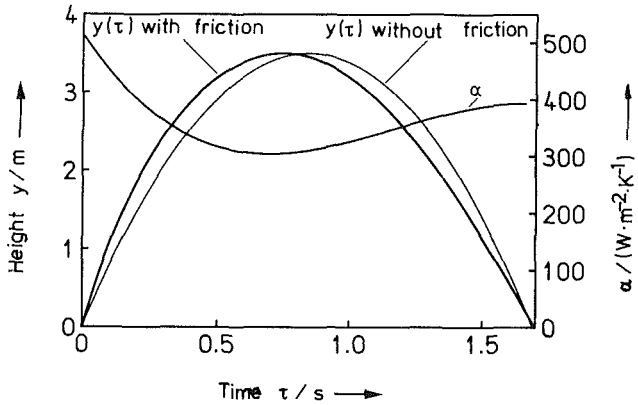

Fig. 2 Time dependence of the droplet location above the pond surface compared with the case of frictionless flow; variation of the heat transfer coefficient during the spray residence time

$$\chi = \frac{1 - \dfrac{t_W - t}{x_s(t_W) - x_s(t)} \left(\dfrac{\partial x_s}{\partial t}\right)_p}{1 + \dfrac{r_o}{c_{pM}} \left(\dfrac{\partial x_s}{\partial t}\right)_p} \tag{20}$$

The denominator of this expression depends only on air temperature; in the temperature range of interest its numerical value varies between 2 and 6. Because of the exponential temperature dependence of the saturation humidity, the numerator on the right-hand side of equation (20) is positive and below unity.

The heat rejected by the droplets is given by

$$\dot{q}_W = \dot{q} + \dot{m} r_o \tag{21}$$

Thus, the droplet temperature is obtained by integrating the equation

$$w \frac{dt_W}{dy} = -\frac{6 \dot{q}_W \rho_A}{n \rho_W c_W \pi d^3} \tag{22}$$

from 0 to the spraying height for upward-moving droplets and back to the pond surface for downward-moving droplets. The initial temperature is equal to the water temperature before spraying t_{WW}; the temperature of the droplets reaching the pond surface is denoted by t_E.

The computational domain is shown in Fig. 1. The left boundary coincides with the axis of symmetry; correspondingly, the horizontal gradients of air temperature and absolute humidity are set equal to zero at the left boundary. The distance of the right boundary from the spray region is regarded as sufficient to allow the assumption of constant ambient conditions at this boundary. At the top boundary the vertical gradient of the absolute humidity is neglected, while the vertical temperature gradient is calculated corresponding to energy conservation. The gradients of the air temperature and the absolute humidity at the bottom boundary are closely related to the heat and water vapor fluxes transferred to the air at the pond surface. These fluxes cause the additional water temperature decrease from t_E to the pond temperature t_P. For their calculation appropriate kinetic expressions are used [2]. The cold water temperature is obtained by averaging t_P over the pond surface

$$t_{CW} \equiv \bar{t}_P = \frac{1}{\pi R_o^2} \int_0^{R_o} 2\pi r t_P dr \tag{23}$$

The boundary conditions for the air temperature and the absolute humidity are discussed in more detail in [2]. The numerical methods used for the solution of the equation system presented above are outlined in [2, 7].

3 Results

In this section results from the model ASCONA are presented. All predictions are based on a spraying height $h_{sp} = 3.5$ m, a Sauter mean diameter $d = 2$ mm, and a water temperature before spraying $t_{WW} = 40°C$. Four different pond geometries and three values for the mass flow rate of water were considered. Most of the calculations discussed below were performed for the frequent ambient conditions $t_a = 20°C$, $\phi_a = 60$ percent, and the more critical case $t_a = 30°C$, $\phi_a = 75$ percent, which is rather rare in Central Europe.

Figures 2–4 illustrate predictions of the droplet motion in the spray region, the cooling of droplets along their trajectory, and the associated change of the thermodynamic state of air. These results originate from a calculation carried out for the ambient conditions $t_a = 20°C$, $\phi_a = 60$ percent, and a mass flow rate of water $\dot{M}_W = 450$ kg/s; the inner and the outer radius of the spray region R_i and R_o were assumed equal to 9 m and 24 m, respectively.

The influence of friction on the droplet motion is illustrated in Fig. 2. Although friction has practically no influence on the spray residence time, it affects the droplet velocity considerably: In contrast to the case of frictionless flow, the velocity of upward-moving droplets is at all levels higher than the velocity of downward-moving droplets. As a consequence, the duration of upward droplet motion is shorter than the falling time: In the case of the assumed value for the drag coefficient ($c_D = 0.47$) it amounts to 44 percent of the spray residence time. In addition, the resulting orifice exit velocity $w_o = 12.36$ m/s is considerably higher than the exit velocity $\hat{w}_o = 8.29$ m/s in the case of frictionless flow.

Figure 2 also shows the variation of the heat transfer coefficient during the spray residence time. High relative velocities between droplets and air lead to high values of the heat transfer coefficient; therefore, the coefficient is highest during the upward motion of the droplets. The lowest value of the coefficient occurs when the relative vertical velocity between droplets and air is zero, i.e., just before the droplets reach the highest point of the spray. The prediction for the heat transfer coefficient shown in Fig. 2 is in good agreement with results reported by Chen and Trezek [4]. The cooling effectiveness depends on the position in the spray region: Fig. 3 shows that droplet cooling deteriorates with decreasing radius because the driving force for both heat and mass transfer decreases with the gradual heating and humidification of the air. It should be noticed that roughly 60 percent of the cooling occurs during the upward motion of the droplets.

Figure 4 illustrates the predicted distribution of the air temperature. The dashed curves correspond to the streamlines of the air flow. The high gradients at the inflow side of the spray region show that the rates of heat transfer are highest there. Because of the analogy between equations (3) and (4), a similar distribution results for the absolute humidity.

Predictions for the cold water temperature deduced from

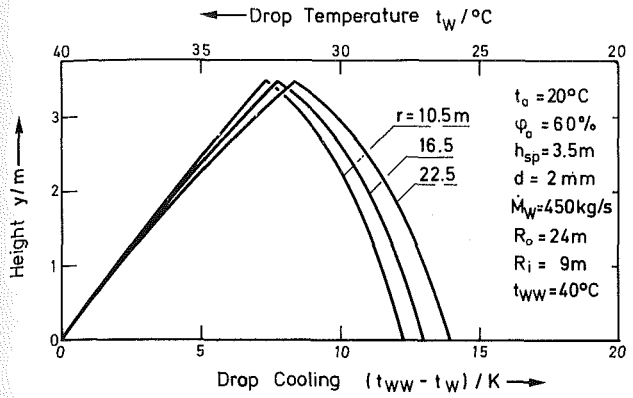

Fig. 3 Height dependence of the droplet temperature at three different radii in the spray region: Droplet cooling deteriorates with decreasing radius

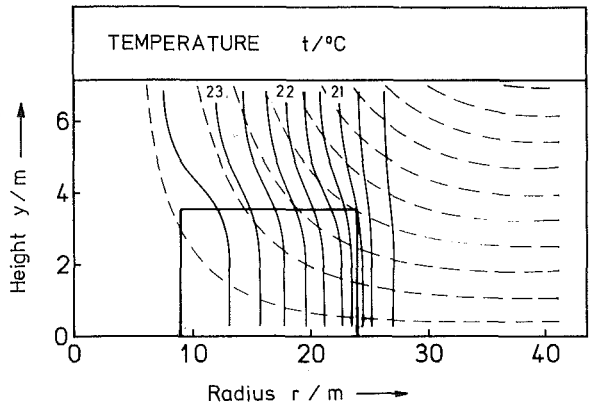

Fig. 4 Predicted air temperature for the case defined in Fig. 3: The dashed curves correspond to the streamlines of the air flow

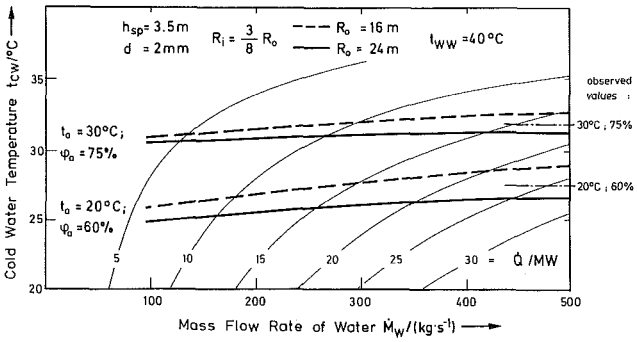

Fig. 5 Cold water temperature from ASCONA compared with results summarized from field measurements: Isopleths for the total heat rejection $\dot{Q}$ are reproduced for convenience

several calculations are summarized in Fig. 5. Two different spray cooling ponds were assumed (outer radius of the spray region $R_o = 16$ m and 24 m), both with a nozzle-free inner zone ($R_i = 3/8\ R_o$). Results are shown for the ambient conditions $t_a = 20°C$, $\phi_a = 60$ percent and $t_a = 30°C$, $\phi_a = 75$ percent. For convenience, isopleths for the total heat rejection are drawn.

The model predictions for the cold water temperature are compared with observed values reported by Hebden and Shah [10]. These values were calculated by averaging data received from both small and large ponds operating at different locations and are based on the low wind velocity of 2 m/s. Assuming that the reported values are representative for the case of zero wind velocity as well, Fig. 5 shows a good agreement between observation and prediction for the two ambient conditions considered. The model predictions show, however, that

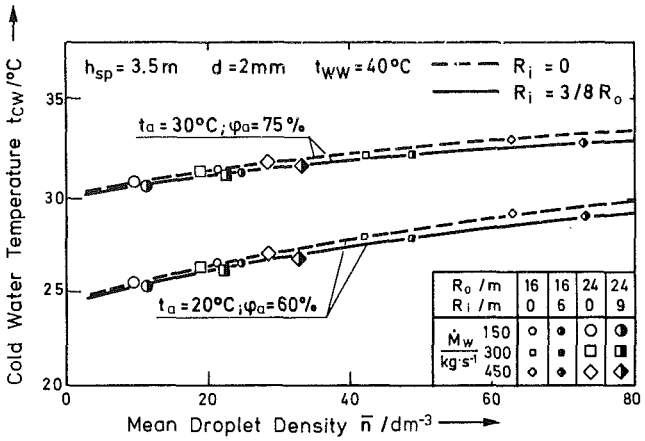

Fig. 6 Cold water temperature from ASCONA and mean droplet density

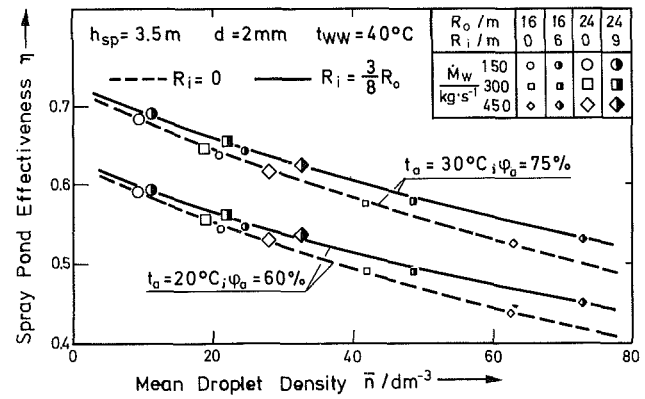

Fig. 7 Spray cooling effectiveness from ASCONA and mean droplet density

the cold water temperature achieved does not only depend on the ambient conditions but also on the pond geometry and the mass flow rate of cooling water.

In Fig. 6, the cold water temperature is plotted as a function of the mean droplet density (see equation (1)). In addition to the cases in Fig. 5, the corresponding cases without a nozzle-free inner zone were considered. In the case of small variations of the pond geometry and the mass flow rate of water, the cold water temperature correlates with the mean droplet density. Further, this figure shows that the performance of a pond without a nozzle-free inner zone is inferior: In this case the inner zone only weakly contributes to the heat rejection, because air velocity and, consequently, heat and mass transfer coefficients are very low in this region. The optimal R_i/R_o ratio presumably depends on the spraying height; values between 0.33 and 0.75 seem to be recommendable.

Figure 7 illustrates the ratio between actual and maximum possible cooling, i.e., the spray cooling effectiveness

$$\eta = \frac{t_{WW} - t_{CW}}{t_{WW} - t_{wb_a}} \tag{24}$$

as a function of the mean droplet density for all 24 cases considered in Fig. 6. The spray cooling effectiveness decreases with increasing mean droplet density.

It should be noted that the spray cooling effectiveness does not provide information on the total heat rejected by a spray cooling pond: As shown by Fig. 7, the spray cooling effectiveness is higher in the case of the ambient conditions $t_a = 30°C$, $\phi_a = 75$ percent than in the case $t_a = 20°C$, $\phi_a = 60$ percent. This is due to the relatively high wet-bulb temperature

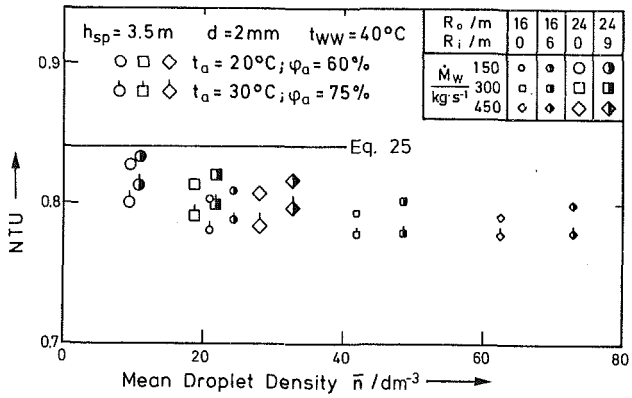

Fig. 8 NTU calculated with the model ASCONA and equation (27) as a function of the mean droplet density; the value resulting from equation (25) is drawn for comparison

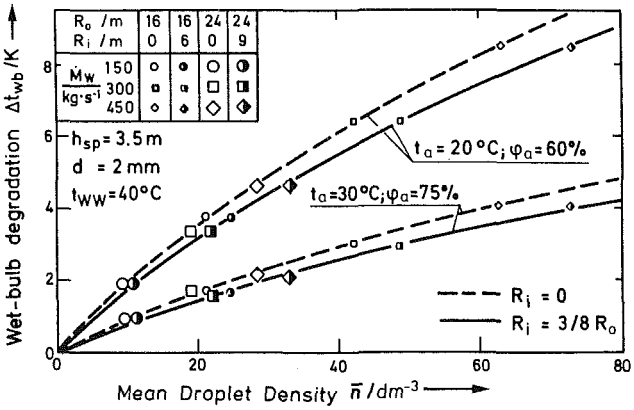

Fig. 9 Wet-bulb degradation from ASCONA and mean droplet density

of 26.3°C in the case of the hot and humid atmospheric conditions $t_\alpha = 30°C$, $\phi_\alpha = 75$ percent.

4 Comparison With Results From NTU Models

In contrast to the model ASCONA, NTU models require considerable empirical information. In these models, the thermal performance of spray cooling systems is described by means of the dimensionless quantity $NTU = \sigma A/\dot{M}_W$. A parametric study (see [2]) yields for the case of zero wind velocity

$$NTU = 0.927(h_{sp}/m)^{0.75}(d/mm)^{-1.5} \tag{25}$$

In NTU models, NTU is commonly assumed to depend on spraying height, droplet size, and wind velocity. For a certain spray cooling system, spraying height and droplet size are given; hence, only the influence of the wind velocity on NTU remains to be described on the basis of measurements. For this purpose, NTU has to be formulated to depend on easily measurable quantities. With a psychrometric ratio equal to unity (see equation (19)), the assumption of a state of saturated air reached adiabatically yields

$$NTU = -\int_{t_{WW}}^{t_{CW}} \frac{c_W dt_W}{h_s(t_W) - h_s(t_{wb})} \tag{26}$$

Mostly this integral is approximated using mean values

$$NTU \simeq \frac{c_W(t_{WW} - t_{CW})}{0.5(h_s(t_{WW}) + h_s(t_{CW})) - h_s(\bar{t}_{wb})} \tag{27}$$

Equations (26) and (27) indicate that NTU corresponds to the ratio between actual cooling and the driving force for the heat rejection.

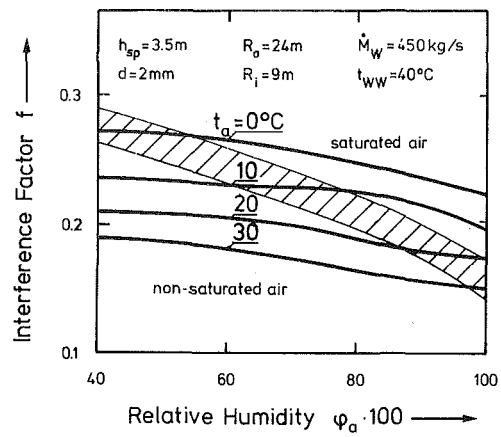

Fig. 10 Interference factor from ASCONA as a function of the ambient conditions. Above the shaded area air is saturated throughout the spray region; below it air leaves the spray region nonsaturated.

The expression on the right-hand side of equation (27) contains easily measurable quantities and allows the determination of NTU for the given spraying system. For predictions of the thermal performance of spray cooling ponds using the same spraying system, only reasonable assumptions for the wet-bulb degradation Δt_{wb} have to be made. Δt_{wb} is defined as the mean increase of wet-bulb temperature in the spray region

$$\Delta t_{wb} \equiv \bar{t}_{wb} - t_{wb_a} \tag{28}$$

Many authors relate Δt_{wb} to the difference between the water temperature before spraying t_{WW} and the ambient wet-bulb temperature t_{wb_a}, e.g., introducing the interference factor f [3]

$$\Delta t_{wb} = f\{t_{WW} - t_{wb_a}\} \tag{29}$$

The analysis of the mechanism of wet-bulb degradation has been proved to be the major difficulty for semi-empirical models, especially in the case of zero wind velocity. Therefore, in some cases the results of the calculations showed poor agreement with reported experimental results.

Results achieved with the model ASCONA were used for a comparison with predictions from NTU models. For this purpose, the volume-averaged wet-bulb temperature of air in the spray region was calculated for all 24 cases in Fig. 6. With these values and the cold water temperatures in Fig. 6, NTU was calculated using equation (27) for all 24 cases. The results are shown in Fig. 8 as a function of the mean droplet density. For the assumed spraying height $h_{sp} = 3.5$ m and the assumed Sauter mean diameter $d = 2$ mm, equation (25) yields the value NTU = 0.838. The relatively good agreement indicates that NTU is basically suitable for the description of the thermal performance of a spray cooling pond.

For a check of the approximations introduced by NTU models for the wet-bulb degradation, Δt_{wb} was calculated for all 24 cases in Fig. 6 and was plotted in Fig. 9 as a function of the mean droplet density. In spite of the assumptions used by several NTU models, the wet-bulb degradation does not only depend on the atmospheric conditions but also varies considerably with pond geometry and mass flow rate of water. The results plotted in Fig. 9 correspond to the correlation

$$f = b\{\bar{n}/dm^{-3}\}^{0.75} \tag{30}$$

where $b = 0.012$ in the case of a nozzle-free inner zone; otherwise $b = 0.013$.

The interference factor was evaluated in a similar manner for a variety of ambient conditions assuming pond geometry and dropwise parameters as given in Fig. 3. Results are shown in Fig. 10. The interference factor decreases both with increasing temperature and increasing relative humidity of ambient air. This behavior is related to the drastic increase of the wet

part of the cooling with increasing temperature and the decrease of the heat rejection with increasing temperature and relative humidity [2]. Figure 10 further shows that the dependence of the interference factor on the relative humidity is more pronounced if the air is either saturated or non-saturated in the entire spray region. In the intermediate range (shaded area in Fig. 10; in this range air reaches saturation in the interior of the spray region) a small increase of the relative humidity leads to a considerable increase of the portion of the spray region, where air is saturated. This leads to a sharp decrease of the wet part of the cooling in this range of ambient conditions and, therefore, to a weaker decrease of the interference factor with increasing relative humidity.

Figures 9 and 10 show that the wet-bulb degradation cannot be adequately parameterized by means of oversimplified expressions.

5 Conclusions

The model ASCONA predicts the performance of spray cooling ponds for zero wind velocity in good agreement with results from field measurements. Results prove that the dimensionless number NTU is basically suitable to describe the thermal performance of spray cooling ponds. NTU models, however, require a sensible parameterization of the wet-bulb degradation in order to predict reliably the spray cooling performance. An analysis of the wet-bulb degradation with the model ASCONA might contribute to the formulation of improved NTU models.

References

1 Zimmermann, C., "Stand und Tendenzen in der Technik und der Anwendung der Kühlteich-/Sprühkühlteichtechnologie," *VGB Kraftwerkstechnik*, Vol. 62, No. 6, 1982, pp. 512–519.

2 Moussiopoulos, N., "Mathematisches Modell zur Berechnung von Sprühkühlteichen," Dissertation, Universität Karlsruhe, Fortschr.-Ber. VDI-Z., Reihe 6, No. 105, Düsseldorf, 1982.

3 Porter, R. W., and Chen, K. H., "Heat and Mass Transfer of Spray Canals," ASME JOURNAL OF HEAT TRANSFER, Vol. 96, No. 3, 1974, pp. 286–291.

4 Chen, K. H., and Trezek, G. J., "The Effect of Heat Transfer Coefficient, Local Wet Bulb Temperature and Droplet Size Distribution Function on the Thermal Performance of Sprays," ASME JOURNAL OF HEAT TRANSFER, Vol. 99, No. 3, 1977, pp. 381–385.

5 Chaturvedi, S., and Porter, R. W., "Air Vapor Dynamics in Large-Scale Atmospheric Spray Cooling Systems," ASME *Journal of Fluids Engineering*, Vol. 100, No. 3, 1978, pp. 65–72.

6 Porter, R. W., Jain, M., and Chaturvedi, S. K., "Unit Thermal Performance of Atmospheric Spray Cooling Systems," ASME JOURNAL OF HEAT TRANSFER, Vol. 102, No. 2, 1980, pp. 210–214.

7 Moussiopoulos, N., "Numerical Simulations of Spray Cooling Pond Performance," submitted to the ASME *Journal of Fluids Engineering*, 1985.

8 Schlünder, E.-U., *Einführung in die Wärmeübertragung*, Vieweg, 1981.

9 Ranz, W. E., and Marshall, W. R., Jr., "Evaporation from Drops," *Chemical Engineering Progress*, Vol. 48, 1952, pp. 141–146; 173–180.

10 Hebden, W. E., and Shah, A. M., "Effects of Nozzle Performance on Spray Ponds," *Proceedings of the American Power Conference*, Vol. 38, 1976, pp. 1449–1457.

A Prediction Method for Heat Transfer During Film Condensation on Horizontal Low Integral-Fin Tubes

H. Honda
Professor.

S. Nozu
Lecturer.

Department of Mechanical Engineering,
Okayama University,
Okayama 700, Japan

A method for predicting the average heat transfer coefficient is presented for film condensation on horizontal low integral-fin tubes. Approximate equations based on the numerical analysis of surface tension drained condensate flow on the fin surface are developed for the heat transfer coefficients in the upper and lower portions of the flooding point below which the interfin space is flooded with condensate. For the unflooded region, the equation is modified to take account of the effect of gravity. These equations are used, along with the previously derived equation for the flooding point, to determine the wall temperature distribution, and in turn the average heat transfer coefficient. It is shown that the present model can predict the average heat transfer coefficient within ±20 percent for most of the available experimental data including 11 fluids and 22 tubes.

Introduction

Horizontal tubes having low integral fins are commonly used to enhance shellside condensation heat transfer. Beatty and Katz [1] developed a model for predicting the heat transfer coefficient on the low finned tubes, which was based on the Nusselt's equations [2] for a horizontal tube and a vertical surface. Although the Beatty and Katz model has been supported by several experiments [1, 3–5], recent studies [6, 7] have shown that this model tends to substantially overpredict or underpredict the experimental data depending on the condition when the condensate flow is considerably affected by the surface tension.

The surface tension effect on the behavior of condensate is composed of two factors. One is the effect of reducing the condensate film thickness on the fin surface at the upper part of the tube, which leads to enhanced heat transfer. The other is the effect of retaining condensate between the fins at the lower part of the tube, which leads to a decrease in effective surface area. Recently, there have been presented several theoretical models in which one or both of these factors were taken into consideration. Karkhu and Borovkov [8], Borovkov [9], and Rudy [6] applied surface tension drained flow models to the fin surface in the unflooded region, in which a constant radial pressure gradient was assumed. In these models heat transfer in the flooded region was neglected. Owen et al. [10] extended the Beatty and Katz model to include the effect of condensate retension. The proposed equation for the average heat transfer coefficient, however, appears to be based on an incorrect area average of the coefficients for the unflooded and flooded regions. Webb et al. [11] applied Adamek's [12] surface tension drained flow analysis to the fin surface in the unflooded region. They also accounted for heat transfers on the fin root surface and in the flooded region.

An important factor which is ignored in these theoretical models is the nonuniformity of wall temperature. As a result of a large difference in heat transfer coefficients between the unflooded and flooded regions, the wall temperature changes considerably around the tube [6, 7]. This will cause the deviation of heat transfer characteristics from that predicted by the uniform wall temperature model.

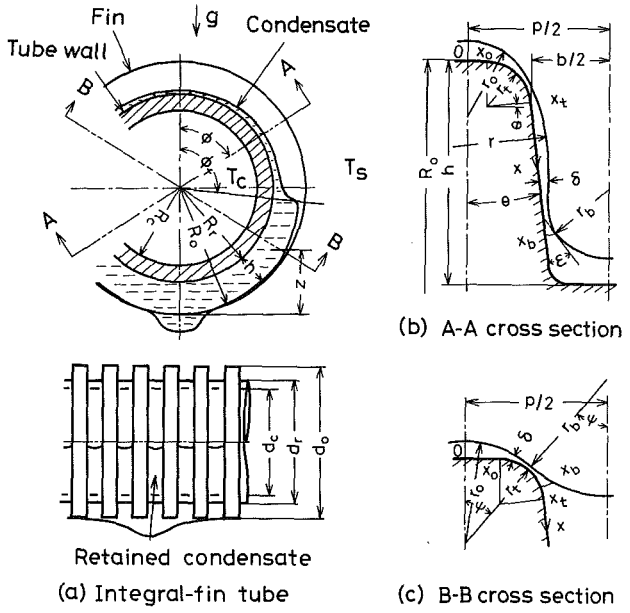

Fig. 1 Physical model and coordinates

The purpose of the present paper is to develop a method for predicting the average heat transfer coefficient on low integral-fin tubes which is applicable to a wide range of conditions. The effect of variable wall temperature is included by treating the problem as that of vapor to coolant heat transfer via tube wall.

Analysis

Physical Model. The physical model and coordinates considered are shown in Fig. 1. A saturated vapor with temperature T_s condenses on a horizontal low integral-fin tube through which a coolant with temperature T_c is flowing. The outer radii of the tube at the tip and root of fins are R_0 and R_r, respectively, and the inner radius R_c. The cross section of a fin is composed of straight portions at the tip and sides, and rounded corners at the tip. The dimensions specify-

Contributed by the Heat Transfer Division and presented at the ASME Winter Annual Meeting, New Orleans, LA, December 9–14, 1984. Manuscript received by the Heat Transfer Division January 14, 1985.

ing the fin geometry are: fin pitch p, fin height h, radius of curvature of the rounded corner r_t, half tip angle θ, and fin spacing at fin tip b. The coordinate x is measured along the fin surface from the center of fin tip, and the angle ϕ from the top of the tube. The connecting points of the straight portions and rounded portion of the fin are denoted by x_0 and x_t.

The angle $\phi = \phi_f$ shown in Fig. 1(a) is the flooding angle below which the interfin space is flooded with condensate. According to [7], ϕ_f is given by

$$\phi_f = \cos^{-1}(2\sigma\cos\theta/\rho_l g b R_0 - 1) \quad \text{for} \quad \sigma\cos\theta/\rho_l g b R_0 < 1 \tag{1}$$

$$\phi_f = 0 \quad \text{for} \quad \sigma\cos\theta/\rho_l g b R_0 \geq 1$$

Equation (1) is based on a static force balance between gravity and surface tension forces acting on the retained condensate. Similar expressions for ϕ_f are derived in [6, 10] based on somewhat different physical models. The unflooded and flooded regions of the tube are termed the u and f regions, respectively.

Figure 1(b) shows a cross section A–A in the u region ($0 < \phi < \phi_f$). The condensate on the fin surface is drained by combined gravity and surface tension forces. Thus, the flow is three dimensional in character. The condensate is pulled into the fin root and is drained circumferentially by gravity. The condensate film is divided into the thin film region $0 \leq x \leq x_b$ and the thick film region at the fin root $x_b < x$. According to the experimental observation [7], however, the condensate film at the fin root is much thinner than the fin height, and has a cricular liquid–vapor interface. The radius of curvature of the interface in the thick film region is denoted by r_b.

Figure 1(c) shows a cross section B–B in the f region ($\phi_f \leq \phi \leq \pi$). Excepting the vicinity of the dripping points of condensate, r_b in this region is given by [7]

$$r_b = \sigma/\rho_l g z = \sigma/\rho_l g R_0(1+\cos\phi) \tag{2}$$

where z is the height of the liquid–vapor interface measured from the tube bottom. Since the condensate film on the fin tip is smoothly connected with the retained condensate, the angle ψ shown in the figure may be approximated as

$$\psi = \sin^{-1}\{(p/2 - x_0)/(r_t + r_b)\} \tag{3}$$

The boundary of the thin film and thick film regions x_b is located near x_t.

Numerical Analysis of Thin Film. Since a complete numerical analysis of complicated condensate flow and heat transfer on the low-finned tube includes difficult problems, the present analysis is limited to the two-dimensional radial flow and heat transfer in the thin film region. The heat transfer in the thick film region is neglected. The numerical results are used afterward to develop approximate expressions for the average Nusselt number for the u and f regions.

The analysis is based on simplifying assumptions as follows: (1) The wall temperature T_w is uniform along the fin; (2) the condensate flow is laminar; (3) the condensate film thickness δ is so small that the inertia term in the momentum equation and the convection term in the energy equation can be neglected; (4) the circumferential flow can be neglected in comparison with the radial one; (5) h is substantially smaller than R_0. Assumption (4) is correct for the surface tension dominated flow. For the combined gravity and surface tension drained flow, however, this assumption is correct only at $\phi \simeq 0$. The effect of radial wall conduction is not incorporated in the numerical analysis. This factor is accounted for separately by introducing the fin efficiency.

The procedure for the formulation of the problem is basically the same as the case of vertical fluted surfaces reported in [13, 14], and will not be repeated here. The equation for the condensate film thickness is written as

$$\frac{1}{3\nu_l}\frac{d}{dx}\left\{\left(\rho_l g f_x - \sigma\frac{da}{dx}\right)\delta^3\right\} = \frac{\lambda_l(T_s - T_w)}{\delta h_{fg}} \tag{4}$$

where f_x is the x component of normalized gravity and $a = 1/r$ is the curvature of the liquid–vapor interface, which are respectively given by

$$\begin{aligned} f_x &= 0 && \text{for } 0 \leq x \leq x_0 \\ f_x &= \cos\phi\,\sin\{(x - x_0)/r_t\} && \text{for } x_0 \leq x \leq x_t \\ f_x &= \cos\phi\,\cos\theta && \text{for } x_t \leq x \end{aligned} \tag{5}$$

Nomenclature

A = average thickness of finned tube
a = curvature of liquid–vapor interface
b = fin spacing at fin tip
d = tube diameter
f_x = x component of normalized gravity
G = $\rho_l g h_{fg} p^3/\lambda_l \nu_l (T_s - T_w)$
G_d = $\rho_l g h_{fg} d_0^3/\lambda_l \nu_l \eta_u (T_s - T_{wu})$
g = gravitational acceleration
h = fin height
h_{fg} = specific enthalpy of evaporation
m_i = dimensionless quantity, equation (40)
Nu_c = coolant Nusselt number
Nu_d = average Nusselt number of finned tube = $\alpha_m d_0/\lambda_l$
Nu_i = average Nusselt number for region i
Nu_p = average Nusselt number of finned surface, equation (11)
Nu_x = local Nusselt number = $\alpha_x p/\lambda_l$
p = fin pitch
Q_i = dimensionless heat transfer rate in region i
q_0 = average heat flux based on nominal surface area
R = tube radius
r = radius of curvature of liquid–vapor interface
r_t = radius of curvature at corner of fin tip
S = $\sigma h_{fg} p/\lambda_l \nu_l (T_s - T_w)$
T = temperature
$\bar{T}$ = dimensionless temperature = $(T - T_c)/(T_s - T_c)$
t_m = average thickness of fin
x = coordinate measured along fin, Fig. 1
x_0, x_t = coordinates at connecting points between straight and round portions of fin, Fig. 1
x_i = coordinate at boundary of successive small regions
z = height of liquid–vapor interface, Fig. 1
α_x = local heat transfer coefficient
α_m = average heat transfer coefficient of finned tube = $q_{0m}/(T_s - T_{wm})$
δ = condensate film thickness
ϵ = angle, Fig. 1
η = fin efficiency
θ = half tip angle of fin
λ = thermal conductivity
ν = kinematic viscosity
ρ = density
σ = surface tension
τ = dimensionless time
ϕ = angular coordinate, Fig. 1
$\bar{\phi}$ = dimensionless angle = ϕ/π
ψ = angle, Fig. 1

Subscripts and Superscripts

b = boundary of thin and thick film regions
c = coolant; also inner surface of tube
f = flooding point; also flooded region
l = liquid
m = average value
0 = tip of fin
r = root of fin
s = saturation
u = unflooded region
w = tube wall
$\bar{}$ = normalized by p

Table 1 Conditions for numerical calculation

Symbol	$\bar{x}_o$	$\bar{r}_t$	$\bar{b}$	$\bar{x}_b$	θ	ϕ	S	G/S
⊕ ○ ●	0.05	0.10	0.7	0.2	0	0	10^6	0
⧋ △ ▲	0.12	0.03	0.7	≀			10^7	
▽	0.14	0.01	0.7	2				1
⧈ □ ■	0.03	0.03	0.88				10^8	

$$a = -(d^2\delta/dx^2)/\{1+(d\delta/dx)^2\}^{3/2} \quad \text{for } 0 \le x \le x_0 \text{ and } x_t \le x \tag{6}$$

$$a = \{1/r_t + (2/r_t^2 + \delta/r_t^3)\delta + 2(d\delta/dx)^2/r_t - (1+\delta/r_t)(d^2\delta/dx^2)\}$$
$$/\{(1+\delta/r_t)^2 + (d\delta/dx)^2\}^{3/2} \quad \text{for } x_0 \le x \le x_t$$

The boundary conditions are

$$d\delta/dx = d^3\delta/dx^3 = 0 \qquad \text{at } x = 0 \tag{7}$$

$$d\delta/dx = \tan\epsilon, \; r = -r_b \quad \text{at } x = x_b \tag{8}$$

where ϵ is the angle shown in Fig. 1(*b*). Equation (8) is the necessary condition for smooth connection of the thin and thick film regions.

The solution of equation (4) is obtained numerically as the steady-state solution of an unsteady condensate flow subject to an arbitrary initial distribution of δ. Adding the unsteady term to the left-hand side of equation (4) and introducing dimensionless variables into the resulting equation yield

$$\frac{G}{3}\frac{\partial}{\partial\bar{x}}(\bar{\delta}^3 f_x) - \frac{S}{3}\frac{\partial}{\partial\bar{x}}\left(\bar{\delta}^3\frac{d\bar{a}}{d\bar{x}}\right) + \frac{\partial\bar{\delta}}{\partial\tau} = \frac{1}{\bar{\delta}} \tag{9}$$

where $G = \rho_l g h_{fg} p^3/\lambda_l \nu_l (T_s - T_w)$, $S = \sigma h_{fg} p/\lambda_l \nu_l (T_s - T_w)$, and τ is the dimensionless time. The dimensionless parameters G and S stand for the effects of gravity and surface tension, respectively.

Equation (9) was solved using an implicit finite difference scheme. Three different grid sizes with finer grids at the tip and corner and a coarser grid at the side were chosen along $\bar{x}$, with a total of 51 to 101 grid points. The value of ϵ was assumed as $\pi/6$ to $\pi/4$. The calculation was continued until the convergence criterion $|1-\bar{\delta}_i^*/\bar{\delta}_i|/\Delta\tau < 1$ was satisfied, where $\bar{\delta}_i^*$ and $\bar{\delta}_i$ are the old and new values of $\bar{\delta}_i$ at grid point, i, and $\Delta\tau$ is the time step. The solution differs from that corresponding to the convergence criterion $|1-\bar{\delta}_i^*/\bar{\delta}_i|/\Delta\tau < 10$ by a maximum of 0.1 percent.

To study the effects of fin geometry and the parameters G and S, the calculations were made for a set of conditions listed in Table 1, where $G/S = 0$ represents the case where the effect of gravity can be neglected, and $G/S = 1$ the case where the effects of gravity and surface tension are comparable. It should be mentioned that the condition of $\phi = 0$ has no significance for $G/S = 0$. In the limiting case of $S = 0$, the problem is reduced to the gravity drained condensation and the solution is obtained analytically.

The local Nusselt number Nu_x and the average Nusselt number based on the projected area of finned surface Nu_p are respectively defined as

$$\mathrm{Nu}_x = \alpha_x p/\lambda_l = 1/\bar{\delta} \tag{10}$$

$$\mathrm{Nu}_p = 2\int_0^{x_b}\alpha_x dx/\lambda_l = 2\int_0^{\bar{x}_b}(1/\bar{\delta})d\bar{x} \tag{11}$$

Figure 2 shows the distributions of Nu_x and $\bar{a}$ along $\bar{x}$ for three values of $\bar{x}_b$. The solid and dotted lines show the cases of $G/S = 0$ and 1, respectively. The values of Nu_p are also shown in the figure. A comparison of (*a*), (*b*), and (*c*) reveals that the distributions of Nu_x and $\bar{a}$ are strongly dependent on the length of the fin side $(\bar{x}_b - \bar{x}_t)$. In the cases of (*a*) and (*b*) with relatively large $(\bar{x}_b - \bar{x}_t)$, Nu_x has two extrema at the corner of the fin tip and at a point close to $\bar{x} = \bar{x}_b$. Correspondingly, $\bar{a}$ changes in two steps across these points. In the case of (*c*) with relatively small $(\bar{x}_b - \bar{x}_t)$, on the other hand, Nu_x has a maximum at the corner of fin tip, and $\bar{a}$ changes in one step across this point. Comparison of the results for $G/S = 0$ and 1 shows that the difference between the two cases is smaller for smaller $\bar{x}_b$. This trend is related to the increase in the gradient of curvature $|d\bar{a}/d\bar{x}|$ at the fin side with the decrease of $\bar{x}_b$. The width of the high Nu_x region at the corner of fin tip decreases as the fin tip radius $\bar{r}_t$ decreases, with the peak value of Nu_x becoming higher. Thus the present analysis should be applied with reserve for $\bar{r}_t \to 0$.

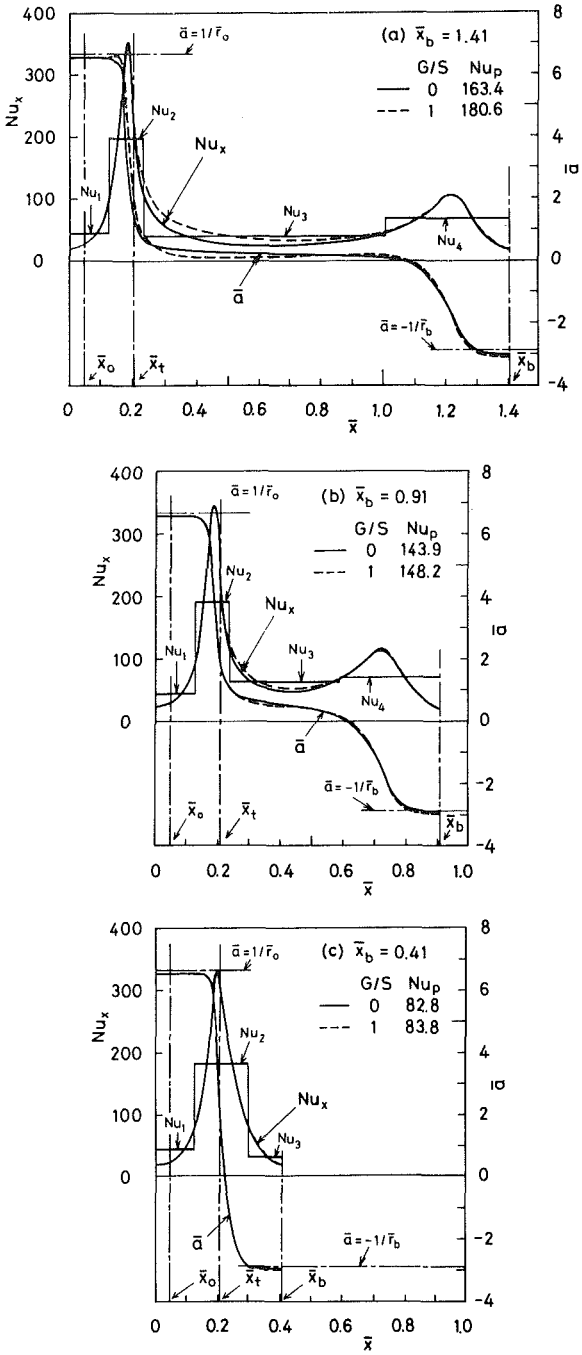

Fig. 2 Distributions of Nu_x and $\bar{a}$ along $\bar{x}$: $S = 10^7$, $\bar{x}_0 = 0.05$, $\bar{r}_t = 0.1$, $\bar{b} = 0.7$, $\phi = 0$, $\theta = 0$, $\epsilon = \pi/6$

Figure 3 shows the variations of Nu_p with $\bar{x}_b$ for four fin shapes listed in Table 1. The Nu_p value first increases rapidly with the increase of $\bar{x}_b$, but the increase is decelerated at $1 <$

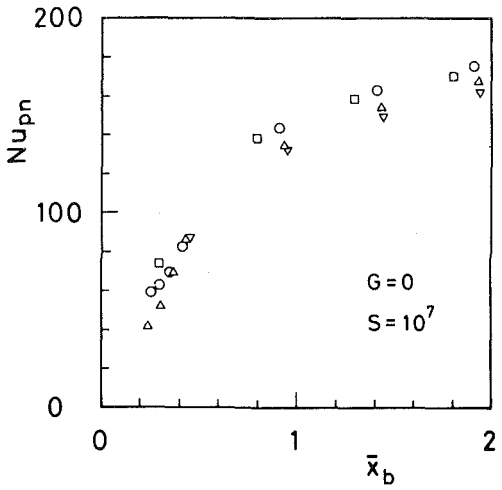

Fig. 3 Variation of Nu_p with $\bar{x}_b$

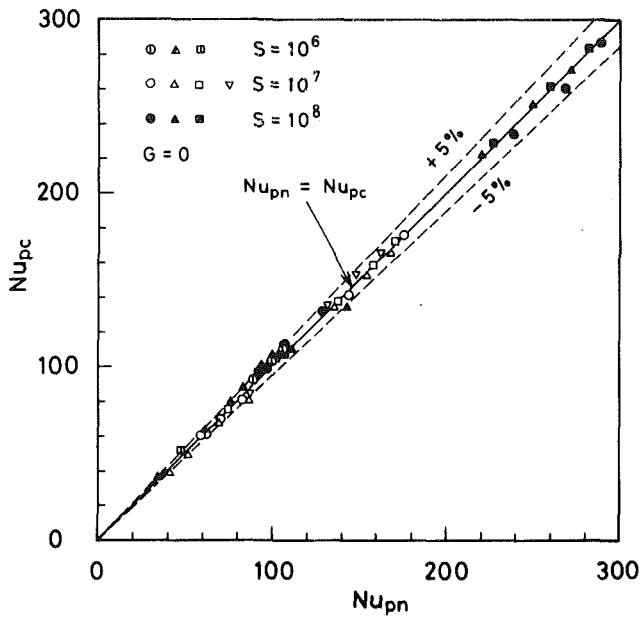

Fig. 4 Comparison of Nu_{pn} and Nu_{pc}

$\bar{x}_b$. Comparison of fins with the same value of $\bar{b}$ (depicted by ○, △, and ▽) shows that Nu_p is greater for a fin with larger $\bar{r}_t$. Also, comparison of fins with the same value of $\bar{r}_t$ (depicted by △ and □) shows that Nu_p is greater for a fin with larger $\bar{b}$ (thinner fin). However, the difference in Nu_p value is less than 11 percent for the range of $\bar{x}_b$ of practical interest ($0.8 \lesssim \bar{x}_b$).

It is relevant to discuss the relation among the Nu_p values for $G/S = 1$, $G = 0$, and $S = 0$. The Nu_p value for $S = 0$ was approximated by the Nusselt equation for a vertical surface. It was found after some trials that these values were correlated within 5 percent by the following equation.

$$(Nu_p)_{G/S=1} = \{(Nu_p)^3_{G=0} + (Nu_p)^3_{S=0}\}^{1/3} \tag{12}$$

Equation (12) may also be applicable to high values of G/S since the combined gravity and surface tension drained flow solutoin approaches the gravity drained flow solution at $S \to 0$.

Approximate Expressions for Nu_p. Approximate expressions for Nu_p for the surface tension drained flow ($G = 0$) are derived based on the numerical results. Taking account of the fact that $\bar{a}$ changes in steps along $\bar{x}$, the arc length $0 \le \bar{x} \le \bar{x}_b$ is divided into two to four regions depending on $\bar{x}_b$, and simple analytical models are introduced.

Four Region Model. In the case of relatively large ($\bar{x}_b - \bar{x}_t$), where $\bar{a}$ changes in two steps along $\bar{x}$, the fin surface is divided into four regions: fin tip, the corner of fin tip, and the upper and lower regions of fin side. The coordinates at the boundaries of neighboring regions $\bar{x}_1$, $\bar{x}_2$, and $\bar{x}_3$, and the regional curvature changes of the condensate film Δa_1, Δa_2, Δa_3, and Δa_4 are defined as follows:

$$\bar{x}_1 = (\bar{x}_0 + \bar{x}_t)/2, \quad \bar{x}_2 = \bar{x}_t + 0.03, \quad \bar{x}_3 = \bar{x}_b - 0.9\bar{r}_b$$
$$\Delta a_1 = 0, \quad \Delta a_2 = 1/\bar{r}_0 - 15/(\Delta x_3^{0.5} S^{0.2}) \tag{13}$$
$$\Delta a_3 = 15/(\Delta x_3^{0.5} S^{0.2}), \quad \Delta a_4 = 1/\bar{r}_b$$

where $\Delta x_3 = \bar{x}_3 - \bar{x}_2$. The value of $\bar{r}_0$ is approximated by the radius of circumcircle at the fin tip, and $\bar{r}_b$ by the radius of inscribed circle between fins which touches the fin side at $\bar{x} = \bar{x}_b - 0.3\bar{r}_b$ as

$$\bar{r}_0 = \bar{r}_t + \bar{x}_0/\cos\theta, \quad \bar{r}_b = \{\bar{b}/2 - (\bar{x}_b - \bar{x}_t)\sin\theta\}/(\cos\theta - 0.3\sin\theta)$$

The values of $\bar{a} = 1/\bar{r}_0$ and $\bar{a} = -1/\bar{r}_b$ are shown by horizontal chain lines in Fig. 2. These values are seen to agree closely with the numerical solutions at $\bar{x} \simeq 0$ and $\bar{x}_b$, respectively.

The regional average Nusselt numbers Nu_1, Nu_2, Nu_3, and Nu_4 are respectively given by the following equations

$$Nu_1 = 2.4/\{\bar{x}_0(1-\sin\theta)/\cos\theta + 0.045\bar{r}_t\}$$
$$Nu_2 = \frac{1.14S^{0.23}\Delta a_2^{0.25}}{\Delta x_2^{0.5}(1+2Q_1/Q_2)^{0.25}}$$
$$Nu_3 = \frac{0.90S^{0.25}\Delta a_3^{0.25}}{\Delta x_3^{0.5}\{1+2(Q_1+Q_2)/Q_3\}^{0.25}} \tag{14}$$
$$Nu_4 = \frac{1.14S^{0.23}\Delta a_4^{0.25}}{\Delta x_4^{0.5}\{1+2(Q_1+Q_2+Q_3)/Q_4\}^{0.25}}$$

where $\Delta x_2 = \bar{x}_2 - \bar{x}_1$, $\Delta x_4 = \bar{x}_b - \bar{x}_3$ and Q_i is the dimensionless heat transfer rate in region i (= 1–4) defined as

$$Q_i = Nu_i \Delta x_i, \quad \Delta x_1 = \bar{x}_1 \tag{15}$$

The expression for Nu_1 is based on the numerical result that the condensate film in region 1 has a circular profile, and is designed to be also valid for the case of $\bar{x}_0 = 0$ presented in [13]. The expressions for Nu_2, Nu_3, and Nu_4 are based on the approximate analytical solution of equation (9) for $G = 0$ and $d\bar{\delta}/d\tau = 0$ assuming a regionally constant $\bar{\delta}$ value along $\bar{x}$. The matching condition of the solutions for the neighboring regions is given by the continuity of condensate flow rate. Small modifications are made for Nu_2 and Nu_4 to provide a better agreement with the numerical results. The value of Q_1 is readily obtained from equations (14) and (15). Those of Q_2, Q_3, and Q_4 are obtained by iteratively solving these equations.

Finally, Nu_p is given by

$$Nu_p = 2(Q_1 + Q_2 + Q_3 + Q_4) \tag{16}$$

Equation (16) is applied to the case where the following condition holds

$$\Delta a_2/\Delta x_2 \ge \Delta a_3/\Delta x_3 \tag{17}$$

Three Region Model. In the case of relatively small ($\bar{x}_b - \bar{x}_t$) where $\bar{a}$ changes in one step along $\bar{x}$, the surface is divided into three regions: fin tip, the corner of fin tip, and fin side. The new definitions of $\bar{x}_2$, Δx_3, Δa_2, and Δa_3 are given by

$$\bar{x}_2 = \max(\bar{x}_b - 0.3\bar{r}_b, \bar{x}_t), \quad \Delta x_3 = \bar{x}_b - \bar{x}_2$$
$$\Delta a_2 = 1/\bar{r}_0 + 0.98/\bar{r}_b, \quad \Delta a_3 = 0.02/\bar{r}_b \tag{18}$$

The expressions for Nu_1 and Nu_2 are given by equation (14). Those for Nu_3 and Nu_p are respectively given by

$$Nu_3 = \frac{1.14S^{0.23}\Delta a_3^{0.25}}{\Delta x_3^{0.5}\{1+2(Q_1+Q_2)/Q_3\}^{0.25}} \tag{19}$$

$$Nu_p = 2(Q_1+Q_2+Q_3) \tag{20}$$

Equation (20) is applied to the case where inequality (17) does not hold and $\bar{x}_b - 0.3\,\bar{r}_b > \bar{x}_t$.

Two Region Model. This model is applied to the f region. The average Nusselt number for this region is approximated by the value of Nu_p at the average height $\bar{z}_m$ defined as

$$\bar{z}_m = \int_{\phi_f}^{\pi} \bar{R}_0(1+\cos\phi)d\phi/(\pi-\phi_f) = \bar{R}_0\{1-\sin\phi_f/(\pi-\phi_f)\} \tag{21}$$

The vales of Δx_1, Δx_2, Δa_1, and Δa_2 are respectively defined as

$$\Delta x_1 = 0.8\bar{x}_0, \qquad \Delta x_2 = 0.2\bar{x}_0 + (\psi_m + \pi/16)\bar{r}_t$$
$$\Delta a_1 = 10^{-3}/\bar{r}_{0m}, \qquad \Delta a_2 = 0.999/\bar{r}_{0m} + 1/\bar{r}_{bm} \tag{22}$$

where $\bar{r}_{bm} = \bar{r}_b(\bar{z}_m)$ and $\psi_m = \psi(\bar{z}_m)$ are given by equations (2) and (3), respectively, and $\bar{r}_{0m} = \bar{x}_0(\bar{r}_t + \bar{r}_{bm})/(0.5 - \bar{x}_0) + \bar{r}_t$.

The expression for Nu_2 is given by equation (14). Those for Nu_1 and Nu_p are respectively given by

$$Nu_1 = 0.90S^{0.25}\Delta a_1^{0.25}/\Delta x_1^{0.5} \tag{23}$$

$$Nu_p = 2(Q_1+Q_2) \tag{24}$$

The values of Nu_1, Nu_2, Nu_3, and Nu_4 obtained from the four and three region models are also shown in Fig. 2. These values are seen to provide good approximations for the regional average values of Nu_x. Figure 4 shows the comparison of Nu_p between that calculated from equation (16) or (20) Nu_{pc} and the numerical solution Nu_{pn}. The agreement between the two is within ±5 percent.

Application to Finned Tubes. The average heat transfer coefficient α_m and the average Nusselt number Nu_d for a finned tube are defined as

$$\alpha_m = q_{0m}/(T_s - T_{wm}), \quad Nu_d = \alpha_m d_0/\lambda_l \tag{25}$$

where $q_{0m} = \int_0^{\pi} q_0 d\phi/\pi$, $T_{wm} = \int_0^{\pi} T_w d\phi/\pi$, q_0 is the heat flux based on the nominal surface area (surface area of a smooth tube having outer diameter d_0), and T_w the wall temperature at the fin root.

The average Nusselt number can be written in terms of relevant parameters for the u and f regions as

$$Nu_d = \{Nu_{du}\eta_u(1-\tilde{T}_{wu})\tilde{\phi}_f + Nu_{df}\eta_f(1-\tilde{T}_{wf})(1-\tilde{\phi}_f)\} / \{(1-\tilde{T}_{wu})\tilde{\phi}_f + (1-\tilde{T}_{wf})(1-\tilde{\phi}_f)\} \tag{26}$$

where Nu_{du} and Nu_{df} are the Nusselt numbers based on the average condensation temperature differences, η_u and η_f the fin efficiencies, $\tilde{T}_{wu}$ and $\tilde{T}_{wf}$ the dimensionless average wall temperatures at the fin root, and $\tilde{\phi}_f = \phi_f/\pi$.

It is assumed that Nu_{du} can be expressed in terms of limiting values for surface tension drained condensation $(Nu_{du})_s$ and gravity drained condensation $(Nu_{du})_g$ as

$$Nu_{du} = \{(Nu_{du})_s^3 + (Nu_{du})_g^3\}^{1/3} \tag{27}$$

The functional form of equation (27) is based on the analogy of equation (12) which holds within 5 percent among the solutions of Nu_p for $G/S = 1$, $G = 0$, and $S = 0$. $(Nu_{du})_s$ is related to Nu_{pu} (given by equation (16) or (20)) by the following equation

$$(Nu_{du})_s = Nu_{pu}(\bar{d}_0 + \bar{d}_r)/2 \tag{28}$$

The expression for $(Nu_{du})_g$ is assumed with reference to the Beatty and Katz model as

$$(Nu_{du})_g = 0.725G_d^{1/4}\{1.3f_l(d_0/h_e)^{1/4} + f_0 + f_r(d_0/d_r)^{1/4}/\eta_u\} \tag{29}$$

where $G_d = \rho_l g h_{fg} d_0^3/\lambda_l \nu_l \eta_u (T_s - T_{wu})$, $h_e = \pi(d_0^2 - d_r^2)/4d_0$ and f_1, f_0, and f_r are the ratios of surface areas at the side, tip, and root of fins to the nominal surface area. The value of $\bar{x}_b$ required to calculate Nu_{pu} is assumed as

$$\bar{x}_b = \bar{x}_r + 0.3\bar{r}_b \tag{30}$$

where $\bar{x}_r$ is the contact point on the fin side of the inscribed circle which is also in contact with the root surface. Since $\bar{x}_r \geq \bar{x}_t$, the applicability of the present model is limited by the following condition:

$$h/(1-\sin\theta) \geq r_t + b/(2\cos\theta) \tag{31}$$

For the f region, the effect of gravity is neglected and Nu_{df} is related to Nu_{pf} (given by equation (24)) by the following equation

$$Nu_{df} = Nu_{pf}\bar{d}_0 \tag{32}$$

The value of η_u is approximated by an analytical solution for a circular fin [15] with rectangular cross section of $(h + t_m/2) \times t_m$, where t_m is the average thickness of the real fin. That of η_f is obtained from the solution of radial conduction as

$$\eta_f = \left\{1 + \frac{\lambda_l}{2\lambda_w}\frac{Nu_{df}}{\bar{t}_m}\ln\left(\frac{d_0}{d_r}\right)\right\}^{-1} \tag{33}$$

The values of $\tilde{T}_{wu}$ and $\tilde{T}_{wf}$ are determined by solving the equation for circumferential wall conduction. Assuming constant heat transfer coefficients for the inner surface and for the u and f regions on the outer surface, and neglecting the interaction with radial conduction, the basic equation is written as

$$\eta_i Nu_{di}\frac{\lambda_l}{\lambda_w} - \left[\eta_i Nu_{di}\frac{\lambda_l}{\lambda_w} + \left\{\frac{1}{2}\ln\left(\frac{d_r}{d_c}\right) + \frac{1}{Nu_c}\frac{\lambda_w}{\lambda_c}\right\}^{-1}\right]\tilde{T}_w = -\frac{4A}{\pi^2 d_r}\frac{d^2\tilde{T}_w}{d\tilde{\phi}^2} \tag{34}$$

where Nu_c is the coolant Nusselt number and A the average tube thickness. The boundary and compatibility conditions are

$$d\tilde{T}_w/d\tilde{\phi} = 0 \quad \text{at} \quad \tilde{\phi} = 0 \quad \text{and} \quad 1 \tag{35}$$

$$(\tilde{T}_w)_u = (\tilde{T}_w)_f \quad \text{and} \quad (d\tilde{T}_w/d\tilde{\phi})_u = (d\tilde{T}_w/d\tilde{\phi})_f \quad \text{at} \quad \tilde{\phi} = \tilde{\phi}_f \tag{36}$$

Table 2 Summary of experimental data used for comparison with theoretical predictions

Tube	Tube arrangement	Fluid	S x 10^{-7}	G/S	Reference
1-3	Single tube	Methyl chloride Sulfer dioxide R22, n-pentane Propane, n-butane	0.47- 1.8	1.2 -22	Beatty-Katz [1]
4	Top of six tubes in a vertical row	R22, n-butane Acetone, Water	0.32- 1.2	0.42- 5.9	Katz-Geist [3]
5,6	Bundle of 60 tubes	R22	5.1 - 7.5	1.7 - 3.3	Pearson-Withers [4]
7,8	Two tubes in a vertical row	R22	3.7 -10	1.5 - 2.8	Takahashi et al. [5]
9-11	Single tube	R11	1.9 -16	0.34- 0.77	Carnavos [16]
12-15	Single tube	R11	0.87- 5.7	0.47- 1.6	Rudy [6]
16-18	Single tube	R113 Methanol	0.24- 6.1 0.85-13	0.27- 1.0 0.10- 0.38	Honda et al. [7]
19-22	Single tube	Water	3.1 -13	0.15- 0.94	Yau et al. [17]

Table 3 Dimensions of test tubes

Tube	d_o	d_c	p	h	t_m	r_t	θ
	mm	mm	mm	mm	mm	mm	deg
1	18.80	13.42	1.65	1.46	0.46	0.033*	5.0
2	19.00	13.79	1.75	1.60	0.47*	0.033*	5.0*
3	26.42	17.30	3.71	3.45	0.84	0.074*	1.7
4	18.95	13.97	1.69	1.58	0.51	0.11*	6.1
5	18.67	14.15	0.97	1.42	0.31	0.018*	5.0*
6	18.67	14.15	1.33	1.42	0.31	0.019*	5.0*
7	18.98	14.58	0.98	1.39	0.34	0.044	4.8
8	19.08	14.48	1.34	1.52	0.39	0.088	3.3
9	19.0	15.4	0.62	0.91	0.25	0.017*	5.0*
10	19.2	15.8	0.82	0.79	0.25	0.019*	5.0*
11	18.8	14.4	0.94	1.32	0.36	0.024*	5.0*
12	18.7	---	0.73	0.89	0.25	0.054	4.8
13	18.7	---	0.98	1.53	0.35	0.10	6.5
14	18.7	---	1.34	1.53	0.32	0.040	5.0
15	17.7	---	1.34	0.85	0.45	0.021	9.0
16	19.35	14.20	0.50	1.13	0.11	0.043	0.0
17	18.89	15.48	0.64	0.92	0.29	0.048	5.3
18	18.69	14.10	0.98	1.46	0.39	0.043	4.5
19	15.9	9.78	1.0	1.59	0.5	0.0	0.0
20	15.9	9.78	1.5	1.59	0.5	0.0	0.0
21	15.9	9.78	2.0	1.59	0.5	0.0	0.0
22	15.9	9.78	2.5	1.59	0.5	0.0	0.0

* Estimated value

The solution of equation (34) is obtained analytically. The average values of dimensionless vapor to fin root temperature differences for the u and f regions are respectively written as

$$(1-\tilde{T}_{wu}) = (1-\tilde{T}_{wu0}) + \frac{(\tilde{T}_{wu0}-\tilde{T}_{wf0})}{m_u\tilde{\phi}_f}\left[\coth(m_u\tilde{\phi}_f) + \frac{m_u}{m_f}\coth\{m_f(1-\tilde{\phi}_f)\}\right]^{-1} \quad (37)$$

$$(1-\tilde{T}_{wf}) = (1-\tilde{T}_{wf0}) - \frac{(\tilde{T}_{wu0}-\tilde{T}_{wf0})}{m_f(1-\tilde{\phi}_f)}\left[\coth\{m_f(1-\tilde{\phi}_f)\} + \frac{m_f}{m_u}\coth(m_u\tilde{\phi}_f)\right]^{-1} \quad (38)$$

where

$$(1-\tilde{T}_{wi0}) = \left[1+\eta_i \mathrm{Nu}_{di}\left\{\frac{\lambda_l}{2\lambda_w}\ln\left(\frac{d_r}{d_c}\right)+\frac{1}{\mathrm{Nu}_c}\frac{\lambda_w}{\lambda_c}\right\}\right]^{-1} \quad (i=u,f) \quad (39)$$

$$m_i = \frac{\pi}{2}\left[\left[\frac{d_r}{A}\left[\eta_i \mathrm{Nu}_{di}\frac{\lambda_l}{\lambda_w} + \left\{\frac{1}{2}\ln\left(\frac{d_r}{d_c}\right)+\frac{1}{\mathrm{Nu}_c}\frac{\lambda_w}{\lambda_c}\right\}^{-1}\right]\right]\right]^{1/2} \quad (i=u,f) \quad (40)$$

Since η_i and Nu_{di} in equations (39) and (40) are functions of $(1-\tilde{T}_{wi})$, iterative calculation is required to obtain the solutions. The solution procedure is started with an appropriate guess of $\tilde{T}_{wi}$ and the assumption of $\eta_i = 1$. Then Nu_{di} and η_i are obtained from the defining equations. Substitution of these values into equations (37) and (38) yields a new $\tilde{T}_{wi}$. The calculation is repeated several times until converged solutions are obtained.

Numerical results showed that the effect of circumferential wall conduction is significant for copper tube but may be neglected for other tube materials. For the latter case, equations (37) and (38) are simplified as

$$\tilde{T}_{wi} = \tilde{T}_{wi0} \quad (i=u,f) \quad (41)$$

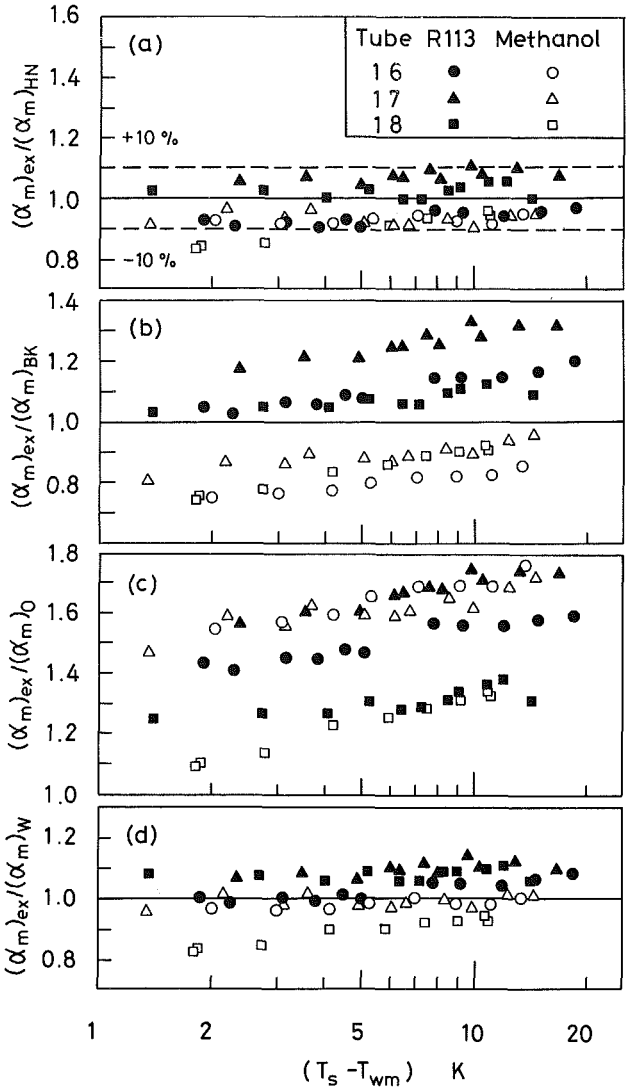

Fig. 5 Comparison of measured and predicted average heat transfer coefficients

Comparison With Experiments and Discussion

The predictions of the present model and those of previously proposed models are compared with available experimental data. A summary of experimental data to be compared is shown in Table 2, and the dimensions of test tubes in Table 3. Some of the fin dimensions depicted with asterisk, which could not be obtained from the literature, were estimated from the other cases. The value of G/S for these data ranges from 0.10 (surface tension controlled condensation) to 22 (gravity controlled condensation).

Among the data sources listed in Table 2, the procedure used for data reduction is not always consistent with each other. Beatty and Katz [1] and Katz and Geist [3] used the Wilson plot method to determine the combined tube wall and film resistance, and subtracted the wall resistance from the result. Pearson and Withers [4] and Takahashi et al. [5] used the modified Wilson plot method, in which the functional form of the Beatty and Katz equation was assumed for α_m. Carnavos [16] estimated α_m from the overall coefficient

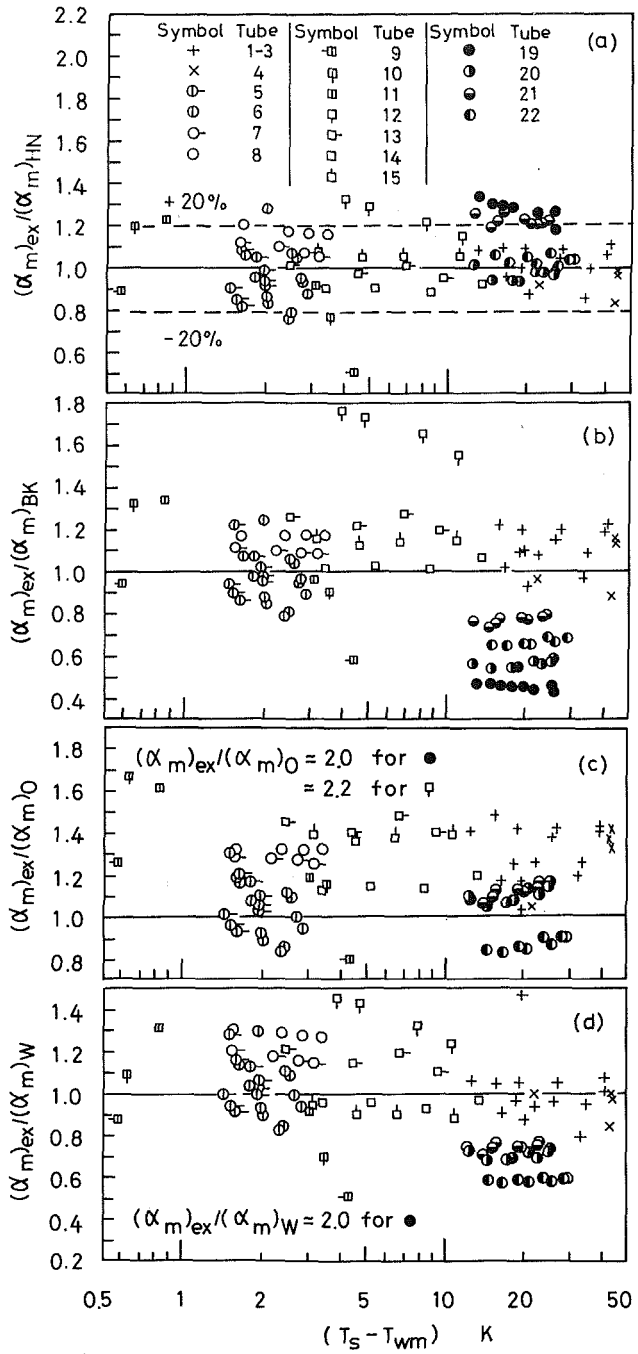

Fig. 6 Comparison of measured and predicted average heat transfer coefficients

assuming a fully developed forced convection correlation for the inner surface. Yau et al. [17] used an experimentally determined correlation of Nu_c for calculating α_m from the overall results. Rudy [6] and Honda et al. [7] measured the local wall temperatures and used the area average value for calculating α_m.

Experimental data for tube bundles (tubes 5 to 8) are also used for comparison since the number of vertical tube rows of these tube bundles is small (≤ 4). The present model must be modified for the effects of condensate inundation and vapor velocity when applying it to large tube bundles.

Figure 5 shows the comparisons of the measured values $(\alpha_m)_{ex}$ of Honda et al. with the predictions of the present model $(\alpha_m)_{HN}$, the Beatty and Katz model $(\alpha_m)_{BK}$, the Owen et al. model $(\alpha_m)_O$, and the Webb et al. model $(\alpha_m)_W$. In this figure the ratio of the measured to predicted values is plotted as a function of the average condensation temperature difference. The present model can predict most of the measured values within ±10 percent. It is mentioned here that the predicted wall temperature distributions are also in good agreement with the measurements. The Beatty and Katz model tends to underpredict the R-113 data, and overpredict the methanol data. The Owen et al. model gives considerably lower predictions for both the R-113 and methanol data for tubes 16 and 17. The Webb et al. model gives satisfactory predictions although there is a trend to overpredict the methanol data at small $(T_s - T_{wm})$. Figure 6 shows similar comparisons for the other data listed in Table 2. The present model underpredicts the water data for tubes 19 and 21, and a part of R-11 data for tube 12 by about 25 percent, but can predict most of the other data within ±20 percent. The Beatty and Katz model considerably underpredicts the R-11 data for tube 12, and considerably overpredicts the water data for tubes 19 and 22. The Owen et al. model considerably underpredicts the R-11 data for tube 12 and the water data for tube 19. The Webb et al. model predicts satisfactorily most of the measured values except for the water data for tubes 19 and 22.

Concluding Remarks

A new prediction method for the condensation heat transfer coefficient on horizontal low integral-fin tubes has been developed. The method is based on an approximate analytical solution of the vapor to coolant heat transfer problem.

Numerical results for laminar film condensation on the finned surface show that the surface tension induced pressure changes in a stepwise manner along the surface. This characteristic allows us to develop sufficiently accurate expressions for the heat transfer coefficients in the unflooded and flooded regions of the tube.

For given conditions of vapor, tube and coolant, the flooding angle is obtained from equation (1). The heat transfer coefficients, the fin efficiencies, and the average wall temperatures in the unflooded and flooded regions are determined by simultaneously solving equations (27), (32), (33), (37), (38), and one more equation for the fin efficiency in the unflooded region. Then, the average heat transfer coefficient for the tube is obtained by substituting these values into equation (26).

It was found that the present model can predict most of the available experimental data including 11 fluids and 22 tubes within ±20 percent.

Acknowledgments

We wish to thank Prof. J. W. Rose and Dr. T. M. Rudy for informing us of the details of their experimental data.

References

1 Beatty, K. O., and Katz, D. L., "Condensation of Vapors on Outside of Finned Tubes," *Chemical Engineering Progress*, Vol. 44, 1948, pp. 55–70.

2 Nusselt, W., "Die Oberflächenkondensation des Wasserdampfes," *Zeit. Ver. Deut. Ing.*, Vol. 60, 1916, pp. 541–546, 567–575.

3 Katz, D. L., and Geist, J. M., "Condensation of Six Finned Tubes in a Vertical Row," *Trans. ASME*, Vol. 70, 1948, pp. 907–914.

4 Pearson, J. F., and Withers, J. G., "New Finned Tube Configuration Improves Refrigerant Condensing," *ASHRAE Journal*, Vol. 11, 1969, pp. 77–82.

5 Takahashi, A., Nosetani, T., and Miyata, K., "Heat Transfer Performance of Enhanced Low Finned Tubes With Spirally Integral Inside Fins," *Sumitomo Light Metal Technical Reports*, Vol. 20, 1979, pp. 59–65.

6 Rudy, T. M., "A Theoretical and Experimental Study of Condensation on Single, Integral-Fin Tubes," Ph.D. Thesis, Pennsylvania State University, 1982.

7 Honda, H., Nozu, S., and Mitsumori, K., "Augmentation of Condensation on Horizontal Finned Tubes by Attaching a Porous Drainage Plate," *Proc. ASME-JSME Thermal Engineering Joint Conference*, Vol. 3, 1983, pp. 289–295.

8 Karkhu, V. A., and Borovkov, V. P., "Film Condensation of Vapors at

Finely Finned Horizontal Tubes," *Heat Transfer–Soviet Research*, Vol. 3, 1971, pp. 183–191.

9 Borovkov, V. P., "Refined Method of Calculating Heat Exchange in the Condensation of Stationary Vapor on Horizontal Finned Tubes," *Inzhenerno-Fizicheskii Zhurnal*, Vol. 39, 1980, pp. 597–602.

10 Owen, R. G., Sardesai, R. G., Smith, R. A., and Lee, W. C., "Gravity Controlled Condensation on Horizontal Integral Fin Tubes," *Condensers: Theory and Practice*, Inst. Chem. Engrs. Symp. Ser., No. 75, 1983, pp. 415–428.

11 Webb, R. L., Rudy, T. M., and Kedzierski, M. A., "Prediction of Condensation Coefficient on Horizontal Integral-Fin Tubes," ASME JOURNAL OF HEAT TRANSFER, Vol. 107, 1985, pp. 255–270.

12 Adamek, T., "Bestimmung der Kondensationgrössen auf feingewellten Oberflächen zur Auslegung optimaler Wandprofile," *Wärme- und Stoffübertragung*, Vol. 15, 1981, pp. 255–270.

13 Honda, H., and Fujii, T., "Laminar Filmwise Condensation on Vertical Grooved Surfaces," *Reports of Research Institute of Industrial Science, Kyushu* University, No. 62, 1975, pp. 99–109; also *Trans. JSME*, Vol. 44, 1978, pp. 2411–2419.

14 Mori, Y., Hijikata, K., Hirasawa, S., and Nakayama, W., "Effect of Surface Tension on Condensate Motion in Laminar Film Condensation (Study of Liquid Film in a Small Trough)," *Int. J. Heat Mass Transfer*, Vol. 23, 1980, pp. 1471–1478.

15 Rohsenow, W. M., and Hartnett, J. P., *Handbook of Heat Transfer*, McGraw-Hill, New York, 1973, Section 3, pp. 112–117.

16 Carnavos, T. C., "An Experimental Study: Condensing R-11 on Augmented Tubes," ASME Paper No. 80-HT-54.

17 Yau, K. K., Cooper, J. R., and Rose, J. W., "Effect of Fin Spacing on the Performance of Horizontal Integral-Fin Condenser Tubes," ASME JOURNAL OF HEAT TRANSFER, Vol. 107, 1985, pp. 377–383.

Solidification Effects on the Fragmentation of Molten Metal Drops Behind a Pressure Shock Wave

J. W. Yang

S. G. Bankoff

Chemical Engineering Department,
Northwestern University,
Evanston, IL 60201

Molten Wood's metal drops falling through water fragment upon being overtaken by a shock wave, under conditions of simultaneous surface solidification. The study of this fragmentation is the subject of the present paper. If the solid crust thickness is sufficiently large by the time of the shock arrival, fine-scale fragmentation is prevented. A stability theory (Epstein, 1977) which includes the elastic crust stiffness in the pressure boundary conditions, and a nonlinear Taylor instability theory (Cooper and Dienes, 1977), are both surprisingly successful in predicting the threshold for fragmentation inhibition.

1 Introduction

When two nearly immiscible liquids are brought into intimate contact, and the temperature of one of the liquids is well above the normal boiling point of the second liquid, a vapor explosion may occur. This phenomenon, sometimes referred to as a fuel-coolant interaction, is characterized by very rapid production of new surface area through fragmentation, which is necessary for energy transfer on a time scale consistent with explosive behavior. The various fragmentation mechanisms which have been proposed may be classified into two broad categories: boiling mechanisms, which can be related to the theory of Fauske [1], and hydrodynamic mechanisms, related to the thermal detonation theory of Board and Hall [2]. The boiling fragmentation mechanism includes violent boiling [3], compression waves [4], bubble collapse [5, 6], jet penetration [7], and coolant entrapment [8]. The hydrodynamic fragmentation mechanism may include Taylor and/or Helmholtz instabilities [9, 10] and boundary layer stripping [11, 12]. In the present work the shock-wave-induced fragmentation of a low-melting-point metal drop in a water-glycerol solution containing small quantities of argon bubbles was investigated in a shock tube at driver pressures up to 3 MPa.

Since the coolant temperature is usually below the freezing temperature of the hot liquid, surface solidification may inhibit the fragmentation and mixing. This has not been investigated previously for purely hydrodynamic fragmentation, and is the subject of the present paper.

2 Solidification Effects

Two theories that consider the effects of a solid crust on Taylor instability are available. Dienes [13] proposed an approximate theory for nonlinear growth of the fastest-growing (according to linear theory) wavelength at an initially plane interface. An energy method, using a quasi-Lagrangian set of coordinates, was used to predict the amplitude function, with or without surface freezing. Assuming that the solidification commences with a mean solidification velocity of 20 mm/s [14] at the same time as the instability growth, the effect of solidification was shown to be minor [15]. However, Sharon and Bankoff [16] showed that the solidification effects could be significant if there was a premixing and solidification time before the pressure shock wave passed through the system.

According to Dienes, the linearized equation describing the instability growth is given by

$$\ddot{q}+4k^2\nu_f\dot{q}+\left[-\tilde{a}k+\frac{4k^2}{\rho_f}\gamma_1 GH\left(\frac{Y_0}{2G}-q\right)\right]q + \operatorname{sgn}(\dot{q})\frac{4k^2}{\rho_f}\gamma_2 Y_0 H\left(q-\frac{Y_0}{2G}\right)=0 \tag{1}$$

where $q(t)$ is the generalized coordinate, $\dot{q}$ and $\ddot{q}$ are its first and second derivatives, and k, Y_0, G are the wave number ($2\pi/\lambda$), the yield stress, and modulus of rigidity, respectively. $H(x)$ is the Heaviside function, $\operatorname{sgn}(x)$ is the sign function and

$$\gamma_1=\begin{cases}1 & \text{frozen}\\ 1-\exp[-2kd(t)] & \text{freezing}\end{cases}$$
$$\gamma_2=\begin{cases}1 & \text{frozen}\\ 1-\exp[-kd(t)] & \text{freezing}\end{cases} \tag{2}$$

and

$$\tilde{a}=a-\frac{\sigma k^2}{\rho_f} \tag{3}$$

where a is the acceleration calculated by

$$a=\frac{3}{8}C_D\frac{\rho_c}{\rho_f}\frac{u_r^2}{R_f} \tag{4}$$

The initial conditions are taken as

$$q(0)=0;\qquad \dot{q}(0)=\frac{ku_{ri}}{\pi}=\frac{2u_{ri}}{\lambda} \tag{5}$$

Equations (1) and (5) can be solved numerically, assuming constant relative velocity ($u_r = u_{ri}$), $C_D = 2$, and $\lambda = R_d = 0.5$ cm. The critical crust thickness above which no instability will grow could be determined for a given initial relative velocity. Neglecting the viscosity term, Cooper and Dienes analytically determined the stability of equation (1) by considering the trajectories in the q–$\dot{q}$ phase plane

$$\dot{q}^2(0)=\frac{k^2u_{ri}^2}{\pi^2}\geq\frac{16k^3\gamma_2^2Y_0^2}{\rho_f^2\tilde{a}}. \tag{6}$$

Hence the critical crust thickness d_{cr} for a freezing drop is

$$d_{cr}=\frac{-1}{k}\ln\left(1-\frac{\rho_f u_{ri}\tilde{a}^{1/2}}{4\pi Y_0 k^{1/2}}\right) \tag{7}$$

Epstein [17], on the other hand, attacked the problem of the stability of a small traveling wave at the interface containing a thin elastic membrane between two inviscid, incompressible fluids with relative tangential velocity and normal accelera-

Contributed by the Heat Transfer Division for publication in the JOURNAL OF HEAT TRANSFER. Manuscript received by the Heat Transfer Division September 3, 1985.

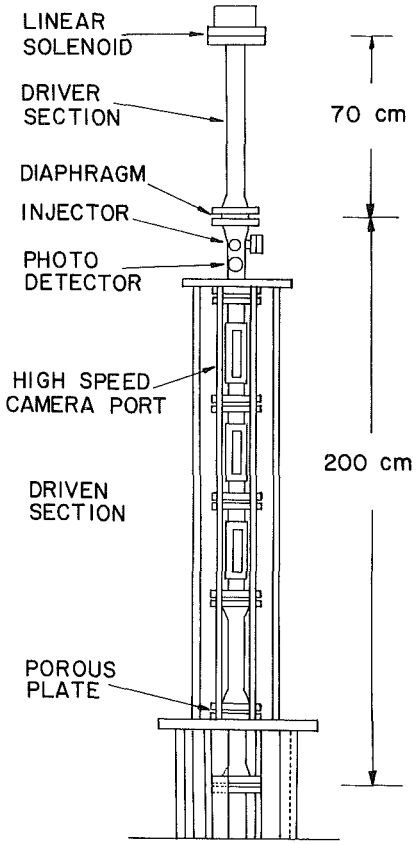

Fig. 1 Shock tube

tion. The characteristic equation for the growth constant n then becomes

$$[\rho_1 + \rho_2 \coth (kh)]n^2 + 2ik[\rho_1 u_1 + \rho_2 u_2 \coth (kh)]n + Dk^5 + 2\sigma k^3 - [\rho_1 u_1^2 + \rho_2 u_2^2 \coth (kh)]k^2 - g(\rho_1 - \rho_2)k = 0 \quad (8)$$

where σ is the average surface tension for the upper and lower crust surfaces. D is the crust stiffness given by

$$D = \frac{E^3 \delta}{12(1-\epsilon^2)} \quad (9)$$

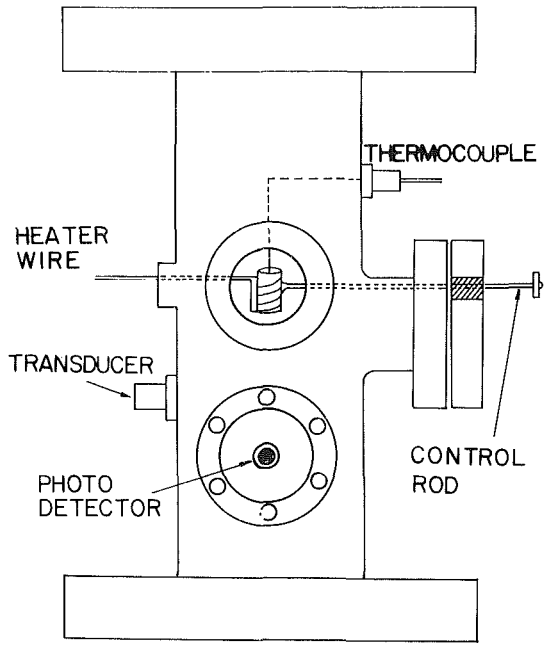

Fig. 2 Drop generation device which includes the crucible heated by a flexible electric heating wire

where E is the Young modulus and ϵ is the Poisson ratio. The cutoff wavelength is determined by solving the equation

$$n^2 = \frac{\rho_1\rho_2(u_1-u_2)^2k^2 \coth (kh)}{[\rho_1 + \rho_2 \coth (kh)]^2} - \frac{Dk^5 + 2\sigma k^3 - g(\rho_1 - \rho_2)k}{\rho_1 + \rho_2 \coth (kh)} \quad (10)$$

3 Experimental

The vertical shock tube, shown in Fig. 1, is the same as that described by Tan and Bankoff [19]. However, instead of injecting molten metal through a small tube to form the liquid metal drop, an electrically heated cup was used to melt the Wood's metal at the top of the driven section. To minimize surface oxidation, which caused plugging in early experiments with an injection tube, a nitrogen blanket was maintained around the cup. To start the run the cup support rod was

Nomenclature

a = acceleration of drop
C_p = specific heat
C_D = drag coefficient
D = crust stiffness; diameter
d = diameter
E = Young modulus
G = modulus of rigidity
g = acceleration due to gravity
H = Heaviside step function
h = heat transfer coefficient
h_{sf} = heat of fusion
k = thermal conductivity; wave number
n = growth constant
P_{21} = shock pressure ratio
R = radius
T = temperature
t = time
t_b = breakup time
U = shock velocity
u = velocity
We = Weber number $= \rho_c u_r^2 d_0/2\sigma$
We_{ff} = free-fall Weber number
Y_0 = yield stress
x, y = Cartesian space coordinates
α = volume fraction; thermal diffusivity
γ_1, γ_2 = parameters, equation (2)
δ = crust thickness
δ_T = thermal boundary layer thickness
ϵ = density ratio of the continuous phase to the dispersed phase; Poisson ratio
η = amplitude of interfacial wave
λ = wavelength
λ_{cut} = cutoff wavelength
μ = viscosity
ρ = density
σ = surface tension
ψ = shape function

Subscripts

b = breakup
c = coolant; continuous phase
cr = critical
d = drop; dispersed phase
del = delay
f = fuel
fr = freezing
g = gas phase
i = interface
l = liquid phase
m = melting
r = relative
t = terminal
∞ = ambient or terminal
0 = initial

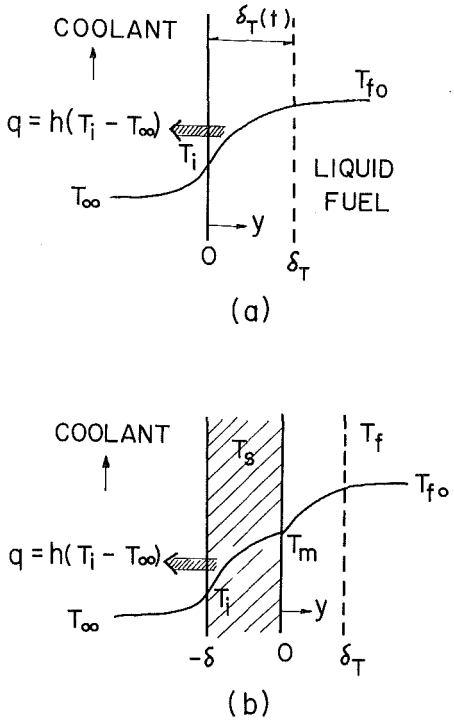

Fig. 3 Conceptual model for unsteady conduction with or without freezing: (*a*) before freezing takes place; (*b*) after freezing starts

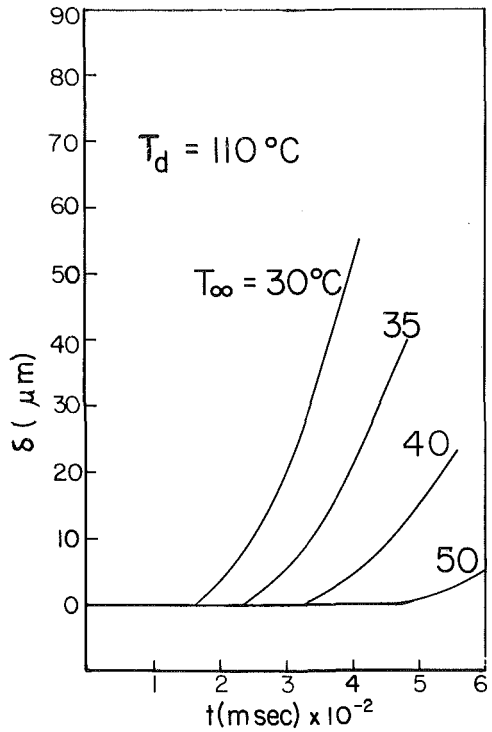

Fig. 4 Rate of crust growth for T_{f0} = 110°C

rotated manually, producing drops of 1 to 7 mm diameter. The falling drops were detected by interruption of a light beam (Fig. 2) which triggered the diaphragm rupture after a suitable time delay. The free-fall Weber number

$$\mathrm{We}_{ff} = \frac{2(\rho_d - \rho_c) d_0^2}{3\sigma C_D} \tag{11}$$

was of order unity, resulting in oscillating drops.

The coolant temperature was controlled by an immersion heater located in an external circulation loop. Both metallic (0.625 mm aluminum foil) and plastic (0.125 mm Mylar polyester film) diaphragms were used in the experiments. Aluminum diaphragms were scored in a milling machine to ensure reproducibility of the spontaneous burst. Double-layer Mylar diaphragms were employed in runs with higher-pressure (2 MPa) differences across the diaphragm. It was obviously desirable to work with a diaphragm as close to its bursting pressure as possible. A cutter with crossed knife edges was connected to a push-type solenoid at top of the driver section. In order to obtain sufficient force, the duty cycle of the solenoid was specified to be less than 10 percent. In addition, a triggered solenoid driver was designed which stored energy in a capacitor and activated the solenoid by a quick discharge. Event synchronization was achieved by setting an appropriate delay time in the precision timer. The delay time was estimated from the free fall velocity and the terminal velocity of drops. Trial and error was required for precise adjustment.

Additional details are given by Tan [20] and Yang [21].

4 Analysis

It was considered that there was no solidification before drops hit the free surface since the ambient temperature in the injector portion was maintained above the melting point of the Wood's metal.

The model for cooling and solidification of the drop falling through the liquid prior to arrival of the shock wave is depicted in Fig. 3. An energy balance before freezing starts at the fuel and coolant interface is simply

$$h(T_i(t) - T_\infty) = k_f \frac{\partial T_f}{\partial y} \tag{12}$$

The integral heat balance across the thermal boundary layer δ_T, is

$$\frac{d}{dt}\int_0^{\delta_T} T_f(y, t)\,dy = \alpha_f \left(\frac{\partial T_f}{\partial y}\right)_{y=\delta_T} - \alpha_f \left(\frac{\partial T_f}{\partial y}\right)_{y=0} + T_{f0}\left(\frac{d\delta_T}{dt}\right) \tag{13}$$

We assume a second-order polynomial for the temperature distribution in the fuel thermal boundary layer

$$\frac{T_f - T_{f0}}{T_i - T_{f0}} = 1 - \left(\frac{y}{\delta_T(t)}\right)^2 \tag{14}$$

Substituting this temperature profile into equations (12) and (13) yields

$$\delta_T = 2\,\frac{k_f(T_{f0} - T_i)}{h(T_i - T_\infty)} \tag{15}$$

$$\frac{1}{3}(T_i - T_{f0})\frac{d\delta_T}{dt} + \frac{\delta_T}{3}\frac{dT_i}{dt} = \frac{2\alpha_f}{\delta_T}(T_i - T_{f0}) \tag{16}$$

The initial conditions for the numerical solution are

$$T_i(0) = T_{f0} \tag{17}$$

$$\delta_T(0) = 0 \tag{18}$$

The integrations are stopped when the interface temperature T_i becomes equal to the solidification temperature of the metal T_m. This condition sets up the initial condition for the solid crust formation. The energy balance at the solid drop and coolant interface ($y = -\delta$) gives

$$k_s \frac{\partial T_s}{\partial y} = h(T_i(t) - T_\infty) \tag{19}$$

where the subscript s denotes the solid crust. At the moving phase boundary ($y = 0$)

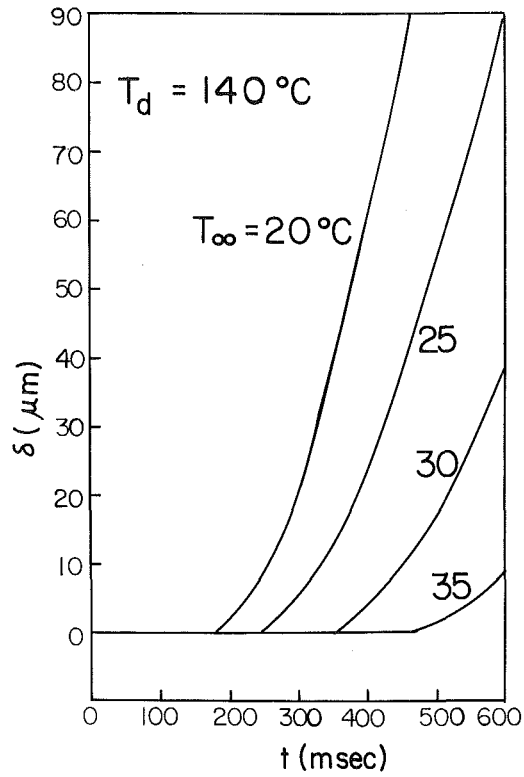

Fig. 5 Rate of crust growth for T_{f0} = 140°C

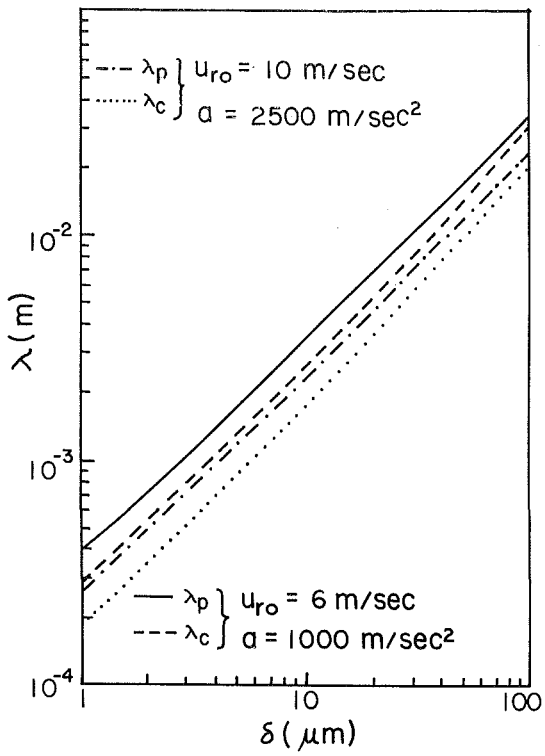

Fig. 6 Cutoff wavelength and most dangerous wavelength versus crust thickness

$$k_s \frac{\partial T_s}{\partial y} = h_{sf} \frac{d\delta(t)}{dt} + k_f \frac{\partial T_f}{\partial y} \tag{20}$$

where h_{sf} is the latent heat of solidification. The macroscopic energy balance across the solidified layer is

$$\frac{d}{dt}\int_{-\delta}^{0} T_s(y, t)dy = \alpha_s\left(\frac{\partial T_s}{\partial y}\right)_{y=0}$$

$$-\alpha_s\left(\frac{\partial T_s}{\partial y}\right)_{y=-\delta} + T_i \frac{d\delta}{dt} \tag{21}$$

and across the thermal boundary layer

$$\frac{d}{dt}\int_{0}^{\delta_T} T_f(y, t)dy = \alpha_f\left(\frac{\partial T_f}{\partial y}\right)_{y=\delta_T}$$

$$-\alpha_f\left(\frac{\partial T_f}{\partial y}\right)_{y=0} + T_{f0} \frac{d\delta_T}{dt} \tag{22}$$

The assumed temperature profile for $T_s(y, t)$ is

$$\frac{T_s - T_m}{T_i - T_m} = -\psi(t)\frac{y}{\delta(t)} + [1-\psi(t)]\left(\frac{y}{\delta(t)}\right)^2 \tag{23}$$

where $\psi(t)$ is a shape function to be determined by boundary conditions. For $T_f(y, t)$, the temperature distribution is

$$\frac{T_f - T_{f0}}{T_m - T_{f0}} = \left[1 - \frac{y}{\delta_T(t)}\right]^2 \tag{24}$$

One thus obtains a system of ordinary differential equations:

$$\psi(t) = \frac{h(T_i - T_\infty)}{k_s(T_i - T_m)}\delta(t) + 2 \tag{25}$$

$$\frac{d\delta}{dt} = \frac{k_s}{\rho h_{sf}}(T_m - T_i)\frac{\psi(t)}{\delta(t)} + \frac{2k_f}{h_{sf}\delta_T}(T_m - T_{f0}) \tag{26}$$

$$\frac{d\delta_T}{dt} = \frac{6\alpha_f}{\delta_T} \tag{27}$$

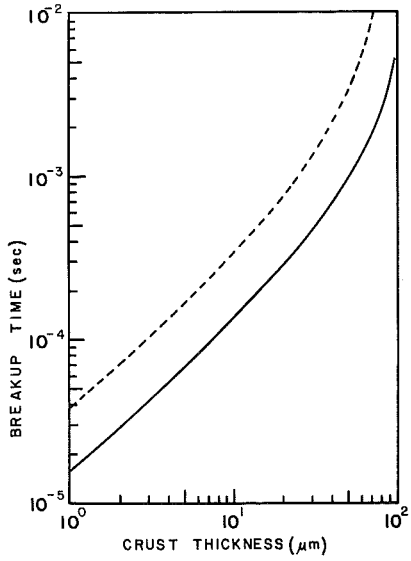

Fig. 7 Breakup time versus crust thickness: solid curve, u_{r0} = 10 m/s, a = 2500 m/s²; dashed curve, u_{r0} = 6 m/s, a = 1000 m/s²

$$\delta\frac{h(T_\infty - T_m)}{k_s(T_i - T_m)^2} + \frac{\psi + 2}{T_i - T_m}\frac{dT}{dt} = \frac{4}{\delta}\frac{d\delta}{dt} - \frac{\psi}{\delta}\frac{d\delta}{dt}$$

$$+\frac{12\alpha_s}{\delta^2}(1-\psi) - \frac{h(T_i - T_\infty)}{k_s(T_i - T_m)}\frac{d\delta}{dt} \tag{28}$$

Figures 4 and 5 show the rate of crust growth for two initial drop temperatures. Substituting into equation (10), one obtains the cutoff wavelength λ_c. The results for two typical experimental conditions are shown in Fig. 6. The lateral velocity u_1 for the Kelvin-Helmholtz instability in the Epstein theory is

approximated by the area-averaged surface velocity across the equivalent hemisphere

$$u_1 = \frac{3}{2} u_{r0} \int_0^{\pi/2} \sin^2 \theta d\theta = \frac{3}{8} \pi u_{r0} \tag{29}$$

The fastest-growing wave number k_p, found by maximizing n^2 in equation (10), is given by

$$\frac{2\rho_1\rho_2^2 h u_1^2 k^2 \coth(kh) \operatorname{csch}^2(kh)}{\rho_1 + \rho_2 \coth(kh)} + 2\rho_1\rho_2 u_1^2 k \coth(kh) - [5Dk^4 + 6\sigma k^2 - a(\rho_1 - \rho_2)][\rho_1 + \rho_2 \coth(kh)] - \rho_2 h \operatorname{csch}^2(kh)[Dk^5 + 2\sigma k^3 - a(\rho_1 - \rho_2)k] = 0 \tag{30}$$

The solution for k_p is seen to be consistently smaller than the cutoff wave number k_c, which indicates the accuracy of the solution of the transcendental equation. As shown in Fig. 6, the critical crust thickness increases with relative velocity.

For purposes of comparison with the linear theory, the e-folding breakup time t_b is employed:

$$t_b = \frac{1}{n(k_p)} \tag{31}$$

Figure 7 shows the breakup time of the crust as a function of crust thickness. Since the calculated crust growth time is orders of magnitude larger than the breakup period of the crust, t_b can be neglected in the stability analysis. The breakup criterion for application of the Epstein theory thus focuses on the cutoff wavelength at the time that the shock wave passes the falling drop. The stability condition is arbitrarily taken to be $\lambda_c/d_0 < 0.1$, where d_0 is the diameter of the volume-equivalent sphere.

Note that neither analysis deals with flow around an accelerating sphere. Hence, only order-of-magnitude agreement with experimental observations might be expected. It will be seen, however, that much better agreement is obtained. Since the drop is opaque, the experimental breakup criterion was taken to be the doubling of the observed volume, assuming axial symmetry.

Table 1 Initial experimental conditions

Run No.	α, percent	p_{21}	d_0,mm	T_{f0},°C	T_c,°C	t_{del}, ms
W704	1.03	7.95	2.6–4.6	115	50	460
W707	0.82	12.42	3.3	105	45	460
W708	1.43	11.43	2.3–5.4	125	35	450
W709	1.43	11.43	2.4–4.5	120	35	480
W711	1.43	11.43	2.5–9.0	120	30	450
W123	1.28	10.93	4.2	105	45	450
W153	1.37	7.95	6.0	104	45	480
W141	4.71	10.44	2.8–4.1	110	40	490
W161	4.79	9.94	3.3–6.0	105	45	490

5 Results and Discussion

Initial fuel temperatures were between 104°C and 125°C, while coolant temperatures varied from 30°C to 50°C. The range of void fraction was from 0.8 to 4.8, the shock pressure ratio varied from 7.95 to 12.42, and the drop diameters were between 2.3 mm and 9.0 mm. Delay times were set at around 460 ms, since the upper window was used for high-speed photographs. Nine runs were successful, which included 30 drops for analysis. A typical 4-mm-dia drop of initial temperature 110°C and gas temperature 70°C was calculated to cool only 0.3°C by the time it reached the free liquid surface after a free fall of 0.1 cm.

Experimental conditions and results are shown in Tables 1 and 2. It is seen that both models give surprisingly good agreement with experimental results. The Dienes model predicted correctly whether breakup would occur for 27 of 30 drops at Weber numbers of 35–270 while the Epstein model predicted correctly for all 30 drops. This remarkable agreement might seem surprising, but it is seen that for only three of the drops did breakup occur with nonzero crust thickness. For applica-

Table 2 Comparison of experimental breakup results with Cooper–Dienes [15] and Epstein [17] theories: B = breakup; S = stable

Drop number	d_0, mm	We	a, m/s^2	δ, μm	$\delta_{cr} \times 10^2$, μm	λ_c, mm	Reference [15]	Reference [17]	Experimental
W704-A	2.7	64	1298	0	1.99	0.215	B	B	B
W704-B	3.4	81	1030	0	2.95	0.216	B	B	B
W704-C	2.6	62	1348	0	1.04	0.216	B	B	B
W704-D	2.6	62	1348	0	1.84	0.216	B	B	B
W704-E	2.7	64	1298	0	1.99	0.215	B	B	B
W704-F	4.6	109	762	0	4.53	0.214	B	B	B
W704-G	3.9	93	898	0	3.62	0.215	B	B	B
W707-A	3.3	75	1009	0.44	2.60	0.266	S	B	B
W708-A	4.3	113	898	3.3	4.71	1.085	S	S	S
W708-B	4.4	115	878	3.3	4.86	1.085	S	S	S
W708-C	2.6	68	1486	3.6	2.22	1.199	S	S	S
W708-D	3.6	94	1073	3.4	3.71	1.122	S	S	S
W708-E	2.3	60	1680	3.7	1.75	1.239	S	S	S
W708-F	5.4	142	715	3.2	6.27	1.050	S	S	S
W709-A	2.4	63	1610	12.9	1.91	4.750	S	S	S
W709-B	3.0	79	1287	12.6	2.83	4.386	S	S	S
W709-C	4.5	118	858	12.4	5.00	4.095	S	S	S
W711-A	9.0	236	429	30.3	11.29	10.08	S	S	S
W711-B	2.5	66	1545	31.2	2.07	16.49	S	S	S
W711-C	2.6	68	1486	31.2	2.22	18.59	S	S	S
W711-D	2.7	71	1431	31.2	2.38	—	S	S	S
W123-A	4.2*	90	753	0.24	3.84	0.234	S	B	B
W153-A	6.0*	270	1104	2.10	13.09	0.574	S	B	B
W141-A	3.8	47	485	9.3	0.84	4.094	S	S	S
W141-B	4.1	51	449	9.1	1.14	3.967	S	S	S
W141-C	2.8	35	658	9.4	—	4.345	S	S	S
W161-A	3.3	82	1116	1.9	3.05	0.670	S	S	S
W161-B	6.0	150	614	1.7	6.72	0.603	S	S	S
W161-C	4.7	117	783	1.8	4.97	0.636	S	S	S
W161-D	3.3	82	1116	1.9	3.05	0.670	S	S	S

*Approximate

tion to specific problems of reactor safety, these models would need to be validated over a wider range of Weber numbers and much higher molten-drop temperatures than is possible in the present apparatus.

6 Acknowledgments

This work was supported by the National Science Foundation (CME-8017842). The shock tube was originally constructed by Dr. M. J. Tan.

References

1 Fauske, H. K., "On the Mechanism of Uranium Dioxide-Sodium Explosive Interactions," *Nucl. Sci. Eng.*, Vol. 51, 1973, pp. 95–101.

2 Board, S. J., Hall, R. W., and Hall, R. S., "Detonation of Fuel Coolant Explosions," *Nature*, Vol. 254, 1975, pp. 319–321.

3 Corradini, M. L., "Heat Transfer and Fluid Flow Aspects of Fuel-Coolant Interactions," M.I.T. Nucl. Eng. C00-1781-12TR, 1978.

4 Caldarola, L., and Kastenberg, W. E., "On the Mechanism of Fragmentation During Molten Fuel-Coolant Interactions," CONF-74041-P3, 1974, pp. 937–951.

5 Board, S. J., Farmer, C. L., and Poole, D. H., "Fragmentation in Thermal Explosions," CEGB Report RD/B/N2423, 1972.

6 Vaughan, G. J., Caldarola, L., and Todreas, N., "A Model for Fuel Fragmentation During Fuel-Coolant Interactions," CONF-761001, 1976.

7 Buchanan, D. J., "Penetration of Solid Layer by a Liquid Jet," *J. Phys. D: Appl. Phys.*, Vol. 6, 1973, pp. 1762–1771.

8 Brauer, F. E., Green, N. W., and Mesler, R. W., "Metal/Water Explosions," *Nucl. Sci. Eng.*, Vol. 31, 1968, pp. 551–554.

9 Harper, E. Y., Grube, G. W., and Chang, I-Dee, "On the Breakup of Accelerating Liquid Drops," *J. Fluid Mech.*, Vol. 52, 1972, pp. 565–591.

10 Patel, P. D., and Theofanous, T. G., "Hydrodynamic Fragmentation of Drops," *J. Fluid Mech.*, Vol. 103, 1981, pp. 207–223.

11 Ranger, A. A., and Nicholls, J. A., "Aerodynamic Shattering of Liquid Drops," *AIAA J.*, Vol. 7, 1969, pp. 285–290.

12 Fishburn, B. D., "Boundary Layer Stripping of Liquid Drops Fragmented by Taylor Instability," *Acta Astronautica*, Vol. 1, 1974, pp. 1267–1284.

13 Dienes, J. K., "Method of Generalized Coordinates and an Application to Rayleigh-Taylor Instabilities," *Phys. Fluids*, Vol. 21, 1978, pp. 736–744.

14 Cronenberg, A. W., and Fauske, H. K., "UO_2 Solidification Phenomena Associated With Rapid Cooling in Liquid Sodium," *J. Nucl. Matls.*, Vol. 52, 1974, pp. 24–32.

15 Cooper, F., and Dienes, J., "The Role of Rayleigh-Taylor Instabilities in Fuel-Coolant Interactions," *Nucl. Sci. Eng.*, Vol. 68, 1978, pp. 308–321.

16 Sharon, A., and Bankoff, S. G., "Propagation of Shock Waves Through a Fuel/Coolant Mixture," in: *Topics in Two-Phase Heat Transfer and Flows*, S. G. Bankoff, ed., ASME, New York, 1978.

17 Epstein, M., "Stability of a Submerged Frozen Crust," ASME JOURNAL OF HEAT TRANSFER, Vol. 99, 1977, pp. 527–532.

18 Chandrasekhar, S., *Hydrodynamic and Hydromagnetic Stability*, Dover, New York, 1961.

19 Tan, M. J., and Bankoff, S. G., "On the Fragmentation of Drops," *J. Fluids Eng.* (in press).

20 Tan, M. J., "Propagation of Pressure Waves in Bubbly Mixtures and Fragmentation of Accelerating Drops," Ph.D. Thesis, Chemical Engineering Department, Northwestern University, Evanston, IL, 1982.

21 Yang, J. W., "Fragmentation of Solidifying Drops Behind a Pressure Shock Wave," Ph.D. Thesis, Chemical Engineering Department, Northwestern University, Evanston, IL, 1985.

A. Sasaki
Research Assistant.

S. Aiba
Professor.

H. Fukuda
Professor.

Department of Mechanical Engineering,
Akita Technical College,
Akita 011, Japan

A Study on the Thermophysical Properties of a Soil

The effect of water content on the apparent thermal diffusivity of a soil has been investigated in relation to time and position in the direction of heat flux. To evaluate the apparent thermal diffusivity the method of minimizing the sum of squares based on a forward-difference equation was used. The sample used for experiments was a sand whose mean grain size was 208 μm and mean dry bulk density about 1360 kg/m³. The measurements were conducted over a range of water content ratios φ (percent pore volume filled with water) from 0 to 93.9 percent and temperatures from 20 to 40°C. The result shows that the overall apparent thermal diffusivity in the case of φ = 9.6 percent and the local apparent thermal diffusivity change with time.

Introduction

It is important to know the thermophysical properties of soils relevant to the following problems. The temperature differences between a stored material and a soil must be accurately estimated in order to calculate the thermal stress in underground tanks. Artificial control of temperature in soils has been sought for increased plant production. More recently, using geothermal energy with a heat pump and storing solar energy in soils have been tried.

Heat is transmitted not only by heat conduction through the solid, liquid, and gas in soils but also by water migration and vapor diffusion based on the temperature gradients and by a phase transition. Therefore the quantitative analysis of heat transport phenomena in soils has been treated as the coupled problem of heat and mass transfer [1-3]. For that purpose, the basic thermophysical properties of soils must be made clear: thermal conductivity, diffusivity, and volumetric heat capacity. Furthermore, it is necessary to examine accurately the water content distribution, the vapor pressure distribution, and the heat and mass transfer coefficients for the water migration and the vapor diffusion. However, it is difficult to know accurately those values which depend on temperature, water content, void fraction, and kind of soil. Therefore we have considered that it is effective to solve the heat conduction equation by using the apparent thermophysical properties including the contribution of mass transfer.

Although a large number of studies [4-12] have been devoted to the thermal conductivity of soils, there have been few investigations of the detailed correlation of mass transfer [5, 10]. Moreover, although many transient phenomena occur in soils, there are few studies on thermal diffusivity.

In order to measure the thermal conductivity and thermal diffusivity, there are steady-state methods and transient methods. The results for single phase materials by these different methods are generally in good agreement with each other. For porous materials such as dry soil, which are nonhomogeneous, steady-state methods are essentially suitable. But when the soil is damp, the thermal conductivity under the condition of uniform water distribution can not be obtained, because the water is rearranged according to the temperature gradient. Therefore the transient method has been generally adopted for moist soils. That is, when the time of measuring temperature is short and the temperature change is small, it has been popularly considered that the influences of the liquid and vapor movements on the thermal conductivity or diffusivity are very little. This fact may suggest that the result obtained by the steady-state method is different from that by the transient method and it is suspected that the thermophysical properties will change with time and the position within soils.

From these points of view, as a first step, the variation of the apparent thermal diffusivity of moist soil is measured for the time passing and the position, and mainly the influence of water content is discussed.

Apparent Thermal Diffusivity and Measurement Theory

Apparent Thermal Diffusivity. The total energy passing the moist soil is given as the sum of the energies transferred by heat conduction through the solid particles, the water, and the air; by sensible heat transport resulting from the water migration and the vapor diffusion; and by the latent heat transfer caused by the phase change. In the case of one-dimensional heat flow, it is expressed as follows

$$(c\rho)_a \frac{\partial T}{\partial \tau} = \frac{\partial}{\partial y}\left(\lambda \frac{\partial T}{\partial y}\right) - \frac{\partial}{\partial y}(Lq_v) - (c_v q_v + c_w q_w)\frac{\partial T}{\partial y} \quad (1)$$

where $(c\rho)_a$ is the apparent heat capacity and is given by

$$(c\rho)_a = c_w\rho_w\epsilon\phi + c_s\rho_s(1-\epsilon) + c_g\rho_g\epsilon(1-\phi) \quad (2)$$

In equations (1) and (2), T is the temperature, τ the time, y the length coordinate, q the mass flux, c the specific heat, ρ the density, λ the thermal conductivity, L the latent heat of evaporation of water, ϵ the porosity, and ϕ the degree of saturation. The subscripts s, g, w, and v represent solid, air, water, and vapor, respectively. The third term on the right side of equation (1), which presents the influence of the sensible heat transfer, will be disregarded as compared with the second term, on the right, which expresses the contribution of the latent heat transfer. Considering that the amount of water vapor diffusing can be expressed by Stefan's law [5] as follows

$$q_v = -\left(\frac{\beta D}{RT}\right)\left(\frac{P}{P-P_v}\right)\frac{\partial P_v}{\partial y} \quad (3)$$

equation (1) is rewritten as follows

$$(c\rho)_a \frac{\partial T}{\partial \tau} = \frac{\partial}{\partial y}\left[\left(\lambda + \frac{\beta LD}{RT}\frac{P}{P-P_v}\frac{\partial P_v}{\partial T}\right)\frac{\partial T}{\partial y}\right] \quad (4)$$

where P is the air pressure, P_v the partial pressure of water vapor, R the gas constant for water vapor, D the coefficient for the diffusion of water vapor in air, and β the correction coefficient for vapor diffusion. The apparent thermal conductivity of the moist soil may be defined as follows

$$\lambda_a = \lambda + \left(\frac{\beta LD}{RT}\frac{P}{P-P_v}\frac{\partial P_v}{\partial T}\right) \quad (5)$$

Contributed by the Heat Transfer Division for publication in the JOURNAL OF HEAT TRANSFER. Manuscript received by the Heat Transfer Division December 16, 1985.

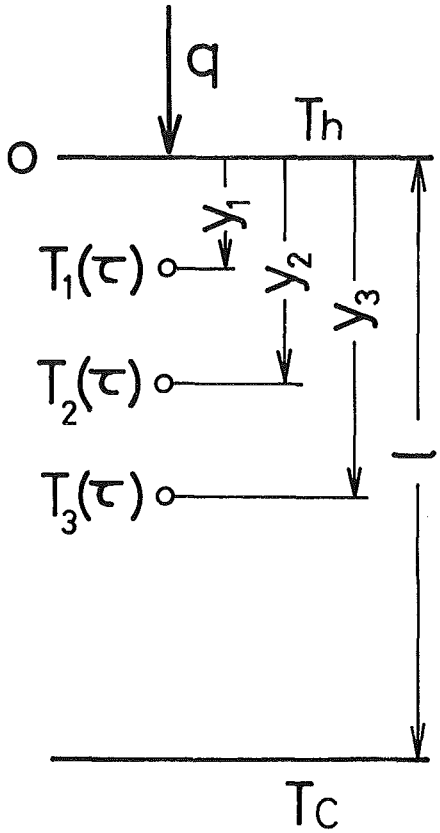

Fig. 1 Coordinate system

The apparent thermal diffusivity treated in this study may be defined as follows

$$\mathfrak{A}_a = \lambda_a/(c\rho)_a \tag{6}$$

Measurement Theory. Measurement of the apparent thermal diffusivity is conducted by the method of minimizing the sum of squares based on the explicit difference method described below [13–15].

Consider an infinite plate of thickness l as shown in Fig. 1. The one-dimensional heat conduction equation is expressed as follows, by using the apparent thermal diffusivity $\mathfrak{A}_a$ defined by equation (6)

$$\frac{\partial T}{\partial \tau} = \frac{\partial}{\partial y}\left(\mathfrak{A}_a \frac{\partial T}{\partial y}\right) \tag{7}$$

Assuming that $\mathfrak{A}_a$ does not change through a certain time period Δt, equation (7) is approximated by the forward difference technique as follows

$$T(y_i, \tau_{j+1}) = T(y_i, \tau_j) + 2\mathfrak{A}_a \Delta\tau[\{T(y_{i+1}, \tau_j) - T(y_i, \tau_j)\}/\Delta y_{i+1} + \{T(y_{i-1}, \tau_j) - T(y_i, \tau_j)\}/\Delta y_i]/(\Delta y_i + \Delta y_{i+1}) \tag{8}$$

where

$$\Delta y_i = y_i - y_{i-1} \tag{9}$$

y_i denotes the position from the upper surface, and $\Delta\tau$ designates the time step. $\mathfrak{A}_a$ is estimated at intervals of Δt. $\mathfrak{A}_a$ at $\tau = n\Delta t (n = 1, 2, \ldots)$ is calculated by using the measured temperature distribution in the sample at $\tau = (n-1)\Delta t$ as initial condition, and the measured temperatures at $\tau = (n-1)\Delta t \sim n\Delta t$ as boundary conditions. Assuming suitable $\mathfrak{A}_a$, the temperature distribution in the sample for $\tau = n\Delta t$ is calculated. The computation is iterated until the calculated temperatures $T_s(y_i, \tau_j)$ are in good agreement with the measured temperatures $T_m(y_i, \tau_j)$, changing $\mathfrak{A}_a$. The apparent thermal diffusivity at $\tau = n\Delta t$ is finally obtained when E defined by equation (10), which is the sum of square of the discrepancy between $T_s(y_i, \tau_j)$ and $T_m(y_i, \tau_j)$, becomes a minimum [13]

$$E = \sum_{i=1}^{I} \sum_{j=1}^{J} [T_s(y_i, \tau_j) - T_m(y_i, \tau_j)] \tag{10}$$

The divisions of the position and the time are carried out in order to satisfy the conditions as follows [15]

$$\mathfrak{A}_a \Delta\tau/\Delta y_i^2 < 0.5 \tag{11}$$

$$\Delta t/\Delta\tau > 3 \tag{12}$$

$$\mathfrak{A}_a \Delta t/\Delta y_i^2 > 0.4 \tag{13}$$

Experimental Apparatus and Procedure

Experiments were performed on the apparatus shown in Fig. 2. The acrylic vessel (2) and the sample (3) were sandwiched in series with rubber plates (6) between the jackets (1), (4) made of copper plate. The inside dimensions of the vessel were 240 mm square by 40 mm depth. Glass wool (5)

Nomenclature

$\mathfrak{A}_a$ = apparent thermal diffusivity, m^2/s
$\mathfrak{A}_a^*$ = nondimensional apparent thermal diffusivity = $\mathfrak{A}_a/(\mathfrak{A}_a)_{\phi=0}$
$\mathfrak{A}_{la}$ = local apparent thermal diffusivity, m^2/s
$\mathfrak{A}_{la}^*$ = nondimensional local apparent thermal diffusivity = $\mathfrak{A}_{la}/(\mathfrak{A}_a)_{\phi=0}$
c = specific heat, kJ/(kg•K)
D = coefficient for diffusion of water vapor in air, m^2/s
d = grain size, μm
G = specific gravity
L = latent heat of evaporation of water, kJ/kg
l = thickness of sample, m
P = pressure, Pa
q = mass flux of liquid water or water vapor, kg/(m^2•s)
R = gas constant for water vapor, J/(kg•K)
T = temperature, K
T^* = nondimensional temperature = $(T-T_c)/(T_h-T_c)$
Δt = time period to estimate apparent thermal diffusivity, s
y = vertical distance from heating surface, m
y^* = nondimensional distance = y/l
W = water content by weight, percent
β = correction coefficient for diffusion
ϵ = porosity ratio, percent
λ = thermal conductivity, W/m•K
ρ = density, kg/m^3
τ = time, s
τ^* = nondimensional time = $(\mathfrak{A}_a)_{\phi=0}\tau/l^2$
ϕ = water content ratio (degree of saturation), percent

Subscripts

a = apparent
c = cooling surface
d = bulk of dryness
g = gas (air)
h = heating surface
l = local
s = solid (sand particle)
v = vapor
w = liquid (water)

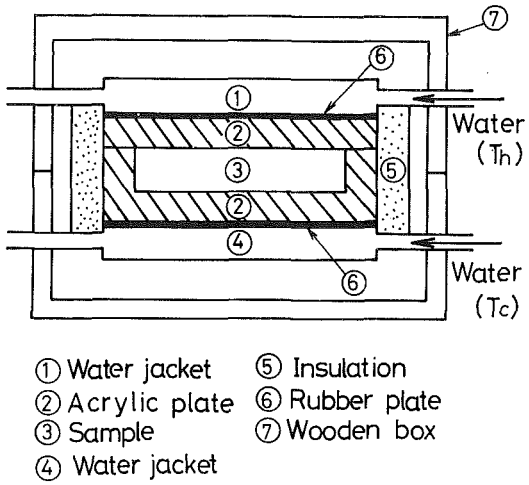

Fig. 2 Schematic view of experimental apparatus

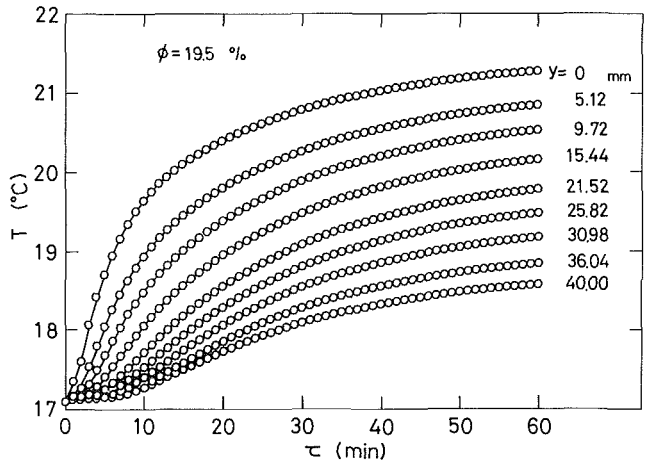

Fig. 3 Typical temperature distribution

(20 mm thick) was wound around the vessel in order to reduce the lateral heat loss. For recording the temperature responses, copper-constantan thermocouples (0.2 mm in diameter) were located at about 5 mm intervals in the direction of y in the middle of the sample.

The measurements were carried out by pouring the high-temperature water into the upper jacket after the temperature distribution in the sample became uniform. The temperature at each position in the sample was continuously measured at intervals of one minute. The positions of the thermocouples, which induced an error in the results, were accurately measured with a height gauge after the end of all temperature measurements. At the same time, the water content distributions in the sample were determined by the removal of the pieces of soil at various intervals in the direction of y.

For the water content ratio of soil, the proportion ϕ of water volume to pore space (that is, the degree of saturation) was used in the present investigation. The ϕ values were 0, 9.6, 19.5, 40.9, and 93.9 percent, and the porosity ϵ was from 44.3 to 49.2 percent. Temperatures were 20, 30, and 40°C. The temperature difference between the heating and cooling surfaces was within 3°C. The apparent thermal diffusivity was obtained at intervals of $\Delta t = 5$ min. The apparent thermal diffusivities were measured at three regions in the sample. They were calculated with the temperature responses at $y = 0-20$ mm, $y = 10-30$ mm, and $y = 20-40$ mm, and were defined as the local apparent thermal diffusivity α_{la} at $y^* = 0.25$, 0.50, and 0.75, respectively.

The sample used for the experiments was a sand collected at

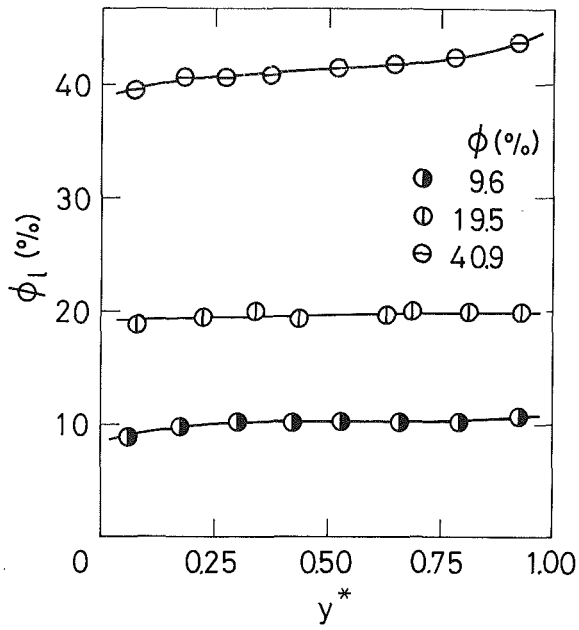

Fig. 4 Vertical distribution of water content for $T = 40$°C

Oga Peninsula in Japan and its specific gravity G was 2.57. The mean grain size d was 208 μm and mean dry bulk density ρ_d 1360 kg/m^3.

A typical temperature response in the sand is shown in Fig. 3 for an experiment at $\phi = 19.5$ percent with $T = 20$°C. The error of the position of the thermocouple was considered to be the largest in this method, as mentioned above. Accordingly, the influence of the deviation of the position on the estimation of the local apparent thermal diffusivity α_{la} at $y^* = 0.75$ was investigated. The variations of α_{la} were examined by moving the position of the thermocouple by 0.2 mm, which was possibly the maximum bias. As a result, the error of α_{la} was within 5 percent until $\tau = 10$ min. The error of α_{la} increased with time because the variations of T decreased, and it reached 15 percent at $\tau = 30$ min. When the time proceeded further on, the error of α_{la} increased. Therefore in these experiments, the measurement of T was stopped at $\tau = 60$ min when the temperature variations reached a quasi-steady state.

Experimental Results and Discussion

Figure 4 shows the water content distribution along the axis of heat flux in the sand at a temperature of 40°C. In the case of $\phi = 9.6$ percent the curve is relatively flat, although a slight decrease near the hot wall and a slight rise near the cold one are observed. For the case $\phi = 19.5$ percent, the distribution of water content varies little in the direction of y^*. But for the case of $\phi = 40.9$ percent (in this case, the pore which exists among the particles of the sand is surrounded with water), the water content decreases slightly in the neighborhood of the hot wall due to the water migration caused by the vapor pressure difference between the hot and cold regions. Such a tendency has been observed by Ohtani et al. [16].

Figure 5 indicates the relationship between the apparent thermal diffusivity α_a obtained for the whole region of the sample and the water content ϕ at various temperatures T. The data shown in this figure are obtained for $\tau = 10$ min. The results (▲) by a Laplace transformation method [17, 18] at $T = 20$°C are also indicated in order to compare with the results by the method used in this work. The result in the present work indicates the similar tendency for Tanasawa's result [4] and is in good agreement with that by the Laplace transformation method. α_a increases rapidly up to $\phi = 20$ percent and reaches a maximum value in the vicinity of $\phi = 20$

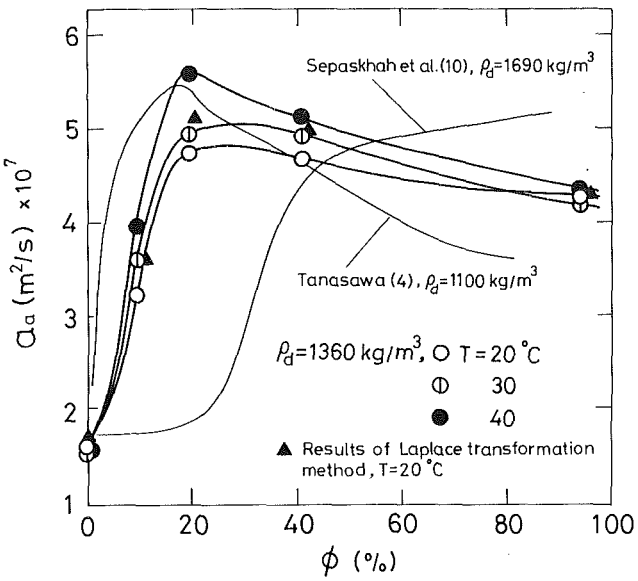

Fig. 5 Dependence of apparent thermal diffusivity on water content

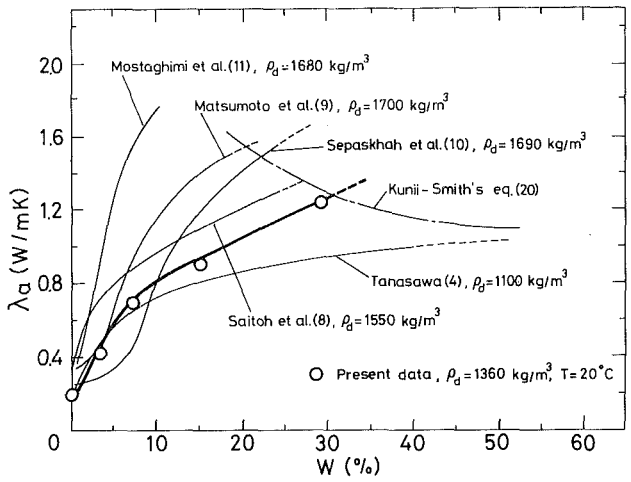

Fig. 6 Comparison of apparent thermal conductivity with existing data

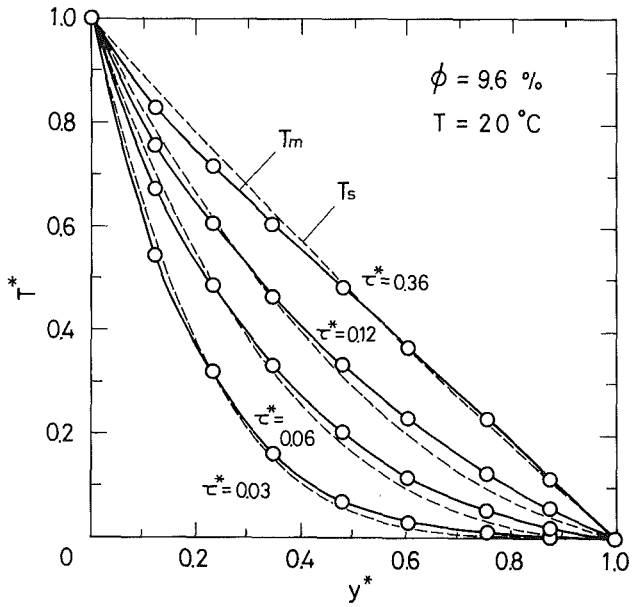

Fig. 7 Nondimensional temperature variation

percent, and decreases slightly in the range of $\phi > 20$ percent. This result suggests that the influence of water on α_a changes in the neighborhood of $\phi = 20$ percent.

In previous works [4–11], it has been shown that the apparent thermal conductivity of the damp sand increases rapidly at a certain range of water content where the continuous water layer aiding heat flow (so-called thermo-bridge) is formed in the sand. The specific heat and the density of air are smaller than those of water and sand particles; therefore the apparent heat capacity of the moist sand is proportional to the amount of water. It is evident that the behavior of α_a near $\phi = 20$ percent is due to the decrease of the thermal resistance caused by water maintained between the particles. The result of Sepaskhah et al. [10] does not change in the range for $\phi < 20$ percent, and its value is lower than the present data. This may be because their sample contained more loam than the present sample. That is, the relative surface area per volume of the loam is larger than that of the sand, and the amount of water absorbed on the surface of a particle therefore increases as compared with the sand.

The influence of temperature T on α_a can not be seen in the cases $\phi = 0$ and 93.9 percent. However, α_a increases with increasing T for $\phi = 9.6$, 19.5, and 40.9 percent, while the thermal diffusivities of sand particles, water, and air are almost independent of temperature. Accordingly, the variations of α_a for T represent the existence of the vapor diffusion. Therefore, it is clear that the vapor diffusion can not be avoided even if the measuring time is very short. The rate of increase of α_a for T increases with ϕ, and it is largest in the vicinity of $\phi = 20$ percent. This value of $\phi = 20$ percent is in good agreement with that of Shah et al. [19].

It is well known that the water contained in sands exists in the form of bound, capillary, and free water. The water content ratio ϕ = 9.6 percent corresponds to the case where the capillary water appears locally between the particles in the state of small meniscus (so-called wedge water); $\phi = 19.5$ percent to the case where the capillary water forms continuous water layers in the whole region of the sand; and $\phi = 40.9$ percent to the case where the free water exists partially in pores. The dry sand ($\phi = 0$ percent) is constructed by sand particles and air. When $\phi = 93.9$ percent, the air is almost replaced by water.

In order to compare with the previous results, the relationship between the apparent thermal conductivity λ_a and the weight water content W is shown in Fig. 6. The apparent thermal conductivity was determined by equation (6). It is evident that the present result is similar to those by Tanasawa [4], Saitoh et al. [8], Matsumoto et al. [9], and Sepaskhah et al. [10]. λ_a at $W > 10$ percent increases with the increase of the dry bulk density ρ_d. For each result the dotted line is drawn up to the saturated state in which all pores are filled with water. The λ_a of the saturated state are in good agreement with the values estimated by the equation of Kunii-Smith [20]. In that equation the value of a marble ($\lambda_s = 2.8$ W/mK) is provided as the thermal conductivity of a sand particle. The result by Mostaghimi et al. [11] is larger than that by Sepaskhah et al., although the dry bulk densities are almost equal.

Figure 7 shows the typical nondimensional temperature distributions for various times in the case of $\phi = 9.6$ percent with $T = 20$°C. In this figure, the solid line shows the measured temperature T_m^* and the dotted line shows the estimated temperature T_s^* which is calculated by α_a shown in Fig. 5. T_m^* is lower than T_s^* in the hot region, while T_m^* is larger than T_s^* in the cold one. This shows that even though the temperature is relatively low, the vapor occurring near the heating surface diffuses to the cold region and it condenses.

Figures 8(*a*) – 8(*c*) indicate the relationship between the nondimensional local apparent thermal diffusivity α_{la}^* and the nondimensional time τ^* at the positions $y^* = 0.25$, 0.50, and

0.75 for $T=20°C$. From the results for $\phi=9.6$ percent shown in Fig. 8(*a*) it can be seen that α_{la}^* at $y^*=0.25$ decreases with increasing τ^*compared to $y^*=0.75$ and that at $y^*=0.50$ it changes little with τ^*. These results are clear from the temperature behavior shown in Fig. 7. As shown in Fig. 8(*b*) for $\phi=19.5$ percent, the tendency of α_{la}^* is almost similar to that for $\phi=9.6$ percent, except in the region at $y^*=0.50$ where α_{la}^* increases slightly with τ^*. In the cases of $y^*=0.50$ and 0.75 the changing rate of α_{la}^* for τ^* is larger than that for $\phi=9.6$ percent, resulting from the more active vapor diffusion. When ϕ increases, α_{la}^* indicates a somewhat different tendency from the above. For example, in the case of ϕ = 40.9 percent, α_{la}^* increases at $y^*=0.50$ with increasing τ^* compared to $y^*=0.75$. It is suspected that vapor diffusion is suppressed because of the local existence of pores in the sand filled with water in the cold region. For $\phi=93.9$ percent, which is considered a two-phase state constructed by sand particles and water, α_{la}^* does not change with τ^* and y^* as shown in Fig. 8(*c*). A similar tendency is observed for $\phi=0$ percent constructed by sand particles and air.

The variation of the nondimensional apparent thermal diffusivity α_a^* over the whole region of the sample is shown in Fig. 9 with τ^* for $T=20°C$. In the case $\phi=0$ and 93.9 percent, α_a^* changes little with τ^*. For $\phi=19.5$ and 40.9 percent, a noticeable variation does not appear, although the local apparent thermal diffusivities α_{la}^* vary extremely with τ^* at each region of y^*. It is considered that the decrease of α_{la}^* at the hot region is canceled by the increase of α_{la}^* at the condensed region under the calculation process. On the other hand, for $\phi=9.6$ percent, α_a^* starts to decrease at about $\tau^*=0.15$. Near $\tau^*=0.3$ it becomes smaller than that for $\phi=0$ percent. This may be explained as follows. In the case of $\phi=9.6$ percent α_a is smaller than those for $\phi=19.5$ and 40.9 percent, and near $\phi=9.6$ percent α_a changes drastically with ϕ as shown in Fig. 5. For the case of $\phi=9.6$ percent where the water exists as wedge water, the water content in the hot region decreases with time and approaches $\phi\sim0$ percent near the heating surface, because the condensed water in the cold region can not return to the hot region. Therefore, the apparent thermal diffusivity in the vicinity of the heating surface ($y^*\sim0$) decreases with time. The decrease of α_{la}^* at $y^*=0.25$ shown in Fig. 8(*a*) is due to the vapor diffusion and the decrease of the apparent thermal diffusivity near the heating surface ($y^*\sim0$). Consequently, α_a^* for $\phi=9.6$ percent decreases with time because the rate of decrease of α_{la}^* at $y^*=0.25$ is larger than the rate of increase of α_{la}^* at $y^*=0.75$. From this, α_a^* should be measured as quickly as possible in the case of $\phi=9.6$ percent.

The tendencies in Fig. 9 are recognized for the cases of $T=30$ and 40 °C, although α_a^* at $\phi=9.6$ percent rapidly starts to decrease for τ^*.

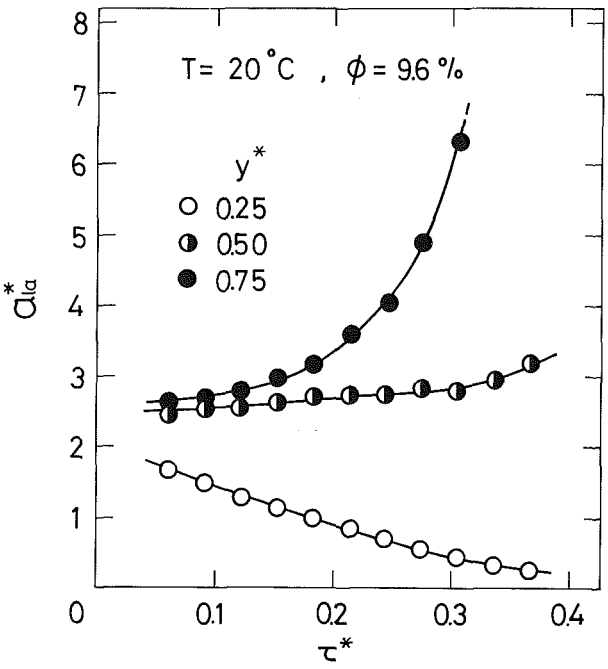

Fig. 8(a)

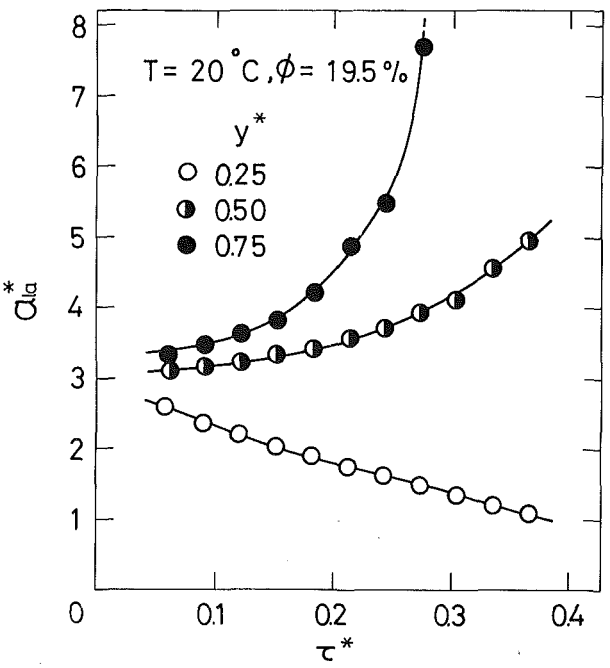

Fig. 8(b)

Conclusions

The variation of apparent thermal diffusivity with time was experimentally determined for the moist sands of the various water contents. The following conclusions can be summarized within the limits of this experiment:

1 The apparent thermal diffusivity α_a attains a maximum in the vicinity of $\phi=20$ percent, where a continuous water layer is formed by the capillary water in the sand.

2 Attention has to be paid to the influence of vapor diffu-

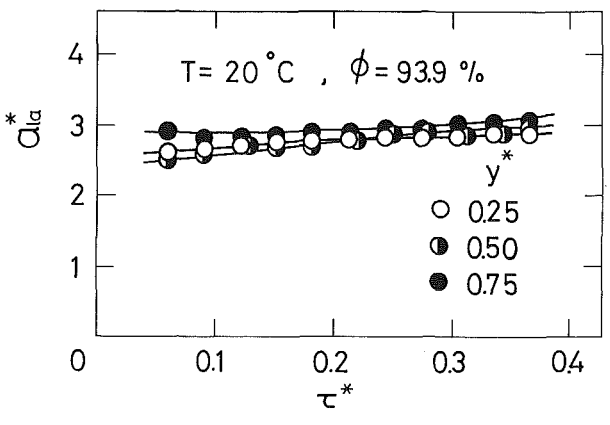

Fig. 8(c)

Fig. 8 Variation of nondimensional local apparent thermal diffusivity with time (*a*) $\phi=9.6$ percent; (*b*) $\phi=19.5$ percent; and (*c*) $\phi=93.9$ percent

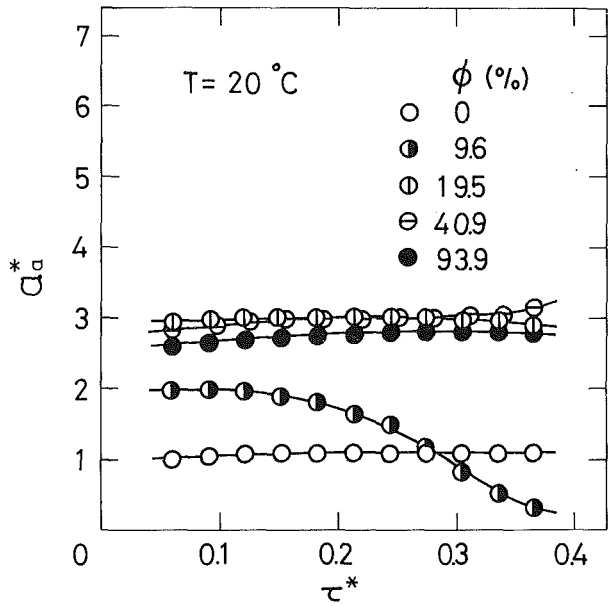

Fig. 9 Relationship between nondimensional apparent thermal diffusivity and time for various water contents

sion even if the transient method is used to measure α_a, because the influence of temperature on α_a of moist sand is relatively large.

3 The nondimensional local apparent thermal diffusivity α_{la}^* in moist sand changes with the measuring time and position. For the case of $\phi \leq 19.5$ percent where free water does not exist in the pores among the particles of the sand, α_{la}^* in the region near the heating surface decreases with the time proceeding against that in the region near the cooling surface, while in the middle region it changes little.

4 In the case of $\phi = 9.6$ percent where the water exists locally between the sand particles as the wedge water, the nondimensional apparent thermal diffusivity α_a^* decreases with time because the water content near the heating surface decreases with time. Therefore, the measurement of apparent thermal diffusivity must be conducted as quickly as possible in this case.

5 Beyond the water content ratio $\phi = 19.5$ percent, where the continuous water layer is sufficiently made up of capillary water, α_a^* does not change with time as in the case of $\phi = 0$ percent.

Acknowledgment

The authors wish to thank Professor E. Yamada, of Akita University, Japan, for his encouragement and helpful advice.

References

1 Slegel, D. L., and Davis, L. R., "Transient Heat and Mass Transfer in Soils in the Vicinity of Heated Porous Pipes," ASME JOURNAL OF HEAT TRANSFER, Vol. 99, 1977, pp. 541-546.

2 Hartley, J. G., and Black, W. Z., "Transient Simultaneous Heat and Mass Transfer in Moist, Unsaturated Soils," ASME JOURNAL OF HEAT TRANSFER, Vol. 103, 1981, pp. 376-382.

3 Baladi, J. Y., Ayers, D. L., and Schoenhals, R. J., "Transient Heat and Mass Transfer in Soils," *International Journal of Heat and Mass Transfer*, Vol. 24, 1981, pp. 449-458.

4 Tanasawa, Y., "A New Method for the Measurement of the Thermal Constants of Wet Substance," *Trans. JSME*, Vol. 1, 1935, pp. 217-226.

5 Krischer, O., and Esdorn, H., "Die Wärmeübertragung in feuchten, porigen Stoffen verschiedener Struktur," *Forsch. Ing-Wes.*, Vol. 1, 1956, pp. 1-8.

6 Woodside, W., and Cliffe, J. B., "Heat and Moisture Transfer in Closed Systems of Two Granular Materials," *Soil Science*, Vol. 87, 1957, pp. 75-82.

7 Woodside, W., and De Bruyn, C. M. A., "Heat Transfer in a Moist Clay," *Soil Science*, Vol. 87, 1957, pp. 75-81.

8 Saitoh, T., and Okagaki, O., "Heat Transfer Characteristic of Wet Materials," *Journal of JSME*, Vol. 62, 1959, pp. 75-81.

9 Matsumoto, J., and Ohkubo, T., "Experimental Study on Heat Transfer Characteristics of Soils," *Proc. JSCE*, Vol. 257, 1977, pp. 53-60.

10 Sepaskhah, A. R., and Boersma, L., "Thermal Conductivity of Soils as a Function of Temperature and Water Content," *Soil Sci. Am. J.*, Vol. 43, 1979, pp. 439-444.

11 Mostaghimi J., and Pfender, E., "Measurement of Thermal Conductivities of Soils," *Wärme- und Stoffübertragung*, Vol. 13, 1980, pp. 3-9.

12 Barnes, P. L., Smajstrla, A. G., and Reddell, D. L., "Thermal Conductivity Related to Moisture Content in Soils," presented at the Winter Meeting of the Am. Soc. Agric. Eng., 1981, Paper No. 81-2511.

13 Beck, J. V., "Calculation of Thermal Diffusivity From Temperature Measurements," ASME JOURNAL OF HEAT TRANSFER, Vol. 85, 1963, pp. 181-182.

14 Beck, J. V., "Transient Determination of Thermal Properties," *Nuclear Engineering Design*, Vol. 3, 1966, pp. 373-381.

15 Okada, M., Katayama, K., and Horiguchi, H., "A New Simultaneous Measuring Method of Thermal Properties by Iterative Calculations," *Journal of JSME*, Vol. 79, 1976, pp. 247-255.

16 Ohtani, S., Suzuki, M., and Maeda, S., "A Consideration on the Driving Force of Water Movement in Moist Granular Bed," *Chem. Eng. (Japan)*, Vol. 30, 1966, pp. 1130-1136.

17 Kavianipour, A., and Beck, J. V., "Thermal Property Estimation Utilizing the Laplace Transform With Application to Asphaltic Pavement," *International Journal of Heat and Mass Transfer*, Vol. 20, 1977, pp. 259-267.

18 Iida, Y., and Shigeta, H., "Measurement of Thermophysical Properties of Solids by Arbitrary Heating," *Trans. JSME*, Series B, Vol. 47, 1981, pp. 470-477.

19 Shah, D. J., Ramsey, J. W., and Wang, M., "An Experimental Determination of the Heat and Mass Transfer Coefficients in Moist, Unsaturated Soils," *International Journal of Heat and Mass Transfer*, Vol. 27, 1984, pp. 1075-1085.

20 Kunii, D., and Smith, J. M., "Heat Transfer Characteristics of Porous Rocks," *AIChE Journal*, Vol. 6, 1960, pp. 71-78.

Journal of Heat Transfer

Technical Notes

This section contains shorter technical papers. These shorter papers will be subjected to the same review process as that for full papers.

Numerical Solutions of Turbulent Convection Over a Flat Plate With Angle of Attack

N. T. Truncellito,[1,2] H. Yeh,[1,3] and N. Lior[1,3]

Nomenclature

A = constant used in initial data line for the turbulent kinetic energy, equation (14)
A_q = turbulent empirical constant = 0.22, equation (3)
A^+ = effective sublayer thickness, in equation (9)
B = exponential constant used in turbulent kinetic energy distribution initial data line = 1, equation (14)
B_q = turbulent empirical constant = 0.38, equation (7)
c_f = skin friction coefficient = $(\mu\Delta\bar{u}/\Delta y)_w/\frac{1}{2}\rho U_\infty^2$
c_p = specific heat at constant pressure
D = Van Driest damping function, equation (9)
g_x = component of gravitational constant in x direction
k = thermal conductivity
l = Prandtl mixing length
L = length of flat plate
Nu_x = local Nusselt number = $(-k\Delta\bar{T}/\Delta y)_w x/[k(T_W - T_\infty)]$
p = pressure
Pr = Prandtl number
Pr_t = turbulent Prandtl number = 0.85
$q^2/2$ = turbulent kinetic energy/fluid density
Re = Reynolds number
Re_L = local Reynolds number based on L
$\mathrm{Re}_{\mathrm{ref}}$ = $\rho_{\mathrm{ref}} L_{\mathrm{ref}} U_{\mathrm{ref}}/\mu_{\mathrm{ref}}$
Re_x = local Reynolds number based on x
S_{cq} = turbulent empirical constant = 1.7, equation (7)
T = temperature
$\bar{u}$ = mean velocity component in streamwise x direction
U = free-stream velocity
u' = fluctuating velocity component in x direction
v = total velocity in y direction, including mean and fluctuating components
$\bar{v}$ = mean velocity
v' = fluctuating velocity component in y direction
x = coordinate along plate in streamwise direction
X = body force, e.g., buoyancy
y = coordinate measured normal to plate
y^+ = normalized y coordinate, equation (10)
γ = ratio of specific heats = c_p/c_v
$\Delta\xi$ = x/L
δ = boundary layer thickness
θ = flat-plate angle of attack with respect to the free stream, deg
κ = empirical constant in turbulent flow = 0.41, equation (3)
μ = dynamic viscosity
ν = kinematic viscosity
ξ = Patankar–Spalding coordinate in direction of flow = x/L
ρ = density of fluid
τ = shear stress
ψ = stream function
ω = Patankar–Spalding coordinate of local stream function ψ normalized by ψ_e at a specific location ξ

Subscripts

e = conditions at the boundary layer edge (boundary with free stream)
ref = reference conditions
t = turbulent component
w = wall conditions
wake = turbulent wake conditions
x = local value measured at x
∞ = free-stream conditions

Superscripts

$\bar{}$ = time-averaged value

[1] Department of Mechanical Engineering and Applied Mechanics, University of Pennsylvania, Philadelphia, PA 19104.
[2] Systems Engineer, General Electric Co., Advanced Energy Programs Dept., Valley Forge, PA.
[3] Mem. ASME.

Contributed by the Heat Transfer Division for publication in the JOURNAL OF HEAT TRANSFER. Manuscript received by the Heat Transfer Division August 10, 1983.

1 Introduction

As evident from the literature [1–10], the knowledge of turbulent convection over flat plates with an angle of attack is limited principally to empirical results of overall heat transfer coefficients (possibly in the form of Nusselt numbers or Colburn j factors) in some ranges of the Reynolds number. This study was motivated in part by the lack of a conclusive method to determine heat loss due to wind effects on the exterior of inclined solar collectors and photovoltaic panels, as also evident from the widespread use of the Jurges correlation (reported in [4, 11]), which does not incorporate any dimensions or fluid properties and is thus strictly correct only for the size of plate and thermal conditions of Jurges' experiment. The purpose of this investigation is to examine the turbulent boundary layer flow and corresponding skin friction and convection heat loss as a function of free-stream velocity and angle of attack, by using a combined analytical/numerical approach. Many such approaches exist for the computation of turbulent flow [12–21]. The approach taken in this study was to establish and solve two models, a zeroth-order one and a first-order one, determine their validity by comparison to existing experimental results and correlations, and compare the effort required for their solution. Since it is generally accepted that the zero-order model is a reasonable approximation, it serves here as a base with which the first-order model solution accuracy and effort are compared. The most salient elements of the analysis and results are summarized below. More details can be found in [22].

2 Analysis

Briefly described, the continuity, momentum, and energy equations for a two-dimensional, turbulent, steady, time-averaged compressible boundary-layer flow over a plate with arbitrary angle of attack, and including a natural convection term, are transformed to the Patankar–Spalding [14] coordinate system. The eddy viscosity is formulated in terms of a three-region mixing length Prandtl–Von Karman model which incorporated the Van-Driest damping function in the near-wall viscous sublayer region.

In the zero-order model, which uses only the partial differential equations for the mean velocity field , and no turbulence partial differential equations (i.e., this is the usual algebraic mixing length model), the turbulent viscosity μ_t is expressed as

$$\mu_t = \bar{\rho} l^2 \left| \frac{\partial \bar{u}}{\partial y} \right| \tag{1}$$

where l is the Prandtl mixing length, and similarly the turbulent thermal conductivity

$$k_t = \bar{\rho} l^2 c_p \left| \frac{\partial \bar{u}}{\partial y} \right| / \mathrm{Pr}_t \tag{2}$$

In the first-order model the turbulent viscosity is given as [13]

$$\mu_t = \rho (A_q l/\kappa)\sqrt{q^2/2} \tag{3}$$

where $q^2 = (\bar{u}'^2 + \bar{v}'^2)$. Similarly, the turbulent conductivity is

$$k_t = \mu_t c_p / \mathrm{Pr}_t \tag{4}$$

Pr_t was assumed to be constant. Any variations in its value in the problem considered here would most likely produce only second-order effects.

The zeroth-order model is the usual algebraic mixing length model and the equations would therefore not be reproduced here. The equations for the first-order model are

Momentum:

$$\overline{\rho u}\frac{\partial \bar{u}}{\partial \xi} + \rho \bar{u}(\omega \overline{\rho_e v_e}/\psi_e)\frac{\partial \bar{u}}{\partial \omega}$$

$$= -\frac{d\bar{p}}{d\xi} + (\overline{\rho u}/\psi_e)\left\{\left[\frac{\partial \mu}{\partial \omega}(1/\mathrm{Re}_{\mathrm{ref}}) + \frac{\partial \rho}{\partial \omega}(A_q l/\kappa)\sqrt{q^2/2} + (\bar{\rho} A_q/\kappa)\frac{\partial l}{\partial \omega}\sqrt{q^2/2} + (A_q \bar{\rho} l/\kappa)\frac{\partial \sqrt{q^2/2}}{\partial \omega}\right](\overline{\rho u}/\psi_e)\frac{\partial \bar{u}}{\partial \omega} + [(\mu/\mathrm{Re}_{\mathrm{ref}}) + (A_q \bar{\rho} l/\kappa)\sqrt{q^2/2}]\left[\frac{\partial \bar{\rho}}{\partial \omega}(\bar{u}/\psi_e)\frac{\partial \bar{u}}{\partial \omega} + (\bar{\rho}/\psi_e)\left(\frac{\partial \bar{u}}{\partial \omega}\right)^2 + (\overline{\rho u}/\psi_e)\frac{\partial^2 \bar{u}}{\partial \omega^2}\right]\right\} + X \tag{5}$$

where X is the buoyancy force defined as $g_x(\bar{T} - T_\infty)/T_\infty$.

Energy:

$$\overline{\rho u}\frac{\partial \bar{T}}{\partial \xi} + \rho \bar{u}(\omega/\psi_e)\overline{\rho_e v_e}\frac{\partial \bar{T}}{\partial \omega}$$

$$= (\overline{\rho u}/\psi_e)\frac{\partial}{\partial \omega}\left\{[(\kappa/c_p(\rho U L)_{\mathrm{ref}}) + (A_q l/\kappa)\sqrt{q^2/2}(\bar{\rho}/\mathrm{Pr}_t)](\overline{\rho u}/\psi_e)\frac{\partial \bar{T}}{\partial \omega}\right\} + [(\mu/\mathrm{Re}_{\mathrm{ref}}) + (\bar{\rho} A_q l/\kappa)\sqrt{q^2/2}]\left[(\overline{\rho u}/\psi_e)\frac{\partial \bar{u}}{\partial \omega}\right]^2 (u_{\mathrm{ref}}^2/c_p T_{\mathrm{ref}}) + \bar{u}\frac{d\bar{p}}{d\xi}[(\gamma - 1)/\gamma] \tag{6}$$

Turbulent Energy [12, 13]:

$$\overline{\rho u}\left[\frac{\partial (q^2/2)}{\partial \xi} + (\omega/\psi_e)\overline{\rho_e v_e}\frac{\partial (q^2/2)}{\partial \omega}\right]$$

$$= \bar{\rho}(A_q/\kappa) l\sqrt{q^2/2}\left[(\overline{\rho u}/\psi_e)\frac{\partial \bar{u}}{\partial \omega}\right]^2 - (\rho B_q \kappa/l)(q^2/2)^{3/2} + (\bar{\rho}^2 \bar{u}/\psi_e)\left\{\left[(1/\mathrm{Re}_{\mathrm{ref}})\frac{\partial \nu}{\partial \omega} + (A_q/\kappa Sc_q)\left(\frac{\partial l}{\partial \omega}\sqrt{q^2/2} + l\frac{\partial \sqrt{q^2/2}}{\partial \omega}\right)\right] \cdot (\overline{\rho u}/\psi_e)\frac{\partial (q^2/2)}{\partial \omega} + [(\nu/\mathrm{Re}_{\mathrm{ref}}) + (A_q l/\kappa)(\sqrt{q^2/2}/Sc_q)]\left[\frac{\partial \bar{\rho}}{\partial \omega}(\bar{u}/\psi_e)\frac{\partial (q^2/2)}{\partial \omega} + (\bar{\rho}/\psi_e)\frac{\partial \bar{u}}{\partial \omega}\frac{\partial (q^2/2)}{\partial \omega} + (\overline{\rho u}/\psi_e)\frac{\partial^2 (q^2/2)}{\partial \omega^2}\right]\right\} \tag{7}$$

The mixing length l is defined for three boundary layer regions.

In the viscous sublayer

$$l = \kappa y D \tag{8}$$

where D is the Van Driest damping function

$$D = 1 - \exp(-y^+/A^+) \tag{9}$$

y^+ is the normalized y coordinate

$$y^+ = y(\sqrt{\tau_w/\rho_w})/\nu_w \tag{10}$$

and A^+ is the effective sublayer thickness which was found to be approximately 26 based on experimental results in [13].

In the near wall regions, $26 < y^+ < y^+_{\mathrm{wake}}$

$$l = \kappa y \tag{11}$$

where $\kappa = 0.41$.

In the wake region, defined by $y > 0.2\delta$, as suggested in [13]

$$l = 0.085\delta \tag{12}$$

The pressure gradient $dp/d\xi$ is supplied by the potential flow relation for an infinite wedge [3]. The ideal gas state equation was used, and the Sutherland model for the molecular viscosity [3], and constant thermal conductivity and specific heat were assumed. The coefficients used in the turbulent models are defined in the Nomenclature. The boundary conditions on the turbulent kinetic energy are that $q^2/2$ is zero at the wall and approaches free stream turbulence as $y \to \infty$

$$\lim_{y \to \infty} = 1.5(\overline{u'^2}) \tag{13}$$

where, based on results from wind-tunnel experiments, it was assumed that $\bar{u}'^2/U_\infty = 0.01$. An initial data line for the boundary condition was provided, and the following distribution was prescribed based upon results reported in [23]

$$q^2/2 = Aye^{-By^2} \tag{14}$$

where it was assumed that $B = 1$, and A was calculated from equations (13) and (14). For both models the boundary conditions at the plate are no-slip for the velocity, and arbitrarily specified temperature.

At the boundary layer edge, the initial guess for the stream function ψ_e, and the normal mass flow $(\rho v)_e$, needed in equations (5)–(7), are obtained from an integral solution of the turbulent boundary-layer momentum and energy equations for this wedge flow problem. The solution of the integrated equations is obtained by a fourth-order Runge–Kutta method which only took about 1 percent of the total computation time. The integral solution insured that a good upper limit to the boundary layer thicknesses was predicted initially, thus placing the numerical models' velocity and temperature profiles in the proper domain. This produced solutions with only a small number of iterations, or occasionally with none at all. U_e is obtained from the potential flow solution for the wedge [3].

3 Method of Solution

The momentum, energy, and turbulent kinetic energy equations (such as equations (5)–(7)) in the first-order model are placed in a linearized central finite difference form compatible with a tridiagonal matrix inversion solution scheme, implicit in the ω direction and explicit in the ξ direction.

The conditions required for the stability of the explicit part of this numerical scheme were evaluated to be

$$\Delta\xi \leq (\Delta\omega)^2 \tag{15}$$

The discretization error for the finite difference equations in both models is $0[(\Delta\omega)^2]$. For the zeroth-order model, well-behaved results were obtained for $\Delta\xi \leq 0.005$. A further reduction of 50 percent in $\Delta\xi$, to 0.0025, has changed Nu_x by only 4 percent. In comparison, the first-order solution scheme was significantly more sensitive, requiring $\Delta\xi$ steps which were smaller by a factor of about a thousand.

The present technique differs from existing procedures such as that described in [13] in that there is no need for a "match-up" or "join-point" near the wall. In [13], such a point is employed between the second and third nodes (normal to the wall) to join the near-wall (Couette layer) solution with that for the outer region (between the edges of the laminar sublayer and the overall turbulent boundary layer). In the present analysis, a finer mesh is employed near the wall (for example, five-fold finer in the zeroth-order model) to account adequately for the steep velocity and temperature gradients.

The velocity and temperature profiles obtained from both models were well-behaved distributions. More importantly, the turbulent kinetic energy profile was generated numerically and also shown to be well behaved.

4 Results

The Range of Variables. Results were obtained for Reynolds numbers up to about 3×10^5, and angles of attack $\theta = 0$, 30, 45, and 60 deg. A constant air temperature of 20°C was assumed. Both models allow the specification of an arbitrary wall temperature, and unless indicated otherwise, a constant wall temperature of 100°F (37.8°C) was assumed in the cases shown below.

Zeroth-Order Model Results. For $\theta = 0$ deg, very good agreement was observed with the Eckert and Colburn equations (shown in [3]). The results were found to agree with the Jurges values only for $L = 2$ ft (0.61 m), and over a normalized velocity of 0–20. This is due to the fact that Jurges conducted his tests at these specific conditions. Substantial disagreement with the Jurges correlation was found for other plate lengths and velocities. The results were found to be consistent with the experimental data reported in the ASHRAE handbook [24] and with the JPL test data of [25] (the comparisons are presented in [22]).

Comparisons of the zeroth-order model results with the more recent measurements of Sparrow and Tien [1] for plates at different angles to the stream (performed by mass transfer experiments as an analog to heat transfer) indicate [22] that the zeroth-order results show a moderate effect of angle of attack between 30–60 deg with regard to wall heat transfer, while the data of [1] show no such effect. In general, it was found that in comparison with the first-order model, the zeroth-order model overpredicts the friction coefficient by about 6–35 percent and the Nusselt number by about 5–17 percent in the analyzed range of parameters.

The finite difference model results were also shown to compare well with the experimental data of Scesa and Sauer [6] obtained for a step discontinuity in wall temperature (see [22]).

First-Order Model Results. The first-order model results have been used to develop a correlation

$$c_{fx} = \left(\sum_{i=0}^{3} a_{1i}\theta^i\right) \mathrm{Re}^{-\left(\sum_{i=0}^{3} b_{1i}\theta^i\right)} \tag{16}$$

and

$$\mathrm{Nu}_x = \left(\sum_{i=0}^{3} c_{1i}\theta^i\right) \mathrm{Re}^{\left(\sum_{i=0}^{3} d_{1i}\theta^i\right)} \mathrm{Pr}^{1/3} \tag{17}$$

where θ is in degrees, valid for 0 deg $\leq \theta \leq 60$ deg, and the coefficients a_{1i}, b_{1i}, c_{1i}, and d_{1i} are shown in Table 1. Here $\mathrm{Re}_{\mathrm{ref}} = 6240$, evaluated for $\rho_{\mathrm{ref}} = 0.00234$ lbf•s^2/ft^4, $U_{\mathrm{ref}} = 1$ ft/s, $L_{\mathrm{ref}} = 1$ ft, and $\mu_{\mathrm{ref}} = (3.75)\ 10^{-7}$ lbf•s/ft^2.

Figures 1 and 2 show that the results of the first-order turbulence model for c_{fx} and Nu_x agree better, respectively, with the empirical Eckert and Colburn equations than the results of the zeroth-order model. In addition to the fact that the additional equation in the first-order model creates a stronger coupling between the constitutive relations, a much finer computational mesh had to be used in the first-order model (as

Table 1 Coefficients for equations (18) and (19)

Model	i =	0	1	2	3
First-Order	a_{1i}	$(5.00)10^{-2}$	$(2.63)10^{-3}$	$-(3.89)10^{-5}$	$(2.22)10^{-7}$
	b_{1i}	$(2.00)10^{-1}$	$(2.32)10^{-3}$	$-(5.83)10^{-5}$	$(4.81)10^{-7}$
	c_{1i}	$(2.90)10^{-2}$	$(3.09)10^{-3}$	$-(8.83)10^{-5}$	$(9.51)10^{-7}$
	d_{1i}	$(8.00)10^{-1}$	$-(5.01)10^{-3}$	$(1.36)10^{-4}$	$-(1.28)10^{-6}$

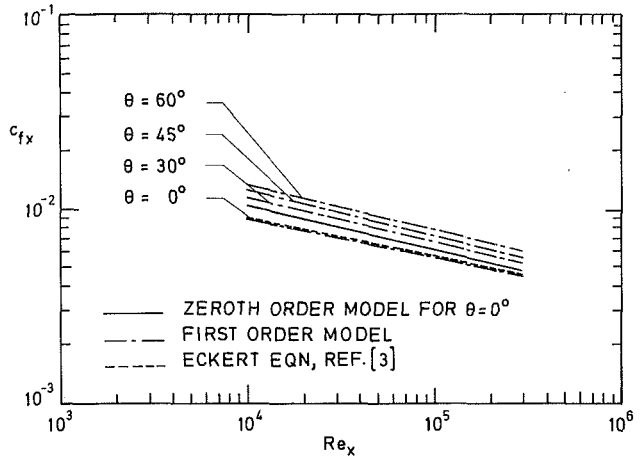

Fig. 1 Skin friction coefficient versus Reynolds number results obtained from first-order model

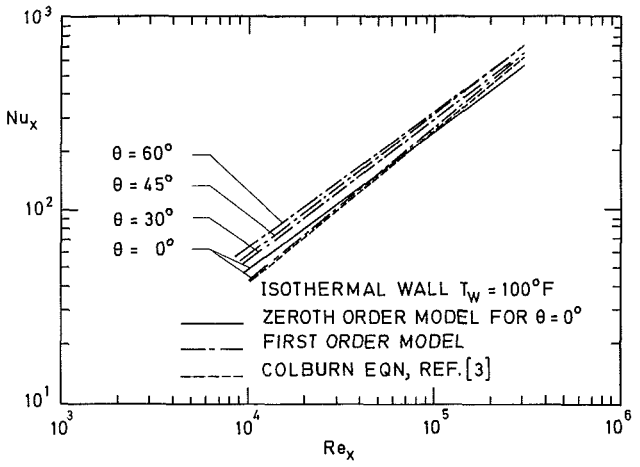

Fig. 2 Nusselt number versus Reynolds number results obtained from first-order model

described above), and this would produce a solution closer to reality, as indeed observed.

The natural convection effects on Nu were found to be negligible in the range of these calculations. This was to be expected, since the Grashof number in the cases computed is smaller than 0.225 Re^2, indicating according to [27] that the effect of natural convection upon the average heat transfer coefficient should be less than 5 percent.

In attempting to apply the results of this two-dimensional analysis to heat transfer from real objects, such as solar collectors, in the natural environment (wind), one must note that most real objects introduce appreciable three-dimensional effects, as well as separation along the edges, and that the nature and level of free-stream turbulence have an important effect on flow characteristics and heat transfer [8–10]. With that in mind, it is obvious that the results obtained in this study must be applied with great care, to cases where the geometry and free-stream turbulence are similar. Although the existence of appreciable three-dimensional effects would require the solution of a different model, this model could be used with realistic values of the free-stream turbulence to give acceptable results for cases which allow a two-dimensional approximation (such as large surfaces, faired or baffled edges). The remarkable coincidence between these results and the empirical Eckert and Colburn correlations at zero angle of attack (the only angle for which these correlations were developed), are noteworthy.

5 Conclusions

1 An integral solution, which is relatively easy to obtain, provides good data for starting the numerical solution.

2 Cost-effective zeroth-order and first-order numerical solutions have been developed whereby any matching procedure between the laminar (Couette) sublayer and the outer turbulent mixing layer solutions has been eliminated.

3 The models were proven to be effective in predicting local Nusselt numbers for arbitrary wall temperature distributions.

4 The zeroth-order results agree very well, within 10–15 percent, with the Colburn and Eckert equations (for zero angle of attack) as well as several other sources (for nonzero angles) of measured skin friction and heat transfer data, while the first-order model results came even closer, within 1–2 percent. The first-order numerical model required, however, a grid which is about a thousand times finer than that needed for the zeroth-order model, and was much more sensitive to assumed starting profiles. This, of course, increased computation difficulty and time significantly.

Acknowledgments

This study was partially supported by the U.S. Department of Energy, Office of Conservation and Solar Applications, Solar Heating and Cooling R&D Branch. The senior author wishes to express his gratitude to Mr. William Auxer of the General Electric Co. for his encouragement of this research effort, and to Drs. I. M. Cohen and P. S. Ayyaswamy for their constructive comments.

References

1 Sparrow, E. M., and Tien, K. K., "Local Heat Transfer and Fluid Flow Characteristics for Airflow Oblique or Normal to a Square Plate," *Int. J. Heat and Mass Transfer*, Vol. 22, 1979, pp. 349–360.

2 Drake, R. M., "Investigation of the Variation of Point Unit Heat Transfer Coefficients for Laminar Flow Over an Inclined Flat Plate," ASME *J. Appl. Mech.*, Vol. 71, 1949, pp. 1–8.

3 Schlichting, H., *Boundary Layer Theory*, 6th ed., McGraw-Hill, New York, 1968.

4 McAdams, W. H., *Heat Transmission*, 3rd ed., McGraw-Hill, New York, 1954.

5 Avezov, R. R., and Vakhidov, A. T., "Choice of Controlling Dimension in the Oblique Flow Past the Glass Surface of a Solar Installation," *Applied Solar Energy*, Vol. 9, 1973, pp. 90–91.

6 Avezov, R. R., Akhmadaliev, A., and Kakhkharov, N. A., "Effect of Angle of Attack on the Efficiency and Heat Transfer of the Glass Cover of a Solar Installation Under Laminar-Flow Conditions," *Applied Solar Energy*, Vol. 9, 1973, pp. 45–48.

7 Hewitt, H. C., Jr., and Onur, N., "A Study of Wind Effects on Collector Performance," ASME Paper No. 80-C2/Sol-4, 1980.

8 Test, F. L., and Lessman, R. C., "An Experimental Study of Heat Transfer During Forced Convection Over a Rectangular Body," ASME JOURNAL OF HEAT TRANSFER, Vol. 102, 1980, pp. 146–151.

9 Test, F. L., Lessman, R. C., and Johari, A., "Heat Transfer During Wind Flow Over Rectangular Bodies in the Natural Environment," ASME JOURNAL OF HEAT TRANSFER, Vol. 103, 1981, pp. 262–267.

10 McCormick, D. C., Test, F. L., and Lessman, R. C., "The Effect of Free-Stream Turbulence on Heat Transfer From a Rectangular Prism," ASME JOURNAL OF HEAT TRANSFER, Vol. 106, 1984, pp. 268–275.

11 Duffie, J. A., and Beckman, W. A., *Solar Engineering of Thermal Processes*, Wiley-Interscience, New York, 1980.

12 Reynolds, W. C., "Computation of Turbulent Flows," *Annual Review of Fluid Mechanics*, Vol. 7, 1975, pp. 183–208.

13 Crawford, M. E., and Kays, W. M., "STAN-5–A Program for Numerical Computation of Two-Dimensional Internal/External Boundary Layer Flows," Stanford University, Dept. of Mechanical Engineering, Report No. HMT-23, 1975.

14 Patankar, S. V., and Spalding, D. B., *Heat and Mass Transfer in Boundary Layers*, 2nd ed., Intertext Books, London, 1970.

15 Launder, B. E., and Spalding, D. B., *Lectures in Mathematical Models of Turbulence*, Academic Press, London-New York, 1972.

16 Bradshaw, P., "The Understanding and Prediction of Turbulent Flow," *Aeronaut. J.*, Vol. 76, 1972, pp. 403–418.

17 Mellor, G. L., and Herring, H. L., "A Survey of the Mean Turbulent Field Closure Methods," *AIAA Journal*, Vol. 11, 1973, pp. 590–599.

18 Cebeci, T., et al., "Calculation of Three-Dimensional Compressible Boundary Layers on Arbitrary Wings," *Proc. NASA-Langley Conf. Aerodyn. Anal. Requiring Adv. Computers*, 1975.

19 Lumley, J. L., "Computational Modeling of Turbulent Flows," in: *Advances in Applied Mechanics*, Vol. 18, C.-S. Yih, ed., 1978, pp. 123–176.
20 Bradshaw, P., Cebeci, T., and Whitelaw, J. M., *Engineering Calculation Methods for Turbulent Flow*, Academic Press, New York, 1981.
21 Taylor, C., and Morgan, K., eds., *Computational Techniques in Transient and Turbulent Flow*, Pineridge Press, New York, 1981.
22 Truncellito, N. T., "Numerical Solutions of Turbulent Models for Flow Over a Plate With Angle of Attack," Ph.D. dissertation, Department of Mechanical Engineering and Applied Mechanics, University of Pennsylvania, Philadelphia, PA, 1981.
23 Hinze, J. O., *Turbulence*, 2nd ed., McGraw-Hill, New York, 1975.
24 *ASHRAE Handbook of Fundamentals*, ASHRAE, New York, 1972.
25 "Thermal Performance Testing and Analysis of Photovoltaic Modules in Natural Sunlight," Jet Propulsion Laboratory, California Institute of Technology, Pasadena, CA, July 1977.
26 Scesa, S., and Sauer, F. M., "An Experimental Investigation of Convective Heat Transfer to Air from a Flat Plate with a Stepwise Discontinuous Surface Temperature," *Trans. ASME*, Vol. 74, 1952, pp. 1251–1255.
27 Sparrow, E. M., and Gregg, J. L., "Buoyancy Effects in Forced Convection Flow and Heat Transfer," ASME *J. Appl. Mech.*, Vol. 81E, 1959, pp. 133–134.

Effect of Flow Oscillations on Axial Energy Transport in a Porous Material

R. Siegel[1]

Nomenclature

A_s = internal surface area of porous medium per unit volume
$C_1 \ldots C_4$ = coefficients defined in equation (7)
c_p = specific heat
d_{max} = maximum fluid displacement
E_1, E_2 = coefficients in equation (13)
F_1, F_2 = coefficients in equation (14)
h = internal heat transfer coefficient
K = constant of integration in equation (6)
k = thermal conductivity (based on entire cross-sectional area)
l = thickness of porous layer
P = amplitude of oscillating pressure
p = fluid pressure
q = axial energy transport per unit cross-sectional area and time
T = the part of t that depends only on time
t = temperature
u = Darcy velocity of fluid (volume flow/entire cross-sectional area)
x = local coordinate across thickness of porous region
α = $C_1 h_m/\omega$
γ = temperature gradient in x direction
κ = permeability of porous material
μ = fluid viscosity
ρ = density
τ = time
φ = porosity of porous material (fluid volume/unit volume)
ω = oscillation frequency

Subscripts

a = amplitude of oscillating component
C = cold reservoir
f = fluid
H = hot reservoir
m = mean value
P = particular solution
s = solid

Introduction

It has been shown analytically and experimentally that flow oscillations of a fluid within a channel can enhance the axial transfer of energy. The transport arises from an axial gradient in fluid temperature resulting from having reservoirs at different temperatures at either end of the channel. A few recent references on enhanced axial transfer are given by [1–5], and these provide bibliography for earlier investigations.

The axial transport produced by fluid oscillations can be two or three orders of magnitude larger than molecular heat conduction. This augmentation is in the absence of throughflow in the channel. The amplitude of the flow oscillations is small compared with the channel length, so the enhancement is not produced by ordinary convective transport. As discussed in [3], the augmentation mechanism is involved with the transverse conduction between adjacent fluid layers moving relative to each other during the oscillations. The analyses in [1, 2] were for diffusion of a contaminant in oscillating laminar flow; since the channel walls were impervious, there was a zero normal derivative in contaminant concentration at the walls. The thermal energy equation has the same form as that for contaminant concentration; hence the analyses in [1, 2] could be extended for laminar energy diffusion in an insulated tube [4]. If the wall is not an insulator, energy can be exchanged with the wall during each oscillation. This transverse conduction enhances the energy transport in the axial direction, as shown in [5] for oscillating laminar flow in a channel with conducting walls.

The present analysis develops relations for axial energy diffusion in a porous medium with oscillating flow. In some devices, such as the Sterling engine, there are regenerators with oscillating flow. Axial transport in the regenerator provides an energy loss; hence it is desirable to determine what factors can limit this diffusion. A regenerator in the form of a porous medium is difficult to model since the flow is continually disrupted by the irregularities of the porous structure. The formulation here will employ an internal heat transfer coefficient that couples the fluid and solid temperatures. The final result shows how the diffusion depends on the magnitude of the heat transfer coefficient and the maximum fluid displacement. An assumption sometimes used in porous media heat transfer is that the good thermal conduct between fluid and solid within the small pores causes the fluid and solid to be at the same temperature locally. In this limit the induced axial diffusion becomes zero. Thus oscillation-induced losses may not be significant if the heat transfer ability within the porous structure is sufficiently high.

Analysis

The porous region is a plane layer of infinite extent in the y and z directions and of finite thickness from $x=0$ to l. A reservoir of hot fluid at T_H is adjacent to the face at $x=0$, and a reservoir of cold fluid at T_C is adjacent to $x=l$. There is no throughflow in the porous layer, but the fluid is oscillating in the x direction with an amplitude that is small compared with

[1]NASA Lewis Research Center, Cleveland, OH 44135; Fellow ASME.
Contributed by the Heat Transfer Division for publication in the JOURNAL OF HEAT TRANSFER. Manuscript received by the Heat Transfer Division October 24, 1985.

19 Lumley, J. L., "Computational Modeling of Turbulent Flows," in: *Advances in Applied Mechanics*, Vol. 18, C.-S. Yih, ed., 1978, pp. 123–176.
20 Bradshaw, P., Cebeci, T., and Whitelaw, J. M., *Engineering Calculation Methods for Turbulent Flow*, Academic Press, New York, 1981.
21 Taylor, C., and Morgan, K., eds., *Computational Techniques in Transient and Turbulent Flow*, Pineridge Press, New York, 1981.
22 Truncellito, N. T., "Numerical Solutions of Turbulent Models for Flow Over a Plate With Angle of Attack," Ph.D. dissertation, Department of Mechanical Engineering and Applied Mechanics, University of Pennsylvania, Philadelphia, PA, 1981.
23 Hinze, J. O., *Turbulence*, 2nd ed., McGraw-Hill, New York, 1975.
24 *ASHRAE Handbook of Fundamentals*, ASHRAE, New York, 1972.
25 "Thermal Performance Testing and Analysis of Photovoltaic Modules in Natural Sunlight," Jet Propulsion Laboratory, California Institute of Technology, Pasadena, CA, July 1977.
26 Scesa, S., and Sauer, F. M., "An Experimental Investigation of Convective Heat Transfer to Air from a Flat Plate with a Stepwise Discontinuous Surface Temperature," *Trans. ASME*, Vol. 74, 1952, pp. 1251–1255.
27 Sparrow, E. M., and Gregg, J. L., "Buoyancy Effects in Forced Convection Flow and Heat Transfer," ASME *J. Appl. Mech.*, Vol. 81E, 1959, pp. 133–134.

Effect of Flow Oscillations on Axial Energy Transport in a Porous Material

R. Siegel[1]

Nomenclature

A_s = internal surface area of porous medium per unit volume
$C_1 \ldots C_4$ = coefficients defined in equation (7)
c_p = specific heat
d_{max} = maximum fluid displacement
E_1, E_2 = coefficients in equation (13)
F_1, F_2 = coefficients in equation (14)
h = internal heat transfer coefficient
K = constant of integration in equation (6)
k = thermal conductivity (based on entire cross-sectional area)
l = thickness of porous layer
P = amplitude of oscillating pressure
p = fluid pressure
q = axial energy transport per unit cross-sectional area and time
T = the part of t that depends only on time
t = temperature
u = Darcy velocity of fluid (volume flow/entire cross-sectional area)
x = local coordinate across thickness of porous region
α = $C_1 h_m/\omega$
γ = temperature gradient in x direction
κ = permeability of porous material
μ = fluid viscosity
ρ = density
τ = time
φ = porosity of porous material (fluid volume/unit volume)
ω = oscillation frequency

Subscripts

a = amplitude of oscillating component
C = cold reservoir
f = fluid
H = hot reservoir
m = mean value
P = particular solution
s = solid

Introduction

It has been shown analytically and experimentally that flow oscillations of a fluid within a channel can enhance the axial transfer of energy. The transport arises from an axial gradient in fluid temperature resulting from having reservoirs at different temperatures at either end of the channel. A few recent references on enhanced axial transfer are given by [1–5], and these provide bibliography for earlier investigations.

The axial transport produced by fluid oscillations can be two or three orders of magnitude larger than molecular heat conduction. This augmentation is in the absence of throughflow in the channel. The amplitude of the flow oscillations is small compared with the channel length, so the enhancement is not produced by ordinary convective transport. As discussed in [3], the augmentation mechanism is involved with the transverse conduction between adjacent fluid layers moving relative to each other during the oscillations. The analyses in [1, 2] were for diffusion of a contaminant in oscillating laminar flow; since the channel walls were impervious, there was a zero normal derivative in contaminant concentration at the walls. The thermal energy equation has the same form as that for contaminant concentration; hence the analyses in [1, 2] could be extended for laminar energy diffusion in an insulated tube [4]. If the wall is not an insulator, energy can be exchanged with the wall during each oscillation. This transverse conduction enhances the energy transport in the axial direction, as shown in [5] for oscillating laminar flow in a channel with conducting walls.

The present analysis develops relations for axial energy diffusion in a porous medium with oscillating flow. In some devices, such as the Sterling engine, there are regenerators with oscillating flow. Axial transport in the regenerator provides an energy loss; hence it is desirable to determine what factors can limit this diffusion. A regenerator in the form of a porous medium is difficult to model since the flow is continually disrupted by the irregularities of the porous structure. The formulation here will employ an internal heat transfer coefficient that couples the fluid and solid temperatures. The final result shows how the diffusion depends on the magnitude of the heat transfer coefficient and the maximum fluid displacement. An assumption sometimes used in porous media heat transfer is that the good thermal conduct between fluid and solid within the small pores causes the fluid and solid to be at the same temperature locally. In this limit the induced axial diffusion becomes zero. Thus oscillation-induced losses may not be significant if the heat transfer ability within the porous structure is sufficiently high.

Analysis

The porous region is a plane layer of infinite extent in the y and z directions and of finite thickness from $x=0$ to l. A reservoir of hot fluid at T_H is adjacent to the face at $x=0$, and a reservoir of cold fluid at T_C is adjacent to $x=l$. There is no throughflow in the porous layer, but the fluid is oscillating in the x direction with an amplitude that is small compared with

[1]NASA Lewis Research Center, Cleveland, OH 44135; Fellow ASME.
Contributed by the Heat Transfer Division for publication in the JOURNAL OF HEAT TRANSFER. Manuscript received by the Heat Transfer Division October 24, 1985.

the thickness l. The oscillation is produced by an unsteady pressure in one of the reservoirs, so the pressure gradient in the porous region is harmonic without a steady component

$$\frac{\partial p}{\partial x} = -P \sin \omega\tau \tag{1}$$

It is assumed that the flow velocities are low enough so that the unsteady velocity is governed by Darcy's law

$$u = -\frac{\kappa}{\mu}\frac{\partial p}{\partial x} \tag{2}$$

This requires that frictional forces between solid and fluid dominate over fluid inertial forces. This assumption will fail for high frequencies unless the frictional resistance of the porous medium is also high. The Darcy velocity in equation (2) is the fluid volume flow divided by the entire cross-sectional area (not by the open area alone).

The energy equation in the solid equates the stored energy to the heat transfer by solid conduction and fluid convection

$$(1-\varphi)\rho_s c_{ps}\frac{\partial t_s}{\partial \tau} = k_s\frac{\partial^2 t_s}{\partial x^2} + h(\tau)A_s(t_f - t_s) \tag{3a}$$

The energy equation in the fluid contains an additional fluid convection term

$$\rho_f c_{pf}\left(\varphi\frac{\partial t_f}{\partial \tau} + u\frac{\partial t_f}{\partial x}\right) = k_f\frac{\partial^2 t_f}{\partial x^2} + h(\tau)A_s(t_s - t_f) \tag{3b}$$

The k_s and k_f are based on the entire cross-sectional area of the porous medium, e.g., k_s is the heat flow in the solid divided by the entire cross-sectional area of the medium. The thermal resistance within individual particles of the porous material has been neglected. This assumes that the Biot number based on particle conductivity and mean radius is less than about 0.1. For oscillations of small amplitude compared with l, there will be only small entrance and exit effects since the bulk of the porous medium does not have any direct contact with the reservoirs. Throughout most of the medium a uniform temperature gradient will develop in the x direction as a result of the temperature difference between reservoirs. Letting this gradient be γ, a solution is tried in the form

$$t_s(x,\tau) = \gamma x + T_s(\tau) \tag{4a}$$

$$t_f(x,\tau) = \gamma x + T_f(\tau) \tag{4b}$$

Then using equations (1) and (2), equations (3a) and (3b) become

$$(1-\varphi)\rho_s c_{ps}\frac{dT_s}{d\tau} = h(\tau)A_s(T_f - T_s) \tag{5a}$$

$$\rho_f c_{pf}\left(\varphi\frac{dT_f}{d\tau} + \frac{\gamma\kappa P}{\mu}\sin \omega\tau\right) = h(\tau)A_s(T_s - T_f) \tag{5b}$$

Equations (5a) and (5b) are added and the result integrated to give

$$T_f + \frac{1-\varphi}{\varphi}\frac{\rho_s c_{ps}}{\rho_f c_{pf}}T_s = \frac{\gamma\kappa P}{\mu\varphi}\frac{\cos \omega\tau}{\omega} + K \tag{6}$$

This is solved for T_s, and inserted into equation (5b) to obtain an equation for T_f

$$\frac{dT_f}{d\tau} + C_1 h(\tau)T_f = C_2 h(\tau)\frac{\cos \omega\tau}{\omega} - C_3 \sin \omega\tau + C_4 h(\tau) \tag{7}$$

where

$$C_1 = \frac{A_s}{\varphi\rho_f c_{pf}}\left[\frac{\varphi\rho_f c_{pf}}{(1-\varphi)\rho_s c_{ps}} + 1\right],$$

$$C_2 = \frac{A_s}{(1-\varphi)\rho_s c_{ps}}\frac{\gamma\kappa P}{\mu\varphi},\quad C_3 = \frac{\gamma\kappa P}{\mu\varphi},\quad C_4 = \frac{A_s K}{(1-\varphi)\rho_s c_{ps}}$$

Part of the particular solution of equation (7) is $T_f = C_4/C_1$. When this is inserted into equation (6), the resulting constant term in T_s, $[\varphi/(1-\varphi)](\rho_f c_{pf}/\rho_s c_{ps})(K - C_4/C_1)$, is equal to C_4/C_1. Hence the $C_4 h(\tau)$ term in equation (7) that arises from the integration constant in equation (6) only serves to equally shift T_f and T_s, and can be omitted. The particular solution of equation (7) is then

$$T_{fP}(\tau) = e^{-\int C_1 h(\tau)d\tau}\int e^{\int C_1 h(\tau)d\tau} \times \left[C_2 h(\tau)\frac{\cos \omega\tau}{\omega} - C_3 \sin \omega\tau\right]d\tau \tag{8}$$

The homogeneous solution of equation (7) is not of interest here as it gives the starting transient that dies out with time.

Local heat transfer measurements in a porous medium are extremely difficult, and information is lacking on $h(\tau)$ for oscillating velocity conditions. Steady values of h are given in a number of references, such as [6-8], for various porous media. For slow oscillations, the $h(\tau)$ would be expected to vary somewhat in phase with the absolute velocity; for higher oscillation rates, there is probably a phase difference. To obtain some insight on how the steady and time varying components of $h(\tau)$ influence the enhanced axial diffusion, an $h(\tau)$ is utilized in the form

$$h(\tau) = h_m \pm h_a \cos 2\omega\tau \tag{9}$$

For the plus sign the maximum $h(\tau)$ and $u(\tau)$ are out of phase; for the minus sign the maximum values occur simultaneously. Substituting (9) into (8) yields

$$T_{fP}(\tau) = e^{-C_1 h_m[\tau \pm (h_a/h_m)(1/\omega)\sin \omega\tau \cos \omega\tau]} \times \int e^{C_1 h_m[\tau \pm (h_a/h_m)(1/\omega)\sin \omega\tau \cos \omega\tau]} \times \left\{C_2 h_m\left[1 \pm \frac{h_a}{h_m}(\cos^2 \omega\tau - \sin^2 \omega\tau)\right]\frac{\cos \omega\tau}{\omega} - C_3 \sin \omega\tau\right\}d\tau \tag{10}$$

Equation (10) can be integrated numerically, but a closed-form solution would be helpful to reveal the interesting features of the solution. This can be done if the unsteady portion of $h(\tau)$ is small compared to the mean component. Then we expand T_{fP} in powers of h_a/h_m

$$T_{fP}(\tau) = T_0(\tau) + \frac{h_a}{h_m}T_1(\tau) + \ldots \tag{11}$$

Equations (9) and (11) are inserted into (7) and terms collected in $(h_a/h_m)^0$ and $(h_a/h_m)^1$ to yield

$$\frac{dT_0}{d\tau} + C_1 h_m T_0 = C_2 h_m\frac{\cos \omega\tau}{\omega} - C_3 \sin \omega\tau \tag{12a}$$

$$\frac{dT_1}{d\tau} \pm C_1 h_m T_0 \cos 2\omega\tau + C_1 h_m T_1 = \pm C_2 h_m \cos 2\omega\tau\frac{\cos \omega\tau}{\omega} \tag{12b}$$

The particular solution of equation (12a) is

$$T_{0P} = E_1 \cos \omega\tau + E_2 \sin \omega\tau \tag{13}$$

where

$$E_1 = \frac{1}{\omega}\,\frac{(C_2/C_1)\alpha^2 + C_3}{\alpha^2+1};\quad E_2 = \frac{\alpha}{\omega}\,\frac{(C_2/C_1) - C_3}{\alpha^2+1}$$

The T_{0P} is substituted into equation (12*b*), and the particular solution is

$$T_{1P} = e^{-C_1 h_m \tau}\int e^{C_1 h_m \tau}[F_1(2\cos^3\omega\tau - \cos\omega\tau) + F_2(2\sin^3\omega\tau - \sin\omega\tau)]d\tau \tag{14}$$

where $F_1 = \pm h_m(C_2/\omega - C_1E_1)$, $F_2 = \pm h_m C_1 E_2$. Equation (14) is integrated and then combined in equation (11) with equation (13) to yield

$$T_{fP} = E_1\cos\omega\tau + E_2\sin\omega\tau - \frac{h_a}{h_m}\,\frac{1}{\omega}\,\frac{1}{\alpha^2+1} \times [F_2(\alpha\sin\omega\tau - \cos\omega\tau) + F_1(\alpha\cos\omega\tau + \sin\omega\tau)] + \frac{h_a}{h_m}\,\frac{1}{\omega}\,\frac{2}{\alpha^2+9}\left\{F_2\left[\alpha\sin^3\omega\tau - 3\sin^2\omega\tau\cos\omega\tau + \frac{6(\alpha\sin\omega\tau - \cos\omega\tau)}{\alpha^2+1}\right] + F_1\left[\alpha\cos^3\omega\tau + 3\sin\omega\tau\cos^2\omega\tau + \frac{6(\alpha\cos\omega\tau + \sin\omega\tau)}{\alpha^2+1}\right]\right\} \tag{15}$$

With the unsteady temperature variation known, the axial transport of energy per unit time and per unit face area of the porous region can now be calculated from the relation (since $u(\tau)$ multiplied by the γx portion of t_f integrates to zero)

$$q = \rho_f c_{pf}\,\frac{\omega}{2\pi}\int_0^{2\pi/\omega} u(\tau)\,T_{fP}(\tau)\,d\tau \tag{16}$$

Using equations (1), (2), and (15), and the expressions for the C, E, and F, the q simplifies to the final result

$$q = \frac{t_H - t_C}{l}\,\frac{h_m A_s}{2}\left(\frac{d_{\max}}{\varphi}\right)^2 \times \frac{1}{\left(\frac{h_m A_s}{\varphi\rho_f c_{pf}\omega}\right)^2\left[1 + \frac{\varphi\rho_f c_{pf}}{(1-\varphi)\rho_s c_{ps}}\right]^2 + 1}\left(1 \pm \frac{1}{2}\,\frac{h_a}{h_m}\right) \tag{17}$$

where $-\gamma = (t_H - t_C)/l$ has been used for the temperature gradient. Equation (17) is given in terms of the maximum fluid displacement as would result from driving the fluid with an oscillating piston. The maximum displacement is related to P by $d_{\max} = \int_0^{\pi/2\omega} u\,dt = \kappa P/\mu\omega$.

Discussion

The axial energy transport given by equation (17) shows that q is directly proportional to the axial temperature gradient and the square of the maximum fluid displacement. If $h_m A_s$ becomes very large, the first term in the denominator is dominating and q decreases inversely with $h_m A_s$; in the limit $h_m A_s \to \infty$, the oscillations do not induce any axial energy transport. For infinite $h_m A_s$, the solid and fluid are locally in thermal equilibrium. For axial transport to occur, there must be energy transfers transverse to the direction of the axial temperature gradient that do not cancel over each oscillation cycle. Equation (17) may simplify somewhat when the fluid is a gas and the porous material is a metal. Then $\rho_s c_{ps} >> \rho_f c_{pf}$ and the second bracket in the denominator can be close to unity unless the porosity is very high.

Now consider the effect of the unsteady portion of the internal heat transfer coefficient. The plus and minus signs in equation (9) result in corresponding signs in (17). For the minus sign, the maximum $h(\tau)$ occurs when $|u|$ is a maximum; thus there is a higher $h(\tau)$ at the center of the oscillation stroke and a lower $h(\tau)$ at the maximum fluid displacement into the porous region. However, it is at the maximum fluid displacement that the local temperature differences between the fluid and the solid are the largest, and hence the largest transverse heat transfer could occur. The fact that the $h(\tau)$ is reduced at that time leads to a lower average transverse heat transfer as compared with using a value of h that does not vary with time. For the plus sign in equation (9) the maximum $h(\tau)$ occurs at the time of both the largest fluid displacement and local temperature difference between fluid and solid. This leads to increased transverse heat transfer and axial transport.

References

1 Chatwin, P. C., "On the Longitudinal Dispersion of Passive Contaminant in Oscillatory Flows in Tubes," *Journal of Fluid Mechanics*, Vol. 71, Part 3, 1975, pp. 513–527.

2 Watson, E. J., "Diffusion in Oscillatory Pipe Flow," *Journal of Fluid Mechanics*, Vol. 133, 1983, pp. 233–244.

3 Joshi, C. H., Kamm, R. D., Drazen, J. M., and Slutsky, A. S., "An Experimental Study of Gas Exchange in Laminar Oscillatory Flow," *Journal of Fluid Mechanics*, Vol. 133, 1983, pp. 245–254.

4 Kurzweg, U. H., "Enhanced Heat Conduction in Fluids Subjected to Sinusoidal Oscillations," ASME JOURNAL OF HEAT TRANSFER, Vol. 107, 1985, pp. 459–462.

5 Kurzweg, U. H., "Enhanced Heat Conduction in Oscillating Viscous Flows Within Parallel-Plate Channels," *Journal of Fluid Mechanics*, Vol. 156, 1985, pp. 291–300.

6 Kunii, D., and Levenspiel, O., *Fluidization Engineering*, Wiley, 1969, pp. 210–218.

7 Shen, J., Kaguei, S., and Wakao, N., "Measurements of Particle-to-Gas Heat Transfer Coefficients from One-Shot Thermal Responses to Packed Beds," *Chemical Engng. Science*, Vol. 36, 1981, pp. 1283–1286.

8 Beasley, D. E., and Clark, J. A., "Transient Response of a Packed Bed for Thermal Energy Storage," *Int. J. of Heat and Mass Transfer*, Vol. 27, 1984, pp. 1659–1669.

Influence of Oscillation-Induced Diffusion on Heat Transfer in a Uniformly Heated Channel

R. Siegel[1]

Nomenclature

A_0, A_1 = steady and oscillating amplitudes of axial pressure gradient
a = half-width of flow channel
C_1 = integration constant in temperature distribution
c_p = specific heat of fluid
f = function of y in unsteady velocity; $\bar{f}$ = complex conjugate
g = function of y in unsteady temperature; $\bar{g}$ = complex conjugate
k = thermal conductivity
Pr = Prandtl number = $c_p\mu/k$
p = pressure
q = heat flux at channel wall
R = axial diffusion function defined in equation (13)
T = temperature

[1]NASA Lewis Research Center, Cleveland, OH 44135; Fellow ASME.

Contributed by the Heat Transfer Division for publication in the JOURNAL OF HEAT TRANSFER. Manuscript received by the Heat Transfer Division November 27, 1985.

$$E_1 = \frac{1}{\omega}\,\frac{(C_2/C_1)\alpha^2 + C_3}{\alpha^2+1};\quad E_2 = \frac{\alpha}{\omega}\,\frac{(C_2/C_1) - C_3}{\alpha^2+1}$$

The T_{0P} is substituted into equation (12*b*), and the particular solution is

$$T_{1P} = e^{-C_1 h_m \tau}\int e^{C_1 h_m \tau}[F_1(2\cos^3\omega\tau - \cos\omega\tau) + F_2(2\sin^3\omega\tau - \sin\omega\tau)]d\tau \tag{14}$$

where $F_1 = \pm h_m(C_2/\omega - C_1E_1)$, $F_2 = \pm h_m C_1 E_2$. Equation (14) is integrated and then combined in equation (11) with equation (13) to yield

$$T_{fP} = E_1\cos\omega\tau + E_2\sin\omega\tau - \frac{h_a}{h_m}\,\frac{1}{\omega}\,\frac{1}{\alpha^2+1}\times[F_2(\alpha\sin\omega\tau - \cos\omega\tau) + F_1(\alpha\cos\omega\tau + \sin\omega\tau)] + \frac{h_a}{h_m}\,\frac{1}{\omega}\,\frac{2}{\alpha^2+9}\left\{F_2\left[\alpha\sin^3\omega\tau - 3\sin^2\omega\tau\cos\omega\tau + \frac{6(\alpha\sin\omega\tau - \cos\omega\tau)}{\alpha^2+1}\right] + F_1\left[\alpha\cos^3\omega\tau + 3\sin\omega\tau\cos^2\omega\tau + \frac{6(\alpha\cos\omega\tau + \sin\omega\tau)}{\alpha^2+1}\right]\right\} \tag{15}$$

With the unsteady temperature variation known, the axial transport of energy per unit time and per unit face area of the porous region can now be calculated from the relation (since $u(\tau)$ multiplied by the γx portion of t_f integrates to zero)

$$q = \rho_f c_{pf}\,\frac{\omega}{2\pi}\int_0^{2\pi/\omega} u(\tau)\,T_{fP}(\tau)\,d\tau \tag{16}$$

Using equations (1), (2), and (15), and the expressions for the C, E, and F, the q simplifies to the final result

$$q = \frac{t_H - t_C}{l}\,\frac{h_m A_s}{2}\left(\frac{d_{\max}}{\varphi}\right)^2 \times \frac{1}{\left(\frac{h_m A_s}{\varphi\rho_f c_{pf}\omega}\right)^2\left[1 + \frac{\varphi\rho_f c_{pf}}{(1-\varphi)\rho_s c_{ps}}\right]^2 + 1}\left(1 \pm \frac{1}{2}\,\frac{h_a}{h_m}\right) \tag{17}$$

where $-\gamma = (t_H - t_C)/l$ has been used for the temperature gradient. Equation (17) is given in terms of the maximum fluid displacement as would result from driving the fluid with an oscillating piston. The maximum displacement is related to P by $d_{\max} = \int_0^{\pi/2\omega} u\,dt = \kappa P/\mu\omega$.

Discussion

The axial energy transport given by equation (17) shows that q is directly proportional to the axial temperature gradient and the square of the maximum fluid displacement. If $h_m A_s$ becomes very large, the first term in the denominator is dominating and q decreases inversely with $h_m A_s$; in the limit $h_m A_s \to \infty$, the oscillations do not induce any axial energy transport. For infinite $h_m A_s$, the solid and fluid are locally in thermal equilibrium. For axial transport to occur, there must be energy transfers transverse to the direction of the axial temperature gradient that do not cancel over each oscillation cycle. Equation (17) may simplify somewhat when the fluid is a gas and the porous material is a metal. Then $\rho_s c_{ps} >> \rho_f c_{pf}$ and the second bracket in the denominator can be close to unity unless the porosity is very high.

Now consider the effect of the unsteady portion of the internal heat transfer coefficient. The plus and minus signs in equation (9) result in corresponding signs in (17). For the minus sign, the maximum $h(\tau)$ occurs when $|u|$ is a maximum; thus there is a higher $h(\tau)$ at the center of the oscillation stroke and a lower $h(\tau)$ at the maximum fluid displacement into the porous region. However, it is at the maximum fluid displacement that the local temperature differences between the fluid and the solid are the largest, and hence the largest transverse heat transfer could occur. The fact that the $h(\tau)$ is reduced at that time leads to a lower average transverse heat transfer as compared with using a value of h that does not vary with time. For the plus sign in equation (9) the maximum $h(\tau)$ occurs at the time of both the largest fluid displacement and local temperature difference between fluid and solid. This leads to increased transverse heat transfer and axial transport.

References

1 Chatwin, P. C., "On the Longitudinal Dispersion of Passive Contaminant in Oscillatory Flows in Tubes," *Journal of Fluid Mechanics*, Vol. 71, Part 3, 1975, pp. 513–527.

2 Watson, E. J., "Diffusion in Oscillatory Pipe Flow," *Journal of Fluid Mechanics*, Vol. 133, 1983, pp. 233–244.

3 Joshi, C. H., Kamm, R. D., Drazen, J. M., and Slutsky, A. S., "An Experimental Study of Gas Exchange in Laminar Oscillatory Flow," *Journal of Fluid Mechanics*, Vol. 133, 1983, pp. 245–254.

4 Kurzweg, U. H., "Enhanced Heat Conduction in Fluids Subjected to Sinusoidal Oscillations," ASME JOURNAL OF HEAT TRANSFER, Vol. 107, 1985, pp. 459–462.

5 Kurzweg, U. H., "Enhanced Heat Conduction in Oscillating Viscous Flows Within Parallel-Plate Channels," *Journal of Fluid Mechanics*, Vol. 156, 1985, pp. 291–300.

6 Kunii, D., and Levenspiel, O., *Fluidization Engineering*, Wiley, 1969, pp. 210–218.

7 Shen, J., Kaguei, S., and Wakao, N., "Measurements of Particle-to-Gas Heat Transfer Coefficients from One-Shot Thermal Responses to Packed Beds," *Chemical Engng. Science*, Vol. 36, 1981, pp. 1283–1286.

8 Beasley, D. E., and Clark, J. A., "Transient Response of a Packed Bed for Thermal Energy Storage," *Int. J. of Heat and Mass Transfer*, Vol. 27, 1984, pp. 1659–1669.

Influence of Oscillation-Induced Diffusion on Heat Transfer in a Uniformly Heated Channel

R. Siegel[1]

Nomenclature

- A_0, A_1 = steady and oscillating amplitudes of axial pressure gradient
- a = half-width of flow channel
- C_1 = integration constant in temperature distribution
- c_p = specific heat of fluid
- f = function of y in unsteady velocity; $\bar{f}$ = complex conjugate
- g = function of y in unsteady temperature; $\bar{g}$ = complex conjugate
- k = thermal conductivity
- Pr = Prandtl number = $c_p\mu/k$
- p = pressure
- q = heat flux at channel wall
- R = axial diffusion function defined in equation (13)
- T = temperature

[1]NASA Lewis Research Center, Cleveland, OH 44135; Fellow ASME.

Contributed by the Heat Transfer Division for publication in the JOURNAL OF HEAT TRANSFER. Manuscript received by the Heat Transfer Division November 27, 1985.

u = axial fluid velocity
$\bar{u}_s$ = mean value of steady velocity
x, y = axial and transverse coordinates
α = thermal diffusivity = $k/\rho c_p$
β = dimensionless parameter = $(2\omega/\nu)^{1/2}a$ ($\beta/\sqrt{2}$ = Womersley number)
γ = axial temperature gradient
δ = Stokes layer thickness = $(2\nu/\omega)^{1/2}$
μ = fluid viscosity
ν = kinematic viscosity = μ/ρ
ρ = fluid density
τ = time
ω = oscillation frequency

Subscripts

m = time mean value
s = steady component
t = time-dependent component
w = at wall
∞ = at $x \to -\infty$

Introduction

Analyses [1–3] and experiments [4, 5] have both shown that oscillating laminar flow in a channel can produce a significant diffusion effect in the axial direction in the presence of an axial gradient in concentration or temperature. For example, flow oscillations in a tube will transfer energy from a hot reservoir at one end of the tube to a cold reservoir at the other end without having any throughflow of fluid in the tube. The enhanced axial diffusion can be thousands of times larger than the transport by axial molecular conduction [6, 7]. The net axial transport during oscillations arises from the irreversible transverse diffusion that occurs in connection with the oscillating transverse temperature distribution. Watson [1] briefly considers the additive effect of having a throughflow forced convection. Although forced convection would usually dominate the transfer process, the effect of oscillation-induced diffusion may be significant for very slow flows.

It is usually thought that flow oscillations would tend to enhance heat transfer for flow in ducts, although in some instances no change in heat transfer has been observed, or there has been a heat transfer decrease (see literature quoted in [8, 9]. The heat transfer behavior is influenced by many parameters such as whether the flow is laminar or turbulent, fully developed or not, the oscillation frequency and the Prandtl number. The purpose of this note is to show that, for forced convection in slow laminar flow in a channel with uniform heat addition, the effect of flow oscillations will be to reduce the channel heat transfer coefficient. This is because the heat addition along the channel wall produces an increasing fluid temperature along the channel length. The flow oscillations interacting with this positive temperature gradient will induce a heat flow back toward the channel inlet. This will tend to inhibit the heat transfer process and will raise the wall temperature required to transfer away a given amount of heating at the channel wall.

Analysis

The momentum equation for the unsteady fully developed channel flow shown in Fig. 1 is

$$\frac{\partial u}{\partial \tau} = -\frac{1}{\rho}\frac{dp}{dx} + \frac{\mu}{\rho}\frac{\partial^2 u}{\partial y^2} \tag{1}$$

Let the throughflow with an oscillating component be driven by the pressure gradient, $-dp/dx = A_0 + A_1 \cos \omega\tau$, and then try a velocity solution of the form $u(y, \tau) = u_s(y) + u_t(y, \tau)$. When these quantities are inserted into equation (1), the equations for u_s and u_t are

$$\frac{d^2 u_s}{dy^2} = -\frac{A_0}{\mu} \tag{2a}$$

$$\frac{\partial u_t}{\partial \tau} = \frac{A_1}{\rho}\cos \omega\tau + \frac{\mu}{\rho}\frac{\partial^2 u_t}{\partial y^2} \tag{2b}$$

The solutions satisfying $u_s = u_t = 0$ at $y = \pm a$ and $du_s/dy = \partial u_t/\partial y = 0$ at $y = 0$ are well known [10]

$$u_s = \frac{A_0}{2\mu}(a^2 - y^2) \tag{3a}$$

$$u_t = \mathrm{Re}[f(y)e^{i\omega\tau}] \tag{3b}$$

where

$$f(y) = \frac{iA_1}{\rho\omega}\left[\frac{\cosh\ (1+i)\frac{y}{\delta}}{\cosh\ (1+i)\frac{a}{\delta}} - 1\right]; \quad \delta = \left(\frac{2\nu}{\omega}\right)^{1/2}$$

The transient energy equation in the channel is

$$\frac{\partial T}{\partial \tau} + u\frac{\partial T}{\partial x} = \alpha\left(\frac{\partial^2 T}{\partial x^2} + \frac{\partial^2 T}{\partial y^2}\right) \tag{4}$$

It is assumed that the channel is long enough so that thermal entrance effects can be neglected. A solution is then tried in the form $T(x, y, \tau) = \gamma x + T_s(y) + T_t(y, \tau)$, and the energy equation becomes

$$\frac{\partial T_t}{\partial \tau} + [u_s(y) + u_t(y, \tau)]\gamma = \alpha\left(\frac{d^2 T_s}{dy^2} + \frac{\partial^2 T_t}{\partial y^2}\right) \tag{5}$$

The T_s is thus found from

$$\frac{d^2 T_s}{dy^2} = \frac{\gamma A_0}{2\alpha\mu}(a^2 - y^2) \tag{6}$$

The T_s will be made to satisfy the imposed heating at the wall so that $\partial T_s/\partial y|_{y=a} = q/k$, and from symmetry $\partial T_s/\partial y|_{y=0} = 0$. The integral of equation (6) evaluated at $y = a$ then yields the temperature gradient in terms of the wall heat addition, $\gamma = 3\alpha\mu q/ka^3 A_0$. Although the oscillating flow will transfer energy in the negative x direction, this transfer is independent of x and does not change the value of γ. Integrating equation (6) a second time yields the known solution for T_s (see [11])

$$T_s = \frac{3}{4}\frac{qa}{k}\left(\frac{y^2}{a^2} - \frac{1}{6}\frac{y^4}{a^4}\right) + C_1 \tag{7}$$

From equations (5) and (3b), the equation for T_t is

$$\frac{\partial T_t}{\partial \tau} + \mathrm{Re}[f(y)e^{i\omega\tau}]\gamma = \alpha\frac{\partial^2 T_t}{\partial y^2} \tag{8}$$

and since T_s has already accounted for the wall heat addition, the boundary conditions for T_t are $\partial T_t/\partial y = 0$ at $y = 0$ and $y = \pm a$. The solution for T_t is given in [1] as

$$T_t(y, \tau) = \mathrm{Re}[g(y)e^{i\omega\tau}] \tag{9}$$

where

$$g(y) = \frac{\gamma A_1}{\rho\omega^2} \times \left\{1 - \frac{\mathrm{Pr}}{\mathrm{Pr} - 1}\left[\frac{\cosh y^*}{\cosh a^*} - \frac{\tanh a^*}{\sqrt{\mathrm{Pr}}}\frac{\cosh (y^*\sqrt{\mathrm{Pr}})}{\sinh (a^*\sqrt{\mathrm{Pr}})}\right]\right\}$$

and $y^* = \sqrt{i\omega/\nu}\, y$, $a^* = \sqrt{i\omega/\nu}\, a$.

The value of C_1 in equation (7) is still to be found; this sets the level of the fluid temperature distribution and hence influences the wall temperature required for transferring away

the wall heating q. The C_1 is obtained by taking a heat balance on the control volume shown in Fig. 1. This yields

$$qx = \rho c_p \int_0^a (T - T_\infty) u \, dy - \int_0^a k \frac{\partial T}{\partial x} \, dy \tag{10}$$

Since $\partial T/\partial x = \gamma$, the last integral yields $k\gamma a$. Then

$$\frac{1}{\rho c_p}(qx + k\gamma a) = \int_0^a [\gamma x + T_s(y) - T_\infty + T_t(y, \tau)][u_s(y) + u_t(y, \tau)]dy$$

Insert u_t and T_t in the form

$$u_t(y, \tau) = \frac{1}{2}[f(y)e^{i\omega\tau} + \bar{f}(y)e^{-i\omega\tau}]$$

$$T_t(y, \tau) = \frac{1}{2}[g(y)e^{i\omega\tau} + \bar{g}(y)e^{-i\omega\tau}]$$

and then take a time average to obtain

$$\frac{1}{\rho c_p}(qx + k\gamma a) = \int_0^a [\gamma x + T_s(y) - T_\infty]u_s(y)dy + \frac{1}{4}\int_0^a (\bar{f}g + f\bar{g})dy \tag{11}$$

Inserting $T_s(y)$ and $u_s(y)$, the first integral becomes

$$\int_0^a [\gamma x + T_s(y) - T_\infty]u_s(y)dy = \left(\gamma x - T_\infty + \frac{39}{280}\frac{qa}{k} + C_1\right)\frac{A_0 a^3}{3\mu} \tag{12}$$

The second integral was evaluated in [1] and is given by

$$\frac{1}{4}\int_0^a (\bar{f}g + f\bar{g})dy = -\frac{k}{\rho c_p}\gamma a\left[\frac{A_1^2 a^6}{\rho^2\nu^4}\frac{4}{\beta^6}\frac{\cosh\beta - \cos\beta}{\cosh\beta + \cos\beta}\frac{C(\beta) - C(\beta\sqrt{\Pr})}{1 - \Pr^{-2}}\right]$$

$$\equiv -\frac{k}{\rho c_p}\gamma a \, R(\beta, \Pr) \tag{13}$$

where $C(\xi) = (\sinh\xi - \sin\xi)\,/\,\xi(\cosh\xi - \cos\xi)$, $\beta = (2\omega/\nu)^{1/2}a$. A special relation is also given in [1] for $\Pr = 1$.

The two integrals are substituted into equation (11) and the γ is eliminated using the expression following equation (6). The result is solved for C_1 to yield

$$C_1 = T_\infty - \frac{qa}{k}\left[\frac{39}{280} - \left(\frac{3\mu\alpha}{A_0 a^3}\right)^2 (R+1)\right] \tag{14}$$

Then from equation (7)

$$\frac{T_s - T_\infty}{\frac{qa}{k}} = \frac{3}{4}\left(\frac{y}{a}\right)^2 - \frac{1}{8}\left(\frac{y}{a}\right)^4 - \frac{39}{280} + \left(\frac{3\mu\alpha}{A_0 a^3}\right)^2 (R+1) \tag{15}$$

This is evaluated at the wall $y = a$, and the time mean wall temperature as a function of x is

$$\frac{T_{w,m} - T_\infty}{\frac{qa}{k}} = \frac{3\mu\alpha}{A_0 a^3}\frac{x}{a} + \frac{17}{35} + \left(\frac{3\mu\alpha}{A_0 a^3}\right)^2 (R+1) \tag{16}$$

The average velocity over the cross section is given by

$$\bar{u}_s = (A_0/2a\mu)\int_0^a (a^2 - y^2)dy = A_0 a^2/3\mu$$

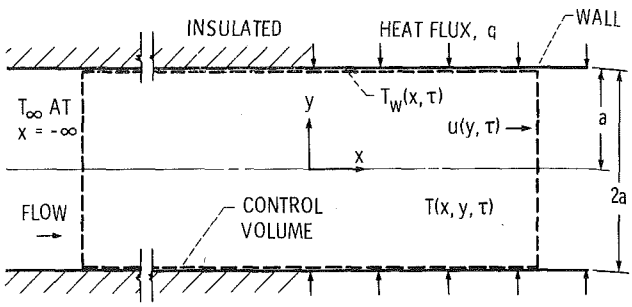

Fig. 1 Geometry of heated parallel plate channel

If this is used to eliminate A_0, the final result is (using $\mathrm{Re}_a = \bar{u}_s a/\nu$)

$$\frac{T_{w,m} - T_\infty}{\frac{qa}{k}} = \frac{17}{35} + \frac{1}{\mathrm{Re}_a \Pr}\left[\frac{x}{a} + \frac{R(\beta, \Pr)}{\mathrm{Re}_a \Pr} + \frac{1}{\mathrm{Re}_a \Pr}\right] \tag{17}$$

Discussion

The effect of flow oscillations superposed on a throughflow has been examined analytically for laminar flow heat transfer in a channel. The channel walls are uniformly heated so that, after the starting transients have decayed, the bulk mean fluid temperature must rise linearly along the channel length. The overall heat balance requires that this mean temperature gradient stay the same with or without flow oscillations present. The flow oscillations will provide an axial transport of energy in the presence of the temperature gradient set up by the mean flow. The axial transport is the result of transverse diffusion during the oscillation cycle. The oscillations provide periodic variations in the transverse temperature gradient. The resulting transverse energy diffusion does not integrate to zero over each cycle, and this results in an oscillation-induced energy transfer in the axial direction. This mechanism has been discussed in references such as [1].

In the present heat transfer situation, the temperature is rising along the channel length; hence the induced axial diffusion is toward the channel entrance in opposition to the flow direction. After a steady oscillating thermal condition has been achieved, the energy being transferred back toward the channel entrance must be acquired by the incoming flow and carried into the channel entrance. This preheats the incoming fluid and raises the temperature level within the channel. The quantitative effect is given by equation (17). The last term on the right, $1/\mathrm{Re}_a\Pr$, is axial molecular conduction, this is usually very small unless $\mathrm{Re}_a\Pr$ is very small, such as for low-velocity or liquid metal flows. The term $R(\beta, \Pr)/\mathrm{Re}_a\Pr$ is the oscillation-induced axial energy flow, and hence, $R(\beta, \Pr)$ is the ratio of this energy flow to that by molecular conduction. As shown in the literature [6, 7], the $R(\beta, \Pr)$ can be in the range of 10^3, thereby producing a significant increase in wall temperature if $\mathrm{Re}_a\Pr$ is small. This will provide the appearance of a reduction in the channel heat transfer coefficient when oscillations are added to a steady flow.

References

1 Watson, E. J., "Diffusion in Oscillatory Pipe Flow," *Journal of Fluid Mechanics*, Vol. 133, 1983, pp. 233–244.

2 Chatwin, P. C., "On the Longitudinal Dispersion of Passive Contaminant in Oscillatory Flows in Tubes," *Journal of Fluid Mechanics*, Vol. 71, Part 3, 1975, pp. 513–527.

3 Kurzweg, U. H., "Enhanced Heat Conduction in Oscillating Viscous Flows Within Parallel-Plate Channels," *Journal of Fluid Mechanics*, Vol. 156, 1985, pp. 291–300.

4 Joshi, C. H., Kamm, R. D., Drazen, J. M., and Slutsky, A. S., "An Experimental Study of Gas Exchange in Laminar Oscillatory Flow," *Journal of Fluid Mechanics*, Vol. 133, 1983, pp. 245–254.

5 Kurzweg, U. H., and de Zhao, L., "Heat Transfer by High-Frequency Oscillations: A New Hydrodynamic Technique for Achieving Large Effective Thermal Conductivities," *Physics of Fluids*, Vol. 27, No. 11, Nov. 1984, pp. 2624–2627.

6 Jaeger, M. J., and Kurzweg, U. H., "Determination of the Longitudinal Dispersion Coefficient in Flows Subjected to High-Frequency Oscillations," *Physics of Fluids*, Vol. 26, No. 6, June 1983, pp. 1380–1382.

7 Kurzweg, U. H., "Enhanced Heat Conduction in Fluids Subjected to Sinusoidal Oscillations," ASME JOURNAL OF HEAT TRANSFER, Vol. 107, 1985, pp. 459–462.

8 Siegel, R., and Perlmutter, M., "Heat Transfer for Pulsating Laminar Duct Flow," ASME JOURNAL OF HEAT TRANSFER, Vol. 84, No. 2, 1962, pp. 111–123.

9 Hwang, M. F., and Dybbs, A., "Heat Transfer in a Tube With Oscillatory Flow," ASME Paper No. 83-WA/HT-90.

10 Arpaci, V. S., and Larsen, P. S., *Convection Heat Transfer*, Prentice-Hall, Englewood Cliffs, NJ, 1984, pp. 246–252.

11 Siegel, R., and Sparrow, E. M., "Simultaneous Development of Velocity and Temperature Distributions in a Flat Duct With Uniform Wall Heating," *AIChE Journal*, Vol. 5, No. 1, 1959, pp. 73–75.

Laminar Heat Transfer in Annular Sector Ducts

H. M. Soliman[1]

Nomenclature

A_c = cross-sectional area = $\phi(r_2^2 - r_1^2)$
c_p = specific heat
d_h = hydraulic diameter = $4A_c/P$
dp/dx = axial pressure gradient
dt_b/dx = axial gradient of bulk temperature
D_h = dimensionless hydraulic diameter = $d_h/(2r_2)$
f = friction factor = $(d_h/4)(-dp/dx)/(\rho u_b^2/2)$
$\bar{h}$ = average heat transfer coefficient = $q/[P(t_w - t_b)]$
k = thermal conductivity
Nu = Nusselt number $\bar{h}\, d_h/k$
P = wetted perimeter = $2\phi(r_1 + r_2) + 2(r_2 - r_1)$
q = rate of heat input per unit length
r = radial coordinate
r_1 = inner radius of duct
r_2 = outer radius of duct
r_h = hydraulic radius = A_c/P
R = dimensionless radial coordinate = r/r_2
R_1 = radius ratio = r_1/r_2
R_h = dimensionless hydraulic radius = r_h/r_2
Re = Reynolds number = $\rho u_b d_h/\mu$
t = fluid temperature
t_b = fluid bulk temperature
t_w = wall temperature for the (H1) case and average wall temperature for the (H2) case
T = dimensionless temperature = $(t - t_w)/[(\rho c_p u_b r_2^2/k)(dt_b/dx)]$
T_b = dimensionless bulk temperature
u = fluid velocity
u_b = mean velocity
U = dimensionless velocity = $u/[(r_2^2/\mu)(-dp/dx)]$
U_b = dimensionless mean velocity
θ = angular coordinate
μ = dynamic viscosity
ρ = density
ϕ = half opening angle of duct

[1]Department of Mechanical Engineering, University of Manitoba, Winnipeg, Manitoba, Canada, R3T 2N2; Mem. ASME.

Contributed by the Heat Transfer Division for publication in the JOURNAL OF HEAT TRANSFER. Manuscript received by the Heat Transfer Division May 31, 1985.

1 Introduction

The continuing interest in compact heat exchangers has created the need for friction factor and Nusselt number data for different passage shapes. It has long been recognized that circular tube results are generally not applicable to noncircular passages even when the hydraulic diameter is used as the characteristic dimension. Hence, design data should be generated for each passage individually, and a good source of such information is Shah and London [1].

One duct geometry for which complete design information does not appear to be available in the open literature is that of annular sector ducts. Such configuration is encountered in multipassage internally finned tubes [2] and many other compact heat exchanger applications. The fluid flow problem for this configuraiton has been solved by Sparrow et al. [3], and more recently by Niida [4]. However, to the best of the author's knowledge, the heat transfer results are not available yet. The purpose of this note is to summarize the analysis and results of fluid flow and heat transfer in annular sector ducts.

2 Analysis

The geometry under consideration, together with the cylindrical coordinate system used in the analysis, is shown in Fig. 1. Due to symmetry, solutions are necessary only within the region $r_1 \le r \le r_2$ and $0 \le \theta \le \phi$. The analysis is limited to steady, laminar, fully developed, forced convection flow of incompressible, Newtonian fluids with constant properties. Axial conduction and viscous dissipation within the fluid are assumed negligible. Heat transfer results are sought for the case of uniform heat input axially using the two limiting boundary conditions of uniform wall temperature circumferentially and uniform wall heat flux circumferentially, referred to as the (H1) and (H2) boundary conditions, respectively [1, 5].

2.1 The Fluid Flow Problem. Under the conditions stated

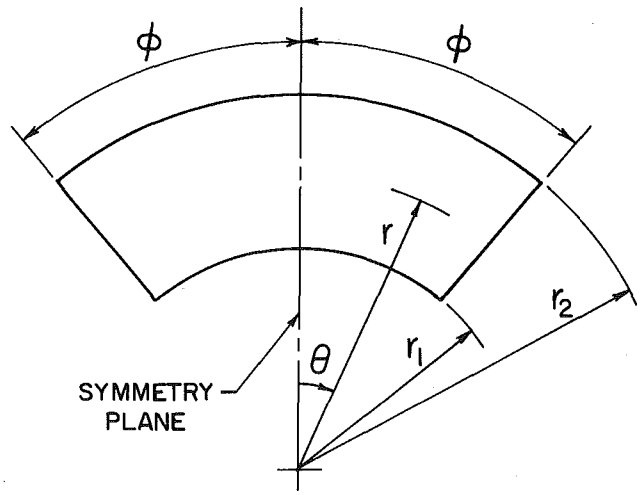

Fig. 1 Geometry and coordinate system

4 Joshi, C. H., Kamm, R. D., Drazen, J. M., and Slutsky, A. S., "An Experimental Study of Gas Exchange in Laminar Oscillatory Flow," *Journal of Fluid Mechanics*, Vol. 133, 1983, pp. 245–254.

5 Kurzweg, U. H., and de Zhao, L., "Heat Transfer by High-Frequency Oscillations: A New Hydrodynamic Technique for Achieving Large Effective Thermal Conductivities," *Physics of Fluids*, Vol. 27, No. 11, Nov. 1984, pp. 2624–2627.

6 Jaeger, M. J., and Kurzweg, U. H., "Determination of the Longitudinal Dispersion Coefficient in Flows Subjected to High-Frequency Oscillations," *Physics of Fluids*, Vol. 26, No. 6, June 1983, pp. 1380–1382.

7 Kurzweg, U. H., "Enhanced Heat Conduction in Fluids Subjected to Sinusoidal Oscillations," ASME JOURNAL OF HEAT TRANSFER, Vol. 107, 1985, pp. 459–462.

8 Siegel, R., and Perlmutter, M., "Heat Transfer for Pulsating Laminar Duct Flow," ASME JOURNAL OF HEAT TRANSFER, Vol. 84, No. 2, 1962, pp. 111–123.

9 Hwang, M. F., and Dybbs, A., "Heat Transfer in a Tube With Oscillatory Flow," ASME Paper No. 83-WA/HT-90.

10 Arpaci, V. S., and Larsen, P. S., *Convection Heat Transfer*, Prentice-Hall, Englewood Cliffs, NJ, 1984, pp. 246–252.

11 Siegel, R., and Sparrow, E. M., "Simultaneous Development of Velocity and Temperature Distributions in a Flat Duct With Uniform Wall Heating," *AIChE Journal*, Vol. 5, No. 1, 1959, pp. 73–75.

Laminar Heat Transfer in Annular Sector Ducts

H. M. Soliman[1]

Nomenclature

A_c = cross-sectional area = $\phi(r_2^2 - r_1^2)$
c_p = specific heat
d_h = hydraulic diameter = $4A_c/P$
dp/dx = axial pressure gradient
dt_b/dx = axial gradient of bulk temperature
D_h = dimensionless hydraulic diameter = $d_h/(2r_2)$
f = friction factor = $(d_h/4)(-dp/dx)/(\rho u_b^2/2)$
$\bar{h}$ = average heat transfer coefficient = $q/[P(t_w - t_b)]$
k = thermal conductivity
Nu = Nusselt number $\bar{h}\, d_h/k$
P = wetted perimeter = $2\phi(r_1 + r_2) + 2(r_2 - r_1)$
q = rate of heat input per unit length
r = radial coordinate
r_1 = inner radius of duct
r_2 = outer radius of duct
r_h = hydraulic radius = A_c/P
R = dimensionless radial coordinate = r/r_2
R_1 = radius ratio = r_1/r_2
R_h = dimensionless hydraulic radius = r_h/r_2
Re = Reynolds number = $\rho u_b d_h/\mu$
t = fluid temperature
t_b = fluid bulk temperature
t_w = wall temperature for the (H1) case and average wall temperature for the (H2) case
T = dimensionless temperature = $(t - t_w)/[(\rho c_p u_b r_2^2/k)(dt_b/dx)]$
T_b = dimensionless bulk temperature
u = fluid velocity
u_b = mean velocity
U = dimensionless velocity = $u/[(r_2^2/\mu)(-dp/dx)]$
U_b = dimensionless mean velocity
θ = angular coordinate
μ = dynamic viscosity
ρ = density
ϕ = half opening angle of duct

[1]Department of Mechanical Engineering, University of Manitoba, Winnipeg, Manitoba, Canada, R3T 2N2; Mem. ASME.

Contributed by the Heat Transfer Division for publication in the JOURNAL OF HEAT TRANSFER. Manuscript received by the Heat Transfer Division May 31, 1985.

1 Introduction

The continuing interest in compact heat exchangers has created the need for friction factor and Nusselt number data for different passage shapes. It has long been recognized that circular tube results are generally not applicable to noncircular passages even when the hydraulic diameter is used as the characteristic dimension. Hence, design data should be generated for each passage individually, and a good source of such information is Shah and London [1].

One duct geometry for which complete design information does not appear to be available in the open literature is that of annular sector ducts. Such configuration is encountered in multipassage internally finned tubes [2] and many other compact heat exchanger applications. The fluid flow problem for this configuraiton has been solved by Sparrow et al. [3], and more recently by Niida [4]. However, to the best of the author's knowledge, the heat transfer results are not available yet. The purpose of this note is to summarize the analysis and results of fluid flow and heat transfer in annular sector ducts.

2 Analysis

The geometry under consideration, together with the cylindrical coordinate system used in the analysis, is shown in Fig. 1. Due to symmetry, solutions are necessary only within the region $r_1 \le r \le r_2$ and $0 \le \theta \le \phi$. The analysis is limited to steady, laminar, fully developed, forced convection flow of incompressible, Newtonian fluids with constant properties. Axial conduction and viscous dissipation within the fluid are assumed negligible. Heat transfer results are sought for the case of uniform heat input axially using the two limiting boundary conditions of uniform wall temperature circumferentially and uniform wall heat flux circumferentially, referred to as the (H1) and (H2) boundary conditions, respectively [1, 5].

2.1 The Fluid Flow Problem. Under the conditions stated

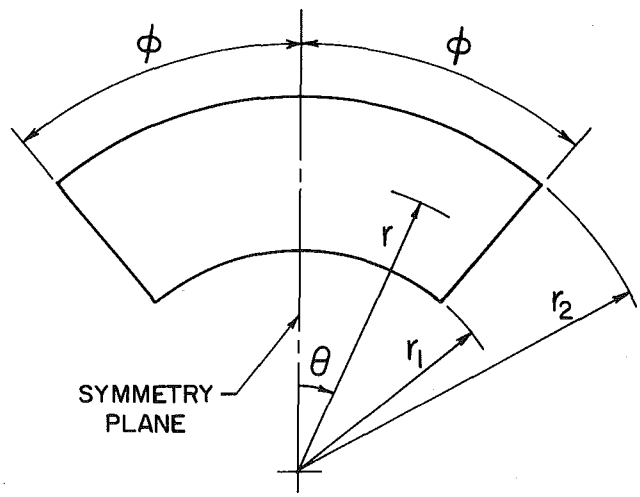

Fig. 1 Geometry and coordinate system

above, the governing momentum equation using the dimensionless variables defined in the Nomenclature can be written as

$$\nabla^2 U = -1 \tag{1}$$

The applicable boundary conditions are; $U = 0$ along the solid boundaries and $\partial U/\partial\theta = 0$ along the symmetry plane. Using the method of separation of variables a solution for equation (1) satisfying all boundary conditions was developed in the form

$$U = \sum_{j=1}^{\infty} 2(-1)^j \cos(\epsilon_j\theta)[-R^2 + \alpha_j R^{\epsilon_j} + \beta_j (R/R_1)^{-\epsilon_j}]/[\phi\epsilon_j(\epsilon_j^2 - 4)] \tag{2}$$

where

$$\epsilon_j = \pi(2j-1)/(2\phi) \tag{3a}$$

$$\alpha_j = (R_1^{\epsilon_j+2} - 1)/(R_1^{2\epsilon_j} - 1) \tag{3b}$$

and

$$\beta_j = (R_1^{\epsilon_j} - R_1^2)/(R_1^{2\epsilon_j} - 1) \tag{3c}$$

Using the definitions of friction factor f and Reynolds number Re given in the Nomenclature, the product fRe based on the hydraulic diameter reduces to

$$f\mathrm{Re} = 2D_h^2/U_b \tag{4}$$

where the dimensionless mean velocity is given by

$$U_b = 2[\int_0^{\phi}\int_{R_1}^{1} UR\, dR\, d\theta]/[\phi(1 - R_1^2)] \tag{5}$$

Substituting equation (2) into equation (5), an expression for U_b as a function of R_1 and ϕ can be easily obtained with which fRe can be evaluated using equation (4). It must be pointed out that while solution (2) is different from the one developed in [3], both series solutions were found to produce practically the same numerical values of fRe. One advantage to solution (2) is its fast rate of convergence. For an accuracy of 0.01 percent in the fRe values only ten terms are necessary at $R_1 = 0.05$ and $\phi = 2.5$ deg. However, the number of terms necessary for the same accuracy was found to increase as R_1 or ϕ increased. For example, 85 terms were required at $R_1 = 0.95$ and $\phi = 175$ deg.

2.2 The Heat Transfer Problem. The dimensionless energy equation applicable to both (H1) and (H2) boundary conditions can be expressed as

$$\nabla^2 T = U/U_b \tag{6}$$

For the (H1) case, the boundary conditions are: $T = 0$ along the solid boundaries and $\partial T/\partial\theta = 0$ along the symmetry plane. The following temperature distribution was developed using the method of separation of variables:

$$T = \sum_{j=1}^{\infty} \frac{(-1)^j \cos(\epsilon_j\theta)}{\phi U_b \epsilon_j(\epsilon_j^2 - 4)}\left[\frac{2R^4}{\epsilon_j^2 - 16} + \frac{\alpha_j R^{\epsilon_j+2}}{2\epsilon_j + 2} - \frac{\beta_j R^2 (R/R_1)^{-\epsilon_j}}{2\epsilon_j - 2} + \frac{\gamma_j R^{\epsilon_j} + \lambda_j (R/R_1)^{-\epsilon_j}}{1 - R_1^{2\epsilon_j}}\right] \tag{7}$$

where

$$\gamma_j = -\frac{2(1 - R_1^{\epsilon_j+4})}{\epsilon_j^2 - 16} - \frac{\alpha_j(1 - R_1^{2\epsilon_j+2})}{2\epsilon_j + 2} + \frac{\beta_j R_1^{\epsilon_j}(1 - R_1^2)}{2\epsilon_j - 2} \tag{8a}$$

and

$$\lambda_j = -\frac{2(R_1^4 - R_1^{\epsilon_j})}{\epsilon_j^2 - 16} + \frac{\alpha_j R_1^{\epsilon_j}(1 - R_1^2)}{2\epsilon_j + 2} + \frac{\beta_j(R_1^2 - R_1^{2\epsilon_j})}{2\epsilon_j - 2} \tag{8b}$$

The conventional definition of Nusselt number based on the hydraulic diameter ($\mathrm{Nu} = \bar{h}\, d_h/k$) reduces to the following dimensionless form

$$\mathrm{Nu} = -D_h^2/T_b \tag{9}$$

where

$$T_b = 2[\int_0^{\phi}\int_{R_1}^{1} UTR\, dR\, d\theta]/[\phi U_b(1 - R_1^2)] \tag{10}$$

Dimensionless velocity and temperature distributions expressed by equations (2) and (7), respectively, were substituted in equation (10) and an analytical (series) expression for T_b as a function of R_1 and ϕ was obtained through which values of Nu_{H1} were calculated using the definition (9). The resulting expression is a fast-converging one; for an accuracy of 0.01 percent in Nu_{H1} only three terms were necessary at $R_1 = 0.05$, $\phi = 2.5$ deg, and the number of necessary terms increased to 57 at $R_1 = 0.95$, $\phi = 175$ deg.

The (H2) case is much more difficult to solve. Equation (6) still applies, however the solution for the temperature distribution must satisfy these boundary conditions

$$\partial T/\partial R = R_h \quad \text{at } R = 1, 0 \le \theta < \phi \tag{11a}$$

$$\partial T/\partial R = -R_h \quad \text{at } R = R_1, 0 \le \theta < \phi \tag{11b}$$

$$\partial T/R\partial\theta = R_h \quad \text{at } \theta = \phi, R_1 < R < 1 \tag{11c}$$

and

$$\partial T/\partial\theta = 0 \quad \text{at } \theta = 0, R_1 < R < 1 \tag{11d}$$

Several methods of solution were suggested in the literature and the least-squares matching technique [6] was adopted here due to its computational efficiency. A solution was assumed in the following form

$$T = A_0 + A_1 R\cos(\theta) + A_2 R^4\cos(4\theta) + \sum_{j=1}^{N}[B_j R^{2\epsilon_j} + C_j(R/R_1)^{-2\epsilon_j}]\cos(2\epsilon_j\theta) + \sum_{j=1}^{N} D_j R^{\epsilon_j+2}\cos(\epsilon_j + 2)\theta + \sum_{j=1}^{N} E_j(R/R_1)^{-\epsilon_j+2}\cos(\epsilon_j - 2)\theta + \sum_{j=1}^{\infty}\frac{(-1)^j\cos(\epsilon_j\theta)}{\phi U_b\epsilon_j(\epsilon_j^2 - 4)}\left[\frac{2R^4}{\epsilon_j^2 - 16} + \frac{\alpha_j R^{\epsilon_j+2}}{2\epsilon_j + 2} - \frac{\beta_j R^2(R/R_1)^{-\epsilon_j}}{2\epsilon_j - 2}\right] \tag{12}$$

where A_0, A_1, A_2, B_j, C_j, D_j, and E_j are arbitrary constants. This solution satisfies energy equation (6) and boundary condition (11d). In order to satisfy the remaining boundary conditions, M points were selected on the solid boundaries and solution (12) was substituted in equations (11a), (11b), and (11c) thus resulting in M equations in the $(4N+2)$ unknowns A_1, A_2, B_j, C_j, D_j, and E_j. To ensure an accurate fit, M was selected to be equal to 10 N. The remaining unknown A_0 was determined by imposing the condition that the line integral of T along the solid boundaries be equal to zero. With all the unknown constants in solution (12) now determined the dimensionless bulk temperature and Nusselt number were obtained from equations (10) and (9), respectively.

Numerical experimentation was conducted to determine the appropriate value of N for accurate results. It was found that for small values of R_1 and ϕ, good accuracy can be achieved with $N = 5$, but higher values of N become necessary at large values of R_1 or ϕ. Due to computer time limitation, it was decided to perform all present computations with $N = 15$ which still allowed for a reasonably wide range of geometries to be covered. Based on our numerical experimentation with different values of N it is believed that the Nu_{H2} values presented later are at least within ± 1 percent accuracy.

Table 1 Values of Nu_{H1}

R_1	2ϕ=5°	10°	15°	20°	30°	40°	50°	60°	90°
0.05	2.487	2.668	2.825	2.961	3.181	3.349	3.479	3.581	3.777
0.10	2.723	2.896	3.041	3.163	3.354	3.490	3.589	3.660	3.782
0.15	2.979	3.137	3.264	3.367	3.516	3.611	3.669	3.704	3.770
0.20	3.254	3.387	3.488	3.564	3.656	3.697	3.711	3.715	3.761
0.25	3.546	3.643	3.706	3.742	3.761	3.742	3.716	3.702	3.773
0.30	3.850	3.893	3.903	3.888	3.821	3.746	3.69[illegible]	3.685	3.815
0.35	4.159	4.126	4.065	3.988	3.832	3.721	3.673	3.679	3.891
0.40	4.460	4.326	4.177	4.031	3.802	3.683	3.658	3.697	4.006
0.45	4.739	4.474	4.226	4.016	3.747	3.650	3.667	3.750	4.159
0.50	4.976	4.554	4.207	3.951	3.686	3.640	3.712	3.844	4.351
0.55	5.151	4.555	4.126	3.854	3.639	3.666	3.803	3.986	4.584
0.60	5.243	4.471	3.997	3.747	3.627	3.743	3.948	4.183	4.855
0.65	5.232	4.312	3.848	3.658	3.668	3.884	4.159	4.440	5.165
0.70	5.101	4.098	3.709	3.616	3.785	4.106	4.446	4.763	5.510
0.75	4.843	3.867	3.621	3.658	4.006	4.429	4.820	5.158	5.889
0.80	4.466	3.675	3.641	3.834	4.371	4.875	5.290	5.624	6.299
0.85	4.018	3.616	3.861	4.230	4.928	5.463	5.861	6.163	6.739
0.90	3.648	3.889	4.462	4.979	5.726	6.208	6.537	6.775	7.208
0.95	3.917	5.028	5.773	6.250	6.809	7.123	7.324	7.464	7.706

R_1	120°	150°	180°	210°	240°	270°	300°	330°	350°
0.05	3.887	3.965	4.039	4.117	4.201	4.289	4.378	4.468	4.527
0.10	3.863	3.956	4.067	4.192	4.322	4.453	4.581	4.704	4.782
0.15	3.861	3.994	4.154	4.323	4.490	4.652	4.804	4.945	5.034
0.20	3.893	4.079	4.284	4.490	4.685	4.867	5.034	5.186	5.279
0.25	3.964	4.203	4.448	4.683	4.897	5.092	5.266	5.422	5.516
0.30	4.072	4.360	4.639	4.894	5.120	5.320	5.496	5.652	5.745
0.35	4.215	4.546	4.850	5.118	5.348	5.549	5.723	5.876	5.966
0.40	4.392	4.757	5.077	5.351	5.580	5.777	5.946	6.093	6.179
0.45	4.600	4.989	5.316	5.591	5.813	6.003	6.164	6.305	6.385
0.50	4.836	5.239	5.565	5.835	6.045	6.225	6.377	6.510	6.583
0.55	5.098	5.503	5.820	6.083	6.276	6.444	6.585	6.709	6.775
0.60	5.383	5.778	6.080	6.334	6.505	6.660	6.788	6.904	6.960
0.65	5.687	6.064	6.344	6.588	6.732	6.871	6.986	7.093	7.138
0.70	6.010	6.357	6.611	6.845	6.956	7.078	7.178	7.279	7.311
0.75	6.348	6.658	6.880	7.106	7.177	7.281	7.366	7.460	7.477
0.80	6.700	6.964	7.150	7.368	7.394	7.479	7.548	7.638	7.638
0.85	7.065	7.275	7.420	7.628	7.609	7.673	7.726	7.810	7.794
0.90	7.443	7.590	7.691	7.884	7.820	7.864	7.899	7.976	7.945
0.95	7.832	7.909	7.961	8.132	8.027	8.048	8.067	8.135	8.090

Table 2 Values of Nu_{H2}

R_1	2ϕ=10°	15°	20°	30°	40°	60°	120°
0.05	0.09412	0.2288	0.4295	1.013	1.671	2.629	3.032
0.10	0.1097	0.2678	0.5059	1.187	1.939	2.818	3.020
0.15	0.1293	0.3203	0.6062	1.460	2.277	2.946	3.007
0.20	0.1552	0.3889	0.7516	1.839	2.483	3.022	2.996
0.25	0.1900	0.4877	0.9824	2.253	2.803	3.059	2.986
0.30	0.2393	0.6414	1.379	2.587	2.941	3.073	2.977
0.35	0.3152	0.9186	1.937	2.809	3.021	3.073	2.967
0.40	0.4414	1.436	2.427	2.945	3.061	3.066	2.956
0.45	0.6839	2.111	2.721	3.022	3.078	3.054	2.944
0.50	1.187	2.580	2.893	3.062	3.080	3.039	2.915
0.55	1.999	2.820	2.993	3.079	3.074	3.020	2.794
0.60	2.602	2.950	3.047	3.081	3.060	2.997	2.670
0.65	2.851	3.024	3.074	3.073	3.038	2.970	2.581
0.70	2.967	3.063	3.082	3.052	3.008	2.956	
0.75	3.032	3.079	3.072	3.018	2.968		
0.80	3.066	3.069	3.036	2.967			
0.85	3.065	3.023	2.963				
0.90	2.979	2.870					
0.95	4.852						

3 Results and Discussion

Values of fRe and Nu_{H1} were obtained for the geometric range $0.05 \leq R_1 \leq 0.95$ and 2.5 deg $\leq \phi \leq$ 175 deg. The fRe results were compared with those of Sparrow et al. [3] (listed in Table 79 [1]) and Niida [4]. Agreement to four significant figures was noted for most of the geometric range, and the maximum deviation between the two sets of values came within ± 0.1 percent. Hence, this segment of the results will not be presented here. The present Nu_{H1} results are listed in Table 1.

For the H2 boundary condition, accurate results were obtained for the range $0.05 \leq R_1 \leq 0.95$ and 2.5 deg $\leq \phi \leq$ 60 deg using $N = 15$. These results are listed in Table 2. Higher values of N are necessary if the results are to be extended to $\phi > 60$ deg, particularly with large values of R_1.

As expected, Nu_{H1} is always higher than Nu_{H2} and both can deviate substantially from Nu = 4.364 for circular tubes. This demonstrates the inadequacy of extending the smooth tube results to noncircular ducts through the use of hydraulic diameter. The results in Tables 1 and 2 exhibit local maxima and minima as R_1 and/or ϕ vary. These optimum points should not be attributed solely to heat transfer performance; the fact that Nusselt number is based on the hydraulic diameter is a factor and thus easy explanation of these optimum points is not possible.

Quantitative comparisons are not possible due to lack of similar results. However, some trends can be seen such as: (*a*) At any ϕ the present results appear to be approaching those of Eckert et al. [7] for circular sector ducts as R_1 approaches zero; (*b*) whenever $\phi\,(1 + R_1) = (1 - R_1)$, the present results become close to $Nu_{H1} = 3.608$ and $Nu_{H2} = 3.091$ for square ducts; and (*c*) for large values of R_1 and ϕ, the present values of Nu_{H1} appear to be approaching 8.235 for parallel plates.

Acknowledgments

Financial assistance provided by the Natural Sciences and Engineering Research Council of Canada is gratefully acknowledged.

References

1 Shah, R. K., and London, A. L., *Laminar Flow Forced Convection in Ducts*, Academic Press, New York, 1978.

2 Carnavos, T. C., "Cooling Air in Turbulent Flow With Multi-passage Internally Finned Tubes," ASME Paper No. 78-WA/HT-52, 1978.

3 Sparrow, E. M., Chen, T. S., and Jonsson, V. K., "Laminar Flow and Pressure Drop in Internally Finined Annular Ducts," *International Journal of Heat Mass Transfer*, Vol. 7, 1964, pp. 583–585.

4 Niida, T., "Analytical Solution for the Velocity Distribution in Laminar Flow in an Annular-Sector Duct," *International Chemical Engineering*, Vol. 20, 1980, pp. 258–265.

5 Shah, R. K., and London, A. L., "Thermal Boundary Conditions and Some Solutions for Laminar Duct Flow Forced Convection," ASME JOURNAL OF HEAT TRANSFER, Vol. 96, 1974, pp. 159–165.

6 Shah, R. K., "Laminar Flow Friction and Forced Convection Heat Transfer in Ducts of Arbitrary Geometry," *International Journal of Heat and Mass Transfer*, Vol. 18, 1975, pp. 849–862.

7 Eckert, E. R. G., Irvine, T. F., and Yen, J. T., "Local Laminar Heat Transfer in Wedge-Shaped Passages," Trans. ASME, Vol. 80, 1958, pp. 1433–1438.

Thermal Design Considerations in Vertical-Channel Natural Convection

J. R. Leith[1]

Introduction

Laminar natural convection in vertical channels has received considerable attention in the literature, principally because of its value as a simplified mathematical model for electronics cooling. Bar-Cohen and Rohsenow [1] applied the

[1]Department of Mechanical Engineering, University of New Mexico, Albuquerque, NM 87131; Assoc. Mem. ASME.

Contributed by the Heat Transfer Division for publication in the JOURNAL OF HEAT TRANSFER. Manuscript received by the Heat Transfer Division October 15, 1985.

Table 1 Values of Nu_{H1}

R_1	2ϕ=5°	10°	15°	20°	30°	40°	50°	60°	90°
0.05	2.487	2.668	2.825	2.961	3.181	3.349	3.479	3.581	3.777
0.10	2.723	2.896	3.041	3.163	3.354	3.490	3.589	3.660	3.782
0.15	2.979	3.137	3.264	3.367	3.516	3.611	3.669	3.704	3.770
0.20	3.254	3.387	3.488	3.564	3.656	3.697	3.711	3.715	3.761
0.25	3.546	3.643	3.706	3.742	3.761	3.742	3.716	3.702	3.773
0.30	3.850	3.893	3.903	3.888	3.821	3.746	3.69[illegible]	3.685	3.815
0.35	4.159	4.126	4.065	3.988	3.832	3.721	3.673	3.679	3.891
0.40	4.460	4.326	4.177	4.031	3.802	3.683	3.658	3.697	4.006
0.45	4.739	4.474	4.226	4.016	3.747	3.650	3.667	3.750	4.159
0.50	4.976	4.554	4.207	3.951	3.686	3.640	3.712	3.844	4.351
0.55	5.151	4.555	4.126	3.854	3.639	3.666	3.803	3.986	4.584
0.60	5.243	4.471	3.997	3.747	3.627	3.743	3.948	4.183	4.855
0.65	5.232	4.312	3.848	3.658	3.668	3.884	4.159	4.440	5.165
0.70	5.101	4.098	3.709	3.616	3.785	4.106	4.446	4.763	5.510
0.75	4.843	3.867	3.621	3.658	4.006	4.429	4.820	5.158	5.889
0.80	4.466	3.675	3.641	3.834	4.371	4.875	5.290	5.624	6.299
0.85	4.018	3.616	3.861	4.230	4.928	5.463	5.861	6.163	6.739
0.90	3.648	3.889	4.462	4.979	5.726	6.208	6.537	6.775	7.208
0.95	3.917	5.028	5.773	6.250	6.809	7.123	7.324	7.464	7.706

R_1	120°	150°	180°	210°	240°	270°	300°	330°	350°
0.05	3.887	3.965	4.039	4.117	4.201	4.289	4.378	4.468	4.527
0.10	3.863	3.956	4.067	4.192	4.322	4.453	4.581	4.704	4.782
0.15	3.861	3.994	4.154	4.323	4.490	4.652	4.804	4.945	5.034
0.20	3.893	4.079	4.284	4.490	4.685	4.867	5.034	5.186	5.279
0.25	3.964	4.203	4.448	4.683	4.897	5.092	5.266	5.422	5.516
0.30	4.072	4.360	4.639	4.894	5.120	5.320	5.496	5.652	5.745
0.35	4.215	4.546	4.850	5.118	5.348	5.549	5.723	5.876	5.966
0.40	4.392	4.757	5.077	5.351	5.580	5.777	5.946	6.093	6.179
0.45	4.600	4.989	5.316	5.591	5.813	6.003	6.164	6.305	6.385
0.50	4.836	5.239	5.565	5.835	6.045	6.225	6.377	6.510	6.583
0.55	5.098	5.503	5.820	6.083	6.276	6.444	6.585	6.709	6.775
0.60	5.383	5.778	6.080	6.334	6.505	6.660	6.788	6.904	6.960
0.65	5.687	6.064	6.344	6.588	6.732	6.871	6.986	7.093	7.138
0.70	6.010	6.357	6.611	6.845	6.956	7.078	7.178	7.279	7.311
0.75	6.348	6.658	6.880	7.106	7.177	7.281	7.366	7.460	7.477
0.80	6.700	6.964	7.150	7.368	7.394	7.479	7.548	7.638	7.638
0.85	7.065	7.275	7.420	7.628	7.609	7.673	7.726	7.810	7.794
0.90	7.443	7.590	7.691	7.884	7.820	7.864	7.899	7.976	7.945
0.95	7.832	7.909	7.961	8.132	8.027	8.048	8.067	8.135	8.090

Table 2 Values of Nu_{H2}

R_1	2ϕ=10°	15°	20°	30°	40°	60°	120°
0.05	0.09412	0.2288	0.4295	1.013	1.671	2.629	3.032
0.10	0.1097	0.2678	0.5059	1.187	1.939	2.818	3.020
0.15	0.1293	0.3203	0.6062	1.460	2.277	2.946	3.007
0.20	0.1552	0.3889	0.7516	1.839	2.483	3.022	2.996
0.25	0.1900	0.4877	0.9824	2.253	2.803	3.059	2.986
0.30	0.2393	0.6414	1.379	2.587	2.941	3.073	2.977
0.35	0.3152	0.9186	1.937	2.809	3.021	3.073	2.967
0.40	0.4414	1.436	2.427	2.945	3.061	3.066	2.956
0.45	0.6839	2.111	2.721	3.022	3.078	3.054	2.944
0.50	1.187	2.580	2.893	3.062	3.080	3.039	2.915
0.55	1.999	2.820	2.993	3.079	3.074	3.020	2.794
0.60	2.602	2.950	3.047	3.081	3.060	2.997	2.670
0.65	2.851	3.024	3.074	3.073	3.038	2.970	2.581
0.70	2.967	3.063	3.082	3.052	3.008	2.956	
0.75	3.032	3.079	3.072	3.018	2.968		
0.80	3.066	3.069	3.036	2.967			
0.85	3.065	3.023	2.963				
0.90	2.979	2.870					
0.95	4.852						

3 Results and Discussion

Values of fRe and Nu_{H1} were obtained for the geometric range $0.05 \leq R_1 \leq 0.95$ and 2.5 deg $\leq \phi \leq$ 175 deg. The fRe results were compared with those of Sparrow et al. [3] (listed in Table 79 [1]) and Niida [4]. Agreement to four significant figures was noted for most of the geometric range, and the maximum deviation between the two sets of values came within ± 0.1 percent. Hence, this segment of the results will not be presented here. The present Nu_{H1} results are listed in Table 1.

For the H2 boundary condition, accurate results were obtained for the range $0.05 \leq R_1 \leq 0.95$ and 2.5 deg $\leq \phi \leq$ 60 deg using $N = 15$. These results are listed in Table 2. Higher values of N are necessary if the results are to be extended to $\phi > 60$ deg, particularly with large values of R_1.

As expected, Nu_{H1} is always higher than Nu_{H2} and both can deviate substantially from Nu = 4.364 for circular tubes. This demonstrates the inadequacy of extending the smooth tube results to noncircular ducts through the use of hydraulic diameter. The results in Tables 1 and 2 exhibit local maxima and minima as R_1 and/or ϕ vary. These optimum points should not be attributed solely to heat transfer performance; the fact that Nusselt number is based on the hydraulic diameter is a factor and thus easy explanation of these optimum points is not possible.

Quantitative comparisons are not possible due to lack of similar results. However, some trends can be seen such as: (*a*) At any ϕ the present results appear to be approaching those of Eckert et al. [7] for circular sector ducts as R_1 approaches zero; (*b*) whenever $\phi\ (1 + R_1) = (1 - R_1)$, the present results become close to $Nu_{H1} = 3.608$ and $Nu_{H2} = 3.091$ for square ducts; and (*c*) for large values of R_1 and ϕ, the present values of Nu_{H1} appear to be approaching 8.235 for parallel plates.

Acknowledgments

Financial assistance provided by the Natural Sciences and Engineering Research Council of Canada is gratefully acknowledged.

References

1 Shah, R. K., and London, A. L., *Laminar Flow Forced Convection in Ducts*, Academic Press, New York, 1978.

2 Carnavos, T. C., "Cooling Air in Turbulent Flow With Multi-passage Internally Finned Tubes," ASME Paper No. 78-WA/HT-52, 1978.

3 Sparrow, E. M., Chen, T. S., and Jonsson, V. K., "Laminar Flow and Pressure Drop in Internally Finined Annular Ducts," *International Journal of Heat Mass Transfer*, Vol. 7, 1964, pp. 583–585.

4 Niida, T., "Analytical Solution for the Velocity Distribution in Laminar Flow in an Annular-Sector Duct," *International Chemical Engineering*, Vol. 20, 1980, pp. 258–265.

5 Shah, R. K., and London, A. L., "Thermal Boundary Conditions and Some Solutions for Laminar Duct Flow Forced Convection," ASME JOURNAL OF HEAT TRANSFER, Vol. 96, 1974, pp. 159–165.

6 Shah, R. K., "Laminar Flow Friction and Forced Convection Heat Transfer in Ducts of Arbitrary Geometry," *International Journal of Heat and Mass Transfer*, Vol. 18, 1975, pp. 849–862.

7 Eckert, E. R. G., Irvine, T. F., and Yen, J. T., "Local Laminar Heat Transfer in Wedge-Shaped Passages," Trans. ASME, Vol. 80, 1958, pp. 1433–1438.

Thermal Design Considerations in Vertical-Channel Natural Convection

J. R. Leith[1]

Introduction

Laminar natural convection in vertical channels has received considerable attention in the literature, principally because of its value as a simplified mathematical model for electronics cooling. Bar-Cohen and Rohsenow [1] applied the

[1]Department of Mechanical Engineering, University of New Mexico, Albuquerque, NM 87131; Assoc. Mem. ASME.

Contributed by the Heat Transfer Division for publication in the JOURNAL OF HEAT TRANSFER. Manuscript received by the Heat Transfer Division October 15, 1985.

correlation technique of Churchill and Usagi [2] to obtain predictions for heat transfer in the vertical channel configuration. The correlating equations obtained in [1] gave favorable comparison with previous experimental data and numerical solutions.

The symmetric uniform wall heat flux case from [1] is considered in the present note. Maximum channel wall temperature rise, as predicted from the correlating equation, is expressed in terms of dimensional variables. This gives an alternate representation of results for design purposes.

Analysis

Results for the symmetric uniform wall heat flux case in air determined by Bar-Cohen and Rohsenow [1] are given by

$$\mathrm{Nu}_L = [48/\mathrm{Ra} + 2.51/(\mathrm{Ra}^{0.4})]^{-0.5} \tag{1}$$

in which Nu_L is the Nusselt number at the channel exit, and Ra is the channel Rayleigh number defined by $\mathrm{Ra} = g\beta qb^5/Lk\nu\alpha$. The Rayleigh number definition corresponds to a channel with plate spacing b and length L, with uniform flux q applied to each plate. Fluid properties β, k, ν, and α are respectively the thermal expansion, thermal conductivity, kinematic viscosity, and thermal diffusivity.

Maximum channel wall temperature rise predicted by equation (1) for the symmetric uniform flux case is simply

$$T_{w,L} - T_0 = \frac{qb}{k}\left(\frac{48}{\mathrm{Ra}} + \frac{2.51}{\mathrm{Ra}^{0.4}}\right)^{0.5} \tag{2}$$

by definition of dimensionless temperature. In equation (2), $T_{w,L}$ is the plate temperature at the channel exit and T_0 is the uniform inlet temperature. A parametric interpretation for these results can be obtained by expressing Rayleigh number in the form $\mathrm{Ra} = (g\beta/\nu\alpha)(qb/k)b^4/L$. The group property $g\beta/\nu\alpha$ is a nonlinear function of mean temperature (assuming fixed external pressure conditions). If the mean temperature is fixed, maximum channel wall temperature rise can be expressed functionally as

$$T_{w,L} - T_0 = \frac{qb}{k} F_1\left(\frac{qb}{k}, \mathrm{Ra}\right) \tag{3}$$

or alternately as

$$T_{w,L} - T_0 = \frac{qb}{k} F_2\left(\frac{b^4}{L}, \mathrm{Ra}\right) \tag{4}$$

Equations (3) and (4) describe two families of curves, which can be exploited numerically to derive a carpet plot for prediction of $T_{w,L} - T_0$ at constant mean temperature. In other words, an equivalent functional form of equations (3) and (4) is given by

$$T_{w,L} - T_0 = \frac{qb}{k} F\left(\frac{qb}{k}, \frac{b^4}{L}\right) \tag{5}$$

Any one of equations (3), (4), or (5) is thus sufficient to give the channel wall temperature rise, if mean temperature is assumed.

Effects of variable mean temperature can be determined if Rayleigh number is expressed in the form $\mathrm{Ra} = (g\beta/k\nu\alpha)qb^5/L$. This gives dimensionless temperature rise as

$$\frac{T_{w,L} - T_0}{qb/k} = f\left(\frac{qb^5}{L}, \bar{T}\right) \tag{6}$$

In practice, the group properties $g\beta/\nu\alpha$ and $g\beta/k\nu\alpha$ can be expressed as simple functions of the mean temperature $\bar{T}$ by curve-fitting established property data (e.g., by quadratic regression).

Results and Discussion

Graphic results of the parametric forms for wall temperature rise (equations (3)–(5)) are shown in Figs. 1 and 2,

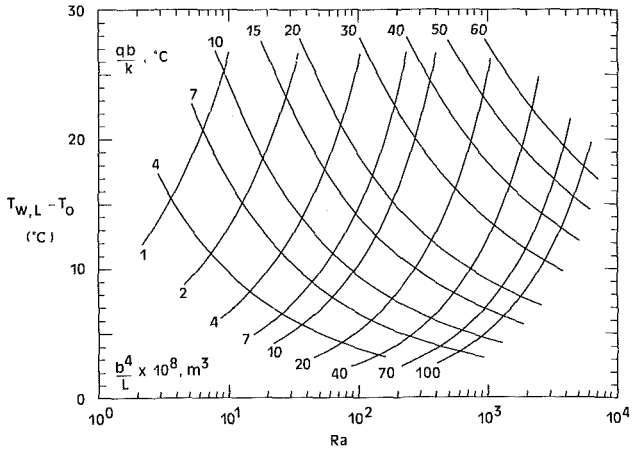

Fig. 1 Maximum wall temperature rise in symmetric constant flux channel; sea-level air at $\bar{T}$ = 30°C

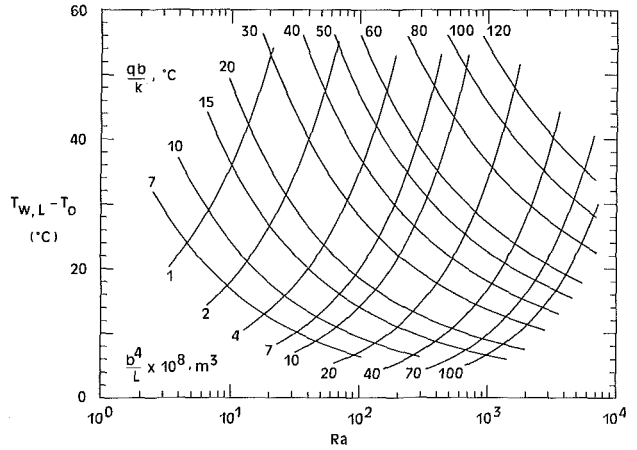

Fig. 2 Maximum wall temperature rise in symmetric constant flux channel; sea-level air at $\bar{T}$ = 50°C

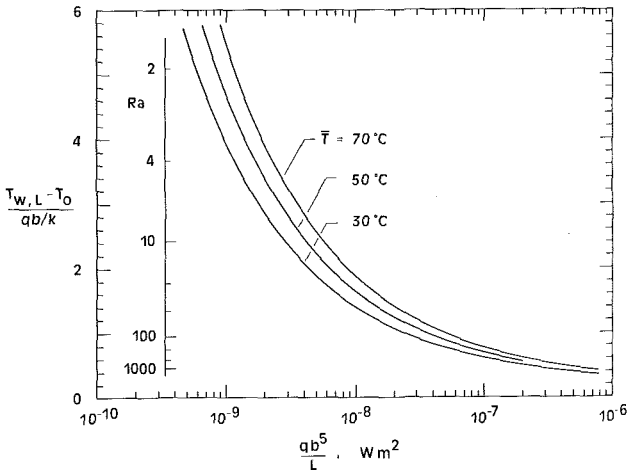

Fig. 3 Effects of mean temperature variation on dimensionless temperature rise

corresponding to sea level air at assumed mean temperatures of 30°C and 50°C. For increasing qb/k, Figs. 1 and 2 give the required increase in b^4/L (e.g., increased plate spacing) necessary to maintain a constant channel wall temperature rise. For constant qb/k, Figs. 1 and 2 also give the expected temperature rise as a function of Rayleigh number. The latter interpretation is evident from the form of equation (3), which

indicates that the temperature dependence of thermophysical properties is defined in the choice of qb/k and Ra.

Effects of increasing mean temperature are illustrated in Fig. 3, which shows the dimensionless channel wall temperature rise as expressed in the parametric form of equation (6). Included in Fig. 3 is a Rayleigh number scale, calculated from equation (1). Inspection of Fig. 3 indicates an increased channel wall temperature rise for increasing mean temperature. This is a consequence of the temperature variation of the group property $g\beta/k\nu\alpha$. Figure 3 can also be interpreted as the error involved in estimation of temperature rise through neglect of temperature-dependent properties.

References

1 Bar-Cohen, A., and Rohsenow, W. M., "Thermally Optimum Spacing of Vertical, Natural Convection Cooled Parallel Plates," ASME JOURNAL OF HEAT TRANSFER, Vol. 106, 1984, pp. 116–123.

2 Churchill, S. W., and Usagi, R., "A General Expression for the Correlation of Rates of Transfer and Other Phenomena," *AIChE Journal*, Vol. 18, 1972, pp. 1121–1128.

Turbulent Mixed Convection Along a Vertical Plate

T. S. Chen,[1,2] B. F. Armaly,[1,3] and M. M. Ali[1]

Introduction

Information on heat transfer characteristics of mixed convection in fully developed turbulent boundary layer flow is currently lacking in the literature. Oosthuizen [1] employed a mixing-length model, in which the buoyancy effect was included in the turblent diffusivities, to analyze turbulent mixed convection flow along an isothermal vertical flat plate under low free-stream velocities and Grashof numbers in the range of $10^{8.5}$ to $10^{9.5}$ (i.e., in the free convection dominated regime). He adjusted the empirical constant in his proposed model and obtained a fair agreement between the experimental data of Hall and Price [2] and his predicted values. Both studies [1, 2], however, were limited to a small range of the turbulent mixed convection regime close to the pure turbulent free convection limit. Turbulent mixed convection along a vertical flat plate in cross flow has been studied analytically [3] by using the mixing-length model and experimentally [4].

In the present Note, mixed convection in turbulent boundary layer flow along an isothermal vertical flat plate is analyzed for the entire mixed convection regime, ranging from pure forced convection to pure free convection, by employing a modified Van Driest mixing-length model for the turbulent diffusivities that account for the buoyancy effect. This approach is a simple attempt to treat the turbulent mixed convection problem, but it does provide good numerical results, particularly for the forced convection dominated regime.

Analysis

Consider a semi-infinite vertical flat plate that is maintained at a uniform surface temperature T_W. A free stream is moving upward and parallel to the plate with a uniform velocity u_∞ at temperature T_∞ ($T_\infty < T_w$). Let x be the streamwise coordinate measured from the leading edge of the plate and y be the transverse coordinate measured normal to the plate. The gravitational acceleration g is acting downward. With the assumption of constant fluid properties and the Boussinesq approximation, the conservation equations for a steady, two-dimensional turbulent boundary-layer flow can be written as

$$\frac{\partial u}{\partial x}+\frac{\partial v}{\partial y}=0 \tag{1}$$

$$u\frac{\partial u}{\partial x}+v\frac{\partial u}{\partial y}=g\beta(T-T_\infty)+\frac{\partial}{\partial y}\left[(\nu+\epsilon_m)\frac{\partial u}{\partial y}\right] \tag{2}$$

$$u\frac{\partial T}{\partial x}+v\frac{\partial T}{\partial y}=\frac{\partial}{\partial y}\left[(\alpha+\epsilon_h)\frac{\partial T}{\partial y}\right] \tag{3}$$

where the notations used in the equations are the conventional ones. The boundary conditions for equations (1)–(3) are

$$\begin{aligned} &u=v=0,\ T=T_w \quad \text{at } y=0\\ &u\to u_\infty,\quad T\to T_\infty \quad \text{as } y\to\infty \end{aligned} \tag{4}$$

The eddy diffusivity for momentum ϵ_m for the inner layer (ϵ_i) and the outer layer (ϵ_o) can be expressed by [5]

$$\epsilon_m=\begin{cases}\epsilon_i=l^2\,|\partial u/\partial y| & \text{for } \epsilon_i\le\epsilon_o\\ \epsilon_o=(0.075\delta)^2\,|\partial u/\partial y|\,\Gamma & \text{for } \epsilon_o<\epsilon_i\end{cases} \tag{5}$$

where δ is the boundary layer thickness, l is the mixing length given by [6]

$$l=0.4y[1-\exp(-y/A)] \tag{6}$$

and Γ is the intermittency factor across the boundary layer thickness, given by Klebannof [7] as

$$\Gamma=[1+5.5(y/\delta)^6]^{-1} \tag{7}$$

According to Cebeci's extension of the Van Driest model [6], the damping parameter A is modified to

$$A=\nu A^+/[N(\tau_w/\rho)^{1/2}] \tag{8}$$

where ρ is the fluid density, τ_w is the wall shear stress, A^+ is an empirical constant equal to 26, and N is given by

$$N=(1-11.8p^+)^{1/2} \tag{9}$$

Equation (9) applies to pure forced convection flow with pressure gradient $\partial p/\partial x$, but without surface mass transfer, and p^+ is defined as $-(\nu/\rho)(\partial p/\partial x)/(\tau_w/\rho)^{3/2}$. In the present problem the buoyancy force induces a pressure gradient inside the boundary layer and the term $g\beta(T-T_\infty)$ in equation (2) replaces the pressure gradient term in pure forced convection flow. Thus, it may be justifiable to employ a parallel of Cebeci's modified model in the present analysis and the expression for p^+ is taken as

$$p^+=\nu g\beta(T_w-T_\infty)/(\tau_w/\rho)^{3/2} \tag{10}$$

It is thus clear that the buoyancy force effect as represented by p^+ in equation (10) will affect the damping parameter A through the expression for N, equation (9), which in turn modifies the mixing length l. In this way the buoyancy force effect on the mixing length is accounted for in the present analysis. The eddy diffusivity for heat ϵ_h, is defined as $\epsilon_h=\epsilon_m/\mathrm{Pr}_t$ where Pr_t is the turbulent Prandtl number which is usually assigned a value of 0.9.

To cast the governing system of equations (1)–(5) into a dimensionless form, one introduces the following conventional dimensionless variables

$$\xi(x)=x/b,\qquad \eta(x,y)=y(u_\infty/\nu x)^{1/2} \tag{11}$$

$$f(\xi,\eta)=\psi(x,y)/(\nu u_\infty x)^{1/2},$$

$$\theta(\xi,\eta)=[T(x,y)-T_\infty]/(T_w-T_\infty) \tag{12}$$

in which b is a reference length and $\psi(x, y)$ is the usual stream function that satisfies equation (1) with $u=\partial\psi/\partial y$ and

[1]Department of Mechanical and Aerospace Engineering, University of Missouri – Rolla, Rolla, MO 65401.

[2]Fellow ASME.

[3]Mem. ASME.

Contributed by the Heat Transfer Division for publication in the JOURNAL OF HEAT TRANSFER. Manuscript received by the Heat Transfer Division June 11, 1984.

indicates that the temperature dependence of thermophysical properties is defined in the choice of qb/k and Ra.

Effects of increasing mean temperature are illustrated in Fig. 3, which shows the dimensionless channel wall temperature rise as expressed in the parametric form of equation (6). Included in Fig. 3 is a Rayleigh number scale, calculated from equation (1). Inspection of Fig. 3 indicates an increased channel wall temperature rise for increasing mean temperature. This is a consequence of the temperature variation of the group property $g\beta/k\nu\alpha$. Figure 3 can also be interpreted as the error involved in estimation of temperature rise through neglect of temperature-dependent properties.

References

1 Bar-Cohen, A., and Rohsenow, W. M., "Thermally Optimum Spacing of Vertical, Natural Convection Cooled Parallel Plates," ASME JOURNAL OF HEAT TRANSFER, Vol. 106, 1984, pp. 116–123.

2 Churchill, S. W., and Usagi, R., "A General Expression for the Correlation of Rates of Transfer and Other Phenomena," *AIChE Journal*, Vol. 18, 1972, pp. 1121–1128.

Turbulent Mixed Convection Along a Vertical Plate

T. S. Chen,[1,2] B. F. Armaly,[1,3] and M. M. Ali[1]

Introduction

Information on heat transfer characteristics of mixed convection in fully developed turbulent boundary layer flow is currently lacking in the literature. Oosthuizen [1] employed a mixing-length model, in which the buoyancy effect was included in the turblent diffusivities, to analyze turbulent mixed convection flow along an isothermal vertical flat plate under low free-stream velocities and Grashof numbers in the range of $10^{8.5}$ to $10^{9.5}$ (i.e., in the free convection dominated regime). He adjusted the empirical constant in his proposed model and obtained a fair agreement between the experimental data of Hall and Price [2] and his predicted values. Both studies [1, 2], however, were limited to a small range of the turbulent mixed convection regime close to the pure turbulent free convection limit. Turbulent mixed convection along a vertical flat plate in cross flow has been studied analytically [3] by using the mixing-length model and experimentally [4].

In the present Note, mixed convection in turbulent boundary layer flow along an isothermal vertical flat plate is analyzed for the entire mixed convection regime, ranging from pure forced convection to pure free convection, by employing a modified Van Driest mixing-length model for the turbulent diffusivities that account for the buoyancy effect. This approach is a simple attempt to treat the turbulent mixed convection problem, but it does provide good numerical results, particularly for the forced convection dominated regime.

Analysis

Consider a semi-infinite vertical flat plate that is maintained at a uniform surface temperature T_W. A free stream is moving upward and parallel to the plate with a uniform velocity u_∞ at temperature T_∞ ($T_\infty < T_w$). Let x be the streamwise coordinate measured from the leading edge of the plate and y be the transverse coordinate measured normal to the plate. The gravitational acceleration g is acting downward. With the assumption of constant fluid properties and the Boussinesq approximation, the conservation equations for a steady, two-dimensional turbulent boundary-layer flow can be written as

$$\frac{\partial u}{\partial x}+\frac{\partial v}{\partial y}=0 \tag{1}$$

$$u\frac{\partial u}{\partial x}+v\frac{\partial u}{\partial y}=g\beta(T-T_\infty)+\frac{\partial}{\partial y}\left[(\nu+\epsilon_m)\frac{\partial u}{\partial y}\right] \tag{2}$$

$$u\frac{\partial T}{\partial x}+v\frac{\partial T}{\partial y}=\frac{\partial}{\partial y}\left[(\alpha+\epsilon_h)\frac{\partial T}{\partial y}\right] \tag{3}$$

where the notations used in the equations are the conventional ones. The boundary conditions for equations (1)–(3) are

$$\begin{aligned} &u=v=0,\ T=T_w \quad \text{at } y=0\\ &u\to u_\infty,\quad T\to T_\infty \quad \text{as } y\to\infty \end{aligned} \tag{4}$$

The eddy diffusivity for momentum ϵ_m for the inner layer (ϵ_i) and the outer layer (ϵ_o) can be expressed by [5]

$$\epsilon_m=\begin{cases}\epsilon_i=l^2\,|\partial u/\partial y| & \text{for } \epsilon_i\le\epsilon_o\\ \epsilon_o=(0.075\delta)^2\,|\partial u/\partial y|\,\Gamma & \text{for } \epsilon_o<\epsilon_i\end{cases} \tag{5}$$

where δ is the boundary layer thickness, l is the mixing length given by [6]

$$l=0.4y[1-\exp(-y/A)] \tag{6}$$

and Γ is the intermittency factor across the boundary layer thickness, given by Klebannof [7] as

$$\Gamma=[1+5.5(y/\delta)^6]^{-1} \tag{7}$$

According to Cebeci's extension of the Van Driest model [6], the damping parameter A is modified to

$$A=\nu A^+/[N(\tau_w/\rho)^{1/2}] \tag{8}$$

where ρ is the fluid density, τ_w is the wall shear stress, A^+ is an empirical constant equal to 26, and N is given by

$$N=(1-11.8p^+)^{1/2} \tag{9}$$

Equation (9) applies to pure forced convection flow with pressure gradient $\partial p/\partial x$, but without surface mass transfer, and p^+ is defined as $-(\nu/\rho)(\partial p/\partial x)/(\tau_w/\rho)^{3/2}$. In the present problem the buoyancy force induces a pressure gradient inside the boundary layer and the term $g\beta(T-T_\infty)$ in equation (2) replaces the pressure gradient term in pure forced convection flow. Thus, it may be justifiable to employ a parallel of Cebeci's modified model in the present analysis and the expression for p^+ is taken as

$$p^+=\nu g\beta(T_w-T_\infty)/(\tau_w/\rho)^{3/2} \tag{10}$$

It is thus clear that the buoyancy force effect as represented by p^+ in equation (10) will affect the damping parameter A through the expression for N, equation (9), which in turn modifies the mixing length l. In this way the buoyancy force effect on the mixing length is accounted for in the present analysis. The eddy diffusivity for heat ϵ_h, is defined as $\epsilon_h=\epsilon_m/\mathrm{Pr}_t$ where Pr_t is the turbulent Prandtl number which is usually assigned a value of 0.9.

To cast the governing system of equations (1)–(5) into a dimensionless form, one introduces the following conventional dimensionless variables

$$\xi(x)=x/b,\qquad \eta(x,y)=y(u_\infty/\nu x)^{1/2} \tag{11}$$

$$f(\xi,\eta)=\psi(x,y)/(\nu u_\infty x)^{1/2},$$

$$\theta(\xi,\eta)=[T(x,y)-T_\infty]/(T_w-T_\infty) \tag{12}$$

in which b is a reference length and $\psi(x, y)$ is the usual stream function that satisfies equation (1) with $u=\partial\psi/\partial y$ and

[1]Department of Mechanical and Aerospace Engineering, University of Missouri – Rolla, Rolla, MO 65401.

[2]Fellow ASME.

[3]Mem. ASME.

Contributed by the Heat Transfer Division for publication in the JOURNAL OF HEAT TRANSFER. Manuscript received by the Heat Transfer Division June 11, 1984.

$v = -\partial\psi/\partial x$. The dimensionless forms of equations (2)–(5) are given by

$$[(1+\epsilon_m^+)f'']' + \frac{1}{2}ff'' + \Omega_b\xi\theta = \xi\left(f'\frac{\partial f'}{\partial\xi} - f''\frac{\partial f}{\partial\xi}\right) \quad (13)$$

$$\left[\left(\frac{1}{\mathrm{Pr}}+\epsilon_h^+\right)\theta'\right]' + \frac{1}{2}f\theta' = \xi\left(f'\frac{\partial\theta}{\partial\xi} - \theta'\frac{\partial f}{\partial\xi}\right) \quad (14)$$

$$f(\xi,0) = f'(\xi,0) = 0, \qquad \theta(\xi,0) = 1$$
$$f'(\xi,\infty) = 1, \qquad \theta(\xi,\infty) = 0 \quad (15)$$

and

$$\epsilon_m^+ = \begin{cases} \epsilon_i^+ = 0.16\eta^2(\mathrm{Re}_b\xi)^{1/2}[1-\exp(-y/A)]^2 \\ \quad \cdot |f''(\xi,\eta)|, \qquad \epsilon_i^+ \le \epsilon_o^+ \\ \epsilon_o^+ = (0.075\eta_\delta)^2(\mathrm{Re}_b\xi)^{1/2}\,|f''(\xi,\eta)| \\ \quad \cdot[1+5.5(\eta/\eta_\delta)^6]^{-1}, \qquad \epsilon_o^+ < \epsilon_i^+ \end{cases} \quad (16)$$

in which

$$\frac{y}{A} = \frac{1}{26}(\mathrm{Re}_b\xi)^{1/4}\eta[f''(\xi,0)]^{1/2}[1-11.8p^+]^{1/2} \quad (17)$$

and

$$p^+ = \Omega_b\xi(\mathrm{Re}_b\xi)^{-1/4}[f''(\xi,0)]^{-3/2} \quad (18)$$

In the above equations, the primes denote partial differentiation with respect to η, Pr is the Prandtl number, $\epsilon_m^+ = \epsilon_m/\nu$, and $\epsilon_h^+ = \epsilon_h/\nu = \epsilon_m^+/\mathrm{Pr}_t$. The buoyancy force parameter Ω_b, the Grashof number Gr_b, and the Reynolds number Re_b are defined, respectively, by

$$\Omega_b = \mathrm{Gr}_b/\mathrm{Re}_b^2, \qquad \mathrm{Gr}_b = g\beta(T_w - T_\infty)b^3/\nu^2, \qquad \mathrm{Re}_b = u_\infty b/\nu \quad (19)$$

In terms of the axial coordinate x, the local buoyancy force parameter Ω_x, the local Grashof number Gr_x, and the local Reynolds number Re_x, can be related, respectively, to Ω_b, Gr_b, and Re_b by

$$\Omega_x = \Omega_b\xi = \mathrm{Gr}_x/\mathrm{Re}_x^2, \qquad \mathrm{Gr}_x = \mathrm{Gr}_b\xi^3, \qquad \mathrm{Re}_x = \mathrm{Re}_b\xi \quad (20)$$

The local Nusselt number $\mathrm{Nu}_x = hx/k$, where $h = q_w/(T_w - T_\infty)$ and $q_w = -k(\partial T/\partial y)_{y=0}$, and the local friction factor, $C_{fx} = \tau_w/(\rho u_\infty^2/2)$, where $\tau_w = \mu(\partial u/\partial y)_{y=0}$, can be expressed, respectively, by

$$\mathrm{Nu}_x = (\mathrm{Re}_b\xi)^{1/2}[-\theta'(\xi,0)], \qquad C_{fx} = 2(\mathrm{Re}_b\xi)^{-1/2}f''(\xi,0) \quad (21)$$

Results and Discussion

The system of partial differential equations (13)–(16) was solved numerically by employing a modified version of the finite-difference technique developed by Keller and Cebeci [8] for turbulent boundary layer flows, to accommodate the coupling between the momentum and energy equations. The details of the numerical solution method are omitted here. For a given value of Pr, the values of $f''(\xi,0)$ and $\theta'(\xi,0)$ can be determined for a prescribed set of $(\Omega_b, \mathrm{Re}_b)$ values by performing the solution for $0 \le \eta \le \eta_\infty$ from $\xi = 0$ to $\xi = 1$. In the numerical calculations, the flow was assumed to be fully turbulent, and various step sizes for ξ, ranging from $\Delta\xi = 0.001$ for $0 \le \xi \le 0.01$, to $\Delta\xi = 0.01$ for $0.01 \le \xi \le 0.1$, and to $\Delta\xi = 0.05$ for $0.1 \le \xi \le 1.0$, were used. However, a constant step size of $\Delta\eta = 0.02$ was found to be satisfactory in the η direction for $0 \le \eta \le \eta_\infty$. In general, the convergence criteria for a solution were specified as $|[f''_{n+1}(\xi,0) - f''_n(\xi,0)]/f''_n(\xi,0)| \le 10^{-5}$ and $|[\theta'_{n+1}(\xi,0) - \theta'_n(\xi,0)]/\theta'_n(\xi,0)| \le 10^{-5}$, with smoothness conditions at η_∞ as $|f''_{n+1}(\xi,\eta_\infty)| \le 5\times10^{-4}$ and $|\theta'_{n+1}(\xi,\eta_\infty)| \le 5\times10^{-4}$.

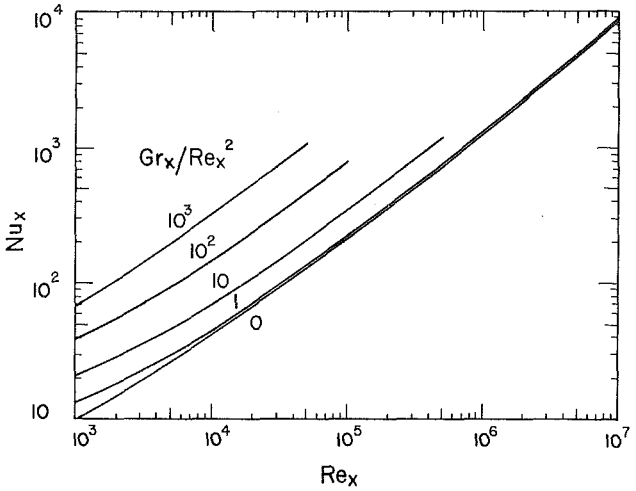

Fig. 1 Variation of the local Nusselt number with Ω_x ($= \mathrm{Gr}_x/\mathrm{Re}_x^2$) as a parameter; Pr = 0.7

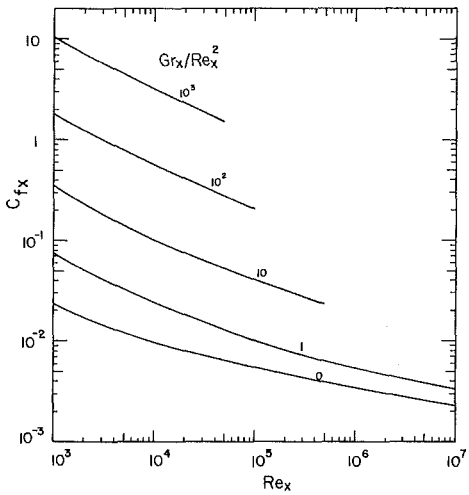

Fig. 2 Variation of the local friction factor with Ω_x ($= \mathrm{Gr}_x/\mathrm{Re}_x^2$) as a parameter; Pr = 0.7

Numerical results were obtained for Pr = 0.7 (air and typical gases). They cover the values of $\Omega_x = \Omega_b\xi$ in the range of $0 \le \mathrm{Gr}_x \le 10^{14}$ and $0 \le \mathrm{Re}_x \le 10^7$. In the calculations, the effects of intermittency factor Γ and buoyancy-induced pressure gradient p^+ on the numerical results were also examined. It was found that when $\Gamma = 1$ the local Nusselt number Nu_x increases by only about 0.4 percent for all Ω_x values considered in the calculations. When p^+ is set equal to zero (i.e., when $N = 1$), the Nu_x value increases by 0 to 6 to 9 to about 19 percent as Ω_x increases from 0 to 1.0 to 10 to ∞. This reveals that the effect of p^+ is to cause a decrease in turbulent diffusivities and hence a drop in the local Nusselt number, and that it is most strongly felt at the limiting case of turbulent free convection where $\Omega_x = \infty$. Calculations with variable turbulent Prandtl numbers, as given by the expression in [9], gave rise to an increase in the local Nusselt number of less than 6 percent as compared to a constant value of $\mathrm{Pr}_t = 0.9$. The results to be presented below are based on $\mathrm{Pr}_t = 0.9$, with Γ and p^+ incorporated in the ϵ_m^+ expression, equation (16).

Figures 1 and 2 illustrate, respectively, the variations of Nu_x and C_{fx} with respect to Re_x for a range of parametric values of $0 \le \Omega_x \le 1000$. The case of $\Omega_x = 0$ corresponds to pure turbulent forced convection. As can be seen from Fig. 1, the local Nusselt number Nu_x (that is, the local surface heat flux) increases with increasing buoyancy force parameter Ω_x for a

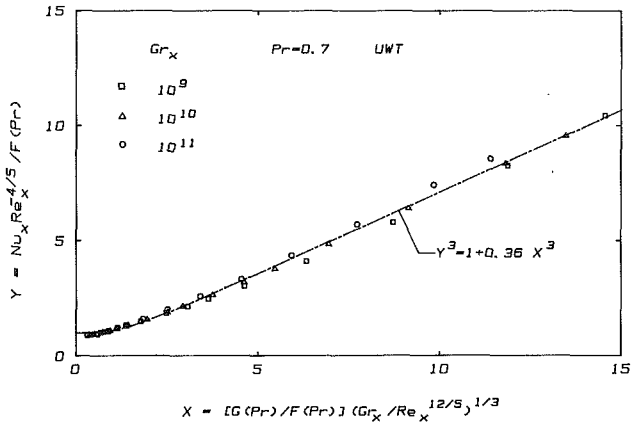

Fig. 3 A comparison between predicted and correlated local Nusselt numbers; Pr = 0.7

given value of Re_x. Also, for a given value of Ω_x the Nu_x is seen to increase with an increase in Re_x. This is to be expected, because a larger value of Ω_x for a given Re_x or a larger value of Re_x for a given Ω_x signifies a larger value of Gr_x or a larger buoyancy force effect that enhances the surface heat transfer rate. The local friction factor (Fig. 2) decreases with an increase in Re_x for a given Ω_x. Also, like the local Nusselt number, the local friction factor is seen to increase as the buoyancy force intensity increases. This is due to an increase in the velocity gradient at the wall as a result of the increasing buoyancy force. The transition Reynolds and Grashof numbers, respectively for pure forced convection and pure free convection, may be taken as $Re_x \doteq 10^5$ and $Gr_x \doteq 10^9$. Thus, the present results can be considered valid for flow conditions in which either $Re_x > 10^5$ or $Gr_x > 10^9$ or both.

The local Nusselt number Nu_x for mixed convection regime in boundary layer flows can be correlated accurately by an equation of the form [10]

$$Nu_x^n = Nu_{x,F}^n + aNu_{x,N}^n \text{ or } Y^n = 1 + aX^n \tag{22}$$

where $a = 1$ for laminar flow along a vertical flat plate, $Y = Nu_x/Nu_{x,F}$, $X = Nu_{x,N}/Nu_{x,F}$, and $Nu_{x,F}$ and $Nu_{x,N}$ are, respectively, the local Nusselt numbers for pure forced convection and pure free convection, and n is a constant exponent. For turbulent flow along an isothermal vertical flat plate, the expression for $Nu_{x,F}$ is given by [11]

$$Nu_{x,F}Re_x^{-4/5} = F(Pr), \qquad F(Pr) = 0.0287\ Pr^{0.6} \tag{23}$$

in the ranges of $0.5 \le Pr \le 1.0$ and $5 \times 10^5 \le Re_x \le 5 \times 10^6$ and the expression for $Nu_{x,N}$ is given by [12]

$$Nu_{x,N}Gr_x^{-1/3} = G(Pr),$$
$$G(Pr) = 0.150\ Pr^{1/3}[1 + (0.492/Pr)^{9/16}]^{-16/27} \tag{24}$$

for all Prandtl numbers and $10^9 \le Gr_x \le 10^{12}$. If a correlation equation in the form of equation (22) is proposed for turbulent mixed convection, the present results for the local Nusselt number shown in Fig. 1 can be correlated, with $a = 0.36$ and $n = 3$, as

$$Nu_xRe_x^{-4/5} = F(Pr)\left\{1 + 0.36\left[\frac{G(Pr)}{F(Pr)} \cdot (Gr_x/Re_x^{12/5})^{1/3}\right]^3\right\}^{1/3} \tag{25}$$

where, for $Pr = 0.7$, $F(Pr) = 0.0232$ and $G(Pr) = 0.0934$. This proposed correlation equation in the form of $Y^3 = 1 + 0.36X^3$ is illustrated in a Y versus X plot in Fig. 3 and is seen to agree very well with the calculated results. The corresponding correlation equation for the average Nusselt number $\overline{Nu} = \bar{h}L/k$, where $\bar{h}$ is the average heat transfer coefficient over the plate length L, can be expressed by

$$\overline{Nu}Re_L^{-4/5} = 1.25F(Pr)\left\{1 + 0.36\left[\frac{G(Pr)}{1.25F(Pr)} \cdot (Gr_L/Re_L^{12/5})^{1/3}\right]^3\right\}^{1/3} \tag{26}$$

The local Nusselt number results from the present calculations converge to the pure forced convection limit, given by equation (23), as $Gr_x/Re_x^2 \to 0$, but converge to a value of about 20 percent lower than that given by equation (24) in the pure free convection limit as $Re_x^2/Gr_x \to 0$. Thus, the proposed mixing-length model employed in the present study may underpredict the local Nusselt number for mixed convection in the buoyancy-dominated (i.e., weak forced flow) regime by as much as 20 percent. However, the present results are accurate for the forced-convection-dominated (i.e., weak buoyancy force) regime and possibly beyond. Experimental measurements are needed to verify and improve the proposed model.

As a final note, it is mentioned that if the Nusselt number results based on $p^+ = 0$ are used in the correlation, the constant a in equations (25) and (26) would change from 0.36 to about 0.52. This would provide a better correlation than that based on $p^+ \neq 0$ in the free convection-dominated mixed convection regime.

Acknowledgments

The present study was supported by the National Science Foundation (NSF MEA 83-00785). Figure 3 was prepared by Mr. N. Ramachandran.

References

1 Oosthuizen, P. H., "Turbulent Combined Convection Flow Over a Vertical Plane Surface," *Proceedings of the 5th International Heat Transfer Conference*, Vol. 3, 1974, pp. 129–133.

2 Hall, W. B., and Price, P. H., "Mixed Forced and Free Convection From a Vertical Heated Plate to Air," *Proceedings of the 4th International Heat Transfer Conference*, Vol. 4, 1970, Paper No. NC3.3.

3 Plumb, O. A., and Evans, G. H., "Turbulent Mixed Convection From a Vertical Heated Surface in a Crossflow," *ASME-JSME Thermal Engineering Joint Conference*, Vol. 3, 1983, pp. 47–53.

4 Siebers, D. L., Schwind, R. G., and Moffat, R. J., "Experimental Mixed Convection Heat Transfer From a Large, Vertical Surface in a Horizontal Flow," Report No. HMT-36, Thermosciences Division, Department of Mechanical Engineering, Stanford University, Feb. 1983.

5 Cebeci, T., and Smith, A. M. O., *Analysis of Turbulent Boundary Layers*, Academic Press, New York, N.Y. 1974.

6 Van Driest, E. R., "On Turbulent Flow Near a Wall," *Journal of the Aeronautical Sciences*, Vol. 23, 1956, pp. 1007–1011.

7 Klebanoff, P. S., "Characteristics of Turbulence in a Boundary Layer With Zero Pressure Gradient," NACA, TN 3178, 1954.

8 Keller, H. B., and Cebeci, T., "Accurate Numerical Methods for Boundary-Layer Flows. II: Two-Dimensional Turbulent Flows," *AIAA Journal*, Vol. 10, 1972, pp. 1193–1199.

9 Cebeci, T., and Khattab, A., "Prediction of Turbulent Free Convection Heat Transfer From a Vertical Flat Plate," ASME JOURNAL OF HEAT TRANSFER, Vol. 97, 1975, pp. 469–471.

10 Churchill, S. W., "A Comprehensive Correlating Equation for Laminar, Assisting, Forced and Free Convection," *AIChE Journal*, Vol. 23, 1977, pp. 10–16.

11 Kays, W. M., and Crawford, M. E., *Convective Heat and Mass Transfer*, 2nd ed., McGraw-Hill, new York, 1980, Chapt. 12.

12 Churchill, S. W., and Chu, H. H. S., "Correlating Equations for Laminar and Turbulent Free Convection From a Vertical Plate," *International Journal of Heat and Mass Transfer*, Vol. 18, 1975, pp. 1323–1329.

A Combined Laser-Doppler Anemometer/Laser-Induced Fluorescence System for Turbulent Transport Measurements

M.-C. Lai[1] and G. M. Faeth[1,2]

Introduction

A combined laser-Doppler anemometer (LDA) and laser-induced fluorescence (LIF) system is described which can provide nonintrusive simultaneous measurements of velocities and concentrations at a point in gases. This yields information needed to better understand turbulent transport of mass and heat—the latter by computation or analogy. The combined LDA/LIF system has potential for a variety of applications due to good spatial resolution and frequency response, acceptable performance at high turbulence intensities, capabilities for operation in dusty or particle-containing environments and near surfaces, and equipment costs that are not much greater than an LDA itself.

The advantages of LDA won't be elaborated since they are well known. However, Mie scattering (Starner and Bilger, 1980), Rayleigh scattering (Driscoll et al., 1982; Pitts and Kashiwagi, 1983), and Raman scattering (Eckbreth et al., 1979) can provide results similar to LIF; therefore, they will be compared with the present approach. Mie scattering involves elastic scattering of a laser beam from particles, providing a signal proportional to particle concentration and thus mixing in seeded flows. However, Mie scattering requires either high particle concentrations or a large measuring volume to control shot noise when concentration fluctuations are measured. Furthermore, reflection of the incident light causes signal-to-noise ratio problems when Mie scattering is used near surfaces. Rayleigh scattering involves elastic scattering from molecules; therefore, shot-noise due to a limited number of particles in the measuring volumes is not a problem. However, this approach encounters difficulties due to spurious signals from Mie scattering in dirty flows and reflections near surfaces. There are also problems in obtaining adequate sensitivity for mixing studies since Rayleigh scattering cross sections of common gases are similar. Raman scattering is inelastic; therefore, optical filters can distinguish between reflected and scattered signals and identify trace species. However, the intensity of Raman scattering is small, requiring strong pulsed lasers which are costly and limit frequency response due to their low pulse rates. Except for CARS, these systems also require careful control of particulate matter in the flow (Eckbreth et al. 1979).

LIF mitigates these problems and can be combined with LDA with little difficulty. LIF is an inelastic scattering process, involving absorption of laser light followed by emission after a short delay ($10^{-10} - 10^{-5}$ s) generally at longer wavelengths (Eckbreth et al., 1979). Thus optical filtering can be used to control Mie scattering and reflections, and trace species can be measured, similar to Raman scattering. However, LIF signals are orders of magnitude stronger than Raman signals; therefore LIF provides good sensitivity with relatively inexpensive cw lasers. The LIF technique is simplest to apply when pressure and temperature are constant throughout the flow field, since the signal is then directly proportional to concentration. The present study was limited to such conditions. In other instances, corrections for pressure and temperature variations are known (Eckbreth et al., 1979).

Owen (1976) proposed combined LDA/LIF in liquids, using a fluorescein dye as a tracer. The present system applies to gases and is based on the use of iodine vapor as a tracer. The LIF signal comes from the strong overlapping P13 and P15 lines in the (43′-0″) band of the B-X system of iodine (McDaniel, 1983a). These lines are within the gain profile of the 514.5 nm line of an argon-ion laser; therefore, costs associated with tunable lasers are avoided. Iodine fluorescence has been proposed in the past to measure density, pressure and velocity in high-speed free flows—the last by the Doppler shift of the fluorescence spectrum (McDaniel et al., 1982; McDaniel, 1983a, b). The present system is adapted for low-speed flows near surfaces; using LDA for velocity measurements and resolving attendant problems of Mie scattering from LDA seeding particles and reflections from surfaces.

The LDA/LIF system can be used to study turbulent mixing between two streams or turbulent transport from surfaces. The present system was developed for the former application; however, use of the technique to study transport from surfaces is discussed at the end of the paper. The following description is brief; more details and representative LDA/LIF measurements for turbulent wall plumes are reported by Lai (1985).

Test Apparatus

Figure 1 is a sketch of the test apparatus and the LDA/LIF system. The test flow was a buoyant turbulent wall plume generated by carbon dioxide/air mixtures issuing from a slot (20–21 mm wide) and flowing down along a plane wall in still air. The slot flow was seeded with iodine vapor (0.2 Torr partial pressure at 20°C) as a tracer. The test wall was 800 mm wide and had 305-mm-high side walls to preserve two dimensionality. Windows in the side walls provided optical access. Optics were rigid; therefore, the wall was traversed vertically and horizontally to measure flow properties.

Iodine vapor is corrosive even at low concentrations; therefore, the wall flow was exhausted using a blower. Ordinary paint protected most surfaces from corrosive attack. Brass, plexiglass, and flexible plastic hoses were also found to be reasonably resistant to iodine corrosion.

LDA

A single-channel, dual-beam LDA was adapted for use with LIF, based on an argon-ion laser yielding up to 800 mW at the 514.5 mm line. After splitting the beams, one beam was returned to the axis and transmitted parallel to the wall. The other beam could rotate around the axis so that various velocity components could be measured—even close to the surface (Lai et al., 1985). The off-axis beam was frequency-shifted to

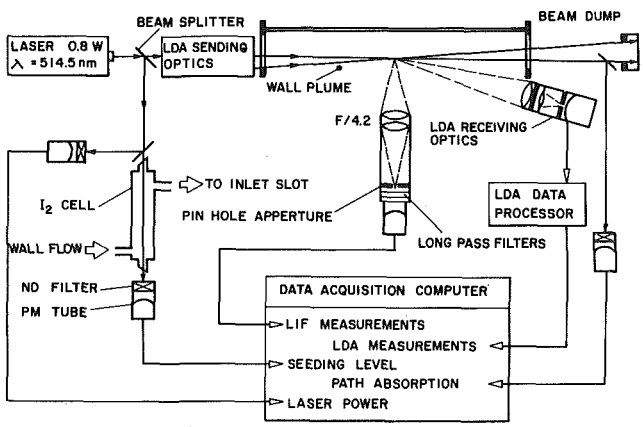

Fig. 1 Sketch of combined LDA/LIF system

[1]Department of Aerospace Engineering, The University of Michigan, Ann Arbor, MI 48109-2140.
[2]Fellow ASME.

Contributed by the Heat Transfer Division for publication in the JOURNAL OF HEAT TRANSFER. Manuscript received by the Heat Transfer Division January 15, 1986.

control directional bias and ambiguity. The LDA signal was detected off-axis, yielding a cylindrical measuring volume having a diameter of 300 μm and a length of 250 μm.

Both the wall flow and the surroundings were seeded (~ 500 nm aluminum oxide particles) to prevent concentration bias. Natural particles were detected as well, yielding particle densities of 0.2/measuring volume. Turbulent microscales were 2-20 mm (Lai, 1985); therefore, a low burst density but high data density signal was obtained. As a result, the low-pass filtered analog output of the burst-counter signal processor provided a continuous record of the flow velocities within the spectral range relevant to the turbulence. This signal was stored using a microcomputer. Uncertainties in instantaneous velocities were less than 3 percent.

LIF

The slot flow was saturated with iodine vapor by passing it through a bed of iodine crystals. The LIF signal was observed from the same measuring volume as the LDA, but at a right angle to the optical axis. Laser beam intensity before and after (the axial beam) passing through the flow was measured to allow correction for drift in the laser power and to account for reduced intensity due to light absorption before the measuring volume was reached. The absorption measurement also provided an independent check of mean concentration measurements. Iodine seeding levels are influenced by laboratory temperature changes due to the strong variation of iodine vapor pressure with temperature (10 percent/K); therefore, seeding levels were monitored by passing the slot flow through an absorption cell (40 mm diameter and 300 mm long) fitted with Brewster windows at both ends. Outputs from the four detectors were sampled and stored similar to the LDA signal.

Scattered and reflected light from the laser line were separated from the LIF signal using three long-pass optical filters (Oriel Corp. Model 5130 LP). The spectra of unfiltered and filtered (two filters) signals are illustrated in Fig. 2. A low resolution (8 nm) monochrometer was used for these measurements; therefore, the laser line and other features of the spectra are broadened. Nevertheless, fluorescence peaks from various transitions (43′-1″, 43′-2″, etc.) can still be seen at wavelengths longer than the laser line. Peak intensities decrease at long wavelengths due to reduced transition probabilities (Flygare, 1978). Clearly, even two filters virtually eliminate signals from the laser line.

The LIF signal was calibrated for effects of iodine concentrations and laser power using a small jet. Unsaturated fluorescence was used in the present work; however, saturated fluorescence at higher light intensities can be used as well, yielding a system where signal levels are independent of laser power fluctuations. The filtered LIF signal was linear in both iodine concentration and laser power (Lai, 1985). Potential sources of error involve reabsorption of fluorescence by iodine vapor between the measuring volume and the detector and background fluorescence caused by scattering and reflections at the laser line. Measurements across the slot exit confirmed relatively small effect of re-absorption ($\approx$ 1 percent). Typical self-absorption coefficients are on the order of 0.1 cm•torr^{-1} (Kurzel and Steinfield, 1970), which would suggest a 4 percent reabsorption at the worst, without even considering collison partner effects. The detector field stop controlled background fluorescence.

Measurements of power spectral densities of concentration indicated negligible signal content (dimensionless energy density less than 0.01) for frequencies greater than 30 Hz, with no trail off into the shot noise regime at frequencies up to 100 Hz (Lai 1985). Thus the LIF signals was processed using an anti-aliasing filter with a break frequency at 40 Hz. Analysis showed that uncertainties of the concentration measurements were generally less than 10 percent.

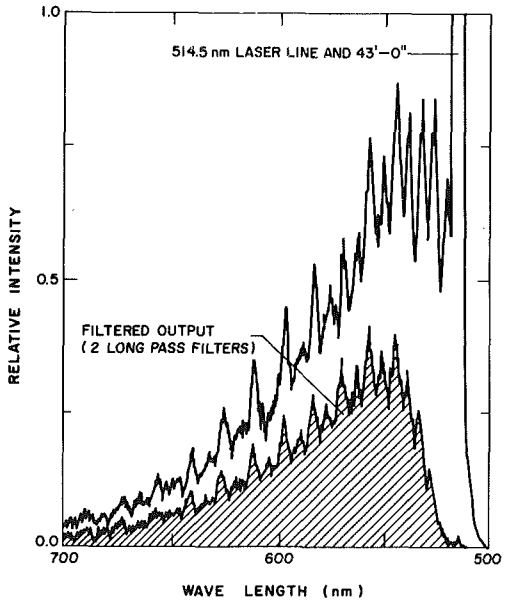

Fig. 2 Unfiltered and long-pass filtered LIF spectra of iodine vapor in air at NTP

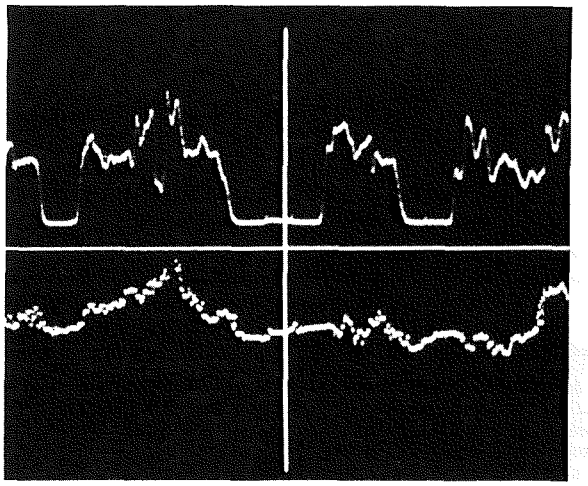

Fig. 3 Time-resolved LIF (upper) and LDA (lower) signals in a turbulent wall plume

Combined LDA/LIF Operation

Figure 3 is an illustration of typical real-time signals of concentrations and velocities using the combined LDA/LIF. The measurements were obtained within a vertical wall plume at $y/x = 0.1$ and $x/b = 37.5$ where y is distance normal to the wall, x is distance from the slot exit, and b is the slot height. The traces are 2.05 s long. The LDA trace is unfiltered; therefore, the step changes in processor output, following validation of signals from individual seeding particles, can be seen.

The turbulence intermittency for the condition pictured in Fig. 3 is slightly greater than one-half—shown by the flat low-amplitude LIF signals when unseeded ambient fluid is present at the measuring volume. The success of the long-pass filters in removing Mie scattered light at the laser line is evident since the baseline LIF signals remain flat in spite of the almost continuous presence of LDA seeding particles in the ambient

fluid. The essentially continuous record of concentrations and velocities yield a variety of concentration and velocity correlations and conditional averages with relative ease; see Lai (1985) for examples. Measurements of mean concentrations by LIF and absorption were also in excellent agreement (Lai et al., 1985).

Other Applications

Iodine does not fluoresce at wavelengths of other common laser lines, e.g., 488 nm and 632.8 nm; therefore, two-color LDA for two-velocity components and three-color operation for phase discrimination as well can be accommodated with little difficulty.

In addition to turbulent mixing applications, described here, the LDA/LIF can be used to study turbulent transport from surfaces. Iodine is simply dissolved in alcohol and painted on the surface. Iodine maintains thermodynamic equilibrium at the surface, except at very low pressures, defining the surface boundary condition. Subsequent transport of the subliming vapor can be measured similar to the present mixing experiments. Solid iodine does not fluoresce; therefore, surface reflections are at the the laser line and can be eliminated using optical filters. All things considered, the LDA/LIF system exhibits significant potential for studies of turbulent transport relevant to heat and mass transfer processes.

Acknowledgments

This research was supported by the United States Department of Commerce, National Bureau of Standards under Grant No. 60NANB4D0032. B. J. McCaffrey, of the Center for Fire Research, served as Scientific Officer. The study was initiated while the authors were affiliated with The Pennsylvania State University.

References

Driscoll, J. F., Schefer, R. W., and Dibble, R. W., 1982, "Mass Fluxes $\rho'u'$ and $\rho'v'$ Measured in a Turbulent Nonpremixed Flame," *Nineteenth Symposium (International) on Combustion*, The Combustion Institute, Pittsburgh, PA, pp. 447-457.

Eckbreth, A. C., Bonczyk, P. A., and Verdieck, J. F., 1979, "Combustion Diagnostics by Laser Raman and Fluorescence Techniques," *Prog. Energy Combust. Sci.*, Vol. 5, pp. 253-322.

Flygare, W. H., 1978, *Molecular Structure and Dynamics*, Prentice-Hall, Englewood Cliffs, N.J.

Kurzel, R. B., and Steinfield, J. I., 1970, "Energy-Transfer Processes in Monochromatically Excited Iodine Molecules. III. Quenching and Multiquantum Transfer From $v' = 43$," *The Journal of Chemical Physics*, Vol. 53, pp. 3293-3303.

Lai, M.-C., 1985, "Structure of Turbulent Adiabatic Wall Plumes," Ph.D., Thesis, The Pennsylvania State University, University Park, PA.

Lai, M.-C., Jeng, S.-M., and Faeth, G. M., 1986, "Structure of Turbulent Adiabatic Wall Plumes," ASME JOURNAL OF HEAT TRANSFER, Vol. 108, pp. 827-834.

McDaniel, J. C., Baganoff, D., and Byer, R. L., 1982, "Density Measurement in Compressible Flow Using Off-Resonant Laser-Induced Fluorescence," *Phys. Fluids*, Vol. 25, pp. 1105-1107.

McDaniel, J. C., 1983a, "Quantitative Measurement of Density and Velocity in Compressible Flows Using Laser-Induced Iodine Fluorescence," AIAA Paper No. 83-0049.

McDaniel, J. C., 1983b, "Nonintrusive Pressure Measurement With Laser-Induced Iodine Fluorescence," AIAA Paper No. 83-1468.

Owen, F. K., 1976, "Simultaneous Laser Velocimeter and Laser Induced Photoluminescence Measurements of Instantaneous Velocity and Concentration in Complex Mixing Flow," AIAA Paper No. 76-035.

Pitts, W. M., and Kashiwagi, T., 1983," The Application of Laser-Induced Rayleigh Light Scattering to the Study of Turbulent Mixing," Report No. NBSLR 83-2641, National Bureau of Standards, Gaithersburg, MD.

Starner, S. H., and Bilger, R. W., 1980, "Measurement of Scalar-Velocity Correlations in a Turbulent Diffusion Flame," *Eighteenth Symposium (International) on Combustion*, The Combustion Institute, Pittsburgh, PA, pp. 921-930.

A Cell Model That Estimates Radiative Heat Transfer in a Nonscattering, Particle-Laden Flow

E. Saatdjian[1]

Nomenclature

A_i = area of section i, m^2
A_P = area of one particle, m^2
A_R = area of the reactor, m^2
d_R = diameter of the reactor, m
F_{A-i} = view factor between particle A and particle i
N_i = total number of particles in section i
N_{Ei} = total number of particles eliminated from view of A by particles in section i
$N_{Ei\|j}$ = total number of particles in section j eliminated from view of A by particles in section i
N_i^{tot} = total number of particles in section i which are seen by A
q = heat flow, W
T = temperature, K
α = fraction of absorbed radiation
ϵ = porosity
σ = Stefan–Boltzmann constant, W/m^2K^4
ϕ = angle (see Fig. 1)

Introduction

Radiation heat transfer is very important in two-phase, gas–solid, high-temperature flows. However, in most cases this form of heat transfer is neglected because the problem is very complex. For example, when spherical black particles are being transported by a transparent gas inside a cylindrical tube, even if the exact location of each particle were known, one would be forced to solve a heat transfer equation for every pair of particles.

Industrial applications involve, for example, the injection of finely ground coal particles into a hydrogen plasma flow; the particles heat up very rapidly, devolatilize and form a gaseous mixture rich in acetylene (Ubhayakar et al., 1977). Another application is particle coal combustion. When the volatile release rate is faster than the incoming oxygen supply, the flame front detaches from the particle surface. The evolved volatiles react releasing energy outside the particle; this energy can eventually heat up the particle itself. The soot cloud formed between the particle and the flame front actively participates in the heat transfer process (Choi and Kruger, 1985). Other examples are luminous gas flames (Jakob, 1957) and packed solids (Vortmeyer, 1978).

When the diameter of particles in the cloud is very small, as is the case for soot, the attenuation of a radiation beam has been found, experimentally, to obey Bouguer's law (Siegel and Howell, 1972); this continuum model breaks down, however, for large-diameter particles.

In the analysis presented here, we consider a particle, labeled A, in the middle of a cloud and develop a theory to estimate the distance from A that is necessary for other particles to absorb the radiation leaving A. We assume that the particles are all of the same size and that they are uniformly distributed in the reactor cross-sectional area; porosity gra-

[1]Laboratoire d'Aérothermique du C.N.R.S., 92190 Meudon, France.

Contributed by the Heat Transfer Division for publication in the JOURNAL OF HEAT TRANSFER. Manuscript received by the Heat Transfer Division December 13, 1985.

fluid. The essentially continuous record of concentrations and velocities yield a variety of concentration and velocity correlations and conditional averages with relative ease; see Lai (1985) for examples. Measurements of mean concentrations by LIF and absorption were also in excellent agreement (Lai et al., 1985).

Other Applications

Iodine does not fluoresce at wavelengths of other common laser lines, e.g., 488 nm and 632.8 nm; therefore, two-color LDA for two-velocity components and three-color operation for phase discrimination as well can be accommodated with little difficulty.

In addition to turbulent mixing applications, described here, the LDA/LIF can be used to study turbulent transport from surfaces. Iodine is simply dissolved in alcohol and painted on the surface. Iodine maintains thermodynamic equilibrium at the surface, except at very low pressures, defining the surface boundary condition. Subsequent transport of the subliming vapor can be measured similar to the present mixing experiments. Solid iodine does not fluoresce; therefore, surface reflections are at the the laser line and can be eliminated using optical filters. All things considered, the LDA/LIF system exhibits significant potential for studies of turbulent transport relevant to heat and mass transfer processes.

Acknowledgments

This research was supported by the United States Department of Commerce, National Bureau of Standards under Grant No. 60NANB4D0032. B. J. McCaffrey, of the Center for Fire Research, served as Scientific Officer. The study was initiated while the authors were affiliated with The Pennsylvania State University.

References

Driscoll, J. F., Schefer, R. W., and Dibble, R. W., 1982, "Mass Fluxes $\rho'u'$ and $\rho'v'$ Measured in a Turbulent Nonpremixed Flame," *Nineteenth Symposium (International) on Combustion*, The Combustion Institute, Pittsburgh, PA, pp. 447-457.

Eckbreth, A. C., Bonczyk, P. A., and Verdieck, J. F., 1979, "Combustion Diagnostics by Laser Raman and Fluorescence Techniques," *Prog. Energy Combust. Sci.*, Vol. 5, pp. 253-322.

Flygare, W. H., 1978, *Molecular Structure and Dynamics*, Prentice-Hall, Englewood Cliffs, N.J.

Kurzel, R. B., and Steinfield, J. I., 1970, "Energy-Transfer Processes in Monochromatically Excited Iodine Molecules. III. Quenching and Multiquantum Transfer From $v' = 43$," *The Journal of Chemical Physics*, Vol. 53, pp. 3293-3303.

Lai, M.-C., 1985, "Structure of Turbulent Adiabatic Wall Plumes," Ph.D., Thesis, The Pennsylvania State University, University Park, PA.

Lai, M.-C., Jeng, S.-M., and Faeth, G. M., 1986, "Structure of Turbulent Adiabatic Wall Plumes," ASME JOURNAL OF HEAT TRANSFER, Vol. 108, pp. 827-834.

McDaniel, J. C., Baganoff, D., and Byer, R. L., 1982, "Density Measurement in Compressible Flow Using Off-Resonant Laser-Induced Fluorescence," *Phys. Fluids*, Vol. 25, pp. 1105-1107.

McDaniel, J. C., 1983a, "Quantitative Measurement of Density and Velocity in Compressible Flows Using Laser-Induced Iodine Fluorescence," AIAA Paper No. 83-0049.

McDaniel, J. C., 1983b, "Nonintrusive Pressure Measurement With Laser-Induced Iodine Fluorescence," AIAA Paper No. 83-1468.

Owen, F. K., 1976, "Simultaneous Laser Velocimeter and Laser Induced Photoluminescence Measurements of Instantaneous Velocity and Concentration in Complex Mixing Flow," AIAA Paper No. 76-035.

Pitts, W. M., and Kashiwagi, T., 1983," The Application of Laser-Induced Rayleigh Light Scattering to the Study of Turbulent Mixing," Report No. NBSLR 83-2641, National Bureau of Standards, Gaithersburg, MD.

Starner, S. H., and Bilger, R. W., 1980, "Measurement of Scalar-Velocity Correlations in a Turbulent Diffusion Flame," *Eighteenth Symposium (International) on Combustion*, The Combustion Institute, Pittsburgh, PA, pp. 921-930.

A Cell Model That Estimates Radiative Heat Transfer in a Nonscattering, Particle-Laden Flow

E. Saatdjian[1]

Nomenclature

A_i = area of section i, m^2
A_P = area of one particle, m^2
A_R = area of the reactor, m^2
d_R = diameter of the reactor, m
F_{A-i} = view factor between particle A and particle i
N_i = total number of particles in section i
N_{Ei} = total number of particles eliminated from view of A by particles in section i
$N_{Ei\|j}$ = total number of particles in section j eliminated from view of A by particles in section i
N_i^{tot} = total number of particles in section i which are seen by A
q = heat flow, W
T = temperature, K
α = fraction of absorbed radiation
ϵ = porosity
σ = Stefan–Boltzmann constant, W/m^2K^4
ϕ = angle (see Fig. 1)

Introduction

Radiation heat transfer is very important in two-phase, gas–solid, high-temperature flows. However, in most cases this form of heat transfer is neglected because the problem is very complex. For example, when spherical black particles are being transported by a transparent gas inside a cylindrical tube, even if the exact location of each particle were known, one would be forced to solve a heat transfer equation for every pair of particles.

Industrial applications involve, for example, the injection of finely ground coal particles into a hydrogen plasma flow; the particles heat up very rapidly, devolatilize and form a gaseous mixture rich in acetylene (Ubhayakar et al., 1977). Another application is particle coal combustion. When the volatile release rate is faster than the incoming oxygen supply, the flame front detaches from the particle surface. The evolved volatiles react releasing energy outside the particle; this energy can eventually heat up the particle itself. The soot cloud formed between the particle and the flame front actively participates in the heat transfer process (Choi and Kruger, 1985). Other examples are luminous gas flames (Jakob, 1957) and packed solids (Vortmeyer, 1978).

When the diameter of particles in the cloud is very small, as is the case for soot, the attenuation of a radiation beam has been found, experimentally, to obey Bouguer's law (Siegel and Howell, 1972); this continuum model breaks down, however, for large-diameter particles.

In the analysis presented here, we consider a particle, labeled A, in the middle of a cloud and develop a theory to estimate the distance from A that is necessary for other particles to absorb the radiation leaving A. We assume that the particles are all of the same size and that they are uniformly distributed in the reactor cross-sectional area; porosity gra-

[1]Laboratoire d'Aérothermique du C.N.R.S., 92190 Meudon, France.

Contributed by the Heat Transfer Division for publication in the JOURNAL OF HEAT TRANSFER. Manuscript received by the Heat Transfer Division December 13, 1985.

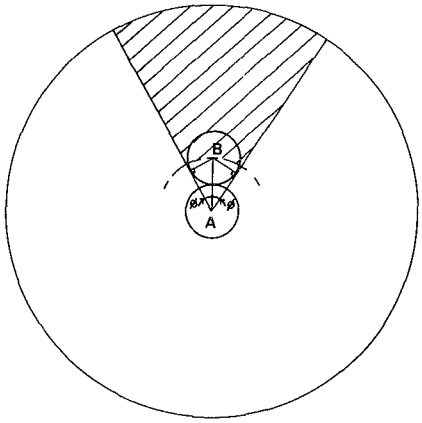

Fig. 1 View of radiation transfer between *A* and a particle *B* in section 1; the shaded area is an approximation of the hidden area which should no longer be considered

dients are neglected. From this theory, one can separate a reactor into two zones: a first zone near the walls where thermal radiation leaving the walls can be captured by the particles in it; and a second zone nearer the reactor center where particle-to-particle radiation heat transfer is predominant. The theory is compared to results obtained using the continuum assumption.

Analysis

Consider a particle labeled A lying at the center of a cylindrical reactor; we wish to determine the amount of radiation leaving A that is captured by the reactor walls, taking into account that other particles of the same size are also present in the reactor and absorb some of the radiation leaving A. For simplicity, the problem is tackled in a plane.

The geometric parameters that are known are: the reactor diameter and radius, d_R and R_R; the particle diameter and radius, d_P and R_P; the porosity ϵ; the area occupied by A and the other particles is $(1-\epsilon)\,A_R$ where $A_R = \pi d_R^2/4$.

The maximum amount of radiation leaving A that can reach the reactor walls is $(1-\alpha)=1$; i.e., if no other particles are present in the reactor and the gas is transparent. Other quantities defined at this stage are:

$A_0 = \pi R_P^2$ = area of section 0, area occupied by particle A

$N_{\text{tot}} = \dfrac{A_R}{A_P}(1-\epsilon)$ = total number of particles in the reactor; A_P is the area of a particle $= \pi R_P^2$

$N_0 = 1$ = number of particles in section 0; particle A occupies this section completely.

At first, particles separated (center to center) from A by a distance of 2 R_P, i.e., particles in contact with A, are considered. The area of this section (labeled 1) is $A_1 = \pi R_P{}^2(2^2 - 1^2)$. The total number of particles in section 1, N_1, is

$$N_1 = \frac{(A_0 + A_1)}{A_R} N_{\text{tot}} - 1 \tag{1}$$

or the number of particles in sections 0 and 1 minus the particles already present in section 0. If $N_1 < 0$, then N_1 is set equal to zero.

The view factor between any two particles is given in Siegel and Howell (1972)

$$F_{A-B} = \frac{1}{\pi}\left(\sqrt{X^2-1} + \sin^{-1}\frac{1}{X} - X\right) \tag{2}$$

where $X = 1 + S/2R_P$ and S is the minimum distance between the surfaces of the two particles.

The radiation that can be captured by the reactor walls after considering the particles in section 1 is

$$(1-\alpha) = 1 - N_1 F_{A-1} \tag{3}$$

where F_{A-1} is determined using equation (2).

Before considering particles in the next section, the reactor area which is now "hidden" from A by the particles in section 1 is evaluated. Indeed, for particles not in contact with A, one must take into account the possibility that there is a particle nearer A which covers it from A partly or completely.

The area hidden per particle in section 1 is $(\phi/\pi)\cdot(\pi R_R^2 - \pi(2R_P)^2$ and corresponds to the shaded area in Fig. 1. The total area hidden by all the particles in section 1 is N_1 times the number and the number of particles lying in this area is equal to the total amount of particles eliminated by particles in section 1, N_{E1}

$$N_{E1} = \frac{N_1 \phi\,(R_R^2 - (2R_P)^2)(N_{\text{tot}} - N_1 - 1)}{A_R - (A_0 + A_1)} \tag{4}$$

Now, subsequent concentric reactor sections can be considered. For sections $i = 2, 3, 4, \ldots$, separated from A by a distance of $(i+1)R_p$, the areas are

$$A_i = \pi R_P^2\,((i+1)^2 - i^2) \tag{5}$$

and the total number of particles in each section is

$$N_i = \frac{\left(\sum_{j=0}^{i} A_j\right) N_{\text{tot}}}{A_R} - \sum_{j=0}^{i-1} N_i \tag{6}$$

Of all the particles in section i, N_i, some are hidden from A by particles in the previous sections.

For example, the number of particles in section i hidden by particles in section 1 is $N_{E1\,|i}$ and can be obtained from equation (4)

$$N_{E1\,|i} = N_{E1} \frac{A_i}{A_R - \sum_{j=0}^{1} A_j} \tag{7}$$

The total amount of particles in section i which are "seen" by A, N_i^{tot}, is calculated by

$$N_i^{\text{tot}} = N_i - \sum_{j=1}^{i-1} N_{Ej\,|i} \tag{8}$$

and the total number of particles "hidden" by particles in section i, N_{Ei}, is

$$N_{Ei} = \frac{N_i^{\text{tot}}(\phi\,(R_R^2 - ((i+1)R_P)^2)\left(N_{\text{tot}} - \sum_{j=0}^{i} N_j\right)}{A_R - \sum_{j=0}^{i} A_j} \tag{9}$$

For a section m further on $(m > i)$, the number of particles in m hidden by particles in i is simply

$$N_{Ei\,|m} = N_{Ei} \frac{A_m}{A_R - \sum_{j=0}^{i} A_i} \tag{10}$$

Finally, the radiation leaving A that can reach the reactor walls is

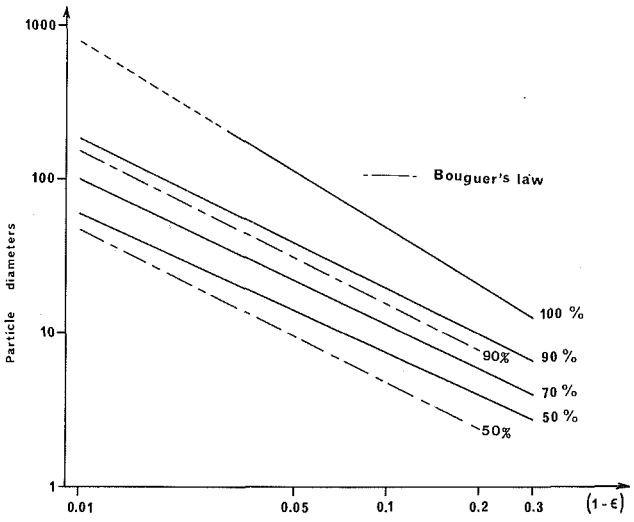

Fig. 2 Number of particle diameters necessary to absorb different percentages of radiation leaving A as a function of porosity; comparison with the continuum model

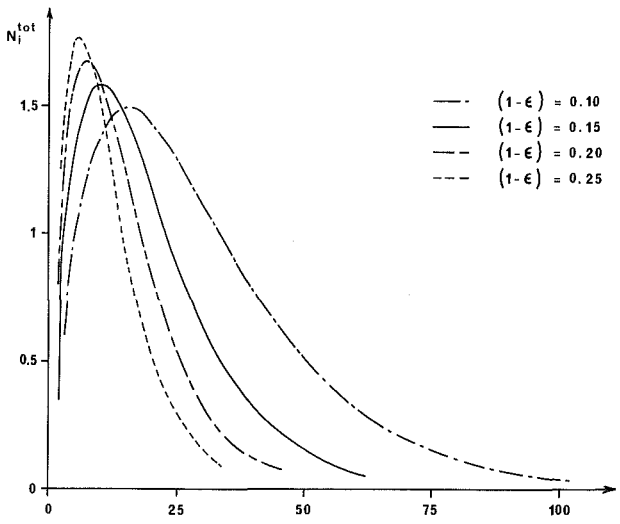

Fig. 3 Number of particles seen by A, N_i^{tot}, versus section number

$$1-\alpha = 1 - \sum_{j=1}^{NN} N_j^{tot} F_{A-j} \tag{11}$$

where NN is the total number of sections between A and the reactor walls.

Results and Discussion

Using the above analysis, a computer program was written which calculates, for each section, the view factor between A and a particle in the section (equation (2)), the total number of particles in the section N_i (equation (6)), the total number of particles that are seen by A in the section N_i^{tot} (equation (8)), the number of particles eliminated by particles in the section, N_{Ei} (equation (9)), and the fraction of radiation left after considering the particles in the section $(1-\alpha)$ (equation (11)). If the number of particles calculated is less than 0 (see equation (1)), then it is set equal to zero. The calculated number of "seen" particles N_i^{tot} is always a real number; the obtained fractions are kept, i.e., a particle presence probability is calculated.

The number of particle diameters necessary to absorb different percentages of radiation leaving A as a function of $(1-\epsilon)$ is given in Fig. 2. The data form straight lines on a log-log plot for the considered porosity range. In Fig. 3, the number of particles seen by A, N_i^{tot}, is plotted versus the section number (i.e., the distance in particle radii from A) for different values of $(1-\epsilon)$. As the distance from A increases, N_i^{tot} rapidly increases, reaches a maximum and then decays asymptotically toward a value of zero. The peak is sharper for higher values of $(1-\epsilon)$. Figure 3 is useful in two ways: First, it explains why several particle diameters are necessary to absorb the last 10 percent of the radiation leaving A. As the distance from A is increased, the view factor and also the number of "seen" particles decrease and, consequently, the product of these two quantities becomes very small. Second, it justifies the analysis because in all the considered cases, the number of particles "seen" after absorbing all the radiation is less than 0.1.

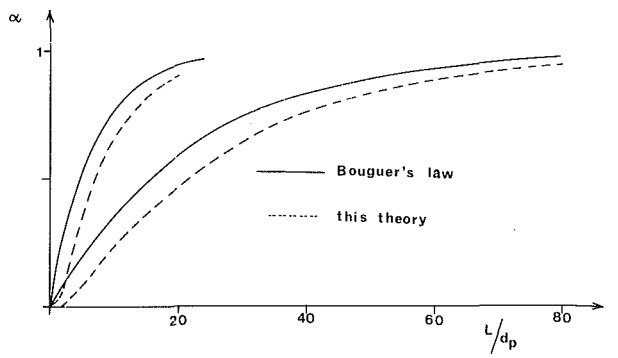

Fig. 4 Fraction of absorbed radiation versus distance in particle diameters

When the diameter of the particles in the cloud is very small, the cell model can be compared to Bouguer's law. Along a line of sight, the continuum assumption gives

$$1-\alpha = \exp(-1.5(1-\epsilon)L/d_P) \tag{12}$$

where L is the distance from the considered particle.

In Fig. 2, the length in particle diameters necessary to absorb 50 and 90 percent of the radiation is plotted versus $(1-\epsilon)$ using both models. The continuum model also yields straight lines in a log-log plot; however, the cell model predicts higher L/d_P values. The difference in length between the two models is negligible for particles of very small diameter, as is the case for soot. For bigger particles, the cell model should still be valid since no assumption concerning the particle size was made. The two models are again compared in Fig. 4 where the fraction of radiation absorbed α is plotted versus L/d_P for $1-\epsilon = 0.1$ and 0.03. Again, both models give the same form of curve. These results tend to show that the presented model is correct in describing energy attenuation in a particle laden flow. The major assumption involved here was that each concentric section had the same porosity, i.e., that the particles were homogeneously distributed.

References

Choi, S., and Kruger, C. H., 1985, "Modelling Coal Particle Behavior Under Simultaneous Devolatilization and Combustion," *Comb. and Flame*, Vol. 61, pp. 131–144.

Jacob, M., 1957, *Heat Transfer*, Wiley, New York.

Siegel, R., and Howell, J. R., 1972, *Thermal Radiation Heat Transfer*, McGraw-Hill, New York.

Ubhayakar, S., Stickler, D., and Gannon, R., 1977, "Modelling of Entrained-Bed Pulverized Coal Gasifiers," *Fuel*, Vol. 56, pp. 281–291.

Vortmeyer, D., 1978, "Radiation in Packed Solids," *Proc. Heat Transfer*, Vol. 6, pp. 525–539.

Radiative and Convective Transfer in a Cylindrical Enclosure for a Gas/Soot Mixture

A. M. Al-Turki[1] and T. F. Smith[1]

Introduction

Energy units such as boilers, gas turbines, and steam generators have gas flows resulting from combustion of hydrocarbon fuels with combustion products of water vapor, carbon dioxide, and soot particles, all of which are strong absorbers and emitters of thermal radiation. At high temperatures and with the presence of these products, radiative heat transfer dominates conductive and convective heat transfer. Due to the size and complexity of these units, experimental data are difficult and costly to obtain, and mathematical models are sought.

Several investigators [1–6] have studied radiant exchange in combustion products, but very limited results are available that incorporate the effects of soot particles in fully developed laminar or turbulent flow of a gas/soot mixture through a circular duct. Soot particles play a dominant role in the radiative heat transfer and may augment the radiant emission of absorbing gases. The purpose of this study is to examine the interaction of radiative heat transfer with convective and conductive heat transfer for flow of a radiatively participating absorbing gas and soot particle mixture. Axial and radial mixture temperature profiles along with wall heat fluxes and Nusselt numbers are sought.

Analysis

The system selected for study consists of laminar or turbulent flow of a gas composed of absorbing gases and soot, with fully developed velocity profile through a black wall circular duct. The system is described in detail in [6] and the solution scheme is described in [7]. The energy equations for the gas temperature distribution and wall heat flux and Nusselt number distributions are given in [6]. The present analysis represents an extension from that in [6] for absorbing gases to a mixture that contains absorbing gases and soot. The analysis employs the zone method [8] with the weighted sum of gray gases model for the radiative properties. It is instructive for the current presentation to illustrate the technique for computing the radiative properties and, in particular, the mixture absorption coefficients that are used to compute the direct exchange areas.

The weighted sum of gray gases model yields the total emissivity and absorptivity of the mixture. The total properties are expressed in terms of weighting factors and absorption coefficients for the absorbing gases and soot acting individually [9, 10]. The total absorption coefficient κ_T is given by

$$\kappa_T = \sum_{n=1}^{N_s} \sum_{m=0}^{N_g} A_{\epsilon n,m}(T) K_{n,m} \tag{1}$$

where N_s and N_g are the number of gray gases for the soot and absorbing gases, respectively, and T is the gas temperature. The mixture emissivity weighting factors are denoted by $A_{\epsilon n,m}$. The mixture absorption coefficient $K_{n,m}$ for the n,m gray gas component is evaluated from

$$K_{n,m} = K_{sn} + K_{gm} P \tag{2}$$

The soot absorption coefficient K_{sn} for the nth gray gas component is given by

$$K_{sn} = C_{sn} f_v \tag{3}$$

where C_{sn} are the soot coefficients and f_v is the soot volume fraction. A second soot coefficient used in [9] has a value near unity. In the present study this coefficient was assumed to be unity without any loss of accuracy. The soot coefficients are furnished in Table 1 for $N_s = 2$. K_{gm} are the absorbing gas absorption coefficients for the mth gray gas component with P denoting the sum of the partial pressures of the absorbing gases, and are available elsewhere [11].

The mixture emissivity and absorptivity weighting factors are given, respectively, by

$$A_{\epsilon\eta,m}(T) = a_{sn}(T) a_{\epsilon m}(T);\ A_{\alpha n,m}(T, T_s) = a_{sn}(T_s) a_{\alpha m}(T, T_s) \tag{4}$$

where a_{sn} are the soot weighting factors evaluated from

$$a_{sn} = \sum_{j=1}^{J_s} b_{sn,j} T^{j-1} \tag{5}$$

The soot temperature polynomial coefficients b_{sn} are listed in Table 1 for $J_s = 4$. No distinction needs to be made between emissivity and absorptivity weighting factors for the soot. T_s is the temperature of the zone where radiant energy originates from and irradiates the zone at T. $a_{\epsilon m}$ and $a_{\alpha m}$ are the absorbing gas emissivity and absorptivity weight factors expressed by temperature polynomials [11]. For the absorbing gas/soot mixture used in the present study, $N_s = 2$ and $N_g = 3$. Thus, by equation (2), there are eight mixture absorption coefficients including the clear gas component.

Results and Discussion

The absorbing gases consist of carbon dioxide and water vapor with partial pressures of 0.1 atm for both gases. The remaining gas is nitrogen, and the total pressure of the mixture is at one atmosphere. The soot volume fraction was assigned values between 0.01×10^{-6} and 5.0×10^{-6} as representative of several energy systems [12]. The cylindrical system was chosen with a length-to-diameter ratio of $\xi = 5$. There were ten radial and twenty axial zones. The reference temperature was assigned a value of 800 K. Results are presented for an inlet gas temperature of 2000 K and a wall temperature of 800 K. The thermophysical properties of air were used and are evaluated at a temperature of 1200 K. For the results presented, the Peclet number is given as $\mathrm{Pe} = 4470\, u_m D$ where u_m is the mean velocity and D is the duct diameter. The conduction to radiation parameter [6] has a value of $0.00066/D$, which implies that radiation effects would dominate the heat transfer processes.

Representative dimensionless gas temperature results for $f_v = 0.10 \times 10^{-6}$ are displayed in Fig. 1 for $u_m = 0.5$ and 10.0 m/s, corresponding to laminar and turbulent flows, respectively. The gas temperatures are normalized with the wall temperature to yield θ. The intersection of the grid points occurs at the zone center. The axial and radial locations are denoted by x and r, respectively. The duct length $L = 5$ m. As u_m increases, the enthalpy flux also increases, resulting in smaller changes in gas temperatures in the axial direction and higher outlet bulk temperatures. At high u_m, only the gas

Table 1 Soot and polynomial coefficients

Coefficient	$n=1$	$n=2$
C_{sn}	1.00802×10^{6}	3.23520×10^{6}
$b_{sn,1}$	1.4207	−0.4207
$b_{sn,2}$	-0.77942×10^{-3}	0.77942×10^{-3}
$b_{sn,3}$	-0.38408×10^{-7}	0.38408×10^{-7}
$b_{sn,4}$	0.24166×10^{-10}	-0.24166×10^{-10}

[1]Department of Mechanical Engineering, The University of Iowa, Iowa City, IA 52242.

Contributed by the Heat Transfer Division and presented at the 23rd National Heat Transfer Conference, Denver, CO, August 1985. Manuscript received by the Heat Transfer Division September 26, 1985.

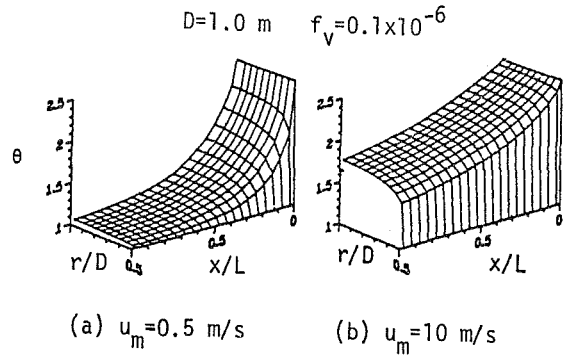

Fig. 1 Velocity effects on temperature distributions

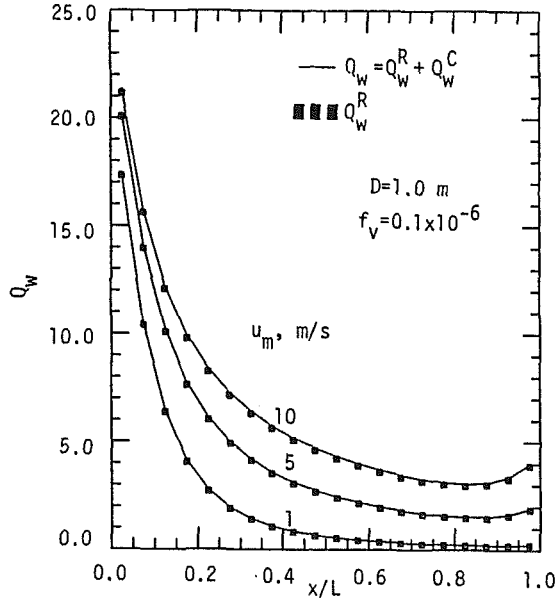

Fig. 2 Velocity effects on wall heat flux

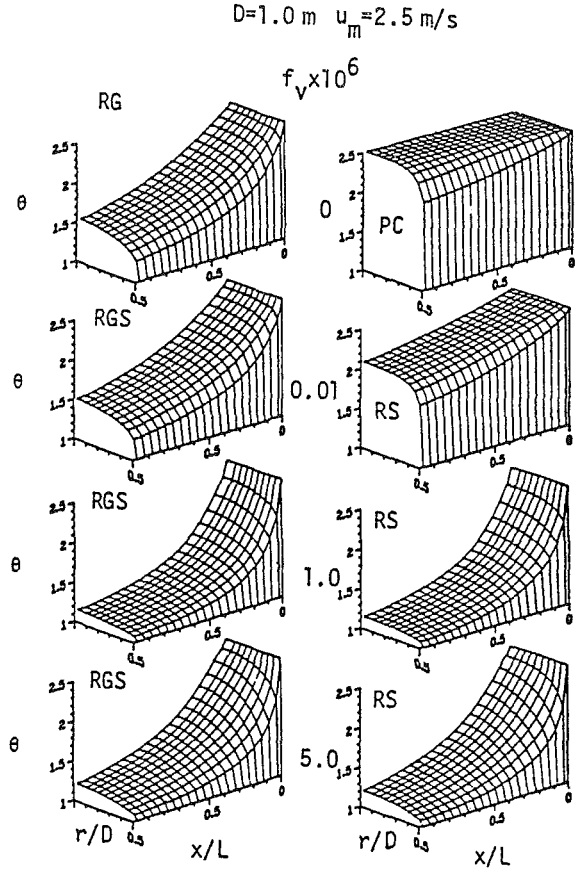

Fig. 3 Soot volume fraction effects on temperature distribution

elements near the wall experience a change in temperature. For laminar flow, radiative transfer dominates and gas temperatures approach the wall temperatures, particularly near the outlet.

The influence of u_m on the wall heat flux is shown in Fig. 2, where Q_w is the dimensionless total wall heat flux expressed as the sum of the radiative Q_w^R and conductive Q_w^c fluxes. Negative wall heat fluxes exist for cooling cases, but the absolute value of the wall heat flux as signified by Q_w is used in the discussion and all figures. In Fig. 2, the solid lines represent the total wall flux and the symbols represent the radiative wall flux. The total wall heat flux is nonuniform and decreases along the axial distance and may increase near the exit due to radiant exchange with the outlet surface. From Fig. 1, the gas temperature for turbulent flow is high yielding a high outlet surface temperature that causes the wall heat flux to increase near the exit. As shown in Fig. 2, the radiative flux dominates with the convective flux being less than 5.0 percent of the total wall heat flux. For example, with $u_m = 5.0$ m/s and at $x/L = 0.475$, the convective wall flux is 0.0727 and the total wall flux is 2.742.

The influence of soot volume fraction on gas temperatures is illustrated in Fig. 3 where results are displayed for $u_m = 2.5$ m/s. The left column of Fig. 3 displays temperature profiles starting with RG where only absorbing gas radiation effects are included and with increasing soot concentration as designated by RGS, which includes both absorbing gases and soot radiation. The right column starts with the pure convective case PC and increases the soot concentration as designated by RS where only soot radiation is included. As soot increases, the gas temperatures decrease and the radial temperature profiles become more uniform. This trend occurs up to approximately $f_v = 1.0 \times 10^{-6}$. After this, the gas elements flowing near the center are at higher temperatures for $f_v = 5 \times 10^{-6}$ as a result of blockage by the soot of the radiant exchange between these elements and the wall. Gas elements near the wall still experience decreasing temperatures as f_v increases up to 5.0×10^{-6}. When f_v is less than 0.01×10^{-6}, the trend of gas emission is that of absorbing gases, and when f_v is greater than 1.0×10^{-6}, the gas emission is dominated by soot emission.

Representative total wall heat flux distributions are illustrated in Fig. 4 for several values of f_v. The solid and broken lines are for $u_m = 2.5$ and 25 m/s, respectively. For PC, wall heat fluxes are approximately 0.2 and 1.8 for these velocities, respectively, and are significantly smaller than those for a radiating gas. Wall heat fluxes for PC were obtained using eighty radial zones. For $u_m = 2.5$ m/s, the wall heat flux increases as the soot volume fraction increases for zones near the inlet end and decreases near the outlet end. The decrease near the outlet end with increasing soot is because the gas is becoming opaque and the radiant wall flux is decreasing since the wall sees only the adjacent gas elements, which are nearly at the wall temperature as seen in Fig. 3. The effects of soot on wall fluxes are small for the lower velocity. For the higher velocity, the wall flux varies strongly with soot since the gas temperatures are higher.

Figure 5 shows the variation of the volumetric radiant term

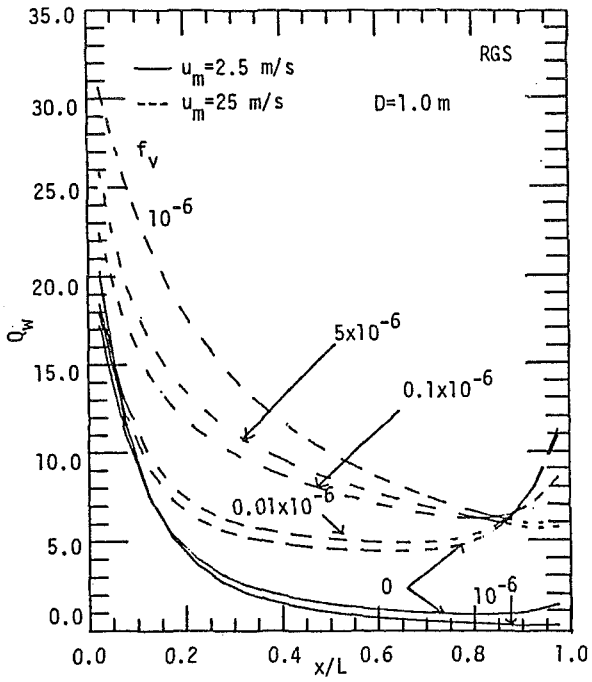

Fig. 4 Soot volume fraction effects on wall heat flux

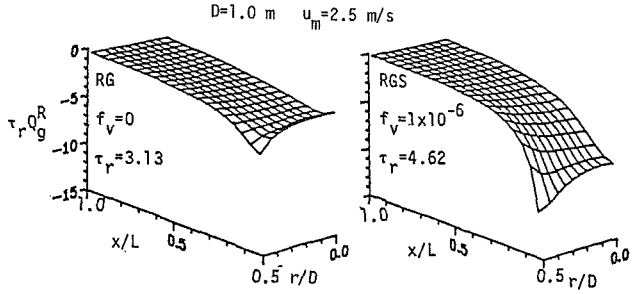

Fig. 5 Volumetric radiant energy term

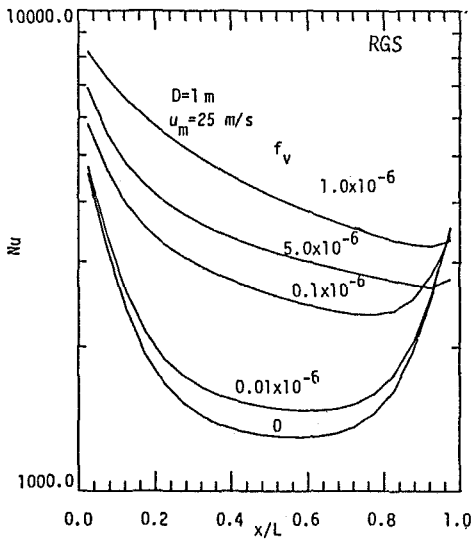

Fig. 6 Nusselt number for combined radiation and convection

$\tau_r Q_g^R$ appearing in the gas energy balance [6] with several values of f_v and $u_m = 2.5$ m/s. This term is related to the radiant energy absorbed minus the radiant energy emitted by the volume zone. The emission increases near the inlet due to the high gas temperature and then decreases along the axial axis. The peak value, where the emission is maximum, moves toward the inlet end as soot volume fraction increases, and also the volume zones near the wall emit more energy. At downstream locations, the radiant energy absorbed is almost equal to the radiant energy emitted especially near the wall, except near the inlet end, the radiant term is relatively uniform, which implies that a coarser zonal pattern may be used without a loss of accuracy.

In view of the large number of parameters, only representative results of the local Nusselt number Nu are presented to illustrate the influence of soot. The results are shown in Fig. 6 for several values of f_v. The Nusselt number decreases along the axial distance and then increases near the outlet end due to the radiant exchange with the outlet end. The Nusselt number for PC is around 200. Similar to the findings in Fig. 4, the Nusselt number increases with f_v up to 10^{-6} and the decreases for $f_v > 10^{-6}$. The Nusselt number for $D = 10$ m [7] is almost ten times that for $D = 1$ m.

Conclusions

The effects of radiation combined with conduction and convection are examined for flow of a radiatively participating gas through a black wall circular tube. The influence of soot volume fraction on gas temperatures and wall heat fluxes is examined. When the soot volume fraction is less than 0.01×10^{-6}, the trend of gas temperature is that due to the absorbing gases. When the soot volume fraction is greater than 10^{-6}, the gas emission is dominated by soot emission and the centerline gas elements are at higher temperatures since the soot blocks the radiant exchange between these elements and the cold wall. The wall heat flux with radiation is larger than that without radiation for the same values of the system parameters. The effects of the soot volume fraction on the wall heat flux are small for low velocities. However, for high velocities, the wall heat flux varies strongly with the soot volume fraction since the gas temperatures are higher. When the soot volume fraction is greater than 1×10^{-6}, the wall heat fluxes decrease as the soot volume fraction increases due to the increase in the gas optical thickness that reduces the radiant exchange between the gas and the wall. The Nusselt numbers with gas/soot radiation are higher than those without radiation for the same values of the system parameters. The Nusselt number increases with soot volume fraction up to 1.0×10^{-6} and then decreases.

References

1 Johnson, T. R., and Beer, J. M., "Radiative Heat Transfer in Furnaces; Further Development of the Zone Method of Analysis," *14th Symp. (Int'l) on Combust.*, 1973, pp. 639–649.

2 Modest, M. F., Meyer, B. R., and Azad, F. H., "Combined Convection and Radiation in Tube Flow of an Absorbing, Emitting and Anisotropically Scattering Gas-Particulate Suspension," ASME Paper No. 80-HT-27, 1980.

3 Lockwood, F. C., and Shan, N. G., "A New Radiation Solution Method for Incorporation in General Combustion Prediction Procedures," *18th Symp. (Intl') on Combust.*, 1981, pp. 1405–1414.

4 Richter, W., and Heap, M. P., "The Impact of Heat Release Pattern and Properties on Heat Transfer in Boilers," ASME Paper No. 81-WA/HT-27, 1981.

5 Yuen, W. W., "Radiative Heat Transfer Characteristics of a Soot/Gas Mixture," *Seventh Int'l. H.T. Conf.*, Munich, Germany, 1982, Vol. 2, pp. 577–582.

6 Smith, T. F., Shen, Z. F., and Al-Turki, A. M., "Radiative and Convective Transfer in a Cylindrical Enclosure," ASME JOURNAL OF HEAT TRANSFER, Vol. 107, 1985, pp. 482–485.

7 Al-Turki, A. M., "Radiative and Convective Heat Transfer in a Cylindrical Enclosure for Flow of a Gas-Soot Mixture," Ph.D. Thesis, The University of Iowa, 1984.

8 Hottel, H. C., and Sarofim, A. F., *Radiative Transfer*, McGraw-Hill, New York, 1967.
9 Felske, J. D., and Charalamopoulos, T. T., "Gray Gas Weighting Coefficient for Arbitrary Gas-Soot Mixtures," *Int. J. Heat Mass Transfer*, Vol. 25, 1928, pp. 1849–1855.
10 Al-Turki, A. M., and Smith, T. F., "Emissivity and Absorptivity of Gas-Soot Mixtures," Technical Report E-TFS-84-003, Department of Mechanical Engineering, The University of Iowa, 1984.
11 Smith, T. F., Shen, Z. F., and Friedman, J. N., "Evaluation of Coefficients for the Weighted Sum of Gray Gases Model," ASME JOURNAL OF HEAT TRANSFER, Vol. 104, 1982, pp. 602–608.
12 Beier, R. A., and Pagni, P. J., "Soot Volume Fraction Profiles in a Forced-Combusting Boundary Layers," ASME JOURNAL OF HEAT TRANSFER, Vol. 105, 1983, pp. 159–165.

Quenching of a Hollow Sphere

S. Subramanian[1] and L. C. Witte[2]

Introduction

Most analyses of boiling on cylinders and spheres assume uniform surface temperature. For bodies that are small or have high conductivity, this is a fair assumption. But for large bodies, the variation of heat flux q around the body might be large enough to cause significant variations in temperature T on a surface that cannot provide unlimited energy to the boiling process by internal conduction. As an example, Ungar and Eichhorn [1] measured large T variations around a 2.54-cm copper sphere quenched in methanol. Such T variation led to nonuniform boiling regimes around the sphere and cast doubt about the significance of minimum and maximum heat fluxes that one would calculate from experiments where T uniformity is assumed. Thibault and Hoffman [2] also measured large variations in heat flux about a 12.7-cm copper cylinder quenched in water.

A hollow sphere, used in this study, removes the conduction path from the front to the back of the body; therefore any spatial variations in heat flux would enhance the T variation in the angular (θ) direction around the body. The output of two thermocouples (TC) mounted inside the sphere was linked to the boiling behavior on the surface by using a specially designed timing circuit that provided simultaneous timing marks for the T–t records and for high-speed motion pictures of selected experiments.

Apparatus

Figure 1 shows the 2.54-cm hollow sphere; it was machined in two parts that were press-fitted together after installation of the thermocouples. The press-fit seam was silver-soldered to eliminate contact resistance between the two halves. The TC beads were peened and silver-soldered into depressions machined into the inner surface. Additional details of the sphere's construction are given in [3].

Following heating in an electric furnace, the sphere was quenched in methanol and water contained in a transparent tank equipped with an immersion heater. The TC outputs and timing signals were recorded on a Tektronix 565 oscilloscope. The timing pulses were also fed to the timing LED channel of a Photec IV high-speed camera used to photograph selected experiments. The details of the timing circuit are given in [3].

Data Reduction

Significant T variations occurred around the sphere during transition/nucleate boiling. Thus the T–t data had to be reduced so as to account for T and q variation in the θ direction, as follows: The sphere was split into nine azimuthal rings for a finite-difference calculation of the local heat fluxes. The input to the calculational model was a third-order polynomial curve-fit of the temperature variation around the sphere at discrete points in time. The four boundary conditions

$$\theta = 0 \qquad dT/d\theta = 0$$
$$\theta = 45 \text{ deg}, \qquad T = \text{TC1}$$
$$\theta = 135 \text{ deg}, \qquad T = \text{TC2}$$
$$\theta = 180 \text{ deg}, \qquad dT/d\theta = 0$$

were used. The finite difference model accounted for the energy flowing around the periphery of the sphere as well as for the loss of internal energy of any particular element. The details of the model are omitted for brevity, see [3]. An uncertainty analysis showed that the maximum uncertainty of ±5 percent for calculated q occurred in the transition/nucleate boiling regime.

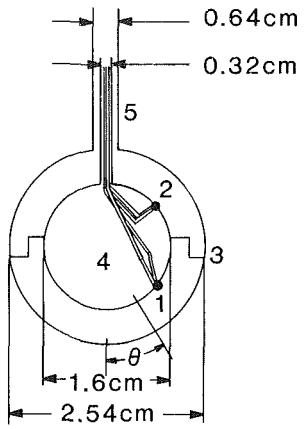

1. TC1, θ = 45°
2. TC2, θ = 135°
3. Silver soldered equator
4. Ceramic bead insulation
5. Support stem

Fig. 1 Schematic diagram of the test sphere

Discussion of Results

Over 100 trials involving methanol and water were made. Twenty-eight of the methanol tests were used for data reported herein. The remainder were used for repeatability verification and apparatus checkout. All tests reported herein were performed with the bottom of the sphere immersed 3.81 cm below the surface of the methanol.

Figure 2 shows the T–t history and the fluxes calculated for the TC1 and TC2 locations for 24°C methanol. This test included motion pictures taken at 800 frames/s. Figure 2 will be used to explain the general nature of subcooled methanol boiling. Motion pictures of boiling subcooled water showed the same qualitative behavior as observed in methanol.

Physics of Subcooled Quenching. Near the end of film boiling, when the sphere was virtually at uniform T, some sort of disturbance originated on the liquid–vapor interface at the right-hand side of the sphere and propagated rapidly over the sphere surface. It is shown by sketch B on Fig. 2. The frame number (1918) when the disturbance started is also shown on

[1]Research Assistant, University of Houston, Houston, TX 77004.
[2]Professor, Department of Mechanical Engineering, University of Houston, Houston, TX 77004; Fellow ASME.
Contributed by the Heat Transfer Division for publication in the JOURNAL OF HEAT TRANSFER. Manuscript received by the Heat Transfer Division April 1, 1985.

8 Hottel, H. C., and Sarofim, A. F., *Radiative Transfer*, McGraw-Hill, New York, 1967.
9 Felske, J. D., and Charalamopoulos, T. T., "Gray Gas Weighting Coefficient for Arbitrary Gas-Soot Mixtures," *Int. J. Heat Mass Transfer*, Vol. 25, 1928, pp. 1849–1855.
10 Al-Turki, A. M., and Smith, T. F., "Emissivity and Absorptivity of Gas-Soot Mixtures," Technical Report E-TFS-84-003, Department of Mechanical Engineering, The University of Iowa, 1984.
11 Smith, T. F., Shen, Z. F., and Friedman, J. N., "Evaluation of Coefficients for the Weighted Sum of Gray Gases Model," ASME JOURNAL OF HEAT TRANSFER, Vol. 104, 1982, pp. 602–608.
12 Beier, R. A., and Pagni, P. J., "Soot Volume Fraction Profiles in a Forced-Combusting Boundary Layers," ASME JOURNAL OF HEAT TRANSFER, Vol. 105, 1983, pp. 159–165.

Quenching of a Hollow Sphere

S. Subramanian[1] and L. C. Witte[2]

Introduction

Most analyses of boiling on cylinders and spheres assume uniform surface temperature. For bodies that are small or have high conductivity, this is a fair assumption. But for large bodies, the variation of heat flux q around the body might be large enough to cause significant variations in temperature T on a surface that cannot provide unlimited energy to the boiling process by internal conduction. As an example, Ungar and Eichhorn [1] measured large T variations around a 2.54-cm copper sphere quenched in methanol. Such T variation led to nonuniform boiling regimes around the sphere and cast doubt about the significance of minimum and maximum heat fluxes that one would calculate from experiments where T uniformity is assumed. Thibault and Hoffman [2] also measured large variations in heat flux about a 12.7-cm copper cylinder quenched in water.

A hollow sphere, used in this study, removes the conduction path from the front to the back of the body; therefore any spatial variations in heat flux would enhance the T variation in the angular (θ) direction around the body. The output of two thermocouples (TC) mounted inside the sphere was linked to the boiling behavior on the surface by using a specially designed timing circuit that provided simultaneous timing marks for the T–t records and for high-speed motion pictures of selected experiments.

Apparatus

Figure 1 shows the 2.54-cm hollow sphere; it was machined in two parts that were press-fitted together after installation of the thermocouples. The press-fit seam was silver-soldered to eliminate contact resistance between the two halves. The TC beads were peened and silver-soldered into depressions machined into the inner surface. Additional details of the sphere's construction are given in [3].

Following heating in an electric furnace, the sphere was quenched in methanol and water contained in a transparent tank equipped with an immersion heater. The TC outputs and timing signals were recorded on a Tektronix 565 oscilloscope. The timing pulses were also fed to the timing LED channel of a Photec IV high-speed camera used to photograph selected experiments. The details of the timing circuit are given in [3].

Data Reduction

Significant T variations occurred around the sphere during transition/nucleate boiling. Thus the T–t data had to be reduced so as to account for T and q variation in the θ direction, as follows: The sphere was split into nine azimuthal rings for a finite-difference calculation of the local heat fluxes. The input to the calculational model was a third-order polynomial curve-fit of the temperature variation around the sphere at discrete points in time. The four boundary conditions

$$\theta = 0 \qquad dT/d\theta = 0$$
$$\theta = 45 \text{ deg}, \qquad T = \text{TC1}$$
$$\theta = 135 \text{ deg}, \qquad T = \text{TC2}$$
$$\theta = 180 \text{ deg}, \qquad dT/d\theta = 0$$

were used. The finite difference model accounted for the energy flowing around the periphery of the sphere as well as for the loss of internal energy of any particular element. The details of the model are omitted for brevity, see [3]. An uncertainty analysis showed that the maximum uncertainty of ±5 percent for calculated q occurred in the transition/nucleate boiling regime.

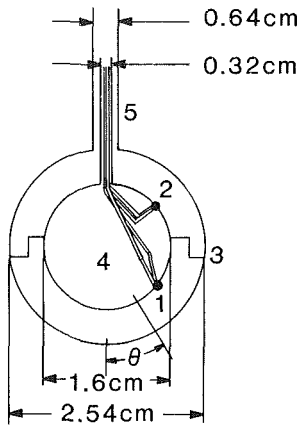

1. TC1, θ = 45°
2. TC2, θ = 135°
3. Silver soldered equator
4. Ceramic bead insulation
5. Support stem

Fig. 1 Schematic diagram of the test sphere

Discussion of Results

Over 100 trials involving methanol and water were made. Twenty-eight of the methanol tests were used for data reported herein. The remainder were used for repeatability verification and apparatus checkout. All tests reported herein were performed with the bottom of the sphere immersed 3.81 cm below the surface of the methanol.

Figure 2 shows the T–t history and the fluxes calculated for the TC1 and TC2 locations for 24°C methanol. This test included motion pictures taken at 800 frames/s. Figure 2 will be used to explain the general nature of subcooled methanol boiling. Motion pictures of boiling subcooled water showed the same qualitative behavior as observed in methanol.

Physics of Subcooled Quenching. Near the end of film boiling, when the sphere was virtually at uniform T, some sort of disturbance originated on the liquid–vapor interface at the right-hand side of the sphere and propagated rapidly over the sphere surface. It is shown by sketch B on Fig. 2. The frame number (1918) when the disturbance started is also shown on

[1]Research Assistant, University of Houston, Houston, TX 77004.
[2]Professor, Department of Mechanical Engineering, University of Houston, Houston, TX 77004; Fellow ASME.
Contributed by the Heat Transfer Division for publication in the JOURNAL OF HEAT TRANSFER. Manuscript received by the Heat Transfer Division April 1, 1985.

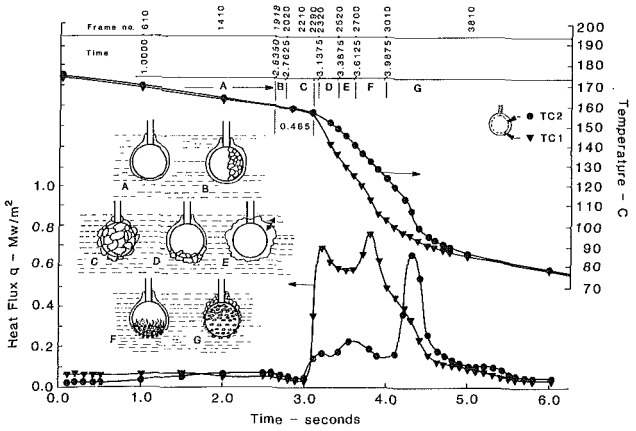

Fig. 2 Plot of heat flux and temperature histories for methanol at 24°C

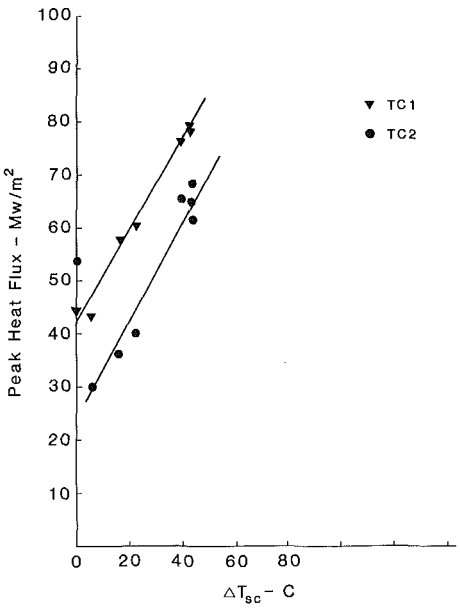

Fig. 3 Peak heat fluxes versus subcooling for methanol

the figure. Once it fully covered the sphere (0.1275 s later), a distinctly different type of liquid–vapor interface developed, which we called "randomly rippled," shown in sketch C. There was a 0.465 s lag between the beginning of the disturbance and when the TCs registered a significant drop in temperature. The characteristic conduction time for the sphere was 0.044 s, so although the TCs could have responded to the disturbance, they did not do so until almost 10 time constants later. This implies that the disturbance was confined to the liquid–vapor interface itself rather than causing massive liquid–solid contact that would have quickly caused a drop in surface temperature.

The sharp drop in TC1 was precipitated by a collapse of the vapor film beginning at the bottom of the sphere at about frame 2320. It is shown as sketch D on the figure. It was relatively violent and quickly set the vapor film into an oscillatory motion. Once this collapse began, the boiling behavior around the sphere became highly localized, as demonstrated in Fig. 2 by the differences in q at TC1 and TC2. The localized nature of the boiling persisted throughout the transition and most of the nucleate boiling regimes.

The oscillations of the vapor film that followed the vapor film collapse led to a decrease in the heat fluxes, especially for TC1, which shows a distinct lessening of the cooling rate between frames 2500 and 2600. Eventually, a nucleate boiling "front" moved around from the bottom to the top of the sphere, as shown in sketch F. Three regimes of boiling might coexist on the sphere at once: nucleate at the bottom, film at the top, separated by an oscillating transition boiling "ring."

The peak heat flux clearly propagated from the bottom to the top of the sphere. The peak heat flux was highest for TC1, which experienced it first. In fact, *all* experiments showed that the peak heat flux was highest for the TC location that experienced it first. Although separated in time on Fig. 2, the peak heat fluxes for TC1 and TC2 occurred at about the same temperature.

Effect of Subcooling. The collapse of the vapor film was much faster for subcooled than for saturated methanol. Subcooled methanol always exhibited "dual maxima" in its boiling curves as shown in Fig. 2. This is indicative of the highly localized nature of transition boiling around the sphere. The first maxima abated as the methanol was brought toward saturation.

Peak Heat Fluxes. Figure 3 shows that nucleate peak heat fluxes (second maximum) were strongly dependent upon liquid subcooling. There was an increase in peak heat flux with subcooling (ΔT_{sc}) for both TC locations. For saturated methanol, the top TC experienced the peak heat flux first, i.e., the vapor film collapsed at the top first and then moved downward over the sphere. In *all* tests the TC that experienced the peak flux first gave the highest value. As subcooling was imposed, the vapor film collapsed at the bottom first thus reversing the TC location where peak flux was highest.

Thibault and Hoffman [2] found that the highest peak heat flux occurred at the top of a 12.7-cm copper cylinder quenched in saturated water. As subcooling increased, the peak heat flux increased more rapidly over the lower parts of the cylinder than at the top, which is in basic agreement with our observations. Ded and Lienhard's [4] theory for peak heat flux agreed to within 5 percent of our average measured values for saturated methanol.

Conclusions

The major findings in this study are:

1 The TC location that experienced it first always gave the highest peak heat flux. When the transition front reached the second TC location, energy had been removed from that location by adjacent points which had already experienced the peak heat flux, thus limiting the amount of energy that could be provided to the boiling process.

2 Double maxima were observed for subcooled boiling. The first maximum corresponded to the initial collapse of the vapor film, while the second represented the nucleate peak heat flux regime. Between the two maxima, a vapor envelope oscillated locally over the surface.

3 Saturated boiling was more global than was subcooled boiling, but the peak heat flux was not uniformly distributed. The average saturated peak heat flux was predicted well by Ded and Lienhard's global theory.

4 All three regimes of boiling – film, transition, and nucleate – might coexist on the surface studied herein. Such behavior became more pronounced as subcooling was increased.

5 T variation around the sphere was virtually nil for film boiling. Consequently, analyses of film boiling assuming uniform T distribution should be adequate even for highly subcooled conditions.

References

1 Ungar, E., and Eichhorn, R., "Local Surface Boiling Heat Transfer From a Submerged Sphere," ASME Paper No. 82-HT-27.

2 Thibault, J., and Hoffman, T. W., "Local Boiling Heat Flux Density Around a Horizontal Cylinder," *Proc. 6th Int. Heat Transfer Conference*, Toronto, 1978, pp. 199–204.

3 Subramanian, S., "Quenching of a Hollow Sphere," MS Thesis, Department of Mechanical Engineering, University of Houston, Houston, TX, Dec. 1984.

4 Ded, J. S., and Lienhard, J. H., "The Peak Pool Boiling Heat Flux From a Sphere," *AIChE J.*, Vol. 18, No. 2, 1972, p. 337.

Depressurization Experiment in a Sodium-Heated Steam Generator Tube

D. M. France[1,2] and R. D. Carlson[1]

1.0 Introduction

Large-capacity steam generators for electric power plants are designed to operate over a wide range of conditions, including normal and off-normal steady-state loads and plant transients. Several shutdown transients for liquid metal fast breeder reactor (LMFBR) power plants were analyzed with the DEMO computer code [1]; results were presented in [2].

One of the more severe transients for the steam generators is the "waterside isolation and dump" transient, which is a planned transient designed into the plant control system. As explained in [2], the purpose of the transient is to minimize the water inventory in the steam generator during a sodium–water reaction resulting from a tube or weld leak. The transient is initiated by closing water valves at the steam generator inlet and outlet thus isolating it from the remainder of the water circuit. Other valves are opened, allowing the isolated water in the steam generator to flow into auxiliary vessels at atmospheric pressure. This sequence of events results in relatively fast depressurization and removal of the water in the steam generator and is often termed the "blowdown" transient.

A blowdown experiment was performed in this study using a sodium-heated test section with geometry and parameters typical of LMFBR steam generators. Water boiling inside a tube at 16 MPa was depressurized to atmospheric pressure in 30 s with the objective of determining the severity of the transient in terms of flow, temperature, and pressure gradients. The experiment was unique in terms of the full-scale test section size, the high pressures and temperatures, and the speed of the depressurization. Quantitative results presented show that the very large pressure and flow gradients that occur are confined to the initiation stage of the transient where system control could be used to mitigate the severity.

2.0 Experimental Analysis

Experiments were performed at Argonne National Laboratory-East in the Steam Generator Test Facility (SGTF). The facility has a nominal power rating of 1 MW and is designed to test full-scale LMFBR steam generator tubes at conditions prototypic of plant operation. The facility is described in detail in [3, 4].

The test section consisted of a single-tube shell and tube heat exchanger mounted vertically. Subcooled water entered the bottom of the tube and flowed upward as it was heated by sodium flowing countercurrent in the shell. The test section is shown schematically in Fig. 1. The dimensions and material of the heat transfer tube are given in the figure.

[1]Argonne National Laboratory, Components Technology Division, Argonne, IL 60439.

[2]Currently at University of Illinois at Chicago, Department of Mechanical Engineering, Chicago, IL 60680, USA; Mem. ASME.

Contributed by the Heat Transfer Division for publication in the JOURNAL OF HEAT TRANSFER. Manuscript received by the Heat Transfer Division January 17, 1985.

Two types of thermocouples are depicted in Fig. 1. The shell thermocouples were used in the present experiments to calculate axial heat flux, water temperature, and water quality distributions before initiation of the transient. The internal thermocouples, which were embedded in the wall of the heat transfer tube, were used during the transient to indicate the movement of liquid in the tube.

The test section inlet and exit piping arrangements are shown in Fig. 2. A single valve at the steam outlet from the test section isolated the top of the test section from the remainder of the water circuit; two valves were used for this purpose at the water inlet. Two blowdown valves were used, one each at the water inlet and outlet, to allow water to flow to the atmosphere from the test section water tube. The test section outlet isolation valve is numbered WV3A; the outlet blowdown valve is located between the test section exit and this valve. The test section inlet was isolated by closing both valves WV2 and WV6. The inlet blowdown valve was located between these two valves and the test section inlet, and the water flowmeter was located between the inlet blowdown valve and the test section inlet, as shown in Fig. 2.

The pressure and temperature of the water flow were measured close to the inlet and exit of the test section, as indicated by "*T*,*P*" in Fig. 2. Linear displacement transformers were placed on the isolation and blowdown valves to monitor positions as a function of time during the transient. The tran-

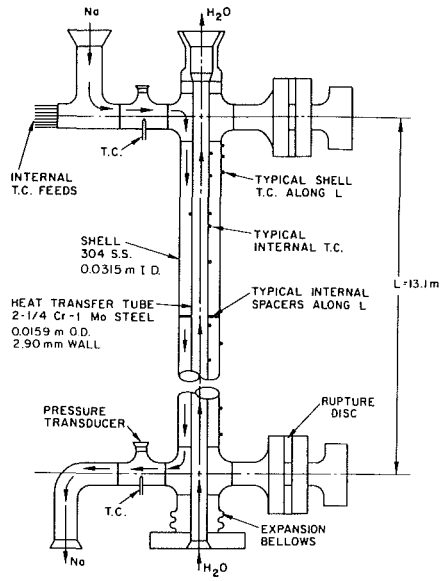

Fig. 1 Test section

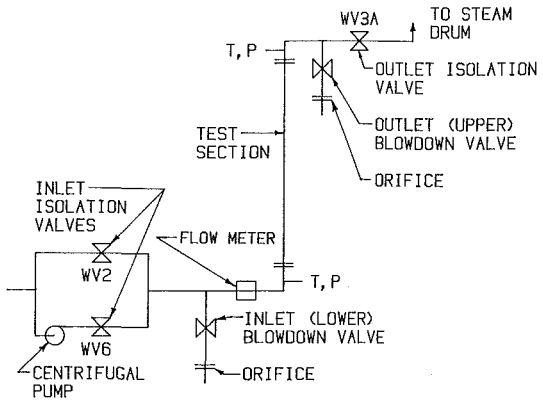

Fig. 2 Water valve arrangement

2 Thibault, J., and Hoffman, T. W., "Local Boiling Heat Flux Density Around a Horizontal Cylinder," *Proc. 6th Int. Heat Transfer Conference*, Toronto, 1978, pp. 199–204.

3 Subramanian, S., "Quenching of a Hollow Sphere," MS Thesis, Department of Mechanical Engineering, University of Houston, Houston, TX, Dec. 1984.

4 Ded, J. S., and Lienhard, J. H., "The Peak Pool Boiling Heat Flux From a Sphere," *AIChE J.*, Vol. 18, No. 2, 1972, p. 337.

Depressurization Experiment in a Sodium-Heated Steam Generator Tube

D. M. France[1,2] and R. D. Carlson[1]

1.0 Introduction

Large-capacity steam generators for electric power plants are designed to operate over a wide range of conditions, including normal and off-normal steady-state loads and plant transients. Several shutdown transients for liquid metal fast breeder reactor (LMFBR) power plants were analyzed with the DEMO computer code [1]; results were presented in [2].

One of the more severe transients for the steam generators is the "waterside isolation and dump" transient, which is a planned transient designed into the plant control system. As explained in [2], the purpose of the transient is to minimize the water inventory in the steam generator during a sodium–water reaction resulting from a tube or weld leak. The transient is initiated by closing water valves at the steam generator inlet and outlet thus isolating it from the remainder of the water circuit. Other valves are opened, allowing the isolated water in the steam generator to flow into auxiliary vessels at atmospheric pressure. This sequence of events results in relatively fast depressurization and removal of the water in the steam generator and is often termed the "blowdown" transient.

A blowdown experiment was performed in this study using a sodium-heated test section with geometry and parameters typical of LMFBR steam generators. Water boiling inside a tube at 16 MPa was depressurized to atmospheric pressure in 30 s with the objective of determining the severity of the transient in terms of flow, temperature, and pressure gradients. The experiment was unique in terms of the full-scale test section size, the high pressures and temperatures, and the speed of the depressurization. Quantitative results presented show that the very large pressure and flow gradients that occur are confined to the initiation stage of the transient where system control could be used to mitigate the severity.

2.0 Experimental Analysis

Experiments were performed at Argonne National Laboratory-East in the Steam Generator Test Facility (SGTF). The facility has a nominal power rating of 1 MW and is designed to test full-scale LMFBR steam generator tubes at conditions prototypic of plant operation. The facility is described in detail in [3, 4].

The test section consisted of a single-tube shell and tube heat exchanger mounted vertically. Subcooled water entered the bottom of the tube and flowed upward as it was heated by sodium flowing countercurrent in the shell. The test section is shown schematically in Fig. 1. The dimensions and material of the heat transfer tube are given in the figure.

[1]Argonne National Laboratory, Components Technology Division, Argonne, IL 60439.

[2]Currently at University of Illinois at Chicago, Department of Mechanical Engineering, Chicago, IL 60680, USA; Mem. ASME.

Contributed by the Heat Transfer Division for publication in the JOURNAL OF HEAT TRANSFER. Manuscript received by the Heat Transfer Division January 17, 1985.

Two types of thermocouples are depicted in Fig. 1. The shell thermocouples were used in the present experiments to calculate axial heat flux, water temperature, and water quality distributions before initiation of the transient. The internal thermocouples, which were embedded in the wall of the heat transfer tube, were used during the transient to indicate the movement of liquid in the tube.

The test section inlet and exit piping arrangements are shown in Fig. 2. A single valve at the steam outlet from the test section isolated the top of the test section from the remainder of the water circuit; two valves were used for this purpose at the water inlet. Two blowdown valves were used, one each at the water inlet and outlet, to allow water to flow to the atmosphere from the test section water tube. The test section outlet isolation valve is numbered WV3A; the outlet blowdown valve is located between the test section exit and this valve. The test section inlet was isolated by closing both valves WV2 and WV6. The inlet blowdown valve was located between these two valves and the test section inlet, and the water flowmeter was located between the inlet blowdown valve and the test section inlet, as shown in Fig. 2.

The pressure and temperature of the water flow were measured close to the inlet and exit of the test section, as indicated by "*T*,*P*" in Fig. 2. Linear displacement transformers were placed on the isolation and blowdown valves to monitor positions as a function of time during the transient. The tran-

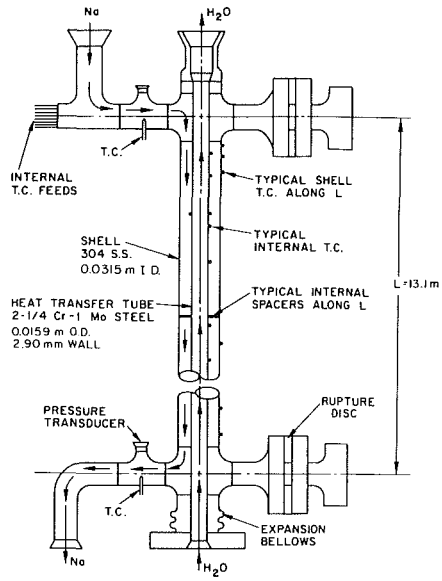

Fig. 1 Test section

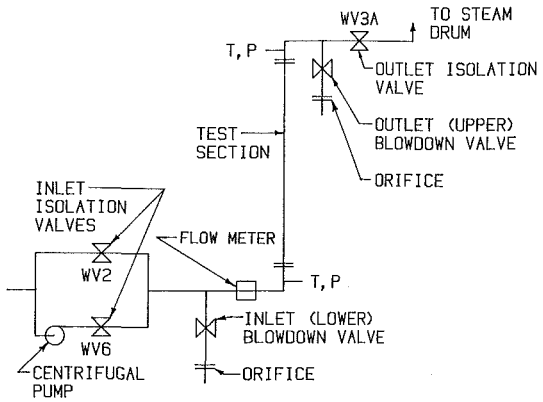

Fig. 2 Water valve arrangement

Table 1 Steady-state parameters

Water Parameters
Mass flux = 435.7 kg/m^2•s
Pressure = 16.0 MPa
Inlet temperature = 134.8°C
Sodium Parameters
Mass flowrate = 0.353 kg/s
Inlet temperature = 487.2°C
Outlet temperature = 295.3°C
CHF Conditions
Heat flux at tube ID = 441 kW/m^2
Quality = 0.396
Axial location = 5.093 m
System Conditions
Total power = 84.86 kW
Quality at exit = 1.507

sient was imposed by the sequential movement of these valves, and the depressurization rate was controlled by the orifices shown in Fig. 2.

3.0 Experimental Procedure

The depressurization experiment was initiated from steady-state operation in the once-through mode. The test parameters are given in Table 1 and are typical of LMFBR steam generator operation with the exception of the low water inlet temperature. This temperature was maintained at 135°C to circumvent facility limitations and allow the depressurization to run to completion. The control valves were activated in a preprogrammed sequence to initiate the transient. First, the inlet isolation valves were closed and power to the water pump was terminated. Then the blowdown valves were opened to the atmosphere, and finaly the exit isolation valve was closed. This sequence of events was accomplished in less than 4 s. The sodium flowrate and inlet temperature to the test section were unaltered during the entire test, simulating the plant conditions predicted in [2]. The valve sequence was chosen in view of these sodium conditions such that the test section was never completely isolated with the blowdown valves in the closed position.

After the valve movements were completed, the test was allowed to continue until the two-phase flow region approached the water flowmeter. The test section pressure approached atmospheric relatively slowly by this time, and the test was terminated by closing the blowdown valves and recovering water flow to the test section.

4.0 Results

The valve movements initiating the transient are shown in Fig. 3; important times are labeled A through E. The first movement of any valve occurred at time A, marking the initial movement of one of the two inlet isolation valves, WV2, from its open position toward the closed position. Before WV2 finished its movement, the other inlet isolation valve, WV6, changed from the full open to the full closed position. Subsequently, valve WV2 reached the full closed position at time B in Fig. 3, marking the complete isolation of the test section inlet from the test facility.

After the test section inlet was isolated, the blowdown valves were opened at times C and D in Fig. 3. Finally, the test section outlet isolation valve was closed, and its complete closure at time E in Fig. 3 marked the earliest time when the test section was completely isolated from the facility with the blowdown valves open.

The water mass flux at the test section inlet is shown in Fig. 4 as a function of time during the test. Under steady-state conditions, before time A, the water mass flux was steady and in

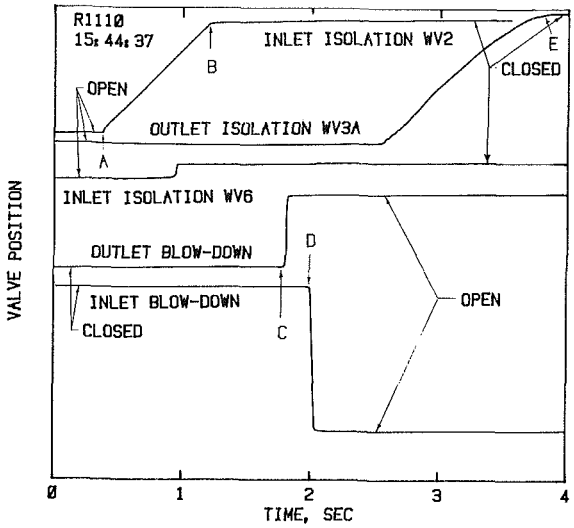

Fig. 3 Transient initiation valve movements

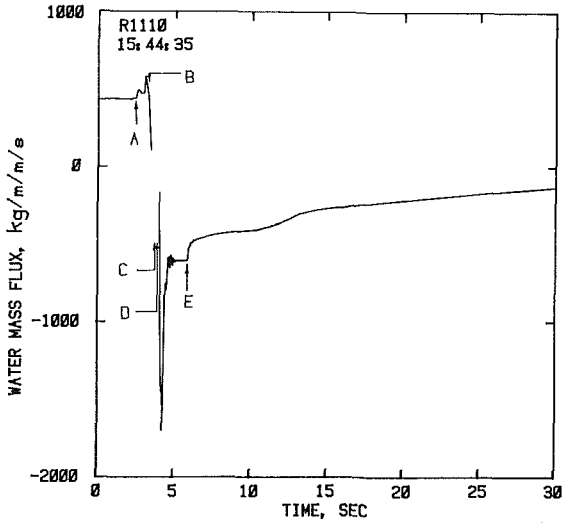

Fig. 4 Test section inlet water flow

the positive direction, which is upflow through the test section. At time A, the transient was started by the initial movement of inlet isolation valve WV2. As a consequence of the position of WV2 relative to the pump, as shown in Fig. 2, the water flow to the test section increased slightly and then started to decrease sharply after time B, when the inlet to the test section was completely isolated from the experimental facility. The water flow decreased even faster after the two blowdown valves were opened at times C and D, and became negative, as shown in Fig. 4. Water was flowing downward out to the test section inlet. The water mass flux reached a maximum value in the downward direction of approximately 3.5 times its steady-state upward value, after which oscillations were experienced followed by very steady flow in the downward direction. During this time, the outlet isolation valve was closing. The outlet valve was completely closed at point E, marking the complete isolation of the test section from the facility, and it had a significant effect on the water flow, causing a small but sharp decrease in the negative flow at the test section inlet. This event was followed by a gradual decrease in the negative flow toward zero flow for the remainder of the test. (No mass flux data were obtained very close to zero flow due to the limitations of the turbine flowmeter used.)

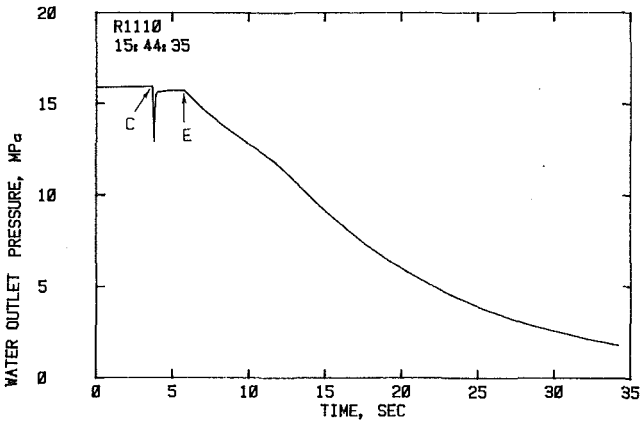

Fig. 5 Test section outlet pressure

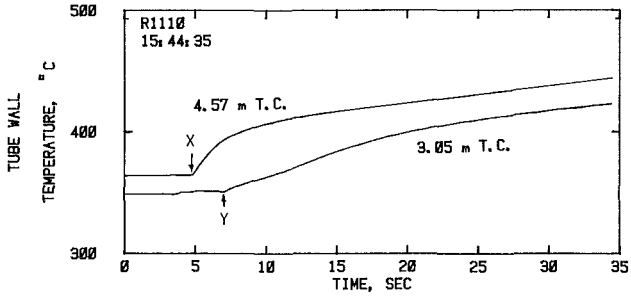

Fig. 6 Temperatures below CHF

The water pressures at the test section inlet and outlet exhibited sharp responses to blowdown valve movements and to complete test section isolation. The outlet pressure shown in Fig. 5 was unchanged from its stedy-state value until the initial movement of the outlet blowdown valve at time C. After a sharp decrease, the pressure recovered to a steady value until time E, after which the pressure decreased relatively gradually toward atmospheric pressure for the remainder of the test. The inlet water pressure response was similar.

Before the depressurization transient began, under steady-state conditions, CHF was located 5.09 m above the water inlet to the test section (Table 1). This location marks the change from liquid to vapor as the continuous phase in contact with the water tube wall, and in this region the wall temperature changes from relatively close to the water temperature to relatively close to the sodium temperature in steady state. A similar effect was seen during the transient. There were two wall thermocouples at 4.57 m and 3.05 m that were below the steady-state CHF position of 5.09 m. As the transient progressed, a clear increase in temperature was observed, first in the 4.57 m thermocouple at 5 s, shown as point X in Fig. 6, and then in the 3.05 m thermocouple at ~7 s (point Y in Fig. 6). The water temperature at the test section inlet was constant until 11 s into the transient. This sequential temperature response was indicative of a liquid/vapor interface moving downward in the test section.

In contrast to the sequential increases in temperature observed below the steady-state CHF location, tube wall temperatures above 5.09 m all increased in temperature at approximately the same time (time X in Fig. 6). The closest thermocouple to the CHF location was at 7.62 m, and the increase in all wall temperature measurements above this point occurring at the same time indicates that the liquid/vapor interface did not move up in the test section above the 7.62 m location.

The test was terminated approximately 30 s after the complete test section isolation at time E. The test section flow was approaching zero; the pressures were slowly approaching atmospheric pressure, and oscillations observed in the water inlet temperature indicated that two-phase flow had reached this level.

5.0 Discussion

Water boiling in a 13 m tube at 16 MPa with superheated steam at the exit was depressurized to atmospheric pressure in 30 s while heat was continuously supplied. This rather severe transient produced large gradients in water flow, pressure, and temperature that were predicted at least on a qualitative basis [2]. However, it was found that the largest gradients in flow and pressure occurred during the time when the transient was initiated by valve movements. After the water side of the test section was completely isolated from the test facility and the blowdown valves were fully open, the 30 s depressurization transient produced relatively small gradients in flow and pressure, although the thermal gradients were large during this period.

The water flow gradients are seen in Fig. 4 to be very large during the transient initiation period before time E. The water mass flux changed by 400 percent in a very short time. However, after time E, the water mass flux exhibited relatively small gradients. Similar results are given for the water pressure in Fig. 5. Before time E, a pressure spike was observed as the upper blowdown valve was opened. The pressure gradient associated with this spike was much more severe than the gradients in the 30 s depressurization after time E.

These results for water mass flux and pressure gradients represent relatively severe conditions for steam generators, but the fact that the steepest gradients occurred during the controlled transient initiation presents the possibility for mitigating the severity by alternate programming of the valves. Both the valve sequence and valve accelerations can influence the results.

The thermal gradients measured during the experiment started at approximately time E and would not be expected to be greatly affected by the transient initiation technique. These gradients are influenced by the initial system parameters, the duration of depressurization, and the direction of water flow.

Flow reversal was measured and predicted [2]. In addition, the tube wall thermocouple responses indicated that the liquid in the test section moved in the downward direction, and a liquid/vapor interface remained intact. These results can be interpreted further as an indication that most of the mass of water in the test section flowed out through the inlet blowdown valve (at the bottom of the test section). This condition was predicted by the DEMO code.

The nominal 30 s depressurization time period used to describe the experiment was based on the pressure measurements shown in Fig. 5. With the exception of the pressure spike associated with blowdown valve movement, the water pressure was essentially unchanged until the test section was completely isolated at time E. Thus, a time of 30 s from time E to the test termination indicates that the period of depressurization from 16 MPa to atmospheric pressure produced a nominal rate of 0.5 MPa/s. Although this depressurization rate is relatively fast for large steam generators, it may be desirable to increase the rate while decreasing pressure and flow gradients during the initiation stage in the manner discussed previously.

6.0 Acknowledgments

This study was performed under the auspices of the U. S. Department of Energy under Contract No. W-31-109-Eng-38.

7.0 References

1 DEMO, Westinghouse Electric Corp. LMFBR Plant Simulation Computer Code, 1978.

2 Gross, M., and Noc, D., "Shutdown Transients for an LMFBR Plant With a Superheated Steam Cycle," ASME Paper No. 82-NE-23.
3 France, D., Carlson, R., Chiang, T., and Priemer, R., "Characteristics of Transition Boiling in Sodium-Heated Steam Generator Tubes," ASME JOURNAL OF HEAT TRANSFER, Vol. 101, No. 2, May 1979, pp. 270-275.
4 Stevens, H. C., and France, D. M., "Development of a Thermal/Hydraulic Test Facility for Full-Scale LMFBR Steam Generator Tubes," *Trans. Am. Nucl. Soc.*, Vol. 22, 1975, p. 538.

Fouling Due to Corrosion Products Formed on a Heat Transfer Surface

E. F. C. Somerscales[1,2] and M. Kassemi[1]

Nomenclature

A = area of heat transfer surface, m^2
a = calibration constant for wire electrical resistance-temperature relation, equation (3), ohms
b = calibration constant for wire electrical resistance-temperature relation, equation (3), ohms/°C
Q = heat flow, W
R = total thermal resistance, m^2 °C/W
R_c = convective thermal resistance, m^2 °C/W
R_f = thermal resistance of fouling deposit, m^2 °C/W
R_t = wire electrical resistance, ohms
T_b = bulk temperature of the water, °C
T_s = temperature of the heat transfer surface, °C

Introduction

This paper is concerned with a type of fouling that has received very little attention in the past in spite of its importance to designers and operators of heat transfer equipment, namely, the fouling due to corrosion products that form on heat transfer surfaces exposed to flowing water. The lack of previous interest probably arises from uncertainty about the importance of this type of fouling. For this reason it is the objective of the research described in this paper to obtain quantitative information on the thermal resistance associated with corrosion fouling, and to compare it to thermal resistance values reported for other categories of fouling. The tests were made with the following conditions comparable to those found in industrial heat transfer equipment: the temperature of the heat transfer surface, material of the heat transfer surface, and the following properties of the water: oxygen content, pH, and temperature. It is not considered justifiable at this stage in the investigation of corrosion fouling:

(*a*) to study details of the fouling process, e.g., corrosion rates and deposit removal;
(*b*) to obtain data on the rates of fouling;
(*c*) to produce design data for heat transfer equipment (although the data obtained should be of considerable qualitative interest to designers);
(*d*) to simulate conditions in industrial equipment, other than those indicated above (e.g., Reynolds number corresponded to a value of about 75 in a duct of circular cross section);
(*e*) to devise a theory of corrosion fouling on the basis of the data obtained in these experiments, because preliminary theoretical studies by one of us (Somerscales, 1981, 1983b), and by Mahato et al. (1968a,b, 1980) and Shemilt et al. (1980) show that detailed numerical information, of the type associated with item (*a*) above, is essential if such an effort is to be successful;
(*f*) to contribute to the literature on corrosion mechanisms in water.

In view of the character of the research, it has been both appropriate and possible to devise a measurement technique that is simultaneously low in cost and provides rapid results. If the data obtained from the test warrant a more detailed investigation of corrosion fouling, of the type indicated in items (*a*) through (*f*) above, then it would be desirable to design and construct, at a cost substantially greater than that of the equipment described in this paper, apparatus that would allow more complete information on the fouling process to be obtained.

Fouling by Aqueous Corrosion Products

Corrosion fouling describes fouling caused by the formation of corrosion products on a heat transfer surface as a result of the corrosion of that surface.[3] Previous work on this type of fouling has been reviewed in detail by Somerscales (1981).

The effect of corrosion fouling deposits is to add a thermal resistance R_f to the convective resistance R_c at the heat transfer surface, so that the total thermal resistance R is given by

$$R = R_c + R_f \tag{1}$$

This overall thermal resistance is related to the heat flow Q by

$$R = A\frac{T_s - T_b}{Q} \tag{2}$$

Experimental Method

To provide experimental apparatus capable of producing quantitative data rapidly and at minimum cost, the tests were carried out with specimens in the form of an electrically heated wire suspended in a bath of water.[4] Two questions that arise concerning this technique are the effect on the interpretation of the data of: (*a*) the metallurgical structure, and (*b*) the presence of wire drawing compounds in the wire. It is not expected that the first point would be important, because the corrosion rate, as pointed out by Uhlig (1963), is controlled by oxygen transport. To ensure that there were no wire drawing compounds incorporated into the material, etched metallurgical sections of two specimens (3 and 4) were made. These are shown in Fig. 1. Careful examination failed to show the presence of wire drawing compounds (this confirms expert

[1]Rensselaer Polytechnic Institute, Troy, NY 12181.
[2]Mem. ASME.
Contributed by the Heat Transfer Division for publication in the JOURNAL OF HEAT TRANSFER. Manuscript received by the Heat Transfer Division August 6, 1984.

[3]Because of the potential for confusing the two corrosion-related fouling phenomena, the authors in earlier publications (Somerscales, 1981; Somerscales and Kassemi, 1984), have introduced the term *ex situ* corrosion fouling to describe fouling caused by corrosion products transported from elsewhere in the system and deposited on the heat transfer surface, and to call the corrosion fouling due to corrosion products formed at the heat transfer surface *in situ* corrosion fouling. This paper is concerned with *in situ* corrosion fouling. In spite of the usefulness of this classification, it is probably better not to expand the nomenclature of fouling unduly, but to call *in situ* corrosion fouling just corrosion fouling, and to recognize that *ex situ* corrosion fouling is due to one or both of the processes called particulate fouling and precipitation fouling.

[4]The current flowing in the wire will not affect the rate of corrosion, since it does not contribute to the corrosion current flowing in the electrolyte between anodic and cathodic areas.

2 Gross, M., and Noc, D., "Shutdown Transients for an LMFBR Plant With a Superheated Steam Cycle," ASME Paper No. 82-NE-23.
3 France, D., Carlson, R., Chiang, T., and Priemer, R., "Characteristics of Transition Boiling in Sodium-Heated Steam Generator Tubes," ASME JOURNAL OF HEAT TRANSFER, Vol. 101, No. 2, May 1979, pp. 270-275.
4 Stevens, H. C., and France, D. M., "Development of a Thermal/Hydraulic Test Facility for Full-Scale LMFBR Steam Generator Tubes," *Trans. Am. Nucl. Soc.*, Vol. 22, 1975, p. 538.

Fouling Due to Corrosion Products Formed on a Heat Transfer Surface

E. F. C. Somerscales[1,2] and M. Kassemi[1]

Nomenclature

A = area of heat transfer surface, m^2
a = calibration constant for wire electrical resistance-temperature relation, equation (3), ohms
b = calibration constant for wire electrical resistance-temperature relation, equation (3), ohms/°C
Q = heat flow, W
R = total thermal resistance, m^2 °C/W
R_c = convective thermal resistance, m^2 °C/W
R_f = thermal resistance of fouling deposit, m^2 °C/W
R_t = wire electrical resistance, ohms
T_b = bulk temperature of the water, °C
T_s = temperature of the heat transfer surface, °C

Introduction

This paper is concerned with a type of fouling that has received very little attention in the past in spite of its importance to designers and operators of heat transfer equipment, namely, the fouling due to corrosion products that form on heat transfer surfaces exposed to flowing water. The lack of previous interest probably arises from uncertainty about the importance of this type of fouling. For this reason it is the objective of the research described in this paper to obtain quantitative information on the thermal resistance associated with corrosion fouling, and to compare it to thermal resistance values reported for other categories of fouling. The tests were made with the following conditions comparable to those found in industrial heat transfer equipment: the temperature of the heat transfer surface, material of the heat transfer surface, and the following properties of the water: oxygen content, pH, and temperature. It is not considered justifiable at this stage in the investigation of corrosion fouling:

(*a*) to study details of the fouling process, e.g., corrosion rates and deposit removal;
(*b*) to obtain data on the rates of fouling;
(*c*) to produce design data for heat transfer equipment (although the data obtained should be of considerable qualitative interest to designers);
(*d*) to simulate conditions in industrial equipment, other than those indicated above (e.g., Reynolds number corresponded to a value of about 75 in a duct of circular cross section);
(*e*) to devise a theory of corrosion fouling on the basis of the data obtained in these experiments, because preliminary theoretical studies by one of us (Somerscales, 1981, 1983b), and by Mahato et al. (1968a,b, 1980) and Shemilt et al. (1980) show that detailed numerical information, of the type associated with item (*a*) above, is essential if such an effort is to be successful;
(*f*) to contribute to the literature on corrosion mechanisms in water.

In view of the character of the research, it has been both appropriate and possible to devise a measurement technique that is simultaneously low in cost and provides rapid results. If the data obtained from the test warrant a more detailed investigation of corrosion fouling, of the type indicated in items (*a*) through (*f*) above, then it would be desirable to design and construct, at a cost substantially greater than that of the equipment described in this paper, apparatus that would allow more complete information on the fouling process to be obtained.

Fouling by Aqueous Corrosion Products

Corrosion fouling describes fouling caused by the formation of corrosion products on a heat transfer surface as a result of the corrosion of that surface.[3] Previous work on this type of fouling has been reviewed in detail by Somerscales (1981).

The effect of corrosion fouling deposits is to add a thermal resistance R_f to the convective resistance R_c at the heat transfer surface, so that the total thermal resistance R is given by

$$R = R_c + R_f \tag{1}$$

This overall thermal resistance is related to the heat flow Q by

$$R = A\frac{T_s - T_b}{Q} \tag{2}$$

Experimental Method

To provide experimental apparatus capable of producing quantitative data rapidly and at minimum cost, the tests were carried out with specimens in the form of an electrically heated wire suspended in a bath of water.[4] Two questions that arise concerning this technique are the effect on the interpretation of the data of: (*a*) the metallurgical structure, and (*b*) the presence of wire drawing compounds in the wire. It is not expected that the first point would be important, because the corrosion rate, as pointed out by Uhlig (1963), is controlled by oxygen transport. To ensure that there were no wire drawing compounds incorporated into the material, etched metallurgical sections of two specimens (3 and 4) were made. These are shown in Fig. 1. Careful examination failed to show the presence of wire drawing compounds (this confirms expert

[1]Rensselaer Polytechnic Institute, Troy, NY 12181.
[2]Mem. ASME.
Contributed by the Heat Transfer Division for publication in the JOURNAL OF HEAT TRANSFER. Manuscript received by the Heat Transfer Division August 6, 1984.

[3]Because of the potential for confusing the two corrosion-related fouling phenomena, the authors in earlier publications (Somerscales, 1981; Somerscales and Kassemi, 1984), have introduced the term *ex situ* corrosion fouling to describe fouling caused by corrosion products transported from elsewhere in the system and deposited on the heat transfer surface, and to call the corrosion fouling due to corrosion products formed at the heat transfer surface *in situ* corrosion fouling. This paper is concerned with *in situ* corrosion fouling. In spite of the usefulness of this classification, it is probably better not to expand the nomenclature of fouling unduly, but to call *in situ* corrosion fouling just corrosion fouling, and to recognize that *ex situ* corrosion fouling is due to one or both of the processes called particulate fouling and precipitation fouling.

[4]The current flowing in the wire will not affect the rate of corrosion, since it does not contribute to the corrosion current flowing in the electrolyte between anodic and cathodic areas.

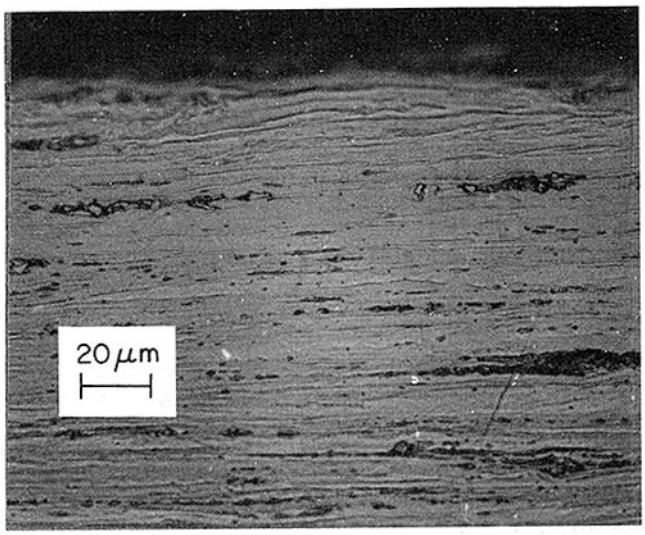

Fig. 1(*a*) Metallurgical longitudinal section of wire test specimen 3, etched in 2 percent nital

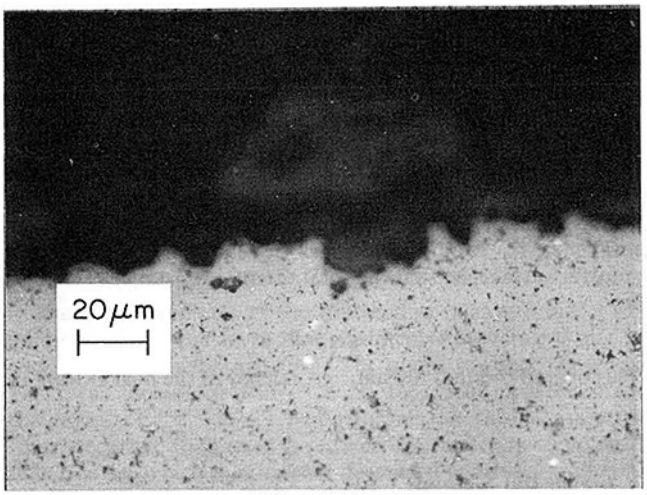

Fig. 1(*b*) Metallurgical cross section of wire test specimen 4, etched in 2 percent nital

opinion that normal drawing practice would be unlikely to lead to such a situation).

Tests were carried out on specimens of 1010 carbon steel[5] wire 1.37 mm diameter and 250 mm long. The wire was formed into the shape of a **U** and mounted in the test chamber shown in Fig. 2. It was heated electrically and the measured electrical resistance was used to determine its temperature and its power dissipation. Because of the very low electrical resistance of the wire (about 30 milliohms) this quantity was measured using a Kelvin bridge. Distilled water maintained at a constant temperature, pH (6.5 ± 0.4), and saturated with atmospheric oxygen was continually circulated through the test cell.

The apparatus has been discussed in detail by Somerscales and Kassemi (1983a), but it must be noted that the apparatus used in these experiments is significantly different from that described in the earlier reference. Experience showed that temporal fluctuations in the water velocity caused oscillations in the wire temperature, which made it impossible to balance the Kelvin bridge. The problem was eliminated by installing three grids, consisting of two acrylic plastic plates, which are each drilled with a large number of small holes, and a plastic mesh, between the test wire and the water inlet.

[5]Composition: 0.08–0.13 percent C, 0.30–0.60 percent Mn, 0.04 percent P, 0.05 percent S, remainder Fe (American Society of Metals, 1979).

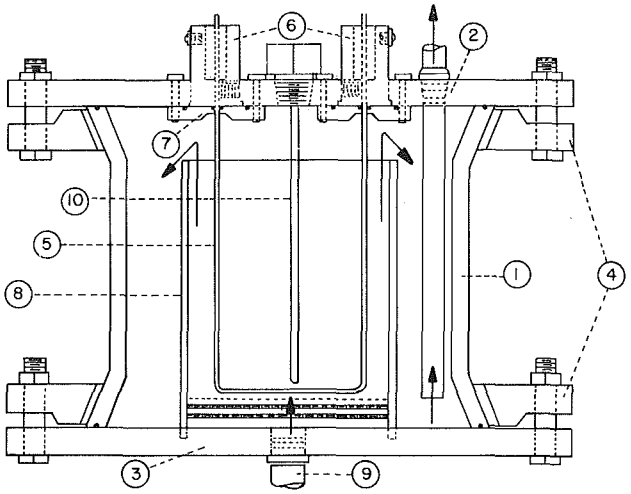

Fig. 2 The test chamber: (1) Pyrex glass pipe (15 cm long × 15 cm diameter); (2) acrylic plastic top cover; (3) acrylic plastic lower cover; (4) aluminum flanges; (5) wire specimen; (6) terminal blocks (steel); (7) O-ring seals; (8) cylindrical acrylic plastic baffle, including screens (3) to ensure uniform spatial flow distribution over the wire specimen; (9) fluid inlet

To start a test, the wire was cut to length, shaped into a **U** in a special former, and mounted in the top cover of the test cell (see Fig. 2). It was then cleaned by dipping the wire for two minutes in 5 percent nitric acid at 90°C, washing with distilled water, and then drying in hot air. The test cell was sealed and the test commenced as described in Somerscales and Kassemi (1983a). The test duration was between 250 and 400 hr, and measurements of the system temperatures, wire electrical resistance, wire current, pH and oxygen content were made every 24 hr.

Because bubbles resulting from boiling on the wire, air coming out of solution, or from the corrosion reaction could introduce a specious thermal resistance, the wire was frequently checked during the course of the test for the presence of bubbles. Bubbles were never observed, and in addition the wire temperature did not exceed 40°C and the maximum water temperature was 24°C, so boiling was absent.

Equation (2) was used to calculate the overall thermal resistance R at the wire surface. The fouling thermal resistance R_f, which is assumed to be the difference between the initial (clean) measured thermal resistance and the thermal resistance at any time, was plotted. This supposes that the convective thermal resistance is equal to the initial measured thermal resistance and does not change as corrosion proceeds. Since the convective thermal resistance on the fouled surface is likely to be substantially smaller than the same resistance on the clean surface, this assumption will result in an overestimation of the convective thermal resistance R_c and an underestimation of the fouling thermal resistance R_f.

Results

Results of the tests on six of the nine specimens used are summarized in Table 1. Graphs of the deposit thermal resistance R_f plotted against time are shown in Fig. 3. From a preliminary examination of these the following can be seen:

(*a*) As time proceeds, i.e., as the wire corrodes, the deposit thermal resistance R_f increases and then tends to approach a constant value.

(*b*) There is considerable variation in the measured values of R_f, both within a single specimen and between specimens (discussed below).

(*c*) Final values of R_f are comparable (see Table 2) to those

Table 1 Summary of experimental results

Test	Duration, hr	Final value* of R_f m^2 °C/W	Change in value of constant a in equation (3), μohms
4	242	4.88×10^{-4}	1260
5	261	5.01×10^{-4}	2340
6	214	2.32×10^{-4}	990
7	166	1.56×10^{-4}	520
8	246	1.90×10^{-4}	380
9	483	4.64×10^{-4}	600

*Multiply R_f values by 5.679 to convert to units of ft^2 °F hr/Btu.

Table 2 Observed thermal resistances

Reference	Material	Duration of test	R_f at conclusion* of test,† m^2 °C/W	Category of fouling	Type of test
McAllister et al. (1961)	90-10 Cu-Ni Aluminum-brass Admiralty brass 304 Stainless steel	2400 hr	6.0×10^{-3} 8.0×10^{-3} 8.0×10^{-3} 1.5×10^{-3}	*In situ* corrosion fouling	Field‡
Griess et al. (1964)	Aluminum alloys	300–500 hr	7.0×10^{-4} (average)	*In situ* corrosion fouling	Laboratory
Gutzeit (1965)	Admiralty brass Aluminum	960 hr	9.0×10^{-3}	*In situ* corrosion fouling	Field
Ritter and Suitor (1976)	Copper alloy 706	1000 hr	1.70×10^{-4} -5.7×10^{-4}	*In situ* corrosion fouling	Field‡
Characklis (1981)	Unknown	100 hr	1.8×10^{-4}	Microbial	Laboratory
Parry et al. (1981)	Admiralty brass	Unknown	2.5×10^{-4}	Precipitation	Field

*Multiply R_f values by 5.679 to convert to units of ft^2 °F hr/Btu.
†Assumed $R_f = R - R_{ci}$, where R_{ci} = convective heat transfer coefficient on clean surface.
‡Specimens exposed to seawater or river water, so other categories of fouling may be present.

observed with other categories of fouling and by other investigators for *in situ* corrosion fouling.

These three points will now be considered in greater detail.

The observed approach of the fouling thermal resistance to a constant value may be due to two causes:

(*a*) The corrosion process has ceased because the deposit of corrosion products is so heavy that oxygen dissolved in the water cannot diffuse through it to reach the underlying metal.

(*b*) A balance is eventually achieved between the rate of corrosion and the removal of the deposit by the flowing water.

In order to choose between these two hypotheses the variation of the constant a in the following relation between the wire electrical resistance R_f and the wire temperature T_s was examined

$$R_t = a + bT \tag{3}$$

This quantity was measured at frequent intervals throughout the duration of a test in order to determine the true temperature–electrical resistance characteristics of the wire, as described in Somerscales and Kassemi (1983a). Since any change in the constant is assumed to represent a change in the cross section of the specimen due to corrosion, then any variation during a given test should be a measure of the extent to which the wire has corroded. It was observed that for all the specimens da/dt was a constant. This can be expressed explicitly in terms of the rate of corrosion if for a wire of circular cross section this refers to the rate of decrease of the diameter of the wire. Then, since the constant a is inversely proportional to the square of the wire diameter, it can be shown that a constant rate of change in the constant a would correspond to a decreasing rate of change of wire diameter. This indicates that the rate of corrosion is decreasing as the test proceeds. However, visible deposits of red oxide formed at various

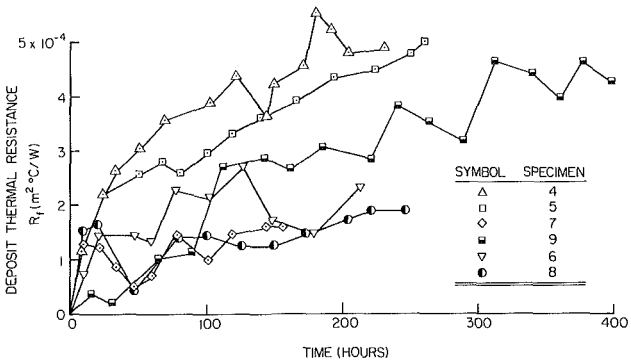

Fig. 3 Variation of corrosion fouling thermal resistance R_f with time on 1010 carbon steel exposed to distilled water (pH = 6.5 ± 0.4, T_∞ = 24°C) saturated with atmospheric oxygen

points in the flow loop, indicating that deposit removal processes were active. The weight of evidence would appear to favor the oxygen transport hypothesis, but the balance between the generation and the removal of the corrosion products may play some part in the observed behavior of the deposit thermal resistance. The choice of hypothesis to explain the observations is difficult to make with the experimental technique described here, and, in the circumstances, more detailed tests, using a different type of apparatus, are required to ascertain the processes involved.

The difference in the results between different specimens seen in Fig. 3 is probably a manifestation of the widely observed variability commonly noted in corrosion tests. The sources of this variability are not completely understood but could, among other things, be related to variations in the composition of different samples of 1010 carbon steel wire used in the tests. Variations in water purity between tests may also have caused the observed differences between the specimens.

However, care was taken to clean the loop between runs, so this does not appear to be a likely source of the variability. In spite of these differences the data are consistent, because the change Δa over the duration of the test in the value of the constant a was in agreement with the change of R_f in the same period. Thus, a plot of these two quantities indicated very strongly that they were correlated. In other words, the data show that large increases in the thermal resistance over the duration of the tests are associated with large amounts of corrosion.

The fluctuations in the measured values of R_f which some of the specimens (particularly 4, 6, 7, and 9) exhibit are real effects because their magnitude greatly exceeds the measurement uncertainty, which was estimated to be ± 6 percent (Somerscales and Kassemi, 1984). They are probably caused by the removal of corrosion products from the surface of the specimen, leading to a reduction in R_f, followed by an increased rate of growth of the deposit because the resistance to oxygen diffusion through the deposit has been reduced. Eventually, this increased rate of corrosion causes an increase in R_f. This appears to be a repetitive process as indicated by the fluctuating values of R_f in Fig. 3. Sites of pitting corrosion were also noted on the specimens and these may have caused the observed irregular increase in the fouling thermal resistance.

The average value (2.8×10^{-4} m^2 °C/W) of the "limiting" deposit thermal resistance found in these experiments is, considering the difference in the exposure times, comparable to values found (see Table 2) with other categories of fouling and in other investigations of corrosion fouling. For other categories of fouling, the mean of the thermal resistance given in Table 2 is 2.2×10^{-4} m^2 °C/W with a mean exposure time of 100 hr. For corrosion fouling the mean shown in Table 2 is 4.2×10^{-3} m^2 °C/W (which may include contributions from other categories of fouling) for an average exposure time of 600 hr.

In addition to the quantitative data discussed above, the appearance of the test specimen was observed, and noted, each time measurements of the fouling thermal resistance were made. At the conclusion of the test when the wire had been removed from the test chamber, it was subjected to closer examination. These observations showed:

(*a*) The fouling deposit (corrosion products) consisted of two layers. The outside layer was red oxide and the inner layer was a black oxide. In the corrosion literature the red deposit is usually described as ferric hydroxide $Fe(OH)_3$ and the black deposit is a mixture of ferrous hydroxide, $Fe(OH)_2$, and hydrated magnetite, $Fe_3O_4 \cdot nH_2O$.

(*b*) The outer red oxide layer was very rough with "carbuncular" regions. On removing the deposit, the latter appeared to be formed over pits in the wire surface. The red oxide was easily removed, suggesting that the action of the flowing water would remove it to a greater or lesser extent from the surface and deposit it elsewhere in the flow system, as indicated by the red oxide deposited at various points in the flow loop.

(*c*) The inner, black oxide layer consisted of a finely divided powder that was more adherent to the wire surface than the red oxide.

Aside from these observations, no detailed physical examination or chemical analysis of the deposit was attempted, because the observed red and black oxide layers have been reported many times in the corrosion literature. In addition, the objectives of the test, as described in the introduction, did not warrant the time and effort of a more detailed examination.

Conclusions

In conclusion it can be stated that the tests reported here have shown that *in situ* corrosion fouling can produce a thermal resistance that is comparable to that arising from other modes of fouling. As pointed out in the Introduction, this is contrary to widely held beliefs among research workers and engineers interested in fouling. This result indicates that the effect of corrosion fouling should be given consideration in the design of heat transfer equipment using "clean" fluids, that is, in situations where other categories of fouling are likely to be absent. In addition, for those situations involving the exposure of heat transfer surfaces to natural waters, the role of corrosion fouling should be taken into account in adding, possibly significantly, to the effect of other types of fouling.

The quantitative data given in the paper should not be used as a basis for design. In particular, the flow conditions corresponded to a very low Reynolds number (estimated to be equivalent to a Reynolds number of 75 in a duct of circular cross section) so that the processes governing the rates of growth of corrosion product deposits and their rates of removal will differ from those occurring with higher Reynolds numbers encountered in items of industrial heat transfer equipment.

Although it is difficult to make inferences from the measurements, the weight of evidence appears to suggest that fouling by corrosion products formed on a 1010 carbon steel heat transfer surface depends on the transport of dissolved oxygen to the corrosion site. As the thickness of the deposit increases then the corrosion rate will decrease. The corrosion rate will increase when some part of the fouling deposit is removed. The elucidation of the process is worthy of further investigation, but the apparatus described here is not considered satisfactory for the purpose.

Acknowledgments

The work described here was supported by the National Science Foundation under Grant No. MEA 81-06429 and by the Rensselaer Polytechnic Institute. The authors would like to acknowledge the important contributions of Edward P. Childs, Jr. and Jesus Chacin. Also N. Fidel, A. Hinge, T. B. Bennett, and W. George assisted with various aspects of the investigation.

References

Unterweiser, P. M., and Penzenik, M., eds., 1979, *Worldwide Guide to Equivalent Irons and Steels*, American Society of Metals, Metals Park, OH.

Characklis, W. G., 1981, "Microbial Fouling: A Process Analysis," *Fouling of Heat Transfer Equipment*, E. F. C. Somerscales and J. G. Knudsen, eds., Hemisphere Publishing Corp., Washington, D.C., pp. 251–291.

Griess, J. G., Savage, H. C., and English, J. L., 1964, "Effect of Heat Flux on the Corrosion of Aluminum by Water. Part IV. Test Relative to the Advanced Test Reactor," AEC Report ORNL 3541.

Gutzeit, J., 1965, "Corrosion and Fouling of Admiralty, Aluminum and Steel Tubes in Open Recirculating Cooling Water Systems," *Materials Protection*, Vol. 4, July, pp. 28–34.

Mahato, B. K., Cha, C. Y., and Shemilt, L. W., 1968a, "Steel Pipe Corrosion Under Flow Conditions – I," *Corrosion Science*, Vol. 8, pp. 173–193.

Mahato, B. K., Steward, F. R., and Shemilt, L. W., 1968b, "Steel Pipe Corrosion Under Flow Conditions – II," *Corrosion Science*, Vol. 8, pp. 737–749.

Mahato, B. K., Cha, C. Y., and Shemilt, L. W., 1980, "Unsteady Mass Transfer Coefficients Controlling Steel Pipe Corrosion Under Isothermal Flow Conditions," *Corrosion Science*, Vol. 20, pp. 421–441.

McAllister, R. A., Eastham, D. H., Dougherty, N. A., and Hollier, M., 1961, "A Study of Scaling and Corrosion in Condenser Tubes Exposed to River Water," *Corrosion*, Vol. 17, pp. 579t–588t.

Parry, D. J., Hawthorn, D., and Rantell, A., 1981, "Fouling of Power Station Condensers Within the Midlands Region of C.E.G.B.," in: *Fouling of Heat Transfer Equipment*, E. F. C. Somerscales and J. G. Knudsen, eds., Hemisphere Publishing Corp., Washington, D.C., pp. 569–586.

Ritter, R. B., and Suitor, J. W., 1976, "Fouling Research on Copper and Its Alloys – Seawater Studies," Progress Report INCRA Project 214A (Jan. 1974–Feb. 1976), Heat Transfer Research Inc., Alhambra, CA.

Shemilt, L. W., Cha, C. Y., Fiadzigbe, E., and Ponter, A. B., 1980, "Steel Pipe Corrosion Under Flow Conditions – III," *Corrosion Science*, Vol. 20, pp. 443–455.

Somerscales, E. F. C., 1981, "Corrosion Fouling," in: *Fouling in Heat Ex-*

change Equipment, J. M. Chenoweth and M. Impagliazzo, eds., ASME, New York, pp. 17-27.

Somerscales, E. F. C., and Kassemi, M., 1983a, "Measurement of the Thermal Resistance of Corrosion Products," *Fouling of Heat Exchanger Surfaces*, Proceedings of the Engineering Foundation Conference, Hershey Pocono Resort, White Haven, PA, Oct. 31-Nov. 5, 1982, R. W. Bryers and S. S. Cole, eds., Engineering Foundation, New York, pp. 105-125.

Somerscales, E. F. C., 1983b, "Fundamental Ideas in Corrosion Testing in the Presence of Heat Transfer," in: *Corrosion in Heat Transfer Conditions*, A.D. Mercer, ed., Society of Chemical Industry, London, pp. 1-36.

Somerscales, E. F. C., and Kassemi, M., 1984, "Fouling Due to In-Situ Corrosion Products," in: *Fouling in Heat Exchange Equipment*, J. W. Suitor and A. M. Pritchard, eds., ASME, New York, pp. 1-9.

Uhlig, H. H., 1963, *Corrosion and Corrosion Control*, Wiley, New York, p. 105.

Determining Noncondensible Gas Fractions at Elevated Temperatures and Pressures Using Wet and Dry Bulb Temperature Measurements

J. Bowman[1] and P. Griffith[2]

Nomenclature

A_c = convection area
A_d = diffusion area
$C_{v,fs}$ = concentration of vapor in the free stream
$C_{v,wb}$ = concentration of vapor at the wet bulb
D = diffusion coefficient
h_c = convective heat transfer coefficient
h_d = mass transfer coefficient
h_r = radiant heat transfer coefficient
i_{fg} = latent heat of vaporization
k = thermal conductivity
Pr = Prandtl number $= cu/k$
Sc = Schmidt number $= \mu/\rho D$
T_{db} = dry-bulb temperature
T_{wb} = wet-bulb temperature

Introduction

The work reported in this note was undertaken to provide a method of determining the noncondensible gas fractions in a steam-gas mixture such as might be found in a large reactor safety experiment like LOFT. In essence, the method used involves measuring the wet and dry bulb temperatures and using an algorithm, in place of the psychometric chart, to determine the partial pressure of the noncondensible gas in the mixture. In accomplishing this, we did the following:

1 Extended the use of wet and dry-bulb temperature readings to determine mixture composition up to a temperature of 589 K and a pressure of 4.13×10^6 Pa.
2 Developed an algorithm to reduce the data.
3 Found which materials would survive those temperatures.

[1]Bowman Engineering and Development Corporation.
[2]Professor of Mechanical Engineering, MIT, Cambridge, MA 02139; Fellow ASME.

Contributed by the Heat Transfer Division for publication in the JOURNAL OF HEAT TRANSFER. Manuscript received by the Heat Transfer Division March 12, 1985.

Experiments

The work described here was completely reported in [1, 2]. This note presents the major results and sketches the analytical methods described in [1, 2].

The experiments had several goals. The first was to see how well the composition of the mixture could be predicted from a knowledge of the pressure, the wet and dry-bulb temperatures, and the noncondensible gas composition (but not the velocity, as that, in general, is unknown). The second was to see how the natural convection occurred, that is, whether the plume went up or down and whether its direction could be predicted. Finally, we wished to construct and prove out a prototype wet and dry-bulb thermometer design that could be used in the large system experiments of interest to the sponsor. In this note, only the final design will be described.

Figure 1 is a general view of the apparatus used in the forced-convection experiments. The whole tank was about 1.67 m (67 in.) in height and 04.3 m (17 in.) in diameter. The water for the wet-bulb thermometer was provided by the condenser which dripped into a recepticle at the left of the wick (see Fig. 2). Gas was circulated by the fan mounted at the top of the apparatus. The fraction of noncondensible gas was determined experimentally by withdrawing a sample into the cylinder shown at the right. By looking at the shape of the pressure temperature curve when cooling the sample, a distinct change in slope was evident when the mixture reached its dew point.

Essentially the same apparatus was used for the natural convection experiments except that the fan and duct were removed. The direction of the plume for the natural convection experiment was determined using an array of thermocouples mounted around the wick as illustrated in Fig. 2.

Analysis

Only the highlights of the analytical procedure used to determine the composition of the steam-noncondensible mixture will be presented here.

As the velocity in the vicinity of both the wet-bulb and dry-bulb thermometers is unknown, it is essential that the measured temperatures be independent of the velocity. This turned out to be the case. A single expression relating the heat and mass transfer coefficients could then be selected. That of Gebhart and Peca [3] was used. It is

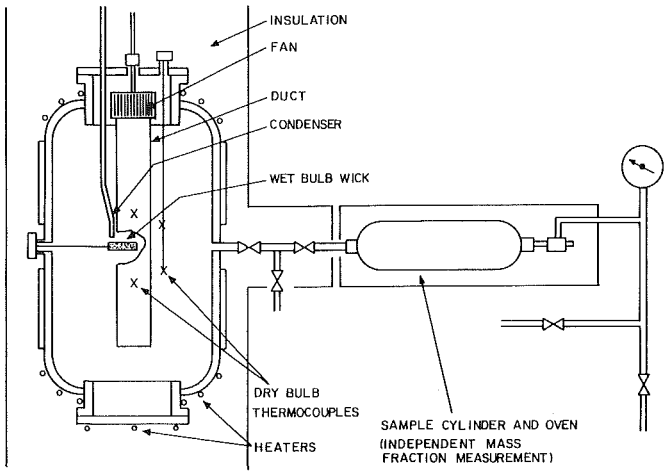

Fig. 1 Schematic of the forced convection test apparatus; for natural convection tests the fan and duct were removed

change Equipment, J. M. Chenoweth and M. Impagliazzo, eds., ASME, New York, pp. 17-27.

Somerscales, E. F. C., and Kassemi, M., 1983a, "Measurement of the Thermal Resistance of Corrosion Products," *Fouling of Heat Exchanger Surfaces*, Proceedings of the Engineering Foundation Conference, Hershey Pocono Resort, White Haven, PA, Oct. 31-Nov. 5, 1982, R. W. Bryers and S. S. Cole, eds., Engineering Foundation, New York, pp. 105-125.

Somerscales, E. F. C., 1983b, "Fundamental Ideas in Corrosion Testing in the Presence of Heat Transfer," in: *Corrosion in Heat Transfer Conditions*, A.D. Mercer, ed., Society of Chemical Industry, London, pp. 1-36.

Somerscales, E. F. C., and Kassemi, M., 1984, "Fouling Due to In-Situ Corrosion Products," in: *Fouling in Heat Exchange Equipment*, J. W. Suitor and A. M. Pritchard, eds., ASME, New York, pp. 1-9.

Uhlig, H. H., 1963, *Corrosion and Corrosion Control*, Wiley, New York, p. 105.

Determining Noncondensible Gas Fractions at Elevated Temperatures and Pressures Using Wet and Dry Bulb Temperature Measurements

J. Bowman[1] and P. Griffith[2]

Nomenclature

A_c = convection area
A_d = diffusion area
$C_{v,fs}$ = concentration of vapor in the free stream
$C_{v,wb}$ = concentration of vapor at the wet bulb
D = diffusion coefficient
h_c = convective heat transfer coefficient
h_d = mass transfer coefficient
h_r = radiant heat transfer coefficient
i_{fg} = latent heat of vaporization
k = thermal conductivity
Pr = Prandtl number $= cu/k$
Sc = Schmidt number $= \mu/\rho D$
T_{db} = dry-bulb temperature
T_{wb} = wet-bulb temperature

Introduction

The work reported in this note was undertaken to provide a method of determining the noncondensible gas fractions in a steam-gas mixture such as might be found in a large reactor safety experiment like LOFT. In essence, the method used involves measuring the wet and dry bulb temperatures and using an algorithm, in place of the psychometric chart, to determine the partial pressure of the noncondensible gas in the mixture. In accomplishing this, we did the following:

1 Extended the use of wet and dry-bulb temperature readings to determine mixture composition up to a temperature of 589 K and a pressure of 4.13×10^6 Pa.
2 Developed an algorithm to reduce the data.
3 Found which materials would survive those temperatures.

[1]Bowman Engineering and Development Corporation.
[2]Professor of Mechanical Engineering, MIT, Cambridge, MA 02139; Fellow ASME.

Contributed by the Heat Transfer Division for publication in the JOURNAL OF HEAT TRANSFER. Manuscript received by the Heat Transfer Division March 12, 1985.

Experiments

The work described here was completely reported in [1, 2]. This note presents the major results and sketches the analytical methods described in [1, 2].

The experiments had several goals. The first was to see how well the composition of the mixture could be predicted from a knowledge of the pressure, the wet and dry-bulb temperatures, and the noncondensible gas composition (but not the velocity, as that, in general, is unknown). The second was to see how the natural convection occurred, that is, whether the plume went up or down and whether its direction could be predicted. Finally, we wished to construct and prove out a prototype wet and dry-bulb thermometer design that could be used in the large system experiments of interest to the sponsor. In this note, only the final design will be described.

Figure 1 is a general view of the apparatus used in the forced-convection experiments. The whole tank was about 1.67 m (67 in.) in height and 04.3 m (17 in.) in diameter. The water for the wet-bulb thermometer was provided by the condenser which dripped into a recepticle at the left of the wick (see Fig. 2). Gas was circulated by the fan mounted at the top of the apparatus. The fraction of noncondensible gas was determined experimentally by withdrawing a sample into the cylinder shown at the right. By looking at the shape of the pressure temperature curve when cooling the sample, a distinct change in slope was evident when the mixture reached its dew point.

Essentially the same apparatus was used for the natural convection experiments except that the fan and duct were removed. The direction of the plume for the natural convection experiment was determined using an array of thermocouples mounted around the wick as illustrated in Fig. 2.

Analysis

Only the highlights of the analytical procedure used to determine the composition of the steam-noncondensible mixture will be presented here.

As the velocity in the vicinity of both the wet-bulb and dry-bulb thermometers is unknown, it is essential that the measured temperatures be independent of the velocity. This turned out to be the case. A single expression relating the heat and mass transfer coefficients could then be selected. That of Gebhart and Peca [3] was used. It is

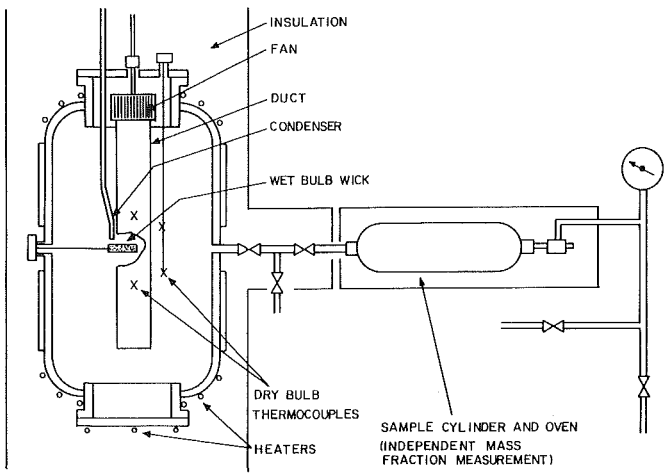

Fig. 1 Schematic of the forced convection test apparatus; for natural convection tests the fan and duct were removed

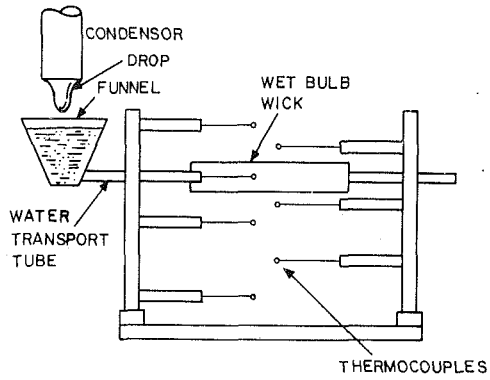

Fig. 2 Schematic of the thermocouple array and condenser and wick arrangement

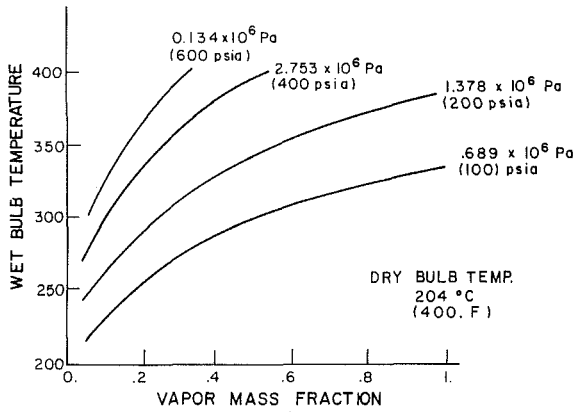

Fig. 3 Sample of calculated relation between wet-bulb temperature and vapor mass fraction for a dry-bulb temperature of 204°C

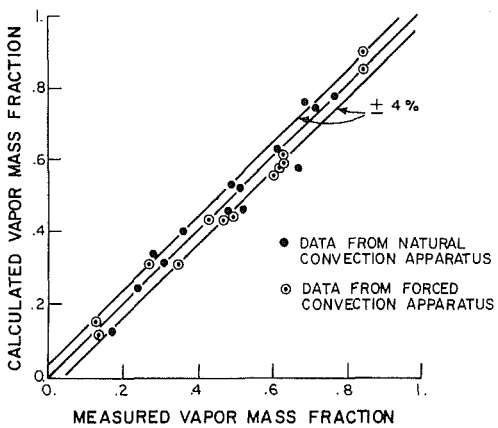

Fig. 4 Comparison of theory and experiment for all the data taken

$$\frac{h_c}{h_d} = \frac{k}{D}\left(\frac{\mathrm{Pr}}{\mathrm{Sc}}\right)^{1/2} \tag{1}$$

This expression was derived for laminar natural convection but was used for laminar and turbulent flow in forced and natural convection. It worked because the only term affected by the kind of convection is the power on the ratio of the Prandtl to the Schmidt number. However, both the Prandtl and Schmidt numbers are close to unity so that the power to which they are raised does not matter. The choice of the laminar, natural convection formula was quite arbitrary.

This ratio plus the energy equation applied to the wet-bulb thermometer are the heart of the algorithm. The energy equation is

$$C_{v,fs} = C_{v,wb} - \frac{A_c}{A_d}\left(\frac{h_c + h_r}{h_c}\right)\left(\frac{h_c}{h_d}\right)\frac{1}{i_{fg}}(T_{db} - T_{wb}) \tag{2}$$

At the higher temperatures at which this device is expected to work, radiation is not necessarily negligible and a linearized radiation heat transfer correction, such as defined in [4], is needed. The ratio (A_c/A_d) is the heat transfer area divided by the mass transfer area. One would normally expect this to be one but for the fritted glass used for the wick in these experiments this ratio was 2. Apparently the water was confined to the spaces between the fritted glass beads which make up the wick.

To complete the calculation, it is necessary to have relations as functions of temperature, for the various properties that appear in equations (1) and (2). Well-established equations were used for these and will not be repeated here.

In order to calculate the concentration of vapor in the free stream, it is necessary to guess what the vapor concentration is. The necessary properties are then computed and substituted into the right-hand side of equation (2). When the correct concentration is chosen, equation (2) is satisfied.

When the above procedure is followed, the prediction of the vapor mass fraction as a function of wet- and dry-bulb temperature is as shown (for 204°C) on Fig. 3. The comparison of this method with the data is shown on Fig. 4.

Discussion

One of the questions we had at the beginning of this program was whether the natural convection plume always went in the same direction. For N_2, for instance, which has a molecular weight greater than that of water vapor, the density increase due to the low temperature at the wet-bulb thermometer might overwhelm the density decrease due to the greater concentration of H_2O near the wick, and the plume might rise. The thermocouples mounted in the vicinity of the wick showed this was never the case and suggestion that the plume might rise, which was made in reference [5], was not born out.

Conclusions

1 An algorithm suitable for determining local noncondensible gas fractions using wet and dry-bulb temperature readings, system pressure, and a knowledge of the noncondensible gas composition has been developed.

2 For non-condensible gas molecular weights less than that of nitrogen, the natural convection plume always goes down, and the ambiguous circulation patterns around the wet-bulb thermometer, which one might expect to occur, actually do not. The algorithm developed should always work for these gases.

3 Because of the analogy between heat and mass transfer and the fact that the Schmidt and Prandtl numbers are very close to unity, the velocity direction or magnitude in the vicinity of the wet-bulb thermometer have no effect on the reading.

References

1 Bowman, J., "Non-condensible Gas Fraction Predictions Using Wet and Dry Bulb Temperature Measurements," Ph.D. Thesis, Dept. of Mechanical Engineering, MIT, June 1982.

2 Bowman, J., and Griffith, P., "Non-condensible Gas Fraction Predictions Using Wet and Dry Bulb Temperature Measurements," NUREG/CR-2853, Mar. 1983.

3 Gebhart, B., and Pera, L., "The Nature of Vertical Natural Convection Flows Resulting From the Combined Buoyancy Effects of Thermal and Mass Diffusion," *Int. J. of Heat and Mass Transfer*, Vol. 10, 1971, pp. 2025-2050.

4 Rohsenow, W. M., and Choi, H. W., *Heat, Mass and Momentum Transfer*, Prentice Hall, Englewood Cliffs, NJ, 1961.

5 Adams, J. A., and McFadden, P. W., "Simultaneous Heat and Mass Transfer on Free Convection With Opposing Body Forces," *AIChE J.*, Vol. 12, 1966, pp. 642-647.